an Open Access Journal Published by MDPI

Impact Factor 1.3
CiteScore 2.3

International Journal of Turbomachinery, Propulsion and Power

mdpi.com/journal/ijtpp

EUROTURBO
european turbomachinery society

Message from the Editor-in-Chief

The *International Journal of Turbomachinery, Propulsion and Power* (*IJTPP*, ISSN 2504-186X) is owned by Euroturbo (www.euroturbo.eu), a not-for-profit international scientific organization legally established in February 2012. Euroturbo was founded by a group of committed scientists and engineers who have actively contributed to the success of several scientific events in the field of turbomachinery over the past twenty-five years. The Journal was conceived as an interdisciplinary dissemination tool and, although the core of the Journal focusses on the design, the Journal also engages the analysis, the modeling and testing of turbomachinery and turbomachinery-based propulsion and energy conversion systems. Technological innovation at system and component level, the development and application of new flow concepts, and advanced experimental and numerical techniques all fit naturally within the scope. The Journal welcomes manuscripts of high scientific quality addressing fundamental and applied issues of turbomachinery flows.

Editor-in-Chief
Prof. Marcello Manna

Associate Editors
Prof. Dr. Tony Arts
Prof. Dr. Gerard Bois
Prof. Dr. Cengiz Camci
Dr. Ruud Eggels
Prof. Dr. Peter Ireland
Prof. Dr. Reinhard Niehuis
Prof. Dr. Kenichiro Takeishi

Aims

International Journal of Turbomachinery, Propulsion and Power focuses on the current and future science and technology development of turbomachinery in the related fields of turbomachinery-based propulsion and power systems. Of primary interest are the thermodynamics, the fluid mechanics, the heat transfer and the applied combustion of aerospace, marine and industrial energy devices and systems, both from a component and system perspective. Likewise, fundamental and applied studies of energy conversion systems based on single or multi-phase fluid flows, single or multi-species, involving one or more turbomachines are solicited. The *IJTPP* is intended to offer a high quality research and development dissemination tool to colleagues with a primary interest in turbomachinery from academia, research institutes and industry.

Scope

- Turbomachinery
- Aerospace propulsion
- Marine propulsion
- Turbochargers
- Power generation
- Thermodynamics
- Fluid mechanics
- Heat Transfer
- Vibrations
- Aero-acoustics
- Applied combustion (aeronautic, aerospace, stationary power systems)
- Wind energy
- Marine energy

Author Benefits

Open Access

Unlimited and free access for readers

No Copyright Constraints

Retain copyright of your work and free use of your article

Thorough Peer-Review

Discounts on Article Processing Charges (APC)

If you belong to an institute that participates with the MDPI Institutional Open Access Program

No Space Constraints, No Extra Space or Color Charges

No restriction on the maximum length of the papers, number of figures or colors

Rapid Publication

A first decision is provided to authors approximately 63.9 days after submission; acceptance to publication is undertaken in 27.6 days (median values for papers published in this journal in the first half of 2024)

MDPI is a member of

Partner Society:
European Turbomachinery Society (Euroturbo)

Editorial Office
ijtpp@mdpi.com

MDPI
Grosspeteranlage 5
4052 Basel, Switzerland
Tel: +41 61 683 77 34
mdpi.com

July 2024

International Journal of
Turbomachinery
Propulsion and Power

MDPI

Article

Topology Rule-Based Methodology for Flow Separation Analysis in Turbomachinery

Pierre Duquesne [1,*,†], Joffrey Chanéac [1,†], Gabriel Mondin [1,†] and Jérôme Dombard [2,†]

[1] Univ Lyon, Ecole Centrale de Lyon, CNRS, Univ Claude Bernard Lyon 1, INSA Lyon, LMFA, UMR5509, 69130 Ecully, France; joffrey.chaneac@ec-lyon.fr (J.C.); gabriel.mondin@ec-lyon.fr (G.M.)
[2] CERFACS, 31100 Toulouse, France; dombard@cerfacs.fr
* Correspondence: pierre.duquesne@ec-lyon.fr
† These authors contributed equally to this work.

Abstract: Boundary-layer flow separation is a common flow feature in many engineering applications. The consequences of flow separation in turbomachinery can be disastrous in terms of performance, stability and noise. In this context, flow separation is particularly difficult to understand because of its three-dimensional and confined aspects. Analyzing the skin friction lines is one key point to understanding and controlling this phenomenon. In the case of separation, the flow at the wall agglutinates around a manifold while the fluid from the boundary layer is ejected toward the flow away from the wall. The analysis of a three-dimensional separation zone based on topology is well addressed for a simple geometry. This paper aims at providing simple rules and methods, with a clear vocabulary based on mathematical background, to conduct a similar analysis with complex turbomachinery geometry (to understand a surface with a high genus). Such an analysis relies on physical principles that help in understanding the mechanisms of flow separation on complex geometries. This paper includes numerous typical turbomachinery surfaces: the stator row, vaneless diffuser, vaned diffuser, axial rotor and shrouded and unshrouded centrifugal impeller. Thanks to surface homeomorphisms, the generic examples presented can easily be converted into realistic shapes. Furthermore, classical turbomachinery problems are also addressed, such as periodicity or rotor clearance. In the last section, the proposed methodology is conducted on a radial diffuser of an industrial compressor. The flow at the wall is extracted from LES computations. This study presents the different closed separation zones in a high-efficiency operating condition.

Keywords: flow separation; topology rule; critical point; turbomachinery

check for updates

Citation: Duquesne, P.; Chanéac, J.; Mondin, G.; Dombard, J. Topology Rule-Based Methodology for Flow Separation Analysis in Turbomachinery. *Int. J. Turbomach. Propuls. Power* **2022**, *7*, 21. https://doi.org/10.3390/ijtpp7030021

Received: 7 January 2022
Accepted: 27 June 2022
Published: 30 June 2022

Publisher's Note: MDPI stays neutral with regard to jurisdictional claims in published maps and institutional affiliations.

Copyright: © 2022 by the authors. Licensee MDPI, Basel, Switzerland. This article is an open access article distributed under the terms and conditions of the Creative Commons Attribution (CC BY-NC-ND) license (https://creativecommons.org/licenses/by-nc-nd/4.0/).

1. Introduction

Boundary-layer flow separation is a generic problem in turbomachinery. Flow separation can be described as the ejection of fluid from the boundary layer toward the flow away from the wall [1]. A back-flow zone in the flow is associated with this fluid ejection. The origin of the flow separation can be divided into two families, a strong adverse pressure gradient or an important curvature of the wall geometry.

The effects of flow separation are generally undesirable and can be detrimental in turbomachinery. From an energetic point of view, the flow separation induces supplementary losses. The energy used in flow separation is not available for the work exchange. The blades of the rotor can suffer from flow separation: the flow does not follow the aerodynamic airfoil; therefore, the work exchange between the rotor and the fluid is less performant. On some occasions, the separation can rotate with a rotation speed different from the rotor speed around the circumference of the compressor. This rotating stall induces periodic fluctuations and is a classical precursor to the compressor surge [2]. This phenomenon also affects centrifugal pumps. For diffusers, flow separation can induce blockage zones that decrease the pressure recuperation. For example, flow separation in hydraulics

bulb turbines is suspected to induce an important and sudden drop-off of the efficiency curves with operating fluctuations near the best efficient point [3]. In other cases, the flow separation is not periodic in the diffuser and induces a non-periodic flow, as observed in a hydraulic turbine by [4] and in a centrifugal compressor by [5]. Another effect of separation is to increase the width of the blade wakes, which, in multistage configurations, can induce complex rotor–stator interactions all along the machine [6]. Finally, flow separation might also generate undesirable low-frequency noise. This is the case in wind turbines operating at high loading conditions [7].

In turbomachinery, the two main objectives are often to increase the performance and the operability of the machine, which are both limited by flow separation. In such configurations, the flow exhibits complex patterns as it is generally three-dimensional, confined, highly unsteady and might be highly turbulent. A frequent misleading practice to analyze a three-dimensional separation in engineering applications is to track back-flow velocity vectors in the 3D field to look for the flow separation. This method is doomed to fail in several situations, notably because a velocity vector in the 3D field can be in back flow without any flow ejection from the boundary layer. Indeed, the swirling flow within a conical duct induces a re-circulation zone without boundary-layer flow separation [8]. Secondly, a fluid ejection from the wall can occur even if there is no back flow. In addition, the flow direction can be hard to define in complex geometry cases. Another, or complementary, misleading practice is to track points on the surface where skin friction is null. In three-dimensional cases, flow ejection from the boundary layer can happen all along the separation line where the skin friction is not necessarily null. Pragmatically, a local indicator of the separation occurrence at a flow-specific location does not exist. Hence, the analysis can not only be focused on each point individually but has to be performed with regard to the neighborhood and has to take into account the connection to the wall. Without any preliminary survey, to lead such an analysis in the 3D field directly is a nearly impossible task to fill. In external aerodynamics, a study of friction-line patterns on wall surfaces is commonly run first [9]. Such an analysis requires an accurate determination of the critical points distribution, which is overseen by a topological rule-based approach. To respect the topology rule ensures to develop a scenario that fits physical principles. All in all, the skin-friction-lines analysis helps to pinpoint the origin of the flow separation at the wall to then ease the global 3D field examination. This technique is used in turbomachinery as well (for example, [3,4,10]), but according to the authors' knowledge, its adaptation for internal flow has not been clearly exposed yet. However, it is not straightforward. In comparison with the classical methodology on a flat plane, the following particularities of the turbomachinery context must be treated carefully:

- The surfaces considered are more complex (characterized by the surface genus) than a simple flat plane.
- Only a part of the system is represented, so the skin friction lines can be generated (source) and destroyed (sink) out of the analysis domain. Nevertheless, the skin friction source-and-sink representation is mandatory and has to be fictitiously re-located into the computational domain (see Section 3.2).
- For the real-world surfaces here studied, critical points can indeed be representative of a boundary flow separation but also indicative of a flow bypassing. Hence, they are no use for the analysis to be performed.
- The partial representation of a component is mainly motivated by minimizing the CPU time. For instance, the periodicity assumption is commonly used to that end in turbomachinery. However, its use can be conflicting with the topological rule-based approach.

According to the needs previously exposed, to develop guidelines to better understand flow separations in turbomachinery appears to be necessary. A topology rule-based methodology is here proposed that ensures to find an admissible counting of critical points and that helps to distinguish the critical points that are connected to the flow separation

zone in the turbomachinery context. This preliminary study aims at piloting the 3D analysis of the flow separation zone.

In the first part, the dedicated vocabulary and the concept of critical point analysis in general fluid mechanics are presented. The particularities of the analysis in turbomachinery are then discussed. The following part is organized in the recommended chronology to conduct the analysis: (1) determine the genus of the surface of interest, (2) determine the splitting critical points induced by the surface division, (3) determine the stagnation and exit nodes, (4) apply a periodicity and (5) check the topology rule. Finally, the last section illustrates the whole methodology with an application on the radial diffuser of an industrial radial compressor.

2. Theoretical Background

In this part, the authors try to clearly present the useful vocabulary and mathematical rules for an engineering approach.

To determine the correct topology rules to apply, the solid turbomachinery geometry (3D) needs to be simplified into a global one-piece surface (2D). In other words, only the "skin" of the solid is considered for studying topology. For instance, a solid ball (3D) is then turned into a sphere (2D). A one-piece surface is said to be connected. The complexity of a connected surface can be characterized by an integer called the genus, denoted as g. The most general definition of the genus corresponds to the maximum number of cuttings along the surface without disconnecting it [11]. As classical examples [12,13], a sphere has genus 0; a torus has genus 1; and a two-torus (two tori connected like an infinity symbol) has genus 2.

To avoid unnecessary alternative definitions, let us consider connected orientable closed surfaces. The definition of an orientable closed surface is given in Appendix A. In practical cases, the classical real-world surfaces encounter these properties. For a surface as previously defined, the genus is related to the Euler characteristic χ as follows:

$$\chi = 2 - 2g. \tag{1}$$

By definition, two spaces are homeomorphic if a set of continuous stretching and bending that transforms one of the two surfaces into the other exists. For instance, a well-known surface homeomorphism links the coffee mug to the torus. These spaces are the same from a topological viewpoint. They have the same topological properties, notably the Euler characteristic. According to Equation (1), two homeomorphic classical real-world surfaces also have the same genus. In this case, Equation (1) is the easiest relation to determine the Euler characteristic.

These considerations on surfaces are useful for flow separation analysis because the Euler characteristic is linked to the number and the type of critical points. A critical point $P_0(x, z)$ is defined as a point on the wall where the skin friction $\tau = (\tau_x, \tau_z)^\top$ vanishes, i.e., $\tau_x(P_0) = \tau_z(P_0) = 0$. This relation results from Poincaré's research [14] on differential equations and the application of this work to fluid mechanics by Legendre [9] and Hunt [15]. An analysis of the skin friction Jacobian matrix $\mathcal{J}_\tau$ (given in Equation (2)) reveals that critical points can be related to only three types of skin friction patterns. They are then called the node, focus and saddle point. Node and focus can be either attracting if skin friction lines converge or repelling otherwise. Figure 1 presents the corresponding skin friction patterns.

$$\mathcal{J}_\tau = \begin{bmatrix} \dfrac{\partial \tau_x}{\partial x} & \dfrac{\partial \tau_x}{\partial z} \\ \dfrac{\partial \tau_z}{\partial x} & \dfrac{\partial \tau_z}{\partial z} \end{bmatrix}. \tag{2}$$

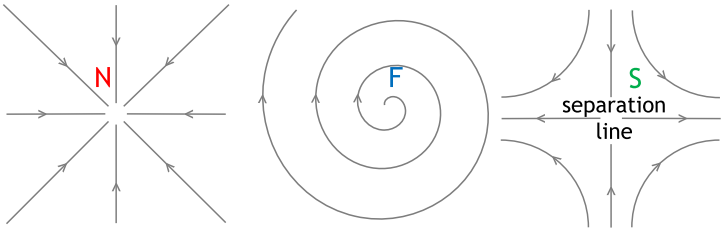

Figure 1. Types of skin friction pattern around a critical point: node (N), for example, here attracting; focus (F), for example, here repelling; and saddle point (S) with the separation line.

The link between the Euler characteristic and the critical points is expressed by the topology rule:

$$\Sigma N - \Sigma S = \chi, \tag{3}$$

with ΣN the number of nodes and foci, and ΣS the number of saddle points.

A necessary condition for the three-dimensional separation occurrence is the convergence of the skin friction lines [16]. Streamwise convergence of skin friction lines and near-wall streamlines induces a rapid lift of the near-wall streamlines away from the wall to conserve the mass flux through the stream tube [17]. The convergence of friction lines is observed along one particular skin friction line, called the separation line, generally originating from a saddle point. The flow accumulated along the separation line is ejected from the wall to the flow field and is then accumulated along a three-dimensional surface called the manifold [18].

As previously mentioned, real-world surfaces encountered are orientable closed surfaces. However, two common practices get out of the previous framework. The infinitely thin plane approximation of a real 3D geometry leads to either a non-orientable or a non-closed surface. The approximation of neglecting a small gap between two solid parts can alter the genus and then it yields to fallacious conclusions in the scope of a topological analysis.

In some exceptional cases, the skin friction pattern of a focus exhibits a closed path around a critical point. In this case, it is called a center or a limit cycle (skin friction lines form concentric circles around the critical point). Such cases have been determined by a theoretical approach by [18]. On a limit cycle, the friction line can converge without a saddle point. This type of separation is called "open" flow separation, in opposition to "closed" flow separation that features a separation line bounded by two critical points.

3. Methodology

3.1. Surface Genus Determination

The first step is to determine the correct genus for the whole surface of interest, without any assumption of periodicity. The surfaces selected in this paper are particularly interesting for turbomachinery engineers. For these surfaces, the genus exists and is related to the Euler characteristic by Equation (1) and allows to determine the topology rule Equation (3). The topology rule ensures to respect a physical equilibrium between the different critical points types. They can have a genus of 0, 1 or related to the number of blades (b). Table 1 gives the genus for most common surfaces in turbomachinery. The last column of Table 1 presents a simple example for each geometry as well as their genus determination. The maximum number of cutting planes before obtaining two parts for each surface family is illustrated with a plane distribution, in red. Of course, other cutting plane distributions can be found, but authors do not find any involving more cutting planes. In this article, only a blade without hole is presented. For example, turbine blades with external cooling holes are not included. A hole in a blade modifies the genus and requires a case-by-case study.

Table 1. Genus of some classical surfaces in turbomachinery.

Turbomachinery Part	g	Related Simplified Representation
Casing, pipe and vaneless diffuser	1	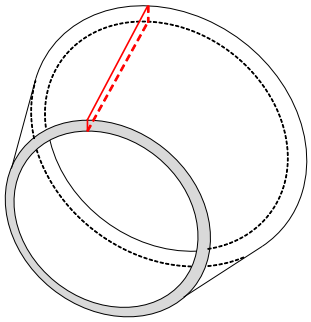
Axial rotor	0	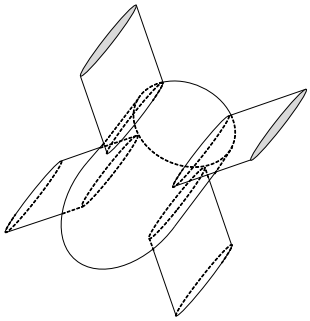
Unshrouded centrifugal impeller	0	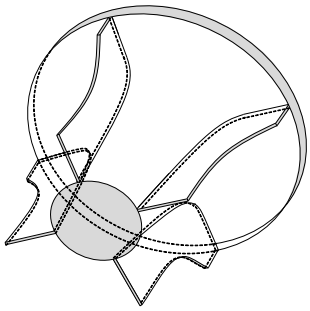
Shrouded centrifugal impeller	b	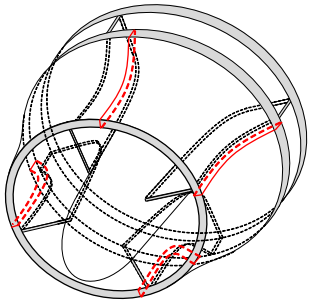
Axial stator	b	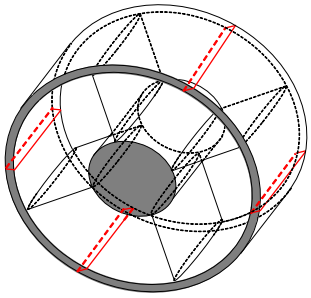

Table 1. *Cont.*

Turbomachinery Part	g	Related Simplified Representation
Radial vaned diffuser	b	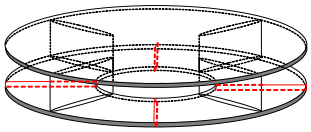
Diffuser with parallel piers	$b+1$	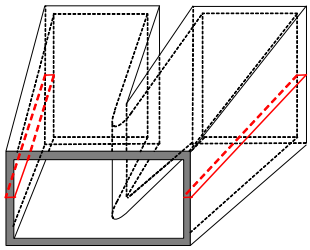

The "casing, pipe and vaneless diffuser" surface family corresponds to the numerous parts fully filled by the working fluid which conduct the flow without blades. Their genus is equal to 1 because all these surfaces are easy to obtain by continuous deformations of a torus. This one is independent of the longitudinal shape (diverging, converging, straight or not) and is also independent of the cross-section shape (circular, rectangular, etc). In the case of a part that is partially filled, e.g., a pipe that is not fully filled with water, the cross section of interest corresponds to the wetted cross section and is homeomorphic to a sphere (i.e., has genus 0). "Axial rotor" and "unshrouded centrifugal impeller" surfaces have genus 0. Any cutting plane divides the surface in two parts. These families include the large majority of rotating parts: fans, propellers, wind turbine rotors, jet engine compressors and turbines. The "shrouded centrifugal impeller" family is the only one known by the authors with a rotating part and a genus different from 0. This family corresponds to the case where the rotating part is composed of the blades, the hub and shroud. It includes some centrifugal compressors, centrifugal pumps and Francis turbines. For these shrouded rotors, the genus is equal to the number of blades. In this type of rotor, the number of splitter blades must be added if they are connected to both the hub and the shroud, and must not otherwise. The axial position of the leading edge or trailing edge has no effect on the genus. The "axial stator" and "radial vaned diffuser" are representative of classical stators of compressors. Their genus is also equal to the number of blades connected to the hub and the shroud. It is worth noticing that the assumption of neglecting a gap would wrongly transfer a geometry from one family to the other and yield an incorrect value of the genus. The last family of interest also presents a genus related to the number of blades. "Diffuser with parallel piers" category is representative of a hydraulic turbine draft tube with structural piers. The genus is here equal to the number of piers plus one.

3.2. Surface Partition and Splitting Critical Points (SCP)

Unlike turbomachinery cases, classical cases involve a surface that is completely immersed in the flow field. In turbomachinery, only the internal flow is considered and only a part of the system is analyzed. To be consistent with the topology rule, authors introduce imaginary critical points to take into account this partition of the domain (splitting critical points, SCP). This article is only focused on turbomachinery with confined flow. Hence, non-confined turbomachinery (wind turbine, propeller, for example) are disregarded. The friction field of interest is the one induced by the flow inside the turbomachinery; the outside flow is not considered. Next, as implicitly presented in the previous section, the zone of interest in turbomachinery is generally not the whole system from the fluid inlet to the fluid outlet but only a part of it. However, skin friction lines start and end at nodes (skin friction source and sink), which can be out of the zone of interest. From this observation, authors propose to introduce imaginary critical points that account for

the development of the flow field upstream and downstream of the domain considered. They are referred to as splitting critical points (SCP). A preliminary caution to apply this methodology is to select a domain which includes the complete separation zone: the friction lines need to be relatively straight at the domain limits. Authors have found three types of SCP. The first one corresponds to a domain for which it was necessary to cut a shaft. In this case, an imaginary node needs to be added at the shaft center, as depicted in Figure 2, to induce friction lines along its side. A practical application is the analysis of the second stage of an axial multistage compressor rotor. In reality, a node exists on the hub upstream of the first rotor, but this one is not present in the selected zone of interest and needs to be added as an imaginary node.

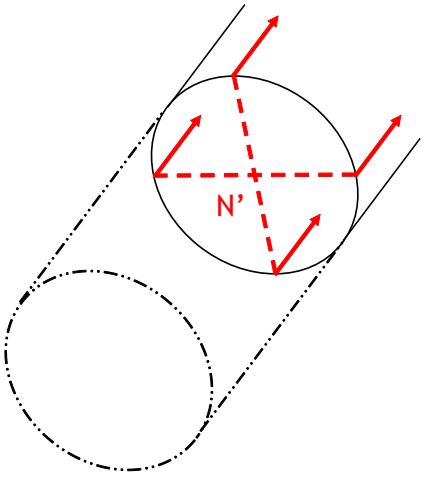

Figure 2. SCP, imaginary shaft node.

The next case is intrinsically linked to the confined-flow aspect. Let us consider a portion of a pipe extracted from a pipeline system, as illustrated in Figure 3. The flow of interest is only the inner flow. An imaginary node (N1′, Figure 3) is added to generate a friction line along the duct. The node also induces two friction lines which travel along the entrance periphery, one to the right and another on the left. Due to the closing, these two friction lines come together and induce a saddle point (S2′, Figure 3) which induces a straight friction line along the cylinder. At the duct outlet, a saddle point (S1′, Figure 3) collects the friction line originating from the entrance node and a node (N2′, Figure 3) collects the friction line originating from the entrance saddle point. This pattern presented here with two pairs of saddle–node can be extended with an infinite even number of pairs. This mechanism is topologically neutral as it generates the same amount of saddle and node points.

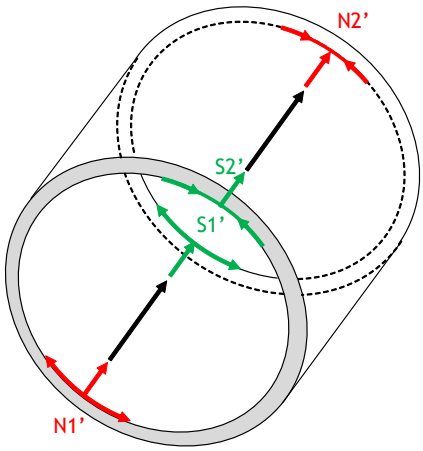

Figure 3. SCP, two imaginary saddle–node combination for a portion of cylindrical duct.

The last type of SCP is useful to describe the outlet condition of radial turbomachines, such as an isolated unshrouded compressor impeller. The flow at the entrance is axial and radial at the exit. In this configuration, the friction lines tend to exit the machine radially, as illustrated in Figure 4. In this case, the authors propose to place an imaginary node at the center of the exit circular section. This one corresponds to the imaginary intersection of friction lines at the exit of the impeller.

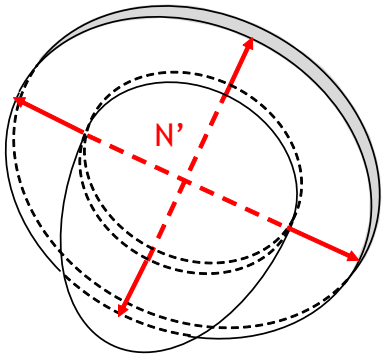

Figure 4. SCP, imaginary radial node.

For a real surface, all these conditions can occur simultaneously. Figure 5 presents the example of the SCP for a shrouded centrifugal pump impeller with a hub. In this case, the axial flow at the entrance reaches the hub and creates a node. This one is not represented in Figure 5 as it is not an SCP. The hub surface induces a modification of the flow direction from the axial to the radial direction. To represent the radial friction lines on the hub surface at the impeller exit, an imaginary node is added (N3′). The flow on the shroud corresponds to the imaginary saddle–node combinations of an isolated portion of the casing (N1′, N2′, S1′ and S2′).

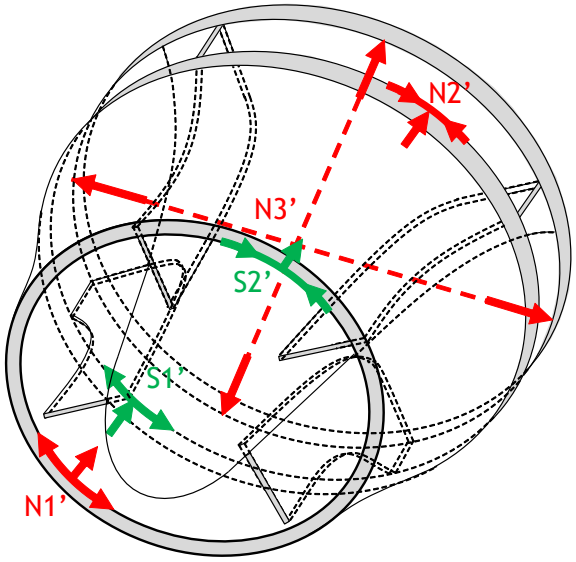

Figure 5. SCP for a shrouded centrifugal pump impeller with hub.

Furthermore, the recommended SCP for the topology analysis of each turbomachinery part presented is proposed in Table 2.

Table 2. Recommended splitting critical point.

Turbomachinery Part	Splitting Critical Points (SCP)
Casing, pipe and vaneless diffuser	Two imaginary saddle–node combinations.
Axial rotor with hub nose	An imaginary shaft node (and another shaft node if the hub is not in the domain).
Unshrouded centrifugal impeller without hub nose	An imaginary shaft node (because the hub is not in the domain) and an imaginary radial node.
Shrouded centrifugal impeller with hub nose	An imaginary radial node and two imaginary saddle–node combinations (and another shaft node if the hub is not in the domain).
Axial stator without hub nose	A shaft node (because the hub is not in the domain) and two saddle–node combinations.
Radial vaned diffuser	Two radial nodes and two saddle–node combinations.
Diffuser with parallel piers	A saddle–node combination (entrance channel) and $b + 1$ saddle–node combinations (exit channels).

3.3. Stagnation and Exit Nodes Inside the Domain

An interesting learning of the classical case of an object completely immersed in the flow is the stagnation node, where the upstream flow impacts the surface. This point is the source of the skin friction lines. These skin friction lines converge to an attracting node downstream where the flow exits the immersed object.

Let us consider the simple example of a sphere completely immersed in a uniform flow. A stagnation point appears on the side facing the flow, yielding a skin friction node from which friction lines diverge (stagnation node). In the same fashion, a skin friction node to which friction lines converge (exit node) appears on the opposite side. With the same idea, any overhang of the general shape inside the domain can feature a stagnation and/or an exit node. In the context of turbomachinery, a blade can be interpreted as such an overhang, with the stagnation point at the leading edge and the exit point at the trailing edge. Moreover, the nose of a hub exhibits a stagnation point at its tip. These nodes are physical and must be counted. Consequently, two nodes per blade should be counted, as well as one node per hub with a nose inside the considered domain.

3.4. Periodicity

The cost of a 360° numerical simulation is often prohibitive in turbomachinery. In most cases, a periodicity in the azimuthal direction naturally exists and can be used to obtain periodic solutions by replicating the flow field computed on a single channel. However, in the scope of the topological analysis, some caution is needed to properly restrain the surface of interest with this assumption and to adapt the topology rule. When periodicity is properly applied, conclusions on the whole system can be drawn from the study of a single periodic subdomain

For a genus-0 surface, with a periodicity assumption over a single or several channels, the observed subdomain should be considered as a genus-0 surface.

For connected orientable closed surfaces whose genus is strictly higher than zero, the issue of periodicity can be tackled by considering that the surface is homeomorphic to one or several tori. A genus-1 surface is homeomorphic to one torus and cannot be split. Here, this case corresponds only to the family "casing, pipe and vaneless diffuser". This implies that if the goal of the simulation is to analyze flow separation on this type of surface, the simulation domain must include the whole surface.

For genus-b surfaces, the correct divisions only occur between two tori, illustrated in Figure 6. The genus of the extracted surface corresponds to the number of tori kept. All genus-b surfaces presented before are periodic in the azimuthal direction, and the number of tori corresponds to the number of interblade channels. Each torus is then formed by

the junction of the blade pressure side surface, the two casing interblade surfaces and the blade suction side surface. Let us point out that, even though the flow physics is insensitive to the periodic pattern selected, this specific division is crucial in the context of a topological analysis. Indeed, an isolated blade bounded on both sides is a genus-0 surface, but an isolated interblade channel has a genus equal to one (see Figure 6). Considering a subdomain centered on a blade can be tempting but leads to a false value of the genus.

In the case of the "diffuser with parallel piers" where genus is $b + 1$, the surface is not periodic. However, a symmetry plane between exit channels can exist. Each exit channel and the inlet channel can be represented by a torus. The exit tori then merge with the inlet torus. The symmetry plane must be placed at the junction between exit tori that respects the geometrical symmetry. To apply the symmetry assumption, the number of piers (b) must be odd, and the genus of the periodic subdomain is $(b + 1)/2$. Otherwise, the entire domain must be kept.

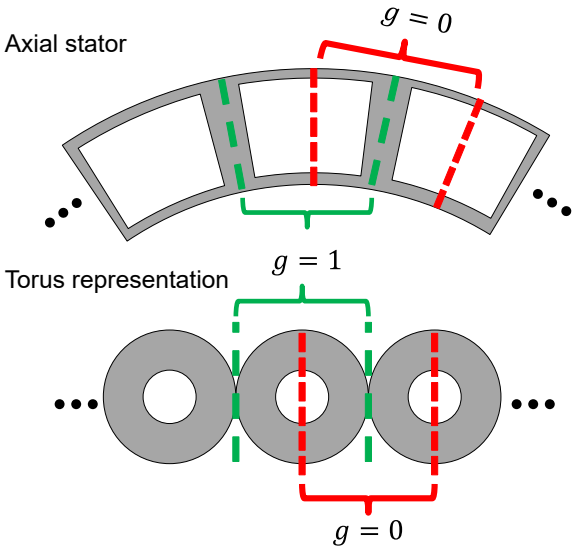

Figure 6. Correct periodic division of an axial stator. Green division is correct for both genus determination and observation domain. Red division is only correct for observation domain.

The next point of attention is the distribution of the critical points to check the topology rule. Three types of critical points must be distinguished: inside the periodic domain, from the subdomain splitting (SCP) and on the periodic boundary surface. The critical points which are located inside the periodic subdomain count completely. The number of these critical points in the complete surface is simply a periodic repetition of this pattern. The SCP are indivisible and count for the same quantity for a periodic subdomain and for the complete surface. A critical point on the periodic boundary surface counts as a half point in the periodic subdomain and one for the complete surface. For example, the stagnation node at the leading edge of a blade is counted as a half node if the point is on the periodic surface. If a critical point is on the two periodic surfaces, this point counts for one, in the periodic subdomain and in the complete surface. The classical example is the stagnation node at the hub which belongs to the two periodic surfaces.

3.5. Application of the Topology Rule

At this point of the analysis, the genus of the complete surface is known, the SCP are determined, the number of stagnation nodes are determined. The periodicity is applied on the analysis surface on the topological rule and on the critical point distribution. One should now check if the topology rule is correct.

If the topology rule is checked, the topological organization obtained corresponds to a situation without flow separation. From then, this organization can be compared to the actual skin friction field to look for supplementary critical points. If the skin friction field of

interest exhibits more critical points than the one counted so far, the flow field features one or several separation zones, and the supplementary critical points are linked to these zones.

If the topology rule is not validated, the resulting topological organization is not physical. The topological organization, with or without flow separation, needs to check the topology rule. A first stage is to find a physical topological organization without flow separation. In turbomachinery, the problem often comes from the stagnation and exit nodes on a blade introduced in Section 3.3. In this case, from authors' experience, the topology rule is fulfilled by adding two saddle points representing the flow bypassing around the blade at the blade connection to the wall. One saddle point is placed upstream of the blade leading edge, the other downstream of the blade trailing edge. From then, this organization can be compared to the actual skin friction field to look for supplementary critical points.

The critical points symptomatic of a separation zone appear in saddle–node or saddle–focus pairs to respect the topology rule.

A tricky notion is that critical points from flow separation can interact with critical points from the geometry aspect. The knowledge of the topology without flow separation can help to distinguish critical points from different origins.

Let us underline that identifying critical points for a given skin friction field is not trivial. They can be detected manually by inspecting the low friction magnitude regions. If a large number of skin friction fields must be explored, automatic detection algorithms can be used [19]. This is the case when characterizing the unsteadiness of a separation zone, for instance.

4. Application to an Industrial Radial Diffuser

In the framework of the Clean Sky 2 project FLORA, a Large-Eddy Simulation (LES) of an industrial centrifugal compressor was performed. The compressor has been designed and built by SAFRAN Helicopter Engines. This compressor is composed of inlet guide vanes, a backswept splittered unshrouded impeller, a splittered vaned radial diffuser and axial outlet guide vanes. Thanks to a natural periodicity in the azimuthal direction, the simulation domain is limited to 1/3 of the machine. A compressible LES has been performed using the code TurboAVBP developed at CERFACS [20]. TurboAVBP is a single program–multiple data paradigm that encapsulates two instances of the unstructured massively parallel LES solver AVBP. Both rotor and stator domains are run simultaneously within the code and primitive variables are interpolated and exchanged using overset grids with the CWIPI library of Onera [21]. The setup is similar to the one used in [22] where the convective operator is discretized by the Lax–Wendroff scheme (2nd-order accurate) and an explicit time advancement [23]. The Sigma [24] Sub-Grid Scale model (SGS) is used and standard log-law is applied on all solid boundaries.

In this article, only the splittered vaned radial diffuser is considered. The flow field used is the average of unsteady solutions over approximately a 10-rotations period. To simplify the analysis, the LES solution is interpolated from an unstructured mesh with 114 million cells to a structured mesh with 6 million cells. Two-dimensional streamlines at the first cells are used as a proper approximation of the skin friction field. They are colored by the velocity magnitude.

The selected operating conditions are near the best efficiency and nominal speed. As presented in the following, the flow separation zones are small and have a restricted effect on performance. This case is easy to analyze and is selected for illustrating the presented methodology.

4.1. Surface Genus Determination

From Table 1, the genus associated to a radial diffuser is equal to the number of main and splitter blades b. The splitter blades count in the number of blades (these ones are connected to both the hub and the shroud). The surface remains continuous even if the surface is cut between each blade on the shroud surface. Any supplementary cut divides

the surface into two parts. The exact number of blades cannot be provided due to the industrial property. The topology rule here is:

$$\Sigma N - \Sigma S = 2 - 2g = 2 - 2b. \quad (4)$$

4.2. Surface Partition and Splitting Critical Point (SCP)

According to Table 2, the extraction of the radial diffuser from the complete compressor induces four SCP: two radial nodes and two saddle–node combinations. The two radial nodes emit skin friction lines and are located at the hub and shroud surfaces on the compressor axis. The saddle–node combinations are located at the circular boundary on the hub and shroud surfaces. These saddle–node combinations produce an equal quantity of saddle and node points and are therefore topologically neutral.

4.3. Stagnation Node Inside the Domain

Two stagnation nodes are present on each blade. Thus, in the complete diffuser, there are $2b$ nodes.

4.4. Periodicity

Using homeomorphism, the radial diffuser is equivalent to b-tori. Each torus is delimited by the blade suction side surface, the interblade shroud and hub surfaces and the blade pressure side surface. Let us recall that two different blade geometries exist, the main blade and the splitter blade. Consequently, to preserve the geometrical periodicity, the azimuthal periodicity is applied to 2-tori and the analysis domain is delimited by the suction side of one main blade and the pressure side of the next main blade. The analysis domain includes both sides of the splitter blade, as illustrated in Figure 7. The shroud surface is set with low opacity to see the internal splitter blade. Consequently, the genus of this subdomain is $g = 2$, and the topology rules yield:

$$\Sigma N - \Sigma S = -2. \quad (5)$$

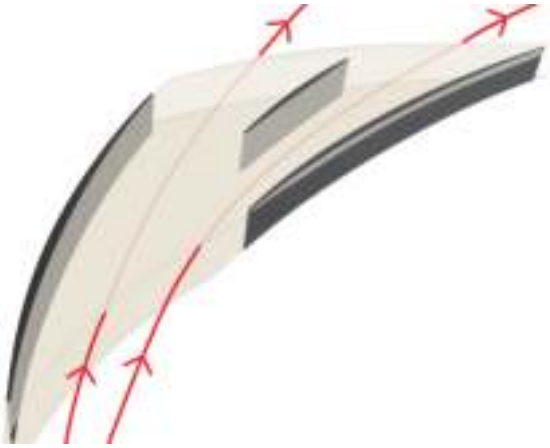

Figure 7. Three-dimensional representation of the analysis subdomain. The shroud surface is set with low opacity. Red arrows represent the flow direction.

4.5. Application of the Topology Rule

With previous considerations, the periodic subdomain contains six nodes (two half nodes at the main blade suction side, two half nodes at the main blade pressure side, two nodes from the splitter blades and two nodes from the SCP) and no saddle point (the SCP saddle–node combinations compensate themselves and are not counted here). As a result, Equation (5) is not fulfilled.

The analysis of the skin friction field at the wall reveals a flow organization around each blade as depicted in Figure 8. In the middle of the leading edge, the stagnation point

(N1, Figure 8) emits friction lines. They go along the sides of the blade, toward the blade tip and toward the blade root. The friction lines going toward the blade root induce a back-flow zone upstream of the leading edge of the hub surface. The friction lines on the hub surface coming from upstream are deviated around the back-flow zone and induce the saddle point (S1, Figure 8). The friction lines emitted by S1 around the blade are collected by the saddle point at the trailing edge (S2, Figure 8). The saddle point S2 emits friction lines that go downstream and along the trailing edge. A similar organization is found at the shroud surface (S3 and S4, Figure 8). The exit node (N2, Figure 8) collects the skin friction lines emerging from S2, S4 and N1.

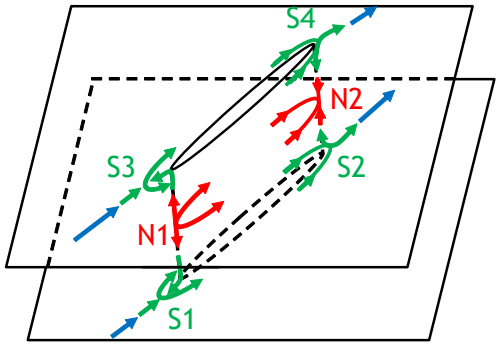

Figure 8. Topology without separation of a blade surface bounded on both sides.

From the authors experience, for a blade bounded by two surfaces, this topological organization is the simplest observed configuration and is symptomatic of a flow bypassing solid volumes.

As a summary, four saddle points and two nodes are attributed to the splitter blade. As the analysis domain is the interblade channel, two half main blades are considered and are attributed with eight half saddle points and four half nodes. With the two nodes from the SCP, the topology rule (5) is now satisfied.

No flow separation zones have been introduced so far. This example was selected because the flow separation zones are expected to be small. It is therefore easier to divide the critical points into those related to the geometrical aspect and those occurring due to the flow separation. Indeed, this distinction is often challenging as all critical points can interact with one another. The skin-friction-lines analysis reveals five isolated zones of flow separation. In Figure 9, the critical points at the hub surface are presented. The critical points related to geometrical aspects, indicated in green in Figure 8, are indicated in green as well. The other critical points reveal three flow separation zones.

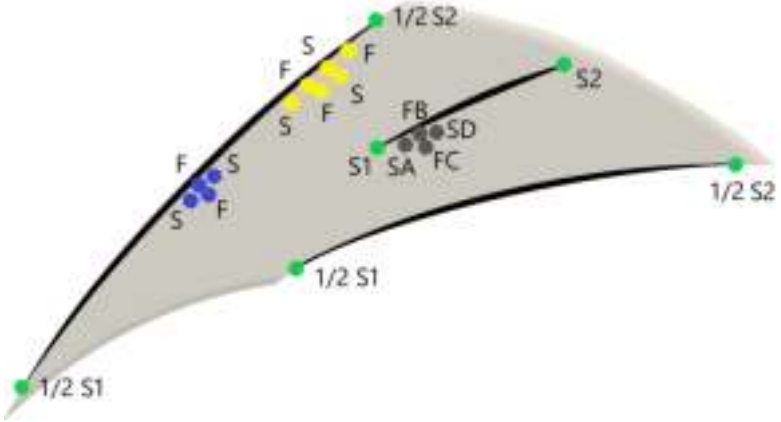

Figure 9. Location of the different critical points on the hub surface.

The first one, indicated in blue, is located at the junction between the main blade suction side and the hub, approximately at midchord. A zone with similar critical points

distribution is observed on the shroud surface corner. The second one, indicated in yellow, is located downstream of the first one. In this case, such a zone is not observed at the shroud. Both separation zones are symptomatic of a corner separation. Indeed, in such a region, the adverse pressure gradient acts on the low-energy fluid from the corner boundary layer.

The last zone is indicated in grey and is located on the suction side of the splitter blade, close to the leading edge. The same topology is observed at the shroud surface. The friction lines on the suction side of the splitter are presented in Figure 10. The enlargement presents the local critical points distribution on the hub surface with two saddle points and two foci. This separation zone is symptomatic of a local off-design flow incidence close to the hub and shroud. Such flow conditions can be explained by the passage flow occurring in the main channel, which drags the boundary-layer flow from the suction side of a main blade to the pressure side of the neighboring one. Moreover, the corner separation zones at the suction side (in blue and yellow, Figure 9) can induce a blockage effect which contributes to the flow deviation.

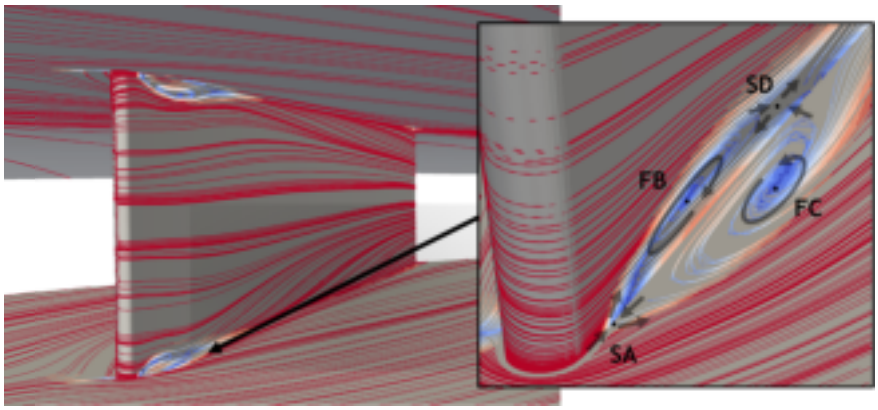

Figure 10. Skin friction lines colored by the velocity magnitude at the first cell. From minimum to maximum: blue to red.

The topological analysis as well as the analysis of the skin friction fields enable to characterize the visible critical points as a function of their origins. According to the methodology presented in this paper, this analysis can be extended from the periodic subdomain to the complete diffuser. Table 3 summarizes the critical points count for both domains. Let us underline that Equations (4) and (5) are satisfied, respectively, for the periodic and the complete domain.

Table 3. Critical points listing.

(a) Analysis Domain	**Saddle**	**Node**	**Focus**
From SCP *	0	2	0
From stagnation node	0	4	0
From geometrical aspect	8	0	0
From flow separation	11	0	11
Total	19	17	
(b) Complete diffuser	**Saddle**	**Node**	**Focus**
From SCP *	0	2	0
From stagnation node	0	2 b	0
From geometrical aspect	4 b	0	0
From flow separation	11 (b/2)	0	11 (b/2)
Total	4 b + 11 (b/2)	2 + 2 b + 11 (b/2)	

(*) Saddle–node combinations of SCP compensate themselves.

5. Conclusions

In this paper, a method is proposed to properly initiate the analysis of a three-dimensional flow separation using critical points. This method considers the specificities of the turbomachinery domain. The main steps of this analysis are:

- Determination of the surface genus and the topology rule;
- Determination of the splitting critical points (SCP) induced by the surface isolation from the total system;
- Determination of the stagnation and exit nodes inside the domain, in particular, at the blade leading and trailing edge and at the nose hub;
- A reduction in the analysis domain to a smaller subdomain, if a natural periodicity exists. The consequences on the topology rule and the critical points distribution are described;
- A definition of topology with no flow separation that respects the topology rule. Flow regions that exhibit additional critical points are then highlighted, and their physical origins can be analyzed further.

The topology rule is a unique tool for finding all critical points and deducting flow separation mechanisms. However, it should be used with caution as a false topology rule can lead to misleading conclusions. This method helps to clarify the concept of genus, even for complex geometries and with domain restrictions, and consequently helps to properly apply the topology rule. Finally, as presented with the analysis of a radial diffuser, the evaluation of the topology without separation seems to be a good practice to group critical points from the geometrical aspect and from the flow separation zone.

Author Contributions: Conceptualization by P.D. with the help of J.C. and G.M., LES calculation by J.D. and analysis by P.D. All authors have read and agreed to the published version of the manuscript.

Funding: This project has received funding from the Clean Sky 2 Joint Undertaking (JU) under the European Union's Horizon 2020 research and innovation program, under grant agreement No. 820099.

Data Availability Statement: Not applicable.

Acknowledgments: This publication reflects only the point of view of the authors and the JU is not responsible for any use that may be made of the information it contains.

Conflicts of Interest: The authors declare no conflict of interest.

Appendix A

The Euler characteristic determination is usually performed by Equation (1), which holds under the assumption of a connected, orientable, closed surface analysis. To be used reliably, the definitions of connected (Definition A1), orientable (Definition A2) and closed (Definition A3) are presented underneath [11,12].

Definition A1. *A one-piece surface is said to be connected.*

Definition A2. *A connected surface is said to be orientable if it has two "sides". For example, a sphere and a torus are orientable surfaces, but the Möbius strip is not.*

Definition A3. *A closed surface is connected, without boundary (i) and compact (ii). For instance, a sphere and a torus are closed surfaces, but the disk surface is not.*

i *The boundary is the set of points which can be approached from both the inside and the outside of the surface. For example, a mathematical disk is a surface that has a boundary, but a sphere is not.*

ii *For what matters here, a surface is called compact if the two following properties are both verified:*

- *It can be embedded in a finite-sized box. The set is then called bounded. A plane is unbounded as it extends in all directions, but a disk is a surface that is bounded.*

– *It contains all of its boundary points. The set is then called closed. Consequently, the disk surface (not) containing its boundary is (not) closed.*

As a consequence, a surface that is closed is not necessarily a closed surface. Pragmatically, the disk surface containing its boundary is closed but not a closed surface.

References

1. Prandtl, L. *Über Flüssigkeitsbewegung bei sehr kleiner Reibung*; Teubner: Heidelberg, Germany; Leipzig, Germany, 1904; p. 484.
2. Greitzer, E.M. Surge and Rotating Stall in Axial Flow Compressors—Part II: Experimental Results and Comparison with Theory. *J. Eng. Power* **1976**, *98*, 199–211. [CrossRef]
3. Duquesne, P.; Maciel, Y.; Deschênes, C. Investigation of Flow Separation in a Diffuser of a Bulb Turbine. *J. Fluids Eng.* **2016**, *138*, 011102. [CrossRef]
4. Mauri, S.; Kueny, J.L.; Avellan, F. Werlé–Legendre Separation in a Hydraulic Machine Draft Tube. *J. Fluids Eng.* **2005**, *126*, 976–980. [CrossRef]
5. Moënne-Loccoz, V.; Trébinjac, I.; Poujol, N.; Duquesne, P. Detection and Analysis of an Alternate Flow Pattern in a Radial Vaned Diffuser. *Int. J. Turbomach. Propuls. Power* **2020**, *5*, 2. [CrossRef]
6. Fiquet, A.L.; Aubert, S.; Brandstetter, C.; Buffaz, N.; Vercoutter, A. Acoustic resonance in an axial multistage compressor leading to non-synchronous blade vibration. *J. Turbomach.* ***2021***, 143, 091014. [CrossRef]
7. Lacagnina, G.; Chaitanya, P.; Berk, T.; Kim, J.H.; Joseph, P.; Ganapathisubramani, B.; Hasheminejad, S.M. Mechanisms of airfoil noise near stall conditions. *Phys. Rev. Fluids* **2019**, *4*, 123902. [CrossRef]
8. Mohan, P.R.; Prasad, C.M.V. An Investigation of the Establishment of a Recirculation Zone by Swirling Flows within a Conical Duct. In Proceedings of the ASME 1983 International Gas Turbine Conference and Exhibit, Phoenix, AZ, USA, 27 March 1983.
9. Délery, J. *Three-Dimensional Separated Flows Topology: Singular Points, Beam Splitters and Vortex Structures*; ISTE Ltd.: London, UK; Wiley: Hoboken, NJ, USA, 2013.
10. Dawkins, I.; Taylor, J.; Ottavy, X.; Miller, R. The Unsteady Topology of Corner Separations. In Proceedings of the ASME Turbo Expo 2021: Turbomachinery Technical Conference and Exposition, Online, 7–11 June 2021. [CrossRef]
11. Munkres, J. *Topology*, 2nd ed.; Pearson: London, UK, 2000.
12. Massey, W.S.; William, S. *A Basic Course in Algebraic Topology*; Graduate Texts in Mathematics; Springer: New York, NY, USA, 1991. [CrossRef]
13. Abbena, E.; Salamon, S.; Gray, A. *Modern Differential Geometry of Curves and Surfaces with Mathematica*; Chapman and Hall/CRC: Boca Raton, CA, USA, 2006; ISBN 978-1584884484.
14. Poincaré, H. Académie des Sciences (France), France, Ministère de l'éducation Nationale, Paul Appell, et Gaston Darboux. Oeuvres de Henri Poincaré: Paris: Gauthier-Villars et Cie. 1916. Available online: http://archive.org/details/uvresdehenripoin03poin (accessed on 7 January 2022).
15. Hunt, J.C.R.; Abell, C.J.; Peterka, J.A.; Woo, H. Kinematical studies of the flows around free or surface-mounted obstacles; applying topology to flow visualization. *J. Fluid Mech.* **1978**, *86*, 179–200. [CrossRef]
16. Lighthill, M.J. Attachment and separation in three-dimensional flows. In *Laminar Bound*; Layer Theory; Oxford Univeristy Press: Oxford, UK, 1963; pp. 72–82.
17. Tobak, M.; Peake, D.J. Topology of Three-Dimensional Separated Flows. *Annu. Rev. Fluid Mech.* **1982**, *14*, 61–85. [CrossRef]
18. Surana, A.; Grunberg, O.; Haller, G. Exact Theory of Three-Dimensional Flow Separation. Part 1. Steady Separation. *J. Fluid Mech.* **2006**, *564*, 57–103. [CrossRef]
19. Depardon, S.; Lasserre, J.J.; Brizzi, L.E.; Borée, J. Automated Topology Classification Method for Instantaneous Velocity Fields. *Exp. Fluids* **2007**, *42*, 697–710. [CrossRef]
20. Schoenfeld, T.; Rudgyard, M. Steady and unsteady flow simulations using the hybrid flow solver AVBP. *AIAA J.* **1999**, *37*, 1378–1385. [CrossRef]
21. Duchaine, F.; Jauré, S.; Poitou, D.; Quémerais, E.; Staffelbach, G.; Morel, T.; Gicquel, L. Analysis of high performance conjugate heat transfer with the openpalm coupler. In *Computational Science & Discovery*; IOP Publishing: Bristol, UK, 2015. [CrossRef]
22. Dombard, J.; Duchaine, F.; Gicquel, L.; Staffelbach, G.; Buffaz, N.; Trébinjac, I. Large eddy simulations in a transonic centrifugal compressor. In *American Society of Mechanical Engineers Digital Collection*; ASME: New York, NY, USA, 2018. [CrossRef]
23. Lax, P.D.; Wendroff, B. Difference schemes for hyperbolic equations with high order of accuracy. *Commun. Pure Appl. Math.* **1964**, *17*, 381–398. [CrossRef]
24. Nicoud, F.; Toda, H.B.; Cabrit, O.; Bose, S.; Lee, J. Using singular values to build a subgrid-scale model for large eddy simulations. *Phys. Fluids* **2011**, *23*, 085106. [CrossRef]

International Journal of
Turbomachinery
Propulsion and Power

MDPI

Article

Optimization of Turbine Blade Aerodynamic Designs Using CFD and Neural Network Models

Chao Zhang * and Matthew Janeway

Siemens Digital Industries Software, Cypress, CA 90630, USA; matt.janeway@siemens.com
* Correspondence: chao.zhang1@siemens.com

Abstract: Optimization methods have been widely applied to the aerodynamic design of gas turbine blades. While applying optimization to high-fidelity computational fluid dynamics (CFD) simulations has proven capable of improving engineering design performance, a challenge has been overcoming the prolonged run-time due to the computationally expensive CFD runs. Reduced-order models and, more recently, machine learning methods have been increasingly used in gas turbine studies to predict performance metrics and operational characteristics, model turbulence, and optimize designs. The application of machine learning methods allows for utilizing existing knowledge and datasets from different sources, such as previous experiments, CFD, low-fidelity simulations, 1D or system-level studies. The present study investigates inserting a machine learning model that utilizes such data into a high-fidelity CFD driven optimization process, and hence effectively reduces the number of required evaluations of the CFD model. Artificial Neural Network (ANN) models were trained on data from over three thousand two-dimensional (2D) CFD analyses of turbine blade cross-sections. The trained ANN models were then used as surrogates in a nested optimization process alongside a full three-dimensional Navier–Stokes CFD simulation. The much lower evaluation cost of the ANN model allows for tens of thousands of design evaluations to guide the search of the best blade profiles to be used in the more expensive, high-fidelity CFD runs, improving the progress of the optimization while reducing the required computation time. It is estimated that the current workflow achieves a five-fold reduction in computational time in comparison to an optimization process that is based on three-dimensional (3D) CFD simulations alone. The methodology is demonstrated on the NASA/General Electric Energy Efficient Engine (E3) high pressure turbine blade and found Pareto front designs with improved blade efficiency and power over the baseline. Quantitative analysis of the optimization data reveals that some design parameters in the present study are more influential than others, such as the lean angle and tip scaling factor. Examining the optimized designs also provides insight into the physics, showing that the optimized designs have a lower amount of pressure drop near the trailing edge, but have an earlier onset of pressure drop on the suction side surface when compared to the baseline design, contributing to the observed improvements in efficiency and power.

Keywords: CFD; optimization; aerodynamics; gas turbines; machine learning; neural networks

check for updates

Citation: Zhang, C.; Janeway, M. Optimization of Turbine Blade Aerodynamic Designs Using CFD and Neural Network Models. *Int. J. Turbomach. Propuls. Power* **2022**, *7*, 20. https://doi.org/10.3390/ijtpp7030020

Academic Editor: Tom Verstraete

Received: 25 April 2022
Accepted: 28 June 2022
Published: 30 June 2022

Publisher's Note: MDPI stays neutral with regard to jurisdictional claims in published maps and institutional affiliations.

Copyright: © 2022 by the authors. Licensee MDPI, Basel, Switzerland. This article is an open access article distributed under the terms and conditions of the Creative Commons Attribution (CC BY-NC-ND) license (https://creativecommons.org/licenses/by-nc-nd/4.0/).

1. Introduction

The present study applies machine learning methods in a CFD-based optimization for turbine blade aerodynamics. Literature on optimization and machine learning methods used in gas turbine studies will be reviewed, followed by a summary of the motivation of the present work.

Numerical optimization has been widely used in the design and analysis of gas turbines. In some earlier studies, specific optimization algorithms have been investigated to leverage lower fidelity models to achieve fast optimization time. One study on aerodynamic wing optimization has used an approximation and model management optimization

method to incorporate low fidelity, computationally cheaper models with occasional recourse to higher fidelity, more expensive models, resulting in threefold saving in optimization time [1]. Another study adopted a similar concept, employing a trust-region approach to interleave the exact models with cheaper surrogate models during optimization iterations [2]. These methods demonstrate the possibility of obtaining optimized solutions on a limited computational budget by incorporating lower-fidelity surrogate models. In more recent years, an increasing number of optimization studies have relied on using parametric CFD models. In optimization of the coolant flow passage of the NASA C3X vane, different designs were evaluated repeatedly through CFD runs [3]. In the study of a marine high-pressure turbine [4], ten design parameters controlling multi-row film cooling designs were built into the CFD model and optimized based on a non-dominated sorting genetic algorithm. Multiple studies were also conducted on ultra-super-critical steam turbines [5,6], in which the blade aerodynamic efficiency was optimized using 2D and 3D CFD simulations driven by Siemens' Simcenter HEEDS commercial Sherpa optimization algorithm. A CFD-based co-optimization strategy was presented in [7], which demonstrates a workflow for coupling different disciplines into a nested optimization loop to conduct parallel blade aerodynamic and thermal optimizations. In addition to improving turbine blade designs, optimization has also been applied to improving the operations of gas turbine engines, for instance, to find the best valve setup parameters that reduce fuel consumption [8].

With the advancements in computer science and data storage, an increase in interest in application of machine learning methods to gas turbine designs has been observed. One area of such applications seeing increased interest has been the prediction of key performance metrics using models trained on input data gained through past simulations or experiments. In an earlier study [9], the outlet temperature and fuel mass flow rate at different operating conditions for a 255 MW single-shaft gas turbine were predicted by building a three-layer neural network model. Another application of the Artificial Neural Network (ANN) model has been seen in a turbine film cooling study to predict the instantaneous temperature distributions along the blade surface as well as the cooling effectiveness [10]. In another study of a jet engine power plant [11], a machine learning method combining physics-based and measurement-driven modeling was developed and used to conduct preventive maintenance and diagnose faults. Machine learning methods were also applied to a Viper 632-43 military turbojet engine to predict the exhaust temperature using models trained on data collected from a gas turbine simulation program [12]. Extending from predicting individual engineering metrics, machine learning has also been used to predict field quantities representing more complicated underlying physics. A method using gradient boosted trees was used to develop models of aerodynamic loads on vibrating turbine blades and demonstrated to have good agreement with detailed CFD results [13]. In another study, the turbine surface pressure distribution was predicted using transfer learning models, which transfer knowledge from a large-scale but low-fidelity dataset to a small-scale but high-fidelity dataset, shown to have a low prediction error with reduced cost [14]. Machine learning has also been applied to the prediction of operating characteristics of gas turbine engines, using real-time data of power plants to develop neural networks [15,16]. In addition to the above applications, machine learning has also been studied to develop turbulence closure models. In one study for wake mixing, a machine learning model was demonstrated to be robust across several different operating conditions when integrated into a RANS CFD model of a low-pressure turbine [17]. A review article on machine learning methods for science and engineering particularly highlighted the need for interpretable, generalizable, expandable, and certifiable machine learning techniques for safety-critical applications [18].

Recent works have also focused on using machine learning embedded into design optimization procedures. In the optimization of a centrifugal compressor impeller [19], an ANN model was first developed using CFD and FEA data from a Design of Experiment (DOE) study. Then, the ANN model was applied in an optimization procedure, which resulted in a

1% increase in isentropic efficiency and 10% reduction in the blade stress. In another study investigating a carved blade tip [20], 55 CFD runs were conducted to generate ANN meta models, which were then used in a genetic algorithm routine to optimize the blade tip shape. In a missile control surface optimization study [21], machine learning, reinforcement learning, and transfer learning were integrated into the optimization procedure and leveraged CFD in the evaluation iterations. In another study of 2D airfoil optimization [22], a deep convolutional generative adversarial network was trained and embedded as a surrogate model in an optimization framework. In still another study of a compact turbine rotor [23], machine learning models were trained and used to optimize the efficiency and torque based on a gradient-based multi-objective optimization algorithm. In addition to using machine learning models in optimization, several CFD and optimization studies have compared machine learning models with response surface models (RSM). In a study of aircyclone optimization [24], it is concluded that ANN offers an alternative and powerful approach to response surface methods for modeling the cyclone pressure drop, benchmarked against experimental data. In another study of modeling and optimizing a perforated baffle used for turbine blade passage cooling [25], both ANN and RSM methods were found capable of predicting friction factor and Nusselt number values, although the RSM method performed slightly better than ANN in that study. A more recent study on cyclone optimization also tested a RSM and several machine learning models. A GMDH-neural network model was found to be superior and chosen for the optimization process [26].

As discussed in the above literature, optimization that leverages high-fidelity CFD simulations can provide accurate and realistic optimal designs in general. While leveraging a neural network as a surrogate to replace the CFD evaluations in the optimization loop can significantly improve the computational time, the fundamental challenge is that a neural network model is a lower fidelity model compared to a CFD simulation, and therefore, it may not be as accurate as CFD in predicting certain design variants required by the optimization process. Further, neural network models may also be trained based on previously available datasets that come from different studies, such as 1D and 2D simulation data, and experimental data, all of which will result in the neural network being a reduced order model compared to 3D CFD. As such, relying solely on the neural network when the predictive accuracy is necessary can lead to errant results. The present study presents a nested optimization workflow that can leverage both neural networks and high-fidelity, 3D CFD simulations at the same time to ensure every "best" design is studied in detail by the CFD tool. The introduction of a neural network into the optimization allows for over 70% reduction in the number of CFD evaluations and thus makes significant reductions in computational cost compared to a process relying exclusively on CFD simulations. The methodology is demonstrated through an aerodynamic optimization using a rebuilt model of the NASA/General Electric E3 high pressure turbine blade [27–29].

2. Methodology

Artificial Neural Network models are used alongside 3D CFD simulations in a numerical optimization procedure to improve the aerodynamic performance of a turbine blade. ANN models are typically trained using large datasets obtained from previous experimental or numerical studies. In companies/organizations that conduct R&D on engineering designs, these datasets are usually available from previous studies. The present study proposes a methodology of using such existing knowledge from previous studies to train ANN models and then use the ANN models in an CFD-based design optimization process. A dataset from a previously published work is obtained to conduct the ANN modeling training in the present study. The overall framework of the research methodology is shown in Figure 1, which illustrates how different analysis models/tools required by the optimization process are created. First, data were obtained from a previous study [7] containing 3204 CFD design evaluations of different 2D turbine blade profiles. Performance metrics including efficiency and power were extracted as targets, with the blade geometric parameters serving as input features, to train ANN models. The ANN hyperparameters

were subsequently optimized. The blade cross-sectional profiles were parameterized using a Class-Shape Transformation (CST) method [30]. Using the 2D blade cross-sectional profile, the 3D blade CAD geometry was created with additional parameterization allowing for the variation of further design transformation, such as the thickness, twist, and lean. The blade CAD geometry was then used to build a 3D Reynolds Averaging Navier–Stokes (RANS) CFD model, which solves for the flow field in a single blade passage. Once the ANN models and the 3D CFD simulation are independently developed, they are integrated into a nested optimization procedure for repeated evaluations of different blade design variants to optimize the design parameters. In the nested optimization process, an inner optimization loop is executed using the ANN models to improve the blade cross-sectional profile. In each iteration of the global optimization, the best blade profile is selected from the inner optimization step to create a 3D CFD blade model with additional parameters such as the scaling factors, twist, and lean angles. The optimization targets improving the efficiency and power of the blade. Details of the optimization process will be discussed in a later session in this chapter.

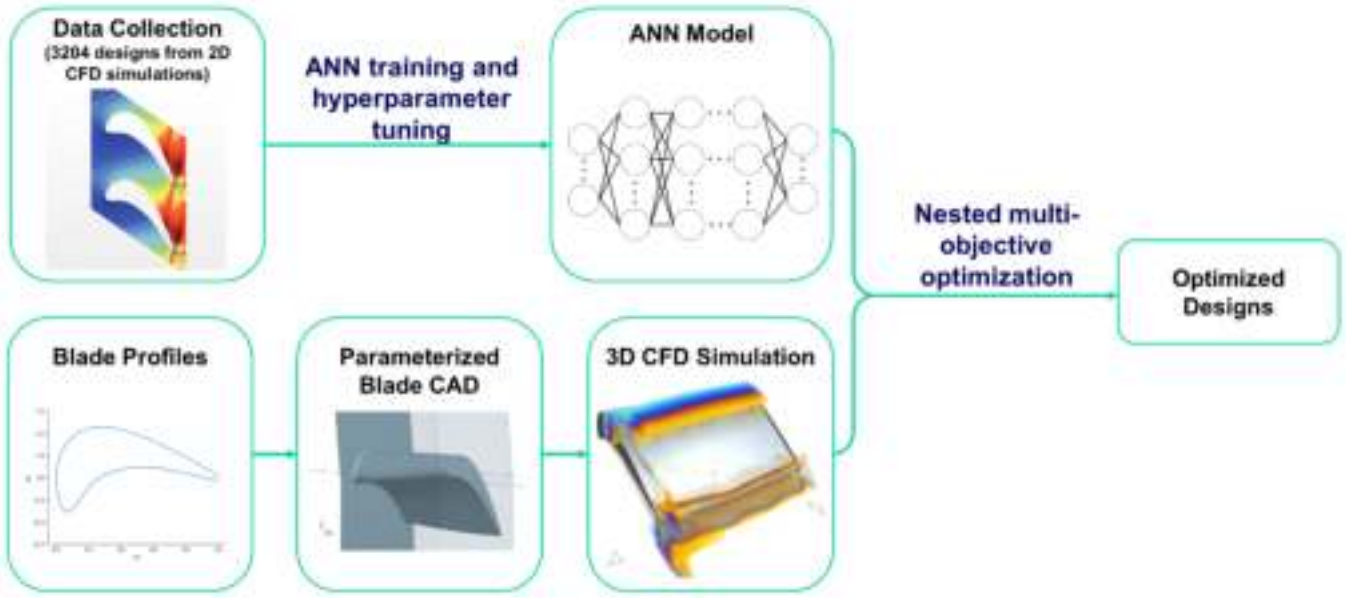

Figure 1. The overall framework of the research methodology. (2D CFD data was collected from a previous study [7].)

2.1. Artificial Neural Network

A dataset representing different design variants of 2D aerodynamic CFD results was obtained from a previous study [7] and used to train ANN models. The dataset features blade design and performance parameters for 3204 designs. The input parameters for the ANN models include 20 blade design parameters. These parameters are the weighting factors used by the CST method [30] to control variations in the blade profile. Under the CST method, these weighting factors are multiplied by Bernstein polynomials to define a shape function, and then subsequently multiplied by a class function to define the aerodynamic blade profile. An order-9 Bernstein polynomial was deemed sufficiently flexible for the purposes of the study [7] and that choice is repeated here, resulting in 10 design parameters for each of the suction and pressure sides of the blade: $\{w_{u,1}, w_{u,2}, \ldots, w_{u,10}\}$ and $\{w_{l,1}, w_{l,2}, \ldots, w_{l,10}\}$. These 20 parameters are used as input features in the ANN models and optimization parameters in the subsequent blade optimization process. Two performance metrics in the dataset were used as output parameters, isentropic efficiency,

and power output, for which two ANN models were developed, respectively. The efficiency and power are defined based on enthalpy quantities of the flow, as follows:

$$\eta = \frac{h_i - h_o}{h_i - h_{o,isen.}}, \tag{1}$$

$$Pow = \Delta h = h_i - h_o \tag{2}$$

The Keras API for TensorFlow [31] was used to construct the ANN models. In consideration of the different distributions of the efficiency and power data and the robustness of the model, a separate ANN model was constructed for each of these two quantities. After some preliminary tests on ANN models of 5, 6, and 7 layers, 7 and 6 layers were constructed, respectively, into the ANN models representing efficiency and power. The choice of the number of layers in ANN usually varies in different problems. It will be shown that the prediction errors are within acceptable range for the chosen number of layers, and that the errors will be further reduced by optimizing the hyperparameters of the models. The first layer of each ANN model has 20 inputs representing the blade input features (CST weights) and the last layer has one output, which is either efficiency or power. The number of neurons in the hidden layers of each ANN, along with other topological and training parameters, were optimized in a separate hyperparameter optimization process. As a starting point for that process, the hyperparameters for each ANN model were set using the values provided in the first two columns of Table 1.

Table 1. Hyperparameters of the initial and optimized ANN models.

Hyperparameters	Initial ANN for Efficiency	Initial ANN for Power	Optimized ANN for Efficiency	Optimized ANN for Power
Number of Neurons-Layer 2	20	20	5	23
Number of Neurons-Layer 3	40	40	35	15
Number of Neurons-Layer 4	20	20	53	36
Number of Neurons-Layer 5	10	5	50	42
Number of Neurons-Layer 6	5	–	62	–
Activation Function-Layer 2	relu	relu	relu	selu
Activation Function-Layer 3	relu	relu	sigmoid	softmax
Activation Function-Layer 4	relu	relu	elu	elu
Activation Function-Layer 5	relu	relu	elu	softmax
Activation Function-Layer 6	relu	–	softmax	–
Learning Rate	0.001	0.001	6.4895×10^{-5}	1.47285×10^{-3}
Number of Epochs	200	200	6123	4000

To improve the predictive performance of the ANN, the hyperparameters were optimized using Siemens commercial optimization tool HEEDS and its Sherpa algorithm [32]. A diagram of the optimization process is provided in Figure 2. The optimizer repeatedly tunes all the hyperparameters for the ANN models listed in the index column of Table 1 with an objective to minimize the model test error on a held-out testing dataset. In each optimization cycle, the dataset is randomly split into a training and testing set with a ratio of 95/5. The training set is used the train the ANN model. The training process involves a typical backpropagation procedure with an 80/20 split of the training set, over multiple epochs with TensorFlow's ADAM optimizer. After the training step is completed, the model's performance is then evaluated against the held-out test set. The evaluation error is passed back to the optimization solver to tune the hyperparameters for the next cycle. A total number of 240 iterations were executed during the optimization of each of the two ANNs. The evaluation number, 240, was based on the Sherpa algorithm best practice [32], which recommends the number of evaluations being about 10 times the number of input variables for single objective optimization problems, due to the hybrid and adaptive methods employed by the algorithm. In the ANN optimization, 12 hyperparameters must be

optimized, and thus it requires at least 120 evaluations according to the best practice. In consideration of the relatively fast run time for the ANN training process in comparison to the 3D CFD run time, that evaluation number is further doubled to 240 to provide better accuracy.

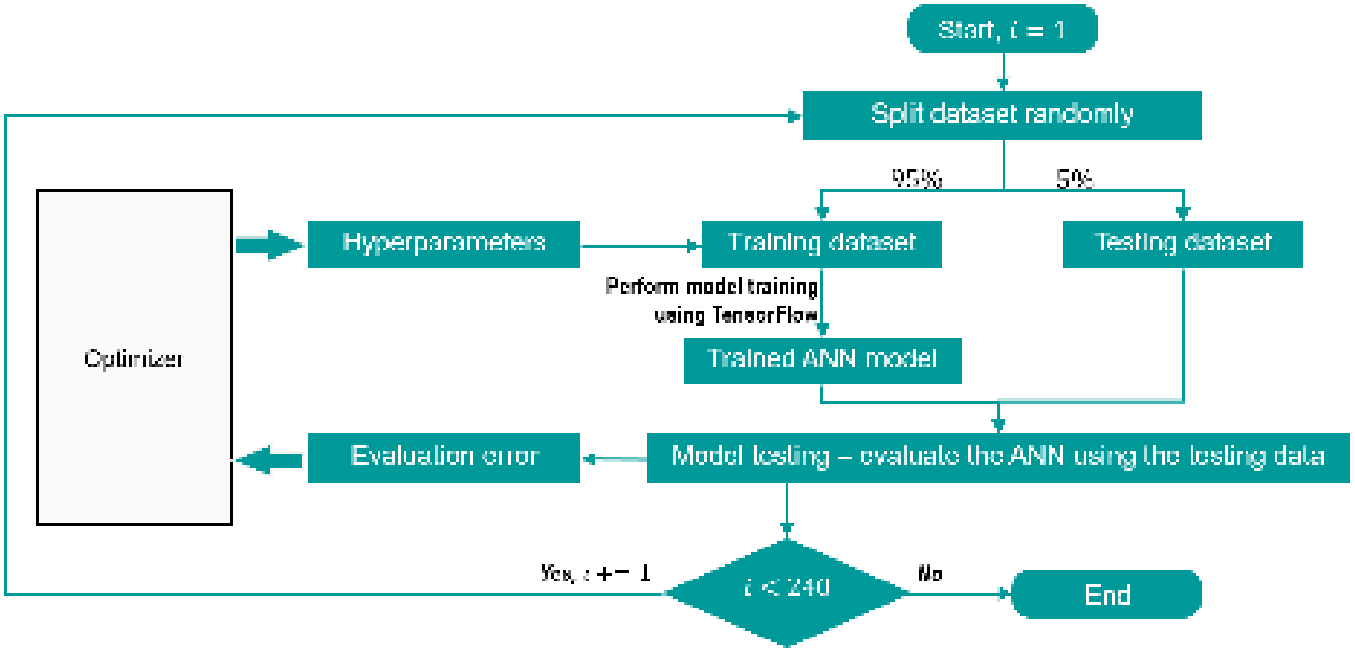

Figure 2. ANN model optimization diagram.

The optimized hyperparameters are obtained and provided in the last two columns of Table 1. After optimization, the evaluation errors for efficiency and power were reduced, respectively, from 0.33% to 0.10%, and from 0.43% to 0.10%. The performance of the initial and optimized ANN models are also examined by comparing the predicted values vs. true values from the test set, shown in Figure 3. It is observed that the optimized ANN models result in better alignment between the predicted values and the true values, as well as narrower bandwidths of the prediction errors on the histogram plots. From Figure 3, it is also observed that the bias of the optimized ANN for efficiency was greatly reduced, as the data points are evenly distributed on both sides of the line of unity slope, shown in the second subplot. This is consistent with the histograms of the prediction errors in Figure 4, which shows that both the bias and bandwidth of the errors were improved in the optimized ANN models. The optimized ANN models are used in the subsequent blade optimization process in this study. The Python scripts for training the ANN models with the optimized hyperparameters are provided in [33]. The CPU time for training an individual ANN largely depends on the number of Epochs. In the present study, the CPU times for training the ANN models representing efficiency and power with their respective optimized hyperparameters were 14.3 min and 8.5 min, respectively. The total compute times for optimizing the hyperparameters of these ANN models were, respectively, 13.07 h and 11.65 h. This optimization was carried out based on parallel execution of 10 training models at the same time using a 6-core CPU.

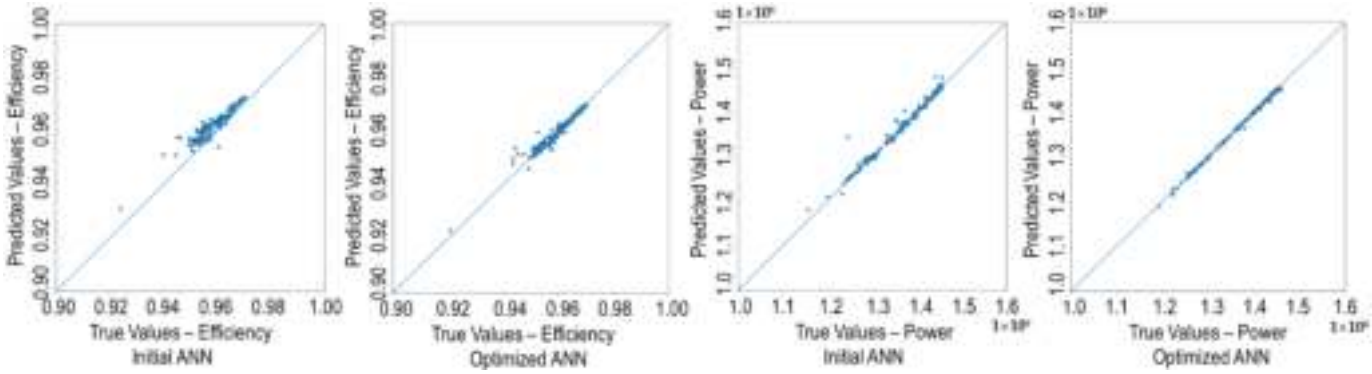

Figure 3. Predicted vs. true values of the initial and optimized ANN models.

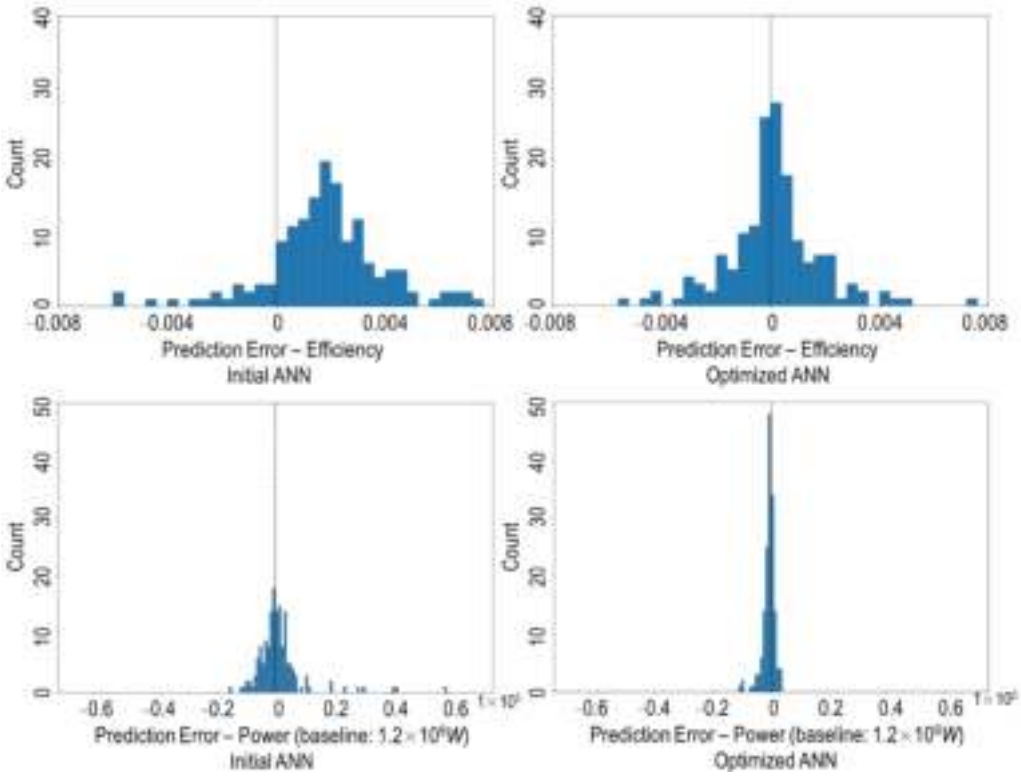

Figure 4. Histogram plots of the prediction errors of the initial and optimized ANN models.

2.2. Parametric Blade CAD and CFD Model

An initial turbine blade CAD model was built by adapting the E3 high pressure turbine blade profiles. Using the first stage rotor blade coordinates provided at three spanwise locations [27]—hub (12.693in), pitch (13.571in), and tip (14.41in)—and accounting for the incoming flow angle [28,29], a 3D CAD model was constructed by lofting these cross-sectional profiles, as shown in Figure 5a, to provide a baseline case. Applying the same philosophy of lofting cross sections and at the same time utilizing the CST method for the cross-sectional profile definition [27], a parameterized blade CAD model was created for the design optimization study. First, the CST method creates a base cross-sectional profile, which is used as the pitch profile. The CST method allows varying the base profile in design optimization through manipulating the 20 weighting parameters, $\{w_{u,1}, w_{u,2}, \ldots, w_{u,10}\}$ and $\{w_{l,1}, w_{l,2}, \ldots, w_{l,10}\}$. Then, the base profile is scaled to create the hub and tip profiles. In the scaling process, the twist angles and chord lengths of the hub and tip profiles are matched to their counterparts of the original E3 blade; 4 additional scaling factors, $\left\{\xi_{hub,l}, \xi_{hub,u}, \xi_{tip,l}, \xi_{tip,u}\right\}$, were applied to the lower and upper profiles

of the hub and tip sections, respectively, to allow for small variations of the thicknesses of the hub and tip sections so that they can be optimized. The ranges of these variations are defined conservatively out of practical considerations of the original E3 engine blade shape. In general, the scaling allows the hub profile to be thicker and the tip profile to be thinner. Finally, a tilt angle, θ, and a lean angle, β, were also built into the CAD model to be optimized later. Based on a reverse engineering study analyzing different engine blade geometries [34], the tilt angle can vary from 0 to 0.164°, and the lean angle can vary from −0.086° to 0.086° in the optimization study. A schematic plot of these angles is shown in Figure 5b.

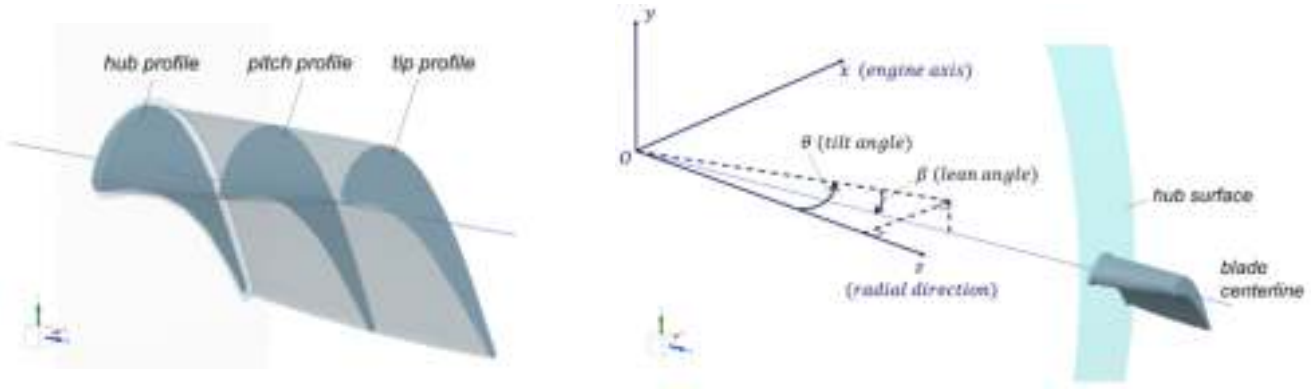

(**a**) (**b**)

Figure 5. Blade geometry schematics: (**a**) blade geometry adapted from E3 profile coordinates; (**b**) blade angles schematic.

Using the 3D blade, a single-blade passage CFD model was developed using Siemens multi-physics package Simcenter STAR-CCM+. The continuity, momentum, and fluid energy transport equations are solved using a coupled solver (density-based) following a finite volume approach with a 2nd order upwind discretization scheme on a polyhedral grid. Menter's SST K-Omega model [35] with all y+ treatment is used as a closure to the turbulence model. The all y+ wall treatment adjusts the application of a turbulence wall function based on the local y+ value of the near wall mesh cell. The CFD simulations were performed using the test conditions. Following E3 engine rotor testing conditions and 2D CFD practices from NASA studies [28,29], a total pressure of 344,777 Pa and a total temperature of 709 K were used for the inlet boundary condition, while an atmospheric pressure of 101,325 Pa was defined at the outlet. The same boundary conditions representing the engine testing conditions were also applied in the previous 2D CFD simulations in [7]. (These 2D CFD datasets were used to develop ANN models in the present work.) A grid sequencing method was used to provide initial conditions, by solving inviscid flow equations repeatedly on a set of gradually refined mesh grids. Automatic CFL number control was also applied to adjust the CFL number in response to linear solver convergence behavior during the algebraic multigrid procedure. To ensure overall solution convergence is reached, in addition to monitoring the residuals of the governing fluid equations, stopping criteria were also set based on the asymptotic values of engineering quantities, such as isentropic efficiency, power output, maximum surface temperature, and total pressure difference.

The CFD methodology has been applied in a previous study based on a 2D version of the E3 blade and validated against other experimental and numerical results of the E3 blade [7]. In the present study, a grid independence investigation has also been performed for the 3D CFD. Three sets of CFD grids with different resolutions were tested. The chosen grid features 12 million polyhedral cells with near-wall y+ values all below 1.4, based on which the solution calculates a baseline efficiency of 96.0% and a power of 5.638×10^4 W. (Note power is calculated based on the single blade CFD model in the current study, which has a pie sector angle of 4.737°). The relative difference between the chosen grid and its next-level refined grid is 0.1% for efficiency and 0.02% for power.

2.3. Optimization Strategy

The present study adopts a nested optimization process. The nested optimization is a slight variation of a previous co-optimization strategy introduced in [7]. The nested optimization accomplishes two essential tasks. First, because an ANN model calculation consumes significantly less computing resources and time than a 3D CFD run, nesting an inner optimization based on the ANN model can effectively utilize the time while waiting for a 3D CFD run to complete. For each 3D CFD simulation run, 250 evaluations of different blade cross-sectional profiles were completed in the inner optimization loop using the ANN model. Second, the inner, ANN-driven optimization passes the best blade profile of the present optimization cycle to the 3D CFD run. This architecture effectively allows using the ANN-driven optimization to guide the 3D CFD search, and thus reduces the number of 3D CFD runs compared to an optimization process that is solely based on evaluating 3D CFD models.

The goal of the optimization is to maximize blade efficiency, η, and power output, Pow. The design variables that are being explored in optimization are the ones discussed in the previous session, $w_{u,1}$, $w_{u,2}$, …, $w_{u,10}$, $w_{l,1}$, $w_{l,2}$, …, $w_{l,10}$, $\xi_{hub,l}$, $\xi_{hub,u}$, $\xi_{tip,l}$, $\xi_{tip,u}$, θ and β. The optimization procedure repeatedly executes the ANN and CFD models to evaluate different blade design variants, while extracting performance metrics to search for better designs. As the ANN model is much less computationally expensive compared to CFD, it is leveraged in an optimization loop by itself to yield optimized cross-sectional blade profiles, which are subsequently used to construct 3D shapes for CFD simulations. Using the ANN embedded optimization to guide the search for the best blade profiles allows for reducing the number of expensive CFD evaluations. As such, a nested optimization workflow is constructed, as illustrated in Figure 6. The workflow is realized using commercial optimization software Simcenter HEEDS and its Sherpa optimization algorithm [30] is used in both Optimizer 1 and Optimizer 2. The Sherpa algorithm constantly evaluates the characteristics of the problem by using a hybrid combination of search strategies at each stage of the optimization process to best traverse the design landscape. In addition, it also adapts the tuning parameters of the search strategies to the specific region of the search. The HEEDS' Sherpa algorithm has been effectively applied to optimize gas turbine applications, as shown in studies [5–7].

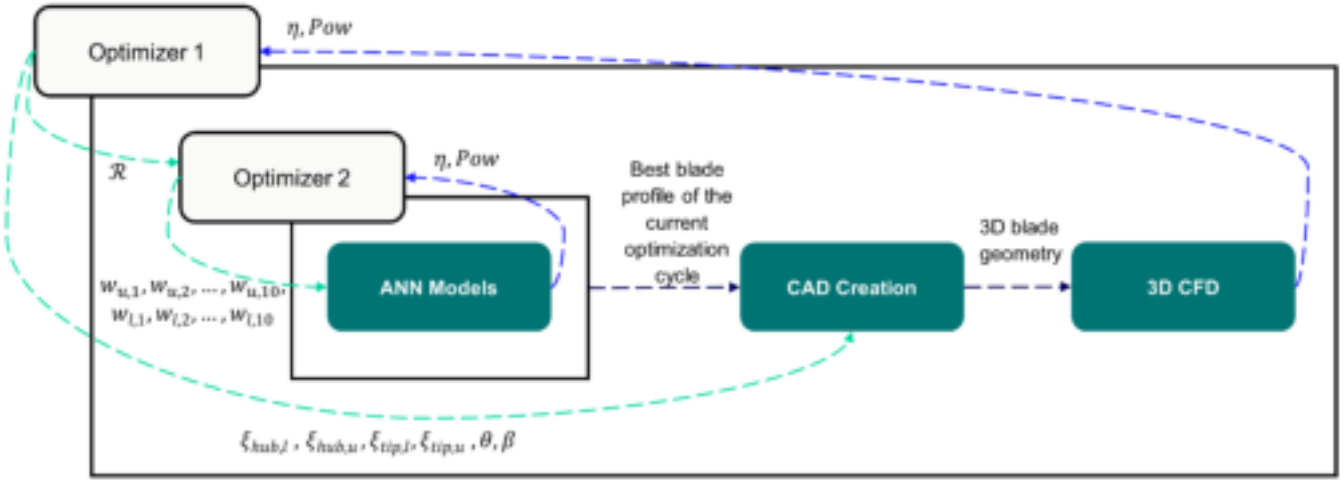

Figure 6. Optimization iteration hierarchy and data flow.

In the global optimization loop (Optimizer 1 as shown in Figure 6), a multi-objective trade-off problem is solved targeting maximizing both efficiency and power. Two constraints are set: efficiency must be greater than 95% and power must also be greater than a baseline power value. These constraints are included in the optimization performance function, based on considerations of practical gas turbine design metrics and general

performance characters of the E^3 engine. The global optimization solver, Optimizer 1, affects the blade shape change by directly optimizing the section scaling factors and blade angles in the CAD. In addition, Optimizer 1 also affects an inner optimization process, which is represented by Optimizer 2. Optimization 1 controls the selection of the CST weights used as input parameters for Optimizer 2, through manipulating a random seed, $\mathcal{R}$, which sets the initial state for the global search strategies employed by the Sherpa algorithm. Although Optimizer 1 does not directly manipulate the CST weights, because $\mathcal{R}$ controls their selection, it acts as a 1D encoding of the entire 20-dimensional design space for Optimizer 1 to explore. Optimizer 1 repeatedly evaluates and optimizes different design variables during the global optimization cycles; in each evaluation cycle, Optimizer 2 optimizes the CST weights using the ANN models, with an objective to maximize the efficiency and a constraint on minimum power value. Overall, 250 blade cross-sectional profiles were evaluated in each execution of Optimizer 2. It directly explores the shape profiles through manipulating the weighting parameters used in the CST method. In each evaluation cycle of Optimizer 1, the best blade profile found by Optimizer 2 is applied in the more expensive and high-fidelity CFD simulation. The performance function in each optimization is defined as the sum of normalized objectives minus the sum of normalized constraints. In a generic form, the performance function is formulated as follows:

$$P = \sum_{i=1}^{i=N_{obj}} \frac{Obj_i}{Norm_i} - \sum_{j=1}^{j=N_{cons}} \frac{10^4 \times ConsViol^2}{Norm_j{}^2}, \quad (3)$$

In the above formula, Obj_i represents the objective quantity, such as η and Pow; $ConsViol$ represents the amount of violation resulted from each constraint definition ($\eta > 0.95$, $Pow > Pow_{baseline}$); the normalization factors Norm are selected using the respective η and Pow values of the baseline design.

3. Results

3.1. Optimization Results

In the present optimization study, a total of 163 blade designs have been evaluated in 3D CFD, with 40,750 2D blade profiles being evaluated by the ANNs. An efficiency vs. power plot showing all 3D blade design points is provided in Figure 7. A Pareto front is formed in the upper right region of Figure 7, which contains optimal designs with the best trade-off relations between efficiency and power. Among the optimal designs, the maximum increase in efficiency is over 3%, and the maximum increase in power is around 8%. To obtain insight into the design variable distributions of the optimal designs, two groups of optimal designs are selected—a group of top 10 high-efficiency designs, and another group of top 10 high power designs. The responses and selected design input variables (which include the two blade angles and four scaling factors) for these two groups of designs are highlighted on a parallel plot in Figure 8. The parallel plot reveals some qualitative trends in the design parameters: (1) both the high-efficiency and high power designs favor large lean angles, β; (2) the high-efficiency designs also favor a large scaling factor for the tip upper surface, $\xi_{tip,u}$, while the high power designs favor a small-to-medium value for $\xi_{tip,u}$; (3) a weaker influence of the scaling factor for the hub lower surface, $\xi_{hub,u}$, is also observed. Note that the lean angle was constrained conservatively within a smaller range in consideration of commercial turbine geometric characteristics provided in [27].

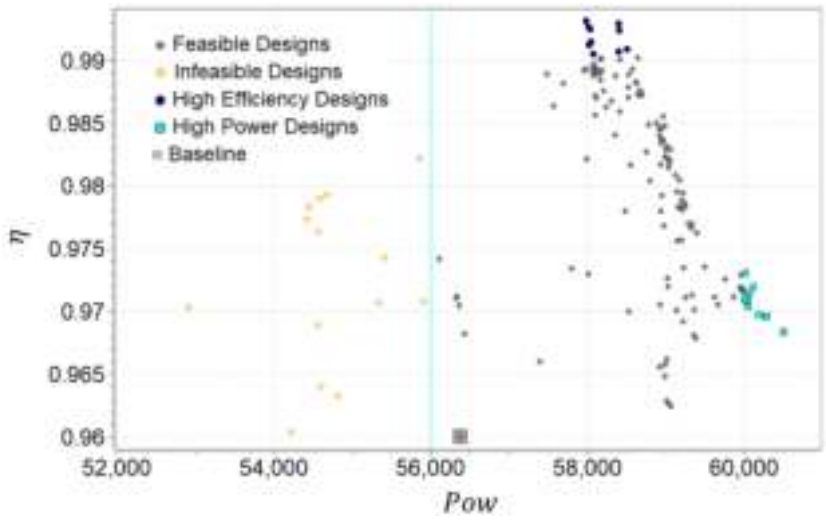

Figure 7. Efficiency vs. power for all designs points in the optimization study.

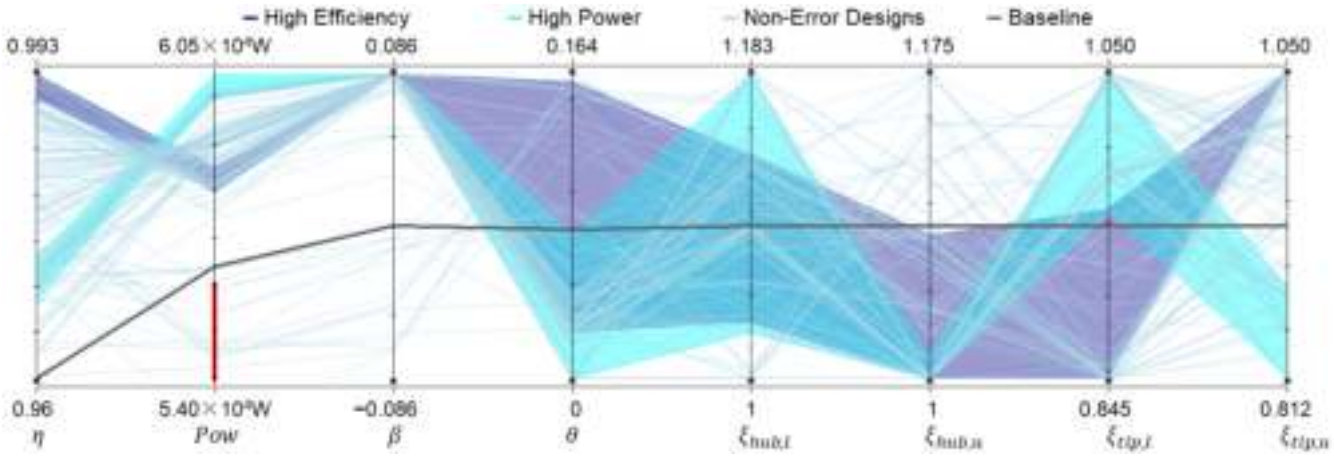

Figure 8. Parallel plot highlighting selected design parameters of different groups of designs.

A quantitative analysis has also been conducted. The Pearson correlation coefficients of the data are calculated, based on the covariance and standard deviations. The definition is given as follows:

$$\mathfrak{r} = \frac{\sum_{i=1}^{n}(x_i - \overline{x})(\mathcal{Y}_i - \overline{\mathcal{Y}})}{\sqrt{\sum_{i=1}^{n}(x_i - \overline{x})^2}\sqrt{\sum_{i=1}^{n}(\mathcal{Y}_i - \overline{\mathcal{Y}})^2}}, \tag{4}$$

In the above formula, $x,\ \mathcal{Y} \in \left\{\eta,\ Pow,\ \beta,\ \theta,\ \xi_{hub,l},\ \xi_{hub,u},\ \xi_{tip,l},\ \xi_{tip,u}\right\},\ (\ x \neq \mathcal{Y})$. x_i and $\mathcal{Y}_i$ represent sample values corresponding to each blade design, and n is the total number of designs, which is 163 in the present study. The Pearson correlation coefficients, the histogram distributions of selected parameters, and the data sample plots are shown on a correlation plot in Figure 9, respectively, on the upper right region, along the diagonal line joining the upper left and lower right corners, and on the lower left region. Large magnitudes of the Pearson correlation coefficients for $\{\xi_{tip,u},\ \eta\}$ (1st row, last column) and $\{\beta,\ Pow\}$ (2nd row, 3rd column) indicate strong relationships in these two pairs of variables. The large coefficient values are confirmed by their respective data sample plots of $\xi_{tip,u}$ vs. η (last row, 1st column) and β vs. Pow (3rd row, 2nd column), in which most of the design points follow the linear regression lines closely. In addition, the correlation plot also shows that the effect of the scaling factor for the hub lower surface, $\xi_{hub,u}$, is rather mild.

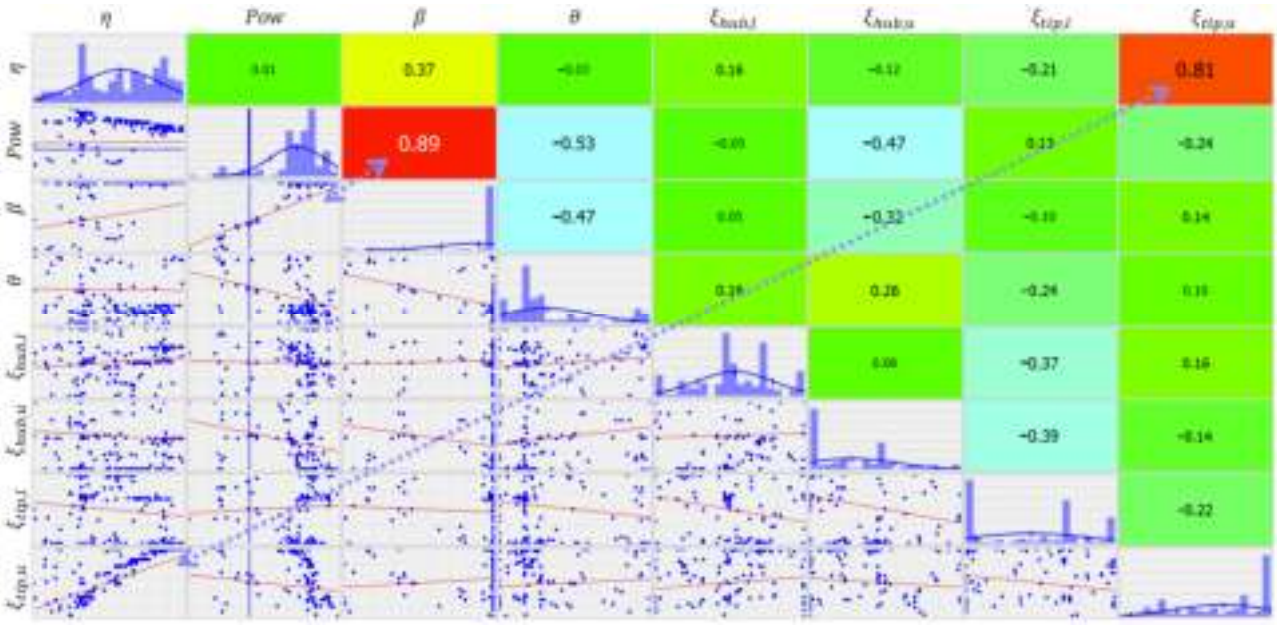

Figure 9. Correlation plot of selected design parameters of all designs. (The two most influential numbers and their corresponding plots are highlighted using the dashed arrows.)

The efficiency and power are plotted versus the two parameters with the strongest correlations, lean angle (β), and tip upper surface scaling factor ($\xi_{tip,u}$), shown in Figure 10. It is observed that (1) most of the improved designs favor larger lean angles, and (2) among the improved designs, a smaller $\xi_{tip,u}$ leads to greater power improvement, while a larger $\xi_{tip,u}$ leads to high-efficiency gain. To analyze the effects of the blade shape and the fluid dynamics, two designs are selected for further investigation—a high-efficiency design and a high power design, which will be referred to as "Design A" and "Design B,", respectively. These two designs are also marked in Figure 10 and will be discussed in the next session.

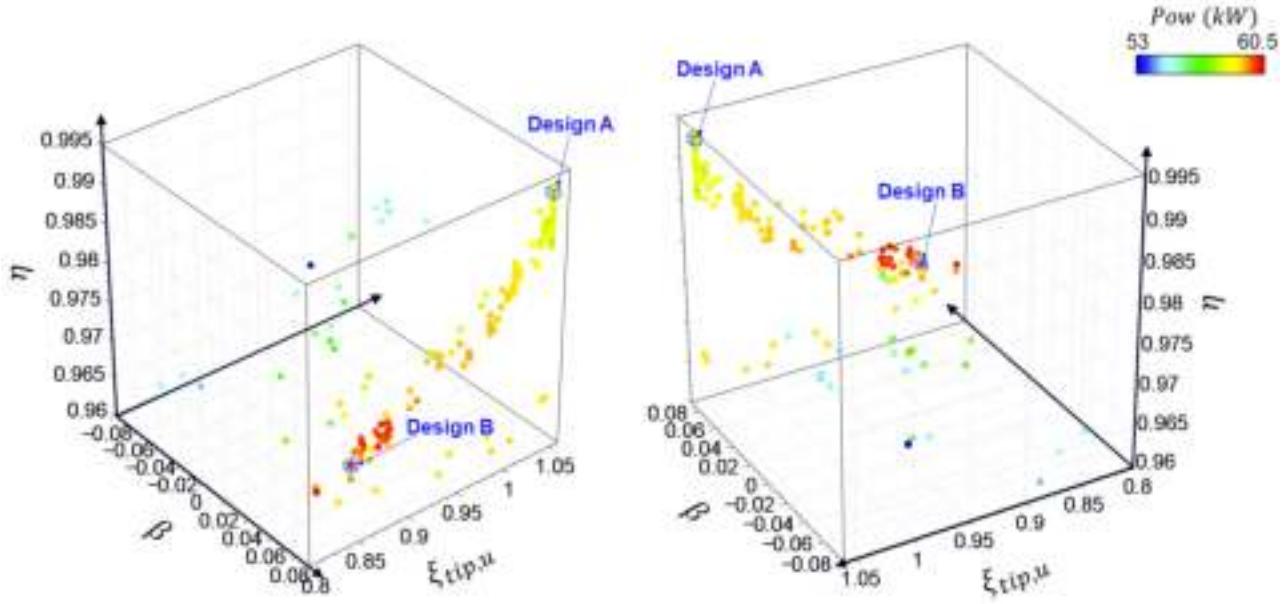

Figure 10. Two views of a 3D plot showing efficiency, power, lean angle, and tip upper surface scaling factor of all designs: (**a**) a normal view; and (**b**) a view obtained by rotating the left-side plot around the η axis by 180°.

The total run time for the optimization process was around 30 h (with six CFD evaluations running in parallel, each consuming 160 compute cores). There are 27 input variables in the global optimization problem. As illustrated in Figure 6, the integration of the inner optimization loop allows for optimizing the 20 blade profile parameters using the inexpensive ANN models. Throughout the optimization process, the ANN models were evaluated 40,750 times; in each optimization cycle, the best blade cross-sectional profile obtained from the inner ANN optimization was passed on to the 3D CFD for evaluation. As a result, the number of design variables being directly exposed in the 3D CFD runs is reduced to six. Since the required number of CFD evaluations largely depends on the number of input variables in an optimization problem, the nested optimization strategy only requires 163 evaluations of 3D CFD simulations. In comparison, if an optimization study of the same problem does not adopt the nested optimization strategy and is solely based on CFD, then all 27 design variables (rather than 6) will be evaluated based on 3D CFD runs. Based on a quick estimation, this will result in 4.5 times (=27/6) the number of CFD runs, which is 733 CFD runs, and will cost roughly 135 h of optimization run time if the same compute resource settings were used.

3.2. Fluid Dynamics Analysis

Two optimized designs are selected for detailed investigation of the aerodynamic results: a high-efficiency design, and a high-power design (a.k.a. Designs A and B as shown in Figure 9). They are compared with the baseline design. The CFD results show the optimized designs feature less pressure drop on the suction side near the trailing edge. A pressure coefficient is defined based on the average inlet velocity and density:

$$c_p = \frac{p}{\frac{1}{2}\rho_{in}u_{in}^2}, \tag{5}$$

The pressure coefficient distributions on the hub, mid, and tip sections are compared in the upper row of plots in Figure 11. The baseline design shows significant low pressure regions on the suction surface near the trailing edge on all three streamwise sections. In comparison, the two optimized designs saw increased minimum pressure in those areas at the hub and mid sections. An enlarged view of the pressure coefficient distribution on the mid-section near the trailing edge is provided for each design in the lower row of plots in Figure 11. The baseline design features a shock in this region, highlighted by a relatively high pressure spot next to the low pressure zone, which is present inside the dotted circle marked on Figure 11a. This shock feature is absent in the two optimized designs due to the modifications in the blade shapes in those designs. This observation is consistent with the Mach number distributions that will be discussed in a later paragraph.

To further investigate the pressure drop on the suction side near the trailing edge, volumetric renderings of the pressure coefficient scenes are shown in Figure 12, to highlight the flow in the low-pressure regime by focusing on c_p values between -0.35 and -0.1. It is observed that in the optimized designs, lower pressure coefficients are present near the tip, but the pressure coefficient has been increased in the mid-session and nearer the hub. The overall reduction of maximum negative pressure coefficients in the mid and hub regions offsets the effects of increased tip leakage flow in the optimized designs.

Next, the pressure coefficient distributions on the blade surfaces are investigated. Scalar scenes of the pressure coefficients on the baseline, Design A, and Design B blades are shown in Figure 13. A large portion of the suction-side surface in the baseline design features a significantly negative c_p values between -0.35 and -0.23 starting around the three quarters chord. In the optimized designs, the onset of the negative pressure coefficient zone moves upstream, nearer the half chord, yet the magnitude of this zone is much less, with most areas featuring c_p values between -0.12 and 0. To achieve a more quantitative comparison, the pressure coefficient curves along the streamwise direction on the hub, mid, and tip sections of the three blades are plotted and compared, with the plots of the blade profiles, shown in Figure 14. The earlier onsets of the lower pressure coefficient region on

the suction-side surfaces in the two optimized designs are demonstrated by the plots. The earlier onset allows for larger enclosed areas of negative c_p curves for the optimized design, contributing to the power improvements.

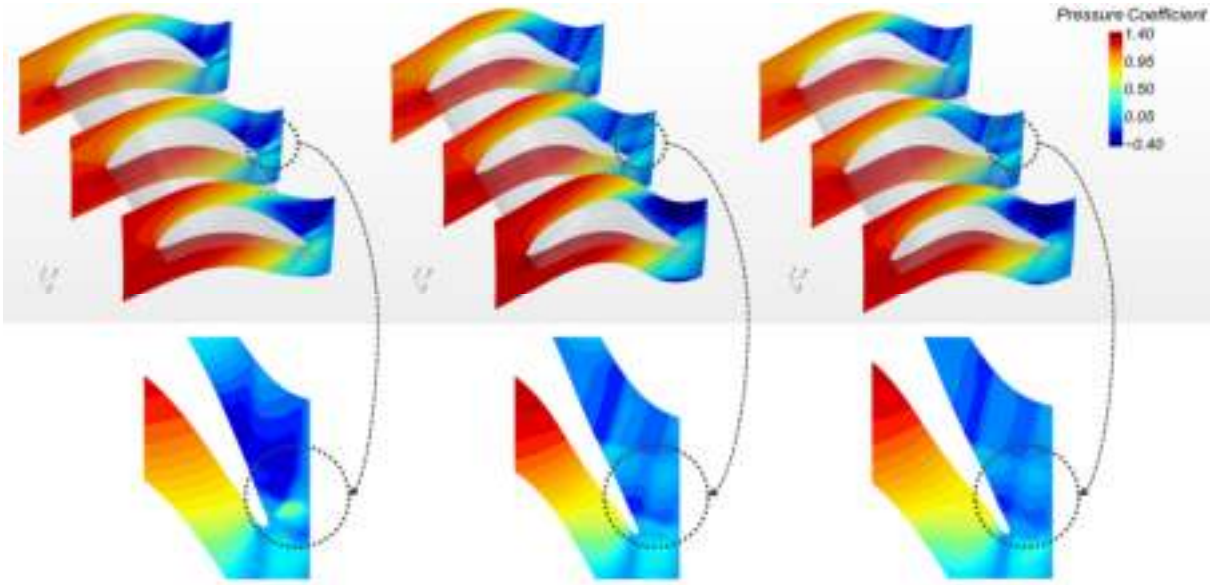

(**a**) (**b**) (**c**)

Figure 11. Static pressure distributions: (**a**) Baseline design; (**b**) Design A; and (**c**) Design B.

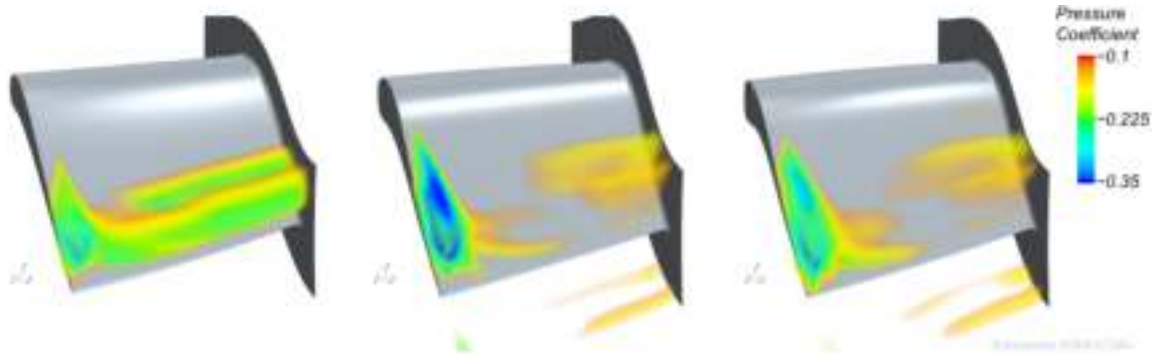

(**a**) (**b**) (**c**)

Figure 12. Static pressure distributions: (**a**) Baseline design; (**b**) Design A; and (**c**) Design B.

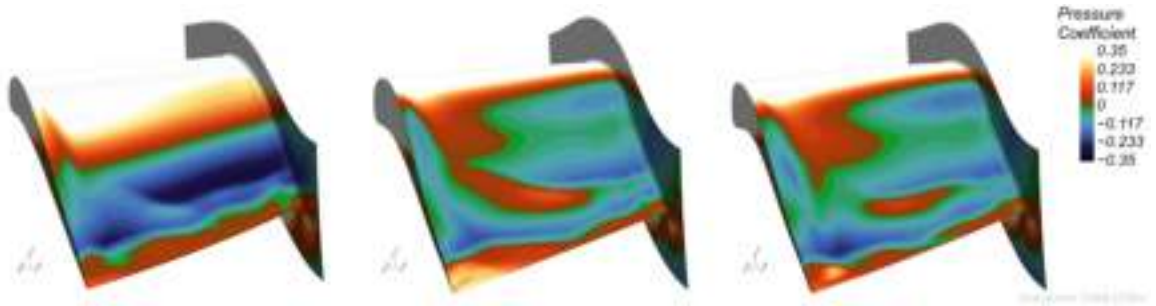

(**a**) (**b**) (**c**)

Figure 13. Pressure coefficient scenes on the surfaces of the blades: (**a**) Baseline design; (**b**) Design A; and (**c**) Design B.

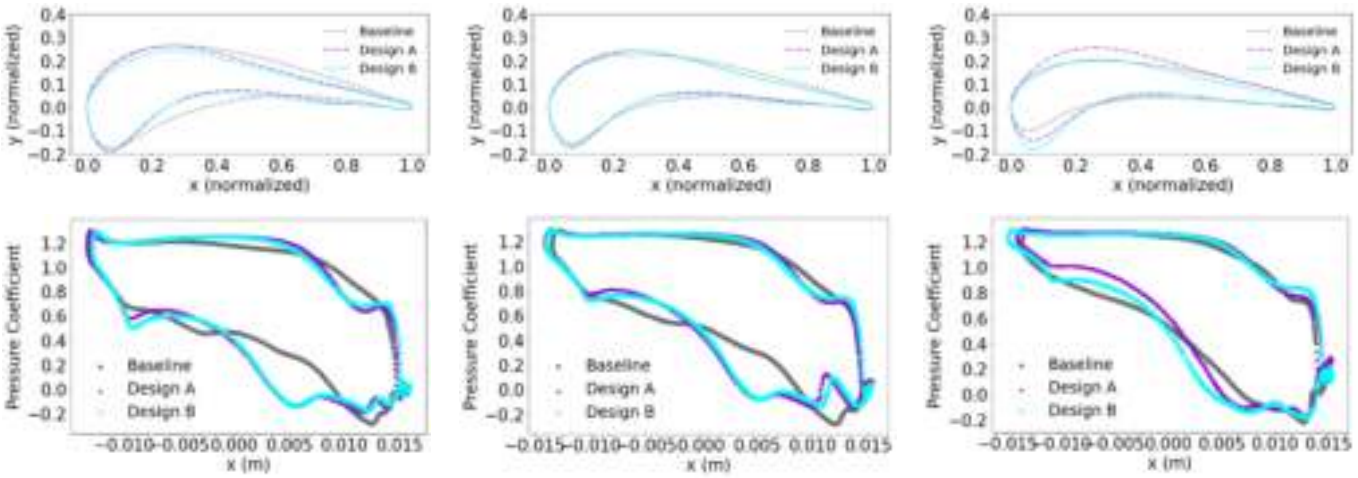

(**a**) (**b**) (**c**)

Figure 14. Blade profiles (first row) and pressure coefficients in the streamwise direction (second row): (**a**) hub sections comparison; (**b**) mid sections comparison; and (**c**) tip sections comparison.

To further investigate the differences in solutions, a volume rendering scene is created by focusing on visualizing changes in Mach number within the range between 0.8 and 1.2, shown in Figure 15. The goal of this plot is to reveal where sudden changes in Mach number may occur in the transonic flow regime. A consistent shock structure near the trailing edge covering the full span length of the blade is observed in the baseline design, which is consistent with the high pressure spot in the same area highlighted by the dotted circle in Figure 11a. This shock feature is missing in the two optimized designs (Designs A and B), due to the weaker gradients in those designs.

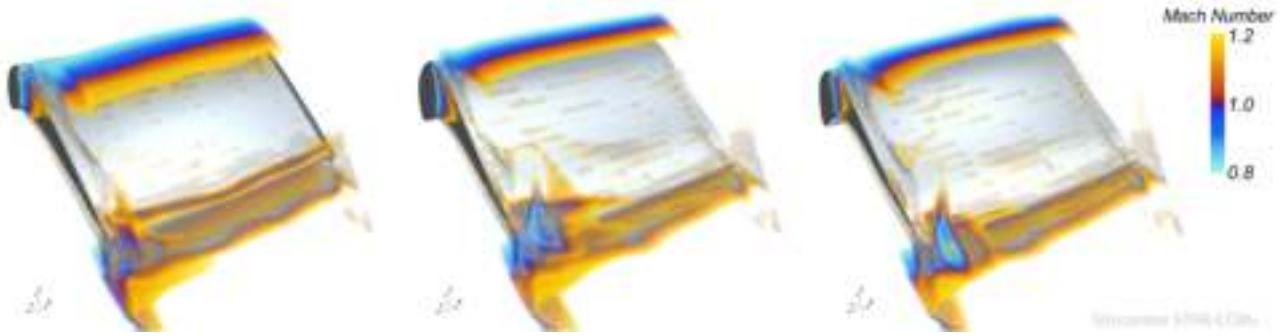

(**a**) (**b**) (**c**)

Figure 15. Mach number rendering: (**a**) Baseline design; (**b**) Design A; and (**c**) Design B.

A further comparison is made by plotting the streamlines in the tip leakage regions and showing pressure coefficients on spanwise cross-sections in Figure 16. It appears the two optimized designs feature slightly more chaotic Mach number distributions in the local region near the trailing edge and tip leakage. The leakage flow's influence on the overall performance is relatively small in comparison to the previously discussed suction-side effects. It can be observed that the streamlines in the high-efficiency design (Design A) are slightly more curved, yet the induced low-pressure spots by the secondary flow effects of the tip leakage flows are weak and about the same magnitude. Overall, the difference caused by the tip leakage flow is small in these three designs. The performance improvements in the optimized designs are more influenced by other flow effects discussed earlier, such as the increased minimum pressure on the suction side near the trailing edge (Figures 11–13), and the reduction of the shock structure (Figure 15).

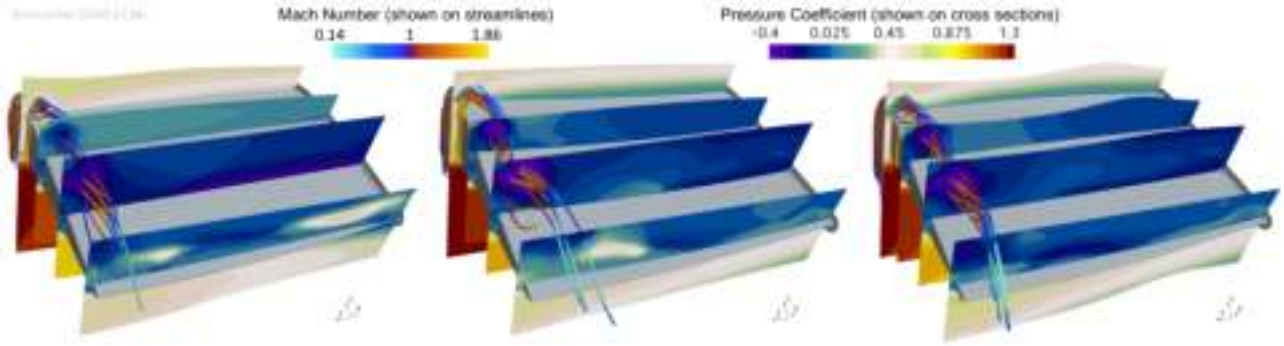

(**a**) (**b**) (**c**)

Figure 16. Tip leakage flow streamlines and pressure coefficients on spanwise cross-sections: (**a**) Baseline design; (**b**) Design A; and (**c**) Design B.

4. Conclusions

The present study has demonstrated an optimization workflow combining the use of neural networks and high-fidelity CFD. The neural network models were trained on over three-thousand design data points from a previous publication. The practical implication of the overall strategy is that in engineering design analysis, existing data sets, which are generally available from the previous simulation, experimental, or reduced-order studies, can be leveraged to build neural network models, which can then be used in combination with high-fidelity CFD simulations to guide optimization processes. This approach achieves a reduction in the required number of high-fidelity CFD runs, and hence reduces the computational cost while maintaining accuracy. The integration of computationally inexpensive ANN models, which were evaluated 40,750 times, allows for a relatively small number (163) of CFD evaluations in the present optimization process, resulting in a total run time of about 30 h (with 6 CFD evaluations running in parallel, each consuming 160 compute cores). It is estimated that if the nested optimization strategy based on ANN was not used, a total number of 733 CFD evaluations will be required due to the large number of design variables exposed in 3D CFD evaluations, resulting in roughly 135 h of the optimization run time if the same compute resource settings were used.

The efficacy of the methodology is demonstrated on a turbine blade aerodynamic problem. ANN models with 7 layers and 6 layers were built to represent two blade performance metrics, efficiency, and power, respectively. The hyperparameters of the ANN models were optimized, and the models were used as surrogate models along with high-fidelity CFD simulations in a nested optimization procedure to obtain optimized blade designs. Pareto front designs representing improved efficiency and power were found by the optimization procedure. A lean angle and a tip scaling factor were shown to be more favored by the optimization procedure than other parameters in the context of the chosen blade and analysis methodology used in the current study. Examining the fluid dynamics of the optimized designs vs. the baseline design reveals that the optimization (1) reduced the magnitude of the most negative pressure coefficients in the flow on the suction side near the trailing edge, and (2) altered the blade geometry that reduced the shock near the trailing edge. Both of these aspects have effects on improved efficiency and power in the optimized designs.

As a future extension of this study, the following may be considered. (1) Test the performance of other response surface methods and meta models against ANN and apply them in the nested optimization workflow. (2) The present study demonstrates a nested ANN-CFD optimization methodology, applied to an idealized turbine CFD problem as a proof-of-concept. In production-level gas turbine designs, more detailed constraints on the geometry or loading curve must be incorporated to ensure more realistic optimization outcomes. Different power output conditions of the engine may also be explored in optimization.

Author Contributions: Conceptualization, C.Z.; methodology, C.Z. and M.J.; software, C.Z. and M.J.; validation, C.Z. and M.J.; formal analysis, C.Z.; investigation, C.Z. and M.J.; resources, C.Z. and M.J.; data curation, C.Z.; writing—original draft preparation, C.Z.; writing—review and editing, C.Z. and M.J.; visualization, C.Z.; supervision, M.J.; project administration, C.Z. and M.J.; funding acquisition, M.J. All authors have read and agreed to the published version of the manuscript.

Funding: This research received no external funding.

Data Availability Statement: Not applicable.

Acknowledgments: This work is a part of the authors' professional development initiatives sponsored by the Simcenter Customer Support organization of Siemens Digital Industries Software. The authors wish to thank their colleagues at Siemens Digital Industries Software. Additional thanks go to Yutao He at Jet Propulsion Laboratory, Caltech, for discussions on the research methodology.

Conflicts of Interest: The authors declare no conflict of interest.

Nomenclature

c_p	pressure coefficient	
h	fluid enthalpy	J/kg
p	pressure	Pa
$\mathcal{P}$	performance function	
Pow	power	W
r	radius	m
$\mathfrak{r}$	Pearson coefficient	
u	velocity	m/s
Δh	enthalpy change	J/kg
w	blade profile parameter	
η	efficiency	
ρ	density	kg/m^3
σ_c	centrifugal stress	Pa
Ω	rotating speed	rad/s
Subscripts		
h	hub	
i	domain inlet	
l	lower surface	
max	maximum quantity	
o	domain outlet	
s	solid	
t	tip	
u	upper surface	

References

1. Alexandrov, N.M.; Lewis, R.M.; Gumbert, G.R.; Green, L.L.; Newman, P.A. Approximation and Model Management in Aerodynamic Optimization with Variable-Fidelity Models. *J. Aircr.* **2001**, *38*, 1093–1101. [CrossRef]
2. Ong, Y.S.; Nair, P.B.; Keane, A.J. Evolutionary Optimization of Computationally Expensive Problems via Surrogate Modeling. *AAIA J.* **2003**, *41*, 687–696. [CrossRef]
3. Mazaheri, K.; Zeinalpour, M.; Bokaei, H.R. Turbine Blade Cooling Passages Optimization Using Reduced Conjugate Heat Transfer Methodology. *Appl. Therm. Eng.* **2016**, *203*, 1228–1236. [CrossRef]
4. Jiang, Y.; Lin, H.; Yue, G.; Zheng, Q.; Xu, X. Aero-Thermal Optimization on Multi-Rows Film Cooling of a Realistic Marine High Pressure Turbine Vane. *Appl. Therm. Eng.* **2016**, *111*, 537–549. [CrossRef]
5. Braining, E.; Weidtmann, K.; Buehler, P.; Lautenschlaeger, A.; Braun, R. Improvement of an Automated Design Process and Investigation of the Optimization Approach and the Dependencies of the Individual Objectives. In Proceedings of the GPPS Forum 18, Global Power and Propulsion Society, GPPS-2018-0027, Montreal, QC, Canada, 7–9 May 2018.
6. Braining, E.; Weidtmann, K.; Braun, R.; Rincon DL, H.; Bohn, D. Automated 2D Airfoil Optimization of Intentionally Choked Blades. In Proceedings of the Global Power and Propulsion Society, GPPS-BJ-2019-0067, Beijing, China, 16–18 September 2019.
7. Zhang, C.; Hodges, J.; Janeway, M. Co-Optimization of Turbine Blade Aero and Thermal Designs Based on Computational Fluid Dynamics (CFD) Models. In Proceedings of the 5th–6th Thermal and Fluids Engineering Conference, New Orleans, LA, USA, 26–28 May 2021.

8. Pierezan, J.; Maidl, G.; Yamao, E.M.; Coelho, L.S.; Mariani, V.C. Cultrual Coyote Optimization Algorithm Applied to a Heavy Duty Gas Turbine Operation. *Energy Convers. Manag.* **2019**, *199*, 111932. [CrossRef]
9. Bettocchi, R.; Pinelli, M.; Spina, P.R.; Venturini, M. Set up of a Robust Neural Netwok for Gas Turbine Simulation. In Proceedings of the ASME Turbo Expo 2004, Power for Land, Sea, and Air, Vienna, Austria, Jun 14–17 June 2004.
10. Li, D.; Qiu, L.; Tao, K.; Zhu, J. Artificial Intelligence Aided Design of Film Cooling Scheme on Turbine Guide Vane. *Propuls. Power Res.* **2020**, *9*, 344–354. [CrossRef]
11. Belov, S.; Nikolaev, S.; Uzhinsky, I. Hybrid Data-Driven and Physics-Based Modeling for Gas Turbine Prescriptive Analytics. *Int. J. Turbomach. Propuls. Power* **2020**, *5*, 29. [CrossRef]
12. Giorgi, M.G.D.; Quarta, M. Hybrid MultiGene Genetic Programing—Artificial Neural Networks Approach for Dynamic Performance Prediction of an Aeroengine. *Aerosp. Sci. Technol.* **2020**, *103*, 105902. [CrossRef]
13. Zhang, M.; Hao, S.; Hou, A. Study on the Intelligent Modeling of the Blade Aerodynamic Force in Compressor Based on Machine Learning. *Mathematics* **2021**, *9*, 476. [CrossRef]
14. Wang, Q.; Yang, L.; Rao, Y. Establishment of a Generalizable Model on a Small-Scale Dataset to Predict the Surface Pressure Distribution of Gas Turbine Blades. *Energy* **2021**, *214*, 118878. [CrossRef]
15. Park, Y.; Choi, M.; Kim, K.; Li, X.; Jung, C.; Na, S.; Choi, G. Prediction of Operating Characteristics for Industrial Gas Turbine Combustor Using an Optimized Artificial Neural Network. *Energy* **2020**, *213*, 118769. [CrossRef]
16. Sun, L.; Liu, T.; Xie, Y.; Zhang, D.; Xia, X. Real-Time Power Prediction Approach for Turbine Using Deep Learning Techniques. *Energy* **2021**, *233*, 121130. [CrossRef]
17. Akolekar, H.; Zhao, Y.; Sandberg, R.D.; Pacciani, R. Integration of Machine Learning and Computational Fluid Dynamics to Develop Turbulence Models for Improved Turbine Wake Mixing Prediction. In Proceedings of the ASME Turbo Expo 2020: Turbomachinery Technical Conference and Exposition, London, UK, 22–26 June 2020.
18. Brunton, S.L.; Kutz, J.N.; Manohar, K.; Aravkin, A.Y.; Morgansen, K.; Klemisch, J.; Goebel, N.; Buttrick, J.; Poskin, J.; Blom-Schieber, A.W.; et al. Data-Driven Aerospace Engineering: Reframing the Industry with Machine Learning. *AIAA J.* **2021**, *59*, 2820–2847. [CrossRef]
19. Wang, H.; Xi, G. Optimization of High Speed Centrifugal Compressor for a Micro Gas Turbine Based on CFD and FEM Analysis. In Proceedings of the ASME Turbo Expo 2010: Power for Land, Sea, and Air, Glasgow, UK, 14–18 June 2010.
20. Maral, H.; Alpman, E.; Kavurmacioglu, L.; Camici, C. A Genetic Algorithm Based Aerothermal Optimization of Tip Carving for an Axial Turbine Blade. *Int. J. Heat Mass Transf.* **2019**, *143*, 11849. [CrossRef]
21. Yan, X.; Zhu, J.; Kuang, M.; Wang, X. Aerodynamic Shape Optimization Using a Novel Optimzer Based on Machine Learning Techniques. *Aerosp. Sci. Technol.* **2019**, *86*, 826–835. [CrossRef]
22. Li, J.; Zhang, M.; Martins, J.R.R.A.; Shu, C. Efficient Aerodynamic Shape Optimization with Deep-Learning-Based Geometric Filtering. *AIAA J.* **2020**, *58*, 4243–4259. [CrossRef]
23. Wang, Y.; Liu, T.; Zhang, D.; Xie, Y. Dual-Convolutional Neural Network Based Aerodynamic Prediction and Multi-Objective Optimization of a Compact Turbine Rotor. *Aerosp. Sci. Technol.* **2021**, *116*, 106869. [CrossRef]
24. Elsayed, K.; Lacor, C. Modeling, Modeling, Analysis and Optimization of Aircyclones Using Artificial Neural Network Response Surface Methodology and CFD Simulation Approaches. *Powder Technol.* **2011**, *212*, 115–133. [CrossRef]
25. Chamoli, S. ANN and RSM Approach for Modeling and Optimization of Designing Parameters for a V down Perforated Baffle Roughened Rectangular channel. *Alex. Eng. J.* **2015**, *54*, 429–446. [CrossRef]
26. Park, D.; Cha, J.; Kim, M.; Go, G.S. Multi-objective Optimization and Comparison of Surrogate Models for Separation Performance of Cyclone Separator Based on CFD, RSM, GMDH-Neural Network, Back Propagation-ANN and Genetic Algorithm. *Eng. Appl. Comput. Fluid Mech.* **2020**, *14*, 180–201. [CrossRef]
27. Halila, E.E.; Lenahan, D.T.; Thomas, T.T. Energy Efficient Engine High Pressure Turbine Test Hardware Detailed Design Report; NASA-CR-167955; NASA Lewis Research Center: 1982. Available online: https://ntrs.nasa.gov/citations/19850002687 (accessed on 25 April 2022).
28. Timko, L.P. Energy Efficient Engine High Pressure Component Test Performance Report; NASA-CR-168289; NASA Lewis Research Center: 1990. Available online: https://ntrs.nasa.gov/citations/19900019237 (accessed on 25 April 2022).
29. Chen, S.-C.S. Axial-Flow Turbine Rotor Discharge-Flow Overexpansion and Limit-Loading Condition, Part 1: Computational Fluid Dynamics (CFD) Investigation; NASA/TM-2017-219506; Glenn Research Center: 2017. Available online: https://ntrs.nasa.gov/citations/20170007293 (accessed on 25 April 2022).
30. Kulfan, B. Universal Parametric Geometry Representation Method. *J. Aircr.* **2008**, *45*, 142–158. [CrossRef]
31. Abadi, M.; Barham, P.; Chen, J.; Chen, Z.; Davis, A.; Dean, J.; Devin, M.; Ghemawat, S.; Irving, G.; Isard, M.; et al. Tensorflow: A system for large-scale machine learning. In Proceedings of the 12th USENIX Conference on Operating Systems Design and Implementation, Savannah, GA, USA, 2–4 November 2016; USENIX Association: Berkeley, CA, USA, 2016; pp. 265–283.
32. Red Cedar Technology. *SHERPA—An Efficient and Robust Optimization/Search Algorithm*; WP-1023, Rev. 05.08; Red Cedar Technology: East Lansing, MI, USA, 2021.
33. Zhang, C. A Python Program—Machine Learning Regression for Gas Turbine Blade Efficiency and Power, Version 1.0.0; Computer software; 2022. Available online: https://github.com/Cool-Chaoz/Machine-Learning-Regression-for-Gas-Turbine-Blade-Efficiency-and-Power (accessed on 25 April 2022).

34. Mohaghegh, K.; Sadeghi, M.H.; Abdullah, A.; Boutorabi, R. Improvement of Reverse-Engineered Turbine Blades Using Construction Geometry. *Int. J. Manuf. Technol.* **2010**, *49*, 675–687. [CrossRef]
35. Menter, F.R. Two-equation eddy-viscosity turbulence modeling for engineering applications. *AIAA J.* **1994**, *32*, 1598–1605. [CrossRef]

International Journal of
Turbomachinery
Propulsion and Power

MDPI

Article

Multi-Channel High-Dimensional Data Analysis with PARAFAC-GA-BP for Nonstationary Mechanical Fault Diagnosis

Hanxin Chen [1,*], Shaoyi Li [1,2] and Menglong Li [1]

[1] Wuhan Institute of Technology, School of Mechanical and Electrical Engineering, Wuhan 430074, China; lisy@ncpu.edu.cn (S.L.); mlong95@163.com (M.L.)
[2] Nanchang Institute of Science and Technology, School of Artificial Intelligence, Nanchang 330108, China
* Correspondence: pg01074075@ntu.edu.sg

Abstract: Conventional signal processing methods such as Principle Component Analysis (PCA) focus on the decomposition of signals in the 2D time–frequency domain. Parallel factor analysis (PARAFAC) is a novel method used to decompose multi-dimensional arrays, which focuses on analyzing the relevant feature information by deleting the duplicated information among the multiple measurement points. In the paper, a novel hybrid intelligent algorithm for the fault diagnosis of a mechanical system was proposed to analyze the multiple vibration signals of the centrifugal pump system and multi-dimensional complex signals created by pressure and flow information. The continuous wavelet transform was applied to analyze the high-dimensional multi-channel signals to construct the 3D tensor, which makes use of the advantages of the parallel factor decomposition to extract feature information of the complex system. The method was validated by diagnosing the nonstationary failure modes under the faulty conditions with impeller blade damage, impeller perforation damage and impeller edge damage. The correspondence between different fault characteristics of a centrifugal pump in a time and frequency information matrix was established. The characteristic frequency ranges of the fault modes are effectively presented. The optimization method for a PARAFAC-BP neural network is proposed using a genetic algorithm (GA) to significantly improve the accuracy of the centrifugal pump fault diagnosis.

Keywords: parallel factor analysis; genetic algorithm; BP neural network; fault diagnosis

check for updates

Citation: Chen, H.; Li, S.; Li, M. Multi-Channel High-Dimensional Data Analysis with PARAFAC-GA-BP for Nonstationary Mechanical Fault Diagnosis. *Int. J. Turbomach. Propuls. Power* **2022**, *7*, 19. https://doi.org/10.3390/ijtpp7030019

Academic Editor: Giorgio Pavesi

Received: 1 February 2022
Accepted: 3 May 2022
Published: 28 June 2022

Publisher's Note: MDPI stays neutral with regard to jurisdictional claims in published maps and institutional affiliations.

Copyright: © 2022 by the authors. Licensee MDPI, Basel, Switzerland. This article is an open access article distributed under the terms and conditions of the Creative Commons Attribution (CC BY-NC-ND) license (https://creativecommons.org/licenses/by-nc-nd/4.0/).

1. Introduction

Mechanical equipment plays a significant role in the construction of the national economy and is an integral part of the entire industrial sector [1]. With the great developments in the improvement of modern production that have taken place, the structures of modern equipment are becoming much more complex. The mechanical equipment needs to remain resilient in severe working conditions. Due to the influence of many unavoidable severe environmental factors, machinery and equipment such as the centrifugal pumps, gearboxes, engines, and other major components that work under a heavy load, high temperature and high pressure experience a variety of the failures. Especially given the extension in their working life, the mechanical components inevitably suffer aging, wear, tear, etc. If failure in the machinery and equipment is not handled promptly, minor damages progress to severe failures, which delays production, causes huge economic losses and serious accidents that endanger the lives of staff [2]. The timely prevention of mechanical equipment failure to maintain the safe operation of equipment in industrial production is of paramount importance.

Centrifugal pumps have excellent properties such as a simple structure, high efficiency and stable performance. They are widely used in industrial production. It is necessary to diagnose and monitor the running status of the centrifugal pumps during the complex industrial process such as in the oil industry, etc. [3]. The current mainstream vibration

signal-based centrifugal pump fault diagnosis method mainly relies on machine learning [4]. Reference [5] selects the time-domain characteristic signal of an electrical submersible pump using the decision tree algorithm and inputs it into a classifier to realize fault separation. Studies in the literature [6] introduce the idea of the k-nearest neighbor algorithm into traditional Markov distance fault judgment to forecast three common centrifugal pump faults. Bordoloi D J et al. used support vector machines to effectively diagnose the blockage level and obstruction cavities at different pump speeds [7]. In the context of Industry 4.0, given the progress in computer science, sensors, cloud technology, big data, etc., the large scale of data collection and the storage of the complex industrial systems are becoming easier and the scale of data is becoming larger, which characterizes the structure of data as high-dimensional. Currently, the processing of high-dimensional data from the large scale industrial processes, which are used to mine valuable information, is a hot topic in the literature [8].

Traditional data-processing methods have a great capability of reducing the dimension of data, such as the Principal Component Analysis (PCA), Intrinsic Modal Analysis (EMD), Wavelet Packet Energy (WPE) and local characteristic analysis (LFA) [9]. Combining the above dimensionality reduction method with a neural network to process massive data and realize data mining has become the mainstream research direction in the research community [10]. C Cui constructed the PCA-BP-MSET model to achieve effective fault warning in an air compressor fault diagnosis system [11]. For abnormalities in the sensor system, Yu used EMD to process the data and PNN as a classifier to achieve fault classification [12]. Compared with the above algorithms, the parallel factorization processing tensor has the advantage of reducing data loss and computational complexity because the tensor represents the properties of the higher order data without damaging the intrinsic structure and underlying information of the data. One of the most promising theories of parallel factorization comes from Kruskal and the new concept of k-order [13]. The k-order for matrix A is the maximum that satisfies the condition that any k column vectors of the matrix A are uncorrelated linearly, which reveals sufficient conditions for the application of the parallel factorization method and lays foundations for its applications in signal processing [14]. Zhang et al. applied PARAFAC decomposition for radar spatial-temporal signal processing to achieve the automatic angle and frequency matching [15]. Li et al. [16] used the parallel factor analysis to deal with the separation of multiple fault sources in the mechanical equipment and achieved the desired results. Sidiropoulos et al. used PARAFAC analysis for the recognition and identification of multiple targets in MIMO radar systems [17]. Weis et al. used the PARAFAC algorithm in their EEG data analysis to determine the individual components of the correlation [18]. Yang et al. constructed tensor using wavelet transform and processed multi-dimensional fault signals with parallel factor theory to achieve effective classification [19].

Genetic algorithm (GA) comes from the idea and mechanism of natural evolution as the optimal parallel search in the laws of biology. It is constructed by simulating the principle of "natural selection and survival of the fittest" in the natural evolutionary process. GA provides a solution to complex nonlinear problems that are not easily solved by the traditional optimization methodology [20]. A genetic algorithm was proposed for combination with the support vector machine (SVM) to achieve the optimal algorithm for fault diagnosis of the rolling bearing machines [21]. The ICA algorithm was implemented for the feature extraction of the signal in the motor bearing, which is combined with GA to optimize the radial basis neural network for fault diagnosis. The diagnostic accuracy was significantly improved [22]. Compared with the traditional neural network (NN), the optimized and improved NN has an optimal network structure and higher accuracy.

This paper investigates the relevant theory relating to signal matrix decomposition and applies continuous wavelet transformation to multi-channel signal analysis to construct a three-dimensional tensor. The parallel factor decomposition achieves the characteristic information extraction of the complex systems, which determine the frequency range of the faulty centrifugal pump. The effective feature frequency information extraction is

combined with the excellent adaptive updating ability and nonlinear characteristics of BP-NN. The BP-NN model is established to diagnose the fault modes of the centrifugal pump. In order to overcome the disadvantage of the slow convergence of the BP-NN, the optimization method based on GA is proposed to optimize the BP neural network model so that it finds the appropriate weights and thresholds at a quicker rate and rapidly achieves fault classification.

2. Principle of Parallel Factor Analysis

Tensor is the high-dimensional form of data construction. The dimensionality of the data is called the order of the tensor and is considered the generalization of the matrix and vector in the high-dimensional spatial construction. Traditional methods such as ICA, PCA, etc. used for processing data with high dimensionality generally spread the data into a two-dimensional matrix for processing to remove the structural data. The solution often fails to achieve the expected results. PARAFAC is a common decomposition treatment in tensor decomposition. The core idea is to approximate the original tensor data by the sum of finite rank-1 tensors.

2.1. Parallel Factor Model

Tensor is a high-dimensional extension of the matrix. The order of the tensor represents the dimensions of the tensor as shown in Figure 1. The vector formed by the one-dimensional time series of the vibration signal collected by the single-channel sensor is the 1st order tensor. The matrix is the 2nd order tensor. The multi-dimensional array above the three-dimensional level is the high-order tensor.

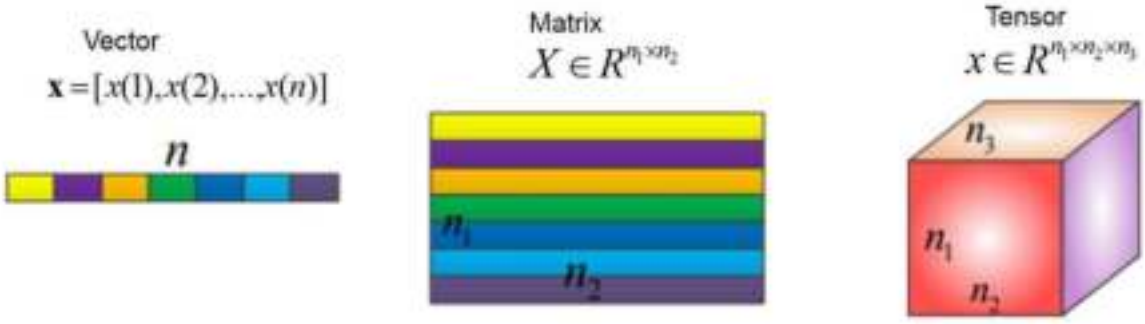

Figure 1. Tensor.

In the two-dimensional matrix, the variable $x_{p,q}$ generally is applied to indicate the components of the two-dimensional matrix that the subscript denotes the x-axis and the subscript q denotes the y-axis during the x—y 2D coordinate system. The variable $x_{p,q,k}$ indicates the element of the three-dimensional matrix that the subscript p denotes x—axis, subscript q denotes y—axis and subscript q denotes z $-$ axis during the x—y—z 3D coordinate system. The 2-D array of the 3D matrix constitutes the subarray of the 3D matrix. The subarray is labeled as the slice of the 3D matrix in the axis. The low-rank decomposition of the matrix is extended to construct the 3D matrix. Let the variable $x_{p,q,k}$ be the elements of the three-dimensional matrix $X \in C^{P \times Q \times K}$, where $p = 1, \cdots, P; \quad q = 1, \cdots, Q; k = 1, \cdots, K$. Three-dimensional matrices can be represented as vector outer product as follows:

$$X = a_1 \circ b_1 \circ c_1 +, \ldots, + a_R \circ b_R \circ c_R = \sum_{r=1}^{R} a_r \circ b_r \circ c_r \tag{1}$$

where $a_r \in C^P b_r \in C^Q c_r \in C^K r = 1, 2, \ldots, R$. Equation (1) provides the low order decomposition process of the 3D matrix. The orders of the 3D matrices X are R. The model for the low-rank decomposition of the 3D matrix as shown in Equation (1) is Parallel Factor Model. Figure 2 shows the procedure of the PARAFAC model.

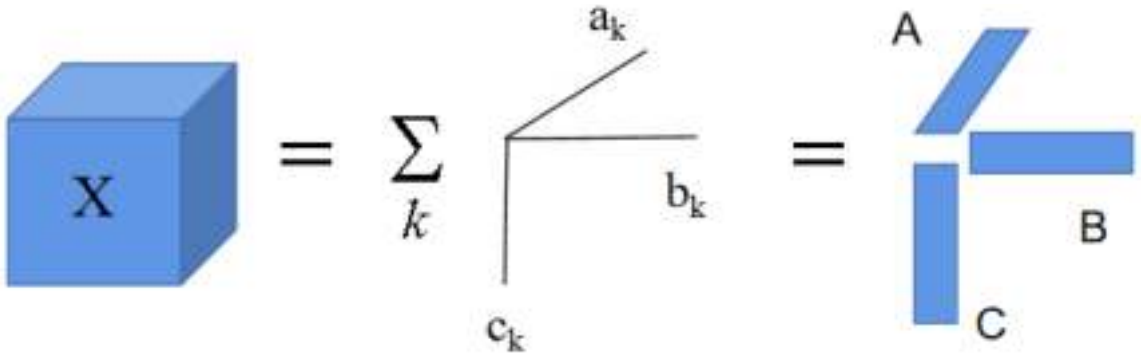

Figure 2. Procedure for Parallel Factor Decomposition.

Here, the definitions of the three matrices are as follows:

$$\begin{aligned} A &= [a_1, \ldots, a_R] \\ B &= [b_1, \ldots, b_R] \\ C &= [c_1, \ldots, c_R] \end{aligned} \tag{2}$$

The symbols A, B, and C are the three loading arrays in the PARAFAC model. Equation (2) shows that the components in the 3D array X are decomposed as the sum of the multiplication of R components.

2.2. Uniqueness of Parallel Factor Decomposition

For a two-dimensional matrix, when the rank of the matrix is greater than 1, the two-dimensional matrix's low-rank decomposition is not unique if there are no special structural constraints. For the matrix decomposition process $X = AB^T$, there exists another set of matrices $\overline{A}$, $\overline{B}$ that is $X = \overline{AB}^T$. However, $\overline{A} \neq A\Pi_A\Delta_A$, $\overline{B} \neq B\Pi_B\Delta_B$, Here, the symbols Π_A and Π_B are column swap matrices and the symbols Δ_A and Δ_B are the diagonal scale matrices. The uniqueness of the two-dimensional matrix decomposition is illustrated by the converse method. Given any full-rank approach $T \in C^{F\times F}$ with

$$X = AB^T = ATT^{-1}B^T = \overline{AB}^T \tag{3}$$

Among them

$$\overline{A} = AT = [\overline{a}_1, \ldots, \overline{a}_F] \tag{4}$$

$$\overline{B} = B(T^{-1})^T = \left[\overline{b}_1, \ldots, \overline{b}_F\right] \tag{5}$$

where $\overline{a}_f$ and $\overline{b}_f$ are the column vectors of the arrays A and B. If the arrays A, B are full rank, $\overline{A}$ and $\overline{B}$ are also full rank matrices, then we have

$$X = \overline{AB}^T = \overline{a_1}\overline{b_1^T} + \overline{a_2}\overline{b_2^T} + \cdots + \overline{a_F}\overline{b_F^T} \tag{6}$$

The above formula satisfies the definition of the low order decomposition. However, $T \neq \Pi\Delta$. Therefore, the 2D matrix low-rank decomposition is not unique.

The fundamental difference between the parallel factorization and the 2D matrix decomposition is the uniqueness of its decomposition, which is one of the reasons that the PARAFAC model is widely used in data analysis. The uniqueness theorem of PARAFAC decomposition comes from the new concept of the k-order. The k-order for a matrix A is the maximum order of k and satisfies the condition that any k column vectors of the array A are linearly uncorrelated, which reveals the sufficient conditions for the uniqueness of the parallel factorization method for application in data analysis. Consider the sub-profile matrix of the PARAFAC model along the X-axis.

$$X_P^{Q\times K} = BD_p(A)C^T \quad p = 1, 2, \ldots, P \tag{7}$$

Here, the matrix is $A \in R^{P\times R}$, $B \in R^{Q\times R}$, $C \in R^{K\times R}$, if the following inequality is satisfied

$$k_A + k_B + k_C \geq 2(R+1) \tag{8}$$

The matrices A, B, and C are unique.

3. Hybrid Method with PARAFAC_GA_BP_NN

3.1. Algorithm on PARAFAC

3.1.1. Nuclear Consistency Estimation

The PARAFAC algorithm is very sensitive to the pre-estimated factor F. When the parameter F is estimated as too low, no physically meaningful solution is obtained. If the parameter F is estimated as too high, it leads to an increase in the model error and makes the deviation between the calibration values and the true values larger. Therefore, a suitable value for factor F is very important for constructing the PARAFAC model. It is necessary to pre-estimate the number of factors. Since the ranks of the tensors are obtained asymptotically, different methods are usually used to evaluate the decomposition factor number from several perspectives. Here, Core Consistency estimation is an effective methodology for the estimation of the factors by calculating the level of the similarity between the super-diagonal array T and the core 3D data array G in the PARAFAC model. The calculation of Core Consistency (δ) is defined as follows:

$$\delta = 100 \times \left(1 - \frac{\sum_{d=1}^{F}\sum_{e=1}^{F}\sum_{f=1}^{F}\left(g_{def} - t_{def}\right)^2}{F} \right) \tag{9}$$

where the parameter F is the factor number in the PARAFAC model, the parameter g_{def} is the element of the matrix G, the parameter t_{def} and is the element of T. For the ideal PARAFAC model, the superdiagonal arrays T and G should be very similar, at which point the kernel agreement value equals 100%. Usually, when the kernel agreement value is equal to or more than 60%, the model is considered to be close to trilinearity. However, when the kernel agreement value is lower than 60%, the model is considered to deviate from trilinearity. A much more accurate factor number is obtained according to the change in the kernel agreement value.

3.1.2. Trilinear Alternating Least Squares (TALS)

$\left|X_{pqk}\right|$ is an arbitrary three-dimensional data set. The two-dimensional matrices defined as $X_p(Q\times K)$, $X_q(P\times K)$ and $X_k(P\times Q)$ that the corresponding elements satisfy the following conditions.

$$X_p(q,k) = X_q(p,k) = X_k(p,q) = X_{pqk} \tag{10}$$

Then, the three-dimensional matrix is described as the joint cubic equation along the three different dimensions.

$$\left\{\begin{array}{l} X_p = Bdiag(A(p,:))C^T, p = 1,2,\ldots,I \\ X_q = Cdiag(B(q,:))A^T, q = 1,2,\ldots,J \\ X_k = Adiag(C(k,:))B^T, k = 1,2,\ldots,K \end{array}\right\} \tag{11}$$

where the variables X_p X_q and X_k denotes the slice of the three-dimensional matrix X in the three directions P, Q and K. The symbol $diag(A(k,:))$ denotes the square matrix after the diagonalization of the kth row elements of the matrix A and so on from Equation (11).

$$\begin{bmatrix} Bdiag(A(1,:))C^T \\ Cdiag(B(2,:))C^T \\ \vdots \\ Adiag(C(I,:))C^T \end{bmatrix} = \begin{bmatrix} Bdiag(A(1,:)) \\ Cdiag(B(2,:)) \\ \vdots \\ Adiag(C(I,:)) \end{bmatrix} C^T = \begin{bmatrix} X_{i=1} \\ X_{i=2} \\ \vdots \\ X_{i=I} \end{bmatrix} = X^{PQ\times K} \tag{12}$$

$$\begin{bmatrix} Bdiag(A(1,:)) \\ Cdiag(B(2,:)) \\ \vdots \\ Adiag(C(I,:)) \end{bmatrix} = A \bullet B \tag{13}$$

Then, the PARAFAC model is expressed in the form of the Khatri-Rao product.

$$\begin{aligned} X^{P\times QK} &= A(B\bullet C)^T \\ X^{Q\times KP} &= B(C\bullet A)^T \\ X^{K\times PQ} &= C(A\bullet B)^T \end{aligned} \tag{14}$$

The basic idea of the TALS method is to update one array at one step by initializing a matrix and updating the remaining matrices using the Least Mean Square (LMS) Method. This step is repeated until the algorithm converges.

The hypothetical 3D dataset X with the dimensions $P \times Q \times K$ is represented by a trilinear model in the following form.

$$x_{p,q,k} = \sum_{f=1}^{F} a_{p,f} b_{q,f} c_{k,f} + e_{pqk} \quad p = 1 \ldots P \quad q = 1 \ldots Q \quad k = 1 \ldots K \tag{15}$$

Here, the symbol F denotes the number of components, the symbol $a_{p,f}$ is the pth component of the vector a_f, the symbol $b_{q,f}$ is the qth component in the vector b_f, the symbol $c_{k,f}$ is the kth component in the vector c_f. The symbol $x_{p,q,k}$ $(p = 1, \ldots, P,\ q = 1, \ldots, Q,\ k = 1, \ldots, K)$. $P \times Q \times K$ forms the three-dimensional space of the data set X. The symbol $e_{pqk}(p = 1, \ldots, P, \quad q = 1, \ldots, Q, \quad k = 1, \ldots, K)$ is the error, which forms the 3D error set E on the $P \times Q \times K$ coordinate system. The symbol $A = [a_1, a_2, \ldots, a_P]$ is defined as a $P \times F$ matrix. $B = [b_1, b_2, \ldots, b_Q]$ is a $Q \times F$ matrix. The symbol $C = [c_1, c_2, \ldots, c_K]$ is a $K \times F$ matrix.

Matrix A is calculated as:

$$\begin{bmatrix} X_{\ldots 1} \\ X_{\ldots 2} \\ \vdots \\ X_{\ldots K} \end{bmatrix} = \begin{bmatrix} BdiagC(1,:) \\ BdiagC(2,:) \\ \vdots \\ BdiagC(K,:) \end{bmatrix} A^T + E_K \tag{16}$$

Here, $X_{\ldots k} = Bdiag(C(k,:))A^T + E_{\ldots k}, \quad k = 1, 2, \ldots, K$, E_k is the error.

The least mean square estimate of the matrix A^T is determined by the following equation.

$$\hat{A}^T = \begin{bmatrix} BdiagC(1,:) \\ BdiagC(2,:) \\ \vdots \\ BdiagC(K,:) \end{bmatrix}^{+} \begin{bmatrix} X_{\ldots 1} \\ X_{\ldots 2} \\ \vdots \\ X_{\ldots K} \end{bmatrix} \tag{17}$$

Here, $[\ ]^{+}$ is the generalized inverse.

The matrix B is determined as:

$$\begin{bmatrix} Y_{\ldots 1} \\ Y_{\ldots 2} \\ \vdots \\ Y_{\ldots P} \end{bmatrix} = \begin{bmatrix} CdiagA(1,:) \\ CdiagA(2,:) \\ \vdots \\ CdiagA(P,:) \end{bmatrix} B^T + E_P \tag{18}$$

Here, $Y_{\ldots p} = Cdiag(A(p,:))B^T + E_{\ldots p}, \quad p = 1, 2, \ldots, P$, E_P is the error.
The least mean square estimate of the matrix B^T is defined as:

$$\hat{B}^T = \begin{bmatrix} CdiagA(1,:) \\ CdiagA(2,:) \\ \vdots \\ CdiagA(P,:) \end{bmatrix}^+ \begin{bmatrix} Y_{\ldots 1} \\ Y_{\ldots 2} \\ \vdots \\ Y_{\ldots P} \end{bmatrix} \tag{19}$$

The matrix C is determined as follows.

$$\begin{bmatrix} Z_{\ldots 1} \\ Z_{\ldots 2} \\ \vdots \\ Z_{\ldots Q} \end{bmatrix} = \begin{bmatrix} AdiagB(1,:) \\ AdiagB(2,:) \\ \vdots \\ AdiagB(Q,:) \end{bmatrix} C^T + E_Q \tag{20}$$

Here, $Z_{\ldots q} = Adiag(B(q,:))C^T + E_{\ldots q}, \quad q = 1, 2, \ldots, Q$, E_Q is the error.
The least mean square estimate of the parameter C^T is defined as:

$$\hat{C}^T = \begin{bmatrix} AdiagB(1,:) \\ AdiagB(2,:) \\ \vdots \\ AdiagB(Q,:) \end{bmatrix}^+ \begin{bmatrix} Z_{\ldots 1} \\ Z_{\ldots 2} \\ \vdots \\ Z_{\ldots Q} \end{bmatrix} \tag{21}$$

Loop (1) to (3) are repeated, and the matrix is updated until convergence.

3.1.3. Algorithm Implementation of Parallel Factor Analysis

Each element X_{pqk} of the tensor $X^{P \times Q \times K}$ consists of a trilinear component model as follows:

$$x_{pqk} = \sum_{f=1}^{F} a_{pf} b_{qf} c_{kf} + e_{pqk} \tag{22}$$

In signal processing, the parameter F contributes to the transient response signal, the variable a_{pf} is the value of the f component related to the pth sample information, the variable b_{qf} is the response value of the fth component related to the qth sample information, the variable c_{kf} is the value of the fth component related to the kth sample information. The variables a_{pf}, b_{qf} and c_{kf} are the components of the array A, B and C. The variable e_{pqk} is the measurement error. The above equation is in the form of the PARAFAC model. It can be expressed in terms of three slice matrices that the trilinear model is expressed as in the following form, which is similar to the singular value decomposition in PCA.

$$\begin{aligned} X_{p\ldots}(Q \times K) &= Bdiag(a_p)C^T + E_{p\ldots}(J \times K), p = 1, 2, \ldots, P \\ X_{q\ldots}(K \times P) &= Cdiag(b_q)A^T + E_{q\ldots}(K \times I), q = 1, 2, \ldots, Q \\ X_{k\ldots}(P \times Q) &= Adiag(c_k)B^T + E_{k\ldots}(P \times Q), k = 1, 2, \ldots, K \end{aligned} \tag{23}$$

Here, the parameters a_p, b_q and c_k are the pth row of the array A, the qth row of the array B and the kth row of the array C. The symbols $diag(a_p)$, $diag(b_q)$ and $diag(c_k)$ are diagonal vectors of the $F \times F$ matrix. The parameters a_i, b_j and c_k are the elements of the diagonal vectors. The symbol "T" denotes the transpose of the matrix. The variables

$E_{p\ldots}(Q \times K)$, $E_{q\ldots}(K \times P)$ and $E_{k\ldots}(P \times Q)$ are three slices of the error array. Equation (22) is expressed as a matrix.

$$X = AT^{(F \times FF)}(C \otimes B)^T + E \tag{24}$$

Here, the symbol $\otimes$ is the Kronecker product, the array $T^{(F \times FF)}$ is a two-dimensional matrix of the recombination of the core 3D data frame T. The variable T is a unit diagonal 3D-data array (also called a super diagonal array) with the matrix size ($F \times F \times F$) where the super diagonal element equals 1 and the remaining elements are zero.

In the standard PARAFAC model, the sum of squared residuals (SSR) is the minimization of the loss function, which is defined as:

$$SSR = \sum_{p=1}^{P}\sum_{q=1}^{Q}\sum_{k=1}^{K}\left(x_{pqk} - \sum_{f=1}^{F} a_{pf}b_{qf}c_{kf}\right) = \sum_{p=1}^{P}\sum_{q=1}^{Q}\sum_{k=1}^{K} e_{pqk}^2 \tag{25}$$

PARAFAC decomposition can be implemented using Alternate Least Squares (ALS) with the following iterative process.

Determining the number of the components F.
Initialize arrays B and C
Solve matrix A.

Solving the estimate $a_p^T = diag\left[B^+ X_{p\ldots}(C^T)^+\right] \quad p = 1, \ldots, P$ of matrix A, which means the vector $diag(\bullet)$ obtains the elements on the main diagonal of the matrix. The superscript "+" indicates the generalized inverse, $B^+ = (B^T B)^{-1} B^T$.

The arrays B and C are estimated by the following equations.

$$b_q^T = diag\left[C^+ X_{q\ldots}(A^T)^+\right], \quad q = 1, \ldots, Q \tag{26}$$

$$c_k^T = diag\left[A^+ X_{k\ldots}(B^T)^+\right], \quad k = 1, \ldots, K \tag{27}$$

Then, (3) and (4) are repeated until the SSR is less than the threshold, which is set by default as 1×10^{-6}.

Based on the unique multi-decomposition in the PARAFAC model, the sub-arrays A, B and C are obtained, which represent the sample information, the response process information and sensing information.

3.2. Algorithm on GA

GA is an evolutionary heuristic algorithm, which was developed from Darwin's natural selection and biological evolution of genetics in 1975. It was originally created to handle large scale and complex optimization problems that could not be solved effectively by classical mathematical methods. The idea of GA is as follows: In a random initialized set, individuals are selected according to their fitness size, and then crossover and mutation by genetics produce new sets that are better than the previous one and also relatively closer to the global optimal solution.

When GA is used to solve a problem, the objective function and variables of the problem are determined firstly and the variables are encoded. The solution to the problem is represented by the strings of numbers in GA. The genetic operator operates directly on the strings. The encoding method is divided into binary encoding and real encoding. If the individual is represented by the binary encoding, the decoding formula for converting binary numbers to decimal numbers is defined as:

$$F(x_{i1}, x_{i2}, \ldots, x_{il}) = R_i + \frac{T_i - R_i}{2^i - 1}\sum_{j=1}^{l} x_{ij}\, 2^{j-1} \tag{28}$$

Here, the parameters $x_{i1}, x_{i2}, \ldots, x_{il}$ are the ith string. The length of each string is l. Each parameter is 0 or 1. The parameters T_i and R_i are the two endpoints of the ith string X_i.

The fundamental procedure of GA consists of selection, crossover and mutation operations. The new population is chosen from the old population with the probability threshold, which is determined by the fitness values. The principle is that the better the fitness value of an individual the higher the probability of a new population. The crossover operation consists of exchanging and combining two chromosomes to produce a new superior individual. The mutation is to select any individual from the population and a point in the chromosome is chosen to b mutated to produce a better individual. In this paper, GA is used to optimize BP to improve the classification diagnosis of centrifugal pumps. The basic implementation process is as follows:

(1) Random initialization of populations.
(2) Calculate the population fitness values from which the optimal individuals are identified.
(3) Select the chromosomes.
(4) Crossover chromosomes.
(5) mutation of chromosomes.
(6) Determine if the evolution is finished, if not, return to step 2.

3.3. Principle on BP_NN

Back Propagation is the multilayer feed-forward NN, which is trained according to the error. It has the broadest applications among NN at present. BP-NN is typical of the forward network and has more than three layers without feedback. There is no interconnection within layers. Its structure is shown in Figure 3. The structure shows that the BP-NN neural network can realize the mapping from an n-dimensional input matrix to an m-dimensional output matrix by connecting the updated weight and threshold. In general, BP_NN uses the Sigmoid function or linear function as the transfer function.

$$f(x) = \frac{1}{1 + e^{-x}} \tag{29}$$

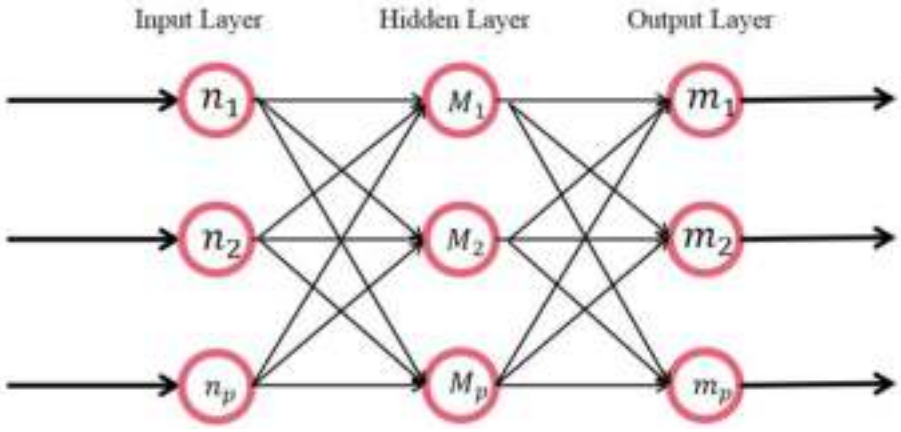

Figure 3. Structure of BP_NN.

In the BP_NN model, the node number of the hidden layer has a great influence on diagnostic accuracy. A smaller number of nodes reduces the ability of the net to learn, which required an increase in the number of training cycles. Too many nodes makes the training time longer, meaning that overfitting can easily occur. Reference [23] points out that the optimal number of hidden layer nodes must exist. For the exploration of this number of nodes, many scholars have given various solutions [24–26], including the use of the experimental method, the introduction of the hyperplane, dynamic full parameter self-adjustment and so on. A series of empirical formulas are obtained. After

the summary, the optimal number of hidden layer nodes can be obtained. Refer to the following formula [24–26]:

$$\begin{aligned} l &< \sqrt{m+n} + a \\ l &= \log_2^n \end{aligned} \tag{30}$$

Here, the parameter n is the number of nodes on the input level, the variable l is the number of nodes on the intermediate level, the variable m is the number of nodes on the output level and the variable a is a constant between 0 and 10. In the paper, the input nodes (n) equal 8, the output nodes (m) equal 4 and the nodes of intermediate level are set to be 3.

4. Experimental System of Centrifugal Pump

The industrial experimental system of the slurry pump is shown in Figure 4. The model for the centrifugal pump in the experiment is Weir/Warman 3/2 CAH with a closed impeller that is C2147. The diameter of the impeller is 8.5 inches. The centrifugal pump is driven by the motor. There is a V-belt drive between the motor and the centrifugal pump with a transmission ratio of 13/6. The parameters of the motor are shown in Table 1.

Figure 4. Centrifugal pump experimental system.

Table 1. Motor parameters.

Model	Rated Voltage (V)	Maximum Speed (RPM)	Rated Speed (RPM)	Rated Ambient Temperature (°C)	Rated Power (HP)	Overload Factor	Motor Size
	230/460	1200	1180	40	40	1.15	362 T

The vibration signal acquisition system is shown in Figure 5, which mainly consists of a signal analyzer and a laptop computer for storing data. The system acquires multiple channel signals including 3-axis vibration, acoustics, flow, pressure and temperature. The following conditions are satisfied for the acquisition of the experimental data.

(1) Data collection does not begin until the centrifugal pump is running smoothly.
(2) The sampling frequency satisfies the sampling theorem.
(3) Multiple sets of data are collected for experiments conducted in each state.

Figure 5. Data acquisition system.

In order to collect nonlinear multi-fault-mode characteristic signals, when the centrifugal pump is running steadily, the motor speed is set to be 1200 rpm for data acquisition. The data acquisition time of each group is 20 s. The sampling frequency is 9 kHz. The system synchronously collects online data on the vibration, acoustics, flow, pressure, etc. The nonlinear operation state of the machinery during the industrial process is simulated by controlling the flow rate and pressure of flow during the processing circuit, which consists of the nonlinear and nonstationary multi-failure mode.

5. Simulated Signal for PARAFAC Analysis

Considering that the vibration signals acquired in the condition monitoring of mechanical equipment in the practical industrial environment generally were corrupted by the heavy noise signals, the typical numerical signal is generated to simulate the characteristic vibration information in the fault diagnosis of a mechanical system by using Equation (31), which is used to assess the effectiveness of the proposed method based on PAFARAF and continuous wavelet transform (CWT). The simulated signal consists of impulse signals when the fault occurs in the equipment and Gaussian White Noise (GWN) with 1 dB signal-to-noise ratio (SNR).

$$\begin{cases} x(t) = s(t) + n(t) \\ s(t) = \sum\limits_{i} (1 + 0.2\cos(2 * pi * f_r t)) e^{-700(t - i/f_i)} \cos(2 * pi * f_n(t - i/f_i)) \end{cases} \tag{31}$$

Here, the function $s(t)$ is the periodic shock signal, the symbols f_r and f_i are the rotation frequency and faulty frequency, which are 30 Hz and 200 Hz. The inherent frequency f_n is 2000 Hz. The symbol $n(t)$ denotes the noise signal. The faulty signal is simulated to consist of the rotational frequency, faulty frequency and intrinsic frequency with noise corruption. The sampling frequency and analysis points are set as follows: $f_s = 12,000$, $N = 8192$. The time and frequency domains of the simulated signal are shown in Figure 6, and it can be found that the fault characteristics are correlated with both the inherent frequency of the system and the rotation frequency of the motor shaft. It can be seen that the frequency components related to the fault characteristics include harmonic frequencies $2f_i$, modulation frequencies $f_n - nf_i$, and other frequencies. The key point for accurate fault identification is to extract the useful frequencies related to the faulty characteristics from the original noise signal.

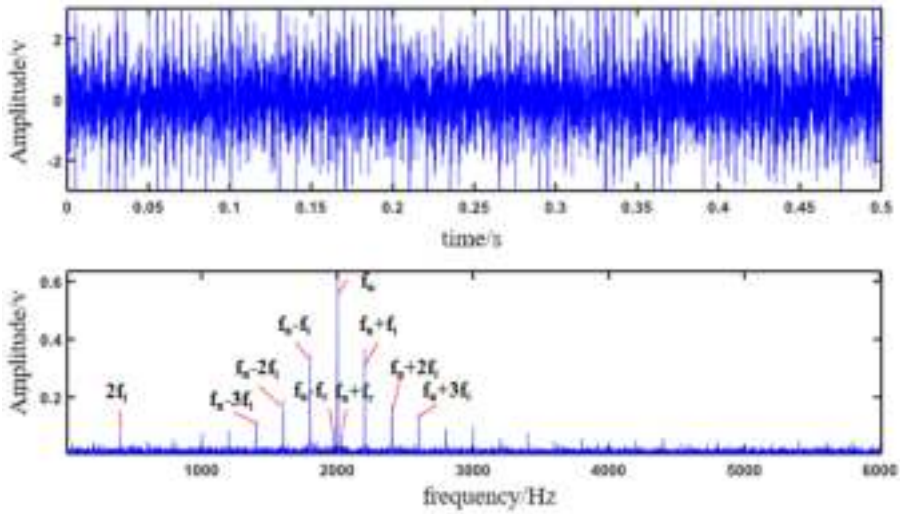

Figure 6. Corrupted simulation signal with noise.

Although the frequency domain of the simulated signal in Figure 6 presents the frequency information related to the fault characteristics, it is buried by heavy noise and inherent frequency-related components. The failure characteristics are buried and located in heavy noise. It is necessary for the corrupted data to be processed to extract the fault characteristic frequencies accurately. CWT is used to analyze the simulated impulse signal. The wavelet basis function is "comr3−3". The center frequency of the wavelet function is 3 Hz. Figure 7 shows the CWT of the simulated signal. However, the fault-related frequency components are not filtered out, which indicates that the traditional time-frequency transformation is not effective enough to extract the weak fault characteristics of the frequency components from the simulated complex noised signal.

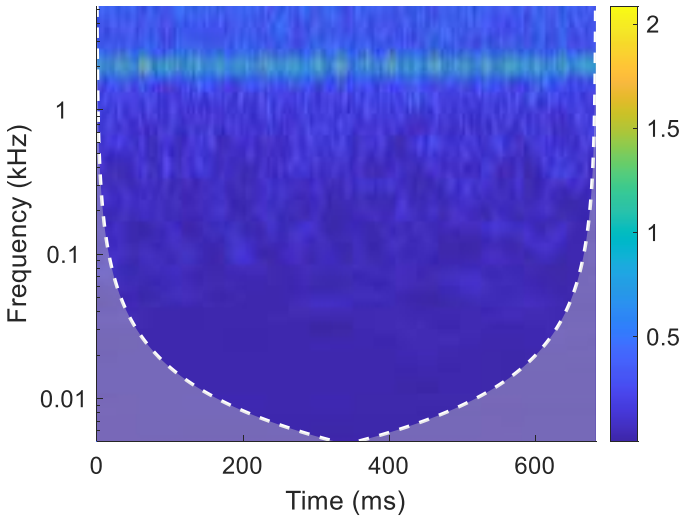

Figure 7. Wavelet transform of the simulated signal.

PARAFAC is a tensor decomposition algorithm and the decomposition is unique. In the case that the tensor models the N-dimensional relationship well, the parallel factor decomposition retains the original characteristic signal to a large extent while the feature caused by the failure component of the mechanical system is extracted effectively from the original complex system information. Based on the advantage of PARAFAC, the wavelet coefficients of the simulated signal after continuous wavelet transform are obtained, which is applied to construct one 3rd-order tensor with the dimension $1 \times 200 \times 8192$. The tensor is decomposed by the parallel factor analysis to extract multiple factor components, which

contain the channel, time and frequency information of the high-dimensional original signal. To build a correct parallel factor model, it is necessary to select the appropriate factor group fraction. The simulated signal determines the factor number F by considering the cross-validation and the kernel consistency method proposed in Section 3.

Figure 8 shows the cross-validation of the simulated signal. When the number of factors F is set to be from 1 to 3, the parallel factor cross-validation of the simulation signal is better in both the fitting group and the validation group. The values of the explanatory variables reach more than 80% and the kernel consistency of the parallel factor model reaches 100%. In summary, it is considered that the number of factors F is chosen as 3 to establish the parallel factor model for the tensor, which is constructed by the simulation signal for the data analysis.

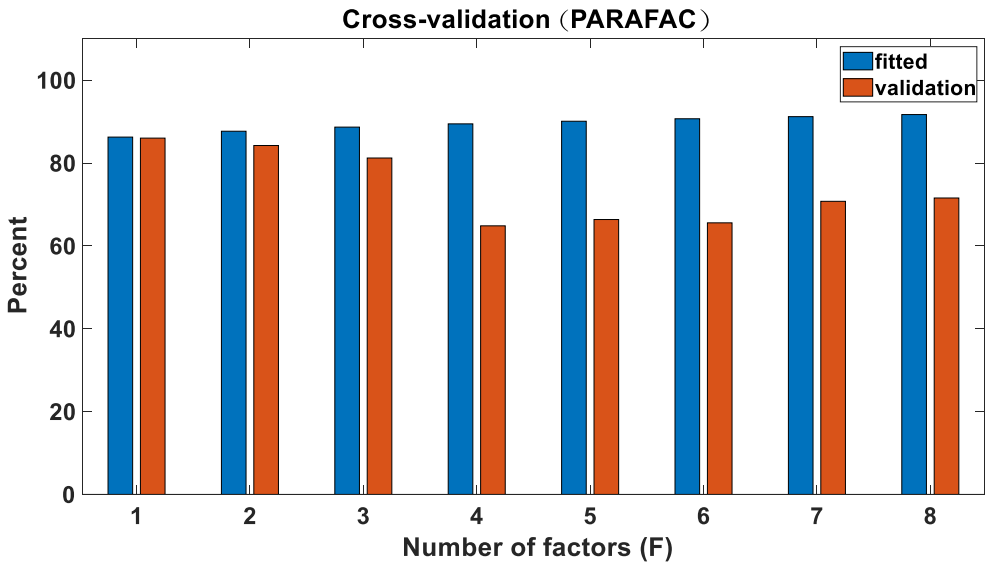

Figure 8. Cross-validation for simulated signal.

Figure 9 shows the three subspaces which are obtained after the parallel factor decomposition of the simulated fault signal with noise addition. The loading values correspond to the channel, time and frequency information of the original signal. The residual values of the model fitting are obtained. The simulated signal is decomposed by PARAFAC into a frequency matrix, time matrix and time–frequency information. The amplitudes corresponding to the simulated impulse signal in the frequency matrix have obvious peaks at frequencies of 2000 Hz and 0~100 Hz, which shows the disadvantage that the low-frequency characteristics associated with the fault component are not clearly extracted. The time–information matrix obtained after the decomposition of the parallel factor is analyzed with the power spectrogram as shown in Figure 10. The comparison between Figure 7 and the results in Figures 9 and 10 verifies that the PARAFAC algorithm has a great advantage in a more accurate and efficient form of feature extraction of the complex corrupted vibration signals in fault diagnosis as compared to the traditional time–frequency domain signal processing methods.

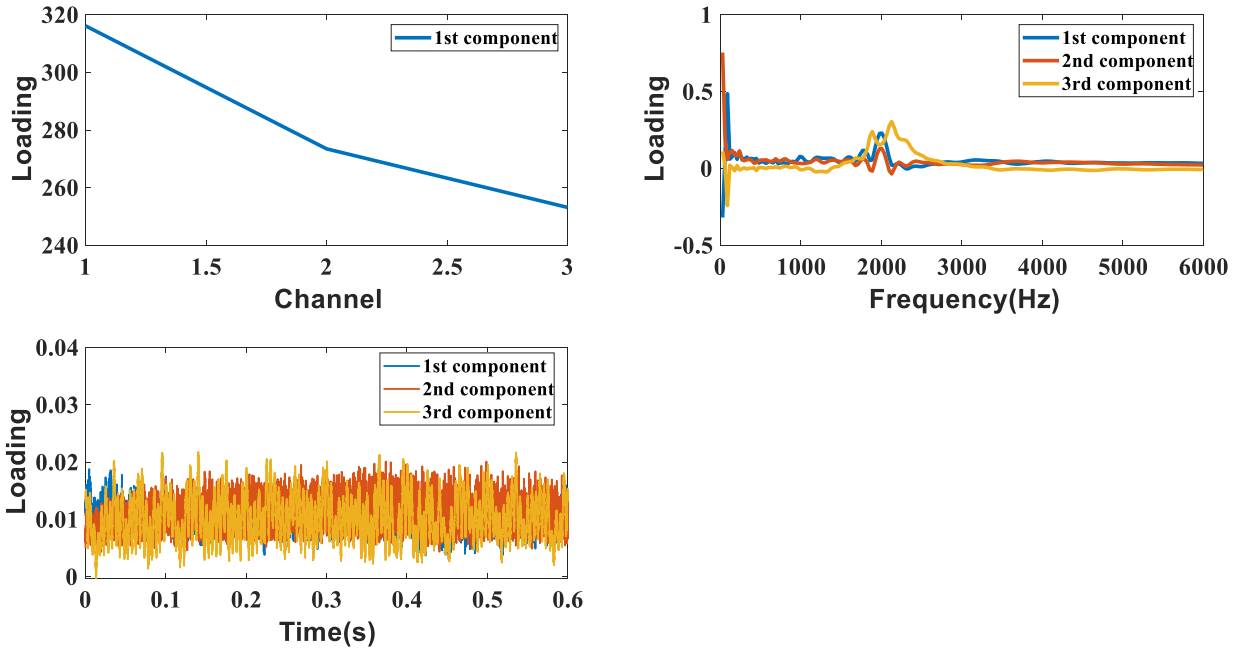

Figure 9. Parallel factor decomposition of simulated signal.

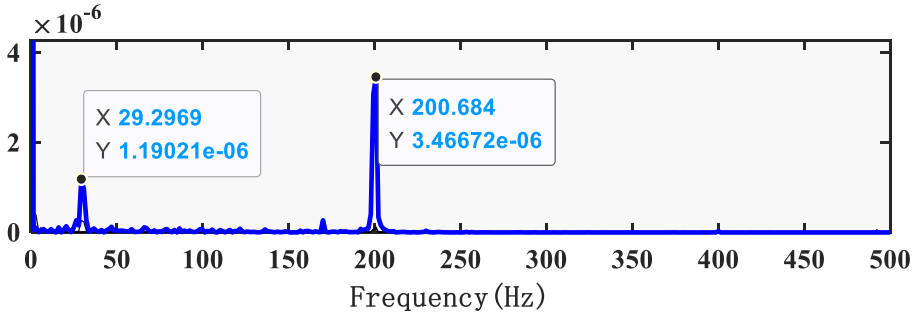

Figure 10. Power spectrum of decomposed time domain loading matrix with PARAFAC.

6. Discussion

Based on the simulated signal analysis as shown in Figures 9 and 10, it has been verified that the time and frequency feature matrices can accurately characterize the fault model information. The multiple dimensional data model can be constructed by containing the acquired data from the accelerometer, flow sensor and pressure sensor, which is analyzed and processed by the PARAFAC algorithm. The time and frequency loading matrices are extracted as the characteristic signals. The forty sets of data are collected from the centrifugal pump system under one of the four running states that are normal (F1), impeller blade damage (F2), impeller edge damage (F3) and impeller perforation damage (F4), which are used to analyze the operation status of the centrifugal pump for the nonlinear multiple fault diagnosis.

Based on Nyquist's sampling theorem, the maximum frequency of the signal spectrum is half of the sample frequency of 4500 Hz. The time for data acquisition in each mode of the impeller in the experiment is 20 s with eighteen thousand data points. A reduction in the complexity of data processing for a better comparison is required, and the proposed PARAFAC algorithm as described in Section 3 is used directly to obtain data points for the four failure modes for feature extraction.

PARAFAC was used to process the test data. We considered the vibration signals, flow signals and pressure signals from the multiple measurement points collected in the above experimental system for a total of the fifteen channel signals. The purpose of choosing 15 data channels is that the 15 physical system variables are sufficient as systematic

characteristics to control the nonstationary operation status. The operating status of the centrifugal pump is evaluated comprehensively from the multiple physical information facets, which makes the fault diagnosis of the centrifugal pump more reasonable and effective.

The number of factors of the PARAFAC model can be determined by choosing the kernel consistent diagnosis method in Section 3. The number of factors ranges from 1 to 8. There are three groups of data to test the factors. Figure 10 shows nuclear consistency estimation.

As shown in Figure 11, when the number of factors is from 1 to 5, the kernel consistency values are above 60%. When the number of factors is greater than 5, the kernel consistency values decrease rapidly by 60%. Therefore, the amount of factors in the PARFAC model is chosen to be 5. The PARAFAC algorithm is solved by the trilinear alternating least squares method. Figure 12 shows the signal analysis by PARAFAC used to obtain the five components in mode 2 under four operating states when the angular speed is 1200 rpm. Mode 2 provides the frequency information. Figure 13 shows the signal analysis by PARAFAC used to obtain the five components in mode 3 under four operating states when the angular speed is 1200 rpm. Model 3 provides the time domain information.

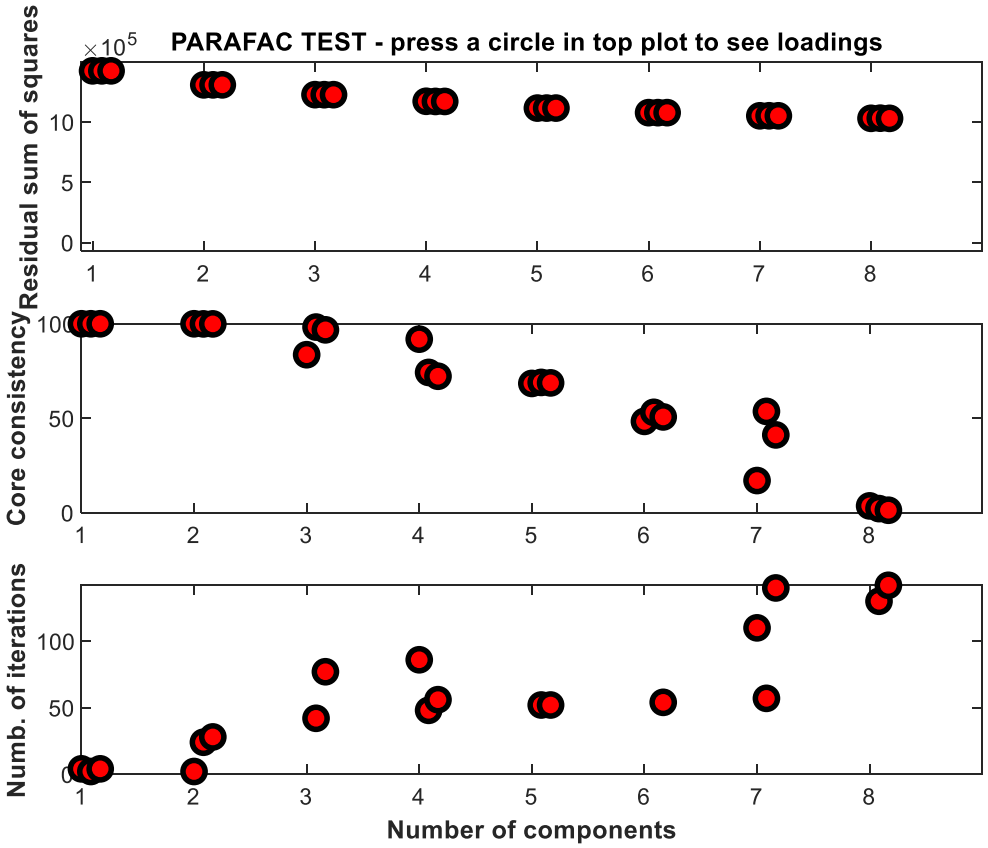

Figure 11. Nuclear consistency estimation.

The multi-channel complex signals are obtained from the centrifugal pump, which are analyzed by parallel factor decomposition to obtain the time and frequency information matrices. The time matrices as shown in Figure 13 are analyzed by Discrete Fourier Transform (DFT) to obtain the frequency domain information. DFT is defined as follows:

$$S(k) = \frac{N-1}{k=0} x(k\Delta tz) e^{\frac{-2\pi jnk}{N}}, (n = 1, 2, \ldots, N-1) \quad (32)$$

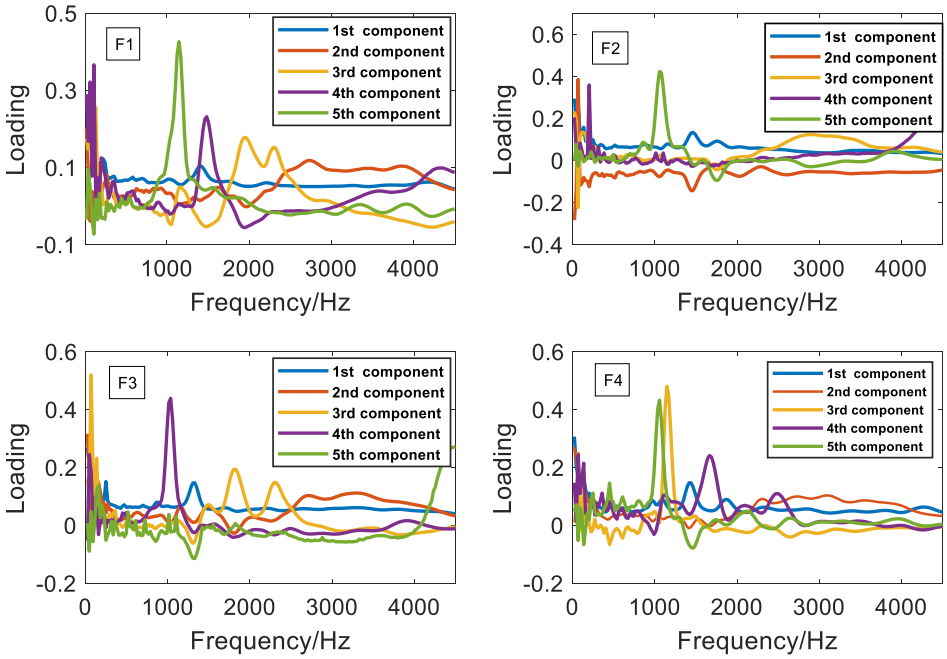

Figure 12. The 1200 rpm centrifugal pump signal decomposition in Mode 2: (**F1**) for normal impeller, (**F2**) for blade damage, (**F3**) for impeller edge damage, (**F4**) for impeller perforation damage.

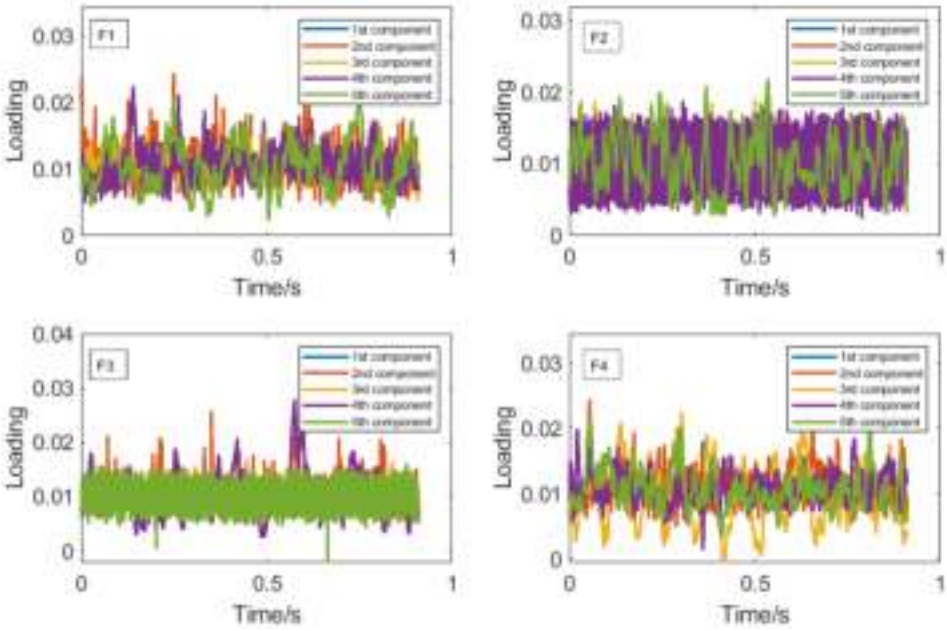

Figure 13. 1200 rpm centrifugal pump signal decomposition in Mode3: (**F1**) for normal impeller, (**F2**) for blade damage, (**F3**) for impeller edge damage, (**F4**) for impeller perforation damage.

Figure 14 shows the spectra frequency of the fourth component under F1 and F2. The characteristic frequency under F2 is 250 Hz. Figure 15 shows the spectra frequency of the fifth component under F1 and F3. The characteristic frequency under F3 is 184 Hz. Figure 16 shows the spectra frequency of the third component under F1 and F4. The characteristic frequency under F4 is 20 Hz. The rotation speed of the motor in this experiment was set to 1200 rpm and the rotation frequency was 20 Hz. It is known that the fault characteristic frequency of the centrifugal pump impeller is generally related to the frequency component of the rotation frequency. The frequency of the impeller blade failure is expressed by the blade passing frequency, which is calculated by multiplying the rotation frequency by the number of blades, which was 20 × 10 = 200 Hz in this paper. Regarding the blade damage

and impeller edge damage mode, the characteristic frequency is approximately distributed around 200 Hz. The characteristic frequency of the impeller perforation damage is 12 Hz, which is about 1/2 of the rotation frequency. Based on the above analysis, it has been verified that the parallel factor algorithm is more effective for the characteristic processing of the centrifugal pump multidimensional signal.

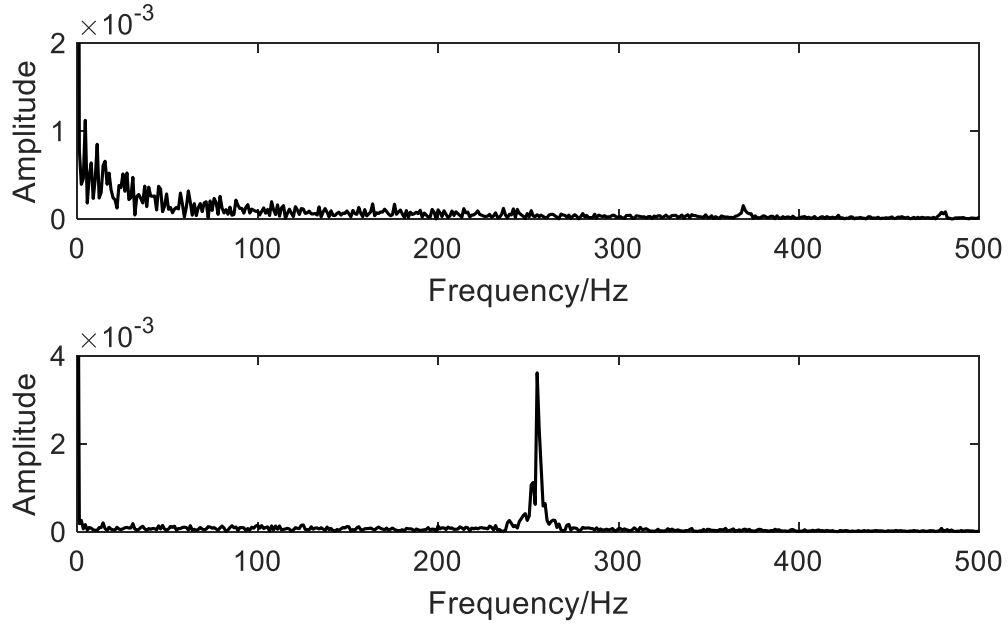

Figure 14. Spectra analysis of fourth component under F1 and F2.

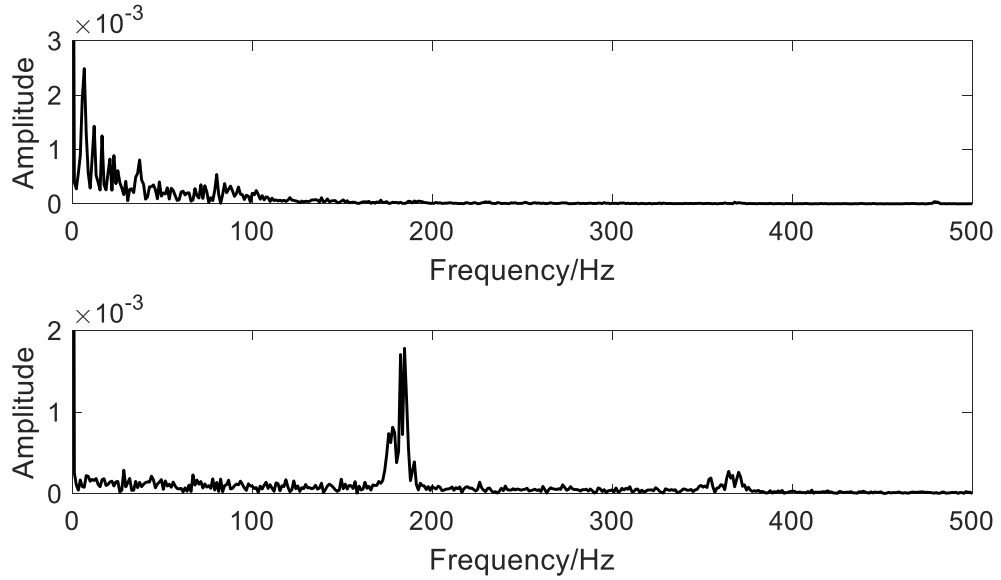

Figure 15. Spectra analysis of fifth component under F1 and F3.

The time–frequency features extracted from the multi-source signals by PARAFAC decomposition are inputted to the BP model as features. The classification accuracy of the model was calculated. The output of the BP model and the corresponding state of the centrifugal pump are shown in Table 2.

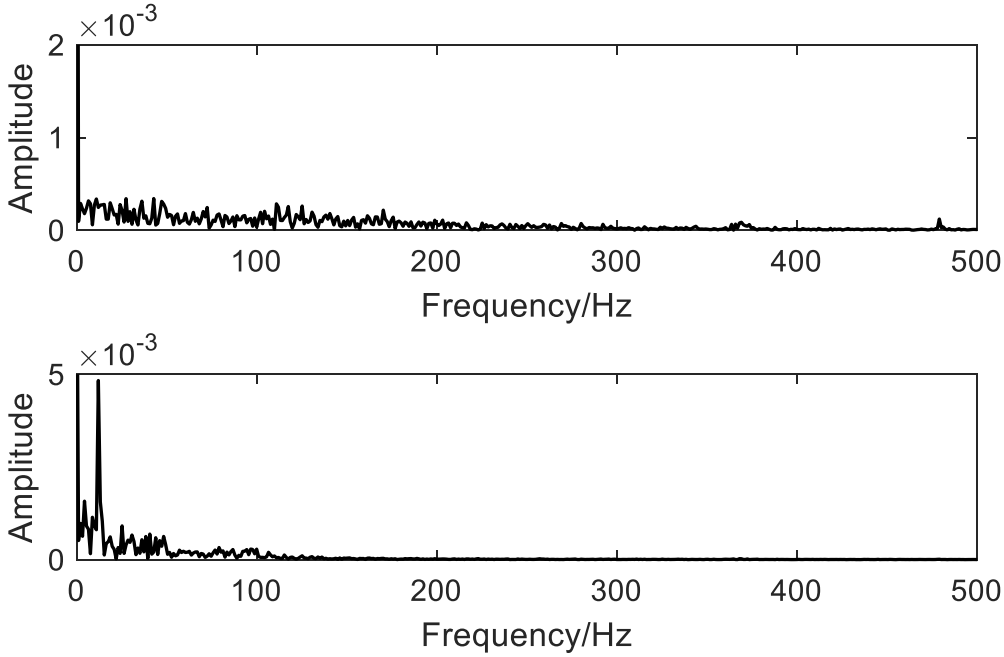

Figure 16. Spectra analysis of third component under F1 and F4.

Table 2. Expected output of neural network corresponding to each state of centrifugal pump.

Output Label	1	2	3	4
F1	1	0	0	0
F2	0	1	0	0
F3	0	0	1	0
F4	0	0	0	1

The eight statistics of each component constitute the feature vectors for subsequent NP_NN and GA_BP_NN classification. The time and frequency domain statistics of each component are calculated as follows:

(1) Center of gravity frequency:

$$F_1 = \frac{\sum_{k=1}^{K} f_s \cdot S(k)}{\sum_{k=1}^{K} S(k)} \tag{33}$$

(2) Root Mean Square (RMS) of spectrum

$$F_2 = \sqrt{\frac{1}{K-1}\sum_{k=1}^{K}\left[S(k) - \frac{1}{K}\sum_{k=1}^{K} S(k)\right]^2} \tag{34}$$

(3) Frequency of root mean square (RMS)

$$F_3 = \sqrt{\frac{\sum_{k=1}^{K} f_k{}^2 \cdot S(k)}{\sum_{k=1}^{k} S(k)}} \tag{35}$$

(4) Peak Factor

$$PF = \frac{\max|x(i)|}{\sqrt{\frac{1}{N}\sum_{i=1}^{N} x(i)^2}} \tag{36}$$

Clearance Factor

$$CLF = \frac{\max|x(i)|}{\left(\frac{1}{N}\sum_{i=1}^{N}\sqrt{|x(i)|}\right)^2} \tag{37}$$

Waveform Factor

$$WF = \frac{\sqrt{\frac{1}{N}\sum_{i=1}^{N} x_i^2}}{\frac{1}{N}\sum_{i=1}^{N}|x(i)|} \tag{38}$$

Impulse Factor

$$IF = \frac{\max|x(i)|}{\frac{1}{N}\sum_{i=1}^{N}|x(i)|} \tag{39}$$

Kurtosis Factor

$$KF = \frac{\sum_{i=1}^{N}(x(i)-\overline{x})^4 \; N}{\left(\sqrt{\frac{\sum_{i=1}^{N}(x(i)-\overline{x})}{N}}\right)^4 \cdot \left(\sqrt{\frac{1}{N}\sum_{i=1}^{N} x_i^2}\right)^4} \tag{40}$$

Figure 17 shows the diagnostic correction of centrifugal pump features in the BP_NN classification model. There is one mistake between the actual value and predicted value for F1 and five mistakes between the actual value and predicted value for F2. We improved the identification correction accuracy of fault status, as GA was applied to optimize the weights and thresholds between each connection layer of the BP_NN model. Figure 18 shows the diagnostic correction of centrifugal pump features in the GA_BP_NN classification model. There is just one mistake between actual value and predicted value for F3, which is much better than that for BP_NN without GA optimization.

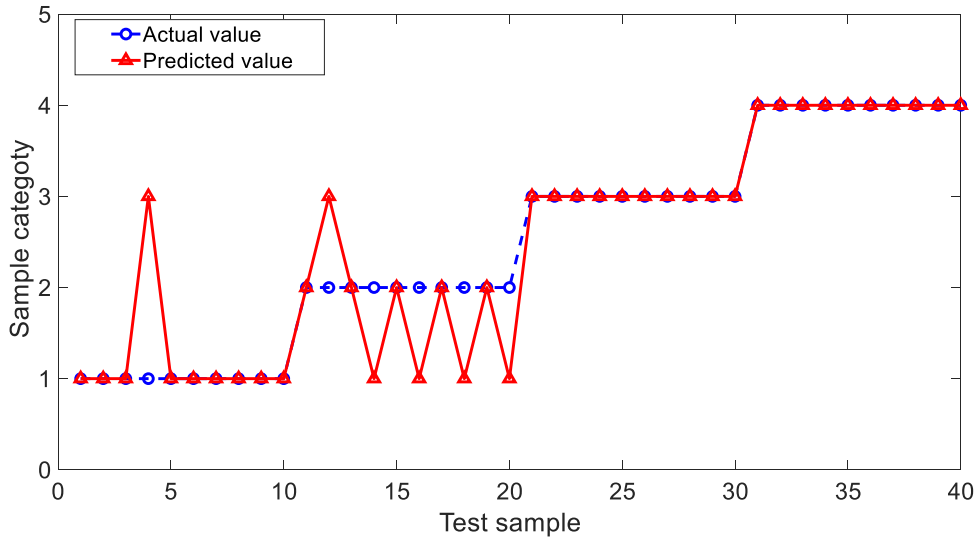

Figure 17. Comparison between the actual and predicted values by BP_NN.

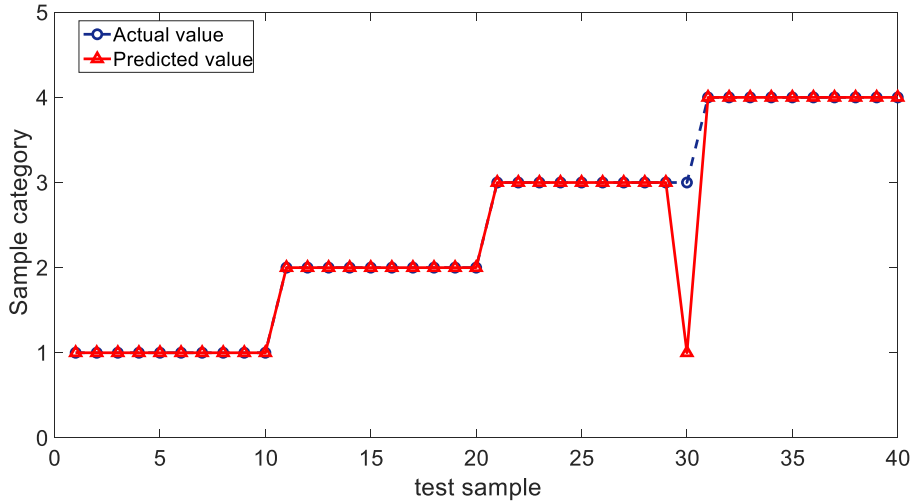

Figure 18. Comparison between the actual and predicted values by GA_BP_NN.

7. Conclusions

Aiming at resolving the multiple failure modes of the centrifugal pump impeller, an experimental system of a centrifugal pump was developed to collect multi-channel complex fault signals for its operation state. The continuous wavelet transform was applied to analyze the multi-channel signals to construct 3D tensors. The hybrid method of the multiple-dimensional-data fusion was proposed based on PARAFAC, BP_NN and GA. The multi-dimensional signal analysis of the complex systems accurately located the fault frequency range of the centrifugal pump. An improvement in the diagnostic accuracy was achieved. Due to the limitations of experimental conditions, this paper only investigated the accuracy of the single fault classification of multi-channel signals, while the failure modes of mechanical equipment in actual production would be more complex, which also provides direction for future research.

Author Contributions: Conceptualization, S.L.; methodology, H.C.; software, M.L.; validation, S.L.; formal analysis, S.L.; investigation, S.L. and M.L.; resources, H.C.; data curation, M.L.; writing—original draft preparation, S.L.; writing—review and editing, S.L. and H.C.; visualization, M.L.; supervision, H.C.; project administration, H.C.; funding acquisition, H.C. All authors have read and agreed to the published version of the manuscript.

Funding: The National Natural Science Foundation of China (Grant 51775390).

Informed Consent Statement: Informed consent was obtained from all subjects involved in the study.

Data Availability Statement: Not applicable.

Acknowledgments: The experimental data were obtained from Lab of Reliability at University of Alberta in Canada.

Conflicts of Interest: The authors declare no conflict of interest.

References

1. Wu, B. A brief discussion on the fault diagnosis and inspection and testing of lifting machinery. *China Equip. Eng.* **2021**, 153–154.
2. Xia, X.; Lu, Y.; Su, Y.; Yang, J. Mechanical fault diagnosis of high-voltage circuit breaker based on phase space reconstruction and improved GSA-SVM. *China Electr. Power* **2021**, *54*, 169–176.
3. Zhao, P. Research on Vibration Fault Diagnosis Method and System Implementation of Centrifugal Pump. Ph.D. Thesis, North China Electric Power University, Beijing, China, 2011.
4. Tong, Z.M.; Xin, J.G.; Tong, S.G.; Yang, Z.-Q.; Zhao, J.-Y.; Mao, J.-H. Internal flow structure, fault detection, and performance optimization of centrifugal pumps. *J. Zhejiang Univ. Sci. A* **2020**, *21*, 85–117. [CrossRef]
5. Castellanos Barrios, M.; Serpa, A.L.; Biazussi, J.L.; Verde, W.M.; Natachedo Socorro Dias Arrifano Sassim. Fault identification using a chain of decision trees in an electrical submersible pump operating in a liquid-gas flow. *J. Pet. Sci. Eng.* **2019**, *184*, 106490. [CrossRef]

6. Chen, Y.; Yuan, J.; Luo, Y.; Zhang, W. Fault Prediction of Centrifugal Pump Based on Improved KNN. *Shock. Vib.* **2021**, *2021*, 7306131. [CrossRef]
7. Bordoloi, D.J.; Tiwari, R. Identification of suction flow blockages and casing cavitations in centrifugal pumps by optimal support vector machine techniques. *J. Braz. Soc. Mech. Sci. Eng.* **2017**, *39*, 2957–2968. [CrossRef]
8. Niu, C. Research on Wind Turbine Drive Chain Fault Diagnosis Based on Big Data and Artificial Intelligence. Ph.D. Thesis, Shanxi University, Taiyuan, China, 2019.
9. Xiaoshuai, G. Research on Online Monitoring and Fault Diagnosis Method of Electric Motor and Centrifugal Pump Set. Ph.D. Thesis, Beijing University of Chemical Technology, Beijing, China, 2020.
10. Taqvi, S.A.A.; Zabiri, H.; Tufa, L.D.; Uddin, F.; Fatima, S.A.; Maulud, A.S. A Review on Data-Driven Learning Approaches for Fault Detection and Diagnosis in Chemical Processes. *ChemBioEng Rev.* **2021**, *8*, 239–259. [CrossRef]
11. Cui, C.; Lin, W.; Yang, Y.; Kuang, X.; Xiao, Y. A novel fault measure and early warning system for air compressor. *Measurement* **2019**, *135*, 593–605. [CrossRef]
12. Yu, Y.; Li, W.; Sheng, D.; Chen, J. A novel sensor fault diagnosis method based on Modified Ensemble Empirical Mode Decomposition and Probabilistic Neural Network. *Measurement* **2015**, *68*, 328–336. [CrossRef]
13. Favier, G.; de Almeida, A.L.F. Overview of constrained PARAFAC models. *Eurasip J. Adv. Signal Process.* **2014**, *2014*, 142. [CrossRef]
14. Krushal, J.B. Three-way arrays: Rank and uniqueness of trilinear decompositions, with application to artithmetic complexity and statistics. *Linear Algebra Its Appl.* **1997**, *18*, 95–138. [CrossRef]
15. Yang, C. Research on the Application of Parallel Factor Analysis in Blind Separation of Multiple Fault Sources. Ph.D. Thesis, Nanchang University of Aeronautics, Nanchang, China, 2018.
16. Li, J.F.; Zhang, S.F. Joint angular and Doppler frequency estimation of dual-base MIMO radar based on quadratic linear decomposition. *J. Aeronaut.* **2012**, *33*, 1474–1482.
17. Nion, D.; Sidiropoulos, N.D. A PARAFAC-based technique for detection and localization of multiple targets in a MIMO radar system. In Proceedings of the 2009 IEEE International Conference on Acoustics, Speech and Signal Processing, Taipei, Taiwan, 19–24 April 2009; pp. 2077–2080. [CrossRef]
18. Weis, M.; Romer, F.; Haardt, M.; Jannek, D.; Husar, P. Multi-dimensional space-time-frequency component analysis of event related EEG data using closed-form PARAFAC. In Proceedings of the 2009 IEEE International Conference on Acoustics, Speech and Signal Processing, Taipei, Taiwan, 19–24 April 2009; pp. 349–352. [CrossRef]
19. Yang, L.; Chen, H.; Ke, Y.; Huang, L.; Wang, Q.; Miao, Y.; Zeng, L. A novel time–frequency–space method with parallel factor theory for big data analysis in condition monitoring of complex system. *Int. J. Adv. Robot. Syst.* **2020**, *17*, 172988142091694. [CrossRef]
20. Li, Y.; Yuan, H.; Yu, J.; Zhang, C.; Liu, K. A review on the application of genetic algorithm in optimization problems. *Shandong Ind. Technol.* **2019**, *12*, 242–243.
21. Zhao, G.S.; Huang, D.L.; Zhao, X. Fault diagnosis of mining rolling bearings based on RCMDE and GA-SVM. *Coal Technol.* **2021**, *40*, 221–223.
22. Ma, J.; Meng, L.; Xu, T.; Meng, X. Research on bearing fault diagnosis by genetic radial basis neural network based on FastICA. *Mach. Tools Hydraul.* **2021**, *49*, 188–192.
23. Rastegar, R.; Hariri, A. A Step Forward in Studying the Compact Genetic Algorithm. *Evol. Comput.* **2006**, *14*, 277–289. [CrossRef] [PubMed]
24. Xu, Y.; He, M. Improved artificial neural network based on intelligent optimization algorithm. *Neural Netw. World* **2018**, *28*, 345–360. [CrossRef]
25. Lv, Y.; Liu, W.; Wang, Z.; Zhang, Z. WSN Localization Technology Based on Hybrid GA-PSO-BP Algorithm for Indoor Three-Dimensional Space. *Wirel. Pers. Commun.* **2020**, *114*, 167–184. [CrossRef]
26. Han, X.; Wei, Z.; Zhang, B.; Li, Y.; Du, T.; Chen, H. Crop evapotranspiration prediction by considering dynamic change of crop coefficient and the precipitation effect in back-propagation neural network model. *J. Hydrol.* **2021**, *596*, 126104. [CrossRef]

International Journal of
Turbomachinery
Propulsion and Power

MDPI

Review

Machine Learning Methods in CFD for Turbomachinery: A Review

James Hammond [1], Nick Pepper [2], Francesco Montomoli [1,*] and Vittorio Michelassi [3]

[1] Aeronautics Department, Imperial College London, London SW7 2AZ, UK; j.hammond18@imperial.ac.uk
[2] The Alan Turing Institute, London NW1 2DB, UK; npepper@turing.ac.uk
[3] Turbomachinery & Process Solutions, Baker Hughes, 50127 Florence, Italy; vittorio.michelassi@bakerhughes.com
* Correspondence: f.montomoli@imperial.ac.uk

Abstract: Computational Fluid Dynamics is one of the most relied upon tools in the design and analysis of components in turbomachines. From the propulsion fan at the inlet, through the compressor and combustion sections, to the turbines at the outlet, CFD is used to perform fluid flow and heat transfer analyses to help designers extract the highest performance out of each component. In some cases, such as the design point performance of the axial compressor, current methods are capable of delivering good predictive accuracy. However, many areas require improved methods to give reliable predictions in order for the relevant design spaces to be further explored with confidence. This paper illustrates recent developments in CFD for turbomachinery which make use of machine learning techniques to augment prediction accuracy, speed up prediction times, analyse and manage uncertainty and reconcile simulations with available data. Such techniques facilitate faster and more robust searches of the design space, with or without the help of optimization methods, and enable innovative designs which keep pace with the demand for improved efficiency and sustainability as well as parts and asset operation cost reduction.

Keywords: machine learning; computational fluid dynamics; turbomachinery; uncertainty quantification; physics informed neural networks

check for updates

Citation: Hammond, J.; Pepper, N.; Montomoli, F.; Michelassi, V. Machine Learning Methods in CFD for Turbomachinery: A Review. *Int. J. Turbomach. Propuls. Power* **2022**, *7*, 16. https://doi.org/10.3390/ijtpp7020016

Academic Editor: Marcello Manna

Received: 21 March 2022
Accepted: 9 May 2022
Published: 13 May 2022

Publisher's Note: MDPI stays neutral with regard to jurisdictional claims in published maps and institutional affiliations.

Copyright: © 2022 by the authors. Licensee MDPI, Basel, Switzerland. This article is an open access article distributed under the terms and conditions of the Creative Commons Attribution (CC BY-NC-ND) license (https://creativecommons.org/licenses/by-nc-nd/4.0/).

1. Introduction

Turbomachines, and in particular Gas Turbines (GT), have been widely used in the last decades for propulsion, both aviation and marine, power generation and mechanical drive; while Steam Turbines (ST) have been used mostly for large scale power generation, both standalone and in conjunction with GT in combined cycles [1]. GT technology is nearing maturity and efficiency, reliability, availability, and operating range are now close to entitlement. Consequently, further improvement becomes increasingly complex and expensive. Most of these units are fossil fuels fired, and the increasing pressure to reduce their carbon footprint [2] calls for changes that require innovations in many technology areas to drastically reduce, or zero, emissions and interface seamlessly with renewable resources. Some examples to cite a few are:

- Fuel flexibility (methane, hydrogen, ammonia, oxi-combustion, and a blend of these with low NO_x emissions),
- Part load performance (when operating below 50% of nominal power),
- Fast start-up and shut-down (which should take less than a minute to allow interfacing with intermittent renewables),
- Better efficiency (higher firing temperatures and pressures and improved materials properties),
- Reduced maintenance (for operation in remote areas close to wind or solar farms),
- Improved interface with bottom cycles (operated with steam or organic fluids),

- Interfacing with Carbon Capture and Sequestration (CCS).

Consequently, designers are faced with the prospect of moving away from well-established comfort-zone designs, either by applying conventional design to *uncharted* applications, or by designing new units in *uncharted* design spaces [3]. All of these challenge the entire design process, from the early conceptual to the preliminary and detailed design stages.

In the specific areas of aerodynamics, aeromechanics (both forced response and flutter), heat transfer, and combustion, design systems are evolving from correlation-based designs, relying heavily on companies' proprietary experimental data, to more complex multidimensional and multidisciplinary approaches that require Computational Fluid Dynamics (CFD) [3,4]. Correlation-based designs are naturally bound to the investigated design space envelope and are not suited for exploring design opportunities outside this space. As a more complex design verification tool based on first principles, CFD has the potential to investigate any design space. Unfortunately, conventional CFD such as steady and unsteady Reynolds-averaged Navier–Stokes (RANS and URANS), which are the main subject of this paper, also suffer from fundamental weaknesses. These can be imputed primarily to turbulence and heat transfer models, and secondly to the geometry and operating condition simplifications often made to reduce the computational effort [5,6]. To overcome such deficiencies, most companies develop so-called "best practices" to run CFD and minimize the deviation from measured data, which apply only to the design space in which reliable data are available. Consequently, conventional CFD reliability as a general design tool, although much more powerful compared to correlation-based and simple 1D and 2D methods, is undermined and design safety margins are applied as a measure of the "ignorance" of designers and the tools [6].

In previous years, scale resolving simulations such as Large Eddy Simulation (LES) and Direct Numerical Simulation (DNS), as opposed to time-averaging methods like (U)RANS, emerged as a viable design aid (see, for example, applications to low-pressure turbines [7–9], and combustion systems [10]). Figure 1a shows where each method lies on the trade-off between accuracy and computational expense and Figure 1b shows the correlation of these methods to the energy spectrum. LES resolves the majority of the fluid flow energy spectrum and models only the finer dissipation scales where the assumption of quasi-isotropic turbulence is acceptable [11]. Despite their undeniable superiority to (U)RANS, LES with appropriate grid resolution is still computationally prohibitive for wall-driven and statistically periodic flows such as those in multistage compressors and turbines, while it is more common for the wall-bounded and statistically steady flows present in combustion chambers [12]. Scale resolving simulations offer superior resolution allowing designers to determine not only *what* is happening in the fluid flow, but also *why* it is happening [6,11]. This distinction has unlocked an alternative use of scale resolving simulations as accurate datasets to benchmark and improve (U)RANS models. It is important to remember that the most popular two-equation model, k-ϵ [13], was originally developed and calibrated for boundary layers and free jet flows, and has since been applied with a fair degree of accuracy to much more complex flows. Therefore, LES and DNS provide the perfect databases to improve lower-order models, especially when using different forms of machine learning (ML).

Improved (U)RANS predictability, as well as both Hybrid-LES (HLES) and LES in narrower application ranges, allows the design space to be extended with less fear of running into inaccurate predictions. A potential by-product of such improvement is represented by design optimization methods, from simple airfoils aero and aeromechanics [14], to more advanced multidimensional topology optimization [15] that can ultimately be used with more confidence while overcoming the excessive computational effort of scale-resolved simulations. With this premise, this paper attempts to describe current research activities to evolve CFD methods with the aid of high-fidelity simulation and ML, to further improve accuracy in both academic and industrial applications.

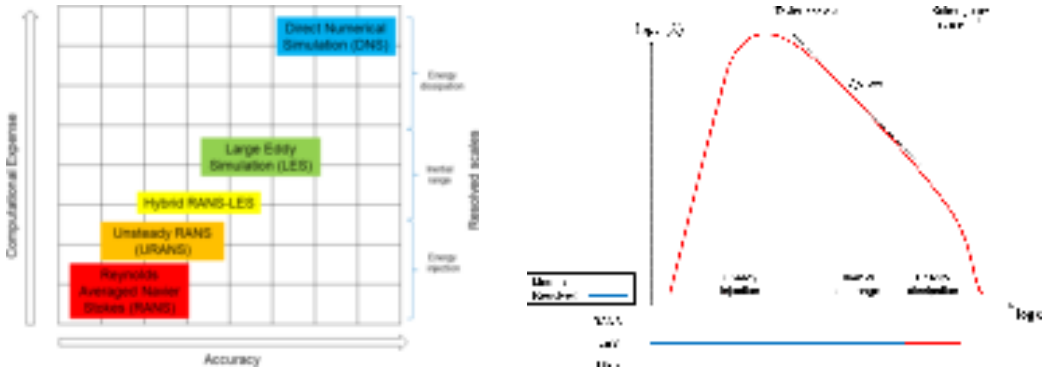

(**a**) (**b**)

Figure 1. Comparison of the different approaches for modelling turbulence: (**a**) Computational expense against accuracy for each approach; (**b**) the correlation of each method to the energy spectrum, highlighting which portion of the spectrum is resolved or modelled in each case.

2. Application of Machine Learning Methods to CFD for Turbomachinery Design

The accurate prediction of flow fields is key to the development of new technologies and products in the critical early phase where a wide design space needs to be explored. Such necessity does not apply only to turbomachines, but to each application in which a fluid flow is required to store or convert various forms of energy into various forms of power. Industry, more than academia, has always faced the challenge of handling heterogeneous datasets with varying levels of fidelity. These range from simple scaled-down tests, to full-scale full-system tests, as well as field data from the results of associated computational design tools. Moreover, the quality of both experimental and computational tools is continuously improving (for example advanced ceramic probes for high-pressure high-temperature flows, or LES with appropriate discretization for real geometries and operating conditions) as is the cost of running experiments and high-fidelity simulations. Given the sheer size of the heterogeneous datasets present in industry, an updated engineering approach based on ML methods is required to leverage the available data efficiently. With an eye on the application of improved prediction methods, several key avenues currently being explored to various extents, but which nevertheless are worthy of due consideration, are described below:

1. How can ML indicate ways to improve accuracy at various levels of physics resolution? With reference to Figure 1a, DNS can be used to improve the subgrid-scale (SGS) model in LES, which can be used to improve Reynolds-averaged models in (U)RANS. In particular, we focus on Artificial Neural Networks (ANNs) and Gene Expression Programming (GEP) based methods that use data from DNS or LES to improve the accuracy of (U)RANS in some respect.
2. Are ML methods a viable strategy for reduction of computational cost associated with a single CFD simulation by accelerating the convergence of solvers?
3. Uncertainty quantification (UQ) is employed during the design of new products to determine the impact of different sources of uncertainty on the performance of a design. Computing the statistical moments of an uncertain Quantity of Interest (QoI) does not generally admit analytical solutions, but instead requires meta-models that are not only accurate but can scale well with the number of uncertain system parameters. These models must also be able to handle large, heterogeneous datasets containing data with varying levels of uncertainty. Furthermore, the results of the uncertainty analysis must be clearly communicated to multi-disciplinary teams who are stakeholders in the project. How can ML based methods be used to address these challenges?
4. Finally, is the model able to incorporate multi-fidelity data and help match scarce experimental measurements affected by errors? Is the model generalisable to a range

of flow features (for instance adverse or favourable pressure gradients), geometries (wall-bounded vs. wall-driven) and flow conditions (statistically steady vs. statistically periodic)?

To facilitate the discussion of these points, reference is made to Figure 2, showing an instantaneous snapshot of the thermal field in proximity to the trailing edge of a high-pressure turbine (HPT). The figure summarizes the different sets of information available, including the flow field computed employing CFD methods with different levels of resolution.

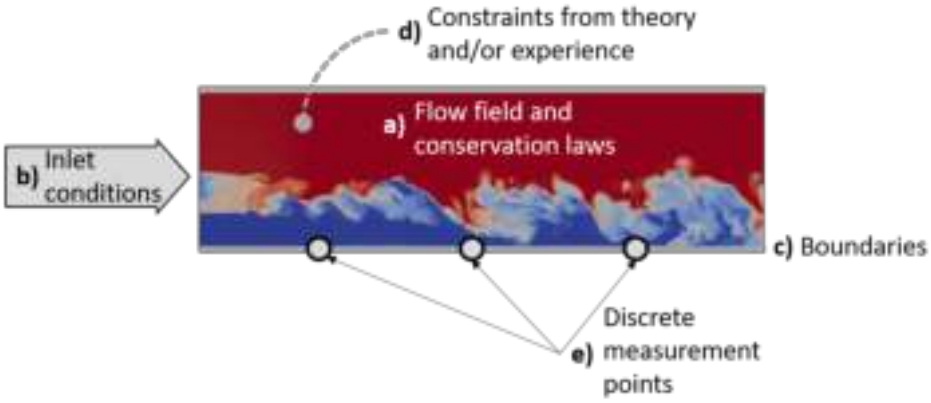

Figure 2. Data and constraints contributing to the definition of the flow field. The picture illustrates a snapshot of the mixing of cold and hot streams.

3. Turbulence Modeling with Machine Learning

The modelling of turbulence effects in the internal flows of turbomachines is particularly complex due to the interaction of a wide range of frequencies and the associated flow structures. Although captured sufficiently in simple cases by classical (U)RANS methods, regions of high anisotropy and wide ranges of interacting length scales cause the inherent assumptions relied upon in the development of the RANS closures to break down. The aim of machine learning in this context is to improve the accuracy of CFD calculations without resorting to high-fidelity, scale resolving and computationally expensive techniques. This simple premise has driven the development of a vast range of techniques over the last 10 years each underpinned by a simple philosophy; use data generated from experiments and, mostly, from high-fidelity simulations to inform on uncertainty and corrections to existing LES, HLES, and (U)RANS data, and eventually to develop improved models.

In this scenario, with reference to Figure 2, the flow field (a) is available from high-fidelity simulations with a good degree of accuracy, as well as inlet conditions (b) and boundaries (c) while discrete measurements points, (e), may be available only to validate the high-fidelity data. The constraints from theory, (d), are generally considered in the model learning phase. Approaches can then be largely split into two distinct categories:

1. Those that find corrective functions for the Reynolds stress or other quantities of interest and apply these in one predictive step to the baseline model. This involves introducing the corrected Reynolds stress into lower-order closures (DNS to LES or HLES, and LES to (U)RANS) as a static field from which the velocity and pressure field can be converged.
2. Those that make inherent changes to lower-order closures (mostly (U)RANS), either through terms in the turbulence equations or by learning nonlinear models for the Reynolds stresses based on mean flow features, as discussed in [16]. These models are then inferenced at every iteration in a subsequent (U)RANS calculation.

Each approach has merits and deficiencies although it is considered that, at convergence, they both yield similar results. Methods using the first approach can learn discrepancies and make corrections to the quantity of interest in an environment completely removed from CFD. Just one additional solver is required to predict the mean flow

variables which solves the RANS equations injected with a static Reynolds stress field. This modularity keeps implementation simpler and allows the CFD engineer and the machine learning engineer to operate individually. The second approach requires the machine learning and the RANS calculations to be more intrinsically linked [17]. As the model must be inferenced at every step, the machine learnt model must be implemented in the RANS solver. This can introduce a significant amount of overhead code as different models may need different implementations. However, once developed, the model is self-contained and can be run independently.

3.1. The Energy Spectrum in Turbomachinery

Figure 3 illustrates the typical energy plot as a function of the wavenumber (K) for homogeneous turbulence. The solid black line shows a peak that corresponds to the maximum energy eddies that, moving to the right, progressively transfer energy to smaller eddies down to the Kolmogorov scale at which viscous dissipation becomes dominant. Figure 4 sketches the range of different modelling paths, which will be illustrated with the help of Figure 3.

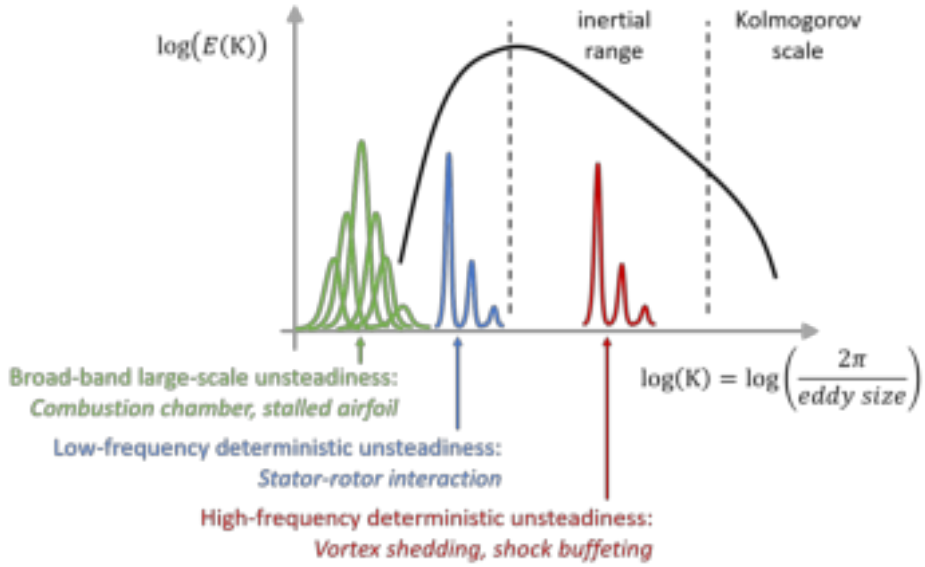

Figure 3. Energy spectrum for turbomachinery showing the different scales at which deterministic frequencies can contaminate the *canonical* spectrum.

3.2. DNS to Improve LES

A well-resolved DNS constitutes a formidable dataset to develop turbulence models as it resolves the majority of the Kolmogorov scales at which turbulence is substantially isotropic. The resolution in LES in terms of K sits in the inertial scale range, as close as possible to the Kolmogorov scale limit to minimize the importance of the SGS model. While the open literature offers a wide range of models [18], a good example of the development of an SGS model with the help of ML based on a DNS database is described by Park and Joi [19], who used a Neural Network trained on a DNS of a $Re_\tau = 178$ flow. They proved that the resulting SGS model could be applied to channel flows at much larger Reynolds numbers. With reference to Figure 4, this is the branch A in which the conservation of a generic quantity f requires the introduction of the additional SGS term in its transport equation

$$\frac{Df}{Dt} = \underbrace{\frac{\partial f(\mu, \nabla f_i)}{\partial x_j}}_{\text{resolved}} + \underbrace{\frac{\partial f(\mu_{\text{SGS}}, \nabla f_i)}{\partial x_j}}_{\text{SGS spatial average}} . \tag{1}$$

In case the resolution in space and time is enough for DNS, the diffusion process depends on the viscosity μ, which is a *fluid* property. When the resolution is not enough, it is necessary to introduce the SGS viscosity μ_{SGS} that is a *flow* property averaged over the length scale of the spatial grid resolution.

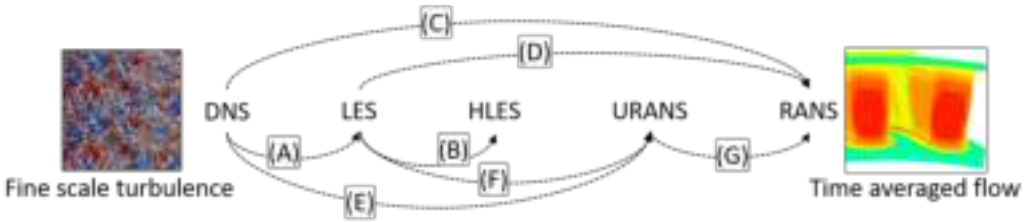

Figure 4. Schematic of the branches by which higher-fidelity scale-resolving simulations can be used as datasets to inform the development of lower-order models.

3.3. DNS and LES to Improve HLES

Branch *B* covers the so-called hybrid-LES (HLES) approach in which models switch to RANS where the grid resolution in space is insufficient. This approach requires cumbersome interfacing of LES, which is a space-averaged method, with RANS, which is a time-averaged method. Weatheritt and Sandberg [20] used machine learning, in particular Gene Expression Programming (GEP), to tune their HLES approach with the help of a companion LES and obtained very encouraging results for the flow past twin cylinders.

3.4. DNS and LES to Improve (U)RANS

Potentially the most common path by which machine learning has been employed in CFD to date is via inference of (U)RANS turbulence closures from higher-fidelity DNS and LES databases. To this end, Weatheritt and Sandberg [21] developed a novel form of GEP capable of regressing tensorial expressions. As a symbolic regression technique, GEP provides explicit algebraic expressions for the quantity of interest which in this case is the anisotropy. Using the explicit algebraic Reynolds stress (EASM) framework of Pope [22], they learnt improved nonlinear expressions for the anisotropy which showed promise in predictive circumstances where the included physics is similar. The GEP methodology has since been applied to flows relevant in the turbomachinery space, looking at the HPT cascade [23] and extended the approach to develop nonlinear scalar-flux models for heat transfer analysis by developing a general form of the scalar-flux based on functional dependence [24]. Applying GEP to LES data of a jet in crossflow representative of film cooling techniques, they observed significant improvement in the prediction of the scalar-flux term, culminating in adiabatic effectiveness values more accurately reproducing experiments for a range of blowing ratios.

Hammond et al. [25] looked to further the GEP methodology introduced by Weatheritt and Sandberg to validate its capability on more complex 3D flows, such as those generated by topology optimisation. Using a topology optimised heat exchanger duct as a test case for a complex internal cooling system, they showed an improved assessment of the aerodynamic blockage when compared to DES reference data. This analysis is performed with the intention of applying data-driven closures in fluid optimisation methods, to achieve designs representative of high-fidelity flow prediction at a fraction of the computational cost. Whilst GEP has the merit of providing the user with an explicit expression which can be easily assimilated and assessed, the functional forms that can be expressed are sometimes limited. ANNs provide the option of greater flexibility and are potentially able to perform wider searches of the parameter space. Frey et al. [26] built on the work of Ling et al. [27] and used relatively shallow neural networks trained on DNS data to improve the eddy viscosity term in the Boussinesq approximation. They applied this approach to a serpentine channel representative of internal cooling channels in turbine blades. Using a hierarchical agglomerative clustering algorithm to separate regions of the flow for training,

they showed that improved results were achieved when the separation regions around each bend were excluded from training. This was attested to the importance of accurately predicting turbulent mixing in the flow preceding the separation point and just outside the rear part of the bubble.

Therefore, ML can be used to develop Reynolds-averaged models using LES (and DNS when available) by using both different forms of ANNs and GEP, as discussed in [28]. However, different ways to evaluate the fit of the model when introduced in RANS [17] may also be explored, as summarized in Figure 5. Zhao et al. [17] observed that it was convenient to verify the trained $\tau_{i,j}^{ML}$ by using the updated flow field resulting from a new RANS calculation with the latest candidate constitutive flow as opposed to testing it with the frozen velocity field from LES. Obviously, the training effort increases significantly, but it overcomes the problems of the nonlinear response of the NS equations to changes in the constitutive law.

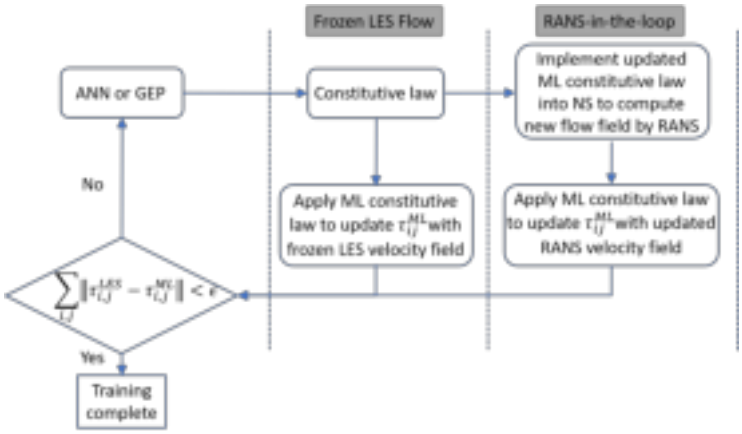

Figure 5. Training verification strategies which can broadly be split into two main categories: frozen training and RANS-in-the-loop.

Additionally, as turbomachinery flows are inherently unsteady, it is necessary to distinguish between RANS and URANS. In this class of models, fine-scale high frequency motion effects are entirely filtered out and replaced with the so-called Reynolds-stresses that apply to both turbulent diffusion of momentum and thermal energy.

The filtering process assumes a *canonical* spectrum, similar to the black line in Figure 3 representative of isotropic turbulence decay. In turbomachines, the energy spectrum may change due to several possible reasons listed in Figure 3. Combustion systems generate "broad-band" large-scale unsteadiness that alters the fundamental process of extracting energy from the mean flow field, and large-scale flow structures are also generated in axial compressors and turbines post-stall. In this case, RANS may be accurate as long as the broad-band low frequency energy is small, although it is unclear if the Reynolds-averaging process based on the *canonical* spectrum will still work, and an unsteady RANS that resolves the low frequencies may be a better choice. This is represented by branches *C* and *D* in Figure 4. The energy spectrum of 3 may also change due to the large scale "deterministic" unsteadiness generated by stator–rotor interaction, trailing edge vortex shedding, and shock buffeting.

Stator–rotor interaction is driven by the blade-passing frequency that depends on the airfoil count and the rotational speed, and it generally sits outside the inertial range. Therefore, the so-called spectral gap (the gap between the deterministic frequency and the frequency range that defines the inertial range) is preserved and the Reynolds-averaging process is appropriate [11,29]. In spite of the spectral gap, complex constitutive laws may still be required to capture the airfoil–wake interaction, as documented by Michelassi et al. [30] due to curvature and pressure gradient effects. This scenario is represented by branches *E* and *F* in Figure 4.

With high frequencies, like in high-pressure turbine trailing edge vortex shedding or in supersonic flows with shock buffeting, the deterministic contribution may sit inside the inertial range and the spectral gap vanishes. Consequently, there is a strong interaction between the deterministic unsteadiness and the turbulence energy cascade. In this scenario, Reynolds-averaging will wrongly filter the deterministic contribution, and it will fail (branches *E* and *F*). In this case, the conservation of a generic quantity f can be formulated as

$$\frac{Df}{Dt} = \underbrace{\frac{\partial f(\mu, \nabla f_i)}{\partial x_j}}_{\text{laminar}} + \underbrace{\frac{\partial f(\mu_t, \nabla f_i)}{\partial x_j}}_{\text{Reynolds average}} . \tag{2}$$

Similarly to Equation (1), the molecular viscosity μ depends on the *fluid*, while the turbulent viscosity μ_t is a *flow* property averaged in time.

To overcome the difficulties that a turbulence model has to mimic both deterministic and stochastic unsteadiness, Akolekar et al. [7] and Lav et al. [31] adopted different approaches. In [7], the authors applied GEP to develop a RANS turbulence closure based on several phase-locked averaged flow fields from the LES of a low-pressure turbine with discrete incoming wakes. The results showed a substantial improvement compared to a standard two-equation model, although the gap with LES was still evident. In [31], the authors used the LES past an infinite plate to reproduce the vortex shedding typical of a low-pressure turbine. The developing wake has both large stochastic unsteadiness (i.e., turbulence) and large coherent unsteadiness due to the shedding of discrete vortices. The authors proposed a triple decomposition in which the flow field is split into a steady time-averaged flow, a periodic component extracted by FFT, and a stochastic component in a way similar to the so-called *Partially-Averaged Navier–Stokes* (PANS) equations. They concluded that the best match with LES was obtained by running URANS with a turbulence model trained only on the stochastic component of the LES flow field.

In the past, Van de Wall et al. [32] extended the Reynolds stresses that model the effect of stochastic unsteadiness due to turbulence on the mean flow field, to the so-called *deterministic stresses* meant to model the effect of deterministic unsteadiness due to stator–rotor interaction on the mean flow field, represented by branch *G* in Figure 4. Therefore, the resulting conservation equation becomes

$$\frac{Df}{Dt} = \underbrace{\frac{\partial f(\mu, \nabla f_i)}{\partial x_j}}_{\text{laminar}} + \underbrace{\frac{\partial f(\mu_t, \nabla f_i)}{\partial x_j}}_{\text{Reynolds average}} + \underbrace{\frac{\partial f(\mu_{\text{DET}}, \nabla f_i)}{\partial x_j}}_{\text{deterministic average}} , \tag{3}$$

in which the *deterministic average* term is averaged over the low frequency periodic flow and accounts for the unsteadiness generated by stator–rotor interaction. While μ is a *fluid* property, both μ_t and μ_{DET} are *flow* properties as discussed for both Equations (1) and (2).

4. Acceleration of the CFD Solver

The second avenue for ML which has received significant attention in the context of CFD is through the acceleration of solvers. The computational cost of running a CFD simulation, neglecting mesh generation, is driven by: the total number of elements; the time taken to solve the system of equations (the algorithm); and the number of time steps. These factors are driven by the approach used, from RANS at one end through to DNS at the other. As discussed in the previous sections, RANS models struggle to accurately describe large scale separations (i.e., compressors near stall, flow in the secondary airflow system, and internal coolant systems). For this reason, attention turns to scale-resolving LES and DNS despite computational expense considerations rendering them infeasible for design space exploration, uncertainty quantification and optimisation methods (although advances in the latter are being made using data-driven turbulence modelling, see [33] for example). The trade-off between required regional mesh resolution and computational expense has been explored by many authors [34–36]. Whilst such approaches are feasible

in low and high-pressure turbines without consideration of the full coolant system, it is still prohibitive to analyse component-to-component interactions on a regular basis [37]. As such, ML methods currently under development may be able to provide the necessary relaxation to computational constraints to shift scale-resolving simulations into a range more suited to industrial design processes.

The directions explored can be split into two broad categories: spatial discretization and temporal discretization. Spatial discretization approaches aim to speed up the solver by leveraging coarse meshes with ML to provide super-resolution of the missing details. In contrast, temporal discretization approaches use ML to forecast the temporal evolution of a numerical scheme with speeds much faster than the time stepping of the underlying CFD algorithm. Both approaches will be discussed in detail in the following sections.

4.1. Spatial Discretization Acceleration

The idea behind the acceleration of solvers by considering spatial discretization is conceptually simple. As mentioned, one of the main driving factors of computational time in a CFD simulation is the total number of elements. To reduce computational time then, it is intuitive to reduce the number of elements. However, this comes with a deterioration of the prediction accuracy. Recently, several formulations [38,39] have been proposed that use ML to improve the accuracy of prediction on coarse meshes with the result of a massive speed up in simulation time for the same accuracy. The ML component in the solver is trained on high-fidelity simulation and the methodology described acts as a general multiscale framework that can be used to speed up scale resolving LES and DNS simulations.

A secondary advantage of super-resolution methods is the improvement that can be made in overall I/O cost. The datasets generated by DNS are very large. For instance, up to 20Tb of data may be stored per time step for wall-bounded flows with $Re = 10^4$, present in low-pressure turbine stages. The overall I/O cost can be significantly reduced by storing a fraction of this dataset and using super-resolution to reconstruct the missing data.

The approach presented by Kochkov et al. [38] aims to predict the accurate evolution of a CFD simulation, using a mesh with an order of magnitude coarser resolution in each spatial dimension and learned interpolation to achieve a computational speed up around 40 times. However, the success of this technique is highly dependent on the availability of large datasets of high-resolution data. One approach with aims to mitigate the need for large high-resolution training sets is offered by Gao et al. [39]. They aim to reconcile sparse, noisy training datasets using convolutional neural networks where the physics are injected by constraining the network to match conservation laws and boundary conditions; this method is based on PINNs which will be described in detail in Section 6.

4.2. Temporal Discretization Acceleration

The other avenue by which ML can be utilised to accelerate CFD solvers is through forecasting the temporal evolution of the solution. A detailed comparison of such methods is offered by Fotiadis et al. [40] who investigate the performance of four different neural networks for solving the inviscid 2D shallow water equations, equivalent to compressible wave propagation problem. The authors compared three recurrent networks (LSTM, ConvLSTM, PredRNN++) and one feed-forward U-Net model.

The LSTM (long-short term memory) model was initially proposed for the prediction of wave propagation by Sorteberg et al. [41]. Their network comprised a convolutional encoder and decoder structure with three LSTM blocks in between. The vector output of the encoder branch is then propagated forward in time by the LSTMs before being decoded to obtain the forecasted fields. Both the ConvLSTM and PredRNN++ models use convolution operations inside a recurrent cell to find a connection between temporal and spatial modelling. PredRNN+ also utilizes spatial memory that traverses the stacked cells in the network, hence increasing short-term accuracy [42]. Whilst CovLSTM and PredRNN++ have been empirically demonstrated as suitable for short-term spatio-temporal prediction, accuracy inevitably deteriorates in longer-term forecasting.

The final model compared by the authors, U-Net, has been used in various spatio-temporal prediction problems. For instance, to infer optical flows, motion fields and velocity fields [43–45]. The model is trained end to end and is conditional on its own prediction. The fact that the input of the network depends on its former predictions allows a significant improvement in the long-term accuracy.

4.3. Reduced-Order Models

Many of the approaches proposed in the literature for accelerating fluid simulations use the fact that the underlying model is a surrogate of the real one, with an approximate solution of Navier–Stokes equations. To give a real advantage, these so-called Reduced-order models (ROMs), which have been used for many years in turbomachinery flows, must be faster than the original Navier–Stokes equations [46]. There are two main aspects of a ROM: the identification of different scales and the identification of a suitable formulation within which to describe them. Machine learning methods, mainly through image recognition development, have expanded both areas in recent years. In turbomachinery, the segregation of scales is evident, particularly in multistage simulations, wakes, boundary layers, and local separations where a range of length scales exist simultaneously.

It can be shown that a shallow linear autoencoder acts as a Proper Orthogonal Decomposition (POD) method, while, increasingly, deep nonlinear autoencoders are being used. After the appropriate system is defined, the dynamics of these systems need to be defined. Several ML methods can be utilised here, including sparse identification of nonlinear dynamics, SINDy that has been used for a wide range of applications, from laminar and turbulent flows to wakes [47].

A further approach has been provided by CFDNet [48]. Standard CFD solvers are used to warm up the solutions and CFDNet then forecasts the evolution, before leaving the CFD solver to construct the final output. The authors explained how these three steps (warmup, inference, and refinement) contribute to generating an ML framework capable of dealing with unseen cases. The refinement case uses the CFD solver to refine the inference output of the neural network, ensuring that the model is consistent with physics. A more general version of this framework is proposed by Leer and Kempf [49]. The authors proposed a combination of a minimalistic multilayer perceptron (MLP) and a radial-logarithmic filter mask (RLF) to generate a surrogate model able to predict internal and external flows. The RLF encodes the geometry into a compressed form to be interpreted by the MLP and allows fast estimation of flow fields for various applications.

Whilst all the above methods show promising features, it should be highlighted that they are, for the most part, applied only to simple canonical situations. For wide scale integration in the field of turbomachinery, their capabilities must now be demonstrated consistently on complex cases representative of flows present in an industrial setting.

5. Uncertainty Quantification and Management

A potential area of application for the machine learning methods discussed in the previous sections is in the quantification and management of uncertainties during the design process. In order to develop a robust design that can deliver good performance across a range of operating conditions, it is necessary to consider the uncertainties affecting the system [50]. Figure 6 illustrates the importance of this for industry, through a probability density function (PDF) that represents the variation between the measured and quoted performance. Examples of performance metrics include the efficiency, life, or operability of a product. The quoted performance, F_{quoted}, is defined as the predicted performance, $F_{\text{predicted}}$, minus a safety margin that includes all uncertainties, $F_{\text{quoted}} = F_{\text{predicted}} - \Delta F_1$. The safety margin is introduced to avoid falling below contractually accepted limits, ΔF_L (for example 4% on power). The tail of the PDF left of the vertical grey line indicates cases in which a unit does not meet the performance acceptance limit. The red curve assumes $\Delta F_1 = 0$ and the risk of not meeting the quoted performance is large. The blue curve sets $\Delta F_1 > 0$ to reduce such risk. In other words, the average expected performance is penalized

by shifting the red curve to the right. The amount of shift is directly proportional to the overall uncertainty. The more truncated tails of the green curve show the case in which uncertainty is reduced, or controlled, and the performance prediction is more accurate. The probability mass to the left of the grey line is identical for both the blue and green curves, i.e., both distributions have the same risk of not meeting contractual performance; however, the safety margin of the green curve is smaller ($\Delta F_2 < \Delta F_1$) and therefore it is possible to quote a higher performance with the same risk.

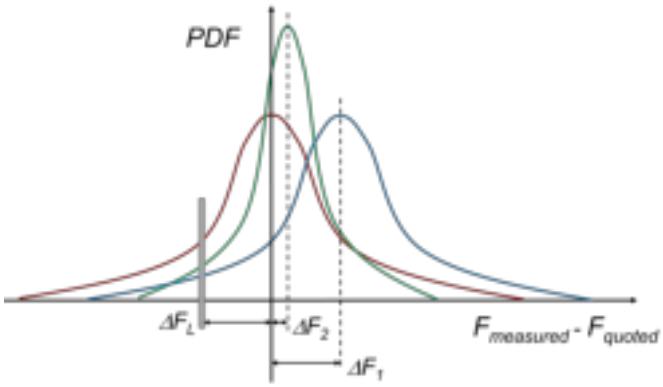

Figure 6. Effect of uncertainty on quoted performance. The red line corresponds to an uncertain parameter with no saftety margin and high probability of failing performance standards. The blue line shows the same uncertain parameter with a large saftey margin ΔF_1 required to reduce failure probability to an acceptable level. The green line shows how the safety margin ΔF_2 achieving same failure probability can be reduced by reducing the overall uncertainty.

The uncertainties affecting a product are typically divided into two categories: aleatoric and epistemic. Aleatoric uncertainties refer to uncertainties arising from random fluctuations in the environment. In the context of turbomachinery, these might arise from: uncertain operating conditions [51]; variations or imperfections introduced in the geometry during manufacturing or caused by wear [52]; and noise present in experimental measurements [53] (constraints (b), (c), and (e) in Figure 2). On the other hand, epistemic uncertainties refer to uncertainties introduced by the simplifications necessary to model a real world system. In addition to numerical effects introduced by truncation, uncertainties introduced by applying theoretical assumptions, a lack of available data, or constraints to a turbulence model come under this category (point (d) in Figure 2). While aleatoric uncertainties are irreducible, in principle, epistemic uncertainties are reducible and could be minimised, for instance by collecting more data or developing models that more accurately capture the physics.

5.1. Quantifying Aleatoric Uncertainty

The goal of Uncertainty Quantification (UQ) is to estimate the impact of uncertainties on the performance of a product, which might be expressed as a probability distribution or a confidence interval for a given Quantity of Interest (QoI). We first consider the forward propagation of aleatoric uncertainties, in which a joint density over the uncertain parameters affecting the system, $\boldsymbol{\xi}$, is available. At a minimum, the designer is concerned with estimating the first two statistical moments of a QoI, i.e., the mean and standard deviation performance of a design operating in uncertain conditions [54]. Reliability analysis, in which the relatively low probability of the uncertain conditions leading to failure is estimated, is something of an exception to this as this probability will be determined by the distribution tails [55,56]. Nevertheless, the example of estimating the mean and standard deviation of a QoI is instructive, as it illustrates the need for accurate meta-models of expensive CFD simulations for UQ in an industrial setting.

Evaluating the first two statistical moments of an uncertain QoI entails solving the integral for the mean:

$$\mathbb{E}(w) = \int w(\boldsymbol{\xi}) f(\boldsymbol{\xi}) d\boldsymbol{\xi}, \tag{4}$$

and for the variance:

$$\mathrm{Var}(w) = \int (w(\boldsymbol{\xi}) - \mathbb{E}(w))^2 f(\boldsymbol{\xi}) d\boldsymbol{\xi}, \tag{5}$$

where w represents the QoI and $\boldsymbol{\xi} \in \Re^{n_u}$ the uncertain parameters with joint density $f(\boldsymbol{\xi})$. These integrals are unlikely to admit an analytical solution. Numerical methods such as stochastic collocation may be employed for low-dimensional uncertain spaces [57]; however, these become computationally intractable for large scale problems. In such cases, Monte Carlo sampling is a popular strategy for approximating these integrals and is particularly effective if the computational model $w(\boldsymbol{\xi})$ is cheap to evaluate. An accurate assessment of the aleatoric uncertainties affecting a product requires the evaluation of n Monte Carlo samples, perhaps on the order of $n \approx 10^5$–10^6, with the confidence of the estimate of the mean converging as $n^{-\frac{1}{2}}$ [58]. Given the computational costs associated with a single CFD simulation, the statistical assessment of a design using direct Monte Carlo sampling is impractical; a surrogate model or meta-model of the system is required. This meta-model is trained using a limited dataset of CFD simulations, after which the meta-model may be evaluated at what is assumed to be negligible cost. Methods such as non-intrusive Polynomial Chaos Expansions (niPCEs), while effective for low-dimensional uncertain spaces [59], suffer from the *curse of dimensionality*, where the minimum number of simulations required to determine the coefficients of the expansion grows rapidly with n_u. While there is current research targeted at mitigating this aspect of niPCEs (see, e.g., [60,61]), at present, niPCEs are generally infeasible for the high-dimensional problems faced by industry. On the other hand, intrusive Polynomial Chaos Expansions, which require alterations to the CFD code, are criticised for being difficult to implement in an industrial context, although again academics working to mitigate this critique (see, e.g., [62,63]). Addressing these issues presents an opportunity to employ machine learning methods, which have been demonstrated to scale well to high-dimensional spaces, as meta-models that can be used to accelerate simulations, allowing for the accurate statistical assessment of the uncertainties affecting a product.

5.2. Quantifying Epistemic Uncertainty

Quantifying the effects of epistemic uncertainty can be difficult [64]. However, quantifying the structural uncertainties in RANS is a key challenge for industrial CFD simulations as the constraints introduced by theory or experience on a turbulence model are largely responsible for mismatches between simulations and experiments [5,6]. There are already works in the literature that have addressed the issue of model form uncertainty in RANS simulations, which we group into three strategies: perturbation-based; Bayesian-based; or discrepancy modelling.

Banerjee et al. [65] demonstrated that the three limiting states of the turbulent anisotropy could be represented as a barycentric map. As an example of the first set of approaches, Gorlé et al. [66] and Emory et al. [67] proposed a perturbation based method for quantifying the epistemic uncertainty in RANS turbulent closures. Uniform eigenvalues perturbations were made to the Reynolds stress anisotropy tensor in the direction of the limiting states of turbulence (1, 2, and 3 component turbulence) to produce a conservative upper bound to the upper bound. These perturbations, and the barycentric coordinate system, are illustrated in Figure 7. Later versions of this method incorporated machine learning, employing a random regression forest to vary the size of the eigenvalue perturbation locally according to the feature importance of a set of 12 dimensionless features [68]. An advantage of the perturbation based approach is that UQ can be performed without requiring a high-fidelity dataset to compare the RANS simulations against, as is the case for the other two categories of approaches.

Bayesian frameworks have been proposed that treat the parameters of the Reynolds stress tensor as a set of uncertain parameters [69–71]. Beginning from a set of prior distributions and a joint PDF for the likelihood, posterior probability distributions for these parameters are inferred through a calibration process, in which the predictions of the RANS model are compared against a dataset of high-fidelity observations [72,73]. Figure 7 illustrates this change in perspective using the barycentric coordinate system referenced above. The workflow for the Kalman inversion scheme in Xiao et al. [72] is represented schematically in Figure 8. Rather than perturbing the RANS predicted state towards each of the three limiting cases, in the Bayesian interpretation of the problem, new, physically realisable states are sampled from a posterior distribution. As has been mentioned, a prerequisite for these Bayesian based methods is that a set of high-fidelity data is available to compare the RANS simulations against. This could be the results of experiments [74,75] or from DNS data.

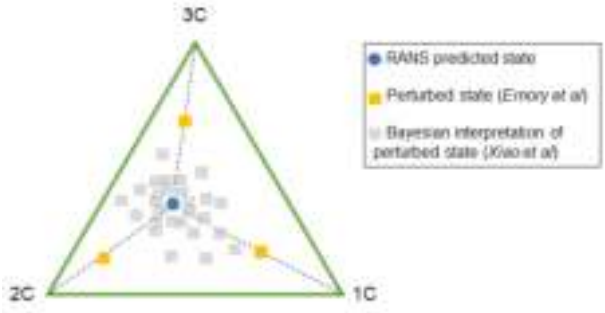

Figure 7. Barycentric map of the physically realisable states of turbulence as a combination of three limiting states of turbulence: one, two, and three components (1C, 2C, and 3C, respectively) and represented the perspectives for pertubation based and Bayesian based methods of UQ in this space. Adapted from [67,76]. Copyright 2016 Elsevier B.V.

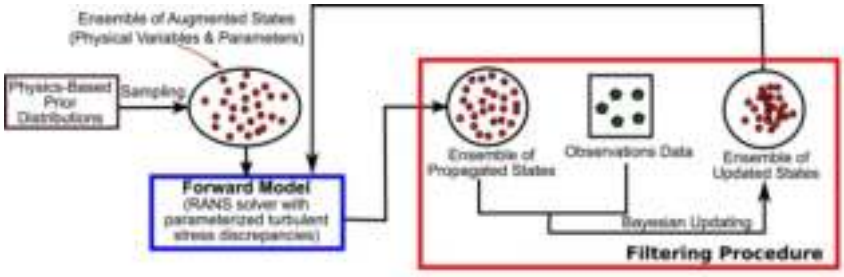

Figure 8. A schematic illustrating the Kalman inverison scheme: the posterior distribution for the uncertain parameters in RANS is adjusted to reconcile the ensemble of propagated states as closely as possible with the observations. Adapted from [72]. Copyright 2016 Elsevier Inc.

Finally, there are those methods that develop a statistical model for the discrepancy between RANS and high-fidelity data. In the work of Dow and Wang, for instance, the discrepancy between the turbulent viscosity field predicted by RANS and the field inferred from the DNS data via inverse RANS is modelled as a Gaussian random field [77]. Similarly, the work of Duraisamy et al. [78–80] uses field inversion and machine learning methods to develop a functional form of the discrepancies in the model. For further discussion on the topic of quantifying the model form uncertainty in RANS models, we refer the reader to the excellent reviews of Duraisamy et al. [81] and Xiao and Cinella [82]. Section 3 of this paper details recent developments in using machine learning to improve RANS simulations by leveraging high-fidelity data from LES. Often, this is achieved by using machine learning to estimate a set of invariant quantities that can be combined linearly to form the anisotropy tensor in the turbulent closure. The majority of these methods do not consider the uncertainty introduced by this mapping, although some progress has been

made in this regard. Geneva and Zabaras [83] introduced a Bayesian formulation of the neural network used by Ling et al. [27] to compute the anisotropy tensor. Through Monte Carlo sampling of a Bayesian Neural Network, they were able to quantify the uncertainty in this term and consequently place probabilistic bounds on the estimated pressure and velocity fields.

5.3. Quantifying Mixed Uncertainty and Visualisation

The methods that have been described so far in this section target the quantification of aleatoric and epistemic (specifically model form) uncertainty separately. Ultimately, tools will need to be developed for industries capable of processing both types of uncertainties simultaneously. This is a challenging problem. However, some progress has been made in this direction within the turbomachinery space [84]. Quantifying the effects of mixed uncertainty may require engineers to reconsider how uncertainty is visualised and communicated. Rather than specifying a single probability distribution for the QoI, a p-box approach that can be used to bound families of likely Cumulative Distribution Functions (CDFs) might be more effective [85,86]. A disadvantage of these methods is that p-boxes are an abstract concept, the meaning of which is difficult to convey to non-experts. Ling and Townsend [87] proposed a classification based approach, using ML classifiers such as Support Vector Machines, to identify the regions of the greatest uncertainty in RANS simulations of flows over several geometries. An advantage of this method is that the levels of uncertainty present in a simulation may be presented intuitively, as can be seen in Figure 9. In risk-averse industries such as aeronautics, new products are heavily scrutinised by regulators before they can be certified [88]. As part of the process of certification, it is necessary to justify the design decisions with the evidence that was available to the designers at the time. For machine learning methods to become incorporated within the design process, it will be essential for the uncertainty present in these methods to be clearly indicated, particularly the predictive uncertainty that can account for epistemic uncertainties arising from a lack of data. At present, the majority of machine learning methods provide point estimations with no way of quantifying the uncertainty in the estimate. As is discussed in the reviews of Hüllermeier and Waegeman [89] and Psaros et al. [90], moving away from 'black-box' models and accounting for aleatoric and epistemic uncertainty will be crucial for the massive industrial application of machine learning. The papers review methods that currently accomplish this, such as Bayesian Neural Networks.

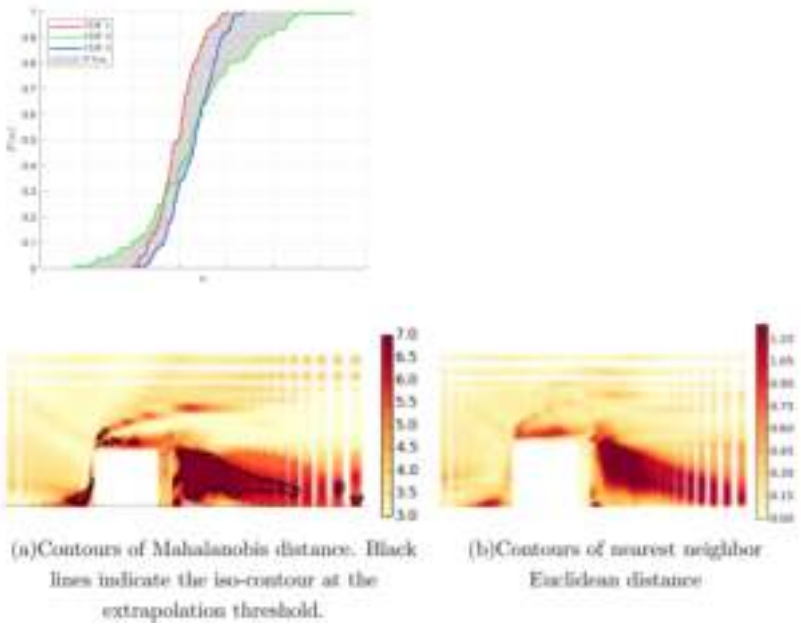

Figure 9. Perspectives for visualising the results of uncertainty analyses: illustration of a p-box (**top**) and representation of RANS uncertainty from Ling and Townsend (**bottom**, adapted from [87]. Copyright 2015 AIP Publishing LLC.).

5.4. Multi-Fidelity Methods

Finally, industry usually has a wealth of heterogeneous data from the manufacturing, assembly, operation, and servicing of components. These data will be affected by uncertainty to various extents (see, e.g., [91]). It would be beneficial if these data could be used to inform future designs, particularly at the conceptual design phase where the resources available to evaluate candidate designs are limited, but where the decisions taken have a significant impact on the final product [92,93]. Exploiting these data are the motivating philosophy behind the digital twin approach to design, in which sustainable practices throughout the lifecycle of a product are encouraged [94]. However, using a large heterogeneous dataset of historic data is a challenging task due to both the size of the datasets involved and the varying levels of epistemic uncertainty associated with the collection of the data. This is especially true if uncertainty must be propagated between computational models at multiple scales or levels [95]. There is currently a great deal of research within the UQ community directed at multi-fidelity methods, in which generative models that are informed by heterogeneous datasets are developed. Approaches based on Gaussian processes (co-kriging) [96,97], multi-fidelity Polynomial Chaos Expansions [98,99], multi-level Monte Carlo [100], and different forms of physics informed neural networks such as those by Wang and Zhang [101] and Yang et al. [102] have all been proposed for the solution of the PDEs that govern fluid flows. More recently, Pepper et al. [103] presented a Knowledge-Based Neural Network (KBaNN) capable of computing additive corrections to the output of a model based on a coarse computational mesh. The KBaNN was able to generalise to flows that share similar physics. In principle, this approach can be used to add more advanced modelling features and make it possible to develop a bi-fidelity method that leverages data from any existing simulation database.

Of these methods, co-kriging has proved to be particularly popular due to the natural way in which the heterogeneous uncertainties may be handled. An additional advantage is that the predictive uncertainty may be expressed through the kriging variance (see, e.g., [104–107] for examples in the aeronautics and turbomachinery spaces). In recent years, there has also been emphasis placed on developing ML methods for multi-scale [108–110] or multi-level [111,112] uncertainty propagation. However, many of these papers aim at improving low-fidelity model evaluations with datasets from high-fidelity model evaluations,

rather than experimental data which is likely to be noisier and more difficult to reconcile due to unresolved physics in the computational models. One approach might be to focus on identifying the "worst offenders" in the low-fidelity model to target. For instance, Lengani et al. used Proper Orthogonal Decomposition (POD) to construct a reduced-order model of a turbine wake in which the modes that contributed the most to unsteady losses could be identified [113]. Nevertheless, for a more comprehensive improvement in the accuracy of simulations, it may be necessary to consider more drastic machine learning approaches. This new paradigm of machine learning methods might offer a means to reconcile simulations of a complex flow field with the available experimental data while simultaneously satisfying the remaining constraints in Figure 2. These new forms of machine learning are discussed in more detail in the following section.

6. New Forms of Machine Learnt Tools

The overwhelming complexity of turbulent flows requires a technology step change to overcome the inherent limits of the approaches followed to date. The so-called turbulence models required by the (U)RANS approach do not attempt to model turbulence; instead, they model the effect of turbulence on a Reynolds-averaged flow field. Such models proved reasonably accurate for engineering applications [5,114], but they have difficulties predicting axial compressor operability [115], heat transfer, aeromechanics, and more generally any off-design operation of aerodynamic bodies [5]. Therefore, the seamless application of (U)RANS is *model accuracy limited*. The obvious cure is to switch from modelling to resolving the high frequency broad spectrum turbulent motion by LES or DNS. Regretfully, the associated computational cost of realistic scale-resolving simulation is excessive, and the practical application of high-fidelity simulations in industry is *computational resources limited*.

As discussed earlier in this paper, various forms of machine learning have been used to improve turbulence models—first, for example, GEP and ANNs trained on data from scale-resolving simulations. More recently, an evolution of ANNs, known as Physics Informed Neural Networks (PINNs), introduced a step change in the computer simulation of complex flow fields. Karniadakis et al. [116] provided a detailed explanation of the potential offered by PINNs. This may be understood with reference to the practical example schematized in Figure 2, which describes the mixing of cold and hot streams and represents a typical GT hot-gas-path design problem. The flow field, (a), must obey fundamental conservation principles such as mass, momentum, and enthalpy balances, under a combined set of inlet conditions, (b), and boundaries, (c). The combined set of (a), (b), (c) is enough to perform a computer simulation of the flow and the accuracy of their specification is key to the quality of the final result. However, the physics models adopted in the simulation may not necessarily satisfy the constraints dictated by theory and experience, (d), and may not guarantee a good match with measurements, (e). In this case, the only option left to a designer is to start a long and tedious set of iterations to determine the impact of the mesh, model assumptions and boundary conditions on the results, in an attempt to match measurements better. Following from [116], Cai et al. [117] illustrate a way to overcome this bottleneck by training a neural network capable of reproducing the flow field of Figure 2 by using all the available sets of information. With reference to the specific fluid dynamics case of Figure 2, a PINN may be trained to

(a) Obey the basic conservation principles of the time-averaged Navier–Stokes equations (PDE);
(b) Match inlet operating conditions (IC);
(c) Match boundary and geometrical conditions (BC);
(d) Obey the fundamental turbulence constraints for theory (see, for example, turbulence invariants formulated by Lumley [118]), (TC);
(e) Match measurements obtained from experiments (ME).

The overall training process may be followed with the help of Figure 10 in which a Neural Network is trained to fulfil the constraints that concur in a penalty function Σ, which measures the quality and maturity of the PINN training process

$$\Sigma = \pi_{\mathrm{PDE}}\Sigma_{\mathrm{PDE}} + \pi_{\mathrm{IC}}\Sigma_{\mathrm{IC}} + \pi_{\mathrm{BC}}\Sigma_{\mathrm{BC}} + \pi_{\mathrm{TC}}\Sigma_{\mathrm{TC}} + \pi_{\mathrm{ME}}\Sigma_{\mathrm{ME}}. \quad (6)$$

The quantities Σ_ϕ represent the deviation from the expected value (for example, the PDE conservation error), and π_ϕ are a set of weights used to control the severity of the deviation from each separate constraint. The advantage of training a Neural Network based model with this approach is its ability to account for all the information, data, and constraints simultaneously. In fact, the flow field predicted by a PINN trained with this approach will match the measured data (e) while fulfilling all theoretical constraints and the boundary conditions. The results reported in [116,117] suggest that this is possible, although PINNs and their training process are not ready for massive industrial application. In particular, Cai et al. [117] followed the approach summarized in Equation (6) for the simulation of a portion of the incompressible vortex shedding flow downstream of a cylinder. The set-up of the training dataset had to be appropriately selected, but the results indicated the method was able to capture the most relevant flow features with an L_2-norm error ranging from 1% to ≈10% depending on the velocity component. They further verified their approach on a bow-shock case showing similar accuracy. Eivazi et al. [119] followed a similar approach for the simulation of a boundary layer with adverse, zero, and favourable pressure gradients, confirming that the PINN approach could replicate the boundary layer development with a fair degree of accuracy. The authors also tackled the challenging problem of periodic hills where a sizeable flow separation develops. The predicted flow field, which required inlet conditions, geometry, and boundary values of the static pressure in selected locations, compared well with a reference DNS dataset. In their detailed paper, Raissi et al. [120] described how the solution of well known PDEs, such as the Schrodinger, the Allen-Cahn, and Navier–Stokes equations can be reproduced with PINNs. Their approach differed from that summarized by Equation (6) as they trained the PINN using 200 initial data points randomly sampled from the exact solution available at the initial time step. They used a relatively light network with four hidden layers and 200 neurons per layer to ensure a very good match with the reference exact solution. This is illustrated in Figure 11, highlighting the excellent match between the instantaneous static pressure field downstream of a circular cylinder predicted by the direct solution of the Navier–Stokes equations, and by the PINN.

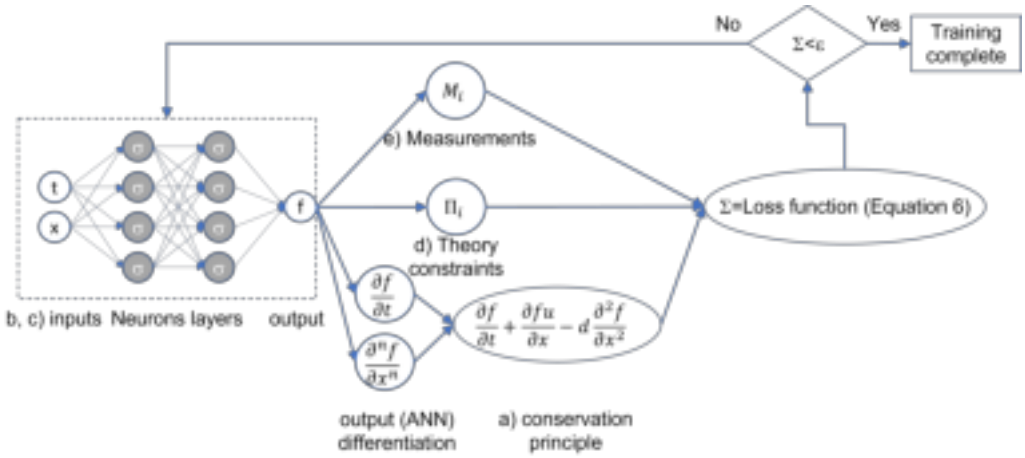

Figure 10. A generalized schematic of the Physics Informed Neural Network (PINN) approach.

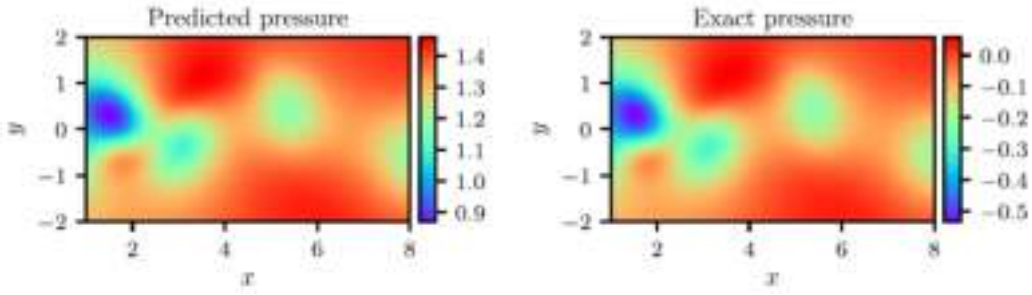

Figure 11. Instantaneous static pressure in the vortex shedding region downstream of circular cylinder. Reproduced with permission from [120]. Copyright 2018 Elsevier Inc.

Although the applications seen to date are relatively simple, they show the huge potential of this method that is not to be seen as a viable replacement for CFD models, but rather as a model capable of incorporating and reconciling multi-fidelity data from different sources, as summarized by Equation (6).

7. Summary and Outlook

Design systems, and particularly turbomachinery design, are increasingly aided by first-principle CFD tools and by general multi-disciplinary optimization methods. This paper summarizes the avenues along which design methods and performance optimization tools can be further improved.

- In a design optimization loop, the quality of a design is measured by interrogating an estimator, in this case, CFD. The quality and robustness of the optimal solution are dictated by the reliability of CFD, the accuracy of which can be boosted by ML.
- Each design iteration, especially when dealing with multidisciplinary verification, is very computationally intensive. ML can improve optimizer convergence by reducing the number of iterations and, more importantly, the cost associated with each design performance analysis.

Along these lines, this paper begins by focusing on the areas in which machine learning is already making a direct impact on CFD within the space of turbomachinery—specifically, where data from higher-fidelity simulations are used to train models which augment lower-fidelity calculations in an attempt to reconcile the *model accuracy limiting* of (U)RANS with the *computational resource limiting* of LES or DNS. Machine learning has been successfully used mostly to overcome the difficulties stemming from the modelling of turbulence, the driving mechanism of entropy change. These methods have shown significant promise with improved prediction observed for flows including but not limited to high and low-pressure turbines, cooling flows such as jet in crossflow and turbine internal cooling ducts, waste heat recovery systems, carbon capture and sequestration systems.

Despite their clear potential, it is recognized that at present such methods rarely consider the epistemic uncertainties introduced by these mappings, whilst also assuming single-point specification of initial and boundary conditions. In risk-averse industries such as aviation and marine, as well as power generation for civil and industrial applications where turbomachines are often employed, this uncertainty needs to be quantified and managed to support design decisions and allow certification of products by regulatory bodies. Considering this, current methods are reviewed that account for the uncertainty of some Quantity of Interest in the presence of both aleatoric and epistemic uncertainties. The methods shed light on how UQ can be leveraged to provide some level of assessment of the predictive confidence of these machine learnt models, when applied in previously unseen cases. Improved accuracy will help determine the effect of single components' performance on the overall engine (i.e., compressor operability, combustion emissions, high-pressure-turbine durability, power turbine efficiency) and eventually aid decisions on the most appropriate corrective action in case of problems. More accurate CFD with a manageable computational effort will also allow the analysis of component to-component

interaction, often a cause of unexpected problems (i.e., inlet system and axial compressor instability, combustion chamber and high-pressure turbine durability, power turbine and exhaust system noise, aeroacoustic cavity excitation, to cite a few).

These approaches demonstrate an underutilized but highly important aspect of predictive models if they are to be accepted for large scale integration in an industrial setting. They also bring attention to a fundamental question: how can traditional computational simulation be seamlessly reconciled with the wealth of heterogeneous data often available in industry, each contaminated by varying levels of resolution in space and time, and aleatoric and epistemic uncertainty during their collection. This is by no means a straightforward task. Specification of conservation laws, initial and boundary conditions for some geometry may be sufficient to run a computational simulation but does not guarantee agreement with measured data and design experience.

A recent development that offers the potential to unify these two opposing facets of industrial design comes through the introduction of Physics-Informed Neural Networks (PINNs). PINNs offer a unique opportunity to combine all sources of available information in a single constrained optimisation network. Measured data, data from high-fidelity sources, theoretical physical laws and tried and tested empirical relationships can all be considered simultaneously by incorporating them, with appropriately selected weightings, in the loss function of a learning machine. The development of PINNs brings the field of machine learning in fluid dynamics to a very exciting juncture, where seamless data fusion appears to present itself as a serious contender. Whilst currently in their infancy and applied only to relatively simple applications to date, researchers will inevitably exploit the rich vein that PINNs uncover. This will no doubt come through application to a multitude of more complex problems, to show their pertinence in a general setting and provide novel perspectives to old challenges. Whilst this may be a clear direction, a more thoughtful approach is encouraged at this point, particularly within the industrial setting of turbomachines.

Future data-driven approaches should endeavor to account for the wealth of prior knowledge to reduce the vast high dimensional parameter spaces and reduce the computational complexity of the search for optimal solutions. Predictions using developed models should also be presented with an uncertainty caveat such that practitioners have confidence in the results obtained and can justify the design decisions taken as a result. Although fully replacing current conventional methods will take time, there is already a clear path toward new methods with a wider validity range—those that, with the help of ML, make the best use of measurements from both dedicated scaled-down tests and high-fidelity field data, enforce theory and improve the prediction accuracy of computational tools from early to detailed design.

Author Contributions: Investigation: J.H., N.P., F.M. and V.M.; Writing—Original Draft: J.H., N.P., F.M. and V.M.; Writing—Review & Editing: J.H., N.P., F.M. and V.M. All authors have read and agreed to the published version of the manuscript.

Funding: This research was funded by the Engineering and Physical Sciences Research Council (EPSRC) Grant No. EP/L016230/1.

Acknowledgments: The authors would like to acknowledge Baker Hughes for funding and for the permission to publish this work.

Conflicts of Interest: The authors declare no conflict of interest.

References

1. *Gas Turbine World 2020 GTW Handbook*; Pequot Publishing Inc.: Fairfield, CT, USA, 2020.
2. Sources of Greenhouse Gas Emissions. Available online: https://www.epa.gov/ghgemissions/sources-greenhouse-gas-emissions (accessed on 26 October 2021).
3. Michelassi, V.; Ling, J. Challenges and opportunities for artificial intelligence and high-fidelity simulations in turbomachinery applications: A perspective. *J. Glob. Power Propuls. Soc.* **2021**, 1–14. [CrossRef]
4. Denton, J.D.; Dawes, W.N. Computational fluid dynamics for turbomachinery. *J. Mech. Eng. Sci.* **1998**, *213*, 107–124. [CrossRef]

5. Sandberg, R.D.; Michelassi, V. The current state of high-fidelity simulations for main gas path turbomachinery components and their industrial impact. *Flow Turbul. Combust.* **2019**, *102*, 797–848. [CrossRef]
6. Laskowski, G.; Kopriva, J.; Michelassi, V.; Shankaran, S.; Paliath, U.; Bhaskaran, R.; Wang, Q.; Talnikar, C.; Wang, Z.; Jia, F. Future Directions of High Fidelity CFD for Aerothermal Turbomachinery Analysis and Design. In Proceedings of the 46th AIAA Fluid Dynamics Conference, Washington, DC, USA, 13–17 June 2016; p. 3322.
7. Akolekar, H.D.; Sandberg, R.D.; Hutchins, N.; Michelassi, V.; Laskowski, G. Machine-Learnt Turbulence Closures for Low-Pressure Turbines with Unsteady Inflow Conditions. *J. Turbomach.* **2019**, *141*, 101009. [CrossRef]
8. Michelassi, V.; Chen, L.; Pichler, R.; Sandberg, R.D.; Bhaskaran, R. High-fidelity simulations of low-pressure turbines: Effect of flow coefficient and reduced frequency on losses. *ASME J. Turbomach.* **2016**, *138*, 111006. [CrossRef]
9. Pichler, R.; Michelassi, V.; Sandberg, R.D.; Ong, J. Highly Resolved LES Study of Gap Size Effect on Low-Pressure Turbine Stage. *ASME J. Turbomach.* **2017**, *140*, 021003.
10. Meloni, R.; Ceccherini, G.; Michelassi, V.; Riccio, G. Analysis of the self-excited dynamics of a heavy-duty annular combustion chamber by large-eddy simulation. *J. Eng. Gas Turbines Power* **2019**, *141*, 111016. [CrossRef]
11. Sandberg, R.D.; Michelassi, V. Fluid Dynamics of Axial Turbomachinery: Blade- and Stage-Level Simulations and Models. *Annu. Rev. Fluid Mech.* **2022**, *54*, 255–285. [CrossRef]
12. Slotnick, J.; Khodadoust, A.; Alonso, J.; Darmofal, D. *CFD Vision 2030 Study: A Path to Revolutionary Computational Aerosciences*; Technical report; NASA Langley Research Center: Hampton, VA, USA, 2014.
13. Jones, W.; Launder, B. The calculation of low-Reynolds-number phenomena with a two-equation model of turbulence. *Int. J. Heat Mass Transf.* **1973**, *16*, 1119–1130. [CrossRef]
14. Lopez, D.I.; Ghisu, T.; Shahpar, S. Global Optimisation of a Transonic Fan Blade Through AI-Enabled Active Subspaces. *J. Turbomach.* **2021**, *14*, 011013.
15. Gaymann, A.; Montomoli, F.; Pietropaoli, M. Robust Fluid Topology Optimization Using Polynomial Chaos Expansions: TOffee. In *Turbo Expo: Power for Land, Sea, and Air*; Turbomachinery: London, UK, 2018; Volume 2D. [CrossRef]
16. Gatski, T.; Speziale, C. On explicit algebraic stress models for complex turbulent flows. *J. Fluid Mech.* **1993**, *254*, 59–78. [CrossRef]
17. Zhao, Y.; Akolekar, H.D.; Weatheritt, J.; Michelassi, V.; Sandberg, R.D. RANS turbulence model development using CFD-driven machine learning. *J. Comput. Phys.* **2020**, *411*, 109413. [CrossRef]
18. Wallin, S.; Johansson, A. An explicit algebraic Reynolds stress model for incompressible and compressible turbulent flows. *J. Fluid Mech.* **2000**, *403*, 89–132. [CrossRef]
19. Park, J.; Choi, H. Toward neural-network-based large eddy simulation: Application to turbulent channel flow. *J. Fluid Mech.* **2021**, *914*, A16. [CrossRef]
20. Weatheritt, J.; Sandberg, R.D. Hybrid Reynolds-Averaged/Large-Eddy Simulation Methodology from Symbolic Regression: Formulation and Application. *AIAA J.* **2017**, *55*, 3734–3746. [CrossRef]
21. Weatheritt, J.; Sandberg, R.D. A novel evolutionary algorithm applied to algebraic modifications of the RANS stress-strain relationship. *J. Comput. Phys.* **2016**, *325*, 22–37. [CrossRef]
22. Pope, S.B. A more general effective-viscosity hypothesis. *J. Fluid Mech.* **1975**, *72*, 331–340. [CrossRef]
23. Weatheritt, J.; Pichler, R.; Sandberg, R.D.; Laskowski, G.; Michelassi, V. Machine Learning for Turbulence Model Development Using a High-Fidelity HPT Cascade Simulation. In Proceedings of the Turbomachinery Technical Conference and Exposition, Charlotte, NC, USA, 26–30 June 2017; pp. 1–12. [CrossRef]
24. Weatheritt, J.; Zhao, Y.; Sandberg, R.D.; Mizukami, S.; Tanimoto, K. Data-driven scalar-flux model development with application to jet in cross flow. *Int. J. Heat Mass Transf.* **2019**, *147*, 118931. [CrossRef]
25. Hammond, J.; Montomoli, F.; Pietropaoli, M.; Sandberg, R.; Michelassi, V. Machine Learning for the Development of Data Driven Turbulence Closures in Coolant Systems. *J. Turbomach.* **2022**, *144*, 081003. [CrossRef]
26. Frey Marioni, Y.; Ortiz, E.A.D.T.; Cassinelli, A.; Montomoli, F.; Adami, P.; Vazquez, R. A machine learning approach to improve turbulence modelling from DNS data using neural networks. *Int. J. Turbomach. Propuls. Power* **2021**, *6*, 17. [CrossRef]
27. Ling, J.; Kurzawski, A.; Templeton, J. Reynolds averaged turbulence modelling using deep neural networks with embedded invariance. *J. Fluid Mech.* **2016**, *807*, 155–166. [CrossRef]
28. Weatheritt, J.; Sandberg, R.D.; Ling, J.; Saez, G.; Bodart, J. A Comparative Study of Contrasting Machine Learning Frameworks Applied to RANS Modeling of Jets in Crossflow. In Proceedings of the ASME Turbo Expo 2017: Turbomachinery Technical Conference and Exposition, Charlotte, NC, USA, 26–30 June 2017; GT2017-63403.
29. Tucker, P. Computation of unsteady turbomachinery flows: Part1–Progress and Challenges. *Prog. Aerosp. Sci.* **2011**, *47*, 522–545. [CrossRef]
30. Michelassi, V.; Pichler, R.; Chen, L.; Sandberg, R.D. Compressible Direct Numerical Simulation of Low-Pressure Turbines: Part II—Effect of Inflow Disturbances. *ASME J. Turbomach.* **2015**, *137*, 071005-1–071005-12. [CrossRef]
31. Lav, C.; Sandberg, R.D.; Philip, J. A framework to develop data-driven turbulence models for flows with organised unsteadiness. *J. Comp. Phys.* **2019**, *383*, 148–165. [CrossRef]
32. Van de Wall, A.G.; Kadambi, J.R.; Adamczyk, J.J. A transport model for the deterministic stresses associated with turbomachinery blade row interactions. *J. Turbomach.* **2000**, *122*, 593–603. [CrossRef]
33. Hammond, J.; Pietropaoli, M.; Montomoli, F. Topology optimisation of turbulent flow using data-driven modelling. *Struct. Multidiscip. Optim.* **2022**, *65*, 49. [CrossRef]

34. Ali, Z.; Tyacke, J.; Tucker, P.G.; Shahpar, S. Block Topology Generation for Structured Multi-block Meshing with Hierarchical Geometry Handling. *Procedia Eng.* **2016**, *163*, 212–224. [CrossRef]
35. Toosi, S.; Larsson, J. Grid-adaptation and convergence-verification in large eddy simulation: A robust and systematic approach. In Proceedings of the 2018 Fluid Dynamics Conference, Atlanta, GA, USA, 25–29 June 2018; pp. 1–24. [CrossRef]
36. Rezaeiravesh, S.; Liefvendahl, M. Effect of grid resolution on large eddy simulation of wall-bounded turbulence. *Phys. Fluids* **2018**, *30*, 055106. [CrossRef]
37. Tyacke, J.; Vadlamani, N.R.; Trojak, W.; Watson, R.; Ma, Y.; Tucker, P.G. Turbomachinery simulation challenges and the future. *Prog. Aerosp. Sci.* **2019**, *110*, 100554. [CrossRef]
38. Kochkov, D.; Smith, J.A.; Alieva, A.; Wang, Q.; Brenner, M.P.; Hoyer, S. Machine learning—Accelerated computational fluid dynamics. *Proc. Natl. Acad. Sci. USA* **2021**, *118*, e2101784118. [CrossRef]
39. Gao, H.; Sun, L.; Wang, J.X. Super-resolution and denoising of fluid flow using physics-informed convolutional neural networks without high-resolution labels. *Phys. Fluids* **2021**, *33*, 073603. [CrossRef]
40. Fotiadis, S.; Pignatelli, E.; Valencia, M.L.; Cantwell, C.; Storkey, A.; Bharath, A.A. Comparing Recurrent and Convolutional Neural Networks for Predicting Wave Propagation. *arXiv* **2020**, arXiv:2002.08981.
41. Sorteberg, W.E.; Garasto, S.; Cantwell, C.C.; Bharath, A.A. Approximating the Solution of Surface Wave Propagation Using Deep Neural Networks. In Proceedings of the 32nd Conference on Neural Information Processing Systems (NeurIPS), Montreal, QC, Canada, 3–8 December 2018; pp. 246–256._26. [CrossRef]
42. Wang, Y.; Gao, Z.; Long, M.; Wang, J.; Yu, P.S. PredRNN++: Towards a resolution of the deep-in-time dilemma in spatiotemporal predictive learning. *Int. Conf. Mach. Learn.* **2018**, *11*, 8122–8131.
43. Thuerey, N.; Weissenow, K.; Prantl, L.; Hu, X. Deep learning methods for reynolds-averaged navier–stokes simulations of airfoil flows. *AIAA J.* **2020**, *58*, 25–36. [CrossRef]
44. Dosovitskiy, A.; Fischer, P. FlowNet: Learning Optical Flow with Convolutional Networks. *arXiv* **2015**, arXiv:1504.06852.
45. De Bézenac, E.; Pajot, A.; Gallinari, P. Deep learning for physical processes: Incorporating prior scientific knowledge. In Proceedings of the 6th International Conference on Learning Representations, ICLR 2018—Conference Track Proceedings, Vancouver, BC, Canada, 30 April–3 May 2018; IOP Publishing: Bristol, UK, 2018.
46. Vinuesa, R.; Brunton, S.L. The Potential of Machine Learning to Enhance Computational Fluid Dynamics. *arXiv* **2021**, arXiv:2110.02085.
47. Brunton, S.L.; Noack, B.R.; Koumoutsakos, P. Machine Learning for Fluid Mechanics. *Annu. Rev. Fluid Mech.* **2020**, *52*, 477–508. [CrossRef]
48. Obiols-Sales, O.; Vishnu, A.; Malaya, N.; Chandramowliswharan, A. CFDNet: A deep learning-based accelerator for fluid simulations. In Proceedings of the International Conference on Supercomputing, Barcelona, Spain, 29 June–2 July 2020. [CrossRef]
49. Leer, M.; Kempf, A. Fast Flow Field Estimation for Various Applications with A Universally Applicable Machine Learning Concept. *Flow Turbul. Combust.* **2021**, *107*, 175–200. [CrossRef]
50. Bertini, F.; Credi, M.; Marconcini, M.; Giovannini, M. A Path Toward the Aerodynamic Robust Design of Low Pressure Turbines. *J. Turbomach.* **2012**, *135*, 021018. [CrossRef]
51. Satish, T.; Murthy, R.; Singh, A. Analysis of uncertainties in measurement of rotor blade tip clearance in gas turbine engine under dynamic condition. *Proc. Inst. Mech. Eng. Part G J. Aerosp. Eng.* **2014**, *228*, 652–670. [CrossRef]
52. Montomoli, F.; Massini, M.; Salvadori, S. Geometrical uncertainty in turbomachinery: Tip gap and fillet radius. *Comput. Fluids* **2011**, *46*, 362–368. [CrossRef]
53. Notaristefano, A.; Gaetani, P.; Dossena, V.; Fusetti, A. Uncertainty Evaluation on Multi-Hole Aerodynamic Pressure Probes. *J. Turbomach.* **2021**, *143*, 091001. [CrossRef]
54. Montomoli, F.; Carnevale, M.; Massini, M.; D'Ammaro, A.; Salvadori, S. *Uncertainty Quantification in Computational Fluid Dynamics and Aircraft Engines*; Springer: London, UK, 2015.
55. Sepe, M.; Graziano, A.; Badora, M.; Di Stazio, A.; Bellani, L.; Compare, M.; Zio, E. A physics-informed machine learning framework for predictive maintenance applied to turbomachinery assets. *J. Glob. Power Propuls. Soc.* **2021**, 1–15. [CrossRef]
56. Gottschalk, H.; Saadi, M.; Doganay, O.T.; Klamroth, K.; Schmitz, S. Adjoint Method to Calculate the Shape Gradients of Failure Probabilities for Turbomachinery Components. In *Turbo Expo: Power for Land, Sea, and Air*; Turbomachinery: London, UK, 2018; Volume 7A. [CrossRef]
57. Eldred, M.; Burkardt, J. Comparison of Non-Intrusive Polynomial Chaos and Stochastic Collocation Methods for Uncertainty Quantification. In Proceedings of the 47th AIAA Aerospace Sciences Meeting Including the New Horizons Forum and Aerospace Exposition, Orlando, FL, USA, 5–8 January 2009. [CrossRef]
58. Hanson, J.; Beard, B. Applying Monte Carlo Simulation to Launch Vehicle Design and Requirements Verification. In Proceedings of the AIAA Guidance, Navigation, and Control Conference, Toronto, ON, Canada, 2–5 August 2010.
59. Knio, O.M.; Maître, O.P.L. Uncertainty propagation in CFD using polynomial chaos decomposition. *Fluid Dyn. Res.* **2006**, *38*, 616–640. [CrossRef]
60. Zhou, Y.; Lu, Z.; Hu, J.; Hu, Y. Surrogate modeling of high-dimensional problems via data-driven polynomial chaos expansions and sparse partial least square. *Comput. Methods Appl. Mech. Eng.* **2020**, *364*, 112906. [CrossRef]
61. Salis, C.; Zygiridis, T. Dimensionality Reduction of the Polynomial Chaos Technique Based on the Method of Moments. *IEEE Antennas Wirel. Propag. Lett.* **2018**, *17*, 2349–2353. [CrossRef]

62. Papageorgiou, A.K.; Papoutsis-Kiachagias, E.M.; Giannakoglou, K.C. Development and assessment of an intrusive polynomial chaos expansion-based continuous adjoint method for shape optimization under uncertainties. *Int. J. Numer. Methods Fluids* **2022**, *94*, 59–75. [CrossRef]
63. Chatzimanolakis, M.; Kantarakias, K.D.; Asouti, V.; Giannakoglou, K. A painless intrusive polynomial chaos method with RANS-based applications. *Comput. Methods Appl. Mech. Eng.* **2019**, *348*, 207–221. [CrossRef]
64. Uusitalo, L.; Lehikoinen, A.; Helle, I.; Myrberg, K. An overview of methods to evaluate uncertainty of deterministic models in decision support. *Environ. Model. Softw.* **2015**, *63*, 24–31. [CrossRef]
65. Banerjee, S.; Krahl, R.; Durst, F.; Zenger, C. Presentation of anisotropy properties of turbulence, invariants versus eigenvalue approaches. *J. Turbul.* **2007**, *8*, N32. [CrossRef]
66. Gorlé, C.; Emory, M.; Larsson, J.; Iaccarino, G. *Epistemic Uncertainty Quantification for RANS Modeling of the Flow over a Wavy Wall*; annual research briefs; Center for Turbulence Research: Stanford, CA, USA, 2012; pp. 81–91.
67. Emory, M.; Larsson, J.; Iaccarino, G. Modeling of structural uncertainties in Reynolds-averaged Navier–Stokes closures. *Phys. Fluids* **2013**, *25*, 110822. [CrossRef]
68. Heyse, J.F.; Mishra, A.A.; Iaccarino, G. Estimating RANS model uncertainty using machine learning. *J. Glob. Power Propuls. Soc.* **2021**, 1–14. [CrossRef]
69. Cheung, S.H.; Oliver, T.A.; Prudencio, E.E.; Prudhomme, S.; Moser, R.D. Bayesian uncertainty analysis with applications to turbulence modeling. *Reliab. Eng. Syst. Saf.* **2011**, *96*, 1137–1149. [CrossRef]
70. Oliver, T.A.; Moser, R.D. Bayesian uncertainty quantification applied to RANS turbulence models. *J. Phys. Conf. Ser.* **2011**, *318*, 042032. [CrossRef]
71. Oliver, T.; Moser, R. Uncertainty Quantification for RANS Turbulence Model Predictions. In *APS Division of Fluid Dynamics Meeting Abstracts*; 2009. Available online: http://meetings.aps.org/link/BAPS.2009.DFD.LC.4 (accessed on 2 February 2022).
72. Xiao, H.; Wu, J.L.; Wang, J.X.; Sun, R.; Roy, C. Quantifying and reducing model-form uncertainties in Reynolds-averaged Navier–Stokes simulations: A data-driven, physics-informed Bayesian approach. *J. Comput. Phys.* **2016**, *324*, 115–136. [CrossRef]
73. Edeling, W.N.; Cinnella, P.; Dwight, R.P.; Bijl, H. Bayesian estimates of parameter variability in the k-ϵ turbulence model. *J. Comput. Phys.* **2014**, *258*, 73–94. [CrossRef]
74. Edeling, W.; Cinnella, P.; Dwight, R.P. Predictive RANS simulations via Bayesian model-scenario averaging. *J. Comp. Phys.* **2014**, *275*, 65–91. [CrossRef]
75. Li, J.P.; Zeng, F.Z.; Chen, S.S.; Zhang, K.L.; Yan, C. Bayesian model evaluation of three k–ω turbulence models for hypersonic shock wave–boundary layer interaction flows. *Acta Astronaut.* **2021**, *189*, 143–157. [CrossRef]
76. Xiao, H.; Wang, J.X.; Ghanem, R.G. A random matrix approach for quantifying model-form uncertainties in turbulence modeling. *Comput. Methods Appl. Mech. Eng.* **2017**, *313*, 941–965. [CrossRef]
77. Dow, E.; Wang, Q. Quantification of structural uncertainties in the k-ω turbulence model. In Proceedings of the AIAA/ASME/ASCE/AHS/ASC Structures, Structural Dynamics and Materials Conference, Denver, CO, USA, 4–7 April 2011. [CrossRef]
78. Tracey, B.D.; Duraisamy, K.; Alonso, J.J. A machine learning strategy to assist turbulence model development. In Proceedings of the 53rd AIAA Aerospace Sciences Meeting, Kissimmee, FL, USA, 5–9 January 2015; p. 1287.
79. Parish, E.J.; Duraisamy, K. A paradigm for data-driven predictive modeling using field inversion and machine learning. *J. Comput. Phys.* **2016**, *305*, 758–774. [CrossRef]
80. Singh, A.P.; Duraisamy, K. Using field inversion to quantify functional errors in turbulence closures. *Phys. Fluids* **2016**, *28*, 045110. [CrossRef]
81. Duraisamy, K.; Iaccarino, G.; Xiao, H. Turbulence Modeling in the Age of Data. *Ann. Rev. Fluid Mech.* **2019**, *51*, 357–377. [CrossRef]
82. Xiao, H.; Cinnella, P. Quantification of model uncertainty in RANS simulations: A review. *Prog. Aerosp. Sci.* **2019**, *108*, 1–31. [CrossRef]
83. Geneva, N.; Zabaras, N. Quantifying model form uncertainty in Reynolds-averaged turbulence models with Bayesian deep neural networks. *J. Comput. Phys.* **2019**, *383*, 125–147. [CrossRef]
84. McKeand, A.M.; Gorguluarslan, R.M.; Choi, S.K. Stochastic analysis and validation under aleatory and epistemic uncertainties. *Reliab. Eng. Syst. Saf.* **2021**, *205*, 107258. [CrossRef]
85. Pepper, N.; Montomoli, F.; Sharma, S. Data fusion for Uncertainty Quantification with Non-Intrusive Polynomial Chaos. *Comput. Methods Appl. Mech. Eng.* **2021**, *374*, 113577. [CrossRef]
86. He, Q. Model validation based on probability boxes under mixed uncertainties. *Adv. Mech. Eng.* **2019**, *11*, 1687814019847411. [CrossRef]
87. Ling, J.; Templeton, J. Evaluation of machine learning algorithms for prediction of regions of high Reynolds averaged Navier Stokes uncertainty. *Phys. Fluids* **2015**, *27*, 085103. [CrossRef]
88. Freeman, R. 1—New welding techniques for aerospace materials. In *Welding and Joining of Aerospace Materials*, 2nd ed.; Woodhead Publishing Series in Welding and Other Joining Technologies; Chaturvedi, M., Ed.; Woodhead Publishing: Cambridge, UK, 2021; pp. 1–19. [CrossRef]
89. Hüllermeier, E.; Waegeman, W. Aleatoric and epistemic uncertainty in machine learning: An introduction to concepts and methods. *Mach. Learn.* **2021**, *110*, 457–506. [CrossRef]

90. Psaros, A.F.; Meng, X.; Zou, Z.; Guo, L.; Karniadakis, G.E. Uncertainty Quantification in Scientific Machine Learning: Methods, Metrics, and Comparisons. *arXiv* **2022**, arXiv:2201.07766.
91. McCroskey, W. *A critical Assessment of Wind Tunnel Results for the NACA 0012 Airfoil*; Technical Report; National Aeronautics and Space Administration: Moffett Field, CA, USA, 1987.
92. Mavris, D.; DeLaurentis, D. Methodology for Examining the Simultaneous Impact of Requirements, Vehicle Characteristics, and Technologies on Military Aircraft Design. *ICAS* **2000**, *144*, 1–12.
93. Saravi, M.; Newnes, L.; Mileham, A.; Goh, Y. Estimating Cost at the Conceptual Design Stage to Optimize Design in terms of Performance and Cost. In *Collaborative Product and Service Life Cycle Management for a Sustainable World*; Advanced Concurrent Engineering; Curran, R., Chou, S., Trappey, A., Eds.; Springer: Berlin, Germany, 2008.
94. Xie, R.; Chen, M.; Liu, W.; Jian, H.; Shi, Y. Technologies for Turbomachinery in a Life Cycle Perspective: A Review. *Sustainability* **2021**, *13*, 2495. [CrossRef]
95. Babuška, I.; Nobile, F.; Tempone, R. Reliability of computational science. *Numer. Methods Partial. Differ. Equ.* **2007**, *23*, 753–784. [CrossRef]
96. Kennedy, M.C.; O'Hagan, A. Bayesian calibration of computer models. *J. R. Stat. Soc. Ser. B (Stat. Methodol.)* **2001**, *63*, 425–464. [CrossRef]
97. Forrester, A.I.; Sóbester, A.; Keane, A.J. Multi-fidelity optimization via surrogate modelling. *Proc. R. Soc. A Math. Phys. Eng. Sci.* **2007**, *463*, 3251–3269. [CrossRef]
98. Eldred, M.S.; Ng, L.W.T.; Barone, M.F.; Domino, S.P. Multifidelity Uncertainty Quantification Using Spectral Stochastic Discrepancy Models. In *Handbook of Uncertainty Quantification*; Ghanem, R., Higdon, D., Owhadi, H., Eds.; Springer International Publishing: Cham, Switzerland, 2015; pp. 991–1040.
99. Yan, L.; Zhou, T. Adaptive multi-fidelity polynomial chaos approach to Bayesian inference in inverse problems. *J. Comput. Phys.* **2019**, *381*, 110–128. [CrossRef]
100. Giles, M.B. Multilevel Monte Carlo methods. *Acta Numer.* **2015**, *24*, 259–328. [CrossRef]
101. Wang, F.; Zhang, Q.J. Knowledge-based neural models for microwave design. *IEEE Trans. Microw. Theory Tech.* **1997**, *45*, 2333–2343. [CrossRef]
102. Yang, L.; Meng, X.; Karniadakis, G.E. B-PINNs: Bayesian physics-informed neural networks for forward and inverse PDE problems with noisy data. *J. Comput. Phys.* **2021**, *425*, 109913. [CrossRef]
103. Pepper, N.; Gaymann, A.; Sharma, S.; Montomoli, F. Local bi-fidelity field approximation with Knowledge Based Neural Networks for Computational Fluid Dynamics. *Sci. Rep.* **2021**, *11*, 14459. [CrossRef]
104. Laurenceau, J.; Sagaut, P. Building efficient response surfaces of aerodynamic functions with kriging and cokriging. *AIAA J.* **2008**, *46*, 498–507. [CrossRef]
105. Wang, Q.; Song, L.; Guo, Z.; Li, J. Transfer Optimization in Accelerating the Design of Turbomachinery Cascades. In *Turbo Expo: Power for Land, Sea, and Air*; Turbomachinery: London, UK, 2020; Volume 2D. [CrossRef]
106. Han, Z.H.; Zimmermann, R.; Goretz, S. A New Cokriging Method for Variable-Fidelity Surrogate Modeling of Aerodynamic Data. In Proceedings of the 48th AIAA Aerospace Sciences Meeting Including the New Horizons Forum and Aerospace Exposition, Orlando, FL, USA, 4–7 January 2010. [CrossRef]
107. Rumpfkeil, M.; Yamazaki, W.; Dimitri, M. A Dynamic Sampling Method for Kriging and Cokriging Surrogate Models. In Proceedings of the 49th AIAA Aerospace Sciences Meeting including the New Horizons Forum and Aerospace Exposition, Orlando, FL, USA, 4–7 January 2011. [CrossRef]
108. Chan, S.; Elsheikh, A.H. A machine learning approach for efficient uncertainty quantification using multiscale methods. *J. Comput. Phys.* **2018**, *354*, 493–511. [CrossRef]
109. Peng, G.C.; Alber, M.; Tepole, A.B.; Cannon, W.R.; De, S.; Dura-Bernal, S.; Garikipati, K.; Karniadakis, G.; Lytton, W.W.; Perdikaris, P.; et al. Multiscale modeling meets machine learning: What can we learn? *Arch. Comput. Methods Eng.* **2021**, *28*, 1017–1037. [CrossRef] [PubMed]
110. Trehan, S.; Durlofsky, L. Machine-learning-based modeling of coarse-scale error, with application to uncertainty quantification. *Comput. Geosci.* **2018**, *22*, 1093–1113. [CrossRef]
111. Lye, K.O.; Mishra, S.; Molinaro, R. A multi-level procedure for enhancing accuracy of machine learning algorithms. *Eur. J. Appl. Math.* **2021**, *32*, 436–469. [CrossRef]
112. Jabarullah Khan, N.K.; Elsheikh, A.H. A machine learning based hybrid multi-fidelity multi-level Monte Carlo method for uncertainty quantification. *Front. Environ. Sci.* **2019**, *7*, 105. [CrossRef]
113. Lengani, D.; Simoni, D.; Pichler, R.; Sandberg, R.D.; Michelassi, V.; Bertini, F. On the Identification and Decomposition of the Unsteady Losses in a Turbine Cascade. *J. Turbomach.* **2019**, *141*, 031005. [CrossRef]
114. Denton, J. The 1993 IGTI Scholar Lecture: Loss Mechanics in Turbomachines. *ASME J. Turbomach.* **1993**, *115*, 621–656. [CrossRef]
115. Leggett, J.; Priebe, S.; Shabbir, A.; Michelassi, V.; Sandberg, R.; Richardson, E. LES Loss Prediction in an Axial Compressor Cascade at Off-Design Incidences with Free Stream Disturbances. *ASME J. Turbomach.* **2018**, *7*, 071005. [CrossRef]
116. Karniadakis, G.E.; Kevrekidis, I.G.; Lu, L.; Perdikaris, P.; Wang, S.; Yang, L. Physics-informed machine learning. *Nat. Rev. Phys.* **2021**, *3*, 422–440. [CrossRef]
117. Cai, S.; Mao, Z.; Wang, Z.; Yin, M.; Karniadakis, G.E. Physics-informed neural networks (PINNs) for fluid mechanics: A review. *arXiv* **2021**, arXiv:2105.09506.

118. Lumley, J. Toward a turbulent constitutive relation. *J. Fluid Mech.* **1970**, *41*, 413–434. [CrossRef]
119. Eivazi, H.; Tahani, M.; Schlatter, P.; Vinuesa, R. Physics-informed neural networks for solving Reynolds-averaged Navier–Stokes equations. *arXiv* **2021**, arXiv:2107.10711.
120. Raissi, M.; Perdikaris, P.; Karniadakis, G. Physics-informed neural networks: A deep learning framework for solving forward and inverse problems involving nonlinear partial differential equations. *J. Comput. Phys.* **2019**, *378*, 686–707. [CrossRef]

International Journal of
Turbomachinery
Propulsion and Power

MDPI

Article

UHBR Open-Test-Case Fan ECL5/CATANA †

Valdo Pagès [1], Pierre Duquesne [1], Stéphane Aubert [1], Laurent Blanc [2], Pascal Ferrand [1], Xavier Ottavy [1] and Christoph Brandstetter [1,*]

[1] Ecole Centrale de Lyon, Univ. Lyon, CNRS, Univ. Claude Bernard Lyon 1, INSA Lyon, LMFA, UMR5509, 69130 Ecully, France; valdo.pages@ec-lyon.fr (V.P.); pierre.duquesne@ec-lyon.fr (P.D.); stephane.aubert@ec-lyon.fr (S.A.); pascal.ferrand@ec-lyon.fr (P.F.); xavier.ottavy@ec-lyon.fr (X.O.)
[2] Ecole Centrale de Lyon, Univ. Lyon, CNRS, UMR5513, LTDS, 69130 Ecully, France; laurent.blanc@ec-lyon.fr
* Correspondence: christoph.brandstetter@ec-lyon.fr
† This paper is an extended version of our paper published in Proceedings of the European Turbomachinery Conference ETC14 2021, Paper No. 625 and 626, Gdansk, Poland, 12–16 April 2021.

Abstract: The application of composite fans enables disruptive design possibilities but increases sensitivity to multi-physical resonance between aerodynamic, structure dynamic and acoustic phenomena. As a result, aeroelastic problems increasingly set the stability limit. Test cases of representative geometries without industrial restrictions are a key element of an open scientific culture but are currently non-existent in the turbomachinery community. In order to provide a multi-physical validation benchmark representative of near-future UHBR fan concepts, the open-test-case fan stage ECL5 was developed at Ecole Centrale de Lyon. The design intention was to develop a geometry with high efficiency and a wide stability range that can be realized using carbon fibre composites. This publication aims to introduce the final test case, which is currently fabricated and will be experimentally tested. The fan blades are composed of a laminate made of unidirectional carbon fibres and epoxy composite plies. Their structural properties and the ply orientations are presented. To characterize the test case, details are given on the aerodynamic design of the whole stage, structure dynamics of the fan and aeroelastic stability of the fan. These are obtained with a state-of-art industrial design process: static and modal FEM, RANS and LRANS simulations. Aerodynamic analysis focuses on performance and shows critical flow structures such as tip leakage flow, radial flow migration and flow separations. Mechanical modes of the fan are described and discussed in the context of aeroelastic interactions. Their frequency distribution is validated in terms of resonance risk with respect to synchronous vibration. The aeroelastic stability of the fan is evaluated at representative operating points with a systematic approach. Potential instabilities are observed far from the operating line and do not compromise experimental campaigns.

Keywords: fan; composite; aeroelasticity; flutter; aeroacoustics

check for updates

Citation: Pagès, V.; Duquesne, P.; Aubert, S.; Blanc, L.; Ferrand, P.; Ottavy, X.; Brandstetter, C. UHBR Open-Test-Case Fan ECL5/CATANA. *Int. J. Turbomach. Propuls. Power* **2022**, *7*, 17. https://doi.org/10.3390/ijtpp7020017

Academic Editor: Raúl Vázquez Díaz

Received: 25 January 2022
Accepted: 17 May 2022
Published: 31 May 2022

Publisher's Note: MDPI stays neutral with regard to jurisdictional claims in published maps and institutional affiliations.

Copyright: © 2022 by the authors. Licensee MDPI, Basel, Switzerland. This article is an open access article distributed under the terms and conditions of the Creative Commons Attribution (CC BY-NC-ND) license (https://creativecommons.org/licenses/by-nc-nd/4.0/).

1. Introduction

With the application of modern lightweight blade geometries, aeroelastic coupling phenomena tend to reduce the operating range of compressors and fans in aircraft propulsion engines. As synchronous excitation mechanisms are well understood today, the most challenging aeroelastic phenomena for future turbomachinery applications are of a non-synchronous (not a multiple of the shaft rotation speed) nature. A list of these phenomena is presented as follows. This paper is an extended version of our paper published in Proceedings of the European Turbomachinery Conference ETC14 2021, Paper No. 625 and 626, Gdansk, Poland, 12–16 April 2021 [1,2].

Flutter is defined as self-excited blade vibration and usually involves blade-to-blade coupling. It is considered as initially small-amplitude blade oscillation in a specific eigenmode that exponentially amplifies through a positive feedback loop with the aerodynamic

field (negative aerodynamic damping). Linear modelling approaches are capable of predicting the onset of this mechanism and of determining critical modes and developing countermeasures. The disturbance is only dependent on the blade vibration and disappears as soon as the vibration stops. For large vibration amplitudes, limit-cycle oscillation may occur due to aerodynamic or structure dynamic non-linearity. For turbo-engine fans, critical modes are typically dependent on swirling acoustic modes that develop between the inlet and the fan stage [3].

Buffeting describes the interaction between an aerodynamic instability (typically vortex shedding) that comprises a characteristic frequency and the blade vibration in a specific eigenmode. Typically, no circumferential blade-to-blade coupling is necessary, but often planar acoustic duct modes establish and synchronize the phase of the aerodynamic instabilities leading to a zero-nodal-diameter vibration [4].

Rotating stall is a purely aerodynamic phenomenon occurring due to overloading of a blade row and subsequent flow separation, leading to the establishment of circumferentially propagating stall cells. It typically excites structural eigenmodes due to unsteady loading, but for small amplitudes the propagation is not coupled with the blade vibration [5].

Non-synchronous forced response is a non-synchronous coupling mechanism in multistage compressors that has been observed between a trapped acoustic mode and a coincident structural vibration pattern [6]. The phenomenon is less relevant for fan applications.

Convective non-synchronous vibration (NSV) typically occurs close to the stability limit but before the onset of rotating stall. A complex lock-in mechanism between propagating aerodynamic vorticity disturbances and blade vibration is described under the term NSV [7,8]. Blade vibration leads to a change in free vorticity, or even the formation of radial vortices in the passage flow, which are convected from blade to blade if a sufficient blockage is present in the passage. Interaction with trailing blades leads to modal forcing and the shedding of subsequent vorticity. Propagating aerodynamic disturbances can lock in with structural vibration patterns and lead to a coherent fluid–structural interaction. The phenomenon must be differentiated from flutter, as the aerodynamic disturbance appears without blade vibration and has a characteristic convective propagation speed (typically described under the term rotating instability).

For all the described phenomena, the flow structure in the tip region, particularly the influence of the tip leakage flow and the passage shock, is of great importance. Significant blockage enables the circumferential transport of disturbances or provokes separation of the boundary layer, which may be susceptible to acoustic or structure-dynamic feedback.

For high-speed fans, rotating stall, buffeting and flutter are the most common instability mechanisms and are well understood today. The establishment of UHBR configurations with low-speed fans, however, leads to a substantial change in the relevant characteristics.

- Low-speed fans predominantly operate on the flat part of the compression characteristic, making them more susceptible to stall-driven instability [9].
- The flutter frequencies (in the stationary frame) are lower compared to high-speed designs. Acoustic liners in the intake, which are designed to attenuate higher-frequency community noise, do not affect the modes relevant for aeroelastic instability.
- The intake length is shorter for low-speed fans, leading to stronger inflow asymmetry and altered acoustic interactions [10]. This gives rise to stronger broadband excitation and shifted resonance frequencies.
- The relative Mach number and shock strength are lower, and the tip clearance relative to the blade chord and solidity (solidity = blade chord length/pitch) are smaller than for conventional direct-drive fans and more sensitive to geometric variability [11].
- A strongly non-linear fluid–structure interaction has been observed at low frequencies for fans with low solidity related to the pressure untwist of the blades. Under transonic conditions, slight deviations of the local stagger angle at the blade tip can cause a fundamentally different shock structure between adjacent blades that affects the stability of distinct rotor sections [12]. This circumstance affects the applicability

of promising methods such as intentional blade mistuning [13] for suppressing the development of circumferentially propagating modes.

A selection of state-of-the-art high-bypass-ratio engines is presented in Figure 1 (image sources (accessed on 20 September 2021): (a) https://www.geaviation.com/commercial/engines/ge90-engine; (b) https://www.geaviation.com/commercial/engines/genx-engine https://c-fan.com/products/; (c) https://www.cfmaeroengines.com/engines/leap/; (d) https://www.flugrevue.de/flugzeugbau/getriebefan-triebwerke-pratt-whitney-will-probleme-beseitigen/; (e) https://www.airlineratings.com/news/a350s-trent-xwb-engine-hits-twin-milestones/). The propulsion industry has focused on different strategies but all show common goals: a reduction in tip speed, a reduction in the number of blades and a reduction in individual blade weight. General Electric started in the 1990s with the establishment of layered carbon fibre composite fan blades in the GE90 engine for wide-body aircraft and is the only manufacturer with in-service composite fans. The more recent GEnx shows a reduced blade number of 18. Following this development, the CFM LEAP engine was established for the A320neo class, with 18 blades constructed from 3D woven carbon fibres. Pratt & Whitney introduced the first geared turbofan with 20 (hybrid) metallic blades, also for the A320neo class. Still following a conventional approach in fan design, recent Rolls-Royce engines comprise hollow titanium blades, but technology demonstrators based on variants of the Trent 1000 engine incorporate composite fibre fan blades. The fan of the Trent XWB engine for the Airbus A350 high-bypass engine with 22 blades is shown as an example in Figure 1 (Trent 7000 has 20 blades).

Figure 1. Selection of established modern (ultra)-high-bypass-ratio engines.

All the fan blades shown have significant 3D features, particularly forward sweep, which is known to be beneficial for aerodynamic performance but emphasizes aeroelastic sensitivity for torsional or chord-wise bending modes and particularly NSV. Recent research [14,15] has shown that the use of the anisotropic properties of composites in fans could help to improve both the mechanics and aerodynamics. Composites also present the potential to control flutter by modification of the eigenmodes [16].

In order to enable further technological advancements in this direction, extensive research is necessary to identify and characterize the relevant instability mechanisms for the novel type of low-speed fan. In particular, the complex flow structure at part load and part speed is challenging for state-of-the-art numerical approaches and requires experimental benchmark data on representative geometries.

To address these research objectives, an extensive research program with collaboration between Ecole Centrale de Lyon and the Von Karman Institute for Fluid Dynamics has been initiated. A fan module, ECL5, fabricated from composite material, has been developed as an open test case. It will be investigated, with a focus on non-synchronous coupling mechanisms between aerodynamics, acoustics and structure dynamics, within the European Clean Sky 2 project CATANA (Composite Aeroelastics and Aeroacoustics, catana.ec-lyon.fr). The fan stage was designed at Ecole Centrale de Lyon and was intended to be representative of near-future composite low-speed fans in terms of the following:

1. General aerodynamic design parameters (Mach number, blade loading, solidity, aspect ratio, hub-to-tip ratio, mass flow density, etc.)

2. Aerodynamic flow structure, due to its influence on instability mechanisms (shock patterns, radial flow migration, secondary flow, separations, etc.)

From the current point of view, the most promising research configuration is a UHBR low-speed fan stage with high subsonic design speed, designed to be installed in midrange jets (such as Airbus A320neo). Hence, the open-test-case ECL5 that will be introduced in the following was developed from an extrapolation of industrial concepts for current low-speed designs. In Figure 2, (image sources (accessed on 20 September 2021): (a) https://www.additivemanufacturing.media/mission-critical/; (b) https://www.air-cosmos.com/article/rolls-royce-tests-ultrafan-low-pressure-system-592, image flipped), the final design is shown in comparison to the recently certified GE9x and the Rolls Royce UltraFan technology demonstrator.

Figure 2. Modern industrial low-speed composite fans and open-test-case ECL5/CATANA (CAD).

In the following, the final design and the composite structure of the fan are presented. Details are given on the modelling strategies used to simulate the different physics: stationary flow simulations (RANS), mechanical simulations (FEM) and time-linearized simulations (LRANS). Finally, the aerodynamic behaviour and structural dynamics of the fan are deduced, and its aeroelastic stability is assessed.

2. ECL5 Description

2.1. Design Approach

Based on an initial design [17], the final design was obtained with the use of a modularly coupled design chain, including a parametric blade geometry generator, automatic meshing, a steady RANS solver and structural FEM simulations. The fan geometry fulfils the following design objectives:

- A blade number of 16 (lowest blade count in technology demonstrators as shown above).
- A fan diameter of 508 mm to enable integration into the test facility PHARE-2, with blade root compatible with the existing disk from Project ENOVAL [18].
- Aerodynamic design point (fan only) at peak efficiency with a pressure ratio of 1.36, a mass flow density maximum of 200 kg/s/m^2 and a rotation speed of 11,000 rpm.
- Near-sonic relative tip Mach number at the design point.
- Isentropic efficiency (fan only) exceeding 94% at the design point.
- At peak pressure at the design speed, no flow separation at the trailing edge.
- Peak efficiency at 105% and speed not lower than 92% (transonic speedline).
- Nominal tip clearance of ∼1 mm (1.1% tip chord) to ensure stall inception and surge experiments without casing contact. Future experiments are planned with further reduced tip clearance.
- Fan to be fabricated without integration of a metallic leading edge.

For the OGV, no specific design criteria were set except for a minimization of the (numerical) corner separation under highly loaded conditions and minimum losses at the design point. The blade number was fixed at 32 in the optimization process and reduced to 31 for the final design, to avoid the establishment of planar acoustic interactions.

Stage inlet and outlet geometry is similar to previous installations [18]. The same applies to the casing geometry in the fan section. The OGV is located far downstream of the fan to minimize interactions, as the focus of the research project was on the fan. As the facility comprises only a single flow channel, engine-representative OGV aerodynamics are not intended; only axial stage outflow and homogeneous radial conditions are required to ensure detailed performance analysis and to enable future research projects with a fundamental background in noise generation.

The development process is described in detail in Pagès [19]. The hubline, from nosecone to OGV outlet, was open for optimization. A section of the design is presented in Figure 3. Figure 4 shows the blade profiles at different span heights, clearly emphasizing the transonic blade design at the fan tip and the wide chord geometry around midspan. At the hub, the relative tangential velocity and the rotational speed have the same direction at the trailing edge, which is necessary in order to meet the design criteria laid out above but creates a challenging flow field with high swirl velocities upstream of the OGV.

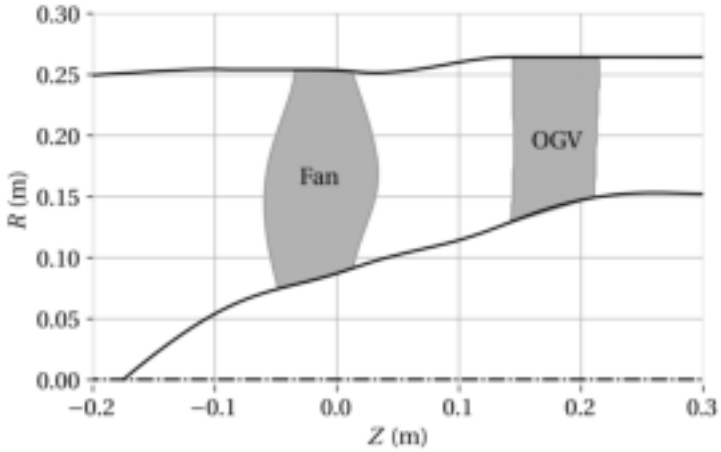

Figure 3. Section of ECL5 fan stage.

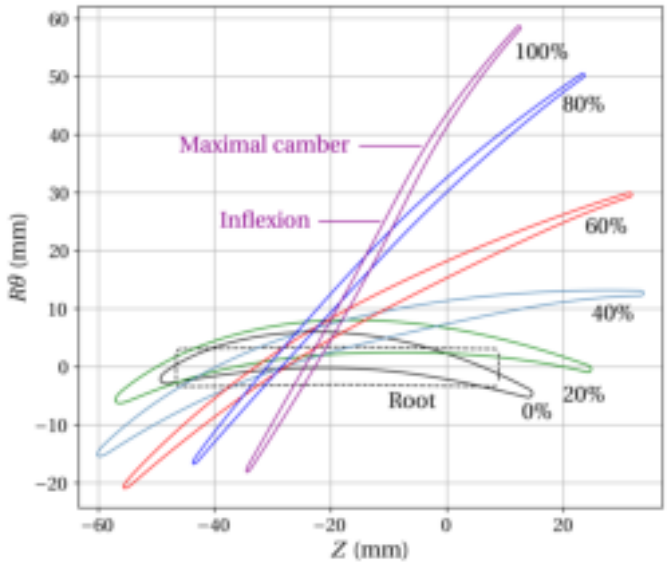

Figure 4. Fan profiles at different span heights.

The tip clearances for various rotation speeds are presented in Table 1:

Table 1. Tip clearance as predicted by FEM model (tip chord = 90 mm).

Rotation Speed	Tip Clearance (mm)		Tip Clearance (% Tip Chord)	
(100% = 11,000 rpm)	**Leading Edge**	**Trailing Edge**	**Leading Edge**	**Trailing Edge**
0%	1.00	1.50	1.11	1.67
50%	0.98	1.30	1.09	1.45
80%	0.87	1.12	0.97	1.25
100%	0.78	0.99	0.87	1.10
105%	0.77	0.92	0.86	1.02

2.2. Fan Composite Structure

The blade is exclusively made of unidirectional carbon fibres and epoxy composite plies stacked into a laminate with intentional ply orientations. A ply is considered to be made of orthotropic material. The three material orthotropy directions are defined locally as follows: direction 1 is the orientation of the carbon fibres, direction 2 is orthogonal to direction 1 within the ply and direction 3 is orthogonal to the ply. The constitutive law of the composite material is described classically by nine constants, as listed in Table 2 (indicated by the composite manufacturer).

Table 2. Material properties.

ρ	E_1	$E_2 = E_3$	G_{23}	$G_{12} = G_{13}$	ν_{23}	$\nu_{12} = \nu_{13}$
1560 kg/m^3	123.0 GPa	9.3 GPa	5.0 GPa	4.5 GPa	0.3	0.26

The maximum thickness of the blade (at the root) is 13.3 mm. The thickness of a ply is 0.15 mm, so the maximum number of plies is 88. The internal structure is symmetric with respect to the laminate midplane, to minimize the coupling of in-plane and out-of-plane movements. Each point of the midplane is associated with a number of plies defined by the local blade thickness. Plies are ranked by their size from largest to smallest (see Figure 5).

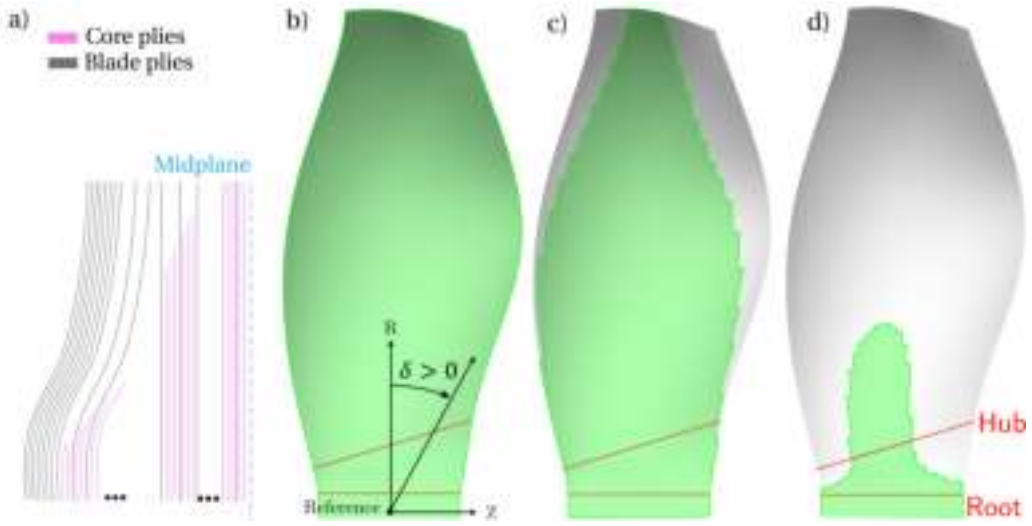

Figure 5. Plies of ECL5 fan (coloured in green): (**a**) ply alternation; (**b**) Ply 1—blade, wrap; (**c**) Ply 6—blade; (**d**) Ply 19—core.

For the design process, plies were divided into two families. The 18 largest plies are called blade plies and the others—the smallest—are called core plies. To reduce the number of degrees of freedom for the design, the orientation of core plies was set, considering half a blade, in the sequence $((0°/90°)_6(0°/90°/0°)_4(0°/0°))_s$, with 0° defined as the radial direction. Their influence on global elastic properties is minor; they mainly contribute to thickness adjustment. Thus the total number of fibre orientations to be defined was set to

18. These orientations are listed in Table 3. The orientation of a ply is defined as illustrated in Figure 5b. The orientation is imposed on a chosen point at the root of the blade. Local orientation along the blade is determined by the draping of the surface [20].

Table 3. Blade ply orientations.

Ply Nr.	**1**	**2**	**3**	**4**	**5**	**6**	**7**	**8**	**9**
Orientation	45°	−45°	−15°	−30°	15°	−15°	70°	0°	0°
Ply Nr.	**10**	**11**	**12**	**13**	**14**	**15**	**16**	**17**	**18**
Orientation	−15°	0°	0°	60°	−60°	0°	0°	60°	−60°

The manufacturing process consisted of three steps. First, each pre-impregnated ply was cut to the predefined shape. Secondly, the plies were stacked into two half-molds. Then, both molds were pressed together before heating to start the epoxy polymerisation process.

The plies were stacked in a particular way to improve the manufacturing process and the final resistance to delamination. This was an alternation of blade plies and core plies, as illustrated in Figure 5a. One particular feature is that Ply 1 (the largest, Figure 5b) was placed at the external surface of the blade. Thus, the external surface is composed of only one ply and has a very low surface roughness with no sharp step.

3. Modelling Strategies

3.1. Aerodynamics

For the aerodynamic simulations, a structured mesh was created using AutoGrid (https://www.numeca.com, accessed on 20 September 2021). A single passage of the fan domain contains 3.5 million cells, with 141 layers in the radial direction, and 41 layers are used in the tip gap. The OGV domain contains 1.7 million cells, with 101 layers in the radial direction and no tip gap. The fan meshing is illustrated in Figure 6.

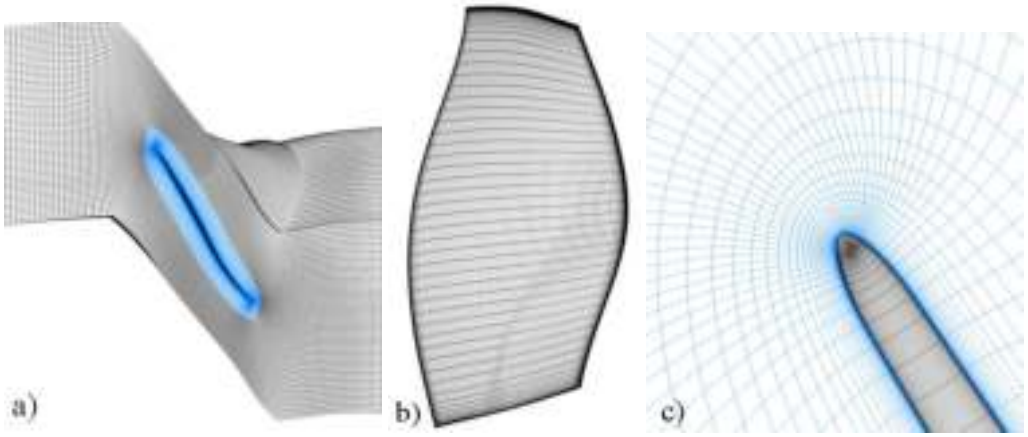

Figure 6. Views of structured mesh for aerodynamic simulations: (**a**) blade to blade; (**b**) meridional; (**c**) O-mesh around the leading edge and the matching tip-clearance mesh.

Stationary flow simulations were conducted using the RANS solver FineTurbo (https://www.numeca.com, accessed on 20 September 2021). The wall resolution of this mesh is below $y^+ = 1$ for design conditions. A $k - \omega$ SST turbulence model was used for the simulations presented in the following. This methodology was validated in a study on a comparable low-speed fan for the operating range between choke and peak pressure [18]. A study on mesh convergence is presented in [19].

3.2. Mechanics

The FEM solver Ansys was used for the mechanical simulations (https://www.ansys.com/products/structures/ansys-mechanical, accessed on 20 September 2021). The simulation

domain and boundary conditions are presented in Figure 7a. A cyclic symmetry condition is imposed on the faces of the disk sector (in purple) since the fan should be tuned and all blades should be identical. The shaft of the test facility is not modelled. To represent the contact between the disk and the shaft, the disk is clamped in the blue area and the axial displacement is set to zero in the green area. The aerodynamic pressure field is imposed on the red surface. Static simulations include large deflection.

The blade composite laminate was modelled by a hexaedric 3D mesh (Ansys ACP (https://www.ansys.com/products/structures/composite-materials , accessed on 20 September 2021)) and a dedicated procedure to model the ply alternation. To reduce the mesh size, a stack of plies was modelled with an equivalent element. Each half-thickness was modelled by an equivalent element (see Figure 7b) with orthotropic properties, homogenized by classical laminate theory [21].

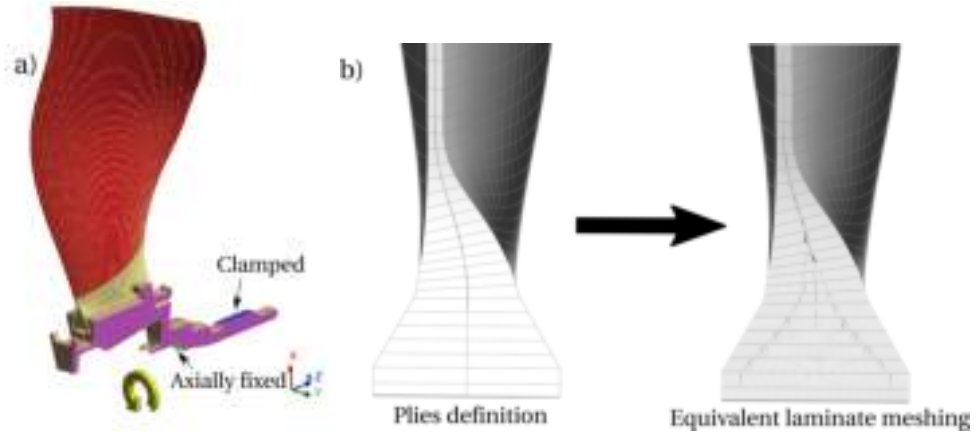

Figure 7. Mechanical model: (**a**) boundary conditions; (**b**) blade thickness meshing.

3.3. Aeroelasticity

3.3.1. Energy Method

The aeroelastic stability was investigated with the energy method [22]. This approach is based on the assumption that flow fluctuations do not affect the structural dynamics and are linear with respect to the vibration amplitude. It consists of two steps. First, eigenmodes and natural frequencies are determined. Secondly, an unsteady flow simulation is performed to compute the harmonic variations of the flow caused by the vibration. Aeroelastic stability is determined by the energy transfer from the structure to the flow. It is assessed by the pressure-force work W per vibration cycle. For positive work ($W > 0$), the blade releases energy to the fluid, so that vibrations are damped. For negative work ($W < 0$), energy is transferred from the fluid into the structure, thus exciting the blade vibration and leading to aeroelastic instability. In agreement with industrial convention, the aerodynamic damping value is defined in the following as:

$$\zeta = \frac{W}{4\pi E_k} = \frac{W}{2\pi M_0 \omega_0^2} \quad (1)$$

where E_k is the modal kinetic energy of the travelling wave, M_0 is the modal mass and ω_0 is the vibration angular frequency.

3.3.2. Time-Linearized Simulations

An isolated fan was considered for the stability study, according to common practice for fan flutter studies based on self-excitation [3,23,24]. The OGV is at a distance of one chord downstream of the fan, so its potential influence is significantly reduced.

To assess the stability of the fan, a time-linearized method (LRANS) was used. Based on the assumption of small harmonic perturbations, the coordinates of the grid vertices,

as well as the flow solution, can be decomposed into a steady part and a time-dependent harmonic perturbation. These two parts were simulated separately.

The steady flow necessary for LRANS simulations was obtained with the compressible RANS solver elsA (http://elsa.onera.fr/, accessed on 20 September 2021). The solver relies on a cell-centred finite volume method on multi-block structured grids. Convective fluxes are obtained using the Jameson scheme with artificial dissipation. The turbulence was modelled by a $k - \omega$ Kok model with vorticity-based computation of turbulent kinetic energy production. A single passage of the fan domain was reduced to 2.3 million cells, with 101 layers in the radial direction and with 21 layers used in the tip gap. The wall resolution remains below $y^+ = 1$. A comparison of the steady-state results with those obtained with FineTurbo was carried out and showed few disparities, resulting in differences lower than 0.3% in the total pressure ratio and 0.3% in the isentropic efficiency for the studied operating points.

The unsteady flow was obtained with the solver Turb'Lin [25]. The solution was obtained in the frequency domain. This vertex-centred LRANS solver has been validated for transonic separated flows [25,26]. The turbulence model was linearized (see [27] for a comparison with results for a frozen turbulence assumption). Upstream and downstream of the fan, the mesh was extended by numerous fan diameters with strongly reduced axial resolution, to attenuate acoustic reflections.

4. Results

4.1. Aerodynamic Characteristics

The stage characteristics of steady RANS calculations throttled via static pressure at the stage outlet are presented in Figure 8. It can be seen that the overall peak efficiency is well located at the 100% speedline, at a point where the total pressure characteristic is almost flat. For high speedlines above 100% of the design speed, choke occurs in the fan; otherwise, it occurs in the OGV. Towards low mass flows, the speedlines are rolled over and limited by numerical convergence. This is comparable to the case presented by Rodrigues et al. [18], showing that through the application of a choked nozzle far downstream, the numerical stability limit can be further extended while still not reaching the stability limit of the experiment. Under highly throttled conditions, the performances in the experiments are expected to significantly deviate from the numerical results. In this paper, five operating points representative of the different flow topologies and limits are presented. OP-A is the design point, OP-B is the maximum pressure ratio and OP-C presents a choked flow at 100% speed. OP-D and OP-E are operating points near the maximum pressure ratio at 80% speed.

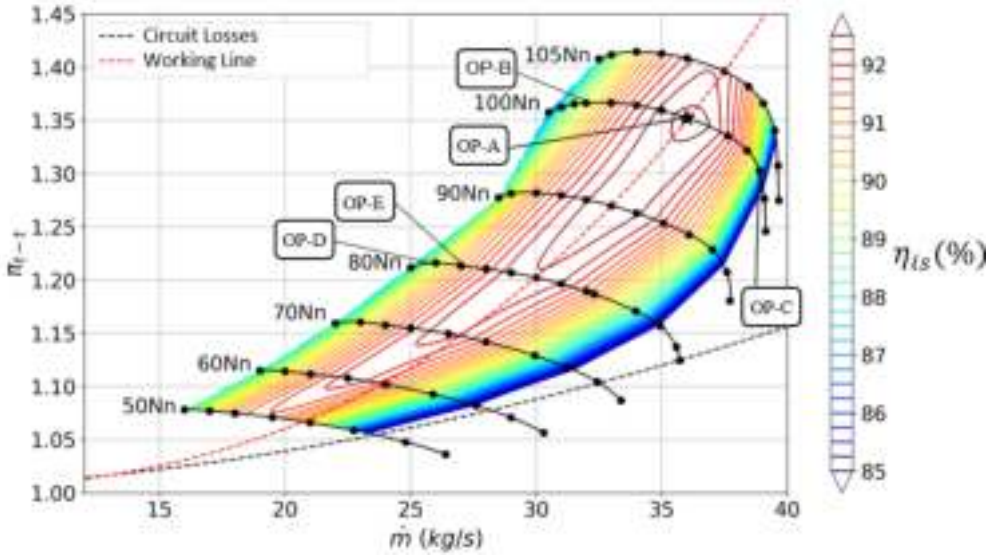

Figure 8. Stage compressor map with operating points of interest.

A detail of the 100% speedline is given in Figure 9, showing the pressure and efficiency characteristics as well as the radial profiles at the rotor exit (aerodynamic simulations were for a constant 1.5 mm tip clearance, and the fabricated fan had tip clearance according to Table 1). In a wide range between OP-B and OP-C (representing 19% of the design mass flow, depicted in cyan in Figure 9), the fan produces a flat efficiency characteristic above 88%. The evolution between the low-throttled operating point OP-C and the higher-throttled conditions shows that the fan is barely affected between the hub and midspan. The maximum pressure ratio is observed near the midspan, and throttling increases the loading of the blade tip. At design point OP-A, the efficiency profile is almost constant between 20% and 80% span. The influence of the tip leakage flow is observed between 85% and 100% span for all conditions shown.

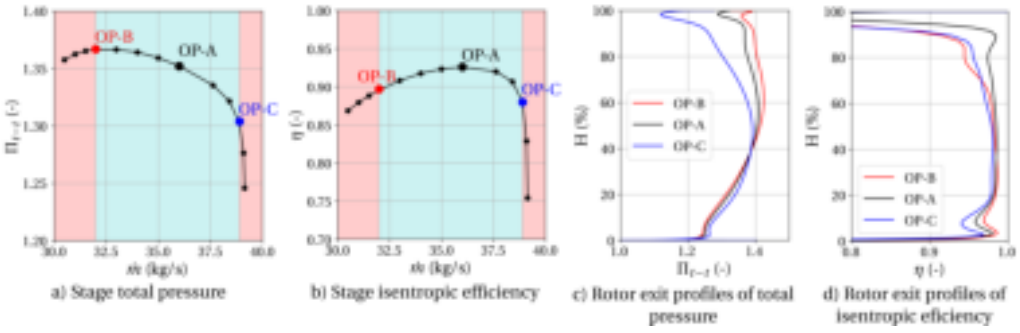

Figure 9. Detail of flow conditions at different operating points at 100% speed.

In Figure 10, the flow structure is presented in more detail for design point OP-A. The isentropic Mach number distribution on the suction side shows the shock structure from midspan and emphasizes the reduced loading at the blade tip. Surface streamlines are homogeneous, without indications for flow separations but with moderate radial migration towards the trailing edge. The blade-to-blade view of the relative Mach number and radial velocity at 95% span indicates low blockage in the tip region and a clearly depicted tip leakage vortex that interacts mildly with the shock.

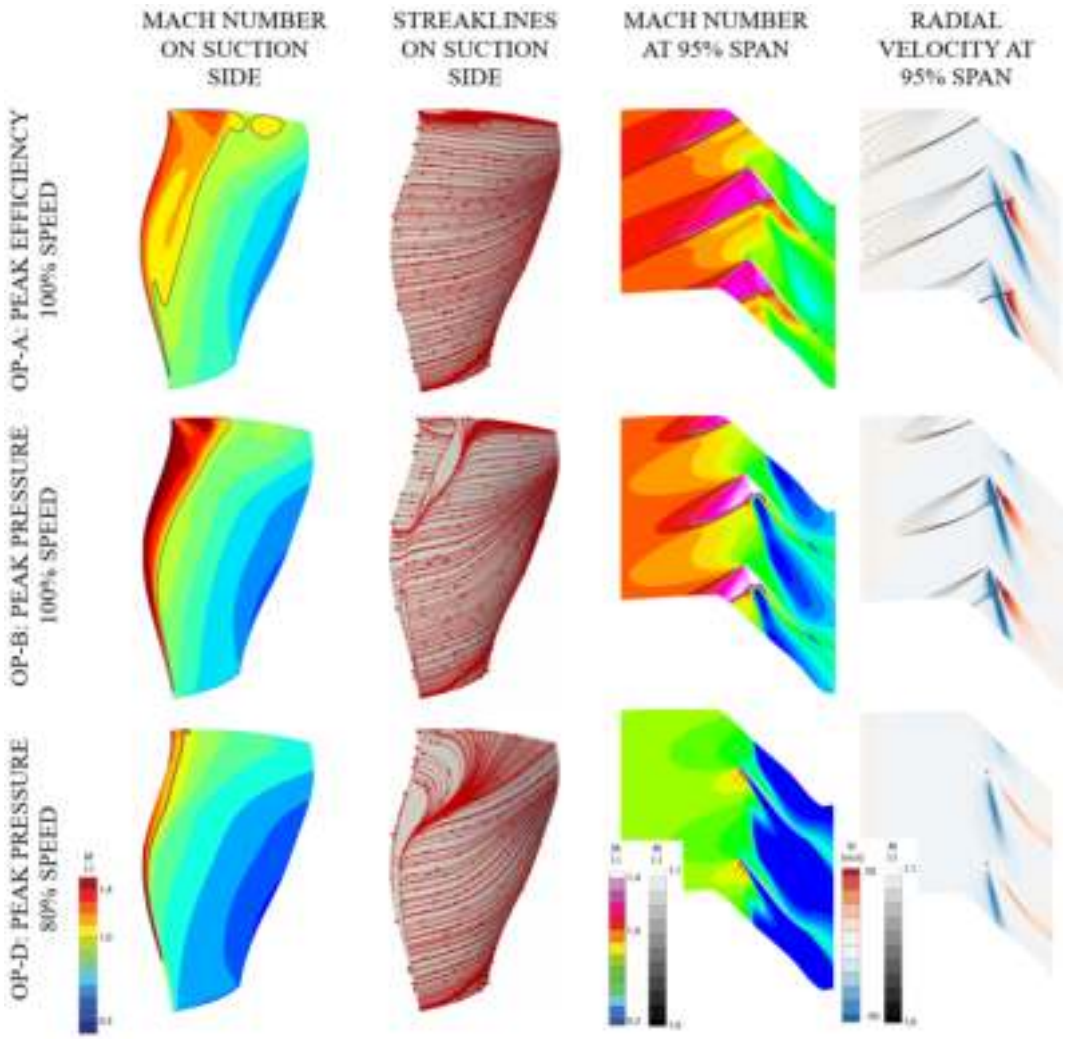

Figure 10. Detail of flow conditions at different operating points.

This situation changes at the maximum pressure condition OP-B, where the pre-shock Mach number strongly increases, and the surface streamlines show signs of boundary-layer separation between 70% span and the casing. In addition, radial migration is accentuated, leading to low relative Mach numbers below 0.2 at the trailing edge at lower channel heights. The blade-to-blade view depicts a strong blockage zone enclosed by the emphasized tip clearance flow. Here, a stronger interaction with the shock is indicated.

The same illustration is given for the maximum pressure point at the 80% speedline, OP-D. Here, the flow is mostly subsonic. The supersonic zone (without shock) in the isentropic Mach number distribution is due to the circumvention of the leading edge. Surface streamlines indicate significant local backflow at the leading edge for higher channel heights. The blockage region at the fan tip is more severe than at the design speed, with a widely inclined zone of negative radial velocity. Radial flow migration is highly accentuated at this condition, particularly close to the casing. However, due to the low relative velocity, the amplitude of the radial velocity close to the casing is lower than for the higher speedline.

4.2. Mechanics

4.2.1. Static Mechanics

Hot shapes of the fan blade were determined for each speedline along the working line. Due to the use of the anisotropic properties of the composite, the maximal blade displacement was 1.15 mm at maximal speed, corresponding to 1.0% of the chord. This is

comparable to the optimization presented by Schmid et al. [15]. The maximum static stress in the fibre direction does not exceed 17% of the elastic limit. The static stress is therefore low compared to the elastic limit, which allows a sufficiently high level of dynamic stress during the experimental campaign.

4.2.2. Mode Shapes

Regarding the synchronous excitation phenomena, intake distortions are the predominant sources. The potential effects of the OGV are negligible because of the axial distance from the fan of more than one chord. Experience on similar configurations shows that above the 6th engine order, forced response amplitudes are negligible [18,28]. At 105% of nominal rotation speed, the frequency of the 6th engine order is 1155 Hz. Mode 3 and Mode 4 frequencies are around 900 Hz and 1500 Hz, respectively, at maximal rotation speed, so only the first three modes are considered in the following.

Modal data are presented only for positive nodal diameters, because they are identical for both co-rotative and contra-rotative modes. Modal frequencies are given in Figure 11a for each nodal diameter (ND). Frequency variations are less than 2%, except for low nodal diameters between modes of the same family. The Mode 1ND0 frequency is lowered by 9% compared to the other NDs. The Mode 2ND1 and Mode 3ND1 frequencies are also reduced by 12% and 14%, respectively. To assess the mode shape variations between nodal diameters, the modal assurance criterion (MAC) was used [29]. For each mode, the mode shape was compared to its ND8 counterpart. The MAC value is equal to 1 if the mode shapes are identical and 0 if they are inconsistent. The MAC values are represented in Figure 11b. Except for ND1, the three modes are superimposed at 1. Modes 2ND1 and 3ND1 are very different from the other NDs due to the high disk contribution. The Mode 1ND0 mode shape is comparable, although its frequency is slightly different. These significant variations between nodal diameters must be taken into account in aeroelastic studies. Furthermore, the accuracy of the prediction can be affected by the support stiffness and gyroscopic effects. Thus, the choice to model the disk without the shaft could have an important impact on this nodal diameter (ND1) and must be addressed in further studies.

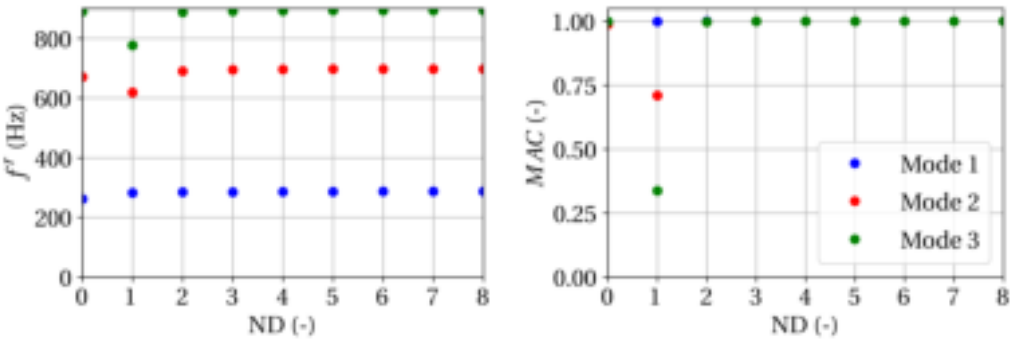

(**a**) (**b**)

Figure 11. Nodal diameter influence on modes at 100% speed: (**a**) frequency; (**b**) MAC in comparison with ND8.

The mode shapes at ND2 are shown in Figure 12. ND2 is representative of all nodal diameters except ND1. Mode 1 is a bending mode with a very low torsional component. The displacement is almost purely circumferential without an axial component. Mode 2 shows a pronounced torsional component at the blade tip, which is known to be critical for fluid–structure interactions [8,30]. Mode 3 represents a torsional mode with the torsional centre positioned at half-chord at midspan and at the leading edge at the tip.

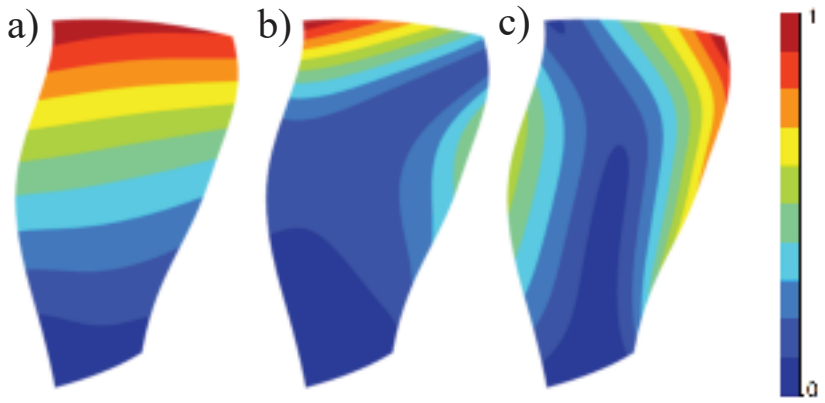

Figure 12. Normalized modal displacement amplitude at ND2: (**a**) Mode 1; (**b**) Mode 2; (**c**) Mode 3.

Mode shapes at ND1 are shown in Figure 13. As identified in Figure 11b, Mode 2ND1 and Mode 3ND1 are very different from the other equivalent NDs. In particular, the mode shape of 3ND1 is closer to Mode 2 than to Mode 3.

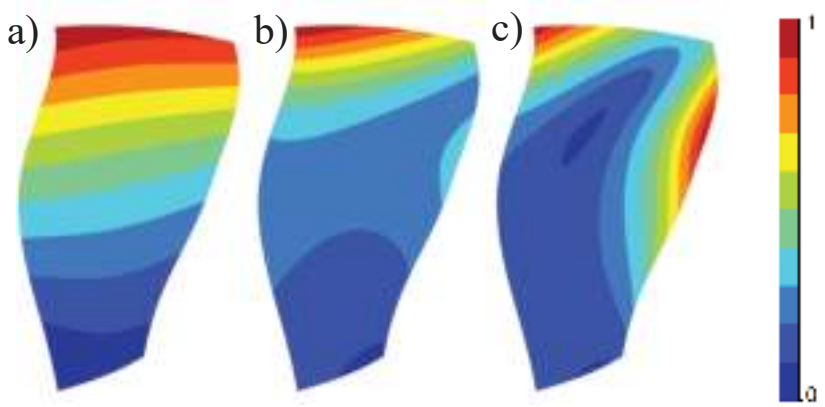

Figure 13. Normalized modal displacement amplitude at ND1: (**a**) Mode 1; (**b**) Mode 2; (**c**) Mode 3.

4.2.3. Campbell Diagram

The Campbell diagram obtained for the fan is presented in Figure 14. The crossings of the different modes with EO lines are highlighted. Modal frequencies were adjusted during the design process—as a result of the carbon fibre orientations—to prevent crossings above 100% speed. These are sufficiently distributed in frequency to enable safe tests, i.e., without fatigue caused by resonance, at low part-speed (∼50%), high part-speed (∼80%) and full speed (100% and above). Experience shows that the predicted frequencies are slightly higher than those of manufactured blades. Fans produced by the same manufacturer show that the frequency predictions are nearly 5% higher for torsional modes [18,28]. Moreover, in previous experimental campaigns, crossing with engine orders higher than 3 did not prevented speedline exploration. Hence, the 80% speedline could be safely investigated, despite the crossing of Mode 3.

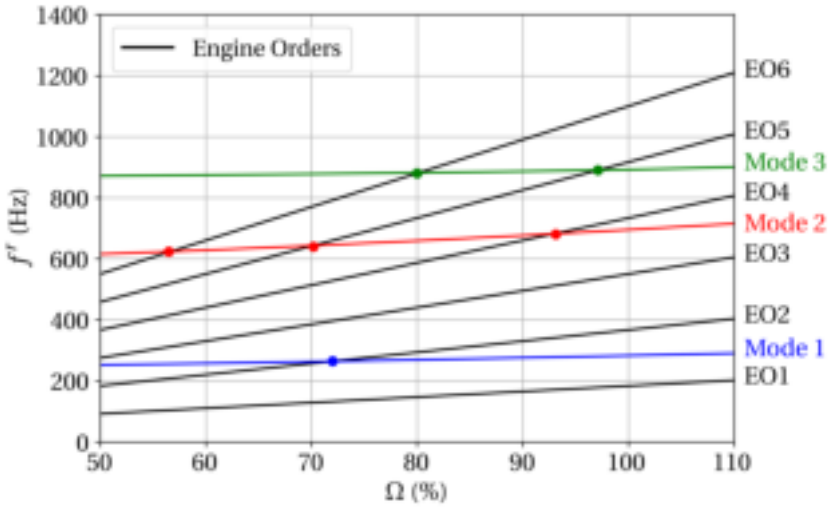

Figure 14. Campbell diagram at ND2.

4.3. Overall Stability Analysis

4.3.1. Strategy

To be representative of industrial configurations and to enable comprehensive experimental campaigns, it is necessary that the fan presents stable operating conditions at every planned experimental rotation speed. An exhaustive review would test every nodal diameter of every mode at each rotation speed. Even with the LRANS method, this exceeds the scope of a design study. The systematic stability analysis is limited to four operating points. The design point OP-A serves as a reference and must be stable in any case. OP-B, OP-C and OP-D are representative of the different flow limits (see Figure 8).

Flutter events detected on modern fans mostly involve the first bending mode at low nodal diameter [3,23,24]. However, it was shown by Stapelfeldt and Brandstetter [8] that torsional mode shapes could lead to aeroelastic instability for a convective mechanism, denoted as non-synchronous vibration. Thus, all three modes were investigated. Table 4 gives the reduced tip frequencies (see Equation (2)) based on the chord and the upstream relative velocity at both considered speeds.

$$k_r = \frac{f^r c}{U^{tip}} \tag{2}$$

To reduce the number of aeroelastic configurations simulated, only even numbers of nodal diameters were simulated in a first step. The nodal diameters ± 1 were added because their aeroelastic behaviour cannot be deduced from other nodal diameters, due to their mode shape (see Figures 12 and 13). Odd nodal diameters were simulated if discontinuities in aerodynamic damping curves were observed.

Table 4. Reduced frequency on working line (ND8).

Speedline	80%	100%
Mode 1	0.09	0.08
Mode 2	0.22	0.19
Mode 3	0.30	0.24

4.3.2. Aerodynamic Damping

Figures 15 and 16 show the aerodynamic damping ratio ζ as function of the nodal diameter at operating points OP-A to OP-D. The minimal values of each curve are shown in Table 5. At OP-A, the design point, the aerodamping is always positive and the minimal value reached is 1.38%. Mode 1 aerodamping variations as function of nodal diameter are

smooth for every operating point. The smallest value occurs between ND0 and ND2, and it exceeds 5% for high NDs. For every operating point studied, Mode 1 is globally more stable than Mode 2 or Mode 3, especially at high NDs. Aerodamping curves for Mode 2 and Mode 3 are more erratic, and minimal values are reached for various NDs. Only one point was found to be unstable: Mode 2ND5 at OP-D. Among all other simulated configurations, the aerodamping is always higher than 0.69%.

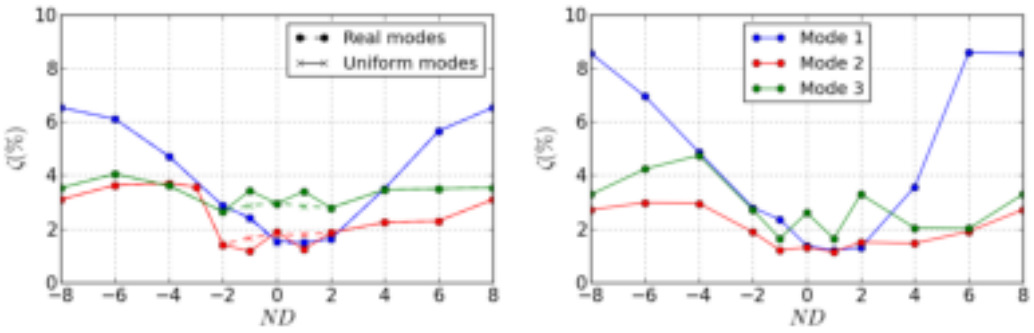

Figure 15. Aerodynamic damping as a function of nodal diameter: (**left**) OP-A; (**right**) OP-B.

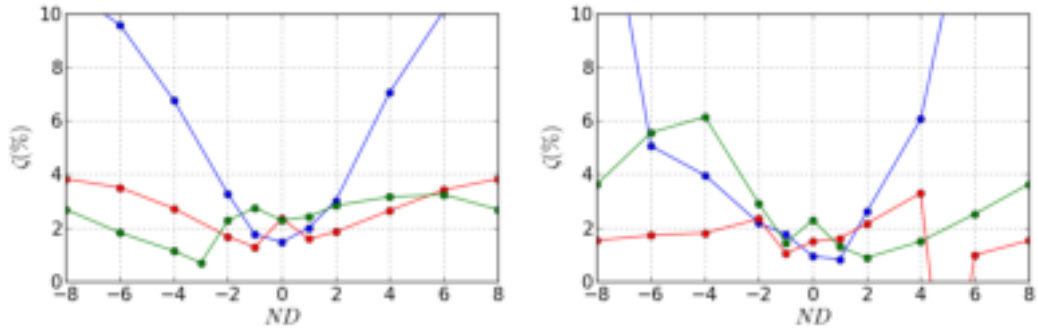

Figure 16. Aerodynamic damping as a function of nodal diameter: (**left**) OP-C; (**right**) OP-D.

Table 5. Minimum of aerodynamic damping. Unstable condition marked in red.

Operating Point	Mode 1	Mode 2	Mode 3
OP-A (100%, 36.0 kg/s)	1.50%	1.38%	2.64%
OP-B (100%, 32.0 kg/s)	1.20%	1.15%	1.64%
OP-C (100%, 38.9 kg/s)	1.47%	1.28%	0.69%
OP-D (80%, 26.0 kg/s)	0.83%	−5.60%	0.89%

4.3.3. Influence of Mode Frequency and Mode Shapes on Damping

Abrupt changes are observed in the damping curves. Among the possible reasons could be the change of mode shape and frequency for low nodal diameters (see Figure 11). This dependency is quantified at OP-A in Figure 15a. The aerodynamic damping was computed with the same frequency and mode shape as ND8 (uniform modes), which is similar to ND2, as shown Figure 12. It is compared to the aerodynamic damping obtained with modes from FEM (real modes). The resulting curves with uniform modes are smoother. The aerodamping is mainly impacted at Mode 2ND $\pm$ 1 and Mode 3ND $\pm$ 1, whose modal shapes and frequencies are very different from other NDs. Mode 1ND0 has a shift in frequency of 9%; however, the impact on the stability behaviour is marginal. The erratic changes observed between nodal diameters -2 and 2 are mostly due to mode shape variations.

4.4. Instability Analysis

Upstream and downstream acoustic conditions can produce discontinuities in the stability behaviour of the blades [31]. At the operating points studied, numerous switches

between cut-on and cut-off conditions can be observed, but only three discontinuities were identified related to acoustic behaviour that could lead to instability:

- For Mode 2ND-3 at OP-A, the stability curve is flat at each side of the discontinuity and the fan remains stable (see Figure 15a).
- For Mode 3ND-3 at OP-C, the stability reaches a minimum but the fan remains stable (see Figure 16a).
- For Mode 2ND5 at OP-D, the fan is predicted to be unstable (see Figure 16b). The stability behaviour for ND4 to ND6 is investigated in the following .

4.4.1. Aeroelastic Instability of Mode 2 at OP-D

For Mode 2ND5 at OP-D, the fan is predicted to be unstable and the aerodamping reaches a negative minimum at $\zeta = -5.6\%$. The local work at the surface of the blade, normalized according to the global work by $U = 4\pi E_k$ (see Equation (1)), is plotted (Figure 17) for ND4 to ND6. The local work is mostly located at the tip of the blade due to the mode shape (see Figure 12b). Corresponding flow fluctuations at ND5 are more than one order of magnitude higher than for adjacent nodal diameters. For example, if the displacement is arbitrarily set to 1.0% of the chord at the tip, the maximal pressure fluctuations are 65% of the inlet static pressure. At ND5, fluctuations cannot be analysed quantitatively because this lies outside the hypothesis of small perturbations on which the linearized method is based.

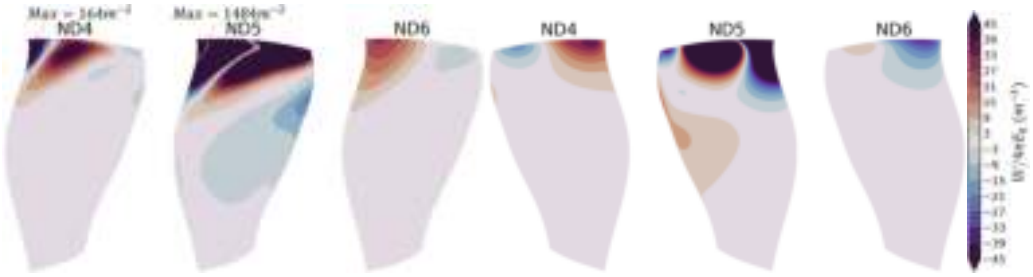

Figure 17. Local work at OP-D for Modes 2ND4 to 2ND6: (**left three blades**) suction side; (**right three blades**) pressure side.

At ND4 and ND6, the hypothesis of small perturbations remains valid, and the work distribution can be analysed. Figure 17 shows that both the suction side and the pressure side are equivalently involved in the overall stability of the blade. The local work patterns between ND4 and ND6 on the pressure side are similar but of opposite sign. On the suction side, the patterns are different. At ND4, the work is negative then positive near the leading edge, with high values, whereas the work is mildly positive at ND6 over a large area. This important change in behaviour between these nodal diameters indicates resonance, which is reached near ND5. The damping value obtained at ND5 is questionable due to resonance. However, it still shows that instability could be expected under these operating conditions, which must be investigated with caution during experiments.

4.4.2. Acoustic Propagation Conditions

The propagation conditions [32] of Mode 2 at OP-D are presented in Figure 18. This figure provides an understanding of the acoustics in the duct. An acoustic pressure wave generated by a vibrating fan can propagate axially if the frequency in the steady frame of reference f^s is higher than a frequency f^{cut}, called the cut-off frequency, where f^s is determined by Equation (3).

$$f^s = |f^r + \Omega\,\mathrm{ND}| \tag{3}$$

where f^r is the frequency in the rotating frame of reference (i.e., the modal frequency). With the assumptions of uniform flow in the radial direction, rigid-body flow and a hard-walled

duct, the acoustic cut-off frequency for a subsonic axial flow can be estimated according to Hellmich and Seume [32] as:

$$f^{cut} = \frac{k_r a}{2\pi}\left(\sqrt{1 - M_x^2} \pm M_\theta\right) \tag{4}$$

where M_x and M_θ are the axial and circumferential Mach number, a is the sound speed and k_r is the radial modal wave number calculated from Bessel functions. M_x and M_θ are determined by the mean value far upstream and downstream of the blade. The propagation conditions are shown in Figure 18 and were verified in the linearized simulation results. Upstream, acoustic waves propagate at ND0 to ND6. Downstream, acoustic waves propagate at ND4 but not at ND5 or ND6. In the opposite direction, propagation occurs at neither ND5 nor ND6. Vibration patterns that fulfil this condition of being cut on only in one axial direction are known to be critical for aeroelastic stability [6,33]. The discontinuity observed in the aerodamping curve (Figure 19) for OP-D seems to coincide with the change in the acoustic propagation conditions shown in Figure 18.

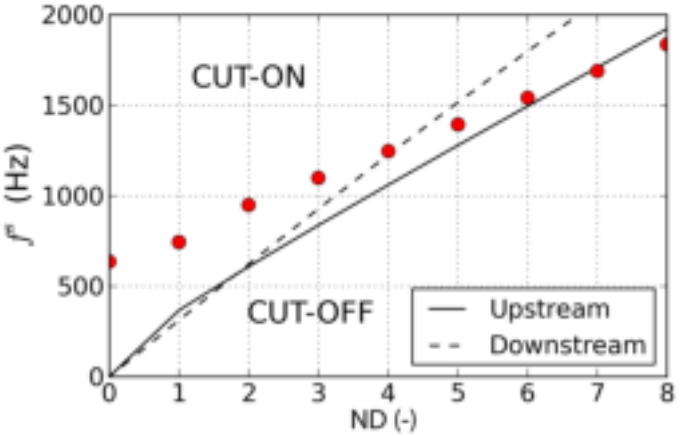

Figure 18. Mode 2 (red dots) acoustic conditions at OP-D and OP-E.

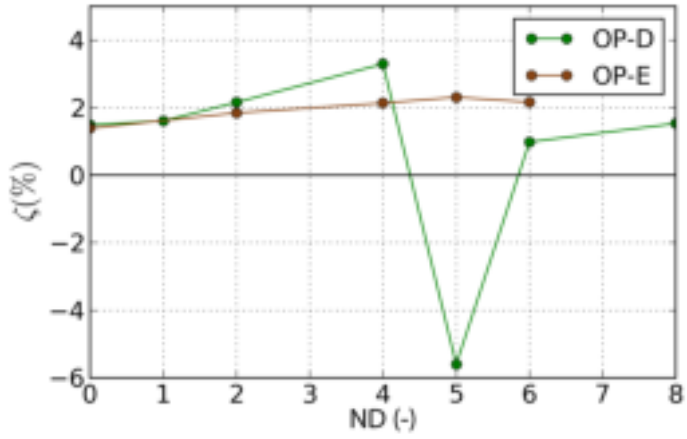

Figure 19. Mode 2 aerodynamic damping at OP-D and OP-E.

4.4.3. Influence of Operating Point

The aeroelastic stability is compared between OP-D and OP-E for Modes 2ND4 to 2ND6. At OP-E, the mass flow is 3.8% higher than at OP-D, and the leading-edge separation size is reduced to 25% of the chord. The acoustic cut-off frequencies at OP-E are not shown in Figure 18, because the differences from OP-D (less than the symbol size) are not significant compared to the model accuracy. It was verified in simulations that the acoustic propagation conditions upstream and downstream for ND4 to ND6 were the same for both

operating points. The normalized local work distributions are presented in Figure 20. In contrast to OP-D (see Figure 17), the results show very little influence of the nodal diameter at this operating point and only stabilizing aerodynamic damping higher than 2.0% (see Figure 19). On the suction side, the work repartition resembles ND4 at OP-D but with lower amplitude. Unlike the results at OP-D, the work on the pressure side is one order of magnitude lower than on the suction side. Here, the stability of the blade is driven by the suction side. The shift of 3.8% in the mass flow leads to a stable system and suppresses the strong influence of nodal diameter on fan stability. Thus, even if the acoustic conditions are similar, the fan remains stable closer to the operating line. Based on the presented study, it is not clear whether the acoustic conditions are the dominant driver for instability or whether a convective mechanism as described by Stapelfeldt and Brandstetter [8] leads to aeroelastic lock-in (non-synchronous vibrations). The latter case is not unlikely, as the ND5 pattern can be in resonance with a backward-travelling aerodynamic disturbance of wave-number 11 (aliased on a 16-blade rotor). This disturbance would propagate with a speed of ≈60% of the fan speed in the absolute frame of reference, which is well within the range of reported convective disturbances [18]. However, it has not been investigated before using time-linearized methods. Nevertheless, the detected instability at OP-D does not prevent experimental exploitation of the speedline, as it occurs only close to the stall limit and in cases where convective lock-in limit-cycle oscillations are expected.

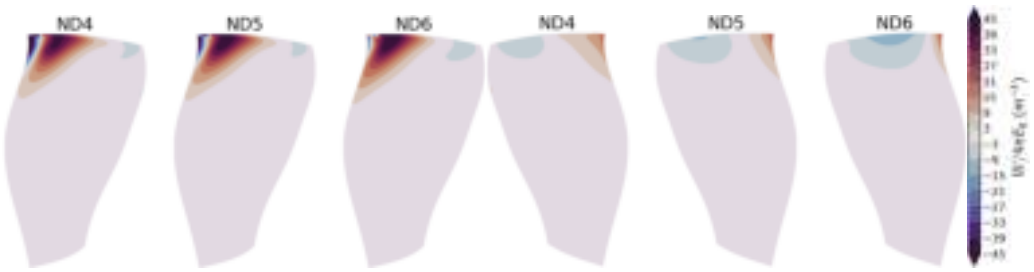

Figure 20. Local work at OP-E for Modes 2ND4 to 2ND6: (**left three blades**) suction side; (**right three blades**) pressure side.

5. Conclusions

A fan representative of modern UHBR fans was designed and presented as an open test case. The fan blades were made of unidirectional carbon fibres and epoxy composite plies. To enable an analysis of the dynamic behaviour, the structural properties, manufacturing process and ply orientations were presented.

The second mode of the fan had a significant torsional component at the blade tip which makes it likely to be critical for fluid–structure interactions. Modes of the same family vary significantly at low nodal diameters. The impact of this disparity was quantified in aeroelastic studies. The fan stability was systematically investigated over representative operating points using a time-linearized method. At nominal speed, no aeroelastic instabilities were predicted. Thus, it was possible to investigate highly loaded operating conditions. At part-speed, a potential instability was identified under throttled conditions, and this will be investigated in more detail in future work. It was shown that the instability area remained localized far from the operating line, and this will be the focus of the planned experimental campaign which is expected to start in mid-2022.

Author Contributions: Conceptualization: V.P., P.D., S.A., L.B., P.F., X.O. and C.B.; methodology: V.P., P.D., S.A., L.B., P.F., X.O. and C.B.; investigation: V.P., P.D., S.A., L.B., P.F., X.O. and C.B.; writing—original draft preparation: V.P. and C.B.; writing—review: P.D., S.A., L.B., P.F. and X.O.; review and editing: V.P. and C.B.; visualization: V.P. and C.B.; supervision: P.D., S.A., L.B., P.F., X.O. and C.B.; project administration/funding acquisition: S.A., X.O. and C.B. All authors have read and agreed to the published version of the manuscript.

Funding: This project received funding from the Clean Sky 2 Joint Undertaking (JU) under grant agreement No. 864719. The JU receives support from the European Union's Horizon 2020 research

and innovation programme and the Clean Sky 2 JU members other than the Union. This publication reflects only the authors' view, and the JU is not responsible for any use that may be made of the information it contains. The development of the open-test-case fan is supported by CIRT (Consortium Industrie-Recherche en Turbomachine).

Institutional Review Board Statement: Not applicable.

Informed Consent Statement: Not applicable.

Data Availability Statement: The geometry, experimental results and available simulations are accessible to European research institutes and international researchers upon negotiation. Registration at catana.ec-lyon.fr, accessed on 20 September 2021.

Acknowledgments: The authors are grateful for the continuous support of Safran Aircraft Engines, particularly the contribution of Laurent Jablonski during the design phase of the open test case.

Conflicts of Interest: The authors declare no conflict of interest.

Abbreviations

The following abbreviations are used in this manuscript:

EO	Engine Order
FEM	Finite Element Method
LRANS	Linearized Reynolds-Averaged Navier–Stokes
ND	Nodal Diameter
NSV	Non-Synchronous Vibration
OGV	Outlet Guide Vanes (Stator)
OP	Operating Point
RANS	Reynolds-Averaged Navier–Stokes
UHBR	Ultra-High Bypass Ratio

References

1. Brandstetter, C.; Pagès, V.; Duquesne, P.; Ottavy, X.; Ferrand, P.; Aubert, S. UHBR Open-Test-Case Fan ECL5/CATANA, Part 1: Geometry And Aerodynamic Performance. In Proceedings of the European Turbomachinery Conference ETC14 2021, Paper No. 625, Gdansk, Poland, 12–16 April 2021. Available online: https://hal.archives-ouvertes.fr/hal-03257374 (accessed on 20 September 2021).
2. Pagès, V.; Duquesne, P.; Ottavy, X.; Ferrand, P.; Aubert, S.; Blanc, L.; Brandstetter, C. UHBR Open-Test-Case Fan ECL5/CATANA, Part 2: Mechanical And Aeroelastic Stability. In Proceedings of the European Turbomachinery Conference ETC14 2021, Paper No. 626, Gdansk, Poland, 12–16 April 2021. Available online: https://hal.archives-ouvertes.fr/hal-03257377 (accessed on 20 September 2021).
3. Vahdati, M.; Cumpsty, N. Aeroelastic Instability in Transonic Fans. *J. Eng. Gas Turbines Power* **2015**, *138*, 022604. [CrossRef]
4. Lee, B.H.K. Self-sustained shock oscillations on airfoils at transonic speeds. *Prog. Aerosp. Sci.* **2001**, *37*, 147–196. [CrossRef]
5. Dodds, J.; Vahdati, M. Rotating Stall Observations in a High Speed Compressor—Part I: Experimental Study. *J. Turbomach.* **2015**, *137*, 051002. [CrossRef]
6. Fiquet, A.L.; Vercoutter, A.; Buffaz, N.; Aubert, S.; Brandstetter, C. Acoustic resonance in an axial multistage compressor leading to non-synchronous blade vibration. In Proceedings of the ASME Turbo Expo 2020 & Turbomachinery Technical Conference and Exposition, Online, 21–25 September 2020; ASME: London, UK, 2020.
7. Kielb, R.E.; Barter, J.W.; Thomas, J.P.; Hall, K.C. Blade Excitation by Aerodynamic Instabilities: A Compressor Blade Study. In Proceedings of the ASME Turbo Expo 2003, Collocated with the 2003 International Joint Power Generation Conference, Atlanta, GA, USA, 16–19 June 2003; American Society of Mechanical Engineers Digital Collection; American Society of Mechanical Engineers: New York, NY, USA, 2003; Volume 4, pp. 399–406. [CrossRef]
8. Stapelfeldt, S.; Brandstetter, C. Non-synchronous vibration in axial compressors: Lock-in mechanism and semi-analytical model. *J. Sound Vib.* **2020**, *488*, 115649. [CrossRef]
9. Lee, K.B.; Wilson, M.; Vahdati, M. Validation of a Numerical Model for Predicting Stalled Flows in a Low-Speed Fan—Part I: Modification of Spalart–Allmaras Turbulence Model. *J. Turbomach.* **2018**, *140*, 051008. [CrossRef]
10. Peters, A.; Spakovszky, Z.S.; Lord, W.K.; Rose, B. Ultrashort Nacelles for Low Fan Pressure Ratio Propulsors. *J. Turbomach.* **2015**, *137*, 021001. [CrossRef]
11. Wilson, M.J.; Imregun, M.; Sayma, A.I. The Effect of Stagger Variability in Gas Turbine Fan Assemblies. *J. Turbomach.* **2006**, *129*, 404–411. [CrossRef]
12. Lu, Y.; Green, J.; Stapelfeldt, S.C.; Vahdati, M. Effect of Geometric Variability on Running Shape and Performance of a Transonic Fan. *J. Turbomach.* **2019**, *141*, 101012. [CrossRef]

13. Zhai, Y.; Bladh, R.; Dyverfeldt, G. Aeroelastic Stability Assessment of an Industrial Compressor Blade Including Mistuning Effects. *J. Turbomach.* **2012**, *134*, 060903. [CrossRef]
14. Goerke, D.; Le Denmat, A.L.; Schmidt, T.; Kocian, F.; Nicke, E. Aerodynamic and Mechanical Optimization of CF/PEEK Blades of a Counter Rotating Fan. In Proceedings of the ASME Turbo Expo 2012: Turbine Technical Conference and Exposition, Copenhagen, Denmark, 11–15 June 2012; ASME: Copenhagen, Denmark, 2012; Volume 7: Structures and Dynamics, Parts A and B, pp. 21–33. [CrossRef]
15. Schmid, T.; Lengyel-Kampmann, T.; Schimdt, T.; Nicke, E. Optimization of a carbon fiber composite blade of a counter-rotating fan for aircraft engines. In Proceedings of the 13th European Conference on Turbomachinery Fluid Dynamics & Thermodynamics, Lausanne, Switzerland, 8–12 April 2019; European Turbomachinery Society: Lausanne, Switzerland, 2019.
16. Reiber, C.; Blocher, M. Potential of aeroelastic tailoring to improve flutter stability of turbomachinery compressor blades. In Proceedings of 12th European Conference on Turbomachinery Fluid Dynamics & Thermodynamics, Stockholm, Sweden, 3–7 April 2017; European Turbomachinery Society: Stockholm, Sweden, 2017. [CrossRef]
17. Rendu, Q. Modélisation des Écoulements Transsoniques Décollés pour L'étude des Interactions Fluide-Structure. Ph.D. Thesis, Université de Lyon, Lyon, France, 2016.
18. Rodrigues, M.; Soulat, L.; Paoletti, B.; Ottavy, X.; Brandstetter, C. Aerodynamic Investigation of a Composite Low-Speed Fan for UHBR Application. *J. Turbomach.* **2021**, *143*, 101004. [CrossRef]
19. Pagès, V. Conception du Fan UHBR ECL5 pour une Analyse des Mécanismes D'interactions Multi-physiques à L'origine du Flottement. Ph.D. Thesis, Ecole Centrale de Lyon, Lyon, France, 2021.
20. Wang, J.; Paton, R.; Page, J.R. The draping of woven fabric preforms and prepregs for production of polymer composite components. *Compos. Part A Appl. Sci. Manuf.* **1999**, *30*, 757–765. [CrossRef]
21. Barbero, E.J. *Finite Element Analysis of Composite Materials Using ANSYS®*, 2nd ed.; CRC Press: Boca Raton, FL, USA, 2013.
22. Carta, F.O. Coupled Blade-Disk-Shroud Flutter Instabilities in Turbojet Engine Rotors. *J. Eng. Power* **1967**, *89*, 419–426. [CrossRef]
23. Sanders, A.J.; Hassan, K.K.; Rabe, D.C. Experimental and Numerical Study of Stall Flutter in a Transonic Low-Aspect Ratio Fan Blisk. *J. Turbomach.* **2004**, *126*, 166–174. [CrossRef]
24. Aotsuka, M.; Murooka, T. Numerical Analysis of Fan Transonic Stall Flutter. In Proceedings of the ASME Turbo Expo 2014: Turbine Technical Conference and Exposition, Düsseldorf, Germany, 16–20 June 2014; ASME: Düsseldorf, Germany, 2014; Volume 7B: Structures and Dynamics; Volume V07BT35A020. [CrossRef]
25. Rendu, Q.; Philit, M.; Rozenberg, Y.; Labit, S.; Chassaing, J.C. Time-linearized and harmonic balance navier-stokes computations of a transonic flow over an oscillating bump. In Proceedings of the 14th International Symposium on Unsteady Aerodynamics, Aeroacoustics & Aeroelasticity of Turbomachines, Stockholm, Sweden, 8–11 September 2015; ISUAAAT: Stockholm, Sweden, 2015; p. 14.
26. Philit, M.; Ferrand, P.; Labit, S.; Chassaing, J.C.; Aubert, S.; Fransson, T. Derivated Turbulence Model to Predict Harmonic Loads in Transonic Separated Flows over a Bump. In Proceedings of the 28th International Congress of the Aeroanautical Sciences, Brisbane, Australia, 23–28 September 2012; ICAS: Brisbane, Australia, 2012; p. 11.
27. Duquesne, P.; Aubert, S.; Rendu, Q.; Ferrand, P. Effect of nodal diameter on the local blades vibration on the choke flutter instability in transonic UHBR fan. In Proceedings of the 15th International Symposium on Unsteady Aerodynamics, Aeroacoustics and Aeroelasticity of Turbomachines, Gothenburg, Sweden, 16–17 October 2018; p. 10.
28. Brandstetter, C.; Paoletti, B.; Ottavy, X. Compressible Modal Instability Onset in an Aerodynamically Mistuned Transonic Fan. *J. Turbomach.* **2019**, *141*, 031004. [CrossRef]
29. Allemang, R.J. The Modal Assurance Criterion—Twenty Years of Use and Abuse. *J. Sound Vib.* **2003**, *37*, 14–23.
30. Duquesne, P.; Mahieux, B.; Aubert, S.; Ferrand, P. Sensitivity of the aerodynamics damping coefficient prediction to the turbulence modelling conjugated with the vibration mode shape. In Proceedings of the 13th European Conference on Turbomachinery Fluid Dynamics & Thermodynamics ETC13, Lausanne, Switzerland, 8–12 April 2019; European Turbomachinery Society: Lausanne, Switzerland, 2019; p. 12.
31. Ferria, H.; Ferrand, P.; Pacull, F.; Aubert, S. Numerical investigation of flutter stability in subsonic space turbine blisk with emphasis on cut-on/cut-off modes and interblade phase angles. *J. Therm. Sci.* **2012**, *21*, 492–499. [CrossRef]
32. Hellmich, B.; Seume, J.R. Causes of Acoustic Resonance in a High-Speed Axial Compressor. *J. Turbomach.* **2008**, *130*, 031003. [CrossRef]
33. Atassi, H.M.; Fang, J.; Ferrand, P. Acoustic blockage effects in unsteady transonic nozzle and cascade flows. In Proceedings of the 33rd Aerospace Sciences Meeting and Exhibit, Reno, NV, USA, 9–12 January 1995; AIAA: Reno, NV, USA, 1995; Volume 95-0303, p. 9.

International Journal of
Turbomachinery
Propulsion and Power

MDPI

Article

Acoustoelastic Modes in Rotor-Cavity Systems: An Overview on Frequency Shift Effects Supported with Measurements

Tina Unglaube * and Dieter Brillert

Chair of Turbomachinery, University of Duisburg-Essen, 47057 Duisburg, Germany; dieter.brillert@uni-due.de
* Correspondence: tina.unglaube@uni-due.de

Abstract: With an increase in fluid densities in centrifugal compressors, fluid-structure interaction and coupled acoustoelastic modes receive growing attention to avoid machine failure. Besides the vibrational behavior of the impeller, acoustic modes building up in the side cavities need to be understood to ensure safe and reliable operation. In a coupled system, these structure and acoustic dominant modes influence each other. Therefore, a comprehensive overview of frequency shift effects in rotor-cavity systems is established based on findings in the literature. Additionally, experimental results on coupled mode pairs in a rotor-cavity test rig with a rotating disk under varying operating conditions are presented. Measurement results for structure dominant modes agree well with theoretical predictions. The development of a forward and a backward traveling wave is demonstrated for each mode in case of disk rotation. Conducted experiments reveal the occurrence of weakly and strongly coupled mode pairs as frequency shifts are observed that cannot solely be explained by "uncoupled mode effects", such as the added mass, speed of sound, and stiffening effect, but indicate an additional coupling effect. However, the hypothesis of a bigger frequency shift for stronger coupled modes cannot be corroborated consistently. Only for the strongly coupled four nodal diameter mode pair in the "wide cavity" setup, a coupling effect is clearly visible in the form of mode veering.

Keywords: rotor-cavity system; acoustoelastic modes; coupling; fluid-structure interaction

check for updates

Citation: Unglaube, T.; Brillert, D. Acoustoelastic Modes in Rotor-Cavity Systems: An Overview on Frequency Shift Effects Supported with Measurements. *Int. J. Turbomach. Propuls. Power* **2022**, *7*, 15. https://doi.org/10.3390/ijtpp7020015

Academic Editor: Antoine Dazin

Received: 26 January 2022
Accepted: 4 May 2022
Published: 6 May 2022

Publisher's Note: MDPI stays neutral with regard to jurisdictional claims in published maps and institutional affiliations.

Copyright: © 2022 by the authors. Licensee MDPI, Basel, Switzerland. This article is an open access article distributed under the terms and conditions of the Creative Commons Attribution (CC BY-NC-ND) license (https://creativecommons.org/licenses/by-nc-nd/4.0/).

1. Introduction

Centrifugal compressors are applied for a wide range of industrial applications, including gas compression for the chemical industry, natural gas extraction and liquefaction, enhanced oil recovery, as well as carbon capture and storage. Required discharge pressures increase continuously, and so do fluid densities inside the machines, increasing the forces acting on the impeller. Besides the vibrational behavior of the impeller, which has been studied extensively over the last decades, these fluid-structure interactions have to be understood. Nowadays, it is well known that natural frequencies of compressor impellers shift due to an increase in gas density of the surrounding fluid. Moreover, acoustic modes building up in the side cavities of radial compressors were found to be another potential source of high cycle fatigue. Recent studies suppose that acoustic and disk vibration modes influence each other, resulting in further frequency shifts in coupled rotor-cavity-systems. However, these effects are not fully understood yet. To ensure a safe and reliable design and avoid machine failure during operation, these coupled natural frequencies have to be predicted accurately, and the excitation and the damping mechanism need to be studied further.

Rotor-cavity systems, consisting of a rotating disk in a fluid-filled cavity, provide a simplified model of centrifugal compressors for fundamental research purposes. Therefore, a comprehensive overview on frequency shift effects in acoustoelastic rotor-cavity systems is established based on findings published in the literature. This provides a robust foundation for a theoretical understanding of the topic, which is then underpinned with measurement

data. For this purpose, a rotor-cavity test rig was set up at the Chair of Turbomachinery at the University Duisburg-Essen (Germany) that demonstrates the occurrence of coupled acoustoelastic modes. It enables the researchers to systematically collect and evaluate experimental data on rotor-fluid interaction and the formation of coupled acoustic and structure dominant modes while varying different influencing parameters independently from each other. By doing so, a deeper understanding of coupling and frequency shift effects in rotor-cavity systems is gained.

2. Literature Overview

Some of the earliest works on disk vibration in turbomachinery were conducted by Lamb and Southwell (1921) [1] and Southwell (1922) [2], analyzing the vibrations of a spinning circular disk. A few years later, Campbell (1924) [3] published his fundamental study on the vibrational excitation of rotating turbomachinery, thereby establishing the so-called Campbell diagram. Until today, it remains a widely-used tool to avoid potential vibrational resonances that might result in machine failure. Subsequently, many studies were conducted analyzing the vibrational behavior of rotating disks and compressor impellers. E.g., Eversman and Dodson (1969) [4] published a technical note on the free vibration of spinning, centrally clamped circular disks, and presented an analytical solution of the Eigenvalue equation as a function of hub-to-disk ratio for different spin rigidity parameters and mode shapes. Ewins (1973) [5] published an analytical and experimental study on the vibration characteristics of tuned and detuned bladed disk assemblies, emphasizing the importance of considering the complete bladed disk assembly, instead of disk and blades separately. Irretier [6,7] studied the natural and forced vibrations of a wheel disk and established a numerical model to calculate the Eigen frequencies and mode shapes of the system and later carried out experiments and calculations on the vibrations of rotating radial impellers, which were in good agreement.

One of the first fundamental studies on aero-acoustic excitation sources in turbomachinery was published by Tyler and Sofrin (1962) [8]. They identified rotor-stator interaction as a significant noise generating mechanism and found that both the spinning rotor alone and rotor-stator interaction produce rotating pressure patterns. Since then, these spinning modes are referred to as Tyler-Sofrin modes. Ehrich (1969) [9] derived an analytic model of an annular acoustic cavity to conclude on natural frequencies of acoustic modes in the cavity. It is used to analyze experimental data of a turbomachine over a range of rotational speeds and explain resonance peaks at supersonic and subsonic wheel speeds. Amongst the more recent publications, Eisinger (2002) [10] and Eisinger and Sullivan (2002) [11] address acoustically induced fatigue of impellers of rotating machinery. Coupling of the structural and acoustic modes is discussed that might ultimately lead to structural failure of the impeller. This becomes especially important for impellers in high-density fluids, where disk vibration and acoustic modes cannot be treated separately anymore but need to be analyzed as a coupled system. Magara's publications [12,13] are of particular interest along this chain of causation as they discuss structural frequencies of radial compressors in a high-density environment. Two analytical models are established to explain the subsequent frequency shift phenomena for a non-rotating and a rotating disk due to mode coupling. Experimental results agree well with numerical ones. Beirow et al. (2015) [14] studied the effect of mistuning on a high-pressure compressor blisk at rest with respect to structural vibration modes and damping ratios. The forced response is analyzed, and it is found that, taking aero-elastic coupling effects into account, damping of the structure generally increases while the response decreases. Based on other theoretic models, Heinrich et al. (2020) [15] proposed a generalized model for the approximation of coupled acousto-mechanical natural frequencies in high-pressure centrifugal compressors, which was later extended to take damping effects into account (Heinrich et al. (2021) [16]). In the latter, the model outcome is further compared to experimental data, yielding excellent agreement regarding the predicted natural frequencies and an acceptable agreement regarding damping ratios.

Examples of aero-acoustic excitation in industrial turbomachinery are, e.g., reported in Hellmich and Seume (2006) [17], where an acoustic resonance in a four-stage axial compressor is explained with a simplified model for helical acoustic modes, as well as König (2009) [18] and Petry et al. (2012) [19], who investigate acoustic Eigenmodes in the side cavities of an industrial centrifugal compressor. Their setup includes one complete compressor stage, from the inlet guide vanes to the return guide vanes. Another case of actual high cycle fatigue in an industrial compressor possibly caused by aero-elastic excitation is described in Eckert (1999) [20], accentuating that the problem of fluid-structure interaction in turbomachinery is of substantial concern in real applications.

The current paper is based on the preceding work of the research group at the Chair of Turbomachinery at UDE, aiming at gathering baseline experimental data on rotor-fluid interaction. Barabas et al. (2015) [21] introduced the test rig and measurement instrumentation in detail and presented first velocity profile measurements, indicating a turbulent flow with high Reynolds numbers inside the cavity. Barabas et al. (2017) [22] presented frequency shifts towards higher and lower frequencies for the two modes of a coupled mode pair for a change in cavity pressure. Moreover, interfering influences of crossing modes were identified. Barabas et al. (2018) [23] then focused on the damping of weakly coupled acoustic dominant modes, which was found to decrease with an increase in fluid pressure, and established a relationship of the damping ratio, the kinematic viscosity, and the natural frequency of the acoustic modes.

It is shown that structural-acoustic mode coupling in rotor-cavity systems is a complex field of research with many interacting effects to be taken into account. Several publications address some of these effects, but so far none has revealed them at large. This paper contributes to a deeper understanding of the coaction of all pertinent frequency shift effects in rotor-cavity systems and thus to the efforts to avoid resonances in centrifugal compressors that might ultimately lead to component failure in turbomachinery.

3. Theory on Frequency Shifts in Rotor-Cavity Systems

3.1. The Rotor-Cavity System

A rotor-cavity (or rotor-stator) system consists of an impeller rotating inside a stationary cavity. It can be used as a simplified model of turbomachine impellers in a casing. The rotating disk divides the fluid volume into two separate cavities, similar to the side cavities in, e.g., centrifugal compressors. The ratio of the cavity's axial gap width s to the disk radius r_d is a characteristic dimension describing the cavity, referred to as non-dimensional axial gap width G.

$$G = \frac{s}{r_d} \tag{1}$$

Between the disk vibration modes and the acoustic modes inside the fluid-filled cavities, fluid-structure interaction occurs if there is a resulting force from one to the other. These interactions present themselves in the form of the out-of-plane structural modes of the disk and fluctuating pressure patterns of the fluid that can only truly be neglected if the disk rotates in a vacuum. Structural and acoustic modes additionally influence each other if a certain mode pair is coupled. This results in a further frequency shift. In the case of coupling, the modes are referred to as structure and acoustic dominant modes.

3.2. Uncoupled Structure/Disk Vibrational Modes

The mode shape of disk vibration modes, also called structural modes, is characterized by the number of nodal diameters (diametral modes, or circumferential order) m and the number of nodal circles (or radial order) n. For a rotating disk, a resonance between a natural frequency $f_{m,n}$ of one of its disk modes and an excitation frequency $f_{e,st}$ occurs when the latter coincides with the rotational frequency of the forward or backward traveling wave of the disk mode as follows [3]:

$$f_{e,st} = f_{m,n} \pm m \times f_\Omega \tag{2}$$

with f_Ω being the rotational frequency of the rotating disk.

Disk natural frequencies $f_{m,n}$ increase slightly with an increase in disk rotational speed Ω due to the stiffening effect of the centrifugal force field [7]. This effect can be approximated (as, e.g., in [2]) but is often sufficiently small to be neglected [7].

For a mistuned disk, i.e., a non-axisymmetric disk, there are two natural frequencies for one disk mode. However, this frequency splitting is often negligible for practical applications [7]. In general, the above-mentioned considerations also apply to rotating impellers. Nevertheless, mistuning due to geometrical non-uniformities becomes more likely for more complex impeller geometries [5]. Such detuning gives rise to more irregular and complex mode shapes and more resonances than those in equivalent tuned systems [5].

3.3. Uncoupled Acoustic/Cavity Modes

In a fluid-filled cavity, acoustic modes (or cavity modes) can form that establish as fluctuating pressure patterns. In rotating machinery, these acoustic waves are excited by the flow through the machine and can be enhanced by the impeller rotation [10]. Similar to structural modes, acoustic modes are characterized by their number of nodal diameters p, nodal circles q, and additionally, axial nodes r. The frequency of the (p,q) acoustic mode inside a cylinder can be calculated as follows [24]:

$$f_{p,q} = \frac{(\pi\alpha)_{p,q}\, c}{2\pi\, r_c} \tag{3}$$

where $(\pi\alpha)_{p,q}$ are the dimensionless solutions to the first derivative of the Bessel function for the (p,q) acoustic mode (see Figure 1). From Equation (3) we see that the natural frequency of the acoustic mode is linearly dependent on the fluid's speed of sound c, and thus on the fluid properties. E.g., an increase in fluid pressure causes a shift in the natural frequency of the acoustic modes. This will be referred to as the speed-of-sound effect in the following. A change in cavity radius r_c also results in a change of acoustic frequency; however, according to this model in Equation (3), a change in axial gap width does not.

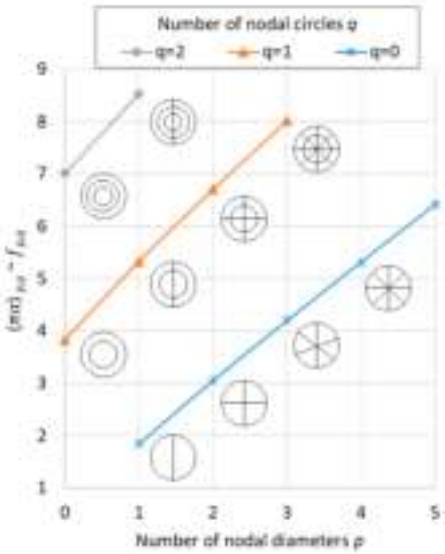

Figure 1. Non-dimensional solutions to Bessel functions for acoustic frequencies inside a cylinder and respective mode shapes for different numbers of nodal diameters and nodal circles.

In a rotor-stator system, disk rotation results in fluid rotation inside the cavity. These flow patterns influence the formation of acoustic modes and can be described depending on the circumferential Reynolds number *Re*, which is defined as follows:

$$Re = \frac{u\ L}{\nu} = \frac{2\pi\ \Omega\ r_d^2}{\nu} \tag{4}$$

where u is the circumferential velocity, L the characteristic length, and ν the kinematic viscosity of the fluid. The widely used rotor-stator cavity flow model by Daily and Nece (1960) [25] distinguishes between four flow regimes, the two turbulent ones having either merged or separated boundary layers. The latter is predominant for bigger cavity widths or higher Reynolds numbers and is characterized by a core flow, for which an almost constant circumferential velocity is assumed, i.e., the fluid is swirling as a bulk flow. The core rotation can be described by the ratio k_0 of the fluid velocity v_f to the impeller circumferential velocity u and only depends on the geometry of the cavity if there is no superimposed through flow [26]. In the case of zero leakage flow, it is also independent of the radius and can be estimated as follows [26]:

$$k_0 = \frac{v_f}{u} = \frac{1}{1 + \left(\frac{r_c}{r_d}\right)^2 \sqrt[2]{\left(\frac{r_c}{r_d} + 5\frac{t_{ax}}{r_d}\right)\frac{c_{f,case}}{c_{f,d}}}} \tag{5}$$

where r_d and r_c are the impeller and the cavity radius, t_{ax} is the cylindrical portion of the impeller side room, and $c_{f,d}$ and $c_{f,case}$ are the friction coefficients of the impeller and casing, respectively. Typically, the core rotation factor takes a value between 0.4 and 0.5, i.e., the fluid rotates at a rotational speed a little less than half of the disk speed.

Analogous to the structural modes, the acoustic modes subject to core rotation form a backward and a forward traveling wave in the cavities that can be calculated as follows:

$$f_{e,ac} = f_{p,q} \pm k_0 \times p \times f_\Omega \tag{6}$$

3.4. Fluid-Structure Interaction

So far, the disk vibration and fluid-filled cavity have been treated separately. However, the influence of the surrounding fluid on the impeller has to be considered. Especially with an increase in fluid pressure and therefore density, significant forces are acting from the fluid on the impeller. Vice-versa, the out-of-plane structural modes also influence the acoustic ones. These effects are called fluid-structure-interaction and cannot be neglected. Of particular practical interest is the influence of an increased fluid density on the turbomachinery impeller, which is addressed by the added-mass-effect: An increase in mass of the surrounding fluid results in a decrease of the natural frequencies of the impeller [12,13,27], as the fluid mass is linearly dependent on the fluid density (and the cavity volume). Hence, while the impeller's mass does not change, the total mass of the system changes as the fluid mass acting on the impeller varies. The change in natural frequency is anti-proportional to the change in total mass. However, these interactions are not of major concern unless coupling between a pair of acoustic and structural modes exists.

3.5. Coupling

The respective modes need to be excited first off for coupling between an acoustic and a structure mode to occur. While acoustic modes are excited by the fluid flow through the casing passing obstacles, such as vanes or the rotor, the most efficient source of impeller vibration are higher order acoustic modes [10]. In addition, for a setup with two cavities surrounding an impeller or disk, there must be a phase shift between the acoustic modes in these cavities, or in a different notion, an axial node must exist (at the axial position of the disk). Only then is there a resulting force from the fluid acting on the impeller. Therefore,

the out-of-plane structural (disk) modes and acoustic (cavity) modes with an axial node have the most potential to influence each other.

The compatibility of mode shapes is a necessary condition for structural-acoustic coupling. This coincidence of mode shapes is especially established through the same number of nodal diameters ($m = p$) [10]. It is often assumed that each structural mode is only well coupled to one acoustic mode and only weakly to all others [10,28]. The most severe interaction (or complete coincidence) occurs when also the (uncoupled) natural frequencies match [10]. However, any coupling of a pair of acoustic and structure dominant modes results in the shift of their natural frequencies compared to the uncoupled modes. This coupling effect also occurs if the theoretically uncoupled natural frequencies are in a certain proximity to each other. The closer the uncoupled natural frequencies are to each other, the stronger is the coupling effect and thus the resulting frequency shift. According to [10], a 25% minimum separation of natural frequencies is recommended to consider modes as not coupled. In Reference [11], the degree of structural-to-acoustic coupling is expressed by a coupling coefficient, which is zero in the case of uncoupled systems. A small mass of the impeller or a thin cavity increases the coupling, while a bigger mass of the disk and a wider cylindrical cavity facilitate weaker coupling [11].

Still, it should be mentioned that for real turbomachinery impellers or detuned bladed disk assemblies, each excited disk mode contains components of many diametral mode orders. Therefore, an m-engine order excitation might excite not only the pure m-nodal diameter mode but also most other modes [5].

3.6. Existing Frequency Shift Models

One widely used mathematical model aiming at explaining coupling effects in rotor-cavity systems is the model of Magara et al. (2008) [12], which originates from research on frequency shifts of centrifugal compressor impellers in high-density gas applications.

The frequency shift model consists of a parabola, which opens upward (left side of Equation (7)) and a straight line with a positive slope (right side of Equation (7)) if the square of the system frequency f_s^2 is indicated on the x-axis (see Figure 2).

$$\left(f_{1,uc}^2 - f_s^2\right) * \left(f_{2,uc}^2 - f_s^2\right) = 2\frac{\rho_f\, c^2}{\rho_d\, b\, s_c} f_s^2 \tag{7}$$

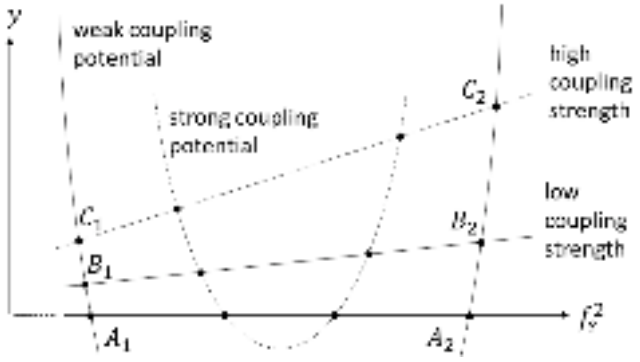

Figure 2. Coupling model of Magara et al. (2008) [12].

The intersections of the parabola with the x-axis (points A) represent the theoretically uncoupled natural frequencies of the disk and the fluid. Which of them is the lower and which the higher-frequency mode depends on the geometry and cannot be stated generally. Therefore, they are not indicated as acoustic and structure modes, but as $f_{1,uc}$ and $f_{2,uc}$. The frequency difference between A_1 and A_2 indicates the coupling potential of the two modes, being bigger the closer the theoretically uncoupled natural frequencies are to each other. The straight line indicates the coupling strength. The slope increases with an increase in fluid density ρ_f and speed of sound c and decreases with an increase in disk density ρ_d,

disk thickness b, and axial cavity width s_c. The intersections of the coupling strength term with the parabola (points B and C) represent the two natural frequencies of the coupled system f_s. When the coupling strength increases, the intersections are shifted upwards and outwards, i.e., the frequency of the lower-frequency mode decreases (from B_1 to C_1) and the one of the higher-frequency mode increases (from B_2 to C_2). This frequency shift is bigger, the more the coupling strength increases (the bigger its slope), and the closer the theoretically uncoupled modes are to each other, i.e., the bigger the coupling potential. The latter effect can be illustrated by comparing the frequency shifts of the cases with weak (solid line parabola) and strong coupling potential (dashed line parabola).

3.7. Overview on Frequency Shift Phenomena in a Rotor-Cavity-System

Based on the comprehensive review of structural and acoustic modes, as well as their fluid-structure interaction and coupling in the previous paragraphs, an overview of frequency shift effects in rotor-cavity systems is presented in what follows (Figure 3).

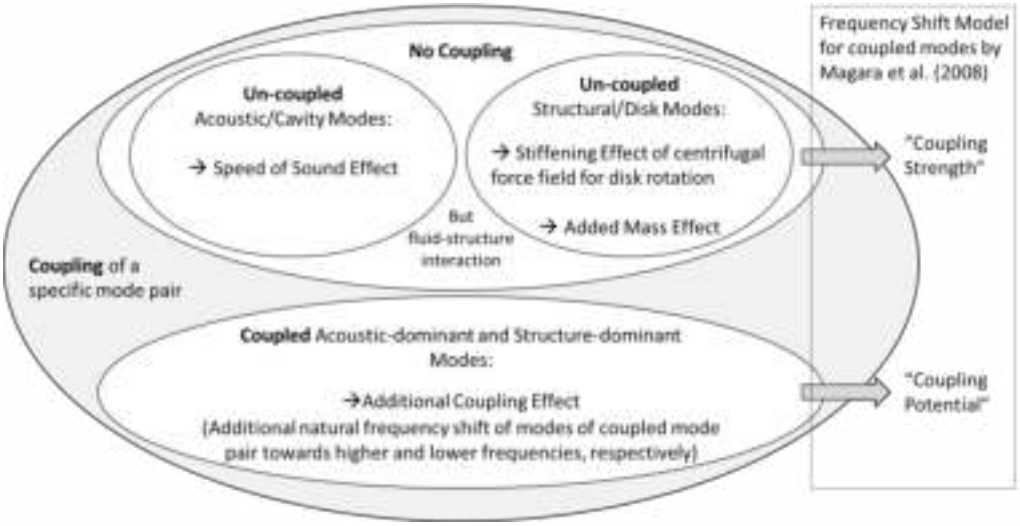

Figure 3. Overview of frequency shift effects in rotor-cavity systems [12].

First, there is a group of "uncoupled mode effects", which occur independently from any coupling of a specific mode pair, i.e., they can be observed for both, uncoupled as well as for coupled modes: The speed of sound effect refers to a shift in the natural frequency of the acoustic mode if the speed of sound changes due to altered fluid properties. Additionally, the stiffening effect of the centrifugal force field might be observed for rotating impellers resulting in a slight upward shift of the structural frequency at higher rotational speeds. Considering fluid-structure interaction effects, which are of particular importance for higher fluid densities surrounding an impeller, the added mass effect plays an important role. It results in a decrease of disk frequencies if the mass of the surrounding fluid increases. In Magara's coupling model [12], these effects are encompassed by the term "coupling strength". If two specific modes are coupled, i.e., a structure and an acoustic dominant mode with similar mode shapes and natural frequencies in a certain proximity to each other are excited, this adds additional frequency shifts: For a coupled mode pair, one natural frequency shifts towards higher, the other towards lower frequencies, compared to their uncoupled counterparts. This is referred to as the coupling effect. The smaller the frequency difference of the uncoupled modes is, the bigger is the coupling effect, and thus the frequency shift it effectuates. In Magara's coupling model [12], these frequency shifts are addressed by the term "coupling potential".

Based on this, the following can be hypothesized: Any frequency shift that is not caused by the added mass, speed of sound, or stiffening effect (for uncoupled structural or acoustic modes) indicates an additional coupling effect. The coupled modes are then referred to as structure dominant and acoustic dominant modes.

When the frequency difference between two coupled modes decreases subject to, e.g., a change in fluid properties or rotational speed, the two modes approach each other. However, in several cases, they do not intersect (no resonance) but diverge again and approach the theoretically uncoupled frequency path of the other mode. This frequency deflection is called mode veering and reported, e.g., in [27,29].

4. Experimental Setup and Procedure

4.1. Test Rig and Instrumentation

Experimental results presented in this paper are obtained at the rotor-cavity test rig of the Chair of Turbomachinery at the University Duisburg-Essen, Germany, introduced in [21–23]. The test rig consists of a plain rotating disk with a constant width b in a cylindrical stationary casing, forming two fluid-filled cavities, which are connected through a small radial gap. A sketch of the test rig, including some measurement equipment, is given in Figure 4. This setup represents a simplified model of the side cavities in radial compressors. The axial gap widths of the front and rear cavity, s_{cf} and s_{cr}, respectively, can be adjusted independently. For the conducted experiments, there is no superimposed through flow in the cavities. The disk is mounted on a shaft connected to a continuously adjustable high-speed electrical drive via a magnetic coupling. Different gases can be passed into the test rig from a pre-mix chamber, allowing for a variation of fluid parameters. The disk's rotational speed Ω can be varied, and circumferential Reynolds numbers up to 2×108 can be achieved with CO_2 at maximum speed.

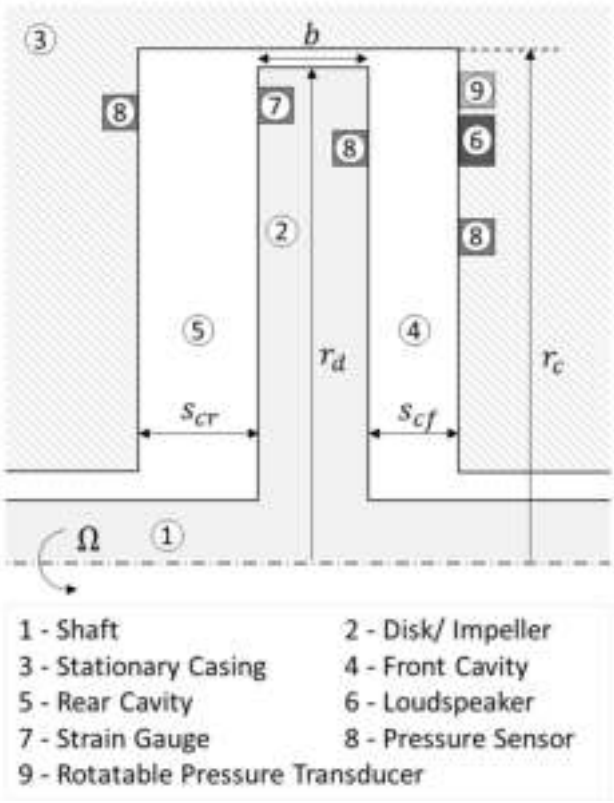

Figure 4. Test rig setup and measurement equipment.

Excitation sources in real turbomachinery, such as rotor-stator interaction, are missing in the test rig due to its simplified (blade- and vane-less) geometry. For that reason, a loudspeaker is installed in the casing of the front cavity. It is capable of exciting both acoustic and structure dominant modes in the front and the rear cavities. The excitation frequency is set by a wave generator connected to an amplifier and adjusted independently from other parameters. The geometry of the test rig is designed so that at least one pair of

acoustic and structural modes with the same number of nodal diameters are coupled at ambient conditions.

When interpreting the results, one should notice that the cavity, in which the measurements are taken, is not perfectly closed. There are two small openings in the front cavity, one at the outer radius and one at the inner. Although valves in the connecting pipes are closed so that there is no in- or outflow to or from the cavity, these openings might affect the propagation and reflection of acoustic waves inside the cavity. In future experiments, results for a completely closed cavity and the current setup will be compared to gain further insight into this matter. However, the side cavities in real turbomachines are also not perfectly closed, so that the setup in this work might even represent a more realistic case than that of a perfectly sealed cavity.

To measure acoustic modes that occur in the form of local pressure fluctuations, the test rig is equipped with two pressure transducers in each, the front and rear cavity, as well as one on the disk. To detect structural modes in the form of disk vibration, two strain gauges are mounted on the disk. The following measures are provided for the identification of mode shapes: The number of nodal diameters of the excited mode is traced with an additional traversable pressure sensor installed in the front cavity, which can rotate 300 degrees around the disk's circumference at a constant excitation frequency. To detect the number of nodal circles, the two pressure sensors in the front cavity are mounted at a different radial position compared to those in the rear cavity. An axial node is detected by identifying a 180 degrees' phase shift between the pressure patterns in the front and rear cavity. In addition, the test rig and pre-mix chamber are equipped with pressure and temperature sensors to determine the thermodynamic properties of the fluid.

The general uncertainty of the measurement chain of the temperature sensors is determined to be ± 1.8 K, and the non-linearity and dynamic uncertainties of the pressure sensors are negligibly small [29]. However, strain gauges are only able to measure dynamic vibrations up to a cut-off frequency of 50 kHz [29]. Additionally, the electrostatic noise increases significantly for experiments with a rotating disk, resulting in a very low signal-to-noise ratio for those strain gauge results. However, pressure sensor results are not affected as much by electromagnetic interferences. Therefore, response functions for the structure dominant modes are also measured with pressure sensors in case of disk rotation. Measurements without disk rotation have shown that this approach does not influence the results as strain gauge and pressure sensor measurements agree well.

4.2. Experimental and Evaluation Procedures

In preparation for the experiments, the test rig is filled with the required gas mixture until the target pressure is reached. The temperature inside the test rig is assumed to be constant, as a maximum friction-induced increase of 0.3% for experiments with high rotational speeds is considered negligible.

All experiments aiming to identify the modal parameters of the excited modes are conducted through frequency sweep experiments. First, the frequency interval and sweep velocity are set. The latter is chosen sufficiently small so that the transducer's response can be considered stationary. The frequency generator produces the respective harmonic signal, amplified to drive the loudspeaker acting as the excitation source. Sweep experiments are conducted with a constant sweep velocity from low to high frequencies and the rotatable pressure sensor set to a fixed position. Each frequency sweep experiment is repeated three times.

Additional measurements with the rotatable pressure sensor are conducted at a constant excitation frequency for mode order identification. The rotatable pressure sensor traverses to different circumferential positions, where it remains for the duration, during which pressure fluctuations are measured at this position. In this way, pressure patterns in circumferential direction are identified, and the number of nodal diameters is determined. Moreover, a coupled finite element method analysis and an experimental hammer test of

the disk have been conducted to have a reference for the modal parameters of the disk vibration modes.

The data from the pressure transducers and strain gauges recorded during the sweep experiments are evaluated by Fourier transformation. Thereby, the raw data is transformed from the time into the frequency domain, and frequency response functions are obtained for each sensor. Natural frequency results are obtained using the peak picking method. However, especially for acoustic dominant modes in the "slim cavity" setup, many modes overlap, influence, cross, and deflect each other. Moreover, interference signals influence the measured frequency response, so that frequency peaks cannot always be identified undoubtedly.

4.3. Conducted Experiments

Experiments are conducted with two different geometrical setups. For both, the rear cavity has a non-dimensional axial gap width of 0.1. The front cavity width in the "wide cavity" setup is symmetrical to the rear cavity, while for the "slim cavity" it has a non-dimensional axial gap width of 0.025. As shown in the following, the front cavity is the "dominant" one, determining the formation of acoustic (dominant) modes, likely because the excitation source is located here.

Different experimental series are conducted, aiming to reveal natural frequency shifts due to different effects discussed theoretically beforehand. In the first test series, "GAP", a brief comparison of results for different axial gap widths is presented. A change in geometry causes a change in coupling strength by altering the fluid mass acting on the disk. In the second test series "PRESSURE", the fluid pressure in the cavity is changed, effectuating the coupling strength. Density and speed of sound of the fluid change at the same time. Therefore, an added mass and speed of sound effects are expected. While the first two experimental series are conducted with a non-rotating disk, the third one, "ROTATION", includes experiments with different disk rotational speeds, changing the coupling potential between modes by altering the frequency difference between them. Through this, the coupling potential is expected to be significantly increased, resulting in much stronger coupling effects than for the previous test series. An overview of the conducted experimental series is given in Table 1.

Table 1. Overview of conducted test series and expected frequency shift effects.

Test Series	Description	Altered Coupling Influence	Expected Frequency Shift Effect(s) for Uncoupled Modes	Possible Further Frequency Shift Due to Coupling
"GAP"	Variation of axial gap width	Variation of coupling strength	Added mass effect	Weak coupling effect
"PRESSURE"	Variation of fluid pressure	Variation of coupling strength	Added mass effect, speed of sound effect	Weak coupling effect
"ROTATION"	Variation of disk rotational speed	Variation of coupling potential	Stiffening effect of centrifugal force field	Coupling effect

Based on the preceding remarks, two main hypotheses are stipulated:

1. Any frequency shift that cannot be explained by "uncoupled mode effects" is presumably due to additional coupling effects;
2. The coupling effect is stronger the closer the natural frequencies of the theoretically uncoupled modes are to each other.

To validate these hypotheses, the experimental results in this work are assessed subject to the following approach:

1. Theoretic frequency shifts of "uncoupled mode effects" are quantified and measured frequency shifts corrected for their influence;
2. The remaining frequency shifts are analyzed, which are expected to be due to "coupling effects".

4.4. Estimation of Coupling Effect

To estimate the coupling effect, i.e., the extent of any frequency shift caused by coupling, a coupling potential parameter CP and a coupling strength parameter CS are introduced as follows:

$$CP = \frac{f_{ac} - f_{st}}{\min(f_{ac}, f_{st})} \tag{8}$$

$$CS = \frac{\rho_f \, c}{s_{cf}} \tag{9}$$

The coupling potential parameter CP represents the frequency separation between the coupled modes. A smaller value indicates stronger coupling. It is positive when the acoustic dominant mode has a higher frequency than the structure dominant one, and negative if it is vice versa. In the following, the coupling potential is defined as "strong" when the frequency separation between the structure and acoustic dominant modes is less than 0.3. The coupling strength parameter CS depends on the fluid properties as well as the geometry of the cavity. Both coupling parameters together allow concluding on a possible coupling effect.

4.5. Presentation of Measurement Results

Measurement results are presented in the following way: Instead of absolute natural frequencies f_{st} and f_{ac}, normalized frequencies f^* are used in the following, which are frequencies relative to that of the two nodal diameter structure mode in air for the "slim cavity" setup, which serves as a reference frequency f_{ref}, as follows:

$$f^* = \frac{f}{f_{ref}} = \frac{f}{f_{st,2,0}(air, 0.1 \text{ MPa}, 295 \text{ K})} \tag{10}$$

Normalized frequencies f^* can be calculated for any structure (dominant) mode (m,n) and any acoustic (dominant) mode (p,q,r).

For the evaluation of frequency shifts, relative frequency changes Δf^* are displayed. These are frequency changes relative to the frequency at a cavity pressure of 0.1 MPa as follows:

$$\Delta f^* = \frac{f - f_0}{f_0} = \frac{f - f(0.1 \text{ MPa})}{f(0.1 \text{ MPa})} \tag{11}$$

Corrected relative frequency changes $\Delta f^*_{st,corr}$ of structural modes (corrected for the added mass effect) are calculated as follows, with $m_{tot} = m_d + m_f$ being the total mass of disk and fluid together:

$$\Delta f^*_{st,corr}(\rho) = \frac{f_{st,corr}(\rho) - f_{st,0}}{f_{st,0}} = \frac{f_{st}(\rho)\frac{m_{tot}(\rho)}{m_{tot,0}} - f_{st,0}}{f_{st,0}} \tag{12}$$

Corrected relative frequency changes $\Delta f^*_{ac,corr}$ of acoustic modes (corrected for the speed of sound effect) are calculated as follows:

$$\Delta f^*_{ac,corr}(\rho) = \frac{f_{ac,corr}(\rho) - f_{ac,0}}{f_{ac,0}} = \frac{f_{ac}(\rho)\frac{c_0}{c(\rho)} - f_{ac,0}}{f_{ac,0}} \tag{13}$$

Corrected relative frequency changes $\Delta f^*_{st,corr}$ and $\Delta f^*_{ac,corr}$ can be calculated for any structure (dominant) mode (m,n) and any acoustic (dominant) mode (p,q,r), respectively.

5. Measurement Results and Discussion

Acoustic and structure dominant modes that can be excited in the test rig within the range of analyzed frequencies (150 s^{-1} to 1400 s^{-1}) are the two to five nodal diameter modes with zero nodal circles. Following the theory of a match of mode shapes [10], only modes with the same mode order are considered as potentially coupled ($m = p$, $n = q$).

Coupled acoustic dominant modes have an additional axial node ($r = 1$), so that there is a net force acting on the disk. For all analyzed mode pairs, except for the five nodal diameters one in the "slim cavity", the acoustic dominant mode has a higher frequency than the structure dominant mode. This, along with other characteristic data of the occurring mode pairs, is displayed in Table 2.

Table 2. Overview of excited mode couples (with $n = q = 0$) in test rig at UDE. The coupling strength is calculated for 0.1 MPa and 295 K. Values of the coupling strength parameter are normalized as a ratio of the respective value to that for the case of air in the "slim cavity".

Test Rig Setup	k_0	Fluid	$CS/(CS_{slim,air})$	Nodal Diameters ($m = p$)	f^*_{st}	f^*_{ac}	CP	Estimated Coupling Effect
Wide Cavity	0.44	helium	0.101	3	1.99	8.86 *	+3.45	uncoupled
				4	3.44	10.75 *	+2.13	uncoupled
		air	0.250	2	1.01	2.41	+1.37	weak
				3	1.99	3.02	+0.52	weak
				4	3.40	3.66	+0.08	(very) strong
Slim Cavity	0.48	air	1	2	1.00	2.53	+1.53	weak
				3	1.98	3.78	+0.90	weak
				4	3.42	4.38	+0.28	strong
				5	5.26	4.61	−0.14	strong

* Frequencies of the acoustic modes in helium are outside of the measured frequency interval, and therefore estimated based on fluid properties and first derivative of Bessel function.

The different geometries of the two test rig setups result in slightly different core rotation factors k_0 and thereby different coupling strength parameters CS. The latter is also controlled by the fluid properties. The frequency separation between the theoretically uncoupled structure and acoustic modes with the same number of nodal diameters determines the coupling potential parameter CP. Both coupling parameters then predict the coupling effect. In Table 2, coupling strength parameters CS are exemplarily given for 0.1 MPa and 295 K, and coupling potential parameters CP for standstill of the disk.

From this preliminary estimation of the coupling effect, the coupling strength is expected to be bigger for the "slim cavity" test rig setup compared to the "wide" one; and lower in Helium compared to air. The coupling potential is estimated to be the biggest for the four nodal diameter mode in air for the "wide cavity" setup, followed by the five and four nodal diameter modes in the "slim cavity". For these mode pairs, frequency shifts are expected to be observable due to the strong coupling potential.

Results of the three different test series (as introduced in Table 1) are presented in the following.

5.1. Variation of Axial Gap Width

In the first experimental series, "GAP", the axial gap width of the front cavity is varied and thereby is the coupling strength. The disk is non-rotating. With a decrease in (front) cavity width, the fluid mass acting on the disk decreases, and the coupling strength increases (see Table 2 for CS values).

Response functions recorded for the different front cavity widths differ considerably from each other. With a decrease in the cavity width, the natural frequencies of the structure dominant modes change only slightly (max 2%), while the acoustic dominant modes shift significantly towards higher frequencies (5% to 25%). Therefore, it can be concluded that the axial gap width has a significant influence on the occurring acoustic dominant modes. Additionally, more peaks appear to occur in the response functions, and many peaks overlap in the measurements with a smaller front cavity width.

The measured natural frequencies do not reflect the theoretically expected behavior if no coupling is anticipated (slight increase in disk natural frequencies and no change in acoustic dominant modes), neither do they exhibit the expected frequency shifts if coupling is assumed. Consequently, neither the "uncoupled mode effects" nor the coupling models

can explain the observed frequency shifts subject to a variation of the axial gap width, i.e., the theory does not explain the measurement results.

5.2. Presure Variation

In the second experimental series "PRESSURE", with a non-rotating disk, the fluid pressure inside the test rig is changed while all other parameters remain constant. Thereby, the coupling strength is varied (for *CS* values at 0.1MPa see Table 2), and added mass as well as speed of sound effects are expected to influence measured natural frequencies. In addition, a weak coupling effect might be observable, depending on the excited mode pair (see *CP* values in Table 2). For all measurement results of the series "PRESSURE", corrected relative frequency changes Δf^*_{corr} are displayed as defined in Equations (11)–(13).

A measurement series using the "wide cavity" setup and helium as the fluid is conducted as disk vibration modes measured in helium can be considered approximately uncoupled due to the big frequency separation to the respective acoustic modes (see Table 2). If no further coupling is assumed, the frequencies should not change subject to a change in fluid density after being corrected for the added mass effect. As shown in Figure 5, natural frequencies of the measured three and four nodal diameter structure modes decrease slightly with an increase in fluid density. Corrected for the added mass effect, an insignificant decrease of 0.3% and 0.2% remains for the (3,0) and (4,0) structural modes, respectively, if the fluid density is increased approximately 15-fold. This remaining decrease in frequency is considered as negligible, and therefore these modes in helium can be considered as practically constant and thus uncoupled.

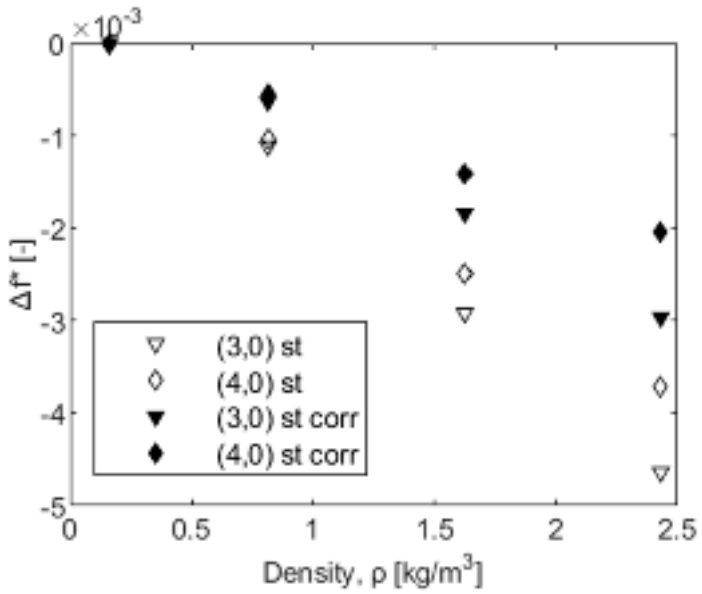

Figure 5. Corrected relative frequency changes of structure modes in helium for "wide cavity" over fluid density. Raw values and values corrected for added mass effect.

Measurements using the "slim cavity" setup and air as the fluid are conducted to analyze the excited modes for potential coupling. As mode pairs in air exhibit a higher coupling potential than those in helium, frequency shifts attributed to coupling effects are expected to be bigger in air, but dependent on the coupling potential of each mode pair. Corrected relative frequency changes of the structure dominant modes $\Delta f^*_{st,corr}$ are presented in Figure 6. For the modes with two to four nodal diameters, the natural frequencies of the disk decrease about 4% to 5% for a 12-fold increase in fluid density, while the frequency of the five nodal diameter structural mode increases about 5%. These frequency changes are considerably bigger than those measured in the almost uncoupled case for helium, and it can be concluded that there must be an additional coupling effect. Measured frequency shifts agree qualitatively with the coupling model of Magara et al.

(2008) [12], indicating a decrease in the frequency of the structure dominant modes in case of $f_{st} < f_{ac}$, and an increase for the opposite case (for the five nodal diameter mode). However, the frequency changes appear to be very similar for the two, three and four nodal diameter modes, although those have different coupling potentials.

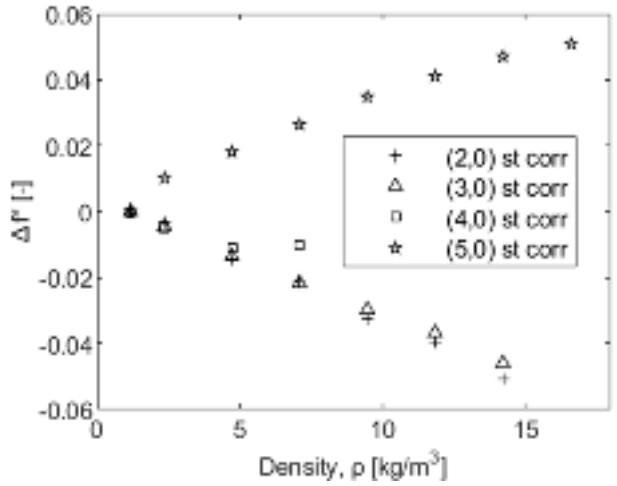

Figure 6. Corrected relative frequency changes of structure dominant modes in air for "slim cavity" over fluid density. Values corrected for added mass effect.

While most frequency peaks are well visible for structural modes, this is not the case for most acoustic modes; the two nodal diameter mode is the only exception. To show potential coupling influences, both (acoustic and structure dominant) modes of the two nodal diameter mode pair are displayed in Figure 7. After the structural mode is corrected for the added mass effect and the acoustic mode for the speed of sound effect, both still exhibit a decreasing and a slightly increasing trend, respectively, when plotted over the fluid density. This behavior supports the hypothesis that weak coupling is present between the disk and the surrounding fluid, and the trends agree qualitatively with those in Magara's [12] coupling model.

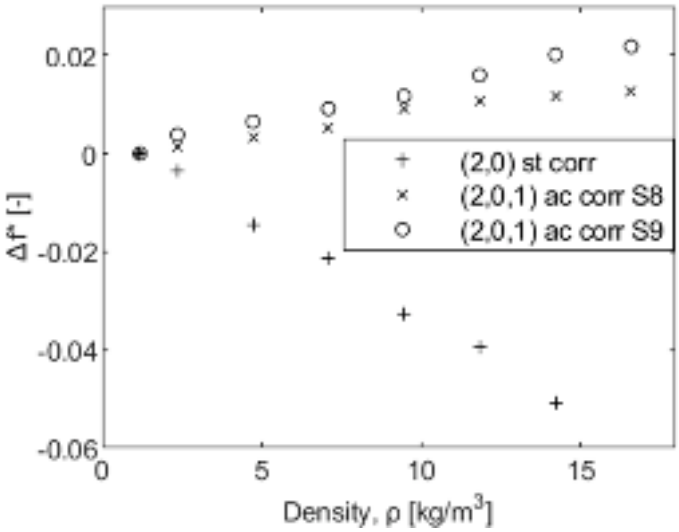

Figure 7. Corrected relative frequency changes of two nodal diameter mode pair in air for "slim cavity" over fluid density. Values corrected for added mass effect and speed of sound effect, respectively. Sensors: S8 on disk, S9 in front cavity.

It should be noted that the frequency change of the acoustic dominant mode differs slightly depending on the pressure sensor's location in the test rig. It is smaller (+2.2%

(S9) and +1.3% (S8 on disk)) than that of the structure dominant mode (−5.5%) for the approximately 14-fold increase in density.

Altogether, for the measurement series "PRESSURE", frequency shifts of structure dominant modes are observed that exceed the "uncoupled mode effects" and thus indicate a coupling effect, even for modes that are only weakly coupled. However, no clear picture about frequency shifts of acoustic dominant modes is obtained, and the hypothesis of a more pronounced coupling effect for stronger coupled modes could not be confirmed on the base of the measurement series with a variation in fluid pressure.

5.3. Variation of Disk Rotational Speed

In the third experimental series, "ROTATION", the disk rotational speed is varied, while the fluid pressure (0.1 MPa, air) and all other parameters remain constant. By this means, the coupling potential is changed as frequency differences between potentially coupled acoustic and structure dominant modes are varied (rotating case *CP* values differ from standstill values in Table 2). There is no added mass or speed of sound effect. However, a small effect of the stiffening effect of the centrifugal force field of the impeller might be observable, but measurement values are not explicitly corrected for its influence.

Disk rotation results in the formation of two modes for each mode order, one forward and one backward traveling wave. While disk modes theoretically travel at the disk rotational speed, cavity modes travel at the fluid's rotational speed in the cavity. Assuming bulk flow in the cavity at approximately half the disk's rotational speed, frequencies of acoustic and structure dominant modes approach each other subject to a change in disk rotational speed. These effects are shown in the following, first for structure, then for acoustic dominant modes, and last for specific mode pairs. For all measurement results of the series "ROTATION", normalized frequencies f^* are displayed as defined in Equation (10). In addition to the measurement results, theoretical values for the natural frequencies of structure and acoustic dominant modes at the respective disk rotational speed are given, calculated according to Equations (2) and (6), respectively. Utilized core rotation factors for the acoustic dominant modes are listed in Table 2.

As shown in Figure 8, the development of a forward and a backward traveling wave is clearly visible for each mode, and the measured frequency splits of the disk vibration modes subject to rotation agree well with the theoretical values.

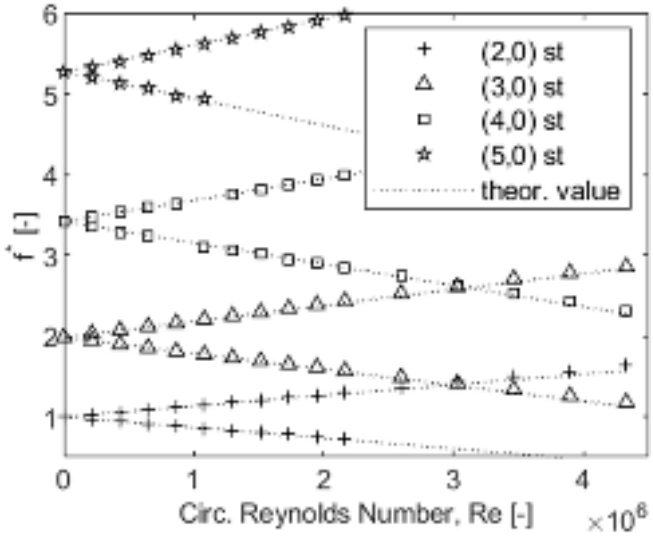

Figure 8. Normalized natural frequencies of structure dominant modes in air at 0.1MPa for "slim cavity" over circumferential Reynolds number. Experimental and theoretical results.

Natural frequencies of the acoustic dominant modes are much less apparent in the measurement results than the disk vibration modes, as they are often overlapping with

neighboring modes or deflected by them. However, the formation of a forward and a backward traveling wave is evident for the acoustic dominant modes with three, four, and five nodal diameters, as shown in Figure 9. Measured and theoretic frequency splits of the acoustic dominant modes subject to disk rotation do not agree well. Moreover, there is no consistent trend noticeable; measured frequency splits for the (3,0,1) and the (5,0,1) modes are smaller than the theoretical values, while the frequency split of the (4,0,1) mode is slightly bigger. Moreover, core rotation factors adopted to match theoretic values of the three and five nodal diameter acoustic waves with the experimental ones appear to be outside of the usual range. Possibly, the core rotation factors are different from the ones calculated theoretically from Equation (5). Additionally, the number of nodal diameters might influence the natural frequency of the traveling waves, in a way different from that stated in Equations (3) and (6). However, for all analyzed modes, the forward wave appears to exhibit a bigger frequency difference to the non-rotating case than the backward wave.

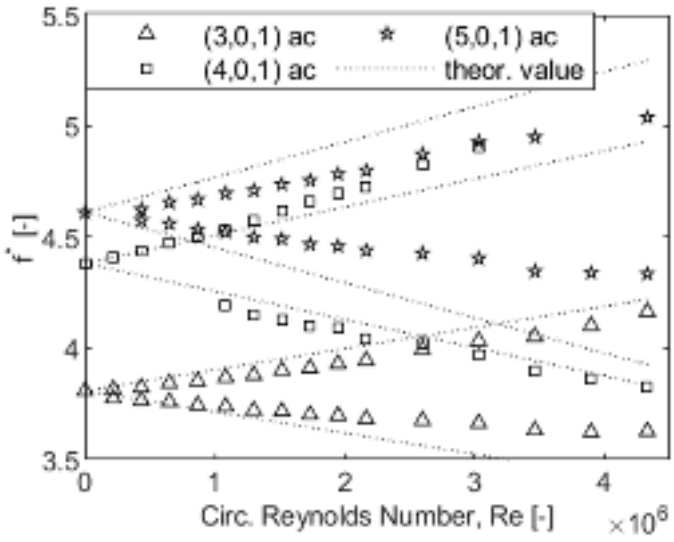

Figure 9. Normalized natural frequencies of acoustic dominant modes in air at 0.1MPa for "slim cavity" over circumferential Reynolds number. Experimental and theoretical results.

To assess the coupling effect for coupled mode pairs, the respective acoustic and structure dominant modes are presented together in the following. Disk rotation further increases the coupling potential (compared to the standstill values in Table 2), making coupling effects observable. The mode pair with three nodal diameters (displayed in Figure 10) is very well visible for all analyzed rotational speeds. However, the coupling potential is estimated to be low ($CP = +0.9$), and thus the expected coupling effect relatively small. Theoretically, the forward traveling waves of the structure and acoustic dominant modes would cross at very high disk rotational speeds while the backward waves veer away from each other. However, within the range of analyzed rotational speeds, the coupling potential remains weak. If the theoretic values are adjusted to approximately fit the backward wave of the measured acoustic dominant mode, which is assumed to be less influenced by coupling, a core rotation factor of about 0.25 must be adopted (as shown in Figure 10). Compared to the backward wave, the acoustic dominant forward wave appears to be deflected towards higher frequencies. This might be due to the increased but still relatively small coupling potential at higher rotational speeds.

The strongest coupling potential of all measured modes is predicted for the four nodal diameter mode pair in the "wide cavity" test rig setup ($CP = +0.08$). Therefore, frequency shifts due to the strong coupling effect are expected to be observable. As can be seen in Figure 11, mode veering is visible, confirming this assumption. The forward modes strongly influence and deflect each other. Instead of crossing at a circumferential Reynolds number of approximately 1.7×10^6, the forward traveling waves approach each

other until a minimum normalized frequency difference of 0.2 is reached and then veer apart, increasing their frequency separation again. For the "slim cavity" test rig setup, this behavior cannot be observed, as the acoustic dominant mode is shifted towards higher frequencies resulting in a weaker coupling potential ($CP = +0.28$). The structure dominant mode follows the theoretical values well, and the acoustic dominant one only exhibits a slight upward deflection. This is a clear indication that a stronger coupling effect is present for stronger coupled modes, i.e., those in closer proximity to each other.

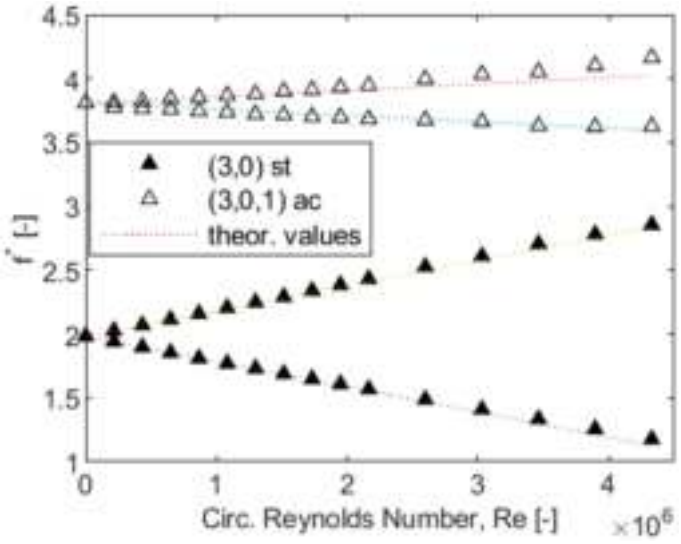

Figure 10. Normalized natural frequencies of three nodal diameter mode pair in air at 0.1MPa for "slim cavity" over circumferential Reynolds number. Experimental and theoretical results (a core rotation factor of 0.25 is adopted for the theoretic values of the acoustic wave).

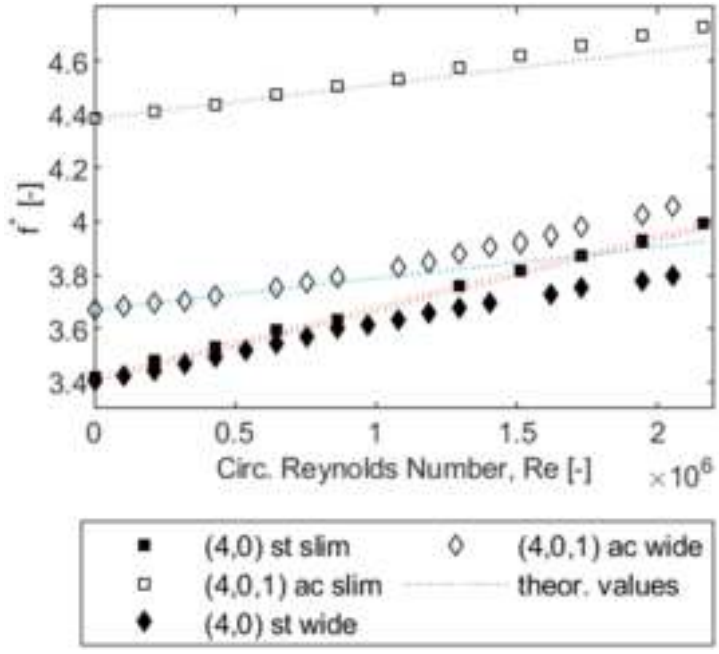

Figure 11. Normalized natural frequencies of forward waves of four nodal diameter mode pair in air at 0.1 MPa for "wide" and "slim cavity" over circumferential Reynolds number. Experimental and theoretical results (core rotation factors of 0.44 and 0.48 are adopted for the theoretic values of the acoustic waves for "slim" and "wide cavity" setup, respectively).

The four and five nodal diameter mode pairs, which are estimated to be strongly coupled in the "slim cavity" setup (*CP* values of +0.28 and −0.14, respectively, see Table 2), are not very well visible in the measurement results. With disk rotation, the coupling potential becomes even bigger, but the response peaks of the structure dominant modes are poorly visible and diminish at a certain rotational speed. As shown in Figure 12, the backward wave of the structure dominant five nodal diameter mode disappears once it comes close to the forward acoustic wave and therefore does not come in closer proximity to the potentially coupled backward acoustic dominant wave. The same happens for the forward wave of the structure dominant four nodal diameter mode, which is no longer visible at Reynolds numbers higher than 2×10^6, where it crosses the backward wave of the acoustic dominant mode (see Figures 8 and 9). Therefore, it does not come close to the coupled forward wave of the acoustic dominant mode. Consequently, no conclusion on the coupling effect and possible veering behavior of the modes with a strong coupling potential can be drawn for the "slim cavity" test rig setup.

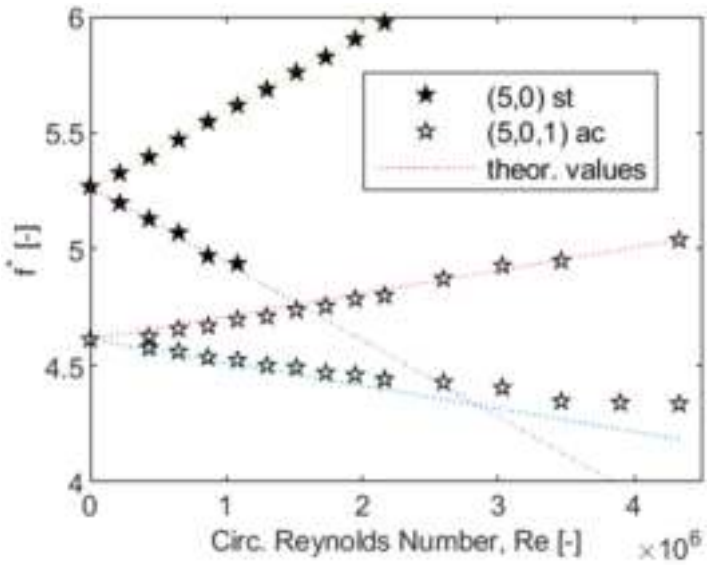

Figure 12. Normalized natural frequencies of five nodal diameter mode pair in air at 0.1 MPa for "slim cavity" over circumferential Reynolds number. Experimental and theoretical results (a core rotation factor of 0.30 is adopted for the theoretic values of the acoustic wave).

Nevertheless, it should be noted that the concept of bulk flow inside the cavity that can be estimated by a core rotation factor is a theoretical idea that does not exist in real cavities. Moreover, measurement results presented in this work are characterized by circumferential Reynolds numbers slightly lower than values for well-established bulk flow. Therefore, most measurement results actually classify into the transitions area between merged and separated boundary layer regimes according to [25], and the applicability of the core rotation concept should be further investigated. Using a fluid with lower kinematic viscosity or conducting measurements with disk rotation at higher pressures could be options to reach higher Reynolds numbers in future experiments.

6. Conclusions and Future Work

In the first part, fundamental concepts necessary to understand the formation of structural and acoustic modes and their coupling in a rotor-cavity system are compiled, and existing coupling models are reviewed. Based on a comprehensive literature review, an overview of frequency shift effects in rotor-cavity systems with a rotating disk is established, including effects for uncoupled and coupled modes. A procedure to analyze those frequency shift effects is developed and later applied to the analysis of experimental results. Moreover, an attempt to quantify the expected coupling effects is made by establishing a coupling strength and a coupling potential parameter.

In the second part of this work, measurement results of acoustic and structure dominant modes are presented, including a test series with varying cavity pressure and one with different disk rotational speeds. For the latter, the development of a forward and a backward traveling wave is demonstrated for each mode. All excited mode pairs in the test rig are at least weakly coupled in air, i.e., frequency shifts are observed that cannot solely be explained by "uncoupled mode effects", such as the added mass, speed of sound, and stiffening effect, but indicate an additional coupling effect. However, the hypothesis of a bigger coupling effect (bigger frequency shift) for stronger coupled modes cannot be corroborated consistently. By varying the disk rotational speed, the frequency difference between coupled modes, and thus their coupling potential, can be varied additionally. However, the expected coupling effect is not observable for all mode pairs. Only the four nodal diameter mode pair in the "wide cavity" exhibits a strong coupling effect. Mode veering is visible, i.e., with an increase in disk rotational speed, the coupled modes approach each other, and then veer apart instead of crossing.

Generally, measurement results for structure dominant modes agree well with theoretical predictions. However, measured acoustic dominant modes do not always exhibit the expected theoretic behavior. It requires further research to clarify whether or not the underlying assumptions on core rotation apply to the flow conditions in the cavity during the measurements. For future research, a different fluid or a higher pressure could be considered to ensure higher Reynolds numbers and further validate the bulk flow concept as well as examine boundary layer influences. Additionally, the influence of the small opening of the cavity needs further investigation.

The next essential step in the line of this research will be to investigate the damping of coupled acoustic and structure dominant modes, as resonances cannot always be avoided and the damping ratio determines the response amplitudes of the system and thus the risk of impeller material failure. Eventually, the transferability of the results to real machines needs to be proven. However, this work poses an essential step towards a better understanding of acoustoelastic coupling effects in the side cavities of centrifugal compressors under varying operating conditions.

Author Contributions: Conceptualization, T.U.; Data curation, T.U.; Formal analysis, T.U.; Funding acquisition, D.B.; Investigation, T.U.; Methodology, T.U.; Supervision, D.B.; Visualization, T.U.; Writing—original draft, T.U.; Writing—review & editing, D.B. All authors have read and agreed to the published version of the manuscript.

Funding: This project is funded by Deutsche Forschungsgemeinschaft (DFG). The authors are grateful for the financial support under project number 429153912.

Data Availability Statement: Not applicable.

Conflicts of Interest: The authors declare no conflict of interest. The funders had no role in the design of the study; in the collection, analyses, or interpretation of data; in the writing of the manuscript, or in the decision to publish the results.

Nomenclature

b	disk/impeller thickness, m
c	speed of sound, m/s
c_f	friction coefficient
CP	coupling potential parameter
CS	coupling strength parameter
f	frequency, 1/s
$f^* = \frac{f}{f_{ref}}$	normalized frequency relative to the frequency $f_{ref} = f_{st,2,0}(air,\ 0.1\ \text{MPa}, 295\ \text{K})$
$\Delta f^* = \frac{f-f_0}{f_0}$	relative frequency change relative to the frequency $f_0 = f(0.1\ \text{MPa})$

f_Ω	rotational frequency of rotating disk, 1/s
$G = \frac{s}{r_d}$	non-dimensional axial gap width of cavity
k_0	core rotation factor
L	characteristic length, m
m	mass, kg
(m,n)	number of nodal diameters, nodal circles of structure (dominant) mode
(p,q,r)	number of nodal diameters, nodal circles, axial nodes of acoustic (dominant) mode
r	radius, m
Re	circumferential Reynolds number
s	axial gap width of cavity, m
t_{ax}	cylindrical portion of impeller side room, m
u	disk/impeller circumferential velocity, m/s
v	velocity, m/s
Ω	rotational speed of disk, 1/min
$(\pi\alpha)_{p,q}$	dimensionless solutions to the first derivative of the Bessel function for the (p,q) acoustic mode
ν	kinematic viscosity of the fluid, m^2/s
ρ	density, kg/m^3
	Subscripts
ac	acoustic (dominant)
c, cf, cr	cavity, front cavity, rear cavity
$corr$	corrected
d	disk
e	excitation
f	fluid
s	system
st	structure (dominant)
tot	total
uc	uncoupled

References

1. Lamb, H.; Southwell, R.V. The vibrations of a spinning disk. *Proc. R. Soc. A* **1921**, *99*, 272–280.
2. Southwell, R.V. On the free transverse vibrations of a uniform circular disc clamped at its centre; and on the effects of rotation. *Proc. R. Soc. A* **1922**, *101*, 133–153.
3. Campbell, W. *Protection of Steam Turbine Disk Wheels from Axial Vibration*; General Electric Company: New York, NY, USA, 1924.
4. Eversman, W.; Dodson, R.O., Jr. Free vibration of a centrally clamped spinning circular disk. *AIAA J.* **1969**, *7*, 2010–2012. [CrossRef]
5. Ewins, D.J. Vibration characteristics of bladed disc assemblies. *J. Mech. Eng. Sci.* **1973**, *15*, 165–186. [CrossRef]
6. Irretier, H. The natural and forced vibrations of a wheel disc. *J. Sound Vib.* **1983**, *87*, 161–177. [CrossRef]
7. Irretier, H. Experiments and calculations on the vibrations of rotating radial impellers. *J. Vib. Acoust. Stress Reliab.* **1988**, *110*, 137–142. [CrossRef]
8. Tyler, J.M.; Sofrin, T.G. Axial Flow Compressor Noise Studies; No. 620532. *SAE Trans.* **1962**, *70*, 309.
9. Ehrich, F.F. Acoustic resonances and multiple pure tone noise in turbomachinery inlets. *J. Eng. Power* **1969**, *91*, 253–262. [CrossRef]
10. Eisinger, F.L. Acoustic fatigue of impellers of rotating machinery. *J. Press. Vessel. Technol.* **2002**, *124*, 154–160. [CrossRef]
11. Eisinger, F.L.; Sullivan, R.E. Acoustically-induced structural fatigue of impeller discs: A Brief Note. *Turbo Expo Power Land Sea Air* **2002**, *3610*, 1063–1069.
12. Magara, Y.; Mitsuhiro, N.; Kazuyuki, Y.; Naohiko, T.; Tetsuya, K. Natural frequencies of centrifugal compressor impellers for high density gas applications. *ASME Int. Mech. Eng. Congr. Expo.* **2008**, *48661*, 107–114.
13. Magara, Y.; Yamaguchi, K.; Miura, H.; Takahashi, N.; Narita, M. Natural frequency shift in a centrifugal compressor impeller for high-density gas applications. *J. Turbomach.* **2013**, *135*, 011014. [CrossRef]
14. Beirow, B.; Kühhorn, A.; Figaschewsky, F.; Nipkau, J. Effect of mistuning and damping on the forced response of a compressor blisk rotor. ASME Turbo Expo 2015: Turbine Technical Conference and Exposition. *Am. Soc. Mech. Eng. Digit. Collect.* **2015**, *56772*, V07BT32A001.
15. Heinrich, C.R.; Kühhorn, A.; Steff, K.; Petry, N. Generalized Model for the Approximation of Coupled Acousto-Mechanical Natural Frequencies in High-Pressure Centrifugal Compressors. *J. Eng. Gas Turbines Power* **2021**, *143*, 071022. [CrossRef]
16. Heinrich, C.R.; Unglaube, T.; Beirow, B.; Brillert, D.; Steff, K.; Petry, N. Surrogate Models for The Prediction of Damping Ratios in Coupled Acoustoelastic Rotor-Cavity Systems. In Proceedings of the ASME Turbo Expo 2021: Turbine Technical Conference and Exposition, online, 7–11 June 2021. GT2021-58835.

17. Hellmich, B.; Seume, J.R. Causes of acoustic resonance in a high-speed axial compressor. ASME Turbo Expo 2006: Power for Land, Sea, and Air. *Am. Soc. Mech. Eng. Digit. Collect.* **2006**, *4241*, 377–387.
18. König, S. Acoustic eigenmodes in the side cavities of centrifugal compressors. *Turbo Expo Power Land Sea Air* **2009**, *48876*, 547–557.
19. Petry, N.; König, S.; Benra, F.-K. Influence of the Swirling Flow in the Side Cavities of a High-Pressure Centrifugal Compressor on the Characteristics of Excited Acoustic Modes. Turbo Expo Power for Land, Sea, and Air. *Am. Soc. Mech. Eng.* **2012**, *44748*, 627–639.
20. Eckert, L. High Cycle Fatigue Cracks at Radial Fan Impellers Caused by Aeroelastic Self-Excited Impeller Vibrations: Part I—Case History, Root Cause Analysis, Vibration Measurements. International Design Engineering Technical Conferences and Computers and Information in Engineering Conference. *Am. Soc. Mech. Eng.* **1999**, *19777*, 1135–1146.
21. Barabas, B.; Stefan, C.; Sebastian, S.; Friedrich-Karl, B.; Hans-Josef, D.; Dieter, B. Experimental and numerical determination of pressure and velocity distribution inside a rotor-stator cavity at very high circumferential Reynolds numbers. In Proceedings of the 11th European Conference on Turbomachinery Fluid dynamics & Thermodynamics, Madrid, Spain, 23–27 March 2015.
22. Barabas, B.; Dieter, B.; Hans-Josef, D.; Friedrich-Karl, B. Identification of Coupled Natural Frequencies in a Rotor-Stator Test-Rig for Different Gas Properties. In Proceedings of the 12th European Conference on Turbomachinery Fluid dynamics & Thermodynamics, Stockholm, Sweden, 3–7 April 2017.
23. Barabas, B.; Dieter, B.; Hans-Josef, D.; Friedrich-Karl, B. Damping Behavior of Acoustic Dominant Modes in an Aeroacoustic Test Rig Representing a Simplified Geometry of a High Pressure Radial Compressor. Turbo Expo: Power for Land, Sea, and Air. *Am. Soc. Mech. Eng.* **2018**, *51159*, V07CT36A018.
24. Norton, M.P.; Frederick, C.N. *Fundamentals of Noise and Vibration Analysis for Engineers*; Cambridge University Press: Cambridge, UK, 1998.
25. Daily, J.W.; Nece, R.E. Chamber dimension effects on induced flow and frictional resistance of enclosed rotating disks. *J. Basic Eng.* **1960**, *82*, 217–230. [CrossRef]
26. Gülich, J.F. Disk friction losses of closed turbomachine impellers. *Forsch. Im Ing.* **2003**, *68*, 87–95. [CrossRef]
27. Sigrist, J.-F.; Daniel, B.; Christian, L. Dynamic analysis of a nuclear reactor with fluid–structure interaction: Part i: Seismic loading, fluid added mass and added stiffness effects. *Nucl. Eng. Des.* **2006**, *236*, 2431–2443. [CrossRef]
28. Fahy, F.J. Vibration of containing structures by sound in the contained fluid. *J. Sound Vib.* **1969**, *10*, 490–512. [CrossRef]
29. Barabas, B.; Friedrich-Karl, B.; Nico, P.; Dieter, B. Experimental Damping Behavior of Strongly Coupled Structure and Acoutic Modes of a Rotating Disk with Side Cavities. In Proceedings of the ASME Turbo Expo 2021: Turbine Technical Conference and Exposition, online, 7–11 June 2021; GT2021-58782.

International Journal of
Turbomachinery
Propulsion and Power

MDPI

Article

Acoustoelastic Modes in Rotor-Cavity Systems: An Overview on Frequency Shift Effects Supported with Measurements

Tina Unglaube * and Dieter Brillert

Chair of Turbomachinery, University of Duisburg-Essen, 47057 Duisburg, Germany; dieter.brillert@uni-due.de
* Correspondence: tina.unglaube@uni-due.de

Abstract: With an increase in fluid densities in centrifugal compressors, fluid-structure interaction and coupled acoustoelastic modes receive growing attention to avoid machine failure. Besides the vibrational behavior of the impeller, acoustic modes building up in the side cavities need to be understood to ensure safe and reliable operation. In a coupled system, these structure and acoustic dominant modes influence each other. Therefore, a comprehensive overview of frequency shift effects in rotor-cavity systems is established based on findings in the literature. Additionally, experimental results on coupled mode pairs in a rotor-cavity test rig with a rotating disk under varying operating conditions are presented. Measurement results for structure dominant modes agree well with theoretical predictions. The development of a forward and a backward traveling wave is demonstrated for each mode in case of disk rotation. Conducted experiments reveal the occurrence of weakly and strongly coupled mode pairs as frequency shifts are observed that cannot solely be explained by "uncoupled mode effects", such as the added mass, speed of sound, and stiffening effect, but indicate an additional coupling effect. However, the hypothesis of a bigger frequency shift for stronger coupled modes cannot be corroborated consistently. Only for the strongly coupled four nodal diameter mode pair in the "wide cavity" setup, a coupling effect is clearly visible in the form of mode veering.

Keywords: rotor-cavity system; acoustoelastic modes; coupling; fluid-structure interaction

check for updates

Citation: Unglaube, T.; Brillert, D. Acoustoelastic Modes in Rotor-Cavity Systems: An Overview on Frequency Shift Effects Supported with Measurements. *Int. J. Turbomach. Propuls. Power* **2022**, *7*, 15. https://doi.org/10.3390/ijtpp7020015

Academic Editor: Antoine Dazin

Received: 26 January 2022
Accepted: 4 May 2022
Published: 6 May 2022

Publisher's Note: MDPI stays neutral with regard to jurisdictional claims in published maps and institutional affiliations.

Copyright: © 2022 by the authors. Licensee MDPI, Basel, Switzerland. This article is an open access article distributed under the terms and conditions of the Creative Commons Attribution (CC BY-NC-ND) license (https://creativecommons.org/licenses/by-nc-nd/4.0/).

1. Introduction

Centrifugal compressors are applied for a wide range of industrial applications, including gas compression for the chemical industry, natural gas extraction and liquefaction, enhanced oil recovery, as well as carbon capture and storage. Required discharge pressures increase continuously, and so do fluid densities inside the machines, increasing the forces acting on the impeller. Besides the vibrational behavior of the impeller, which has been studied extensively over the last decades, these fluid-structure interactions have to be understood. Nowadays, it is well known that natural frequencies of compressor impellers shift due to an increase in gas density of the surrounding fluid. Moreover, acoustic modes building up in the side cavities of radial compressors were found to be another potential source of high cycle fatigue. Recent studies suppose that acoustic and disk vibration modes influence each other, resulting in further frequency shifts in coupled rotor-cavity-systems. However, these effects are not fully understood yet. To ensure a safe and reliable design and avoid machine failure during operation, these coupled natural frequencies have to be predicted accurately, and the excitation and the damping mechanism need to be studied further.

Rotor-cavity systems, consisting of a rotating disk in a fluid-filled cavity, provide a simplified model of centrifugal compressors for fundamental research purposes. Therefore, a comprehensive overview on frequency shift effects in acoustoelastic rotor-cavity systems is established based on findings published in the literature. This provides a robust foundation for a theoretical understanding of the topic, which is then underpinned with measurement

data. For this purpose, a rotor-cavity test rig was set up at the Chair of Turbomachinery at the University Duisburg-Essen (Germany) that demonstrates the occurrence of coupled acoustoelastic modes. It enables the researchers to systematically collect and evaluate experimental data on rotor-fluid interaction and the formation of coupled acoustic and structure dominant modes while varying different influencing parameters independently from each other. By doing so, a deeper understanding of coupling and frequency shift effects in rotor-cavity systems is gained.

2. Literature Overview

Some of the earliest works on disk vibration in turbomachinery were conducted by Lamb and Southwell (1921) [1] and Southwell (1922) [2], analyzing the vibrations of a spinning circular disk. A few years later, Campbell (1924) [3] published his fundamental study on the vibrational excitation of rotating turbomachinery, thereby establishing the so-called Campbell diagram. Until today, it remains a widely-used tool to avoid potential vibrational resonances that might result in machine failure. Subsequently, many studies were conducted analyzing the vibrational behavior of rotating disks and compressor impellers. E.g., Eversman and Dodson (1969) [4] published a technical note on the free vibration of spinning, centrally clamped circular disks, and presented an analytical solution of the Eigenvalue equation as a function of hub-to-disk ratio for different spin rigidity parameters and mode shapes. Ewins (1973) [5] published an analytical and experimental study on the vibration characteristics of tuned and detuned bladed disk assemblies, emphasizing the importance of considering the complete bladed disk assembly, instead of disk and blades separately. Irretier [6,7] studied the natural and forced vibrations of a wheel disk and established a numerical model to calculate the Eigen frequencies and mode shapes of the system and later carried out experiments and calculations on the vibrations of rotating radial impellers, which were in good agreement.

One of the first fundamental studies on aero-acoustic excitation sources in turbomachinery was published by Tyler and Sofrin (1962) [8]. They identified rotor-stator interaction as a significant noise generating mechanism and found that both the spinning rotor alone and rotor-stator interaction produce rotating pressure patterns. Since then, these spinning modes are referred to as Tyler-Sofrin modes. Ehrich (1969) [9] derived an analytic model of an annular acoustic cavity to conclude on natural frequencies of acoustic modes in the cavity. It is used to analyze experimental data of a turbomachine over a range of rotational speeds and explain resonance peaks at supersonic and subsonic wheel speeds. Amongst the more recent publications, Eisinger (2002) [10] and Eisinger and Sullivan (2002) [11] address acoustically induced fatigue of impellers of rotating machinery. Coupling of the structural and acoustic modes is discussed that might ultimately lead to structural failure of the impeller. This becomes especially important for impellers in high-density fluids, where disk vibration and acoustic modes cannot be treated separately anymore but need to be analyzed as a coupled system. Magara's publications [12,13] are of particular interest along this chain of causation as they discuss structural frequencies of radial compressors in a high-density environment. Two analytical models are established to explain the subsequent frequency shift phenomena for a non-rotating and a rotating disk due to mode coupling. Experimental results agree well with numerical ones. Beirow et al. (2015) [14] studied the effect of mistuning on a high-pressure compressor blisk at rest with respect to structural vibration modes and damping ratios. The forced response is analyzed, and it is found that, taking aero-elastic coupling effects into account, damping of the structure generally increases while the response decreases. Based on other theoretic models, Heinrich et al. (2020) [15] proposed a generalized model for the approximation of coupled acousto-mechanical natural frequencies in high-pressure centrifugal compressors, which was later extended to take damping effects into account (Heinrich et al. (2021) [16]). In the latter, the model outcome is further compared to experimental data, yielding excellent agreement regarding the predicted natural frequencies and an acceptable agreement regarding damping ratios.

Examples of aero-acoustic excitation in industrial turbomachinery are, e.g., reported in Hellmich and Seume (2006) [17], where an acoustic resonance in a four-stage axial compressor is explained with a simplified model for helical acoustic modes, as well as König (2009) [18] and Petry et al. (2012) [19], who investigate acoustic Eigenmodes in the side cavities of an industrial centrifugal compressor. Their setup includes one complete compressor stage, from the inlet guide vanes to the return guide vanes. Another case of actual high cycle fatigue in an industrial compressor possibly caused by aero-elastic excitation is described in Eckert (1999) [20], accentuating that the problem of fluid-structure interaction in turbomachinery is of substantial concern in real applications.

The current paper is based on the preceding work of the research group at the Chair of Turbomachinery at UDE, aiming at gathering baseline experimental data on rotor-fluid interaction. Barabas et al. (2015) [21] introduced the test rig and measurement instrumentation in detail and presented first velocity profile measurements, indicating a turbulent flow with high Reynolds numbers inside the cavity. Barabas et al. (2017) [22] presented frequency shifts towards higher and lower frequencies for the two modes of a coupled mode pair for a change in cavity pressure. Moreover, interfering influences of crossing modes were identified. Barabas et al. (2018) [23] then focused on the damping of weakly coupled acoustic dominant modes, which was found to decrease with an increase in fluid pressure, and established a relationship of the damping ratio, the kinematic viscosity, and the natural frequency of the acoustic modes.

It is shown that structural-acoustic mode coupling in rotor-cavity systems is a complex field of research with many interacting effects to be taken into account. Several publications address some of these effects, but so far none has revealed them at large. This paper contributes to a deeper understanding of the coaction of all pertinent frequency shift effects in rotor-cavity systems and thus to the efforts to avoid resonances in centrifugal compressors that might ultimately lead to component failure in turbomachinery.

3. Theory on Frequency Shifts in Rotor-Cavity Systems

3.1. The Rotor-Cavity System

A rotor-cavity (or rotor-stator) system consists of an impeller rotating inside a stationary cavity. It can be used as a simplified model of turbomachine impellers in a casing. The rotating disk divides the fluid volume into two separate cavities, similar to the side cavities in, e.g., centrifugal compressors. The ratio of the cavity's axial gap width s to the disk radius r_d is a characteristic dimension describing the cavity, referred to as non-dimensional axial gap width G.

$$G = \frac{s}{r_d} \tag{1}$$

Between the disk vibration modes and the acoustic modes inside the fluid-filled cavities, fluid-structure interaction occurs if there is a resulting force from one to the other. These interactions present themselves in the form of the out-of-plane structural modes of the disk and fluctuating pressure patterns of the fluid that can only truly be neglected if the disk rotates in a vacuum. Structural and acoustic modes additionally influence each other if a certain mode pair is coupled. This results in a further frequency shift. In the case of coupling, the modes are referred to as structure and acoustic dominant modes.

3.2. Uncoupled Structure/Disk Vibrational Modes

The mode shape of disk vibration modes, also called structural modes, is characterized by the number of nodal diameters (diametral modes, or circumferential order) m and the number of nodal circles (or radial order) n. For a rotating disk, a resonance between a natural frequency $f_{m,n}$ of one of its disk modes and an excitation frequency $f_{e,st}$ occurs when the latter coincides with the rotational frequency of the forward or backward traveling wave of the disk mode as follows [3]:

$$f_{e,st} = f_{m,n} \pm m \times f_\Omega \tag{2}$$

with f_Ω being the rotational frequency of the rotating disk.

Disk natural frequencies $f_{m,n}$ increase slightly with an increase in disk rotational speed Ω due to the stiffening effect of the centrifugal force field [7]. This effect can be approximated (as, e.g., in [2]) but is often sufficiently small to be neglected [7].

For a mistuned disk, i.e., a non-axisymmetric disk, there are two natural frequencies for one disk mode. However, this frequency splitting is often negligible for practical applications [7]. In general, the above-mentioned considerations also apply to rotating impellers. Nevertheless, mistuning due to geometrical non-uniformities becomes more likely for more complex impeller geometries [5]. Such detuning gives rise to more irregular and complex mode shapes and more resonances than those in equivalent tuned systems [5].

3.3. Uncoupled Acoustic/Cavity Modes

In a fluid-filled cavity, acoustic modes (or cavity modes) can form that establish as fluctuating pressure patterns. In rotating machinery, these acoustic waves are excited by the flow through the machine and can be enhanced by the impeller rotation [10]. Similar to structural modes, acoustic modes are characterized by their number of nodal diameters p, nodal circles q, and additionally, axial nodes r. The frequency of the (p,q) acoustic mode inside a cylinder can be calculated as follows [24]:

$$f_{p,q} = \frac{(\pi\alpha)_{p,q}\, c}{2\pi\, r_c} \tag{3}$$

where $(\pi\alpha)_{p,q}$ are the dimensionless solutions to the first derivative of the Bessel function for the (p,q) acoustic mode (see Figure 1). From Equation (3) we see that the natural frequency of the acoustic mode is linearly dependent on the fluid's speed of sound c, and thus on the fluid properties. E.g., an increase in fluid pressure causes a shift in the natural frequency of the acoustic modes. This will be referred to as the speed-of-sound effect in the following. A change in cavity radius r_c also results in a change of acoustic frequency; however, according to this model in Equation (3), a change in axial gap width does not.

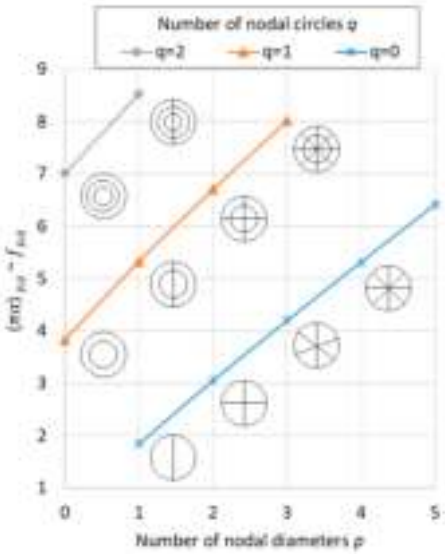

Figure 1. Non-dimensional solutions to Bessel functions for acoustic frequencies inside a cylinder and respective mode shapes for different numbers of nodal diameters and nodal circles.

In a rotor-stator system, disk rotation results in fluid rotation inside the cavity. These flow patterns influence the formation of acoustic modes and can be described depending on the circumferential Reynolds number *Re*, which is defined as follows:

$$Re = \frac{u\ L}{\nu} = \frac{2\pi\ \Omega\ r_d^2}{\nu} \tag{4}$$

where u is the circumferential velocity, L the characteristic length, and ν the kinematic viscosity of the fluid. The widely used rotor-stator cavity flow model by Daily and Nece (1960) [25] distinguishes between four flow regimes, the two turbulent ones having either merged or separated boundary layers. The latter is predominant for bigger cavity widths or higher Reynolds numbers and is characterized by a core flow, for which an almost constant circumferential velocity is assumed, i.e., the fluid is swirling as a bulk flow. The core rotation can be described by the ratio k_0 of the fluid velocity v_f to the impeller circumferential velocity u and only depends on the geometry of the cavity if there is no superimposed through flow [26]. In the case of zero leakage flow, it is also independent of the radius and can be estimated as follows [26]:

$$k_0 = \frac{v_f}{u} = \frac{1}{1 + \left(\frac{r_c}{r_d}\right)^2 \sqrt[2]{\left(\frac{r_c}{r_d} + 5\frac{t_{ax}}{r_d}\right)\frac{c_{f,case}}{c_{f,d}}}} \tag{5}$$

where r_d and r_c are the impeller and the cavity radius, t_{ax} is the cylindrical portion of the impeller side room, and $c_{f,d}$ and $c_{f,case}$ are the friction coefficients of the impeller and casing, respectively. Typically, the core rotation factor takes a value between 0.4 and 0.5, i.e., the fluid rotates at a rotational speed a little less than half of the disk speed.

Analogous to the structural modes, the acoustic modes subject to core rotation form a backward and a forward traveling wave in the cavities that can be calculated as follows:

$$f_{e,ac} = f_{p,q} \pm k_0 \times p \times f_\Omega \tag{6}$$

3.4. Fluid-Structure Interaction

So far, the disk vibration and fluid-filled cavity have been treated separately. However, the influence of the surrounding fluid on the impeller has to be considered. Especially with an increase in fluid pressure and therefore density, significant forces are acting from the fluid on the impeller. Vice-versa, the out-of-plane structural modes also influence the acoustic ones. These effects are called fluid-structure-interaction and cannot be neglected. Of particular practical interest is the influence of an increased fluid density on the turbomachinery impeller, which is addressed by the added-mass-effect: An increase in mass of the surrounding fluid results in a decrease of the natural frequencies of the impeller [12,13,27], as the fluid mass is linearly dependent on the fluid density (and the cavity volume). Hence, while the impeller's mass does not change, the total mass of the system changes as the fluid mass acting on the impeller varies. The change in natural frequency is anti-proportional to the change in total mass. However, these interactions are not of major concern unless coupling between a pair of acoustic and structural modes exists.

3.5. Coupling

The respective modes need to be excited first off for coupling between an acoustic and a structure mode to occur. While acoustic modes are excited by the fluid flow through the casing passing obstacles, such as vanes or the rotor, the most efficient source of impeller vibration are higher order acoustic modes [10]. In addition, for a setup with two cavities surrounding an impeller or disk, there must be a phase shift between the acoustic modes in these cavities, or in a different notion, an axial node must exist (at the axial position of the disk). Only then is there a resulting force from the fluid acting on the impeller. Therefore,

the out-of-plane structural (disk) modes and acoustic (cavity) modes with an axial node have the most potential to influence each other.

The compatibility of mode shapes is a necessary condition for structural-acoustic coupling. This coincidence of mode shapes is especially established through the same number of nodal diameters ($m = p$) [10]. It is often assumed that each structural mode is only well coupled to one acoustic mode and only weakly to all others [10,28]. The most severe interaction (or complete coincidence) occurs when also the (uncoupled) natural frequencies match [10]. However, any coupling of a pair of acoustic and structure dominant modes results in the shift of their natural frequencies compared to the uncoupled modes. This coupling effect also occurs if the theoretically uncoupled natural frequencies are in a certain proximity to each other. The closer the uncoupled natural frequencies are to each other, the stronger is the coupling effect and thus the resulting frequency shift. According to [10], a 25% minimum separation of natural frequencies is recommended to consider modes as not coupled. In Reference [11], the degree of structural-to-acoustic coupling is expressed by a coupling coefficient, which is zero in the case of uncoupled systems. A small mass of the impeller or a thin cavity increases the coupling, while a bigger mass of the disk and a wider cylindrical cavity facilitate weaker coupling [11].

Still, it should be mentioned that for real turbomachinery impellers or detuned bladed disk assemblies, each excited disk mode contains components of many diametral mode orders. Therefore, an m-engine order excitation might excite not only the pure m-nodal diameter mode but also most other modes [5].

3.6. Existing Frequency Shift Models

One widely used mathematical model aiming at explaining coupling effects in rotor-cavity systems is the model of Magara et al. (2008) [12], which originates from research on frequency shifts of centrifugal compressor impellers in high-density gas applications.

The frequency shift model consists of a parabola, which opens upward (left side of Equation (7)) and a straight line with a positive slope (right side of Equation (7)) if the square of the system frequency f_s^2 is indicated on the x-axis (see Figure 2).

$$\left(f_{1,uc}^2 - f_s^2\right) * \left(f_{2,uc}^2 - f_s^2\right) = 2\frac{\rho_f\, c^2}{\rho_d\, b\, s_c} f_s^2 \tag{7}$$

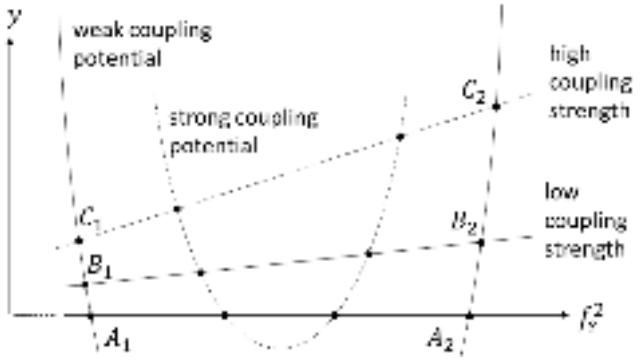

Figure 2. Coupling model of Magara et al. (2008) [12].

The intersections of the parabola with the x-axis (points A) represent the theoretically uncoupled natural frequencies of the disk and the fluid. Which of them is the lower and which the higher-frequency mode depends on the geometry and cannot be stated generally. Therefore, they are not indicated as acoustic and structure modes, but as $f_{1,uc}$ and $f_{2,uc}$. The frequency difference between A_1 and A_2 indicates the coupling potential of the two modes, being bigger the closer the theoretically uncoupled natural frequencies are to each other. The straight line indicates the coupling strength. The slope increases with an increase in fluid density ρ_f and speed of sound c and decreases with an increase in disk density ρ_d,

disk thickness b, and axial cavity width s_c. The intersections of the coupling strength term with the parabola (points B and C) represent the two natural frequencies of the coupled system f_s. When the coupling strength increases, the intersections are shifted upwards and outwards, i.e., the frequency of the lower-frequency mode decreases (from B_1 to C_1) and the one of the higher-frequency mode increases (from B_2 to C_2). This frequency shift is bigger, the more the coupling strength increases (the bigger its slope), and the closer the theoretically uncoupled modes are to each other, i.e., the bigger the coupling potential. The latter effect can be illustrated by comparing the frequency shifts of the cases with weak (solid line parabola) and strong coupling potential (dashed line parabola).

3.7. Overview on Frequency Shift Phenomena in a Rotor-Cavity-System

Based on the comprehensive review of structural and acoustic modes, as well as their fluid-structure interaction and coupling in the previous paragraphs, an overview of frequency shift effects in rotor-cavity systems is presented in what follows (Figure 3).

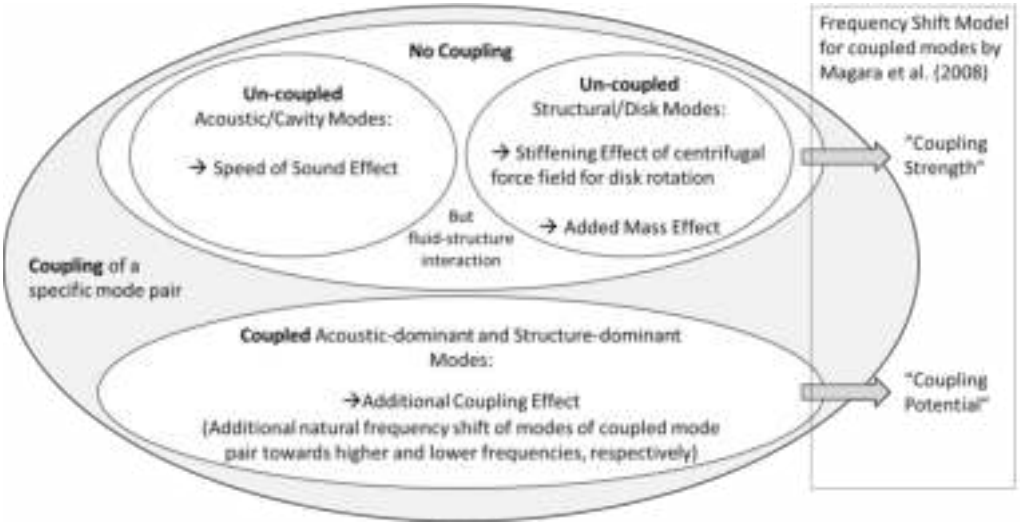

Figure 3. Overview of frequency shift effects in rotor-cavity systems [12].

First, there is a group of "uncoupled mode effects", which occur independently from any coupling of a specific mode pair, i.e., they can be observed for both, uncoupled as well as for coupled modes: The speed of sound effect refers to a shift in the natural frequency of the acoustic mode if the speed of sound changes due to altered fluid properties. Additionally, the stiffening effect of the centrifugal force field might be observed for rotating impellers resulting in a slight upward shift of the structural frequency at higher rotational speeds. Considering fluid-structure interaction effects, which are of particular importance for higher fluid densities surrounding an impeller, the added mass effect plays an important role. It results in a decrease of disk frequencies if the mass of the surrounding fluid increases. In Magara's coupling model [12], these effects are encompassed by the term "coupling strength". If two specific modes are coupled, i.e., a structure and an acoustic dominant mode with similar mode shapes and natural frequencies in a certain proximity to each other are excited, this adds additional frequency shifts: For a coupled mode pair, one natural frequency shifts towards higher, the other towards lower frequencies, compared to their uncoupled counterparts. This is referred to as the coupling effect. The smaller the frequency difference of the uncoupled modes is, the bigger is the coupling effect, and thus the frequency shift it effectuates. In Magara's coupling model [12], these frequency shifts are addressed by the term "coupling potential".

Based on this, the following can be hypothesized: Any frequency shift that is not caused by the added mass, speed of sound, or stiffening effect (for uncoupled structural or acoustic modes) indicates an additional coupling effect. The coupled modes are then referred to as structure dominant and acoustic dominant modes.

When the frequency difference between two coupled modes decreases subject to, e.g., a change in fluid properties or rotational speed, the two modes approach each other. However, in several cases, they do not intersect (no resonance) but diverge again and approach the theoretically uncoupled frequency path of the other mode. This frequency deflection is called mode veering and reported, e.g., in [27,29].

4. Experimental Setup and Procedure

4.1. Test Rig and Instrumentation

Experimental results presented in this paper are obtained at the rotor-cavity test rig of the Chair of Turbomachinery at the University Duisburg-Essen, Germany, introduced in [21–23]. The test rig consists of a plain rotating disk with a constant width b in a cylindrical stationary casing, forming two fluid-filled cavities, which are connected through a small radial gap. A sketch of the test rig, including some measurement equipment, is given in Figure 4. This setup represents a simplified model of the side cavities in radial compressors. The axial gap widths of the front and rear cavity, s_{cf} and s_{cr}, respectively, can be adjusted independently. For the conducted experiments, there is no superimposed through flow in the cavities. The disk is mounted on a shaft connected to a continuously adjustable high-speed electrical drive via a magnetic coupling. Different gases can be passed into the test rig from a pre-mix chamber, allowing for a variation of fluid parameters. The disk's rotational speed Ω can be varied, and circumferential Reynolds numbers up to 2×108 can be achieved with CO_2 at maximum speed.

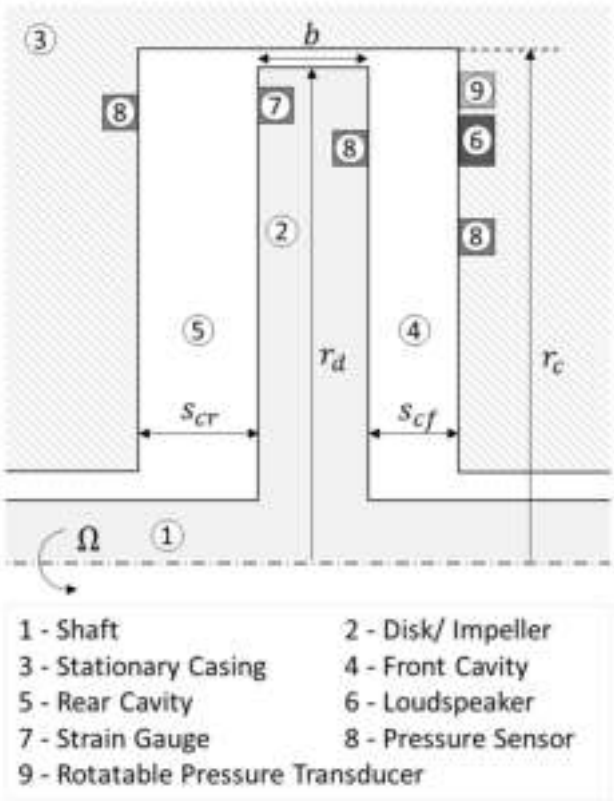

Figure 4. Test rig setup and measurement equipment.

Excitation sources in real turbomachinery, such as rotor-stator interaction, are missing in the test rig due to its simplified (blade- and vane-less) geometry. For that reason, a loudspeaker is installed in the casing of the front cavity. It is capable of exciting both acoustic and structure dominant modes in the front and the rear cavities. The excitation frequency is set by a wave generator connected to an amplifier and adjusted independently from other parameters. The geometry of the test rig is designed so that at least one pair of

acoustic and structural modes with the same number of nodal diameters are coupled at ambient conditions.

When interpreting the results, one should notice that the cavity, in which the measurements are taken, is not perfectly closed. There are two small openings in the front cavity, one at the outer radius and one at the inner. Although valves in the connecting pipes are closed so that there is no in- or outflow to or from the cavity, these openings might affect the propagation and reflection of acoustic waves inside the cavity. In future experiments, results for a completely closed cavity and the current setup will be compared to gain further insight into this matter. However, the side cavities in real turbomachines are also not perfectly closed, so that the setup in this work might even represent a more realistic case than that of a perfectly sealed cavity.

To measure acoustic modes that occur in the form of local pressure fluctuations, the test rig is equipped with two pressure transducers in each, the front and rear cavity, as well as one on the disk. To detect structural modes in the form of disk vibration, two strain gauges are mounted on the disk. The following measures are provided for the identification of mode shapes: The number of nodal diameters of the excited mode is traced with an additional traversable pressure sensor installed in the front cavity, which can rotate 300 degrees around the disk's circumference at a constant excitation frequency. To detect the number of nodal circles, the two pressure sensors in the front cavity are mounted at a different radial position compared to those in the rear cavity. An axial node is detected by identifying a 180 degrees' phase shift between the pressure patterns in the front and rear cavity. In addition, the test rig and pre-mix chamber are equipped with pressure and temperature sensors to determine the thermodynamic properties of the fluid.

The general uncertainty of the measurement chain of the temperature sensors is determined to be ± 1.8 K, and the non-linearity and dynamic uncertainties of the pressure sensors are negligibly small [29]. However, strain gauges are only able to measure dynamic vibrations up to a cut-off frequency of 50 kHz [29]. Additionally, the electrostatic noise increases significantly for experiments with a rotating disk, resulting in a very low signal-to-noise ratio for those strain gauge results. However, pressure sensor results are not affected as much by electromagnetic interferences. Therefore, response functions for the structure dominant modes are also measured with pressure sensors in case of disk rotation. Measurements without disk rotation have shown that this approach does not influence the results as strain gauge and pressure sensor measurements agree well.

4.2. Experimental and Evaluation Procedures

In preparation for the experiments, the test rig is filled with the required gas mixture until the target pressure is reached. The temperature inside the test rig is assumed to be constant, as a maximum friction-induced increase of 0.3% for experiments with high rotational speeds is considered negligible.

All experiments aiming to identify the modal parameters of the excited modes are conducted through frequency sweep experiments. First, the frequency interval and sweep velocity are set. The latter is chosen sufficiently small so that the transducer's response can be considered stationary. The frequency generator produces the respective harmonic signal, amplified to drive the loudspeaker acting as the excitation source. Sweep experiments are conducted with a constant sweep velocity from low to high frequencies and the rotatable pressure sensor set to a fixed position. Each frequency sweep experiment is repeated three times.

Additional measurements with the rotatable pressure sensor are conducted at a constant excitation frequency for mode order identification. The rotatable pressure sensor traverses to different circumferential positions, where it remains for the duration, during which pressure fluctuations are measured at this position. In this way, pressure patterns in circumferential direction are identified, and the number of nodal diameters is determined. Moreover, a coupled finite element method analysis and an experimental hammer test of

the disk have been conducted to have a reference for the modal parameters of the disk vibration modes.

The data from the pressure transducers and strain gauges recorded during the sweep experiments are evaluated by Fourier transformation. Thereby, the raw data is transformed from the time into the frequency domain, and frequency response functions are obtained for each sensor. Natural frequency results are obtained using the peak picking method. However, especially for acoustic dominant modes in the "slim cavity" setup, many modes overlap, influence, cross, and deflect each other. Moreover, interference signals influence the measured frequency response, so that frequency peaks cannot always be identified undoubtedly.

4.3. Conducted Experiments

Experiments are conducted with two different geometrical setups. For both, the rear cavity has a non-dimensional axial gap width of 0.1. The front cavity width in the "wide cavity" setup is symmetrical to the rear cavity, while for the "slim cavity" it has a non-dimensional axial gap width of 0.025. As shown in the following, the front cavity is the "dominant" one, determining the formation of acoustic (dominant) modes, likely because the excitation source is located here.

Different experimental series are conducted, aiming to reveal natural frequency shifts due to different effects discussed theoretically beforehand. In the first test series, "GAP", a brief comparison of results for different axial gap widths is presented. A change in geometry causes a change in coupling strength by altering the fluid mass acting on the disk. In the second test series "PRESSURE", the fluid pressure in the cavity is changed, effectuating the coupling strength. Density and speed of sound of the fluid change at the same time. Therefore, an added mass and speed of sound effects are expected. While the first two experimental series are conducted with a non-rotating disk, the third one, "ROTATION", includes experiments with different disk rotational speeds, changing the coupling potential between modes by altering the frequency difference between them. Through this, the coupling potential is expected to be significantly increased, resulting in much stronger coupling effects than for the previous test series. An overview of the conducted experimental series is given in Table 1.

Table 1. Overview of conducted test series and expected frequency shift effects.

Test Series	Description	Altered Coupling Influence	Expected Frequency Shift Effect(s) for Uncoupled Modes	Possible Further Frequency Shift Due to Coupling
"GAP"	Variation of axial gap width	Variation of coupling strength	Added mass effect	Weak coupling effect
"PRESSURE"	Variation of fluid pressure	Variation of coupling strength	Added mass effect, speed of sound effect	Weak coupling effect
"ROTATION"	Variation of disk rotational speed	Variation of coupling potential	Stiffening effect of centrifugal force field	Coupling effect

Based on the preceding remarks, two main hypotheses are stipulated:

1. Any frequency shift that cannot be explained by "uncoupled mode effects" is presumably due to additional coupling effects;
2. The coupling effect is stronger the closer the natural frequencies of the theoretically uncoupled modes are to each other.

To validate these hypotheses, the experimental results in this work are assessed subject to the following approach:

1. Theoretic frequency shifts of "uncoupled mode effects" are quantified and measured frequency shifts corrected for their influence;
2. The remaining frequency shifts are analyzed, which are expected to be due to "coupling effects".

4.4. Estimation of Coupling Effect

To estimate the coupling effect, i.e., the extent of any frequency shift caused by coupling, a coupling potential parameter CP and a coupling strength parameter CS are introduced as follows:

$$CP = \frac{f_{ac} - f_{st}}{\min(f_{ac}, f_{st})} \tag{8}$$

$$CS = \frac{\rho_f \, c}{s_{cf}} \tag{9}$$

The coupling potential parameter CP represents the frequency separation between the coupled modes. A smaller value indicates stronger coupling. It is positive when the acoustic dominant mode has a higher frequency than the structure dominant one, and negative if it is vice versa. In the following, the coupling potential is defined as "strong" when the frequency separation between the structure and acoustic dominant modes is less than 0.3. The coupling strength parameter CS depends on the fluid properties as well as the geometry of the cavity. Both coupling parameters together allow concluding on a possible coupling effect.

4.5. Presentation of Measurement Results

Measurement results are presented in the following way: Instead of absolute natural frequencies f_{st} and f_{ac}, normalized frequencies f^* are used in the following, which are frequencies relative to that of the two nodal diameter structure mode in air for the "slim cavity" setup, which serves as a reference frequency f_{ref}, as follows:

$$f^* = \frac{f}{f_{ref}} = \frac{f}{f_{st,2,0}(air, 0.1 \text{ MPa}, 295 \text{ K})} \tag{10}$$

Normalized frequencies f^* can be calculated for any structure (dominant) mode (m,n) and any acoustic (dominant) mode (p,q,r).

For the evaluation of frequency shifts, relative frequency changes Δf^* are displayed. These are frequency changes relative to the frequency at a cavity pressure of 0.1 MPa as follows:

$$\Delta f^* = \frac{f - f_0}{f_0} = \frac{f - f(0.1 \text{ MPa})}{f(0.1 \text{ MPa})} \tag{11}$$

Corrected relative frequency changes $\Delta f^*_{st,corr}$ of structural modes (corrected for the added mass effect) are calculated as follows, with $m_{tot} = m_d + m_f$ being the total mass of disk and fluid together:

$$\Delta f^*_{st,corr}(\rho) = \frac{f_{st,corr}(\rho) - f_{st,0}}{f_{st,0}} = \frac{f_{st}(\rho)\frac{m_{tot}(\rho)}{m_{tot,0}} - f_{st,0}}{f_{st,0}} \tag{12}$$

Corrected relative frequency changes $\Delta f^*_{ac,corr}$ of acoustic modes (corrected for the speed of sound effect) are calculated as follows:

$$\Delta f^*_{ac,corr}(\rho) = \frac{f_{ac,corr}(\rho) - f_{ac,0}}{f_{ac,0}} = \frac{f_{ac}(\rho)\frac{c_0}{c(\rho)} - f_{ac,0}}{f_{ac,0}} \tag{13}$$

Corrected relative frequency changes $\Delta f^*_{st,corr}$ and $\Delta f^*_{ac,corr}$ can be calculated for any structure (dominant) mode (m,n) and any acoustic (dominant) mode (p,q,r), respectively.

5. Measurement Results and Discussion

Acoustic and structure dominant modes that can be excited in the test rig within the range of analyzed frequencies (150 s^{-1} to 1400 s^{-1}) are the two to five nodal diameter modes with zero nodal circles. Following the theory of a match of mode shapes [10], only modes with the same mode order are considered as potentially coupled ($m = p$, $n = q$).

Coupled acoustic dominant modes have an additional axial node ($r = 1$), so that there is a net force acting on the disk. For all analyzed mode pairs, except for the five nodal diameters one in the "slim cavity", the acoustic dominant mode has a higher frequency than the structure dominant mode. This, along with other characteristic data of the occurring mode pairs, is displayed in Table 2.

Table 2. Overview of excited mode couples (with $n = q = 0$) in test rig at UDE. The coupling strength is calculated for 0.1 MPa and 295 K. Values of the coupling strength parameter are normalized as a ratio of the respective value to that for the case of air in the "slim cavity".

Test Rig Setup	k_0	Fluid	$CS/(CS_{slim,air})$	Nodal Diameters ($m = p$)	f^*_{st}	f^*_{ac}	CP	Estimated Coupling Effect
Wide Cavity	0.44	helium	0.101	3	1.99	8.86 *	+3.45	uncoupled
				4	3.44	10.75 *	+2.13	uncoupled
		air	0.250	2	1.01	2.41	+1.37	weak
				3	1.99	3.02	+0.52	weak
				4	3.40	3.66	+0.08	(very) strong
Slim Cavity	0.48	air	1	2	1.00	2.53	+1.53	weak
				3	1.98	3.78	+0.90	weak
				4	3.42	4.38	+0.28	strong
				5	5.26	4.61	−0.14	strong

* Frequencies of the acoustic modes in helium are outside of the measured frequency interval, and therefore estimated based on fluid properties and first derivative of Bessel function.

The different geometries of the two test rig setups result in slightly different core rotation factors k_0 and thereby different coupling strength parameters CS. The latter is also controlled by the fluid properties. The frequency separation between the theoretically uncoupled structure and acoustic modes with the same number of nodal diameters determines the coupling potential parameter CP. Both coupling parameters then predict the coupling effect. In Table 2, coupling strength parameters CS are exemplarily given for 0.1 MPa and 295 K, and coupling potential parameters CP for standstill of the disk.

From this preliminary estimation of the coupling effect, the coupling strength is expected to be bigger for the "slim cavity" test rig setup compared to the "wide" one; and lower in Helium compared to air. The coupling potential is estimated to be the biggest for the four nodal diameter mode in air for the "wide cavity" setup, followed by the five and four nodal diameter modes in the "slim cavity". For these mode pairs, frequency shifts are expected to be observable due to the strong coupling potential.

Results of the three different test series (as introduced in Table 1) are presented in the following.

5.1. Variation of Axial Gap Width

In the first experimental series, "GAP", the axial gap width of the front cavity is varied and thereby is the coupling strength. The disk is non-rotating. With a decrease in (front) cavity width, the fluid mass acting on the disk decreases, and the coupling strength increases (see Table 2 for CS values).

Response functions recorded for the different front cavity widths differ considerably from each other. With a decrease in the cavity width, the natural frequencies of the structure dominant modes change only slightly (max 2%), while the acoustic dominant modes shift significantly towards higher frequencies (5% to 25%). Therefore, it can be concluded that the axial gap width has a significant influence on the occurring acoustic dominant modes. Additionally, more peaks appear to occur in the response functions, and many peaks overlap in the measurements with a smaller front cavity width.

The measured natural frequencies do not reflect the theoretically expected behavior if no coupling is anticipated (slight increase in disk natural frequencies and no change in acoustic dominant modes), neither do they exhibit the expected frequency shifts if coupling is assumed. Consequently, neither the "uncoupled mode effects" nor the coupling models

can explain the observed frequency shifts subject to a variation of the axial gap width, i.e., the theory does not explain the measurement results.

5.2. Presure Variation

In the second experimental series "PRESSURE", with a non-rotating disk, the fluid pressure inside the test rig is changed while all other parameters remain constant. Thereby, the coupling strength is varied (for *CS* values at 0.1MPa see Table 2), and added mass as well as speed of sound effects are expected to influence measured natural frequencies. In addition, a weak coupling effect might be observable, depending on the excited mode pair (see *CP* values in Table 2). For all measurement results of the series "PRESSURE", corrected relative frequency changes Δf^*_{corr} are displayed as defined in Equations (11)–(13).

A measurement series using the "wide cavity" setup and helium as the fluid is conducted as disk vibration modes measured in helium can be considered approximately uncoupled due to the big frequency separation to the respective acoustic modes (see Table 2). If no further coupling is assumed, the frequencies should not change subject to a change in fluid density after being corrected for the added mass effect. As shown in Figure 5, natural frequencies of the measured three and four nodal diameter structure modes decrease slightly with an increase in fluid density. Corrected for the added mass effect, an insignificant decrease of 0.3% and 0.2% remains for the (3,0) and (4,0) structural modes, respectively, if the fluid density is increased approximately 15-fold. This remaining decrease in frequency is considered as negligible, and therefore these modes in helium can be considered as practically constant and thus uncoupled.

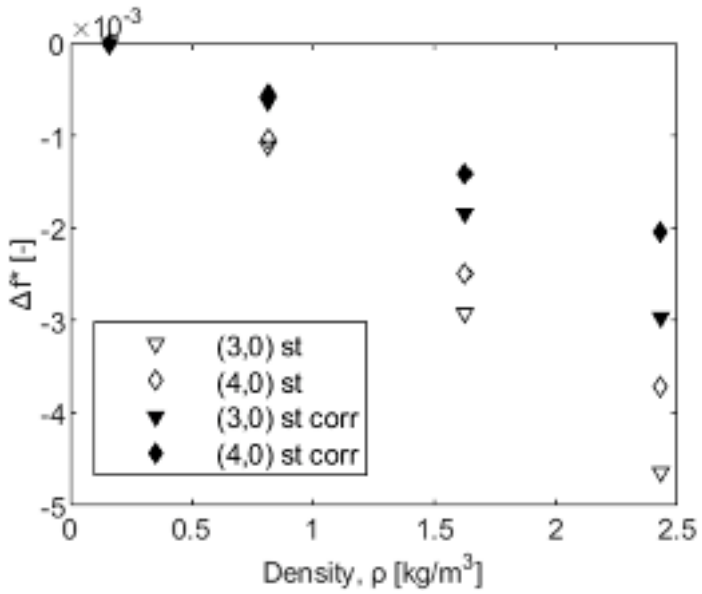

Figure 5. Corrected relative frequency changes of structure modes in helium for "wide cavity" over fluid density. Raw values and values corrected for added mass effect.

Measurements using the "slim cavity" setup and air as the fluid are conducted to analyze the excited modes for potential coupling. As mode pairs in air exhibit a higher coupling potential than those in helium, frequency shifts attributed to coupling effects are expected to be bigger in air, but dependent on the coupling potential of each mode pair. Corrected relative frequency changes of the structure dominant modes $\Delta f^*_{st,corr}$ are presented in Figure 6. For the modes with two to four nodal diameters, the natural frequencies of the disk decrease about 4% to 5% for a 12-fold increase in fluid density, while the frequency of the five nodal diameter structural mode increases about 5%. These frequency changes are considerably bigger than those measured in the almost uncoupled case for helium, and it can be concluded that there must be an additional coupling effect. Measured frequency shifts agree qualitatively with the coupling model of Magara et al.

(2008) [12], indicating a decrease in the frequency of the structure dominant modes in case of $f_{st} < f_{ac}$, and an increase for the opposite case (for the five nodal diameter mode). However, the frequency changes appear to be very similar for the two, three and four nodal diameter modes, although those have different coupling potentials.

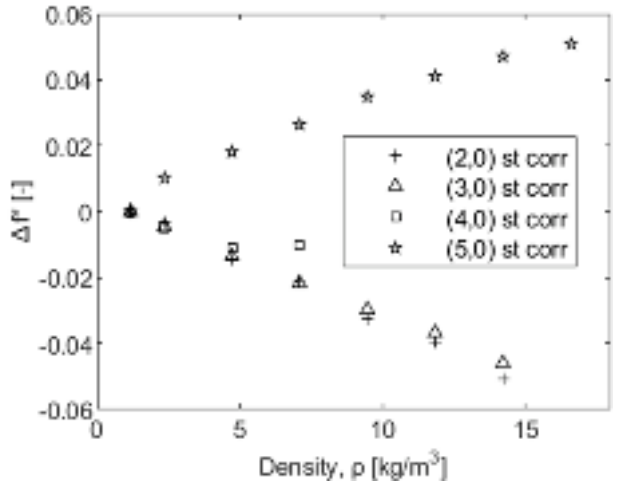

Figure 6. Corrected relative frequency changes of structure dominant modes in air for "slim cavity" over fluid density. Values corrected for added mass effect.

While most frequency peaks are well visible for structural modes, this is not the case for most acoustic modes; the two nodal diameter mode is the only exception. To show potential coupling influences, both (acoustic and structure dominant) modes of the two nodal diameter mode pair are displayed in Figure 7. After the structural mode is corrected for the added mass effect and the acoustic mode for the speed of sound effect, both still exhibit a decreasing and a slightly increasing trend, respectively, when plotted over the fluid density. This behavior supports the hypothesis that weak coupling is present between the disk and the surrounding fluid, and the trends agree qualitatively with those in Magara's [12] coupling model.

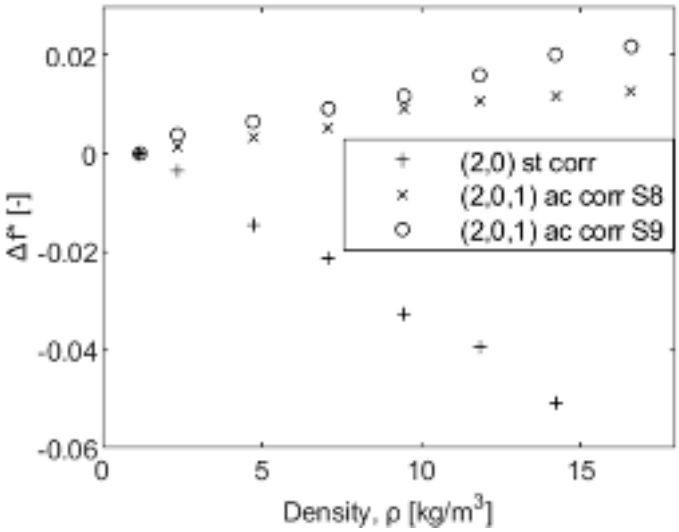

Figure 7. Corrected relative frequency changes of two nodal diameter mode pair in air for "slim cavity" over fluid density. Values corrected for added mass effect and speed of sound effect, respectively. Sensors: S8 on disk, S9 in front cavity.

It should be noted that the frequency change of the acoustic dominant mode differs slightly depending on the pressure sensor's location in the test rig. It is smaller (+2.2%

(S9) and +1.3% (S8 on disk)) than that of the structure dominant mode (−5.5%) for the approximately 14-fold increase in density.

Altogether, for the measurement series "PRESSURE", frequency shifts of structure dominant modes are observed that exceed the "uncoupled mode effects" and thus indicate a coupling effect, even for modes that are only weakly coupled. However, no clear picture about frequency shifts of acoustic dominant modes is obtained, and the hypothesis of a more pronounced coupling effect for stronger coupled modes could not be confirmed on the base of the measurement series with a variation in fluid pressure.

5.3. Variation of Disk Rotational Speed

In the third experimental series, "ROTATION", the disk rotational speed is varied, while the fluid pressure (0.1 MPa, air) and all other parameters remain constant. By this means, the coupling potential is changed as frequency differences between potentially coupled acoustic and structure dominant modes are varied (rotating case *CP* values differ from standstill values in Table 2). There is no added mass or speed of sound effect. However, a small effect of the stiffening effect of the centrifugal force field of the impeller might be observable, but measurement values are not explicitly corrected for its influence.

Disk rotation results in the formation of two modes for each mode order, one forward and one backward traveling wave. While disk modes theoretically travel at the disk rotational speed, cavity modes travel at the fluid's rotational speed in the cavity. Assuming bulk flow in the cavity at approximately half the disk's rotational speed, frequencies of acoustic and structure dominant modes approach each other subject to a change in disk rotational speed. These effects are shown in the following, first for structure, then for acoustic dominant modes, and last for specific mode pairs. For all measurement results of the series "ROTATION", normalized frequencies f^* are displayed as defined in Equation (10). In addition to the measurement results, theoretical values for the natural frequencies of structure and acoustic dominant modes at the respective disk rotational speed are given, calculated according to Equations (2) and (6), respectively. Utilized core rotation factors for the acoustic dominant modes are listed in Table 2.

As shown in Figure 8, the development of a forward and a backward traveling wave is clearly visible for each mode, and the measured frequency splits of the disk vibration modes subject to rotation agree well with the theoretical values.

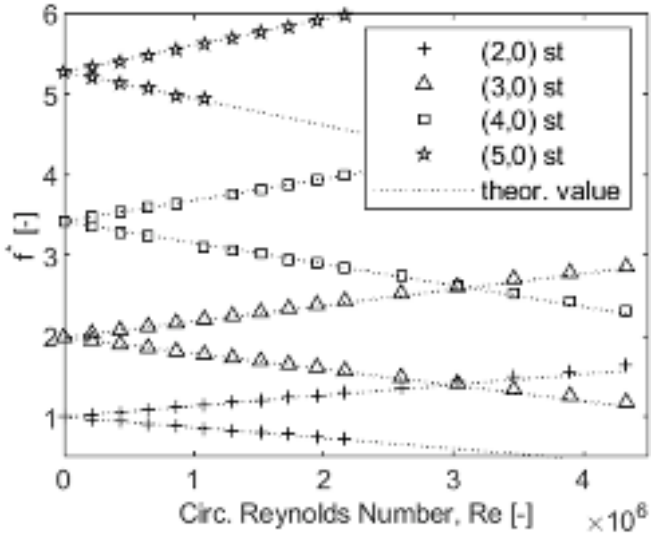

Figure 8. Normalized natural frequencies of structure dominant modes in air at 0.1MPa for "slim cavity" over circumferential Reynolds number. Experimental and theoretical results.

Natural frequencies of the acoustic dominant modes are much less apparent in the measurement results than the disk vibration modes, as they are often overlapping with

neighboring modes or deflected by them. However, the formation of a forward and a backward traveling wave is evident for the acoustic dominant modes with three, four, and five nodal diameters, as shown in Figure 9. Measured and theoretic frequency splits of the acoustic dominant modes subject to disk rotation do not agree well. Moreover, there is no consistent trend noticeable; measured frequency splits for the (3,0,1) and the (5,0,1) modes are smaller than the theoretical values, while the frequency split of the (4,0,1) mode is slightly bigger. Moreover, core rotation factors adopted to match theoretic values of the three and five nodal diameter acoustic waves with the experimental ones appear to be outside of the usual range. Possibly, the core rotation factors are different from the ones calculated theoretically from Equation (5). Additionally, the number of nodal diameters might influence the natural frequency of the traveling waves, in a way different from that stated in Equations (3) and (6). However, for all analyzed modes, the forward wave appears to exhibit a bigger frequency difference to the non-rotating case than the backward wave.

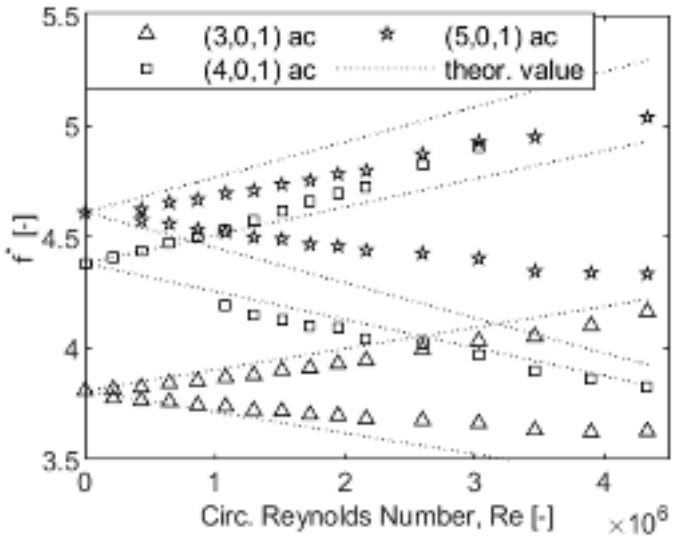

Figure 9. Normalized natural frequencies of acoustic dominant modes in air at 0.1MPa for "slim cavity" over circumferential Reynolds number. Experimental and theoretical results.

To assess the coupling effect for coupled mode pairs, the respective acoustic and structure dominant modes are presented together in the following. Disk rotation further increases the coupling potential (compared to the standstill values in Table 2), making coupling effects observable. The mode pair with three nodal diameters (displayed in Figure 10) is very well visible for all analyzed rotational speeds. However, the coupling potential is estimated to be low ($CP = +0.9$), and thus the expected coupling effect relatively small. Theoretically, the forward traveling waves of the structure and acoustic dominant modes would cross at very high disk rotational speeds while the backward waves veer away from each other. However, within the range of analyzed rotational speeds, the coupling potential remains weak. If the theoretic values are adjusted to approximately fit the backward wave of the measured acoustic dominant mode, which is assumed to be less influenced by coupling, a core rotation factor of about 0.25 must be adopted (as shown in Figure 10). Compared to the backward wave, the acoustic dominant forward wave appears to be deflected towards higher frequencies. This might be due to the increased but still relatively small coupling potential at higher rotational speeds.

The strongest coupling potential of all measured modes is predicted for the four nodal diameter mode pair in the "wide cavity" test rig setup ($CP = +0.08$). Therefore, frequency shifts due to the strong coupling effect are expected to be observable. As can be seen in Figure 11, mode veering is visible, confirming this assumption. The forward modes strongly influence and deflect each other. Instead of crossing at a circumferential Reynolds number of approximately 1.7×10^6, the forward traveling waves approach each

other until a minimum normalized frequency difference of 0.2 is reached and then veer apart, increasing their frequency separation again. For the "slim cavity" test rig setup, this behavior cannot be observed, as the acoustic dominant mode is shifted towards higher frequencies resulting in a weaker coupling potential ($CP = +0.28$). The structure dominant mode follows the theoretical values well, and the acoustic dominant one only exhibits a slight upward deflection. This is a clear indication that a stronger coupling effect is present for stronger coupled modes, i.e., those in closer proximity to each other.

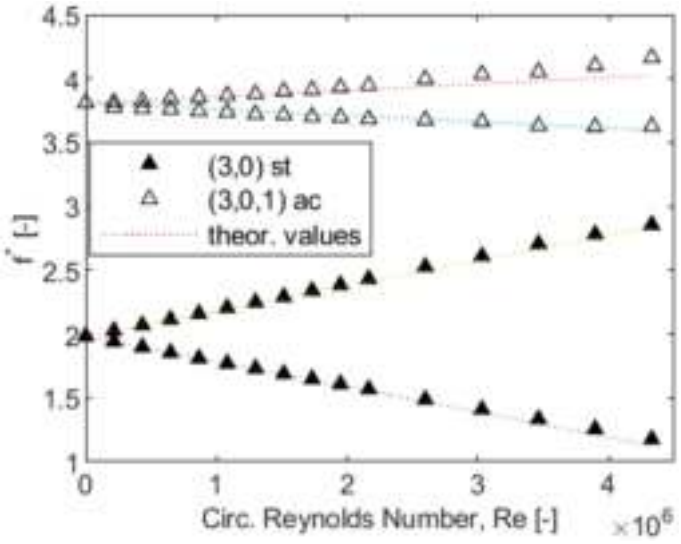

Figure 10. Normalized natural frequencies of three nodal diameter mode pair in air at 0.1MPa for "slim cavity" over circumferential Reynolds number. Experimental and theoretical results (a core rotation factor of 0.25 is adopted for the theoretic values of the acoustic wave).

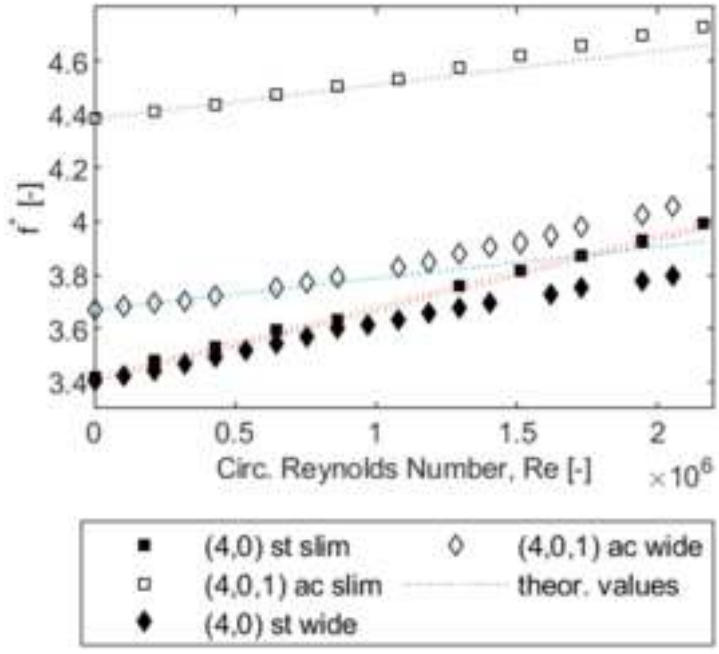

Figure 11. Normalized natural frequencies of forward waves of four nodal diameter mode pair in air at 0.1 MPa for "wide" and "slim cavity" over circumferential Reynolds number. Experimental and theoretical results (core rotation factors of 0.44 and 0.48 are adopted for the theoretic values of the acoustic waves for "slim" and "wide cavity" setup, respectively).

The four and five nodal diameter mode pairs, which are estimated to be strongly coupled in the "slim cavity" setup (*CP* values of +0.28 and −0.14, respectively, see Table 2), are not very well visible in the measurement results. With disk rotation, the coupling potential becomes even bigger, but the response peaks of the structure dominant modes are poorly visible and diminish at a certain rotational speed. As shown in Figure 12, the backward wave of the structure dominant five nodal diameter mode disappears once it comes close to the forward acoustic wave and therefore does not come in closer proximity to the potentially coupled backward acoustic dominant wave. The same happens for the forward wave of the structure dominant four nodal diameter mode, which is no longer visible at Reynolds numbers higher than 2×10^6, where it crosses the backward wave of the acoustic dominant mode (see Figures 8 and 9). Therefore, it does not come close to the coupled forward wave of the acoustic dominant mode. Consequently, no conclusion on the coupling effect and possible veering behavior of the modes with a strong coupling potential can be drawn for the "slim cavity" test rig setup.

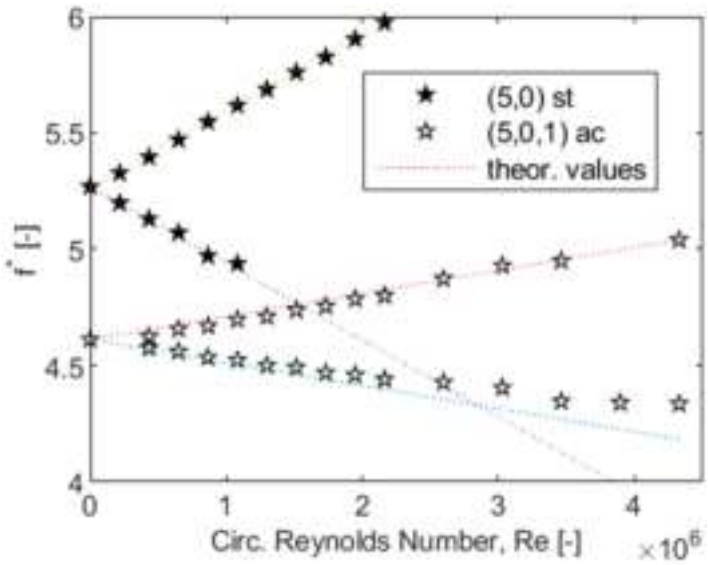

Figure 12. Normalized natural frequencies of five nodal diameter mode pair in air at 0.1 MPa for "slim cavity" over circumferential Reynolds number. Experimental and theoretical results (a core rotation factor of 0.30 is adopted for the theoretic values of the acoustic wave).

Nevertheless, it should be noted that the concept of bulk flow inside the cavity that can be estimated by a core rotation factor is a theoretical idea that does not exist in real cavities. Moreover, measurement results presented in this work are characterized by circumferential Reynolds numbers slightly lower than values for well-established bulk flow. Therefore, most measurement results actually classify into the transitions area between merged and separated boundary layer regimes according to [25], and the applicability of the core rotation concept should be further investigated. Using a fluid with lower kinematic viscosity or conducting measurements with disk rotation at higher pressures could be options to reach higher Reynolds numbers in future experiments.

6. Conclusions and Future Work

In the first part, fundamental concepts necessary to understand the formation of structural and acoustic modes and their coupling in a rotor-cavity system are compiled, and existing coupling models are reviewed. Based on a comprehensive literature review, an overview of frequency shift effects in rotor-cavity systems with a rotating disk is established, including effects for uncoupled and coupled modes. A procedure to analyze those frequency shift effects is developed and later applied to the analysis of experimental results. Moreover, an attempt to quantify the expected coupling effects is made by establishing a coupling strength and a coupling potential parameter.

In the second part of this work, measurement results of acoustic and structure dominant modes are presented, including a test series with varying cavity pressure and one with different disk rotational speeds. For the latter, the development of a forward and a backward traveling wave is demonstrated for each mode. All excited mode pairs in the test rig are at least weakly coupled in air, i.e., frequency shifts are observed that cannot solely be explained by "uncoupled mode effects", such as the added mass, speed of sound, and stiffening effect, but indicate an additional coupling effect. However, the hypothesis of a bigger coupling effect (bigger frequency shift) for stronger coupled modes cannot be corroborated consistently. By varying the disk rotational speed, the frequency difference between coupled modes, and thus their coupling potential, can be varied additionally. However, the expected coupling effect is not observable for all mode pairs. Only the four nodal diameter mode pair in the "wide cavity" exhibits a strong coupling effect. Mode veering is visible, i.e., with an increase in disk rotational speed, the coupled modes approach each other, and then veer apart instead of crossing.

Generally, measurement results for structure dominant modes agree well with theoretical predictions. However, measured acoustic dominant modes do not always exhibit the expected theoretic behavior. It requires further research to clarify whether or not the underlying assumptions on core rotation apply to the flow conditions in the cavity during the measurements. For future research, a different fluid or a higher pressure could be considered to ensure higher Reynolds numbers and further validate the bulk flow concept as well as examine boundary layer influences. Additionally, the influence of the small opening of the cavity needs further investigation.

The next essential step in the line of this research will be to investigate the damping of coupled acoustic and structure dominant modes, as resonances cannot always be avoided and the damping ratio determines the response amplitudes of the system and thus the risk of impeller material failure. Eventually, the transferability of the results to real machines needs to be proven. However, this work poses an essential step towards a better understanding of acoustoelastic coupling effects in the side cavities of centrifugal compressors under varying operating conditions.

Author Contributions: Conceptualization, T.U.; Data curation, T.U.; Formal analysis, T.U.; Funding acquisition, D.B.; Investigation, T.U.; Methodology, T.U.; Supervision, D.B.; Visualization, T.U.; Writing—original draft, T.U.; Writing—review & editing, D.B. All authors have read and agreed to the published version of the manuscript.

Funding: This project is funded by Deutsche Forschungsgemeinschaft (DFG). The authors are grateful for the financial support under project number 429153912.

Data Availability Statement: Not applicable.

Conflicts of Interest: The authors declare no conflict of interest. The funders had no role in the design of the study; in the collection, analyses, or interpretation of data; in the writing of the manuscript, or in the decision to publish the results.

Nomenclature

b	disk/impeller thickness, m
c	speed of sound, m/s
c_f	friction coefficient
CP	coupling potential parameter
CS	coupling strength parameter
f	frequency, 1/s
$f^* = \frac{f}{f_{ref}}$	normalized frequency relative to the frequency $f_{ref} = f_{st,2,0}(air,\ 0.1\ \text{MPa}, 295\ \text{K})$
$\Delta f^* = \frac{f-f_0}{f_0}$	relative frequency change relative to the frequency $f_0 = f(0.1\ \text{MPa})$

f_Ω	rotational frequency of rotating disk, 1/s
$G = \frac{s}{r_d}$	non-dimensional axial gap width of cavity
k_0	core rotation factor
L	characteristic length, m
m	mass, kg
(m,n)	number of nodal diameters, nodal circles of structure (dominant) mode
(p,q,r)	number of nodal diameters, nodal circles, axial nodes of acoustic (dominant) mode
r	radius, m
Re	circumferential Reynolds number
s	axial gap width of cavity, m
t_{ax}	cylindrical portion of impeller side room, m
u	disk/impeller circumferential velocity, m/s
v	velocity, m/s
Ω	rotational speed of disk, 1/min
$(\pi\alpha)_{p,q}$	dimensionless solutions to the first derivative of the Bessel function for the (p,q) acoustic mode
ν	kinematic viscosity of the fluid, m^2/s
ρ	density, kg/m^3
	Subscripts
ac	acoustic (dominant)
c, cf, cr	cavity, front cavity, rear cavity
$corr$	corrected
d	disk
e	excitation
f	fluid
s	system
st	structure (dominant)
tot	total
uc	uncoupled

References

1. Lamb, H.; Southwell, R.V. The vibrations of a spinning disk. *Proc. R. Soc. A* **1921**, *99*, 272–280.
2. Southwell, R.V. On the free transverse vibrations of a uniform circular disc clamped at its centre; and on the effects of rotation. *Proc. R. Soc. A* **1922**, *101*, 133–153.
3. Campbell, W. *Protection of Steam Turbine Disk Wheels from Axial Vibration*; General Electric Company: New York, NY, USA, 1924.
4. Eversman, W.; Dodson, R.O., Jr. Free vibration of a centrally clamped spinning circular disk. *AIAA J.* **1969**, *7*, 2010–2012. [CrossRef]
5. Ewins, D.J. Vibration characteristics of bladed disc assemblies. *J. Mech. Eng. Sci.* **1973**, *15*, 165–186. [CrossRef]
6. Irretier, H. The natural and forced vibrations of a wheel disc. *J. Sound Vib.* **1983**, *87*, 161–177. [CrossRef]
7. Irretier, H. Experiments and calculations on the vibrations of rotating radial impellers. *J. Vib. Acoust. Stress Reliab.* **1988**, *110*, 137–142. [CrossRef]
8. Tyler, J.M.; Sofrin, T.G. Axial Flow Compressor Noise Studies; No. 620532. *SAE Trans.* **1962**, *70*, 309.
9. Ehrich, F.F. Acoustic resonances and multiple pure tone noise in turbomachinery inlets. *J. Eng. Power* **1969**, *91*, 253–262. [CrossRef]
10. Eisinger, F.L. Acoustic fatigue of impellers of rotating machinery. *J. Press. Vessel. Technol.* **2002**, *124*, 154–160. [CrossRef]
11. Eisinger, F.L.; Sullivan, R.E. Acoustically-induced structural fatigue of impeller discs: A Brief Note. *Turbo Expo Power Land Sea Air* **2002**, *3610*, 1063–1069.
12. Magara, Y.; Mitsuhiro, N.; Kazuyuki, Y.; Naohiko, T.; Tetsuya, K. Natural frequencies of centrifugal compressor impellers for high density gas applications. *ASME Int. Mech. Eng. Congr. Expo.* **2008**, *48661*, 107–114.
13. Magara, Y.; Yamaguchi, K.; Miura, H.; Takahashi, N.; Narita, M. Natural frequency shift in a centrifugal compressor impeller for high-density gas applications. *J. Turbomach.* **2013**, *135*, 011014. [CrossRef]
14. Beirow, B.; Kühhorn, A.; Figaschewsky, F.; Nipkau, J. Effect of mistuning and damping on the forced response of a compressor blisk rotor. ASME Turbo Expo 2015: Turbine Technical Conference and Exposition. *Am. Soc. Mech. Eng. Digit. Collect.* **2015**, *56772*, V07BT32A001.
15. Heinrich, C.R.; Kühhorn, A.; Steff, K.; Petry, N. Generalized Model for the Approximation of Coupled Acousto-Mechanical Natural Frequencies in High-Pressure Centrifugal Compressors. *J. Eng. Gas Turbines Power* **2021**, *143*, 071022. [CrossRef]
16. Heinrich, C.R.; Unglaube, T.; Beirow, B.; Brillert, D.; Steff, K.; Petry, N. Surrogate Models for The Prediction of Damping Ratios in Coupled Acoustoelastic Rotor-Cavity Systems. In Proceedings of the ASME Turbo Expo 2021: Turbine Technical Conference and Exposition, online, 7–11 June 2021. GT2021-58835.

17. Hellmich, B.; Seume, J.R. Causes of acoustic resonance in a high-speed axial compressor. ASME Turbo Expo 2006: Power for Land, Sea, and Air. *Am. Soc. Mech. Eng. Digit. Collect.* **2006**, *4241*, 377–387.
18. König, S. Acoustic eigenmodes in the side cavities of centrifugal compressors. *Turbo Expo Power Land Sea Air* **2009**, *48876*, 547–557.
19. Petry, N.; König, S.; Benra, F.-K. Influence of the Swirling Flow in the Side Cavities of a High-Pressure Centrifugal Compressor on the Characteristics of Excited Acoustic Modes. Turbo Expo Power for Land, Sea, and Air. *Am. Soc. Mech. Eng.* **2012**, *44748*, 627–639.
20. Eckert, L. High Cycle Fatigue Cracks at Radial Fan Impellers Caused by Aeroelastic Self-Excited Impeller Vibrations: Part I—Case History, Root Cause Analysis, Vibration Measurements. International Design Engineering Technical Conferences and Computers and Information in Engineering Conference. *Am. Soc. Mech. Eng.* **1999**, *19777*, 1135–1146.
21. Barabas, B.; Stefan, C.; Sebastian, S.; Friedrich-Karl, B.; Hans-Josef, D.; Dieter, B. Experimental and numerical determination of pressure and velocity distribution inside a rotor-stator cavity at very high circumferential Reynolds numbers. In Proceedings of the 11th European Conference on Turbomachinery Fluid dynamics & Thermodynamics, Madrid, Spain, 23–27 March 2015.
22. Barabas, B.; Dieter, B.; Hans-Josef, D.; Friedrich-Karl, B. Identification of Coupled Natural Frequencies in a Rotor-Stator Test-Rig for Different Gas Properties. In Proceedings of the 12th European Conference on Turbomachinery Fluid dynamics & Thermodynamics, Stockholm, Sweden, 3–7 April 2017.
23. Barabas, B.; Dieter, B.; Hans-Josef, D.; Friedrich-Karl, B. Damping Behavior of Acoustic Dominant Modes in an Aeroacoustic Test Rig Representing a Simplified Geometry of a High Pressure Radial Compressor. Turbo Expo: Power for Land, Sea, and Air. *Am. Soc. Mech. Eng.* **2018**, *51159*, V07CT36A018.
24. Norton, M.P.; Frederick, C.N. *Fundamentals of Noise and Vibration Analysis for Engineers*; Cambridge University Press: Cambridge, UK, 1998.
25. Daily, J.W.; Nece, R.E. Chamber dimension effects on induced flow and frictional resistance of enclosed rotating disks. *J. Basic Eng.* **1960**, *82*, 217–230. [CrossRef]
26. Gülich, J.F. Disk friction losses of closed turbomachine impellers. *Forsch. Im Ing.* **2003**, *68*, 87–95. [CrossRef]
27. Sigrist, J.-F.; Daniel, B.; Christian, L. Dynamic analysis of a nuclear reactor with fluid–structure interaction: Part i: Seismic loading, fluid added mass and added stiffness effects. *Nucl. Eng. Des.* **2006**, *236*, 2431–2443. [CrossRef]
28. Fahy, F.J. Vibration of containing structures by sound in the contained fluid. *J. Sound Vib.* **1969**, *10*, 490–512. [CrossRef]
29. Barabas, B.; Friedrich-Karl, B.; Nico, P.; Dieter, B. Experimental Damping Behavior of Strongly Coupled Structure and Acoutic Modes of a Rotating Disk with Side Cavities. In Proceedings of the ASME Turbo Expo 2021: Turbine Technical Conference and Exposition, online, 7–11 June 2021; GT2021-58782.

International Journal of
Turbomachinery
Propulsion and Power

MDPI

Article

A Reliable Update of the Ainley and Mathieson Profile and Secondary Correlations

Yumin Liu [1,*], Patrick Hendrick [1], Zhengping Zou [2] and Frank Buysschaert [3]

[1] Department of Aero-Thermo-Mechanics, Université Libre de Bruxelles, 1050 Brussels, Belgium; patrick.hendrick@ulb.be
[2] School of Energy & Propulsion Engineering, Beihang University, Beijing 100191, China; zouzhengping@buaa.edu.cn
[3] Department of Applied Mechanics & Energy Conversion, Katholieke Universiteit Leuven, 8200 Brugge, Belgium; frank.buysschaert@kuleuven.be
* Correspondence: yu.m.liu@ulb.be

Abstract: Empirical correlations are still fundamental in the modern design paradigm of axial turbines. Among these, the prominent Ainley and Mathieson correlation (Ainley D. and Mathieson G., 1951, "A Method of Performance Estimation for Axial-Flow Turbines," ARC Reports and Memoranda No. 2974) and its derivatives, plays a crucial role. In this paper, the underlying assumptions of the aforementioned models are discussed by means of a descriptive review, whilst an attempt is made to enhance their reliability and, potentially, accuracy in performance estimations. Closer investigation reveals an intriguing misuse of the lift coefficient in the secondary loss. In light of this, an enhanced model that, notably, builds upon the Zweifel criterion and the vortex penetration depth concept is developed and discussed. The obtained accuracy is subsequently assessed through CFD computations, employing a database comprising 109 cascades. The results indicate a 50% probability of achieving the ±15% error interval, which is twice as good as the most recent Aungier model (Aungier R., 2006, "Turbine Aerodynamics: Axial-Flow and Radial-Inflow Turbine Design and Analysis", ASME Press, New York). Furthermore, the reliability of the proposed model is demonstrated by a reconstruction of the Smith chart, on the one hand, and a performance analysis, on the other. The reconstruction exhibits contours that conform to the original. The results of the performance study are compared with the CFD solutions of eight cascades working in off design conditions and confirm the need of the additionally included turbine design parameters, such as the axial velocity and the meanline radius ratios.

Keywords: loss correlation; axial-flow turbine; turbine performance

check for updates

Citation: Liu, Y.; Hendrick, P.; Zou, Z.; Buysschaert, F. A Reliable Update of the Ainley and Mathieson Profile and Secondary Correlations. *Int. J. Turbomach. Propuls. Power* **2022**, *7*, 14. https://doi.org/10.3390/ijtpp7020014

Received: 2 December 2021
Accepted: 3 April 2022
Published: 21 April 2022

Publisher's Note: MDPI stays neutral with regard to jurisdictional claims in published maps and institutional affiliations.

Copyright: © 2022 by the authors. Licensee MDPI, Basel, Switzerland. This article is an open access article distributed under the terms and conditions of the Creative Commons Attribution (CC BY-NC-ND) license (https://creativecommons.org/licenses/by-nc-nd/4.0/).

1. Introduction

The axial turbine became incontestably the accustomed device for medium to high mechanical power generation in modern powerplants and therefore, not surprisingly, it still remains the subject of extensive research. Throughout the past decades, experience and knowledge have grown continuously, adding refinements to the art of turbine design. In this study, the 1D aerodynamic design, more specifically, the loss correlations employed in the meanline analysis used in the early design phase, are reviewed. These models are crucial, as they set the preliminary design parameters that can be maintained up to the final design stage, that is, if the model incorporates sufficient levels of reliability [1]. Among these, it is evident to note the renown Ainley and Mathieson (AM) correlation, published in 1957, which serves this purpose [2] well. For the record, Ainley and Mathieson's model was considered to be a significant innovation, as it enabled the quantification of local losses. It was, e.g., successfully employed in the design process of the Rolls Royce Olympus engine [3]. Being the cradle leading to great successes and broad acceptance, it underwent multiple updates [4–6], which expanded into a veritable genealogy.

Over time, the design of axial turbines underwent several improvements and the geometry became much more diverse, causing the accuracy and reliability of the current historic correlation based (open source) 1D models to become less effective. An important issue is their mathematical foundation, which relies on a fuzzy blend of classical flow theory and heuristic manipulations matching the early cascade measurements [7]. Hence, it is not surprising that modern turbines may become excluded from their range of application. In light of this, studies have evaluated the correlation reliability through parametric analysis [8–10]. Although inconsistencies have been identified and reported, no remedies have been proposed. Accuracy has been evaluated on few test cases, which is insufficient to affirm any statistical significance. These two aspects (reliability and accuracy) have to be investigated with statistical evidence to clarify the true potential of the available 1D correlations with the latest turbines. Moreover, it is deemed mandatory to upgrade the correlations with a more robust physics based backbone, compatible with modern turbines.

The objective of this paper is, therefore, twofold. The first is to provide a comprehensive review of the AM family correlations. The second is to enhance the AM correlation based on recent breakthroughs in turbine aerodynamics and loss mechanisms, and boosting compatibility with current design workflows. In particular, the Zweifel criterion [11] and the depth penetration [12,13] are integrated into the latest Aungier (Ag) profile and secondary loss models [6]. The latter are validated on a data set composed of 109 cascades (static and rotating) to achieve statistical significance in terms of accuracy and reliability. High fidelity simulations and their numerical solutions serve as the benchmark during the evaluations. The correlation accuracy is determined in terms of probability according to the Gaussian distribution of the relative errors, whilst the correlation reliability is proven by its ability to reproduce the Smith chart [14] and maintain consistent trends in off design conditions under the variation of the newly introduced axial velocity ratio.

2. Review

The importance of empirical loss correlations still remains high in the design process of modern axial turbines. Despite their restricted fidelity, they can effectively offer guidance in decision making during the preliminary design stages [1]. In general, the development of empirical models is built upon on a turbine database, which is produced by means of experimental tests where a multitude of measurements are performed and linked to several, mostly dimensionless, design parameters. When parameters are found to correlate well, dedicated design laws can consequently be established.

Quite recently, there was a spirited debate on the capability of cascade tests to approximate real turbine flow. The proponents claimed that cascades could offer a satisfactory basis for estimating losses in real machines and should be preferred thanks to their simplicity, flexibility and low cost [15]. The opponents, however, believe that cascades are inherently limited since they cannot reproduce key aspects of the real operation environment, involving, e.g., rotational, curvature and inlet flow distortion effects [16]. Despite this contention, the current state of the art research has clearly joined the supporting side, considering the solid foothold of cascade tests in public literature. The authors of this work adhere to the standpoint of Craig and Cox (CC) [17], which holds a certain relativism. In fact, the extreme situation in which application of the correlations fails in both accuracy and reliability is rather unlikely. However, careless use must be avoided, as this could lead to an entirely erroneous result [18,19]. Hence, the user has to be fully aware of the features and limitations involved, so that the correlations can be applied effectively in real turbine design. This aspect is the crux of the following discussions.

Correlations are typically determined by the investigator's own judgment, experience and interpretation of flow physics, test quality and database size [20]. The challenge resides in the way the wide information of a complex 3D flow is filtered and condensed into a 1D empirical model. During its setup, certain parameters could be deliberately biased, with the objective to reflect specific turbine characteristics. The reason behind this intervention is quite straightforward. For example, aero-engine and land based steam turbines do not

share the same design requirements, as is the case with high and low pressure turbines. They differ by design and aerodynamics and so will the correlations. The comparative studies of several public domain correlations [9,21] emphasized this issue clearly. As a consequence, there are no universal turbine correlations at this point. Hence, they only serve a specific range of applications adequately.

Since it is common to use empirical models for a wide range of turbine design applications, it is not surprising that the parameters estimated from the cascade correlation may disagree with real machine measurements by a considerable order of magnitude. In these circumstances, one resorts typically to a heuristic calibration. Otherwise, the correlation is of little value [22]. However, there are some risks involved with such an approach. First, simple multipliers/polynomials are often deemed sufficient, even though the resulting correlation would much better suit turbines akin to those used in the database from which the model was established. Second, its use inherently leads to designs whose aerodynamics are similar to that of the turbines in its original database. The fundamental issue is the statistical bias engendered by the limited size of the database. This could be prevented by the construction of a large public database collecting all cascade measurements performed up to the present day [7]. Unfortunately, early investigators did not share or even lost their databases. New investigators often had to generate a new database from the ground up, with neither access to previous data, nor methodologies. In particular, insights that could have revealed a stronger interaction between design parameters, were curtailed. As a consequence, 1D correlations revert to quite simple mathematics or charts and are biased, which, thus, leads to results with rather low fidelity. In contrast, the models established in large industries do not suffer from the aforementioned issues, where one can afford the calibration of public domain or in-house correlations using the vast amount of data accumulated over time for dedicated configurations. From this data, new versions of earlier models can be developed, which enables a safer and cheaper enhancement of the design process.

In [23], it was advanced that any loss correlation exhibits the same probability to accurately predict turbine performance once out of its range of application. Considering the current discussion, it is rather irrational to expect outstanding accuracy from models that attempt to cover complex systems with elemental information. With full awareness of the higher fidelity 3D methods intervening at later design stages, correlation accuracy should be less prioritized, but the focus must initially go towards including all relevant design parameters in the model. Therefore, the ability to cope coherently with the true physics, i.e., reliability, must become the primary concern.

2.1. Ainley and Mathieson Family Correlations

The empirical AM correlation [2] has been so successful that it owns a lineage (the AM correlation and its derivatives will not be differentiated in this framework, as these are fundamentally equivalent). Chronologically, it was established through cascade tests using conventional profiles stemming from the 1940s and claimed a nominal accuracy of $\pm 2\%$ in stage efficiency estimation. The latter corresponds to about $\pm 15\%$ total pressure loss error. It was published at a time when the expertise and the understanding of axial compressors were more profound than those of turbines [24]. As a matter of fact, before AM was published, one had to resort to expensive experimental trial and error processes when the available methods revealed efficiencies largely inferior to those of the actual turbines. The AM correlation was, therefore, considered to be groundbreaking, as it provides a systematic way to quantify turbine aerodynamic loss and its components.

The Dunham and Came (DC) correlation [4] was the first and a canonical update to the model of AM, which used 16 1960s technology Rolls Royce turbines. It extended the application range to small turbines, while retaining the same accuracy level. Dunham claimed that their model was still the most reliable design tool during the 1970s, in a context where there was a progressive adoption of potential flow calculation in industry [3]. However, the investigators did not have access to the database of AM and, thus, the improvement

resulted from model calibration based on the overall performance of a restricted number of turbines. It is noteworthy to mention that CC [17], along with Traupel [25], published new correlations with different approaches with regard to turbine aerodynamics in that same period. The Kacker and Okapuu (KO) correlation [5] came as a second update based on 33 1980s technology Pratt & Whitney turbines and showed an accuracy up to ±1.5% in stage efficiency estimation in design conditions. Furthermore, KO, having high confidence in the validity of the Smith chart [14] which contains 70 1960s technology Rolls Royce turbines [26], calibrated their correlation to fittingly reproduce the same chart. Ag [6] subsequently revised KO to handle recompression produced in extreme off design conditions and real working fluids. In addition, it can cope with hub to shroud S2 calculations (the hub to shroud S2 and blade to blade S1 calculations proposed by Wu [27] refer to stream surfaces on which 2D flow equations are solved by mass-averaging the third coordinate). This has recently been confirmed, notably in ORC turbines [28,29]. Despite many the critics of its limitations, the choice of the AM correlation over other public correlations is driven by three particular aspects. Firstly, it owns a comparatively broader mathematical basis and is less reliant on empirical charts. Secondly, it does not require specific assumptions on the blade surface velocity distribution nor the need to perform cumbersome mathematical computations. As a consequence, faster solution and better accessibility are ensured, in contrast to the semi-empirical models of Baljé and Binsley [30], Denton [31] and Coull and Hodson [32]. Lastly, transparent and valuable details of its development can be retraced in the successive works [2,24,33,34].

There are five sources of total pressure loss encountered in aerodynamics, notably, skin friction, pressure drag, shock, leakage and mixing losses. However, this classification was rearranged to associate these losses to their location instead of their phenomenological origin. The AM family correlations assumed the turbine loss system as follows:

$$\begin{aligned} Y_t &= \frac{p_{tr,out,is} - p_{tr,out}}{p_{tr,out} - p_{out}}, \\ &= Y_p + Y_s + Y_{cl}. \end{aligned} \tag{1}$$

- Profile loss Y_p is generated by the growth of the boundary layer and flow mixing over the blade surface. This encompasses skin friction and pressure drag. In case the exit flow reaches supersonic velocities and triggers shocks near the trailing edge, then an additional supersonic loss Y_{ex} is to be accounted for. These losses exclusively arise from blade to blade S1 flow and thus assume spanwise uniformity.
- Secondary loss Y_s originates from the interaction between endwall flow and the pressure difference across the blade passage. The main actors are the 3D induced vortices and endwall boundary layers. AM, drawing on the model of Carter [35], regarded both flows and the annulus loss as one entity. This local loss is responsible for spanwise non-uniformity at blade tip and hub.
- Tip leakage loss Y_{cl} arises from the presence of a gap between the blade tip and the shroud, preventing the rotating blade from rubbing against the casing. Although this is indispensable to complete the loss system, this loss is not considered within the scope of this work, where priority is given to the more fundamental profile and secondary losses.

Although it was not specified, the correlations implicitly refer to losses of fully mixed flow. However, to be precise, there is neither theoretical nor experimental evidence that can justify the breakdown of Equation (1), as this inherently assumes little interaction between the components [36]. However, its effectiveness might be due to the comparatively small chord of axial turbine blades and the short flow transit time in the blade passage inhibiting strong interaction between the secondary flows (all flows that differ from the primary inviscid flow) [7].

2.2. Profile Losses

The AM 2D profile loss [37] is

$$\begin{aligned} Y_{p,AM} &= \left[Y_{p,\theta_{in}=0^\circ} - \left| \frac{\theta_{in}}{\beta_{out}} \right| \left(\frac{\theta_{in}}{\beta_{out}} \right) \left(Y_{p,\theta_{in}=-\beta_{out}} - Y_{p,\theta_{in}=0^\circ} \right) \right] \left(\frac{5t_{max}}{c} \right)^{-K_m \frac{\theta_{in}}{\beta_{out}}}, \\ &= f(s/c, t_{max}/c, \theta_{in}, \beta_{out}). \end{aligned} \tag{2}$$

AM blended the profile losses of a slightly compressible 50% reaction nozzle $Y_{p,\theta_{in}=0^\circ}$ and impulse nozzle $Y_{p,\theta_{in}=-\beta_{out}}$, as depicted in their Figure 4 on page 24 in [2], to cover all intermediate designs. This correlation inherently comprises the trailing edge loss taken at standard $t_{te}/s = 0.02$. Equation (2) was obtained from low speed wind tunnel tests and focuses on parabolically cambered conventional profiles, i.e., the British T.6 type profiles. Their experimental results showed the notable sensitivity of the losses to the profile thickness in impulse profiles and, thus, a correction for any deviation from standard $t_{max}/c = 0.2$ [34] was introduced in the model. In addition, there was a variation according to $(\theta_{in}/\beta_{out})^2$ for profiles in-between the impulse and nozzle blades, hence justifying the arrangement/blending in Equation (2). The velocity distribution of the nozzle and impulse blades was presented in AM's Figure 5 on page 26 in [34]. This distribution shows that a considerable portion of the suction side of the blade extending from midchord to trailing edge is affected by flow diffusion, which is nowadays regarded as unacceptable in design standards. Use of AM would, therefore, implicitly assume a similar velocity distribution over modern turbine profiles, which is likely to result in a significant loss mismatch if not handled with care [38]. This specific problem with associated implications has to be addressed when enhancing Equation (2).

In order to improve the reliability of the model of AM for recent turbine configurations, several correction factors—in this work designated as the auxiliary factors$K$—have been proposed by different authors [4,5]. For example, in his latest update, Ag [6] adapted the profile loss correlation of KO (and, thus, AM). This equation possesses several auxiliary factors and is expressed as:

$$\begin{aligned} Y_{p,Ag} &= K_{mod} K_M K_p K_{Re} \left(K_i Y_{p,AM} - Y_{t_{te}=0.02s} \right) + Y_{sh}, \\ &= f(e_c/s, \theta_{in}, \theta_{out}, M_{r,in}, M_{r,out}, Re, e/c, k, i) Y_{p,AM}. \end{aligned} \tag{3}$$

- Mach correction factor $K_p \leq 1$ reflects the flow acceleration in the blade passage reducing viscous loss and acts in the subsonic range $M_{r,out} \geq 1$. According to Ag [6], K_p, introduced for the first time by KO, is flawed in extreme off-design conditions, especially when recompression occurs at the blade hub. It was known that KO yielded only satisfactory results at the design point [15]. Wei [9] tested KO and exposed a curious slope disruption and a nonphysical reduction in the predicted profile losses in cases of higher positive incidences i resulting in recompression, because of spurious K_p values. It is also noteworthy that the impact of the Mach number was investigated by AM [24] and is consistent with the purpose of K_p, but it was, surprisingly, not adopted in the earlier Equation (2).
- Expansion correction factor $K_M \geq 1$ deals with local weak shocks on the blade suction side in the subsonic exit Mach number band $M_{r,out} \in [0.6–1]$ and was rendered more physics driven. This parameter was first introduced by DC [4] for supersonic flows and was derived from the overall turbine performance established by means of experiments.
- Reynolds correction factor K_{Re} applies to Reynolds numbers outside the transition range $[10^5–5 \times 10^5]$ and includes surface roughness, as seen in the CC correlation [17]. A standard finish of $e/c = 10^{-4}$ is assumed throughout the analysis.
- Technology correction factor K_{mod} copes with the technology mismatch of $Y_{p,AM}$ when examining the losses in post-1980s turbine profiles [37]. K_{mod} takes the value of 0.825 for meridional entry profiles and 2/3 for the other.

- Incidence correction factor $K_i \geq 1$ conditions the profile loss in off design conditions and was proven to be successful in pre-1980s turbines [39] but overly conservative in modern turbines [15].

In summary, the purpose of the auxiliary factors is to calibrate Equation (2) with its underlying velocity distribution, without the need for an in depth understanding or elaboration of the loss mechanisms. This is evidently caused by a lack of knowledge transfer between AM, DC, KO and Ag [7]. The shock factor $Y_{sh} \geq 0$ accounts for local shocks situated on hub profiles with a thicker leading edge under comparatively high inlet velocities and is exclusively considered as an independent loss contributing to the profile loss, as introduced by KO. However unlike that of KO, it is unaffected by the auxiliary factors. If $M_{r,out} \geq 1$, then K_p and K_M are held at $M_{r,out} = 1$ and the supersonic loss Y_{ex} has to be supplemented to Y_p in Equation (3). Ag proposed

$$Y_{ex,Ag} = \left(\frac{M_{r,out} - 1}{M_{r,out}} \right)^2. \tag{4}$$

It must be recognized that this is a rather arbitrary formulation. However, this is retained throughout the analysis because there are no more reliable alternatives at the moment.

As mentioned earlier, Equation (2) encompasses the trailing edge loss for standard $t_{te}/s = 0.02$. For any variation of t_{te}/s, AM proposed a trailing edge correction factor affected to Equation (1), such that

$$Y_t = K_{te}(Y_p + Y_s + Y_{cl}). \tag{5}$$

This expression interrelates the trailing edge to the profile, and secondary and tip clearance losses and was criticized by KO for its weak physical soundness regarding the latter two options. In fact, neither of the endwall nor tip leakage vortices remain closely attached to the blade surface upon reaching the blade exit, rendering interaction between the vortices and the trailing edge wake flow unlikely. Instead, KO employed a more intuitive approach and proposed the trailing edge loss Y_{te} as an independent component [5], such that

$$Y_t = Y_p + Y_s + Y_{cl} + Y_{te}. \tag{6}$$

However, Y_{te} still remains part of Y_p in a broader sense, so that Equation (1) is not contracted. To enable this expression, one has to virtually bring Equation (2) to $t_{te}/s = 0$ beforehand. However, Ag carried on this approach and formulated the trailing edge loss as the consequence of an abrupt area enlargement:

$$Y_{te,Ag} = \left(\frac{t_{te}}{o - t_{te}} \right)^2. \tag{7}$$

Correction to zero of the trailing edge of Equation (2) is performed by the subtraction of $Y_{t_{te}=0.02s}$.

2.3. Secondary Losses

The AM 3D gross secondary loss is presented by the following equation [2]:

$$\begin{aligned} Y_{s,AM} &= \lambda_{AM} Z, \\ &= f(\beta_{in}, \beta_{out}, \theta_{in}, A_{out}/A_{in}, r_{hub}/r_{tip}). \end{aligned} \tag{8}$$

This compact expression was the result of continuous efforts to interpret turbine endwall secondary flows. λ_{AM} and Z are intrinsic parameters of the AM correlations and originate from the work of Carter [35], who drew on the classical secondary flow theory. The intent of AM was to define a common and unique basis between axial compressors and turbines to quantify secondary losses, as one had (historically) the objective to employ mostly similar blades for both devices. The theory associates endwall vortices with passage

vortices produced in curved channels [40]. The latter originate from the distortion of the inlet endwall boundary layer by the near-wall velocity deficit and the blade passage pressure gradient, causing the inception of a helical cross-flow motion spreading throughout the blade passage, as shown in Figure 1a.

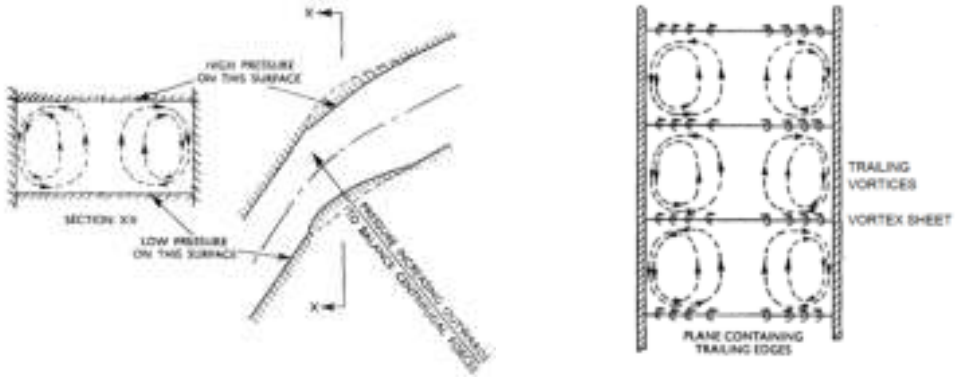

(**a**) (**b**)

Figure 1. Secondary flow mechanisms considered by Carter [35]. (**a**) Classical secondary flow model. (**b**) Cascade lifting line model.

As Carter strived for a practical model to quantify the losses incurred by these passage vortices, he made an analogy with the lifting line theory to obtain a first order approximation. The idea that Carter used leans on the trailing edge inviscid vortex sheet produced by flow circulating around a blade. Being unstable, the closed vortex filaments of the vortex sheet roll up into trailing vortices at the blade ends, as shown in Figure 1b. Based on qualitative analyses of some experimental evidence taken downstream of the blade, the modelled trailing and passage vortices were made equivalent, to establish a secondary loss correlation [35]. Hence, the induced drag under uniform spanwise circulation is:

$$C_{D,s} = \frac{1}{4}\frac{C_{L,m}^2}{s/c}\left(1 - \frac{2H'}{H}\right) = \lambda_{AM}\frac{C_{L,m}^2}{s/c}, \tag{9}$$

with H' the distance from blade midspan to the core of the endwall vortices. This loss coherently reflects lost work by the product of blade loading and the width of the trailing vortices; an analogy to force time displacement. AM subsequently replaced H' by the empirical *Ainley parameter* λ_{AM}, which is shown in their Figure 16 on page 31 in [34], and which reflects the vortex characteristics implicitly. The involved lift coefficient $C_{L,m}$ refers to the mean velocity and relates to the mean angle β_m, where

$$C_{L,m} = 2\frac{s}{c}(\tan\beta_{in} - \tan\beta_{out})\cos\beta_m, \tag{10}$$

and

$$\beta_m = \tan^{-1}\left(\frac{\tan\beta_{in} + \tan\beta_{out}}{2}\right). \tag{11}$$

This was transformed into the *Ainley loading* Z with:

$$Y_{s,AM} = C_{D,s}(\cos^2\beta_{out}/\cos^3\beta_m)(c/s) = \lambda_{AM}Z, \tag{12}$$

where:

$$Z = \frac{C_{L,m}^2}{s/c}\frac{\cos^2\beta_{out}}{\cos^3\beta_m}\frac{c}{s} = 4(\tan\beta_{in} - \tan\beta_{out})^2\frac{\cos^2\beta_{out}}{\cos\beta_m}. \tag{13}$$

This equation assumes an axial velocity ratio AVR and meanline radius ratio κ, with: $\mathrm{AVR} = W_{z,out}/W_{z,in} = \kappa = r_{in}/r_{out} = 1$ and is fully independent of s/c. Note that a change in blade loading due to a pitch to chord variation would not be identifiable [41]. As a matter

of fact, this expression is much closer to the lift coefficient of a single airfoil. The chosen lifting line theory is also used under steady and incompressible conditions and is applied to low camber/loading blades to guarantee the linearity of the problem. As a result, a large disagreement in secondary loss may arise in impulse turbine blades [8] and Equation (13) may wrongfully override other parameters under high loadings [10]. AM were aware of this issue, given the shortage of high-loading blades in their database [34].

It is also interesting to note that a mathematical "mistake" occurred with respect to Equation (12). Normally, the outcome should have been [40]:

$$Y_{s,AM} = C_{D,s}(1/\cos\beta_m)(c/s), \tag{14}$$

and consequently, Equation (13):

$$Z = 4(\tan\beta_{in} - \tan\beta_{out})^2 \cos\beta_m \tag{15}$$

which yields results that are several orders of magnitude higher. This indicates that Equation (12) was most likely adapted heuristically to match the measurements. Therefore, as they possess little physical meaning, λ_{AM} and Z cannot be taken apart in the analysis [7]. This is not surprising, since the secondary loss of AM in Equation (8) was calibrated with:

$$Y_s = Y_t - Y_p \tag{16}$$

This corresponds to Equation (1) in absence of clearance losses but has another implication. In fact, the secondary loss was calibrated to the subtraction of the measured true total loss by the modelled profile loss of Equation (2). Hence, Equation (8) embodies the errors associated to Equation (2). As is the case with λ_{AM} and Z, secondary and profile losses should also not be used separately, as they are bound together by Equation (16).

Dunham [19] criticized the approach of Carter but still relied on it to produce

$$\begin{aligned} Y_{s,AMDC} &= 0.0334 K_{AR} \left(\frac{\cos\beta_{out}}{\cos\theta_{in}}\right) Z, \\ &= f(H/c, \beta_{in}, \beta_{out}, \theta_{in}). \end{aligned} \tag{17}$$

The aspect ratio factor $K_{AR} \geq 1$ relates the intensity of the endwall vortices with blade height and was reported to have questionable reliability [42]. DC simplified the multipliers in Equation (13) using a cascade configuration

$$\lambda_{AM} = f\left(\frac{(A_{n,out}\cos\beta_{out}/A_{n,in}\cos\theta_{in})^2}{(1+d_{hub}/d_{tip})}\right) = f\left(\frac{1}{2}\left(\frac{\cos\beta_{out}}{\cos\theta_{in}}\right)^2\right) = 0.0334 K_{AR}\left(\frac{\cos\beta_{out}}{\cos\theta_{in}}\right) \tag{18}$$

The constant 0.0334 is expected to cover most inlet boundary layer thicknesses and was obtained by calibration to overall turbine performance data [22]. Even though this crude approach is not able to estimate the downstream endwall loss of cascade flows [18], it was, however, proven to be more accurate than most refined correlations tested and compared under diverse inlet boundary layer profiles [43]. Eventually, Ag improved Equation (17) to

$$\begin{aligned} Y_{s,Ag} &= K_p K_{Re}\left(\frac{Y_{s,AMDC}^2}{1+7.5Y_{s,AMDC}^2}\right)^{\frac{1}{2}}, \\ &= f(M_{r,in}, M_{r,out}, Re, e/c) Y_{s,AMDC}, \end{aligned} \tag{19}$$

which shares the K_p and K_{Re} of Equation (3) [6]. Nevertheless, K_{Re} was inherited from DC and was later removed by KO. They certainly did not agree on the impact of viscosity on the endwall flow and, interestingly, the debate is still ongoing. It is true that the endwall vortices are mostly driven by inviscid mechanisms. However, their growth in the blade passage highly depends on the endwall boundary layer flow preceding the blade leading edge

and continuous interaction with the blade surface boundary layer. Thereby, the approach of DC and Ag is more plausible. The square root manipulation prevents loss overshoots in extreme off design conditions. This feature has proven to be particularly crucial in optimization. In fact, the search algorithm could inadvertently exploit inconsistencies of the correlation to reach its objective [44].

Again, the auxiliary factors act as moderate multipliers to the basic Equation (17). It is interesting to note that the aptness of the axial turbine loss correlations was investigated in the context of centrifugal turbines, and, more specifically, the interaction of the auxiliary factors [23]. Drastic changes in the aerodynamic parameters did not trigger a comparable variation in the auxiliary factors, which could have guaranteed reliable solutions. Hence, these auxiliary factors can only sustain minor and individual adjustment and, thus, axial turbine correlation should only be used with axial turbines.

3. Profile Loss Enhancement

The Ag correlation [6], being the latest complete loss system, constitutes the most suitable vessel for successive enhancements. Thus, the profile loss of Equation (3) is revamped into

$$\begin{aligned} Y_{p,Enh} &= 0.914 K_{mod} K_M K_p K_{Re} Y_{p,AM} + Y_{sh} + Y_{inc}, \\ &= f(e_c/s, \theta_{in}, \theta_{out}, M_{r,in}, M_{r,out}, Re_s, e/c, k, i, d_{LE}/s, We_{LE}, \mathrm{AVR}) Y_{p,AM}, \end{aligned} \tag{20}$$

in which Equation (2) is rewritten as

$$\begin{aligned} Y_{p,AM} &= \left[Y_{p,\beta_{in}=0^\circ} - \left| \frac{\beta_{in}}{\beta_{out}} \right| \left(\frac{\beta_{in}}{\beta_{out}} \right) \left(Y_{p,\beta_{in}=-\beta_{out}} - Y_{p,\beta_{in}=0^\circ} \right) \right] \left(\frac{5 t_{max}}{c} \right)^{-K_m \frac{\beta_{in}}{\beta_{out}}}, \\ &= (s/c, t_{max}/c, \beta_{in}, \beta_{out}, \psi_Z). \end{aligned} \tag{21}$$

Carrying on with the auxiliary factor arrangement of Equation (3), several minor changes were performed.

1. Metal angle θ_{in} in Equation (21) was replaced by a design flow angle β_{in}. Practically, a better continuity in design workflow is gained by focusing on the flow angles first and deriving the metal angles afterward. Modern turbines tend to integrate little negative incidence to enable low loss in off designs. Proceeding with θ_{in} would, rather, require extra iterations in the preliminary design process.
2. $Y_{p,\beta_{in}=0^\circ}$ and $Y_{p,\beta_{in}=-\beta_{out}}$ in Equation (21) were scaled by a common s/c. Before developing the modifications, the context in which they were built is reviewed and compared to current practice. During the 1940s, blade profiling was an empirical science. It consisted of a selection from a family of standardized profiles and was arranged into cascade configuration with little allowable change. This approach was inherited from axial compressors and guaranteed cost-effectiveness as it facilitated manufacture. It was impossible to grasp the trend of cascade performance without resorting to cumbersome trial and error wind tunnel tests until the determination of a competent profile. This substantially contrasts with modern profiling techniques, which offer close monitoring and automated optimization of the blade surface velocity distribution. $Y_{p,\beta_{in}=0^\circ}$ and $Y_{p,\beta_{in}=-\beta_{out}}$ were certainly obtained from competent but obsolete profiles, in which blade surface velocity distributions or efficiencies have become unacceptable according to modern state of the art standards [34]. As they form the cornerstone of Equation (2), it would be unreasonable to initiate large modification at the risk of disrupting the auxiliary factor arrangement in Equations (3) and (20). Instead, a scaling technique with a reference s/c, which is analogous to that applied to compressor performance maps, is proposed. In a design process, s/c is set following a trade off between efficiency and cost. If efficiency consideration prevails, the optimum s/c that minimizes profile loss, in this case of Equation (2), is chosen, so that any s/c departure results in profile loss increase or simply efficiency deterioration. However,

the optimum s/c of $Y_{p,\beta_{in}=0^\circ}$ and $Y_{p,\beta_{in}=-\beta_{out}}$ are fixed and specific to competent profiles. The issue would then be its insensitivity to other types of profile. With this in mind, a reasonable approach that maintains the $Y_{p,\beta_{in}=0^\circ}$ and $Y_{p,\beta_{in}=-\beta_{out}}$ trend and scales the optimum pitch to chord ratio s/c_{AM} of Equation (2) to a new optimum s/c is proposed. The purpose is to extend Equation (21) to other profiles in which optimum s/c abides by different design rules. Among these, the prominent Zweifel criterion [11] is chosen to inherit its flexibility and its incompressible is generalized to:

$$s/c_Z = \frac{1}{2}\frac{b}{c}\frac{\psi_Z}{|\frac{1}{\mathrm{AVR}}\tan\beta_{in} - \tan\beta_{out}|\cos^2\beta_{out}}, \tag{22}$$

introducing the axial velocity ratio AVR as an additional design parameter. An ψ_Z beyond the range of [0.6–0.8] recommended by Zweifel is chosen, to achieve the higher optimum pitch to chord ratio s/c_Z in modern turbines. The vital scaling factor is:

$$\begin{aligned} f_{s/c} &= \frac{s/c_Z}{s/c_{AM}}, \\ &= f(s/c, \beta_{in}, \beta_{out}, \mathrm{AVR}, \psi_Z, \gamma), \end{aligned} \tag{23}$$

which is multiplied to the s/c_{AM} of Equation (21). Note that $Y_{p,\beta_{in}=0^\circ}$ and $Y_{p,\beta_{in}=-\beta_{out}}$ are fitted as polynomials about their respective optimum s/c (the fitting formulae of Tournier and El-Genk [45], Korpela [46], Aungier [6] and Concepts/ETI [47] were tested at extreme $\beta_{out} = 30^\circ$ and $\beta_{out} = 80^\circ$; the Tournier and El-Genk performed best), so that the scaling process does not alter their slope. As demonstrated, the original and scaled $Y_{p,\beta_{in}=0^\circ}$ and $Y_{p,\beta_{in}=-\beta_{out}}$ are depicted at exit flow angles $\beta_{out} = 50^\circ$ and 70° in Figure 2, with the $\psi_Z = 1$ typical of modern turbines.

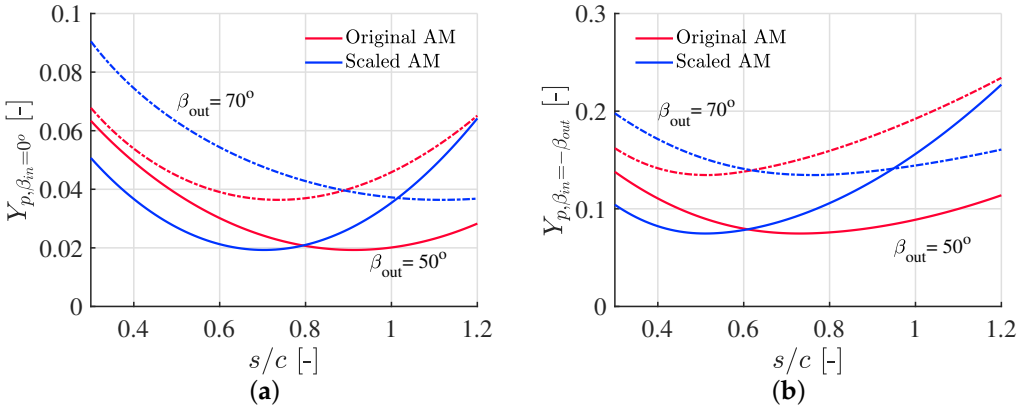

Figure 2. Optimal pitch to- hord ratio matching of AM profile losses [2] with $\psi_Z = 1$. (**a**) Nozzle $\beta_{in} = 0^\circ$. (**b**) Impulse $\beta_{in} = -\beta_{out}$.

Both Figure 2a,b are consistent on the minimum shift. At $\beta_{out} = 70^\circ$, a larger s/c can be achieved with better boundary layer flow control during blade profiling. However, at $\beta_{out} = 50^\circ$, a lower s/c is resorted tp, in order to satisfy $\psi_Z = 1$. This is an undesirable solution, as this would add structural weight. A cost-effective constraint is imposed to refrain $f_{s/c} \geq 1.1$.

3. The Reynolds correction factor K_{Re} was adjusted to suction surface length and becomes a function of the suction surface Reynolds number Re_s. Suction surface momentum thickness could be responsible of up to 90% of the profile loss [32], the suction surface flow should logically be prioritized.

4. Incidence loss Y_{inc} replaces the incidence factor K_i of Equation (3) and acts as a fully independent, contributing to the profile loss. According to Moustapha et al. [15], modern turbines are designed with relatively thicker leading edges and smoother front curvatures, to retard boundary layer separation over a wide range of incidence angles and to keep loss at low level. This feature can not be reflected in the conservative K_i. In this regard, Benner et al. [48] formulated a polynomial incidence loss Y_{inc} compatible with KO and used in Equation (20).
5. The trailing edge loss $Y_{te,Ag}$ of Equation (7) is insensitive to change of turbine operating conditions and, thus, was deemed inappropriate for modifications. As an alternative, the Y_{te} of KO, which encompasses many key aerodynamic parameters, is considered:

$$\Delta\Phi_{te,KO} = \Delta\Phi_{te,\beta_{in}=0^\circ} - \left|\frac{\beta_{in}}{\beta_{out}}\right|\left(\frac{\beta_{in}}{\beta_{out}}\right)\left(\Delta\Phi_{te,\beta_{in}=-\beta_{out}} - \Delta\Phi_{te,\beta_{in}=0^\circ}\right). \tag{24}$$

The replacement of θ_{in} by β_{in} follows the same reasoning behind Equation (21). Drawing on the profile loss of AM in Equation (2), KO blended the exit boundary layer mixing and base pressure losses of nozzle and impulse blades [5]. Instead of a subtraction, as in Equation (3), virtual correction of Y_p to $t_{te}/s = 0$ produces a multiplication by 0.914 in Equation (20). The latter corresponds to the value of K_{te} proposed by AM in Equation (5) at standard $t_{te}/s = 0$ [2]. Now, the conversion of Equation (24) to Y_{te} involves $M_{r,out}$ [49]. This is a property specific to the total pressure loss coefficient and cannot be counted as part of the correlation. However, recent literature has proven its reliance on $M_{r,out}$ but has not delivered any correlation compatible to the AM family [50]. Conveniently, Equation (24) was acquired on low speed tests in the same way as Equation (2). This implies that auxiliary factors defined for the profile loss can be reasonably extended to the trailing edge loss. Considering the relevance of compressibility and Reynolds effects, Equation (24) is revamped into

$$\begin{aligned} Y_{te,Enh} &= K_M K_p K_{Re} Y_{te,KO}, \\ &= f(\beta_{in}, \beta_{out}, t_{te}/o, M_{r,in}, M_{r,out}, Re_s, e/c). \end{aligned} \tag{25}$$

4. Revised Secondary Loss

In light of the issues disclosed earlier in Equation (9), its terms are overhauled. The purpose is to determine a better product of loading and displacement supported by a robust physical basis and depart from the approach used in Equation (16). The latter implies that each contribution has to fully be independent, as in Equation (1). Interestingly, there was a formulation anterior to Equation (8) found in early works [24,33]:

$$Y_{s,AM} = 0.04\left(1 - \frac{\theta_{in}}{\beta_{out}}\right)C_{L,out}^2, \tag{26}$$

using the lift coefficient based on the outlet velocity

$$C_{L,out} = 2\frac{s}{c}(\tan\beta_{in} - \tan\beta_{out})\frac{\cos^2\beta_{out}}{\cos\beta_m}. \tag{27}$$

Unfortunately, Equation (26) was abandoned in favor of the model of Carter [35] because it owns a firmer theoretical background and provides common ground for future compressor and turbine models, according to AM [34]. Contrary to their expectation, axial compressors and turbines have not taken the same course of evolution. As odd as it may be, there is a soundness in Equation (26) in the present context. In particular, $C_{L,out}$ is consistent with turbine analysis, which is not the case with Z of Equation (8), which relies on $C_{L,m}$ in Equation (10).

The secondary loss improvement begins with $C_{L,out}$ rearranged and generalized into the lift solidity coefficient

$$\frac{C_{L,out}}{s/c} = \left(1 + \frac{1}{\text{AVR}}\right)\left(\frac{\kappa}{\text{AVR}}\tan\beta_{in} - \tan\beta_{out}\right)\frac{\cos^2\beta_{out}}{\cos\beta_m}. \tag{28}$$

Assuming AVR $= \kappa = 1$, Equation (27) is recovered. Modern turbines possess a meridional flowpath that forces the radial shift of streamlines such that $\kappa \neq 1$. The latter triggers the Coriolis force and may lower work output [51]. Moreover, expansion through each row inevitably accelerates the flow and, thus, invariance of AVR even in early design stages, which thus constitutes a poor assumption. This aspect would serve in the subsequent evaluation of the correlation reliability. In addition, β_m is also generalized to:

$$\beta_m = \tan^{-1}\left(\frac{\frac{1}{\text{AVR}}\tan\beta_{in} + \tan\beta_{out}}{1 + \frac{1}{\text{AVR}}}\right). \tag{29}$$

Elaborated models of the endwall vortices have been produced since then, to substitute the classical secondary flow theory. Among these, the passage vortex penetration depth of Sharma and Butler [12], later enhanced by Benner et al. [13], is proposed as the replacement to λ_{AM}:

$$\begin{aligned}\frac{Z_{te}}{H} &= \frac{0.1F_\theta^{0.79}}{\sqrt{\text{CR}}(H/c)^{0.55}} + 32.7\left(\frac{\delta^*}{H}\right)^2, \\ &= f(H/c, \delta^*/H, \beta_{in}, \beta_{out}, \gamma, s/c, \text{AVR}).\end{aligned} \tag{30}$$

Once the incident endwall flow impinges on the blade, a first separation occurs at the leading edge, creating a horseshoe vortex, as illustrated in Figure 3a. Under passage pressure gradient and crossflow friction, the pressure leg is progressively strengthened and pushed towards the adjacent blade suction side. Meanwhile, the suction leg remains near the suction side wall. Eventually, both legs of opposite vorticity coincide at the minimum pressure point. The suction leg starts to orbit around the dominant pressure leg, also identified as the passage vortex. The latter draws a demarcation line S4 on the blade suction side. Sharma and Butler assumed symmetric and linear S4, beginning at the leading edge and forming a triangle, as shown in Figure 3b. Z_{te}/H corresponds to the width of the passage vortex taken at the trailing edge. It also differs from λ_{AM} by the weight attributed to the parameters. For instance, AM prioritized the area ratio A_{out}/A_{in} over blade turning $\beta_{in} + \beta_{out}$, as there was only weak evidence on the influence of blade loading [34]. On the opposite, the genetic algorithm used by Benner et al. identified a stronger influence of the blade tangential force F_θ, rather than the convergence ratio CR, analogous to A_{out}/A_{in}.

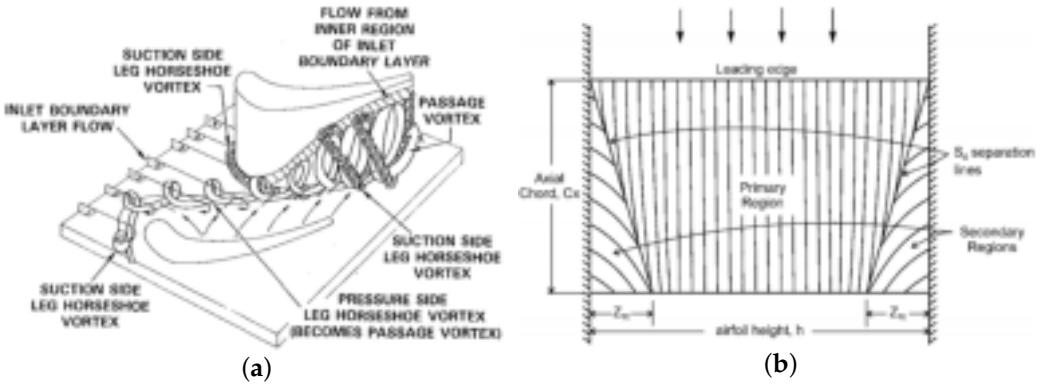

Figure 3. Endwall vortices model. (**a**) New secondary loss model [12]. (**b**) Passage vortex penetration depth [13].

Coull and Hodson [10] pointed out the absence of directives in the calculation of the upstream displacement thickness δ^*/H. This is a minor issue, as classical formulae or reasonable estimates could be resorted to. However, it is still unable to consider downstream endwall loss increase [18]. In a turbine environment, this issue becomes less relevant, as vortex flow is disrupted by succeeding blade rows distanced by a short row gap. The threshold of Equation (30) is $Z_{te}/H = 0.5$, above which the merging of the endwall vortices takes place and produces distinct flow dynamics.

An additional consideration is made on the aspect ratio H/c. Enlarging blade height H and shortening blade chord c both increase H/c but affect secondary loss in different ways [34]. This problem was raised in the early cascade tests of Kraft [52], which exposed the insensitivity of the secondary loss under the change of c. The traditional interpretation reflected by the auxiliary factor K_{AR} in Equations (17) and (19) is that secondary loss is inversely proportional to H/c. This is valid when H is varied but no special regard to c has been made. However, as H/c approaches 0, K_{AR} tends to infinity and vice versa. This contradicts the real physics of the secondary flow. Teia even showed that the structure of the endwall vortices is unaltered by the change of H beyond a certain critical aspect ratio in his Figures 10–12, page 25–26 [42]. He deduced that interaction between the endwall vortices is absent and, thus, secondary loss should remain constant. Below a certain critical aspect ratio varying H, the vortices merge together and amplify loss. His observation offers new insights into the highlighted inconsistency but lacks key verification. Notably, correlation between vortices' interaction and loss was not established and this can hardly argue secondary loss insensitivity for all H/c before merging. In addition, no means were provided to estimate his critical aspect ratio. Drawing partially on his observation, invariance to H/c above $H/c = 2$ in Equation (30) is imposed. $H/c = 2$ corresponds to the traditional threshold below which the slope of K_{AR} becomes sharper. Concurrently, the database size bias of Equation (30) reduces its certainty beyond the same threshold [13]. At this stage, it is cautiously advanced that loss amplification occurs even before the merging of the vortices within $H/c \leq 2$. The problem with c remains unsolved.

Replacing Equation (8), the basic secondary loss is

$$\begin{aligned} Y_{s,b} &= \frac{1}{2}\frac{Z_{te}}{H}\left(\frac{C_{L,out}}{s/c}\right)^2, \\ &= f(H/c, \delta^*/H, \beta_{in}, \beta_{out}, \gamma, s/c, \mathrm{AVR}, \kappa), \end{aligned} \tag{31}$$

accounting for the pair of endwall vortices and their core located at $Z_{te}/2H$ as in Figure 3b. This respects the structure of lost work with loading and displacement parameters. The square of $C_{L,out}/(s/c)$, as in Equation (26), is inherited from the classical lifting-line theory, which associates the endwall and induced vortices. It yields values which are lower than Z by several order of magnitude, hence predominance of $C_{L,out}/(s/c)$ over other parameters is naturally prevented

The independence to s/c in Equation (19) has been criticized, as this does not fit reality [41,53]. Practice refers to the optimum s/c with profile loss consideration only, there are still no available studies, to this day, that have addressed an overall optimum for both profile and secondary losses [19]. The tangential force F_θ of Equation (30) utilizes s/c as loading indicator and is unable to serve this purpose. As a reasonable attempt to incorporate the intensification of secondary loss caused by deviation from the profile optimum s/c, an auxiliary factor is proposed

$$\begin{aligned} K_{sc} &= 1 + 10\left(1 - \frac{s/c}{s/c_Z}\right)^2, \\ &= f(s/c, \beta_{in}, \beta_{out}, \mathrm{AVR}, \psi_Z, \gamma). \end{aligned} \tag{32}$$

This polynomial expression was acquired by fitting the cascade data of Perdichizzi and Dossena [41], as shown in Figure 4.

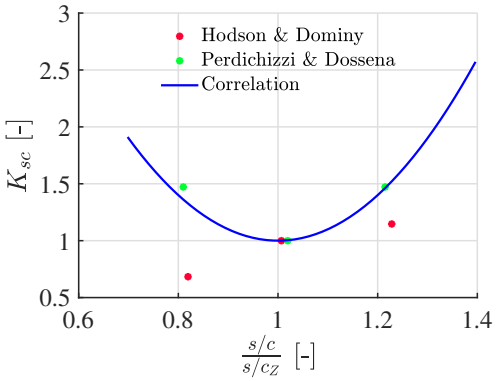

Figure 4. Optimum pitch to chord ratio auxiliary factor for secondary loss.

Tests were conducted for $s/c = 0.58, 0.73, 0.87$ and $i \in [-60\text{–}{+}35]^\circ$. The highlighted points result from averaging over the incidence range and normalizing by s/c_Z with $\psi_Z = 0.6$ such that a clear parabola could be drawn. The data of Hodson and Dominy [53] were also exposed and normalized with $\psi_Z = 0.9$, for comparison. According to the trend, it is seen that their LPT profiles were not optimized at nominal s/c and, thus, their results are omitted. The magnitude of Equation (32) is restrained to 1.5 beyond the range [0.8–1.2] as a precaution, given the scarcity of data. Lastly, the enhanced secondary loss, keeping the same arrangement as Equation (19), is updated as

$$\begin{aligned} Y_{s,Enh} &= K_{sc} K_p K_{Re} \left(\frac{Y_{s,b}^2}{1 + 7.5 Y_{s,b}^2} \right)^{\frac{1}{2}}, \\ &= f(s/c, \psi_Z, \gamma, M_{r,in}, M_{r,out}, Re_s, e/c, H/c, \delta^*/H, \beta_{in}, \beta_{out}, \text{AVR}, \kappa). \end{aligned} \tag{33}$$

Further discussions regarding recent works are carried on. Teia [42] stipulated that profile loss should increase with H/c. He argued that increasing H incurs additional loss, as the boundary layer covers more surface area. This implies a 3D effect which violates the 2D spanwise uniformity of the profile loss assumed in Equation (1). A similar attempt was done by Benner et al. [54], with their alternative loss breakdown

$$Y_t = Y_p \left(1 - \frac{Z_{te}}{H} \right) + Y_s. \tag{34}$$

The boundary layer flow was treated separately in accordance to the area division on the suction side in Figure 3b. They stated that their secondary loss correlation includes the profile loss of the secondary regions, which is unlikely since their genetic algorithm search removed the blade skin friction during the development of their correlation. In that sense, the net profile loss is confined within the primary region delimited by S4. Although intuitive, these results are not compatible with older correlations, especially when the Y_p of Equation (34) is still that of KO.

To ascertain the credibility of the update, it has to achieve statistical significance and thus requires a large database. A major challenge in this framework is to gather a sufficient number of public turbine test cases to possibly enable unbiased analysis. A previous study [23] collected 33 subsonic cascades (15 static and 18 rotating) partitioned from single stage turbines. The same approach is adopted and the previous cascade database is enlarged to 109 specimens (54 static and 55 rotating) to enhance representativeness. Their key design parameter range is summarized in Table 1.

Table 1. Design parameter range of the cascade database.

Parameters	Min	Max
s/c	0.498	0.974
H/c	0.456	6.493
$M_{r,in}$	0.071	0.649
$M_{r,out}$	0.149	1.280
$\beta_{in} + \beta_{out}$	45.6°	138.9°
Re	4.538×10^4	6.025×10^6
Re_s	5.487×10^4	1.1185×10^7

Although it was advanced that reliability should be prioritized over the accuracy in the early review, both aspects would be investigated. For this purpose, high fidelity CFD simulations were conducted on the cascades and the solutions would serve as a benchmark in the analysis.

Although the clearance leakage loss Y_{cl} is not addressed in this paper, it is fundamental to select a compatible leakage loss model to complete the system of Equation (1). For this purpose, the recent correlations of Yaras and Sjolander [55] or Farokhi [56] are recommended.

5. Numerical Method

Since numerical steady solutions serve in determining Y_t, their credibility has to be guaranteed. At issue is their overriding dependence upon numerical discretization and turbulence modelling [57]. Without proper verification and validation, any produced solutions would be untrustworthy [58]. In this regard, a previous study [23] adopted the systematic V and V procedure [59] to identify the numerical scheme (mesh and turbulence model) best suited for the simulation of turbine aerodynamics. It was performed on the Aachen turbine rotor test case [60] with NUMECA FINE/Turbo [61] and presented an on design numerical error of 3.79% the experimental value. The latter is considerably lower than the accuracy standard of ±15% of the correlations [34,38], therefore justifying the use of CFD in the assessment.

The computations were run with the commercial package NUMECA FINE/Turbo [61] whose code architecture is capable of maximum second order accuracy. In order to capture anisotropy, and impact of curvature and body forces on turbulence, the proprietary separation sensitive corrected explicit algebraic Reynolds stress model (SSC-EARSM) was chosen. Compared to the conventional EARSM model [62], this was calibrated by scale adaptive simulation to increase turbulent mixing in the flow separation region and enhance the near wall behavior of anisotropy. Single blade passage meshes were generated with the semi-automatic mesher AutoGrid5. O4H topology, which comprises batches of curvilinear structured hexahedral blocks, was adopted. A large portion of cells were clustered at the wall boundaries and plane intersections to enable, first, inner cell spacing characterized by $y^+ \approx 0.8$ within the viscous sublayer. The employed mesh resolution was about 2.7×10^6 nodes. To ensure algorithm robustness, a uniform profile of absolute total temperature and pressure was imposed at the inlet patch, placed at one chord upstream of the leading edge. This also guarantees the control of the endwall boundary layer over the distance separating the inlet patch to the blade leading edge and enables the use of classical formula in the δ^* estimation in Equation (30). Static pressure was subsequently prescribed at the outlet patch placed at one chord downstream of the trailing edge. This distance should enable mixed out solutions at the outlet. Periodic boundary conditions were imposed on the circumferential patches of the control volume. All simulations were performed with real gas in on design conditions, unless specified otherwise.

6. Correlation Accuracy

Although it has been advanced that correlation accuracy should not be prioritized, the extreme case with 100% error is not tolerable either. In that sense, the limit at which

inaccuracy fails the correlation has to be evaluated. For this purpose, the previous gauge with the probability ΔP_{tol} of reaching a tolerance interval of $\pm 15\%$ error is reused [23], this is depicted in Figure 5. This conforms to the aforementioned accuracy standard of $\pm 15\%$ [38] and accommodates numerical error uncertainties.

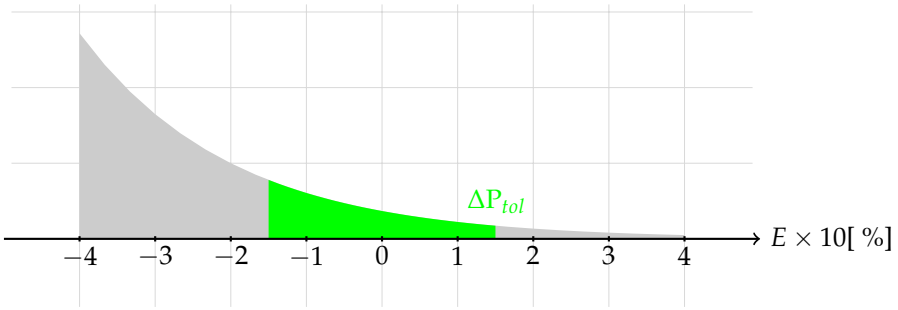

Figure 5. Tolerance interval for correlation accuracy evaluation.

The assessment relies on straightforward descriptive statistics. The latter require a bounded quantity following a near normal distribution and including Equation (1). Thus, the relative error normalized by the benchmark CFD solutions is

$$E = \frac{Y_{t,num} - Y_t}{Y_{t,num}}. \tag{35}$$

with the large database available, a z-distribution is assumed [63].

The update is assessed together with its original form in Figure 6. By comparing the predicted loss of each cascade, the depicted trend in Figure 6a indicates a higher estimation by the enhanced correlation. Distinct disparities occur at high loss levels, whereas most points are clustered below the bisection at low levels, within a ± 0.05 band. Hence, Ag and its update moderately agree for low loss only. As per the convention for scatter plots, the centered bar represents the mean and the other smaller and larger bars delimit the 99% confidence interval and standard deviation, respectively. Figure 6b uncovers a significant difference between Ag and its update, with approximately 10% distance separating their confidence interval. Both populations have comparable spreads but that of Ag is largely decentered, unveiling a systematic underestimation from the Ag correlation. Their difference produces a coherent shift of its mean to the negative side. However, contrary to any expectation, its spread has not shrunk, implying that the update has inherently departed from its original model in terms of turbine aerodynamics interpretation. A priori, if accuracy has to be improved, then the correlation should have its relative error centered on 0 and standard deviation within $\pm 15\%$, to deliver at least $\Delta P_{tol} = 66\%$. The numerical values are gathered in Table 2 and include the ΔP_{tol} of each distribution.

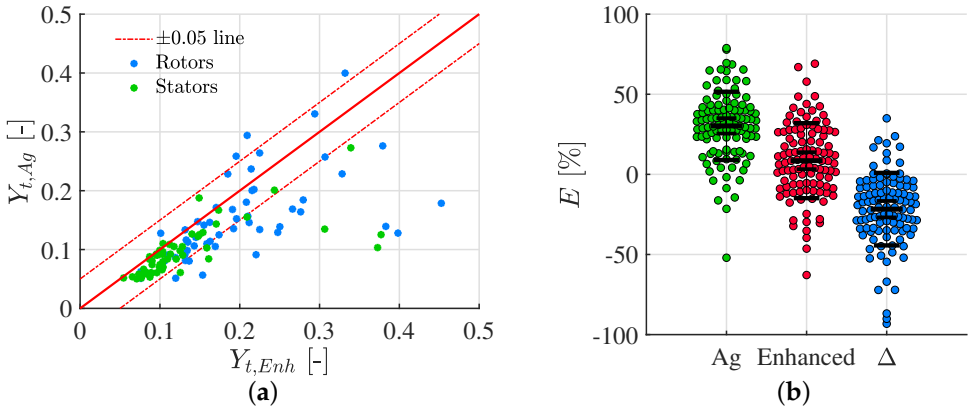

Figure 6. Comparison of Ag and enhanced correlations. (**a**) Total loss. (**b**) Total loss relative error.

Table 2. Statistical solutions of the axial cascade database.

Method	**Descriptive Statistics**		
Parameters	$\bar{E}$ [%]	σ [%]	ΔP_{tol} [%]
Ag	30.255	21.308	22.018
Enhanced	8.548	23.409	45.136
Δ	−21.707	22.634	33.107

With the Ag correlation, it is possible to achieve the required accuracy with approximately 25% chance. This result is opposite to the previous analysis, which reported an optimistic $\Delta P_{tol} = 45.13\%$ while retaining a comparable $\sigma = 23.41$ over 33 cascades [23]. It is very likely that the mean is susceptible to sample size bias, while the spread remains invariant. The enhanced correlation outperforms by doubling ΔP_{tol} with a better position of its mean error. This result has to be handled with care, as this would change with another comparable cascade database with a shift of the mean error. On the other hand, the spread manifests as a barrier marking the limit of low fidelity models. For this reason, accuracy should be relegated to higher order methods.

7. Correlation Reliability

Adopting the approach of Horlock [64] and Coull and Hodson [32], trend consistency is evaluated with the flow coefficient ϕ and stage loading ψ. The latter condition the turbine stage velocity triangle and efficiency. Their early selection is guided by the famous Smith chart [14], after fixing the stage number.

As a reminder, Figure 7 was established by tests on 70 cold single stage turbines which reactions varied from 20% to 60%. These were designed with AVR = 1 and zero incidence. Coull and Hodson supplemented the blade profiles associated to different areas of the chart. The top left area is characterized by the highest turning and lowest efficiency airfoils to satisfy the loading requirement. In this regard, accrued interblade passage convergence is required to guide reduced momentum flows. Nevertheless, flow turning can be alleviated for the same loading and efficiency by increasing ϕ and thus transiting to the top right area. Eventually, the bottom area is characterized by low turning and higher efficiency airfoils and the same consideration concerning the flow passage configuration.

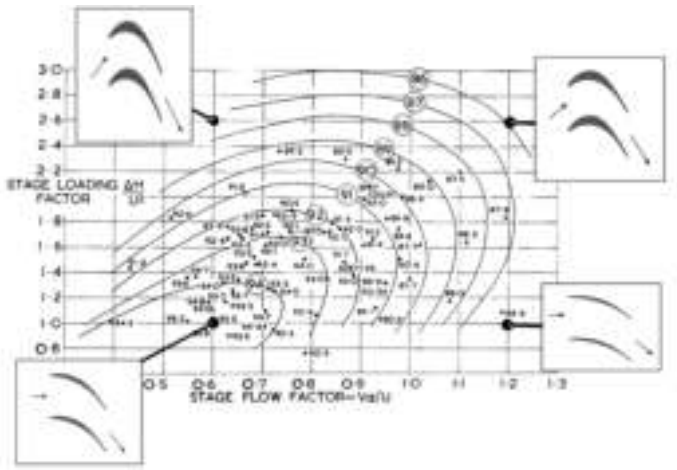

Figure 7. Smith chart calibrated to zero tip loss and 50% reaction [14,32].

To demonstrate reliability, the enhanced correlation is expected to reproduce the same topology by varying ϕ and ψ, as attempted by CC [17] and KO [5]. For this purpose, the analysis begins with the design of a single LPT stage using the setting of Coull and Hodson to acquire a common basis for comparison and explore the LPT for which the AM correlations are known to fail [10]. Repeating stage, 50% reaction, a constant hub to tip

ratio of 0.75 and parabolic camber are assumed. The first stage power requirement and inlet boundary conditions are taken from the GE E3 LPT [65]. The design parameters s/c, β_{out}, velocity ratio VR= W_{out}/W_{in} and H/c of the LPT rotor are plotted in Figure 8 over the same ψ and ϕ range as the Smith chart, for reference. Consecutively, the LPT isentropic efficiency is derived.

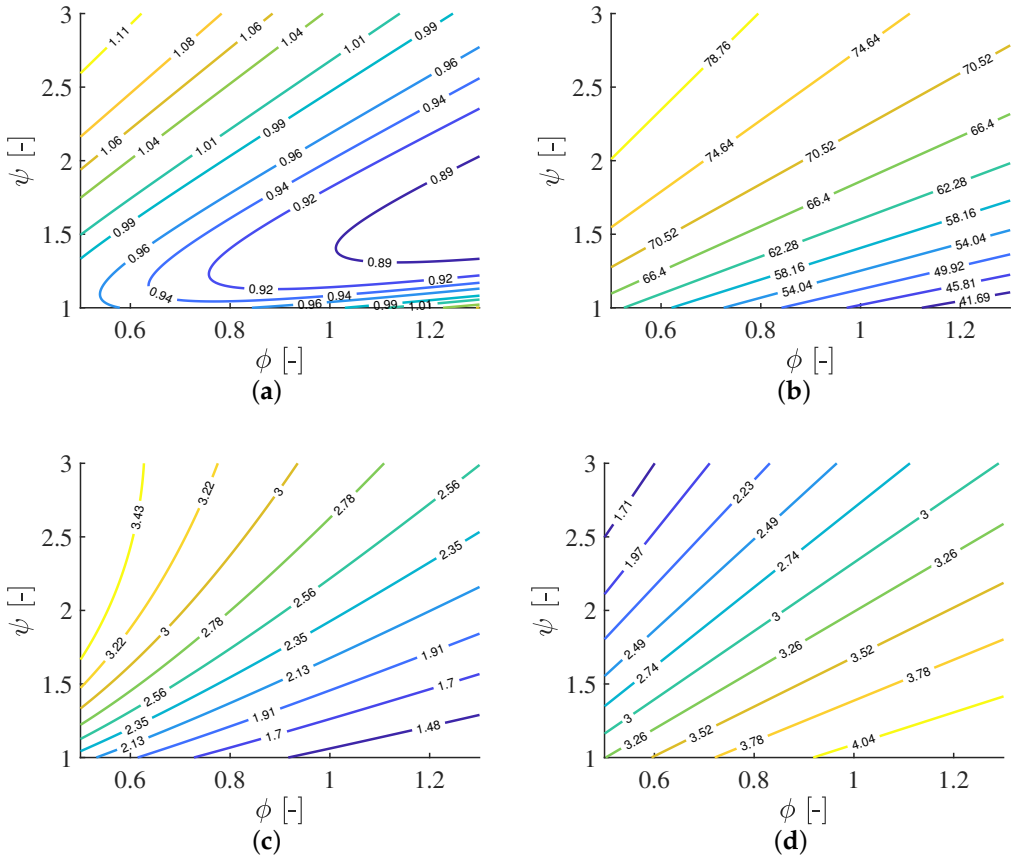

Figure 8. Velocity triangle and geometric parameter ranges of the LPT rotor. (**a**) Pitch to chord ratio s/c. (**b**) Exit flow angle β_{out}. (**c**) Velocity ratio VR. (**d**) Aspect ratio H/c.

First, considering the profile loss efficiency in Figure 9, both contour plots unsurprisingly share the same topology. Equations (2) and (21) differ by minor calibrations involving the Zweifel criterion [11] and extending the auxiliary factors to Equation (24). Furthermore, their bottom right area is identical, since Zweifel criterion matching is disabled for low turning profiles at $f_{s/c} > 1.1$. The abrupt break of the contour 0.02 arises from K_{mod}, which alters its value when departing from nozzle profiles at low ψ [37]. In Figure 9a, profile loss is minimized for most of the bottom area, reflecting low turning profiles, as shown in Figure 8b. Greater ψ and fewer losses are feasible by increasing ϕ but at expense of lower s/c, as in Figure 8a. Loss is aggravated towards the top left area, which conforms to Figure 7. Figure 9b stands out with its comparatively lighter gradient, induced by the adequate application of $f_{s/c}$. With the exception of the bottom right area and according to the results of Coull and Hodson [32], a loss level comparable to that of the semi-analytical correlations of Denton [31] and Coull and Hodson [10], in Figure 10a,b, page 7, respectively, is achieved.

Then, secondary losses differ in all possible aspects in Figure 10. The Ag secondary loss [6] remains low for most of the domain and increases towards the top left area in Figure 10a. This pattern is not shared by other AM family correlations [10]. Further insights are offered by analyzing the components of Equation (8). Here, λ_{AM} displays a topology similar to that of Figure 7 in Figure 11a. Its minimum is reached at the bottom left area

and, curiously, remains invariant towards the top right direction. Meanwhile, amplification takes place in all other directions, switching from curved to straight contours. On the other hand, Z progressively grows accordingly, along ψ, to reach the steepest straight contour in the top left area in Figure 11c. With a difference of $O(10^3)$, it naturally plays a predominant role in the product of Equation (8) and dictates the resulting topology. Thus, Figure 10a disregards most features of Figure 11a and highlights losses with contours that are curved by the auxiliary factors and the square root of Equation (19). Conversely, the lowest loss is produced at greater ψ and gradually intensifies towards the bottom right area in Figure 10b.

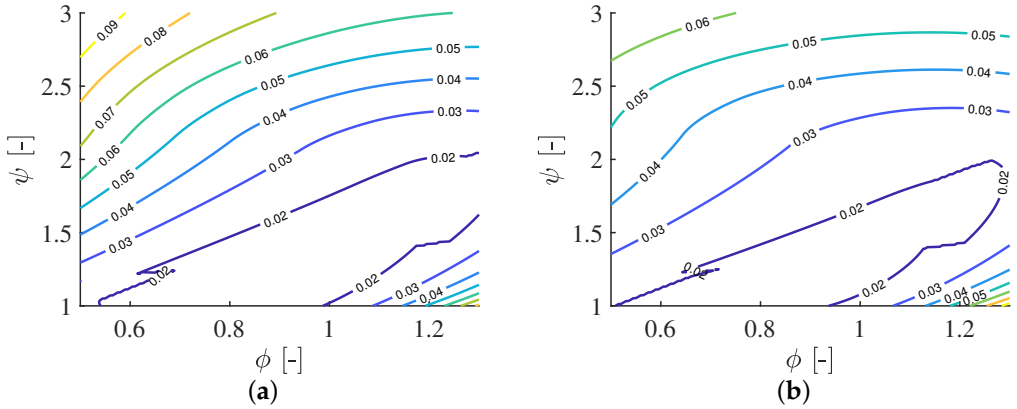

Figure 9. Profile loss efficiency with $\psi_Z = 1.1$, AVR $= 1$, $i = 0$, $H/b = 6.5, 4.6$ for stator and rotor. (**a**) Aungier [6]. (**b**) Enhanced.

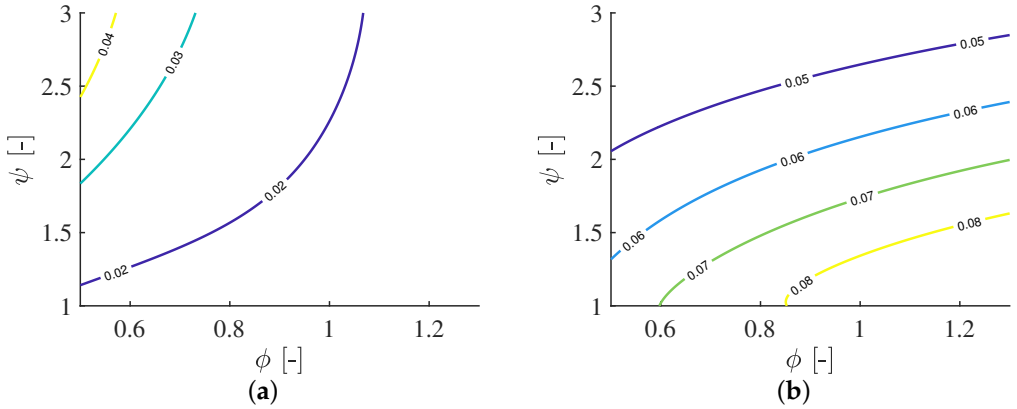

Figure 10. Secondary loss efficiency with $\psi_Z = 1.1$, AVR $= 1$, $H/b = 6.5, 4.6$ for stator and rotor. (**a**) Aungier [6]. (**b**) Enhanced.

The central question to be posed now is which correlation conforms to reality? Back to Figure 11a, λ_{AM} is supposed to reflect the endwall vortices. In this regard, the increase in the top left area is consistent, since it is backed by a sharper exit angle in Figure 8b and lesser aspect ratio in Figure 8d. However, the other increase in the bottom right area is unlikely. It is impossible to magnify the endwall vortices by decreasing turning/loading, increasing aspect ratio and also lowering VR in Figure 8c. Moreover, a higher ϕ should not favor the growth of secondary flows in the flow passage, as these are downwashed through considerable momentum convection [7]. With these points in mind, it is seen that the monotonous penetration depth of Figure 11b better matches the topology of Figure 8b–d. The contour slope disruption in the top left area is triggered by the aspect ratio variation for $H/c < 2$, ensuring discussion over the results of Teia [42]. Once again, there is a clear divergence between the blade loadings in Figure 11c,d. Contrasting with Figure 11c, the maximum is located in the bottom right area. This feature comes from the s/c at the denominator in Equation (28) and is substantiated by Figure 8a, in which the minimum occupies

the same area. Z originally accounted for s/c as uncovered in Equation (13) but dispensed with its contribution, as confirmed herein. Furthermore, secondary loss increase under high ϕ and low ψ was also produced by the trusted CC [17] and Traupel [25] correlations [10]. Despite the absence of similarity with Figure 7, consistency in the enhanced correlation is comparatively augmented. In particular, the difference between the components of Equation (19) is mitigated to $O(10)$.

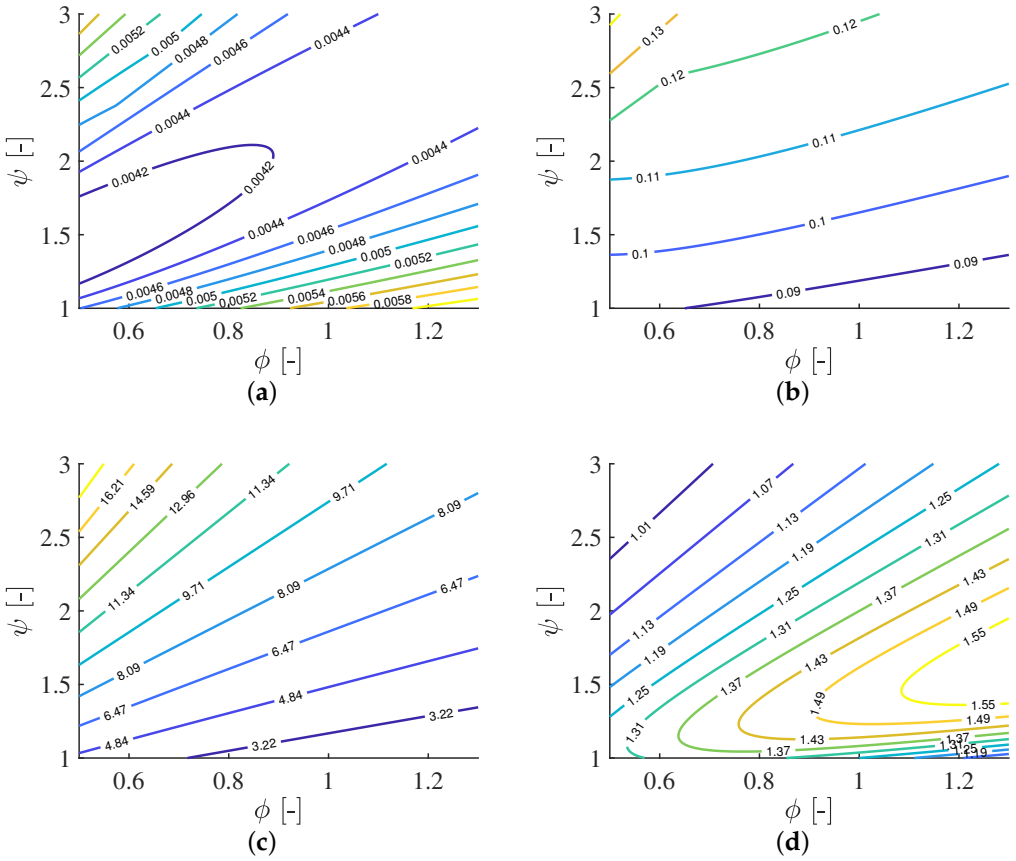

Figure 11. Rotor secondary loss components with $\psi_Z = 1.1$, AVR $= 1$, $H/b = 4.6$. (**a**) Ainley parameter λ_{AM}. (**b**) Vortex penetration depth $Z_{te}/2H$. (**c**) Ainley loading Z. (**d**) Generalized lift solidity coefficient $C_L/s/c$.

Eventually, the isentropic efficiency key to correlation reliability is depicted in Figure 12. The trend of Ag in Figure 12a is clearly driven by the profile loss in Figure 9a. In that respect, the bowed contours that are supposed to be inscribed in the domain of Figure 7 are stretched towards higher ϕ. As a consequence, losses induced by large ϕ are underestimated by the correlation. In addition, the update reveals to be more conservative in the quantification of the losses, as the first identified contour is 0.91 in Figure 12b. The latter exhibits an almost complete bow but is not comparable to those of the Smith chart, as it covers too much area. Hence, it can only enable a global trend consistency. Although overstretching to high ϕ is reduced, its expansion occasions over and under estimations in the bottom and top areas, respectively. Variation of contour level or sensitivity to design parameters is lessened. These weaknesses are occasioned by the secondary loss in which $H/c = 2$ is held constant for most of the domain, as shown in Figure 11b. This is somewhat expected, as Equation (30) of Benner et al. [13] was not intended for the current treatment regarding H/c. The model's conservativeness could be alleviated through a larger H/c, if justified. For now, the threshold $H/c = 2$ is untouched, as the reasonable conservativeness in preliminary design provides an adequate margin for subsequent modifications.

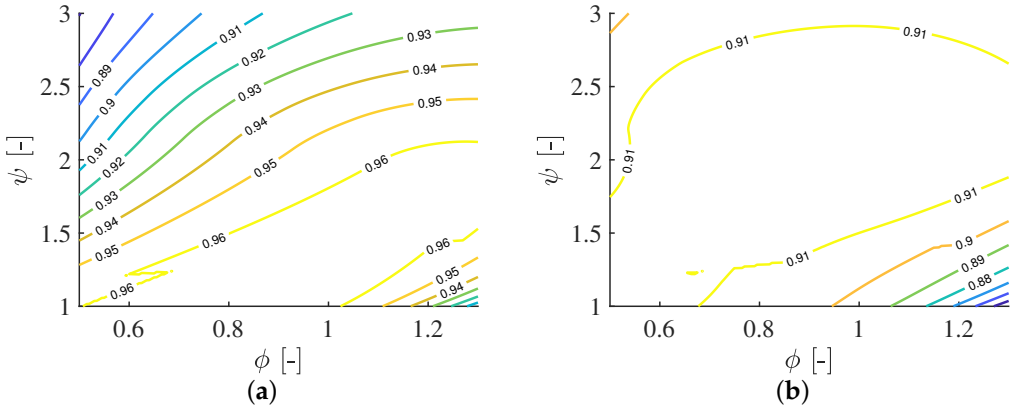

Figure 12. Isentropic efficiency with $\psi_Z = 1.1$, AVR $= 1$, $H/b = 6.5, 4.6$ for stator and rotor. (**a**) Aungier [6]. (**b**) Enhanced.

The enhanced correlation has introduced additional design parameters or degrees of freedom, in hopes of reaching a better control on design. These are summarized in Appendix A Table A1 and their number amounts to three to five for the profile and secondary losses, respectively. The following analysis retains four static and rotating cascades [26,60,65,66] with distinct κ and with their operating conditions altered with a back pressure within $\pm 10\%$ of its nominal value. This aims to evaluate the change of Y_t over the prescribed operation range, drawing on the approach of Wei [9]. Again, CFD solutions form the benchmark. AVR determined in the early velocity triangle and knowingly set to unity in the AM correlations is concurrently highlighted to demonstrate its relevance as a design parameter. The results of the static and rotating cascades normalized by on design CFD values are depicted in Figure 13. The cascades are not identified to their references in the plots to foster randomness, as reliability must not be biased by the turbine origin.

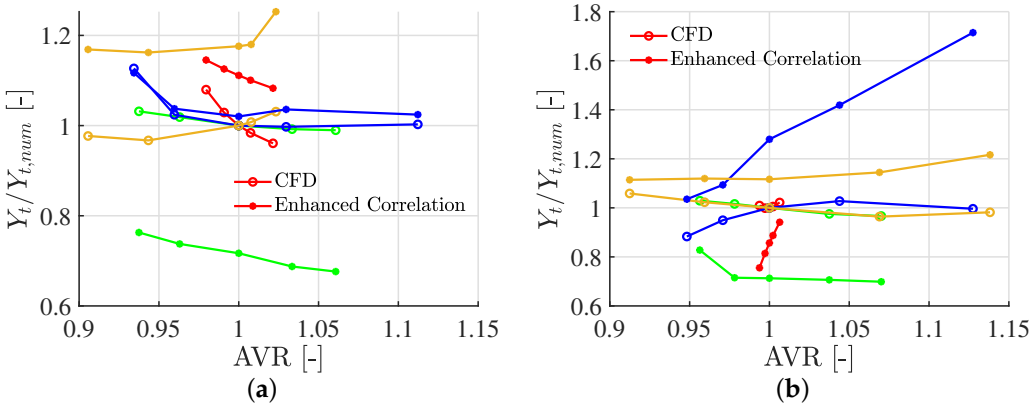

Figure 13. Total loss variation of four cascades. (**a**) Stators. (**b**) Rotors.

The distance separating each pair of curves relates to accuracy. It is worth mentioning that two out of four cascades achieve the early tolerance interval and this conform with the estimated $\Delta P_{tol} = 45\%$. AVR varies for different operating conditions and extends as far as 15% its nominal value in Figure 13b. This parameter has demonstrated its nontriviality and hence justifies the generalization of Equations (22) and (28). By diminishing the back pressure, AVR increases and vice-versa. For the static cascades in Figure 13a, the trend of each pair of curves similarly results in an acceptable global consistency. If strict consistency is imposed, then the curves should have synchronous slopes that conserve their separation at each variation. Whereas, for the rotating cascades in Figure 13b, serious trend disruptions are displayed introducing undesirable uncertainties. One cascade undergoes slope switchover to negative values at AVR $= 1.05$. Moreover, there are two cascades for

which a considerable slope mismatch is seen. The first starts from AVR = 1.05 along the back pressure increase. The second even covers the entire range around AVR = 1. Contrasting with Figure 13a, the reason for these divergences becomes rather straightforward. CFD can capture the impacts of rotation on secondary flows and, thus, loss mechanism, whereas correlations built upon cascade tests and calibrated to turbine data cannot. As a matter of fact, parameters or factors relating to rotation are absent in the correlations. In this view, reliability is globally guaranteed in stators and compromised in rotors because of rotation. Clearly, this observation constitutes the most sound argument against the use of cascades as benchmark of the correlations, as presented in the early review.

8. Conclusions

In this paper, historical insight was provided into the numerous features of the AM correlations, whose most authoritative contributions were given by AM, DC, KO, and Ag. These models were established empirically using measurements on turbine cascades and deliver a standardized solution for the configurations considered in the experiments. As a consequence, the range of applications of the models are biased towards the types of turbine cascades used to develop the correlations. An important restriction of the AM correlations is related to the profile loss, which is established through interpolation between nozzle and impulse blade empirical charts. This implies the prior setting of the velocity distribution over the blade surface, which follows from measurements on a restricted set of turbine cascade configurations. Another restriction is related to the secondary loss, which draws on the classical lifting-line theory of Carter and associates wingtip trailing vortices with blade passage vortices. Further investigation revealed a mathematical mistake in the secondary loss formulation and an undesirable link with the profile loss.

In light of these issues, an update to the profile and secondary losses was proposed in this work, building upon the correlations of Ag. For the profile loss, the addressed points are:

- The substitution of metal angle θ_{in} by the flow angle β_{in}.
- The scaling of the AM optimum pitch to chord s/c_{AM} by the Zweifel optimum pitch to chord s/c_Z. This, notably, preserves of the slope of the AM profile losses $Y_{p,\beta_{in}=0^\circ}$ and $Y_{p,\beta_{in}=-\beta_{out}}$ and adapts the AM correlation to other design rules.
- The use of a Reynolds number Re_s based on the suction surface length.
- The substitution of the auxiliary factor K_i by a more suitable incidence loss Y_{inc}, proposed by Benner et al.
- The reuse of the KO trailing edge loss $Y_{te,KO}$ affected by the profile loss auxiliary factors.

As for the secondary loss, the addressed points are:

- The replacement of the classical secondary flow model of AM and Carter by the endwall vortices model of Sharma and Butler.
- The use of the product of the elemental lift solidity coefficient $C_{L,out}/s/c$ and vortex penetration depth Z_{te} instead of the heuristic Ainley loading Z and parameter λ_{AM}.
- The invariance of the auxiliary factor K_{AR} beyond the threshold aspect ratio $H/c = 2$.
- The definition of a new auxiliary factor K_{sc}, to determine the variation of the secondary loss with the pitch to chord ratio s/c.

With a database of 109 cascades available, the prediction of the new correlation is benchmarked against the cascade numerical solution. Using descriptive statistics and expressing accuracy as the probability of achieving a relative error within ±15%, the improvement yields $\Delta P_{tol} = 45\%$ against the $\Delta P_{tol} = 22\%$ of Ag. Although there is a clear improvement, these results are largely dependent on the choice of a finite database for which the representativeness of the population is unknown. Nevertheless, this quantification should provide an estimate of the results and raise confidence in the use of the enhanced correlation. Regarding reliability, the new correlation ensures global consistency by reproducing the Smith chart [14] and off design stator loss variation. In addition, the analysis points out a correlation conservativeness in the design of the typical LPT, which is

due to insensitivity to the secondary loss correlations beyond $H/c = 2$. Severe trend disruptions are identified during the application of the proposed enhanced correlation on four rotating cascades, the mismatches with CFD compromise its reliability in rotating flows.

Author Contributions: Conceptualization, Y.L.; methodology, Y.L.; software, Y.L.; validation, P.H. and Z.Z. and F.B.; formal analysis, Y.L.; investigation, Y.L.; resources, P.H. and Z.Z.; data curation, Y.L.; writing—original draft preparation, Y.L.; writing—review and editing, Y.L.; visualization, Y.L.; supervision, P.H. and Z.Z. and F.B.; project administration, P.H. and Z.Z.; funding acquisition, P.H. and Z.Z. All authors have read and agreed to the published version of the manuscript.

Funding: This research received no external funding.

Institutional Review Board Statement: Not applicable.

Informed Consent Statement: Not applicable.

Data Availability Statement: The cascade dataset and its CFD results are available on demand.

Conflicts of Interest: The authors declare no conflict of interest.

Nomenclature

Acronyms

Ag	Aungier
AM	Ainley and Mathieson
BSM	Benner and Sjolander and Moustapha
CFD	Computational fluid dynamics
CFL	Courant–Friedrich–Levy
DC	Dunham and Came
E3	Energy efficient engine
KO	Kacker and Okapuu
LPT	Low pressure turbine
MKT	Moustapha and Kacker and Tremblay
VandV	Verification and validation
Z	Zweifel

Symbols

β	Relative flow angle	[°]
$\Delta\Phi$	Kinetic loss coefficient	[-]
ΔP_{tol}	Tolerance interval probability	[-]
δ^*	Endwall displacement thickness	[m]
γ	Stagger	[°]
κ	Meanline radius ratio	[-]
λ_{AM}	Ainley parameter	[-]
ϕ	Flow coefficient	[-]
ψ	Blade loading	[-]
ψ_Z	Zweifel loading	[-]
σ	Standard deviation	[-]
θ	Metal angle	[°]
A	Cross section area	[m^2]
b	Axial chord	[m]
c	True chord	[m]
C_L	Lift coefficient	[-]
$C_{D,s}$	Secondary drag coefficient	[-]
d	Annulus diameter	[m]
d_{LE}	Leading edge diameter	[m]
E	Relative error	[-]
e	Surface roughness	[m]
e_c	Back curvature	[m^{-1}]

F_θ	Tangential loading	[-]
$f_{s/c}$	Scaling factor	[-]
H	Blade height	[m]
H'	Distance to endwall vortices	[m]
i	Incidence	[°]
K	Auxiliary factor	[-]
k	Heat ratio coefficient	[-]
K_{AR}	Aspect ratio correction	[-]
K_i	Incidence factor	[-]
K_{mod}	Technology factor	[-]
K_M	Expansion correction factor	[-]
K_m	Profile correction factor	[-]
K_p	Mach correction factor	[-]
K_{Re}	Reynolds correction factor	[-]
K_{sc}	Pitch to chord ratio correction	[-]
K_{te}	Trailing edge correction factor	[-]
M	Mach number	[-]
o	Throat width	[m]
p	Pressure	[Pa]
r	Meanline radius	[m]
Re	Reynolds number	[-]
Re_s	Suction length Reynolds number	[-]
s	Pitch	[m]
t_{max}	Maximum thickness	[m]
t_{te}	Trailing edge thickness	[m]
W	Relative velocity	[m/s]
We_{LE}	Leading edge wedge	[°]
Y_p	Profile loss	[-]
Y_s	Secondary loss coefficient	[-]
Y_t	Total loss coefficient	[-]
Y_{cl}	Tip clearance loss coefficient	[-]
Y_{ex}	Supersonic loss coefficient	[-]
Y_{inc}	Incidence loss coefficient	[-]
Y_{sh}	Shock factor	[-]
Y_{te}	Trailing edge loss coefficient	[-]
Z	Ainley loading	[-]
Z_{te}	Vortex penetration depth	[m]
AVR	Axial velocity ratio	[-]
CR	Convergence ratio	[-]
VR	Velocity ratio	[-]

Superscripts

$-$	Average

Subscripts

Enh	Enhanced
hub	Hub
in	Inlet
is	Isentropic
m	Mean
n	Normal
num	Numerical
out	Outlet
r	Relative
t	Total
tip	Tip
z	Axial

Appendix A

Table A1. Dimensionless parameters of the AM correlations.

Parameters	$Y_{p,AM}$	$Y_{s,AM}$	$Y_{p,Ag}$	$Y_{s,Ag}$	$Y_{te,Ag}$	$Y_{ex,Ag}$	Y_p	Y_s	Y_{te}
s/c	∈		∈				∈	∈	
t_{max}/c	∈		∈				∈		
θ_{in}	∈	∈	∈	∈			∈		
θ_{out}			∈				∈		
β_{in}		∈		∈				∈	∈
β_{out}	∈	∈	∈	∈			∈	∈	∈
t_{te}/s					∈				
o/s					∈				
e_c/s			∈				∈		
$M_{r,in}$			∈	∈			∈	∈	∈
$M_{r,out}$			∈	∈		∈	∈	∈	∈
Re			∈	∈					
Re_s							∈	∈	∈
e/c			∈	∈			∈	∈	∈
k			∈				∈		
i	∈		∈				∈		
d_{LE}/s							∈		
We_{LE}							∈		
A_{out}/A_{in}		∈							
r_{hub}/r_{tip}		∈							
H/c				∈				∈	
AVR							∈	∈	
ψ_Z							∈	∈	
t_{te}/o					∈				∈
δ^*/H								∈	
γ							∈	∈	
κ								∈	
Reference	Equation (2)	Equation (8)	Equation (3)	Equation (19)	Equation (7)	Equation (4)	Equation (20)	Equation (33)	Equation (24)
Total	5	5	12	8	3	1	17	13	7

References

1. Zou, Z.P.; Wang, S.T.; Liu, H.X.; Zhang, W.H. *Axial Turbine Aerodynamics for Aero-Engines: Flow Analysis and Aerodynamics Design*, 1st ed.; Springer Nature: Singapore, 2017.
2. Ainley, D.; Mathieson, G. *A Method for Performance Estimation for Axial-Flow Turbines*; Technical Report R&M No. 2974; Aeronautical Research Council: London, UK, 1951.
3. Dunham, J. 50 Years of Turbomachinery Research at Pyestock—Part 2: Turbines. *Aeronaut. J.* **2000**, *104*, 199–207. [CrossRef]
4. Dunham, J.; Came, P.M. Improvements to the Ainley-Mathieson Method of Turbine Performance Prediction. *J. Eng. Power* **1970**, *92*, 252–256. [CrossRef]
5. Kacker, S.C.; Okapuu, U. A Mean Line Prediction Method for Axial Flow Turbine Efficiency. *J. Eng. Power* **1982**, *104*, 111–119. [CrossRef]
6. Aungier, R. *Turbine Aerodynamics: Axial-Flow and Radial-Inflow Turbine Design and Analysis*; ASME Press: New York, NY, USA, 2006.
7. Japikse, D. *Turbomachinery Performance Modeling*; SAE Technical Paper 2009-01-0307; SAE: Beograd, Serbia, 2009. [CrossRef]
8. Lozza, G. A Comparison Between the Craig-Cox and the Kacker-Okapuu Methods of Turbine Performance Prediction. *Meccanica* **1982**, *17*, 211–221. [CrossRef]
9. Wei, N. Significance of Loss Models in Aerothermodynamic Simulation for Axial Turbines. Ph.D. Thesis, KTH Energiteknik, Stockholm, Sweden, 2000.
10. Coull, J.D.; Hodson, H.P. Blade Loading and Its Application in the Mean-Line Design of Low Pressure Turbines. *J. Turbomach.* **2013**, *135*, 12. [CrossRef]
11. Zweifel, O. Die Frage der optimalen Schaufelteilung bei Beschaufelungen von Turbomaschinen, insbesondere bei großer Umlenkung in den Schaufelreihen. *Brown Boveri Mitteilungen* **1945**, *32*, 436–444.
12. Sharma, O.P.; Butler, T.L. Predictions of Endwall Losses and Secondary Flows in Axial Flow Turbine Cascades. *J. Turbomach.* **1987**, *109*, 229–236. [CrossRef]
13. Benner, M.W.; Sjolander, S.A.; Moustapha, S.H. An Empirical Prediction Method for Secondary Losses in Turbines—Part I: A New Loss Breakdown Scheme and Penetration Depth Correlation. *J. Turbomach.* **2005**, *128*, 273–280. [CrossRef]
14. Smith, S. A Simple Correlation of Turbine Efficiency. *J. R. Aeronaut. Soc.* **1965**, *69*, 467–470. [CrossRef]
15. Moustapha, S.H.; Kacker, S.C.; Tremblay, B. An Improved Incidence Losses Prediction Method for Turbine Airfoils. *J. Turbomach.* **1990**, *112*, 267–276. [CrossRef]
16. Whittle, F. *Gas Turbine Aero-Thermodynamics: With Special Reference to Aircraft Propulsion*; Elsevier: Oxford, UK, 2013.
17. Craig, H.R.M.; Cox, H.J.A. Performance Estimation of Axial Flow Turbines. *Proc. Inst. Mech. Eng.* **1970**, *185*, 407–424. [CrossRef]

18. Dring, R.P.; Heiser, W.H. Turbine Aerodynamics. In *The Aerothermodynamics of Aircraft Gas Turbine Engines*; Oates, G.C., Ed.; NTIS: Seattle, WA, USA, 1978; Chapter 18; pp. 1–23.
19. Dunham, J. A Review of Cascade Data on Secondary Losses in Turbines. *J. Mech. Eng. Sci.* **1970**, *12*, 48–59. [CrossRef]
20. Denton, J. A Survey and Comparison of Methods for Predicting the Profile Loss of Turbine Blades. In Proceedings of the Conference on Heat and Fluid Flow in Steam and Gas Turbine Plant, Coventry, UK, 3–5 April 1973; Number RD/M/R143; pp. 204–212.
21. Chyu, M.K.; Young, G.M. *A Loss/Performance Evaluation of SSME HPFTP Turbine*; Technical Report NGT 01-002-099; NASA & University of Alabama: Huntsville, AL, USA, 1988.
22. Sieverding, C.H. Axial Turbine Performance Prediction Methods. In *Thermodynamics and Fluid Mechanics of Turbomachinery*; NATO ASI Series E; Kluwer Academic Publishers B.V.: Dordrecht, The Netherlands, 1985; Volume 1, pp. 737–784.
23. Liu, Y.M.; Hendrick, P.; Zou, Z.P.; Buysschaert, F. Statistical and Computational Evaluation of Empirical Axial Turbine Correlations in Design of Centrifugal Turbines. *J. Turbomach.* **2021**, *144*, 041002. [CrossRef]
24. Ainley, D.G. Performance of Axial-Flow Turbines. *Proc. Inst. Mech. Eng.* **1948**, *159*, 230–244. [CrossRef]
25. Traupel, W. *Thermische Turbomaschinen: Band 1: Thermodynamisch-Strömungstechnische Berechnung*; Springer: Berlin/Heidelberg, Germany, 2019.
26. Hirsch, C.; Denton, J.D. *Through Flow Calculations in Axial Turbomachines*; Technical Report AGARD-AR-175; Propulsion and Energetics Panel Working Group 12: Neuilly-sur-Seine, France, 1981.
27. Wu, C. *A General Theory of Three-Dimensional Flow in Subsonic and Supersonic Turbomachines in Radial and Mixed Flow Types*; Technical Report NACA TN-2604; National Advisory Committee for Aeronautics: Cleveland, OH, USA, 1952.
28. Da Lio, L.; Manente, G.; Lazzaretto, A. New efficiency charts for the optimum design of axial flow turbines for organic Rankine cycles. *Energy* **2014**, *77*, 447–459. [CrossRef]
29. Al Jubori, A.M.; Al-Dadah, R.K.; Mahmoud, S.; Daabo, A. Modelling and Parametric Analysis of Small-Scale Axial and Radial-Outflow Turbines for Organic Rankine Cycle Applications. *Appl. Energy* **2017**, *190*, 981–996. [CrossRef]
30. Baljé, O.E.; Binsley, R.L. Axial Turbine Performance Evaluation. Part A—Loss-Geometry Relationships. *J. Eng. Power* **1968**, *90*, 341–348. [CrossRef]
31. Denton, J.D. The 1993 IGTI Scholar Lecture: Loss Mechanisms in Turbomachines. *J. Turbomach.* **1993**, *115*, 621–656. [CrossRef]
32. Coull, J.D.; Hodson, H.P. Predicting the Profile Loss of High-Lift Low Pressure Turbines. *J. Turbomach.* **2012**, *134*, 14. [CrossRef]
33. Ainley, D. *An Approximate Method for the Estimation of the Design Point Efficiency of Axial Flow Turbines*; Technical Report R&M No. 59; Aeronautical Research Council: London, UK, 1950.
34. Ainley, D.; Mathieson, G. *An Examination of the Flow and Pressure Losses in Blade Rows of Axial Flow Turbines*; Technical Report R&M No. 2891; Aeronautical Research Council: London, UK, 1951.
35. Carter, A.D.S. Three-Dimensional-Flow Theories for Axial Compressors and Turbines. *Proc. Inst. Mech. Eng.* **1948**, *159*, 255–268. [CrossRef]
36. Lakshminarayana, B.; Horlock, J.H. Review: Secondary Flows and Losses in Cascades and Axial-Flow Turbomachines. *Int. J. Mech. Sci.* **1963**, *5*, 287–307. [CrossRef]
37. Zhu, J.; Sjolander, S.A. Improved Profile Loss and Deviation Correlations for Axial-Turbine Blade Rows. Turbo Expo 2005, Parts A and B. In *Turbo Expo: Power for Land, Sea, and Air*; ASME Paper No. GT2005-69077; ASME: Reno, NV, USA, 2005; Volume 6, pp. 783–792. [CrossRef]
38. Dunham, J. Loss Mechanisms and Unsteady Flows in Turbomachines. In Proceedings of the Technical Report AGARD-CP-571, Propulsion and Energetics Panel 85th Symposium, Derby, UK, 8–12 May 1995.
39. Stabe, R.G.; Kline, J.F. *Incidence Loss for a Core Turbine Rotor Blade in a Two-Dimensional Cascade*; Technical Report NASA TM X-3047; NASA: Washington, DC, USA, 1974.
40. Hawthrone, W.R. *Aerodynamics of Turbines and Compressors*; *High Speed Aerodynamics and Jet Propulsion*; Princeton University Press: Princeton, NJ, USA, 1964; Volume 10.
41. Perdichizzi, A.; Dossena, V. Incidence Angle and Pitch–Chord Effects on Secondary Flows Downstream of a Turbine Cascade. *J. Turbomach.* **1993**, *115*, 383–391. [CrossRef]
42. Teia, L. New Insight Into Aspect Ratio's Effect on Secondary Losses of Turbine Blades. *J. Turbomach.* **2019**, *141*. [CrossRef]
43. Walsh, J.A.; Gregory-Smith, D.G. Inlet Skew and the Growth of Secondary Losses and Vorticity in a Turbine Cascade. *J. Turbomach.* **1990**, *112*, 633–642. [CrossRef]
44. Agromayor, R.; Nord, L.O. Preliminary Design and Optimization of Axial Turbines Accounting for Diffuser Performance. *Int. J. Turbomach. Propuls. Power* **2019**, *4*, 32. [CrossRef]
45. Tournier, J.M.; El-Genk, M.S. Axial Flow, Multi-Stage Turbine and Compressor Models. *Energy Convers. Manag.* **2010**, *51*, 16–29. [CrossRef]
46. Korpela, S.A. *Principles of Turbomachinery*, 2nd ed.; John Wiley & Sons: Hoboken, NJ, USA, 2020.
47. Concepts/ETI. *Loss Models In Axial (Reduced Throughflow) and AxCent (NS Throughflow) Solvers*; Concepts NREC: White River Junction, VT, USA, 2014.
48. Benner, M.W.; Sjolander, S.A.; Moustapha, S.H. Influence of Leading-Edge Geometry on Profile Losses in Turbines at Off-Design Incidence: Experimental Results and an Improved Correlation. *J. Turbomach.* **1997**, *119*, 193–200. [CrossRef]

49. Brown, L.E. Axial Flow Compressor and Turbine Loss Coefficients: A Comparison of Several Parameters. *J. Eng. Power* **1972**, *94*, 193–201. [CrossRef]
50. Sieverding, C.; Manna, M. A Review on Turbine Trailing Edge Flow. *Int. J. Turbomach. Propuls. Power* **2020**, *5*, 10. [CrossRef]
51. Lewis, R.I. *Turbomachinery Performance Analysis*; Butterworth-Heinemann: Oxford, UK, 1996.
52. Kraft, H. Reaction Tests of Turbine Nozzles for Subsonic Velocities. *Trans. ASME* **1949**, *71*, 781–787.
53. Hodson, H.P.; Dominy, R.G. The Off-Design Performance of a Low-Pressure Turbine Cascade. *J. Turbomach.* **1987**, *109*, 201–209. [CrossRef]
54. Benner, M.W.; Sjolander, S.A.; Moustapha, S.H. An Empirical Prediction Method For Secondary Losses In Turbines—Part II: A New Secondary Loss Correlation. *J. Turbomach.* **2005**, *128*, 281–291. [CrossRef]
55. Yaras, M.I.; Sjolander, S.A. Prediction of Tip-Leakage Losses in Axial Turbines. *J. Turbomach.* **1992**, *114*, 204–210. [CrossRef]
56. Farokhi, S. Analysis of Rotor Tip Clearance Loss in Axial-Flow Turbines. *J. Propuls. Power* **1988**, *4*, 452–457. [CrossRef]
57. Denton, J.D. Some Limitations of Turbomachinery CFD. Turbomachinery, Parts A, B, and C. In Proceedings of the ASME Turbo Expo 2010: Power for Land, Sea, and Air, Glasgow, UK, 14–18 June 2010; Volume 7, pp. 735–745. [CrossRef]
58. Oberkampf, W.L.; Blottner, F.G. Issues in Computational Fluid Dynamics Code Verification and Validation. *AIAA J.* **1998**, *36*, 687–695. [CrossRef]
59. Stern, F.; Wilson, R.V.; Coleman, H.W.; Paterson, E.G. Comprehensive Approach to Verification and Validation of CFD Simulations—Part 1: Methodology and Procedures. *J. Fluids Eng.* **2001**, *123*, 793–802. [CrossRef]
60. Walraevens, R.; Gallus, H. *Test Case 6: 1—1/2 Stage Axial Flow Turbine*; Technical Report, ERCOFTAC SIG on 3D Turbomachinery Flow Prediction; ERCOFTAC Turbomachinery Seminar and Workshop: Les Arcs, France, 1997.
61. Cadence/NUMECA. *FINE/Turbo 16.1 Theory Guide*; Cadence/NUMECA: Brussels, Belgium, 2021.
62. Menter, F.R.; Garbaruk, A.V.; Egorov, Y. Explicit Algebraic Reynolds Stress Models for Anisotropic Wall-Bounded Flows. *Prog. Flight Phys.* **2012**, *3*, 89–104. [CrossRef]
63. Mendenhall, W.; Beaver, R.J.; Beaver, B.M. *Introduction to Probability and Statistics*; Cengage Learning: Boston, MA, USA, 2012.
64. Horlock, J.H. *Axial Flow Turbines: Fluid Mechanics and Thermodynamics*; Butterworths: London, UK, 1973.
65. Cherry, D.; Gay, C.; Lenahan, D. *Energy Efficient Engine Low Pressure Turbine Test Hardware Detailed Design Report*; Technical Report NASA-CR-167956; General Electric Company: Washington, DC, USA, 1984.
66. Leach, K.; Thulin, R.; Howe, D. *Energy Efficient Engine: Turbine Intermediate Case and Low-Pressure Turbine Component Test Hardware Detailed Design Report*; Technical Report NASA-CR-167973; United Technologies Corporation: Washington, DC, USA, 1984.

International Journal of
Turbomachinery
Propulsion and Power

MDPI

Article

Two-Dimensional Investigation of the Fundamentals of OGV Buffeting †

Jonah Harris [1,*], Bharat Lad [2] and Sina Stapelfeldt [1]

[1] Vibration University Technology Centre, Department of Mechanical Engineering, Imperial College London, London SW7 2AZ, UK; s.stapelfeldt@imperial.ac.uk
[2] Aeromechanics Department, Rolls-Royce plc, Derby DE24 8BJ, UK; bharat.lad@rolls-royce.com
* Correspondence: j.harris18@imperial.ac.uk
† This paper is an extended version of our paper published in Proceedings of the European Turbomachinery Conference ETC14 2021, Paper No. 607, Gdansk, Poland, 12–16 April 2021.

Abstract: The increased demands of compact modern aero engine architectures have highlighted the problem of outlet guide vane (OGV) buffeting in off-design conditions. This structural response to aerodynamic excitations is characterised by increased vibration, risking structural fatigue. Investigations focused on understanding, mitigation and avoidance are therefore of high priority. OGV buffet is a type of transonic buffet caused by unsteady shock movement, but the exact parameters driving it are not fully understood. To try and understand them, this paper examines the buffet of a quasi-2D OGV geometry. Parametric studies of the incidence angle and inlet Mach number were performed. Forcing frequencies for both studies were found to be close to the experimentally detected frequency of vibration in the first bow mode, which demonstrates that buffet is driven by quasi-2D flow features. Increasing the inlet Mach number increased the dominant forcing frequency, whereas increasing the incidence yielded little change. Profiles of unsteady pressure amplitudes were shown to smoothly increase in magnitude with an increasing incidence and inlet Mach number.

Keywords: outlet guide vanes; buffeting; transonic buffet; quasi-2D

check for updates

Citation: Harris, J.; Lad, B.; Stapelfeldt, S. Two Dimensional Investigation of the Fundamentals of OGV Buffeting. *Int. J. Turbomach. Propuls. Power* **2022**, *7*, 13. https://doi.org/10.3390/ijtpp7020013

Received: 13 December 2021
Accepted: 29 March 2022
Published: 2 April 2022

Publisher's Note: MDPI stays neutral with regard to jurisdictional claims in published maps and institutional affiliations.

Copyright: © 2022 by Rolls-Royce plc. Licensee MDPI, Basel, Switzerland. This article is an open access article distributed under the terms and conditions of the Creative Commons Attribution (CC BY-NC-ND) license (https://creativecommons.org/licenses/by-nc-nd/4.0/).

1. Introduction

The pursuit of performance and efficiency in aero-engines has led to short, compressed engine architectures, with outlet guide vanes (OGVs) placed closer to the fan and downstream obstructions within the low-pressure system. This has necessitated OGVs being arranged in non-axisymmetric assemblies with individually staggered and cambered blades. Under certain off-design conditions, the aerodynamic instability, known as OGV buffet, can occur on individual blades. This results in buffeting: the structural response to the aerodynamic excitations [1]. This work was originally presented in the conference proceedings of the 14th European Conference on Turbomachinery Fluid dynamics and Thermodynamics [2]. Buffeting is suspected to be the cause of high levels of asynchronous (non-integer multiples of rotational frequency) vibrations detected in off-design tests of a large civil turbofan. The vibration occurred in the first bow mode and high amplitudes were limited to a single vane. The modal displacements in Figure 1 show that the bow mode is most susceptible to excitation at midspan, toward the trailing edge. The vibrations occurred at a high mass flow condition, where the fan was running at a fan-tip Mach number (M_{FT}) of M_{FT} = 1.14, which we will refer to as the "datum engine speed". The simulated fan constant speed characteristic of the datum engine speed is show in green in Figure 2, with the experimental buffeting region highlighted in pink. The vibrations had a reduced frequency of approximately 0.34. The reduced frequency (k) was calculated in line with Equation (1) using angular frequency (ω), OGV semi-chord (b) and mass-averaged inlet velocity (U).

$$k = \frac{\omega b}{U} \tag{1}$$

Previous work used unsteady simulations of a single passage OGV to understand the cause of OGV buffeting. 'Buffeting' refers to the structural response and is distinct to the term 'buffet', which pertains to the responsible aerodynamic excitations due to instabilities [1]. The unsteady pressure fluctuations of buffet cause these dangerous buffeting structural vibrations, which can lead to the destruction of turbomachinery blades [3].

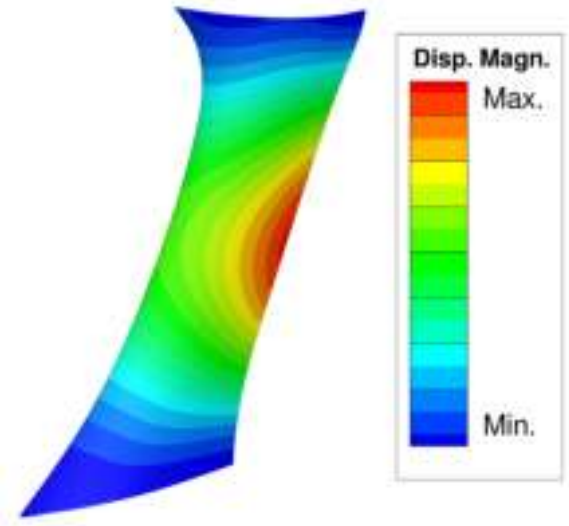

Figure 1. OGV first bow mode.

The previous study indicated that the specific instability responsible for the phenomenon in OGVs is transonic buffet [4]. Typically associated with external aerodynamics, transonic buffet is a flow instability characterised by large-scale, periodic shock motion and a fluctuating shock-induced separation, growing in phase as the shock moves forward and shrinking as it retreats [5]. Transonic buffet occurs when a strong shock-wave–boundary-layer interaction (SBLI) causes the boundary layer to thicken and separate [6]. The shock-induced separation increases in size and spreads to the trailing edge and is followed by unstable self-sustaining shock motion [1].

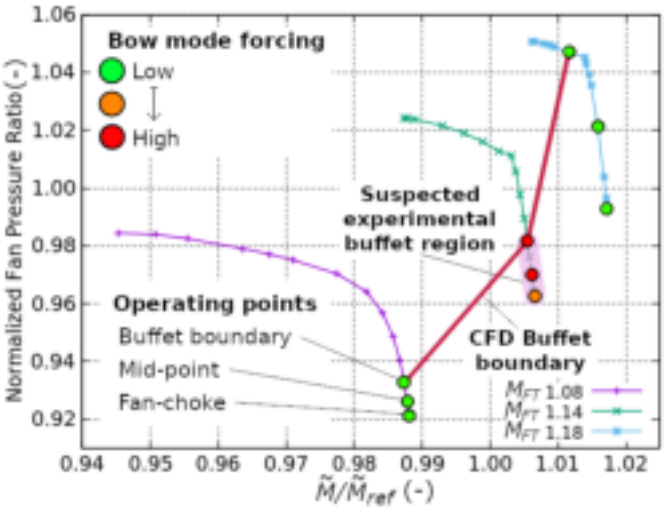

Figure 2. Engine operating map with marked OGV buffet boundary with normalised fan pressure ratio plotted against normalised mass flow rate calculated using non-dimensional mass flow rate ($\tilde{M}$) and a reference non-dimensional mass flow rate ($\tilde{M}_{ref}$).

Figure 3 shows an example flow field from a steady solution of a buffeting operating point. The previous study revealed a highly 3D phenomenon, incorporating shock movement with chordwise and radial components, a linked fluctuating separation region and substantial hub separation. Unsteady simulations produced relatively noisy forcing signals, with a dominant frequency very close to that recorded during engine testing. Importantly, the simulations showed that forcing was highest at the experimental engine speed. The simulated operating map and buffet boundary are shown in Figure 2, with buffet occurring on the choke side of the marked buffet boundary. The datum engine speed exhibited the highest amplitude forcing of the bow mode, increasing toward the buffet boundary. Despite being purely aerodynamic and without structural motion, the frequencies of the vibrations were very close to the bow mode frequency.

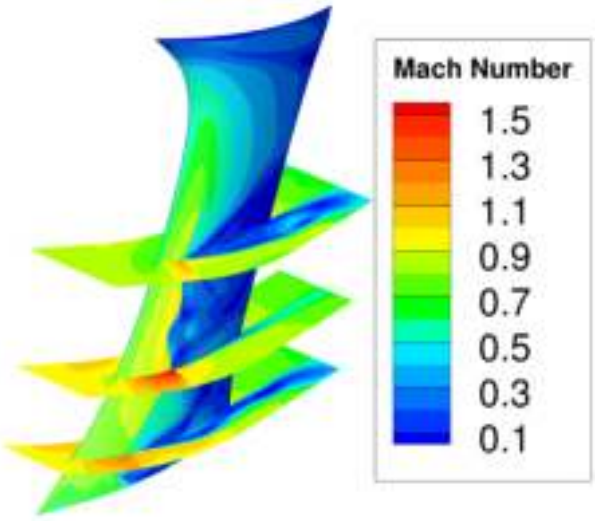

Figure 3. OGV buffeting Reynolds-averaged Navier–Stokes (RANS) simulation flow field.

Similar to the 2D supercritical airfoil experiments of Lee, our 3D simulations found that operating points closest to the buffet boundary provided the highest forcing [7]. In their paper, Lee found that fluctuating normal forces were greatest near the buffet onset and decreased moving further into the buffeting conditions. This paper sets out to achieve a more fundamental understanding of OGV buffeting by moving to a quasi-2D domain and conducting parametric studies of the inlet Mach number and incidence angle.

2. Materials and Methods

The simulations presented here were completed using the steady and unsteady Reynolds-averaged Navier–Stokes (RANS and URANS) solver AU3D. This is the in-house solver of the Imperial Vibration University Technology Centre (VUTC) created and validated for use in turbomachinery settings with aeroelastic capability developed over the last 25 years [8–10]. For this study, the RANS and URANS equations were solved using an implicit scheme that is second-order accurate in space and first-order accurate in time. Turbulence modelling was provided by a modified Spalart–Allmaras (SA) one-equation model, and all simulations were run using wall functions to treat the boundary layer. Iovnovich and Raveh show that the SA model provides a good level of accuracy in buffet simulations, with Thiery and Coustols proving it to be suitable for 2D buffet simulations [11,12]. Thiery and Coustols say that, in the case of transonic buffet, the time-scales of the wall-bounded turbulence and shock oscillations are so different that the turbulence can be left to modelling. Aerodynamic modal forcing was computed using unsteady pressure histories from the flow solver, as detailed in [13].

Figure 4 summarises the structure of the 2D domain and its origins in the low pressure system. To construct the 2D domain, the OGV airfoil section at midspan was extracted and

meshed in a Cartesian domain using the Altair program HyperMesh. The circumferential width of this slice, presented in the profile view of Figure 4, was based on the OGV pitch at midspan, terminating in y-periodic surfaces. The spanwise extent of the quasi-2D domain is 4% chord resolved with 11 mesh layers connected by structured mesh and terminating in z-periodic boundaries, as shown in Figure 4. The central 2D layer was used to extract all simulation data. The resolution and distribution of nodes in a radial slice were based on previous best practice and produced a Cartesian 2D OGV slice with approximately 20,000 nodes, down from 21,300 used in the layers of the annular 3D domain. The close-up in Figure 4 shows the construction of the unstructured airfoil mesh. Having constructed the OGV domain, a straight coarsening duct was attached approximating the length of the low pressure system. Riemann invariant inlet and outlet boundary conditions and the coarsening duct were used to eliminate numerical reflections. As marked on Figure 4, the OGV inlet surface provides total pressure, total temperature and flow angle boundary conditions, with the outlet surface of the coarsening duct setting a static pressure boundary condition. The periodic set-up meant that all unsteadiness was axisymmetric and not propagating circumferentially, but this was considered satisfactory, as engine testing data indicate that OGV buffet is a local phenomenon. An example simulation with wall functions confirmed that over 80% of node non-dimensional wall distance (y^+) values were between 12 and 100, with a mean of 48.

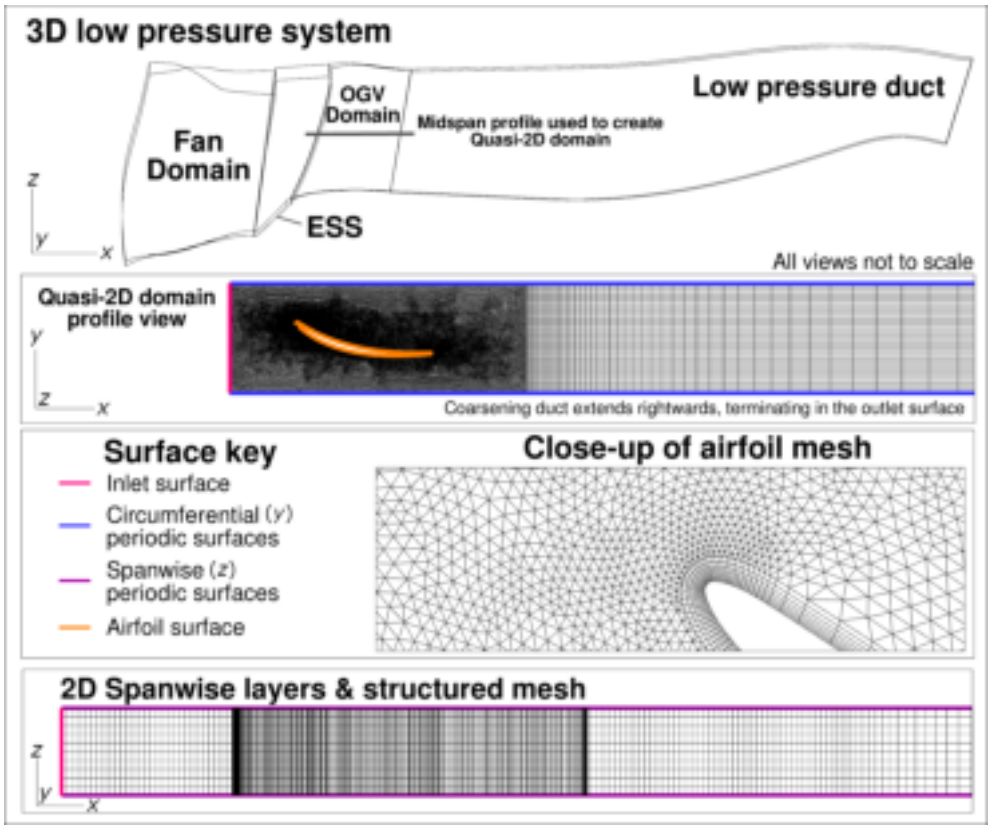

Figure 4. 3D OGV within low pressure system and translation to quasi-2D domain.

The quasi-2D domain grid was used for all steady RANS and URANS simulations. The datum boundary conditions were derived from area-averaged values for the mixing plane data from the 3D case that provided the highest amplitude forcing. This occurred at the buffet boundary of the datum engine speed. The URANS simulations of the parametric studies were started from a converged steady state RANS solution that was second order accurate in space. The URANS time-step, previously subjected to a convergence study for our 3D work, was carried over and provides a temporal resolution of 390 steps per period of experimental buffeting. Total simulation time was set to provide approximately

25 flow-throughs of the 2D domain and produced consistent results. Time histories were individually trimmed to exclude any initial transients in the following analysis.

Airfoil incidence and Mach number are known to influence transonic buffet onset and strength [7]. Therefore, the core of this paper is based on two parametric studies, varying inlet Mach number (M_{in}) with airfoil incidence (β) held constant and vice versa. Incidence was calculated as the difference between the inlet flow angle and metal angle, as shown in Figure 5. Negative incidences are common in this study due to the high axial velocities. M_{in} and β were varied by modifying the specified velocity components of the datum inlet boundary conditions by increasing their resultant magnitude, or their relative magnitude with the resultant held constant, respectively.

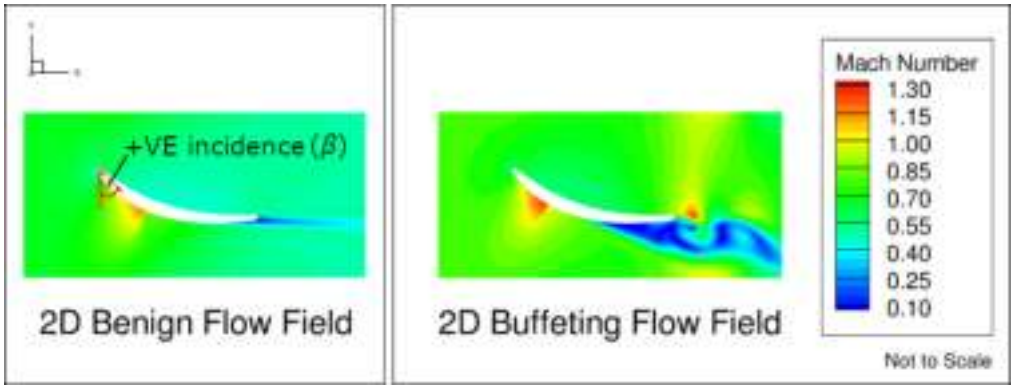

Figure 5. Two-dimensional OGV full pitch flow field examples and incidence sign convention.

For each parametric study, a range of inlet conditions were selected, with increased resolution around the datum values. These operating conditions and the initial 3D-derived datum conditions are summarised in Table 1. Not all of the parametric study operating points produced unsteady forcing, and were therefore deemed to be buffet-free; these are indicated in Table 1 but excluded from the following analysis. Two results have been totally excluded for exhibiting the "carbuncle effect", a numerical instability responsible for the appearance of a small blister-like structure in high Mach number flows [14].

Table 1. Parametric study simulation tranche summary.

Incidence β	M_{in}	OGV Buffet	M_{in}	Incidence β	Buffet
Datum −1.9°	0.721	No	Datum 0.721	−1.9°	No
−6.9°	0.721	No	0.577	−1.9°	No
−4.9°	0.721	No	0.649	−1.9°	No
−3.4°	0.721	Yes	0.667	−1.9°	No
−2.9°	0.721	Yes	0.682	−1.9°	No
−2.4°	0.721	Yes	0.707	−1.9°	No
−1.4°	0.721	Yes	0.714	−1.9°	Yes
−0.9°	0.721	Yes	0.729	−1.9°	Yes
−0.4°	0.721	Yes	0.736	−1.9°	Yes
+0.1°	0.721	Yes	0.757	−1.9°	Yes

Figure 5 shows two example full-pitch circumferential cuts of the 2D URANS flow fields of buffeting and non-buffeting (or benign) operating points. The benign flow field has a well-defined shock and minimal TE separation, whereas the buffeting operating point shows many of the characteristics of transonic buffet, including a shock that has shifted in position and a large separation stemming from the base of the shock. The size of this separation also has an effect on the free-stream by decreasing the effective passage area.

3. Results and Discussion

3.1. Forcing Frequency and Amplitude

Time histories of lift forcing were recorded for each operating point and analysed using Welch's method to produce frequency spectra of the component amplitudes. Monitoring lift was selected to allow us to focus on the 2D causes of the shock motion, which would be complicated by the 3D nature of the first bow mode varying in both span and chordwise directions. Welch's method operates by splitting the signal into segments and averaging the resulting a with a degree of windowing to reduce the effect of noise. The previous study's segment size of 4800 time-steps has been retained for reasons of accuracy and comparison.

Figure 6 presents resulting selected RMS forcing amplitudes and frequency spectra of the incidence parametric study, normalised by bow mode frequency and maximum amplitude. Only selected 2D results were pictured for reasons of clarity. The spectrum for the original 3D datum case has been included for comparison, scaled to the secondary y-axis. We can see well grouped first harmonics for each buffeting operating point sitting very close to the bow mode frequency and the 3D case. However, the 2D cases all possess clear second harmonics that are proportionally higher in amplitude than the broadband noise of the 3D case.

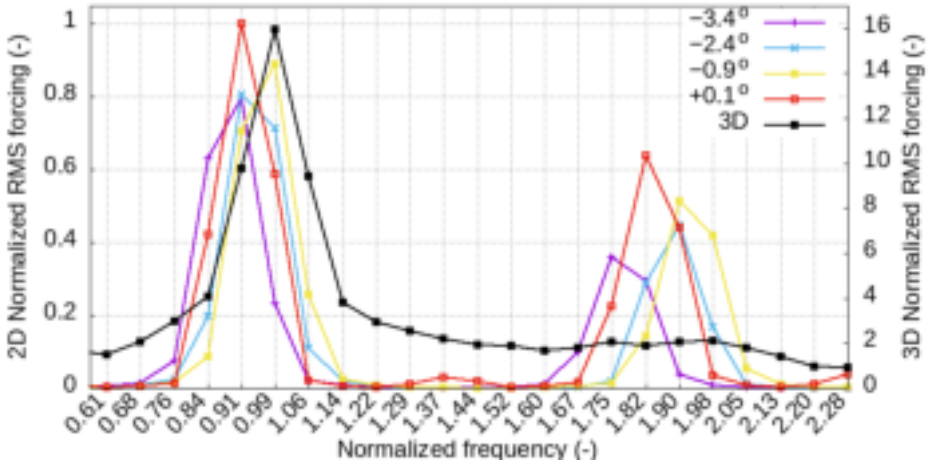

Figure 6. Parametric study forcing frequency spectra and amplitudes, varying β with constant M_{in}.

Within the 2D cases, we can see that the amplitude of the first harmonics broadly increases with β but only changes by approximately 20%, with the trend being more pronounced in the second harmonics. There is little difference in frequency between the 2D cases, limited by the normalised frequency resolution of 0.08, dictated by the chosen Welch segment size. The separation is more visible in the second harmonics, showing that the frequency increases with incidence until $-2.4°$, whereupon it remains constant before actually decreasing for $+0.1°$.

Figure 7 reproduces this analysis for the M_{in} parametric study and shows a pattern of well-grouped first harmonics slightly increasing in frequency with M_{in}. Second harmonics also increase in amplitude and frequency, rising well above the proportional 3D broadband noise. However, there is a major outlier in 0.757 M_{in} that showcases a substantially different first harmonic frequency, which is 14% higher than the bow mode frequency.

Figures 8 and 9 feature non-dimensional frequencies plotted against the varying incidence and inlet Mach number: the dominant forcing frequency, Strouhal number and an acoustic frequency. The dominant forcing frequency and the acoustic frequency are both normalised by the bow mode frequency. The Strouhal number (St) can be used to determine whether the aerodynamic unsteadiness occurs at a fixed non-dimensional frequency and is calculated in line with Equation (2), using the dominant forcing frequency (f), OGV chord (C) and two reference velocities: upstream and downstream (U). The upstream

velocity was based on the mass-averaged inlet velocity and downstream velocity on the time-averaged profile velocity at 80% chord.

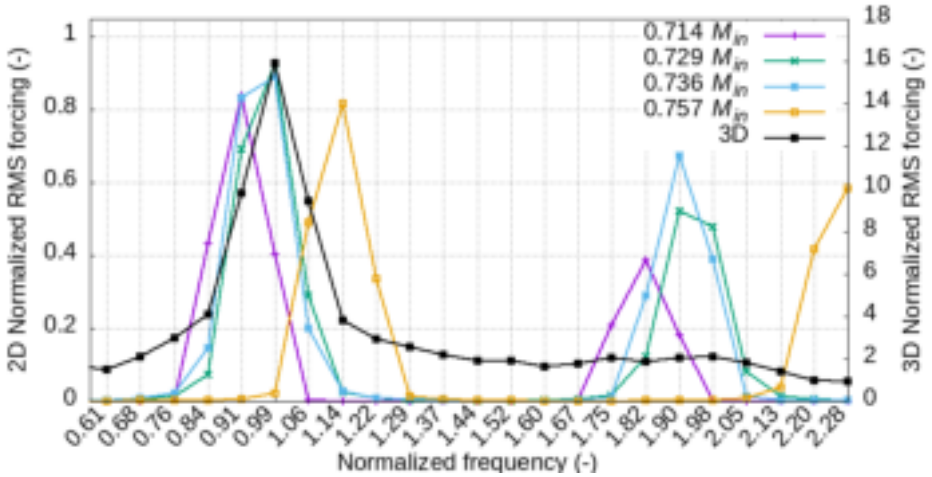

Figure 7. Parametric study forcing frequency spectra and amplitudes, varying M_{in} with constant β.

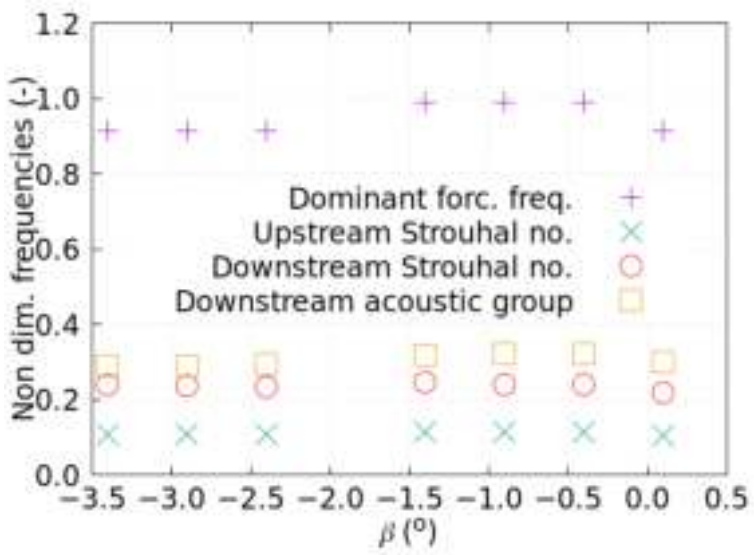

Figure 8. Parametric sweep of β, comparing dominant forcing frequency, acoustic frequency and St at different locations.

$$St = \frac{fC}{U} \tag{2}$$

Acoustic feedback mechanisms have been said to be important for self-sustained shock motion and to determine whether this is influencing OGV buffet. Figures 8 and 9 incorporate an acoustic frequency calculated using the downstream velocity to estimate the period of a wave travelling from the shock at 20% span to the TE and returning [15]. From Figure 8, we can see that the dominant forcing frequencies are reasonably flat for increasing β, whereas the sweep of M_{in} in Figure 9 produces gradually increasing dominant frequencies for increasing M_{in}. This implies that M_{in} is more important for setting the dominant forcing frequency close to the OGV bow mode, but a wide range of β produces the most consistently dangerous frequencies. For both studies, the Strouhal number trends mirror the dominant forcing frequencies but remain relatively consistent, with upstream and downstream Strouhal numbers holding values of approximately 0.1 and 0.24, respectively, albeit with a minor up-tick in the upstream Strouhal number at higher Mach numbers. This consistency indicates a common underlying convective non-dimensional frequency.

Figures 8 and 9 show that downstream acoustic frequencies follow similar trends to the dominant forcing frequencies, but at approximately one third of the magnitude, indicating that acoustic feedback may not have a significant bearing on the OGV shock motion.

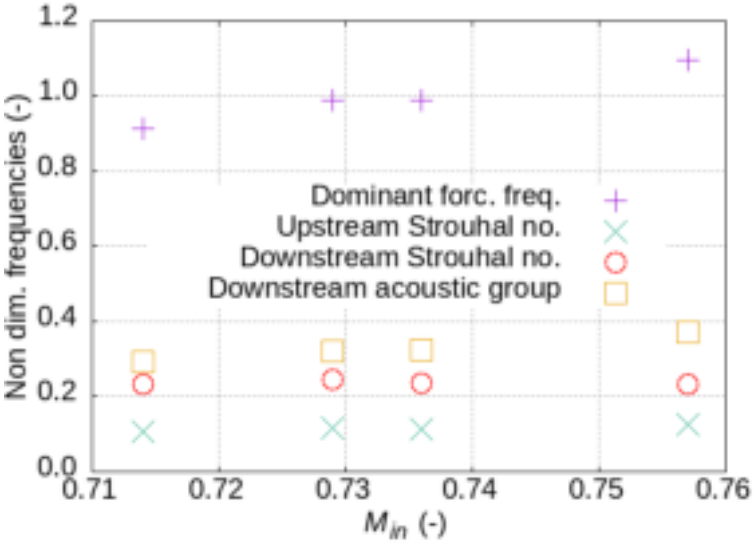

Figure 9. Parametric sweep of M_{in}, comparing dominant forcing frequency, acoustic frequency and *St* at different locations.

3.2. Time-Averaged Mach Number

To identify the changes in the flow field responsible for the trends seen above, the profiles of the time-averaged isentropic Mach number were calculated from the time histories of surface pressure for the central mesh layer. Figure 10 shows profiles of the time-averaged Mach number for an increasing incidence. As could be expected for a study where the inlet velocity magnitude was held constant, there is very little change in the overall trend, with each condition possessing a similarly smeared shock, denoting movement. There is a small forward movement of the peak The Mach number location with increasing incidence was accompanied by a small decrease in size. The higher incidences also possess higher Mach numbers toward the trailing edge.

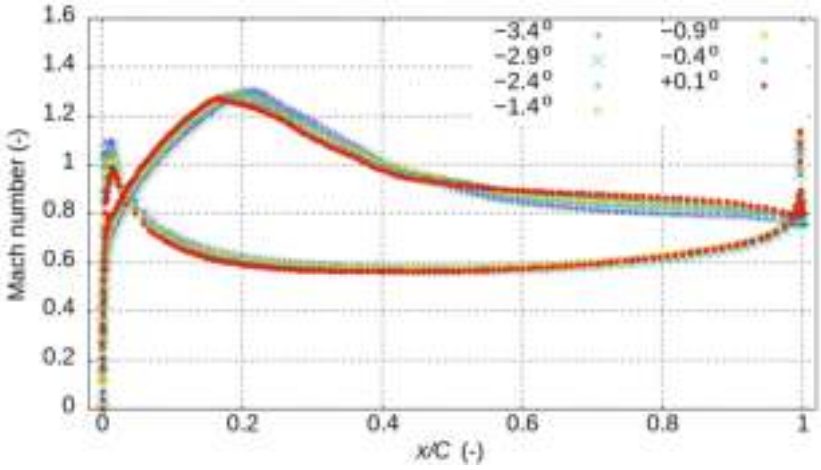

Figure 10. Midspan time-averaged isentropic Mach number profiles for varying β at buffeting operating points.

Turning to Figure 11, an increasing M_{in} gives a similar trend of a forward moving peak, but with a higher sustained Mach number toward the trailing edge for 0.757 M_{in}. However,

an increasing M_{in} also increases the leading edge pressure surface peak, as opposed to the decrease seen in Figure 10 for an increasing incidence. This is due to negative incidences providing more acceleration around the leading edge.

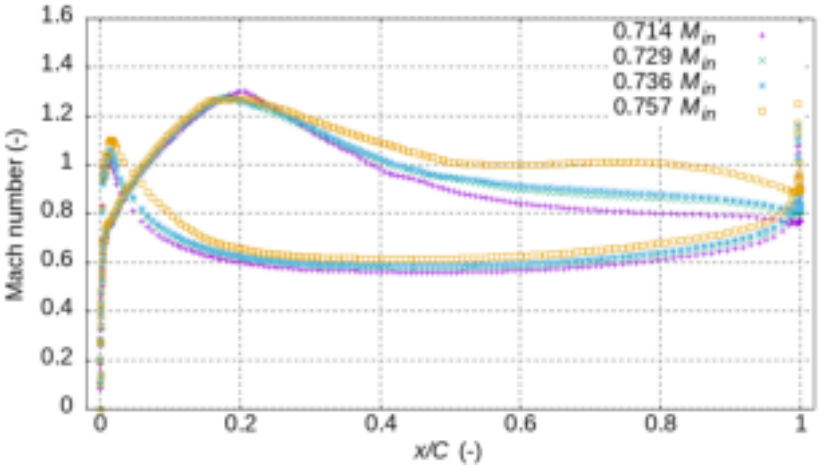

Figure 11. Midspan time-averaged isentropic Mach number profiles for varying M_{in} at buffeting operating points.

3.3. Unsteady Pressure Distribution

Figure 12 presents full pitch circumferential flow examples for two time steps from four operating points: -3.4° , -0.4°, 0.714 M_{in} and 0.736 M_{in}, showing the progression of buffet in both studies. The snapshots on the left were chosen to show different aspects of flow separation, and those on the right were chosen for their shock strength. All of the separations feature recirculation zones in various stages of creation and ejection. All four cases also experience passage choke when the pressure and suction surface shocks join. However, -0.4° and 0.736 M_{in} feature shocks were able to move further rearward, have stronger stagnation point shocks and more dramatic shock-wave–boundary-layer interactions on their suction surfaces and went on to exhibit higher unsteady pressure amplitudes. It should be noted that, although only -0.4° shows pressure surface separation, this was at least briefly present in all cases.

Time histories of surface pressure for the central mesh layer were Fourier-decomposed to calculate unsteady pressure amplitudes in the dominant frequency of each operating point. The plots in Figures 13 and 14 graph unsteady pressure amplitudes, non-dimensionalised by dynamic pressure, against the chordwise location for both the suction and pressure surfaces against β. Starting with the baseline of -3.4°, we can see a large primary suction peak due to a shock movement at approximately 35% span (15% further aft than peak average Mach number location) and a small secondary peak at 45% span. Lee observed similar secondary peaks due to separation bubbles similar to the recirculation zones identified in Figure 12 [7]. A gradual increase in unsteady pressure amplitudes towards the TE can be attributed to the trailing edge separation [7].

As the incidence increases, the primary peak grows, moves forward and absorbs the secondary peak as the shock displacement grows; this is accompanied by a steady rise in the TE separation fluctuations. An operating point of -0.4° is the only operating point to buck this trend by not providing a distinct increase in the peak and TE separation amplitude. Examining Figure 13, the absorption of a second peak with an increasing incidence seems to be due to the increase in shock strength and movement masking the effect of any recirculation zones. For the pressure surface, as the incidence increases, we see increased amplitudes at the stagnation point and two minor peaks consolidating into one. Analyses of complete time histories reveal this to be caused by the passage-choking pressure surface shock dividing in two as it shrinks. The effect is lessened at higher incidences, as one half becomes substantially stronger and overwhelms the other. This increase in the

peak suction and pressure surface unsteadiness with incidence runs counter to the trend of a decreasing peak average Mach number. However, the locations are clearly linked, with the time-averaged suction surface peak Mach number location and peak unsteadiness moving forward with an increasing incidence. The higher unsteady amplitudes towards the trailing edge also correlate with higher time-averaged Mach numbers.

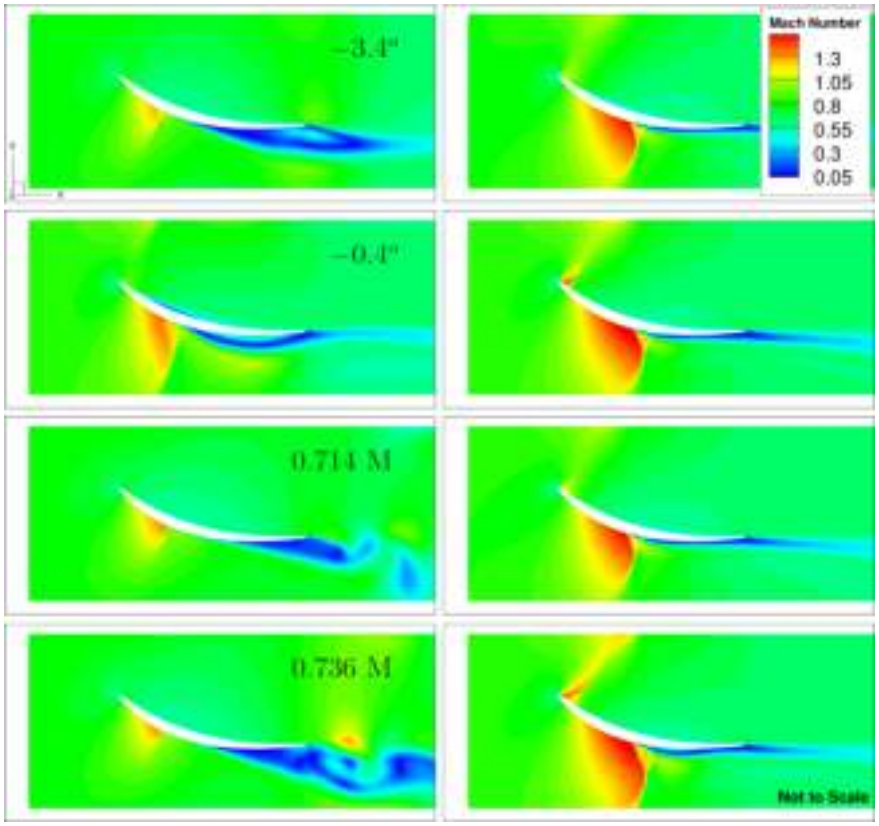

Figure 12. Instantaneous full-pitch midspan unsteady flow fields of interest.

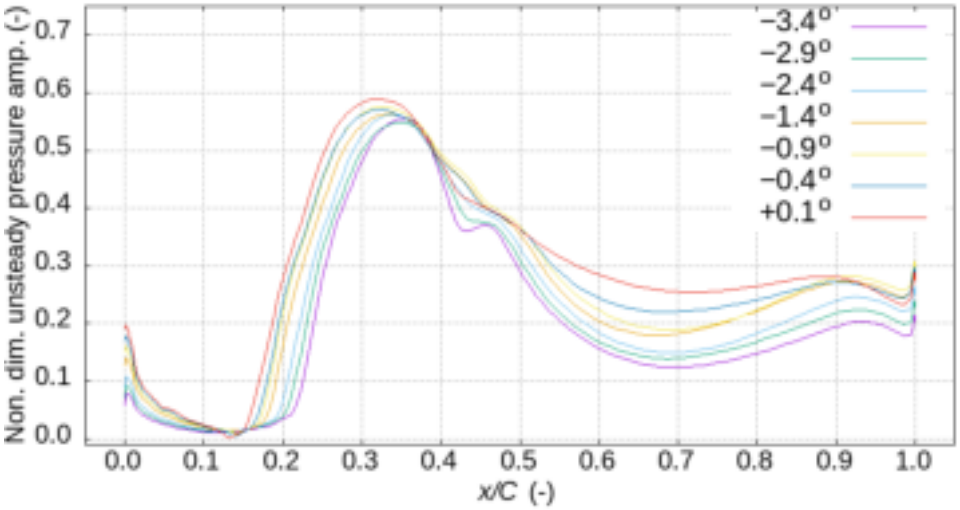

Figure 13. Profiles of Fourier-decomposed unsteady pressure amplitudes on the OGV suction surface for varying β.

Figures 15 and 16 show similar behaviour for varying M_{in}, with the only slight difference being that the peak unsteady amplitude location moves aft with increasing M_{in}, in contrast to the peak average Mach number, which moves forward. In both parametric

studies, the broadening of the unsteady amplitude peaks with an increasing inlet Mach number and incidence can be interpreted as an increase in the range of shock motion.

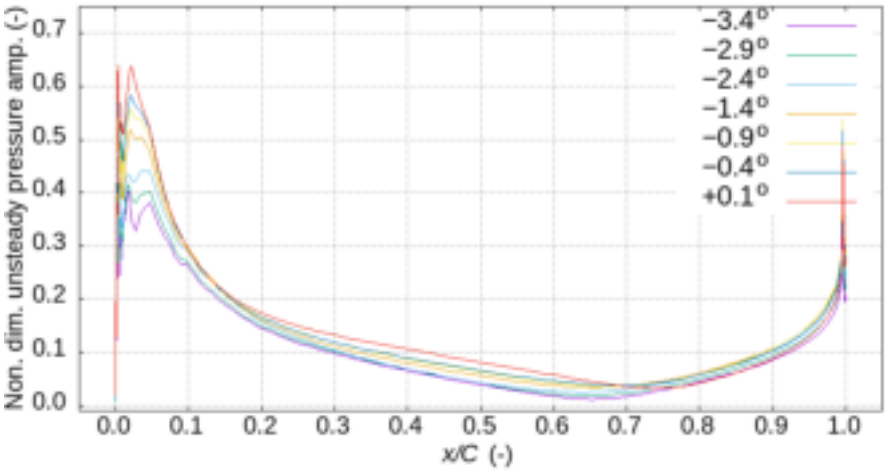

Figure 14. Profiles of Fourier decomposed unsteady pressure amplitudes on the OGV pressure surface for varying β.

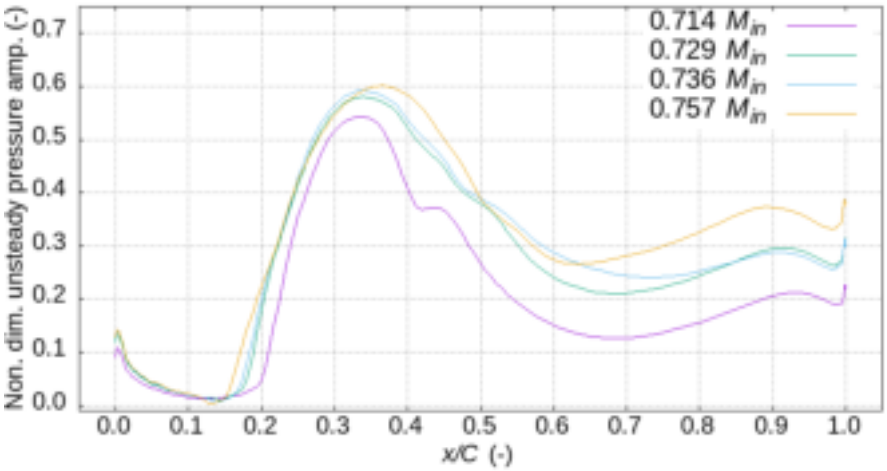

Figure 15. Profiles of Fourier-decomposed unsteady pressure amplitudes on the OGV suction surface for varying M_{in}.

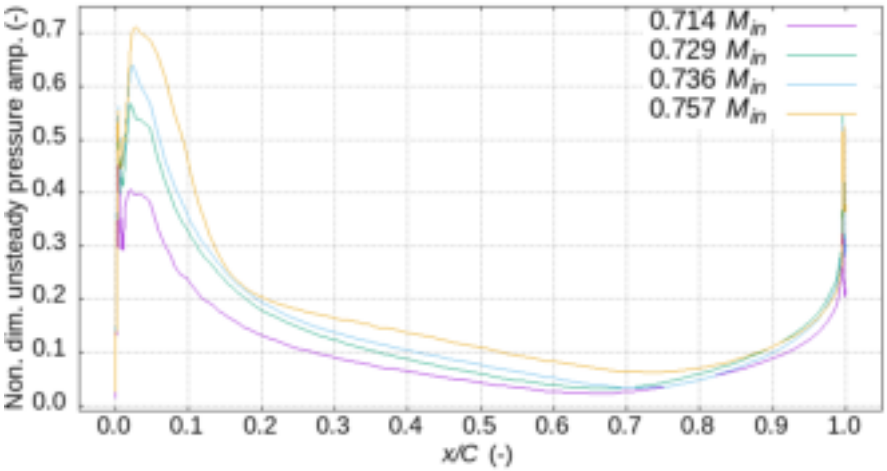

Figure 16. Profiles of Fourier-decomposed unsteady pressure amplitudes on the OGV pressure surface for varying M_{in}.

Figures 17 and 18 plot the maximum suction surface unsteady pressure amplitude (normalised by the maximum value across both studies) against varying β and M_{in}. Increasing the inlet Mach number increases the unsteady pressure amplitude at a much greater rate than increasing the incidence within the span of these studies. The trends appear approximately linear in the data ranges available. The fact that we also know that peak average Mach number tends to decrease with the incidence and inlet Mach number infers that these trends of increasing peak unsteadiness are due to increased shock movement and not changes in shock strength. This is corroborated by both incidence and inlet Mach number increases resulting in wider peaks of unsteady pressure on the suction surface, indicating a larger shock movement. Correspondingly, larger changes in the unsteady pressure downstream of the shock towards the trailing edge indicate that the forcing in the bow mode, which has a large displacement toward the trailing edge, will increase with a larger shock movement.

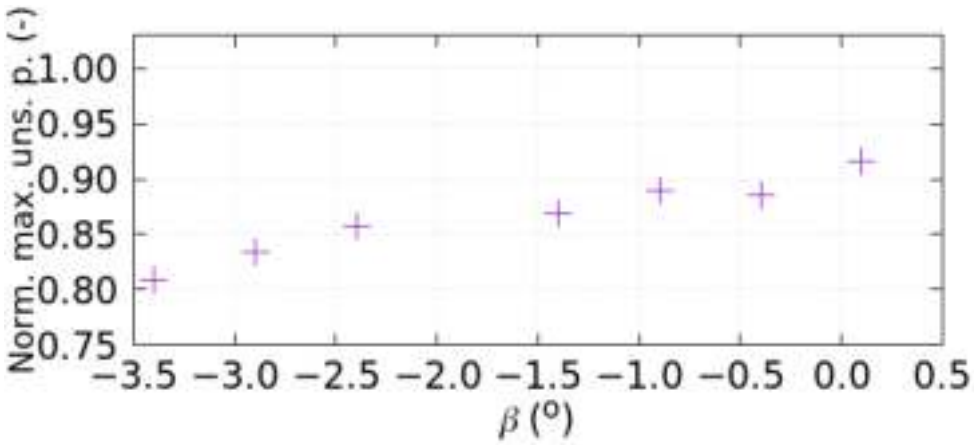

Figure 17. Comparing effect of varying β on maximum Fourier-decomposed unsteady pressure amplitudes.

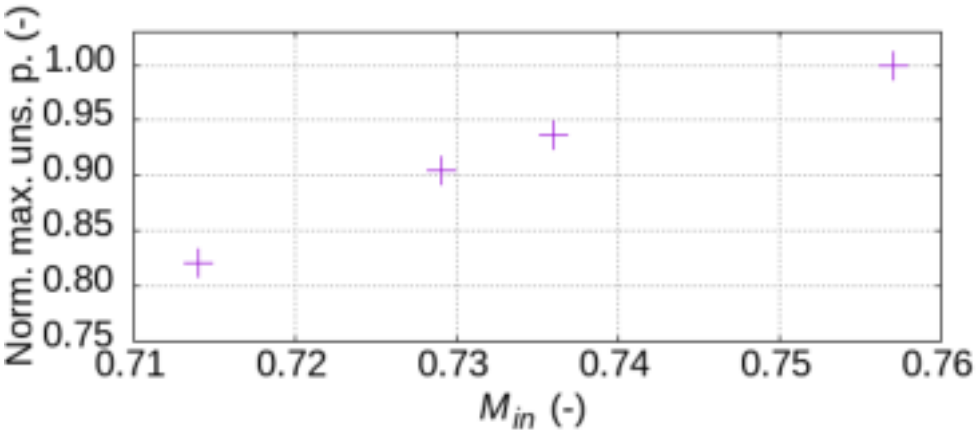

Figure 18. Comparing effect of varying M_{in} on maximum Fourier-decomposed unsteady pressure amplitudes.

4. Conclusions

In this study, the buffet phenomenon observed on an OGV was reproduced on a quasi two-dimensional geometry. The frequency of the 2D phenomenon was very close to that measured on the 3D geometry. This demonstrates that buffet is not driven by highly three-dimensional flow features but by a quasi-2D shock instability. Parametric studies and varying the incidence and inlet Mach number found that an increasing incidence produced more consistent dominant frequencies nearer the bow mode frequency than an

increasing inlet Mach number. The buffeting flow fields were also observed to produce consistent Strouhal numbers across both studies. The studies produced smooth trends of time-averaged Mach numbers, with the maximum average Mach number moving forward and decreasing in magnitude with increasing β and M_{in}. The unsteady pressure amplitude trends were also smooth, increasing in magnitude with both the incidence and inlet Mach number. Secondary peaks, increased TE fluctuations and pressure surface LE peaks were linked to recirculation zones, TE separations and twin LE shocks, respectively.

Author Contributions: Conceptualisation, J.H., B.L. and S.S.; methodology, J.H.; software, J.H., B.L. and S.S.; validation, J.H.; formal analysis, J.H.; investigation, J.H.; resources, S.S. and B.L.; data curation, J.H.; writing—original draft preparation, J.H.; writing—review and editing, J.H. and S.S.; visualisation, J.H.; supervision, S.S. and B.L.; project administration, J.H. and S.S.; funding acquisition, S.S. and B.L. All authors have read and agreed to the published version of the manuscript.

Funding: This research was supported by Rolls-Royce plc and an EPSRC iCASE studentship (iCASE Ref 18000163).

Data Availability Statement: The data in this report are subject to copyright by Rolls-Royce plc and therefore have been presented here in normalised and non-dimensional formats and are unavailable for external distribution, but the corresponding author is very happy to further discuss the implications of the simulations and results.

Acknowledgments: The authors would once again like to thank Rolls-Royce, Imperial College VUTC and Department of Mechanical Engineering for their continued support.

Conflicts of Interest: The results presented here are only possible through the provision of technical resources by Rolls-Royce plc and, as such, have also been passed through them for copyright approval.

Abbreviations

The following abbreviations are used in this manuscript:

OGV	Outlet guide vane
RANS	Reynolds-Averaged Navier-Stokes
URANS	Unsteady Reynolds-Averaged Navier-Stokes
LE	leading edge
TE	trailing edge

References

1. Caruana, D.; Mignosi, A.; Robitaillie, C.; Correge, M. Separated Flow and Buffeting Control. *Flow Turbul. Combust.* **2003**, *71*, 221–245. [CrossRef]
2. Harris, J.; Lad, B.; Stapelfeldt, S. Two Dimensional Investigation of the Fundamentals of OGV Buffeting. ETC. 2021. Available online: https://www.euroturbo.eu/publications/proceedings-papers/etc2021-607 (accessed on 13 December 2021).
3. Jacquin, L.; Molton, P.; Deck, S.; Maury, B.; Soulevant, D. Experimental Study of Shock Oscillation over a Transonic Supercritical Profile. *AIAA J.* **2009**, *47*, 1985–1994. [CrossRef]
4. Harris, J.R.; Lad, B.; Stapelfeldt, S. Investigating the Causes of Outlet Guide Vane Buffeting. In Proceedings of the ASME Turbo Expo 2020, Virtual, 21–25 September 2020; Volume 84218.
5. Babinsky, H.; Harvey, J.K. *Shock Wave-Boundary-Layer Interactions*; Cambridge University Press: Cambridge, UK, 2011; p. 461.
6. Crouch, J.D.; Garbaruk, A.; Magidov, D.; Travin, A. Origin of transonic buffet on aerofoils. *J. Fluid Mech.* **2009**, *628*, 357–369. [CrossRef]
7. Lee, B.H.K. Transonic buffet on a supercritical aerofoil. *Aeronaut. J. (1968)* **1990**, *94*, 143–152.
8. Vahdati, M.; Sayma, A.I.; Imregun, M. An Integrated Nonlinear Approach for Turbomachinery Forced Response Prediction. Part II: Case Studies. *J. Fluids Struct.* **2000**, *14*, 103–125. [CrossRef]
9. Dodds, J.; Vahdati, M. *Rotating Stall Observations in a High Speed Compressor Part 2: Numerical Study*; American Society of Mechanical Engineers (ASME): New York, NY, USA, 2014; Volume 2D. [CrossRef]
10. Stapelfeldt, S.; Vahdati, M. Improving the Flutter Margin of an Unstable Fan Blade. *J. Turbomach.* **2019**, *141*, 071006. [CrossRef]
11. Iovnovich, M.; Raveh, D.E. Reynolds-Averaged Navier-Stokes Study of the Shock-Buffet Instability Mechanism. *AIAA J.* **2012**, *50*, 880–890. [CrossRef]
12. Thiery, M.; Coustols, E. URANS computations of shock-induced oscillations over 2D rigid airfoils: Influence of test section geometry. *Flow Turbul. Combust.* **2005**, *74*, 331–354. [CrossRef]

13. Sayma, A.I.; Vahdati, M.; Imregun, M. An Integrated Nonlinear Approach for Turbomachinery Forced Response Prediction. Part I: Formulation. *J. Fluids Struct.* **2000**, *14*, 87–101. [CrossRef]
14. Garicano-Mena, J.; Lani, A.; Deconinck, H. An energy-dissipative remedy against carbuncle: Application to hypersonic flows around blunt bodies. *Comput. Fluids* **2016**, *133*, 43–54. [CrossRef]
15. Lee, B.H. Self-sustained shock oscillations on airfoils at transonic speeds. *Prog. Aerosp. Sci.* **2001**, *37*, 147–196. [CrossRef]

International Journal of
Turbomachinery
Propulsion and Power

MDPI

Article

Flow in Pillow-Plate Channels for High-Speed Turbomachinery Heat Exchangers

Stephan Sundermeier [1], Maximilian Passmann [2], Stefan aus der Wiesche [1,*] and Eugeny Y. Kenig [3]

[1] Department of Mechanical Engineering, University of Applied Sciences, 48565 Steinfurt, Germany; stephan.sundermeier@fh-muenster.de
[2] Chair of Hydraulic Fluid Machinery, Ruhr University Bochum, Universitätsstraße 150, 44801 Bochum, Germany; maximilian.passmann@ruhr-uni-bochum.de
[3] Chair of Fluid Process Engineering, Paderborn University, 33098 Paderborn, Germany; eugeny.kenig@upb.de
* Correspondence: wiesche@fh-muenster.de; Tel.: +49-02551-9-62272

Abstract: In numerous turbomachinery applications, e.g., in aero-engines with regenerators for improving specific fuel consumption (SFC), heat exchangers with low-pressure loss are required. Pil low-plate heat exchangers (PPHE) are a novel exchanger type and promising candidates for high-speed flow applications due to their smooth profiles avoiding blunt obstacles in the flow path. This work deals with the overall system behavior and gas dynamics of pillow-plate channels. A pillow-plate channel was placed in the test section of a blow-down wind tunnel working with dry air, and compressible flow phenomena were investigated utilizing conventional and focusing schlieren optics; furthermore, static and total pressure measurements were performed. The experiments supported the assumption that the system behavior can be described through a Fanno–Rayleigh flow model. Since only wavy walls with smooth profiles were involved, linearized gas dynamics was able to cover important flow features within the channel. The effects of the wavy wall structures on pressure drop and Mach number distribution within the flow path were investigated, and a good qualitative agreement with theoretical and numerical predictions was found. The present analysis demonstrates that pressure losses in pillow-plate heat exchangers are rather low, although their strong turbulent mixing enables high convective heat transfer coefficients.

Keywords: heat transfer; gas dynamics; aero-engines; ORC power systems; pillow-plate; Fanno–Rayleigh flow; compressible flow phenomena; schlieren photography

check for updates

Citation: Sundermeier, S.; Passmann, M.; aus der Wiesche, S.; Kenig, E.Y. Flow in Pillow-Plate Channels for High-Speed Turbomachinery Heat Exchangers. *Int. J. Turbomach. Propuls. Power* **2022**, *7*, 12. https://doi.org/10.3390/ijtpp7020012

Academic Editor: Francesco Montomoli

Received: 13 December 2021
Accepted: 22 February 2022
Published: 22 March 2022

Publisher's Note: MDPI stays neutral with regard to jurisdictional claims in published maps and institutional affiliations.

Copyright: © 2022 by the authors. Licensee MDPI, Basel, Switzerland. This article is an open access article distributed under the terms and conditions of the Creative Commons Attribution (CC BY-NC-ND) license (https://creativecommons.org/licenses/by-nc-nd/4.0/).

1. Introduction

The outflow velocity level of thermal turbomachinery is typically rather high. This high-velocity level can cause substantial exergy losses in subsequently placed heat exchangers, because traditionally, heat exchangers are not designed for high-speed flows. For instance, the layout of a steam power plant is largely affected by exhaust losses due to the combination of a low-pressure steam turbine with a high Mach number exhaust flow and a condenser, as discussed in detail by aus der Wiesche and Joos [1]. In the case of gas turbines, the thermodynamic benefits of cycles with intercoolers and regenerators are well-known, but this approach is characterized by significant pressure losses in the heat exchangers which makes their use in large power plants challenging. In the case of aero engines, an interesting way to improve the specific fuel consumption is to add a regenerator, but this is normally not performed with gas turbines used for propulsion because of the added weight. One exception was the early Allison T78 turboprop engine, shown in Figure 1, which was an attempt to build an engine with much lower fuel consumption at partial power [2–4]. Today, the reduction in gas turbine-specific fuel consumption using heat exchangers is becoming a topic with increasing importance. In organic Rankine cycle (ORC) power systems, it is usual to add a heat exchanger directly after the ORC turbine to preheat the working fluid, as illustrated by an example shown in Figure 2. Currently, regarding the

regenerator, that approach is extremely disadvantageous because the hot exhaust vapor flow is typically transonic or even supersonic due to the low speed of sound of organic vapors. Hence, significant exergy losses result which reduce the total cycle efficiency [5].

Figure 1. Cutaway of the Allison T78 turboprop engine with a regenerator by Allison Engine Company, adapted from [6]. The regenerator is situated aft of the turbine to minimize the frontal area.

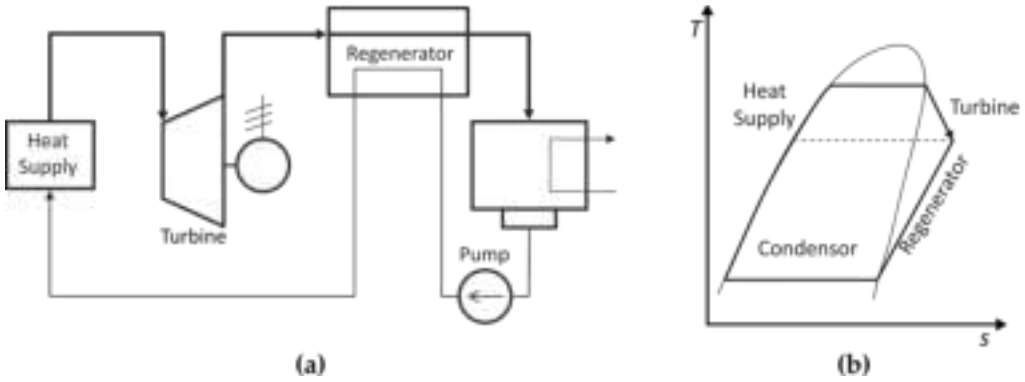

Figure 2. Organic Rankine cycle (ORC) with regenerator after the turbine: (**a**) cycle layout; (**b**) process in *T*,*s* diagram.

In all the cases discussed above, the use of a transonic or supersonic flow heat exchanger with low-pressure losses and high convective heat transfer coefficients would be very attractive. Any heat exchanger design based on blunt bodies, such as tubes placed in the high-speed crossflow, would lead to substantial shock losses. An interesting technical solution to that problem might be provided by the use of pillow-plate devices. Pillow-plate heat exchangers (PPHE) are a novel heat exchanger type based on a wavy pillow-like plate geometry, as shown schematically in Figure 3.

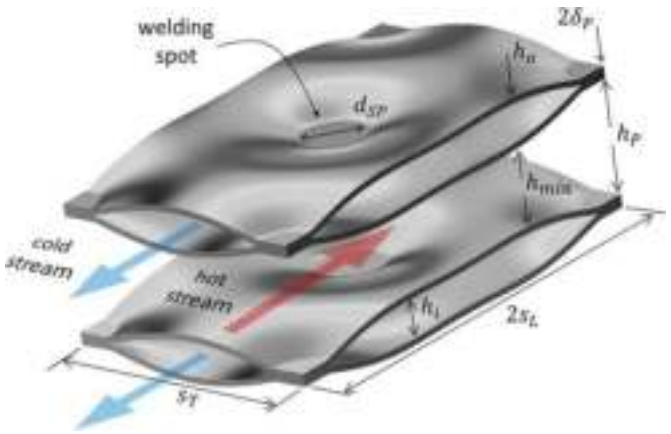

Figure 3. Illustration of a pillow-plate heat exchanger (adapted from Piper et al. [6]).

Typically, PPHE are composed of parallel plates arranged as a stack [7]). One flow path of a PPHE can be designed as a smooth, wavy wall-bounded channel. The smooth changes in the channel profile help to reduce pressure losses. Furthermore, it is known from low-speed flow applications that the convective heat transfer coefficients are comparatively high due to the mixing effect at the welding spots working as heat transfer, increasing dimples in the hot stream path [8].

In the past, low-speed flows in pillow-plate heat exchangers were investigated in detail (see, for instance, [7–9]). The first discussion of high-speed flow phenomena in pillow-plate channels was proposed recently by Passmann et al., who presented computational fluid dynamics (CFD) results for an adiabatic pillow-plate channel flow [10]. These results qualitatively supported the analytical prediction that this type of flow could be under stood as a kind of Fanno flow. The conclusion that high-speed flows in pillow-plate channels would be described by a quasi-one-dimensional compressible flow model with friction and heat transfer (Fanno–Rayleigh flow) has significant implications for the system behavior, i.e., the operation performance of a combined turbine-heat exchanger device.

This will be pointed out in the following section in more detail. Furthermore, the outcome of an experimental study is used to confirm the validity of the proposed Fanno–Rayleigh flow model. This experimental investigation enables detailed insight into high-speed flow phenomena occurring in pillow-plate channels, and the data validated the CFD analysis method employed by Passmann et al. [10].

2. One-Dimensional Fanno–Rayleigh Flow Model

In turbomachinery design processes, a mean line analysis is typically performed at the beginning and provides relevant information for more detailed analyses. In the present case, the considered turbomachinery and the hot gas flow through a pillow-plate heat exchanger establish the technical system for which an essentially one-dimensional compressible flow analysis has to be conducted. Such a configuration is shown schematically in Figure 4, where the turbine is simplified through an equivalent nozzle which creates the inflow conditions (index 1) for the pillow-plate channel. The exit station of the pillow-plate channel is denoted by index 2, and its stream-wise coordinate is denoted by x. The lateral coordinates would be y and z. Although an actual turbine is not a passive nozzle, for the present purpose this simplification is sufficient because the overall characteristic of a high-speed turbine performance is well-approximated by a choking mass flow behavior, similar to a nozzle, as discussed by Dixon and Hall [11] or Horlock [12]. The flow with friction (characterized by the friction factor f) in the pillow-plate channel is subjected to external heat addition or heat loss (denoted by the symbol q).

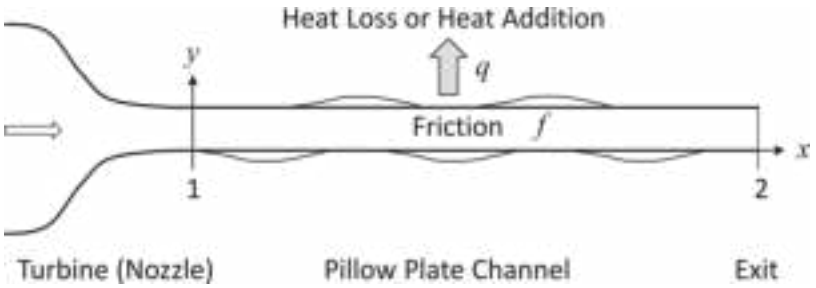

Figure 4. Schematics of the considered system with turbine and pillow-plate heat exchanger.

Due to the general balance equations, all possible flow states occurring in the pillow-plate channel are on a Fanno–Rayleigh flow line in the T,s diagram for a given mass flow rate. The lines for ideal Fanno flow and ideal Rayleigh flow are plotted schematically in Figure 5. Without friction but with heat transfer, the possible flow states would be described by the Rayleigh flow line in Figure 5. Cooling processes would move the flow states away from the point $M = 1$ with maximum entropy s. In the case of subsonic flow (entry Mach number $M_1 < 1$), lower exit Mach numbers would result due to cooling, whereas in the

case of supersonic flow (entry Mach number $M_1 > 1$), the Mach number would increase due to cooling. For the supersonic branch of the Rayleigh line, a shock could occur in the cooling channel leading to a subsonic flow state, as sketched in Figure 5 (see John and Keith [13]). The condition for that shock is given at the common point of the Fanno and the Rayleigh flow lines (at the given mass flow rate).

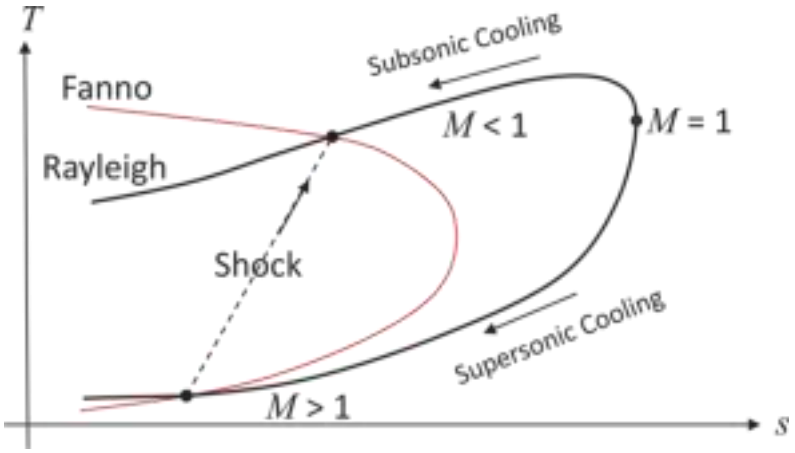

Figure 5. Schematics of Fanno and Rayleigh flow lines in the *T*,*s* diagram.

Considering the fundamental balance equations for an arbitrary control volume along the mean-stream coordinate x, the following Fanno–Rayleigh flow equation, including channel cross-section area changes, friction, and heat transfer, can be derived for an ideal gas with isentropic exponent γ:

$$\frac{dM}{dx} = \frac{M}{1-M^2}\left[\left(1+\frac{\gamma-1}{2}M^2\right)\left(\frac{1}{A}\frac{dA}{dx}+\frac{1}{2}\gamma M^2\frac{f}{D}\right)+\frac{1+\gamma M^2}{2}\frac{1}{c_pT}\frac{dq}{dx}\right] \quad (1)$$

In Equation (1), A denotes the effective cross-section area of the pillow-plate channel with D as the hydraulic diameter. The friction factor f is defined using the wall shear stress τ_ω by $f = 8\tau_\omega/(\rho c^2)$. In the case of fully turbulent pillow-plate channel flow, a relationship between the friction factor f and the heat transfer coefficient h exists due to Reynold's analogy [13]. The heat transfer term in Equation (1) can be evaluated explicitly for a specific thermal boundary condition. For instance, in the case of a constant wall heat rate, the heat transfer term can be expressed as a function of the total temperature T_0 which is a function of the Mach number M due to the isentropic condition.

For a pillow-plate channel, see Figure 3, the area term $A^{-1}dA/dx$ in Equation (1) is periodic and rather small due to the smooth profiles with its moderate relative area changes. Hence, the overall behavior of the system might be expressed qualitatively by the Fanno–Rayleigh flow without area changes. Skipping the area term in Equation (1) and neglecting heat transfer, it is a straightforward task to obtain the choking limit of the system. Integrating the resulting equation from $x = 0$ (the entry with entry Mach number M) and as suming the choking limit $M = 1$ at the end of the pillow-plate channel at $x = L$, a relationship between the entry Mach number and the length L of the pillow late channel results:

$$\frac{fL}{D} = \frac{\gamma+1}{2\gamma}\ln\left(\frac{(\gamma+1)M^2/2}{1+(\gamma-1)M^2/2}\right)-\frac{1}{\gamma}\left(1-\frac{1}{M^2}\right) \quad (2)$$

Equation (2) relates the pillow-plate channel length L and the entry Mach number M for achieving choking conditions at the exit of the channel. For instance, in the case of $\gamma = 1.4$, the limiting value $fL/D = 0.8215$ results for $M \to \infty$. This means that in the case of supersonic inflow, the maximum length L of an adiabatic pillow-plate channel might

be rather small in terms of D/f (however, the friction factor f for supersonic flow past smooth boundaries is of order $f = 0.02$, and hence the maximum length L might be many times the hydraulic diameter D).

The choking condition at the end of a long pillow-plate channel governs the maximum mass flow rate through the system. Due to additional cooling, the maximum mass flow rate can be increased, but in the case of heating, the heat supply leads to a stronger choking effect which reduces the maximum theoretical length. Then, a longer pillow-plate channel would lead to a reduction in the mass flow rate. These mechanisms have important consequences for the turbine exit state (exhaust pressure) and the turbine mass flow rate. The addition of the pillow-plate heat exchanger tends to reduce the mass flow rate through the entire system, and the design of the turbine would be directly affected by the choking effect of the Fanno–Rayleigh flow due to its impact on the resulting pressure distribution.

Although the above discussion (i.e., Figure 5 and Equations (1) and (2)) considers explicitly a perfect gas, the main physical mechanism may be assumed for a non-ideal gas or an organic vapor at least in the dilute gas regime, too. Then, the isentropic exponent γ would be replaced with a generalized exponent (see, for instance, Kouremenos and Antonopoulos [14]).

3. Linearized Gas Dynamics and Pillow-Plate Channel Flows

In addition to the above one-dimensional model for compressible flow with friction and heat transfer, valuable information about the bulk flow velocity and pressure distribution within the pillow-plate channel can be obtained through linearized gas dynamics. The linearization of the gas dynamical governing equations is a powerful method in the case of smooth profiles and inviscid flow because analytical results and certain relationships between the flow variables can be derived [13]. In linearized gas dynamics, it is usual to express the velocity field as a sum of a main, uniform velocity, U, and a perturbation velocity field which can be calculated from a velocity potential φ. Wavy-wall effects on the resulting flow are included in the perturbation velocity potential φ. This perturbation velocity potential φ can be calculated by solving the (subsonic) perturbation equation.

$$\left(1 - M_\infty^2\right)\frac{\partial^2 \phi}{\partial x^2} + \frac{\partial^2 \phi}{\partial y^2} + \frac{\partial^2 \phi}{\partial z^2} = 0 \tag{3}$$

In Equation (3), M_∞ is the local Mach number of the undisturbed main flow (with velocity U) in the channel center at $z = H/2$ (with channel height H) which is a function of the streamwise coordinate x.

3.1. Coherent Pressure Oscillations

The perturbation potential depends on the boundary conditions which are prescribed by the wall surface elevation function z_w. In the case of pillow plates, the periodic wall-surface elevation function z_w can be expressed utilizing double Fourier series with modes $z_{w,xy} = \varepsilon_{xy} \sin(k_x x) \sin(k_y y)$. Due to the linear character of the perturbation Equation (3), each elevation mode can be considered separately and the final solution of φ can be calculated as the sum of modes.

$$\phi_{xy} = \frac{U k_x \varepsilon_{xy}}{k_{xy}} \cos(k_x x) \sin(k_y y) \left(\frac{\exp(-k_{xy} z)}{\exp(-2k_{xy} H) - 1} - \frac{\exp(k_{xy} z)}{\exp(2k_{xy} H) - 1} \right) \text{ with } k_{xy} = \left(1 - M_\infty^2\right) k_x^2 + k_y^2 \tag{4}$$

The above solution (4) leads to the result that pressure oscillations that are coherent with the pillow-plate elevation oscillations occur in the case of subsonic flow through the channel. This can be seen by inserting solution (4) into the static pressure coefficient definition.

$$C_p = \frac{p - p_\infty}{q_\infty} = \frac{(p/p_\infty) - 1}{\gamma M_\infty^2/2} = -\frac{2}{U}\frac{\partial \phi}{\partial x} \tag{5}$$

The sinusoidal wall pressure oscillations due to the wavy wall are exponentially damped with increasing wall distance z in subsonic flow. In the case of a finite channel height H, these oscillations are still observable in the centerline of the channel ($z = H$).

3.2. Similarity Rules for Subsonic Flow and Incompressible Flow Results

In the scientific literature, many results are available for incompressible flow through pillow-plate channels [7,8]. The linearized gas dynamics directly leads to the Prandtl–Glauert and Goethert similarity rules which connects the (subsonic) compressible flow with its incompressible reference [13]. The following general conclusions can be drawn in the framework of this linearized theory:

In the case of a fixed pillow-plate geometry, the static pressure coefficient (5) can be related to its incompressible flow result $C_{p,i}$ by the Prandtl–Glauert factor, i.e., $C_p = C_{p,I}\left(1 - M^2\right)^{-1/2}$. This means that the amplitude of the coherent oscillations increases with increasing Mach number.

The perturbation Equation (3) enables the interpretation that compressible flow in the coordinate system (x,y,z) is equivalent to an incompressible flow (subscript i) if the transformation $x = x_i$, $y = y_i\left(1 - M^2\right)^{-1/2}$ and $z = z_i\left(1 - M^2\right)^{-1/2}$ are assumed. For example, a pillow-plate design characterized by some certain values for its geometric parameters h_{min}, h_p, and s_L (see Figure 3) which would lead to an optimal heat transfer behavior in the incompressible flow regime might be stretched according to the coordinate transformation rules to create a new optimal pillow-plate channel design for compressible flow at a subsonic Mach number M.

4. Experimental Setup and Procedure

The above theoretical considerations and predictions were checked through an experimental study using an adiabatic pillow-plate channel (the addition or loss of heat in the test channel would require substantial additional efforts which were out of the scope of the present validation study).

The experimental investigations were performed utilizing a blow-down wind tunnel which is schematically shown in Figure 6 and explained in more detail by Passmann et al. [15]. The working fluid was compressed air (maximum pressure 8 bar). The filling of the air storage tanks was enabled by the magnetic valve MV1. The temperature and pressure of the storage tank system were recorded continuously. The complete test facility was controlled using a PC and LabView software, from the manufacturer National Instruments, based in Austin, Texas. The blow-down test run was controlled by a coaxial valve CV1, see Figure 6. The pillow-plate channel was placed in the test section of the wind tunnel, as illustrated in Figure 7a.

The test section inlet and outlet flow conditions were obtained by static and total pressure measurements. In prior tests, it was found that the inlet Pitot probe did not significantly disturb the inflow. The static pressure distribution along the center of the pillow-plate channel was measured employing 40 taps placed centrally at the pillow-plate channel end wall, see Figure 7b. In addition to static and total pressure measurements, the transparent sidewalls of the pillow-plate channel enabled an optical visualization using both conventional and focusing schlieren optics. Furthermore, surface oil flow visualization studies were performed to obtain a qualitative picture of the flow behavior.

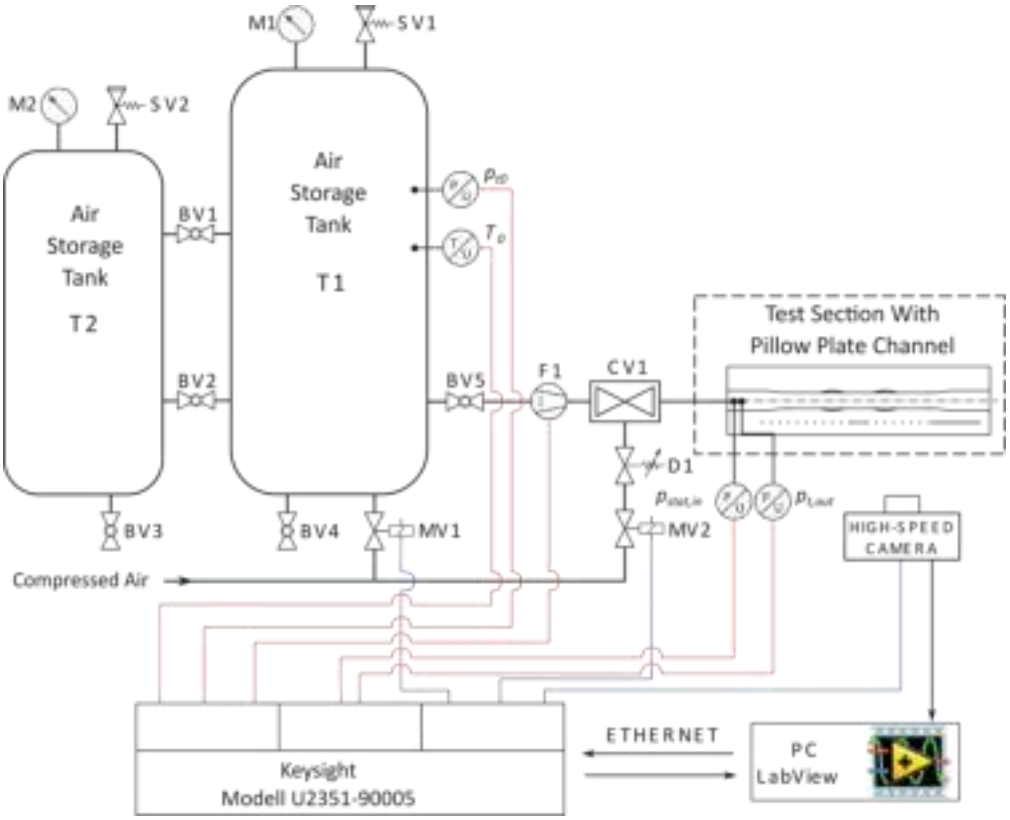

Figure 6. Blow-down wind tunnel facility.

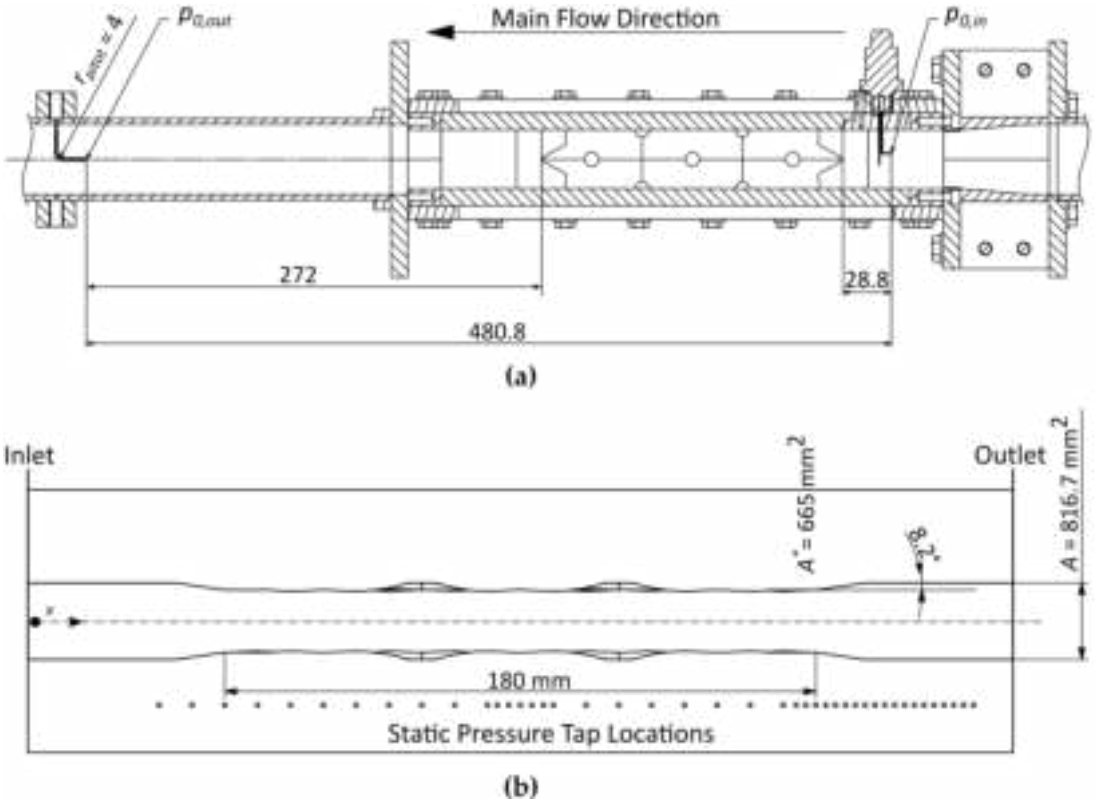

Figure 7. Test section: (**a**) Test section with Pitot probes; (**b**) details of the pillow-plate test section.

Whereas conventional schlieren optics are treated well in the literature, focusing schlieren optical systems are employed less frequently. The principal setup of the employed focusing schlieren optics is shown in Figure 8, and details can be found elsewhere (see Weinstein [16] and Passmann et al. [17]). In combination with a high-speed camera, the focusing schlieren optics enabled a detailed visualization of transient phenomena at certain observation planes in the test section.

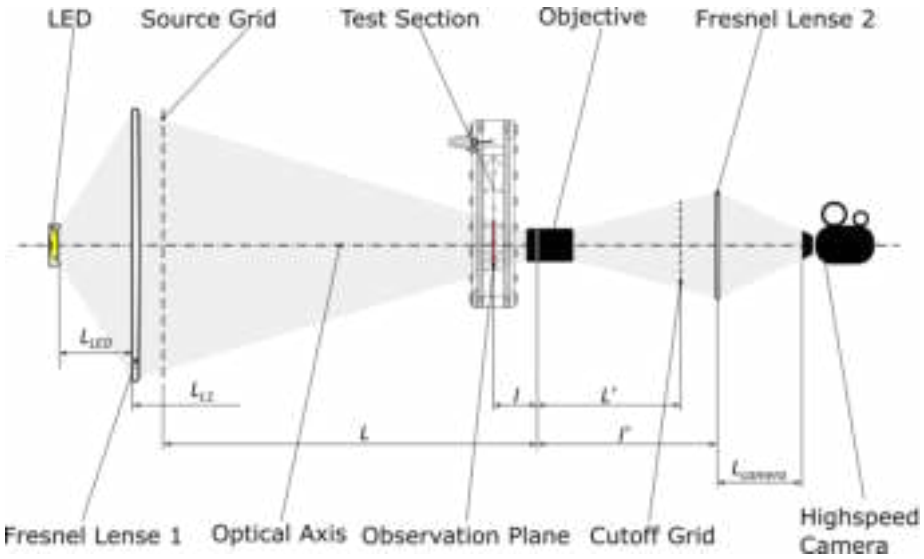

Figure 8. Schematics of the focusing schlieren optical system setup.

5. Results and Discussion

The main objective of the present experimental investigation was to collect qualitative results for the flow phenomena occurring in the considered pillow-plate channel. The present study was restricted to (high) subsonic inflow conditions because this flow regime is of major practical interest (an investigation into supersonic inflow conditions would require an additional Laval nozzle at the inlet zone, which was not part of the test section, see Figure 7).

5.1. Choking Behavior and Pressure Oscillations

A general feature of Fanno flow is its choking behavior. This means that for high subsonic inflow Mach numbers, a shock occurs at the end of the pillow-plate channel ($M = 1$, independently on the stagnation pressure level p_0). This is demonstrated in Figure 9. In Figure 9, conventional schlieren pictures are shown at the outlet region of the pillow-plate channel for different stagnation pressure levels. In any case, Mach number $M = 1$ is reached at the end of the channel, and a shock occurs. For higher pressure levels, a complex pattern results in the expanding flow in the outlet buffer zone. Furthermore, a periodic shading at the pillow-plate channel region (left-hand side of the pictures shown in Figure 9) is indicating an oscillating behavior of the Mach number distribution within the channel due to the periodic surface profile. This observation corresponded well with the variation of static pressure distributions measured along the pillow-plate wall, which is shown for a higher stagnation pressure level in Figure 10. The color picture inlet in Figure 10 shows a simulated Mach number distribution by Passmann et al. [10] with its expanding jet after the shock (red area) and the slight oscillations along the pillow-plate channel region. The oscillating behavior of the static pressure is well-observable in Figure 10. The pressure variations are coherent with the pillow-plate wall surface profile. Accordingly, with the analytical prediction for inviscid compressible flow, see Equation (5) and solution (4), the static pressure oscillations directly reflect the pillow-plate pattern. As a result of the profile and the dimple orientation along the pillow-plate channel, see Figure 7, the amplitudes

of the maxima in Figure 10 alternate between two different levels (i.e., the odd maxima are slightly higher than the other maxima due to the effective cross-section area of the channel including the dimple pattern). Furthermore, a slight decrease in the average static pressure with increasing channel length coordinate can also be identified in Figure 10. This slight decrease represents the pressure drop due to friction within the channel. However, a substantial pressure drop occurred due to the shock at the end of the pillow-plate channel.

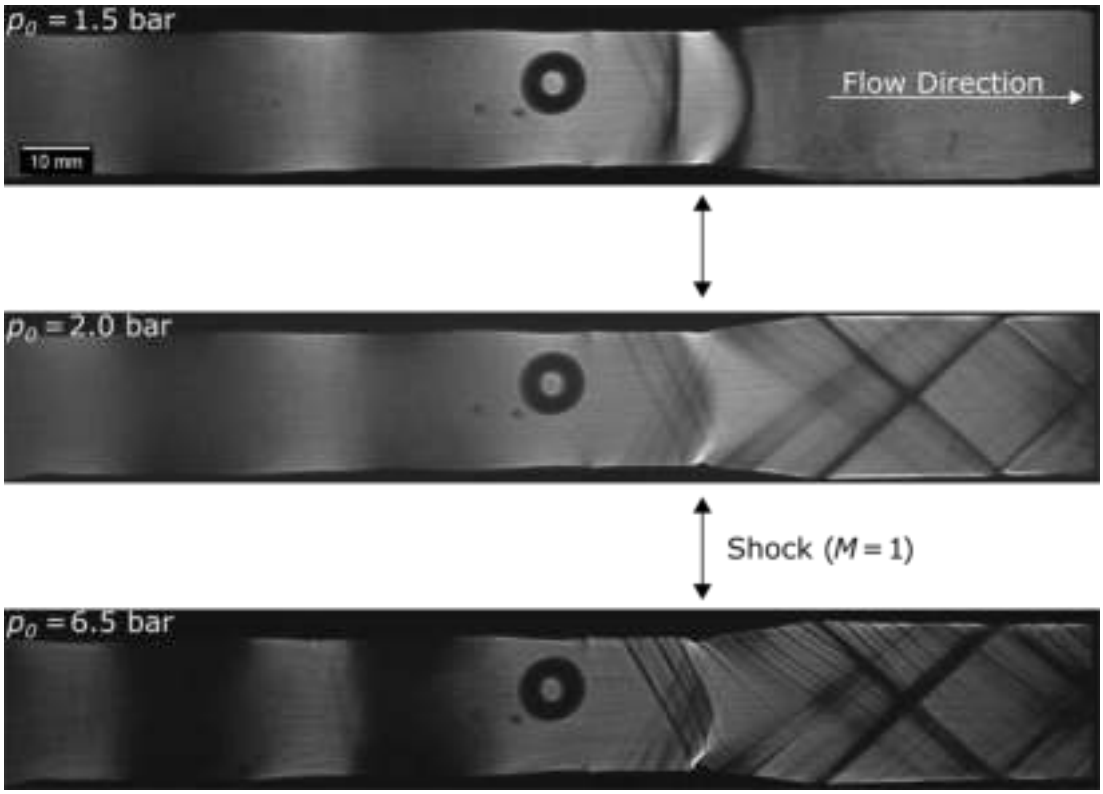

Figure 9. Schlieren pictures for different values of stagnation pressure p_0.

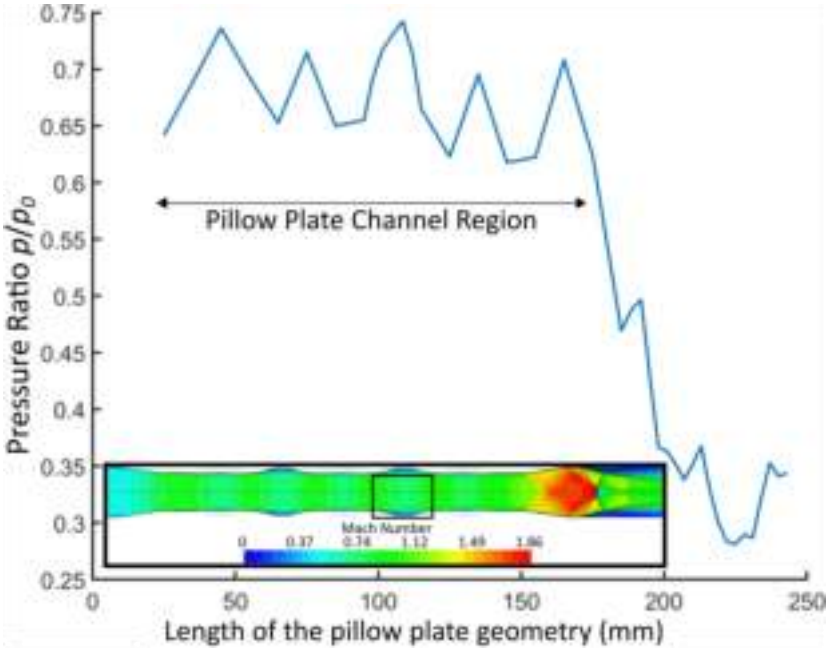

Figure 10. Static normalized pressure distribution against length coordinate.

5.2. Pillow-Plate Profile and Mixing

The surface profile of a pillow-plate channel can be interpreted as a wall with smoot dimples. These dimples substantially increase flow mixing in case of low-speed flows, leading to enhanced convective heat transfer. In the present study, the mixing behavior of high subsonic flow over a pillow-plate surface with dimples was investigated employing focusing schlieren optics and surface oil flow visualizations. Conventional schlieren is not able to obtain the flow over dimples in a well-defined observation plane. In Figure 11, the flow structure past a dimple is shown.

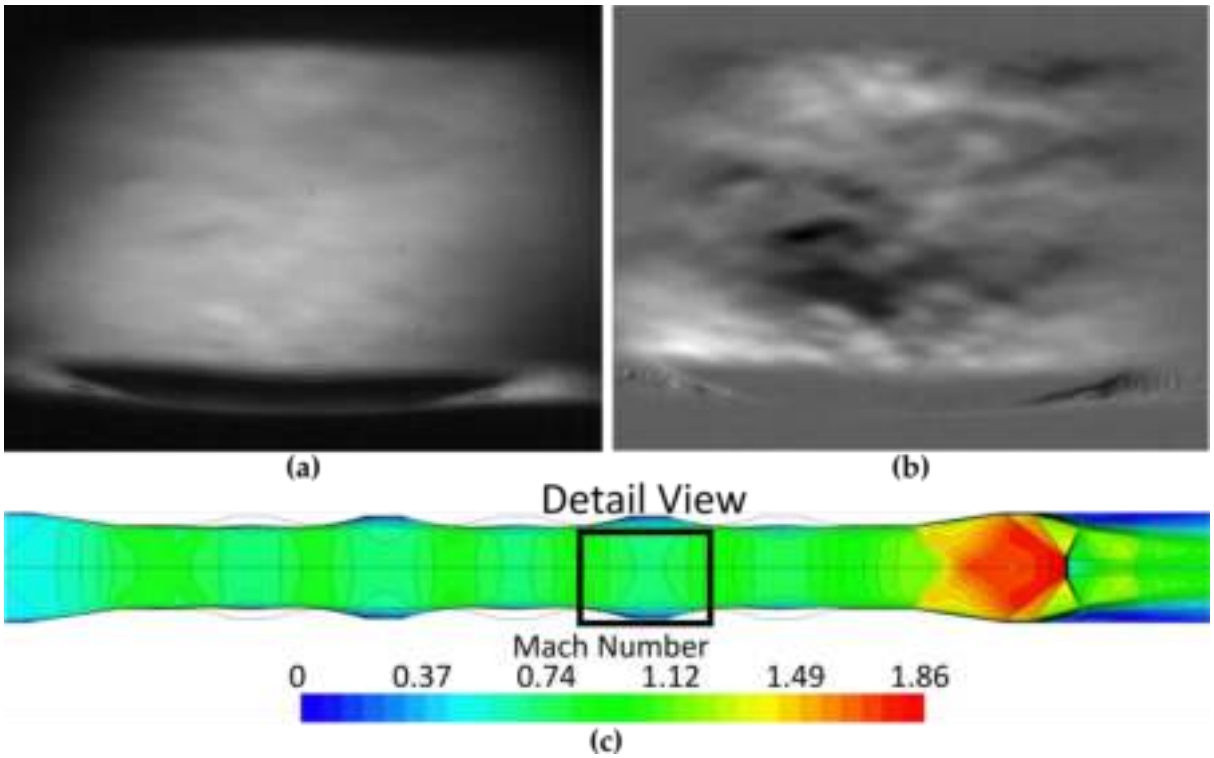

Figure 11. Focusing schlieren optics picture of the flow over a dimple in a pillow-plate channel: (**a**) schlieren picture without subtraction of the background; (**b**) picture after removal of background disturbances and Fourier optical postprocessing; (**c**) Illustration of the location in the pillow-plate channel of the image shown in (**a**).

Here, the observation plane of the focusing schlieren optics was in the middle of a dimple. The two-layer structure of the flow became visible in Figure 11b: a low-speed flow in the dimples and a turbulent, compressible flow above the dimples in the channel. Utilizing surface oil flow visualizations shown in Figure 12, the main vortex structure caused by the dimples could be demonstrated. Figure 12a shows the regular surface oil flow pattern of the pillow-plate wall with its several dimples. As known from incompressible flow analysis, a horse-shoe vortex system is caused by dimples. In the dimples, strong recirculation zones indicated by the accumulation of white oil can be identified in Figure 12b. Figure 12c shows the results of a simulation including all the flow features discussed above.

The vortex and recirculation flow in the dimples is characterized by a low Mach number level (Figures 11b and 12c). The strong vortex pattern illustrated in Figure 12 suggests a strong mixing effect and hence a high convective heat transfer coefficient as in the case of incompressible pillow-plate channel flows.

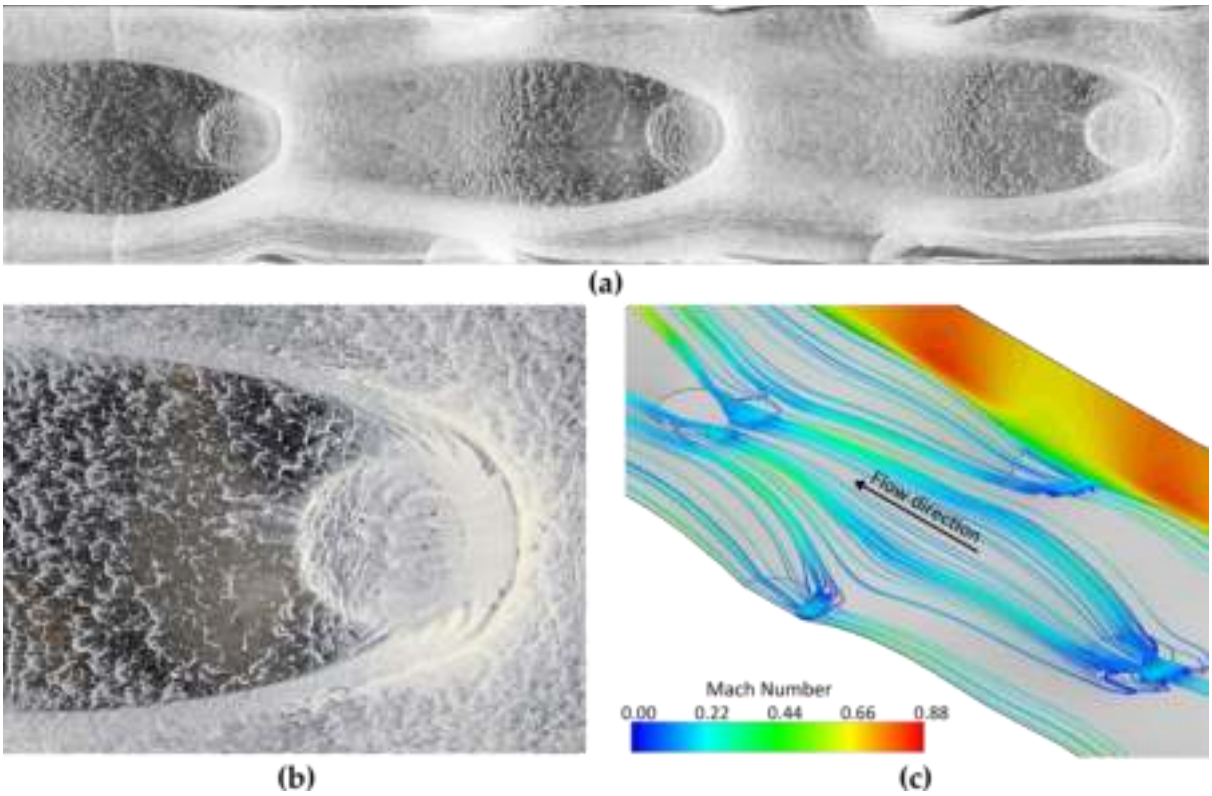

Figure 12. Visualization of the vortex structure caused by dimples in a pillow-plate channel: (**a**) pillow-plate channel wall; (**b**) detailed view of the first dimple; (**c**) CFD simulation.

6. Conclusions

In this work, the overall system behavior and high-speed flow details in pillow-plate channels were investigated experimentally. A pillow-plate channel was placed in the test section of a blow-down wind tunnel working with dry air, and the resulting gas dynamics were investigated utilizing conventional and focusing schlieren optics. Further, static and total pressure measurements were performed. The results of this qualitative study were in good agreement with theoretical predictions for compressible flow past pillow-plate channels.

Regarding potential applications of pillow-plate heat exchangers in combination with high-speed turbomachinery, the following conclusions can be drawn:

The compressible flow through pillow-plate heat exchangers can be interpreted as a kind of Fanno–Rayleigh flow. This means that the choking behavior at the end of the channel has to be considered, which affects the exit conditions of the turbomachine. The pressure drop due to friction is comparably low in the pillow-plate channel, but high convective heat transfer coefficients can be expected due to the substantial mixing and vortex structures. These flow phenomena are rather similar to incompressible flow.

In summary, the observed effects suggest that pillow-plate heat exchangers are rather promising candidates for high-speed flow applications.

Author Contributions: Data curation, S.S., M.P. and E.Y.K.; Formal analysis, S.a.d.W.; Investigation, S.S., M.P., S.a.d.W. and E.Y.K.; Project administration, S.a.d.W.; Software, S.S.; Validation, S.a.d.W. and E.Y.K.; Visualization, S.S., M.P., S.a.d.W. and E.Y.K.; Writing—original draft, S.a.d.W.; Writing—review & editing, S.S., M.P. and E.Y.K. All authors have read and agreed to the published version of the manuscript.

Funding: This research received no external funding.

Institutional Review Board Statement: Not applicable.

Informed Consent Statement: Not applicable.

Data Availability Statement: The authors attest that all relevant data for this study are included in the paper.

Conflicts of Interest: The authors declare no conflict of interest.

Nomenclature

A	area, m^2
c	velocity, m/s
C_p	pressure coefficient
c_p	isobaric specific heat, J/(kg K)
D	hydraulic diameter, m
f	friction factor
H	channel height
h	heat transfer coefficient, $W/(m^2 K)$
k	wave number, 1/m
L	length, m
M	Mach number
p	pressure, Pa
s	specific entropy, J/K
T	Temperature, K
U	bulk flow or free-stream velocity, m/s
x	coordinate in main flow direction, m
y	coordinate (normal to flow direction), m
z	coordinate of surface elevation, m
Greek Symbols	
γ	isentropic exponent
ρ	density, kg/m^3
φ	velocity potential, m^2/s
τ_w	wall shear stress, Pa

References

1. aus der Wiesche, S.; Joos, F. (Eds.) *Handbuch Dampfturbinen*; Springer Vieweg: Wiesbaden, Germany, 2018.
2. Bathie, W.W. *Fundamentals of Gas Turbines*, 2nd ed.; Wiley & Sons: New York, NY, USA, 1996.
3. Bräunling, W.J.G. *Flugzeugtriebwerke*, 2nd ed.; Springer: Berlin, Germany, 2004.
4. Sunden, B.; Fu, J. Aerospace Heat exchangers. In *Heat Transfer in Aerospace Applications*; Academic Press: New York, NY, USA, 2017; Chapter 6.
5. Macchi, E.; Astolfi, M. (Eds.) *Organic Rankine Cycle (ORC) Power Systems*; Elsevier: Amsterdam, The Netherlands, 2017.
6. McDonald, C.F.; Massardo, A.F.; Rodgers, C.; Stone, A. Recuperated gas turbine aeroengines, part I: Early development activities. *Aircr. Eng. Aerosp. Technol.* **2008**, *80*, 139–157. [CrossRef]
7. Piper, M.; Olenberg, A.; Tran, J.M.; Goedecke, R.; Scholl, S.; Kenig, E.Y. Bestimmung charakteristischer Geometrieparameter von Thermoblech-Wärmeübertragern. *Chem. Ing. Tech.* **2014**, *86*, 1214–1222. [CrossRef]
8. Piper, M.; Tran, J.M.; Kenig, E.Y. A CFD Study of the Thermo-Hydraulic Characteristics of Pillow Plate Heat Exchangers. In Proceedings of the ASME 2016 Heat Transfer Summer Conference, Washington, DC, USA, 10–14 July 2016.
9. Mitrovic, J.; Maletic, B. Numerical simulation of fluid flow and heat transfer in thermoplates. *Chem. Eng. Technol.* **2011**, *34*, 1439–1448. [CrossRef]
10. Passmann, M.; aus der Wiesche, S.; Kenig, E.Y. On the Low and High Speed Flow of Gases Through Pillow Plate Channels. In Proceedings of the ASME-JSME-KSME 2019 Joined Fluids Engineering Conference, San Francisco, CA, USA, 28 July–1 August 2019. Paper-ID AJ-KFLUIDS2019-4633.
11. Dixon, S.L.; Hall, C.A. *Fluid Mechanics and Thermodynamics of Turbomachinery*, 6th ed.; Butterworth-Heinemann: Burlington, VT, USA, 2010.
12. Horlock, J.H. *Axial Flow Turbines*; Krieger Publishing: Malabar, FL, USA, 1985.
13. John, J.E.; Keith, T.G. *Gas Dynamics*, 3rd ed.; Pearson: Upper Saddle River, NJ, USA, 2006.
14. Kouremenos, D.A.; Antonopolous, K.A. Isentropic Exponents of real gases and application for the Air at temperatures from 150 K to 450 K. *Acta Mech.* **1987**, *65*, 81–99. [CrossRef]

15. Passmann, M.; aus der Wiesche, S.; Joos, F. An Experimental and Numerical Study of Tip-Leakage Flows in an Idealized Turbine Tip Gap at High Mach Numbers. In Proceedings of the ASME-Turbo Expo 2018, Oslo, Norway, 11–15 June 2018; Paper-ID GT2018-76366.
16. Weinstein, L.M. Large-field high-brightness focusing schlieren system. *AIAA J.* **1993**, *31*, 1250–1255. [CrossRef]
17. Passmann, M.; aus der Wiesche, S.; Joos, F. Focusing schlieren visualization of transonic turbine tip-leakage flows. In Proceedings of the 13th European Conference on Turbomachinery Fluid Dynamics and Thermodynamics, Lausanne, Switzerland, 8–12 April 2019; Paper-ID ETC2019-326.

International Journal of
Turbomachinery
Propulsion and Power

MDPI

Article

The Profile Loss of Additive Manufactured Blades for Organic Rankine Cycle Turbines

Leander Hake [1,*], Felix Reinker [1], Robert Wagner [1], Stefan aus der Wiesche [1] and Markus Schatz [2]

[1] Laboratory of Heat, Energy and Motor Technology, Department of Mechanical Engineering, Muenster University of Applied Sciences, Campus Steinfurt, 48565 Steinfurt, Germany; f.reinker@fh-muenster.de (F.R.); r.wagner@fh-muenster.de (R.W.); wiesche@fh-muenster.de (S.a.d.W.)
[2] Laboratory of Fluid Machinery for Energy Technology, Helmut-Schmidt-University, 22043 Hamburg, Germany; markus.schatz@hsu-hh.de
* Correspondence: leander.hake@fh-muenster.de

Abstract: Results from an experimental profile loss study are presented of an additive manufactured linear turbine cascade placed in the test section of a closed-loop organic vapor wind tunnel. This test facility at Muenster University of Applied Sciences allows the investigation of high subsonic and transonic organic vapor flows under ORC turbine flow conditions at elevated pressure and temperature levels. An airfoil from the open literature was chosen for the cascade, and the organic vapor was Novec 649^{TM}. Pitot probes measured the flow field upstream and downstream of the cascade. The inflow turbulence level was 0.5%. The roughness parameters of the metal-printed blades were determined, and the first set of flow measurements was performed. Then, the blade surfaces were further finished, and the impact of roughness on profile losses was assessed in the second flow measurement set. Although the Reynolds number level was relatively high, further surface treatment reduces the profile loss noticeably in organic vapor flows through the printed cascade.

Keywords: turbomachinery; aerodynamics; profile loss; ORC turbines

check for updates

Citation: Hake, L.; Reinker, F.; Wagner, R.; aus der Wiesche, S.; Schatz, M. The Profile Loss of Additive Manufactured Blades for Organic Rankine Cycle Turbines. *Int. J. Turbomach. Propuls. Power* **2022**, *7*, 11. https://doi.org/10.3390/ijtpp7010011

Academic Editor: Francesco Martelli

Received: 30 November 2021
Accepted: 3 March 2022
Published: 21 March 2022

Publisher's Note: MDPI stays neutral with regard to jurisdictional claims in published maps and institutional affiliations.

Copyright: © 2022 by the authors. Licensee MDPI, Basel, Switzerland. This article is an open access article distributed under the terms and conditions of the Creative Commons Attribution (CC BY-NC-ND) license (https://creativecommons.org/licenses/by-nc-nd/4.0/).

1. Introduction

Additive manufacturing (also known as 3D printing technology) offers excellent potential for many turbomachinery applications because it can realize intricate blade designs (see, for instance, Magerramova et al. [1], Albright [2], or Adair et al. [3]). Faced with complex internal cooling channel designs, all leading gas turbine companies have considered this technology. Additive manufacturing is also a promising approach for organic Rankine cycle (ORC) turbines. Firstly, suitable additive manufacturing materials are widely available for the temperature and pressure levels in ORC turbines. Secondly, several ORC turbines are compact devices, and sophisticated three-dimensional blades might help to optimize their aerodynamics. Additive manufacturing could be a cost-efficient way to realize such highly efficient blading. However, the high surface roughness levels of printed blades can cause severe profile losses. For many decades, it has been well known that roughness is of significant importance for cascade and turbine performance (Speidel [4], Scholz [5], and Bammert and Sandstede [6]). Although considerable progress can be observed in additive manufacturing technology, substantial rework is still necessary to achieve roughness levels comparable to conventionally manufactured blades. The relatively high roughness level of printed objects makes it questionable how much rework and additional production cost would be required to create competitive blades. This severe issue might reduce the broader acceptance of this technology in the turbomachinery industry. Furthermore, the open literature reports virtually nothing about additive manufactured cascade's loss and aerodynamic performance in organic vapor flows. In the following, the outcome of an experimental investigation of profile losses of a printed linear turbine cascade is presented. The cascade was placed in the test section of a closed-loop organic

vapor wind tunnel (CLOWT). This test facility at Muenster University of Applied Sciences enables the investigation of high subsonic and transonic organic vapor flows under ORC turbine flow conditions at elevated pressure and temperature levels. Before presenting the experimental setup and procedure and before discussing the results, the following remarks might help. The present study focused only on cascade aerodynamics and profile losses, and manufacturing or other technology items were explicitly out of scope. Although additive manufacturing offers its full potential for creating complex three-dimensional blades and nozzles, the present study only considered two-dimensional profile losses because roughness issues are especially relevant for that kind of loss.

2. Test Case

The so-called VKI-Sieverding blade profile, shown in Figure 1, was chosen for the cascade because for this airfoil, as many reliable data and results are available for the subsonic and transonic flow of an ideal gas in the open literature (see Sieverding [7], Lehthaus [8], Kiock et al. [9]). The airfoil was designed following Dejc's method, and the suction side is derived from one basic lemniscate, while the pressure side is composed of both a circular arc and a lemniscate.

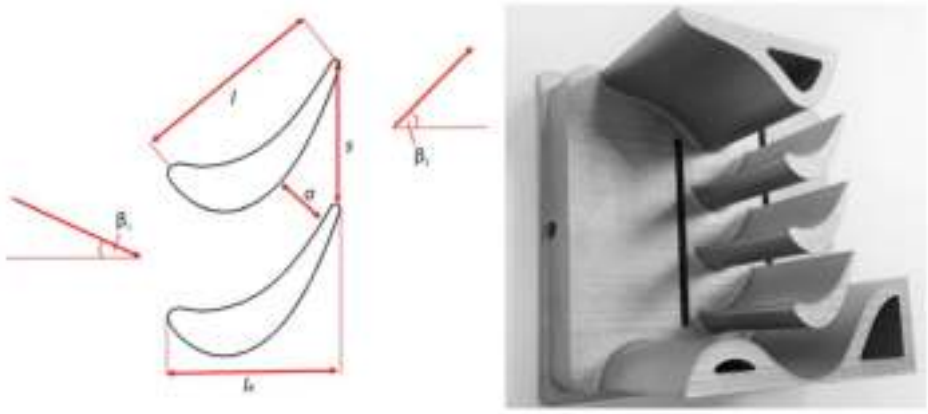

Figure 1. Geometric dimensions of the blade profiles and printed final design cascade.

Although the VKI-Sieverding profile represents a classical gas turbine airfoil design, it has been widely recognized as suitable for general transonic testing purposes. The airfoil is typical for cooled gas turbine rotor sections, and the trailing edge radius is relatively large compared to steam turbine profiles. For the present purpose, the large trailing edge radius was advantageous because it enabled the inclusion of trailing edge losses which are highly relevant for ORC turbines, as discussed by Baumgärtner et al. [10].

Based on this airfoil, a linear cascade, Figure 1, was designed to fit the test section of the employed closed-loop organic vapor wind tunnel (see section "Description of Test Facility"). Table 1 shows all determined dimensions of the blade profile. The cross-section of the test section was 100 mm × 50 mm. The test section height H = 50 mm of the airfoils corresponded to the transonic wind tunnel facility of VKI Rhode-St. Genese (Kiock et al. [9]) and was found to be appropriate for investigating profile loss. However, the present test section permitted only an axial inflow and an axial outflow. The maximum channel height was 100 mm, which was much smaller than at the VKI transonic wind tunnel facility. Since an airfoil with a significant deflection was employed; these severe design constraints led to a cascade configuration with only three entirely free-standing airfoils (and additional guiding profiles at the cascade's boundaries see Figures 2 and 3). The cascade's final design, including its guiding profile and its outflow region, was defined after a numerical optimization procedure, employing compressible CFD analyses using a perfect gas model for air. During numerical optimization, the main objective was to meet the flow's salient features through the central test blade passage.

Table 1. Determined dimensions of the blade profile.

Description	Abbreviated	Nominal	Actual
Spacing	*s*	21.3 mm	22 ± 0.2 mm
Narrowing	*o*	8.2 mm	8.3 ± 0.05 mm
Chord length	*l*	30 mm	30.5 ± 0.2 mm
Axial chord	*lx*	25 mm	25 ± 0.2 mm
Space chord ratio	*s/l*	0.71	0.721 ± 0.011
Inflow angle	*β1*	30°	30°
Exit angle	$cos^{-1}(o/s)$, *β2*	67.35°	67.84 ± 0.36°

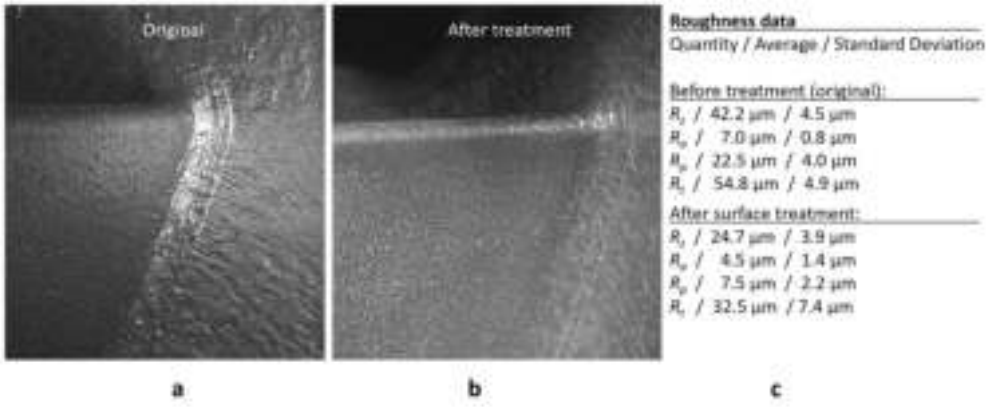

Figure 2. Position: trailing edge, original state (**a**); treatment state (**b**); and measured roughness data (**c**).

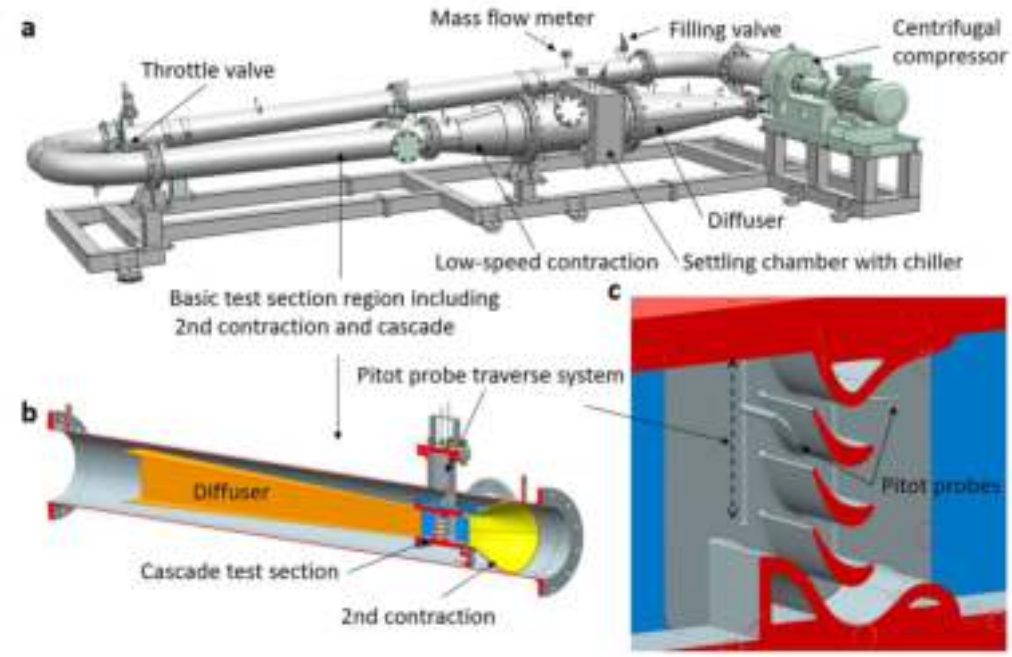

Figure 3. Position: Closed-loop organic vapor wind tunnel CLOWT (Close-loop organic vapor Wind tunnel) (**a**); test section (**b**); and cascade (**c**).

2.1. Roughness and Blade Manufacturing

The quality of a surface is defined as the height of the peaks, the roughness structure, and its waviness. A single roughness parameter was usually prescribed in traditional workshop practice, including the roughness height R_t, defined as the largest height of the roughness peaks or the center-line-average *CLA* value. In the German industry standard

DIN4767, the relationship $CLA \approx 0.14\ R_t^{1.14}$ was quoted for traditionally mechanically manufactured surfaces. Today, the arithmetic mean deviation of the assessed surface, R_a, or the average value over the assessment length, R_z, using the maximum peak to valley height, or the maximum profile peak height, R_p, are frequently used in the turbomachine industry.

The impact of roughness on the flow is a complicated topic because flow roughness and manufacturing roughness are not the same. If the viscous sublayer fully envelops peaks, there is no influence on the skin friction, and the surface is hydraulically smooth. If the peaks reach out of the viscous sublayer, shearing stress typically increases and additional loss occurs. A common approach is using an equivalent sand grain roughness k_s [5]. A milled surface with roughness R_t behaves like a surface with sand grains of size $k_s = R_t/2.56$ for a flow perpendicular to the milling grooves. On the other hand, it was also observed that a surface with sharp regular steps of height R_t could be hydraulically much rougher than a sand grain surface with the same peak level. Here, a relation $k_s = R_t/0.08 = 12.5 \cdot R_t$ was experimentally observed [5]. For blades, it is frequently quoted (Scholz [5], Bammert and Sandstede [6]) that the admissible sand grain roughness $k_{s,adm}$ normalized by the chord length l is a function of the Reynolds number $Re = cl\rho/\mu$ and can be correlated by

$$\frac{k_{s,adm}}{l} \leq \frac{100}{Re} \rightarrow \quad k_{s,adm} \leq 100\ \frac{\mu}{\rho\ \mathrm{c}} \tag{1}$$

In ORC turbine applications, the Reynolds number Re can be relatively high due to the substantial density ρ of organic vapors consisting of complex molecules. Hence, the admissible roughness $k_{s,adm}$ might be relatively small for ORC turbines, posing considerable manufacturing challenges. Most of our knowledge on roughness on the flow past blades has been collected in light of conventional manufacturing methods. Much less is known regarding the surface quality of additive manufactured blades. Adair et al. [3] reported surface roughness measurements of electronic beam melting (EBM) blade artifacts in the as-printed and post-electrochemical machining conditions.

They found values of order $R_a \approx 80$ µm ($R_z \approx 90$ µm) in as-printed condition for the pressure and the suction side of gas turbine blades. After pulsed electrochemical machining (PECM), the roughness values were reduced to levels of $R_a \approx 1.3$ µm ($R_z \approx 7.2$ µm).

The present cascade was manufactured using the selective laser melting (SLM) method. Figure 2a shows the printed part when the supplier provided it. The printing direction was normal to the main flow direction and, after printing, the supplier did a first surface treatment. This surface is hence called "original". After the first set of flow measurements, the printed part's surface was treated using vibratory finishing. The improvement due to the second finishing process can be seen in Figure 2. Figure 2b compares the surfaces of the blades (leading edge region) before and after finishing. Figure 2c provides some roughness data. The deviation between the roughness levels measured in stream-wise direction and measured in printing direction was noticeable; however, it is not further elaborated in this contribution. The roughness data and relation (1) indicated that both the original and finished parts are rough in aerodynamics: the inflow Reynolds number was of order $Re = 10^6$ yielding $k_{s,adm}/l = 10^{-4}$. The admissible roughness, $R_{t,adm}$, would hence be of order 8 µm, which was easily not achieved after the applied standard finishing process, as displayed in Figure 2c. Thus, a different finishing process would be required to achieve hydraulically smooth blades. In principle, this is possible (see Adair et al. [3]), but is not covered within the present study.

2.2. Description of the Test Facility

The present experiments were performed in the closed-loop organic vapor wind tunnel (CLOWT) test section using the perfluorinated ketone Novec™ 649 and dry air as working fluids. The wind tunnel test facility CLOWT is shown in Figure 3. More details on CLOWT and its design features and its control system can be found in previous publications (Reinker et al. [11,12]).

After passing the centrifugal compressor, the working fluid was decelerated in the diffuser and entered the settling chamber, where the stagnation pressure p_0 and temperature T_0 were recorded. The mass flow rate $\dot{m}$ through the wind tunnel was measured utilizing a device in the return of the wind tunnel. The compressor running speed n controlled the flow rate. The wind tunnel's temperature level was controlled using an electrical heating system (not shown in Figure 3) and the coolant mass flow through the chiller. In combination with the inventory forward control (i.e., the amount of working fluid mass in the closed wind tunnel), stable operation conditions were achieved during the tests (for further details see Reinker et al. [12]). In CLOWT, a two-stage contraction zone accelerates the flow. The first subsonic axisymmetric nozzle (standard diameter DN500 to DN250) offers a moderate contraction ratio of about 3.7. The second nozzle accelerated the fluid up to the desired inflow conditions (see Figure 3b). In the present study, the second contraction was established by a three-dimensional nozzle based on additive manufacturing.

The second nozzle provided a three-dimensional cross-section change from round to rectangular contraction (standard diameter DN250 to a rectangular cross-section of 50 mm × 100 mm), leading to a total contraction ratio of 39. After passing the two-stage contraction zone, the fluid entered the cascade's high-speed test section, as shown in Figure 3b,c. Different inflow turbulence intensities could be achieved through variable screen sets in the settling chamber. Still, during the present study, no additional screen was implemented to provide a moderate inflow turbulence intensity of order $Tu = 0.5\%$ for cascade testing. The turbulence level was experimentally confirmed by hot-wire anemometry, as explained by Reinker and aus der Wiesche [13]. The inflow turbulence Taylor micro length scale was of order $\lambda = 4$ up to 6 mm.

For the experiments, Novec 649^{TM} by 3M was used primarily as working fluid. The typical pressure and temperature values at inlet stagnation conditions were 2.5 bar and 97 °C. In addition to the organic vapor, some cascade tests were also performed using dry air at atmospheric conditions (1 bar and 25 °C). In Table 2, some relevant thermodynamic data are listed for typical process conditions during the present cascade tests. Thermodynamic data of Novec 649 and air were calculated by employing REFPROP and its underlying equation of states (see McLinden et al. [14]) using actual pressure and temperature measurements. As pointed out by Baumgärtner et al. [10], the isentropic exponent κ is expected to be of some relevance for profile loss. Table 2 shows that the isentropic exponent κ was significantly lower for Novec 649^{TM} than for air. Due to the high-density ρ of Novec 649^{TM}, high inflow Reynolds numbers $Re_1 = c_1 l \rho_1 / \mu_1$ were achieved for the cascade flow.

The total enthalpy h_0 was determined using the wall pressure p_0, the (total) temperature T_0 was measured at the settling chamber (denoted by subscript 0) and the mass flow rate $\dot{m}$ obtained in the return of the wind tunnel. Since incompressible flow was involved in the settling chamber (with Mach number of order $M_0 = 10^{-2}$), the density ρ_0 in the settling chamber was simply calculated using p_0 and T_0. During steady-state operation, the total enthalpy h_0 was assumed to be constant for the contraction and test section; however, a slight temporal drift of system pressure and the temperature was taken into account during the long-term operation of the wind tunnel.

Table 2. Thermophysical properties of dry air and Novec 649^{TM} at typical pressure and temperature levels (calculated using REFPROP 9.0).

Fluid	Air	Novec 649
Pressure level p [MPa]	0.10	0.25
Temperature level T [K]	298	370
Density ρ [kg/m^3]	1.17	28.46
Isentropic exponent κ [−]	1.40	1.05
Compressibility factor Z [−]	1.000	0.903
Speed of sound a [m/s]	346.2	90.8
Dynamic viscosity η [Pas]	1.848×10^{-5}	1.389×10^{-5}

At the beginning of the high-speed test section, far upstream, the inflow static wall pressure p_1 was obtained through a static pressure tap placed centrally at the entrance of the test section. Further static end-wall pressure taps were located close to the cascade wall downstream (p_1) and upstream of the cascade (p_2) at planes where the total pressures p_{01} and p_{02} were measured employing traversing Pitot probes, as displayed in Figure 3c. In addition to the static pressure measurements close to the cascade trailing edge plane, the static pressure p_2 far downstream was measured independently. The employed Pitot probes had a stem diameter of 3 mm, and the probe head diameter was 1 mm. A prior calibration study indicated that the employed Pitot probes were robust against the flow angle within $\pm 10^{\circ}$. Hence, the probes were insensitive to the expected flow angle changes, as in the case of the study of Shelton et al. [15]. Since the cascade test section's outflow zone was anything than optimal, as shown in Figure 2, it was decided to carry out the wake traverse measurements relatively close to the trailing edge plane (at a distance of about 2 mm). Regarding mixing losses, it was not possible to traverse at a downstream plane (p_{02}) sufficiently far away from the cascade, as recommended by Scholz [5] and Kiock et al. [9]. However, that issue was of minor importance for the present purpose (i.e., a comparison of rough and smooth blades).

The accurate determination of pressures for the organic vapor flow requires special attention. In the case of dry air, measurements of static and total pressures can be performed by standard instrumentation using pressure transducers or manometers. In the case of organic vapor flows, condensation issues in pressure lines outside of the hot stream domain can substantially affect the measurements. For scanning the cascade test section pressures (i.e., p_1, p_2, p_{01}, and p_{02}), a rotatable switching device mounted at a side flange of the test tube was designed and employed for the involved valves. All connecting lines and valves for cascade pressure scanning were mounted inside the hot wind tunnel test tube.

Furthermore, a thermal decoupling device described in detail by Reinker et al. [16] was employed to avoid condensation issues at the pressure transducer mounted outside. Although previous functionality tests suggested that the leaking effect seemed to be negligible for the rotatable switching device, experiments at higher Mach numbers indicated that some systematic errors occurred during the measurements of the static pressure taps p_2. Therefore, the static pressure p_{2^*} measured independently far downstream of the cascade was employed for data reduction.

2.3. Data Reduction

The inflow Mach number M_1 was the primary flow input parameter since the angle of incidence (or inflow angle β_1) was fixed for the present study (see Figure 1. The inflow Mach number M_1 was calculated through an isentropic relation $M_1 = f(p_{01}, p_1)$ for a given stagnation enthalpy h_0 and static pressure p_1. The isentropic relation f for the inflow Mach number was provided by a separate routine implemented in REFPROP (see McLinden et al. [14] for details). In non-perfect gas dynamics, the isentropic relations f are not universal functions as in the case of perfect gas dynamics; instead, they depend on the given initial state h_0 and p_0. Following Shelton et al. [15], the isentropic exit Mach number M_{2is} was calculated through an isentropic relation $M_{2is} = f(p_{01}, p_{2avg})$ with the inflow total pressure p_{01} and the average exit static pressure p_{2avg}. In the case of a perfect gas, the isentropic relation f for the exit Mach number can be given as analytical formulas. Substantially more efforts are required for non-perfect gas flows. For the present study, Passmann et al. [17] proposed a method using REFPROP data of Novec 649. For the total downstream pressure in supersonic flow, a bow shock occurs upstream of a Pitot probe. In supersonic flow, the total pressure p_{02m} measured by the Pitot probe is related to the actual total pressure p_{02} through a normal shock relation. In the case of a perfect gas, the analytical Rayleigh–Pitot equation can be used for calculating the actual exit Mach number M_2 using the static pressure data p_2 and the Pitot probe signal p_{02}. In supersonic organic vapor flows, it is necessary to solve the coupled set of balance equations (mass, energy, and impulse) numerically for stations upstream and downstream of the normal shock using

appropriate equations of states [17]. Even in the case of high subsonic organic vapor flow, the deviations between a perfect gas expression and a correct thermodynamic treatment of the Pitot probe can be significant [16]. In the present study, the deviations between the Rayleigh–Pitot Equation (2) and the numerically obtained Mach number M_2 were of order 4 up to 8%.

$$\frac{p_{02}}{p_2} = \frac{\kappa+1}{2} M_2^2 \left(\frac{(\kappa+1)^2 M_2^2}{4\kappa M_2^2 - 2(\kappa-1)} \right)^{1/(\kappa-1)} \quad (2)$$

In an ideal cascade experiment, p_{01} would not depend on the traverse coordinate y; however, a weak mal-distribution might occur in actual tests. In the present cascade test section, no noticeable inflow total pressure mal-distribution p_{01} was found. An example of upstream total and downstream total pressure distributions for a typical run is shown in Figure 4. Whereas the inflow total pressure p_{o1} was nearly constant over the normalized traverse coordinate y/s, the specific wake flow distribution became visible in the exit total pressure distribution $p_{02}(y)$.

A serious question is how to average flow quantities for a given purpose (see, Cumpsty and Horlock [18] for a discussion of the "correct" averaging procedure). Exit static pressures have to be arithmetically averaged over spacing s to get p_{2avg}. In the case of total pressures, the so-called mass-weighted average is typically preferred (Dixon and Hall [19]); however, experimentalists frequently use area-averaged total pressures as well [18]. The latter approach was chosen in the present treatment, similar to Scholz [5] or Speidel [4]. In addition to that averaging issue, different ways for expressing cascade performance and losses are in use. Following Shelton et al. [15], a total pressure loss coefficient $Y = (p_{01} - p_{02})/p_{01}$ was defined using averaged total exit pressures p_{02} (the inlet total pressure p_{01} was practically constant, Figure 4).

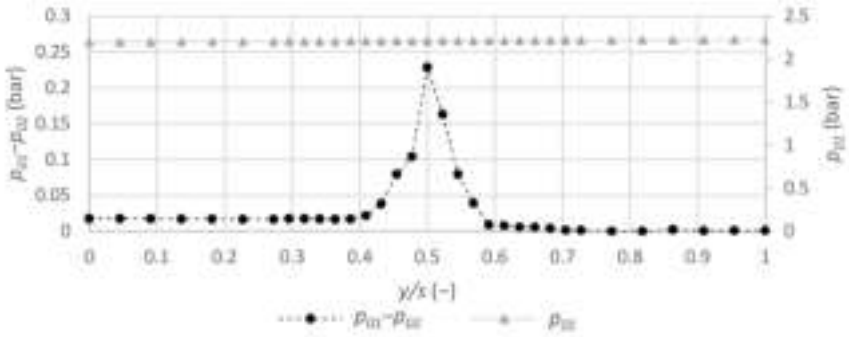

Figure 4. Examples of total upstream and total downstream pressure difference distributions (Novec 649, M_{2is} = 0.68).

Kiock et al. [9] preferred an energy loss coefficient $\zeta = 1 - {c_2}^2/{c_{2is}}^2$ defined by the actual exit and the isentropic exit velocities c_2 and c_{2is}, respectively. For the present purpose, the profile loss performance study reported by Kiock et al. [9] was of significant relevance because this study compared measurements performed independently at four different leading research facilities. Moffat [20] distinguished between three levels of replication: Nth order, first order, and zeroth order. The Nth order includes variations between different researchers with physically other test facilities. The first order includes variation due to changes in the instrumentation's calibration and changes in ambient conditions at a particular test facility. In the zeroth-order replication, the process is steady at a specific test facility, and the chief source of error is the inaccuracy of the instrument readings. In validating analytical tools or computational fluid dynamics (CFD) simulation methods, it is desirable to evaluate the magnitudes of the errors occurring in Nth-order replication. It is also useful to know these errors in order to assess non-perfect gas effects on cascade performance for the present study. Kiock et al. [9] reported significant deviations for the loss results between the four test facilities by considering the same configuration using

air. That observation has to be kept in mind when new loss results are presented for an organic vapor.

2.4. Uncertainty Analysis

Experiments with organic vapor flow at elevated pressure and temperature levels require special efforts. The uncertainty of the flow variables can have two uncertainty sources: bias and precision. The total uncertainty of a variable is a combination of both. Although the employed pressure transducers' uncertainty level was of order 0.1 up to 0.2% (depending on the actual pressure level), a much higher total uncertainty level (of order $\Delta p/p$ = 0.5 up to 1.6%) was developed. This substantially higher uncertainty level was mainly given by bias errors caused by condensation in the pressure lines [16]. In the present case, the condensation issue was the primary source of uncertainty for the pressure measurements. The contribution due to precision was nearly negligible (the precision error was of order 0.01 up to 0.05%). The absolute uncertainty of the temperature measurements (using temperature sensors PT100 1/10 DIN B) was of order ΔT = 0.1 K (nearly independent on the actual temperature level), yielding to a total relative uncertainty level of $\Delta T/T$ = 0.06 up to 0.1%, including the data logger and precision contributions. The contribution due to precision was only of order 0.01% regarding temperature measurements.

In addition to the above general uncertainty sources for the primary variables pressure and temperature, the thermodynamic properties' calculation uncertainty due to the selected equation of states and fluid database and the scattering of wind tunnel operation during a measurement run had to be considered for data reduction.

The thermodynamic variables calculation utilized the REFPROP database with the appropriate equation of states for a given fluid [14]. REFPROP provided information about the uncertainty range of thermodynamic variables, and these uncertainties were treated as bias errors in the uncertainty analysis. For example, REFPROP quoted that the uncertainty in vapor speed of sound was only 0.05%. This value was used as a corresponding bias error contribution to calculate the uncertainty of the Mach number. A substantial level of uncertainty resulted in density calculations. Without considering the systematic error due to the finite accuracy of the thermodynamic equation of states, the total relative uncertainty level for the density was of order $\Delta\rho/\rho$ = 0.7 up to 2.0% (depending on the pressure and temperature level). Considering the systematic uncertainty due to the thermodynamic equation of states led to $\Delta\rho/\rho$ = 1.6 up to 3.0%. The uncertainty level of the density affected the total uncertainty of the mass flow rate, and the total relative uncertainty of order $\Delta m/m$ = 1.6 up to 4.5% resulted in that quantity. That uncertainty directly affected the Mach and the Reynolds number uncertainty levels for which similar figures were obtained.

The scattering of the wind tunnel operation (i.e., pressure, temperature, and mass flow rate) was within the experimental uncertainty level of the involved instrumentation (see above). The transient temperature drift did not exceed 10^{-3} K/s.

3. Results and Discussion

In the present closed-loop wind tunnel facility, a nearly linear relationship between the inflow Mach number M_1 and Reynolds number Re_1 existed, as seen in Figure 5. Close to the choking Mach number at about $M_{1,ch}$ = 0.27, the dependency on the pressure of the sound speed for Novec 649 caused a nonlinear behavior. The exit Reynolds number level was of order 10^6 up to 3×10^6, which was slightly higher than in the literature studies reported by Kiock et al. [9], where Re_2 did not exceed 0.9×10^6. The relationship between the inlet and exit Mach numbers agreed with the literature data obtained for air (Figure 6). Using the cascade data of Figure 1 and employing the perfect gas expression quoted by Scholz [5], a theoretical value of $M_{1,ch}$ = 0.27 resulted in the choking Mach number, which is in excellent agreement with the observed choking Mach number. Kiock et al. [9] reported that choking conditions would be achieved for air at M_2 = 0.9. This behavior was also observed for the organic vapor flow through the cascade. Obviously, the isentropic exponent value or other real gas effects were not relevant for the choking behavior in the present study conducted

in the dilute gas regime of an organic vapor. No impact of roughness on the overall choking behavior was found.

The energy loss coefficient ζ against exit Mach number M_2 can be compared with literature data reported by Kiock et al. [9], although the present study used Novec 649 as working fluid instead of air. In Figure 7, the loss coefficient ζ against the exit Mach number M_2 is shown and compared with literature data. The loss coefficients obtained for the organic vapor flow through the finished printed cascade were in good agreement with literature data obtained for air and a smooth cascade at higher subsonic Mach numbers. A somewhat higher value than in literature was observed at lower exit Mach numbers. The reason for that deviation remained unclear, possibly resulting in residual roughness and a lower Reynolds number. Since the Mach and the Reynolds numbers were strongly related in the present study, a low Mach number corresponded to a lower Reynolds number. It is likely that flow separation occurred at lower Reynolds numbers leading to higher profile losses. A somewhat similar picture was also observed by Yuan and Kind [21]. They suspected that the flow was separating rather upstream of the suction-surface trailing edge of the rough blades, at least at lower Mach numbers (i.e., lower Reynolds numbers). The loss coefficient ζ at $M_2 = 0.68$ was noticeably higher for the original, roughly printed cascade than for the treated cascade (see Figure 8). In Table 3, three different coefficient results are listed. The level of the local pressure loss coefficient Y, used by Shelton et al. [15], is typically much lower than the energy loss coefficient ζ preferred by Kiock et al. [9]. In nearly the same order of magnitude as the energy losses are the losses Y_P. This loss definition is used by Yuan and Kind [21] in their investigations. The reduction due to surface treatment was comparable for all three definitions. Table 3 shows that the loss reduction for the three different definitions is in an area of about 32 $\pm$ 2%.

Corresponding details of the two local loss coefficient distributions in the wakes are shown in Figure 8, where the local energy loss coefficient ζ is plotted against the normalized traverse coordinate y/s for an exit Mach number $M_2 = 0.68$.

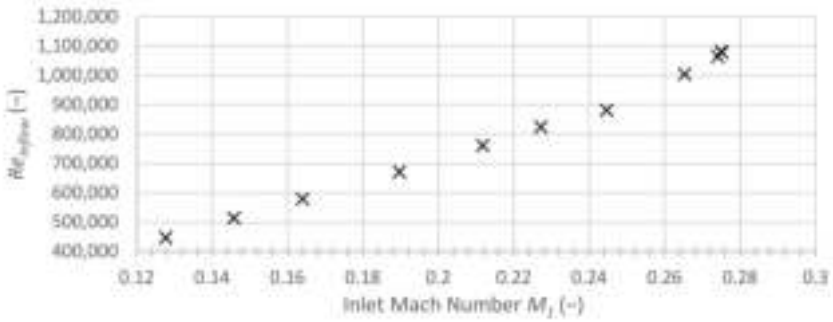

Figure 5. Inflow Reynolds number Re_{Inflow} against inlet Mach number M_1.

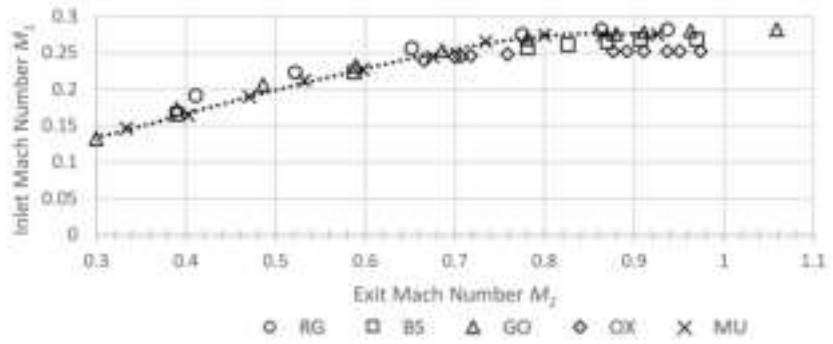

Figure 6. Inlet Mach number M_1 against exit Mach number M_2 and choking behavior (MU = new data obtained at Muenster and literature data adapted from Kiock et al. [9]; RG = von Karman Institute for Fluid Dynamics, GO = German Aerospace Centre (DLR) Göttingen, BS = TU Braunschweig, OX = Oxford University).

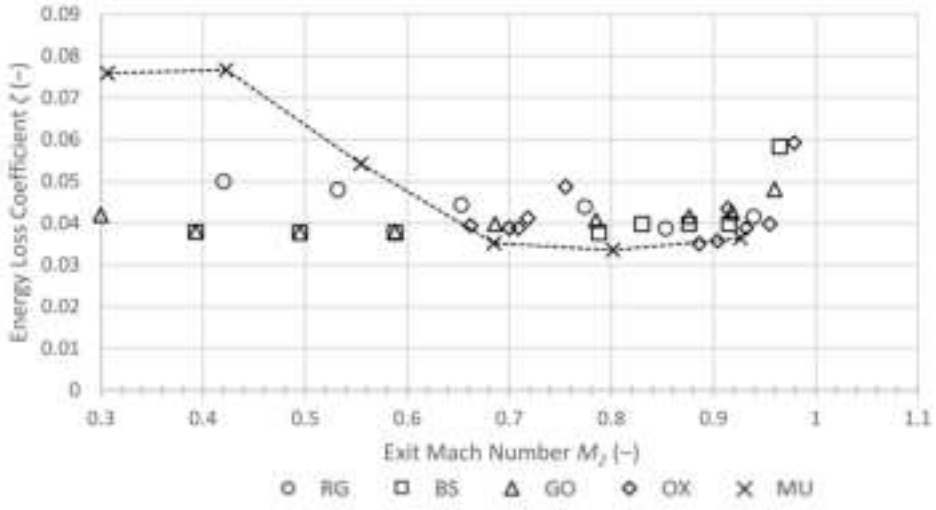

Figure 7. Loss coefficient ζ against exit Mach number M_2 for NOVEC 649 and literature data obtained for air and smooth blades (adapted from Kiock et al. [9]; RG = von Karman Institute for Fluid Dynamics, GO = German Aerospace Centre (DLR) Göttingen, BS = TU Braunschweig, OX = Oxford University).

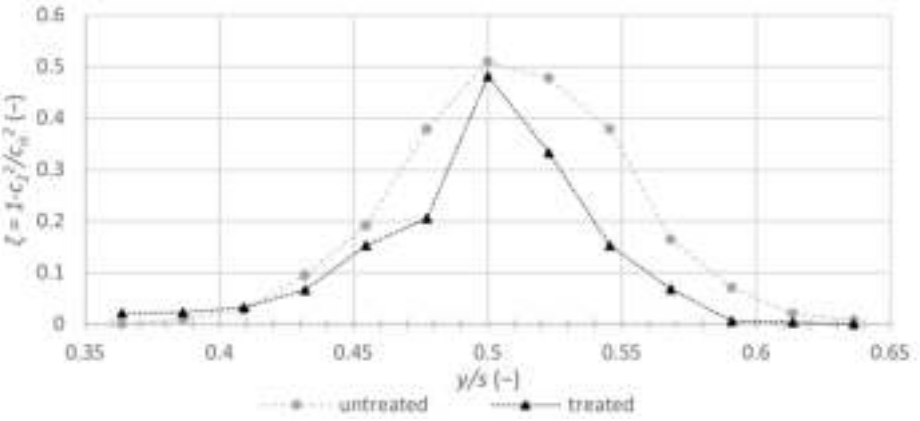

Figure 8. Energy loss coefficient ζ against traverse/space ratio coordinate (M_2 = 0.68).

Table 3. Three different approaches for the loss coefficient and average loss coefficients obtained for Novec 649 at M_2 = 0.68.

Loss Coefficient	Untreated State * (Original)	Treated State * (Finished)	Percentage Improvement
$Y = \mathbf{1} - \frac{p_{02}}{p_{01}}$	1.1%	0.747%	32.1%
$Y_P = \frac{p_{01}-p_{02}}{p_{01}-p_2}$	5.71%	4%	30%
$\zeta = \mathbf{1} - \frac{{c_2}^2}{{c_{2is}}^2}$	5.3%	3.51%	33.8%

* Roughness R_t: original 54.8 ± 4.9 µm, finished 32.5 ± 7.4 µm.

The local loss distributions indicated a thicker boundary layer and, hence, a higher profile loss in the case of the rougher cascade. Both pressure and suction side boundary layer thicknesses were reduced due to the surface treatment; however, the impact seemed to be stronger for the suction side. This effect of roughness is not uncommon in cascade aerodynamics.

The wake flow observations in Figure 8 indicate that a turbulent boundary layer flow past the airfoils was established for an exit Mach number of M_2 = 0.68. Hence, it is interesting to compare the loss reduction due to finishing with the predictions of boundary

layer theory. The ratios $Y_{\text{finished}}/Y_{\text{original}}$, $Y_{P,\text{finished}}/Y_{P,\text{original}}$ and $\zeta_{\text{finished}}/\zeta_{\text{original}}$ were 0.68 and 0.65, respectively (see Table 3). During the present experiments at $M_2 = 0.68$, the corresponding inlet and exit Reynolds numbers were of order $Re_1 = 1 \times 10^6$ and $Re_2 = 2.8 \times 10^6$, respectively. The relative roughness of the finished surface was $k_s/l = 10^{-3}$ and $k_s/l = 1.8 \times 10^{-3}$ for the original part. Then, the ratio of the skin friction coefficients of the finished and the original surface would be of order 0.75 (see Scholz [5], especially page 402). This value is relatively close to the observed loss coefficient ratios. This agreement supports the hypothesis that surface roughness affected the profile loss in the usual boundary layer theory framework. Due to the moderate Mach number level, the skin friction and loss coefficients were not significantly affected by compressibility effects. For smaller Reynolds numbers, there is a significant increase in the profile losses. These are no longer comprehensible with the theory of Scholz [5]. Therefore, it is assumed that in the lower velocity range (see Figure 7), friction losses at the airfoils occur and the local detachment of the center blade contributes to the losses. In this context, it is further interesting to note that the empirical profile loss correlation by Traupel [22] would predict a value of $\zeta = 3.6\%$ for the finished blade. This value is very close to the measured value $\zeta = 3.51\%$, as displayed in Table 3.

4. Conclusions

Profile loss results were reported of an experimental study using an additive manufactured linear turbine cascade placed in the test section of a closed-loop organic vapor wind tunnel. A blade profile from the open literature was chosen for the cascade, and the organic vapor was Novec 649. Pitot probes were employed to measure the flow field upstream and downstream of the cascade. The original roughness parameters of the metal-printed blades, as delivered by the manufacturer, were determined, and the first set of flow measurements was performed. Then, the printed part was finished, and the second set of flow measurements enabled an assessment of the impact of roughness on profile losses.

Although the Reynolds number level was relatively high, it was found that further surface treatment noticeably reduces the profile loss, as in the case of organic vapor flows through the printed cascade. After an additional finishing process, a similar profile loss behavior could be achieved, as reported for smooth blades. In addition, it was shown that the residual roughness has a massive influence on profile losses in the lower subsonic velocity range. This phenomena that the losses increase in the lower speed range was also detected in a study on the roughness effect. The reduction in the profile losses was nearly in the same area for all three loss approaches. Therefore, it is confirmed that the loss considerations are equivalent to each other in terms of velocity or pressure.

No significant new non-perfect gas dynamics effects were observed for the global cascade performance in this high subsonic up to transonic dilute gas flow regime.

Author Contributions: Conceptualization, S.a.d.W. and L.H.; methodology, L.H.; software, L.H.; validation, M.S., S.a.d.W. and L.H.; formal analysis, L.H.; investigation, F.R., R.W. and L.H.; resources, S.a.d.W.; data curation, L.H.; writing—original draft preparation, S.a.d.W.; writing—review and editing, L.H.; visualization, L.H.; supervision, F.R.; project administration, S.a.d.W.; funding acquisition, S.a.d.W. All authors have read and agreed to the published version of the manuscript.

Funding: This research work was funded by the program "progress.nrw-Research" of the State of Northrhine-Westfalia, Germany, under the grant number 005-2003-0076_037/PtJ 2003pr006. The support by J. Hollekamp for obtaining the surface roughness data is also acknowledged.

Institutional Review Board Statement: Not applicable.

Informed Consent Statement: Not applicable.

Data Availability Statement: Not applicable.

Conflicts of Interest: The authors declare no conflict of interest.

Nomenclature

a	speed of Sound	m/s
c	flow velocity	m/s
f	isentropic relation	-
h	specific enthalpy	J/kg
k_s	sand grain roughness	µm
l	chord length	mm
l_x	axial chord	mm
M	Mach number	-
o	narrowing	mm
p	static pressure	bar
p_0	total pressure	bar
R_a	mean roughness	µm
Re	Reynolds number	-
R_p	average peak-to-valley height	µm
R_t	maximum surface roughness	µm
R_z	peak-to-valley height	µm
s	spacing	mm
s	specific entropy	J/(kg·K)
s/l	space chord ratio	-
T	temperature	K
y	vertical traversing line	mm
y/s	traversing spacing ratio	-
Y	total pressure loss coefficient	-
Y_P	pressure loss coefficient	-
Z	compressibility factor	-
Greek Symbols		
β_1	inflow angle	◦
β_2	exit angle	◦
ζ	energetic loss coefficient	-
η	dynamic viscosity	Pa·s
κ	isentropic exponent	-
μ	micro	µ
ρ	density	kg/m^3
Subscripts		
1	inflow	
2	exit	
avg		
ch	choke	
t	total	
is	isentropic	

References

1. Magerramova, L.; Vasilyev, B.; Kinzburskiy, V. Novel Designs of Turbine Blades for Additive Manufacturing. In Proceedings of the ASME Turbo Expo 2016: Turbomachinery Technical Conference and Exposition, (GT2016-56084). Seoul, Korea, 13–17 June 2016.
2. Albright, B. Siemens 3D Prints Power Turbine Blades. *Digital Engineering*. 12 June 2017. Available online: www.digitalengineering247.com/article/siemens-3d-prints-power-turbine-blades (accessed on 25 May 2020).
3. Adair, D.; Kirka, M.; Ryan, D. Additive Manufacture of Prototype Turbine Blades for Hot-Fired Engine Performance Validation Trials. In Proceedings of the ASME Turbo Expo 2019, (GT2019-90966). Phoenix, AZ, USA, 17–21 June 2019.
4. Speidel, L. Einfluss der Oberflächenrauhigkeit auf die Strömungsverluste in ebenen Schaufelgittern. *Forschung. Ing.* **1954**, *20*, 129–140. [CrossRef]
5. Scholz, N. *Aerodynamik der Schaufelgitter*; G. Braun: Karlsruhe, Germany, 1965.
6. Bammert, K.; Sandstede, H. Influences of Manufacturing Tolerances and Surface Roughness of Blades on the Performance of Turbines. *ASME J. Eng. Power Jan.* **1976**, *98*, 29–36. [CrossRef]
7. Sieverding, C.H. Experimental Data on Two Transonic Turbine Blade Sections and Comparison With Various Theoretical Methods. VKI Lecture Series 59 - Volume 3 (Transonic Flows in Turbomachinery); 21–25 May 1973; Part 3. VKI PP 1972-05.

8. Lehthaus, F. Berechnung der transsonischen Strömung durch ebene Turbinengitter nach dem Zeit-Schritt-Verfahren. *VDI-Forsch.* **1978**, *586*, 5–24.
9. Kiock, R.; Lehthaus, F.; Baines, N.C.; Sieverding, C.H. The Transonic Flow Through a Plane Turbine Cascade as Measured in Four European Wind Tunnels. *ASME J. Eng. Gas Turbines Power* **1986**, *108*, 277–284. [CrossRef]
10. Baumgärtner, D.; Otter, J.J.; Wheeler, A.P.S. The Effect of Isentropic Exponent on Transonic Turbine Performance. In Proceedings of the ASME Turbo Expo 2019, Phoenix, AZ, USA, 17–21 June 2019. (GT2019-90251).
11. Reinker, F.; Kenig, E.Y.; aus der Wiesche, S. CLOWT: A Multifunctional Test Facility for the Investigation of Organic Vapor Flows. In In Proceedings of the ASME 2018 5th Joint US-European Fluids Engineering Division Summer Meeting, (V002T14A004). Montreal, QC, Canada, 15 July 2018.
12. Reinker, F.; Kenig, E.Y.; aus der Wiesche, S. Closed Loop Organic Vapor Wind Tunnel CLOWT: Commissioning and Operational Experience. In In Proceedings of the ORC, Athens, Greece, 9–11 September 2019; p. 47.
13. Reinker, F.; aus der Wiesche, S. Application of Hot-Wire Anemometry in the High Subsonic Organic Vapor Flow Regime. In In Proceedings of the 3rd International Seminar on Non-Ideal Compressible Fluid Dynamics for Propulsion and Power, Delft, The Netherlands, 29–30 October 2020.
14. McLinden, M.O.; Perkins, R.A.; Lemmon, E.W.; Fortin, T.J. Thermodynamic Properties of 1,1,1,2,2,4,5,5,5-Nonafluoro-4(trifluoromethyl)-3-pentanone: Vapor Pressure, (p, ρ, T) Behavior, and Speed of Sound Measurements, and an Equation of State. *J. Chem. Eng. Data* **2015**, *60*, 3646–3659. [CrossRef]
15. Shelton, M.L.; Gregory, B.A.; Doughty, R.L.; Kiss, T.; Moses, H.L. A Statistical Approach to the Experimental Evaluation of Transonic Turbine Airfoils in a Linear Cascade. *ASME J. Turbomach.* **1993**, *115*, 366–375. [CrossRef]
16. Reinker, F.; Wagner, R.; Passmann, M.; Hake, L.; aus der Wiesche, S. Performance of a Rotatable Cylinder Pitot Probe in High Subsonic Non-Ideal Gas Flows. In In Proceedings of the 3rd International Seminar on Non-Ideal Compressible Fluid Dynamics for Propulsion and Power, Delft, The Netherlands, 29–30 October 2020.
17. Passmann, M.; aus der Wiesche, S.; Joos, F. A one-dimensional analytical calculation method for obtaining normal shock losses in supersonic real gas flows. *IOP Conf. Ser. J. Phys. Conf. Ser.* **2017**, *821*, 012004. [CrossRef]
18. Cumpsty, N.A.; Horlock, J.H. Averaging Nonuniform Flow for a Purpose. *ASME J. Turbomach.* **2006**, *128*, 120–129. [CrossRef]
19. Dixon, S.L.; Hall, C.A. *Fluid Mechanics and Thermodynamics of Turbomachinery*, 6th ed.; Butterworth-Heinemann: Burlington, MA, USA, 2010.
20. Moffat, R.J. Contributions to the Theory of Uncertainty Analysis of Single-Sample Experiments. In Proceedings of the 1980–81 AFOSR-HTTM-Stanford Conference on Complex Turbulent Flows, Stanford, CA, USA, 1 February 1982 ; Volume 1, pp. 40–56.
21. Yuan, L.Q.; Kind, R.J. Measurements and computations of compressible flow through a turbine cascade with surface roughness. In Proceedings of the ASME Turbo Expo 2006, (GT2006-90018). Barcelona, Spain, 8–11 May 2006.
22. Traupel, W. *Thermische Turbomaschinen, Erster Band*; Springer: Berlin/Heidelberg, Germany, 1966.

International Journal of
Turbomachinery
Propulsion and Power

MDPI

Article

Turbomachine Operation with Magnetic Bearings in Supercritical Carbon Dioxide Environment

Alexander Johannes Hacks * and Dieter Brillert

Chair of Turbomachinery, University of Duisburg-Essen, Lotharstraße 1, 47057 Duisburg, Germany; dieter.brillert@uni-due.de
* Correspondence: alexander.hacks@uni-due.de

Abstract: In the sCO2-HeRo project, the Chair of Turbomachinery at the University of Duisburg-Essen developed, built and tested a turbomachine with an integral design in which the compressor, generator and turbine are housed in a single hermetic casing. However, ball bearings limited operation because their lubricants were incompatible with supercritical CO_2 (sCO_2) and they had to operate in gaseous CO_2 instead. To overcome this problem, the turbomachine was redesigned built and tested in the sCO2-4-NPP project. Instead of ball bearings, magnetic bearings are now used to operate the turbomachine with the entire rotor in sCO_2. This paper presents the revised design, focusing on the usage of magnetic bearings. It also investigates whether the sCO_2 limits the operating range. Test runs show that increasing the density and rotational speed results in greater deflection of the rotor and greater forces on the bearings. Measurements are also analyzed with respect to influence of the density increase on the destabilizing forces in the rotor–stator cavities. The conclusion is that for the operation of the turbomachine, the control parameters of the magnetic bearings must be adjusted not only to the rotor speed, but also to the fluid density. This enabled successful operation of the turbomachine, which reached a speed of about 40,000 rpm during initial tests in CO_2.

Keywords: supercritical carbon dioxide; magnetic bearings; rotor dynamics

check for updates

Citation: Hacks, A.J.; Brillert, D. Turbomachine Operation with Magnetic Bearings in Supercritical Carbon Dioxide Environment. *Int. J. Turbomach. Propuls. Power* **2022**, *7*, 18. https://doi.org/10.3390/ijtpp7020018

Academic Editor: Marcello Manna

Received: 2 December 2021
Accepted: 8 June 2022
Published: 14 June 2022

Publisher's Note: MDPI stays neutral with regard to jurisdictional claims in published maps and institutional affiliations.

Copyright: © 2022 by the authors. Licensee MDPI, Basel, Switzerland. This article is an open access article distributed under the terms and conditions of the Creative Commons Attribution (CC BY-NC-ND) license (https://creativecommons.org/licenses/by-nc-nd/4.0/).

1. Introduction

This research paper focuses on the work conducted by the Chair of Turbomachinery at University Duisburg-Essen in the sCO2-4-NPP project to develop and test a compact turbomachine with integral design and active magnetic bearings (AMB) in CO_2 in the supercritical state (sCO_2). It is part of a novel heat removal system for residual decay heat in nuclear power plants developed in the previous project sCO2-HeRo (Benra et al. [1] and Starflinger et al. [2]). The application requires the overall system and the turbomachine to be compact, robust and simple. Therefore, the original turbomachine, called sCO2-HeRo^B TAC, presented by Hacks et al. [3] consists of a one-stage compressor and turbine on either end of a shaft with an alternator in the middle. While the TAC meets the requirements of compactness and simplicity due to all components being housed in a single hermetic casing, it has hybrid angular ball bearings lubricated with grease to support the rotor. Unfortunately, the grease proved to be incompatible with sCO_2. As a result, an additional auxiliary pump had to be applied to reduce the pressure of the CO_2 at the bearings and run them in gaseous CO_2 instead. This made the system less compact and harder to control because the outlet pressure of the auxiliary pump and compressor had to be balanced against each other. Furthermore, a safety relief valve ensured subcritical pressure at the bearings. Therefore, a failure of the pump results in loss of CO_2 inventory and renders the heat removal system less robust. To overcome this drawback of the original design, the new TAC needs to operate with all rotor–stator cavities filled by sCO_2 as indicated by the darker blue and purple colors in Figure 1. AMBs do not require lubricants. Therefore, they represent a suitable technology to replace the ball bearings in the original design and eliminate the additional auxiliary pump in the system.

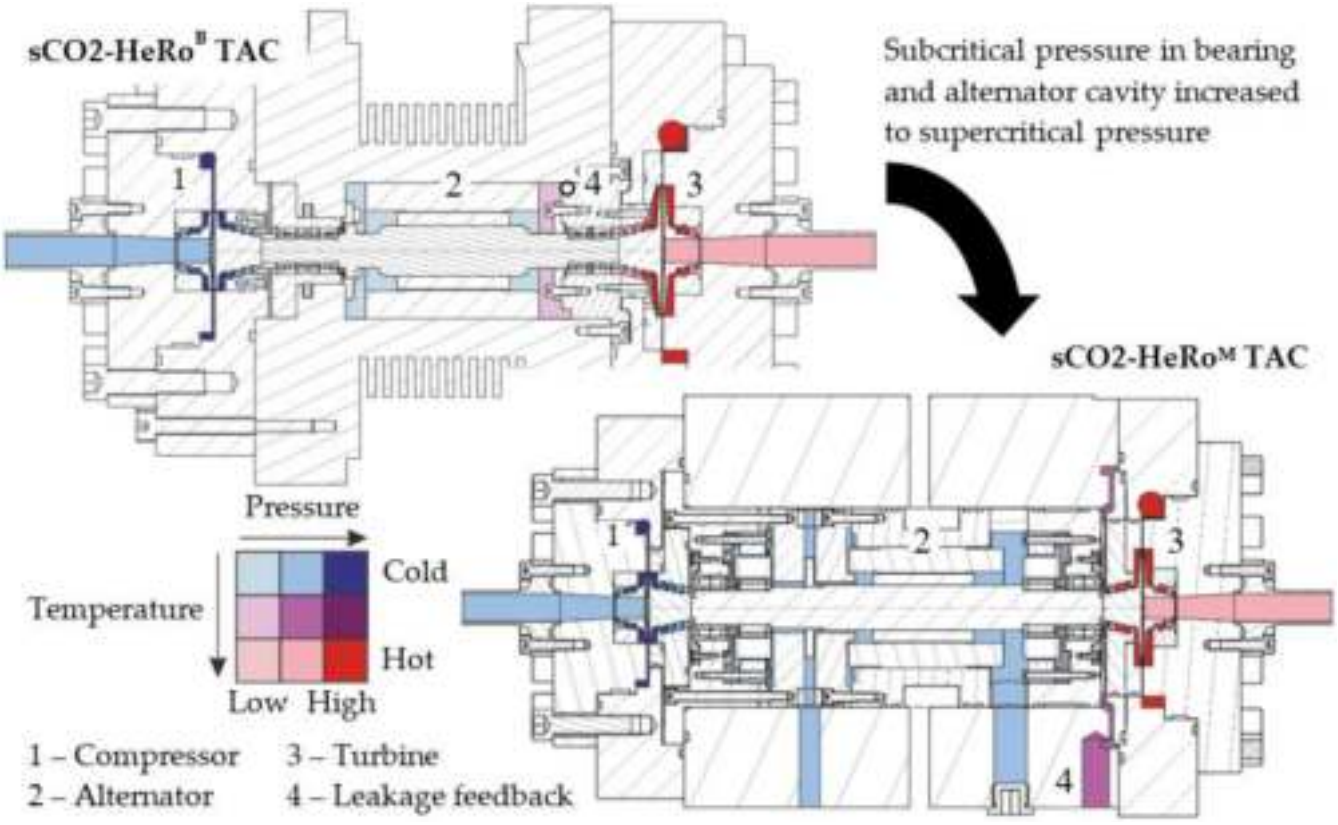

Figure 1. Cross-sections of sCO2-HeRo^{B} TAC [3] (**top left**) and sCO2-HeRo^{M} TAC (**bottom right**) with indication of CO_2 pressure and temperature inside rotor stator cavities.

However, there is scarce research documented in the literature concerning the operation of turbomachines for sCO_2 with AMB. To the author's knowledge, only a collaboration between the Korea Atomic Energy Research Institute (KAERI, Daejeon, Korea) and the Korea Advanced Institute of Science and Technology (KAIST, Daejeon, Korea) has published experiments on AMB operating in sCO_2. They aim to operate a hermetic compressor with high-pressure sCO_2 at the bearings, similar to the TAC described by the authors for the sCO2-HeRo system. In 2016, Cha et al. [4] reported sCO_2 fluid properties to cause instability of the bearing rotor leading to the erection of AMB test rig. In 2019, Kim et al. [5] published first results. Based on their experiments, they show that sCO_2 indeed has the potential to affect the rotor due to high density and sensitivity of density to pressure [6]. Consequently, they are working on a model to predict the effect of sCO_2 in the turbomachinery cavities on the rotor and to find a suitable control strategy for the AMBs [6,7].

This paper describes the design and operation of the newly built TAC with AMB (called sCO2-HeRo^{M} TAC). The key features and dimensions are highlighted in this paper. Similar to previous studies at KAERI and KAIST, a theoretic analysis is performed, showing potential of sCO_2 in the alternator cavity to cause the largest destabilizing forces, compared to the other cavities. Consequently, a cooling concept was developed to reduce the density of sCO_2 within the rotor–stator cavity and the resulting destabilizing forces. During the initial test runs in the sCO2-HeRo cycle, the density of CO_2 gradually increased. Measurements are presented for increasing the speed at different density levels. Based on this, additional measurements at constant rotational speed are employed to evaluate the potential of sCO_2 density to destabilize the rotor. During this process, the sCO2-HeRo^{M} TAC reached the design rotational speed of 50,000 rpm in air and approximately 30,000 rpm at compressor inlet density of almost 650 kg/m^3. Furthermore, observations of adapting control parameters of the AMB system to the sCO_2 fluid density are presented. Overall, operability of sCO2-HeRo^{M} TAC is demonstrated.

2. Design of the sCO2-HeRo^{M} Turbomachine with Active Magnetic Bearings

The design of the sCO2-HeRo^{M} TAC is based on the sCO2-HeRo^{B} TAC. Hacks et al. [3] describe the design of the latter in detail and show main cycle parameters. The compressor geometry [3,8] as well as performance measurements [9,10] are public, too. Figure 1 shows the overall layout of the TACs. It is identical for both the sCO2-HeRo^{M} TAC and the sCO2-HeRo^{B} TAC bearing a turbine, alternator and compressor on a single shaft in a hermetic casing. Design features such as the compressor and turbine geometry are identical, too. The major difference is the type of bearing. In the sCO2-HeRo^{M} TAC, the original ball bearings were replaced by AMB to eliminate the limitations imposed by the grease. The latter was found to dissolve in sCO_2 and was therefore maintained in gaseous CO_2 in the sCO2-HeRo^{B} TAC by reducing CO_2 pressure to subcritical pressure, indicated by lighter blue color in Figure 1, with an additional pump. AMB do not require a lubricant and therefore overcome the restrictions imposed by gaseous CO_2 at the bearings. However, they have certain characteristics, which must be considered for design and operation. In general, AMB systems require two radial bearings and a separate axial thrust bearing, which is different from the hybrid angular ball bearings originally used. Previously, only a single radial and one combined axial–radial bearing were required because this bearing type can support both axial and radial forces [3]. Furthermore, AMB requires sensors to control the position of the levitated rotor and additional safety bearings to keep the rotor from crashing into the stator in case of AMB failure or overload. This has several implications for the new TAC. First, the rotor is about 20% longer due to the additional axial bearing, sensors and safety bearings. Therefore, the shaft must have a larger diameter to keep the critical speed above the design speed. Second, the thrust disk of the axial bearing adds significantly to the already high windage losses. These are larger in the sCO2-HeRo^{M} TAC compared to the sCO2-HeRo^{B} TAC due to the larger shaft diameter in general, the new thrust disk and because sCO_2 is denser than gaseous CO_2. In addition, uneven pressure distribution on both sides of the thrust disk may result in high axial thrust. Third, the labyrinth seal clearance is kept at 0.1 mm because of the small design mass flow rate of the cycle of only 0.65 kg/s. Therefore, maximum deflection of the rotor must remain below 0.1 mm at the seals and is only 0.08 mm at the safety bearings. This requires precise manufacturing and assembly. It also limits the maximum radial deflection of the rotor during operation.

2.1. Design of Internal Flow Paths

Further requirements relate to the design of flow paths within the TAC. The AMB and sensors are electronic components that need to stay below their temperature limit of about 150 °C. However, CO_2 temperatures at the turbine measure up to 200 °C which is above the limit and requires cooling by cold CO_2. Furthermore, the sCO_2 properties inside the TAC affect the rotor and components such as the bearings and alternator and require interactive design of the rotor, sCO_2 flow paths and AMB controller parameters. On one hand, the sCO_2 needs to provide cooling to the alternator and AMB, which requires high heat capacity and consequently high density of the sCO_2. On the other hand, high density means a stronger interaction between the rotor and surrounding sCO_2, which translates into higher windage losses and higher pressure gradients inside rotor–stator cavities causing larger forces on the rotor. At the thrust disk and impellers, the pressure gradients may cause significant axial thrust, which must be covered by the load capacity of the axial thrust bearing. Pressure gradients in the radial direction cause forces that must be supported by journal bearings. If these are too large, the deflection of the rotor increases until the rotor touches the safety bearings causing the TAC to shut down. To meet the contradictive demand of high vs. low density inside the rotor–stator cavities, an additional sCO_2 inlet and outlets were implemented in the central part of the TAC to control CO_2 flow rate, direction and density. The positions of the additional inlet and outlets are marked in the cross-section in Figure 2 and the

simplified scheme in Figure 3 shows two resulting configurations for the internal flow paths. Configuration 1 uses the leakage outlet (c) and is similar to the original design, depicted in Figure 1. It has the advantage of requiring no additional cooling flow through (a). However, cold sCO_2 from compressor leakage with high-density flows along large portions of the rotor, around the axial thrust disk and through the generator cavity before it is mixed with hot turbine leakage in mixing point M3. This translates to high windage losses, large axial thrust and high radial forces in the generator cavity. In configuration 2, the leakage is extracted at the thrust disk (b) of the axial bearing. It is a mixture of the compressor leakage and the cooling flow through the generator, mixed in point M1. The cooling flow (a) is mixed with hot turbine leakage between turbine hub seal (6) and radial bearing (5) in mixing point M2. Thus, density of sCO_2 flowing through the generator cavity (4) is lower and controllable by cooling flow (a). This means lower windage losses, radial fluid forces and axial thrust.

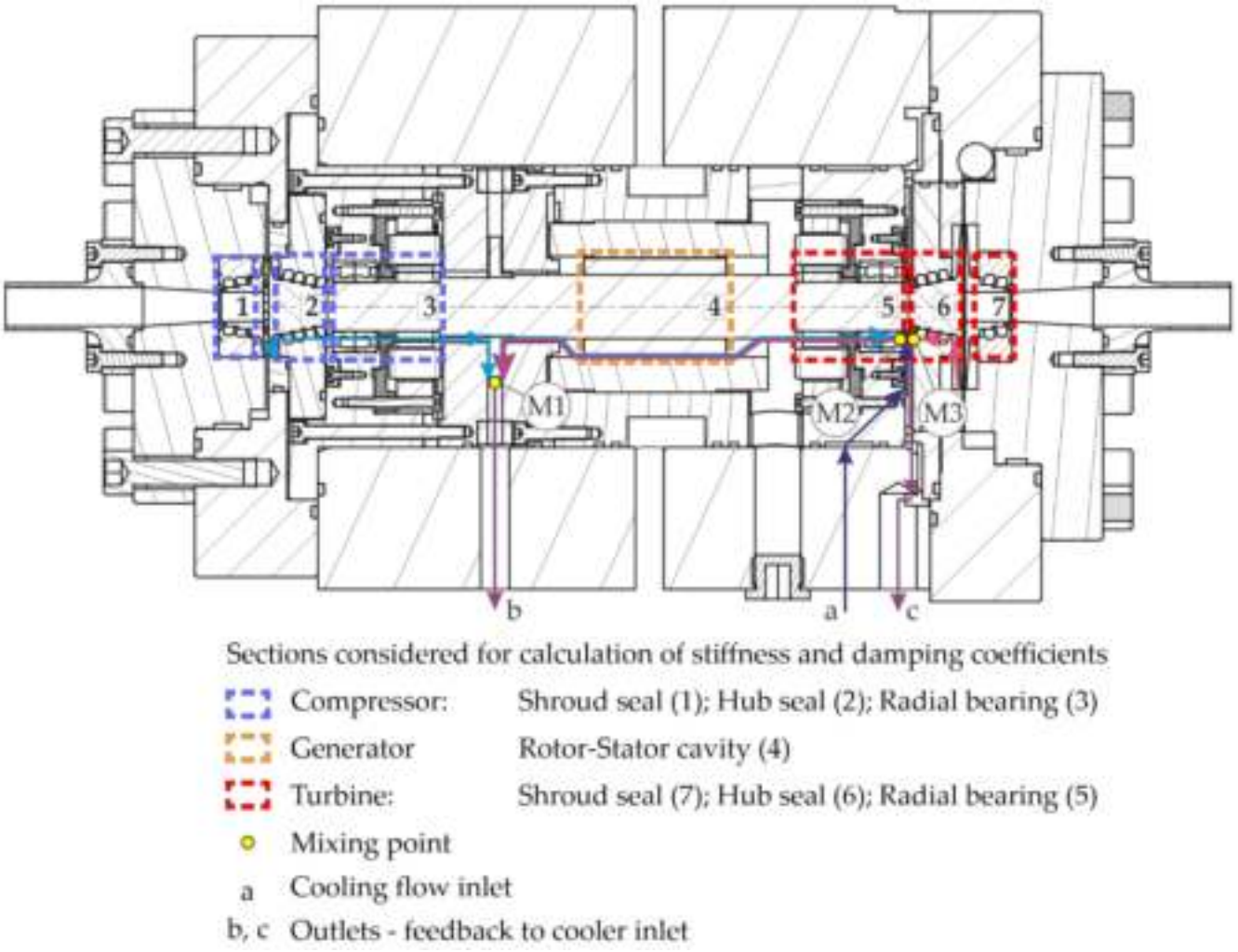

Figure 2. Sections considered for calculation of stiffness and damping coefficients.

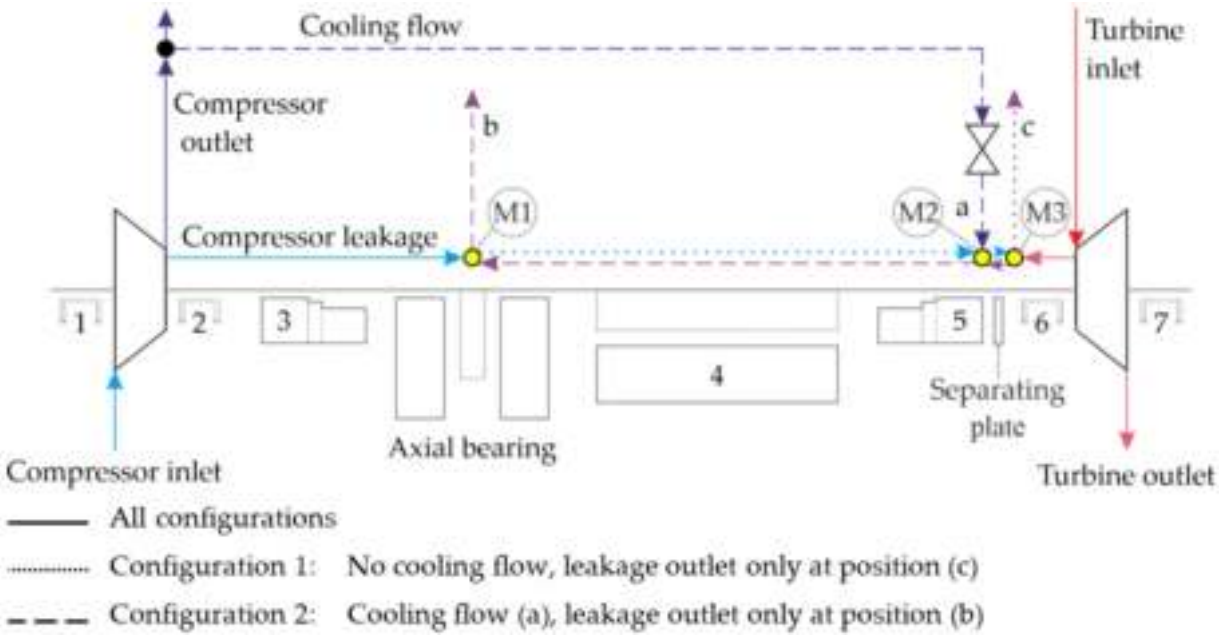

Figure 3. Simplified scheme of CO_2 two configurations of flow paths inside sCO2-HeRo^M TAC with labyrinth seals 1, 2, 6, 7, radial magnetic bearing clearance 3, 5 and generator cavity 4 (colors according to Figure 1).

2.2. Fluid Forces of sCO$_2$ in Rotor–Stator Cavities of the sCO2-HeRo^M Turbomachine

As this paper relates to the AMB used in sCO2-HeRo^M TAC, windage losses, axial thrust and the cooling effect of sCO_2 calculated with in-house code are not discussed in detail. The focus lies on the radial deflection of the rotor and radial forces in the bearings. These are caused by forces on the rotor due to imbalance and rotationally asymmetric pressure fields around the rotor. The latter occurs in the impellers and in the rotor–stator cavities. The rotor–stator cavities are the labyrinth seals and cavities in the manner of cylindrical shells such as the journal bearings (safety bearings, sensor rings, radial bearings) and the generator cavity. In the radial bearing, the space between the electromagnets is closed similar to the journal bearing shown by Jin et al. [7] to obtain a nearly cylindrical surface and avoid large forces caused by irregular geometry reported by Kim et al. [5]. To account for the forces (F) in the rotordynamics analysis, equivalent stiffness (K) and damping coefficients (C) are used together with deflection x and y (see Equation (1)). These are calculated using the commercially available tool xLRotor [11] for different sections indicated in Figure 2. For labyrinth seals, a model designed for a compressible gas seal was used, while the other cavities were approximated as annular seals. Calculations of stiffness and damping coefficients were performed for sections in Figure 2 considering the pressure and density distribution along the flow path of sCO_2 inside the TAC. However, a constant average density and viscosity was used as input for the annular seal model and the compressible gas seal model used a constant compressibility factor to account for fluid properties. Due to the small change of fluid properties within the annular cavities and relatively little pressure difference across the seals, the deviations caused by the inaccuracy of fluid properties are considered to be limited. They reveal that all cavities considered have a destabilizing effect, i.e., the forces of the fluid act on the rotor in a direction that increases the deflection of the rotor. Considering flow path configuration 1, Figure 4 shows the results of an example calculation. Coefficients of the different sections in Figure 2 are displayed as a fraction of those in the generator cavity (4). Note that sections (3) and (5) are divided into the different elements of the radial bearing, safety bearing, sensor ring and the radial bearing itself. According to Figure 4, the generator cavity (4) dominates the rotordynamic influence of the sCO_2 compared to the other cavities. Coefficients are at least six-times larger for cross-coupled stiffness $\left(K_{xy} = K_{yx}\right)$ and direct damping $\left(C_{xx} = C_{yy}\right)$ and almost

10-times higher for direct stiffness $(K_{xx} = K_{yy})$ and cross-coupled damping $(C_{xy} = C_{yx})$. The reason for the dominance of the generator cavity is the size of the cavity, which has twice the diameter and more than twice the length of the cavity in safety bearings. The latter has high coefficients because of a narrow radial gap width of only 0.08 mm. In addition, the liquid-like sCO_2 causes larger coefficients for seals and bearings on the compressor side, even though those on the turbine side bear the same geometry. Since Figure 4 suggests that forces originating in the generator cavity are dominant over those in other cavities, particular attention is paid to the effect of density alterations inside this cavity on radial deflection and bearing forces.

$$\begin{bmatrix} F_x \\ F_y \end{bmatrix} = -\begin{bmatrix} K_{xx} & K_{xy} \\ K_{yx} & K_{yy} \end{bmatrix} \begin{bmatrix} x \\ y \end{bmatrix} - \begin{bmatrix} C_{xx} & C_{xy} \\ C_{yx} & C_{yy} \end{bmatrix} \begin{bmatrix} \dot{x} \\ \dot{y} \end{bmatrix} \tag{1}$$

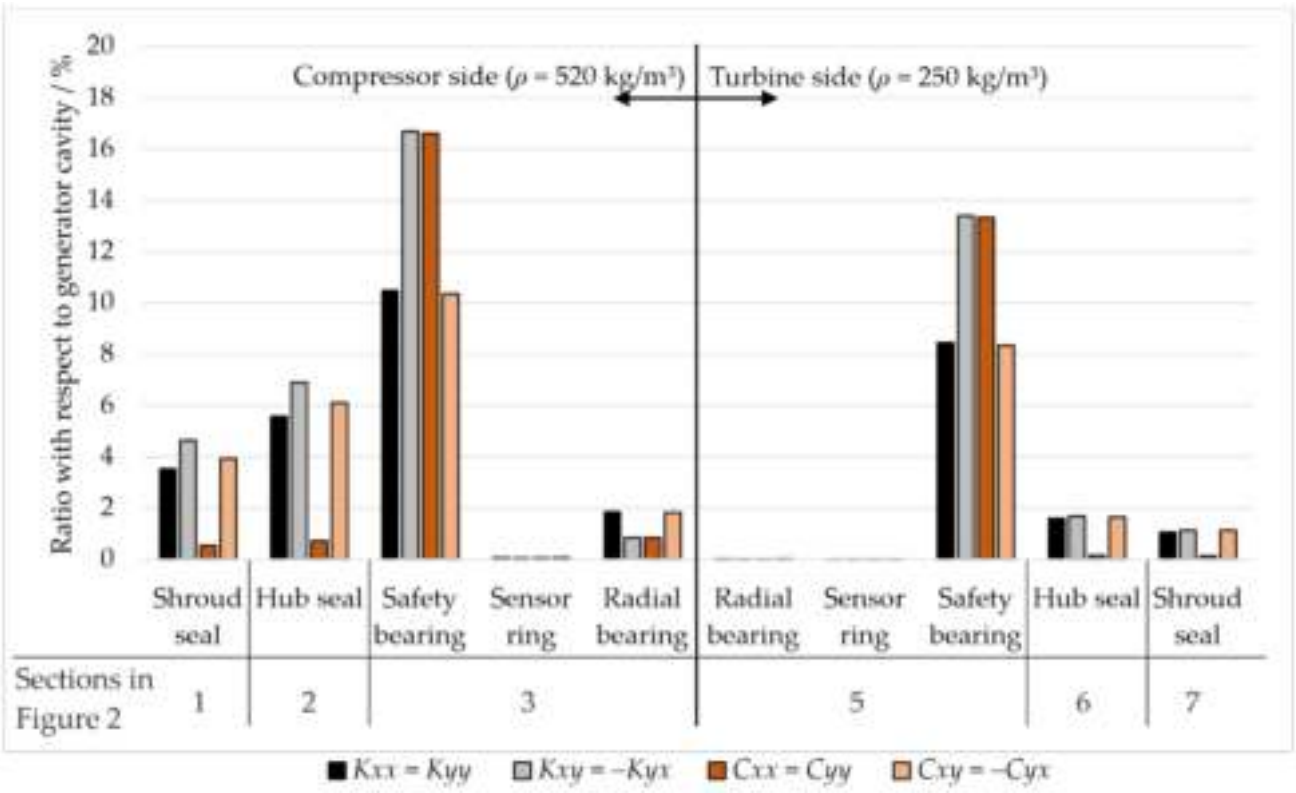

Figure 4. Ratio of stiffness coefficients (K) and damping coefficients (C) with respect to coefficients of generator cavity (density = 310 kg/m^3) calculated for flow path configuration 1.

Figure 5 shows a sensitivity study of radial clearance, density inside the generator cavity and rotational speed on the stiffness and damping coefficients. In the study, only one parameter is changed while the others remain constant. To increase radial clearance, the rotor diameter is reduced. Density is changed at constant pressure. The study is carried out with xLRotor [11] using a model for a short annular seal. Although the cavity fails to meet the requirements of a short seal, relationships in terms of the studied parameters are considered equal for long- and short-seal models. Figure 5 presents clearance height as having a significantly larger effect on the cross-coupled stiffness (and direct damping) than on direct stiffness. On the other hand, decrease in density and rotational speed lead to a larger reduction of direct stiffness coefficients. In terms of forces, this means density and rotational speed have more influence on forces pointing towards (stabilizing) or away from the center of rotation (destabilizing). For sCO2-HeRo^M TAC, the focus lies on these forces and consequently the direct stiffness coefficients. The reason is that in the (original) flow path configuration 1 (see Figure 3) the direct stiffness coefficients were too large for operation of the sCO2-HeRo^M TAC. Therefore, flow path configuration 2 was established

to reduce the density in the generator cavity and to allow operation of the sCO2-HeRo^{M} TAC. This and the general influence of density suggested by Figure 5 means that it must be controlled during operation.

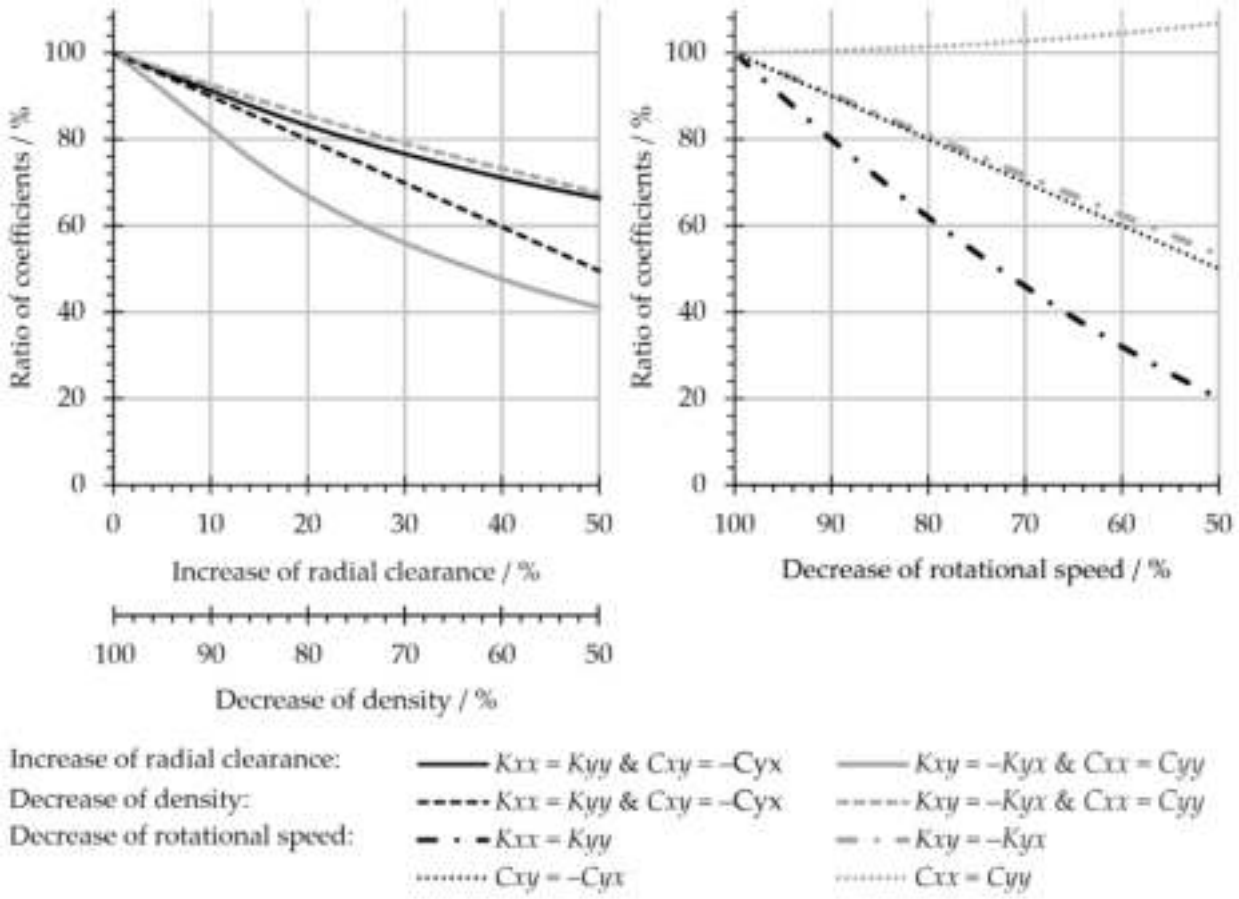

Figure 5. Ratio of stiffness and damping coefficients for decrease of rotational speed, increase of radial clearance and decrease of density in generator cavity of sCO2-HeRo^{M} TAC.

3. Operation of the sCO2-HeRo^{M} Turbomachine

The goal of the initial operation of the sCO2-HeRo^{M} TAC is to prove its operability in the sCO2-HeRo cycle. It also aims to verify the concept of internal flow paths and improve understanding of the effects of rotational speed and density on the operation of the TAC in sCO_2. Based on findings of the previous chapter and the publications of Cha et al. [4] and Kim et al. [5], operation of a TAC with AMB becomes more difficult as density increases. Therefore, the tests start with operation in air at atmospheric pressure, considered as known conditions. Then, they proceed with CO_2 in gaseous conditions and low density. As shown in Figure 6, the density at the compressor inlet, representing the highest density in the cycle, increased gradually starting from the gaseous state of CO_2 at 160 kg/m^3 in region I until reaching supercritical conditions for the first time in region III with a density above 300 kg/m^3. Finally, region V reached design density and design static inlet pressure of 566 kg/m^3 and 78.3 bar at the compressor inlet, respectively. Together with regions III, IV and VI, the tests covered the whole range of possible compressor inlet conditions. This includes higher static inlet pressures of up to 90 bar, maximum inlet density of 650 kg/m^3 and conditions around the critical point. During operation of the TAC in the different regions of compressor inlet conditions in Figure 6, the deflection of the rotor and the radial, magnetic forces calculated for the bearings were monitored. Radial deflections are measured at the radial bearings with eddy current sensors monitoring the position of the rotor relative to the stator. At each bearing, four sensor pairs opposite to

each other are employed. The increase of rotational speed in different regions of compressor inlet conditions is presented first. Afterwards, measurements at constant rotational speed are discussed with respect to the influence of density. Measurements are compared to obtain a qualitative understanding regarding the dependence of deflection and bearing forces on rotational speed and sCO_2 density.

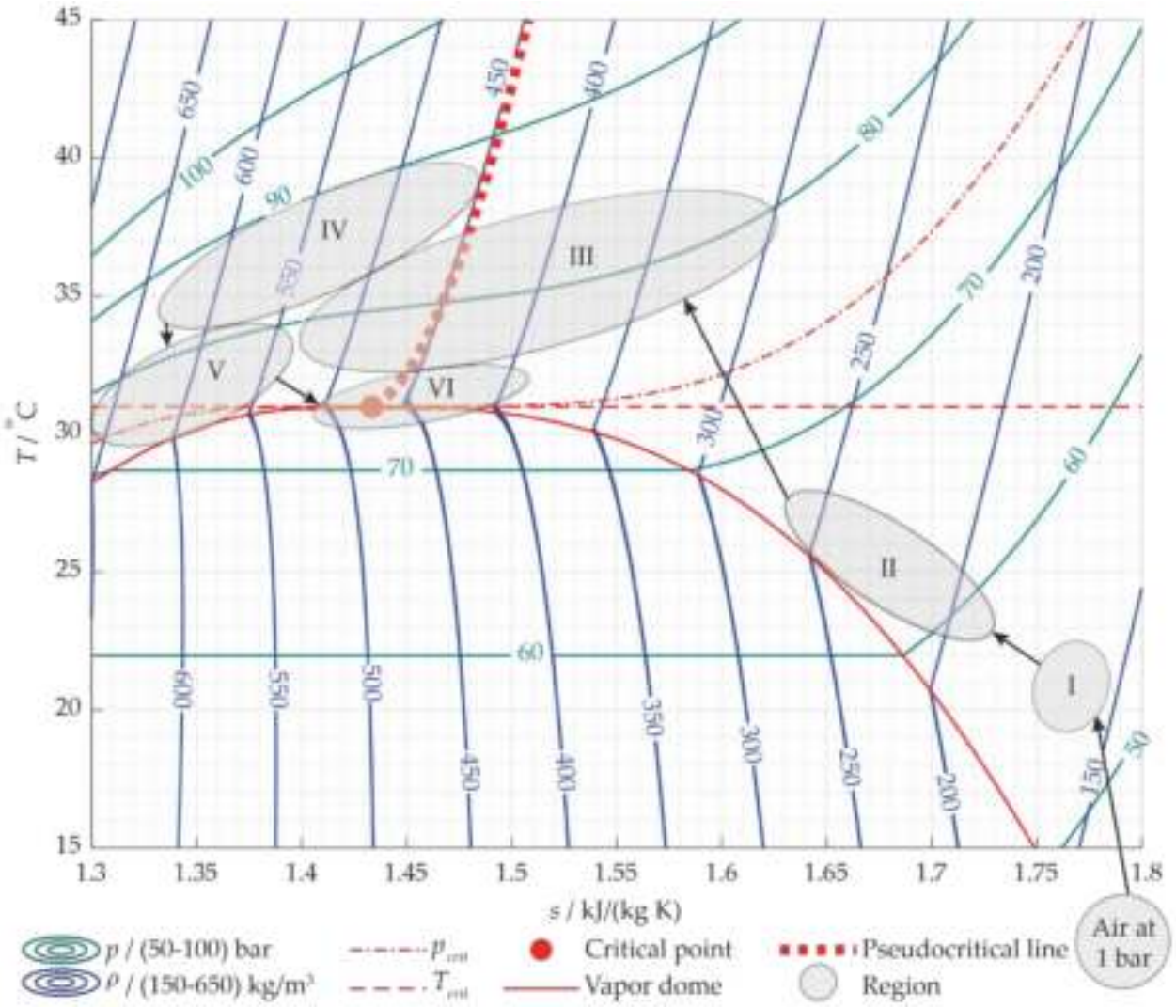

Figure 6. Regions of compressor inlet conditions during steps of initial operation depicted in T-s-diagram for CO_2 with lines of constant pressure (p) and density (ρ).

3.1. Increasing Rotational Speed

Here, a comparison between test runs in different regions of Figure 6 is presented. Each test run also shows the effect of rotational speed on the radial deflection of the rotor and the radial forces in the bearings. From Figure 5, the observation of an increase in force and/or deflection when increasing both rotational speed and density is expected. Whereby rotational speed is expected to demonstrate a larger effect. The analysis starts with a preliminary test conducted in air. The TAC reached a design rotational speed of 50,000 rpm as shown in Figure 7. For readability, the (thousands) of measurement points are not depicted. Instead, the shaded areas represent the area where 90% of the measurement points are located. That means that for each rotational speed, the lower and upper bound of the shaded area are chosen in a way that 90% of measurements at the respective rotational speed are included. During air pre-tests, a basic AMB controller was used without considering rotordynamic coefficients of seals and cavities. Since air density represents only 1% of the density in region I of operation in CO_2 (see Figure 7) and

even less, only 0.3%, of the compressor design inlet density, forces due to fluid inside the impellers and cavities are considered negligible compared to operation in CO_2. Figure 7 shows deflection of rotor at standstill to be on average 3 µm for the compressor bearing and 2 µm for the turbine bearing and to fluctuate in the same range. As speed increases, both deflection and forces increase slightly. At 50,000 rpm, the maximum deflection reached approximately 12 µm or 15% of the maximum clearance in the safety bearings. Forces remained well below 10% of the maximum bearing force.

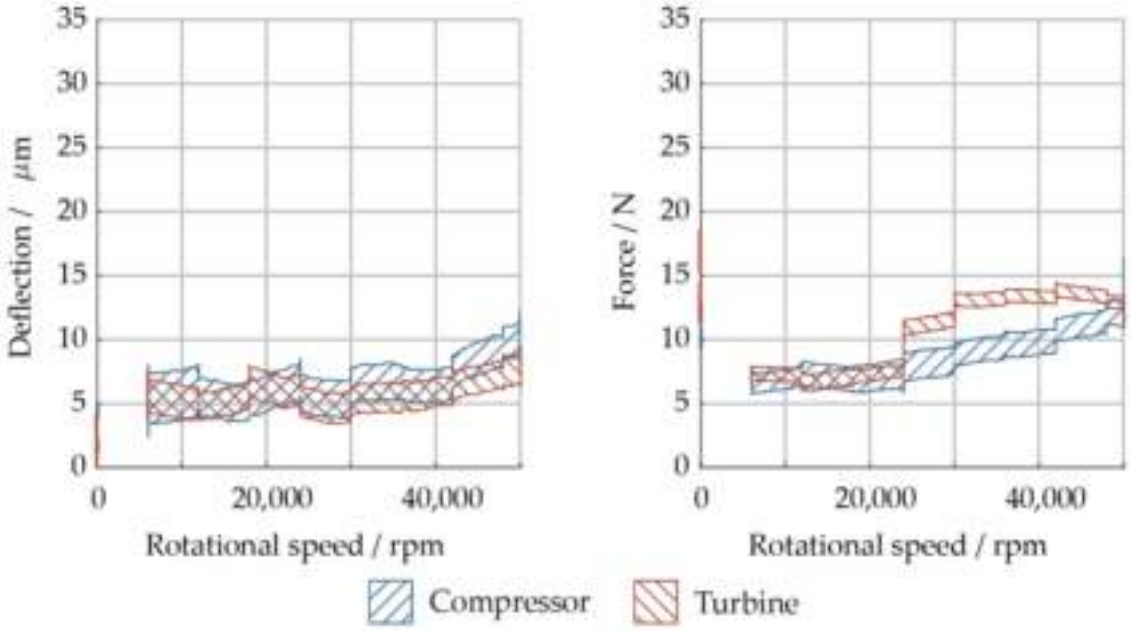

Figure 7. Deflection and forces at radial bearings on compressor and turbine side during air pre-tests for speeds ranging from 0 rpm to 50,000 rpm.

In general, the preliminary air test reached 50,000 rpm and showed the rotor to be well-balanced and clearances to be as designed. It proved general operability of the TAC and provided the basis for further testing in CO_2.

The next step included the first tests regions I–III in Figure 6, where CO_2 was in a gaseous or gas-like state. From regions I–III, the density increases at the compressor inlet and in the whole cycle. Furthermore, the density difference between the turbine inlet and compressor inlet is small because the maximum temperature of CO_2 is kept well below 60 °C. Finally, the maximum speed during these tests is limited to 40,000 rpm because, unlike tests in air, the TAC relies on turbine power to reach maximum speed owing to the higher density at the compressor requiring more power. Due to low compressor inlet density and low turbine inlet temperature, this power cannot be provided.

Figure 8 presents a comparison of measurements for three test runs and the test run in air. Test run Ia and Ib are at the density in region I and run II is in region II. During run Ia, the initial controller design used for the air test was not modified. As in the air test, increased deflections and forces were observed as rotational speed increased. Moreover, the fluctuations in measurements (depicted as larger enclosed area) now seem to also increase. Above 20,000 rpm, the deflections are larger than for the test run with air, especially on the compressor side. Figure 8 shows large deflections of about 25 µm or 31% of the clearance at the compressor bearing at a speed of 33,000 rpm or 66% of design rotational speed. This is already more than twice the deflection found in the air test at design rotational speed. Note the peak at approximately 5000 rpm, which indicates switching on the imbalance controller. It is active for larger rotational speeds and strongly reduces the deflection of the rotor. Similar action is taken again during test runs Ib and II. The controller parameters are changed so that the deflection of the rotor is reduced at speeds above 27,000 rpm.

Therefore, there is drastically less deflection of the rotor for rotational speeds above 27,000 rpm compared to run Ia. For approximately 38,000 rpm, values are now 40–50% larger than values at design speed in the test run with air. Observing the radial force in both bearings, the forces in the compressor bearing are larger than for the air case. On the other hand, forces in the turbine bearing remain similar but for larger fluctuations (larger enclosed area). Run Ia is an exception, exhibiting a much larger force. It is interesting to note that changing the control parameters when exceeding 27,000 rpm leads to a steeper increase in the forces as a function of speed.

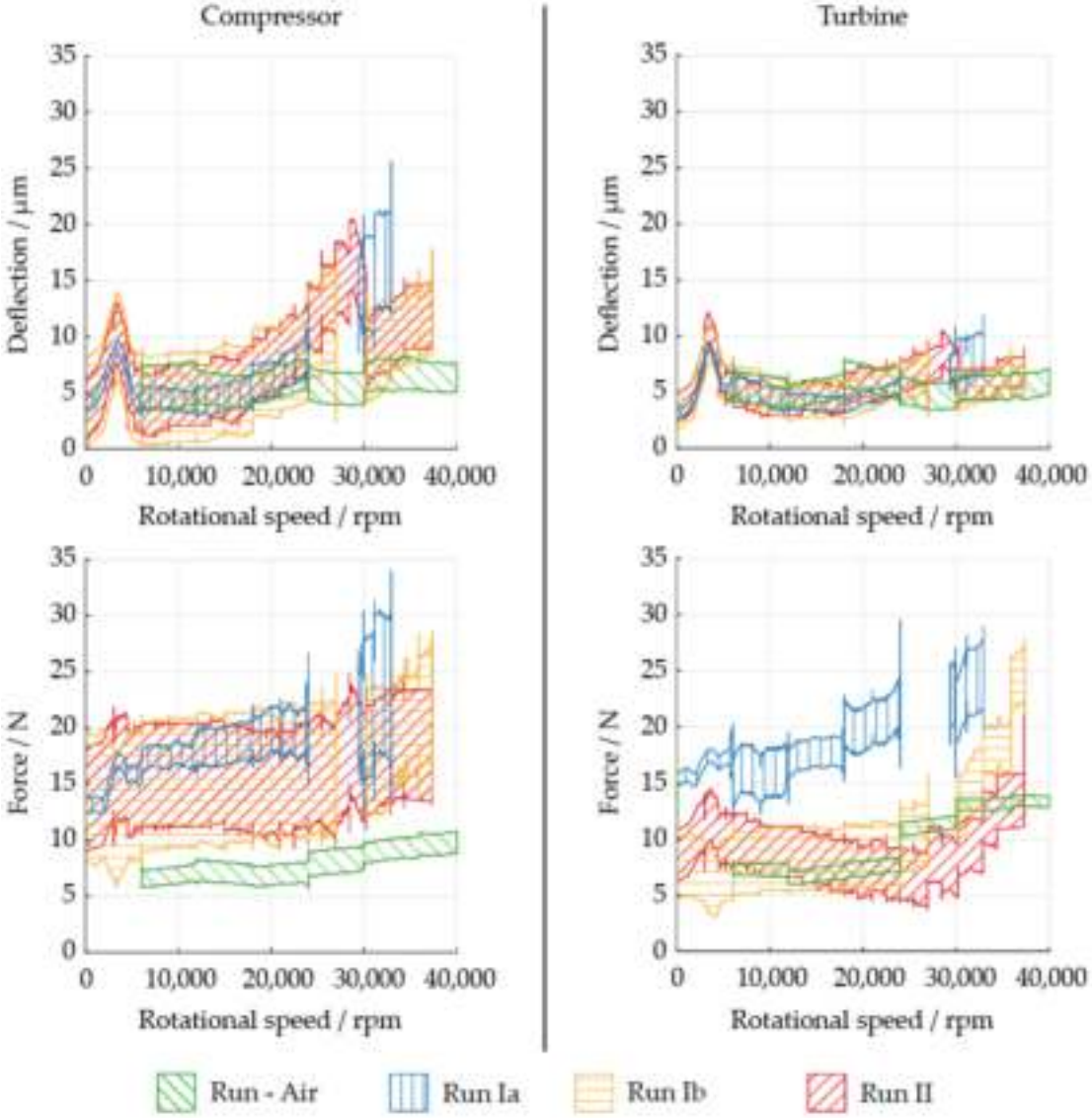

Figure 8. Deflections and forces depicted as function of speed for region I and II in Figure 6 for three test runs compared to the air test: (**top**) deflections; (**bottom**) forces; (**left**) at compressor bearing; (**right**) at turbine bearing.

These observations suggest that conditions in CO_2 indeed have an effect on operating the TAC with AMB. The reason for the observed behavior is likely due to the approximately 100-fold higher density. Furthermore, a change in control parameters is required to balance the effect of CO_2 on the rotor.

The next step is test run III, where CO_2 is in supercritical, gas-like conditions in region III right of the pseudocritical line (see Figure 6). The density is now 150–200% of the density of run II, which was performed with a compressor inlet density of about 200 kg/m^3. Ap-

proaching 20,000 rpm, the deflection at both the turbine bearing and compressor increases more than previously observed (see Figure 9). Therefore, the rotational speed for adjusting control parameters to limit deflections is reduced from 27,000 rpm to just above 18,000 rpm. This results in deflections at speeds greater than 18,000 rpm being in the same range as the previous test runs in CO_2. A change in forces similar to before is observed. However, the size of the enclosed area representing the scatter of radial forces of the bearings increases rather than the mean value. The fluctuations are approximately twice as large as previously measured. Again, it is assumed that this is related to the increasing interaction of CO_2 with the rotor due to greater density.

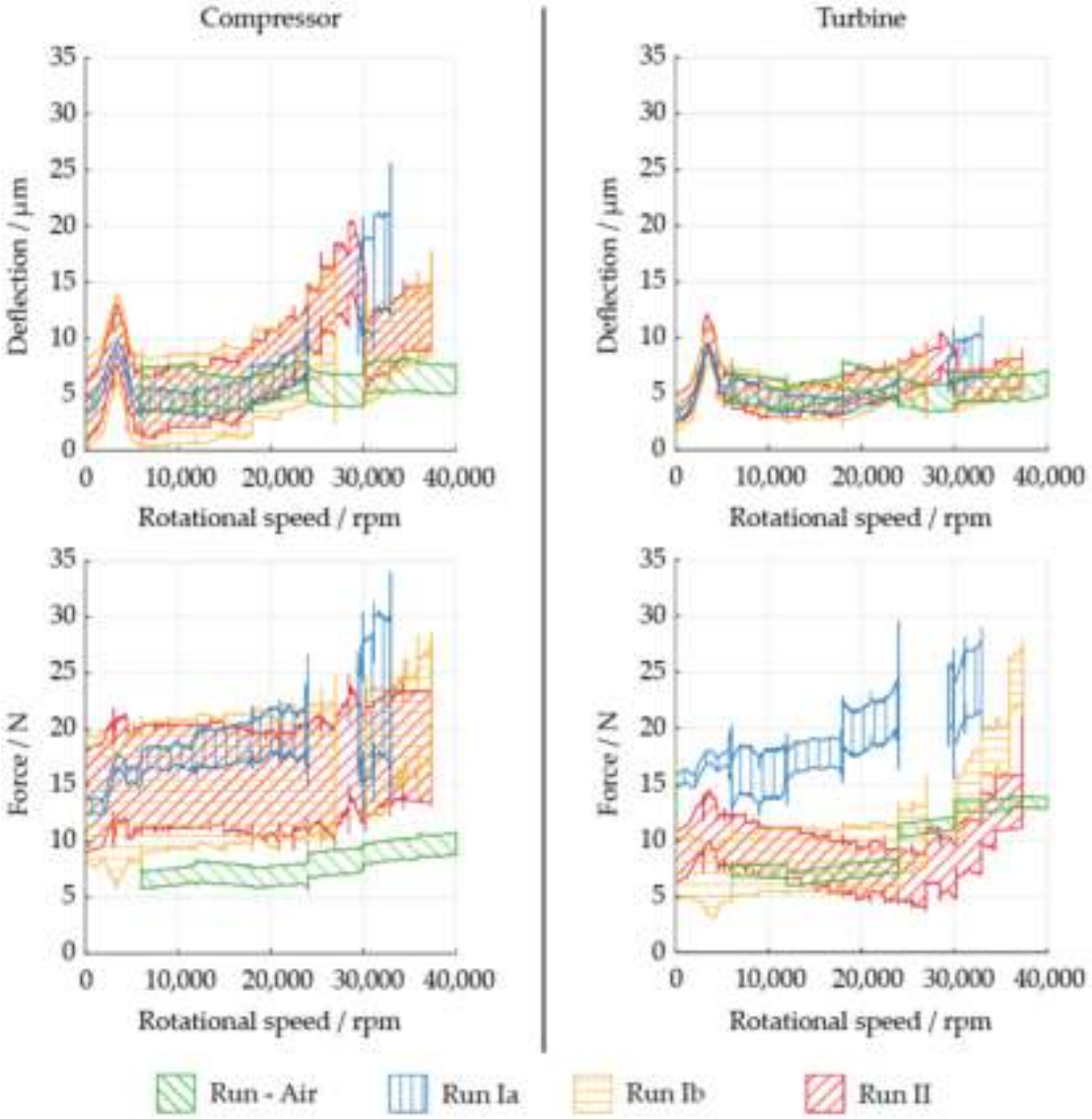

Figure 9. Deflections and forces depicted as function of speed for region III in Figure 6 compared to previous test runs: (**top**) deflections; (**bottom**) forces; (**left**) at compressor bearing; (**right**) at turbine bearing.

Finally, compressor inlet conditions for test run IV and V are brought to liquid-like sCO_2 conditions left of the pseudocritical line in regions III, IV and V. The test runs featured compressor inlet densities of about 450 kg/m^3 and 600 kg/m^3, respectively. Note that the density at the turbine inlet remains similar to test run III due to the elevated inlet temperature. As in the previous run, the maximum deflection increases mainly at the compressor bearing (see Figure 10). The maximum deflection reaches 40% of the clearance

height at approximately 30,000 rpm (60% of design speed). While maximum force in Figure 10 and its fluctuation at the compressor are similar to previous tests, the scatter of measured values for deflection increases. For the turbine bearing, a reduction in force can be seen at 15,000 rpm when the turbine bypass valve that was previously completely open is closed to 30%. At 25,000 rpm, it is closed to 10%, resulting in an increase in force at the turbine bearing. Additionally, the force increases more rapidly as rotational speed rises. Between 11% and 30% opening of the turbine bypass marks the point at which the flow direction changes at the turbine. While the turbine impeller "pumps" sCO_2 due to e.g., friction at the disk when the pressure ratio across the turbine is low due to the open bypass valve, closing the valve means the pumping effect can no longer overcome the rising pressure ratio. Thus, a "wrong" flow direction at the turbine results in a larger force on the turbine bearing. In addition, deflections up to 15,000 rpm are in a similar range to the air tests, but become much larger at speeds near 30,000 rpm. Therefore, future test runs require further modification of the control parameters to achieve speeds above 30,000 rpm when the compressor is operated with high-density liquid-like CO_2.

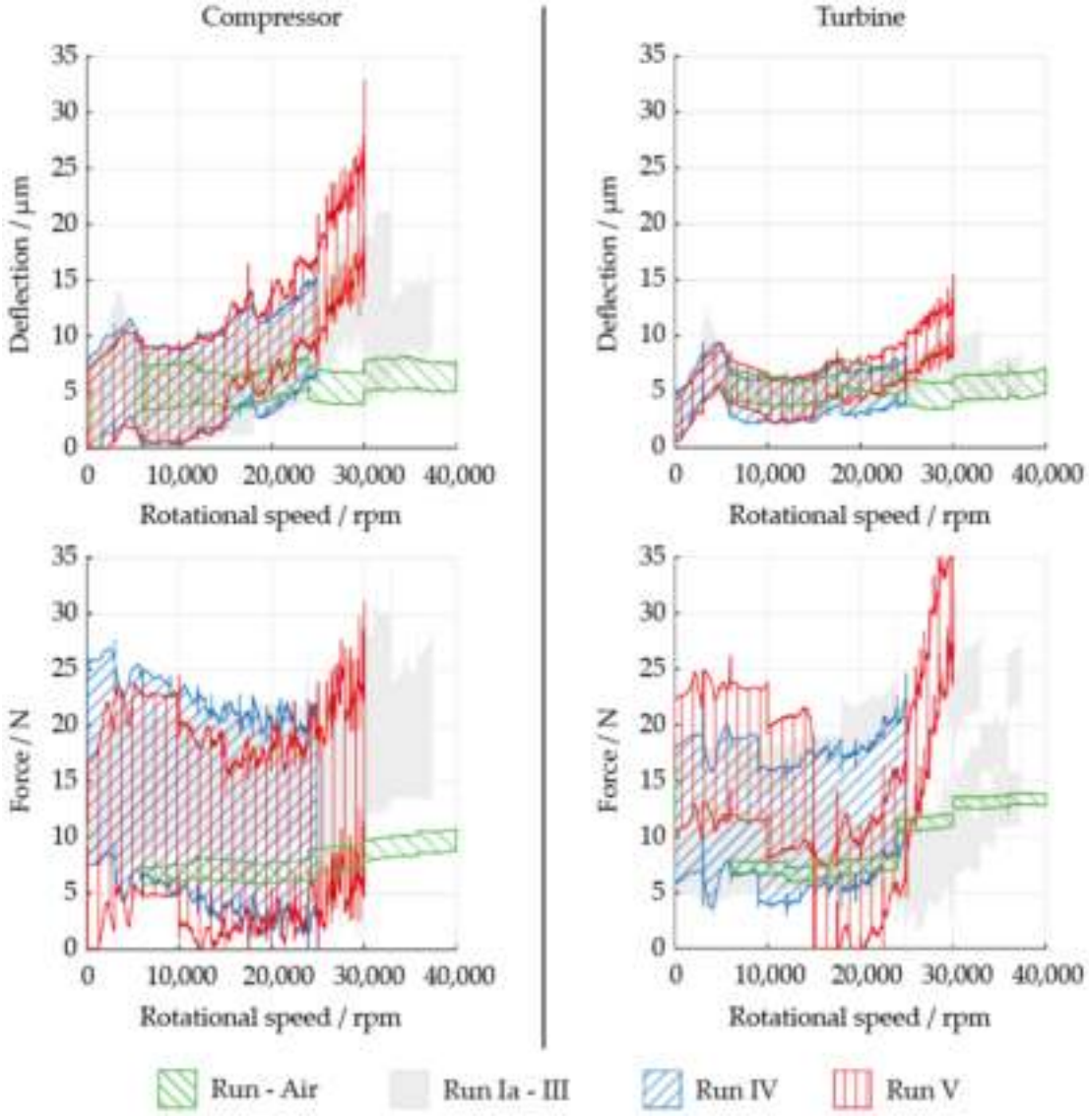

Figure 10. Deflections and forces depicted as function of speed for region IV and V in Figure 6 compared to previous test runs: (**top**) deflections; (**bottom**) forces; (**left**) at compressor bearing; (**right**) at turbine bearing.

The speed up tests showed that at low rotational speeds of up to 15,000 rpm, deflection is similar to the test run in air, regardless of density. It appears that the AMB is able to compensate the influence of sCO_2, even though larger forces are required. At larger rotational speeds, radial deflections and forces remain almost constant in test run with air, while the values and scatter of the measurements increase significantly for test runs in CO_2. The difference becomes larger when the density at the compressor inlet increases. As shown, a change of AMB control parameters can reduce deflections at the cost of larger forces. Therefore, AMBs are able to actively compensate the effect of sCO_2 on the rotor in the speed and density range investigated.

3.2. Increasing Density

The previous section clearly shows that the radial deflection of the rotor and the radial forces in the bearings increase with speed. It also shows an increase in deflection and bearing forces for test runs in regions with higher compressor inlet density. A similar result is presented by Kim et al. [6], who describe the effect of different sCO_2 conditions on radial force on the rotor for a cylindrical shell-type rotor–stator cavity. They show that an increase in density can also increase forces of sCO_2 on the rotor. To investigate the effect more closely, measurements at a constant rational speed are presented. Figure 11 shows that an increase in compressor inlet density indeed increases radial deflection of the rotor and radial forces inside the bearings. However, it should be noted that the increase of compressor inlet density has several effects. For example, it leads to an increase in the pressure ratio and thus in the force acting on the blades of the impeller.

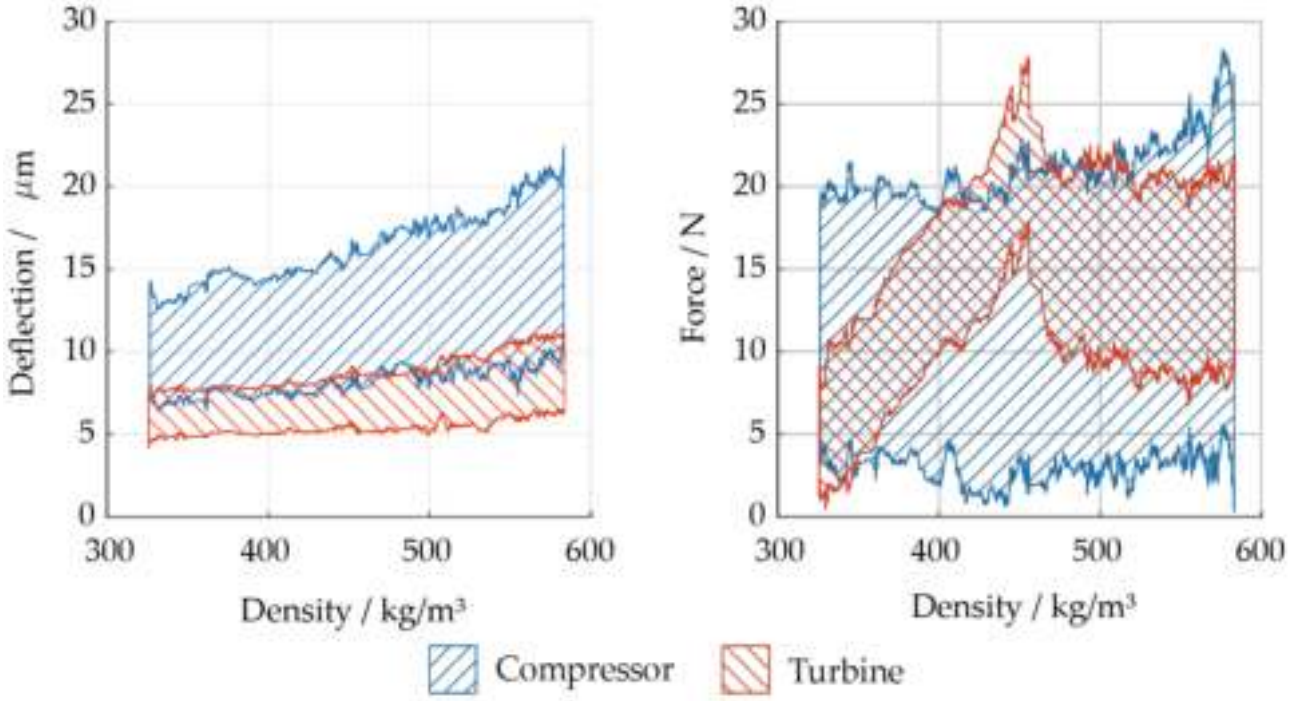

Figure 11. Deflection of the rotor and radial force of the bearings on turbine and compressor side over compressor inlet density at constant rotational speed of 25,000 rpm: (**left**) deflection; (**right**) radial force.

To separate the different effects of increases in density, the pressure ratio is more closely examined. The pressure ratio can usually be changed by altering the flow rate of the compressor. The sCO2-HeRo cycle features a compressor bypass valve for this purpose. However, the change in pressure ratio due to closure of the bypass valve is small and no effect on deflection or radial bearing forces was observed. This is due to flat curves of constant speed in the compressor performance map (compare Hacks et al. [3]). However, the pressure rise in the compressor is strongly dependent on its inlet density (compare

Hacks et al. [9,10]). In the case of Figure 11, it doubles as inlet density increases from 325 kg/m^3 to 580 kg/m^3. Therefore, it can be concluded that a change of flow rate at the compressor inlet is not responsible for the increase in bearing forces and radial deflection of the rotor but the direct effect of density on pressure rise might be.

Second, the effect of density inside the rotor–stator cavities is analyzed. As Figure 5 indicates, fluid forces inside rotor–stator cavities increase with local density, which was also reported by Kim et al. [6]. Here, only the effect of changing the density in the generator cavity is considered, because design calculations indicated the largest destabilizing forces to be caused by CO_2 inside the cavity (see Figure 4). Figure 12 presents the radial deflection of the rotor and radial bearing forces for one set of measurements when the valve controlling the cooling flow rate (a) was throttled. The further this valve is throttled, the lower the density inside the generator cavity becomes. The expectation is that lower density reduces the deflection of the rotor and radial force in the AMB due to smaller destabilizing forces. However, Figure 12 shows no considerable change of deflection and larger forces for smaller density inside the cavity (contrary to expectations). The behavior was also checked for other series of measurements. While the change in radial force is often less pronounced than in Figure 12, no definite increase in deflection or radial force is observed with density. The reason behind this is uncertain, but might be related to one of the following reasons. Leakage flow over the hub seal of the turbine impeller mixes with the cooling flow rate (a) inside the TAC (see Figure 3). Neither of the two mass flows can be measured directly, but must be calculated. Since the mixing with the leakage flow occurs inside the TAC, only the density inside the cavity is calculated and thus subject to uncertainties in calculating mass flow over the seal and valve. Another reason could be that according to the model used for Figure 5, the direct stiffness coefficient has a quadratic dependency on rotational speed. Therefore, radial forces in the cavity might only be significant at higher rotational speeds.

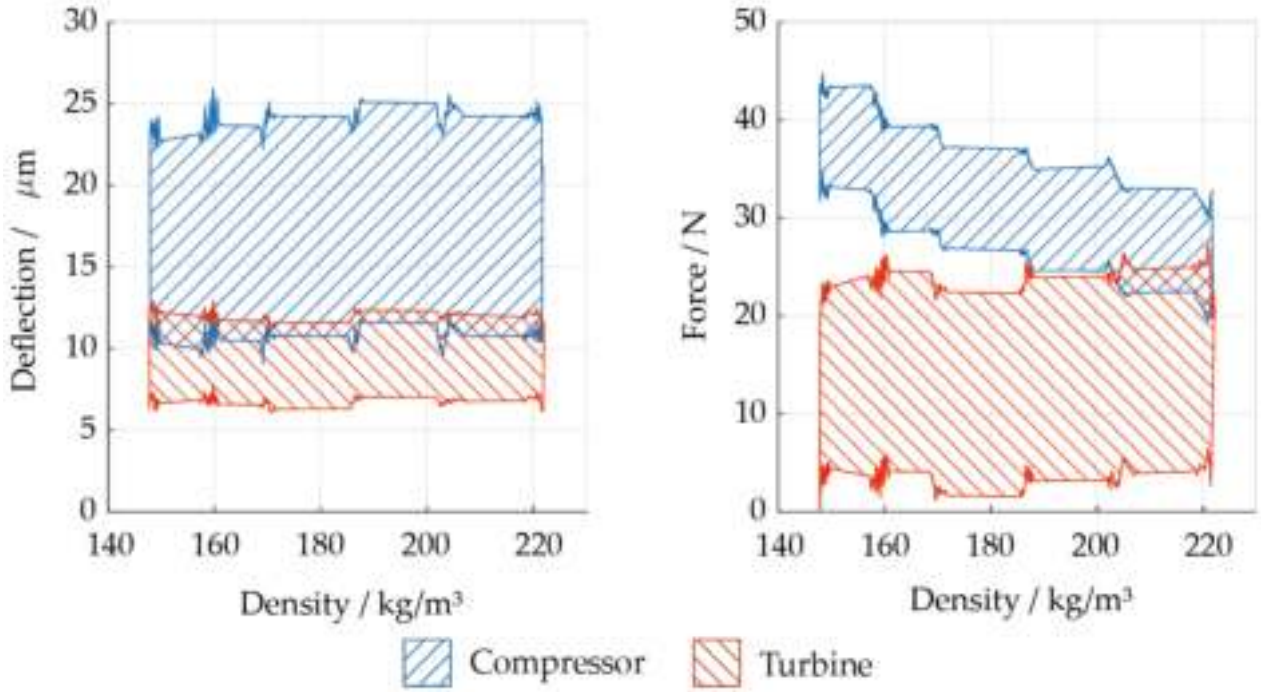

Figure 12. Deflection of the rotor and radial force of the bearings on turbine and compressor over density inside generator cavity at constant rotational speed of 27,500 rpm: (**left**) deflection; (**right**) force.

Finally, it was discovered that an increase in density at the compressor inlet does not lead to an increase in density in the generator cavity, even though the cooling flow rate rises and the temperature drops. Instead, the density remains almost constant because the pressure inside the cavity decreases. This also hints that forces acting on the compressor

impeller dominate the fluid forces that originated in the generator cavity. Therefore, the effects on the compressor impeller dominate the increase in radial deflection of the rotor and the increase in radial bearing forces, at least in the speed and density range studied.

4. Summary and Conclusions

The paper first presents the design of the sCO2-HeRo^{M} TAC. Its shaft is supported by AMBs so that the CO_2 can remain in a supercritical state throughout the TAC, shaking off the shackles of the previously used grease lubrication, which requires gaseous CO_2. To integrate the AMBs into the TAC, the cooling concept was revised to ensure cooling of the AMB on the turbine side and reduce windage losses, axial thrust and destabilizing forces. It is shown that the latter can be expressed by stiffness and damping coefficients and the coefficients of the generator cavity are expected to be dominant. They increase with rising rotational speed and density and decrease with larger clearance height. Furthermore, it is demonstrated that objectives of cooling on one hand and reducing windage losses and fluid forces on the other hand are contradictory since one requires cold and the other warm CO_2 with high and low density, respectively. The new cooling concept allows for a compromise, as regulation of the cooling flow regulates the temperatures and densities inside the TAC. Moreover, the density in the generator cavity can be kept constant even if the density increases at the compressor inlet. Therefore, cooling concept 2 is suitable for sCO2-HeRo^{M} TAC with AMBs. Finally, the first test runs with the sCO2-HeRo^{M} TAC were successfully completed. By adjusting the controller parameters to match the fluid properties, stable operation of the TAC was achieved at 30,000 rpm for a compressor inlet density as high as 650 kg/m^3. The conclusion is that a TAC using AMBs can be operated in sCO_2 if the forces related to the high density are considered.

Furthermore, measurements of radial deflection of the rotor and radial forces in the AMBs during several test runs are presented. In an initial step, the sCO2-HeRo^{M} TAC reached design rotational speed of 50,000 rpm in air, proving operability with negligible fluid-induced forces. Increasing compressor inlet density and rotational speed demonstrated an expected increase in radial deflection of the rotor and radial forces in the bearings with both increasing density and rotational speed. Furthermore, it was shown that adjusting controller parameters bears the ability to reduce deflection of the rotor by applying larger forces in the AMBs to balance fluid-induced forces.

Moreover, density increase is also analyzed at constant rotational speed. An increase of density at the compressor inlet is associated with an increase in radial deflection of the rotor and larger radial forces. The density on the turbine side and inside the generator cavity remains approximately constant for the related measurements. However, pressure rise increases strongly with compressor inlet density. In another attempt to demonstrate the impact of density on destabilizing forces inside rotor–stator cavities of the cylindrical-shell type, the density inside the generator cavity was changed while other properties were kept approximately constant. Contrary to expectations, no significant change in radial deflection was observed. Radial forces even tended to decrease. It appears that, at least at for the rotational speed studied, the force inside the generator cavity does not dominate the overall radial forces on the rotor. This may be related to a quadratic dependency of the direct stiffness coefficient on rotational speed indicated by the model used. Therefore, the relationship between the fluid forces that originated in the cavity and the total radial force on the rotor could increase and become dominant at higher rotational speeds. However, for the speed and density range studied, other radial forces acting on the compressor impeller or in the cavities on the compressor side seem to dominate the fluid forces on the rotor and need to be considered in future studies. A detailed experimental analysis of the different components of the destabilizing force on the rotor requires a rotor geometry with reduced complexity.

Author Contributions: Conceptualization, A.J.H.; methodology, A.J.H.; validation, A.J.H.; formal analysis, A.J.H.; investigation, A.J.H.; data curation, A.J.H.; writing—original draft preparation, A.J.H.; writing—review and editing, A.J.H. and D.B.; visualization, A.J.H. and D.B.; supervision,

D.B.; project administration, D.B.; funding acquisition, D.B. All authors have read and agreed to the published version of the manuscript.

Funding: This project has received funding from the Euratom research and training programme 2014–2018 under grant agreement No. 847606.

Data Availability Statement: Data available on request. The data presented in this study are available on request from the corresponding author.

Conflicts of Interest: The authors declare no conflict of interest.

References

1. Benra, F.-K.; Brillert, D.; Frybort, O.; Hajek, P.; Rhode, M.; Schuster, S.; Seewald, M.; Starflinger, J. A supercritical CO_2 low temperature Brayton-cycle for residual heat removal. In Proceedings of the 5th International Symposium—Supercritical CO_2 Power Cycles, San Antonio, TX, USA, 29–31 March 2016.
2. Starflinger, J.; Brillert, D.; Frybort, O.; Hájek, P.; Hennink, A.; Freutel, T. Raising nuclear reactor safety to a higher level—The supercritical CO2 heat removal system—sCO_2-HeRo. In Proceedings of the 26th International Conference Nuclear Energy for New Europe NENE, Bled, Slovenia, 11–14 September 2017.
3. Hacks, A.; Schuster, S.; Dohmen, H.J.; Benra, F.-K.; Brillert, D. Turbomachine Design for Supercritical Carbon Dioxide within the sCO_2-HeRo.eu Project. *J. Eng. Gas Turbines Power* **2018**, *140*, 121017. [CrossRef]
4. Cha, J.E.; Cho, S.K.; Lee, J.I. Operation Test of the Supercritical CO_2 Compressor Supported with Active Magnetic Bearing. In Proceedings of the Transactions of the Korean Nuclear Society Autumn Meeting, Gyeongju, Korea, 27–28 October 2016.
5. Kim, D.; Baik, S.; Lee, J.I. Investigation of Magnetic Journal Bearing Instability Issues in Supercritical CO2 Turbomachinery. In Proceedings of the ASME-JSME-KSME 2019 8th Joint Fluids Engineering Conference, San Francisco, CA, USA, 28 July–1 August 2019. [CrossRef]
6. Kim, D.; Baik, S.; Lee, J. Instability Study of Magnetic Journal Bearing under S-CO_2 Condition. *Appl. Sci.* **2021**, *11*, 3491. [CrossRef]
7. Jin, S.-H.; Cha, J.-E.; Chang, J.-U.; Choi, S.-H.; Ahn, H.-J. Controlling the Fluid Induced Instability of a Supercritical CO_2 Compressor Supported by Magnetic Bearing. *KSPE* **2020**, *37*, 737–742. [CrossRef]
8. Hacks, A.J.; Abd El Hussein, I.; Ren, H.; Schuster, S.; Brillert, D. Experimental Data of Supercritical Carbon Dioxide (sCO_2) Compressor at Various Fluid States—Supplementary Data. *DuEPublico* **2021**. [CrossRef]
9. Hacks, A.; Vojacek, A.; Dohmen, H.J.; Brillert, D. Experimental investigation of the sCO_2-HeRo compressor. In Proceedings of the 2nd European sCO2 Conference, Essen, Germany, 30–31August 2018; pp. 50–59. [CrossRef]
10. Hacks, A.J.; Abd El Hussein, I.; Ren, H.; Schuster, S.; Brillert, D. Experimental Data of Supercritical Carbon Dioxide (sCO_2) Compressor at Various Fluid States. *J. Eng. Gas Turbines Power* **2022**, *144*, 41012. [CrossRef]
11. Rotating Machinery Analysis, Inc. "XLRotor". Available online: https://www.xlrotor.com/solutions/xlrotor/ (accessed on 4 August 2021).

International Journal of
Turbomachinery
Propulsion and Power

MDPI

Article

Stall Margin Improvement in an Axial Compressor by Continuous and Pulsed Tip Injection †

Joseph Moubogha Moubogha, Gabriel Margalida, Pierric Joseph, Olivier Roussette and Antoine Dazin *

UMR 9014—LMFL—Laboratoire de Mécanique des Fluides de Lille—Kampé de Fériet,
Arts et Métiers Institute of Technology, Centrale Lille, University Lille, CNRS, ONERA, F-59000 Lille, France;
joseph.moubogha-moubogha@ensam.eu (J.M.M.); gabriel.margalida@ensam.eu (G.M.);
pierric.joseph@ensam.eu (P.J.); olivier.roussette@ensam.eu (O.R.)

* Correspondence: antoine.dazin@ensam.eu

† This manuscript is an extended version of our meeting paper published in the Proceedings of the 14th European Turbomachinery Conference, Gdansk, Poland, 12–16 April 2021.

Abstract: Stall and surge are strong limitations in the operating range of compressors and thus one of the major limits of jet engine performance. A promising way to push the stability limit of compression machines is to inject a small amount of flow at the blade tip to alter the physical mechanism responsible for stall onset. This study focuses on the experimental performance of such a system. To do so, an axial compressor test bench was equipped with 40 actuators connected to an auxiliary pressurised air supply system. They were able to generate high-speed jet blowing just at the tip of the rotor blades. The opening of each actuator was controlled by an electromagnetic valve. This allowed generating continuous or pulsed jets with frequencies up to 500 Hz at different duty cycles. The performance of the control system was investigated for various control strategies, where the injected flow rate, the injection angle, the number of injectors, the jet frequency and the duty cycle were systematically varied. This paper is concluded by a study of the energy balance of the system for various configurations. To the best of the authors' knowledge, this constitutes a rarely seen analysis in the literature.

Keywords: axial compressor; active flow control; stall margin improvement; tip blowing; energy cost

check for updates

Citation: Moubogha, J.M.; Margalida, G.; Joseph, P.; Roussette, O.; Dazin, A. Stall Margin Improvement in an Axial Compressor by Continuous and Pulsed Tip Injection. *Int. J. Turbomach. Propuls. Power* **2022**, *7*, 10. https://doi.org/10.3390/ijtpp7010010

Received: 14 October 2021
Accepted: 6 March 2022
Published: 16 March 2022

Publisher's Note: MDPI stays neutral with regard to jurisdictional claims in published maps and institutional affiliations.

Copyright: © 2022 by the authors. Licensee MDPI, Basel, Switzerland. This article is an open access article distributed under the terms and conditions of the Creative Commons Attribution (CC BY-NC-ND) license (https://creativecommons.org/licenses/by-nc-nd/4.0/).

1. Introduction

The problem of stall and surge instabilities developing in axial compressors is nearly as old as the first gas turbine [1,2], and the loss of stability of axial compressors at a high-pressure ratio is still nowadays an important limitation of the global performance of modern aero engines, as the occurrence of these phenomena can cause dramatic events. It thus leads engine manufacturers to apply a consequent security margin (the so-called stall margin (*SM*)) to keep the compressor far from its stability limit. This deprives the machines of their higher-pressure ratio and higher-efficiency operating ranges, which penalises the global performance of the engine. Stall margin improvements (*SMI*) can be achieved by various methods: a large number of works in the literature are devoted to passive control techniques, such as casing treatments [3]. These methods involve permanent modifications of the casing that cannot cope with changes in flow conditions. Using active flow control systems, which can easily be turned off and on, is thus an attractive alternative, and many research works have been carried out concerning this kind of techniques and were summarised recently by Li et al. [4]. One should keep in mind, however, that such methods come with some technical drawbacks in terms of complexity, added weight and, potentially, reliability issues. According to Day's review [2], the most common stall inception in the modern engines is the spike, which originates from phenomena occurring at the blade tip [5,6]. The most efficient way to control these phenomena is, thus, to blow a high-momentum jet at the blade tip, as demonstrated by several authors [7–9], to decrease the

loading and/or act on the dynamic of the tip gap vortex. Among all the literature dedicated to this subject, there is a consensus about some specific characteristics of the control system that must be used to obtain a significant effect in terms of *SMI*:

- The jet has to be as close as possible to the casing wall; consequently, many authors have successfully used the Coandă effect to get a wall-attached jet [10,11].
- A high momentum (or high velocity) and good angular coverage [9] are needed.

Nevertheless, some points remain unclear. As stated by Li et al. [4], there is no consensus about the effect of the yaw angle (positive angle values are given by the rotor rotation direction). Whereas the first paper [12] originally claimed that a positive yaw angle is better, other authors have demonstrated the opposite [13,14]. In addition, to the best of the authors' knowledge, the balance between the energy cost of blowing and the positive effect on machine performance has never been clearly established. It is therefore difficult to answer the question of whether such a system "pays its place" in a real engine. Finally, the potential interest of pulsed blowing has barely been addressed [7], whereas it has shown its efficiency in some other flow control applications, such as separation control [15].

In previous studies conducted in the laboratory by the same research team, the flow mechanisms involved during the onset of stall with and without active flow control have notably been analysed. The control system effectively succeeded in increasing the operating range of the compressor by neutralising the spike mechanisms and by moving the last stability point close to the maximum of the performance curve. For some control configurations, a low-frequency phenomenon appears in pressure measurements, suggesting a transition from spike-type stall to modal-type stall inception. In addition, some important effects, such as the injected momentum, have been investigated [16,17].

This paper aims to complete this previous study by addressing the above-mentioned questions concerning the yaw angle and energy balance of the system using pulsed actuation. This study relies on an experimental parametric study conducted on the same single-stage axial compressor test bench equipped with a modular flow injection system [17]. After a description of the experimental set-up, the paper focuses on the effect of the blowing angle at several rotation speeds to clearly point out the effect of blowing on the rotating frame. The paper is then dedicated to an estimation of the energy costs and savings of the control system to try to evidence the most interesting blowing strategies in pulsed or continuous blowing. This work is the first part of the EU-funded Horizon 2020 research project ACONIT [18], which aims at designing, manufacturing and testing actuators for flow control for implantation in an aircraft engine.

2. Experimental Set-Up

The support of the experiments performed in this research work is the low-speed, single-stage axial compressor CME2 located at the Arts et Métiers Institute of Technology in Lille (France). This compressor is a subsonic machine comparable to a stage of a high-pressure component of an aero engine [2]. Initially designed as a convenient tool to study rotating stall [19,20], this specific test bench has been equipped in the recent years with an active flow control (AFC) system relying on magnetic valves to produce pulsed jets [16].

The compressor itself, depicted in Figure 1a and whose characteristics are listed in Table 1, is operated at rotational speeds ranging from 3200 rpm to 4500 rpm. A typical performance curve is provided in Figure 1b, plotting the total-to-static pressure rise coefficient $\Psi_{t-s} = \Delta P_{t-s} / 0.5 \rho U_{tip}^2$ as a function of the flow coefficient $\Phi = V_x / U_{tip}$. During the tests, the mass flow is varied using a throttling valve located downstream of the compressor stage (see Figure 1a). In this paper, stall is triggered by continuously closing the throttling valve up to the unstable part of the performance curve.

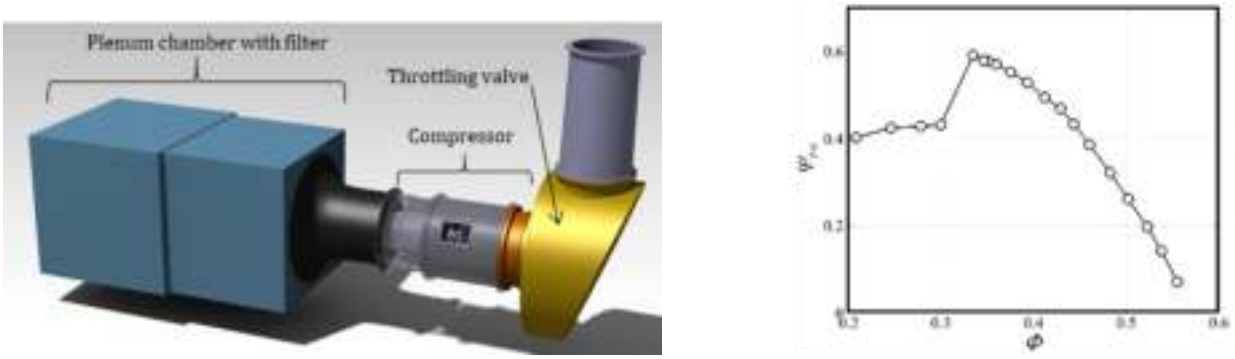

(**a**) (**b**)

Figure 1. CME2 test rig: (**a**) schematic description; (**b**) typical performance curve of the compressor at 3200 rpm.

Table 1. Compressor parameters at 3200 rpm.

Parameters	Value	Units
Design mass flow rate	5.3	$kg \cdot s^{-1}$
Design axial velocity, LE *	43	$m \cdot s^{-1}$
Rotor blade number	30	
Stator blade number	40	
Casing diameter	550	mm
Hub-tip ratio, LE	0.75	
Rotor tip chord	84	mm
Rotor tip stagger angle	54	°
Rotor tip gap	0.5	mm
Rotor tip speed	94	$m \cdot s^{-1}$

* LE, leading edge.

The performance of the compressor is evaluated using two differential pressure sensors located on the test rig. The first sensor measures the difference between the total pressure recorded in the plenum chamber and a mean static pressure measured at the end of the converging pipe located just downstream of the plenum chamber. This value allows capturing the dynamic pressure at the compressor inlet, and then the flow rate. The second sensor is used to evaluate the stage performance by measuring the static pressure in front of the rotor and downward of the stator. The precision of these measurements has been evaluated to ± 0.012 $kg \cdot s^{-1}$ and ± 1.5 Pa for the flow rate and the total-to-static pressure rise, respectively [16].

The control system [17] (see the overall description in Figure 2) consists of 20 injection blocks, each one counting two injectors. This configuration was selected because of the space constraint caused by the curvature of the casing. A solenoid valve (Matrix MX821), whose driving frequency can be set between 0 (continuous) and 500 Hz, with a supply pressure of up to 8 bar, feeds each injector. Each injector can be then operated independently and can produce a jet speed of up to 200 $m \cdot s^{-1}$ through a 10×0.5 mm^2 slot. Accordingly, the injected mass flow can be set from 0 to approximately 2.5% of the main flow rate of the stage either by changing the supply pressure or by changing the duty cycle (DC) of the solenoid valves when pulsed injection is used. The duty cycle is defined as the blowing time duration divided by the total period duration (i.e., the sum of blowing and no blowing time). All solenoid valves are driven by the same command signal, and manufacturer data indicate a response time lower than 1 ms. As stated in the literature, blowing is most effective in front of the rotor leading edge [14], and the critical area is located at the tip, close to the casing [4]. Consequently, actuators are located 10 mm upstream of the rotor ($x = -20\% \cdot Cx$), and injectors are shaped using the Coandă effect to blow along the casing

right in the tip gap [11]. Injectors can also be rotated along their axis to vary the yaw angle of injection with an angular step of 15°.

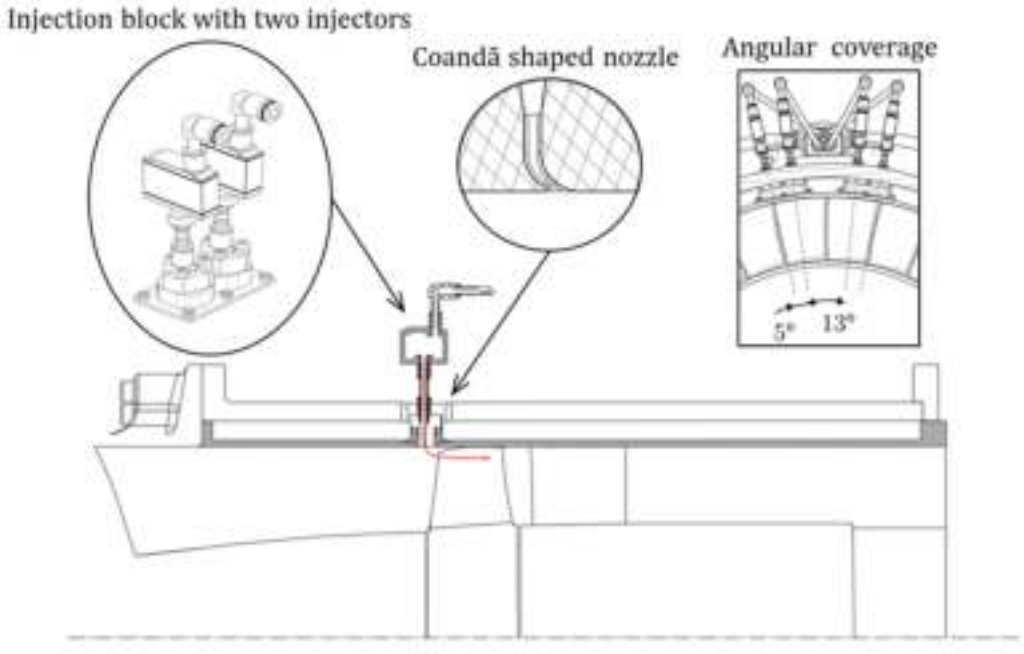

Figure 2. Active flow control system description.

The experimental protocol is extensively described in a previous paper [17], but key information is reported here for the sake of completeness. In a typical stall test, the working point of the compressor is moved along the performance curve using the controlled closing of a throttling valve. Stall is easily perceptible through an abrupt drop in the mass flow and pressure ratio. The baseline curve is compared with a controlled curve, which is obtained with control activated for the entire working range of the compressor. There is thus no issue with activation delay of the active flow control system.

A typical example of results of the flow control system is proposed in Figure 3, where the total-to-static pressure rise coefficient is plotted as a function of the flow coefficient. For each control case, the actual value of the global mass flow rate injected is specified along with the duty cycle (in pulsed blowing). Here and subsequently, the baseline results correspond to the performance of the compressor without control and the injected mass flow rate Q_{inj} is expressed in scaled form, Q^*_{inj}, as a percentage of the compressor flow rate at the last stable operating point before stall without control, q_s. It is obvious from these results that the blowing acts positively on the stable operating range of the compressor.

To evaluate the effect of the control system on the performance curve of the machine, the definition of the stall margin improvement given by Weigl et al. [21] is used and calculated using the following equations:

$$SM = \left(\frac{q_N}{q_S} \times \frac{\Pi_S}{\Pi_N} - 1\right) \times 100 \text{ and} \tag{1}$$

$$SMI = \frac{SM_C - SM_B}{SM_B} \times 100, \tag{2}$$

with q and Π, respectively, being the flow rate and the pressure ratio. Please note that in Equations (1) and (2), along with Figure 4, the subscripts N and S refer to quantities at the nominal operating point and at the last stable operating point, respectively, before stall (i.e., the operating point with the lowest flow rate before stall onset). Similarly, subscript B refers to the baseline case, without control, and C to the controlled case.

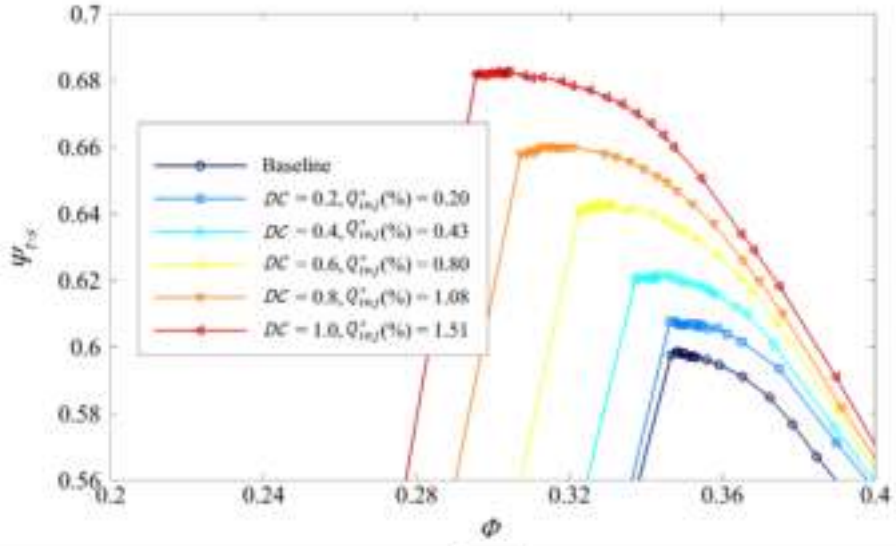

Figure 3. Performance curves obtained using the pulsed jet control system with various duty cycle and global injected mass flow rate values (actuation frequency $f = 100$ Hz, 20 injectors activated, absolute blowing flow angle $\alpha_{jet} = 0°$ and rotation speed $\Omega = 3200$ rpm). The duty cycle $DC = 1$ corresponds to continuous blowing.

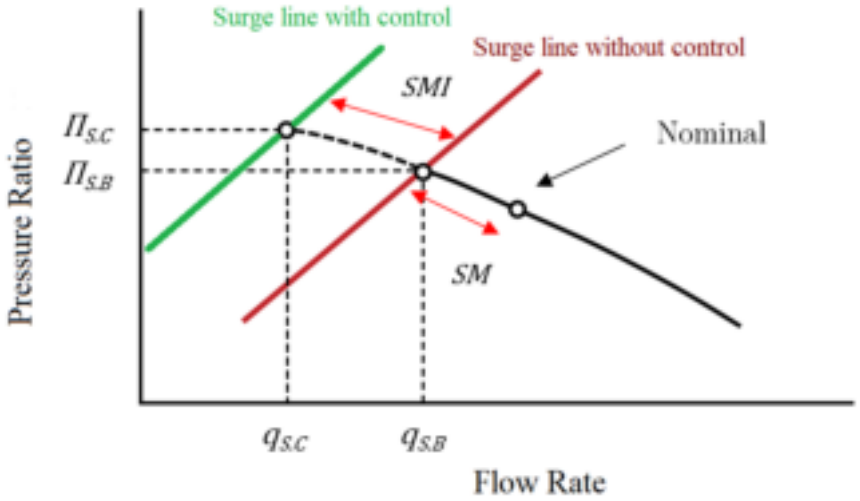

Figure 4. Schematic description of the *SMI* (adapted from [21]).

3. Effect of the Injection Yaw Angle

To highlight the effect of the injection yaw angle, a first series of experiments were conducted at 3200 rpm. The absolute blowing flow angle α_{jet}, the velocity (or the injected mass flow rate) and the number of injectors activated were varied. Absolute and relative blowing flow angles are defined in Figure 5. Positive absolute blowing angle values are given by the rotor rotation direction in the study; therefore, the absolute blowing angle is considered negative when the blowing direction is opposite to the rotor rotation direction.

Several basic test results of the active flow control in continuous blowing at 3200 rpm with 40 injectors activated and various absolute blowing flow angle and injected mass flow rate values are detailed and presented in Figure 6. The total-to-static pressure rise coefficient is plotted as a function of the flow coefficient for the six absolute blowing flow angles investigated: 30°, 15°, 0°, −15°, −30° and −45°. It can be seen that as already observed in Figure 3, for each absolute injection angle, the blowing extends the operating range of the compressor and simultaneously increases the compressor performance. It

is also rather obvious that higher benefits are obtained for negative absolute blowing flow angles.

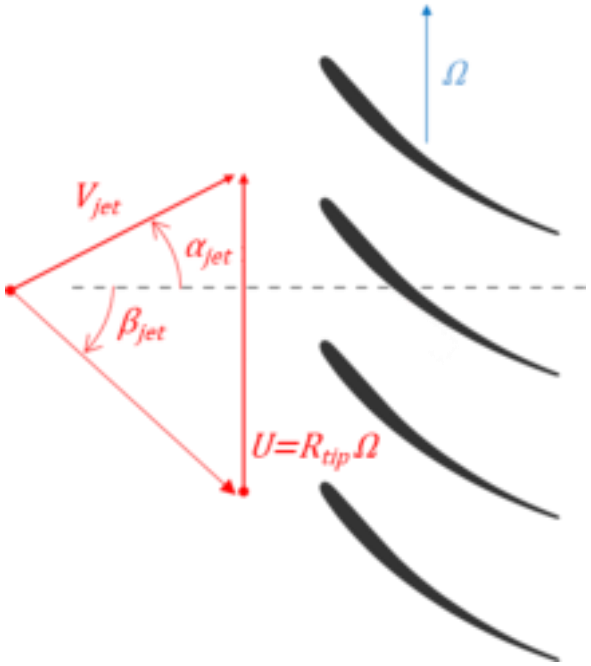

Figure 5. Definition and illustration of the absolute and relative blowing flow angles. Positive angle values are given by the rotor rotation direction.

To investigate the effect of the blowing flow angle, the stall margin improvement was calculated for each experiment reported in Figure 6, and the results are reported in Figure 7. To make the comparison of the different sets of parameters easier, the absolute blowing velocity V_{jet} was scaled by the rotor tip speed. The velocity of the jet, V_{jet}, was obtained by hot-wire measurements conducted on the injectors in a dedicated fluidic actuator test bench [16]. In addition, the results are presented as a function of the relative blowing flow angle β_{jet}, i.e., the jet flow angle seen by the blade, which was derived from the absolute velocity and angle of the jet, and the rotor tip speed using the velocity triangle (see Figure 5).

For the majority of the tested jet velocities, the stall margin improvement presents a clear and monotonic increase as the relative blowing angle decreases and reaches in most cases a maximum value for relative flow angles in the range between $-60°$ and $-70°$. It then appears to remain relatively constant or to decrease slightly at lower relative flow angles.

The effect of the rotation velocity was investigated and is presented in Figure 8. The stall margin improvement is plotted as a function of the relative blowing angle for two main rotor rotational velocities: 3200 and 4500 rpm. After scaling the absolute blowing velocity by the appropriate rotor tip speed, results were fairly close for the two different rotational speeds. The monotonic increase in the stall margin improvement with the decreasing of the relative blowing angle and the plateau reached around $-60°$ and $-70°$ is once again clearly apparent. It has to be pointed out that the inlet blade angle at the tip (depicted in Figure 8 by the vertical blue dashed line) of this compressor is $-65°$. It thus appears that the highest effect of the stall margin improvement is obtained for relative blowing angles close to the inlet blade angle, which is consistent with some previous experimental observations [7].

This can also be easily explained as this blowing angle is certainly most suitable for decreasing the blade loading at the tip and thus preventing the mechanism occurring at the tip and leading to rotating stall.

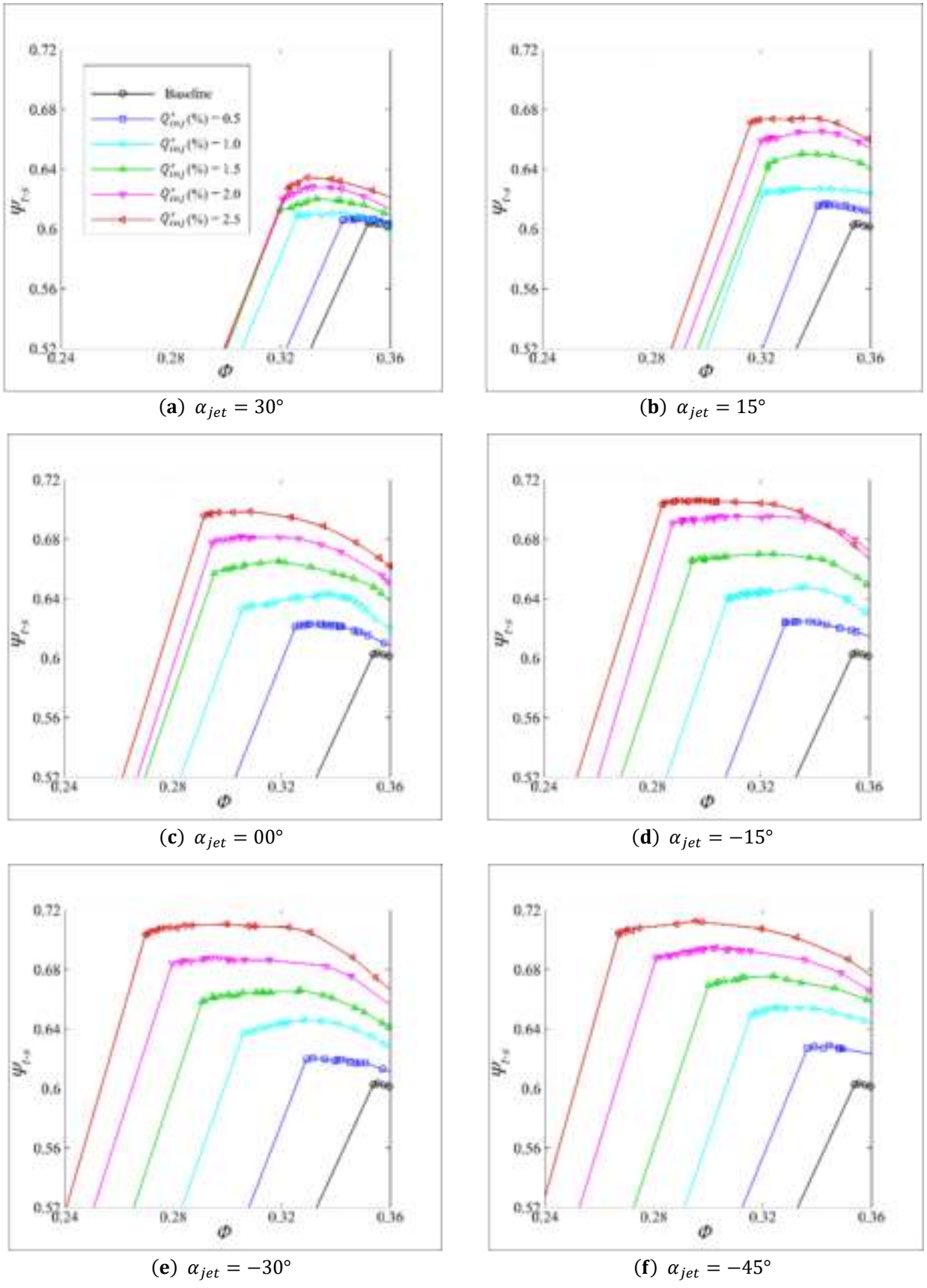

(**a**) $\alpha_{jet} = 30°$ (**b**) $\alpha_{jet} = 15°$

(**c**) $\alpha_{jet} = 00°$ (**d**) $\alpha_{jet} = -15°$

(**e**) $\alpha_{jet} = -30°$ (**f**) $\alpha_{jet} = -45°$

Figure 6. Performance curves obtained using continuous blowing with various absolute blowing angles of: (**a**) 30°, (**b**) 15°, (**c**) 0°, (**d**) −15°, (**e**) −30° and (**f**) −45° and various injected mass flow rate values (40 injectors activated and rotation speed $\Omega = 3200$ rpm).

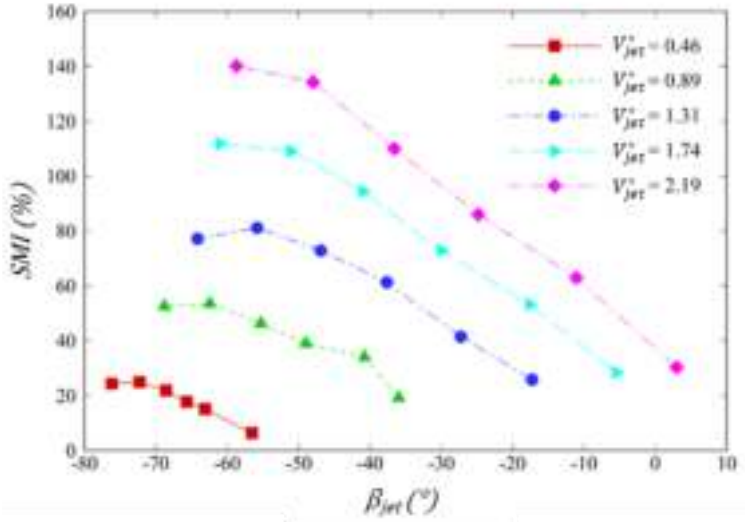

Figure 7. Effect of the relative blowing flow angle with 40 injectors activated for a rotation speed of 3200 rpm.

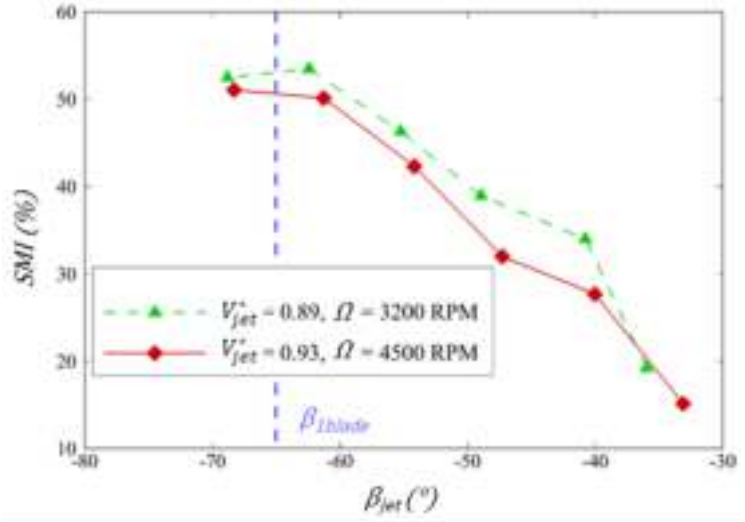

Figure 8. Effect of the relative blowing flow angle with 40 injectors activated at different rotating speeds.

4. Energy Balance

The main goal of the control system is to improve the compressor stall margin. An additional benefit is the improvement in the pressure rise provided by the compressor stage (and thus a gain in the energy provided by the compressor to the flow). Nevertheless, the generation of jets involves an energy cost. The power balance, introduced next, can be seen as the net benefit (energy gain – energy cost) of the control system. So, if it is negative, then the use of the control system costs more than it brings in.

The power balance (*PB*) of the control system is thus evaluated by subtracting the power cost (*PC*) of the blowing to the associated power gain (*PG*), as defined below:

$$PB = PG - PC. \tag{3}$$

Regarding the cost, it is the power consumed by the blowing system. In this case, we use a screw compressor to pressurise the air and solenoid valves to carry out the pulsed blowing. It is therefore possible to estimate the cost of the injection through the electrical power consumed by all these elements. However, this includes many other factors that are not of direct interest, such as the choice of the solenoid valve or the way in which compressed air is generated, which can be subsequently improved and which will

undoubtedly be different from the final solution embedded in an engine. Consequently, the power consumed by the injection system at the last level is estimated by evaluating the aeraulic power added by the jets. Please note that in this study, the temperature of the injected air was close to the ambient one, as several buffer tanks (a large 500 L tank followed by two smaller 15 L ones) are present in the pressured air supply system.

The power cost (PC) of the blowing is defined as the kinetic power added to the flow by the jets:

$$PC = Q_{inj}\frac{1}{2}V_{jet}^2, \tag{4}$$

where Q_{inj} is the global injected mass flow rate and V_{jet} the mean jet velocity at the actuator nozzle.

The power gain (PG) is evaluated by comparing the performance of the compressor with and without control at the flow rate corresponding to the last stable operating point without control (see the representation given in Figure 9). More precisely, it is defined as the difference between the net power available in the fluid downstream of the compressor with and without control;

$$PG = q_s\left[\left(\frac{P_{2C}}{\rho_{2C}} + \frac{V_{2C}^2}{2}\right) - \left(\frac{P_{2B}}{\rho_{2B}} + \frac{V_{2B}^2}{2}\right)\right], \tag{5}$$

where q_s is the flow rate at the last stable operating point before stall without control; P the static pressure; V the velocity; ρ the density; and the indexes 2, C and B, respectively, the stage outlet, the controlled configuration and the baseline (configuration without control).

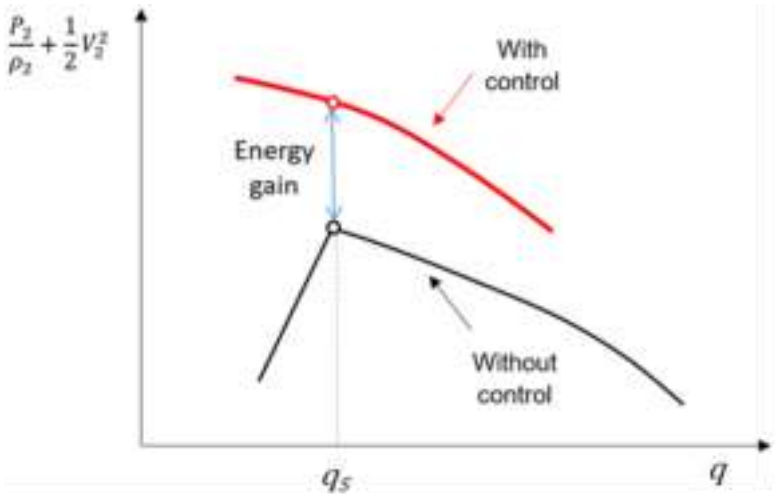

Figure 9. Energy gain due to the active flow control system.

4.1. Continuous Mode

Figure 10 presents the results of a series of tests performed on the compressor operating at 3200 rpm. All the experiments reported on the graph correspond to continuous blowing, with an absolute blowing angle $\alpha_{jet} = -30°$. This absolute blowing angle was retained for the rest of the study as it allowed achieving the best SMI, according to the reasons developed, due to the results in Figure 7. The effect of the number of injectors used (N) and the global blowing flow rate was examined. The figure shows, for each tested configuration, the SMI achieved compared to the power balance (PB) of the considered control strategy. On this graph, the most interesting points are on the top and the right of the figure, as they correspond to control parameters achieving significant SMI with a positive power balance.

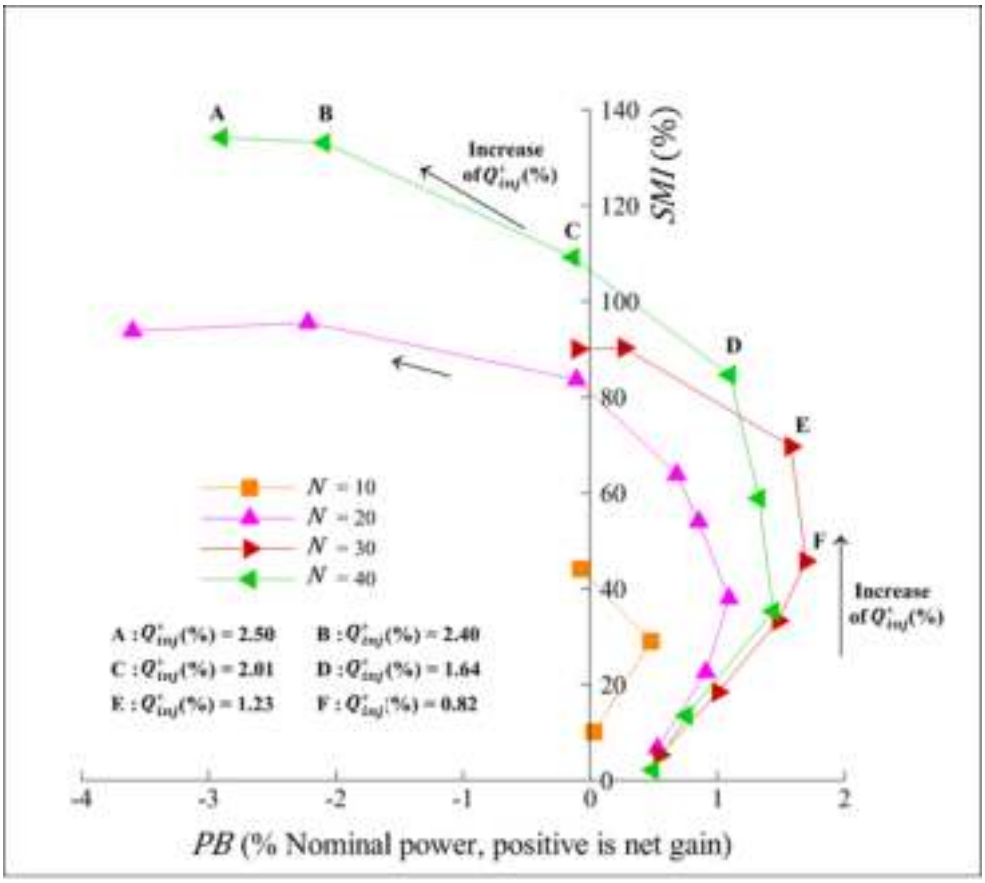

Figure 10. *SMI* and power balance of the control system. Continuous blowing with the absolute injection angle $\alpha_{jet} = -30°$ and the rotation speed $\Omega = 3200$ rpm. N is the number of injectors activated.

Some remarkable points in the graph are highlighted with letters, from A to F. Points A, B and C correspond to strategies that allow reaching the greatest *SMI*. Nevertheless, these configurations correspond to the maximum number of injectors with the maximum flow rate (and velocity) per injector. Consequently, the energy cost is high, and the energy balance for this specific case is unfavourable. Points D, E and F correspond to interesting applicative configurations as they allow to obtain a fairly good *SMI* (from 55% for point F to 80% for point D) with a positive power balance, which can reach 1.8% of the compressor nominal power.

These most interesting points are all obtained for configurations with 30 to 40 injectors activated, which means that good angular coverage is necessary to reach a good compromise between the *SMI* and the positive power balance. This need for a sufficient angular coverage was also highlighted by Suder et al. [8] and more recently by Margalida et al. [16,17]. This parameter is determining for the increase in the *SMI*. It seems that this is also the case for the energy balance.

The second observation coming from Figure 10 is that whatever the number of injectors used, when the flow rate starts to increase, both the *SMI* and the power balance increase, leading to the best configurations, such as points D, E or F. When the blowing flow rate continues to increase, the *SMI* continues to increase [14], whereas the power balance deteriorates rapidly.

Figure 11 shows the evolutions of the power gain (a), the power cost (b) and the power balance (c) as a function of the injected flow rate. What can be clearly observed is that the power gain is low for a low injected flow rate (less than 1%) and that the power gain grows almost linearly and more rapidly than the power cost, which evolves approximatively as the jet speed cubed (or the injected flow rate cubed). This evolution leads to a rapid growth of the cost for values higher than 1–1.5%, leading to rapid degradation of the power balance

(Figure 11c). What can also be noticed in Figure 11b is that for a given injected flow rate, the power cost is lower for the configuration with more injectors activated: in this case, the flow rate is distributed between more injectors, which leads to a lower velocity per injector and a lower cost, according to Equation (4).

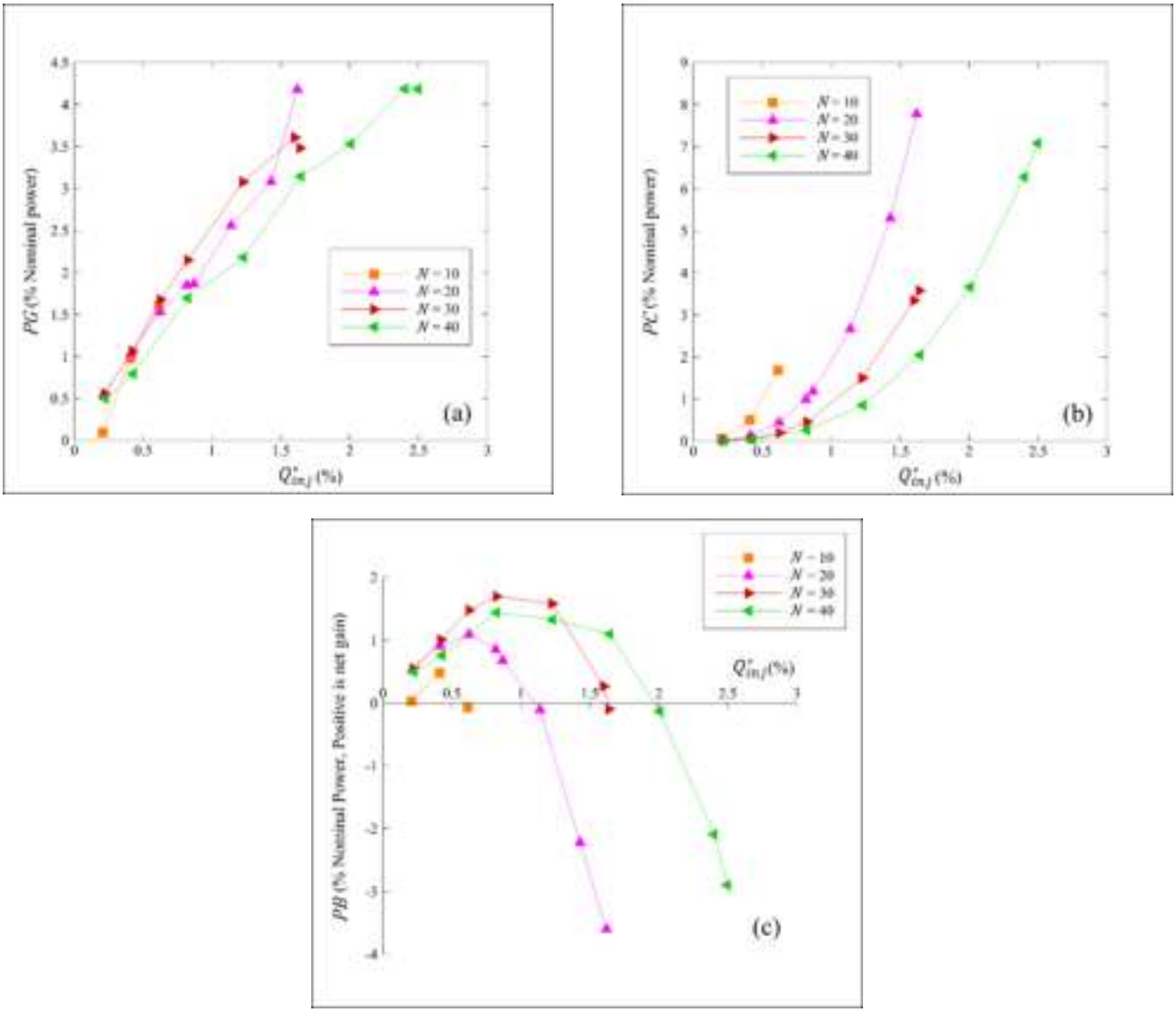

Figure 11. Evolution of the: (**a**) power gain, (**b**) power cost and (**c**) power balance as a function of the injected flow rate. Continuous blowing with the absolute injection angle $\alpha_{jet} = -30°$ and the rotation speed $\Omega = 3200$ rpm.

The fact that the power balance is positive for a large range of Q^*_{inj} indicates that the blowing leads also to an increase in the blade work at the tip and/or a decrease in the losses (the profile losses close to the tip, as the flow is realigned with the blade inlet angle and certainly also to the losses associated with the secondary gap flows, as demonstrated in the case of an isolated blade, for some blowing configurations [22]).

4.2. Pulsed Mode

Figure 12 presents a typical evolution of the stall margin improvement with the actuation frequency, in pulsed mode. Note that in Figure 12, no result is presented for frequencies above 200 Hz, as beyond this value, the response time of the valve becomes significant compared with the blowing duration. In this case, 40 injectors are activated, and the global injected mass flow rate is kept constant (here 0.03 kg/s) at different actuation frequencies with the same duty cycle (DC = 0.7). The absolute pulsed blowing angle is $-30°$, and the rotor rotation speed is set at 3200 rpm. It can be seen that there is a strong dependency between the *SMI* and the actuation frequency. The stall margin improvement grows almost monotonically with the frequency and reaches its maximum for a value close to the maximum frequency allowed by the system. However, this maximum value is almost already reached around an actuation frequency of 200 Hz. Consequently, the results in pulsed actuation that are presented correspond to the best results in terms of the *SMI*. Please note that in this study, all injectors pulsated simultaneously but that a variating actuation in the circumferential direction was also possible with this set-up (as previously performed a few times in the literature [2]).

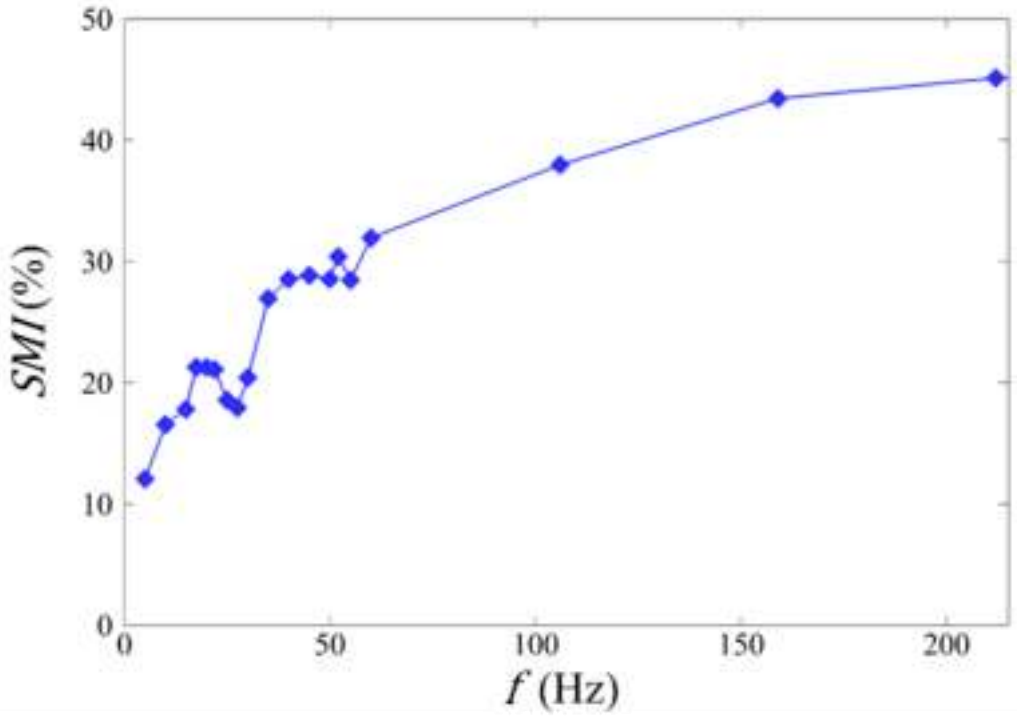

Figure 12. Evolution of the *SMI* with the actuation frequency in pulsed blowing. The number of activated injectors $N = 40$, the injected mass flow rate $Q_{inj} = 0.03$ kg/s, the duty cycle $DC = 0.7$, the absolute blowing flow angle $\alpha_{jet} = -30°$ and the rotation speed $\Omega = 3200$ rpm.

Figure 13 reports the comparison of the stall margin improvement and power balance for several pulsed actuation tests compared to the points obtained in continuous mode for 30 and 40 injectors activated. The absolute injection angle and the rotation speed are kept constant and equal, respectively, to $-30°$ and 3200 rpm. It is clear that the benefit of pulsed actuation is not obvious in terms of the *SMI*, as it allows reaching values up to 50% maximum, sensibly lower than the higher ones obtained in continuous blowing.

Nevertheless, if the power balance is considered, pulsed actuation presents a real interest. Point H is able to reach, in pulsed actuation, an *SMI* performance close to the one obtained by point F (in continuous blowing) with a lower flow rate taken from the external system and a better power balance.

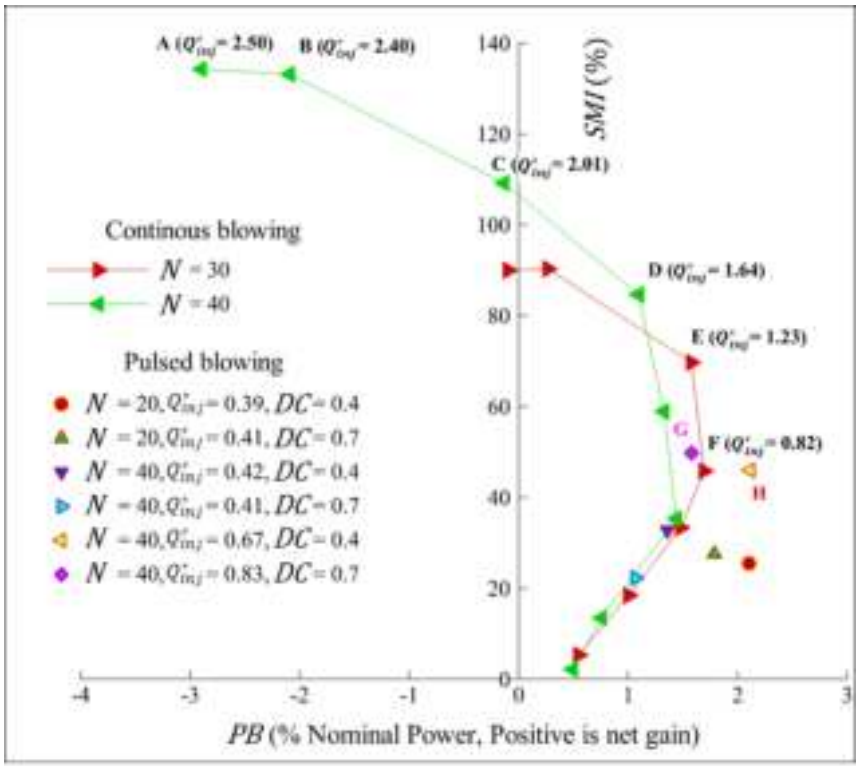

Figure 13. *SMI* and power balance in pulsed and continuous blowing with the absolute injection angle $\alpha_{jet} = -30°$ and the rotation speed $\Omega = 3200$ rpm.

5. Conclusions

This study reports the results of flow control application for stall margin improvement (*SMI*) using an experimental parametric study conducted on a single-stage axial compressor test bench. The machine is equipped with fluidic actuators installed on the casing, upstream of the rotor. A series of experiments with various blowing conditions in pulsed and continuous modes were conducted. In particular, the aim of the study was, firstly, to shed some light on the controversial influence of the blowing yaw angle. Secondly, it was also an opportunity to carry out a never-seen investigation of the energy budget of such control methods applied to an axial compressor.

Concerning the blowing yaw angle effect, it appears that blowing angles, in the relative frame, close to the blade angle at the tip produce the best results in terms of the *SMI*, as, at this blowing angle, the jet directly acts on the blade loading at the tip and thus prevents the phenomena at the origin of stall. It is then not a matter of positive or negative absolute values, as stated often in the literature, and this confirms some findings of Kefalakis et al. [7]. For real applications, the relative blowing angle is not the easiest parameter to adjust, as it depends on the blowing velocity, the absolute blowing angle and the rotor speed. Fortunately, a high *SMI* value appears to be achieved for a quite large range of relative blowing angles. It means that a single absolute blowing angle can cover several operating points.

Concerning the energy budget, this study has shown that some of the blowing configurations present a positive net gain on the energy balance for an *SMI* up to 110% and up to nearly 140% with a net energy consumption. Former configurations imply sufficient angle coverage and are obtained when an advantageous balance is achieved between the positive effect of the blowing (increase in the *SMI*, decrease in the losses) and the energy cost necessary to produce high-speed jets. The benefit of using pulsed blowing is not obvious in terms of the *SMI* but is clearly interesting for the power balance as some configurations allow a positive power balance of 2% with a still interesting *SMI* of 50%.

The analysis of the efficiency of any flow control system devoted to reducing the energy consumption is always an interesting step, as it allows to state whether such a system "pays its place" in a complex industrial machine, such as an aircraft, where every gram counts. This study is in that sense enlightening, as it allows imagining various uses of the different tested configurations. Firstly, the highest *SMI* points, despite their net energy cost, could be devoted to critical situations where the safety and level of engine performance need to be maintained. One thinks of take-off and landing cases and of combat situations at high angles of attack to cope with inlet distortion effects. On the contrary, even with a lesser *SMI*, a configuration exhibiting a net positive energy gain could be continuously used to improve the overall efficiency of the engines and thus reduce their environmental impact.

This study constitutes an encouraging proof-of-concept that active flow control is viable from an energy point of view at the laboratory scale, that is, on a simplified, low-speed and single-stage test rig using low-TRL actuators. The next step is now to reproduce and validate the concept on a real engine using industrial-grade actuators. This constitutes the next step of the current project and will be published in the near future.

Author Contributions: Conceptualisation, P.J. and A.D.; methodology, P.J., O.R. and A.D.; software, G.M. and P.J.; validation, J.M.M., P.J. and A.D.; formal analysis, J.M.M., P.J. and A.D.; investigation, J.M.M. and G.M.; resources, O.R. and G.M.; writing—original draft preparation, P.J., A.D. and J.M.M.; writing—review and editing, O.R., J.M.M., P.J. and A.D.; supervision, O.R. and A.D.; project administration, O.R. and A.D.; funding acquisition, A.D., P.J. and O.R. All authors have read and agreed to the published version of the manuscript.

Funding: This project (ACONIT) has received funding from the Clean Sky 2 Joint Undertaking under the European Union's Horizon 2020 research and innovation programme under grant agreement No. 886352.

Institutional Review Board Statement: Not applicable.

Informed Consent Statement: Not applicable.

Data Availability Statement: Data available on request.

Acknowledgments: We are grateful to the technical staff at the Arts et Métiers Institute of Technology in Lille, France, especially Patrick Olivier and Claude Lamacz, for technical support and expertise provided during the test campaign.

Conflicts of Interest: The authors declare no conflict of interest.

Nomenclature

AFC	Active flow control
SM	Stall margin
SMI	Stall margin improvement
PG	Power gain
PC	Power cost
PB	Power balance
P	Pressure (Pa)
V	Velocity (m/s)
ρ	Density (kg/m^3)
q	Mass flow rate (kg/s)
Ω	Rotor rotational velocity (rpm)
U	Rotor tip speed (m/s)
Π	Pressure ratio
Φ	Flow coefficient
Ψ	Pressure rise coefficient
x	Axial position (mm)
Cx	Axial chord length (mm)
α_{jet}	Absolute blowing flow angle (°)
β_{jet}	Relative blowing flow angle (°)
V_{jet}	Absolute jet speed (m/s)
Q_{inj}	Injected mass flow rate (kg/s)
N	Number of injectors
DC	Duty cycle
f	Driving frequency
N	Number of injectors activated
Subscripts	
$1-2$	Stage inlet − outlet
N	Nominal operating point
S	Last stable operating point
B	Baseline or case without control
C	Controlled case
x	Axial quantity
tip	Quantity at blade tip
mid	Quantity at mid-span
$t-s$	Total-to-static quantity

References

1. Moubogha, J.M.; Margalida, G.; Joseph, P.; Roussette, O.; Dazin, A. Surge Margin Improvement by Continuous and Pulsed Tip injection. In Proceedings of the 14th European Conference on Turbomachinery Fluid Dynamics & Thermodynamics, ETC2020-639, Gdansk, Poland, 12–16 April 2021.
2. Day, I.J. Stall, surge, and 75 years of research. *J. Turbomach.* **2016**, *138*, 011001. [CrossRef]
3. Hathaway, M.D. *Passive Endwall Treatments for Enhancing Stability*; NASA Report No. TM-2007-214409; July 2007. Available online: ntrs.nasa.gov (accessed on 13 October 2021).
4. Li, J.; Du, J.; Nie, C.; Zhang, H. Review of Tip Air Injection to Improve Stall Margin in Axial Compressors. *Prog. Aerosp. Sci.* **2019**, *106*, 15–31. [CrossRef]
5. Hewkin-Smith, M.; Pullan, G.; Grimshaw, S.D.; Greitzer, E.M.; Spakovszky, Z.S. The Role of Tip Leakage Flow in Spike-Type Rotating Stall Inception. *J. Turbomach.* **2019**, *141*, 061010. [CrossRef]
6. Pullan, G.; Young, A.M.; Day, I.J.; Greitzer, E.M.; Spakovszky, Z.S. Origins and Structure of Spike-Type Rotating Stall. *J. Turbomach.* **2015**, *137*, 051007. [CrossRef]
7. Kefalakis, M.; Papailiou, K.D. Active Flow Control for Increasing the Surge Margin of an Axial Flow Compressor. *Turbo Expo Power Land Sea Air* **2006**, *424*, 101–111.
8. Stößel, M.; Bindl, S.; Niehuis, R. Ejector Tip Injection for Active Compressor Stabilization. *Turbo Expo Power Land Sea Air Am. Soc. Mech. Eng.* **2014**, *45608*, V02AT37A004.
9. Suder, K.L.; Hathaway, M.D.; Thorp, S.A.; Strazisar, A.J.; Bright, M.B. Compressor Stability Enhancement Using Discrete Tip Injection. *J. Turbomach.* **2001**, *123*, 14–23. [CrossRef]
10. Kern, F.; Brehm, S.; Niehuis, R. Ejector Tip Injection System for Active Aerodynamic Compressor Stabilization Part I: Design and Experiment. In Proceedings of the 12th European Conference on Turbomachinery Fluid Dynamics & Thermodynamics, ETC2017-244, Stockholm, Sweden, 3–7 April 2017.
11. Strazisar, A.J.; Bright, M.M.; Thorp, S.; Culley, D.E.; Suder, K.L. Compressor Stall Control through Endwall Recirculation. *Turbo Expo Power Land Sea Air* **2004**, *41707*, 655–667.
12. D'Andrea, R.; Behnken, R.L.; Murray, R.M. Rotating Stall Control of an Axial Flow Compressor Using Pulsed Air Injection. *J. Turbomach.* **1997**, *119*, 742–752. [CrossRef]
13. Khaleghi, H.; Teixeira, J.A.; Tousi, A.M.; Boroomand, M. Parametric Study of Injection Angle Effects on Stability Enhancement of Transonic Axial Compressors. *J. Propuls. Power* **2008**, *24*, 1100–1107. [CrossRef]
14. Nie, C.; Xu, G.; Cheng, X.; Chen, J. Micro Air Injection and Its Unsteady Response in a Low-Speed Axial Compressor. *J. Turbomach.* **2002**, *124*, 572–579. [CrossRef]
15. Greenblatt, D.; Wygnanski, I. The Control of Flow Separation by Periodic Excitation. *Prog. Aerosp. Sci.* **2000**, *36*, 487–545. [CrossRef]
16. Margalida, G. Analyse Expérimentale et Contrôle Actif de l'écoulement Dans Un Compresseur Axial Mono-Étagé Durant La Transition Vers Le Décrochage Tournant. Ph.D. Thesis, Ecole Nationale Supérieure d'Arts et Métiers, Lille, France, 2019.
17. Margalida, G.; Joseph, P.; Roussette, O.; Dazin, A. Active Flow Control in an Axial Compressor for Stability Improvement: On the Effect of Flow Control on Stall Inception. *Exp. Fluids* **2021**, *62*, 1–13. [CrossRef]
18. Dazin, A.; Joseph, P.; Romano, F.; Gallas, Q.; Marty, J.; Aigouy, G.; Stôβel, M.; Niehuis, R. The ACONIT Project: An Innovative Design Approach of Active Flow Control for Surge Prevention in Gas Turbines. *IOP Conf. Ser. Mater. Sci. Eng.* **2021**, *1024*, 012068. [CrossRef]
19. Margalida, G.; Joseph, P.; Roussette, O.; Dazin, A. Comparison and Sensibility Analysis of Warning Parameters for Rotating Stall Detection in an Axial Compressor. *Int. J. Turbomach. Propuls. Power* **2020**, *5*, 16. [CrossRef]
20. Vegliò, M.; Dazin, A.; Bois, G.; Roussette, O. Unsteady Pressure Measurements of Spike Type Inception in Axial Compressor: Time Frequency Analysis and Averaging Procedure. In Proceedings of the 11th European Conference on Turbomachinery Fluid Dynamics and Thermodynamics, ETC2015-209, Madrid, Spain, 23–27 March 2015.
21. Weigl, H.J.; Paduano, J.D.; Frechette, L.G.; Epstein, A.H.; Greitzer, E.M.; Bright, M.M.; Strazisar, A.J. Active Stabilization of Rotating Stall and Surge in a Transonic Single Stage Axial Compressor. In *Volume 4: Manufacturing Materials and Metallurgy; Ceramics; Structures and Dynamics; Controls, Diagnostics and Instrumentation; Education; IGTI Scholar Award*; American Society of Mechanical Engineers: Orlando, FL, USA, 1997.
22. Deveaux, B.; Fournis, C.; Brion, V.; Marty, J.; Dazin, A. Experimental Analysis and Modeling of the Losses in the Tip Leakage Flow of an Isolated, Non-Rotating Blade Setup. *Exp. Fluids* **2020**, *61*, 126. [CrossRef]

International Journal of
Turbomachinery
Propulsion and Power

MDPI

Article

Experimental Validation of an Analytical Condensation Model for Application in Steam Turbine Design †

Florian Felix Lapp *, Sebastian Schuster, Simon Hecker and Dieter Brillert

Chair of Turbomachinery, University of Duisburg-Essen, 47057 Duisburg, Germany; s.schuster@uni-due.de (S.S.); simon.hecker@siemens-energy.com (S.H.); dieter.brillert@uni-due.de (D.B.)

* Correspondence: florian.lapp@uni-due.de

† This manuscript is an extended version of our meeting paper published in the Proceedings of the 14th European Turbomachinery Conference, Gdansk, Poland, 12–16 April 2021.

Abstract: This paper presents experimental data on shear-stress-driven liquid water films on a horizontal plate formed by the condensation of superheated steam. The experimental results were obtained in the Experimental Multi-phase Measurement Application (EMMA) at the University of Duisburg-Essen. The liquid film thickness was spatially and temporally investigated with an optical measurement system. Furthermore, the resulting local heat transfer coefficient in the case of film condensation was determined for a variety of steam velocities and temperatures. Subsequently, the presented data are compared to the results of an analytical condensation model for shear-stress-driven liquid films developed by Cess and Koh. Thus, the model is qualitatively validated, with explicable remaining disparities between the model and experiment that are further discussed. The presented results are an important contribution to the contemporary research into steady-state, single-component multiphase flow considering phase-change phenomena including heat transfer.

Keywords: heat transfer; steam turbine; condensation; film formation; multiphase flow; phase change

check for updates

Citation: Lapp, F.F.; Schuster, S.; Hecker, S.; Brillert, D. Experimental Validation of an Analytical Condensation Model for Application in Steam Turbine Design. *Int. J. Turbomach. Propuls. Power* **2022**, *7*, 9. https://doi.org/10.3390/ijtpp7010009

Academic Editor: Antoine Dazin

Received: 16 November 2021
Accepted: 27 February 2022
Published: 3 March 2022

Publisher's Note: MDPI stays neutral with regard to jurisdictional claims in published maps and institutional affiliations.

Copyright: © 2022 by the authors. Licensee MDPI, Basel, Switzerland. This article is an open access article distributed under the terms and conditions of the Creative Commons Attribution (CC BY-NC-ND) license (https://creativecommons.org/licenses/by-nc-nd/4.0/).

1. Introduction

The previous decades brought massive changes to the field of power generation and energy distribution. Conventional power plants are facing load variations more frequently, as well as an increase in start-up- and shut-down-cycles, to provide reliable electricity supply and avoid major power outages. This service was realized at the expense of the installed energy conversion facilities, foremost gas and steam turbines. The growing machinery lifetime consumption intensifies the urge to address flexibility requirements in modern turbine design. Gaining a deeper insight into all physical processes that affect the machine conditions is essential for steam turbine design. Spatial and temporal temperature gradients are major factors in the assessment of mechanical integrity and component failure. The thermal stresses, in combination with phase-change phenomena, induced by the previously mentioned operational events of start-up and shut-down, are not negligible. Moreover, the consideration of condensation associated with increasing heat transfer coefficients (HTC) is impeding the design process. Particular attention regarding condensation needs to be given to the turbine housing and the steam-containing cavities. The thermal housing condition can only be sufficiently predicted for all possible shifts in operation points using reliable condensation models, including HTCs.

This paper qualitatively validates an existing analytical 2D-model by Cess [1] and Koh [2] for shear-stress-driven liquid condensation films on a fully wetted horizontal surface, which is compared to experimental data gained in the Experimental Multi-phase Measurement Application (EMMA) at the University Duisburg-Essen. According to Kulkarni [3], and to date, a comparable experimental validation of this model has never been

performed due to difficulties in implementing a suitable experiment that meets the requirements of the theory, as well as the significant differences that exist between shear-stress-driven and gravity-driven film flows. The validation is accomplished by variations in the steam velocity and is focused on enhancing the prediction accuracy of the model regarding liquid water film thickness in combination with the local HTCs.

2. Analytical Model

The first pioneering approach in the field of condensation modelling was achieved by Nusselt [4], describing the process of gravitational-driven falling film condensation on a vertical subcooled wall regarding parallel steam flow and resting steam atmosphere. The first description of solely shear-stress driven condensation films with the absence of an actuating body force on top of a horizontal surface was provided by Cess [1] and Koh [2]. This approach is based on the numerical solution of the ordinary differential equations for the particular case of a semi-infinite plate with parallel flow, resulting from a constant pressure and boundary layer approximation, as well as a "similarity" solution formulation of the resulting model equations. The central achievement of this model is the predictability of the thickness of a condensing shear-stress-driven liquid film in combination with the local wall HTC-distribution. The mathematic derivation of the model was presented by Cess [1] and Koh [2], as well as additional approaches by Narain et al. [5], Phan et al. [6] and Kulkarni et al. [3].

The most important coefficient within the model is the similarity variable η^+ according to Sparrow and Gregg [7]. This represents the central parameter for the determination of further values, which is calculated as

$$\eta^+ = \sqrt[3]{\frac{c_{p,l} \cdot \left(T_s - T_w\right) \cdot r}{Pr \cdot \Delta h_{evap} \cdot 0.083}} \tag{1}$$

with the Koh coefficient r

$$r = \sqrt{\frac{\rho_l \cdot \mu_l}{\rho_g \cdot \mu_g}}. \tag{2}$$

The liquid film thickness δ_x is one of the pivotal parameters derived from η^+ as

$$\delta_x = \eta^+ \sqrt{\frac{\nu_l \cdot x}{U_\infty}}. \tag{3}$$

The second essential parameter is the local wall-HTC $\alpha_{x,w}$, given as

$$\alpha_{x,w} = Nu_{x,w} \cdot \frac{\lambda_l}{x} \tag{4}$$

with the local wall Nusselt number $Nu_{x,w}$, defined as

$$Nu_{x,w} = \frac{1}{\eta^+} \sqrt{Re_{x,w}} \tag{5}$$

and the local wall Reynolds number $Re_{x,w}$ was finally defined as

$$Re_{x,w} = \frac{U_\infty \cdot x}{\nu_l}. \tag{6}$$

Additional values, such as the wall shear stress $\tau_{x,w}$, the liquid film mass flow rate m_l and the film velocity profile $U_{z,l}$, are provided by the model. These values are not experimentally determinable; hence, they are neglected in the validation approach used in this paper.

3. Experimental Investigation

The measurements were conducted with the Experimental Multi-phase Measurement Application (EMMA) at the University Duisburg-Essen. Lapp et al. [8] presented the design and the available steam conditions of the test facility, including the measurement systems applied for the determination of the liquid water film thickness, as well as the local HTC-distribution. The square-shaped cross-sectional measurement section of $A_\infty = 2500$ mm^2, displayed in Figure 1, was equipped with an optical access that allowed for an observation length of $l_x = 250$ mm and $l_y = 50$ mm. Via this access, the infrared-interferometric sensor from Precitec [9] provided a resolvable liquid film thickness in the range of 16 µm–2600 µm with a linearity error of ±0.429 µm.

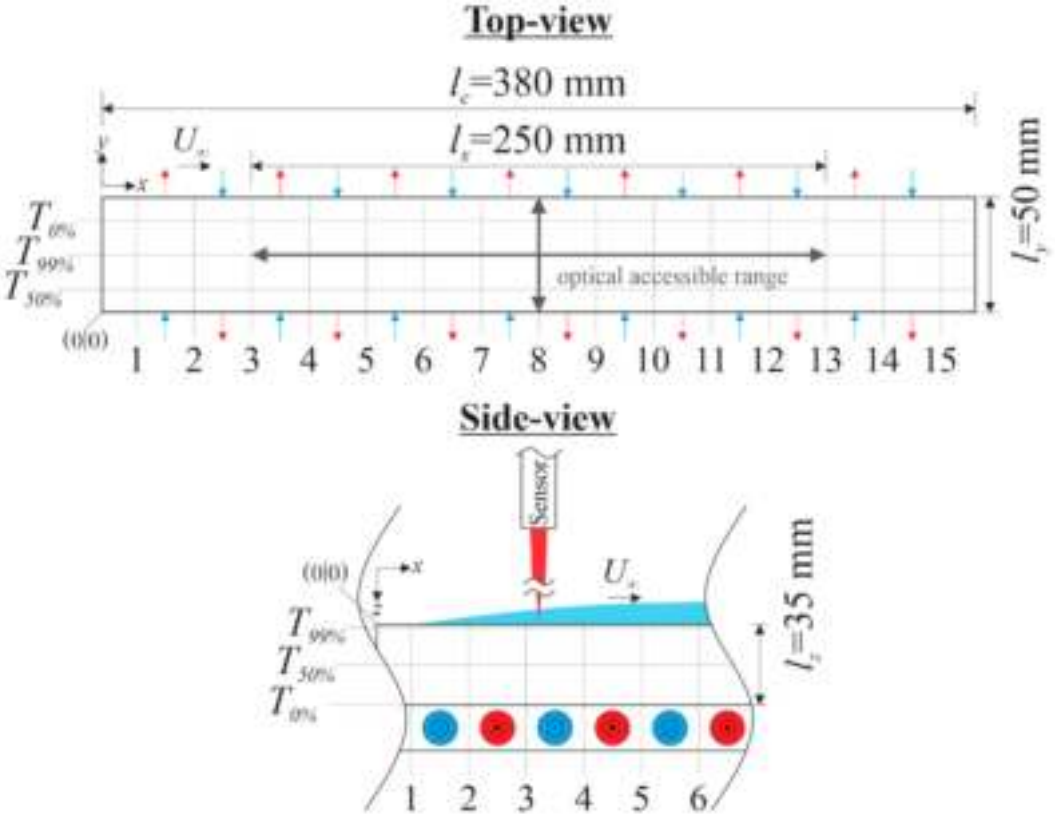

Figure 1. Measurement section with instrumentation locations and optical accessible range.

The horizontally aligned measurement plate of $l_c = 380$ mm and $l_z = 35$ mm, manufactured from stainless-steel, was instrumented with thermocouples (TC) type T at 15 axial positions, consisting of 3 TC each, recording $T_{0\%}$ at the bottom of the measurement plate, $T_{50\%}$ at 50 % thickness of the measurement plate height, and $T_{99\%}$ 0.5 mm below the measurement surface at top side. $T_{0\%}$ and $T_{50\%}$ were used to calculate the local heat flux density, $\dot{q}_x$. To induce film condensation on top of the measurement plate, the necessary heat flux was accomplished by a countercurrent heat-exchanging plate made of aluminum 3.1645 (DIN EN 17007-4 [10]) from Batz+Burgel [11], with 16 water–glycol filled cooling channels connected to an external water-cooled refrigeration unit.

The main goal of this measurement campaign was validation of the analytical model presented earlier. Since the film condensation influenced by shear-stress is a thermodynamic process influenced by multiple steam parameters, such as temperature T_∞, pressure p_∞ and velocity $U_{\infty,}$ as well as solid interface conditions such as cooling capacity $\dot{Q}_c$, surface material, average roughness R_a and fouling, the significant effects need to be identified. For the initial validation of the model, this paper focusses on the fluid–mechanical and thermodynamic boundary conditions.

Thus, the surface material and R_a were fixed, and the corresponding influence was identical within the whole investigation. Stainless-steel 1.4571 (DIN EN 10027 [12]) from DEW [13] was the applied wall material, with a thermal conductivity of $\lambda_w = 15\,\mathrm{Wm^{-1}K^{-1}}$.

The surface was ground and exhibited an average roughness value of $R_a = 1.862$ µm. Since the effect of surface fouling has a fundamental impact on the liquid film behavior, the surface was regularly cleaned with isopropyl alcohol before each measurement sequence, to guarantee equal conditions throughout the whole investigation.

T_∞, p_∞ and U_∞, as well as $\dot{Q}_c$, are the thermodynamic variables that need to be varied for a sufficient validation of the analytical condensation model. Due to the absence of an actuating body force, the liquid film is solely shear-stress-driven by the steam mass flow at the liquid-gaseous interface. Hence, U_∞ is the major factor determining the local film thickness δ_x alongside the flow direction and is, therefore, investigated in this paper. U_∞ is altered from $U_{\infty,min} = 2.5$ m/s up to $U_{\infty,max} = 12.5$ m/s in steps of 2.5 m/s. All measurements within that sequence were conducted at $T_\infty = 473.15$ K, $p_\infty = 1.1{\cdot}10^5$ Pa and $\dot{Q}_c = 1.2$ kW.

In preparation for every test sequence, the whole measurement section was preheated 20 K above saturated steam temperature to ensure dry test conditions and isothermal wall temperature distribution. After that, the measurement plate was subcooled for 30 min until a stationary liquid film was established. The fully wetted surface was observed across the whole optical accessible length, $l_x = 250$ mm, in the middle of the test section at $y = 25$ mm. Each configured U_∞ was investigated multiple times, capturing lines by moving the sensor up- and downstream with a velocity of 0.75 mm/s and a sampling rate of 30 Hz. Additional tests concerning possible wavelet effects at the liquid-gaseous interface were conducted at 5 positions at a distance of 50 mm along the previously mentioned line. Each position was recorded for 1 min using a frequency of 1 kHz to prevent subsampling.

4. Experimental Results and Inaccuracy Consideration

To form the basis for a precise and trustable analysis, the measurement data-processing, as well as the sensor inaccuracies, need to be sufficiently discussed. Since $\delta_{x,exp}$ and $\alpha_{x,exp}$ are the central measurements investigated in this paper, the method of analysis is subsequently presented.

4.1. Liquid Film Thickness

$\delta_{x,exp}$ is continuously recorded along a linear track of $l_x = 250$ mm, leading to a distribution of thickness values, which need to be converted to a mathematical correlation for an optimal model comparison. Based on the model assumptions, Equation (3) analytically describes the local film thickness δ_x as a square-root-function of the axial position x. Hence, the consideration of a root function approach will presumably lead to the most suitable curve-fitting results if the model corresponds to the experimental results. Figure 2 shows the square-root curve-fitting approach at a steam velocity of $U_\infty = 12.5$ m/s. The correlation quality advantage of the square root function, presented at $U_\infty = 12.5$ m/s, is representative for all varied velocities, confirming the application of the square root function. An exponential and a logarithmic function were also considered, leading to worse correlation results than the square root approach. The correlation coefficient R was used to determine the fitting quality and was about $R = 0.923$ for all the remaining velocities. $U_\infty = 2.5$ m/s exhibits the only exception to the decent correlation quality, with $R = 0.165$. One reason for this was presented by Kulkarni et al. [3], describing a minimal velocity threshold for the model prediction validity in the ballpark of 2 m/s. The reason for this can be traced back to the inertial forces within the liquid phase, which cannot be overcome by shear-stress at the liquid-gaseous interface, due to steam velocities below the minimal threshold value. Hence, $U_\infty = 2.5$ m/s will not be further investigated, since it is beyond the model's range of validity.

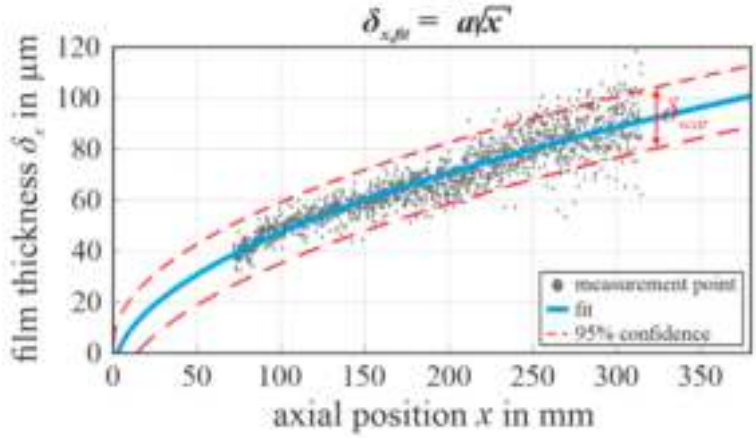

Figure 2. The chosen curve-fitting equation based on a square root function, exemplarily displayed at $U_\infty = 12.5$ m/s.

To determine measurement inaccuracy, the 95% confidence interval was used by calculating the absolute confidence interval width. This is also referred to as the absolute thickness scattering $\delta_{x,scat}$, more specifically the mean thickness scattering $\overline{\delta}_{x,scat}$, averaged along the whole plate length. Considering all investigated steam velocities, $\overline{\delta}_{x,scat}$ is about ± 2.622 µm and, hence, 5.7 times the sensors' linearity error of ± 0.429 µm given by Precitec [9]. One reason for the high scattering of $\delta_{x,exp}$ is a visible wavelet fluctuation at the liquid-gaseous interface depending on $\delta_{x,exp}$ and U_∞. This effect is particularly distinct at high steam velocities. The mentioned dependencies of $\delta_{x,scat}$ substantiate the theory that $\delta_{x,scat}$ is mainly dominated by a physical measurable wavelet effect, which would describe the relatively high measurement scattering. As described earlier, additional wavelet measurements were conducted to quantify the share of wavelet fluctuation within $\delta_{x,scat}$. At five different positions, the liquid film is locally observed, determining a continuous thickness signal. This signal should consist of a variety of Sines\Cosines shares if the optical observable fluctuations correspond to a harmonic wavelet occurrence. Thus, the filtered local signals were transformed from a time- to a frequency-domain using a Fast Fourier Transformation (FFT), as presented in Figure 3, at two axial positions. It can be stated that the signal consists of multiple harmonics of the base frequency of 1 Hz with a decreasing amplitude. At the position $x = 295$ mm, the maximum amplitude $\widetilde{\delta}_{wave,max}$ is three times the amplitude at $x = 95$ mm, showing a clear dependence on the increasing film thickness. The mean maximum amplitude for all positions and each velocity was $\overline{\widetilde{\delta}}_{wave,max} = \pm 3.864$ µm. The FFT result proves that the mean measurement scattering of $\overline{\delta}_{x,scat} = \pm 2.622$ µm can be traced back to the presence of wavelet effects on the liquid-gaseous interface. After that, the first 10 Hz were retransformed by an inverse FFT to verify that the identified amplitude spectrum represents the original signal. Figure 3 presents the transformed amplitude spectrum. The $\widetilde{\delta}_{wave,max}$ that was identified by the FFT can be found within the signal in the time domain. Since the inverse signal fit the original data very well, the FFT approach, determining the maximum wavelet amplitude within the film thickness signal, can sufficiently be presumed. Subsequently, it can be stated that $\overline{\delta}_{x,scat}$ corresponds very well to $\overline{\widetilde{\delta}}_{wave,max}$, verifying that the scattering is caused by a physical measurable wavelet effect on the liquid-gaseous interface. Thus, it can be concluded that $\overline{\delta}_{x,scat}$ must not be considered a measurement error, since $\delta_{x,exp}$ can be derived by providing a sufficiently high measurement frequency. This wavelet consideration is exemplarily presented for the case of $U_\infty = 12.5$ m/s. Regarding the lower steam velocities, it can be observed that the maximum wavelet amplitudes reduce with declining velocities, although the overall film thickness is rising. This can be traced to the fact that the wavelet formation within the liquid water film is solely shear-stress-driven.

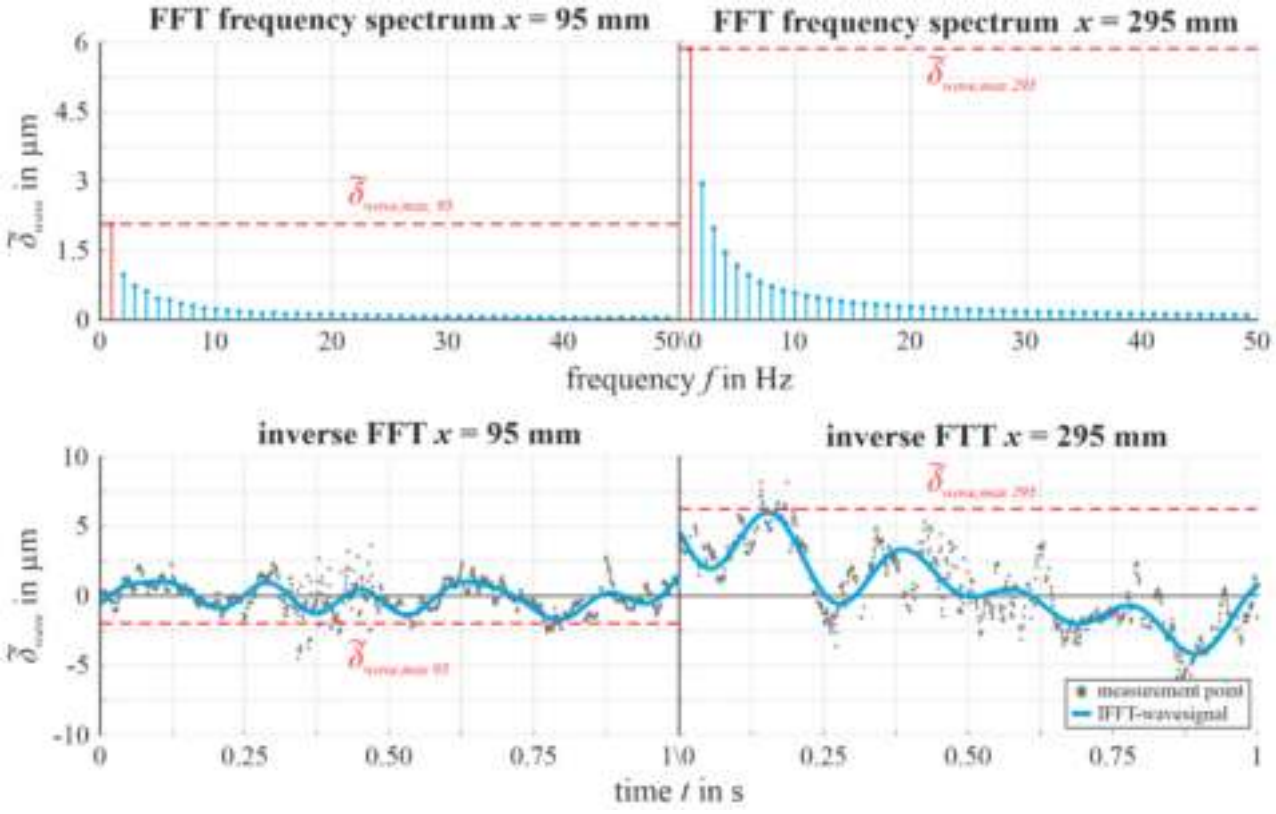

Figure 3. The frequency spectrum of the FFT-processed signals that are subsequently retransformed for the first 10 Hz at two axial positions, exemplarily displayed at $U_\infty = 12.5$ m/s.

Figure 4 shows the experimental results of $\delta_{x,exp}$, including square-root-based fits and 95% confidence intervals. $\delta_{x,exp}$ exhibits further progression for every velocity that corresponds very well to a square-root-based function. The condensation starts at the beginning of the cooled measurement plate or slightly after, which is physically plausible.

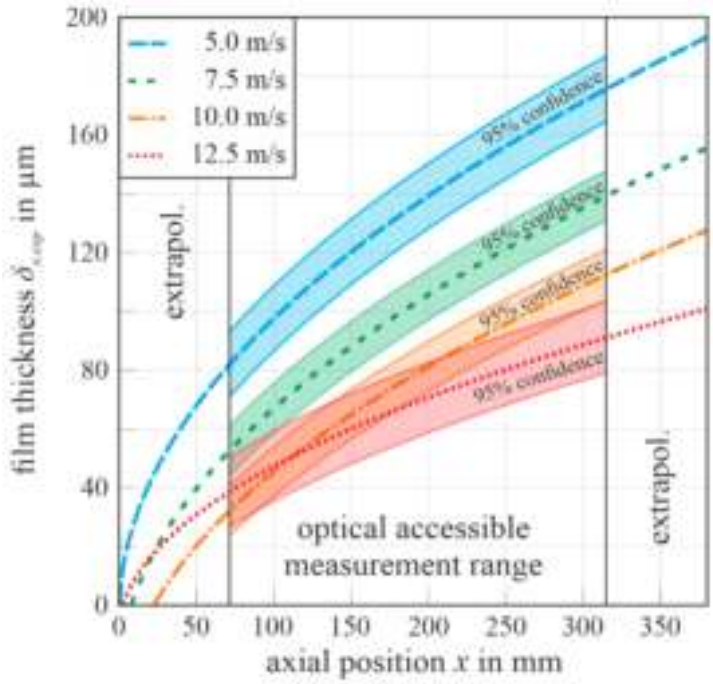

Figure 4. Experimental results of $\delta_{x,exp}$ including square root fits and 95% confidence intervals.

Due to the fact that the axial starting position of the condensation is extrapolated from the data, recorded within the measurement range, the position serves solely as a plausibility criterion at this point and will be further investigated. The increase in $\delta_{x,exp}$ as a function of the progressing overflow position x can clearly be observed for all velocities. Furthermore, the decrease in U_∞ leads to an increase in the $\delta_{x,exp}$. The fact that the main film-actuating mechanism, provided by the interfacial shear stress, declined, gives the liquid film more dwell time on the cooled plate, accompanied by an enhanced condensation intensity. One distinctive feature can be found in the trend of $U_\infty = 12.5$ m/s, consisting of a higher film thickness for $x < 120$ mm compared to $U_\infty = 10$ m/s. The film thickness development gradients deliver plausible results, since the increasing shear-stress leads to lower thickness development gradients.

Figure 5 presents the result of an additional condensation measurement to address the difficulties of the optical limitation at the condensation initialization point. Since every cooling duct within the cooling plate can be individually controlled, the first half of the measurement plate remains uncooled during this test. Hence, the starting point of the condensation film is shifted to the optical accessible measurement range and can be further investigated. As expected, Figure 5 illustrates that no condensation film can be observed in the uncooled area. The condensation starting point is located at $x = 180$ mm, and is thereby located 10 mm further upstream than the beginning of the cooled area at $x = 190$ mm. This is due to the fact that the tempered measurement plate consists of continuous material, and axial heat conductance is not avoidable. Nevertheless, the starting point of the condensation, as well as the beginning of the cooled area, are relatively close to each other, despite the blurring effect of the plates' axial heat conductance. Subsequently, the results of this experiment prove that the condensation starting point in the main experiment is located at the beginning of the measurement plate, since the plate and the rest of the measurement section exhibit a friction-type connection, leading to a significantly lower heat conductance in the axial direction.

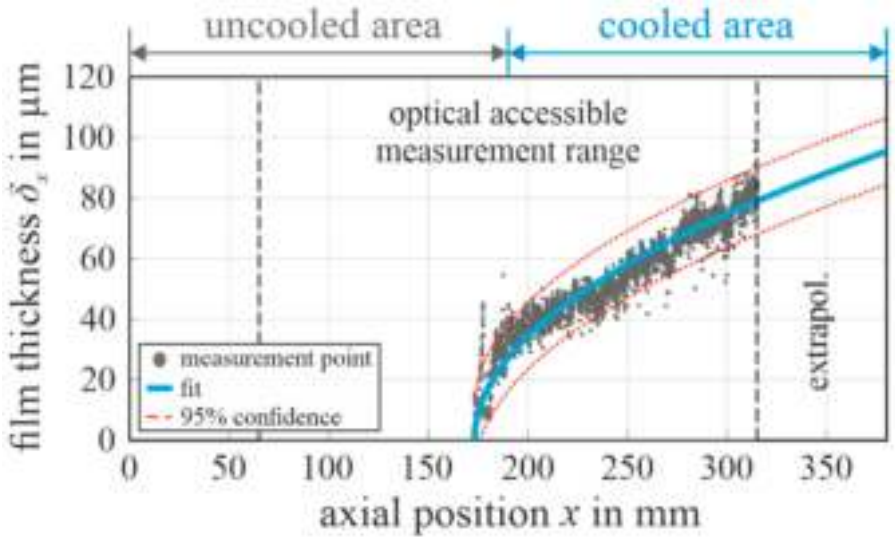

Figure 5. Experimental result of the film thickness on a plate, solely cooled in the second half at $U_\infty = 10$ m/s.

Since the condensation starting area was not optically observable, the application of the square-root-based fitting approach needs to be verified. The measurement data in Figure 5 were fitted with the same square root approach as presented earlier. It is obvious that the square root fit matches the measurement points within the entire investigated area. Hence, it is proven that the square root approach is valid to approximate the raw measurement data alongside the whole measurement section.

4.2. Heat Transfer Coefficient

The determination of $\alpha_{x,exp}$ is mainly based on the measurement of $\dot{q}_x$, the wall temperature T_w and the saturated steam temperature T_s. Hence, the temperature difference method, compared to Diller [14,15], was applied to determine $\dot{q}_x$, by measuring the temperature difference between $T_{50\%}$ and $T_{0\%}$. By measuring $T_{99\%}$, 0.5 mm below the surface, T_w is linearly extrapolated with the temperature gradient between $T_{99\%}$ and $T_{50\%}$. Subsequently, T_s is determined by measuring the static steam pressure p_∞. Overall, $\alpha_{x,exp}$ is calculated by

$$\alpha_{x,exp} = \frac{\lambda_w(T_{50\%} - T_{0\%})}{l_{z,50\%,0\%}(T_s - T_w)}, \tag{7}$$

including the measurement inaccuracy, calculated by the classic error propagation approach as

$$\Delta\alpha_{x,err} = \left|\frac{\partial\alpha_x}{\partial\lambda_w}\Delta\lambda_w\right| + 2\left|\frac{\partial\alpha_x}{\partial T_{XX\%}}\Delta T_{XX\%}\right| + \left|\frac{\partial\alpha_x}{\partial l_z}\Delta l_z\right| + \left|\frac{\partial\alpha_x}{\partial T_s}\Delta T_s\right| + \left|\frac{\partial\alpha_x}{\partial T_w}\Delta T_w\right|. \tag{8}$$

$\alpha_{x,exp}$ is measured at 15 equidistantly distributed positions along the measurement plate. Every measurement position consists of three TC Type T that are mounted within spark-eroded holes, measuring $T_{99\%}$, $T_{50\%}$ and $T_{0\%}$. The manufacturing process assures a precise positioning of the TC within the holes, leading to a positioning error of $\Delta l_z = \pm 100$ µm. Prior to mounting, a calibration of all 45 temperature probes was performed in the range of 20 °C − 120 °C, ensuring a TC inaccuracy of $\Delta T_{xx\%} = \pm 0.1$ K. The pressure probe exhibits an error of $\Delta p_\infty = \pm 1$ Pa, leading to $\Delta T_s = \pm 0.5$ mK. Moreover, the thermal conductivity error was estimated by the accuracy of the alloy composition, leading to $\Delta\lambda_w = \pm 0.15\ \mathrm{Wm^{-1}K^{-1}}$. Overall, the average HTC-error results in $\Delta\overline{\alpha}_{x,err} = \pm 112,526\ \mathrm{Wm^{-2}K^{-1}}$.

Figure 6 shows the experimental results of $\alpha_{x,exp}$, including power-function-based fits and measurement inaccuracies. The sensors at $T_{99\%}$ lost connection to the wall, due to a mounting malfunction at the first measurement position, $x_1 = 15.5$ mm, as well as the ninth measurement position, $x_9 = 215.5$ mm. Both results have not been considered in the correlation approach, based on the function $\alpha_{x,fit} = ax^b$. All $\alpha_{x,exp}$ distributions show a regressive decline due to an increasing axial position x. An evident inverse relation between $\alpha_{x,exp}$ and $\delta_{x,exp}$ can be spatially observed. Additionally, both quantities are a function of U_∞.

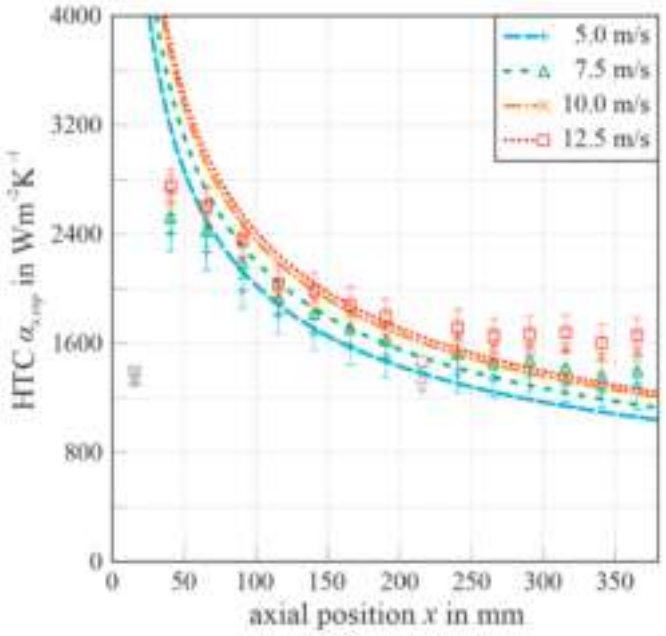

Figure 6. Experimental results of $\alpha_{x,exp}$ including power-function-based fits.

5. Model Validation

The central objective of this paper is the experimental validation of the theoretically calculated values of δ_x and α_x regarding the variation in the steam velocity. Figure 7 presents a comparison of the theoretical as well as the experimental data regarding (a) δ_x and (b) α_x.

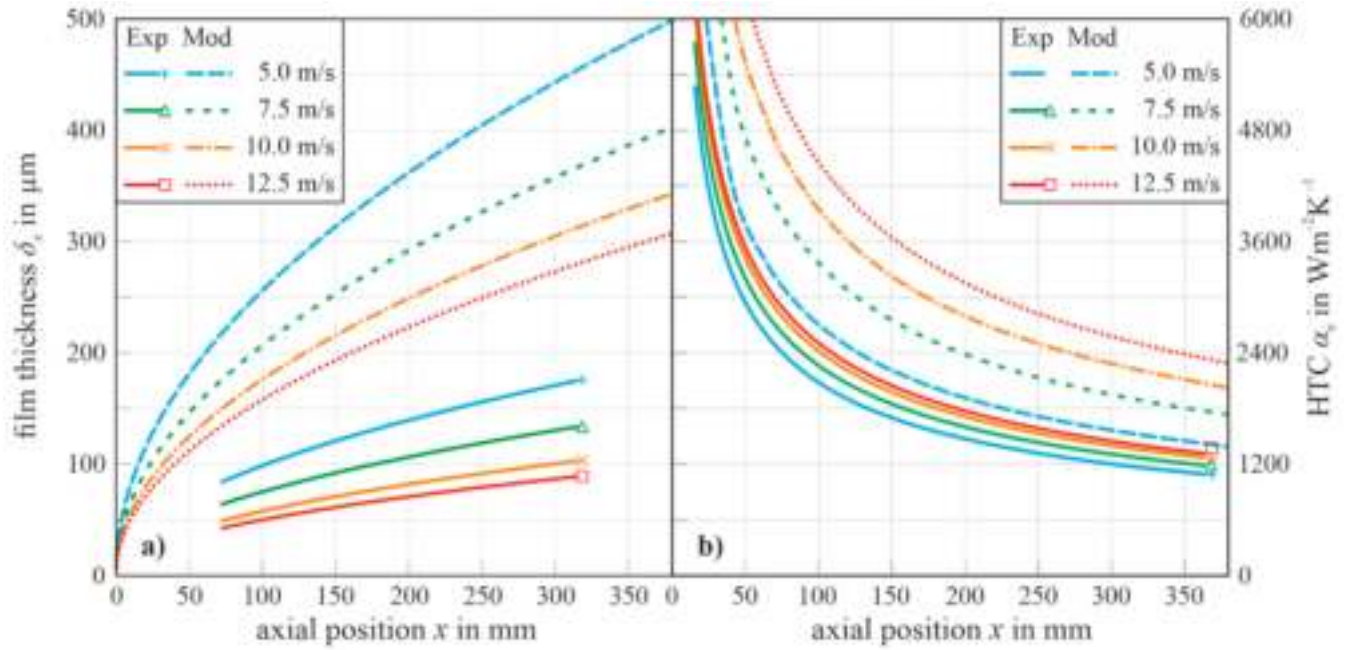

Figure 7. Comparison of the experimental and theoretical results regarding (**a**) δ_x and (**b**) α_x.

In case of the liquid film thickness, it can be observed that the inverse-velocity-dependent declining progress of $\delta_{x,exp}$ was analogically predicted by the theoretical model. Furthermore, the spatial rise in δ_x with rising x was also sufficiently predicted. The thickness predicted by the model was, overall, 2.3 times higher than the experimental investigated films, constituting a major difference between the model and experiment. A possible reason for this could be the influence of the experimental steam superheating of 100 K above the saturated steam temperature, which needs to be applied to prevent secondary condensation on the side walls. The additional superheated enthalpy share that needs to be transferred, besides the latent heat, contributed a heating effect to the liquid phase, inhibiting the condensation process and leading to a spatial reduction in the condensate amount. Subsequently, it can be stated that the theoretical model predictions are plausible and were qualitatively validated considering the fundamental influence of the local position x and U_∞.

Regarding the HTC α_x, the prediction quality of the model is very similar to the case of δ_x. The theoretically predicted local decrease in α_x in the flow direction is qualitatively confirmed by the experimental results. In addition, the impact, due to the velocity variation, further affirms the model's qualitative validity. A major difference between the model and experiment is apparent in the spatial gradient. The model assumes a semi-infinite plate with a singularity at the front edge. In the theoretical calculation of $\alpha_{x,mod}$, x appears in the denominator, leading to a singularity with infinite HTC. Since the front edge of the real measurement plate is in contact with the inlet section, the high HTCs at the axial starting position of the condensation will lead to axial heat conduction in the upstream direction. Hence, $\alpha_{x,exp}$ exhibits a reduced HTC gradient at the beginning of the plate. Another mismatch between the model and experiment is observable in the differing gradients at axial positions further downstream. The model predicts a steeper decline in the HTCs for all velocities, compared the experiment, which shows an ostensible saturation behavior.

This can be traced back to the physical thickness of the measurement plate, which is necessary to measure a temperature gradient to determine $\alpha_{x,exp}$. The material consistency of the plate is inseparably connected with the occurrence of heat flux in the axial direction, causing a homogenization of the HTC distribution. Subsequently, the model can qualitatively be considered as validated, analogous to the case of δ_x.

6. Conclusions and Outlook

In this paper, experimental data for shear-stress-driven liquid water films on a horizontal fully wetted surface are presented. Furthermore, these data were used for the qualitative validation of the analytical condensation model by Cess (1960) and Koh (1962). This model has never been validated before and the experimental results confirmed the qualitative prediction of the liquid film thickness δ_x, as well as the local HTC distribution α_x. Regarding the liquid film thickness, the following conclusions can be drawn:

- δ_x increases as a square root-function of the progressing overflow position x for all velocities.
- The decrease in U_∞ leads to an increase in the δ_x.
- Regarding δ_x, the model overestimates the thickness values regarding factor 2.3 compared to the experimental results due to the deferred steam temperature condition between the model and experiment.

Finally, regarding the heat transfer coefficient, the following conclusions can be drawn:

- α_x shows a regressive decline depending on an increasing axial position, x.
- An evident inverse relation between α_x and δ_x can be spatially observed. Additionally, both quantities are a function of U_∞.
- The axial gradient of α_x is predicted to be higher than the experimental results.

The results of this paper make a valuable contribution to the trustworthiness of the well-applied and widely distributed condensation model of Cess and Koh. This model is an integral part of the description of condensation processes, besides the experimentally validated Nusselt film theory. By proving the qualitative validity of this shear-stress-driven condensation model, the prediction reliability was fundamentally increased, enabling a comprehensive description of condensation cases regarding liquid condensate amount, as well as the connected HTC-distribution within the steam turbine design processes.

Author Contributions: Conceptualization, F.F.L.; methodology, F.F.L.; software, F.F.L.; validation, F.F.L.; formal analysis, F.F.L.; investigation, F.F.L.; resources, F.F.L.; data curation, F.F.L.; writing—original draft preparation, F.F.L.; writing—review and editing, S.S., S.H. and D.B.; visualization, F.F.L.; supervision, S.S.; project administration, D.B.; funding acquisition, D.B. and S.H. All authors have read and agreed to the published version of the manuscript.

Funding: This project is part of the AG Turbo joint research program, contract number 03ET7092I. The investigations were supported by the Federal Ministry of Economics and Energy (BMWi) as well as the Siemens Energy AG, Muelheim a.d.R., Germany.

Institutional Review Board Statement: Not applicable.

Informed Consent Statement: Not applicable.

Data Availability Statement: Not applicable.

Conflicts of Interest: The authors declare no conflict of interest.

Nomenclature

A	area	m^2	Re	Reynolds number	–
c_p	specific heat at const. pressure	$\frac{J}{kgK}$	T	steam temperature	K
h	enthalpy	$\frac{J}{kgK}$	U	steam velocity	$\frac{m}{s}$
$\dot{m}$	mass flow rate	$\frac{kg}{s}$	x	axial position	m
Nu	Nusselt number	–	α	heat transfer coefficient	$\frac{W}{m^2K}$
l	length	m	δ	film thickness	m
p	steam pressure	Pa	η	similarity variable	–
Pr	Prandtl number	–	λ	thermal conductivity	$\frac{W}{mK}$
$\dot{q}$	heat flux density	$\frac{W}{m^2}$	μ	dynamic viscosity	Pa·s
$\dot{Q}$	heat flux/cooling capacity	W	ν	kinematic viscosity	$\frac{m^2}{s}$
r	Koh coefficient	–	ρ	density	$\frac{kg}{m^3}$
R	correlation coefficient	–	τ	shear stress	Pa
R_a	average roughness value	m			

Indices

∞	steam flow conditions	*scat*	scattering
c	cooling plate	*wave*	wavelet
err	error/inaccuracy	*w*	wall
evap	evaporation	*x*	direction x—horizontal parallel to flow
exp	experimental	y	direction y—horizontal orthogonal to flow
g	gaseous	*z*	direction z—vertical orthogonal to flow
l	liquid	0%	Pos. at 0% meas. plate height
max	maximum	50%	Pos. at 50% meas. plate height
mid	middle	99%	Pos. at 0.5 mm below meas. surface
min	minimum	+	dimensionless
mod	model	~	amplitude
s	saturation	–	average

References

1. Cess, R.D. Laminar-film condensation on a flat plate in the absence of a body force. *Z. Angew. Math. Phys.* **1960**, *11*, 423–433. [CrossRef]
2. Koh, J. Film condensation in a forced-convection boundary-layer flow. *Int. J. Heat Mass Transf.* **1962**, *5*, 941–954. [CrossRef]
3. Kulkarni, S.; Narain, A.; Mitra, S. Forced Flow of Vapor Condensing Over a Horizontal Plate (Problem of Cess and Koh): Steady and Unsteady Solutions of the Full 2D Problem. *J. Heat Transf.* **2010**, *132*, 101502. [CrossRef]
4. Nusselt, W. Die Oberflächenkondensation des Wasserdampfes. *VDI-Zs* **1916**, *60*, 541–546.
5. Narain, A.; Liang, Q.; Yu, G.; Wang, X. Direct Computational Simulations for Internal Condensing Flows and Results on Attainability/Stability of Steady Solutions, Their Intrinsic Waviness and Their Noise Sensitivity. *J. Appl. Mech.* **2004**, *71*, 69–88. [CrossRef]
6. Phan, L.; Narain, A. Nonlinear Stability of the Classical Nusselt Problem of Film Condensation and Wave Effects. *J. Appl. Mech.* **2006**, *74*, 279–290. [CrossRef]
7. Sparrow, E.M.; Gregg, J.L. A Boundary-Layer Treatment of Laminar-Film Condensation. *J. Heat Transf.* **1959**, *81*, 13–18. [CrossRef]
8. Lapp, F.F.; Schuster, S.; Hecker, S.; Brillert, D. The Multi-Phase Flow Test Facility "EMMA" to Investigate Local Heat Transfer Coefficients and Liquid Water Films at Wet Steam Conditions [GT2020-16307]. In Proceedings of the ASME Turbo Expo 2020, London, UK, 22–26 June 2020.
9. Precitec Optronik GmbH. *Overview Interferometric Point Sensors—CHRocodile 2 LR*; Gaggenau: Bad Rotenfels, Germany, 2019.
10. DIN–German Institute for Standardization. *Material Numbers–Part 4: System of the Principal Groups 2 and 3: Non-Ferrous Metals*; DIN EN 17007-4; Beuth Verlag GmbH: Berlin, Germany, 2012.
11. Batz + Burgel GmbH & Co. *KG Material Data Sheet: EN AW–2007 (AlCu4PBMgMN- 3.1645)*; Batz + Burgel GmbH & Co.: Friedberg, Germany, 2019.
12. DIN–German Institute for Standardization. *Designation Systems for Steels–Part 2: Numerical System*; DIN EN 10027; Beuth Verlag GmbH: Berlin, Germany, 2015.
13. DEW–Deutsche Edelstahlwerke, Specialty Steel GmbH & Co. *KG. Technical Data Sheet, X6CrNiMoTi17-12-2, 1.4571*; DEW–Deutsche Edelstahlwerke, Specialty Steel GmbH & Co. KG: Witten, Germany, 2019.

14. Diller, T.E. Advances in Heat Flux Measurements. *Adv. Heat Transf.* **1993**, *23*, 279–368.
15. Lapp, F.F.; Schuster, S.; Hecker, S.; Brillert, D. Experimental validation of an analytical condensation model for the improvement of steam turbine design regarding flexibility requirements. In Proceedings of the 14th European Conference on Turbomachinery Fluid Dynamics & Thermodynamics, ETC2020-562, Gdansk, Poland, 12–16 April 2021.

International Journal of
Turbomachinery
Propulsion and Power

MDPI

Article

Reynolds Sensitivity of the Wake Passing Effect on a LPT Cascade Using Spectral/*hp* Element Methods †

Andrea Cassinelli [1], Andrés Mateo Gabín [2], Francesco Montomoli [1], Paolo Adami [3], Raul Vázquez Díaz [4] and Spencer J. Sherwin [1,*]

[1] Department of Aeronautics, Imperial College London, London SW7 2AZ, UK; andrea.cassinelli.93@gmail.com (A.C.); f.montomoli@imperial.ac.uk (F.M.)
[2] School of Aeronautical and Space Engineering, Universidad Politécnica de Madrid, 28040 Madrid, Spain; andres.mgabin@upm.es
[3] Rolls-Royce Deutschland, 15827 Dahlewitz, Germany; Paolo.Adami2@Rolls-Royce.com
[4] Rolls-Royce plc., Derby DE24 8ZF, UK; Raul.Vazquez@Rolls-Royce.com
* Correspondence: s.sherwin@imperial.ac.uk
† This paper is an extended version of our paper published in Proceedings of the European Turbomachinery Conference ETC14 2021, Paper No. 606, Gdansk, Poland, 12–16 April 2021.

Abstract: Reynolds-Averaged Navier–Stokes (RANS) methods continue to be the backbone of CFD-based design; however, the recent development of high-order unstructured solvers and meshing algorithms, combined with the lowering cost of HPC infrastructures, has the potential to allow for the introduction of high-fidelity simulations in the design loop, taking the role of a virtual wind tunnel. Extensive validation and verification is required over a broad design space. This is challenging for a number of reasons, including the range of operating conditions, the complexity of industrial geometries and their relative motion. A representative industrial low pressure turbine (LPT) cascade subject to wake passing interactions is analysed, adopting the incompressible Navier–Stokes solver implemented in the spectral/*hp* element framework *Nektar*++. The bar passing effect is modelled by leveraging a spectral-element/Fourier Smoothed Profile Method. The Reynolds sensitivity is analysed, focusing in detail on the dynamics of the separation bubble on the suction surface as well as the mean flow properties, wake profiles and loss estimations. The main findings are compared with experimental data, showing agreement in the prediction of wake traverses and losses across the entire range of flow regimes, the latter within 5% of the experimental measurements.

Keywords: wake-passing effect; reynolds sensitivity; spectral/*hp* element method; high-order; smoothed profile method

check for updates

Citation: Cassinelli, A.; Mateo Gabín, A.; Montomoli, F.; Adami, P.; Vázquez Díaz, R.; Sherwin, S.J. Reynolds Sensitivity of the Wake Passing Effect on a LPT Cascade Using Spectral/*hp* Element Methods. *Int. J. Turbomach. Propuls. Power* **2022**, *7*, 8. https://doi.org/10.3390/ijtpp7010008

Academic Editor: Tony Arts

Received: 20 June 2021
Accepted: 7 February 2022
Published: 22 February 2022

Publisher's Note: MDPI stays neutral with regard to jurisdictional claims in published maps and institutional affiliations.

Copyright: © 2022 by the authors. Licensee MDPI, Basel, Switzerland. This article is an open access article distributed under the terms and conditions of the Creative Commons Attribution (CC BY-NC-ND) license (https://creativecommons.org/licenses/by-nc-nd/4.0/).

1. Introduction

In a gas turbine engine, the pressure expansion through high- and low-pressure turbines (LPT) is achieved in a number of subsequent stages. The interaction of multiple stages of rotors and stators is a crucial source of deterministic unsteadiness, which has effects on the loss production mechanisms, and it is thus of great importance to designers. One of the early computational investigations of the wake-passing effect was carried out by Wu and Durbin [1,2], who presented evidence that incoming wakes are responsible for the formation of longitudinal structures on the pressure side.

Subsequently, a number of Direct Numerical Simulation (DNS) studies were performed on LPTs, providing further contributions to the understanding of the effect of incoming wakes on the pressure- and suction-side boundary layers [3–6]. A detailed review by Hodson and Howell [7] summarises the wake-induced boundary layer transition mechanisms in LPTs.

The impact of the wake passing frequency on loss mechanisms has been numerically investigated by several authors. Michelassi et al. [8] built on top of previous work [9]

to analyse the effects of various types of inflow disturbances on losses in a series of compressible DNS simulations. In particular, they observed the effect of three reduced frequencies and two Reynolds numbers ($Re_2 = 60{,}000$ and 100,000) on various types of loss indicators. The behaviour of high reduced frequencies was found to be most effective in suppressing the suction surface separation bubble, by manifesting a very similar behaviour to high levels of inflow turbulence, due to the constant-area mixing prior to the leading edge.

The comparisons of mixed-out losses with profile losses as defined by Denton [10] allowed distinguishing the losses generated in the boundary layer from those generated in the flow core by the variable-area wake mixing. The largest difference was found at low levels of reduced frequency (1 bar per pitch): in this case, the wakes remain distinct within the blade passage and experience significant wake distortion losses.

Further LES simulations [11] demonstrated the combined importance of the reduced frequency and flow coefficient on losses. These important design parameters affect the frequency with which incoming wakes impact on the cascade as well as the wake inclination. The normal distance between incoming wakes was found to correlate very well with mixed-out losses, further confirming that wake merging (which produces a free-stream turbulence-like behaviour) is generally beneficial for the reduction of unsteady losses. This approach can importantly be adopted to inform design optimisation, as the various combinations of reduced frequency and flow coefficient are effectively a consequence of design parameters, such as the revolution speed and flow-through velocity.

As part of an ongoing effort to develop a validated incompressible DNS capability for the turbomachinery Industry using spectral/*hp* element methods, the present work builds on consolidated expertise [12–14] in the use of the *Nektar*++ open-source software framework [15] for industrial applications. The wake-passing effect is analysed in the context of a representative research LPT profile, with a particular focus on the Reynolds sensitivity of the transition mechanism on the suction surface and the loss prediction. The optimal and most realistic degree of reaction corresponds to the reduced frequency range where unsteady losses are highest [11], which is targeted in this paper. The availability of experimental data in the wake traverses at the flow regimes analysed allows quantification of the accuracy of the numerical approach.

The paper is organised as follows: first, a brief introduction on the numerical setup and wake modelling strategy is presented. Subsequently, the flow dynamics on the suction surface are characterised in the various phases of the wake passing cycle. The following sections focuses on the time-averaged effects of the wake passing, analysing the blade wall distributions, wake profiles and mixed-out measurements and establishing a comparison with highly accurate experimental data. The paper concludes by providing remarks on the validity of the results presented.

2. Methods

2.1. Numerical Approach

The incompressible Navier–Stokes equations

$$\frac{\partial \mathbf{u}}{\partial t} = -(\mathbf{u} \cdot \nabla)\mathbf{u} - \nabla p + \nu \nabla^2 \mathbf{u} \qquad \text{in } \Omega, \tag{1}$$

$$\nabla \cdot \mathbf{u} = 0 \qquad \text{in } \Omega, \tag{2}$$

were discretised using the spectral/*hp* element framework *Nektar*++ [15]. The solver adopts a stiffly stable time discretisation [16], which decouples the velocity and pressure fields, also known as the Velocity-Correction Scheme [17]. This formulation treats the convective terms explicitly, while pressure and the viscous contributions are treated implicitly; therefore, addressing stability constraints that would otherwise be associated with the viscous time stepping.

Analysis of test cases at high Reynolds numbers with under-resolved meshes requires the use of stabilization techniques: if the dissipative scales at high wavenumbers are not

fully resolved, a buildup of energy might cause the solution to diverge. Spectral Vanishing Viscosity (SVV) was introduced by Tadmor et al. [18] as a technique to add artificial diffusion to potentially unstable under-resolved scales. Since the oscillations causing divergence of the solution emerge at sub-elemental level, SVV is a stabilization technique that acts at the subgrid-scale level, without introducing any explicit model.

The DG-Kernel SVV formulation introduced by Moura et al. [19,20] was adopted to ensure numerical stability in the spectral/*hp* planes, while the traditional exponential kernel was employed in the Fourier expansion in the spanwise direction. In adopting such a stabilisation approach, better resolution ability is achieved by increasing the polynomial order (both in terms of diffusion and dispersion properties) as opposed to reducing the base mesh size. As shown in the earlier work of Cassinelli et al. [12] at $Re = 88{,}000$, the polynomial order adopted is sufficiently high for SVV not to affect the flow physics of interest. The spectral/*hp* dealiasing approach by [21] was adopted for all computations. The spectral/*hp* element implementation of the present work relies on Taylor–Hood type elements, where the C^0 continuous pressure field is computed at one polynomial order lower than the C^0 continuous velocity variables. Further details on the numerical methodology, mesh resolution and convergence properties were discussed by Cassinelli et al. [12,22].

2.2. LPT Setup with Wake Passing

The availability of experimental data motivated the choice of the flow regimes in analysis. Three Reynolds numbers were considered: $Re_2 = 86{,}000, 157{,}000$, and $297{,}000$, based on mixed-out exit velocity U_2 and suction surface perimeter S_0. The research LPT cascade in analysis is scaled by the true chord and inflow velocity, so that $C = 1$ and $U_\infty = 1$.

The wake-passing effect is experimentally reproduced by including a mechanism to introduce upstream-generated wakes shed from uniformly spaced cylindrical bars, controlled by an electric motor. To analyse this phenomenon, two nondimensional parameters are of fundamental importance: the reduced frequency F_{red} and flow coefficient Φ, defined as:

$$F_{\text{red}} = \frac{U_b C}{P_b U_2}, \qquad \Phi = \frac{U_{\infty,x}}{U_b}, \tag{3}$$

where U_b indicates the bar velocity, P_b is the vertical distance between bars and $U_{\infty,x}$ is the axial inlet velocity. These parameters control the bar speed (which affects the inclination of the wake when it impinges on the blade) and their relative distance. Together, they affect the frequency at which the wakes impact on the blade. Adjusting the cylinder distance and speed allows for analysis of realistic configurations where the rotor and stator count are different. However, the numerical experiments are typically carried out with pitchwise periodic boundary conditions.

Limitations owing to the computational cost that would be required to simulate multiple blades require the cascade pitch P_y to be a multiple of the distance between bars P_b. Therefore, from a computational perspective, the control parameter in the simulations is the velocity of the cylinders. In this study, the exact value of the reduced frequency was simulated, while the flow parameter was enforced as a consequence of single-pitch periodicity (i.e., imposing $P_b = P_y$). The numerical values imposed in the simulations are reported in Table 1. The relative error between the nominal flow coefficient and effective flow coefficient is 6.748%. The lower flow coefficient results in slightly higher wake inclination compared to the experiments.

Introducing the wake passing period $\mathcal{T}_b = P_b/U_b$, time can be expressed as function of the number of periods m and the phase $0 \leq \varphi \leq 1$: $t = m\mathcal{T}_b + \varphi\mathcal{T}_b$. After transient times of at least $12C/U_\infty$, time-averaged statistics were subsequently sampled over $m = 20$ bar passing periods (corresponding to $T = 24C/U_\infty$). At phase $\varphi = 0$, the bar is situated at the same pitchwise location as the leading edge, $y/C = 0$.

Table 1. LPT bar passing setup with cylinder parameters in the upper portion of the table. $Re_2 = 86{,}000$ was simulated both with inflow wakes (IW) and inflow turbulence (IT), while other regimes analyse IW alone. The compute time is estimated on 1000 cores on the Archer supercomputer, including runtime post-processing and thus providing a conservative estimate.

Re_2	86,000 (IW, IW+IT)	157,000 (IW)	297,000 (IW)
F_{red} (S_0-based)	0.624132	0.627675	0.633188
$U_b^{\text{sim}}/U_\infty$	0.705339	0.706414	0.708116
Φ^{sim}	1.17731	1.17414	1.16966
α_1 [°]	33.86	33.96	34.08
Δt	2.5×10^{-5}	2.5×10^{-5}	2×10^{-5}
Compute time for $T = 1C/U_\infty$	8 h 40 min	8 h 40 min	10 h 45 min

The x–y planes were discretised with a high-order expansion at $P = 6$; the spanwise domain was set to $L_z = P_y/4 = 0.21164\,C$ and discretised with $N_z = 72$ Fourier planes, resulting in 52.67 M DoF per variable. As shown in Figure 1, this numerical setup yields a wall resolution of $\Delta x^+ < 20$, $\Delta y^+ < 0.6$, $\Delta z^+ < 8$ at $Re_2 = 297{,}000$. The space- and time-convergence properties of a similar numerical setup on a range of statistical distributions and properties were previously assessed extensively in a clean inflow case at $Re = 88{,}000$ [12]. In particular, $x - y$ plane convergence was analysed by means of P-refinement, reporting negligible discrepancies for expansion orders $P > 5$. The independence of the results with respect to the span was also discussed, and further evaluated by analysis of the correlation function [22], which showed that the blade wake is fully contained within the chosen spanwise domain. It should be noted that the aforementioned analyses were carried out in a previous study in the context of a disturbance-free inflow environment, at a flow regime corresponding to the lower end of the Reynolds envelope considered in the present study. Furthermore, since the same mesh is employed for all Reynolds numbers, the effective resolution is lower at high Reynolds numbers.

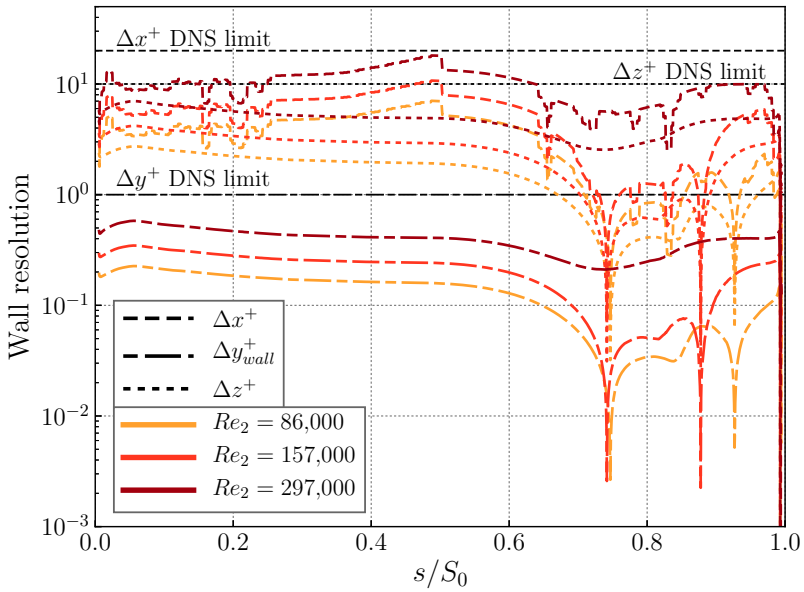

Figure 1. Wall resolution along the suction surface with increasing Re_2 and incoming wakes.

Enforcing the pitchwise domain to be a multiple of the spanwise domain allowed adopting a modified version of the inflow turbulence generation algorithm by Davidson [23], introduced and validated in *Nektar++* [13]. This implementation allows to generate

a spanwise- and pitchwise-periodic synthetic velocity signal, requiring a choice of spanwise domain such that P_y is a multiple of L_z.

Case $Re_2 = 86{,}000$ is analysed with and without inflow turbulence (on top of the discrete disturbances shed by passing bars). The inflow turbulence case (IW+IT) required a refined computational mesh to resolve the turbulent structures introduced at the inlet. This mesh differs from the IW mesh only in the region comprised between the inflow and the vertically refined line where the bar passing occurs. A nominal inflow turbulence intensity TI $= 3.5\%$ was prescribed in combination with a length scale $L_t = 0.05C$ to guarantee domain independence.

The algorithm selected 30 modes to discretise the modified von Kármán spectrum, compared to 1024 specified previously analysed [13]. As a consequence of a coarser discretisation of the wavenumber space, the level of turbulence intensity effectively introduced at the inlet of the computational domain is lower than prescribed: TI $= 2.578\%$.

2.3. Modelling the Bar Passing Effect

To model the bar passing effect, the Smoothed Profile Method (SPM), first introduced by Nakayama and Yamamoto [24], was selected. The method was further developed to adopt a time discretisation based on a high-order semi-implicit splitting scheme [25,26], and incorporated in the *Nektar++* framework. Extensive preliminary validation was carried out in the PhD thesis by Cassinelli [22] to ensure the generation of a realistic cylinder wake.

As part of the SPM formulation, an interface thickness parameter must be selected to represent the rigid particles. The interface thickness was selected to ensure accurate representation of the SPM boundaries (thus driven by resolution requirements). An auxiliary study focused on varying the diameter of the cylinders at fixed interface thickness. A smaller bar diameter of $d_b^{\mathrm{SPM}} = 0.6 d_b$ (with $d_b/C = 0.023$) produced wake profiles and spectral characteristics matching those of a corresponding DNS simulation over the entire range of Reynolds numbers analysed.

The qualitative result of the wake-passing effect at high Reynolds number is shown in Figure 2. The initial stage of wake bending is visible in the Figure, while the suction surface transition leads to fully turbulent boundary layer at the trailing edge.

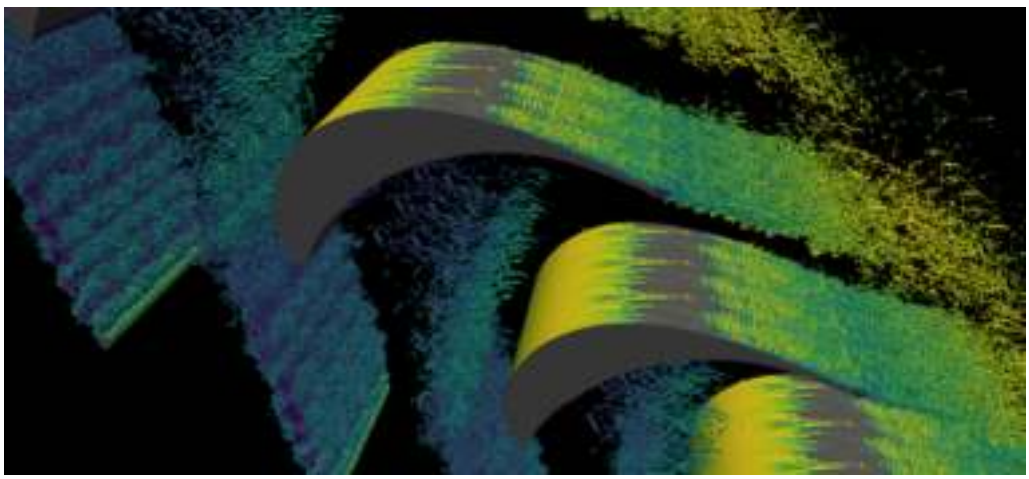

Figure 2. Iso-surfaces of Q-Criterion ($Q = 200$) contoured by velocity magnitude in case $Re_2 = 297{,}000$. The computational domain is duplicated for graphical purposes.

2.4. Low-Speed Experimental Testing of LPTs

The present generation of LPTs typically operates at subsonic conditions, characterised by exit Mach numbers of $Ma_2 \sim 0.6$. The cost of experimental programs can be significantly reduced by performing tests in low-speed wind tunnels, at essentially incompressible conditions. However, the pressure distribution is in general strongly dependent on the Mach number [27]: the peak suction Mach number ultimately controls the adverse pressure

gradient flow region, where most losses are generated. Therefore, experimental testing cannot be carried out on the same blade shape and cascade setup.

A number of scaling techniques as well as more advanced redesign strategies were developed to derive a modified profile shape and flow conditions [28,29], allowing to compensate for the effects of compressibility.

The linear cascade in analysis was redesigned to match the design high Mach number distribution when tested at incompressible conditions, modifying profile shape and increasing the inlet flow angle. This has important implications for the applicability of the capability presented in the paper. One of the main research purposes is the validation of a virtual wind tunnel capability, and the use of an incompressible flow solver is not a road blocker: leveraging scaling techniques, realistic LPT geometries with a peak suction Mach number up to 0.6–0.7 can be accurately simulated in their low-speed testing conditions. However any compressibility effects, even if overall small, are not accounted in the present work.

3. Results

3.1. Evidence of the Transition Mechanism

The time averaging operation masks the wealth of flow phenomena occurring in the boundary layer (BL) of LPTs subject to incoming disturbances, and it particularly fails to highlight the presence of high-amplitude events that precede the onset of turbulence. A discussion on some instantaneous flow statistics is presented before analysing time-averaged statistics, to highlight some of the flow phenomena occurring on the suction surface of the cascade.

Figure 3 provides qualitative insight into the suction surface dynamics at consecutive phases φ for $Re_2 = 86{,}000$. Similar considerations could be discussed for the higher flow regimes $Re_2 = 157{,}000$ and 297,000 but they are here omitted for brevity. The wakes impinge on the suction surface separation bubble between $\varphi = 0.25$ and $\varphi = 0.375$. The extended region of weakly negative recirculation (the pale yellow region) visible at $\varphi = 0$–0.125 between $s/S_0 = 0.7$–0.95 is largely suppressed by the incoming disturbance. Concurrently, at $\varphi = 0.25$ the shear layer rolls up into two separate regions of recirculating flow, as previously highlighted by Michelassi et al. [11]. The upstream recirculation region is found at $s/S_0 \approx 0.85$, while the downstream one merges into the trailing edge. As the wake impacts on the separation bubble, the region of high shear in the upstream portion of the suction surface (the dark blue region) moves towards the trailing edge, following the impinging disturbance. At $\varphi \approx 0.375$, the attached flow region develops a spanwise pattern of alternating high- and low-speed flow, called Klebanoff streaks, which play an important role in the bypass transition mechanism [30,31].

Streaks are found at all the flow regimes analysed, and their spanwise length scale is inversely proportional to the Reynolds number. The generation mechanism of elongated streaks in the suction surface in presence of inflow turbulence was recently discussed in detail by Zhao and Sandberg [32]. In the context of wake passing, the generation of streaks occurs periodically, and its effect on the transition mechanism in the aft portion of the suction surface is evident at $0.375 \leq \varphi \leq 0.75$.

The nature of the disturbances that penetrate the boundary layer shear is determined by the shear sheltering mechanism [33,34]: the boundary layer shear acts as a filter for the high-frequency vortical disturbances. The low-frequency perturbations that penetrate into the boundary layer promote strong shear associated with the streaks, which may develop into turbulent spots through localized secondary streak instability. These steps characterise the early stages of the bypass transition mechanism, described as a secondary instability of lifted shear layers when they reach the top of the boundary layer, and they are subject to high-frequency free-stream disturbances [30,35].

Liu et al. [36] discussed how the physical mechanisms governing streak instability can be revealed through Floquet analysis of secondary instability. As discussed by Zaki [31],

in the presence of Klebanoff streaks the two most unstable modes of the boundary layer are the inner mode (varicose instability) and the outer mode (sinuous instability).

In the early stages of the wake passing cycle, the penetration of streaks within the boundary layer has not reached the trailing edge (TE) region yet. However, the formation of instabilities is detected at $\varphi \approx 0.25$ and highlighted in Figure 4 left; this region is identified by the dashed black rectangle in the third panel of the C_f carpet plots shown on the left. The vorticity contour suggests the presence of part-span K-H instability, which rapidly lifts up from the wall and develops across the boundary layer edge.

The alternating parallel fluctuating velocity patterns are consistent with the findings of Zhao and Sandberg [32], where they are argued to be evidence of varicose streak instability. However, in this case the instability is most likely due to part-span K-H type instability which occurs naturally in the separation bubble. At the later phases of the wake passing cycle, the presence of developed turbulent spots is detected. However, the evidence here presented is not sufficient to uniquely identify the physical streak instability mechanism (i.e., sinuous or varicose) preceding the inception of the spots.

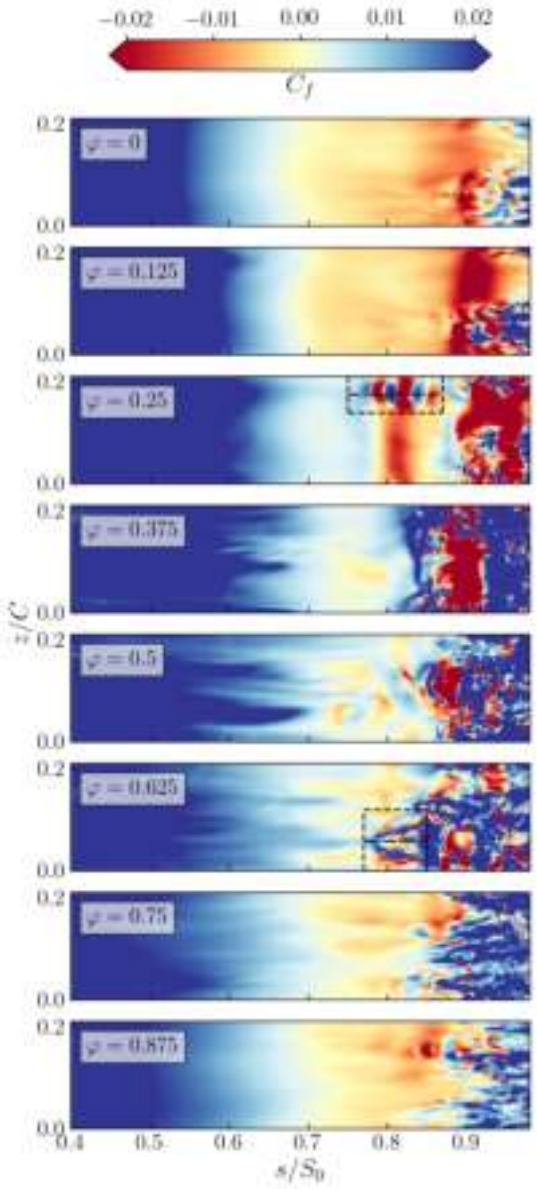

Figure 3. Instantaneous time–space skin friction on the suction surface at eight consecutive phases, $Re_2 = 86{,}000$. The dashed boxes identify the regions shown in detail in Figure 4.

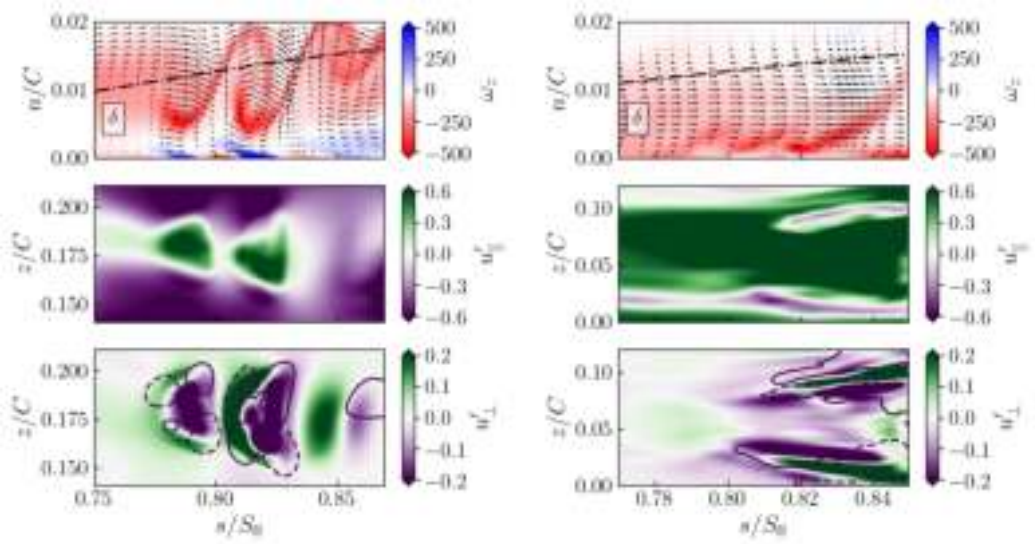

Figure 4. Instantaneous suction surface statistics for $Re_2 = 86{,}000$ in the regions identified by the black dashed boxes of Figure 3. The top subfigure shows spanwise vorticity in the blade-normal plane denoted with dash-dotted lines of Figure 3, superimposed with fluctuating velocity vectors. The middle and bottom figures show respectively wall-parallel and wall-normal fluctuating velocity $n/C = 0.01$ away from the wall. The solid and dashed lines in the bottom subfigures are iso-lines of $w' = \pm 0.15$. (**Left**): $\varphi = 0.25$; (**right**): $\varphi = 0.625$.

3.2. Space-Time Boundary Layer Behaviour

The time evolution of the spanwise-averaged effect of the wakes on the suction surface boundary layer is revealed in the space-time plots of the shape factor of Figure 5. The BL evolution is captured over 4 wake passing periods $\mathcal{T}_b$ with a resolution of 80 flow snapshots per period. Instantaneous statistics are here preferred over phase-averaged realisations to capture the highly unsteady nature of the wake interactions.

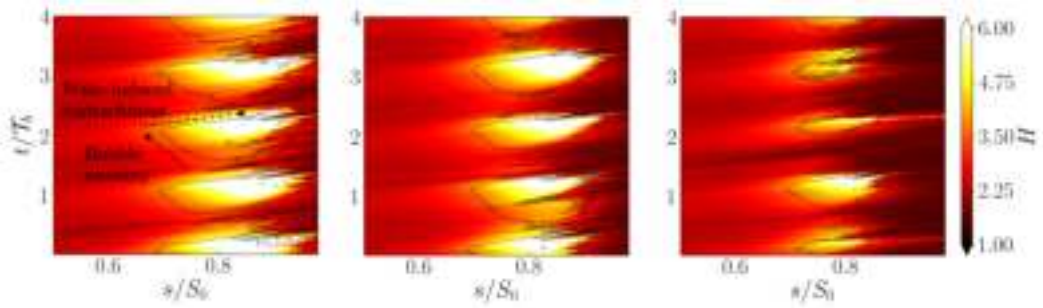

Figure 5. Instantaneous space–time contour of suction surface BL shape factor, superimposed with iso-lines of wall-shear stress at two levels: $C_f = 0$ (continuous line), $C_f = -0.024$ (dashed line). (**Left**): $Re_2 = 86{,}000$; (**middle**): $Re_2 = 157{,}000$; (**right**): $Re_2 = 297{,}000$.

The presence of the separation bubble is highlighted by the solid iso-lines of $C_f = 0$, which identify the spanwise-averaged extent of separation. When the wake interacts with the separation bubble, wake-induced transition promotes reattachment of the flow over the whole extent of the suction surface, as indicated by the dashed arrow on Figure 5. Following the wake-driven reattachment and the subsequent calmed region, the separation bubble recovers as the separation line moves upstream. The separation bubble captured in Figure 5 at $Re_2 = 297{,}000$ is significantly smaller compared to $Re_2 = 86{,}000$; however, it is also subject to larger relative variability in terms of both streamwise and temporal extent: the second instance of separation visualised in Figure 5 is roughly twice as persistent compared to the following instance.

This suggests that the dynamics of the boundary layer between $s/S_0 \approx 0.7 - 0.9$ is largely affected by the presence of streak instabilities trailing the passing of the wake in every cycle.

3.3. Blade Wall Distributions

The time-averaged and spanwise-averaged pressure distribution and skin-friction coefficient are shown in Figure 6. Additional data obtained introducing a momentum forcing near the leading edge (labelled "BF") as described by Cassinelli et al. [13] is included to highlight the impact of the periodic disturbances on time-mean flow performance indicators. Due to the presence of passing bars, the effective inflow angle is decreased compared to the cases without wake passing, from $\alpha_1 = 33.86°$ to $\alpha_1^{\text{eff}} = 31.73°$ in $Re_2 = 86{,}000$, $\alpha_1 = 33.96°$ to $\alpha_1^{\text{eff}} = 32.17°$ in $Re_2 = 157{,}000$ and $\alpha_1 = 34.08°$ to $\alpha_1^{\text{eff}} = 32.18°$ in $Re_2 = 297{,}000$.

The difference translates into discrepancies in the front portion of the suction surface between the cases with and without passing wakes, evident in the suction surface skin friction peak at $s/S_0 \approx 0.05$, where the IW profiles are slightly lower than the cases without incoming wakes. In this same region of the suction surface, lower Reynolds number corresponds to higher wall-shear stress.

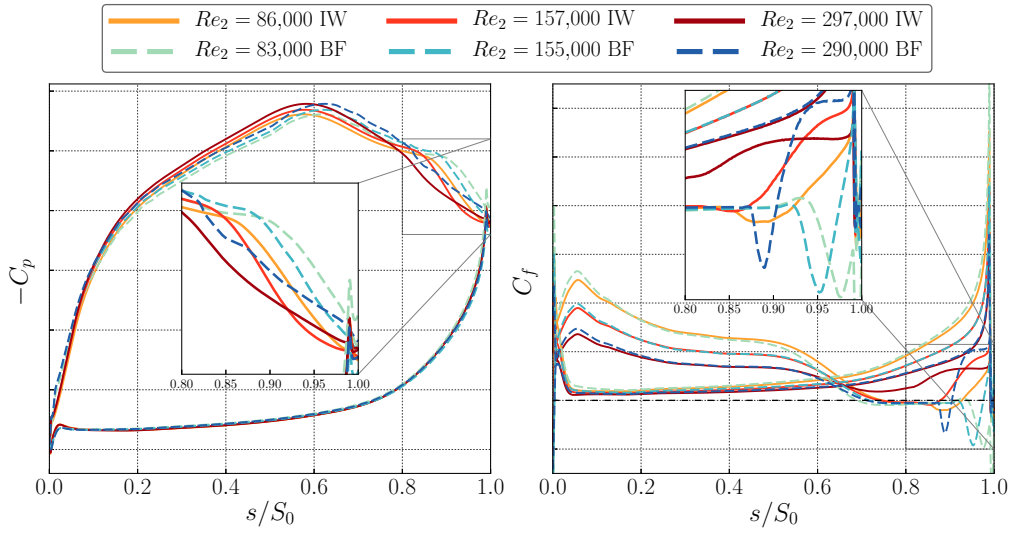

Figure 6. Blade wall distributions with increasing Re_2, compared with momentum forcing cases at the same flow regime. (**Left**): pressure distribution; (**right**): skin-friction coefficient. Y-axis tick labels are omitted due to data sensitivity.

The major differences due to the introduction of periodic disturbances are in the adverse pressure gradient part of the suction surface. Especially at low Reynolds numbers, in the C_p distribution the BF cases present a short plateau region at $s/S_0 \approx 0.85$, indicative of a weak separation bubble. This region is delayed and shortened with the introduction of wake passing. The skin-friction coefficient distribution further clarifies the differences. Due to the periodically modified transition mechanism on the suction surface, the wake passing causes an upstream shift of the time-averaged separation bubble at $Re_2 = 86{,}000$ and $Re_2 = 157{,}000$.

In both cases, flow separation occurs at $s/S_0 \approx 0.74$, and the extent of separation is almost halved compared to the cases with body forcing. The negative C_f peak denoting the presence of roll-ups and anticipating reattachment is moved upstream, flattened and only visible at low Reynolds number. This is a consequence of the wake motion along the suction surface and it does not correspond to stationary flow features.

In both cases, $Re_2 = 86{,}000$ and $Re_2 = 157{,}000$, the flow is attached at the trailing edge but not fully developed. Further increasing the Reynolds number ($Re_2 = 297{,}000$)

removes separation in a time-averaged sense and yields a fully turbulent boundary layer at the trailing edge, as highlighted by the flat C_f profile for $s/S_0 > 0.9$.

3.4. Wake Traverses and Experimental Comparison

Extensive experimental data available from LDA measurements are presented in this section. The experimental setup was described in detail by Bolinches-Gisbert et al. [37]. The wake traverses are extracted at $\hat{x} = x - x_{\mathrm{TE}} = 0.513$, and compared with the experiments in Figure 7.

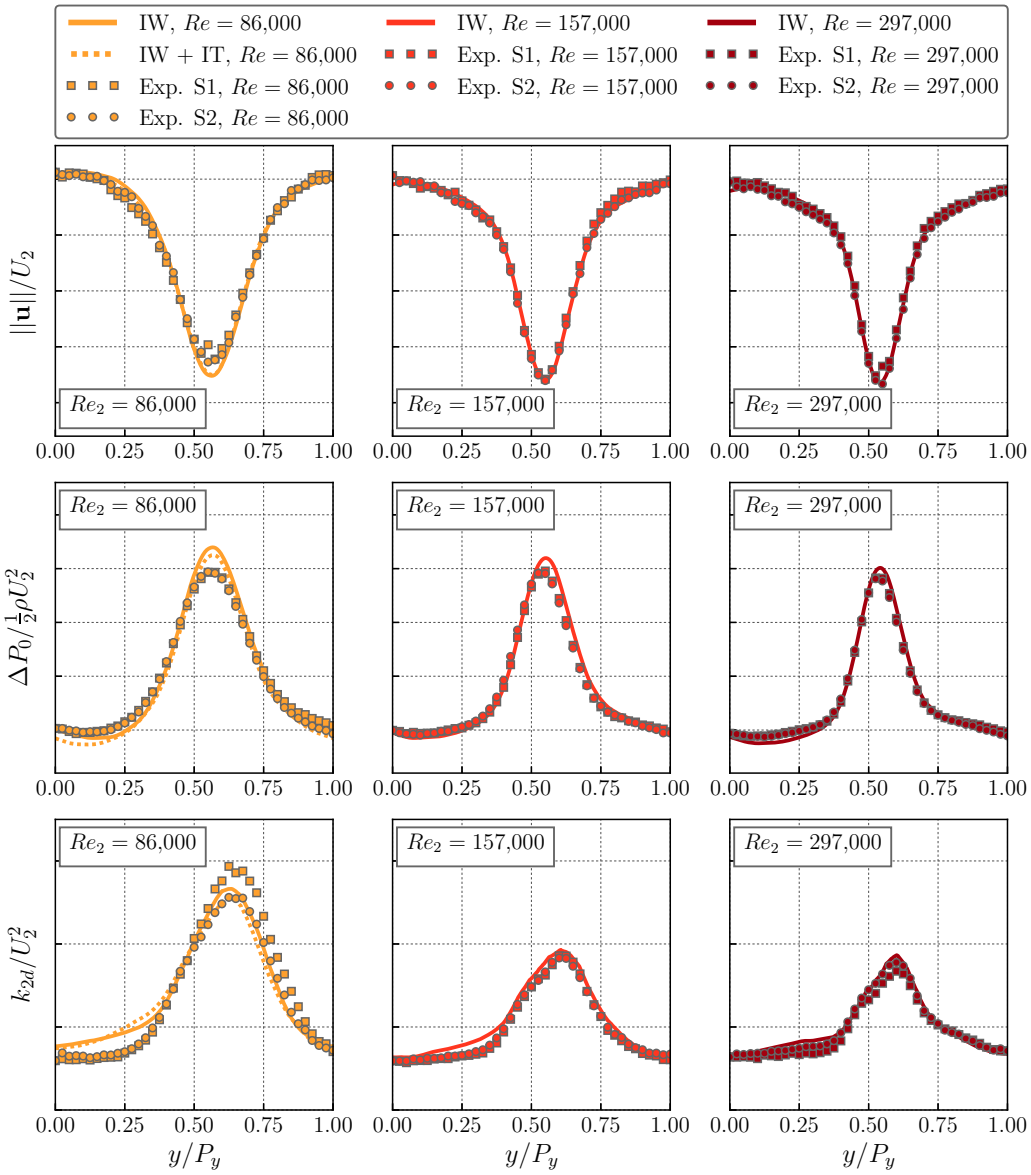

Figure 7. Wake traverses at $\hat{x} = 0.513$ with increasing Reynolds numbers. (**Left**): $Re_2 = 86{,}000$ (in yellow); (**middle**): $Re_2 = 157{,}000$ (in red); (**right**): $Re_2 = 297{,}000$ (in burgundy). Three different wake profiles are shown. (**Top**): velocity magnitude; (**middle**): total pressure loss coefficient; (**bottom**): turbulence kinetic energy. The solid lines indicate IW simulations, and the dashed line indicates IW+IT, for $Re_2 = 86{,}000$ only. The two experimental traverses *S*1 and *S*2 are represented with squares and circles. *Y*-axis tick labels are omitted due to data sensitivity.

The velocity solution accurately captures all the relevant wake flow features, i.e., flank width and negative peak: the latter is within 1% of the experimental value. The presence of

background turbulence (only simulated at $Re = 86{,}000$) does not modify the wake profiles, which overlap to the curves obtained without incoming turbulence, with a marginal discrepancy observed in the mean passage on the pressure side: discrete disturbances are the dominant mechanism in modifying the dynamics of the suction surface separation bubble.

The loss profiles are also reported in the Figure, showcasing good agreement with the experiments especially at higher Reynolds numbers, where the peak is captured within 6% of the experiments. The entity of losses in the mean passage remains unvaried in the three flow regimes explored. The computed results capture a slight decrease of the loss profile peak by ∼6% and 10% in cases $Re_2 = 157{,}000$ and $Re_2 = 297{,}000$, compared to $Re_2 = 86{,}000$.

The experimental values, however, remain approximately constant across the three flow regimes. At higher Re_2, the wake width decreases, owing to the smaller momentum thickness at the trailing edge typical of high-Reynolds configurations, combined with a fully suppressed separation bubble due to bypass transition.

The turbulence length scale in the TE wake was measured from a spanwise line of probe points, yielding a smaller value in the high-Reynolds case, where the two-point correlation decays faster. This in turn promotes lower levels of fluctuations in the wake. At low Re the separation bubble is also periodically open, giving rise to large-scale vortex shedding which results in higher levels of fluctuating turbulence kinetic energy. The higher Reynolds cases $Re_2 = 157{,}000$ and $Re_2 = 297{,}000$ have very similar profiles.

3.5. Mixed-Out Measurements

The mixed-out loss coefficient is shown in Figure 8. The numerical results match the experimental data, with an uncertainty of 2.5% in the total pressure loss coefficient and 0.4 deg of exit angle. At low Reynolds numbers, where the separation periodically extends to the trailing edge, it is traditionally very challenging to accurately capture losses. Case IW + IT at $Re_2 = 86{,}000$ does not improve the agreement with experiments, which were conducted in absence of background fluctuations. The relative error with respect to the experimental measurements is reported in Table 2, which highlights that the two regimes $Re_2 = 86{,}000$ and $Re_2 = 297{,}000$ achieve the minimum error, and are within the range of experimental uncertainty.

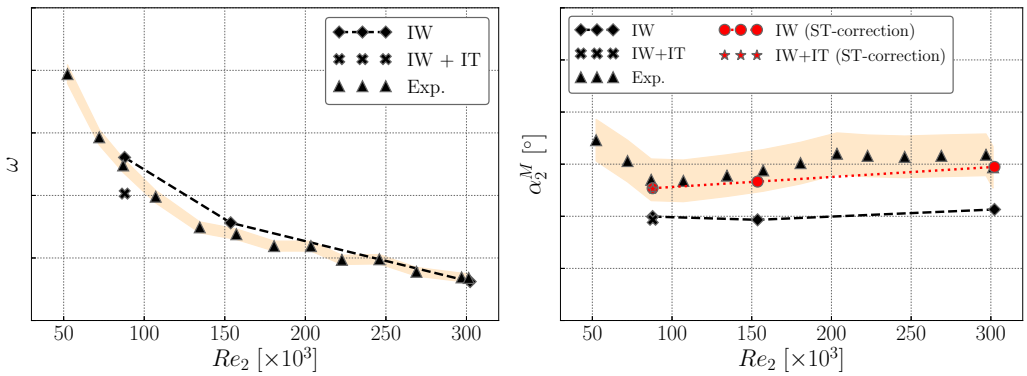

Figure 8. Mixed-out wake traverse measurements: (**left**): total pressure loss coefficient; (**right**): exit angle, with associated streamtube correction shown with red markers. The orange area indicates the uncertainty associated with the measurement chain, of respectively 2.5% and ±0.2°. *Y*-axis tick labels are omitted due to data sensitivity.

The mixed-out exit angle is shown in Figure 8. As highlighted quantitatively in Table 2, the flow turning is consistently overestimated across the flow regimes analysed, suggesting the presence of a bias. The streamwise component of the velocity wakes (not shown) is in deficit compared to the experimental data, especially in the mean passage. Among the various sources of uncertainty between numerical simulations and experiments, the contraction of the experimental streamtube is the most dominant effect. Physically, this

is due to the growth of a boundary layer on the experimental sidewalls, accelerating the flow in the axial direction in the midspan.

A first-order correction is introduced to validate this conjecture, showing that the streamtube effect is mostly responsible for the lack of agreement in the prediction of the exit angle. The ratio between the experimental and computational mass-flow rate k_s can be estimated as:

$$k_s = \frac{\int_0^{p_y} \overline{\mathbf{u}}_{\mathrm{Exp}} \cdot \hat{\mathbf{n}} \, \mathrm{d}y}{\int_0^{p_y} \overline{\mathbf{u}}_{\mathrm{IW}} \cdot \hat{\mathbf{n}} \, \mathrm{d}y} = \frac{\frac{1}{2}(\int_0^{p_y} \overline{u}^{\mathrm{S1}}_{\mathrm{Exp}} \, \mathrm{d}y + \int_0^{p_y} \overline{u}^{\mathrm{S2}}_{\mathrm{Exp}} \, \mathrm{d}y)}{\int_0^{p_y} \overline{u}_{\mathrm{IW}} \, \mathrm{d}y}, \tag{4}$$

considering the average of the mass flow rate calculated in the experimental passages S1 and S2. The streamwise velocity extracted from the numerical simulations is corrected:

$$\overline{u}^{\mathrm{mod}}_{IW} = k_s \overline{u}_{IW}, \tag{5}$$

and the exit angle is recalculated. The associated spanwise domain contraction can be estimated by imposing mass conservation:

$$L'_z = L_z / k_s. \tag{6}$$

The exit angle corrected with the experimental streamtube is consistently shifted to a region within the error bounds of the experimental measurements, therefore suggesting that the streamtube contraction is the physical mechanism responsible for the discrepancy of numerical and experimental measurements. Quantitatively, the mixed-out exit angle error is reduced by ≈80%. The streamtube contraction estimated to yield the correct mass flow rate is between 1–2% and it is larger at higher Reynolds number.

Table 2. Summary of percentage relative error between experimental and computational mixed-out quantity, as well as summary of the streamtube contraction factors.

Parameter	$Re_2 = 86{,}000$	$Re_2 = 157{,}000$	$Re_2 = 297{,}000$
$\frac{\lvert\lvert\omega^M_{\mathrm{IW}} - \omega^M_{\mathrm{Exp}}\rvert\rvert}{\omega^M_{\mathrm{Exp}}}$ [%]	2.919	5.388	2.516
$\frac{\lvert\lvert\alpha^M_{2,\mathrm{IW}} - \alpha^M_{2,\mathrm{Exp}}\rvert\rvert}{\alpha^M_{2,\mathrm{Exp}}}$ [%]	0.563	0.757	0.841
$\frac{\lvert\lvert\alpha^{M,\mathrm{mod}}_{2,\mathrm{IW}} - \alpha^M_{2,\mathrm{Exp}}\rvert\rvert}{\alpha^M_{2,\mathrm{Exp}}}$ [%]	0.129	0.171	0.187
$\frac{L'_z - L_z}{L_z}$ [%]	−1.164	−1.564	−1.734

4. Conclusions

In this paper, we discussed the introduction of the wake-passing effect on an LPT cascade focusing, in particular, on the Reynolds sensitivity of the flow on the suction surface and introducing a comparison of wake measurements with experiments. The three Reynolds numbers analysed correspond to subcritical, critical and supercritical states of the suction surface boundary layer in a clean inflow setup.

The analysis of the LPT flow features first focused on instantaneous statistics. The aft portion of the suction surface features a range of different transition mechanisms, driven by the periodic impingement of the wake passing. At low Reynolds numbers, two roll-up regions were periodically identified where the wake suppresses the suction surface separation bubble; however, at higher Reynolds numbers, this mechanism was not retained. This highlights the high sensitivity of the suction surface separation to external disturbances in the subcritical flow regime.

The comparison of wake traverses from the numerical simulations demonstrates close agreement with experimental measurements with less than a 1% relative error in the profile peak. The total pressure loss coefficient was also predicted accurately, within 5% of the experimental measurements across the flow regimes in analysis. The low- and

high-Reynolds cases were within experimental measurement uncertainty. A first-order estimation suggested that introducing a model of the streamtube contraction of 1–2% of the spanwise domain would yield the same levels of flow turning as in the experiments.

There is a growing need for high-fidelity simulations to train deep neural networks to develop new insights into flow physics. The DNS capability presented in the paper can be used to develop new turbulence closures [38] and promote a better physical understanding of the mechanisms of loss generation in turbomachinery.

Author Contributions: Conceptualization, A.C., F.M., P.A., R.V.D., S.J.S.; data curation, A.C.; formal analysis, A.C.; funding acquisition, F.M., P.A., R.V.D., S.J.S.; investigation, A.C.; methodology, A.C., S.J.S.; project administration, F.M., S.J.S.; resources, A.C., F.M., P.A., R.V.D., S.J.S.; software, A.C., A.M.G., S.J.S.; supervision, F.M., P.A., R.V.D., S.J.S.; validation, A.C.; visualization, A.C.; writing—original draft, A.C.; writing—review and editing, A.C.; All authors have read and agreed to the published version of the manuscript.

Funding: This research received funding from Rolls-Royce plc. and the Aerospace Technology Institute (ATI)/Innovate UK programme "FANFARE".

Data Availability Statement: Due to the nature of funding and the proprietary set of data used, supporting data cannot be made openly available.

Acknowledgments: A.C. would like to acknowledge Vittorio Michelassi, Giacomo Castiglioni and Yuri Frey for the technical discussions. The Authors would also like to acknowledge HPC support from Imperial College Research Computing Service (DOI: 10.14469/hpc/2232) and Archer under the UK Turbulence Consortium (EP/R029326/1).

Conflicts of Interest: The authors declare no conflict of interest.

Abbreviations

The following abbreviations are used in this manuscript:

BF	Body Forcing
BL	Boundary Layer
CFD	Computational Fluid Dynamics
DNS	Direct Numerical Simulation
IW	Inflow Wakes
IT	Inflow Turbulence
LDA	Laser Doppler Anemometry
LES	Large-Eddy Simulation
LPT	Low Pressure Turbine
RANS	Reynolds-Averaged Navier–Stokes
SVV	Spectral Vanishing Viscosity
TI	Turbulence Intensity
URANS	Unsteady RANS

Nomenclature

α	Flow angle
ω	Total pressure loss coefficient
Φ	Flow coefficient
φ	Wake passing phase
$C, (C_{ax})$	Blade (axial) chord length
C_f	Skin friction coefficient
C_p	Static pressure coefficient
F_{red}	Reduced frequency
H	Boundary layer shape factor

k	Turbulence kinetic energy
L_t	Turbulence length scale
L_z	Spanwise domain size
n	Blade wall-normal distance
N_z	Number of Fourier planes
p	Pressure
P	Polynomial order
P_b	Bars pitch
P_y	Blade pitch
Re	Reynolds number
S_0	Suction surface perimeter
T, t	Time
$\mathcal{T}_b$	Wake passing period
U_b	Bar speed
U_2	Mixed-out exit velocity
U_∞	Reference inlet speed

References

1. Wu, X.; Jacobs, R.G.; Hunt, J.C.R.; Durbin, P.A. Simulation of boundary layer transition induced by periodically passing wakes. *J. Fluid Mech.* **1999**, *398*, 109–153. [CrossRef]
2. Wu, X.; Durbin, P.A. Evidence of longitudinal vortices evolved from distorted wakes in a turbine passage. *J. Fluid Mech.* **2001**, *446*, 199–228. [CrossRef]
3. Michelassi, V.; Wissink, J.G.; Fröhlich, J.; Rodi, W. Large-Eddy Simulation of Flow Around Low-Pressure Turbine Blade with Incoming Wakes. *AIAA J.* **2003**, *41*, 2143–2156. [CrossRef]
4. Michelassi, V.; Wissink, J.G.; Rodi, W. Direct numerical simulation, large eddy simulation and unsteady Reynolds-averaged Navier–Stokes simulations of periodic unsteady flow in a low-pressure turbine cascade: A comparison. *Proc. Inst. Mech. Eng. Part A J. Power Energy* **2003**, *217*, 403–412. [CrossRef]
5. Wissink, J.G. DNS of separating, low Reynolds number flow in a turbine cascade with incoming wakes. *Int. J. Heat Fluid Flow* **2003**, *24*, 626–635. [CrossRef]
6. Wissink, J.G.; Rodi, W. Direct numerical simulation of flow and heat transfer in a turbine cascade with incoming wakes. *J. Fluid Mech.* **2006**, *569*, 209–247. [CrossRef]
7. Hodson, H.P.; Howell, R.J. Bladerow Interactions, Transition, and High-Lift Aerofoils in Low-Pressure Turbines. *Annu. Rev. Fluid Mech.* **2005**, *37*, 71–98. [CrossRef]
8. Michelassi, V.; Chen, L.; Pichler, R.; Sandberg, R.D. Compressible Direct Numerical Simulation of Low-Pressure Turbines—Part II: Effect of Inflow Disturbances. *J. Turbomach.* **2015**, *137*, 071005. [CrossRef]
9. Sandberg, R.D.; Michelassi, V.; Pichler, R.; Chen, L.; Johnstone, R. Compressible Direct Numerical Simulation of Low-Pressure Turbines—Part I: Methodology. *J. Turbomach.* **2015**, *137*, 051011. [CrossRef]
10. Denton, J.D. The 1993 IGTI Scholar Lecture: Loss Mechanisms in Turbomachines. *J. Turbomach.* **1993**, *115*, 621–656. [CrossRef]
11. Michelassi, V.; Chen, L.; Pichler, R.; Sandberg, R.; Bhaskaran, R. High-Fidelity Simulations of Low-Pressure Turbines: Effect of Flow Coefficient and Reduced Frequency on Losses. *J. Turbomach.* **2016**, *138*, 111006. [CrossRef]
12. Cassinelli, A.; Montomoli, F.; Adami, P.; Sherwin, S.J. High Fidelity Spectral/hp Element Methods for Turbomachinery. In Proceedings of the ASME Turbo Expo 2018: Turbomachinery Technical Conference and Exposition, Oslo, Norway, 11–15 June 2018; Volume 2C: Turbomachinery; p. GT2018-75733.
13. Cassinelli, A.; Xu, H.; Montomoli, F.; Adami, P.; Vazquez Diaz, R.; Sherwin, S.J. On the Effect of Inflow Disturbances on the Flow Past a Linear LPT Vane Using Spectral/hp Element Methods. In Proceedings of the ASME Turbo Expo 2019: Turbomachinery Technical Conference and Exposition, Phoenix, AZ, USA, 17–21 June 2019; Volume 2C: Turbomachinery; p. GT2019-91622. [CrossRef]
14. Cassinelli, A.; Mateo Gabin, A.; Montomoli, F.; Adami, P.; Vazquez Diaz, R.; Sherwin, S.J. Reynolds Sensitivity of the Wake Passing Effect on a LPT Cascade Using Spectral/hp Element Methods. In Proceedings of the European Turbomachinery Conference ETC14 2021, Gdansk, Poland, 12–16 April 2021; Paper No. 606.
15. Moxey, D.; Cantwell, C.D.; Bao, Y.; Cassinelli, A.; Castiglioni, G.; Chun, S.; Juda, E.; Kazemi, E.; Lackhove, K.; Marcon, J.; et al. Nektar++: Enhancing the capability and application of high-fidelity spectral/hp element methods. *Comput. Phys. Commun.* **2019**, *249*, 107110. [CrossRef]
16. Karniadakis, G.E.; Israeli, M.; Orszag, S.A. High-order splitting methods for the incompressible Navier–Stokes equations. *J. Comput. Phys.* **1991**, *97*, 414–443. [CrossRef]
17. Guermond, J.L.; Shen, J. Velocity-Correction Projection Methods for Incompressible Flows. *SIAM J. Numer. Anal.* **2003**, *41*, 112–134. [CrossRef]
18. Tadmor, E. Convergence of Spectral Methods for Nonlinear Conservation Laws. *SIAM J. Numer. Anal.* **1989**, *26*, 30–44. [CrossRef]

19. Moura, R.C.; Sherwin, S.J.; Peiró, J. Eigensolution analysis of spectral/hp continuous Galerkin approximations to advection-diffusion problems: Insights into spectral vanishing viscosity. *J. Comput. Phys.* **2016**, *307*, 401–422. [CrossRef]
20. Moura, R.C.; Aman, M.; Peiró, J.; Sherwin, S.J. Spatial eigenanalysis of spectral/hp continuous Galerkin schemes and their stabilisation via DG-mimicking spectral vanishing viscosity for high Reynolds number flows. *J. Comput. Phys.* **2020**, *406*, 109112. [CrossRef]
21. Mengaldo, G.; De Grazia, D.; Moxey, D.; Vincent, P.E.; Sherwin, S.J. Dealiasing techniques for high-order spectral element methods on regular and irregular grids. *J. Comput. Phys.* **2015**, *299*, 56–81. [CrossRef]
22. Cassinelli, A. A Spectral/Hp Element DNS Study of Flow Past Low-Pressure Turbine Cascades and the Effects of Inflow Conditions. Ph.D. Thesis, Imperial College London, London, UK, 2020.
23. Davidson, L. Using isotropic synthetic fluctuations as inlet boundary conditions for unsteady simulations. *Adv. Appl. Fluid Mech.* **2007**, *1*, 1–35.
24. Nakayama, Y.; Yamamoto, R. Simulation method to resolve hydrodynamic interactions in colloidal dispersions. *Phys. Rev. E* **2005**, *71*, 036707. [CrossRef]
25. Luo, X.; Maxey, M.R.; Karniadakis, G.E. Smoothed profile method for particulate flows: Error analysis and simulations. *J. Comput. Phys.* **2009**, *228*, 1750–1769. [CrossRef]
26. Wang, Z.; Triantafyllou, M.S.; Constantinides, Y.; Karniadakis, G.E. A spectral-element/Fourier smoothed profile method for large-eddy simulations of complex VIV problems. *Comput. Fluids* **2018**, *172*, 84–96. [CrossRef]
27. Vázquez Diaz, R.; Torre, D. The Effect of Mach Number on the Loss Generation of LP Turbines. In Proceedings of the ASME Turbo Expo 2012: Turbine Technical Conference and Exposition. Volume 8: Turbomachinery, Parts A, B, and C, Copenhagen, Denmark, 11–15 June 2012; pp. 1131–1142. [CrossRef]
28. Vera, M.; Hodson, H.P. Low Speed vs High Speed Testing of LP Turbine Blade-Wake Interaction. In Proceedings of the Symposium on Measuring Techniques in Transonic and Supersonic Flow in Cascades and Turbomachines, Cambridge, UK, 23–24 September 2002; pp. 1–10.
29. Marconcini, M.; Rubechini, F.; Pacciani, R.; Arnone, A.; Bertini, F. Redesign of High-Lift Low Pressure Turbine Airfoils for Low Speed Testing. *J. Turbomach.* **2012**, *134*, 051017. [CrossRef]
30. Jacobs, R.G.; Durbin, P.A. Simulations of bypass transition. *J. Fluid Mech.* **2001**, *428*, 185–212. [CrossRef]
31. Zaki, T.A. From streaks to spots and on to turbulence: Exploring the dynamics of boundary layer transition. *Flow Turbul. Combust.* **2013**, *91*, 451–473. [CrossRef]
32. Zhao, Y.; Sandberg, R.D. Bypass transition in boundary layers subject to strong pressure gradient and curvature effects. *J. Fluid Mech.* **2020**, *888*, A4.
33. Hunt, J.C.; Durbin, P.A. Perturbed vortical layers and shear sheltering. *Fluid Dyn. Res.* **1999**, *24*, 375–404. [CrossRef]
34. Durbin, P.; Wu, X. Transition Beneath Vortical Disturbances. *Annu. Rev. Fluid Mech.* **2007**, *39*, 107–128. [CrossRef]
35. Zaki, T.A.; Durbin, P.A. Continuous mode transition and the effects of pressure gradient. *J. Fluid Mech.* **2006**, *563*, 357–388. [CrossRef]
36. Liu, Y.; Zaki, T.A.; Durbin, P.A. Floquet analysis of secondary instability of boundary layers distorted by Klebanoff streaks and Tollmien-Schlichting waves. *Phys. Fluids* **2008**, *20*, 124102.
37. Bolinches-Gisbert, M.; Robles, D.C.; Corral, R.; Gisbert, F. Prediction of Reynolds Number Effects on Low-Pressure Turbines Using a High-Order ILES Method. *J. Turbomach.* **2020**, *142*, 031002.
38. Frey Marioni, Y.; de Toledo Ortiz, E.A.; Cassinelli, A.; Montomoli, F.; Adami, P.; Vazquez, R. A Machine Learning Approach to Improve Turbulence Modelling from DNS Data Using Neural Networks. *Int. J. Turbomach. Propuls. Power* **2021**, *6*, 17.

International Journal of Turbomachinery Propulsion and Power

MDPI

Editorial

Acknowledgment to Reviewers of *IJTPP* in 2021

***IJTPP* Editorial Office**

MDPI AG, St. Alban-Anlage 66, 4052 Basel, Switzerland

Rigorous peer-reviews are the basis of high-quality academic publishing. Thanks to the great efforts of our reviewers, *IJTPP* was able to maintain its standards for the high quality of its published papers. Thanks to the contribution of our reviewers, in 2021, the median time to first decision was 21 days and the median time to publication was 72 days. The editors would like to extend their gratitude and recognition to the following reviewers for their precious time and dedication, regardless of whether the papers they reviewed were finally published:

Aki Grönman
Andrea Cattanei
Andrea Ferrero
Antoine Archer
Antoine Dazin
Antoine Placzek
Antonio Andreini
Antti Uusitalo
Aravinth Sadagopan
Bogdan C. Cernat
Caetano Peng
Christoph Hassa
Claus Sieverding
Daniele Pampaloni
Daniele Simoni
Davide Lengani
Dingxi Wang
Emmanuel Benichou
Emmanuel Laroche
Erik Dick
Erik Janke
Fabio Cozzi
Fadi Abdel Nour
Fangyuan Lou
Feng Gao
Filippo Merli
Florent Duchaine
Francesco Montomoli
Frank Eulitz
Friedrich-Karl Benra
Gerard Bois
Gerhard Kahl
Gherardo Zambonini
Giovanna Barigozzi
Giovanna Cavazzini
Gwi Bo Byun
Ján Kizek
Jean Decaix
Jérôme Boudet
Joachim Belz
Johan Dahlqvist
Kevin Britchford
Klaus Semmler
Koen Hillewaert
Laurent Gicquel
Lorenzo Pinelli
Loris Simonassi
Mahmoud A. Khader
Manuel Henner
Marcus Meyer
María Vera-Morales
Markus Jöcker
Markus Schatz
Martin Böhle
Martin Buisson
Martina Ricci
Mathias Steger
Matthias Schuff
Mauricio Gutierrez
Mauro Carnevale
Mehrdad Zangeneh
Michael Henke
Michele Ferlauto
Michele Greco
Michele Marconcini
Miguel Asuaje
Mike Barton
Mugurel Stanciu

Citation: *IJTPP* Editorial Office. Acknowledgment to Reviewers of *IJTPP* in 2021. *Int. J. Turbomach. Propuls. Power* **2022**, *7*, 4. https://doi.org/10.3390/ijtpp7010004

Published: 31 January 2022

Publisher's Note: MDPI stays neutral with regard to jurisdictional claims in published maps and institutional affiliations.

Copyright: © 2022 by the author. Licensee MDPI, Basel, Switzerland. This article is an open access article distributed under the terms and conditions of the Creative Commons Attribution (CC BY-NC-ND) license (https://creativecommons.org/licenses/by-nc-nd/4.0/).

Narmin Hushmandi
Nick Baines
Nicola Casari
Nicolas Binder
Nithish Anand
Oliver Pountney
Oluwadamilare Rahman Imam-Lawal
Oyvind Hundseid
Pacciani Roberto
Patrick Buchwald
Patrick Sterzinger
Paul Beard
Paweł Obstawski
Pengbo Ren
Pieter Groth
Pietro Zunino
Piotr Lampart
Reinhard Niehuis
Richard Tunstall
Robert Elliott
Robin Elder
Rocco Moeretti
Rodolfo Bontempo
Romuald Rzadkowski
Ruud Eggels
Sebastian Schuster
Sébastien Poncet
Sergio Lavagnoli
Shahrokh Shahpar
Shailendra Naik
Silvia Ravelli
Simon Pramstrahler
Simone Salvadori
Sina Stapelfeldt
Sławomir Kubacki
Soheil Jafari
Stefan Berten
Stefano Rebay
Stefano Valvano
Stéphane Aubert
Taddei Simone Rosa
Tadeusz Chmielniak
Teemu Turunen-Saaresti
Terrence Simon
Thomas Carolus
Vladimir Kindra
Xiaofeng Sun

International Journal of
Turbomachinery
Propulsion and Power

MDPI

Article

Aeroelastic Stability of Combined Plunge-Pitch Mode Shapes in a Linear Compressor Cascade †

George Hill [1,*], Julian Gambel [2], Sabine Schneider [3], Dieter Peitsch [2] and Sina Stapelfeldt [1]

[1] Rolls-Royce Vibration UTC, Imperial College London, London SW7 2AZ, UK; s.stapelfeldt@imperial.ac.uk
[2] Chair of Aero Engines, TU Berlin, 10587 Berlin, Germany; julian.gambel@tu-berlin.de (J.G.); dieter.peitsch@tu-berlin.de (D.P.)
[3] Rolls-Royce Deutschland Ltd. & Co. KG, Dahlewitz, 15827 Blankenfelde-Mahlow, Germany; Sabine.Schneider@Rolls-Royce.com
* Correspondence: g.hill18@imperial.ac.uk
† This paper is an extended version of our paper published in the Proceedings of the 14th European Turbomachinery Conference, Gdansk, Poland, 12–16 April 2021.

Abstract: Modern aeroengine designs strive for peak specific fuel and thermal efficiency. To achieve these goals, engines have more highly loaded compressor stages, thinner aerofoils, and blended titanium integrated disks (blisks) to reduce weight. These configurations promote the occurrence of aeroelastic phenomena such as flutter. Two important parameters known to influence flutter stability are the reduced frequency and the ratio of plunge and pitch components in a combined flap mode shape. These are used as design criteria in the engine development process. However, the limit of these criteria is not fully understood. The following research aims to bridge the gap between semi-analytical models and modern compressors by systematically investigating the flutter stability of a linear compressor cascade. This paper introduces the plunge-to-pitch incidence ratio, which is defined as a function of reduced frequency and pitch axis setback for a first flap (1F) mode shape. Using numerical simulations, in addition to experimental validation, aerodynamic damping is computed for many modes to build stability maps. The results confirm the importance of these two parameters in compressor aeroelastic stability as well as demonstrate the significance of the plunge-to-pitch incidence ratio for predicting the flutter limit.

Keywords: flutter; aeroelasticity; aerodynamic damping; linear cascade; 1F mode shape

check for updates

Citation: Hill, G.; Gambel, J.; Schneider, S.; Peitsch, D.; Stapelfeldt, S. Aeroelastic Stability of Combined Plunge-Pitch Mode Shapes in a Linear Compressor Cascade. *Int. J. Turbomach. Propuls. Power* **2022**, *7*, 7. https://doi.org/10.3390/ijtpp7010007

Received: 8 December 2021
Accepted: 8 February 2022
Published: 14 February 2022

Publisher's Note: MDPI stays neutral with regard to jurisdictional claims in published maps and institutional affiliations.

Copyright: © 2022 by the authors. Licensee MDPI, Basel, Switzerland. This article is an open access article distributed under the terms and conditions of the Creative Commons Attribution (CC BY-NC-ND) license (https://creativecommons.org/licenses/by-nc-nd/4.0/).

1. Introduction

Modern aeroengine compressor designs strive to reduce weight and maintain peak efficiency. The implementation of new features to achieve these goals pose issues for compressor aeroelastic stability. For example, weight can be reduced and efficiency increased by designing thinner aerofoils; however, these have greatly reduced stiffness. Similarly, titanium blade-integrated disks (blisks) reduce weight but also decrease structural damping gained by hub-blade contacts. This reduction in damping is accompanied by a trend of increased loading per stage, to either increase the overall pressure ratio or maintain the pressure ratio with a reduced number of stages. These design trends make the blades more susceptible to experiencing high vibration amplitudes due to flutter. Flutter is an aeroelastic instability in which energy is transferred from the flow into a mechanical structure, leading to exponentially growing vibration amplitudes. Close to the stall boundary at part speed operating conditions, it is often flutter (rather than stall or surge) that represents the limiting condition for safe engine operation. For this reason, the identification of the key flutter parameters—and a prediction of the stability limit—is essential during early engine design processes in order to avoid costly re-designs later on. Clearly, one of the key influences on compressor flutter stability is the frequency and mode shape of vibration. Generally, increasing the reduced frequency improves flutter stability for a fixed mode shape. A mode

shape consists of both a blade (e.g., flap, torsion, bending) and disk assembly (nodal diameter) mode. This paper will investigate the stability in the first flap (1F) blade mode. Since most of the aeroelastic work input occurs at spanwise sections near the tip of the blade, it will consider the stability of a quasi two-dimensional blade section. It assumes that a spanwise section of the 3D flap mode can be represented by a two-dimensional rigid body motion comprising a plunging and pitching component, as illustrated in Figure 1, where dashed lines represent the vibration displacement. This assumption is valid as long as the flexion of the blade itself is small compared to the rigid motion. The mode shape composition is controlled by the position of the pitch axis, with the plunge component increasing the further aft the pitch axis is located.

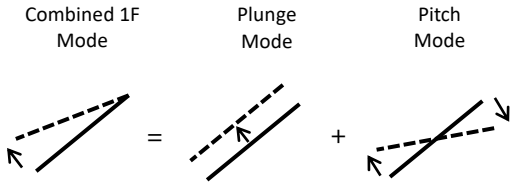

Figure 1. The 1F mode shape as the superposition of plunge and pitch components.

It is well-known that the proportion of the bending and torsion (or the ratio of plunge and pitch in 2D) components in the first flap mode is an important parameter for flutter. The importance of this parameter has been demonstrated in a number of studies, ranging from flat plates with zero mean deflection [1] to fans [2,3] and turbines [4]. All of these consider modes where the plunge and pitch motion are in phase. The aerodynamic damping, which is negative when flutter is produced, in the first flap mode can be conceptually split into four terms: (1) plunge-induced damping in the plunge mode, (2) the plunge-induced damping in the pitch mode, (3) the pitch-induced damping in the plunge mode, and (4) the pitch-induced damping in the pitch mode. While the pure plunge component (1) is often stable and the pure pitch component (4) is small in magnitude, the cross-coupling terms (2)(3) have been identified as the most important contributors to instability [2,3,5]. Under finite loading, blades can become unstable in a pure plunge mode [6], and therefore the pure plunge component cannot be considered unconditionally stable.

Steady loading, in addition to reduced frequency and mode shape composition, is an important factor in flutter stability. This applies to cascades, where it has been shown that the critical reduced frequency increases with increasing flow deflection for a fixed mode shape [6], as well as to rotors, where aerodynamic damping decreases with a reduction in mass flow rate. Although the trend with steady loading is clear, the interaction with the other parameters is not completely understood, and a detailed discussion is out of the scope of this paper. The reader is referred to the literature such as [6] for a systematic exploration of blade loading in a compressor cascade, and [3] for a discussion in the context of modern fan blades.

Neglecting the effects of steady loading, plots of aerodynamic damping against pitch axis location and reduced frequency are often employed to map stability [1,4,7]. When applied to 3D blades, this is usually measured at the tip section of the blade, for example, see [8]. The stability boundary then follows a curved line, as sketched in Figure 2. To combine both reduced frequency and mode shape composition into a single parameter, an incidence ratio $\phi = \theta_{plunge}/\theta_{pitch}$ can be defined, where θ_{plunge} and θ_{pitch} are the quasi-steady incidence induced by the plunge and pitch components, respectively. Exactly how ϕ relates to pitch axis location and reduced frequency will be shown in the next section. Experience on highly loaded transonic fan blades, as reported in [3,7,8], suggests that the stability limit lies at $\phi \approx 1$.

The validity of the incidence ratio ϕ as a flutter stability parameter has not been demonstrated in the public domain. This paper will confirm its importance using a joint

computational and experimental test campaign on a linear compressor cascade, specifically designed for this purpose. The computational fluid dynamics (CFD) is validated against measurements, and aerodynamic damping is computed for a wide range of pitch axis locations and reduced frequencies. The stability boundary is then determined in terms of the plunge-to-twist incidence ratio.

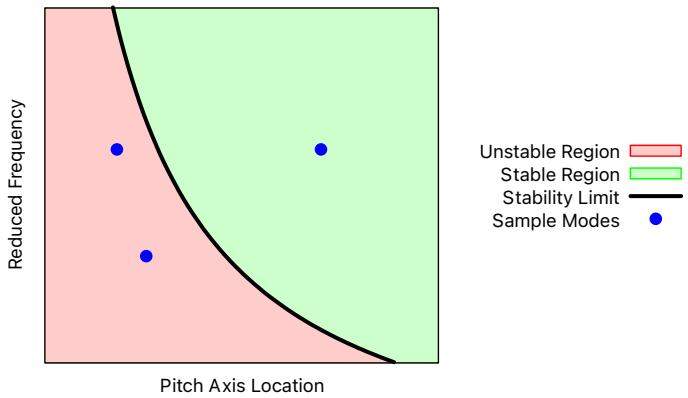

Figure 2. Sketch of stability map.

2. Test Case

As mentioned, this work focuses on a two-dimensional 1F blade mode shape, which can be considered a superposition of pure plunge and pure pitch components. Under the assumption that these components are in phase, and that the blades are rigid bodies, the mode shape is equivalent to a single degree of freedom (SDOF) rotation about a pitching axis located a chordwise distance x downstream of the leading edge. An implementation of this is shown in Figure 3.

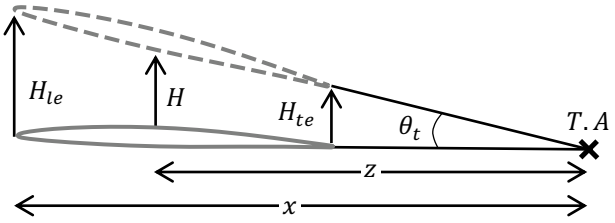

Figure 3. Implementation of 1F mode shape as SDOF rotation.

By changing the positions of the pitching axis location x and the mid-chord plunge amplitude H, the plunge-to-twist ratio of the mode can be varied. The limits are a pure twist mode when $x = 0.5c$ and a pure bending mode as $x \to \infty$. We will now define the the plunge-to-twist incidence ratio ϕ as the ratio of incidences generated by each of the components' vibration amplitude. The pitching axis location, x, relates to the plunge-to-twist incidence ratio as follows:

$$\phi = \frac{\theta_p}{\theta_t} = \frac{(\omega H/u)}{(H/z)} = \frac{\omega z}{u} = k\left(\frac{x}{c} - \frac{1}{2}\right) \tag{1}$$

where $k = \frac{\omega c}{u}$ is the reduced frequency and $z = x - c/2$ is the experimental lever length. From Equation (1), we can see that properties of the mode shape can be varied as a function of the normalised pitching axis location x/c and the reduced frequency k, whereas ϕ is the derived stability parameter which will form the basis of the stability map. Due to experimental constraints, the twist incidence amplitude, θ_t, is fixed at 1.5°.

Investigations into aeroelastic stability were conducted on a subsonic, linear compressor cascade. The blade profiles are the modified NACA 65-Series [9], with a maximum

thickness of 6% at half-chord over a 10° circular arc camber line. The stagger is fixed at 43°, with a span-to-chord ratio of 1.313. The cascade is formed by an 11-blade passage, with a pitch-to-chord ratio, s/c, of 0.75, which aims to represent a section cut of a typical compressor blade in the tip region. The flow incidence is fixed at 2°, and the operating point is far away from stall. The cascade has viscous hard walls on the hub, tip, and blade-to-blade boundaries, as shown in Figure 4. Inflow and outflow boundary conditions are highlighted in green, while all other viscous hard walls are shown in black.

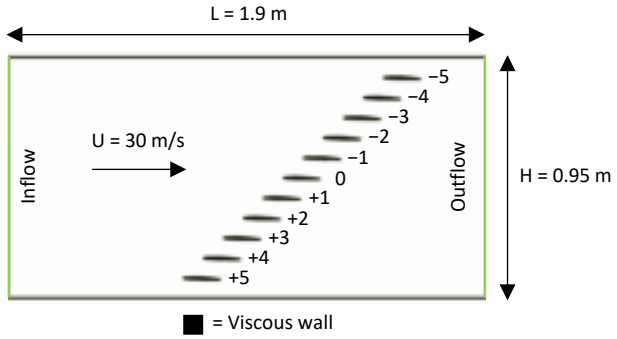

Figure 4. Schematic of cascade geometry with blade numbering convention.

The central Blade 0 will vibrate with a prescribed motion, and an aerodynamic influence coefficient method (AIC) will be used to calculate the aerodynamic damping ratio for many assembly modes. All other blades are fixed. The amplitude is large enough for unsteady pressures to be distinct from numerical noise but small enough for the unsteady flow to be represented as linear. Nominal operating conditions and parameter ranges are listed in Table 1. Both the reduced frequency and the normalised pitching axis location are varied with constant 5% increments between the limits shown. The reduced frequency range corresponds to a physical frequency range of 6.36–22.28 Hz.

Table 1. Cascade operating conditions.

Mach number (-)	0.087
Reynolds number (-)	300,000
Incidence angle (deg)	2
Reduced frequency range (-)	0.2–0.7
Normalised torsion axis location (-)	0.5–3

3. Test Rig

The experimental investigations were conducted at the Chair for Aero Engines, TU Berlin. The wind tunnel and cascade architecture are shown in Figure 5. The air flow is provided by a radial blower, which is then homogenised by passing through a diffuser and a settling chamber with multiple honeycomb grids and a nozzle before entering the measurement section. The air is discharged as a free jet at the end of the measurement section. Total pressure and temperature are measured at the settling chamber side wall, dynamic pressure is measured with a Pitot-static probe at the centre of the measurement section inlet face, and inlet static pressure is measured at the inlet face side wall. The mass flow rate and Reynolds number are calculated. Time-averaged and turbulent velocity distributions at the measurement section inlet as well as flow patterns can be found in [10].

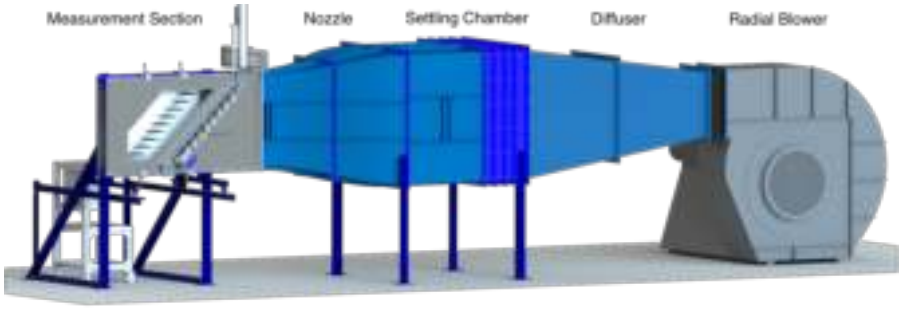

Figure 5. Experimental test rig architecture.

The central blade of the cascade is attached at its root to a lever on the outside of the wind tunnel. The lever is mounted to a traversing plate, which can be moved back and forth along linear bearings on the side wall to change the pitching axis location. Figure 6 shows a section cut of the traversing plate at its maximum x/c. Moving the blade position in the slot fixes the location in the cascade. Oscillatory motion is provided by an electric step motor, with an eccentric attached to its shaft through a scotch yoke mechanism and a connecting rod. Lever displacement is monitored with a laser triangulation distance sensor at the tip of the lever.

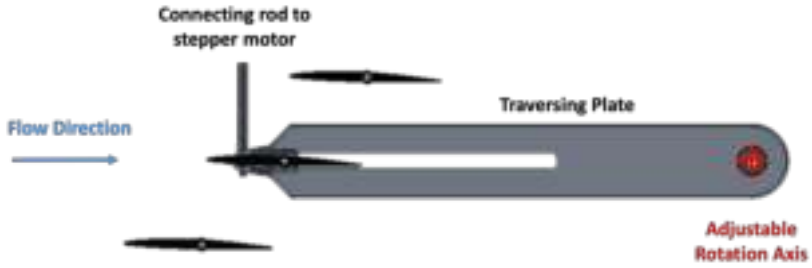

Figure 6. Section view of the vibrating blade module implementation of x/c.

Piezo-resistive differential pressure transducers were employed to measure the blade surface pressures. The pressure transducers exhibited linear behaviour around the zero point and can be considered as bidirectional. Calibration was conducted against externally calibrated precision pressure cells, which showed accurate pressure readings in the single-digit Pa range. The data acquisition system provided a theoretical resolution of 0.0267 Pa. The measurement blades have mid-span 20 pressure taps, with 10 each for the suction and pressure surface. The pressure taps have an exponential spacing along the chord, with greater density towards the leading edge. Transition strips are located between taps 4 and 5 (19% chord) on the suction surface of all blades to prevent flow separation.

4. Numerical Method

4.1. Flow Solver

The solver implemented throughout this work, AU3D, has been developed and validated at Imperial College over the last 25 years [11–13]. It is a 3D, time-accurate, viscous, finite-volume unsteady Reynolds averaged Navier–Stokes (URANS) solver and is second-order accurate in time and space. An edge-based data structure is used in the solver for computational efficiency. Turbulent closure is provided by a modified one-equation Spalart–Allmaras turbulence model [14]. The scheme implements a viscous wall function to model the flow near the wall. Steady state solutions are obtained using a RANS method, with a dual time-stepping procedure and residual smoothing to accelerate convergence. The mesh movement is satisfied by a spring analogy algorithm [11].

4.2. Computational Implementation

The computational mesh is semi-unstructured. In the spanwise direction, the domain is discretised by 23 radial layers. All viscous surfaces (including hub, tip, and spanwise boundaries) have a fully resolved boundary layer as shown in the upper wall mesh in Figure 7a. The boundary layer is resolved with a high density of hexahedral elements, with an average of $y+ = 45$ required by the viscous wall functions. A typical blade surface boundary layer is shown in Figure 7b. A total of 98% of the surface elements have $\{20 < y+ < 100\}$. The far field contains a coarser prismatic mesh and Riemann invariant boundary conditions at the inflow and outflow. This minimises the undesirable reflection of disturbances off the boundaries, which may impact flutter stability. The inlet boundary is placed approximately 4 chords upstream of the first blade. The overall mesh contains approximately 1.7×10^6 nodes. This mesh was selected based on agreement with the experimental data.

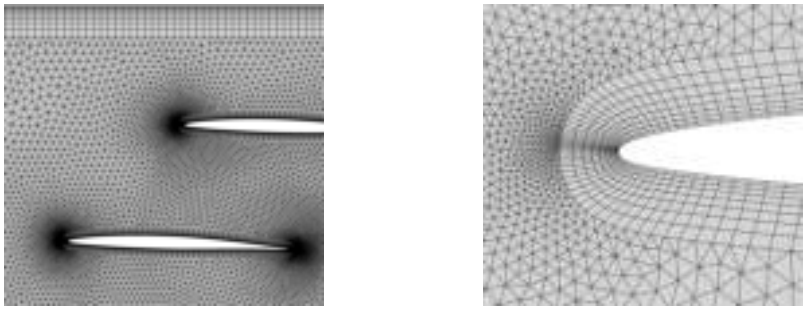

(**a**) Mesh of upper wall. (**b**) Blade leading edge mesh.

Figure 7. Linear cascade mesh.

The steady state flow solutions are obtained by imposing total pressure, total temperature, and flow angle at the far-field inflow boundary as well as static pressure at the outflow boundary. The mode shape is obtained analytically by the axis rotation of each surface node about the torsion axis location, as in the experiment. The mode is then mass normalised and the vibration amplitude is satisfied by the modal displacement. The blade vibrates with the prescribed motion and is discretised in time, with approximately 350 time steps per vibration cycle, based on a time convergence study. To match the experimental work, the modal force is calculated using only the mid-span unsteady pressures and assumes a radially uniform flow.

5. Aero-Damping Evaluation Method

The flutter stability of the cascade is assessed by an aerodynamic influence coefficient (AIC) method [15]. This treats the modal force on the blade surface as the linear sum of influences of the vibrating blade acting on itself and the influence of propagating disturbances from the adjacent blades' vibrations. Clearly, the propagation of disturbances that will influence a given blade will be affected by the geometry, operating conditions, and mode shape. The influence coefficients form a circulant matrix L defined as follows:

$$f_i(t) = \begin{bmatrix} L_0 & L_{N-1} & L_{N-2} & \cdots & L_1 \\ L_1 & L_0 & L_{N-1} & \cdots & L_2 \\ \vdots & \vdots & \vdots & & \vdots \\ L_{N-1} & L_{N-2} & L_{N-3} & \cdots & L_0 \end{bmatrix} \begin{Bmatrix} q_0(t) \\ \vdots \\ q_i(t) \\ \vdots \\ q_{N-1}(t) \end{Bmatrix} \tag{2}$$

where q is the modal displacement, f is the modal force, L is the complex influence coefficient, and N is the number of blades. The dominant terms of the L matrix are the diagonal L_0 terms, which represent the modal force influence on a blade due to its own

vibration, which always provides a stabilising contribution [16]. The equations of motion, defined in terms of the influence coefficients, is then transformed into the travelling wave mode domain. This allows the equations of motion to be decoupled, and each travelling wave mode can be processed separately. This is achieved by expanding the influence coefficients over the inter-blade phase angle domain by the discrete Fourier transform:

$$C_\sigma = \sum_{n=0}^{N-1} L_n e^{-in\sigma} \tag{3}$$

where σ is the inter-blade phase angle (IBPA), which, for the vibration in nodal diameter ND, is given by $\sigma = 2\pi ND/N$. Here, positive IBPAs correspond to forward travelling waves, and negative IBPAs to backward travelling waves. When the equation of motion is written in terms of travelling wave mode coefficients, the eigenvalues λ_σ can be computed to determine the stability of the aeroelastic system at each inter-blade phase angle (IBPA). The aerodynamic damping ratio is given by $\zeta = -\operatorname{Re}(\lambda_\sigma)/\operatorname{Im}(\lambda_\sigma)$, where a negative damping ratio indicates that the modal force is in phase with the modal velocity, causing work to be exerted on the blade, resulting in flutter. Unless otherwise indicated, aerodynamic damping is measured as the aerodynamic damping ratio in this paper.

6. Validation of CFD

6.1. Steady State Flow

Before the parameters that drive flutter are investigated, the steady RANS CFD results are compared against time-averaged experimental measurements. It should be noted that in both cases, there is no blade vibration. Figure 8 shows CFD results for the pressure coefficient at nominal operating conditions. The blade loading is non-uniform as a pressure gradient exists across the cascade, as seen by the negative pressure gradient from blade +5 to −5 in Figure 8. This is caused by the straight endwalls which prevent uniform flow deflection, resulting in a higher mean static pressure and a higher lift on Blade +5 than Blade −5. Separate CFD simulations (not included here) showed that this non-uniformity has a negligible effect on unsteady pressure distributions and the aerodynamic damping procedure.

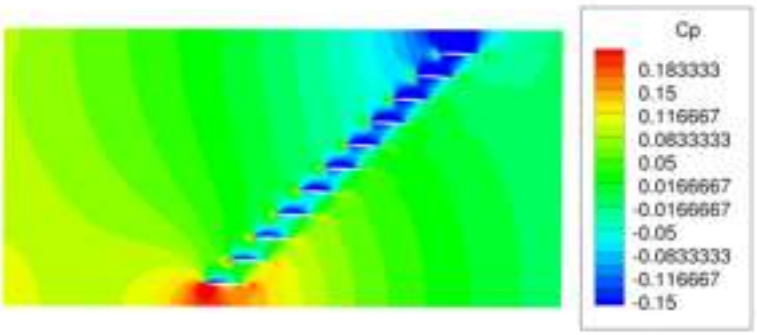

Figure 8. Computed normalised mid-span steady pressure contour.

Figure 9 shows the validation of the steady mid-span blade surface pressure coefficients as a function of normalised chord l/c. There is a generally good agreement over the three central blades, particularly towards the trailing edge. Towards the leading edge, there are some minor differences in blade loading. Possible explanations for this are the differences in incidence between the measurement and the CFD. The non-uniformity in loading can also be seen as blade +1 having a considerably larger pressure coefficient than blade −1.

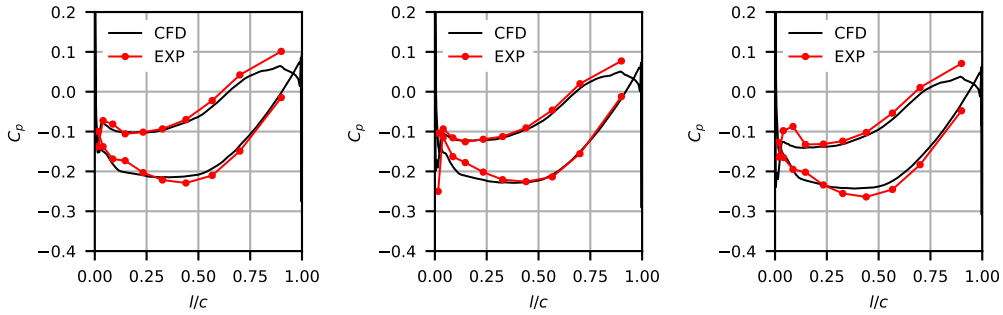

(**a**) blade +1 (**b**) blade 0 (**c**) blade -1

Figure 9. Validation of the steady mid-span surface pressure coefficient against normalised chord.

6.2. Unsteady Flow

To validate the unsteady CFD, the unsteady pressure on the blade surfaces are compared against experimental data. The pressure signals are Fourier-decomposed into the amplitude and phase at the blade vibration frequency. The results are shown in terms of the unsteady pressure coefficient in Figure 10 for $k = 0.4$ and $x/c = 1$ across the five central blades. The phase is shown with respect to the modal velocity. Due to the subsonic attached flow, the Fourier components in frequencies not equal to the vibration frequency are negligible. The amplitudes of unsteady C_p from CFD are well-predicted, with a total error of approximately 9% across all blades shown. The largest amplitudes occur at the leading edge of the vibrating blade 0. The unsteady disturbance from blade 0 propagates towards blade -1, causing a large unsteady pressure amplitude on the pressure side with a very small change to the suction side. On the other hand, for blade +1, there is a weaker propagating disturbance which impinges on the suction side, causing much large amplitudes compared to the pressure side of the blade. We can also see that this propagation mechanism is consistent with blades +2 and -2 as the shape of the unsteady pressure amplitudes and phases are comparable. There is very little phase change from the leading edge pressure side of blade 0 to the trailing edge of blade +1 on the suction side. A similar trend is seen on blade -1.

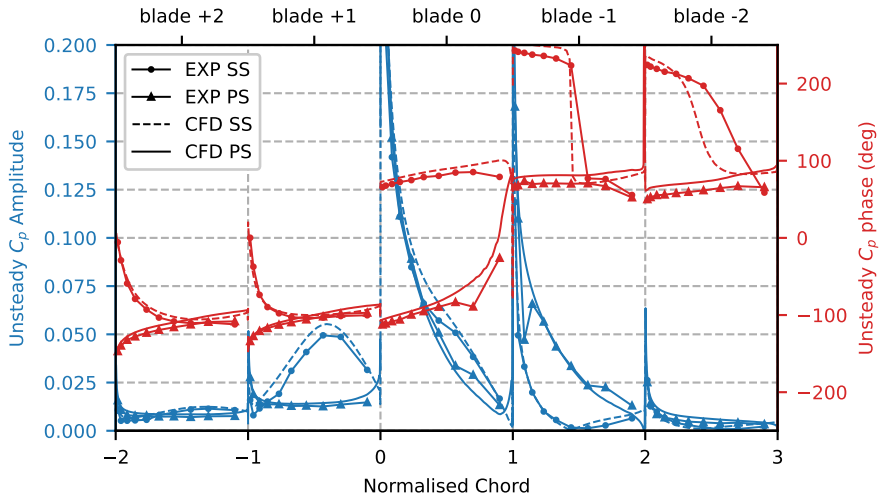

Figure 10. Validation of the unsteady mid-span blade surface pressure coefficient—$k = 0.4$, $x/c = 1$, $\phi = 0.2$.

This indicates a nearly instantaneous propagation of forcing from blade 0 to the adjacent blades, which implies that it is the passage area change which drives the propagation.

The integrated modal force and displacement for each blade are converted into the aerodynamic influence coefficients to begin the aerodamping analysis. Figure 11 shows the validation of the complex influence coefficients for blades +3 up to −3. Coefficients with a positive imaginary component will cause instability as they are in phase with the modal velocity, causing work to be exerted on the blade by the flow. It can be seen that blade 0 provides a large stabilising contribution. In all tested modes, blade 0 always has a stabilising contribution as the forcing is damped by its own vibration [16]. Interestingly, all minus blade AICs for this particular mode also produce a stabilising contribution as the forcing is lagging the vibration. We can see from Equation (3) that blades with a greater discrete distance from the vibrating blade 0 will have considerably smaller contributions to the travelling wave mode coefficients. We can also see from Figure 11 that the AICs of the blades furthest away (+3 and −3) themselves have a much smaller magnitude. For this reason, coefficients for blades (>±3) will be neglected when calculating the aerodamping. This also allows for consistency with the experimental analysis. The aerodynamic damping ratio can now be calculated by the eigenanalysis shown in Section 5. Figure 12 shows the validation of aerodamping against the inter-blade phase angle. There is good agreement in terms of the shape of the aerodamping curve at each IBPA; however, the minimum aerodamping is under-predicted by approximately 30%. Overall, these results show that CFD correctly predicts the operating condition and aerodamping and can therefore be used to continue with further stability analysis.

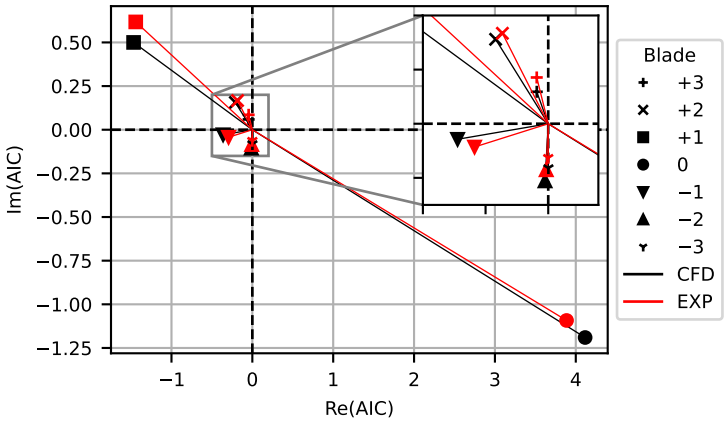

Figure 11. Complex AIC validation—$k = 0.4$, $x/c = 1$, $\phi = 0.2$.

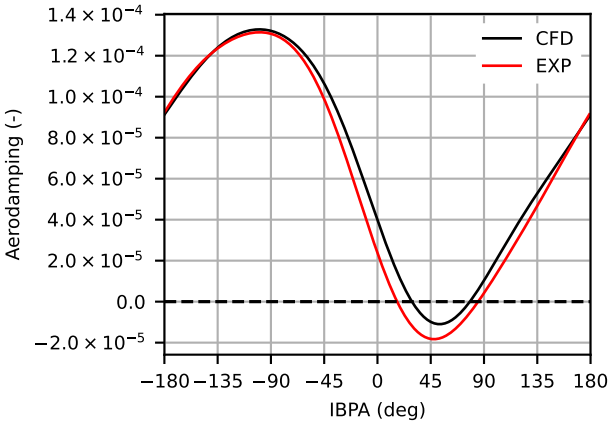

Figure 12. Aerodynamic damping ratio validation—$k = 0.4$, $x/c = 1$, $\phi = 0.2$.

7. Stability Analysis

Following the successful validation of the aerodamping for selected operating conditions, the numerical simulations are used to predict the aerodynamic damping over a wider range of reduced frequencies, k, and normalised pitching axis locations, x/c. The reduced frequencies are varied between 0.2 and 0.7, and the torsion axis is varied between 0.5 and 3, where the former corresponds to a pure twist mode and the latter contains a large plunge component.

7.1. Influence of Inter-Blade Phase Angle

Figure 13 shows the curves of aerodynamic damping against the inter-blade phase angle (IBPA) for two different reduced frequencies, $k = 0.2$ and $k = 0.6$. While negative nodal diameters are stable for the whole range of frequencies and pitching axes, low ND forward travelling wave modes reach negative damping and instability. This is typically expected for 1F flutter of this kind. The largest range of unstable IBPAs exists for low reduced frequencies and $x/c = 0.5$. This pure torsion mode shape is unstable between 10 and 160° IBPA at the lowest reduced frequency, $k = 0.2$. The plunge-dominated mode, $x/c = 3$, has a very narrow unstable IBPA range at the same frequency. Interestingly, the minimum aerodamping at $k = 0.2$ does not occur at $x/c = 0.5$ but is instead at $x/c = 1.25$. This indicates that the mode stabilises as x/c tends to 0.5 for a pure torsional mode shape at this frequency. With increasing frequency, the unstable region shrinks in IBPA range and in aerodamping magnitude, until only $x/c = 0.5$ and $x/c = 0.7$ are marginally unstable at $k = 0.6$.

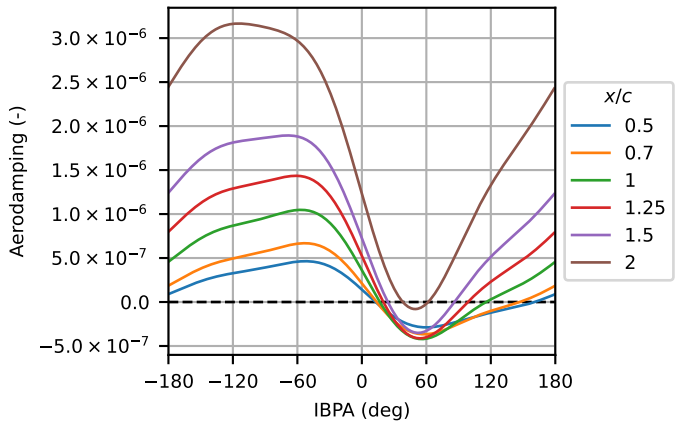

(**a**) $k = 0.2$

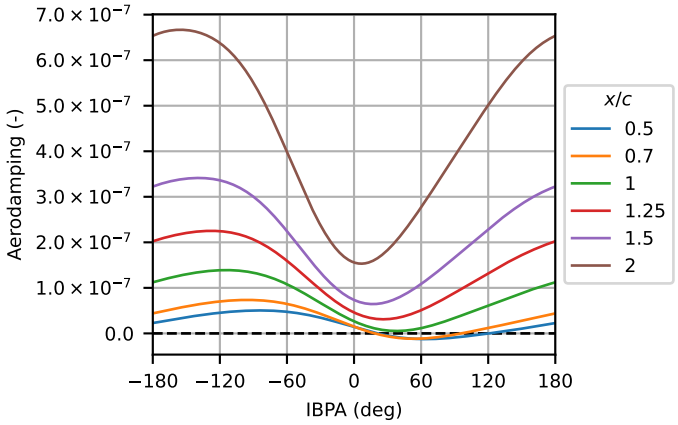

(**b**) $k = 0.6$

Figure 13. Aerodamping as a function of the inter-blade phase angle.

The aerodamping curves at $k = 0.2$ and $k = 0.6$ are significantly different. By looking at Equation (3), we can see that the travelling wave modes are harmonics of a Fourier series, where each coefficient is represented by pairs of blades a greater discrete distance from blade 0. Blade 0 corresponds to the zeroth Fourier coefficient, which will be constant and positive over all IBPAs. The inclusion of the two nearest neighbours in the calculation of the travelling wave mode adds another harmonic and so on. Figure 14 shows how such harmonics are summated to form the aerodamping. We can see from $k = 0.2$ in Figure 13a that the higher order harmonics contribute significantly to the aerodamping compared to $k = 0.6$ in Figure 13b, which has a near cosine shape at $x/c = 2$. We can therefore conclude that at low reduced frequencies, unsteady disturbances propagate more effectively to the blades that are further away as compared to higher frequencies, which in turn decrease aerodamping.

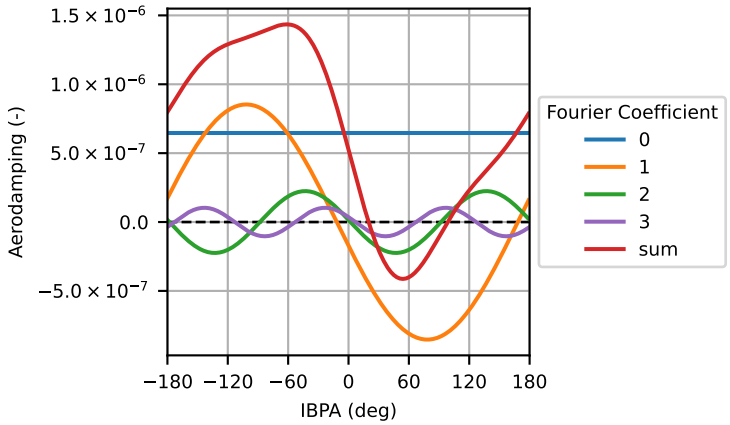

Figure 14. Aerodamping Fourier harmonics against IBPA—$k = 0.2$, $x/c = 1.25$.

7.2. Influence of Reduced Frequency

To investigate these trends further, aerodynamic damping is plotted as a function of reduced frequency for the different values of x/c at a constant IBPA. This is shown in Figure 15. An IBPA of 50° was selected because this was one of the least damped for the whole range of frequencies. Comparing the curves in Figure 15, it is clear that the reduced frequency has a strong influence on the aerodynamic damping trends. However, different trends are seen across the range of torsion axis locations. When the torsion axis is inboard of the aerofoil, $x/c \leq 1$, aerodynamic damping is negative for all reduced frequencies and asymptotically tends to zero with increasing frequency. The magnitude of aerodamping increases as the torsion axis shifts from the centre of the chord ($x/c = 0.5$) to the trailing edge ($x/c = 1$). Mode shapes with a larger plunge component, $1.5 \leq x/c \leq 3$, reach a local maximum at some reduced frequency, typically in the region of $k = 0.25$. These curves then asymptotically tend to zero at greater reduced frequencies as the blade becomes too stiff to be affected by the flow. Additionally, the higher the plunge component, the lower the critical reduced frequency required to stabilise the blade.

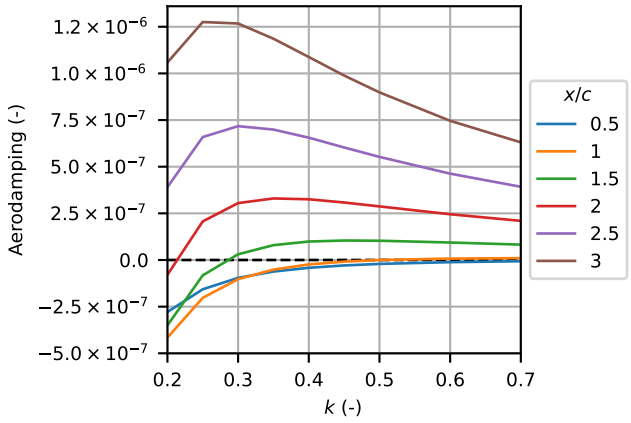

Figure 15. Effect of k on aerodamping at constant x/c—IBPA = 50°.

7.3. Influence of Torsion Axis Location

To further illustrate the influence of the torsional axis setback, Figure 16 shows the trend of aerodamping as the torsion axis setback is increased while reduced frequency and IBPA are kept constant. The modes are negatively damped for low x/c, and the curves follow a parabolic trend, with the critical x/c decreasing for higher frequencies. For a reduced frequency of $k = 0.2$, for example, the rotor is stable for $x/c > 3$, whereas $k = 0.4$ becomes stable at $x/c = 2$. In other words, a higher torsional component leads to a larger range of unstable reduced frequencies. The minimum aerodamping does not occur at the lowest value of x/c, indicating that a pure torsion mode is more stable than a combined mode. This is expected from the literature as it is the cross-coupling of forcing from the plunge and twist motion which causes the greatest instability. We see that there are no monotonic trends with x/c alone, but that it depends on frequency; hence, a stability parameter must contain a combination of the frequency and the plunge-to-twist ratio. From this and Equation (1), it can be deduced that the stability boundary for this IBPA is at a plunge-to-twist incidence ratio of approximately $\phi = 0.27$.

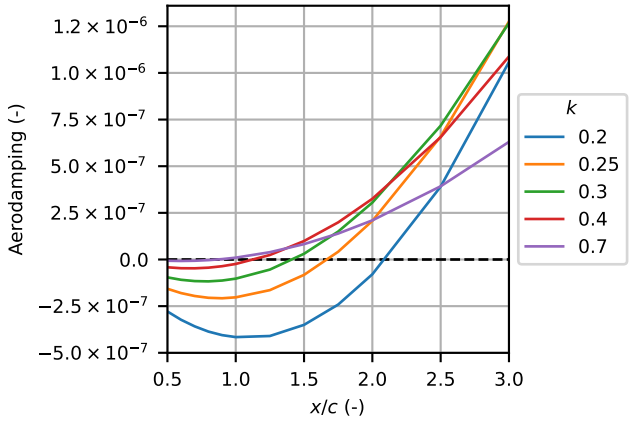

Figure 16. Effect of x/c on aerodamping at constant k—IBPA = 50°.

7.4. Stability Map

To illustrate the behaviour of the whole range of inter-blade phase angles, the minimum aerodynamic damping over all inter-blade phase angles is extracted for each combination of reduced frequency and torsion axis setback. The resulting stability map is shown in Figure 17. As already indicated above, the stability boundary lies at an approximately constant incidence ratio of $\phi = 0.27$, indicating the relevance of the plunge-to-twist incidence ratio parameter. We can see that this is slightly below the experimentally determined

limit of $\phi = 0.3$, indicating an error in the CFD of approximately 10%. The magnitude of the minimum aerodynamic damping does not scale with the incidence ratio, as the isolines do not follow lines of constant ϕ. Instead, there is a region of very large negative aerodamping for mode shapes with a large torsional component at low reduced frequencies. The maximum aerodamping for the parameter range tested is in the plunge-dominated mode, $x/c = 3$, and a reduced frequency of $k = 0.25$. Interestingly, it is not the largest reduced frequency which has the largest positive aerodamping, indicating that blade stiffness could be sacrificed to obtain a larger x/c.

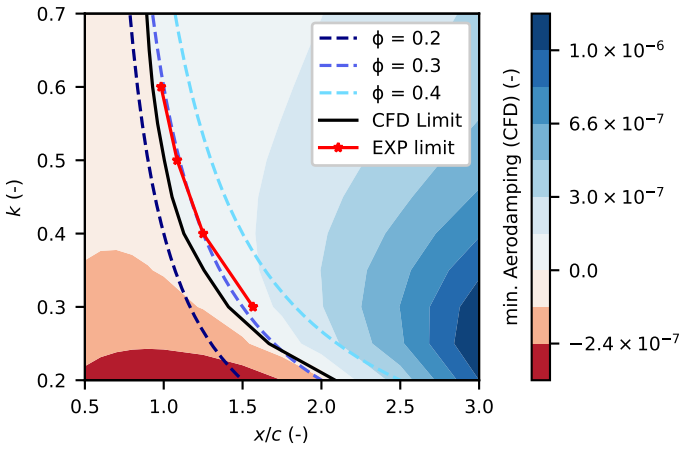

Figure 17. Stability map with contours of minimum aerodamping (CFD) as a function of k and x/c.

7.5. Discussion

Comparing these results to Whitehead's theoretical study of flat plates in an infinite cascade, we see some similarities. Figure 18 plots the critical reduced frequency, below which the cascade becomes unstable. The cascade geometry is similar to the one investigated here, with the same stagger angle but a larger pitch-to-chord ratio ($s/c = 1$ instead of $s/c = 0.75$). The curve of interest for this paper is the incompressible limit, $M = 0$. The unstable region predicted by Whitehead is very similar to Figure 17 for the reduced frequency of $k = 0.7$, for example, which becomes unstable at approximately $x/c = 1$. However, this is not consistent at lower reduced frequencies. This can be partially attributed to the different cascade geometry, since parametric investigations by Whithead [1] showed that reducing the pitch-to-chord ratio will extend the unstable range. However, other differences also exist. The blades in this study have a finite camber, steady loading, and viscous effects that are considered. The stability boundary predicted here also differs from that of transonic fans. According to the work by Vahdati and Cumpsty [3] and Lee et al. [8], the stability boundary for transonic fans near stall lies at $\phi \approx 1$. However, their research also showed a strong dependence of stability on steady state aerodynamics. The importance of these effects, and how they can be built into stability parameters, will be the subject of future work.

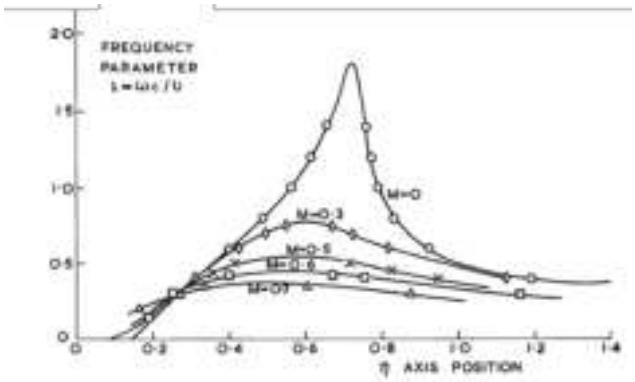

Figure 18. Stability map for an infinite cascade of flat plates with $\xi = 45°$, $s/c = 1.0$, $\eta = x/c$. (Whitehead, 1974).

8. Conclusions

This paper investigated the influence of pitching axis location and reduced frequency on the aeroelastic stability of a subsonic, unstalled, linear compressor cascade. Numerical simulations were validated against experimental measurements and consequently used for a parametric study. The range of reduced frequencies and mode shapes tested are representative of those found in modern compressors, but owing to the low incidence angle, low camber, and subsonic inflow, the cascade loading is comparatively low. This is one possible reason why the stability limit occurs at much lower incidence ratios compared to the literature for highly loaded fan blades. The results confirmed the strong dependency of stability on the reduced frequency and the plunge-to-twist component reported in the literature. We also showed that there are no monotonic trends between these parameters, hence a stability parameter must contain a combination of frequency and the plunge-to-twist ratio. It was also shown that the minimum aerodamping does not occur at a pure twist mode shape, but that it is rather a combination of plunge and twist forcing, which creates the largest instability when x/c is aft of half chord. The ratio of the incidence induced by the plunge motion to that induced by the twist motion was shown to be a valid stability criteria for early engine design stages, despite the changes in loading compared to a transonic fan. In further studies, the effects of blade loading and inlet Mach number will be considered.

Author Contributions: Conceptualization, S.S. (Sabine Schneider), D.P. and S.S. (Sina Stapelfeldt); data curation, G.H. and J.G.; formal analysis, G.H. and J.G.; funding acquisition, S.S. (Sabine Schneider), D.P. and S.S. (Sina Stapelfeldt); investigation, G.H. and J.G.; methodology, G.H. and J.G.; project administration, S.S. (Sabine Schneider); software, G.H. and J.G.; supervision, D.P. and S.S. (Sina Stapelfeldt); visualization, G.H.; writing—original draft, G.H. and S.S. (Sina Stapelfeldt); writing—review and editing, G.H., J.G., S.S. (Sabine Schneider), D.P. and S.S. (Sina Stapelfeldt). All authors have read and agreed to the published version of the manuscript.

Funding: This research was funded by an industrial collective research programme (IGF/CORNET no. 128 EN, FVV Project Number 1331). It was supported by the Federal Ministry for Economic Affairs and Energy (BMWi) through the AiF (German Federation of Industrial Research Associations eV) and the Engineering and Physical Science Research Council through an iCASE studentship (Ref 18000181).

Institutional Review Board Statement: Not applicable.

Informed Consent Statement: Not applicable.

Data Availability Statement: Not applicable.

Acknowledgments: The authors would like to thank Rolls-Royce plc for sponsoring this study and allowing its publication. The authors additionally thank Bernhard Mueck of Rolls-Royce Deutschland and Caetano Peng of Rolls-Royce UK for their scientific input.

Conflicts of Interest: The authors declare no conflict of interest.

Nomenclature

The following nomenclature is used in this manuscript:

1F	First Flap Blade Mode
AIC	Aerodynamic Influence Coefficient
IBPA	Inter Blade Phase Angle
ND	Nodal Diameter
RANS	Reynolds Averaged Navier-Stokes
SDOF	Single Degree of Freedom
PS	Pressure Side
SS	Suction Side
VBM	Vibrating Blade Module
ζ	Aerodynamic Damping Ratio
θ_{plunge}	Plunge Incidence Amplitude
θ_{pitch}	Pitch Incidence Amplitude
ξ	Stagger Angle
ϕ	Plunge-to-Pitch Incidence Ratio
c	Chord
f	Vibration Frequency
k	Reduced frequency, $k = 2\pi fc/u$
M	Mach Number
s	Pitch
u	Inlet Flow Velocity
x	Pitch Axis Location
z	Lever Length

References

1. Whitehead, D.S. The Effect of Compressibility on Unstalled Torsional Flutter. Aeronautical Research Council Reports & Memoranda. 1974; Volume 3754. Available online: https://reports.aerade.cranfield.ac.uk/handle/1826.2/3032 (accessed on 10 November 2021).
2. Halliwell, D. Fan Supersonic Flutter: Prediction and Test Analysis. Aeronautical Research Council Reports & Memoranda. 1975; Volume 3789. Available online: https://reports.aerade.cranfield.ac.uk/handle/1826.2/3068 (accessed on 5 November 2021).
3. Vahdati, M.; Cumpsty, N. Aeroelastic Instability in Transonic Fans. *J. Eng. Gas Turbines Power* **2015**, *138*, 022604. [CrossRef]
4. Panovsky, J.; Kielb, R.E. A Design Method to Prevent Low Pressure Turbine Blade Flutter. *J. Eng. Gas Turbines Power* **2000**, *122*, 89–98. [CrossRef]
5. Zhao, F. Impact of mode shape and acoustic gust on blade flutter stability. In Proceedings of the 15th International Symposium on Unsteady Aerodynamics, Aeroacoustics & Aeroelasticity of Turbomachines, ISUAAAT, Oxford, UK, 24–27 September 2018; pp. 1–10.
6. Whitehead, D.S. Force and Moment Coefficients for Vibrating Aerofoils in Cascade. Aeronautical Research Council Reports & Memoranda. 1962; Volume 3254. Available online: https://reports.aerade.cranfield.ac.uk/handle/1826.2/3828 (accessed on 20 November 2021).
7. Nipkau, J.; Power, B.; Jordan, M. Aeromechanical design and test of a modern highly loaded fan. In Proceedings of the ASME Turbo Expo 2017: Turbomachinery Technical Conference and Exposition, Charlotte, NC, USA, 26–30 June 2017; Volume 2, pp. 1–11. [CrossRef]
8. Lee, K.B.; Wilson, M.; Vahdati, M. Numerical study on aeroelastic instability for a low-speed fan. *J. Turbomach.* **2017**, *139*, 071004. [CrossRef]
9. Carta, F.O. Unsteady Gapwise Periodicity of Oscillating Cascaded Airfoils. In Proceedings of the ASME 1982 International Gas Turbine Conference and Exhibit. American Society of Mechanical Engineers, London, UK, 18–22 April 1982; pp. 1–15. [CrossRef]
10. Malzacher, L.; Geist, S.; Peitsch, D.; Hennings, H. A Low Speed Compressor Test Rig for Flutter Investigations. In Proceedings of the Volume 7B: Structures and Dynamics, American Society of Mechanical Engineers, Seoul, Korea, 13–17 June 2016; pp. 1–12. [CrossRef]
11. Sayma, A.; Vahdati, M.; Imregun, M. An Integrated Nonlinear Approach for Turbomachinery Forced Response Prediction. Part 1: Formulation. *J. Fluids Struct.* **2000**, *14*, 87–101. [CrossRef]
12. Vahdati, M.; Simpson, G.; Imregun, M. Mechanisms for wide-chord fan blade flutter. *J. Turbomach.* **2011**, *133*, 041029. [CrossRef]
13. Stapelfeldt, S.; Vahdati, M. On the importance of engine- representative models for fan flutter predictions. *J. Turbomach.* **2018**, *140*, 081005. [CrossRef]

14. Lee, K.B.; Wilson, M.; Vahdati, M. Validation of a numerical model for predicting stalled flows in a low-speed fan-Part I: Modification of Spalart-Allmaras turbulence model. *J. Turbomach.* **2018**, *140*, 051008. [CrossRef]
15. Hanamura, Y.; Tanaka, H.; Yamaguchi, K. A Simplified Method to Measure Unsteady Forces Acting on the Vibrating Blades in Cascade. *Bull. JSME* **1980**, *23*, 880–887. [CrossRef]
16. Crawley, E.F.; Hall, K.C. Optimization and mechanisms of mistuning in cascades. *J. Eng. Gas Turbines Power* **1985**, *107*, 418–426. [CrossRef]

International Journal of
Turbomachinery
Propulsion and Power

MDPI

Article

Retrofittable Solutions Capability for Gas Turbine Compressors †

Martina Ricci [1], Stefano Gino Mosele [2], Marcello Benvenuto [2], Pio Astrua [2] and Roberto Pacciani [1,*] and Michele Marconcini [1]

[1] Department of Industrial Engineering, University of Florence, Via di Santa Marta, 3, 50139 Florence, Italy; martina.ricci@unifi.it (M.R.); michele.marconcini@unifi.it (M.M.)
[2] Ansaldo Energia, Via Nicola Lorenzi, 8, 16152 Genoa, Italy; StefanoGino.Mosele@ansaldoenergia.com (S.G.M.); Marcello.Benvenuto@ansaldoenergia.com (M.B.); Pio.Astrua@ansaldoenergia.com (P.A.)
* Correspondence: roberto.pacciani@unifi.it; Tel.: +39-055-275-8784
† This paper is an extended version of our paper in Proceedings of the 14th European Turbomachinery Conference, Gdansk, Poland, 12–16 April 2021.

Abstract: The increasing introduction of renewable energy capacity has changed the perspective on the operation of conventional power plants, introducing the necessity of reaching extreme off-design conditions. There is a strong interest in the development and optimization of technologies that can be retrofitted to an existing power plant to enhance flexibility as well as increase performance and lower emissions. Under the framework of the European project TURBO-REFLEX, a typical F-class gas turbine compressor designed and manufactured by Ansaldo Energia has been studied. Numerical analyses were performed using the TRAF code, which is a state-of-the-art 3D CFD RANS/URANS flow solver. In order to assess the feasibility of lower minimum environmental load operation, by utilizing a reduction in the compressor outlet mass-flow rate, with a safe stability margin, two different solutions have been analyzed: blow-off extractions and extra-closure of Variable Inlet Guide Vanes. The numerical steady-state results are compared and discussed in relation to an experimental campaign, which was performed by Ansaldo Energia. The purpose is to identify the feasibility of the technologies and implementation opportunity in the existing thermal power plant fleet.

Keywords: axial compressor; minimum environmental load; computational fluid dynamics

check for updates

Citation: Ricci, M.; Mosele, S.G.; Benvenuto, M.; Astrua, P.; Pacciani, R.; Marconcini, M. Retrofittable Solutions Capability for Gas Turbine Compressors. *Int. J. Turbomach. Propuls. Power* **2022**, *7*, 3. https://doi.org/10.3390/ijtpp7010003

Academic Editor: Antoine Dazin

Received: 15 September 2021
Accepted: 7 January 2022
Published: 11 January 2022

Publisher's Note: MDPI stays neutral with regard to jurisdictional claims in published maps and institutional affiliations.

Copyright: © 2022 by the authors. Licensee MDPI, Basel, Switzerland. This article is an open access article distributed under the terms and conditions of the Creative Commons Attribution (CC BY-NC-ND) license (https://creativecommons.org/licenses/by-nc-nd/4.0/).

1. Introduction

Renewable energy systems (RES) represent a great revolution for the energy market. Despite their rapid development expected over the next decades, gas-fired power plants are required to maintain a key role in the energy horizon in order to ensure grid stability and peak demand and reach extreme off-design conditions. In fact, RES-based power plants (mainly wind and solar photovoltaic) are realized and convert energy when and where the power source is available, and this is not necessarily matching the community needs.

In order to preserve the grid balance, the existing programmable plants, mainly gas turbine (GT) open and combined cycle, have to modulate their load to compensate the large fluctuations due to the introduction of RES [1], as shown in Figure 1.

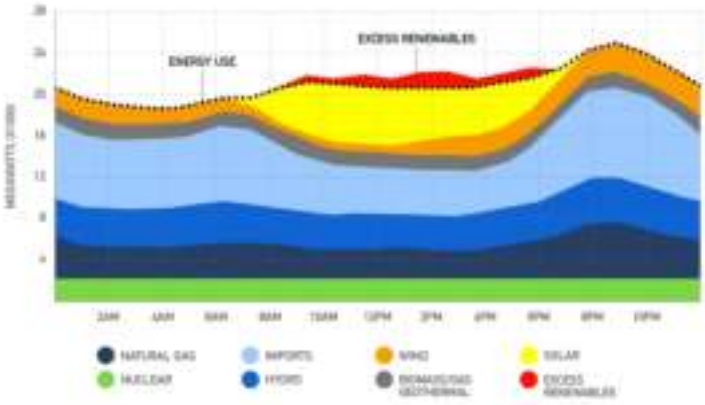

Figure 1. Generic daily power mix using programmable and renewable energy systems [2].

Due to their high potential flexibility, GT-based power plants are expected to keep playing a key role in the energy conversion technology framework despite the pushing toward grid decarbonization thanks to the future use of carbon-free fuel such as hydrogen [3].

The increasingly restrictive regulations imposed by the European community have led to strong interest in the development and optimization of technologies that can be retrofitted to an existing combined-cycle power plant to enhance flexibility as well as increase performance and lower emissions (General Electric [4], Alstom Power [5], Ansaldo Energia [6]).

Under the framework of the European project TURBO-REFLEX, some retrofittable solutions have been developed to enhance the minimum environmental load (MEL) capability in axial flow compressors. In fact, the goal is to reduce the MEL in order to have an increased reserve of power to support the stability of the grid.

Possible actions to reduce the MEL of a gas turbine, without detrimental effects on carbon dioxide emissions, include blow-off extraction, the inlet guide vanes (IGV) extra-closure, and inlet bleed heating. The first allows a high mass flow rate to be extracted from the compressor and discharged into the turbine diffuser. The second allows the compressor mass flow rate to decrease, while the load decreases for the same firing temperature. Finally, the third, also called *anti-icing*, consists in heating the inlet air (e.g., recirculating air from the outlet or using a dedicated heat exchanger). These solutions, which make it possible to significantly reduce the mass flow rate and the power output of the gas turbine, must be carefully analyzed and evaluated in terms of rear stages stability [7,8], ice formation on the first stage blade and vane rows [9,10], unsteadiness, vibrations, and noise emissions, and Heat Recovery Steam Generator (HRSG) temperature limit [11].

This paper aims to evaluate the capability and the robustness of a 3D CFD flow solver to predict the feasibility of lower full-compressor MEL operation by adopting different solutions: blow-off extractions and IGV extra-closure. A typical F-class gas turbine compressor designed and manufactured by Ansaldo Energia has been studied in the framework of the TURBO-REFLEX European project. Numerical analyses were performed using the TRAF code, a state-of-the-art 3D CFD RANS/URANS flow solver [12].

In the first part, numerical steady-state results referring to MEL and other operating conditions with IGV extra-closure will be presented and validated with experimental data available. In the second part, three challenging operating conditions (MEL, MEL with blow-off extraction, MEL with IGV extra-closure and blow-off extraction) have been proposed in order to identify feasibility of the technologies and implementation opportunity in the existing thermal power plant fleet.

2. Computational Framework

In the present work, a state-of-the-art, in-house-developed, RANS/URANS flow solver (TRAF code [12]) has been used. The 3D Reynolds-averaged Navier–Stokes equations are written in conservative form in a curvilinear coordinate system and solved for density,

absolute momentum components, and total energy. A second-order Jameson–Schmidt–Turkel (JST) central scheme [13] with scalar artificial dissipation was considered for the discretization of the convective terms, while for the turbulence closure, the high-Reynolds-number formulation of the Wilcox $k-\omega$ model [14] was selected. The code has been recently validated for the prediction of the characteristics of a multistage axial compressor [15].

2.1. Domain Discretization

The computational domain takes into account the full compressor module composed by 15 stages. Each blade row was discretized using O-type grids with about 1.4×10^6 cells per block. The compressor inlet and outlet guide vanes were discretized using H-type meshes with about 1.0×10^6 cells per block. The mesh density was selected on the base of a preliminary grid dependency analysis. To guarantee a proper resolution of boundary layers, the y^+ value of the grid nodes closest to the blade surface is between 1 and 2.

The impact of blade tip clearance modeling was evaluated by comparing two different approaches. The baseline tip model, referred to as "open tip", was used in a previous study [16]. It exploits a periodic boundary across a non-meshed region over the top of the blade tip to treat the clearance flow as an orifice flow with local interpolation of the conservative variables across the blade tip. In the second model, called "meshed tip", the blade tip gap region is fully discretized using an O-type mesh (Figure 2a) that matches the external grid in the blade-to-blade plane. The two models adopt the same number of cells in the spanwise direction. The mass flow rate distribution along the entire compressor, with and without the meshed tip rotor, is reported in Figure 2b. The operating condition is the reference one, at the working point, with five mass-flow extractions that are located along the meridional flow-path (indicated as EB in the Figure). It can be easily observed how for the "open tip" model, the outlet mass flow is reduced by 1.8%, and so it is less conservative as opposed to the "meshed tip" one. For this reason, the new accurate "meshed tip" has been chosen for modeling the compressor rotor blade tip clearance.

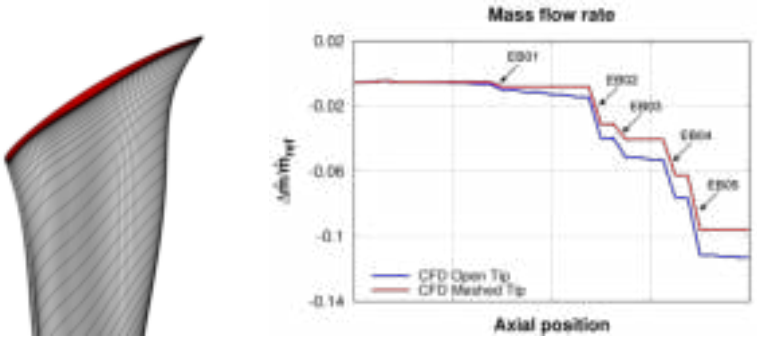

(**a**) (**b**)

Figure 2. View of the rotor tip gap grid block (**a**) and mass flow rate distribution for the compressor, with and without the meshed tip rotor (**b**) (the axial position of the exit bleeds (EB) is indicated).

2.2. Boundary Conditions

The inlet boundary condition enforces the measured radial distributions of total pressure, total temperature, and flow angles. The inlet turbulence intensity and turbulent length scale are 1.0% and 0.01% of blade height, respectively. At the outlet of the computational domain, the static pressure value has been imposed at the hub, and the radial equilibrium was used to obtain the spanwise distribution.

The compressed fluid is humid air and was modeled as a real gas. In all the presented simulations, mixing planes with non-reflecting boundary conditions (Giles [17,18]) have been adopted to couple consecutive rows. A local matching interface was used between the last stator and the OGV since they share the same blade count [6,19].

2.3. Mass Extraction Treatment

The mass flow extraction occurs through bleeding slots located in the compressor casing, and the bleed mass flow rate is controlled by blow-off valves. In order to simulate the blow-off, outflow boundary conditions are applied in the tip endwall regions corresponding to the bleeding slots. A constant static pressure is prescribed, and the other flow variables are extrapolated from the interior of the computational domain. The prescribed pressure value is iteratively adjusted to match the desired amount of extracted mass flow rate.

3. Results

An industrial, F-class axial compressor designed, manufactured, and experimentally tested by Ansaldo Energia has been studied in the present work. The configuration corresponds to 15-stages plus IGV and OGV, with five mass-flow extractions located along the meridional flow-path, some positioned on the hub end-wall and others at the casing. All the vanes, excluding IGV and OGV are shrouded. The effects of seal cavity flow on the mainstream have been considered using a simplified one-dimensional correlation-based cavity model [20].

The regulation of the mass flow has been used to modulate the gas turbine power output. To this aim, two different solutions have been investigated: blow-off extraction and IGV extra-closure. The IGV and the first stator blade have a variable stagger configuration. The stagger angle of these two rows can be modified independently. In the computational model, the IGV blade is considered always in contact with the internal/external wall so that clearances effects are not accounted for in the CFD analyses.

In the first part of the work, numerical steady-state results referring to MEL and other operating conditions with IGV extra-closure are discussed and validated with experimental data. In the second part, three challenging operating conditions of MEL with/without blow-off extraction and IGV extra-closure are proposed in order to assess the feasibility of the technological solutions and their possible implementation in the existing combined-cycle power plant fleet.

Each CFD simulation required about nine hours, running on 64-core processor Intel® Xeon® CPU E5-2680 v2 @2.80 GHz, to reach the steady state convergence. The RMS residual experiences a drop of four decades in about 5000 multi-grid cycles on two grid levels. For all the calculated operating points, the solution convergence was obtained with approximately the same number of iterations showing a good robustness even in presence of separated flow regions inside the computational domain.

3.1. Comparison with Measurements

The first part of the work is devoted to investigating the compressor operation in the off-design condition, referred to as MEL with IGV extra-closure. This strategy can significantly reduce the mass flow elaborated and the power output of the gas turbine; however, a careful analysis of the compressor aerodynamics is required to assure that no stability issues will afflict the operation.

The experimental campaign was carried out by Ansaldo Energia, testing the machine at three different IGV extra-closure configurations, with the current MEL operating condition. An assessment of the CFD results is presented by a detailed comparison with the corresponding experimental data. In particular, the computational model was validated for the T23 configuration (representing the MEL one) and the T24 and T26 configurations, which have an IGV and first stator blade stagger variation with respect to standard MEL, which can been modified independently. The inlet total temperature for the T23 and T24 configurations is almost identical, while the T26 has a lower inlet value ($\Delta T \approx 8°$). In terms of inlet total pressure, the tests with IGV extra-closure have a slightly higher value with respect to the one corresponding to T23 ($\Delta p \approx +0.4\%$).

The numerical results in terms of predicted flow function at compressor inlet and outlet are compared with the experimental data in Figure 3a,b, respectively. The inlet flow function values are scaled as:

$$FF = \left(FF_x - FF_{ref}\right) / FF_{mean,\ T23},$$

where x is equal to T23, T24, and T26. The agreement between numerical results and measured data is good. The averaged total temperature at the outlet shown in Figure 3c appears to be slightly underestimated for all the three cases. Consequently, numerical analyses tend to overestimate the total-to-total adiabatic efficiency and to underestimate the compressor's work input.

Figure 4 shows the static pressure distribution at the casing compared with the values measured by eight pressure taps along the meridional channel, highlighting a good matching with the experimental results for all the operating points. Slight discrepancies can be observed for the last measuring station, located upstream of the rotor row of stage nine.

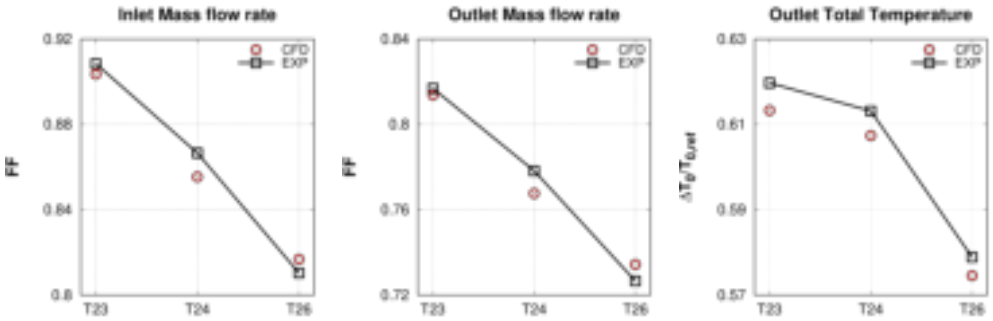

(**a**) (**b**) (**c**)

Figure 3. Compressor inlet (**a**) and outlet (**b**) mass flow rate, and outlet total temperature (**c**).

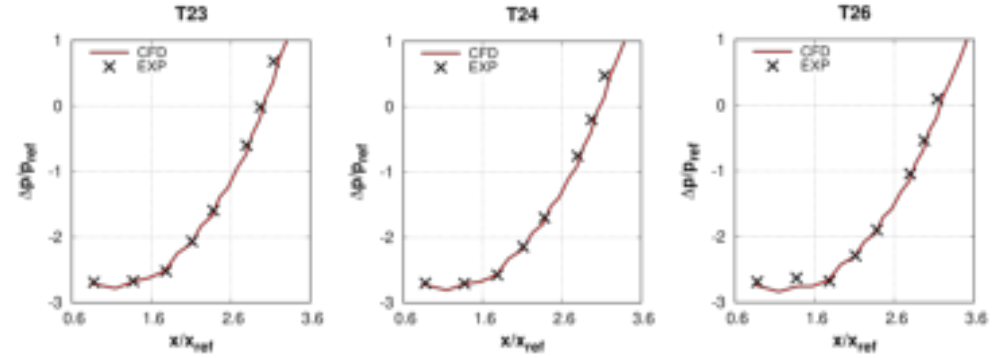

(**a**) (**b**) (**c**)

Figure 4. Compressor pressure at casing for the operating points experimentally tested: (**a**) T23 (MEL), (**b**) T24, (**c**) T26.

3.2. Minimum Environmental Load Reduction Strategies

The feasibility of viable strategies to further reduce the GT load is investigated using the previously assessed numerical framework.

Axial compressors are always equipped with blow-off valves to bypass part of the compressed air to the turbine exhaust. Usually these valves are used during the startup of the GT to avoid compressor instabilities. In the framework of the Turbo-Reflex project, the possibility of using the BO valves to further reduce the minimum environmental load was investigated. The use of BO valves was additionally combined with IGV extra-closure. With this aim, some operating conditions were analyzed with the same compressor inlet boundary conditions (total temperature, total pressure, and absolute flow angle).

The discharge pressure of the compressor was varied in a wide range in order to find the numerical surge margin of the compressor. Three operating conditions have been considered: the reference one, at the minimum environmental load (MEL), the one with an open blow-off valve located before the sixth rotor leading edge (MEL blow-off), and finally the one with an IGV extra-closure, which has a stagger variation with respect to the standard case (MEL IX blow-off). The reduction in the MEL condition by these two different strategies (IGV extra-closure and blow-off valve) will be presented in this section.

Figure 5 shows the total pressure ratio and efficiency characteristics. All values are reported with respect to the working line at the MEL condition. These curves are obtained by progressively increasing the outlet static pressure, starting from the working line condition. The combined opening of the blow-off valves and the extra-closure of the IGV (MEL IX blow-off) reduces the power plant output and penalizes the compressor efficiency. Both strategies reduce the gas turbine pressure ratio with respect to standard MEL, as reported in Figure 5a. In particular, the IGV extra-closure reduces the mass flow with respect to standard MEL. The mass flow reduction led to a lower pressure ratio; then, if flame temperature is fixed, it results in a Turbine Exit Temperature (TET) increase. The blow-off opening more significantly reduces the mass flow in the last stages of the compressor, the combustion chamber, and the turbine. Provided the blow-off mass flow is reinjected into the turbine diffuser, it may greatly reduce the TET.

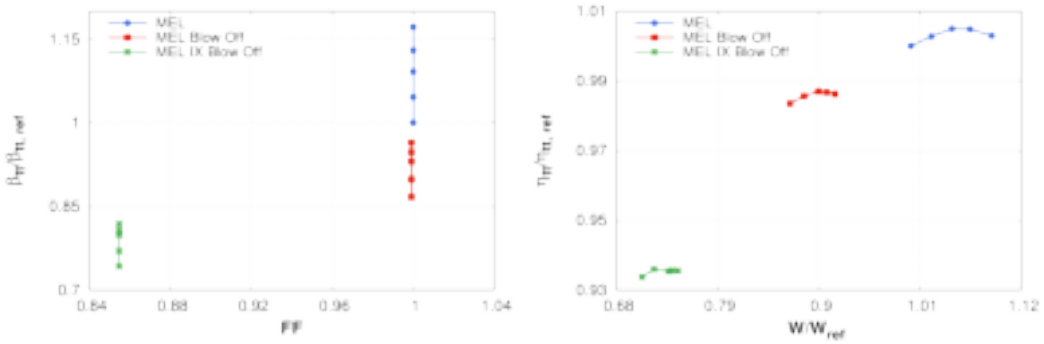

(**a**) (**b**)

Figure 5. Overall pressure ratio (**a**) and efficiency (**b**).

The main operating differences between the three configurations can be appreciated in terms of stage flow coefficient (Figure 6a) and load coefficient (Figure 6b). For stages 4, 5, and 6, there is a load reduction toward the bleed position, followed by a gradual increase toward the end in which the highest value is reached on the last stage. The evolution of the Lieblein's diffusion factor value along the compressor shown in Figure 7a was used as a mean to check the impact of the MEL reduction strategies on the compressor's aerodynamics.

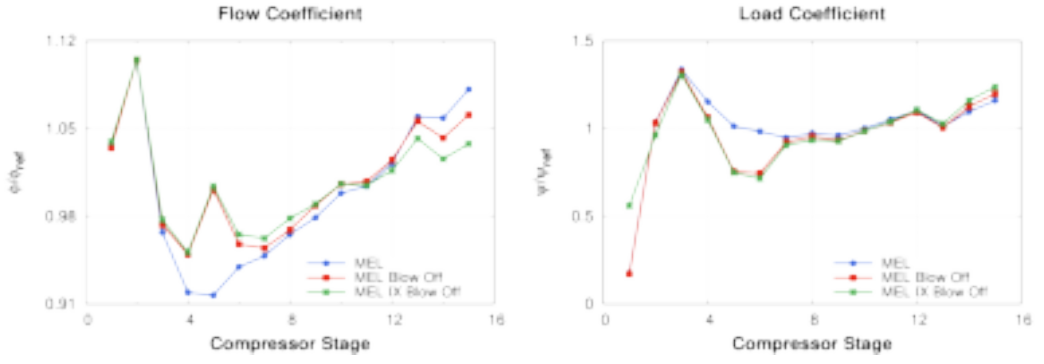

(**a**) (**b**)

Figure 6. Stage flow coefficient (**a**) and load coefficient (**b**).

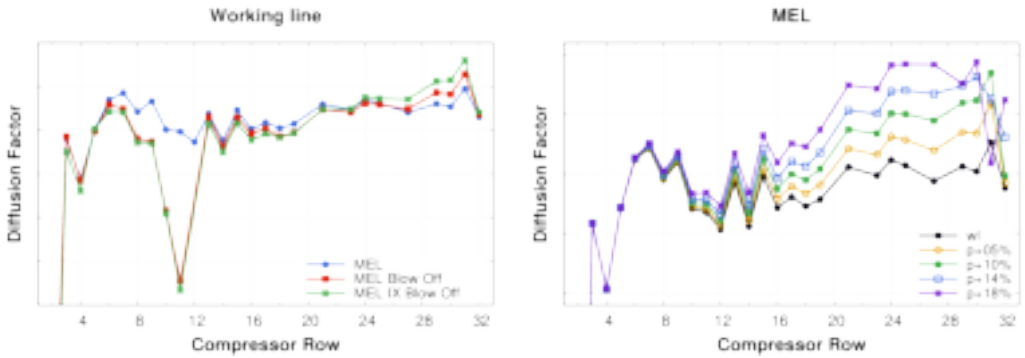

(**a**) (**b**)

Figure 7. Diffusion factor comparison between analyzed MEL configurations (**a**) and part-load standard MEL operating condition (**b**).

Local values of the Lieblein's diffusion factor are initially calculated with reference to meridional streamtubes and accounts for radius changes and AVDR, i.e., three-dimensional aspects of the flow in each blade row:

$$DF = 1 - \frac{w_{out}}{w_{in}} + \frac{\Delta(rw_\theta)}{2\sigma_m r_m w_{in}} \tag{1}$$

Equation (1) is applied along streamtubes between the blade leading and trailing edges, with velocities taken as relative to the blade row (see the sketch in Figure 8). The blade row solidity σ_m is calculated, with reference to the mean streamtube, i.e., the one that equally divides the mass flow rate along the blade height (Figure 8):

$$\sigma_m = \frac{C_m}{s_m},\ s_m = \frac{2\pi r_m}{N},\ r_m = \frac{r_{m,in} + r_{m,out}}{2}$$

where C_m is the distance between the blade leading and trailing edges locations. Finally, the local diffusion factors corresponding to the various streamtubes are averaged in order to obtain a single DF value which is taken as representative of the entire blade row.

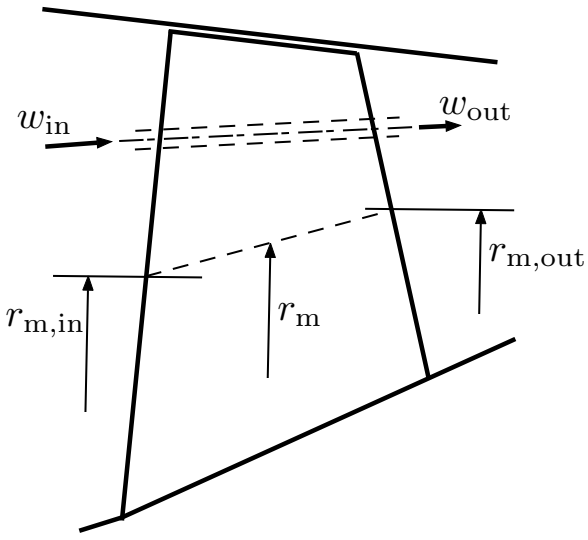

Figure 8. Meridional sketch for diffusion factor definition.

In this work, DF is used as a metric for the loading limit of each blade row and hence for aerodynamic stability of the compressor. The higher the diffusion factor, the lower the blade row stall margin.

The blow-off is located at rotor 6 or row 12, and the figure shows that as the flow approaches the bleed, the diffusion factor decreases. Overcoming the bleed, the diffusion factor increases sharply until the last stage (stator 15), where it reaches the highest value. When the IGV extra-closure is combined with the BO opening, the diffusion factor increases further in the final stage.

Therefore, with these two strategies (MEL blow-off and MEL IX blow-off), there is a reduction in the load in the first part of the compressor (rows 6–24) and then an increase in the load in the last three stages, as confirmed by Figure 6b.

Figure 7b shows the evolution of the DF at MEL condition, varying the discharge pressure of the compressor in a wide range up to 18% of the working line. In the last stator (vane 15 or row 31), the main differences are concentrated. Up to 10%, the diffusion factor has the highest values for the entire compressor. Then, at 14%, it starts to decrease, and at 18%, there is a drastic drop. In fact, based on CFD stage characteristics (Figure 9a), stage 15 reaches the numerical stability margin at 14% of the discharge pressure.

Figure 9 reports the compressor map for the stages 11–15. The numerical stability limit is identified using the peak stage pressure ratio. The numerical surge margin is defined on the base of the numerical stability limit.

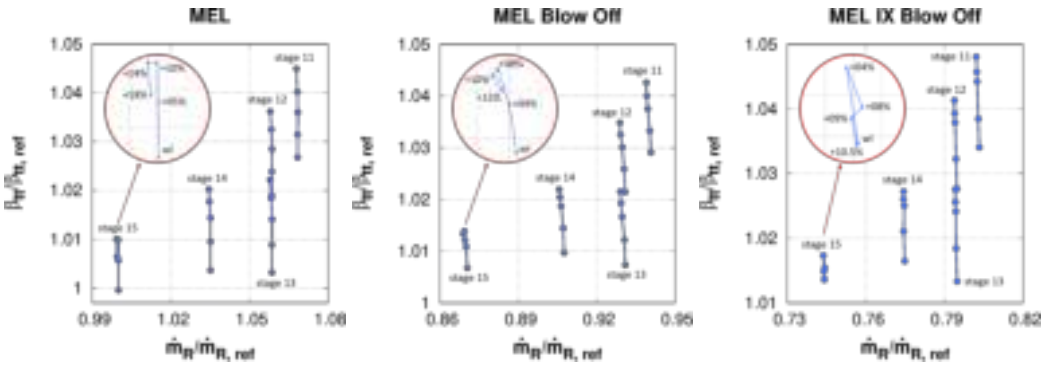

(**a**) (**b**) (**c**)

Figure 9. Compressor stages map for (**a**) MEL, (**b**) MEL+Blow-Off, (**c**) MEL+Blow-Off+IGV Extra Closure.

Recirculation regions close to the compressor endwall for the stages from 10 to 15 with OGV are reported in Figure 10. They suggest that if the hub corner separation is assumed to be most relevant source of instability, the stall mechanism does not change for the three operating conditions. Considering the stage 15 characteristic (Figure 9), the numerical stability margin for MEL, IX, and IX blow-off operating conditions, respectively, is progressively reduced. Such observation is in agreement with the stage 15 diffusion factor at the working point (Figure 7a) which for IX and IX with blow-off operating conditions is progressively higher compared to the value assumed in the MEL condition.

The numerical analysis predicts a wide corner separation at the hub of the stator rows, as observed in similar conditions by other authors (Vo, 2008 [21], Lei, 2008 [22]). This flow structure is more visible for the fourteenth stator row and increases its dimension on the CV15 and OGV. Increasing the back-pressure, the hub corner stall increases both in terms of size and spanwise penetration, indicating that the last stages are about to give up [23].

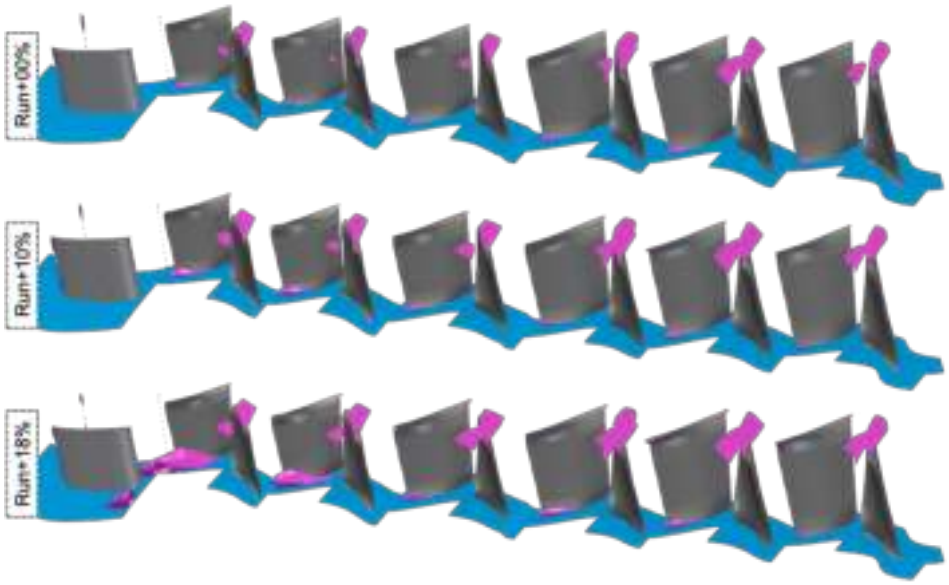

Figure 10. View of stages 10 to 15 + OGV; recirculating flow regions are highlighted by iso-surface of zero axial velocity (flow goes from right to left).

4. Conclusions

In the present work, the capability and robustness of a 3D CFD flow solver to predict the feasibility of lower full-compressor MEL operation have been evaluated. Two different solutions have been analyzed: blow-off extraction and IGV extra-closure.

Numerical steady-state results at three different IGV extra-closure configurations with the current MEL operating conditions have been presented and validated with experimental data. A good accuracy in terms of calculated mass flow rate and total temperature has been achieved by employing a meshed tip gap with respect to an open tip strategy. Even for the most critical condition, the CFD results are perfectly in line with the experimental ones. The significant reduction in mass flow rate and power output gas turbine was well reproduced.

In the second part of the work, three challenging operating conditions have been analyzed: standard MEL, with an open blow-off valve, and an IGV extra-closure. The combined strategies reduce the power plant output. In particular, an additional increase in the diffusion factor and a reduction in the mass flow through the last stages is obtained using the blow-off valve opening. Coupling the BO opening and the IGV extra-closure allows a further reduction in the mass flow rate followed by the diffusion factor augmentation in the rear part of the compressor. The main differences between the considered operating conditions are found to be concentrated in the last stator row. In particular, stage 15 characteristics show that the numerical stability margin for MEL, IX, and IX blow-off operating conditions is progressively reduced. The numerical analysis predicts a wide hub corner separation in CV14, CV15, and OGV that increases in size when increasing the back pressure.

The viability of both technologies in the existing thermal power plant fleet has been verified. By opening blow-off valves or extra-closing the IGV, the gas turbine is able to operate with less mass flow at constant flame temperature and therefore produce less power and burn less fuel than in the standard case.

It is believed that the proposed numerical framework and setup is feasible and is able to provide reliable performance figures in the analysis of industrial compressors operating in strong off-design conditions.

Author Contributions: Conceptualization, P.A., M.B., S.G.M., methodology, R.P., M.M., M.R., software, M.R., R.P., M.M., validation, M.R., M.M., R.P., S.G.M., M.B., formal analysis, R.P., M.M., investigation, M.R., S.G.M., M.B., writing—original draft preparation, M.R., R.P., M.M., writing—review and editing, R.P., M.M., visualization, M.R., supervision, P.A., S.G.M., R.P., M.M., project administration, P.A., M.B., S.G.M., M.M., R.P. All authors have read and agreed to the published version of the manuscript.

Funding: This research was funded by European Union's Horizon 2020 research and innovation programme under grant agreement No. 764545.

Data Availability Statement: Not applicable.

Acknowledgments: We would like to thank our fellow partners in European Union's H2020 programme TURBO-REFLEX for permitting the publication of our results in this paper.

Conflicts of Interest: The authors declare no conflict of interest.

Abbreviations

The following abbreviations are used in this manuscript:

BO	Blow-off
IGV	Inlet guide vane
IX	IGV extra-closure
MEL	Minimum environmental load
OGV	Outlet guide vane
RES	Renewable energy systems
TET	Total exit temperature
Nomenclature	
$AVDR$	Axial velocity by density ratio, $AVDR = \frac{(\rho c_x)_{out}}{(\rho c_x)_{in}}$
c	Absolute velocity
C	Blade chord
DF	Diffusion factor (Lieblein), $DF = 1 - \frac{w_{out}}{w_{in}} + \frac{\Delta(rw_\theta)}{2\sigma_m r_m w_{in}}$
FF	Inlet flow function, $FF = \frac{\dot{m}\sqrt{T_0}}{p_0}$
h	Specific enthalpy
$\dot{m}$	Mass flow rate
N	Number of blades
p	Pressure
r	Radius
s	Blade row tangential spacing
u	Peripheral velocity, $u = \Omega r$
T	Absolute temperature
x	Axial coordinate
w	Relative velocity
W	Compressor power input
β	Pressure ratio
η	Isentropic efficiency
ϕ	Flow coefficient, $\phi = \frac{c_x}{u}$
ψ	Load coefficient, $\psi = \frac{\Delta h_0}{u^2}$
σ	Blade row mean solidity, $\sigma = \frac{C_m}{s_m}$
Subscripts	
0	Total quantity
in	Inlet
m	Mean
out	Outlet
ref	Reference
tt	Total-to-total
x	Axial
ρ	Density
θ	Tangential

References

1. Ruchti, C.; Olia, H.; Franitza, K.; Ehrsam, A.; Bauver, W. Combined Cycle Power Plants as Ideal Solution to Balance Grid Fluctuations—Fast Start-Up Capabilities. In Proceedings of the 43th Colloquium of Power Plant Technology, Dresden, Germany, 18–19 September 2011.
2. Hailye/KQED, T. California ISO. Available online: https://www.kqed.org/science/610026/what-will-california-do-with-too-much-solar (accessed on 15 September 2021).
3. Chiesa, P.; Lozza, G.; Mazzocchi, L. Using Hydrogen as Gas Turbine Fuel. *J. Eng. Gas Turbines Power* **2005**, *127*, 73–80. [CrossRef]
4. Magni, F.; Grimm, F.; Sorato, S.; Micheli, M. GT13E2 Low Part Load Operation: Extended Flexibility Down to 30% Load. In *Turbo Expo: Power for Land, Sea, and Air*; Volume 3: Coal, Biomass and Alternative Fuels; Cycle Innovations; Electric Power; Industrial and Cogeneration; Organic Rankine Cycle Power Systems; ASME: New York, NY, USA, 2016. [CrossRef]
5. Therkorn, D.; Gassner, M.; Lonneux, V.; Zhang, M.; Bernero, S. CCPP Operational Flexibility Extension Below 30% Load Using Reheat Burner Switch-Off Concept. In *Turbo Expo: Power for Land, Sea, and Air*; Volume 3: Coal, Biomass and Alternative Fuels; Cycle Innovations; Electric Power; Industrial and Cogeneration; ASME: New York, NY, USA, 2015. [CrossRef]
6. Cioffi, M.; Piola, S.; Puppo, E.; Silingardi, A.; Bonzani, F. Minimum Environmental Load Reduction in Heavy Duty Gas Turbine by Bleeding Lines. In *Turbo Expo: Power for Land, Sea, and Air*; Volume 3A: Coal, Biomass and Alternative Fuels; Cycle Innovations; Electric Power; Industrial and Cogeneration; ASME: New York, NY, USA, 2014. [CrossRef]
7. Cozzi, L.; Rubechini, F.; Marconcini, M.; Arnone, A.; Astrua, P.; Schneider, A.; Silingardi, A. Facing the Challenges in CFD Modelling of Multistage Axial Compressors. In *Turbo Expo: Power for Land, Sea, and Air*; Volume 2B: Turbomachinery; ASME: New York, NY, USA, 2017. [CrossRef]
8. Cozzi, L.; Rubechini, F.; Giovannini, M.; Marconcini, M.; Arnone, A.; Schneider, A.; Astrua, P. Capturing Radial Mixing in Axial Compressors With Computational Fluid Dynamics. *J. Turbomach.* **2019**, *141*, 031012. [CrossRef]
9. Diakunchak, I.S. Performance deterioration in industrial gas turbines. *J. Eng. Gas Turbines Power* **1992**, *114*, 161–168. [CrossRef]
10. Ojo, C.O.; Schwille, C.; Nemet, A.; Zierer, T.; Nicklas, M. Optimization of Anti-Icing Limits for Alstom Gas Turbines Based on Theory of Ice Formation. In *Turbo Expo: Power for Land, Sea, and Air*; Volume 1: Aircraft Engine; Ceramics; Coal, Biomass and Alternative Fuels; Controls, Diagnostics and Instrumentation; Education; Electric Power; Awards and Honors; ASME: New York, NY, USA, 2009; pp. 871–879. [CrossRef]
11. Mendoza, E.; Lin, T.; Jiang, X. Reduction of Gas Turbine Exhaust Temperature Limit due to HRSG Limitations by Change on Control Curve to Optimize Plant Operation and Performance. In *Turbo Expo: Power for Land, Sea, and Air*; Volume 3: Coal, Biomass and Alternative Fuels; Cycle Innovations; Electric Power; Industrial and Cogeneration; ASME: New York, NY, USA, 2015. [CrossRef]
12. Arnone, A. Viscous Analysis of Three-Dimensional Rotor Flow Using a Multigrid Method. *J. Turbomach.* **1994**, *116*, 435–445. [CrossRef]
13. Jameson, A.; Schmidt, W.; Turkel, E. Numerical Solutions of the Euler Equations by Finite Volume Methods Using Runge–Kutta Time–Stepping Schemes. In Proceedings of the 14th Fluid and Plasma Dynamics Conference, Palo Alto, CA, USA, 23–25 June 1981; AIAA Paper 81–1259.
14. Wilcox, D.C. Multiscale Model for Turbulent Flows. *AIAA J.* **1988**, *26*, 1311–1320. [CrossRef]
15. Burberi, C.; Michelassi, V.; Scotti del Greco, A.; Lorusso, S.; Tapinassi, L.; Marconcini, M.; Pacciani, R. Validation of steady and unsteady CFD strategies in the design of axial compressors for gas turbine engines. *Aerosp. Sci. Technol.* **2020**, *107*, 106307. [CrossRef]
16. Mosele, S.G.; Garbarino, T.; Schneider, A.; Cozzi, L.; Arnone, A.; Goinis, G.; Hedkvist, S. Compressor Retrofittable Solutions in Heavy-Duty Gas Turbines for Minimum Environmental Load Reduction. *E3S Web Conf.* **2019**, *13*, 01012, [CrossRef]
17. Giles, M.B. *Non-Reflecting Boundary Conditions for the Euler Equations*; Technical Report; CFDL Report 88-1; MIT Dept. of Aero. and Astro.: Boston, MA, USA, 1988.
18. Giles, M.B. *UNSFLO: A Numerical Method for Unsteady Inviscid Flow in Turbomachinery*; Technical Report; GTL 195; MIT Dept. of Aero. and Astro.: Boston, MA, USA, 1988.
19. Cioffi, M.; Puppo, E.; Silingardi, A. Fanno Design of Blow-Off Lines in Heavy Duty Gas Turbine. In *Turbo Expo: Power for Land, Sea, and Air*; Volume 4: Ceramics; Concentrating Solar Power Plants; Controls, Diagnostics and Instrumentation; Education; Electric Power; Fans and Blowers; ASME: New York, NY, USA, 2013. [CrossRef]
20. Rubechini, F.; Marconcini, M.; Arnone, A.; Cecchi, S.; Daccà, F. Some Aspects of CFD Modeling in the Analysis of a Low-Pressure Steam Turbine. In *Turbo Expo: Power for Land, Sea, and Air*; Paper No. GT2007-27235; ASME: New York, NY, USA; 2007.
21. Vo, H.D.; Tan, C.S.; Greitzer, E.M. Criteria for Spike Initiated Rotating Stall. *J. Turbomach.* **2008**, *130*, 011023. [CrossRef]
22. Lei, V.M.; Spakovszky, Z.S.; Greitzer, E.M. A Criterion for Axial Compressor Hub-Corner Stall. *J. Turbomach.* **2008**, *130*, 031006. [CrossRef]
23. Schneider, A.; Silingardi, A.; Astrua, P.; Puppo, E.; Depalo, S. Rotor tip stall from a designer's perspective. In Proceedings of the 12th European Turbomach Conference, Stockholm, Sweden, 3–7 April 2017; Paper ETC2017-343.

International Journal of
Turbomachinery Propulsion and Power

MDPI

Article

Trapped Acoustic Modes in an Axial Multi-Stage Compressor Leading to Non-Synchronous Blade Vibrations †

Anne-Lise Fiquet [1,*], Stéphane Aubert [1], Nicolas Buffaz [2], Agathe Vercoutter [2] and Christoph Brandstetter [1]

1 Ecole Centrale de Lyon, CNRS, University Claude Bernard Lyon 1, INSA Lyon, LMFA, UMR5509, 69130 Ecully, France; stephane.aubert@ec-lyon.fr (S.A.); christoph.brandstetter@ec-lyon.fr (C.B.)
2 Safran Helicopter Engines, Safran Group, 64510 Bordes, France; nicolas.buffaz@safrangroup.com (N.B.); agathe.vercoutter@safrangroup.com (A.V.)
* Correspondence: anne-lise.fiquet@doctorant.ec-lyon.fr
† This paper is an extended version of our paper published in Proceedings of the 14th European Turbomachinery Conference, Gdansk, Poland, 12–16 April 2021.

Abstract: Non-synchronous blade vibrations have been observed in an experimental multi-stage high-speed compressor setup at part-speed conditions. A detailed numerical study has been carried out to understand the observed phenomenon by performing unsteady full-annulus Reynolds-Averaged Navier–Stokes (RANS) simulations of the whole setup using the solver elsA. Several operating conditions have been simulated to observe this kind of phenomena along a speedline of interest. Based on the simulation results, the physical source of the non-synchronous blade vibration is identified: An aerodynamic disturbance appears in a highly loaded downstream rotor and excites a spinning acoustic mode. A "lock-in" phenomenon occurs between the blade boundary layer oscillations and the spinning acoustic mode. The establishment of axially propagating acoustic waves can lead to a complex coupling mechanism and this phenomenon is highly relevant in understanding the multi-physical interactions appearing in modern compressors. It is shown that aerodynamic disturbances occurring downstream can lead to critical excitation of rotor blades in upstream stages due to an axially propagating acoustic wave. The paper includes the analysis of a relevant transient test and a detailed analysis of the numerical results. The study shows the capability and necessity of a full-annulus multistage simulation to understand the phenomenon.

Keywords: axial multi-stage compressor; trapped acoustic modes; non-synchronous forced response

check for updates

Citation: Fiquet, A.-L.; Aubert, S.; Buffaz, N.; Vercoutter, A.; Brandstetter, C. Trapped Acoustic Modes in an Axial Multi-Stage Compressor Leading to Non-Synchronous Blade Vibrations. *Int. J. Turbomach. Propuls. Power* **2022**, *7*, 6. https://doi.org/10.3390/ijtpp7010006

Received: 14 September 2021
Accepted: 28 January 2022
Published: 4 February 2022

Publisher's Note: MDPI stays neutral with regard to jurisdictional claims in published maps and institutional affiliations.

Copyright: © 2022 by the authors. Licensee MDPI, Basel, Switzerland. This article is an open access article distributed under the terms and conditions of the Creative Commons Attribution (CC BY-NC-ND) license (https://creativecommons.org/licenses/by-nc-nd/4.0/).

1. Introduction

Non-Synchronous Vibrations (NSV) have received much attention since the 1990s [1–6]. The term of 'NSV' is used to describe a specific aeroelastic phenomenon where the characteristic frequency is not related to the shaft frequency. Unfortunately, a multitude of phenomena can lead to non-synchronous blade vibrations in turbomachinery, as flutter [7], buffeting, or rotating stall. The term of 'NSV' has been widely used to identify an aeroelastic phenomenon where blade vibrations are measured without a precise terminology.

According to cases of 'NSV' reported in literature, a characterization can be derived:

- Blade vibrations caused by convective phenomena: This type of 'NSV' is typically driven by small-scale aerodynamic disturbances that are convected around the circumference and may adapt their phase to blade vibration [8]. Before the establishment of blade vibrations, it was observed that these aerodynamic disturbances were already present with a random azimuthal distribution and a characteristic circumferential phase velocity. Once 'NSV' is established, this characteristic phase velocity is slightly altered to enable the coincidence of the aerodynamic disturbances with the coherent blade eigenmode. Generally, phenomena of this kind occur in modern transonic compressor rotors under highly throttled conditions close to the stall boundary.

- Acoustic resonance: In this specific case, several spinning modes of zeroth radial order can originate and propagate only in one axial direction due to the change of acoustic propagation conditions upstream and downstream of a blade row [8–12]. This change of acoustic propagation conditions enables only a series of resonant modes with a certain circumferential wave number and circumferential phase velocity [13]. Unstable aerodynamic flow structures can phase-lock to the acoustic mode, and thus serve as a periodic energy source. If it coincides with a structural mode, it may cause damaging effects. In this particular case, it is important to note that a backward traveling acoustic mode originating in a downstream stage of the compressor can be coincident with a specific structural mode of an upstream rotor. This type of phenomena can occur far from the stability limit of the compressor.

Both mechanisms can lead to severe blade vibrations and damage the structure. These phenomena are highly relevant to engine manufacturers since modern compressor stages can develop sensitive flow structures, such as flow separations or small-scale disturbances at off-design conditions. The characterization of such phenomena requires special attention to consider the interdependency between aerodynamics, structure dynamics, and acoustics. Safran Helicopter Engines conducted complex experiments with synchronized aerodynamic and blade vibration measurements to improve the understanding and interaction mechanisms of the observed 'NSV' occurring in a research axial compressor.

As will be shown in this paper, pressure modes observed in the experiment and the numerical simulations are cut-on only in one axial direction (upstream or downstream). This paper represents a synthesis of previous publications on the phenomenon [14–17]. The main objective is to clarify the mechanism behind the non-synchronous phenomena observed experimentally and to give a coherent explanation through comparison with numerical simulations.

Non-synchronous activity has been observed at different operating conditions, but in one specific transient test, an acoustic mode coincides with a structural mode and leads to significant blade vibration. This paper will describe the test case and experimental observations concerning this non-synchronous phenomenon. Full annulus unsteady simulations are carried out for two operating conditions to understand the establishment of this phenomenon. To post-process numerical results in detail, a spatial Fourier transform is calculated to determine dominant circumferential wave numbers. Then, a temporal Fourier transform is computed to derive frequencies and velocities in both frames of reference.

2. Fundamentals

In this study, only non-synchronous frequencies are relevant. To isolate these non-synchronous fluctuations, the deviation of temporal signals Δs is calculated by subtracting an ensemble average of the preceding r revolutions from the instantaneous value $s(i, n)$ at sample i and revolution n [18]:

$$\Delta s(i, n) = s(i, n) - 1/r \sum_{m=1}^{r} s(i, n - m). \quad (1)$$

In this work, a sliding ensemble average of 4 rotations is subtracted from experimental and numerical data to keep only the non-synchronous part of the raw data. All frequencies in this paper are normalized by the shaft rotation frequency (f_{rot}) using Equation (2), yielding to Engine Order (EO).

$$f^* = \frac{f}{f_{rot}}(EO). \quad (2)$$

Figure 1 presents two frequency spectra of unsteady wall pressure signal (a) and associated non-synchronous wall pressure fluctuations (b), in the stationary frame of reference. Synchronous and non-synchronous activity is observed in the frequency spectrum (a). The frequency peak corresponding to the blade passing frequency of rotor blades ($f^* = 16EO$) is

clearly visible in the raw data. This peak is not observed after isolating the non-synchronous part as shown in the frequency spectrum (b). Regarding the non-synchronous frequencies (f^* close to 6 and 12EO), their amplitudes are equal in both spectra. By applying this method, non-synchronous frequencies are thus well isolated. All data presented in the following only contain the non-synchronous part of raw data.

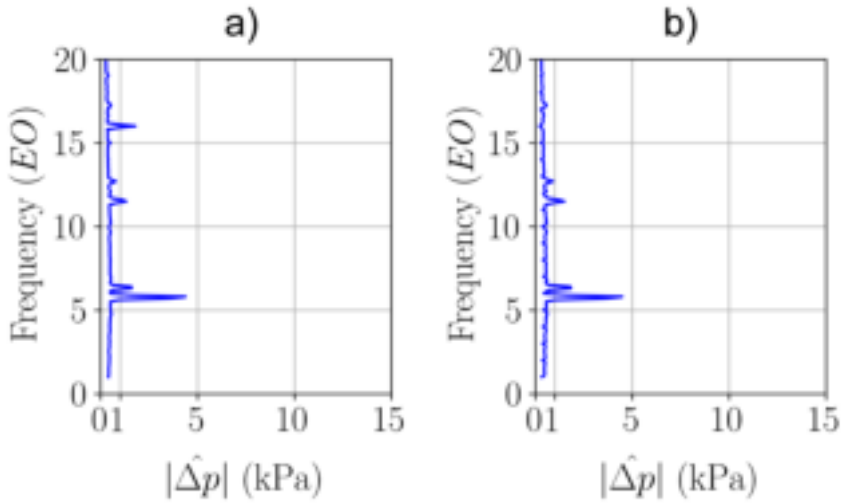

Figure 1. Frequency spectra in the stationary frame of reference of: (**a**) unsteady wall pressure signal; (**b**) non-synchronous wall pressure fluctuations after subtracting a sliding ensemble average of 4 rotations.

A pressure wave can be described in the stationary frame of reference as series of space-time harmonics (N_a, n) as shown in Equation (3), where $P_{N_a,n}$ is the amplitude, $f_n^{*,stat}$ is the normalized frequency in the stationary frame of reference, and $\phi_{N_a,n}^{stat}$ represents the phase:

$$p(r, \theta^{stat}, x, t) = \sum_{N_a=-\infty}^{\infty} \sum_{n=0}^{\infty} P_{N_a,n}(r) e^{i\left(N_a\theta^{stat} - 2\pi f_n^{*,stat} f_{rot} t + \phi_{N_a,n}^{stat}(x)\right)}. \quad (3)$$

For a specific spinning pressure wave in the stationary frame of reference with normalized frequency $f^{*,stat}$, which is traveling around the circumference with circumferential propagating speed c_{prop}^{stat}, it is possible to derive the circumferential wave number $|N_a|$ using Equation (4) [19]. Term Ωr represents the blade velocity at radius r.

$$|N_a| = |f^{*,stat} \frac{\Omega r}{c_{prop}^{stat}}|. \quad (4)$$

It is also possible to established the circumferential organization N_a from Equation (5), where $f^{*,rel}$ and c_{prop}^{rel} correspond respectively to normalized frequency and circumferential propagating speed measured in the rotating frame of reference:

$$N_a = f^{*,rel} \frac{\Omega r}{c_{prop}^{rel}}. \quad (5)$$

The relation between frequencies in both frames of reference is given by Equation (6):

$$f^{*,stat} = f^{*,rel} + N_a. \quad (6)$$

Regarding a structural vibration mode based on blade eigenfrequency $f_{blade}^{*,rel}$, the term Nodal Diameter (ND) is used instead of the circumferential wave number. In contrast to aerodynamic modes, the nodal diameter has to be less than half the number of blades (N_b). If

the structure is in resonance with an aerodynamic mode of $|N_a| > 0.5N_b$, a structural mode traveling in the opposite circumferential direction with $ND = |N_a| - N_b < 0$ develops.

3. Test Case and Experimental Results

3.1. Experimental Setup

The research axial compressor under investigation designed by Safran Helicopter Engines is representative of a modern high-speed multi-stage compressor of helicopter engines. The purpose of the test campaign was to study vibrations in each blade row at off-design operating conditions. The compressor rig is composed of struts, variable Inlet Guide Vanes (IGVs), and three stages, as shown in Figure 2. The stagger angle of IGVs and Stators-1 are varying according to the shaft speed. The presented transient test was conducted at constant part-speed. Thus, stagger angles of both rows are held at fixed position during the experiment. Regarding some specifics of the compressor, the tip clearance of all rotors is lower than 1% of chord, the hub-to-tip ratio lies between 0.6 and 0.8, and the blades aspect ratio evolves between 0.8 and 1.0.

Different measurement systems are available on this test rig. Unsteady pressure measurements are carried out using case-mounted and stator-mounted Kulite transducers. These data are measured in the stationary frame of reference. Blade vibrations of the three rotors are also measured in the rotating frame of reference by using a magnet-coil system [20] and tip-timing technology [21]. The magnet-coil system consists in a small magnet mounted at the rotor tip and a coil installed along the rotor circumference where the voltage induced by the relative motion between both components is measured. Compared to the tip-timing technology, which measures the tip displacement of each rotor blade, vibrations of one blade per row only, is derived by this technique. To derive the circumferential wave number of the vibration pattern (nodal diameter), conventional tip-timing is used. The temporal Fourier transform of the measurement signal of circumferentially distributed optical sensors is calculated to obtain the amplitude of vibration related to structural eigenfrequencies for each blade. Then, a spatial Fourier transform is calculated to obtain the nodal diameter decomposition.

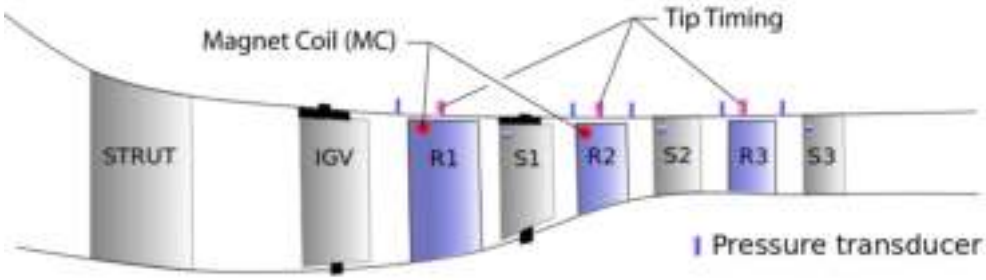

Figure 2. Schematic of Safran Helicopter Engines research compressor.

3.2. Experimental Compressor Characteristic

Non-synchronous phenomena were observed in repeated transient tests at a certain speedline [14,15]. Figure 3 shows the relevant compressor characteristic for the entire rig. Experimental data measured at stabilized operating points are depicted as purple squares. During several transient tests where the throttle is slowly closed towards low mass flow rates, non-synchronous pressure oscillations were observed. The operating conditions where these significant pressure oscillations were measured are shown in Figure 3 (pink and yellow operating points). It is important to notice that these non-synchronous phenomena occur far from the stability limit, unlike the rotating stall or surge. The highest level of amplitude related to the non-synchronous activity was measured in the transient test from operating point OP-A towards the stability limit, thus its analysis is presented in detail in Section 3.3. OP-B and OP-C are two particular operating points, OP-B representing a frequency switch of non-synchronous modes and OP-C representing the onset of signifi-

cant blade vibration, occurring close to numerical condition OP2. Unsteady full-annulus simulations at OP0, OP1, and OP2 are detailed in the numerical of Section 4.

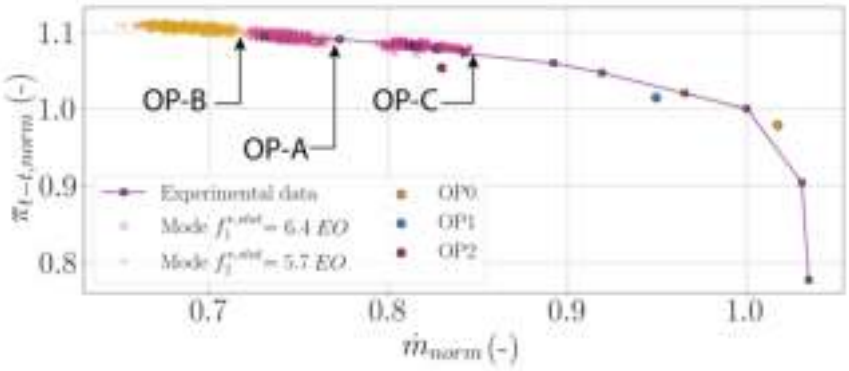

Figure 3. Full compressor characteristic from experiment; indicators for non-synchronous activity in transient experiment ($\times$ and $+$ symbols) and mean averaged performance from unsteady simulations (OP0, OP1, and OP2).

3.3. Transient Test from OP-A to Stability Limit

Figure 4 presents an overview of experimental data measured during the considered transient test at the casing near the leading edge of Rotor-2. The frequency spectrogram of pressure fluctuations (upper part of the figure) reveals several non-synchronous frequencies in the stationary frame of reference. Two phases can be identified in this spectrogram and they are named Phase I and Phase II. Mean average frequency spectra are also plotted in the lower part of the figure for each phase. The change of phase occurs at OP-B, which is identified in Figure 3. During Phase I, a dominant non-synchronous peak at $f_1^{*,stat} = 6.4EO$ is clearly visible. This peak switches from $f_1^{*,stat}$ to $f_2^{*,stat} = 5.7EO$ at the normalized mass flow rate of $\dot{m} = 0.72$. Thus, the pressure peak at $f_2^{*,stat}$ is observed in Phase II. The respective second harmonics of each dominant non-synchronous frequency are also visible in the spectra, as well as the modulation with the blade passing frequency of Rotor-2 ($BPF_{\text{Rotor-2}} = 23EO$). In Phase I, the second harmonic has a frequency of $2f_1^{*,stat} = 12.7EO$ and the modulation peaks are observed at $BPF_{\text{Rotor-2}} \pm f_1^{*,stat}$. During Phase II, the second harmonic of the aerodynamic disturbance presents a frequency of $2f_2^{*,stat} = 11.4EO$. Both peaks resulting of the modulation with the blade passing frequency are identified at $BPF_{\text{Rotor-2}} \pm f_2^{*,stat}$. The amplitude of the non-synchronous pressure oscillations is significant in both phases with a level higher than 8 kPa at the casing near the leading edge of Rotor-2. The switch does not occur instantly, but transiently within a few hundred revolutions, representing a fraction of a second.

This spectral analysis shows that an aerodynamic disturbance identified as a non-synchronous pressure wave of high amplitude, is established in the compressor. During the presented transient test, its frequency changes at operating point OP-B. Moreover, its second harmonic and modulations with the blade passing frequency are still observed. This indicates that the phenomenon is stable and does not change its physical nature between the different phases but its circumferential wave number.

These non-synchronous pressure oscillations are observed in the whole compressor, as shown by Figure 5. It presents the axial evolution of the mean averaged amplitude of the dominant pressure waves for each respective phase. When two wall pressure probes are available at the same axial position, an average of the two probes is computed. The trend between both axial evolutions is identical in Phase I and Phase II. The highest amplitude of around $\approx$13 kPa is reached at Stage-2 and a rapid decay is observed downstream. The lower level of amplitude is measured at the casing near the leading edge of Rotor-1, but

it is still a significant level of more than 1 kPa. The sharp drop in amplitude downstream Stator-2 is discussed in Section 5.

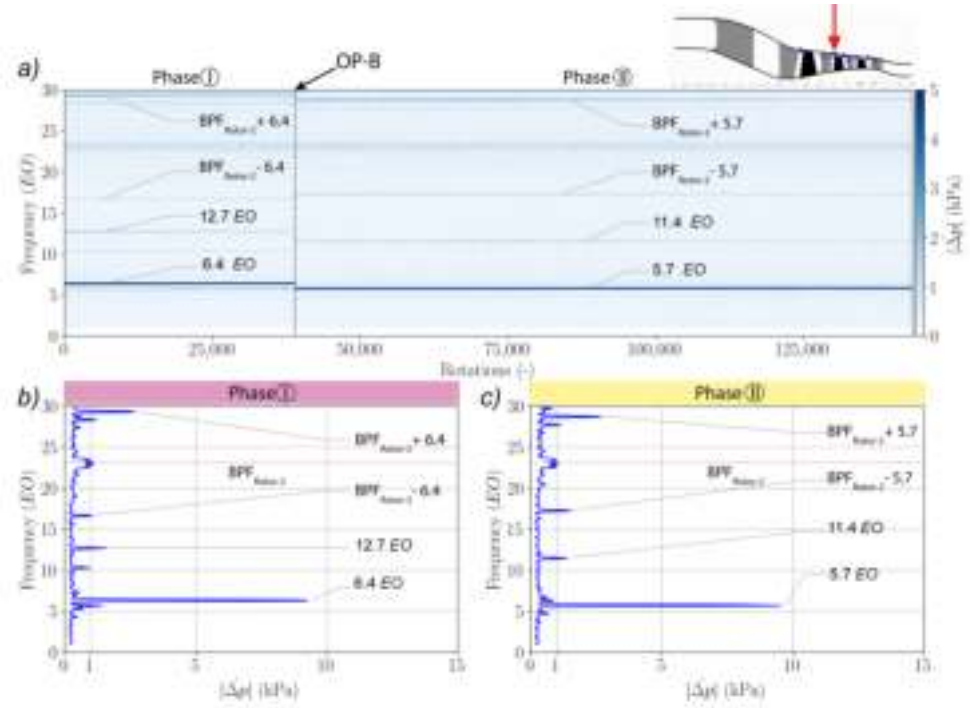

Figure 4. Spectrum analysis of pressure fluctuations measured at the casing near the leading edge of Rotor-2: (**a**) frequency spectrogram during the transient test; (**b**) mean averaged frequency spectrum during Phase I; (**c**) mean averaged frequency spectrum during Phase II .

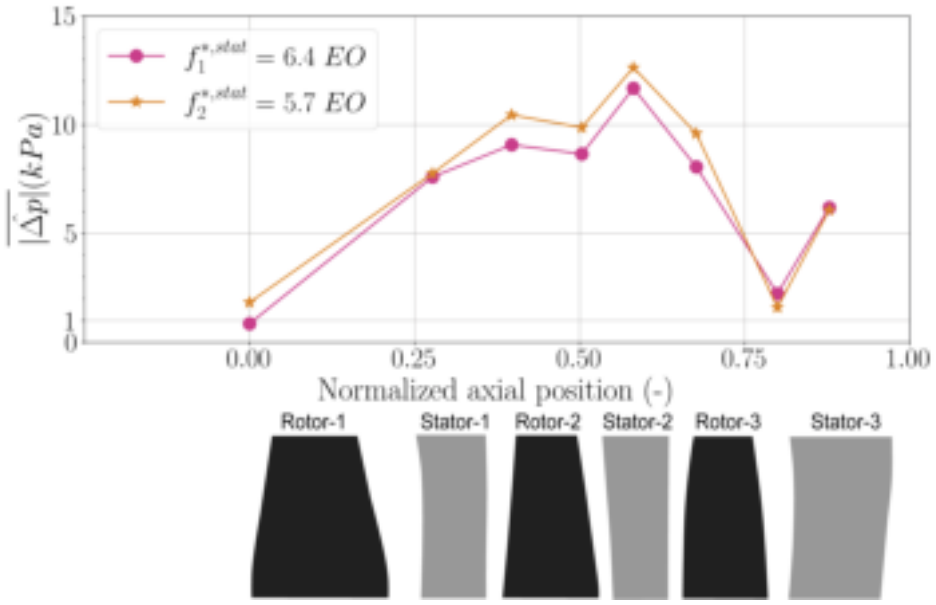

Figure 5. Axial evolution of the mean averaged amplitude of the non-synchronous pressure peak during Phase I and Phase II.

As a conclusion, the considered test reveals the establishment of stable non-synchronous pressure waves of high amplitude in the whole compressor. During the test, two phases are distinguished. The frequency of the non-synchronous pressure mode switches from $f_1^{*,stat} = 6.4EO$ (Phase I) to $f_2^{*,stat} = 5.7EO$ (Phase II). However, the axial evolution of the associated amplitude remains the same between both phases. It is important to note that a

non-synchronous pressure mode similar to the one established during Phase I has been observed at higher mass flow rates from OP-C towards OP-A (see Figure 3).

Tip-timing technology and magnet-coil system enable to measure the rotor blade vibration in the rotating frame of reference. Figure 6 shows the temporal evolution of the vibrating amplitude of three representative blades of Rotor-2. Phase I and Phase II can also be distinguished. A change of behavior occurs at OP-B. A significant level of vibration is measured during Phase I with a mean displacement of 0.3% of the axial chord (≈0.1 mm). In contrast, it decreases rapidly in Phase II and remains at a constant level during this phase. Since the rotor blades are vibrating with a lower amplitude in Phase II while the pressure mode remains at constant level, a self-excited flutter-like phenomenon can be excluded.

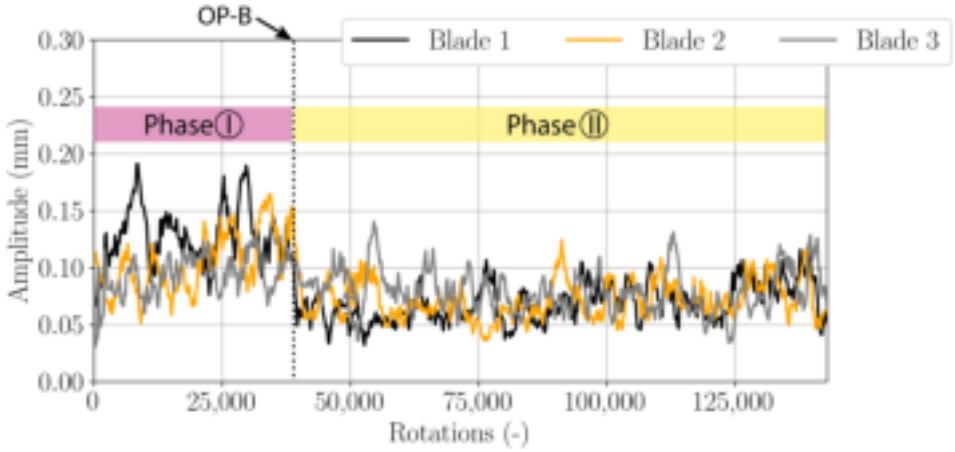

Figure 6. Temporal evolution of the vibrating amplitude for three representative blades of Rotor-2.

Figure 7 presents the frequency spectrogram of the magnet-coil signal of Rotor-2. The frequencies observed in this dataset are measured in the rotating frame of reference. Large amplitudes are clearly observed during the entire test for the first blade eigenmode of Rotor-2 indicated as Mode-1. Its frequency is equal to $f^{*,rel}_{\text{Rotor-2}} = 2.7EO$. Considering the mean averaged frequency spectra, the amplitude of the structural mode Mode-1 decreases slightly from Phase I to Phase II. It is important to note that a non-synchronous activity is also visible in this spectrogram. A very low amplitude peak at $f^{*,rel}_1 = 1.4EO$ in Phase I disappears in Phase II. A peak at $f^{*,rel}_2 = 1.7EO$ is clearly visible in Phase II. This frequency switch occurs at the same instant of the frequency switch observed in the stationary frame of reference (see Figure 4) at OP-B. In Figure 7, a clear frequency peak is also observed at $f^{*,rel} = 0.5EO$ during the entire transient test. The signature resembles that of a rotating stall cell traveling around the circumference with a speed of 50% of rotor speed, however this same signature is not observed in the unsteady wall pressure measurements. Since its amplitude remains constant between both phases, it is not investigated in this work and the peak cannot be explained based on available data. This non-synchronous activity is not related to an eigenmode and its source must be sought in the flow dynamics. At this time, it is necessary to derive the nodal diameter of the structural mode Mode-1 to identify a potential interaction between a pressure mode and blade eigenmode.

The nodal diameter of Mode-1 can be derived from the tip-timing data, which records the tip displacement of each rotor blade. Knowing the tip blade displacement and the vibrating frequency, the nodal diameter of the structural mode is determined. Figure 8 presents the nodal diameter decomposition at the 1st blade eigenfrequency of Rotor-2 (Mode-1) $f^{*,rel}_{\text{Rotor-2}} = 2.7EO$ for both phases. The amplitude of the tip-timing decomposition is normalized by the highest amplitude reached during Phase I, in order to compare both phases. It is obvious that the dominant pattern of the structural mode Mode-1 is equivalent to a nodal diameter of $ND = +10$ during Phase I. A planar pattern ($ND = 0$) is

also observed. In Phase II, the vibration of Rotor-2 blades decreases significantly (comp. Figure 6). The maximal normalized amplitude is strongly reduced by 70%. The nodal diameter decomposition is not conclusive then. However a dominant pattern of $ND = +3$ during this phase could be determined.

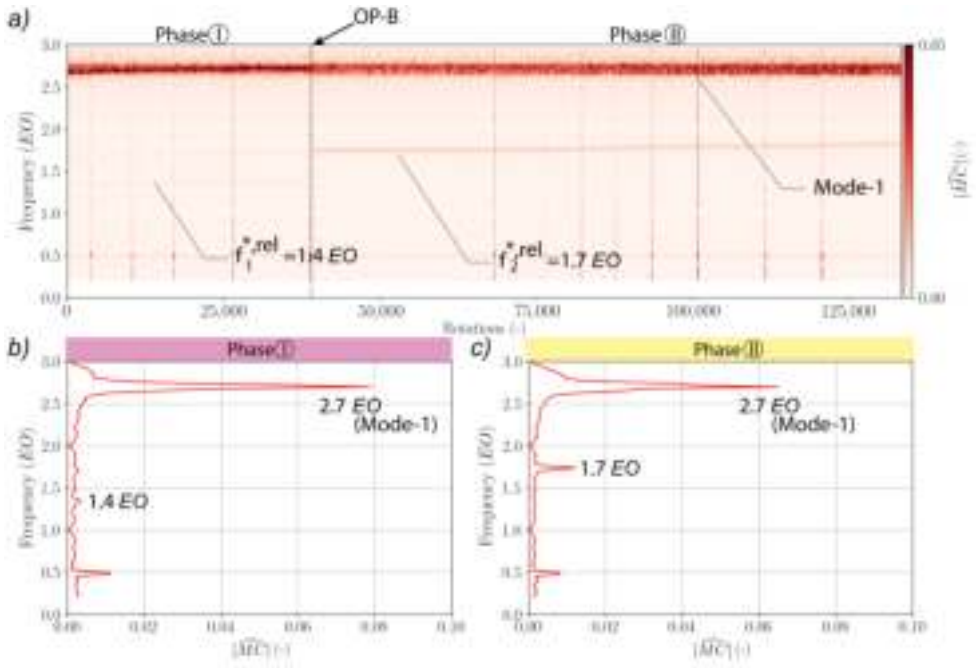

Figure 7. Spectrum analysis of magnet-coil signal of Rotor-2: (**a**) frequency spectrogram during the transient test; (**b**) mean averaged frequency spectrum during Phase I; (**c**) mean averaged frequency spectrum during Phase II.

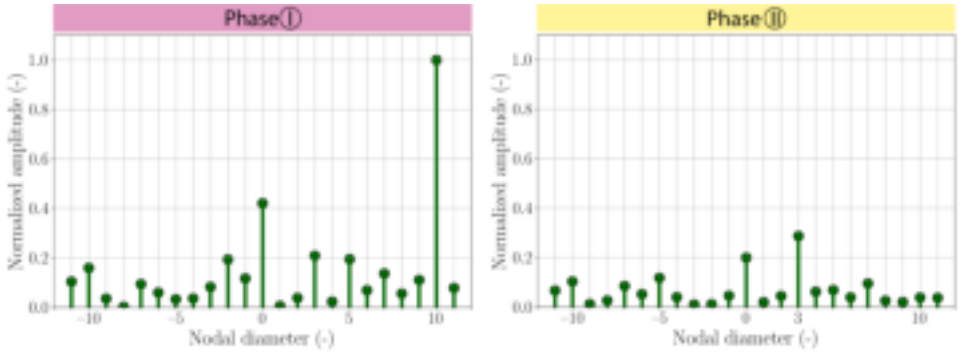

Figure 8. Nodal diameter decomposition, estimated from tip-timing results in Rotor-2 for its 1st blade eigenfrequency $f^{*,rel}_{\text{Rotor-2}} = 2.7EO$ during Phase I and Phase II.

Tip-timing data are also post-processed to get the nodal diameter decomposition for $f_1^{*,rel} = 1.4EO$ and $f_2^{*,rel} = 1.7EO$. As the amplitude of the non-synchronous pressure mode is the highest in Stator-2 (see Figure 5), the tip-timing data of downstream Rotor-3 are used. Figure 9 presents the nodal diameter decomposition at the non-synchronous frequency observed in each phase. The amplitude is normalized as in Figure 8 by the $ND = +10$ value for the 1st blade eigenmode during Phase I. A clear nodal diameter of $ND = +5$ appears in Phase I and it switches to a nodal diameter of $ND = +4$ in Phase II with a similar amplitude.

The circumferential wave number N_a can be derived from a comparison between the stationary and rotating frames of reference regarding Equation (6). Non-synchronous activities have been measured in both frames of reference (see Figures 4 and 7). The

comparison is presented for both phases in Figures 10 and 11. The frequency spectrum in the stationary frame of reference (blue curve) is computed using the unsteady wall pressure signal recorded at the leading edge of Stator-2 at 90% of channel height. The frequency spectrum in the rotating frame of reference (red curve) is derived from the magnet-coil signal measured in Rotor-2.

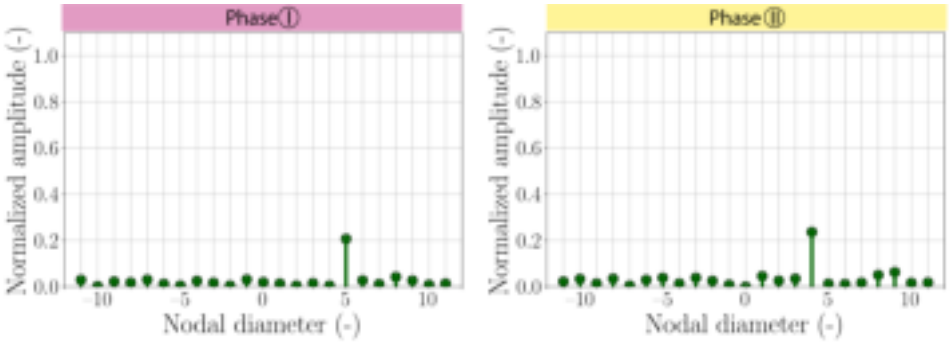

Figure 9. Nodal diameter decomposition, estimated from tip-timing results in Rotor-3 for the dominant non-synchronous frequency in Phase I ($f_1^{*,rel} = 1.4EO$) and Phase II ($f_2^{*,rel} = 1.7EO$).

Several observations from aerodynamic and mechanical data can be dressed from Figure 10:

- A non-synchronous pressure frequency at $f_1^{*,stat} = 6.4EO$;
- Its 2nd harmonic at $2f_1^{*,stat} = 12.7EO$;
- The 1st blade eigenfrequency of Rotor-2 indicated by Mode-1 at $f_{\text{Rotor-2}}^{*,rel} = 2.7EO$;
- The 2nd blade eigenfrequency of Rotor-2 indicated by Mode-2 at $7.2EO$;
- The 3rd blade eigenfrequency of Rotor-2 indicated by Mode-3 at $13.1EO$.

Using Equation (6) and Figure 8, the frequency of Mode-1 in the stationary frame of reference can be derived and is equal to $f_{\text{Rotor-2}}^{*,stat} = f_{\text{Rotor-2}}^{*,rel} + ND = 2.7 + 10 = 12.7EO$. This frequency is visible in the spectrum of unsteady wall pressure signal (blue curve). It is coincident with the 2nd harmonic of the non-synchronous aerodynamic disturbance at $f_1^{*,stat} = 6.4EO$. The non-synchronous excitation of $f_1^{*,rel} = 1.4EO$ presents a pattern of $ND = +5$ (see Figure 9) which corresponds to a frequency in the stationary frame of reference of $f_1^{*,stat} = 1.4 + 5 = 6.4EO$. Hence during Phase I, the pressure wave with a dominant wave number of $N_a = +5$ leads to a non-resonant excitation of the rotor blades at $f_1^{*,rel} = 1.4EO$ and its second harmonic of $N_a = +10$ to a resonant excitation of Mode-1 at $f_{\text{Rotor-2}}^{*,rel} = 2.7EO$, causing the high vibration amplitudes (see Figure 6).

From Phase I to Phase II at OP-B, the occurring aerodynamic disturbance changes its circumferential wave number from $N_a = +5$ to $N_a = +4$ (see Figure 9), and a sharp drop of the vibrating amplitude of Rotor-2 is observed (see Figure 6).

Similar observations noticed in Phase I can be also dressed in Phase II according to Figure 11:

- A non-synchronous pressure frequency at $f_2^{*,stat} = 5.7EO$;
- Its 2nd harmonic at $2f_2^{*,stat} = 11.4EO$;
- a non-synchronous vibrating frequency at $f_2^{*,rel} = 1.7EO$;
- The 1st blade eigenfrequency of Rotor-2 indicated by Mode-1 at $f_{\text{Rotor-2}}^{*,rel} = 2.7EO$;
- The 2nd blade eigenfrequency of Rotor-2 indicated by Mode-2 at $7.2EO$;
- The 3rd blade eigenfrequency of Rotor-2 indicated by Mode-3 at $13.1EO$.

The frequency of Mode-1 in the stationary frame of reference for the most dominant nodal diameter of $ND = +3$ (see Figure 8) is also equal to $f_{\text{Rotor-2}}^{*,stat} = f_{\text{Rotor-2}}^{*,rel} + ND = 2.7 + 3 = 5.7EO$. The non-synchronous excitation of $f_2^{*,rel} = 1.7EO$ presents a pattern

of $ND = +4$ (see Figure 9) which corresponds to a frequency in the stationary frame of reference of $f_2^{*,stat} = 1.7 + 4 = 5.7EO$. Even though this frequency corresponds to the frequency of the occurring aerodynamic disturbance, the circumferential wave number is not coherent between the aerodynamic disturbance ($N_a = +4$) and structural mode ($ND = +3$).

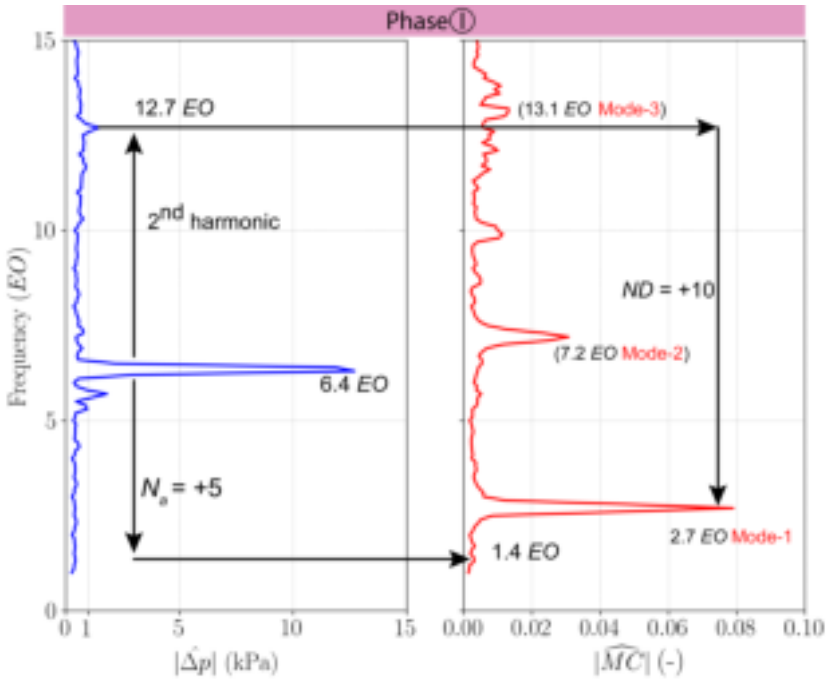

Figure 10. Frequency spectra during Phase I of pressure fluctuations measured at the leading edge of Stator-2 at 90% of channel height in the stationary frame of reference and magnet-coil signal of Rotor-2 measured in the rotating frame of reference.

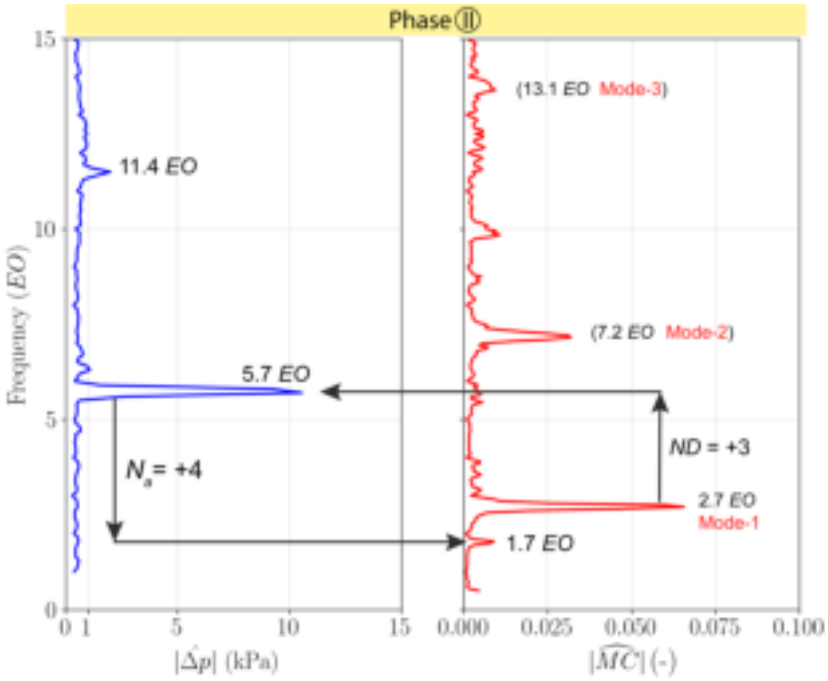

Figure 11. Frequency spectra during Phase II of pressure fluctuations measured at the leading edge of Stator-2 at 90% of channel height in the stationary frame of reference and magnet-coil signal of Rotor-2 measured in the rotating frame of reference.

Table 1 summarizes the characteristics of experimental modes observed as coupled in the transient test. Both the structural mode and pressure mode (2nd harmonic of the acoustic mode) are spinning in the same direction as the rotor with a circumferential speed at the casing higher than the rotor blade speed. This observation indicates that the pressure wave is of an acoustic nature, as the convective phenomena cannot propagate faster than the rotor. The 1st harmonic of this acoustic mode corresponds to a pressure mode with a circumferential wave number of $N_a = +5$ and a frequency in the stationary frame of reference of $f_1^{*,stat} = 6.4EO$.

Table 1. Experimentally observed coupled non-synchronous modes during Phase I.

Observed Mode	Structural Mode 1st Blade Eigenm. Rotor-2	Acoustic Mode 2nd Harmonic Leading Edge Stator-2
	$ND = +10$	$N_a = +10$
$f^{*,stat}(EO)$	12.7	12.7
$f^{*,rel}(EO)$	2.7	2.7
$c^{stat}_{prop}/\Omega r(-)$	1.3	1.3
$c^{rel}_{prop}/\Omega r(-)$	0.3	0.3

Reconsidering Figure 3, it appears that for pink operating points that a co-rotating acoustic mode with $N_a = +5$ and its 2nd harmonic established in the entire machine. Based on tip-timing analysis and magnet-coil data, Rotor-2 develops a structural vibration pattern based on its 1st blade eigenmode, which is coherent with the 2nd harmonic of the acoustic mode. Throttling further (yellow operating points), the circumferential wave number of the acoustic mode changes to $N_a = +4$. Thus, the previous coherence of its 2nd harmonic is lost. As a consequence, the blade vibration of Rotor-2 (see Figure 6) diminishes at the same time while the amplitude of the aerodynamic disturbance remains constant (see Figure 5). Based on this interpretation, the phenomenon is denoted as "Non-Synchronous Forced Response".

4. Numerical Investigation

4.1. Numerical Setup

To reproduce the acoustic resonance observed in the transient test, a numerical investigation is performed at the relevant speedline (see Figure 3). As acoustic modes are observed in the entire compressor, the computational domain includes the IGVs and the three stages, as presented in Figure 12. The downstream experimental nozzle is extended by a convergent nozzle in order to improve numerical stability.

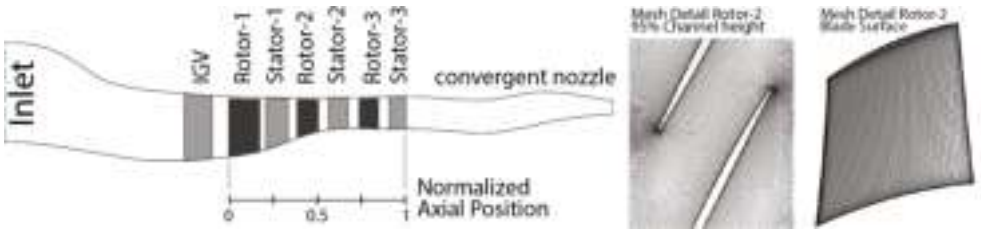

Figure 12. Computational domain for steady and unsteady simulations and detail of Rotor-2 mesh.

The axial and azimuthal wavelengths of observed spinning modes in this work are large: Around 0.8 times the axial length of the compressor and close to 0.2 times the compressor circumference. It has been observed that the circumferential wave number of the acoustic mode is not fixed (it changes from $N_a = +5$ to $N_a = +4$ in the experiment). It is essential not to constrain it by periodic boundary conditions. Thus, full-annulus simulations are required. Moreover pressure modes have to be axially propagative between rows. Hence, sliding meshes are used between stationary and rotating domains instead

of mixing planes. Non-reflective 1-D boundary conditions that specify conservative and turbulent variables are applied at the inlet and outlet of the computational domain.

Numeca AutoGrid5 is used to mesh the domain. The full compressor without struts is modeled with a total number of cells of 133×10^6. Each blade passage of each rotor is meshed with approximately 1.1×10^6 cells. Mesh visualizations of Rotor-2 are also shown in Figure 12.

All simulations are performed using the flow solver *elsA*, an unsteady Reynolds-Average Navier–Stokes (URANS) solver developed by ONERA (Paris, France) [22]. The Roe scheme is used with 2nd order accuracy in space and the turbulence model used is the $k-l$ Smith model. Wall functions are applied to all surfaces ($y^+ \approx 30$). Comparison between results wall resolved versus wall modeled was performed to validate the approach [19]. Simulations are time-accurate using a dual-time stepping scheme with 10 sub-iterations and 1000 physical time steps per rotation. This corresponds to 40 physical time steps per minimal blade passing period. The highest frequency captured according to this temporal discretization is $500EO$, which is more than sufficient for this case. Unsteady full-annulus simulations are initialized with steady single passage simulations with mixing planes. Each calculation is distributed on 700 processors and 40 rotations are calculated to reach a periodic convergence. The computational cost amounts to 385,000 CPU hours for one operating point.

4.2. Simulation Results

Simulations were performed at three operating points, depicted in Figure 3 as OP0, OP1, and OP2. They are respectively located near choke (OP0), near peak efficiency (OP1), and at a mass flow rate where strong non-synchronous pressure oscillations have been measured in the experiment (OP2). The performance of the entire compressor is well predicted by the unsteady simulations but shows a tendency towards a reduced total-pressure rise. Simulations at higher loaded conditions than OP2 diverge due to the establishment of rotating stall cells.

4.2.1. Mean Averaged Results

In [15], steady results were briefly discussed. Figure 13 presents the contours of the average relative Mach number calculated over the four last computed rotations in the whole compressor for the unsteady full-annulus results at OP0, OP1, and OP2. The flow condition in Rotor-3 is transonic. For OP1 and OP2, the relative velocity in Rotor-1 is very low due to the IGV setting, and Rotor-2 is running transonic. The loading of Rotor-2 strongly increases between OP1 and OP2. A thickened boundary layer appears on the suction side of Rotor-2 for OP2. Rotor-3 is highly loaded with far detached shocks. A thickened boundary layer is also observed on the suction side of Rotor-3.

4.2.2. Modal Decomposition

To determine all the non-synchronous modes established in the compressor for the three operating points, it is necessary to derive the axial evolution of circumferential wave number $|N_a|$. The following procedure is applied on the static pressure field at 99.5% of channel height in order to remain in the tip gap but out of the influence region of the wall function. The ensemble average of the four last computed rotations is subtracted from the instantaneous signal to remove rotor periodic phenomena.

According to Equation (3), non-synchronous pressure waves are described as a series of space-time harmonic. To derive circumferential wave numbers $|N_a|$, a spatial Fourier transform is calculated around the circumference at different axial positions for each time step over 4 rotations. The average value of these instantaneous spectra is analyzed to determine the azimuthal organization of non-synchronous pressure modes.

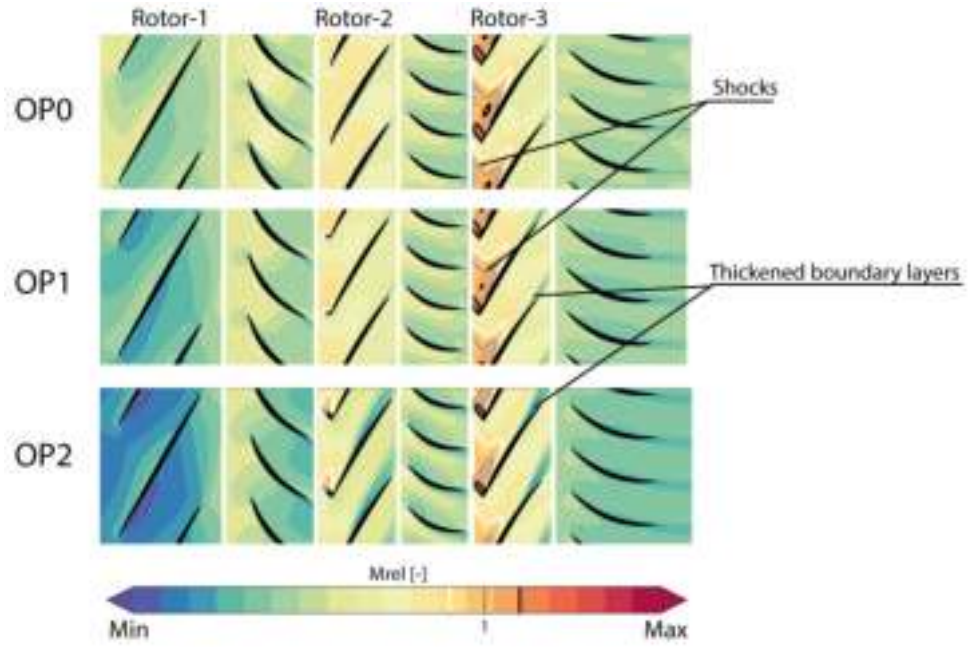

Figure 13. Relative Mach number contours at 80% of channel height for the whole compressor, the mean average of the URANS simulations for OP0, OP1, and OP2. The gray isocontours at low supersonic velocity visualize the shock structure.

The modal decomposition at OP0 reveals small traces of non-synchronous pressure modes between Stage-2 and Stage-3 with an amplitude much lower than 1 kPa. It is considered that OP0 does not experience significant non-synchronous pressure activity.

Figures 14 and 15 shows, respectively, this axial evolution for OP1 and OP2. The leading edge and trailing edge of each rotor are represented by two vertical lines. At OP1, a strong non-synchronous activity is observed in Stage-3. A pressure mode with $|N_a| = 3$ (indicated by letter "A") is clearly identified with a peak in Rotor-3. The associated amplitude is high (≈2 kPa) near Rotor-3 and slightly decays downstream. This pressure mode is not observed upstream of this rotor. Significant peaks at $|N_a| = 20$ and $|N_a| = 26$ are also present in Rotor-3, as indicated respectively by the letters "B" and "C". The pressure mode $|N_a| = 20$ is propagating upstream of the rotor until it reaches the leading edge of Stator-2. The mode $|N_a| = 26$ is only visible in Rotor-3. Both modes indicate a modulation of the non-synchronous pressure mode $|N_a| = 3$ with the number of blades of Rotor-3 ($N_b = 23$) to $N_{a,mod} = N_b \pm |N_a| = 23 \pm 3$ yielding 20 and 26. A last peak is observed at $|N_a| = 15$ located downstream of Rotor-3 and indicated by letter "D". It will not be discussed in this paper.

Figure 15 shows the axial evolution of the circumferential wave number based on a non-synchronous pressure signal at OP2 where strong non-synchronous blade vibrations were measured experimentally (see Figure 3). It is important to note that the pressure scale is 4 times higher than the scale in Figure 14. A clearly dominant circumferential wave number at $|N_a| = 6$ is fully established in the compressor from Stator-1 to Stator-3. This dominant peak is indicated by letter "A". Its 2nd harmonic (letter "B") and its modulations with the number of blades of Rotor-3 (letters "C" and "D") are also visible. The amplitude of the non-synchronous mode at $|N_a| = 6$ is high in Stage-2 and Stage-3.

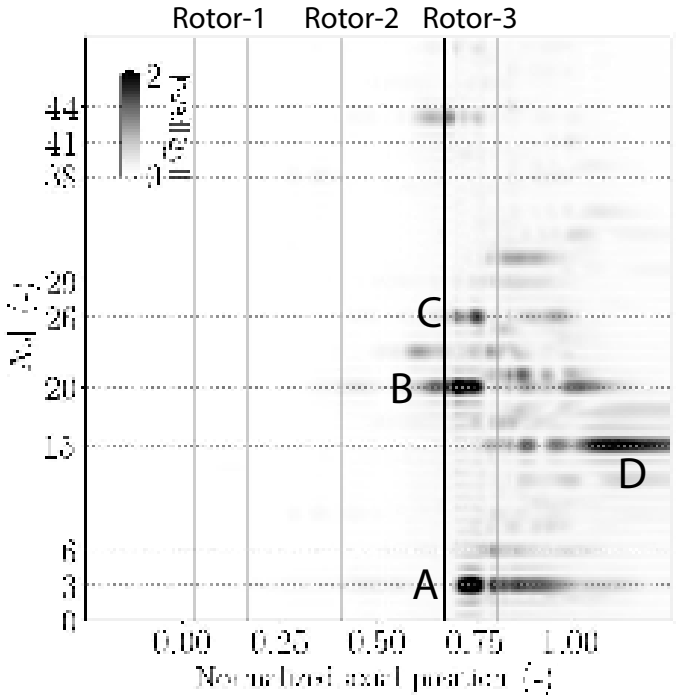

Figure 14. Axial evolution of the circumferential wave number ($|N_a|$) based on the static pressure signal at 99.5% of channel height for OP1.

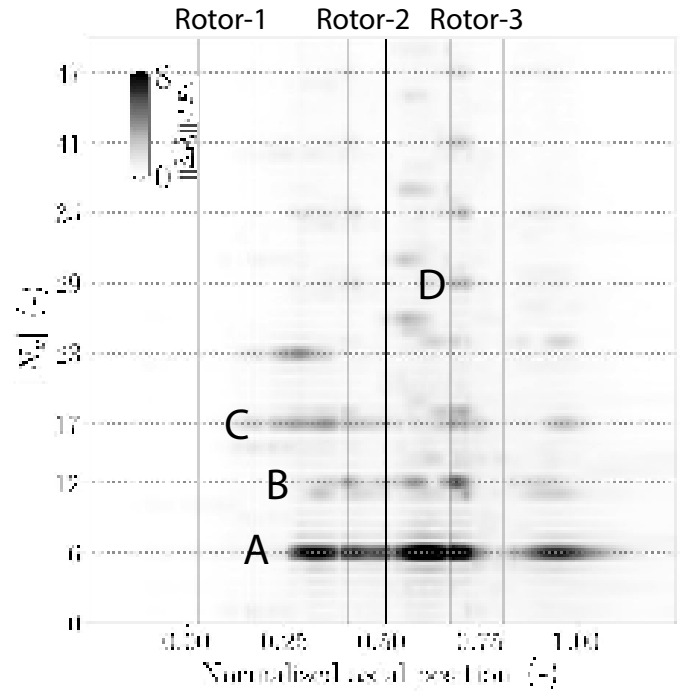

Figure 15. Axial evolution of the circumferential wave number ($|N_a|$) based on the static pressure signal at 99.5% of channel height for OP2.

4.2.3. Characteristics of Non-Synchronous Dominant Modes

To derive frequencies of established modes in both frames of reference, the following decomposition of the non-synchronous pressure field at 99.5% of channel height is applied. First, a spatial filter of the circumferential signal for each individual time step depending on the targeted circumferential wave number ($|N_a|$) is applied. Hence, the temporal evolution of the spatially filtered amplitude is extracted (see Equation (3)). Secondly, the temporal

Fourier transform of this amplitude over 8 rotations is used. The number of 8 rotations improves the frequency resolution. This decomposition applied in a rotor (resp. stator) gives the frequency in the rotating (resp. stationary) frame of reference $f^{*,rel}$ (resp. $f^{*,stat}$).

Figures 16 and 17 presents the axial evolution of the frequency associated to each dominant mode depending on the operating point: Pressure mode with $|N_a| = 3$ for OP1 (see Figure 14) and $|N_a| = 6$ for OP2 (see Figure 15). At OP1, the dominant non-synchronous mode with $|N_a| = 3$ has a frequency of $f^{*,stat} = 2.3EO$ in the stationary frame of reference (highest in Stator-3), as indicated by letter "A" in Figure 16. This dominant mode has also a frequency of $f^{*,rel} = 5.3EO$ in the rotating frame of reference (highest in Rotor-3) as indicated by letter "B". Since $f^{*,stat} < f^{*,rel}$, N_a is equal to -3 according to Equation (6). According to Figure 17, the dominant pressure mode at OP2 with $|N_a| = 6$ presents a frequency in the stationary frame of reference equal to $f^{*,stat} = 6.7EO$ (highest in Stator-2, indicated by letter "A") and a frequency of $f^{*,rel} = 0.7EO$ in the rotating frame of reference (highest in Rotor-3, indicated by letter "B"). In this case $f^{*,stat} > f^{*,rel}$, so N_a is equal to $+6$.

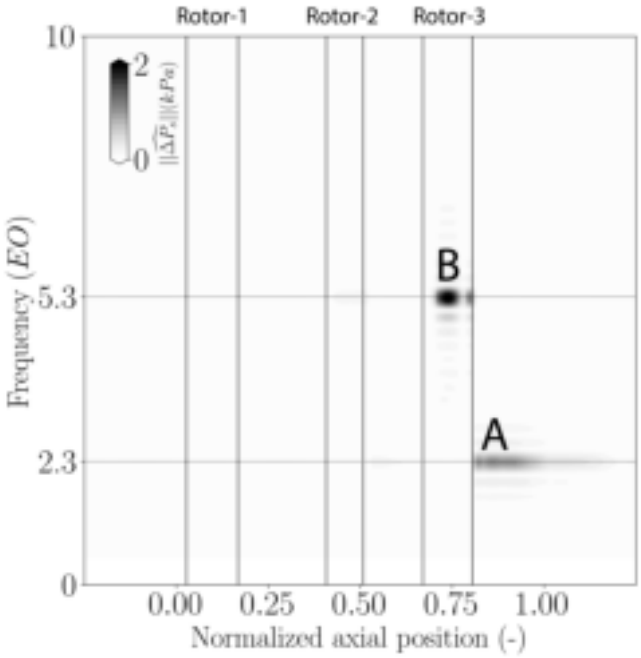

Figure 16. Axial evolution of the frequency of the dominant mode based on static pressure signal at 99.5% of channel height for OP1: Mode at $|N_a| = 3$ ($f^{*,rel}$ in rotors, $f^{*,stat}$ in stators).

Thus, both unsteady full-annulus simulations at OP1 and OP2 develop a dominant non-synchronous pressure mode. Table 2 summarizes the relevant characteristics of each. As the frequencies in both frames of reference are known as well as the circumferential wave number, the circumferential propagating speed can be derived according to Equations (4) and (5). For OP1, a pressure mode with 3 lobes contra-rotating in the stationary frame of reference is observed in the simulations as illustrated in Figure 18 which represents a snapshot of the simulation after reaching periodic convergence. This 3-lobes pressure mode stronger in Rotor-3 is visible at each time instant of the simulation in Stage-3. No significant non-synchronous activity is observed upstream at this stage in the pressure signal. At OP2, the dominant pressure mode corresponds to 6 lobes which are co-rotating in the stationary frame of reference. This 6-lobes pressure mode is clearly distinguished in Figure 19 over Stator-1, Stage-2, and Stage-3. It is highest in Stage-2. Both modes do not propagate with a typical convective speed but are of an acoustic nature since they travel with a speed, which is opposite or higher than the rotor speed in the stationary frame of reference. Thus, the circumferential speed exceeds the speed of sound relative to the mean flow $c^{stat}_{prop} - v_\theta$, according to Table 2.

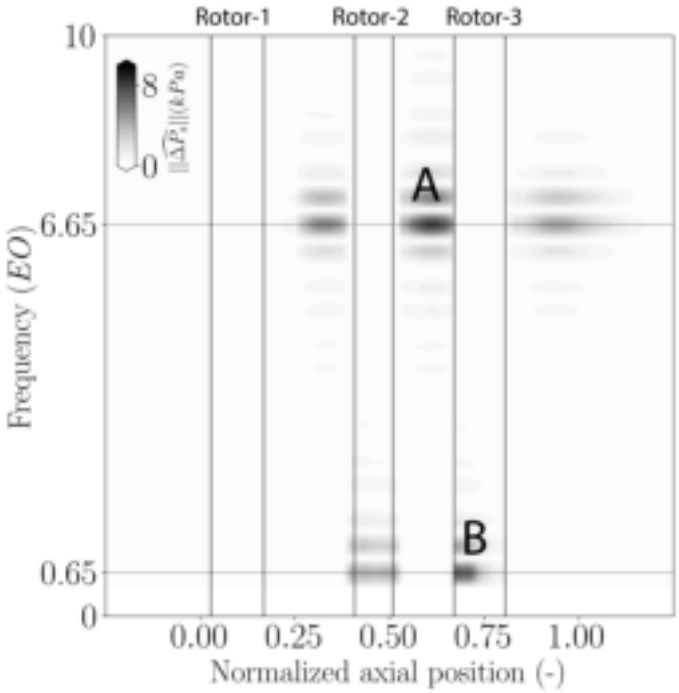

Figure 17. Axial evolution of the frequency of the dominant mode based on static pressure signal at 99.5% of channel height for OP2: Mode at $|N_a| = 6$ ($f^{*,rel}$ in rotors, $f^{*,stat}$ in stators).

Table 2. Numerical dominant non-synchronous modes.

Operating Point	OP1	OP2
N_a	-3	+6
$f^{*,stat}$	2.3	6.7
$f^{*,rel}$	5.3	0.7
$c^{stat}_{prop}/\Omega r$	-0.8	1.1
$c^{rel}_{prop}/\Omega r$	-1.8	0.1
$(c^{stat}_{prop} - v_\theta)/c$	1.03	1.02

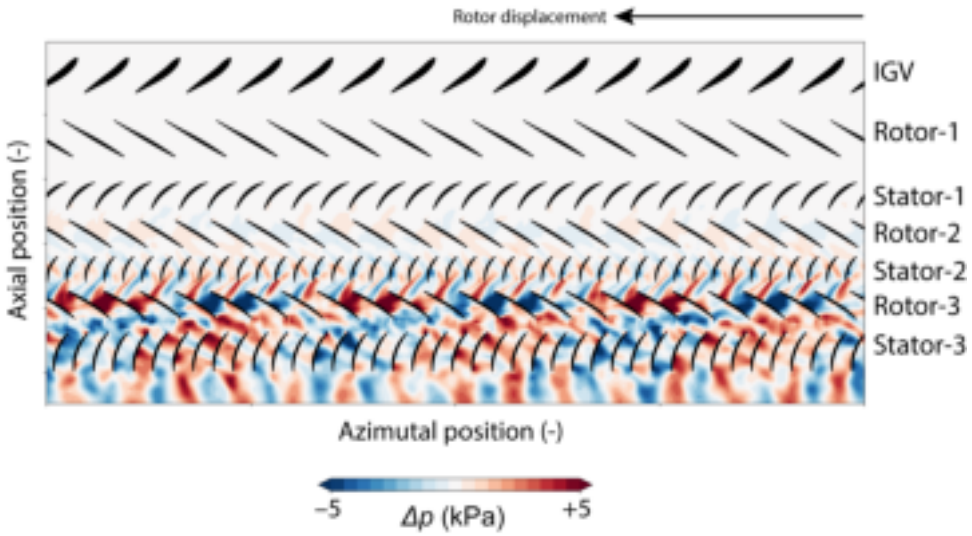

Figure 18. Snapshot of unsteady non-synchronous pressure fluctuations at OP1 at one time instant after periodic convergence at 80% of span.

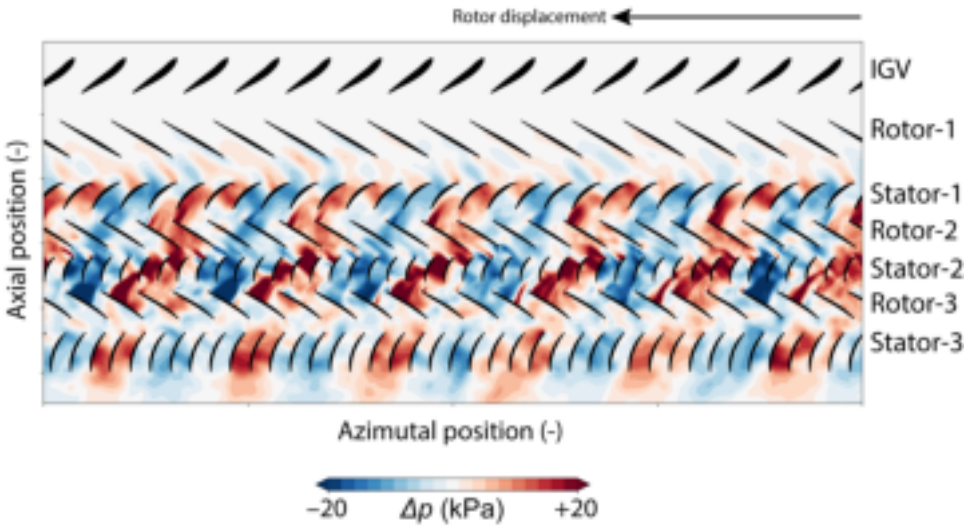

Figure 19. Snapshot of unsteady non-synchronous pressure fluctuations at OP2 at one time instant after periodic convergence at 80% of span.

4.2.4. Lock-In between Aerodynamic Disturbances and Acoustic Modes

As the two operating points reveal the establishment of high amplitude acoustic modes, it is relevant to observe how these modes affect the flow field in Stage-2 and Stage-3. Figure 20 compares the axial Mach number in the axial plane at 20% of chord in Rotor-2 and Rotor-3 for the two operating points at a representative instant. It clearly shows how the flow is mostly undisturbed at OP1, compared to OP2. For OP1, the dominant circumferential wave number of $N_a = -3$ is invisible in Rotor-2 and only slightly observed in Rotor-3. A weak flow separation is present on the suction side of Rotor-3. At the higher loaded operating point OP2, the dominant circumferential wave number of $N_a = +6$ is much stronger. It is radially extended from the hub to the casing in both rotors. In Rotor-3, a large separation zone on the suction side is observed near the hub. Hence, the lock-in phenomenon can be interpreted as a resonance between a swirling acoustic mode, which reaches high amplitudes in the axial gap between the rotor and stator, and a fluctuating boundary layer in the highly loaded rotor, which serves as an energy source. Thus, the dominant circumferential wave number depends on the acoustic propagation conditions.

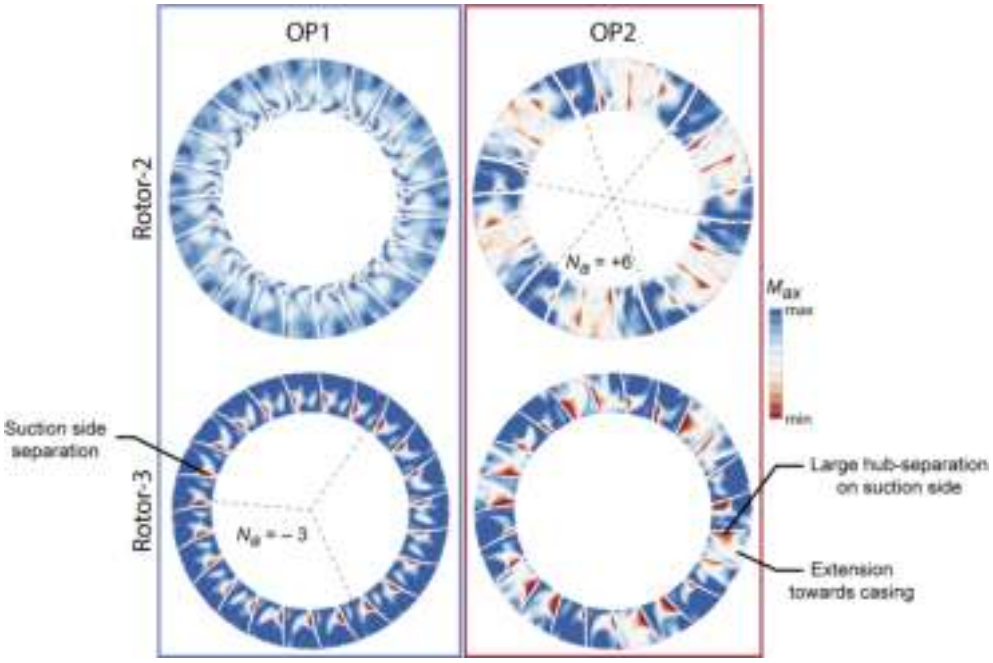

Figure 20. Axial Mach number at 20% of chord in Rotor-2 and Rotor-3 for OP1 and OP2.

5. Comparison and Discussion

The axial evolution of the modal amplitude of the dominant pressure mode at OP2 is presented in Figure 21 for the experiment ($N_a = +5$, $f^{*,stat} = 6.4EO$, see Figure 10) and the simulation ($N_a = +6$, $f^{*,stat} = 6.7EO$, see Figure 17), along the amplitude of the dominant mode ($N_a = -3$, $f^{*,stat} = 2.3EO$, see Figure 16) observed at OP1. These evolutions are determined at the casing. The coherence between experimental and numerical results at OP2 is remarkable. The circumferential wave number is not the same (experiment $N_a = +5$ and simulation $N_a = +6$), nevertheless the modal amplitude extracted from simulation is in good agreement with the experiment. At OP1, the non-synchronous activity appears only in Stage-3.

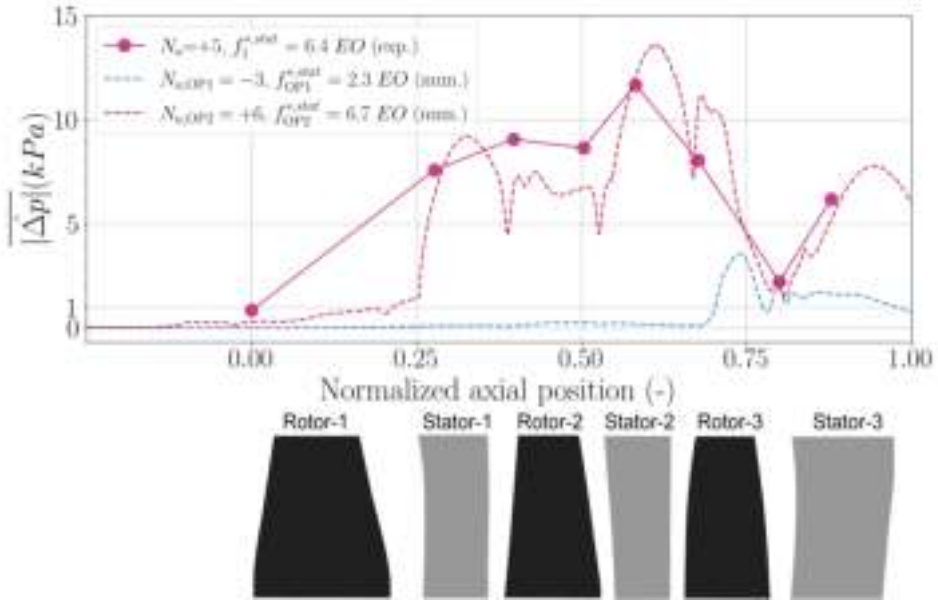

Figure 21. Axial evolution of the amplitude associated to dominant non-synchronous pressure mode, experimental results during Phase I and numerical results at OP1 and OP2.

As Rotor-3 is the most sensitive rotor, Figure 22 presents the evolution of the cut-on frequency depending on the circumferential wave number [23]. Flow conditions used to compute this frequency are derived from simulations. This evolution is given upstream (blue curve) and downstream (red curve) of this rotor. Experimental and numerical acoustic modes are depicted with symbols. The evolution of the 1st eigenfrequency of Rotor-2 blades in the stationary frame of reference according to Equation (6) is drawn as a black curve.

Three important observations can be made:

- All occurring modes, both experimentally and in simulations, are propagative only in one axial direction. Co-rotating modes ($N_a > 0$) are cut-on only upstream, while contra-rotating modes ($N_a < 0$) are cut-on only downstream;
- At highly-loaded conditions OP2, the modes in the experiment and simulations are clustered in the wave-number and frequency ($N_a = +4, +5$ and $+6$);
- Coincidence of the second harmonic at $N_a = +10$ of an acoustic mode at $N_a = +5$ with the structural blade-eigenfrequency leads to significant non-synchronous forced response in the experiment during Phase I. As soon as the mode switches to $N_a = +4$ in Phase II, the vibration amplitude drops as the excitation at $N_a = +8$ is far off resonance.

It is impossible that a self-excited phenomenon (as flutter) is present, as the bladed disk vibration cannot excite a sub-harmonic acoustic mode. This is confirmed in the experiment by the fact that after the wave number changes, the acoustic pressure amplitude remains constant however the vibration diminishes. The reason behind the inaccurate prediction of the wave number of the acoustic mode ($N_a = +6$ versus $N_a = +5$) cannot be explained clearly from the results. The first assumption is that the numerical resolution (spatial and temporal) is not sufficiently accurate to predict the correct wave number. Secondly, a specific wave number can be preferred in the experiment due to geometrical asymmetry and structural mistuning. As the cut-on conditions are sensitive to the flow field in Rotor-2 and Rotor-3, a slight inaccuracy in the simulation can shift the critical frequencies and also enforce the development of the next integer wave number.

Nevertheless, these observations are of importance for the interpretation of experiments, the setup of simulations, and the development of countermeasures. The acoustic propagation conditions upstream and downstream of a rotor that is highly loaded and sensitivity to external feedback determine the development of critical modes. These propagation conditions can be estimated from averaged flow values from experiments or RANS simulations, which are usually performed during the design phase of a multistage compressor. Typically the range of modes, which are propagative only in one axial direction is narrow as depicted in Figure 22. If structural vibration occurs and the eigenfrequency is known, possible interaction can be assessed as presented. Obviously, harmonics of dominant-trapped modes need to be taken into account if amplitudes are significant. Countermeasures must primarily aim to reduce the sensitivity of the rotor-aerodynamics. Typical measures, such as mistuning, will not be efficient for the observed case, as it is not a coupled phenomenon, like flutter or convective NSV [5]. Mistuning is generally considered detrimental for forced-response problems. For this configuration, a full annulus multistage setup was required to reproduce the phenomenon in simulations. Special attention needs to be laid on boundary conditions interacting with acoustic modes. The presented results indicate that the mismatching of the compressor with significant overloading of Rotor-3 is responsible for the emergence of unsteadiness. The actual process observed leading to trapped acoustic modes is then a symptom that cannot be avoided; there will always be room for cut-on/cut-off modes and coincidence with structural eigenmodes is always possible. Design must focus on the avoidance of operating conditions and lead to the excitation of trapped acoustic modes. The focus of the presented study was on the physical explanation of what happens if these conditions occur. Typical procedures to stabilize part-speed operation focus on IGV scheduling, however the study shows that very complex phenomena can occur at a stable aerodynamic performance.

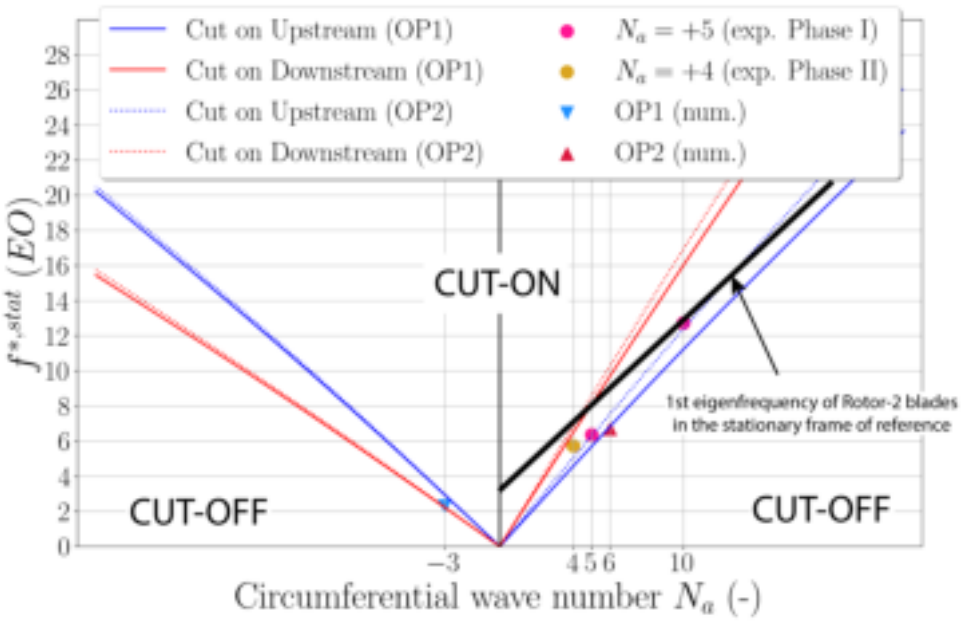

Figure 22. Frequency and circumferential wave number of acoustic modes in the experiment and simulation, as well as the cut-on conditions upstream and downstream of Rotor-3.

6. Conclusions

During repeated test campaigns, significant non-synchronous activity was measured in a research axial multi-stage compressor at part-speed for moderately loaded operating points.

High-amplitude acoustic modes were observed in multiple stages of the machine. The source for the acoustic mode was identified in a highly loaded downstream stage, in which the phase of local flow separations lock-in with an upstream-propagating acoustic mode.

In the experiment, coincidence between the second harmonic of the dominant acoustic mode and a structural vibration eigenmode leads to a severe non-synchronous forced response.

Using unsteady full-annulus simulations, the phenomenon is reproduced. Slight differences in the wave number are observed, however amplitude and frequency of the dominant mode are well captured. Results indicate that an estimation of critical modes can be made based on acoustic propagation conditions derived from experiments or steady RANS calculations.

Author Contributions: Conceptualization, A.-L.F. and C.B.; methodology, A.-L.F. and C.B.; validation, S.A., N.B.; formal analysis, investigation, A.-L.F., C.B. and A.V.; writing—original draft preparation, A.-L.F.; writing—review and editing, S.A. and C.B.; visualization, A.-L.F.; supervision, N.B., S.A. and C.B. All authors have read and agreed to the published version of the manuscript.

Funding: This research was funded by Safran Helicopter Engines.

Data Availability Statement: Not applicable.

Acknowledgments: The authors thank Safran Helicopter Engines (Safran Goup) for permission to publish these results. We are truly grateful for the technical advice and the comments of Jacques Demolis of Safran Helicopter Engines during the preparation of this paper. We would also like to thank Nick Cumpsty of the Imperial College London for the helpful discussions on this work. This work was granted access to the HPC resources of CINES under the allocation 2019-A0052A07410 made by GENCI and to the HPC resources of CCRT.

Conflicts of Interest: The authors declare no conflict of interest.

Abbreviations

The following abbreviations are used in this manuscript:

IGV	Inlet Guide Vane
MC	Magnet-coil
NSV	Non-Synchronous Vibrations
ND	Nodal diameter
EO	Engine Order $[-]$
c	Speed of sound $[\mathrm{m{\cdot}s^{-1}}]$
c_{prop}	Circumferential propagating speed $[\mathrm{m{\cdot}s^{-1}}]$
f_{rot}	Shaft rotation frequency [Hz]
ΔP_s	Pressure fluctuations [Pa]
M_{ax}	Axial Mach number $[-]$
M_{rel}	Relative Mach number $[-]$
N_a	Circumferential wave number $[-]$
N_b	Number of blades $[-]$
Ω	Rotational speed $[\mathrm{rad{\cdot}s^{-1}}]$
r	Radius [m]
v_θ	Absolute tangential velocity $[\mathrm{m{\cdot}s^{-1}}]$
$\hat{.}$	Fourier coefficient
$.^{stat}$	Stationary frame of reference
$.^{rel}$	Rotating frame of reference

References

1. Baumgartner, M.; Kameier, F.; Hourmouziadis, J. Non-Engine Order Blade Vibration in a High Pressure Compressor. In Proceedings of the Twelfth International Symposium on Airbreathing Engines, Melbourne, Australia, 10–15 September 1995.
2. Jüngst, M.; Holzinger, F.; Leichtfuss, S.; Schiffer, H.-P. Analysing non-synchronous blade vibrations in a transonic compressor rotor. In Proceedings of the 11th European Conference on Turbomachinery, Madrid, Spain, 23–27 March 2015.
3. Kielb, R.E.; Barter, J.W.; Thomas, J.P.; Hall, K.C. Blade Excitation by Aerodynamic Instabilities: A Compressor Blade Study. In *Turbo Expo: Power for Land, Sea, and Air*; American Society of Mechanical Engineers: Atlanta, GA, USA, 2003.
4. Möller, D.; Jüngst, M.; Holzinger, F.; Brandstetter, C.; Schiffer, H.-P.; Leichtfuss, S. Mechanism of Nonsynchronous Blade Vibration in a Transonic Compressor Rig. *J. Turbomach.* **2017**, *139*, 011002. [CrossRef]
5. Stapelfeldt, S.; Brandstetter, C. Non-synchronous vibration in axial compressors: Lock-in mechanism and semi-analytical model. *J. Sound Vib.* **2020**, *488*, 115649. [CrossRef]
6. Brandstetter, C.; Paoletti, B.; Ottavy, X. Acoustic and Convective Mechanisms Contributing to Non-Synchronous-Vibrations in a Multistage Compressor. In *Turbo Expo: Power for Land, Sea, and Air*; American Society of Mechanical Engineers: Phoenix, AZ, USA, 2019.
7. Marshall, J.G.; Imregun, M. A review of aeroelasticity methods with emphasis on turbomachinery applications. *J. Fluids Struct.* **1996**, *10*, 237–267. [CrossRef]
8. Brandstetter, C.; Jüngst, M.; Schiffer, H.-P. Measurements of Radial Vortices, Spill Forward, and Vortex Breakdown in a Transonic Compressor. *J. Turbomach.* **2018**, *140*, 061004. [CrossRef]
9. Cooper, A.J.; Peake, N. Trapped acoustic modes in aeroengine intakes with swirling flow. *J. Turbomach.* **2000**, *419*, 151–175. [CrossRef]
10. Hellmich, B.; Seume, J. Causes of Acoustic Resonance in a High-Speed Axial Compressor. In *Turbo Expo: Power for Land, Sea, and Air*; American Society of Mechanical Engineers: Barcelona, Spain, 2006.
11. Holzinger, F.; Wartzek, F.; Schiffer, H.-P.; Leichtfuss, S.; Nestle, M. Self-Excited Blade Vibration Experimentally Investigated in Transonic Compressors: Acoustic Resonance. *J. Turbomach.* **2015**, *138*, 041001. [CrossRef]
12. Parker, R. Acoustic resonances and blade vibration in axial flow compressors. *J. Sound Vib.* **1984**, *92*, 529–539. [CrossRef]
13. Tyler, J.M.; Sofrin, T.G. *Axial Flow Compressor Noise Studies*; SAE Technical Paper; University of Leeds: Leeds, UK, 1962; Volume 620532.
14. Fiquet, A.-L.; Brandstetter, C.; Aubert, S.; Philit, M. Non-Engine Order oscillations in an axial multi-stage compressor—Aeroacoustic interaction. In Proceedings of the 15th International Symposium on Unsteady Aerodynamics, Aeroacoustics and Aeroelasticity of Turbomachines, Oxford, UK, 24–27 September 2018.
15. Fiquet, A.-L.; Brandstetter, C.; Aubert, S.; Philit, M. Non-Synchronous Aeroacoustic Interaction in an Axial Multi-Stage Compressor. *J. Turbomach.* **2019**, *141*, 101013. [CrossRef]
16. Fiquet, A.-L.; Buffaz, N.; Vercoutter, A.; Aubert, S.; Brandstetter, C. Acoustic resonance in an axial multistage compressor leading to non-synchronous blade vibration. In Proceedings of the 14th European Conference on Turbomachinery Fluid dynamics and Thermodynamics, Gdansk, Poland, 12–16 April 2021.

17. Fiquet, A.-L.; Buffaz, N.; Vercoutter, A.; Aubert, S.; Brandstetter, C. Non-synchronous forced response due to trapped acoustic modes in an axial multi-stage compressor. In Proceedings of the ASME Turbo Expo 2020, London, UK, 22–26 September 2020.
18. Brandstetter, C.; Paoletti, B.; Ottavy, X. Compressible Modal Instability Onset in an Aerodynamically Mistuned Transonic Fan. *J. Turbomach.* **2019**, *141*, 031004. [CrossRef]
19. Fiquet, A.-L. Analyse et Modélisation de Phénomènes Aéroélastiques Non-Synchrones dans un Compresseur Axial Multi-étages. Ph.D. Thesis, École Centrale de Lyon, Lyon, France, 2021.
20. Garnier, J.; Vercoutter, A.; Talon, A. Magnet-Coil measurement technology for analyzing turbomachine blade vibrations. In Proceedings of the Surveillance-8, Roanne, France, 20–21 October 2015.
21. Bouchain, A.; Picheral, J.; Lahalle, E.; Vercoutter, A.; Burgardt, B.; Talon, A. New Possibilities for Analyzing Complex Asynchronous Blade Vibrations From Tip-Timing Data Using a Sparse Spectral Analysis Method. In *Turbo Expo: Power for Land, Sea, and Air*; American Society of Mechanical Engineers: Phoenix, AZ, USA, June 2019.
22. Cambier, L.; Heib, S.; Plot, S. The Onera *elsA* CFD software: Input from research and feedback from industry. *Mech. Ind.* **2013**, *14*, 159–174. [CrossRef]
23. Camp, T.R. A Study of Acoustic Resonance in a Low-Speed Multistage Compressor. *J. Turbomach.* **1999**, *121*, 36–43. [CrossRef]

International Journal of
Turbomachinery
Propulsion and Power

MDPI

Article

A Low Order Flow Network Model for Double-Wall Effusion Cooling Systems †

Michael van de Noort * and Peter Ireland

Department of Engineering Science, University of Oxford, Oxford OX1 3PJ, UK; peter.ireland@eng.ox.ac.uk
* Correspondence: michael.vandenoort@eng.ox.ac.uk
† This paper is an extended version of our paper published in Proceedings of the European Turbomachinery Conference ETC14 2021, Paper No. 666, Gdansk, Poland, 12–16 April 2021.

Abstract: The high pressure turbine nozzle guide vane of a modern aeroengine experiences large heat loads and thus requires both highly effective internal and external cooling. This can be accomplished with double-wall effusion cooling, which combines impingement, pin-fin and effusion cooling. The combination of three cooling mechanisms causes high pressure losses, increasing potential for the migration of coolant towards low pressure regions, subsequently starving effusion holes on the leading edge of coolant supply. This paper presents a low order flow network model to rapidly assess the pressure and mass flow distributions through such cooling schemes for a flexible set of geometric and flow conditions. The model is subsequently validated by a series of experiments with varying mainstream pressure gradients. Results from the model are used to indicate design parameters to reduce the effect of coolant migration, and to minimise the risk of destructive hot gas ingestion.

Keywords: coolant migration; flow networks; double-wall effusion cooling

check for updates

Citation: van de Noort, M.; Ireland, P. A Low Order Flow Network Model for Double-Wall Effusion Cooling Systems. *Int. J. Turbomach. Propuls. Power* **2022**, *7*, 5. https://doi.org/10.3390/ijtpp7010005

Academic Editor: Francesco Martelli

Received: 9 December 2021
Accepted: 31 January 2022
Published: 2 February 2022

Publisher's Note: MDPI stays neutral with regard to jurisdictional claims in published maps and institutional affiliations.

Copyright: © 2022 by the authors. Licensee MDPI, Basel, Switzerland. This article is an open access article distributed under the terms and conditions of the Creative Commons Attribution (CC BY-NC-ND) license (https://creativecommons.org/licenses/by-nc-nd/4.0/).

1. Introduction

Studies into the thermal efficiency of gas turbines have come to the consensus that the specific fuel consumption can be improved by increasing the turbine entry temperature. To maximise this benefit, modern aeroengines use TETs well in excess of the turbine components' melting temperatures. Cooling systems are required to prevent component failure, but these reduce power output by reducing the air available for combustion and causing mixing losses in the turbine, which reduce aerodynamic efficiency. Double-wall effusion cooling is viewed as a potential solution to these challenges—the high porosity make-up of the system brings it close to the goal of accomplishing micro-cooling. Bunker [1,2] noted that mirco-cooling has two goals—"spread[ing] out the cooling network in a series of smaller and highly distributed channels" and "bringing the cooling fluid closer to the outer surface of the airfoil". This is accomplished by combining three commonly used cooling techniques—impingement cooling, pin-fin cooling and effusion (or film) cooling, with features densely packed to spread out the coolant, and double-walled to allow coolant to sit close to the outer surface.

Figure 1 shows an example of double-wall effusion cooling being employed in a modern commercial engine turbine blade. This combination of cooling techniques leads to high convection cooling efficiency (1) and overall cooling effectiveness (2), but also produces high pressure losses.

$$\eta_{conv} = \frac{T_{c,e} - T_{c,i}}{T_m - T_{c,i}} \tag{1}$$

$$\varepsilon_o = \frac{T_\infty - T_m}{T_\infty - T_{c,i}} \tag{2}$$

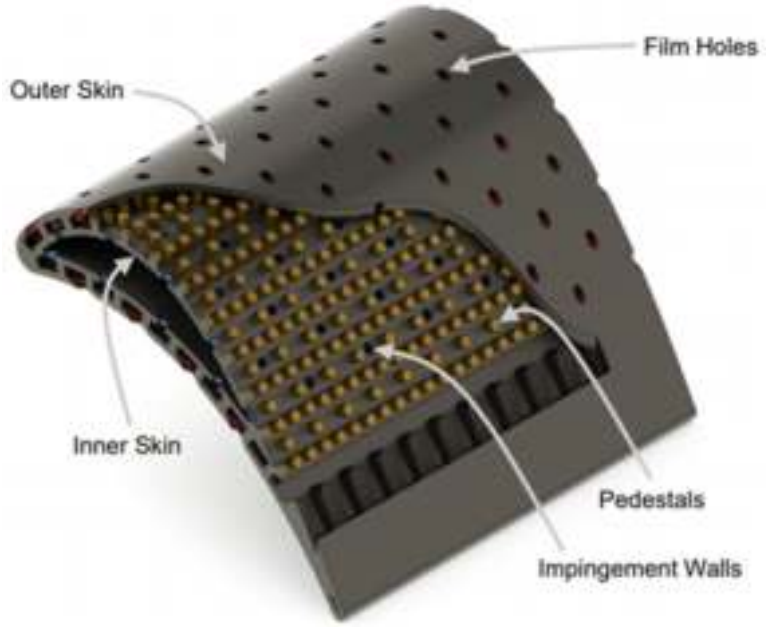

Figure 1. Turbine blade using double-wall effusion cooling scheme—From Murray et al., 2017 [3]. Used with Permission.

The high pressure losses caused by combining three cooling schemes can make double-wall effusion cooling systems vulnerable to coolant migration—the movement of coolant in the pedestal cavity toward low pressure regions under the influence of an external pressure gradient. Coolant migration can be particularly concerning in components where the coolant supply to mainstream stagnation pressure ratio is low—the main example of this being the Turbine's High Pressure NGV, where the mainstream stagnation pressure is only ~3% less than that of the coolant supplied from the HP Compressor. In a configuration such as that shown in Figure 1, where the cavity between the walls is continuous along both surfaces, the streamwise pressure gradient will lead to coolant in the cavity migrating away from the LE sections and toward film holes further along the PS and SS. Spanwise pressure gradients can have similar effects, causing cooling coolant to move from the hub to the tip. Results produced by Holgate et al. [4] showed that for an engine representative NGV, the external static pressure coefficient C_p (3) could fall from -0.2 to -1.2 along the early suction surface alone—given the small pressure margin at the leading edge, this provides a major driving force for coolant migration.

$$C_p = \frac{P_{ext} - P_{ext,\,max}}{\left(\frac{1}{2}\rho_\infty {U_\infty}^2\right)_{throat}} \tag{3}$$

To combat coolant migration, recent patented designs using this cooling scheme (e.g., [5,6]) use walls across the span of the cavity to create separate cooling zones for the PS, LE and SS, but this reduces the effectiveness of pin-fin cooling due to reduced throughflow and turbulence generation.

Coolant migration can have severely detrimental impacts on the film cooling effectiveness in both the region the coolant migrates away from and the region it migrates to. If coolant migration is high enough, the region losing coolant can essentially be starved, leading to destructive hot gas ingestion, which will eventually cause component failure. In the region that the coolant migrates to, a high pressure margin across the outer skin causes film hole flows to be ejected into the mainstream with high velocity, potentially leading to jet-lift off. In both regions, film cooling effectiveness would be significantly reduced, so the component would experience much greater heat loads and would likely have a much

shorter operating life. Predicting and controlling coolant migration is key to ensuring the proper development of a coolant film for external cooling.

This paper summarizes work done to model coolant migration within double-wall effusion cooling systems under the influence of mainstream pressure gradients, done through the use of low order flow network models (LOMs). The LOM developed is a high speed, iterative solver that produces mass flow and pressure distributions throughout cooling arrays for given boundary conditions. This allowed assessment of a high number of design possibilities that would've been too computationally expensive to do in a time-efficient manner using CFD.

2. Related Work

2.1. Double-Wall Effusion Cooling Systems

Research has been conducted into the application of double-wall effusion cooling systems since the 1970s, but their application in modern engines is limited due to issues of manufacturing difficulty and high thermomechanical stresses. As transpiration cooling research is becoming more prevalent, double-wall effusion cooling has become a topic of increased interest—the high manufactured porosity, complex internal flow field, and low film hole blowing ratio lead to such schemes being dubbed as "quasi-transpiration" cooling by Murray et al. [3], who conducted a series of computational tests to find the effects of various geometric parameters on the thermomechanical stresses developed. Increases of the passage height, pedestal diameter and hole diameters were shown to reduce the average thermomechanical stress, as did reducing the pedestal spacing.

Flow travelling through arrays of pedestals can undergo high pressure loss due to the wakes generated behind the pedestals. Research by Chyu et al. [7] and Siw et al. [8] showed that staggered arrays of pedestals caused much greater pressure drops than in-line arrays. The pedestal shape can also have a large influence—cylindrical pedestals produce less pressure loss than those of square or diamond (square rotated by 45°) shapes [7], but also produce lower HTCs.

Bamba et al. [9] found experimentally that in regions where pin-fins did not significantly obstruct the passage of flow from impingement to film hole entry, such as at the LE, the contribution of the pin-fins to the pressure loss was negligible. In these regions, pedestals enhance cooling only by increasing the surface area over which heat transfer can take place.

The dominant form of pressure loss in these systems, however, is from impingement cooling. Andrews et al. [10] stated that "for impingement/effusion applications it is ... valid to assume that all the pressure loss would occur at the impingement plate". Greater pressure losses generally equate to increased cooling performance, as is the case for pin-fin arrays.

Murray et al. [11] conducted a comprehensive study of the effect of the cooling scheme's porosity on its performance. Higher porosity geometries (particularly those with high porosity in the walls) required less coolant mass flow for a given pressure drop and exhibited "relatively high cooling effectiveness" at low coolant flow rates. The authors suggested cooling around the blade could be optimised by varying the porosity as required—high pressure drop regions (i.e., the SS) should use low porosity cooling geometries to minimise aerodynamic losses, whilst areas such as the PS should use higher porosity geometries for increased coolant flow and better effusion cooling performance.

Wambersie et al. [12] conducted experimental tests using high-porosity panels, inspired by transpiration-cooling designs. Whilst these panels gave exceptionally high film effectiveness levels at standard blowing rates, at low flow rates the low pressure margin made the panels susceptible to mainstream flow ingestion, localised to certain regions as a result of high streamwise and spanwise pressure gradients.

2.2. Flow Networks

The models developed for this paper were based on flow network solvers developed by Rose [13], and later by Kutz and Speer [14]. In these systems, flow networks were produced by creating lists of nodes, each representing a specific point in the cooling system. Nodes are connected by links, along which fluid is allowed to flow, forming a network of connected nodes. Boundary nodes form the inlet and outlet of flow within a network. In order to solve for the flow through a network, the law of mass conservation is applied at each internal node—for a node i connected to n nodes j, the governing equation is given by (4) The mass flow rate along a link connecting nodes i and j is determined by Equation (5) where the function $f_{i,j}$ is used to model the three-dimensional flow as one-dimensional. Kutz and Speer [14] expanded from solving for continuity to account for the heat transfer along each link $\dot{Q}_{i,j}$ by making use of the energy equation, adding another governing Equation (6) at each node. This network approach was applied to a full secondary air system, and results for the rear sealing chamber air pressure were in good agreement with engine test results.

$$\sum_{j}^{n} \dot{m}_{i,j} = 0 \tag{4}$$

$$\dot{m}_{i,j} = f_{i,j}(P_i, P_j, T_i) \tag{5}$$

$$\sum_{j}^{n} \dot{m}_{i,j} h_{i,j} + \dot{Q}_{i,j} = 0 \tag{6}$$

Using a similar methodology, Ebenhoch and Speer [15] produced a network solver that was applied to three test cases; isothermal flow in a multipass blade cooling system, coolant flow undergoing high heat transfer in a hypersonic vehicle nozzle, and coolant flow in a rotating HP blade. This flexible network solver was deemed to have "sufficient accuracy in predicting coolant mass flow, regional coolant side heat transfer coefficients, and local coolant temperatures".

Gouws et al. [16] created a network solver for a modern combustor that, once calibrated with experimental data, predicted the mass flow splits through cooling holes with high accuracy. Heat transfer elements within the network allowed a prediction of the outlet temperature distribution. It was found that in a cooling system with large numbers of cooling holes, discharge coefficients had a high influence on one-dimensional flow and pressure drop predictions.

Jin et al. [17] used a compressible flow network analysis to find the mass flow distribution for the various positions around the trailing edge of an HP turbine blade, as part of an investigation into blade oxidation. This investigation revealed that an inlet metering plate at the blade root reduced the coolant internal pressure, raising the risk of hot gas ingestion, particularly in "off-design or transient conditions". The network allowed testing and recommendation of changes to reduce this risk.

3. Modelling Methodology

3.1. Flow Network Construction

The LOM presented focused only on mass flow continuity and was based on test cases without heat transfer and in incompressible conditions. This allowed the temperature of each node to be neglected, with the model solving only for the pressures at each node. Newton's method (see [18]) was used to iteratively solve for the internal pressure distribution. Static pressures at each node served as the list of unknowns, which could then be used to calculate mass flows through the network. In these conditions, the mass flow $\dot{m}_{i,j}$ along a link between nodes i and j becomes a function only of the link's compliance, $C_{i,j}$, and the pressure difference between the nodes, such that:

$$\dot{m}_{i,j} = C_{i,j} \cdot f_{i,j}(P_i - P_j) \tag{7}$$

The geometries discussed in this paper used a staggered arrangement of film holes and impingement holes, such that no holes of the same type were located next to one another—this layout is the same as shown in Figure 1. The standard flow network layout is shown for a single row of holes and pedestals in Figure 2—in the case of there being multiple rows, further nodes would be located into the page, with impingement and film holes alternating left/right positions. The position of each node has three components: position in the streamwise direction, level in the cooling system (1 at the bottom, 5 at the top), and spanwise row number. Other than for nodes on the pedestal layer (Level 4), all nodes on the same layer are of the same type. Links are created based on the physical flow paths available from each node's position, so flow is allowed to transfer to nodes on the same level only on Level 4—the other levels only have links to nodes directly above or below.

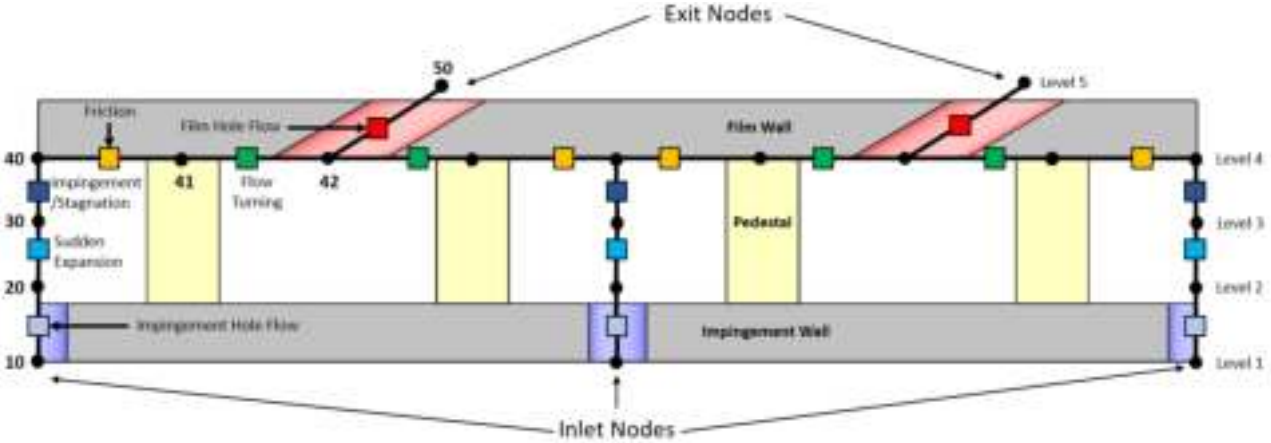

Figure 2. Flow network diagram for a single row.

The number label for each node determines its type:

- 10: Impingement Hole Entry/Inlet Nodes. Boundary nodes with fixed pressure.
- 20: Impingement Hole Exit Nodes. Node pressure is representative of the flow as it leaves the hole.
- 30: Impingement Point Nodes. Nodes represent the point at which flow stagnates on the inner surface of the outer wall as the jet flow from the hole impinges.
- 40: Expansion from Impingement Nodes. Represents flow as it accelerates away from the impingement points, but before it interacts with any pedestals. In the diagram, this point is represented as being above the impingement point for ease of display.
- 41: Post Pedestal Nodes. Frictional pressure losses due to pedestals are modelled in the link between nodes 40 and 41.
- 42: Film Entry Hole Nodes. As noted in Figure 2, these nodes are only used in the case when the film hole inclination is not 90°—when film holes are perpendicular, the 42 nodes are merged with linked 41 nodes. When holes are inclined, flow from one direction turns by a different angle than flow from the opposite direction, requiring the use of a different dynamic head loss coefficient.
- 50: Film Hole Exit Nodes. Boundary nodes with fixed pressure.

The mass flow functions $f_{i,j}(P_i - P_j)$ and compliances $C_{i,j}$ are dependent on the type of link. Flow through a hole, occurring for impingement holes between Levels 1 and 2, and occurring for film holes between Levels 4 and 5, allows the discharge Equation (8) to be used—all holes of both types are cylindrical in this geometry. In cases where high coolant migration and thus an uneven outlet flow distribution is expected, it is unreasonable to assume that all film holes will have similar discharge coefficients. To account for this, the discharge coefficient for each hole was updated in each iteration. The two pressure values from the previous iteration were used to calculate the area-averaged velocity through the

hole. This velocity, the pressure ratio across the hole and geometric properties were used to calculate an updated discharge coefficient using a correlation developed by Mazzei et al. [19]. This was applied to both impingement and film holes. The area ratios β_i and β_f use a square inlet area with a side length of half the hole pitch, and the expansibility factor ε is taken as unity as the air is assumed to be incompressible.

$$\begin{aligned} \dot{m}_l &= \frac{C_{d,i}}{\sqrt{1-\beta_i{}^4}} \varepsilon \frac{\pi {d_i}^2}{4} \sqrt{2\rho} \sqrt{P_{10} - P_{20}}, \\ \dot{m}_f &= \frac{C_{d,f}}{\sqrt{1-\beta_f{}^4}} \varepsilon \frac{\pi {d_f}^2}{4} \sqrt{2\rho} \sqrt{P_{42} - P_{50}} \end{aligned} \tag{8}$$

The connection between Levels 2 and 3 represents the sudden expansion of flow area, when flow leaves the impingement hole and enters the inter-wall cavity. At Level 3, flow is expected to stagnate as it impinges on the outer wall, allowing the form of the Bernoulli equation shown in (9). to be used—this features a loss coefficient $k_{l,ex}$ to account for sudden expansion pressure loss.

$$P_{20} + \frac{1}{2}\rho {U_{20}}^2 - \frac{1}{2} k_{l,ex} \rho {U_{20}}^2 = P_{30} \ \therefore \ \dot{m} = \sqrt{P_{30} - P_{20}} \sqrt{\frac{\rho A^2}{\frac{1}{2}(1 - k_{l,ex})}} \tag{9}$$

To account for the total pressure loss produced by a jet impinging on a wall, a similar loss equation is used for the link between Levels 3 and 4. A single node is used in this position at Level 4, as it assumed that there is no circumferential variation in total pressure loss due to impingement.

$$P_{30} = P_{40} + \frac{1}{2}\rho {U_{40}}^2 + \frac{1}{2} k_{l,i} \rho {U_{40}}^2 \ \therefore \ \dot{m} = \sqrt{P_{30} - P_{40}} \sqrt{\frac{\rho A^2}{\frac{1}{2}(1 + k_{l,i})}} \tag{10}$$

Equation (11) accounts for flow around pedestals on Level 4 between nodes 40 and 41. The friction factor f for flow around pedestals is determined by the correlation developed by Wang [20].

$$\dot{m} = \sqrt{P_{40} - P_{41}} \sqrt{\frac{\rho A^2 D_h}{2fL}}, \ f = 1.76 {Re_{max}}^{-0.318} \tag{11}$$

When turning flows are employed, the mass flow between nodes 41 and 42 is given by (12). For turning flows, loss coefficients were selected from studies by Miller [21]. In cases with close packed pedestals, (11). is replaced by a flow coefficient in the same form as (12), as pressure losses become functions of impingement onto pedestals and turning between them, rather than by friction. This equation uses the assumption that A_{41} is larger than A_{42}.

$$\begin{aligned} P_{41} + \tfrac{1}{2}\rho {U_{41}}^2 &= P_{42} + \tfrac{1}{2}\rho {U_{42}}^2 + \tfrac{1}{2} k_{l,t} \rho {U_{42}}^2 \\ \therefore \ \dot{m} &= \sqrt{P_{41} - P_{42}} \sqrt{\frac{2\rho {A_{41}}^2 {A_{42}}^2}{{A_{41}}^2 (1 + k_{l,t}) - {A_{42}}^2}} \end{aligned} \tag{12}$$

3.2. Computational Implementation

The LOM was produced in MATLAB (MathWorks—Natick, MA, USA), using summations for the mass flows out of nodes described in the equations above, as in (4). The initial guess of pressures through the network was selected to ensure that pressure drops and rises occurred along the links that were expected. To enhance the stability of the model, changes between iterations were damped. The value of the damping factor ζ used was 0.5 in simpler models, such as the geometry featured in Figure 3, but more complex geometries or high mainstream pressure gradients often required ζ to be reduced further. This slowed convergence of the model, though the solving time remained on the order of seconds, a huge reduction from CFD cases. Convergence of the LOM was attained when the maximum absolute value of mass flow imbalance at any node was less than 10^{-12} kg/s.

An additional mass flow check was performed by comparing the inlet and outlet total mass flows.

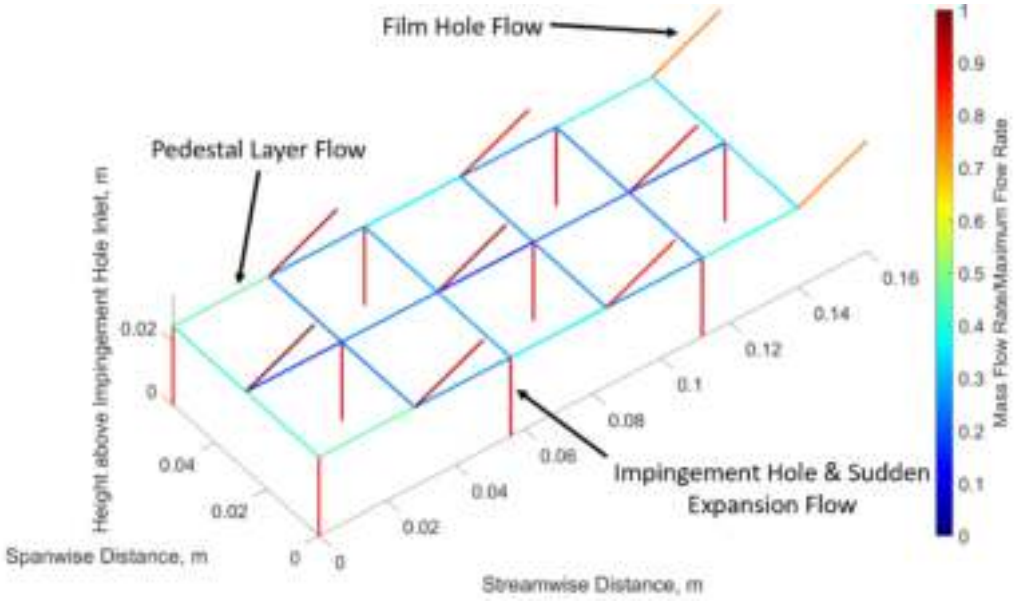

Figure 3. Example results from the LOM.

3.3. Example Results

Figure 3 shows a set of example results for the LOM. Flow paths are contoured by their mass flow rate. In this test case, all film holes are ejecting to the same outlet pressure, and all impingement holes have the same inlet pressure. Despite this, the film holes in the central row (2nd spanwise position) clearly have larger outlet flows than those in the outer rows. The position of the impingement holes leads to film holes at the right end (highest streamwise distance) of the array each having ~75% of the coolant flow that each film hole in the centre receives. The unevenness in the outlet flow distribution is not matched at the inlet—the two impingement holes at the left end of the array (lowest streamwise distance) are the most poorly fed, but receive only 5% less flow than those in the centre of the array. The size of this array and the inclination angle of the film holes are flexible—this particular test case size is '6 × 3', with six hole positions in streamwise direction and three in the spanwise direction. The film hole angle of inclination is 30°.

4. Computational Methodology

CFD simulations in ANSYS Fluent (Ansys—Canonsburg, PA, USA) were used alongside the development of the model for early tests of performance, and to produce some loss correlations where the literature was unable to provide. These tests were run largely in a '2 × 2' test case size, featuring only two impingement holes, two film holes (inclined at 90°), and the pedestals that would feature in the flow paths between these positions. An example fluid domain for use in CFD is shown in Figure 4.

Based on previous studies, the realizable $k - \varepsilon$ model was chosen for turbulence modelling. Fluid density was made to vary according to the ideal gas law, thermal conductivity by kinetic theory, and viscosity by the Sutherland model. Simulations were run such that all flow velocities were well below a Mach Number of 0.3, allowing results from the incompressible LOM solver to be compared. To ensure a y^+ of close to unity on all surfaces, inflation prism layers were used along all walls. Each inflation had 15 layers and a growth rate of 1.2, with a maximum total thickness of 10% of the hole diameter used.

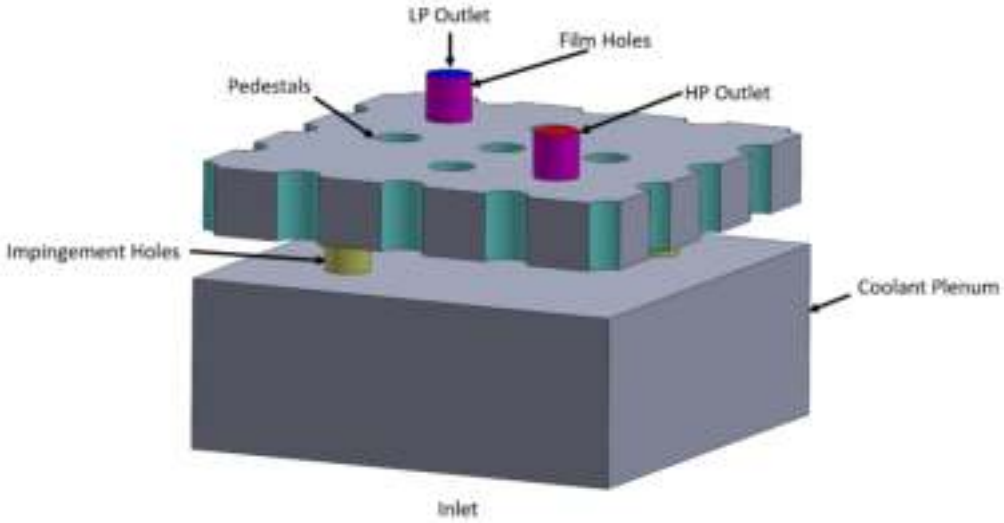

Figure 4. Fluid domain for CFD fluid domain.

To ensure sufficient mesh refinement, a mesh independence study was performed. The two quantities used to judge mesh independence were the total mass flow through the system and the coolant migration factor (13), the derivation of which is discussed further in Section 6.2. For the study conducted, the inlet pressure was set at 1.03 bar, the HP Outlet at 1.0 bar, and the LP Outlet at 0.99 bar. The inlet temperature was 300 K, and all walls were set as adiabatic. Results of the mesh independence study are shown in Figure 5 giving a mesh size of approximately 3.5 million elements.

$$CMF = \frac{\Delta \dot{m}}{2\dot{m}_{in}} \tag{13}$$

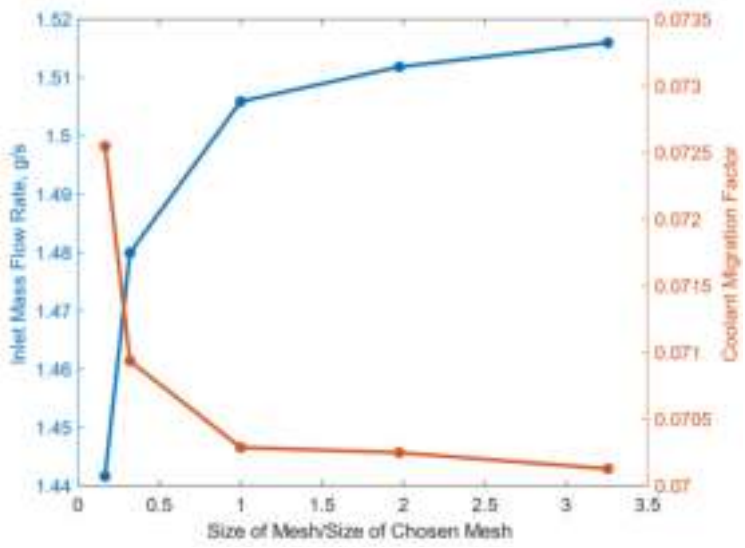

Figure 5. Mesh independence study results.

5. Experimental Methodology

5.1. Experimental Set-Up

To validate the results of the LOM, a simple experimental rig consisting of a Bosch ALS 25 Blower/Vacuum [22], test piece, and six outlet pipes with orifice plates was constructed—this rig was named the 'Blower Rig'. For these experiments, two test pieces were used, D3 and D6. A cut-out diagram of these is shown in Figure 6b. Figure 6a shows the diagram of a unit block of both test pieces—many of these combined to give a 'wall block' with six

rows of holes, each with four impingement holes and four effusion holes in a staggered formation (a size of '8 × 6'). Total lengths were 248 mm in the streamwise direction and 178 mm in the spanwise direction (both including edge walls). A CAD diagram of the test section is shown in Figure 7. Flow from the blower enters the inlet plenum, contained behind the test piece, and is then forced through the test piece to one of six outlet channels, which are connected by hoses to pipes with orifice plates. Each outlet channel corresponds to one spanwise hole pitch and covers the whole streamwise extent of the test piece. At the entrance to said pipes, valves are used to restrict the flow, creating a spanwise pressure gradient. Mass flow rates from each channel are calculated using pressure measurements taken at either side of the orifice plates. Additional pressure tappings are located at the inlet and in the plenum, and at the end of each outlet channel. For this validation, the LOM was expanded to add links for flow leaving the film holes to collect at the channel exit—the point at the end of the channel serves as the new pressure boundary condition for the LOM.

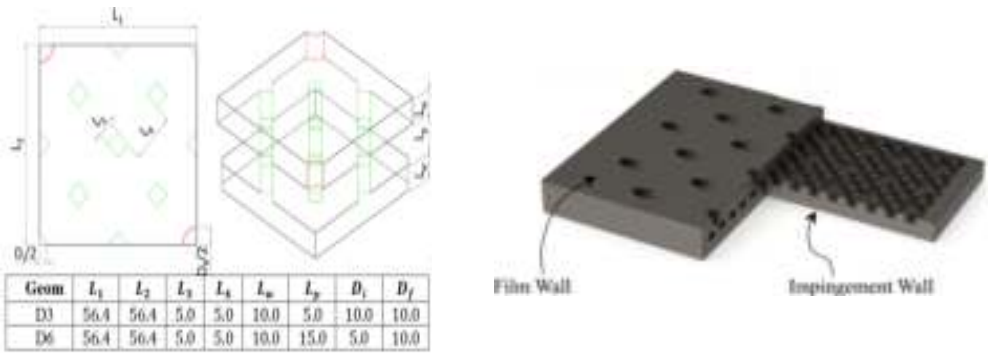

Geom	L_1	L_2	L_3	L_4	L_w	L_y	D_i	D_f
D3	56.4	56.4	5.0	5.0	10.0	5.0	10.0	10.0
D6	56.4	56.4	5.0	5.0	10.0	15.0	5.0	10.0

(**a**) (**b**)

Figure 6. Test piece diagrams from Murray et al. [11]: (**a**) Unit block layout with dimensions. (**b**) Sectioned 3D model. Used with Permission.

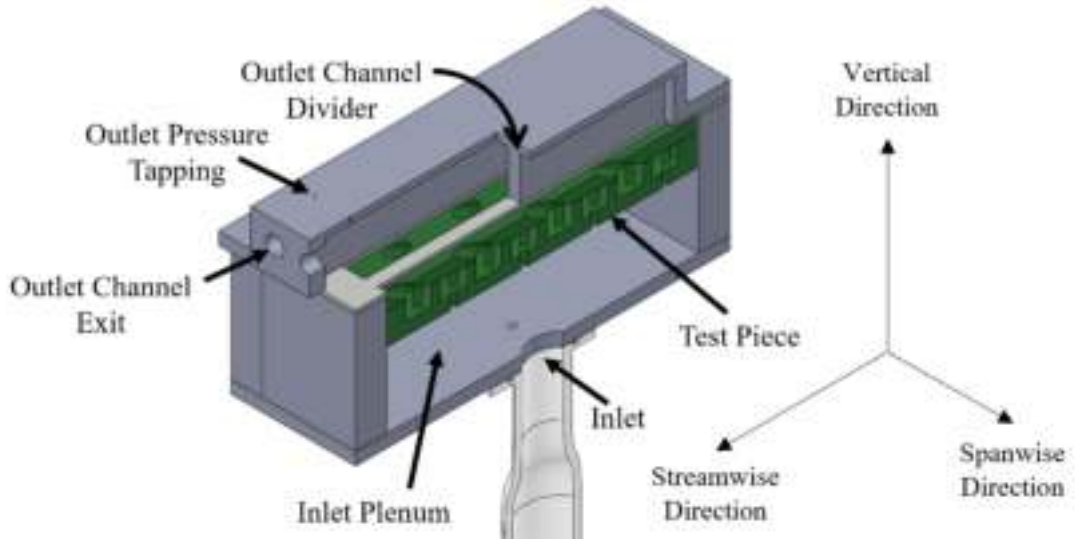

Figure 7. CAD model (Section Diagram) of the blower rig test section.

5.2. Experimental Uncertainty Analysis

Pressure measurements were made using First Sensor HCE Series pressure transducers [23] and recorded using a PicoLog ADC-24 High Resolution Data Logger [24]. Measurements were recorded at 5 Hz for 30 s. In the tests conducted, uncertainties for each pressure reading peaked at approximately ±250 Pa. Mass flow values across each orifice plate, computed using the pressure drops across the orifice plates, had a maximum uncertainty of ±0.48 g/s and a minimum of ±0.45 g/s, giving an uncertainty on the total

mass flow rate of up to ± 1.2 g/s. Test cases where the relative uncertainty of any individual mass flow was over 25% were not used for LOM comparison.

6. Results and Discussion

6.1. Experimental Validation

The blower rig was run for many separate tests, between which the valve positions for each channel were varied to produce a new outlet pressure distribution. The pressure readings recorded from each test were averaged and used as the input boundary conditions to the LOM. Figure 8 compares the total inlet mass flow for each test case, for both experiments and the LOM. Within the range of cases investigated, the results were in good agreement, with a maximum deviation of 10.9% from the experiment results. Agreement for D6 results was hampered by some manufacturing damage that affected film hole size and quality.

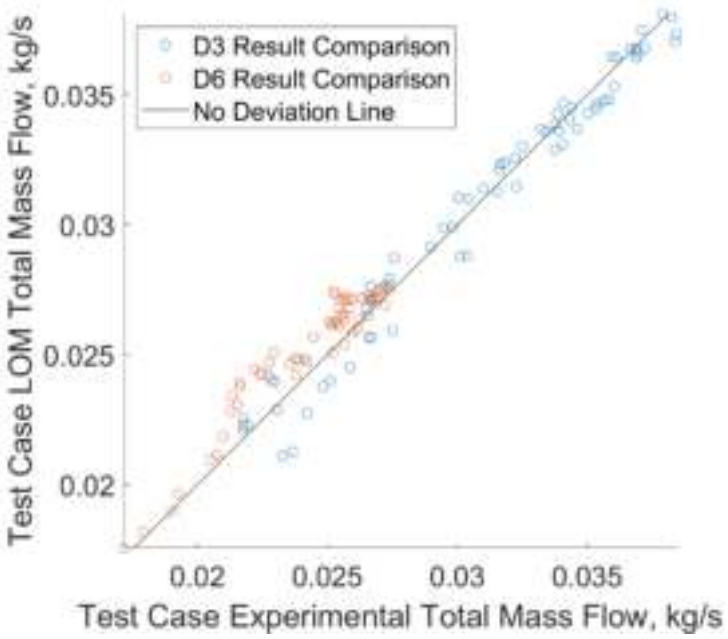

Figure 8. Test case mass flows, experiment result vs. LOM results.

Figure 9 shows how experimental results from two individual D3 test cases compared with those produced by the LOM. The pressure distribution is assessed using the Inlet-Outlet Channel Pressure Loss Coefficient (14) —the pressure loss from inlet to channel outlet, normalized by the dynamic head of the total experimental mass flow passing through the total impingement hole area. The outlet mass flow in each case is assessed as a proportion of that method's total mass flow. Across the range of test cases conducted, individual channel outlet flow shares of the LOM generally fell within 20% of experimental results, rising only in extreme cases. The high spanwise pressure gradient imposed in the test case of Figure 9b clearly leads to a more uneven outlet mass flow distribution, as row 1 receives ~10% of the total inlet mass flow, whilst rows 5 and 6 receive close to 20% each—in the near-uniform outlet pressure case of Figure 9a the flow distribution is more even.

$$C_P = \frac{P_{in} - P_{out}}{\frac{1}{2}\rho\left(\frac{\dot{m}_{in}}{\rho A_i}\right)^2} \tag{14}$$

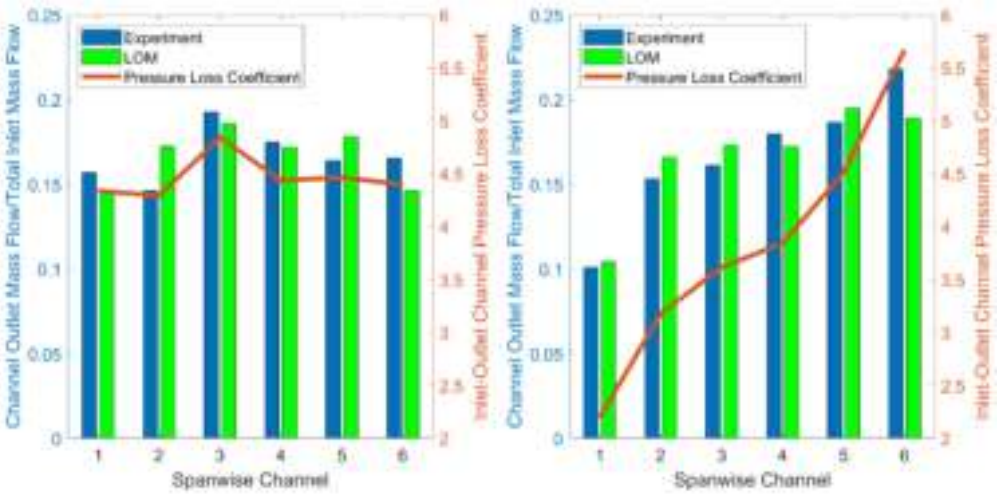

Figure 9. Experiment vs. LOM flow distribution for: (**a**) near-uniform spanwise pressure and (**b**) high spanwise pressure gradient in 2 D3 blower rig tests.

6.2. Effects of Geometric Parameters

Following validation of the LOM using the blower rig, it was used to analyse the effect of selected geometric parameters on coolant migration. To simplify analysis, the investigated domain was reduced to a '2 × 2' size, as used for CFD simulations in Section 4. In such a set-up, the proportion of total coolant that migrates, $\Delta\dot{m}/2\dot{m}_{in}$, ($\Delta\dot{m}$ being the difference between the two outlet mass flows) is a function only of the pressure drops from the coolant supply (inlet pressure P_{0c}) to the two outlets with exit pressures P_1 and P_2, the density, the viscosity, and the length scales s, d_i, d_f, L_i, L_f and L_{pd}. In non-dimensional terms, the Coolant Migration Factor CMF is a function of the Pressure Drop Ratio PDR, the system Reynolds number Re_{sys} (15), and the ratio of the impingement hole diameter to the other geometric parameters (d_f/d_i, L_i/d_i, L_f/d_i and L_{pd}/d_i).

$$CMF = \frac{\Delta\dot{m}}{2\dot{m}_{in}}, \quad PDR = \frac{P_{0c} - P_2}{P_{0c} - P_1}, \quad Re_{sys} = \frac{d_i\sqrt{P_{0c} - P_1}\sqrt{\rho}}{\mu} \tag{15}$$

To give context to these parameters, the CMF serves as a measure of how much flow is being 'stolen' from one film hole by the other. A value of 0 means that the outlet flow distribution is uniform. Any value between 0 and 0.5 means that some migration is occurring, with a value of 0.5 indicating that the low pressure film hole is the outlet for all coolant in the system. If the $CMF > 0.5$, the High Pressure film hole is ingesting mainstream flow. The PDR quantifies the external pressure gradient relative to the coolant supply—a PDR of unity means the external pressure gradient is flat.

Multiple series of simulations with the model were run to determine each geometric factor's effect on the $CMFPDR$ relationship, which sets the level of coolant migration across a range of operating conditions. In a 2 × 2 set-up where all features maintain constant size (i.e., film holes are of the same diameter, etc.), a pressure drop ratio of 1 causes no coolant migration. As the PDR grows, coolant migration increases, as shown in Figure 10a. This was found to be repeatable if all geometric ratios were kept constant, as the system Reynolds number was found to have a minimal effect—this is shown in Figure 10b, where the proportion of migrating coolant hardly changes for wide ranges of Re_{sys}.

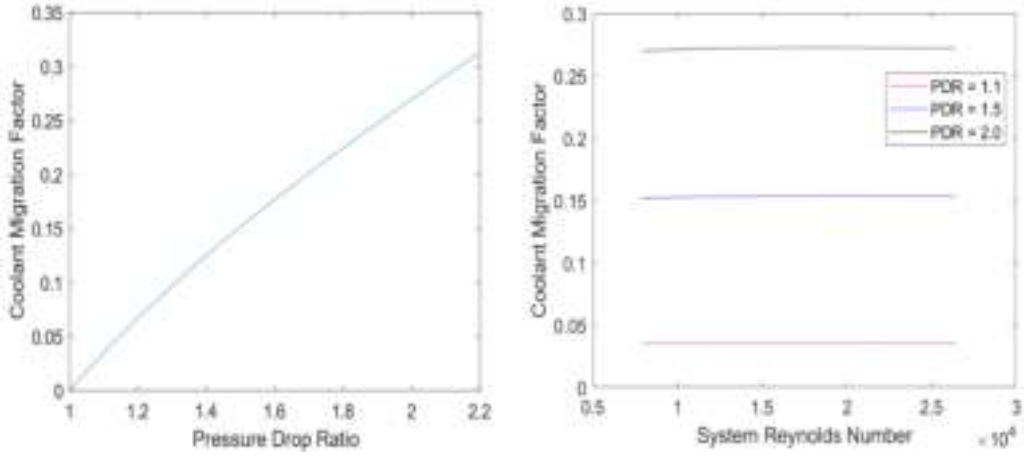

(**a**) (**b**)

Figure 10. Non-Dimensional Relations for *CMF*: (**a**) *CMF* vs. *PDR* for 2 × 2 Model, (**b**) *CMF* vs. *PDR* for 2 × 2 Model at multiple PDRs.

Figure 11a shows the effects of scaling the impingement hole and film hole diameters independently. Scaling each hole diameter has opposite effects—increasing the impingement hole diameter reduces the proportion of coolant migrating, whereas increasing the film hole diameter leads to greater migration. These effects are a product of how the pressure losses through each skin affect the average pressure in the internal cavity. As noted in the related work [10], the impingement process dominates pressure losses in double-wall effusion cooling systems, so even in cases with high external pressure gradients, the impingement hole mass flows remain close to equal and the flow expanding from impingement points is largely at the same pressure. Only after the impingement process does the external pressure gradient influence the flow distribution, unless the array features a variation in pedestal row constrictions, such as in Figure 3. Increasing the impingement hole diameter reduces the pressure drop across the inner skin, creating a larger pressure margin across all film hole positions. The pressure drop ratio across the outer skin is thus reduced, limiting coolant migration. In contrast, increasing the film hole diameter reduces pressure drops across the outer skin and shifts more pressure loss to the impingement process, increasing the pressure drop ratio across the outer skin and increasing coolant migration. This implies that a low porosity outer skin is much less vulnerable to coolant migration than a high porosity one, though coolant migration effects must be considered alongside the likely reduction of film cooling effectiveness caused by reduced outer skin porosity. If the external pressure distribution is known, it can be beneficial to reduce the diameter of film holes in low pressure regions whilst maintaining high hole diameters in high pressure ones—holes at the SS would have a greater pressure drop per unit mass, compensating for the imbalance in outer skin pressure drop ratio and limiting coolant migration.

The effect of scaling the hole lengths is shown in Figure 11b. In the range investigated, increasing the length of the impingement hole reduced coolant migration, whereas increasing the length of film holes increased it. Changing the length of each hole alters its discharge coefficient—for a length/diameter ratio below 2, C_d increases with the hole length as a longer hole length allows secondary flows to be suppressed. C_d begins to decrease as the length to diameter ratio exceeds 2.5 due to excess friction. Therefore, in the range investigated, discharge coefficients are increasing, leading to similar trends as those seen for scaling the hole diameters. A high $C_{d,i}$ reduces pressure losses due to impingement and reduces the pressure drop ratio across the outer skin, and a high $C_{d,f}$ has the opposite effect. As significant heat transfer takes place on the internal surfaces of the holes, cooling performance would need to be considered alongside migration in optimising the wall thicknesses for overall cooling performance.

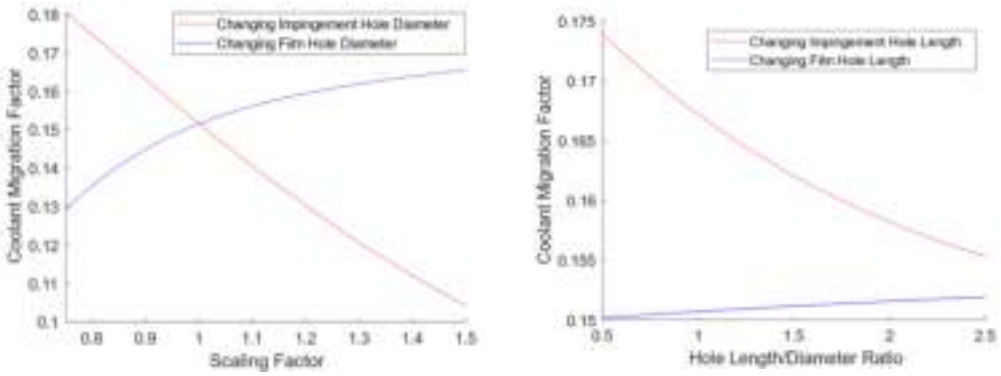

(**a**) (**b**)

Figure 11. Effect of scaling factors on *CMF*: (**a**) *CMF* vs. scaling factors for hole diameters at 1.5 *PDR*; (**b**) *CMF* vs. hole length/diameter ratios at 1.5 *PDR*.

In the context of an engine vane, multiple *PDR*s would need to be considered when investigating any given hole position. Positions partway along the chord would both gain coolant from higher pressure positions and lose coolant to lower pressure ones.

Figure 12 shows the effect of changing the pedestal width on the coolant migration. As the pedestal width to impingement hole diameter ratio goes to two, the available flow area goes to zero. In this region, the flow velocity through the pedestal array is high, leading to high pressure losses in the region—this has a similar effect to reducing the film hole diameter, as less of the system pressure losses occur in the impingement process, leading to a higher pressure margin across the outer skin and less coolant migration. When the pedestal width is less than 1.5 times the impingement hole diameter, the effect of the pedestal width on coolant migration is much weaker, as pressure losses are distinctly less than those occurring through either set of holes.

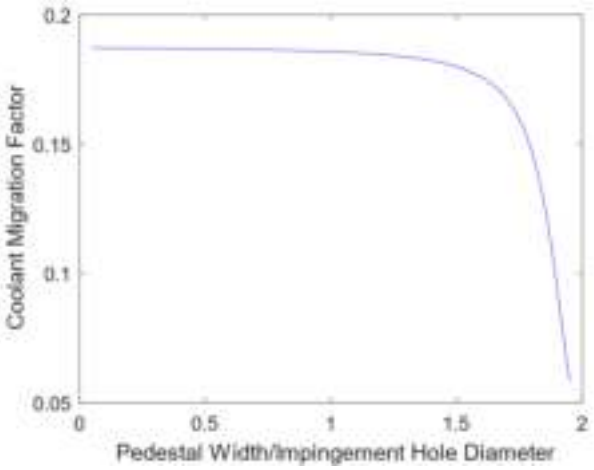

Figure 12. *CMF* vs. pedestal width/impingement hole diameter at 1.5 *PDR*.

6.3. Full-Vane Analysis

In order to demonstrate the issue of coolant migration within a double-wall effusion cooled nozzle guide vane, the LOM was adapted to fit a modern engine NGV, using flow properties found experimentally by Holgate et al. [4]. A network diagram of this application is shown in Figure 13. Due to the very high pressure gradient around the early Suction Surface, the LOM was unable to resolve the internal flow-field for a continuous cavity, so results shown are for a test case where the LE's internal cavity has been separated from both the PS and SS. This shows a series of zero mass flows through the pedestal array. In this configuration, the maximum film hole coolant flows are observed at the early SS, whilst film holes around the LE produce little flow due to the much lower overall pressure margin

for that section. In order to achieve a more even outlet coolant flow around the vane, it would be necessary to increase hole sizes at the LE to allow more flow through, or to reduce hole sizes around the SS to restrict coolant flow. This presents a significant advantage of the LOM, which can be used to rapidly assess the effects of many minor design changes in an attempt to optimize the outlet flow distribution.

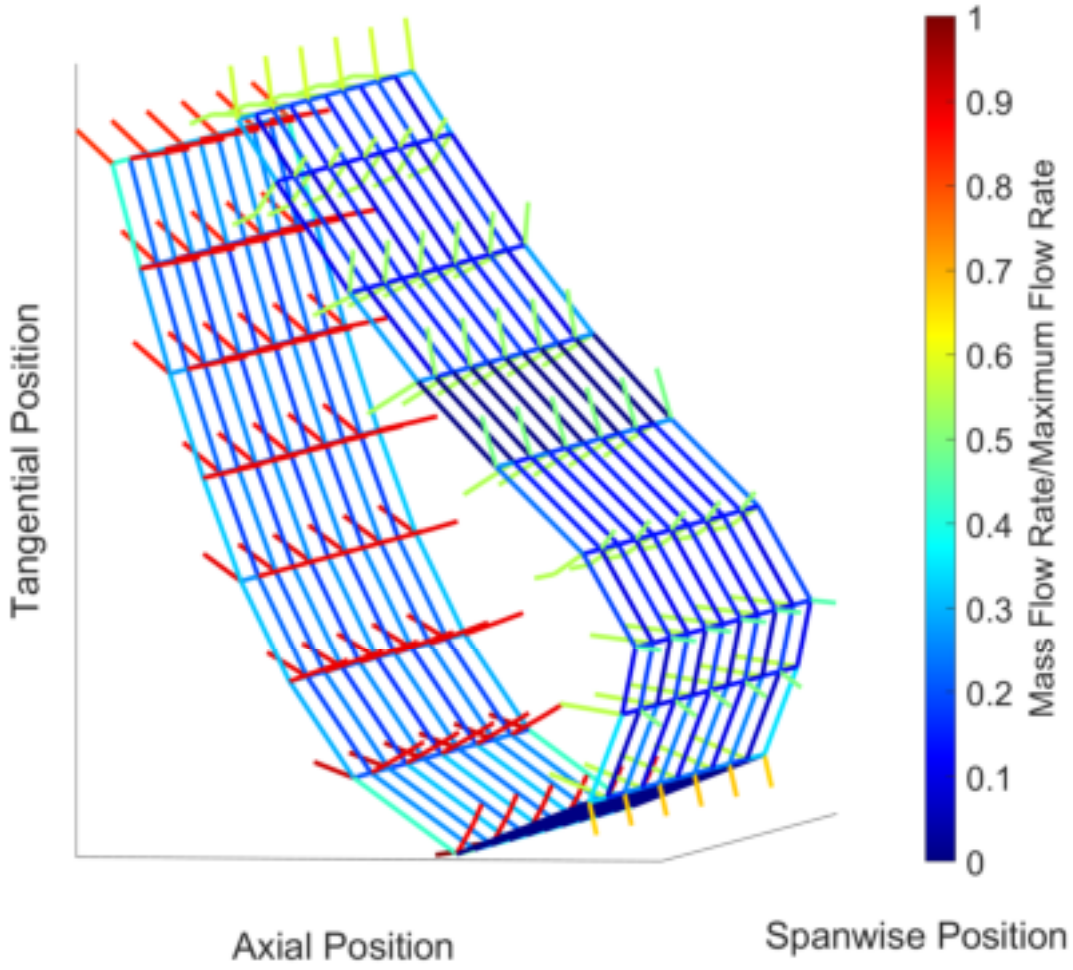

Figure 13. Flow network for a double-wall effusion cooled NGV.

CFD was used to review the effect of walls across the span on the outlet mass flow distribution, the results of which are shown in Figure 14. This figure compares the average outlet mass flow per row of holes, normalized by the value seen at the stagnation line, for three different set-ups; a continuous cavity (no walls), separated sections (LE, PS and SS separate, as in Figure 13 and completely separated (walls between every row of holes). It is immediately clear from these results that without walls through the cavity, there is massive migration of coolant to the early suction surface, resulting in a significant imbalance in the outlet coolant distribution. In this particular case, the use of walls across the span is imperative to maintaining any sort of adequate film cooling at the LE.

Even in the cases where the LE, PS and SS were separated from one another, the average per-hole coolant outlet mass flows were significantly greater for the SS than for other sections. To demonstrate potential methods of evening the outlet flow distribution, the LOM was used to scale up the diameters of film holes around the PS and LE, whilst scaling down the diameters of all film holes on the SS by the same proportion. Results of these tests are shown in Figure 15, which indicates that the hole diameters would need to be scaled by around 80% if the designer were pursuing a more uniform outlet flow. This scaling gives a maximum deviation in the per-hole average coolant mass flow of 19% from the stagnation row value, compared to 118% when no scaling is used. In an engine case,

greater heat loads around the SS would lead to a greater demand for film cooling there, but maintaining adequate film cooling to the LE presents more of a challenge.

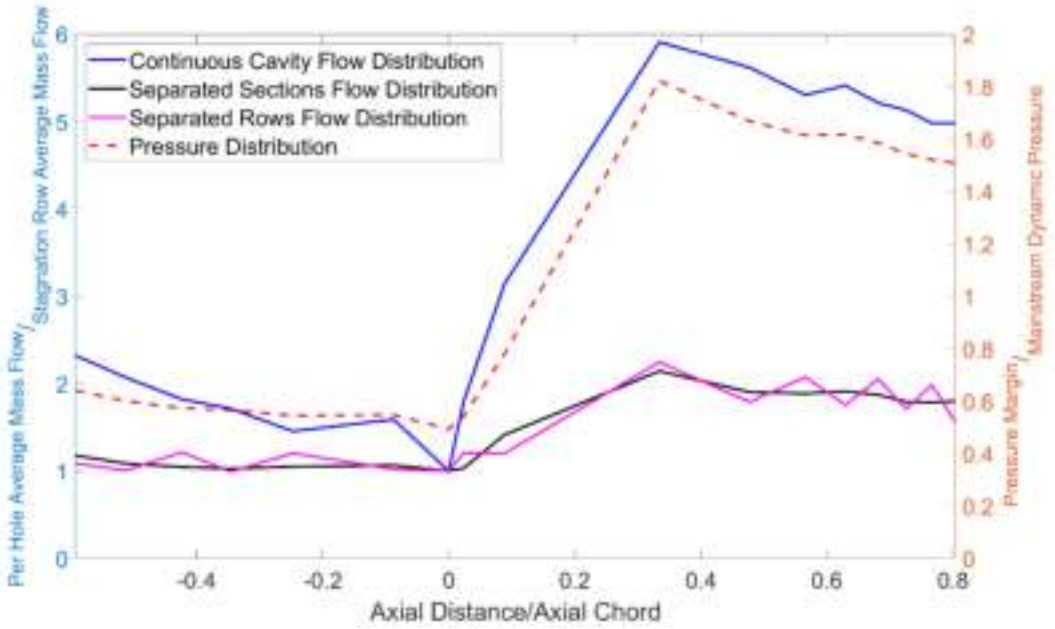

Figure 14. CFD results for outlet mass flow distribution for different internal cavities.

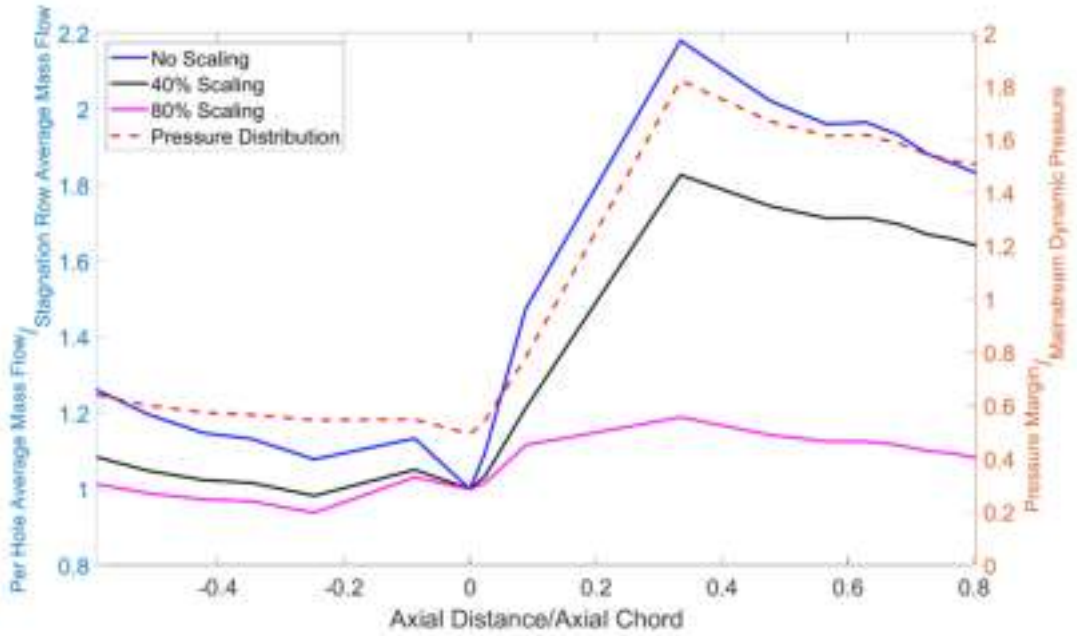

Figure 15. LOM results for outlet mass flow distributions in an NGV for scaling hole diameters.

6.4. Future Work

Future work will address the effect of heat transfer on coolant migration, combining the Flow Network Model with a Low Order Thermal Network through the solid based on that developed by Murray et al. [25]. Given the high rise in coolant temperature as it passes through an engine vane's double-wall cooling system, it is expected that coolant migration would be affected by heat transfer. Significant increases in the coolant temperature in the cavity would lead a reduction in the density of the coolant. A lower density would produce smaller outlet mass flows for the same pressure drops, leading to a reduction in the coolant migration factor. As noted previously, geometric changes made to combat coolant

migration will have knock-on effects on the cooling performance of the geometry—it is important for these concerns to be considered alongside one another, as either could lead to catastrophic failure of the engine component.

7. Conclusions

A low order flow network model was created to assess mass flow and pressure distributions through double-wall effusion cooling systems. The LOM has been developed to use empirical loss coefficients and discharge coefficient correlations to solve mass flows in and out of nodes in a network, solving for the pressures at internal nodes within the cooling system. This allows assessment of the vulnerability of a cooling scheme's geometry to coolant migration under the influence of an external static pressure gradient. Reducing the coolant migration from high to low pressure regions is key to preventing localized areas of poor external film cooling effectiveness. The results of the LOM were validated using the Blower Rig, whereby a blower forced flow through a Double-Wall Effusion Cooling test piece, through which the flow was divided into six outlet channels and mass flows were measured independently. This allowed evaluation of the effect of an imposed spanwise pressure gradient on the outlet flow distribution. Results compared favourably with those of the LOM.

The LOM performed a series of scaling simulations to show the effect of different geometric parameters on coolant migration. These tests showed that the effective method in reducing the Coolant Migration Factor was to minimise the Pressure Drop Ratio across the outer wall. This was done by reducing the share of the overall pressure losses caused by impingement—the geometric changes that caused this included increasing the diameter and length of the impingement holes, and reducing the diameter and length of the film holes. Large pedestal diameters, and thus low-inter pedestal spacing, produced the same results as small film hole diameters, but only at very high values.

It has been suggested that a non-uniform distribution of hole diameters could be used to compensate for the effects of high external static pressure gradients on coolant migration. This was tested for a full vane example, where increasing the diameters of holes at the LE and SS whilst reducing those on the SS gave a far more uniform outlet mass flow distribution.

Author Contributions: M.v.d.N. and P.I. established the goals of the work and the design of experiments. M.v.d.N. developed the Low Order Flow Network Model and performed CFD work and experiments under the supervision of P.I. All authors have read and agreed to the published version of the manuscript.

Funding: This work is funded by Rolls Royce plc. and the EPSRC, under the CDT in Gas Turbine Aerodynamics (No. EP/L015943/1) and the Transpiration Cooling Systems for Jet Engine Turbines and Hypersonic Flight Programme Grant (No. EP/P000878/1).

Data Availability Statement: Not Applicable.

Acknowledgments: The authors wish to thank of Alexander Murray and the technicians at the Oxford Thermofluids Institute for their contributions to setting up experiments, and Luca Di Mare for help with numerical work. Additional thanks go to Ignacio Mayo, formerly of Rolls Royce plc., for his oversight of this study.

Conflicts of Interest: The funders had no role in the design of the study; in the collection, analyses, or interpretation of data; in the writing of the manuscript, or in the decision to publish the results.

Nomenclature

A	Area (m^2)
C_d	Discharge Coefficient
C_p	Pressure Coefficient
CMF	Coolant Migration Factor
d, D	Diameter (m)
f	Friction Factor
h	Specific Enthalpy (J/kg)
HTC	Heat Transfer Coefficient $(W/m^2\ K)$
k_l	Loss Coefficient
L	Length (m)
LE	Leading Edge
$\dot{m}$	Mass Flow Rate (kg/s)
NGV	Nozzle Guide Vane
P	Pressure (Pa)
PDR	Pressure Difference Ratio
PS	Pressure Surface
Re	Reynolds Number
s	Spacing (m)
SFC	Specific Fuel Consumption (kg/N s)
T	Temperature (K)
TET	Turbine Entry Temperature (K)
u, U	Velocity (m/s)
β	Area Ratio
ε	Expansibility Factor
μ	Viscosity (Pa s)
ρ	Density (kg/m^3)
Subscripts	
0	Total
c	Coolant
ext	Exterior
f	Film/Effusion Hole
h	Hydraulic
i	Impingement Hole
in	Inlet
out	Outlet
pd	Pedestal
sys	System
t	Turning
$throat$	Throat
w	Wall
∞	Mainstream

References

1. Van de Noort, M.; Ireland, P.T. A Low Order Flow Network Model for Double-Wall Effusion Cooling Systems. In Proceedings of the European Turbomachinery Conference ETC14 2021, Paper No. 666, Gdansk, Poland, 12–16 April 2021.
2. Bunker, R.S. Gas Turbine Heat Transfer: 10 Remaining Hot Gas Path Challenges. In Proceedings of the ASME Turbo Expo 2006: Power for Land, Sea, and Air, Barcelona, Spain, 8–11 May 2006.
3. Murray, A.V.; Ireland, P.T.; Rawlinson, A.J. An Integrated Conjugate Computational Approach for Evaluating the Aerothermal and Thermomechanical Performance of Double-Wall Effusion Cooled Systems. In Proceedings of the ASME Turbo Expo 2017: Turbomachinery Technical Conference and Exposition, Charlotte, NC, USA, 26–30 June 2017.
4. Holgate, N.; Cresci, I.; Ireland, P.; Rawlinson, A. Prediction and augmentation of nozzle guide vane film cooling hole pressure margin. In Proceedings of the 12th European Conference on Turbomachinery Fluid dynamics & Thermodynamics, Stockholm, Sweden, 3–7 April 2017.
5. Campbell, C.X.; Morrison, J.A. Turbine Airfoil With a Compliant Outer Wall. U.S. Patent 8,147,196 B2, 3 April 2012.
6. Devore, M.A.; Paauwe, C.S. Turbine Airfoil with Improved Cooling. U.S. Patent 7,600,966 B2, 13 October 2009.

7. Chyu, M.K.; Hsing, Y.C.; Natarajan, V. Convective Heat Transfer of Cubic Fin Arrays in a Narrow Channel. *J. Turbomach.* **1998**, *120*, 363–367. [CrossRef]
8. Siw, S.C.; Fradeneck, A.D.; Chyu, M.K.; Alvin, M.A. The Effects of Different Pin-Fin Arrays on Heat Transfer and Pressure Loss in a Narrow Channel. In Proceedings of the ASME Turbo Expo 2015: Turbine Technical Conference and Exposition, Montreal, QC, Canada, 15–19 June 2015.
9. Bamba, T.; Kumagai, T.; Mimura, F.; Yamane, T.; Fukuyama, Y.; Usui, T.; Yoshida, T. Leading Edge Cooling Performance of an Integrated Cooling Configuration. In Proceedings of the ASME Turbo Expo 2008: Power for Land, Sea, and Air, Berlin, Germany, 9–13 June 2008.
10. Andrews, G.E.; Asere, A.A.; Husain, C.I.; Mkpadi, M.C. Full Coverage Impingement Heat Transfer: The Variation in Pitch to Diameter Ratio at a Constant Gap. In *AGARD Heat Transfer and Cooling in Gas Turbines*; AGARD: Bergen, Norway, 1985.
11. Murray, A.V.; Ireland, P.T.; Romero, E. Experimental and Computational Methods for the Evaluation of Double-Wall, Effusion Cooling Systems. In Proceedings of the ASME Turbo Expo 2019: Turbomachinery Technical Conference and Exposition, Phoenix, AZ, USA, 17–21 June 2019.
12. Wambersie, A.; Wong, H.; Ireland, P.; Mayo, I. Experiments of Transpiration Cooling Inspired Panel Cooling on a Turbine Blade Yielding Film Effectiveness Levels over 95%. *Int. J. Turbomach. Propuls. Power* **2021**, *6*, 16. [CrossRef]
13. Rose, J.R. *NASA TM-73774: FLOWNET: A Computer Program for Calculating Secondary Flow Conditions in a Network of Turbomachinery*; NASA: Cleveland, OH, USA, 1978.
14. Kutz, K.J.; Speer, T.M. Simulation of the Secondary Air System of Aero Engines. In Proceedings of the ASME 1992 International Gas Turbine and Aeroengine Congress and Exposition, Cologne, Germany, 1–4 June 1992.
15. Ebenhoch, G.; Speer, T.M. Simulation of Cooling Systems in Gas Turbines. In Proceedings of the ASME 1994 International Gas Turbine and Aeroengine Congress and Exposition, The Hague, The Netherlands, 13–16 June 1994.
16. Gouws, J.; Morris, R.; Visser, J. Modelling of a gas turbine combustor using a network solver. *S. Afr. J. Sci.* **2006**, *102*, 533–536.
17. Jin, H.; Riddle, A.; Cooke, L. A Compressible Flow Network Analysis for Design Upgrade of Industrial Aeroderivative High Pressure Turbine Blades. In Proceedings of the ASME Turbo Expo 2008: Power for Land, Sea, and Air, Berlin, Germany, 9–13 June 2008.
18. Remani, C. *Numerical Methods for Solving Systems of Non-Linear Equations*; Lakehead University: Ontario, QC, Canada, 2013.
19. Mazzei, L.; Winchler, L.; Andreini, A. Development of a numerical correlation for the discharge coefficient of round inclined holes with low crossflow. *Comput. Fluids* **2017**, *152*, 182–192. [CrossRef]
20. Wang, Z. The Application of Thermochromic Liquid Crystals to Detailed Turbine Blade Cooling Measurements. Ph.D. Thesis, University of Oxford, Oxford, UK, 1991.
21. Miller, D.S. *Internal Flow Systems*, 2nd ed.; Miller Innovations: Bedford, UK, 2009.
22. Robert Bosch Power Tools GmbH. *ALS 2400 | 25 | 2500 | 28 | 30*; Robert Bosch Power Tools GmbH: Stuttgart, Germany, 2017.
23. First Sensor. *HCE Series: Miniature Amplified Pressure Sensors Datasheet*; First Sensor: Berlin, Germany, 2020.
24. Pico Technology. *ADC-20 and ADC-24: High Resolution Data Logger Datasheet*; Pico Technology: St Neots, UK, 2019.
25. Murray, A.V.; Ireland, P.T.; Romero, E. An Experimentally Validated Low Order Model of the Thermal Response of Double-Wall Effusion Cooling Systems for HP Turbine Blades. In Proceedings of the ASME Turbo Expo 2020: Turbomachinery Technical Conference and Exposition, Online, 21–25 September 2020.

International Journal of
Turbomachinery
Propulsion and Power

MDPI

Article

Preliminary Design Guidelines for Considering the Vibration and Noise of Low-Speed Axial Fans Due to Profile Vortex Shedding †

Gábor Daku * and János Vad

Department of Fluid Mechanics, Faculty of Mechanical Engineering, Budapest University of Technology and Economics, Bertalan Lajos u. 4-6, H-1111 Budapest, Hungary; vad@ara.bme.hu

* Correspondence: daku@ara.bme.hu

† This paper is a revised version of our paper published in Proceedings of the European Turbomachinery Conference ETC14, Gdansk, Poland, 12–16 April 2021.

Abstract: This paper presents a critical overview on worst-case design scenarios for which low-speed axial flow fans may exhibit an increased risk of blade resonance due to profile vortex shedding. To set up a design example, a circular-arc-cambered plate of 8% relative curvature is investigated in twofold approaches of blade mechanics and aerodynamics. For these purposes, the frequency of the first bending mode of a plate of arbitrary circular camber is expressed by modeling the fan blade as a cantilever beam. Furthermore, an iterative blade design method is developed for checking the risky scenarios for which spanwise and spatially coherent shed vortices, stimulating pronounced vibration and noise, may occur. Coupling these two approaches, cases for vortex-induced blade resonance are set up. Opposing this basis, design guidelines are elaborated upon for avoiding such resonance. Based on the approach presented herein, guidelines are also developed for moderating the annoyance due to the vortex shedding noise.

Keywords: axial flow fan; blade vibration; low tip speed; preliminary fan design; vortex shedding

check for updates

Citation: Daku, G.; Vad, J. Preliminary Design Guidelines for Considering the Vibration and Noise of Low-Speed Axial Fans Due to Profile Vortex Shedding. *Int. J. Turbomach. Propuls. Power* **2022**, *7*, 2. https://doi.org/10.3390/ijtpp7010002

Received: 28 September 2021
Accepted: 4 January 2022
Published: 7 January 2022

Publisher's Note: MDPI stays neutral with regard to jurisdictional claims in published maps and institutional affiliations.

Copyright: © 2022 by the authors. Licensee MDPI, Basel, Switzerland. This article is an open access article distributed under the terms and conditions of the Creative Commons Attribution (CC BY-NC-ND) license (https://creativecommons.org/licenses/by-nc-nd/4.0/).

1. Introduction

Vortex shedding (VS) from low-speed axial flow fan rotor blades has become of engineering relevance in the past decades. The VS phenomenon discussed in this paper—termed herein as profile vortex shedding (PVS), and illustrated in Figure 1—is not to be confused with the trailing-edge-bluntness, VS, which takes place past the blunt trailing edge (TE) of the blade profile, acting as the aft portion of a bluff body [1]. In the aforementioned literature, PVS is referred to as a laminar-boundary-layer VS, because it can only occur if the boundary layer is initially laminar at least over one side of the blade profile. In this case, the initially laminar boundary layer, being separated near or after mid-chord position, reattaches in the vicinity of the TE—thus resulting in a separation bubble—and finally undergoes a laminar-to-turbulent transition. Moreover, the position and the size of the formed separation bubble plays a key role in tonal PVS noise emission. Recently, Yakhina at al. [2] published a detailed investigation about tonal TE noise radiated by low Reynolds number airfoils. They observed that a precondition for tonal noise emission is the formed separation bubble being sufficiently close to the TE. PVS may occur within a certain Reynolds number range. Based on the literature [3–5], a lower limit of $Re_c = 5 \times 10^4$ is assumed herein, while the upper limit is determined by the critical Reynolds number of the natural laminar-to-turbulent transition. When PVS is discussed for low-speed fans, as in the present paper, incompressible flow is considered by implying a Mach number of $\leq$0.3.

Figure 1. Profile vortex shedding (PVS).

Various models are available in the literature on the PVS phenomenon. In this paper, only the classic model by Tam [6] and Wright [7] is referred to, in order to provide a straightforward and comprehensive interpretation on the mechanism. According to this model, PVS is related to a self-excited feedback loop. Due to the unstable laminar boundary layer, Tollmien–Schlichting instability waves are generated; these waves travel downstream toward the TE where sound scattering occurs, and acoustic waves are created. The acoustic waves propagate upstream to amplify the original instabilities. If appropriate phase conditions are fulfilled, the disturbances are amplified at some frequencies, thus closing the feedback loop. Later, a number of authors, e.g., Nash et al. [8], carried out a critical revision on the aforementioned feedback loop model. PVS may generate vibration on the blade. As the studies by Ausoni et al. [9] suggest, the mechanisms of periodic vortex shedding and periodic blade vibration may mutually be coupled at a blade eigenfrequency, within a "lock-in" phenomenon.

In the case of low-speed axial flow fan blades, the difference between PVS and TE-bluntness VS in their physical mechanisms manifests itself in scaling techniques and the values of the Strouhal number being also different.

For blade profiles with thick or blunt trailing edges, the TE-bluntness vortex shedding [10] can be characterized by the Strouhal number based on the free-stream velocity U_0 and the TE thickness d_{TE}:

$$St_{TE} = f_{TE}\, d_{TE}/U_0 \cong 0.20 \quad (1)$$

For PVS [11,12], which is associated with the boundary layer transition and feedback mechanism:

$$St^* = f_{PVS} b/U_0 \cong 0.18 \quad (2)$$

where f is the dominant frequency of the two types of VS, and b is the distance between the vortex rows. Yarusevych et al. [11] found that St^* is universally valid for symmetrical, relatively thick NACA airfoils for certain ranges of the Reynolds number and angle of attack, suggesting the appellation of a "universal" Strouhal number St^*, as specified in Equation (2). However, these airfoils are not widely used in axial fan application; therefore, the present authors have extended the proposed St^* definition as follows. Systematic wind-tunnel experiments were performed on blade section models typical for low-speed axial fans, using a single-component hot-wire probe. Based on the measured f and b values, the authors also confirmed the validity of St^* for asymmetrical profile geometries, such as 8% cambered plate and RAF-6E profiles, in a quasi-2D experimental analysis [13]. Thus, the available experimental database on PVS frequency [5] was extended.

From an engineering point of view, the practical aspects of PVS are remarkable in two ways: vibration and noise. On the one hand, PVS creates a periodically fluctuating force normal to the chord, increasing the risk of blade vibration. On the other hand, VS appears as the primary source of the aeroacoustics noise of low-speed axial flow fans [14–16]. Hence, it is an important engineering objective to check and possibly to control the vibration and noise of low-speed axial fans due to the PVS that is already in the preliminary design phase. It is worth noting that the signatures of blade vibration and PVS-related noise may coincide in the frequency spectra. In [17], the vibrometer connected to the airfoil indicated a vortex-induced vibration, the dominant frequency of which coincided with that of the far-field tone.

Measurements on PVS in the literature are mostly related to isolated and steady airfoils [2,11–13,17,18]. Only a few studies dealt with PVS in the case of rotating blades of asymmetrical profiles being characteristic for realistic axial fans. Longhouse [19] detected

PVS noise on an axial fan of four cambered plate blades with a constant blade chord. Nevertheless, except for a small segment (~10%) of the span of one blade in near-tip region, the PVS noise was suppressed by aft-chord serrations. Furthermore, the spanwise variation of free-stream velocity tended to broaden the noise signature of PVS, thus acting against a remarkable, well-detectable tonal PVS character. Grosche and Stiewitt [20] examined a four-bladed propeller-type axial fan rotor with a moderate sweep and twist. They observed PVS noise at $\alpha \approx 4^\circ$ angle of attack, viewed in the rotating frame of reference near the blade tip, for three different Reynolds numbers based on the chord length ($Re_c = 9 \times 10^4$, 1.3×10^5, 2.6×10^5). All of the aforementioned observations—both the isolated blade profile and rotor consideration—suggest that the following blade features tend to increase the inclination for the occurrence of well-detectable tonal PVS: high aspect ratio (AR), low solidity, moderate twist, and constant blade chord. These parameters are typical for propeller-type fans [21]. Such propeller-type fans, where low-solidity is characteristic over a significant portion of the span, have been designed, for instance, by [22,23].

In order to moderate the harmful noise and vibration effects due to PVS, pessimistic design scenarios have systematically been discovered for which such harmful effects are pronounced. Furthermore, these design characteristics were coupled with rotor dynamics consideration. Based on this coupling, an exemplary unfavorable design case was set up in terms of both operational and geometrical characteristics, for which PVS demonstrates an increased risk of blade resonance. Taking the rotor of such an unfavorable design case—termed hereafter the PVS-affected rotor—as reference, approximate semi-empirical design guidelines can already be elaborated in the preliminary design phase for checking and possibly avoiding PVS-induced resonance. The design guidelines for noise reduction, reported in [13], have also been further developed toward a more detailed model, as illustrated in this paper.

2. Blade Vibration: An Overview

Turbomachinery blade profiles are suggested to be modeled in preliminary analysis as simple cantilever beams [24–30], which means that all degrees of freedom of the blades at the blade root, i.e., where connected to the hub, are constrained. The pure bending—or, in other words, transversal or flexural—vibrations of a prismatic beam with uniform cross-section according to time (τ) and the coordinate along the longitudinal direction of the beam (z) are described by the partial differential equation below, which is derived from the Euler-Bernoulli's beam theory [26,31]:

$$EI\frac{\partial^4 g(z,\tau)}{\partial x^4} + \rho_b A\frac{\partial^2 g(z,\tau)}{\partial \tau^2} = 0 \tag{3}$$

where g(z, τ) is the lateral displacement along the axis perpendicular to the blade chord; E is the Young modulus; I is the second moment of area with respect to the axis being parallel to the chord and fitting to the center of gravity (CG) of the blade section; A is the cross-sectional area of the blade profile; and ρ_b is the density of the blade material. The method of variable separation can be used to produce the free vibration solution. By utilizing the proper initial and boundary conditions, the i-th eigenfrequency (see later) and normal mode shape [31] can be expressed as follows:

$$F_i(z) = (\cos\beta_i z - \cosh\beta_i z) - \frac{(\cos\beta_i l + \cosh\beta_i l)}{(\sin\beta_i l - \sinh\beta_i l)}(\sin\beta_i z - \sinh\beta_i z) \tag{4}$$

where i is the order-number, i.e., 1, 2, 3 etc.; F(z) is the characteristic function or the normal mode of the beam; l is the radial extension of blade from hub to tip, i.e., the blade span, and $\beta_i l \approx (2i-1)\pi/2$. For illustrative examples, Figure 2 qualitatively presents the shapes for some bending modes, generated on the basis of Equation (4). The vertical axis represents the normal mode (i.e., dimensionless displacement) and the horizontal axis shows the dimensionless length of the beam.

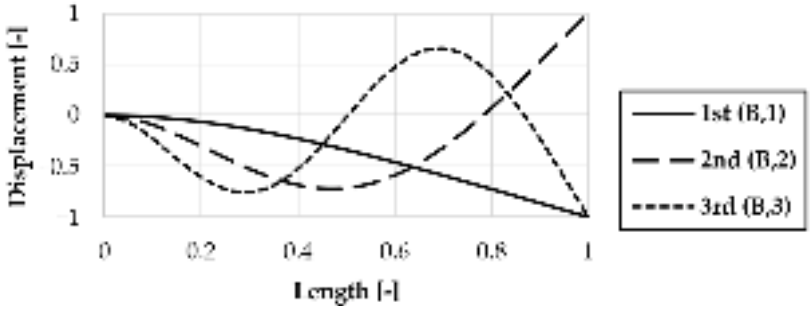

Figure 2. Normal bending modes of the beam.

The pure torsion of the cantilever beam is governed by the following differential Equation [32]:

$$GI_t \frac{\partial^2 \zeta(z,\tau)}{\partial x^2} + \rho_b I_p \frac{\partial^2 \zeta(z,\tau)}{\partial \tau^2} = 0 \quad (5)$$

where $\zeta(z, \tau)$ is the rotation angle around the longitudinal direction of the beam; G is the shear modulus; I_t is the torsional stiffness or torsional constant; and I_p is the polar moment of area of the blade section.

It is important to note that in practice, mixing of modes can occur, and accordingly, various researchers have executed studies on experimental and theoretical evaluations of flexural-torsional vibration analysis, taking into account the coupling of flexural and torsional modes, e.g., [24,27,28,31,33,34]. The present authors have only dealt with pure bending and torsional vibration modes, keeping in mind the simplest possible analytical description mode.

In the literature, basic concepts are available for the analytical treatment of the vibration of beams/blades affected by centrifugal force field due to their rotation. Such concepts regard both untwisted [31] and twisted [24,28,29] geometries. As discussed in [25], the centrifugal force originating from the rotation of the blades has a stiffness-increasing effect, i.e., it tends to moderate the inclination of the blade to vibrate. At the present state of research, the authors neglect the mechanical effect of the centrifugal field, for the following reasons: (a) The centrifugal field tends to be of moderate significance in the low-speed fan blades discussed herein; and (b) the intention is to make a pessimistic—i.e., safety-increasing—preliminary design approach via neglecting the stiffness-increasing trend due to the centrifugal field. Blade twist tends to reduce the bending eigenfrequencies, as FEM computations (not presented herein) demonstrate. Therefore, for twisted blades, the critical frequencies of excitation tend to be shifted toward lower values. At the present state of research, the authors neglect the mechanical effect of blade twist. The reasonability of such neglect is commented on later on. The concerted review of the effects of centrifugal force field and blade twisting, or taking into account the mixing of the pure vibration modes, is planned to be the subject of future research.

Even mechanical or fluid mechanical excitations can unavoidably induce the vibration of the axial flow fan blade to a certain extent, as well as being a source of vibration in the structure on which it is installed. Such excitation effect may derive from the interaction of the fan blades with the wake developing behind the elements placed upstream of the rotor e.g., supporting struts, inlet guide vanes, or even from the discussed PVS phenomenon. For instance, corresponding to the pressure rise, a steady mean lift force acts on the blade. However, the lift force also has a varying component e.g., the fluctuating force due to PVS. As detailed by [25,35], both forces produce a bending moment, resulting in vibration. If the dominant frequency of PVS coincides with an eigenfrequency of the blade, resonance may occur, and the intensity of the vibration can only be limited if the mechanical structure is stiff enough or damped sufficiently. Therefore, it is to be treated with special care in the case of fan blades made of cambered sheet metal plates because their eigenfrequency—due to the moderate inertia of the cross-section and the resulting lower stiffness—is lower compared to that of the profiled blades [25].

Even though fans commonly operate with mechanical stresses far below the capacity of their material—and thus the vibration of the fan blade due to resonance does not lead to the fracture of the mechanical structure—, in the presence of the corresponding stresses, which reach a maximum near the blade root, there can be a risk of fatigue fracture. These stresses combine with the centrifugal ones; therefore, a mixed type, alternating stress condition appears, which must be considered in the design of the fan.

Furthermore, the rotor may become imbalanced due to the deformation patterns associated with each resonance frequency of the blade, forcing the shaft to bend, escalating the initial imbalance and bending. If the excitation is sufficiently intense, resulting in a vibration of large amplitude, one of the fan blades can rub into the duct walls leading to rotor imbalance or the breaking down of the blades.

2.1. Analytical Treatment

2.1.1. Bending Modes

In order to provide a straightforward and comprehensive approach in preliminary design, avoiding any need for numerical computation at the present phase of research and as a solutions of Equation (3), the following analytically expressed eigenfrequencies are considered for the bending modes of an arbitrary prismatic rod, as specified in the literature [26]:

$$f_{\mathrm{B},i} = \frac{K_{\mathrm{B},i}}{l^2}\sqrt{\frac{E\,I}{A\,\rho_{\mathrm{b}}}} \tag{6}$$

Namely, the simple analytical formula above can easily be extended to higher-order bending modes by substituting the appropriate $K_{\mathrm{B},i}$ constant into Equation (6). The values of $K_{\mathrm{B},i}$ for the first three bending modes are $K_{\mathrm{B},1}$ = 0.560, $K_{\mathrm{B},2}$ = 3.506 and $K_{\mathrm{B},3}$ = 9.819, respectively.

2.1.2. Torsional Modes

By solving the expression in Equation (5), the eigenfrequency for torsional modes can be obtained using the analytical formula e.g., in [26], as follows:

$$f_{\mathrm{T},i} = \frac{i-0.5}{2l}\sqrt{\frac{G\,I_{\mathrm{t}}}{\rho_{\mathrm{b}}\,I_p}} \tag{7}$$

In Equation (7) every variable can be determined—except I_{t}—by utilizing the material and geometrical parameters of the blade. To calculate the I_{t} torsional constant for a flat plate, the following relation is given in [26]:

$$I_t = K_{\mathrm{t}} c t^3 \tag{8}$$

where c is the chord length (width of the plate); t is the thickness (height of the plate); and K_{t} is a mechanical constant which can be obtained from Figure 4.2 of [26] or calculated applying the formula—being in accordance with the former literature—e.g., [36]. However, the aforementioned alternatives for determining the torsion constant are related not to a cambered but to a flat plate, inhibiting their direct application in our case study. To overcome this problem, based on [36–38], the torsional constant of a thin-walled open tube cross-section of uniform thickness can be expressed as:

$$I_t = \frac{1}{3} U t^3 \tag{9}$$

where U is the length of the midwall perimeter, shown dashed later in Figure 5.

2.2. Finite Element Method (FEM)

The FEM is a useful and generally accepted tool for solving engineering problems numerically, such as the modal analysis of rotor blades [39–41]. The desired mechanical characteristics can be computed by dividing an arbitrary mechanical structure into simple geometric shapes and defining the material properties and governing connections among these elements. In this study, the frequency analysis of a low speed axial fan blade is carried out using a commercial FEM software program ANSYS Mechanical APDL 2019 R3.

2.2.1. Geometry, Materials, and Elements

In the present paper, the hub is assumed to be rigid in comparison to the fan blade, thus all degrees of freedom of the blades at the hub, i.e., at the blade root, are constrained. Therefore, only one segment of the axial flow fan composed of a single blade without a hub part was examined. In accordance with the later investigated PVS-affected rotor blade profile of the circular-arc-cambered plate of 8% relative curvature and the dimensional and dimensionless values of Tables 3 and 5, the necessary geometrical characteristics for 3D modeling are summarized in Table 1. The reason for choosing this blade profile geometry will be explained in detail later in Section 3.2. For the FEM case study, the fan blade is made of structural steel with a density of 7850 kg/m^3, a Young's modulus of 200 GPa, and a Poisson's ratio (ν_P) of 0.3.

Table 1. Blade geometrical and material parameters for the FEM case study.

l	c	t	h	ρ_b	E	ν_P
264 mm	120 mm	2.40 mm	9.60 mm	7850 kg/m^3	200 GPa	0.30

According to the literature [30,39], SHELL 181 element is suitable for analyzing thin to moderately-thick shell structures related to turbomachinery blades, such as wind turbine and axial flow fan blades. Hence, this type of element is applied to model the fan blade with 124 nodes in the axial direction and 256 nodes in the radial direction. Basically, SHELL 181 is a four-node element with six degrees of freedom at each node: translations in the x, y, and z directions and rotations about the x, y, and z-axes. However, it should be mentioned that the same solution could be obtained by using the 20-node Hex20 (SOLID 186) element of Ansys Workbench 2019 R3.

2.2.2. Mesh Convergence

A mesh convergence study was performed to assure the optimum mesh number in terms of computational accuracy. The first three bending (B) and torsional (T) eigenfrequencies of the fan blade are computed in several mesh sizes (the element number varies from 258 to 507,904). By increasing the number of elements, the first bending eigenfrequency increases slightly and then becomes nearly constant. For higher-order bending and the torsional mode, similar effects can be observed. As shown in Figure 3, 31,744 elements are appropriate to get a sufficiently accurate solution. Nevertheless, it should be mentioned that even a model with a lower number of elements is sufficient for the third-octave band prediction of the first bending eigenfrequency (see Appendix A).

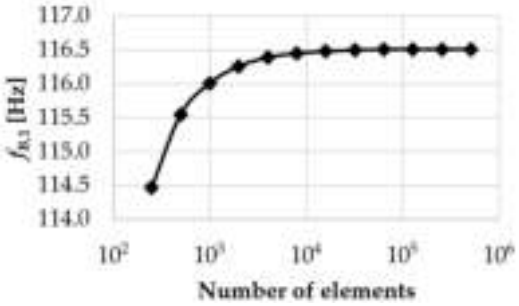

Figure 3. Mesh convergence study.

2.3. Comparison of the Results

In Table 2, the first three analytical bending (B) and torsion (T) eigenfrequencies were calculated based on Equations (5), (7) and (8), and compared to the eigenfrequency obtained by means of FEM. The first column indicates the vibration mode case under discussion. In the second and the fourth columns, FEM and the analytical eigenfrequencies are summarized, respectively. In the third and the fifth columns, the appropriate band number of the third-octave band resolution is listed in accordance with Appendix A. The "Discrepancy" column contains the relative discrepancy of $f_{\text{analytical}}$ in comparison to f_{FEM}.

Table 2. Geometrical and material parameters of the blade.

Mode	f_{FEM} [Hz]	1/3 Octave Band No.	$f_{\text{analytical}}$ [Hz]	1/3 Octave Band No.	Discrepancy [%]
B,1	116.5	11	116.1	11	0.3
B,2	595.2	18	727.6	19	18.2
B,3	1146.7	21	2037.8	23	43.7
T,1	140.1	11	117.4	11	19.4
T,2	472.8	17	352.1	15	34.3
T,3	949.6	20	586.9	18	61.8

From Table 2, it can be observed that the analytical treatment for the first bending (B,1) eigenfrequency is in good agreement with the FEM result. Nevertheless, for the higher-order bending and the torsional modes, the relative discrepancy between analytical and FEM results becomes greater and tends to increase with the increasing of the order of the modes. A possible explanation for this is the partial violation of the briefly presented Euler–Bernoulli thin beam theory. Hence, the AR of the beam is equal to 2.2; namely, the beam is not considered to be slender ($AR > 10$).

Although there have been alternative methodologies to obtain a more accurate analytical prediction for short beams ($AR < 10$), e.g., Timoshenko's beam theory [31], the present paper focuses on Euler–Bernoulli's beam theory, due to the following reasons. (a) On the one hand, the authors aim to create a closed analytical formula with the most straightforward possible analytical description in mind. (b) On the other hand, as shown in [31,42], the relative discrepancy between the analytical first bending eigenfrequencies, calculated based on the two different theories, is less than 5–10%, which, fitting for point (a), is considered to be an acceptable approximation. Based on this and the highlighted role of the first bending mode detailed in Section 3.1, the confirmation of the analytical model by FEM is of primary significance for the first bending mode only and is of secondary importance for the other modes.

Despite the simplification assumption discussed at the beginning of the chapter (untwisted and non-rotating fan blade), supplementary FEM case studies were carried out for the twisted and rotating blade as well. The FEM results demonstrated that both the blade twisting and the presence of a centrifugal force field have a bending eigenfrequency-reducing effect, providing an upper estimation for the first bending eigenfrequency of the blade. As the later calculation example illustrates, even in the case of the untwisted and

stationary fan blade, only impractically low tip speeds would result in the coincidence of the first bending eigenfrequency and PVS frequency. Therefore, the simplified fan blade model applied by the present authors can be considered as a pessimistic design scenario.

3. Blade Mechanics: An Exemplary Case Study

3.1. The Importance of the First-Order Bending Mode

The risk in fan operation due to blade vibration is simultaneously viewed in the present paper from the following two perspectives, which are related to each other. (a) The risk of instantaneous reduction of the gap between the blade tip and the casing. From the perspective of the tip gap reduction, the vibration modes exhibiting monotonously increasing deformation amplitude along the blade height are considered the riskiest. These are the first bending and first torsional modes. (b) The risk of instantaneous rotor imbalance. This occurs in cases when the weight point of the entire blade is displaced in the transversal direction from its original position, fitting on the (approximately) radial blade stacking line, for which the rotor has originally been balanced. From the perspective of rotor imbalance, none of the torsional modes are considered to be risky, as they tend to leave the weight point of the entire blade (approximately) in its original position. In addition, according to their wavy vibration pattern, higher-order bending modes are considered to exhibit only a moderate transversal displacement of the blade weight point.

Therefore, among the various vibrational modes caused by PVS excitation, the first bending mode is judged to be the most critical, and the higher-order bending modes and torsional modes are considered of secondary significance. Consequently, out of the analytical solutions in Equation (5), the "first-order bending mode" is taken herein as an illustrative example of the analytical treatment elaborated upon by the authors. Nevertheless, the reasonability of this choice is justified and supported by the subsequent examples, as follows.

The impact of PVS on both noise and vibration is presumed by the present authors to be pronounced when extensive and coherent vortices are shed with uniform frequency along a dominant portion of the blade span. In this case, PVS is assumed to exhibit pressure fluctuations over the blade suction and pressure surfaces, causing chord-normal forces. Assuming spanwise and spatially coherent shed vortices, the resultant fluctuating forces are in phase over the entire span. Furthermore, PVS and the associated forces may occur farther upstream of the TE (cf. [12]). Such a PVS-induced excitation likely triggers the first-order bending mode.

An upstream stator, e.g., the nearly radially aligned supporting struts located upstream of the rotor, is able to cause wake-blade—also known as "rotor-stator"—interaction, in which the upstream wakes of the stator are swept downstream into the axial flow fan bladerow. The wakes are parallel with the relative velocity (w), thus the interaction manifests itself as a nearly simultaneous, spatially coherent aerodynamic excitation along the entire blade span. Hence, the fan blades are acted by chord-normal fluctuating force, resulting in a spatially coherent bending moment rather than torsional.

In addition, in [25] as a general approach, the frequency of the first bending mode of the blades is to be kept far away from the frequencies of excitation. As it was just mentioned, elements located upstream of the rotor—supporting struts and inlet guide vanes—cause rotor–stator interaction as aerodynamic excitation to the rotor blades, occurring at a frequency of rotational frequency multiplied by the number of upstream elements. On the other hand, such excitation effects correspond to rotor imbalance ("shaker effect") appearing as mechanical excitation at the rotational frequency of the fan.

Moreover, as illustrated in [5], the fluctuation of chord-normal force due to PVS may lead to a variance of the lift coefficient in the order of a magnitude of ± 10 percent of the temporal mean value. As demonstrated in [35], the varying component of lift force causes a bending moment on the blade. When extensive and coherent vortices are shed with uniform frequency along a dominant portion of the blade span, they represent spatially coherent elemental aerodynamic excitation forces, being in phase over the elemental blade

sections, and thus, integrated into a pronounced overall bending moment. The phase identity of the elemental excitation forces along the blade span matches with the phase identity of blade deformation in the first bending mode of the blade, if the frequency of PVS matches with the eigenfrequency related to the first bending mode.

3.2. Eigenfrequency

In order to build up a straightforward model for the interaction of the blade and the fluctuating aerodynamic force due to PVS, some simplifications must be introduced. First of all, a circular-arc-cambered plate of 8% relative curvature is chosen as a blade profile for several reasons:

(a) At moderate Reynolds numbers and angles of attack (α), the cambered plate produces reasonably high C_L, that is comparable with an airfoil profile, i.e., RAF-6E [43], thus enabling the design of blades of relatively high specific performance, i.e., utilizing the loading capability of the blade sections.

(b) At 8% relative curvature, the lift-to-drag (LDR) is near the maximum among the cambered plates of various relative camber, thus enabling the design for reasonably high efficiency [44].

(c) In accordance with the aforementioned practical aspects, it is a cambered plate of 8% relative camber for which hot-wire measurement data are made available by the present authors on PVS at different free-stream velocities and angles of attack [13]. As per the illustration, Figure 4 shows C_L, C_D, and LDR values as a function of the angle of attack for the 8% cambered plate.

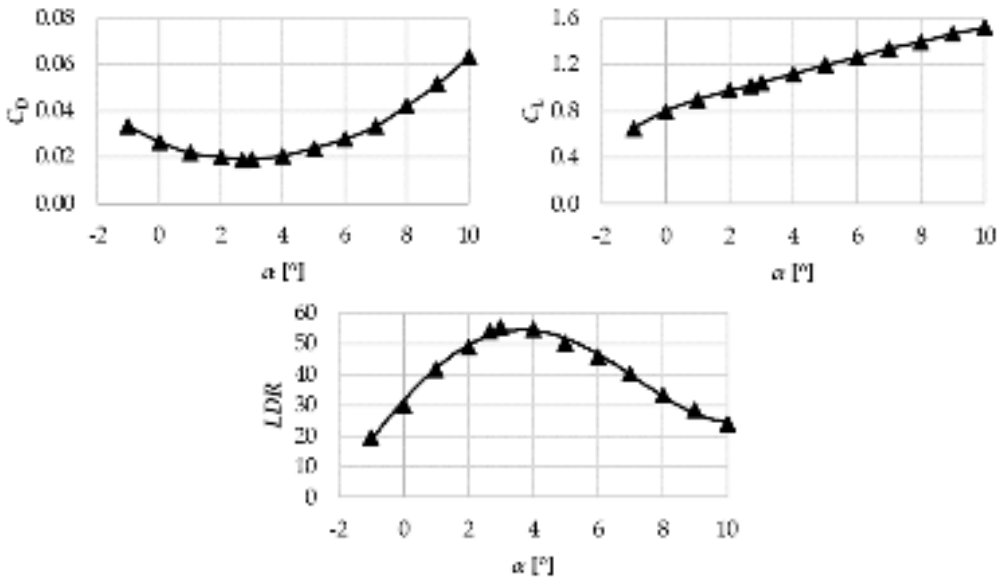

Figure 4. Lift and drag coefficients and lift-to-drag ratios as a function of angle of attack for 8% cambered plate at $Re_c = 3 \times 10^5$ measured by Wallis [44].

Secondly, the fan blade is presumed to consist of geometrically identical blade sections along the full span. This means that the blade chord c, plate thickness t, and height of the camber line h are constants (Figure 5). The measurement data presented by [44] and shown in Figure 4, are related to a relative thickness (t/c) of 2%. This value is representative in fan manufacturing; therefore, t/c is fixed at 2% for the present investigations.

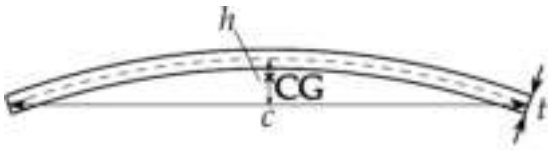

Figure 5. Circular-arc-cambered plate (8% relative camber).

Finally, as discussed earlier, it is assumed that all degrees of freedom of the blades at the hub, i.e., at the blade root, are constrained. This is a reasonable approximation; e.g., if sheet metal blades connect to the hub with a welded joint, or, in the case of polymer material, if the entirety of the hub and blading assembly is injection-molded as a single product. The simplifications above enable us to model the blade as a cantilever beam (or clamped beam) subjected to free vibration. In accordance with Section 3.1, the lowest eigenfrequency, related to the first-order bending mode, can be calculated as follows:

$$f_{B,1} = \frac{0.56}{l^2}\sqrt{\frac{I}{A}}\sqrt{\frac{E}{\rho_b}} \tag{10}$$

The last term on the right-hand side of Equation (10), as the square root of the specific modulus E/ρ_b, is termed herein the wave propagation speed, and denoted as a_b. This is actually the acoustic wave propagation speed in a long one-dimensional fictitious beam made of the blade material. The resultant swinging pattern is shown in Figure 6.

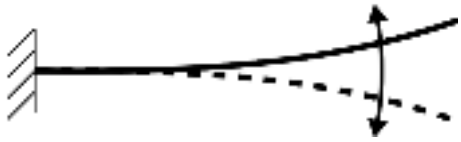

Figure 6. Cantilever beam subjected to free vibration (perpendicular to the blade chord).

3.3. Second Moment of Area

The purpose of the present section is to demonstrate how the I/A term can be related to the basic geometrical characteristics of the circular-arc-cambered plate blade (c, h/c, t/c), creating a direct relationship between the first eigenfrequency and the geometrical parameters of the blade. However, no closed analytical relationship exists in the literature for such purpose. Therefore, an alternative method must be found to express the second term of the right-hand side of Equation (10) with the use of blade geometrical parameters, such as c, h, and t. As a first step, the second moment of area of a cambered plate and a flat plate with same geometrical parameter (t, c) were compared to each other.

The quotient of the second moment of area and the cross-section, in case of a flat plate is:

$$(I/A)_{flat} = (ct^3/12)/(ct) = t^2/12 \tag{11}$$

For a cambered plate it is:

$$(I/A)_{cambered} = K_1(I/A)_{flat}, \text{ where } K_1 = K_1(t/c, h/c) \tag{12}$$

$I_{cambered}$ was obtained for the cambered plate-section using an analytical integration process known from basic solid-state mechanics [45]. As background information for the reader, the values of K_1 are presented in Figure 7 for representative relative thickness and relative camber (h/c) values. For the fitted curves in Figure 7, K_1 was calculated for fixed t/c values for uniform steps of 0.01 h/c over the entire h/c range. In the blade design presented later, K_1 (t/c = 0.02; h/c = 0.08) = 18.07 was used, in accordance with the previously selected blade geometrical parameters.

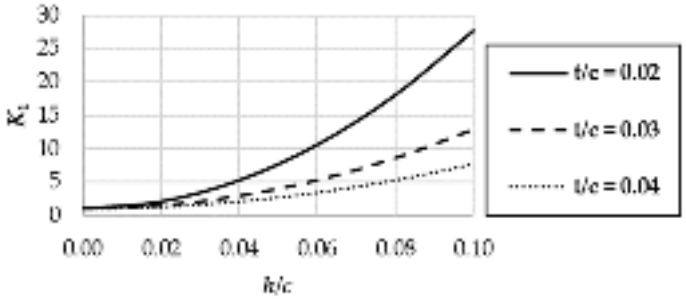

Figure 7. The value of K_1 as a function of relative camber for various relative thicknesses.

Substituting Equations (11) and (12) into Equation (10), the first bending eigenfrequency can be expressed as follows:

$$f_{B,1} = \frac{0.56}{l^2}\sqrt{K_1 \frac{t^2}{12}}\, a_b = \frac{0.56}{l^2} K_b t\, a_b \tag{13}$$

where $K_b = K_b\,(t/c = 0.02; h/c = 0.08) = 1.23$ is the blade mechanics coefficient. Case studies considering other t/c and h/c values can be carried out using Figure 7.

4. PVS-Affected Rotor: An Exemplary Case Study

The aim of this section is to outline a design case study, resulting in a rotor suspected to be unfavorable in terms of noise and vibration due to PVS. Although several unfavorable design cases of such kind can be intentionally generated, this paper intends to present a single, representative design example. The resultant rotor will be termed herein the PVS-affected rotor. Such a design aims to serve as a basis for the realization of a case study rotor that is expected to exhibit remarkable and experimentally well-detectable narrowband signatures of PVS. By such means, the orders of the magnitude of harmfulness of PVS-related effects are to be quantified in future experiments on the PVS-affected rotor, in comparison with other rotors of comparative design. The features of the PVS-affected rotor are as follows:

(a) The rotor blading tends to exhibit a PVS of spanwise constant frequency, and thus, is theoretically presumed to realize large-scale, spatially coherent vortices over the dominant portion of the blade span. Such coherent vortices are assumed to cause spatially correlated, narrowband noise, as well as mechanical excitation over the dominant part of span at a given frequency. The condition of spanwise constant PVS frequency is therefore applied herein in a pessimistic aspect, although it is noted that the signature of PVS noise was observed by [19] even when PVS was confined to ~10% span near the tip of a single blade.

(b) The latter is presumed to provoke blade vibration, if the frequency of PVS coincides with the frequency of the first bending mode of blade vibration.

4.1. Aerodynamics: Blade Design

To be able to design a fan for which the spanwise constancy of PVS frequency is fulfilled—thus satisfying Equation (14), presented later—first, typical dimensionless design and geometrical characteristics, representative of propeller-type fans, were systematically gathered and summarized in Table 3. Here, the authors stress that, in order to guarantee the validity of Equation (9), the blade chord along the blade span was fixed, so $c(r_b)$ = constant. The tendency toward keeping the chord constant along the span in the blade design is supported by the literature examples of [19,20]. Based on the well-known Cordier diagram [46] for turbomachines of favorable efficiency, axial flow fans have the specific diameter and the specific speed within the approximate ranges of $1 \leq \delta \leq 1.5$ and $2 \leq \sigma \leq 3$, respectively. These ranges correspond to the global total pressure rise coefficient and flow coefficient within the ranges of $0.05 \leq \Psi_t \leq 0.25$ and $0.1 \leq \Phi \leq 0.5$, respectively. Thus, values in Table 3 fit to the Cordier diagram well. Regulation 327/2011/EU5 issued energy

efficiency requirements regarding fans in the EU [47], driven by motors with an electric input power between 125 W and 500 kW. According to this, the target total efficiency of an axial fan is $0.5 \leq \eta_t \leq 0.6$ depending on the arrangement and input power. Considering a more economical operation, we are moving toward higher efficiency levels; therefore, $\eta_t \approx 0.7$ is chosen.

Table 3. Geometrical and material parameters of the blade for the PVS-affected rotor.

c/D_{tip}	ν	AR	Ψ_t	Φ	N	η_t	δ	σ
0.133	0.415	2.22	0.143	0.309	5	0.700	1.11	2.39

The first two parameters as well as N in Table 3 define the blade solidity from hub to tip. When calculating the solidity (c/s), it is found that it is below 0.7 along the entire radius of the blade even at the hub, as can be observed in Figure 8. Therefore, according to [46] measurement data on isolated blade profiles—such as data included in Figure 4 in the case of a 8% cambered plate—can be applied in the present design of the PVS-affected rotor. In addition to the aerodynamic data in Figure 4, the empirical data on PVS in [5,13] are also related to isolated profiles, thus fitting to the low-solidity approach utilized herein.

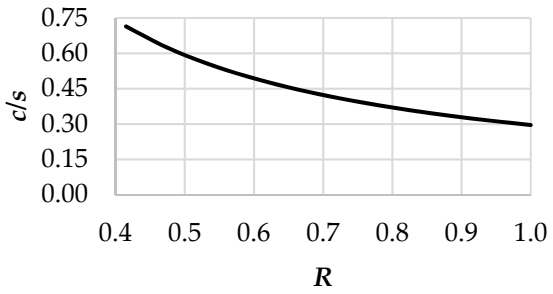

Figure 8. Blade solidity as a function of dimensionless radius ($R = r/r_{tip}$).

In what follows, preliminary design efforts are made for obtaining a rotor blading exhibiting PVS of spanwise constant frequency in order to fulfill the pessimistic condition outlined at the end of the Introduction. The PVS frequency can be expressed from Equation (2) as follows:

$$f_{PVS}(r_b) = St^* \frac{U_0(r_b)}{b(r_b)} = const \tag{14}$$

A nearly constant value of $St^* \approx 0.19$ was found for a 8% cambered plate for various Reynolds numbers and angles of attack in the present authors' previous measurement campaign [13]. Keeping the uncertainty of the measurement-based St^* data in mind, this value is in fair agreement with the literature-based data in Equation (2). $St^* = 0.19$ was used for the calculation presented in the paper. In order to clarify the trend of the free-stream velocity, the velocity vectors are shown in Figure 9. Based on Figure 9, the square of the free-stream velocity can be written as follows [46]:

$${U_0}^2(r_b) = {c_x}^2(r_b) + \left(u(r_b) - \frac{\Delta c_u(r_b)}{2}\right)^2 \tag{15}$$

where c_x is the axial velocity component; u is the circumferential velocity; and Δc_u is the increase of tangential velocity due to the rotor.

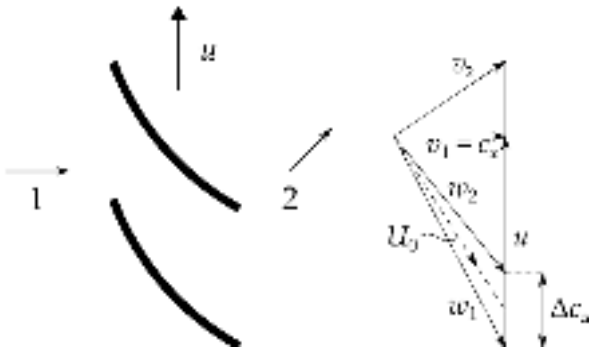

Figure 9. Velocity triangles.

From Equation (15) the square of the dimensionless free-stream velocity can be expressed as follows:

$$\frac{U_0{}^2(r_b)}{u_{tip}{}^2} = \varphi^2(R) + \left(R - \frac{\psi_{t,is}(R)}{4R}\right)^2 \equiv W^2(R) \tag{16}$$

where W is the dimensionless free-stream velocity; $\varphi = c_x(r_b)/u_{tip}$ is the local flow coefficient; R is the dimensionless radius; and $\psi_{t,is}$ is the local isentropic total pressure rise coefficient. As a brief approximation, the circumferential velocity u, representing a solid body rotation, dominates in U_0. Therefore, U_0 tends to approximately linearly increase with R. In a refined calculation, presented later, c_x/u_{tip} and $\Delta c_u/u_{tip}$ are taken into account when obtaining U_0.

In order to provide a spanwise constant f_{PVS}, $b(r_b)$ tends to increase along the span by such means that its increase matches with the spanwise increase of U_0.

According to [5], the distance between vortex rows normalized by the blade chord is:

$$\frac{b(r_b)}{c} = K^* \frac{\Theta(r_b)}{c} \tag{17}$$

where $K^* \approx 1.2$ is an empirical coefficient [5] and Θ is the momentum thickness of the blade wake. According to [17,48] the drag coefficient can be written as:

$$C_D(r_b) = \frac{2\Theta(r_b)}{c} \tag{18}$$

Thus b can be expressed as follows:

$$b(r_b) = c\, K^* \frac{C_D(r_b)}{2} \tag{19}$$

From Equation (19) it can be observed that a spanwise increase of b can be achieved via spanwise increase of C_D. Based on Figure 4, $C_D(R_{mid}) = 0.032$ is chosen, which corresponds to $\alpha = 6.8°$. In the design of the PVS-affected rotor, the following range of $C_D(R)$ was used: $0.0196 \leq C_D \leq 0.0410$. Furthermore, as Figure 4 illustrates, the C_D data within the design range are assigned to α data, and via such assignment, they also determine the design range for the local lift coefficient $C_L(\alpha)$. Therefore, the lift-to-drag ratio $LDR(\alpha) = C_L/C_D$ data are also obtained for the entire design range, incorporating the data at R_{mid}. Thus, each of $C_D(R_{mid})$, $C_L(R_{mid})$, and $LDR(R_{mid})$ are available; these quantities will play an important role in the further investigation of the PVS-affected rotor, as presented later.

Iterative Method

In order to provide a spanwise constant f_{PVS}, the nearly linear spanwise increase of U_0 is matched in blade design with the spanwise increase of C_D. To be able to design such a fan, an iterative method is elaborated as follows, using the data in Table 3 as the basis. Using Equation (16) as an initial guess, the increase of tangential velocity due to

the rotor is neglected; therefore, $W(R)$ is calculated from only the local flow coefficient $\varphi = c_x(r_b)/u_{tip}$ and the dimensionless radius corresponding to the rigid body rotation. In the present methodology, uniform axial inlet condition is assumed, $c_x(r_b)/u_{tip}$ = constant. Furthermore, based on [46] as an approximation, the change of meridional—i.e., axial—velocity is neglected through the rotor. The above implies that spanwise constant axial velocity is presumed, as a brief approximation.

As a next step, based on the value of $W(R_{mid})/C_D(R_{mid})$, the drag coefficients are determined along the blade span. As described earlier, the $C_D(R)$, $\alpha(R)$ and $C_L(R)$ data are assigned to each other, via Figure 4. As a next stage of the design, $\Delta c_u/u_{tip}$ is expressed from the simplified work equation of an elemental rotor:

$$\frac{c}{s(r_b)} C_L(r_b) \cong \frac{2\Delta c_u(r_b)}{U_0(r_b)} \tag{20}$$

where $s = 2r_b\pi/N$ is the blade spacing. With the knowledge of $\Delta c_u(R)/u_{tip}$, the local isentropic total pressure rise coefficient $\psi_{t,is}(R)$ is expressed from the Euler equation of turbomachines:

$$\Delta p_{t,is}(r_b) = \rho_a u(r_b) \Delta c_u(r_b) \tag{21}$$

here $\Delta p_{t,is}$ is the isentropic total pressure rise, and ρ_a is the density of air. This computed $\psi_{t,is}(R)$ is then substituted into Equation (16) for calculating a new approximation of $W(R)$ in the next iteration loop. Fast convergence is obtained in two to three iteration loops. The results are judged to be converged if the relative difference in $\psi_{t,is}(R)$ for the consecutive iteration steps becomes less than 2%.

A feature of the iterative method is that $\psi_{t,is}(R)$ and $\alpha(R)$ are actually the results of the design process. The spanwise distributions of the calculated quantities are shown in Figure 10, where $\gamma(R)$ is stagger angle measured from the circumferential direction. Annulus-averaging of $\psi_{t,is}(R)$ represents the global isentropic total pressure rise obtained as Ψ_t/η_t, using the data in Table 3.

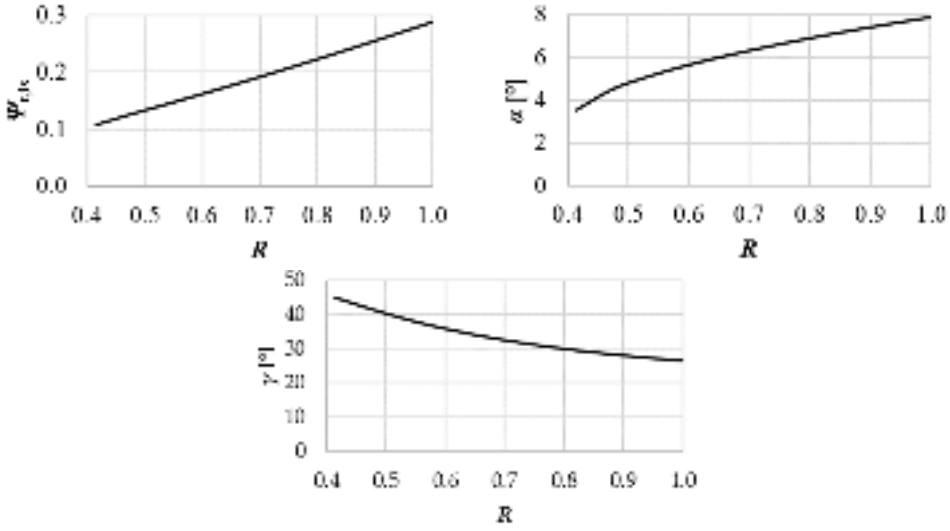

Figure 10. Calculated distributions $\psi_{t,is}(R)$, $\alpha(R)$, and $\gamma(R)$ as a function of R.

Figure 11 represents the proportionate three-dimensional model of the designed PVS-affected fan. The rotor has a realistic, common geometry, as it is representative of propeller-type axial flow industrial fans. The blade geometry is in accordance with the fact that, as a manufacturing simplification, low-speed axial fan blades of cost-effective manufacturing can be made from a plate of spanwise constant chord, as they are rolled in such a way that spanwise constant camber and moderate twist occur.

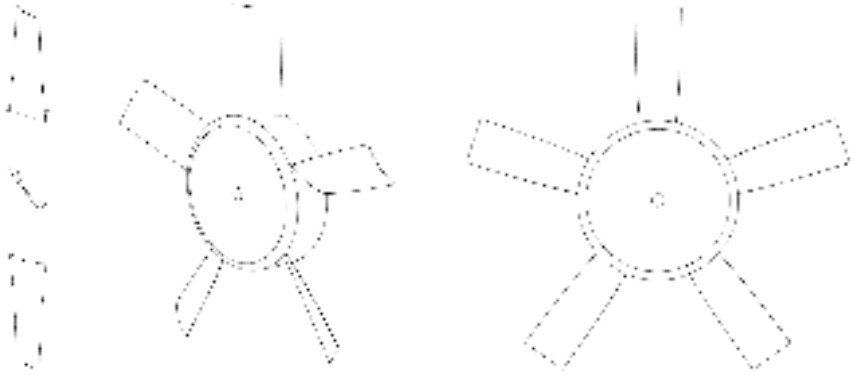

Figure 11. The PVS-affected fan rotor.

4.2. Mechanically or Acoustically Unfavorable Design Cases

In order to set up mechanically unfavorable design cases, representing a coincidence of the frequency of PVS with the frequency of the first bending mode of blade vibration, it is necessary to express U_0 and b in Equation (14). However, b was previously expressed, as shown in Equation (17). Therefore, it is only necessary to deal with U_0. Based on Equations (20) and (21), the free-stream velocity is written as follows:

$$U_0(r_\mathrm{b}) = \frac{2\Delta p_{\mathrm{t,is}}(r_\mathrm{b})\, s(r_\mathrm{b})}{\rho_\mathrm{a} u(r_\mathrm{b})\, c\, C_\mathrm{L}(r_\mathrm{b})} \tag{22}$$

Thus, the PVS frequency can be expressed from Equations (14), (19) and (22):

$$f_\mathrm{PVS}(r_\mathrm{b}) = St^* \frac{2\Delta p_{\mathrm{t,is}}(r_\mathrm{b})}{\rho_\mathrm{a}\, c\, C_\mathrm{L}(r_\mathrm{b})} \frac{s(r_\mathrm{b})}{u(r_\mathrm{b})} \frac{2}{K^* C_\mathrm{D}(r_\mathrm{b})\, c} \tag{23}$$

With the use of $s(r_\mathrm{b})/u(r_\mathrm{b}) = (2\, r_\mathrm{b}\pi/N)/(2\, r_\mathrm{b}\pi n) = 1/(nN)$ and $C_\mathrm{D} = C_\mathrm{L}/LDR$, Equation (23) is written as follows:

$$f_\mathrm{PVS}(r_\mathrm{b}) = St^* \frac{2\Delta p_{\mathrm{t,is}}(r_\mathrm{b})}{\rho_\mathrm{a} c\, C_\mathrm{L}(r_\mathrm{b})} \frac{1}{N\, n} \frac{2\, LDR(r_\mathrm{b})}{K^* C_\mathrm{L}(r_\mathrm{b})\, c} \tag{24}$$

where N is the blade count and n is the rotor speed. The right-hand side of Equation (24) can be rearranged according to Equation (25) in the following way: In the first term, the global aerodynamic performance characteristics are grouped. The second term represents the operational condition of the rotor. In the third term, the basic parameters of the blade geometry are gathered. The fourth term represents the aerodynamics parameters of the elemental blade section. Finally, the last term incorporates the empirics and coefficients.

$$f_\mathrm{PVS}(r_\mathrm{b}) = \frac{\Delta p_{\mathrm{t,is}}(r_\mathrm{b})}{\rho_\mathrm{a}} \frac{1}{n} \frac{1}{N\, c^2} \frac{LDR(r_\mathrm{b})}{C_\mathrm{L}^2(r_\mathrm{b})} \frac{4\, St^*}{K^*} \tag{25}$$

In order to obtain generalized conclusions and trends, dimensionless quantities and groups must be introduced. It should be emphasized that PVS frequency is constant along the blade span due to the presented fan design method. Therefore, any characteristic taken at an arbitrary r_b radius can be replaced by the same characteristic taken at R_mid. Furthermore, as a brief approximation $\eta_\mathrm{t}(r_\mathrm{b}) = \eta_\mathrm{t}(R_\mathrm{mid}) \approx$ constant is presumed. With respect to the foregoing, the first term on the right-hand side of Equation (25) can be expressed:

$$\frac{\Delta p_{\mathrm{t,is}}(r_\mathrm{b})}{\rho_\mathrm{a}} = \frac{\Delta p_{\mathrm{t,is}}(R_\mathrm{mid})}{\rho_\mathrm{a}} = \frac{\Delta p_\mathrm{t}(R_\mathrm{mid})}{\rho_\mathrm{a}\eta_\mathrm{t}(R_\mathrm{mid})} = \frac{\Psi_\mathrm{t}(R_\mathrm{mid})}{\eta_\mathrm{t}} \frac{u_\mathrm{tip}^2}{2} \tag{26}$$

where $u_{tip} = D_{tip}\pi n$ is the tip circumferential speed. The second and the third terms are written as follows:

$$\frac{1}{n}\frac{1}{c^2N} = \frac{1}{n}\frac{1}{D_{tip}\pi}D_{tip}\pi\frac{1}{c^2N} = \frac{1}{u_{tip}}s_{tip}\frac{1}{c^2} \tag{27}$$

Thus Equation (25):

$$f_{PVS}(R_{mid}) = \frac{\Psi_t(R_{mid})}{\eta_t}\frac{u_{tip}^2}{2}\frac{s_{tip}}{u_{tip}}\frac{1}{c^2}\frac{LDR(R_{mid})}{C_L^2(R_{mid})}\frac{4St^*}{K^*} = \frac{\Psi_t(R_{mid})}{\eta_t(R_{mid})}\frac{u_{tip}s_{tip}}{c^2}\frac{LDR(R_{mid})}{C_L^2(R_{mid})}\frac{2\ St^*}{K^*} \tag{28}$$

As it is outlined previously, the mechanically unfavorable design case is considered when the spanwise constant PVS frequency coincides with the first bending eigenfrequency of the fan blade, posing an increased risk of blade resonance:

$$f_{PVS} = const = f_{B,1} \tag{29}$$

If Equations (28) and (13) are substituted in the right-hand side and the left-hand side of Equation (29), respectively, the following equation is obtained:

$$\frac{\Psi_t(R_{mid})}{\eta_t(R_{mid})}\frac{u_{tip}\ s_{tip}}{c^2}\frac{LDR(R_{mid})}{C_L^2(R_{mid})}\frac{2\ St^*}{K^*} = \frac{0.56}{l^2}K_b t\ a_b \tag{30}$$

After rearrangement, Equation (30) can be written in the following as dimensionless, from:

$$\frac{u_{tip}}{a_b} = \frac{\eta_t(R_{mid})}{\Psi_t(R_{mid})}\frac{t}{c}\left(\frac{c}{s}\right)_{tip}\frac{1}{AR^2}\frac{C_L^2(R_{mid})}{LDR(R_{mid})}K_b\frac{0.56\ K^*}{2St^*} \tag{31}$$

Equation (31) provides a means for calculating the critical u_{tip}/a_b velocity ratio for which PVS results in blade resonance, if the nondimensional characteristics—valid for an entire PVS-affected rotor family under survey—are substituted into the right-hand side of the equation. With knowledge of the blade material, a_b can be obtained (cf. Equation (10) and the paragraph below), and thus, the critical u_{tip} value can be computed. Hence, critical rotor diameter X rotor speed data couples can be discovered for an entire rotor family, consisting of rotors of various diameters and speeds.

If the rotor diameter and the nominal rotor speed are fixed for further defining a specific case study, the resultant, nominal u_{tip} value can be compared to the aforementioned critical one. Thus, it can be judged whether a risk of blade resonance may occur by changing the rotor speed, e.g., via a frequency converter. Furthermore, if the rotor diameter and the rotor speed are fixed, all dimensional quantities can be calculated, with the knowledge of nondimensional data in Table 3 as well as on the right-hand side of Equation (25). This makes possible the calculation of f_{PVS}, using Equation (25), for acoustics evaluation. By such means, the third-octave band incorporating PVS can be identified and critically evaluated. For this purpose, the A-weighting graph [49] is to be considered. The plateau of the A-weighting graph represents the most sensitive part of the human audition. Keeping f_{PVS} away from this plateau in blade design, by selecting the appropriate operational and geometrical characteristics, gives a potential for moderating the impact of fan noise on humans. If such design intent cannot be realized for modifying f_{PVS}, the PVS phenomenon in itself is to be suppressed, necessitating modifications in the blade layout, e.g., boundary-layer tripping. However, such modifications are to be treated with criticism, as, e.g., boundary layer tripping may undermine the performance of the fan [3]. Such undesired effects justify the present intent by the authors to accept the occurrence of PVS but "mistune" it toward uncritical frequencies by simple preliminary design means, as a first approach. Such mistuning, being beneficial from both vibration and noise points of view, is to be performed in the preliminary blade design by the negation—i.e., avoidance—of the worst-case design and operational scenarios represented by PVS-affected rotors. For this reason, setting up guidelines for the worst-case design scenarios is of practical value.

5. Calculation Example for the Designed Rotor

First, based on Equation (31) and data in Table 3, as it is specific to the PVS-affected rotor designed herein, the critical tip speeds are computed for various blade materials, which means different values of a_b in terms of the calculation process. The calculated values are summarized in Table 4.

Table 4. Critical rotor tip speeds.

		Steel	Aluminum	Polycarbonate
a_b	[m/s]	5000	5100	1350
$u_{tip,crit}$	[m/s]	1.80	1.83	0.49

The methodology presented herein provides a means for simply checking whether PVS may cause a risk at all from a blade resonance point of view. Based on Table 4, it can be concluded that in the present case study, the critical tip speed is sufficiently low to make these cases irrelevant for the blade resonance point of view of the first-order bending mode (Figure 6). Namely, only impractically low rotor diameters D and/or rotor speeds n would result in coincidence of the f_{PVS} and $f_{B,1}$ [Equation (10)] values for the presented case study. Furthermore, the lower the tip speed, the lower the fluctuating force causing vibration. However, the risk of blade vibration cannot be excluded for other design cases, characterized by modified data in Table 3 and for other—i.e., higher-order bending, as well as torsional—modes of vibration. Therefore, an important future task—as part of the ongoing research project—is to systematically explore risky cases (operational, geometrical, and material characteristics) from the resonance point of view. The methodology presented herein can be generally applied for such systematic studies.

The reader is reminded that the mechanical effect of the blade twist is neglected herein, cf. Section 2. With consideration of the blade twist, the first bending eigenfrequency would be less, thus reducing the impractically low critical tip speed even further.

As the second part of the calculation example, the rotor diameter and rotor speed are fixed as follows: D_{tip} = 0.900 m, n = 1450 1/min. Such values are relevant in industrial ventilation. They result in u_{tip} = 68.3 m/s. Considering data in Table 4 as well as previously fixed further parameters, the additional quantities required to calculate the PVS frequency, according to Equation (28), are derived. The values of the computed quantities are presented in Table 5.

Table 5. PVS frequency for a five-bladed, n = 1450 1/min axial flow fan.

D_{tip}	c	C_L (R_{mid})	LDR (R_{mid})	s_{tip}	f_{PVS}
0.900 m	0.120 m	1.30	43.5	0.565	4520 Hz

The calculated PVS frequency falls within the third-octave band of the middle frequency of 5 kHz. Thus, it approximates the plateau of the A-weighting graph. Therefore, the related noise may cause increased annoyance for a human observer. However, by modifying the design parameters, the axial fan can be redesigned to keep the PVS frequency away from the plateau of the A-weighting graph, based on the presented computation. The systematic exploration of the advantageous parameter modifications, while finding reasonable compromises with other design perspectives, is also a future task.

Based on Table 2, for the first bending eigenfrequency of the designed blade, the following value is calculated: $f_{B,1}$ = 116 Hz. For the sake of completeness, the following mandatory engineering investigation is to be performed. On the one hand, is to be checked whether the computed eigenfrequency is sufficiently far from the nominal rotational frequency. The rotational speed n = 1450 1/min, which corresponds to 24 Hz, is thus ≈ 20% of the first bending eigenfrequency, which is satisfactory.

On the other hand, as mentioned in Section 3.1, elements located upstream of the rotor may lead to rotor–stator interaction, occurring at a frequency of rotational frequency n

multiplied by the number of upstream elements. Therefore, it is necessary to examine for which number of upstream elements (e.g., support strut, inlet guide vane) the computed eigenfrequency would coincide with the excitation frequency of the rotor–stator interaction. As $f_{B,1} \approx 5 \times 24$ Hz = 120 Hz, the critical element number is five, which should be avoided by all means. For example, upon demand, the application of three fan-supporting struts upstream of the rotor fulfills this condition.

6. Conclusions and Future Remarks

Based on the semi-empirical model in literature, the pessimistic design condition of spanwise constant PVS frequency is determined from an aerodynamic approach. To fulfill this condition, an iterative fan design method was elaborated, resulting in a design case study of a PVS-affected rotor. The frequency of PVS was computed with the knowledge of the global operational and geometrical characteristics of an axial fan. A calculation process for determining the eigenfrequency related to the first bending mode of vibration of a circular-arc-cambered plate blade was presented. By combining these two approaches, guidelines can be formulated, already in the preliminary design phase, for the following.

(a) The critical tip speed that may cause resonance can be estimated for various blade materials, according to Equation (31).
(b) On the basis of (a), the critical rotor speed n can be calculated for axial fans of known diameter. Thus, it can be judged whether a risk of blade resonance may occur by changing the rotor speed.
(c) The expected PVS frequency can be determined by knowing the rotor speed of the fan. Therefore, the adverse acoustic effect of PVS can be forecasted on the basis of the A-weighting graph.

As a future objective, opposing the pessimistic design scenarios, redesign efforts are to be made for moderating/avoiding blade resonance and/or noise annoyance. Such efforts incorporate actions against the constancy of PVS frequency along the span. Systematic redesign scenarios as well as comparative experiments—also incorporating pessimistic, PVS-affected rotor cases—will be realized in the future for validating the methodology presented herein. The design aspects related to PVS are to be investigated in the future via studies on 2D—i.e., rectilinear—blade models as well as on truly 3D rotor blade geometries—unavoidable for full consideration of realistic rotor flow effects—by the concerted means of computational fluid dynamics (CFD), analytical mechanics, finite-element mechanical computations, and experimentation. Such studies will also serve as the exploration of the effects of assumptions and simplifications made in the method presented herein.

Author Contributions: G.D. and J.V. conceptualization, methodology, investigation, and writing. All authors have read and agreed to the published version of the manuscript.

Funding: This work has been supported by the Hungarian National Research, Development and Innovation (NRDI) Centre under contract No. NKFI K 129023. The research reported in this paper and carried out at BME has been supported by the NRDI Fund (TKP2021, project no. BME-NVA-02, TKP2021-EGA, and TKP2020 NC, Grant No. BME-NCS) based on the charter of bolster issued by the NRDI Office under the auspices of the Ministry for Innovation and Technology of Hungary. The contribution of Gábor DAKU has been supported by Gedeon Richter Talent Foundation (registered office: 1103 Budapest, Gyömrői út 19-21.), established by Gedeon Richter Plc., within the framework of the "Gedeon Richter PhD Scholarship".

Institutional Review Board Statement: Not applicable.

Informed Consent Statement: Not applicable.

Data Availability Statement: Not applicable.

Acknowledgments: The authors are thankful to Tamás KALMÁR-NAGY for his assistance in the blade mechanics analysis.

Conflicts of Interest: The authors declare no conflict of interest.

Abbreviations

The following abbreviations are used in this manuscript:

Latin Letters

A	Cross-section [m^2]
a_b	Wave propagation speed = $(E/\rho_\mathrm{b})^{1/2}$ [m/s]
AR	Aspect ratio = l/c [-]
b	Transversal dist. between vortex rows [m]
c/s	Blade solidity [-]
D	Rotor diameter [m]
d_TE	Trailing edge thickness [m]
E	Young modulus [Pa]
F	Characteristic function
f	Dominant frequency [Hz]
g	Lateral displacement [m]
G	Shear modulus [Pa]
h	Maximum height of the camber line [m]
h/c	Relative camber [-]
i	Order number, e.g., 1, 2, 3 etc.
I	Second moment of area [m^4]
I_p	Polar moment of area [m^4]
I_t	Torsional constant [m^4]
K*	Empirical coefficient $\approx$ 1.2 [-]
K_1	Preliminary design constant [-]
K_b	Blade mechanics coefficient [-]
K_t	Mechanical constant [-]
$K_{\mathrm{B},i}$	Bending mode constant [-]
c	Blade chord length [m]
c_x	Axial velocity component [m/s]
C_D	Drag coefficient [-]
C_L	Lift coefficient [-]
l	Blade span [m]
LDR	Lift-to-drag ratio = $C_\mathrm{L}/C_\mathrm{D}$ [-]
N	Blade count [-]
n	Rotor speed [1/s]
R	Dimensionless radius = r/r_tip [-]
r	Radial coordinate [m]
Re_c	Reynolds number = $c\ U_0\ /\nu_\mathrm{a}$ [-]
s	Blade spacing = $2r\pi/N$ [m]
St	Strouhal number [-]
St*	Universal Strouhal number [-]
t	Profile thickness [m]
t/c	Relative thickness [-]
u	Rotor circumferential velocity [m/s]
U_0	Free-stream velocity = $(w_1 + w_2)/2$ [m/s]
U	Length of midwall perimeter [m]
w	Relative velocity component [m/s]
W	Dimensionless free-stream velocity [-]
v	Absolute velocity component [m/s]
x, y, z	Cartesian coordinates [m]

Greek Letters

α	Angle of attack [°]
$\beta_i l$	Vibration constant $\approx (2i-1)\pi/2$
γ	Stagger angle [°]
δ	Specific diameter [-]
ζ	Rotation angle [rad]
Δc_u	Increase of tangential velocity [m/s]
$\Delta p_{\mathrm{t,is}}$	Isentropic total pressure rise [Pa]
η	Efficiency [-]
Θ	Momentum thickness of blade wake [m]
ν	Hub-to-tip ratio [-]
ν_{a}	Kinematic viscosity of air [m^2/s]
ν_{P}	Poisson's ratio [-]
ρ	Density [kg/m^3]
σ	Specific speed [-]
τ	Time [s]
φ	Local flow coefficient [-]
Φ	Global flow coefficient [-]
ψ	Local pressure rise coefficient [-]
Ψ	Global pressure rise coefficient [-]

Subscripts and Superscripts

1	Rotor inlet
2	Rotor outlet
a	Air
b	Blade
B	Bending
crit	Critical
i	Order-number i.e., 1, 2, 3
is	Isentropic
mid	Mid-span position
n	Order-number i.e., 1, 2, 3
PVS	Profile vortex shedding
t	Total
T	Torsional
TE	Trailing edge
tip	Blade tip

Abbreviations

2D	Two-dimensional
3D	Three-dimensional
B	Bending mode
CG	Center of gravity
CFD	Computational fluid dynamics
PVS	Profile vortex shedding
T	Torsional mode
TE	Trailing edge
VS	Vortex shedding
FEM	Finite element method

Appendix A

Table A1. Third-octave band.

Band No.	Lower Band Limit (Hz)	Center Frequency (Hz)	Upper Band Limit (Hz)
1	11.2	12.5	14.1
2	14.1	16	17.8
3	17.8	20	22.4
4	22.4	25	28.2
5	28.2	31.5	35.5
6	35.5	40	44.7
7	44.7	50	56.2
8	56.2	63	70.8
9	70.8	80	89.1
10	89.1	100	112
11	112	125	141
12	141	160	178
13	178	200	224
14	224	250	282
15	282	315	355
16	355	400	447
17	447	500	562
18	562	630	708
19	708	800	891
20	891	1000	1122
21	1122	1250	1413
22	1413	1600	1778
23	1778	2000	2239
24	2239	2500	2818
25	2818	3150	3548
26	3548	4000	4467
27	4467	5000	5623
28	5623	6300	7079
29	7079	8000	8913
30	8913	10,000	11,220
31	11,220	12,500	14,130
32	14,130	16,000	17,780
33	17,780	20,000	22,390

References

1. Brooks, T.F.; Pope, D.S.; Marcolini, M.A. *Airfoil Self-Noise and Prediction*; NASA Ref. Publication: Washington, DC, USA, 1989; Volume 1218. Available online: https://ntrs.nasa.gov/citations/19890016302 (accessed on 27 September 2021).
2. Yakhina, G.; Roger, M.; Moreau, S.; Nguyen, L.; Golubev, V. Experimental and Analytical Investigation of the Tonal Trailing-Edge Noise Radiated by Low Reynolds Number Aerofoils. *Acoustics* **2020**, *2*, 293–329. [CrossRef]
3. Lowson, M.; Fiddes, S.; Nash, E. Laminar Boundary Layer Aeroacoustic Instabilities. In Proceedings of the 32nd Aerospace Sciences Meeting and Exhibit, Reno, NV, USA, 10–13 January 1994; p. 10. [CrossRef]
4. Balla, E.; Vad, J. A semi-empirical model for predicting the frequency of profile vortex shedding relevant to low-speed axial fan blade sections. In Proceedings of the 13th European Conference on Turbomachinery Fluid Dynamics & Thermodynamics (ETC13), Lausanne, Switzerland, 8–12 April 2019; p. 12. [CrossRef]
5. Balla, E. Aerodynamic and Aeroacoustic Behavior of Axial Fan Blade Sections at Low Reynolds Numbers. Ph.D. Thesis, Department of Fluid Mechanics, Faculty of Mechanical Engineering, Budapest University of Technology and Economics, Budapest, Hungary, 2020. Available online: http://hdl.handle.net/10890/13530 (accessed on 27 September 2021).
6. Tam, C.K.W. Discrete tones of isolated airfoils. *J. Acoust. Soc. Am.* **1974**, *55*, 1173–1177. [CrossRef]
7. Wright, S. The acoustic spectrum of axial flow machines. *J. Sound Vib.* **1976**, *45*, 165–223. [CrossRef]
8. Nash, E.C.; Lowson, M.V.; McAlpine, A. Boundary-layer instability noise on aerofoils. *J. Fluid Mech.* **1999**, *382*, 27–61. [CrossRef]
9. Ausoni, P.; Farhat, M.; Bouziad, Y.; Kueny, J.-L.; Avellan, F. Kármán vortex shedding in the wake of a 2D hydrofoil: Measurement and numerical simulation. In Proceedings of the IAHR International Meeting of WG on Cavitation and Dynamic Problems in Hydraulic Machinery and Systems, Barcelona, Spain, 28–30 June 2006; p. 14. Available online: https://infoscience.epfl.ch/record/88122 (accessed on 27 September 2021).

10. Roger, M.; Moreau, S. Extensions and limitations of analytical airfoil broadband noise models. *Int. J. Aeroacoust.* **2010**, *9*, 273–305. [CrossRef]
11. Yarusevych, S.; Sullivan, P.E.; Kawall, J.G. On vortex shedding from an airfoil in low-Reynolds-number flows. *J. Fluid Mech.* **2009**, *632*, 245–271. [CrossRef]
12. Yarusevych, S.; Boutilier, M.S.H. Vortex Shedding of an Airfoil at Low Reynolds Numbers. *AIAA J.* **2011**, *49*, 2221–2227. [CrossRef]
13. Daku, G.; Vad, J. Experiment-Based Preliminary Design Guidelines for Consideration of Profile Vortex Shedding From Low-Speed Axial Fan Blades. *J. Turbomach.* **2021**, *143*, 061014. [CrossRef]
14. Lee, C.; Chung, M.; Kim, Y.-H. A Prediction Model for the Vortex Shedding Noise from the Wake of an Airfoil or Axial Flow Fan Blades. *J. Sound Vib.* **1993**, *164*, 327–336. [CrossRef]
15. Sasaki, S.; Kodama, Y.; Hayashi, H.; Hatakeyama, M. Influence of the karman vortex street on the broadband noise generated from a multiblade fan. *J. Therm. Sci.* **2005**, *14*, 198–205. [CrossRef]
16. Dou, H.; Li, Z.; Lin, P.; Wei, Y.; Chen, Y.; Cao, W.; He, H. An improved prediction model of vortex shedding noise from blades of fans. *J. Therm. Sci.* **2016**, *25*, 526–531. [CrossRef]
17. Paterson, R.W.; Vogt, P.G.; Fink, M.R.; Munch, C.L. Vortex Noise of Isolated Airfoils. *J. Aircr.* **1973**, *10*, 296–302. [CrossRef]
18. Arbey, H.; Bataille, J. Noise generated by airfoil profiles placed in a uniform laminar flow. *J. Fluid Mech.* **1983**, *134*, 33–47. [CrossRef]
19. Longhouse, R. Vortex shedding noise of low tip speed, axial flow fans. *J. Sound Vib.* **1977**, *53*, 25–46. [CrossRef]
20. Grosche, F.-R.; Stiewitt, H. Investigation of Rotor Noise Source Mechanisms with Forward Speed Simulation. *AIAA J.* **1978**, *16*, 1255–1261. [CrossRef]
21. Harris, C.M. *Dictionary of Architecture and Construction*, 4th ed.; McGraw-Hill Education: New York, NY, USA, 2006.
22. Castegnaro, S.; Masi, M.; Lazzaretto, A. Preliminary Experimental Assessment of The Performance of Tube-Axial Fans Designed With Different Vortex Criteria. In Proceedings of the European Conference on Turbomachinery Fluid Dynamics and hermodynamics, Stockholm, Sweden, 3–7 April 2017; European Turbomachinery Society: Lausanne, Switzerland, 2017; p. 13.
23. Masi, M.; Lazzaretto, A. A New Practical Approach to the Design of Industrial Axial Fans: Tube-Axial Fans with Very Low Hub-to-Tip Ratio. *J. Eng. Gas Turbines Power* **2019**, *141*, 101003. [CrossRef]
24. Carnegie, W. Vibrations of Pre-Twisted Cantilever Blading. *Proc. Inst. Mech. Eng.* **1959**, *173*, 343–374. [CrossRef]
25. Gruber, J.; Blahó, M.; Herzog, P.; Kurutz, I.; Preszler, L.; Vajna, Z.; Szentmártony, T. *Fans (Ventilátorok, in Hungarian)*, 2nd ed.; Műszaki Könyvkiadó: Budapest, Hungary, 1968.
26. Bohl, W. *Strömungsmaschinen 2; Berechnung und Konstruktion*; Kamprath-Reihe: Vogel Buchverlag, Germany, 1991.
27. Banerjee, J.; Williams, F. Coupled bending-torsional dynamic stiffness matrix for timoshenko beam elements. *Comput. Struct.* **1992**, *42*, 301–310. [CrossRef]
28. Sinha, S.K. Combined Torsional-Bending-Axial Dynamics of a Twisted Rotating Cantilever Timoshenko Beam with Contact-Impact Loads at the Free End. *J. Appl. Mech.* **2006**, *74*, 505–522. [CrossRef]
29. Sinha, S.K.; Turner, K.E. Natural frequencies of a pre-twisted blade in a centrifugal force field. *J. Sound Vib.* **2011**, *330*, 2655–2681. [CrossRef]
30. Sun, Q.; Ma, H.; Zhu, Y.; Han, Q.; Wen, B. Comparison of rubbing induced vibration responses using varying-thickness-twisted shell and solid-element blade models. *Mech. Syst. Signal Process.* **2018**, *108*, 1–20. [CrossRef]
31. Rao, S.S. *Vibration of Continuous Systems*; John Wiley & Sons: Hoboken, NJ, USA, 2007.
32. Gorman, D.J. *Free Vibration Analysis of Beams and Shafts*; John Wiley: New York, NY, USA, 1975.
33. Bishop, R.; Price, W. Coupled bending and twisting of a timoshenko beam. *J. Sound Vib.* **1977**, *50*, 469–477. [CrossRef]
34. Bercin, A.; Tanaka, M. Coupled Flexural–Torsional Vibrations of Timoshenko Beams. *J. Sound Vib.* **1997**, *207*, 47–59. [CrossRef]
35. Daly, B.B. *Woods Practical Guide to Fan Engineering*; Sixth Impression; Woods of Colchester Ltd.: Colchester, UK, 1992.
36. Roark, R.J.; Young, W.C.; Budynas, R.G. *Roark's Formulas for Stress and Strain*; McGraw-Hill: New York, NY, USA, 2002.
37. Blevins, R.D. *Formulas for Natural Frequency and Mode Shape*; Van Nostrand Reinhold Co.: New York, NY, USA, 1979.
38. Boresi, A.P.; Schmidt, R.J. *Advanced Mechanics of Materials*, 6th ed.; John Wiley & Sons: New York, NY, USA, 2003.
39. Hermann, T.M.; Mamarthupatti, D.; Locke, J.E. Postbuckling Analysis of a Wind Turbine Blade Substructure. *J. Sol. Energy Eng.* **2005**, *127*, 544–552. [CrossRef]
40. Mao, R.H.; Meguid, S.A.; Ng, T.Y. Finite Element Modeling of a Bird Striking an Engine Fan Blade. *J. Aircr.* **2007**, *44*, 583–596. [CrossRef]
41. Hsu, M.-C.; Akkerman, I.; Bazilevs, Y. Finite element simulation of wind turbine aerodynamics: Validation study using NREL Phase VI experiment. *Wind. Energy* **2013**, *17*, 461–481. [CrossRef]
42. Loya, J.; Rubio, M.L.; Fernandez-Saez, J. Natural frequencies for bending vibrations of Timoshenko cracked beams. *J. Sound Vib.* **2006**, *290*, 640–653. [CrossRef]
43. Balla, E.; Vad, J. Lift and drag force measurements on basic models of low-speed axial fan blade sections. *Proc. Inst. Mech. Eng. Part A J. Power Energy* **2018**, *233*, 165–175. [CrossRef]
44. Wallis, R.A. *Axial Flow Fans*; George Newnes Ltd.: London, UK, 1961.
45. Beer, F.P.; Johnston, E.R.; Mazurek, D.F. *Vector Mechanics for Engineers: Statics*, 11th ed.; McGraw-Hill: New York, NY, USA, 2016; pp. 485–572.
46. Carolus, T. *Ventilatoren*; B. G. Teubner Verlag: Wiesbaden, German, 2003.

47. Regulation of the European Commission (EU). No. 327/2011, of 30 March 2011, implementing Directive 2009/125/EC of the European Parliament and of the Council of the European Union with regard to ecodesign requirements for fans driven by motors with an electric input power between 125 W and 500 kW. *Off. J. Eur. Union* **2011**, *54*, 8–21.
48. Fathy, A.; Rashed, M.; Lumsdaine, E. A theoretical investigation of laminar wakes behind airfoils and the resulting noise pattern. *J. Sound Vib.* **1977**, *50*, 133–144. [CrossRef]
49. Norton, M.P.; Karczub, D.G. Fundamentals of Noise and Vibration Analysis for Engineers, 2nd Edition. *Noise Control. Eng. J.* **2007**, *55*, 275. [CrossRef]

International Journal of
Turbomachinery
Propulsion and Power

MDPI

Article

Design and Parametric Analysis of a Supersonic Turbine for Rotating Detonation Engine Applications

Noraiz Mushtaq, Gabriele Colella and Paolo Gaetani *

Laboratory of Fluid Machines (LFM), Energy Department, Politecnico di Milano, Via Lambruschini 4, 20156 Milano, Italy; noraiz.mushtaq@polimi.it (N.M.); gabriele.colella@mail.polimi.it (G.C.)
* Correspondence: paolo.gaetani@polimi.it

Abstract: Pressure gain combustion is a promising alternative to conventional gas turbine technologies and within this class the Rotating Detonation Engine has the greatest potential. The Fickett–Jacobs cycle can theoretically increase the efficiency by 15% for medium pressure ratios, but the combustion chamber delivers a strongly non-uniform flow; in these conditions, conventionally designed turbines are inadequate with an efficiency below 30%. In this paper, an original mean-line code was developed to perform an advanced preliminary design of a supersonic turbine; self-starting capability of the supersonic channel has been verified through Kantrowitz and Donaldson theory; the design of the supersonic profile was carried out employing the Method of Characteristics; an accurate evaluation of the aerodynamic losses has been achieved by considering shock waves, profile, and mixing losses. Afterwards, an automated Computational Fluid Dynamics (CFD) based optimization process was developed to find the optimal loading condition that minimizes losses while delivering a sufficiently uniform flow at outlet. Finally, a novel parametric analysis was performed considering the effect of inlet angle, Mach number, reaction degree, peripheral velocity, and blade height ratio on the turbine stage performance. This analysis has revealed for the first time, in authors knowledge, that this type of machines can achieve efficiencies over 70%.

Keywords: rotating detonation engine (RDE); supersonic turbines; method of characteristics (MOC); shock waves prediction models; optimization; parametric analysis

check for updates

Citation: Mushtaq, N.; Colella, G.; Gaetani, P. Design and Parametric Analysis of a Supersonic Turbine for Rotating Detonation Engine Applications. *Int. J. Turbomach. Propuls. Power* **2022**, *7*, 1. https://doi.org/10.3390/ijtpp7010001

Received: 12 August 2021
Accepted: 29 December 2021
Published: 4 January 2022

Publisher's Note: MDPI stays neutral with regard to jurisdictional claims in published maps and institutional affiliations.

Copyright: © 2022 by the authors. Licensee MDPI, Basel, Switzerland. This article is an open access article distributed under the terms and conditions of the Creative Commons Attribution (CC BY-NC-ND) license (https://creativecommons.org/licenses/by-nc-nd/4.0/).

1. Introduction

Factors such as concerns about climate change, more sustainable mobility, and the target imposed upon the aviation sector in terms of pollutant emissions, have caused an incentive for ever more efficient engines. Given the great flexibility and responsiveness of gas turbines, they will continue to represent the core element of aeroengines for a long time, especially for medium/long haul. Their application will also benefit from the progressive shift towards non-fossil fuels, such as Sustainable Aviation Fuels or hydrogen [1]. In addition to the engine core efficiency, weight is also an important task to be addressed by future technologies: compact and high specific work engines are expected to be preferred. These meet the need and potential of the energy sector, where gas turbines will play an important role in balancing the discontinuous supply by non-schedulable renewable energy sources, such as wind and solar power, providing an important prerequisite for the success of renewable technologies in the overall energy mix. In this regard, the adoption of zero-carbon combustion technologies, which are expected to be ever more common soon thanks to the use of carbon free fuels such as Hydrogen and Ammonia [2], can be accelerated. Therefore, it is necessary to invest in a renewal of gas turbine technologies that can fulfil the global need for higher efficiency and lower environmental impact both in the transport and in the energy conversion sectors.

Among the possible innovative gas turbine technologies, pressure gain combustion (PGC) has the greatest potential in terms of overall performance improvement and practical

adoption. This technology utilizes a change in the thermodynamic cycle to achieve a significant efficiency boost for the same turbine inlet temperature. In fact, pressure gain combustion cycles exploit the more thermodynamically efficient processes of constant volume or detonation-based heat release (this latter well approximated by the Fickett–Jacobs cycle): the maximum pressure of these cycles rises during the combustion process with a further increase in compression work. As such, over 15% of thermodynamic efficiency can be potentially achieved respect to a Joule–Brayton cycle working at the same maximum temperature [3,4].

This potential gain justifies the rapidly growing interest in PGC, especially for its ready adaptability to hydrogen combustion and for the chance to realize efficient ultra-compact engines: among the different technologies the so-called rotating detonation engines are the most promising. In this kind of gas turbine, a detonation wave propagates around the perimeter of an annular combustion chamber to achieve the pressure increase. This supersonic combustion wave, with flame speeds around 2 km/s, allows for a lower number of compression stages, a more compact design with reduced combustor weight and a lower specific fuel consumption [5].

In addition to all issues related to the combustion chamber (out of this paper purpose), the transition duct connecting the combustion chamber to the turbine [6–9] and the turbine itself constitute important tasks to be addressed to have efficient cycles.

As for the turbine design, some papers are available in the open literature describing different issues. Paniagua et al. [10] report a preliminary design and a possible turbomachine stage arrangement, while Sousa et al. [11] describe guidelines for entropy minimization by working on the profile shape. Papers [12,13] report results and concepts related to the unsteadiness generated by the combustion chamber and the corresponding turbine frequency response. Liu et al. [14] present and discuss a CFD analysis of such turbines.

The size of the combustion chamber, the number of compression stages are expected to reduce with respect to actual ones, thus contributing to the overall engine weight reduction. This paper focuses on the turbine design too, because it constitutes a primary task for an efficient thermodynamic cycle: in fact, due to the high speed, high temperature and fluctuating flows released by the transition duct the turbine design is complex and requires different methodologies with respect to conventional gas turbine for Joule–Brayton cycles.

Among papers dealing with the turbine design, none of them proposes a parametric analysis on geometrical and fluid-dynamic parameters. The present paper proposes a novel parametric analysis on two geometrical parameters, namely solidity and blade height, on two flow features, such as inlet flow angle and inlet Mach number, and on the reaction degree being this latter one of the main issues describing the stage arrangement and affecting the stage efficiency. Authors are also aware about the criticism of the thermal load and cooling requirements on this kind of application even though they are not addressed in the present paper as they require a specific study.

2. Mean-Line Design

An original mean-line code was developed to perform a blade-to-blade design of a supersonic turbine. The code is based on the standard turbine theory and some specific features for supersonic blades are added: the Kantrowitz limit for a started blade row [15], an accurate evaluation and prediction of the shock losses and a Method of Characteristics to generate the supersonic profile shape. Before describing the logic applied to design the turbine, it is deemed necessary to briefly introduce the theoretical elements mentioned above.

2.1. Started or Unstarted Blade Row

A convergent passage, which is typical of turbines, behaves like a diffuser when subjected to a supersonic flow, thus reducing the velocity and increasing the pressure of the stream. In these conditions, it is critical to assess if the blade row is started or unstarted,

where "started" refers to an oblique shock configuration at the cascade inlet which is less dissipative than the normal shock of the "unstarted" condition (Figure 1).

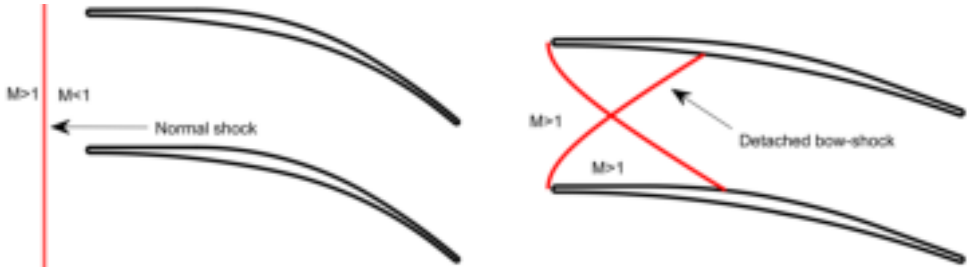

(**a**) (**b**)

Figure 1. Comparison between unstarted (**a**) and started (**b**) condition for a supersonic blade row.

Kantrowitz and Donaldson showed that the strength and the position of the shock depends on the geometry of the diffuser and on the upstream Mach number [15]. Employing a conventional one-dimensional flow theory, the maximum permissible contraction ratio to have a self-started condition can be determined using Equation (1), where M_n is the Mach number behind the normal shock wave.

$$\begin{cases} \left.\frac{A_{th}}{A_{in}}\right|_{self-started} > \left(\frac{\frac{\gamma+1}{2}}{1+\frac{\gamma-1}{2}M_n^2}\right)^{\frac{\gamma+1}{2(\gamma-1)}} \\ \\ M_n^2 = \frac{(\gamma-1)M_{in}^2+2}{2\gamma M_{in}^2-(\gamma-1)} \end{cases} \tag{1}$$

Between the self-started and the unstarted region, there is a third intermediate one: in this region it is possible to achieve a started operating mode, but the diffuser must start from a self-started condition and then either the inlet Mach number should be reduced or a variable diffuser geometry should be employed (Figure 2). This latter concept is relevant in off design conditions.

As the blade turning influences the outlet area in a purely converging blade-to-blade channel, the self-starting limit affects also the maximum allowable turning as shown in Equation (2).

$$\frac{A_{th}}{A_{in}} = \frac{A_o}{A_{in}} = \frac{g_o H_o cos(\alpha_o)}{g_{in} H_{in} cos(\alpha_{in})} > \left(\frac{\frac{\gamma+1}{2}}{1+\frac{\gamma-1}{2}M_n^2}\right)^{\frac{\gamma+1}{2(\gamma-1)}} \tag{2}$$

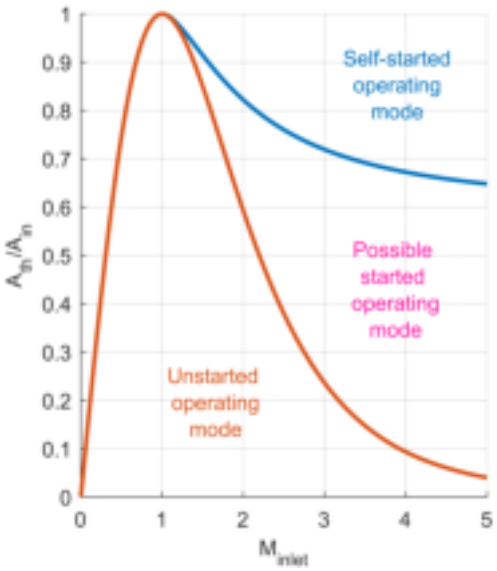

Figure 2. Contraction ratio for a started or unstarted blade row at varying inlet Mach number.

At the same time, the blade turning impacts on the outlet tangential velocity magnitude and therefore on the work exchange. The blade height, contributing to the definition of the outlet discharge section, is also important for the amount of work extracted by the stage.

2.2. Evaluation and Prediction of Aerodynamic Losses

A profile working in a supersonic flow environment is less efficient than its subsonic counterpart due to the generation of a complex shock pattern in the channel. The capability to effectively estimate losses is a key requirement for a reliable mean-line code and this was achieved by taking into account the bow shock wave at the leading edge and the boundary layer (methodology also used in [16]) in addition to the losses related to the first oblique shock wave reflection and the mixing in the case of supersonic axial Mach number.

The detached bow shock wave generated from the leading edge is the main source of entropy production inside the turbine and it is responsible alone of almost two thirds of the total losses. The shape of the detached shock is predicted through the method developed and validated by Moeckel for two-dimensional and axially symmetric bodies [17]. Once the detached shock wave has been determined, the entropy production is calculated locally by applying the oblique shock wave relations and then results are integrally averaged, as shown in Equation (3), where the subscript "up" and "l" refer, respectively, to the upper and lower blade shocks (Figure 1b). Notice that the intersection between shock waves is neglected as a simplifying assumption.

$$\Delta s_{bow-shock} = \frac{1}{y_{up''} - y_{up'}} \int_{y_{up'}}^{y_{up''}} \Delta s_{up}(y) \cdot dy + \frac{1}{y_{l''} - y_{l'}} \int_{y_{l'}}^{y_{l''}} \Delta s_{l}(y) \cdot dy \tag{3}$$

The detached shock wave losses are strongly dependent on the dimensionless ratio between the blade pitch and its thickness. This fact has physical meaning because a smaller thickness compared to the blade passage makes the leading-edge sharper and reduces the subsonic portion of the flow behind the bow shock, which is the main responsible of the losses. At the same time, a too high ratio cannot be used because the leading edge would be too small for structural and thermal integrity.

The first oblique shock wave, which is generated when the detached shock wave is reflected by the blade surface, was also determined and the associated losses were calculated to improve the accuracy in the calculation of the losses. Wave reflection is calculated by considering that the flow immediately adjacent to the wall must be parallel to it: by applying the classical theory of aerodynamics [18], the implicit Equation (4) is derived and solved numerically to find the slope of the reflected shock. The subsequent shock wave reflections were instead not considered because they are significantly weaker, and the assumptions required to evaluate them could seriously affect the reliability of the results.

$$tan\alpha = 2\cot\beta \left[\frac{M^2 sin^2\beta - 1}{M^2(\gamma + cos2\beta) + 2} \right] \tag{4}$$

The second most important source of losses in a supersonic blade row are boundary layer and mixing losses, having preliminarily neglected the shock-boundary layer interaction. The estimate is performed by a two-step procedure:

(i) First the boundary layer quantities for a compressible turbulent boundary layer are calculated using the procedure derived by Stratford and Beavers [19];

(ii) Then the overall loss coefficients are evaluated by applying the method described by Stewart for high velocity flows [20].

In the original methodology, Stewart considered flows with a subsonic axial Mach number; since in our application the axial Mach number is supersonic, the original approach was extended. Without repeating the whole demonstration, already reported in [20], here

are reported only the analytical steps describing the novel extension to supersonic axial Mach numbers.

$$\begin{cases} \left(\frac{V_x}{V_{cr}}\right)^2_{mix} - \frac{2\gamma C}{\gamma+1}\left(\frac{V_x}{V_{cr}}\right)_{mix} + \left(1 - \frac{\gamma-1}{\gamma+1}D^2\right) = 0 \\ C = \dfrac{(1-A_{fs,te})\frac{\gamma+1}{2\gamma} + cos^2\alpha_{te}(1-\delta^{**}-\delta^{**}_{te}-\theta^{**})\left(\frac{V^2}{V^2_{cr}}\right)_{fs,te}}{cos(\alpha_{te})(1-\delta^{**}-\delta^{**}_{te})\left(\frac{V}{V_{cr}}\right)_{fs,te}} \\ D = \left(\frac{V_u}{V_{cr}}\right)_{mix} = \left(\frac{V}{V_{cr}}\right)_{fs,te} sin\alpha_{te}\left(\frac{1-\delta^{**}-\delta^{**}_{te}-\theta^{**}}{1-\delta^{**}-\delta^{**}_{te}}\right) \end{cases} \quad (5)$$

The solution of the second order equation gives two results and in the subsonic case the negative sign was selected to find the correct conditions after mixing. This is physically consistent because the increase in available area from the trailing edge to the mixed region reduces the velocity in subsonic conditions, but for a supersonic axial Mach number the channel behaves like a nozzle and not like a diffuser. Hence, differently from Stewart, the solution of the second order equation selected is the one with the positive sign Equation (6).

$$\left(\frac{V_x}{V_{cr}}\right)_{mix} = \frac{\gamma C}{\gamma+1} + \sqrt{\left(\frac{\gamma C}{\gamma+1}\right)^2 - 1 + \frac{\gamma-1}{\gamma+1}D^2} \quad (6)$$

Once all the quantities have been determined, the total pressure ratio between the inlet and the completely mixed region at outlet is calculated through Equation (7).

$$\frac{p_{t,mix}}{p_{t,in}} = \frac{\left(\frac{\rho V}{\rho_t V_{cr}}\right)_{fs,te} cos\alpha_{te}(1-\delta^{**}-\delta^{**}_{te})}{\left(\frac{\rho V_x}{\rho_t V_{cr}}\right)_{mix}} \quad (7)$$

2.3. Blade Profile Design Through the Method of Characteristics (MOC)

In literature there are mainly two methods based on MOC to design the profile of a supersonic blade row: corner-flow method by Shapiro [21] and vortex-flow method by Goldman [22]. The Goldman one has been implemented in this mean-line code because it provides a smoother velocity distribution with the highest loading at mid-chord and less constraints on the flow turning.

A blade profile designed with the vortex-flow method is composed of the following fundamental parts, each of them having a specific function here briefly summarized for readers convenience (Figure 3): the inlet transition arcs convert a uniform parallel flow at the blade inlet into a vortex flow field, the concentric circular arcs preserve the vortex-flow structure while turning the flow with a constant surface Mach number and the outlet transition arcs reconvert the vortex flow into a uniform parallel flow.

The vortex flow method requires several inputs to define the blade profile: inlet Mach number M_{in}, outlet Mach number M_o, lower surface Mach number M_l, upper surface Mach number M_{up}, inlet flow angle, and the specific heat ratio of the working fluid. Although all the other inputs are given, M_l and M_{up} are selected to avoid issues related to flow separation: as suggested in [22], the maximum M_{up} and the minimum M_l are calculated to obtain a pressure recovery coefficient of 0.5. The actual M_l and M_{up} have been selected with a further 12% margin respect to those limit values.

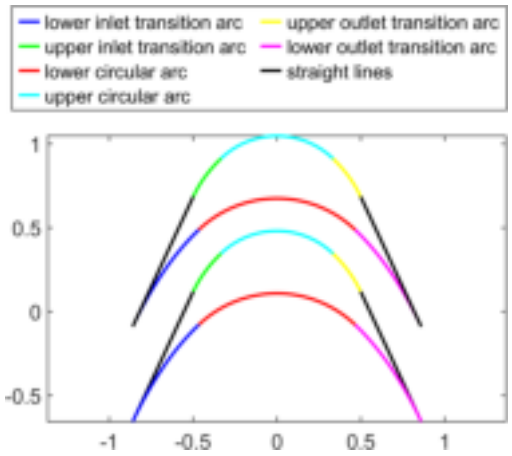

Figure 3. Blade profile sector division in vortex-flow method.

Once the dimensionless profile has been generated, two key geometrical parameters can be calculated: the dimensionless chord c^* ($c^* = c/r$) and pitch g^*. In the mean-line code the chord is the only dimensional quantity assigned for the profile geometry, thus allowing for the calculation of r (the geometrical scale parameter). The geometries presented as examples in this work are for ground power production, hence the dimensionless ratios (c/g and g/thickness) were optimized to achieve the maximum efficiency. For aeronautical application, the turbine design requires a compromise between compactness and efficiency, which leads to different values of the dimensionless ratios and a shorter chord length. Once these quantities have been assigned, the dimensional profile, the pitch and the thickness can be finally calculated.

The profile generated by the Method of Characteristics is optimal from an aerodynamic point of view, but it is purely theoretical since zero thickness at leading and trailing edge is impossible to manufacture and has poor mechanical and thermodynamic performance, especially with a high velocity and high temperature flow. Hence, once an appropriate value of the thickness is selected according to mechanical calculations, the upper and lower surfaces are shifted, and the blade profile is closed by means of circular arcs.

A structural analysis was carried out proving that the blade can withstand without significant issues the static loadings; on the other hand, a detailed thermal analysis was not included in this work, because for this type of turbines this is an advanced topic and will be properly dealt in future studies.

2.4. Mean-Line Code: Description and Logic Explanation

The mean-line code implemented employs a multi-loop iterative approach to achieve more than one design objective, which is possible by changing quantities that would be usually fixed in a direct approach; while the stator blade height ratio H_2/H_1 is an input selected by the user, the rotor blade height ratio H_4/H_3 is iteratively adjusted to maintain the same axial velocity between rotor inlet and outlet, the latter being a common design feature of axial turbines. The absolute stage inlet flow angle is assumed equal to 0°: in fact, notwithstanding the flow entering the turbine is oscillating in pressure, temperature, and direction, its mass flow average is zero because fluctuations are symmetrical [8,23]. By design the rotor absolute outlet flow angle is null to minimize the outlet Mach number and therefore to reduce the shock losses in the following stages. Finally, the code is implemented in a way that the user can select as an input the reaction degree X of the stage: this option does not only help the user to set a key parameter in the design of a turbine but has been extremely useful to perform the parametric analysis shown in Section 6.

Once stator/rotor losses have been calculated and the outlet total pressure is known, the outlet Mach number is found with the continuity equation and then all other quantities are determined by resorting to the ideal gas assumption. As soon as the stator and rotor design have been completed, the mean-line code checks if the Kantrowitz limit for a started

blade row is satisfied. Then, it also verifies that the axial Mach number is higher than 1 to avoid the unique incidence problem [24], which is an unfavorable working condition considering the unsteadiness of the incoming flow. In conclusion the flowchart in Figure 4 shows the order and the logic of all the operations performed to design the rotor.

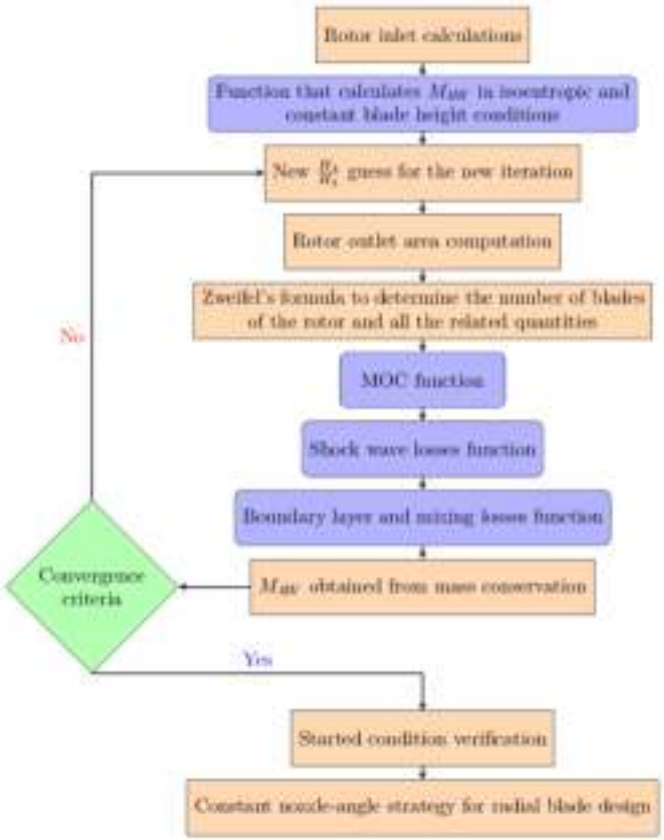

Figure 4. Flowchart to illustrate the iterative process employed to design the rotor in the mean-line code.

3. Computational Flow Model

To check the mean-line code validity and to deepen the understanding of the flow features inside the channel, CFD was run on a selected number of cases. Steady-state blade to blade and steady-state 3D simulations were performed on the commercial software Ansys CFX (19.1, Ansys, Canonsburg, U.S.), which implements a pressure-based implicit coupled solver with co-located grid arrangement. A high-resolution scheme was selected for the advection terms and the turbulence; this scheme belongs to the Total Variation Diminishing (TVD) algorithms, which have proven to be accurate in modelling shock wave reflections [25]. The $k-\omega$ SST model was selected for turbulence closure, while the y^+ was maintained below 1 for proper boundary layer resolution. The working fluid is air which is assumed to be a thermally and calorically perfect gas.

Since the inlet is supersonic, all the relevant quantities are assigned at this boundary. The outlet is supersonic and the lateral boundaries are periodic. Adiabatic and no-slip conditions were selected for the blade walls, while adiabatic and free-slip conditions were set for the hub and shroud walls; this choice was made also for the 3D simulations, because at this stage the aim was to understand the effect of the radial variation of the quantities, working with a mesh that is suitable to investigate a large design space. Finally, a mixing plane interface was employed in the stator-rotor coupled simulations and all the computations were considered at convergence when the residuals are in the order of 10^{-6}.

3.1. CFD Code Validation

Since the flow is supersonic with shocks and expansion waves in the domain, it is pivotal for the results reliability to assess if ANSYS CFX can accurately capture these distinct features with the settings reported above. Two test cases were selected to perform the code validation: the Sod shock tube [26] and the compression corner [27–29]. Notice that a grid sensitivity analysis by way of consecutive refinements was performed for both test cases and all the reported results are grid independent.

In the shock tube problem, a diaphragm is initially separating a high-pressure gas on the left ($x < 0$ m) from a low-pressure gas on the right ($x > 0$ m). When the diaphragm is broken ($t = 0$ s), three new features appear in the domain: a shock wave and a contact surface propagating to the right and an expansion wave propagating to the left. The hypothesis for the analytical solution are that the problem is 1D, the tube is infinitely long and the flow is inviscid [18,26]. Since ANSYS CFX works only with 3D domains, the geometry is modelled as a 10 m long tube, while the other two dimensions are significantly smaller and meshed only with one cell. Figure 5 shows a comparison between the CFD solution and the analytical one at $t = 0.001$ s: the two curves are almost identical for all the quantities proving that Ansys CFX is perfectly able to predict strength, position, and the wave speed of all three features.

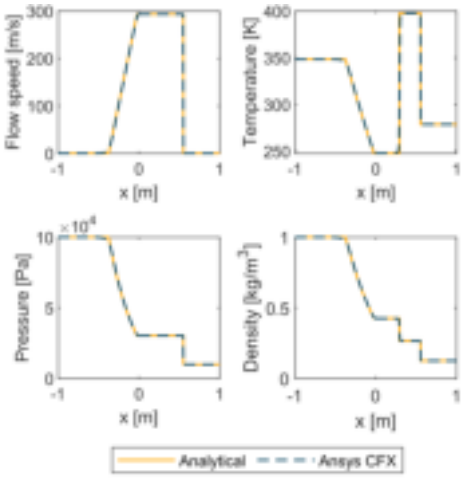

Figure 5. Comparison between the analytical and Ansys CFX solution at $t = 0.001$ s for the Sod shock tube problem.

The 2D compression corner test case by Smits et al. (Figure 6) was selected because the shock/boundary-layer interaction is an advanced problem that contains altogether the difficulties of turbulence, compressibility, and viscous–inviscid interaction phenomena [28,29]. Since the inlet Mach number is supersonic (M = 2.85), an oblique shock wave is generated when the wall turns into the flow domain; depending on the inlet and geometry condition, the interaction between the shock and the boundary layer can lead or not to a boundary layer separation. The computational domain is 3D, but one dimension is significantly smaller than the others and meshed only with one cell. The $k-\omega$ SST model was employed as turbulence model, while the y^+ was maintained below 1 for proper boundary layer resolution. The validation was performed for two ramp angles, respectively, 8 and 16 degrees. Figure 7 plots the surface pressure distribution for both cases and compares them to the experimental data of Smits et al. [28]. For the 8-degree case, ANSYS CFX captures accurately the starting point of pressure increase, the maximum pressure after the shock and the overall trend. For the 16 degree case, CFD is correctly predicting the starting point of pressure increase and the maximum pressure, but there is a slight difference in the trend: in the CFD results there is a weak separation at the corner, which is not seen in the experimental data, but as stated by the authors the 16 degree case is at incipient separation and this aspect may be hidden by the uncertainty of the measurements [29].

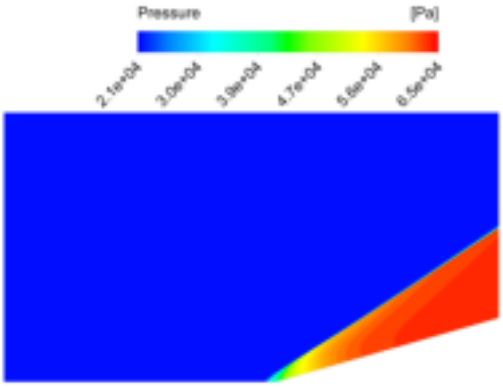

Figure 6. Pressure field for the compression corner problem with a 16 degree ramp angle.

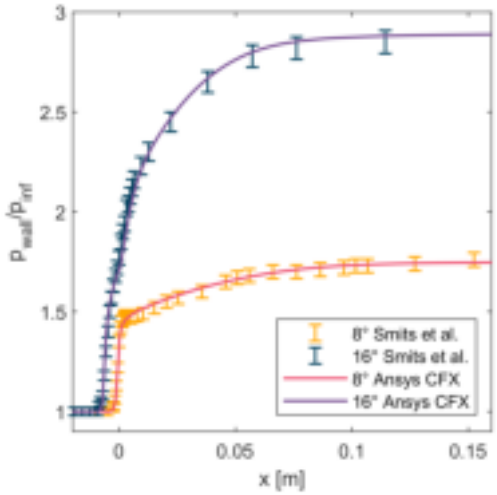

Figure 7. Comparison between the experimental solution [28] and Ansys CFX for the compression corner problem at 8° and 16° ramp angles.

Finally, ANSYS CFX has been extensively used by our turbomachinery group and lots of effort has been dedicated over the years in properly validating the CFD results with the experimental data acquired on the test facilities present at the Laboratory of Fluid Machines (LFM) [30,31].

3.2. Mesh Independence Analysis

ANSYS TurboGrid was used to generate a structured mesh with hexahedral cells, high orthogonality, and low skewness. The mesh independence analysis was performed in two steps: first, the number of cells required in each layer for a 2D blade-to-blade grid independent solution was determined; then, the number of layers was increased in the radial direction till the independence condition was also satisfied for the 3D solution.

The grid convergence index method [32] was applied to perform the mesh sensitivity analysis and the standard deviation of the pressure distribution was selected as the reference quantity. For the blade-to-blade simulation (2 cells in radial direction), 100 k, 200 k, 400 k, 600 k, and 1600 k meshes were tested; the 600 k mesh can be considered as grid independent with a Grid Convergence Index (GCI) of 0.67%, calculated with the pressure distribution extracted at the outlet section mid-span. Then, 10, 30, and 50 layers were prescribed in the radial direction and the pressure distribution was tangentially averaged and extracted in the spanwise direction at half chord distance from the trailing edge; the 9 million cells mesh (30 layers) achieved the independence condition for both stator and rotor, with a GCI of 0.28% and 0.05%, respectively.

3.3. Mean-Line Code Results Validation through CFD in Design Condition

The physical parameters reported in Table 1 have been selected considering typical quantities for RDEs and high-pressure turbines [5,8,10,14,23,33–36], while the geometrical parameters are chosen considering the blade structural feasibility. The validation procedure is accomplished by comparing the code outputs with the mass flow averages extracted from CFD simulations performed on the stator blade. The total entropy predicted by the mean line code is 44.17 J/(kg K), while the value obtained from CFD is 43.87 J/(kg K), which results in a 0.7% deviation; pressure and temperature deviation are also within 1% at stator outlet. This result is very promising and assess the present mean line code as a primary tool in the preliminary turbine design.

Table 1. Input parameters for the reference design stage.

Mass flow rate [kg/s]	100
Peripheral speed [m/s]	450
Reaction degree	0.5
Inlet Mach number	2
Total pressure [bar]	15
Inlet axial speed [m/s]	1445.46
Static temperature [K]	1300

Figure 8 compares the analytically determined shocks with a CFD simulation performed on the same supersonic profile and in the same flow condition. The density gradient (numerical Schlieren) is shown in the background, while in the foreground we can appreciate the detached shock wave and the first oblique shock wave reflection as calculated by the mean-line code. The predicted shock positions are really close to the ones obtained by CFD, which confirms the effectiveness of the Moeckel theory application. Even though the predicted reflected oblique shock wave is not exactly in the same location, slopes are very similar and thanks to this also the estimated entropy production.

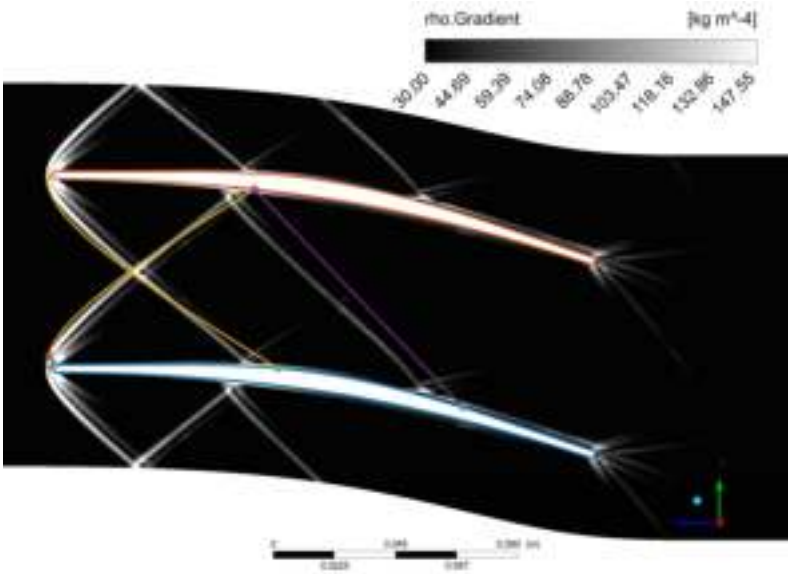

Figure 8. Comparison between CFD numerical Schlieren in background and the analytically determined shocks in foreground (detached shock in yellow and reflected shock in purple in the online colored version).

4. Research of Optimal Loading by an Automated Optimization Process

Several studies have described optimal loading conditions for subsonic axial turbines, meanwhile there is a major knowledge gap regarding supersonic turbines. An original completely automated optimization process, which makes use of Python, MATLAB, and Ansys packages, was developed to find the optimal loading value that minimizes the losses while delivering a sufficiently uniform flow at outlet.

Zweifel's tangential force coefficient Equation (8) was selected as a driver parameter for the whole optimization process because of its capability to quantify the forces acting on a blade: its meaning is not related only to the blade solidity, but it also considers the flow deflection and the variation in the axial component of the velocity [37].

$$C_{ft} = \frac{F_t}{\frac{1}{2}H\rho V_o^2} = \frac{2}{\sigma_x}\cos^2\alpha_o\left(\frac{V_{in,x}}{V_{o,x}}\tan\alpha_{in} - \tan\alpha_o\right) \tag{8}$$

The search interval for the optimal loading condition was established after a series of preliminary CFD simulations. The upper limit was selected starting from the need to have sufficiently uniform flow at stator outlet to allow an efficient rotor operation. Blades cannot be too far apart because the outlet flow would be less uniform in magnitude and direction (Figure 9a). The lower limit is the solidity proposed by the MOC (Figure 9b): the associated C_{ft} is quite low because the main objective of the vortex-flow method is to obtain a completely uniform flow at exit using a high number of blades. Then, it is necessary to consider that the original MOC designed a profile with infinitesimal thickness at leading and trailing edge, so the channel and behavior of the blade were modified when a finite thickness was assigned and, therefore, a new optimal value of the tangential force coefficient is expected. The optimal design should minimize losses while matching uniformity requirements.

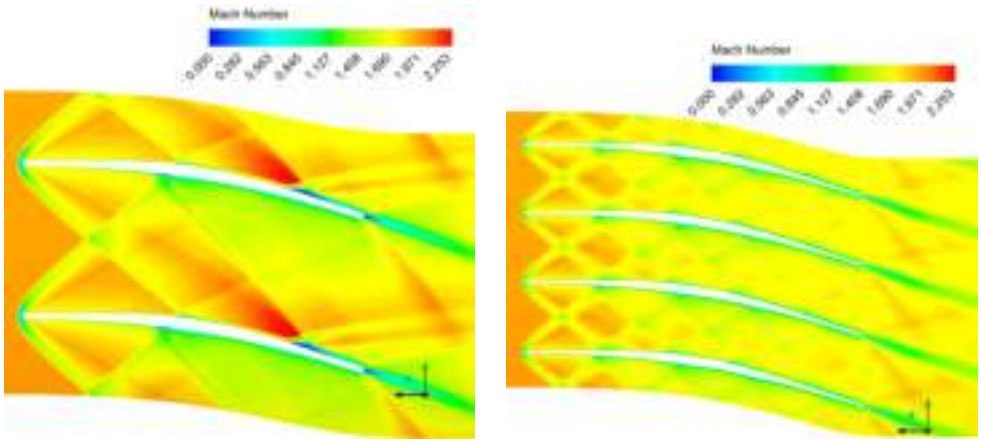

(**a**) (**b**)

Figure 9. (**a**) Minimum solidity conditions assumed in this paper. (**b**) Maximum solidity as proposed by MOC.

The selected optimization algorithm is the "golden section search method", which has a simple robust logic and converges towards a local minimum. This latter feature is a weak point of this method, but preliminary simulations confirmed that within the selected interval the trend of the entropy generated has only one minimum.

Effectively, for each C_{ft} guessed by the algorithm, a high-fidelity evaluation process is performed: (i) the mean-line code (integrated with the MOC) generates the blade profile; (ii) blade-to-blade CFD simulations are set-up and run; (iii) data are extracted from CFD code; (iv) by post-processing, the entropy generation is calculated.

The entire process (described in Figure 10), including the optimization algorithm, has been fully automatized to significantly reduce the human effort and to easily repeat the whole operation with different inlet parameters. Notice that it is fundamental to run the

mean-line code each time, because the search of the optimal value of C_{ft} is performed while maintaining all the other dimensionless numbers fixed. Meshing the domain and the steps regarding the simulation are performed twice for each case: the first mesh is coarse and it is used to quickly initialize the whole domain and then the fine mesh (600k cells) is employed to have high quality data.

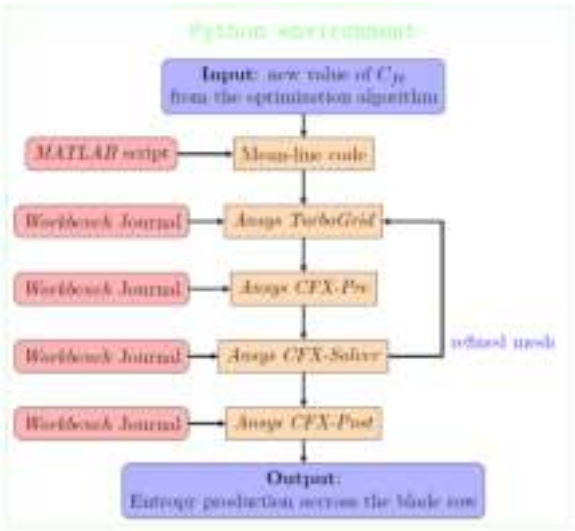

Figure 10. Flowchart to illustrate the procedure used to calculate the entropy production for each value of C_{ft} given by the optimization algorithm.

The results of the optimization procedure applied to the stator blade row are shown in Figure 11; the smallest value of C_{ft} is associated to the value of the solidity given by the MOC and the entropy generated in that condition is almost 18% higher than the optimal value; this improvement clearly justifies the novel optimization process developed for this purpose. Figure 11 also reports the mean-line code losses prediction, and they are very promising with a maximum error with respect to CFD lower than 8%, that decreases to less than 1% in the optimal working condition. For low C_{ft} (higher number of blades and smaller pitch), the error increases because a higher number of oblique shock wave reflections are generated in the passage, all neglected but the first one by the mean-line code. At high C_{ft} (lower number of blades), the increase in losses is explained by the small separation bubble formed behind the reflection point on the blade suction side (Figure 9a).

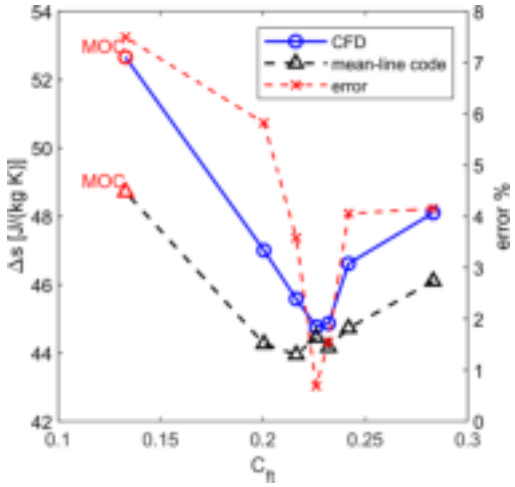

Figure 11. Entropy produced by stator at variable C_{ft}: in blue, values from CFD; in black, value from mean-line code results; in red, CFD-mean-line percentage difference.

It is also very interesting to observe that the recommended value of C_{ft} in literature for conventional machines is 0.8, but the optimal values obtained here are quite different: this suggests that the use of correlations developed for conventional machines should be carefully assessed prior to their application on supersonic turbines.

Figure 12 shows the stator blade in optimal loading condition, which reduces both the wetted surface (and hence profile losses) and the shock wave losses. At the leading edge there is a detached bow shock wave, which is reflected only two times in the channel (labeled as A and B in Figure 12); the reflection in point B is the most critical because it generates a separation bubble, whose size and therefore loss content mainly depend on the blade overspeed and on the reflected shock strength. With a more loaded blade, a larger amount of flow is involved in separation and this leads to a notable increase in losses (Figure 9a); in optimal loading condition the separation bubble is considerably smaller and the boundary layer thickening in the interaction zone is limited.

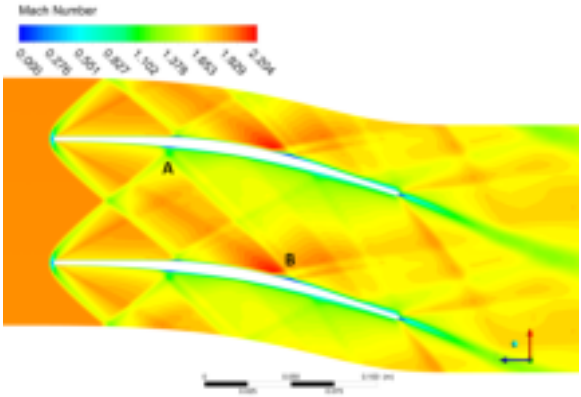

Figure 12. Mach number field for the stator in optimal loading condition.

5. Stator Off-design Analysis

Once the methodology has been assessed and the optimal solidity found, stator off-design performances can be investigated. The two fluid dynamic parameters chosen to be varied are the inlet flow angle and the inlet Mach number. The reason for this choice is twofold: (a) the need to understand the behavior of the supersonic turbine in a wide range of different inlet conditions, (b) the fact that rotating detonation combustion chambers release high fluctuating flows, mainly on these two parameters.

5.1. Inlet Angle Analysis

In this set of off-design blade-to-blade simulations, all inlet boundary conditions except the inlet angle have been fixed. The angle has been varied between $+/-16°$ with a step of 4°. Since the absolute Mach number is maintained constant, a secondary effect of the change in direction is a reduction in the mass flow rate and, consequently, a possible turbine unstarting for extreme value of the inlet angle.

Figure 13 reports the averaged value of the entropy production and total pressure ratio where it can be noted that curves are not "symmetric" with respect to the design condition, because of the shock waves lattice and its interaction with the pressure/suction side boundary layers. Entropy production more than doubles in the selected range thus evidencing how losses in the stator row are crucial for the stage performances.

As for the outlet flow direction, the stator shows good capability to deviate the flow close to the geometrical direction of 22°: Figure 13 also reports the outlet flow angle and its standard deviation calculated at the outlet section mid-span (reported on the figure as error bars). The flow-field is characterized by a medium level of variability at the outlet surface. The design condition shows the lowest deviation angle and a limited standard deviation. Meanwhile, in off-design condition the profile progressively loses the capability to impose the flow direction and the discrepancies with respect to the nominal condition are close to 4° in the worst scenario. These results allow to introduce some further considerations:

since supersonic profiles do not perform well under negative incidence, in the frame of possible off-design conditions both an optimal robust design methodology and a slight positive incidence at the design point can be applied.

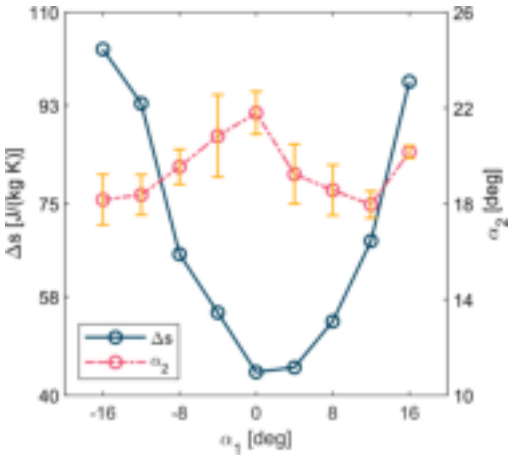

Figure 13. Entropy production and stator outlet angle with its standard deviation calculated at the outlet section mid-span for different inlet flow angles.

By way of example, Mach number contours for the two cases of +/−12° are reported in Figure 14. In the case of −12° (Figure 14a), a separated region is found on the pressure side, due to the sharpness of leading edge. For the positive incidence case, (+12° Figure 14b), the shock pattern causes a flow detachment in the front part of the suction side that is subsequently partially recovered up to the last part of the suction side where a reflected shock causes the final flow detachment. The case of i = +16°, not shown for sake of brevity reports an unstarted situation on the stator with a strong normal shock upstream of the leading edge.

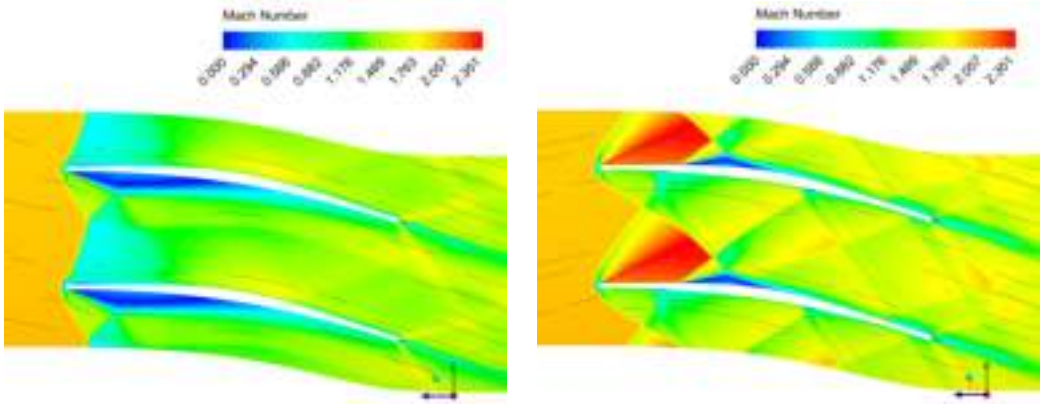

(**a**) (**b**)

Figure 14. Mach number contours for incidence angle of −12° (**a**) and incidence angle of +12° (**b**).

5.2. Inlet Mach Number Analysis

A second set of blade-to-blade simulations have been performed with variable inlet Mach number (range 1.6 to 2.8) but constant axial flow and static quantities (equal to the reference case). At first it has to be underlined that the change in the inlet Mach number, given all other quantities, modifies the mass flow rate and then, the following features can be noted (Figure 15):

(a) The outlet flow angle is reduced by few degrees when the speeds are lower than the design condition, while there is a low over-speed sensitivity;
(b) The condition of uniformity of the outgoing flow is reduced as the speed increases;

(c) Losses have a fairly linear trend around the design condition (M = 2): at higher Mach, the trend is more than linear since the reflected oblique shock affects the trailing edge region, favouring a premature flow separation.

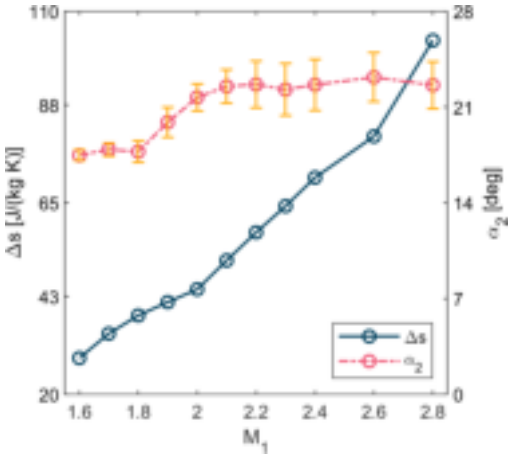

Figure 15. Stator entropy production and outlet flow angle with its standard deviation calculated at the outlet section mid-span for various inlet Mach numbers.

The analysis reported above for different stage inlet flow direction and magnitude demonstrate the complexity of the off-design operation of such turbines and the need for a proficient and robust design methodology. Preliminary evaluations of the stator outlet angle deviation, which in turn modifies the rotor inlet angle, are of paramount importance in the off-design stage analysis.

6. Effect of Reaction Degree and Peripheral Speed

In the context of improving the understanding and the applicability of such stages in ever more efficient gas turbines, a novel parametric analysis has been performed accounting for the effect of the reaction degree (X) and peripheral velocity (U) on the stage performance; the parametrical analysis is based on X and U as these two parameters hold a crucial position in the turbomachinery preliminary design. Such analysis made use of the mean line code and different blade height ratios have been also explored. Then, few selected cases have been also verified by means of CFD (Section 6.3).

The grid selected for these studies is defined in the following way: 12 equally spaced points for U from 260 m/s to 500 m/s and 20 equally spaced points for X from 0 to 0.55: overall, the grid consists in 240 points. Each case was studied in the condition of optimal solidity, this latter searched by the mean-line code thanks to its good agreement with CFD.

An in-depth description of the outcomes of the parametric analysis performed at constant stator blade height will be presented and then a comparison will be drawn at increasing values of H_2/H_1.

6.1. Constant Stator Blade Height

The link among the reaction degree, the peripheral velocity and the stator outlet flow angle is presented in Equation (9) to aid the results understanding, having imposed for the rotor constant axial velocity and axial outlet.

$$\alpha_2 = atan\left(\frac{2U_2(1-X)}{V_{2,x}}\right) \tag{9}$$

A different reaction imposes a different blade turning (low reaction requires high blade turning), that coupled to the peripheral speed allows to quantify the rotor inlet relative Mach number. The stator blade turning affects the area ratio and for high α_2 a significant deceleration on the stator may occur so that the Kantrowitz limit may be not

satisfied leading to a normal shock upstream of the stator, too dissipative to be acceptable: the limit is reported on figures as red dashed lines.

Stator shock losses are primarily influenced by the primary shock and its first reflection which are not so affected by the reaction as, on the contrary, the boundary layer and mixing, even though these latter are less important.

An important source of loss that is strongly affected by the reaction degree is the one related to rotor shocks: this contribution is mainly driven by the relative rotor inlet Mach number. As shown in Figure 16a, the rotor inlet relative Mach number decreases with a reduction in the reaction or an increase in the peripheral speed (higher α_2 that leads to a smaller area at stator outlet, i.e., an increase in deceleration). Hence, rotor losses are strongly modulated by the variables U, X (Figure 16b).

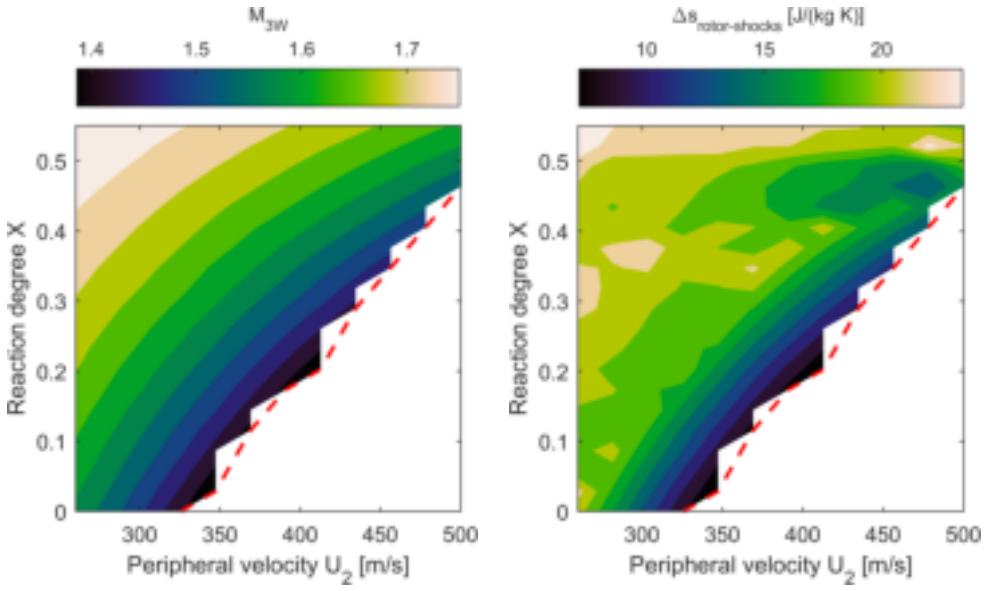

(**a**) (**b**)

Figure 16. Relative Mach number at rotor inlet (**a**) and entropy production [J/(kg K)] due to shocks in the rotor (**b**) for constant stator blade height and different reaction degree and peripheral velocity.

The boundary layer and mixing losses, as in conventional turbines, are mainly function of the outlet flow angle and the velocity. In the stator, losses increase closer to the starting limit because the flow angles are higher (Figure 17a); in the rotor, they decrease because, while the relative outlet flow does not vary significantly, the velocities are lower reducing especially the losses associated to mixing (Figure 17b). Considering that the increase in these losses in the stator is counterbalanced by the decrease in the same losses in the rotor, there is a significant cut in total losses near the starting limit because of a net reduction in shock losses for the rotor.

The Euler work obviously increases for lower X and higher U: Figure 18 describes this feature for different blade height ratios, here commented only for $H_2/H_1 = 1$. The total-to-total efficiency (Figure 19a) is improving towards the Kantrowitz limit thanks to two effects:

(i) The amount of work extracted is increasing because the flow angles or U are larger;
(ii) The total entropy production decreases.

This is undoubtedly an unconventional result: for a subsonic turbine, the designer usually can either aim to maximize the efficiency or the amount of work extracted; here for a supersonic turbine no compromise between the two is required because the designer can theoretically create targets to extract the maximum work at the maximum efficiency. In conclusion, the X and U values should be carefully selected because the decrease in efficiency is strong, passing from 70% to 20% when lowering U and increasing X.

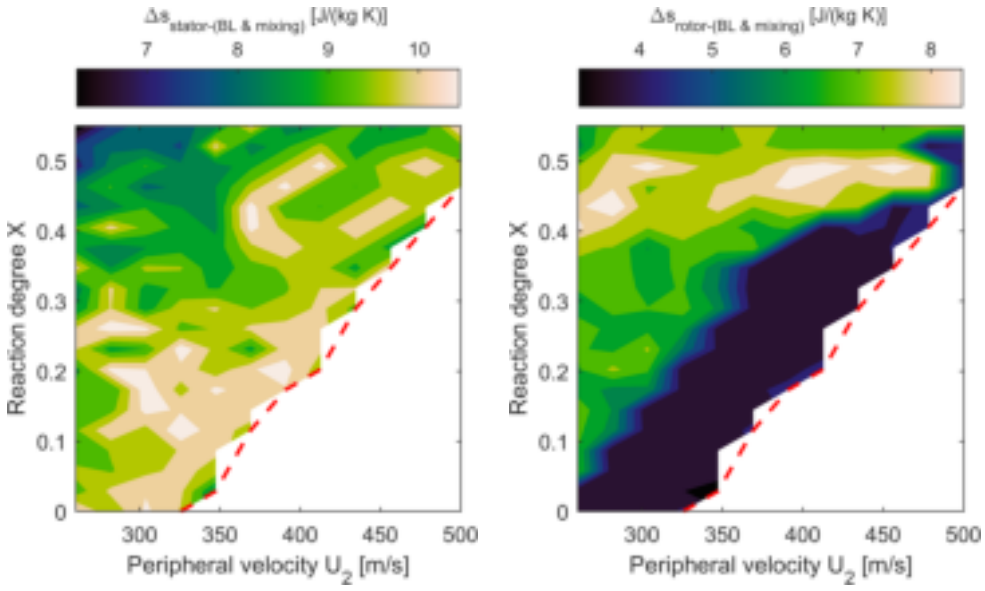

(**a**) (**b**)

Figure 17. Entropy production [J/(kg K)] in the stator (**a**) and in the rotor (**b**) due to boundary layer and mixing for constant stator blade height and different reaction degree and peripheral velocity.

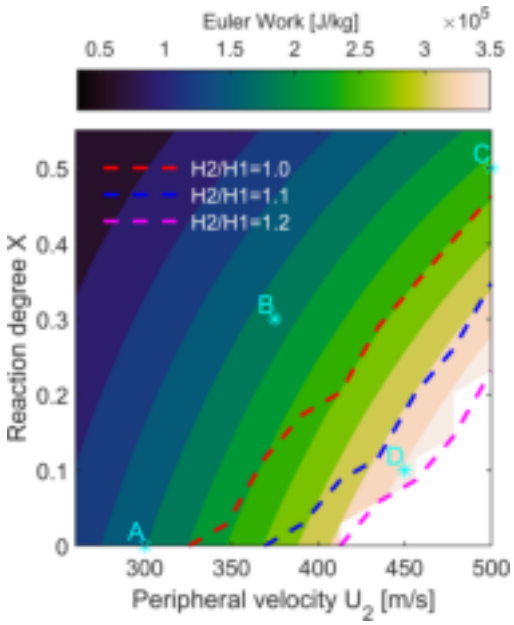

Figure 18. Euler work [J/kg] performed by the stage for different stator blade height, different reaction degree and peripheral velocity.

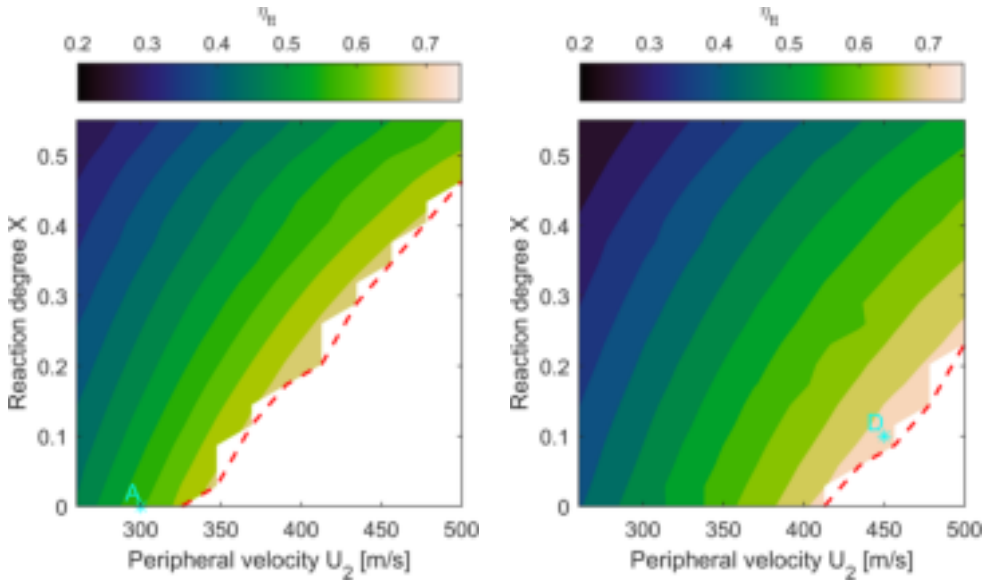

Figure 19. Stage total to total efficiency for stator blade height ratios of 1 (**a**) and 1.2 (**b**) with different reaction degree and peripheral velocity.

6.2. Variable Stator Blade Height

The blades with a variable height are designed with a constant hub radius, while the shroud radius is linearly varied to obtain the desired inlet to outlet blade height ratio. A variable stator blade height is a valuable option to extend the available design space limited by the starting condition: the reduction in area caused by larger flow angles is balanced by a taller blade at outlet section. In this way more pairs (U, X) are feasible, being characterized by larger flow deflections and therefore by a considerable increase in the amount of work extracted (Figure 18). Higher values of the Euler work carry two appealing advantages:

(i) A lower total temperature at stage outlet reduces the cooling requirements on the next stages;

(ii) A sizeable cut in NOx emissions, which are strongly dependent on high temperatures [38]. To this end, the high mean flow velocity allows for a low permanence time at high temperature, thus preventing for high NOx production.

Notwithstanding the increase in the work exchange, M_{3W} is almost constant and low (even still supersonic) close to the starting limit even with an increasing stator blade height ratio. This result depends on the fact that the Kantrowitz limit is only function of the outlet–inlet area ratio and of inlet Mach number: the minimum area ratio is always the same and therefore the maximum possible deceleration will lead to the same M_{3W} close to the Kantrowitz line, which is shifting on the U-X diagram. From this, it is possible to conclude that in the most interesting design area, the shock wave losses generated by stator and rotor remain constant even when the stator blade height and the work are increasing.

The boundary layer and mixing losses are increasing with higher H_2/H_1 ratio because the flow angles are larger for both the stator and the rotor. Hence, the stage total losses are increasing because the shock wave losses are almost constant, while the entropy generated by the boundary and mixing phenomena becomes higher.

Overall, the total-to-total efficiency is improving close to the Kantrowitz limit because the considerable increase in the turbine work overcomes the slight increase in losses (Figure 19b). By way of example, at constant blade height the maximum efficiency is 69% with 271 kJ/kg of work, while at $H_2/H_1 = 1.2$ the maximum efficiency is 76% with 391 kJ/kg. Obviously, the design point cannot be at the edge of the Kantrowitz limit and a reasonable safety margin should be decided. To conclude, an increasing variable stator

blade height is a beneficial option leading to an extension of the design space for U and X, thanks to a considerable increase in work extraction and higher efficiencies.

6.3. Detailed Study of Flow Three-Dimensionality for Multiple Design Points

Interesting results were revealed by the reaction degree and peripheral speed parametric analysis, but these data are generated by a mean-line code, which has been compared only to blade-to-blade simulations. Because one of the shortcomings of a mean-line code is the inability to consider the spanwise variation of the quantities, 3D coupled stator-rotor simulations with a mixing plane interface were performed in 4 meaningful design points (Figure 18 and Table 2). First, a detailed analysis will be provided for case D, which in authors opinion is the most interesting from a performance and flow features standpoint; then, the other points will be examined from a quantitative point of view.

Table 2. Design points studied with 3D coupled stator-rotor simulations.

	U_2 [m/s]	X	H_2/H_1
A	300	0	1
B	375	0.3	1.1
C	500	0.5	1.1
D	450	0.1	1.2

Design point D is directly at the edge of the Kantrowitz limit, but, as previously discussed (Section 6.2), in this region the turbine can extract a large amount of work with the highest efficiencies (Figure 19). From the results of the coupled 3D simulation, the turbine is extracting 36.02 MW with an efficiency of 73.58%, which is in close agreement with the mean-line code prediction of 36.45 MW with an efficiency of 74.47%.

Figure 20 displays the pressure gradient contour on the stator and rotor surfaces, and it is immediately clear that the shock structure has a complex 3D pattern. The first shock reflection line on the stator (1) is closer to the leading edge at the hub than at the shroud and this is the consequence of two factors: (a) the solidity at the hub is higher than the solidity at the shroud; (b) the hub wall is at constant radius, while the shroud wall is rising to achieve the desired blade height. The second and especially the third reflection lines on the stator suction side (2–3) exhibit a double shock structure, which is typical of a separation bubble: the upstream shock is the separation one, while the downstream shock is the reattachment one [39]. It is significant to observe that at the stator last reflection (3), the shock at the hub is closer to the trailing edge reversing the initial trend; the reason behind this shock shifting is that the flow is gradually gaining tangential velocity and observing the radial equilibrium theory, the pressure at the hub is lower and the Mach number is higher.

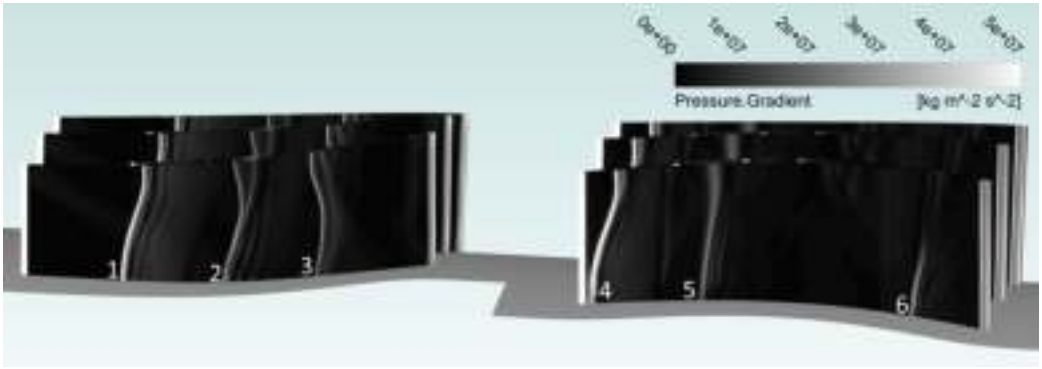

Figure 20. The 3D shock structure visualization on stator suction side and rotor pressure side for design point D.

In the rotor blade, the intersection of the bow shock waves generates a Mach phenomenon, recognized by its typical structure composed of two slip lines and a normal shock between the two triple points (Figure 21). The Mach phenomenon manifests itself with high values of shock deflection for which the conventional solution with two oblique shock waves originating from the intersection point is not possible [39]; this is the reason why the Mach phenomenon appears only for design points at low reaction degree (A and D) and not for the higher ones (B and C). Even though this flow feature is undesired because it increases the pressure losses due to the normal portion of the shock, the low reaction turbines have still a better efficiency thanks to a significantly higher work that overcomes these losses.

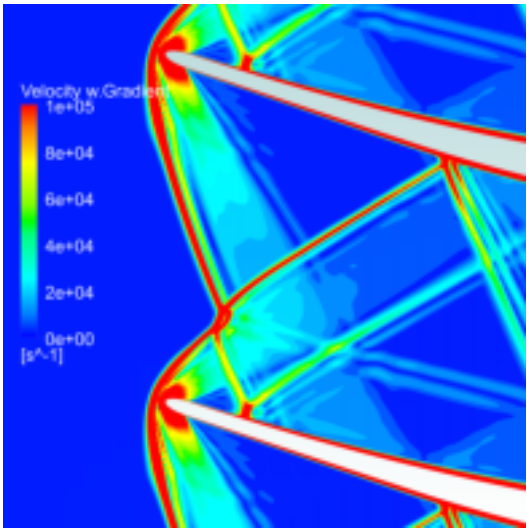

Figure 21. Mach phenomenon generated by the intersection of rotor bow-shock waves in design point D.

Table 3 reports all the relevant data for an in-depth comparison between the mean-line code results and the solution of the coupled 3D CFD simulations. Considering the complexity of the problem, the mean-line code losses predictions are satisfactory, as shown by the entropy production values for both stator and rotor. Pressure, temperature, and Mach number at stator outlet are also accurately estimated and this is beneficial for a reliable rotor design.

Presently the main concern is the notable overturning in point B and C downstream of the stator (higher α_2 in CFD with respect to MLC), which leads to a higher power extraction and therefore higher efficiency compared to the mean-line code. This overturning results from the flow deviation induced by the last shock wave reflection on the suction side and by the complex flow structure built of shocks and expansion fans at trailing edge. This issue is emphasized for point B and C because most of the flow goes through the last reflected shock in the semi-vaned region, while in point A and D this happens only for a small portion; notice that the point D has also 3 reflections in the stator channel compared to the other three cases which have only 2. In conclusion, current work is focused on finding a solution to this issue, even though predicting with accuracy the position of the last shock reflection in a mean-line code is a difficult task.

Table 3. Detailed quantitative comparison between the results of the 3D coupled stator-rotor simulations and the mean-line code predictions.

	A MLC	**A CFD**	**B MLC**	**B CFD**	**C MLC**	**C CFD**	**D MLC**	**D CFD**
η_{tt}	59.50 %	61.66 %	56.71 %	63.85 %	61.91 %	67.32 %	74.47 %	73.58 %
Power [MW]	18.00	19.81	19.41	23.28	25.00	29.38	36.45	36.02
Δs_{stator} [J/(kg K)]	37.86	39.66	39.38	38.09	39.31	37.93	40.71	42.53
Δs_{rotor} [J/(kg K)]	20.29	20.75	30.90	34.75	33.27	35.47	23.26	25.65
M_2	1.67	1.65	1.86	1.83	1.87	1.85	1.79	1.80
T_2 [K]	1501	1509	1381	1392	1375	1389	1424	1422
p_2 [bar]	2.77	2.85	2.07	2.17	2.03	2.12	2.29	2.29
α_2 [deg]	27.53	28.30	22.23	25.69	21.04	24.30	36.67	35.98
M_{4W}	1.53	1.48	1.84	1.80	1.97	1.91	1.58	1.57

7. Conclusions

This paper presents a supersonic turbine design along with its preliminary optimization. The research field of interest is related to the development of rotating detonation engines, for which conventional first stage turbines are unsatisfactory as they are unable to work at an acceptable efficiency.

A novel mean line code was developed to design supersonic turbines; this code includes additional features to assess the starting limit of a supersonic passage, to generate the supersonic profile through an implicit version of the MOC and to accurately predict the losses. For this final point, not only leading-edge bow shock waves and profile boundary layer were considered as recommended in literature, but our code also takes into account the first shock reflection and mixing losses by extending Stewart's theory for supersonic axial Mach numbers. The in-house mean-line code demonstrated excellent predictive capabilities during the validation process with CFD simulations.

Since no loading criterium, empirical or semi-empirical, exists for these pioneer turbines, an optimization procedure was developed and implemented to find the optimal loading condition for both stator and rotor. The optimization procedure, based on the golden-section search algorithm, iteratively and automatically evaluates the performance function by running the mean-line code, creating an adequate mesh and running the CFD simulation for the blade-to-blade section. In optimal loading condition the entropy generated by the stator is almost 18% lower compared to the original solidity proposed by the MOC (once a finite thickness is imposed), clearly justifying the optimization process developed for this purpose.

An extensive blade-to-blade simulation campaign was performed to assess the turbine performance in off-design condition. From this analysis it emerges that supersonic profiles exhibit a low over-speed sensitivity, while an optimal robust design should take into account that a slight positive incidence can be applied at design point to allow for a wider operating range.

Finally, a parametric analysis was carried out to assess the influence of the variable stator blade height, the reaction degree and the peripheral speed on the turbine stage performance. A variable stator blade height design mitigates the Kantrowitz limit, allowing to choose lower reaction degree and higher peripheral velocity designs; this extended design space is also characterized by a higher total-to-total efficiency up to 76% and it is important to underline that, previous to our work, efficiencies this high for this type of machines were not documented in literature. A second important and novel result of this analysis is that, opposite to common subsonic turbine design, the lower the reaction the higher the efficiency: this unconventional result comes from a reduction in rotor shock losses backed by a higher work generation when the reaction degree is lowered. The 3D coupled stator-rotor simulations were performed in 4 meaningful points to confirm these interesting outcomes; these simulations also display the full complexity of the flow field: the shocks exhibit a complex 3D structure from hub to shroud and Mach phenomena appear in the rotor channel at low reaction degree.

The present methodology and results pose credible bases for future stage optimization, both about endwalls and 3D profile shape, and for studies on the cooling issues.

Author Contributions: Conceptualization, N.M. and P.G.; methodology, N.M., G.C. and P.G.; software, N.M. and G.C.; validation, N.M. and P.G.; formal analysis, N.M. and G.C.; writing—original draft preparation, N.M., G.C. and P.G.; writing—review and editing, N.M. and P.G.; supervision, P.G. All authors have read and agreed to the published version of the manuscript.

Funding: This research received no external funding.

Data Availability Statement: Not applicable.

Acknowledgments: The authors would like to thank Giacomo Persico for his help with the CFD simulations and for all the stimulating technical discussion.

Conflicts of Interest: The authors declare no conflict of interest.

Nomenclature

A	Area [m^2]
c	Chord [m]
C_{ft}	Zweifel's tangential force coefficient [-]
F_t	Tangential force [N]
g	Blade pitch [m]
H	Blade height [m]
M	Mach number [-]
p	Pressure [Pa]
r	Radius [m]
s	Specific entropy [$Jkg^{-1}K^{-1}$]
t	Time [s]
U	Peripheral velocity [m/s]
V	Velocity [m/s]
X	Stage reaction: static rotor enthalpy variation/Euler work [-]
y	Tangential coordinate [m]
α	Absolute flow angle with respect to axial direction [°]
β	Slope of the reflected shock [°]
γ	Specific heat ratio [-]
δ	Displacement thickness [m]
δ_{te}	Trailing edge thickness [m]
θ	Momentum thickness [m]
η_{tt}	Total-to-total efficiency: Euler work/total to total isentropic head [-]
ρ	Density [kgm^{-3}]
σ	Blade row solidity [-]

Subscripts

1,2	Stator inlet and outlet, respectively
3,4	Rotor inlet and outlet, respectively
cr	Conditions at Mach number equal to 1
fs	Free stream
in	Inlet
l	Lower
mix	Completely mixed flow condition
n	Behind normal shock wave
o	Outlet
t	Total quantity
te	Trailing edge
th	Throat
u	Tangential direction
up	upper

W	Relative frame of reference
x	Axial direction

Superscripts

′	Foremost point of detached shock
′′	First intersection point of detached shock with blade
*	Dimensionless quantity
**	Dimensionless boundary layer quantities defined in [20]

Acronyms

CFD	Computational Fluid Dynamics
MLC	Mean Line Code
MOC	Method of Characteristics
NOx	Nitrogen Oxides
PGC	Pressure Gain Combustion
RDE	Rotating Detonation Engine

References

1. Brouckaert, J.F. An Outlook on the Future of Turbofans and Aircraft Propulsion Systems. In Proceedings of the EASN Conference, Athens, Greece, 3–6 September 2019.
2. Gabrielli, P.; Gazzani, M.; Martelli, E.; Mazzotti, M. Optimal design of multi-energy systems with seasonal storage. *Appl. Energy* **2018**, *219*, 408–424. [CrossRef]
3. Heiser, W.H.; Pratt, D.T. Thermodynamic cycle analysis of pulse detonation engines. *J. Propuls. Power* **2002**, *18*, 68–76. [CrossRef]
4. Paxson, D. Pressure-Gain Combustion for Gas Turbines. In Proceedings of the ASME Turbo Expo, Oslo, Norway, 11–15 June 2018.
5. Sousa, J.; Paniagua, G.; Collado Morata, E. Thermodynamic analysis of a gas turbine engine with a rotating detonation combustor. *Appl. Energy* **2017**, *195*, 247–256. [CrossRef]
6. Bach, E.; Bohon, M.D.; Paschereit, C.O.; Stathopoulos, P. Influence of nozzle guide vane orientation relative to RDC wave direction. In Proceedings of the AIAA Propulsion and Energy Forum and Exposition, Indianapolis, IN, USA, 19–22 August 2019. [CrossRef]
7. Bach, E.; Bohon, M.D.; Paschereit, C.O.; Stathopoulos, P. Impact of outlet restriction on RDC performance and stagnation pressure rise. In Proceedings of the AIAA Scitech 2019 Forum, San Diego, CA, USA, 7–11 January 2019. [CrossRef]
8. Sun, C.; Zheng, H.; Li, Z.; Zhao, N.; Qi, L.; Guo, H. Effects of diverging nozzle downstream on flow field parameters of rotating detonation combustor. *Appl. Sci. (Switzerland)* **2019**, *9*, 4259. [CrossRef]
9. Braun, J.; Paniagua, G.; Ferguson, D. Aero-Thermal Characterization of Accelerating and Diffusing Passages Downstream of Rotating Detonation Combustors. In Proceedings of the ASME Turbo Expo 2021, Virtual, Online, 7–11 June 2021; p. GT2021–59111.
10. Paniagua, G.; Iorio, M.C.; Vinha, N.; Sousa, J. Design and analysis of pioneering high supersonic axial turbines. *Int. J. Mech. Sci.* **2014**, *89*, 65–77. [CrossRef]
11. Sousa, J.; Paniagua, G. Entropy minimization design approach of supersonic internal passages. *Entropy* **2015**, *17*, 5593–5610. [CrossRef]
12. Braun, J.; Saavedra, J.; Paniagua, G. Evaluation of the unsteadiness across nozzles downstream of rotating detonation combustors. In Proceedings of the AIAA SciTech Forum-55th AIAA Aerospace Sciences Meeting, Grapevine, TX, USA, 9–13 January 2017; pp. 1–12. [CrossRef]
13. Sousa, J.; Paniagua, G.; Saavedra, J. Aerodynamic response of internal passages to pulsating inlet supersonic conditions. *Comput. Fluids* **2017**, *149*, 31–40. [CrossRef]
14. Liu, Z.; Braun, J.; Paniagua, G. Characterization of a Supersonic Turbine Downstream of a Rotating Detonation Combustor. *J. Eng. Gas Turbines Power* **2019**, *141*, 1–13. [CrossRef]
15. Kantrowitz, A.; Donaldson, C. *Preliminary Inversitagtion of Supersonic Diffusers*; NACA Wartime Reports; National Advisory Committee for Aeronautics: Langley Field, VA, USA, 1945.
16. Sousa, J.; Paniagua, G.; Collado-Morata, E. Analysis of the aerodynamic losses in a supersonic turbine. In Proceedings of the ASME Power Conference, Charlotte, NC, USA, 26–30 June 2017; pp. 1–7. [CrossRef]
17. Moeckel, W.E. Approximate method for predicting form and location of detached shock waves ahead of plane or axially symmetric bodies. *NACA TN D-1921* **1921**, *211*, 130. [CrossRef]
18. Anderson, J.D. *Modern Compressible Flow: With Historical Perspective*; Aeronautical and Aerospace Engineering Series; McGraw-Hill Education: New York, NY, USA, 2003.
19. Stratford, B.S.; Beavers, G.S. *The Calculation of the Compressible Turbulent Boundary Layer in an Arbitrary Pressure Gradient—A Correlation of Certain Previous Methods*; Aeronautical Research Council Reports; HER MAJESTY'S STATIONERY OFFICE: London, UK, 1961.

20. Stewart, W. *Analysis of Two-Dimensional Compressible-Flow Loss Characterisitics Downstream of Turbomachine Blade Rows in Terms of Basic Boundary-Layer Characteristics*; NACA Technical Note 3515; National Advisory Committee for Aeronautics: Washington, DC, USA, 1955.
21. Shapiro, A.H. *Dynamic and Thermodynamics of Compressible Fluid Flow*; John Wiley & Sons Inc: Hoboken, NJ, USA, 1953; Volume I, p. 647.
22. Goldman, L.J.; Vanco, M.R. *Computer Program for Design of Two-Dimensional Sharp-Edged-Throat Supersonic Nozzle with Boundary-Layer Correction*; NASA: Greenbelt, MD, USA, 1971.
23. Braun, J.; Saracoglu, B.H.; Paniagua, G. Unsteady performance of rotating detonation engines with different exhaust nozzles. *J. Propuls. Power* **2017**, *33*, 121–130. [CrossRef]
24. Starken, H.; Yongxing, Z.; Schreiber, H.A. Mass Flow Limitation of Supersonic Blade Rows due to Leading Edge Blockage. In Proceedings of the ASME 1984 International Gas Turbine Conference and Exhibit, Amsterdam, The Netherlands, 4–7 June 1984. [CrossRef]
25. Druguet, M.C.; Zeitoun, D.E. Influence of numerical and viscous dissipation on shock wave reflections in supersonic steady flows. *Comput. Fluids* **2003**. [CrossRef]
26. Sod, G.A. A numerical study of a converging cylindrical shock. *J. Fluid Mech.* **1977**. [CrossRef]
27. Settles, G.S.; Dodson, L.J. Hypersonic shock/boundary-layer interaction database. In Proceedings of the AIAA 22nd Fluid Dynamics, Plasma Dynamics and Lasers Conference, Honolulu, HI, USA, 24–26 June 1991. [CrossRef]
28. Settles, G.; Dodson, L. *Hypersonic Shock/Boundary-Layer Interaction Database: New and Corrected Data*; Pennsylvania State University Report; Pennsylvania State University: University Park, PA, USA, 1994.
29. Settles, G.S.; Fitzpatrick, T.J.; Bogdonoff, S.M. Detailed study of attached and separated compression corner flowfields in high reynolds number supersonic flow. *AIAA J.* **1979**, *17*, 579–585. [CrossRef]
30. Persico, G.; Mora, A.; Gaetani, P.; Savini, M. Unsteady Aerodynamics of a Low Aspect Ratio Turbine Stage: Modeling Issues and Flow Physics. *J. Turbomach.* **2012**. [CrossRef]
31. Gaetani, P.; Persico, G. Influence of the Rotor-Driven Perturbation on the Stator-Exit Flow within a High-Pressure Gas Turbine Stage. *Int. J. Turbomach. Propuls. Power* **2021**, *6*. [CrossRef]
32. Celik, I.B.; Ghia, U.; Roache, P.J.; Freitas, C.J.; Coleman, H.; Raad, P.E. Procedure for estimation and reporting of uncertainty due to discretization in CFD applications. *J. Fluids Eng. Trans. ASME* **2008**, *130*, 780011–780014. [CrossRef]
33. Schwer, D.; Kailasanath, K. Numerical Study of the Effects of Engine Size n Rotating Detonation Engines. In Proceedings of 49th AIAA Aerospace Sciences Meeting including the New Horizons Forum and Aerospace Exposition, Orlando, FL, USA, 4–7 January 2011. [CrossRef]
34. Zhou, S.; Ma, H.; Ma, Y.; Zhou, C.; Liu, D.; Li, S. Experimental study on a rotating detonation combustor with an axial-flow turbine. *Acta Astronaut.* **2018**, *151*, 7–14. [CrossRef]
35. Paxson, D.E.; Naples, A. Numerical and analytical assessment of a coupled rotating detonation engine and turbine experiment. In Proceedings of the AIAA SciTech Forum-55th AIAA Aerospace Sciences Meeting, Grapevine, TX, USA, 9–13 January 2017. [CrossRef]
36. Rankin, B.A.; Fotia, M.L.; Naples, A.G.; Stevens, C.A.; Hoke, J.L.; Kaemming, T.A.; Theuerkauf, S.W.; Schauer, F.R. Overview of performance, application, and analysis of rotating detonation engine technologies. *J. Propuls. Power* **2017**. [CrossRef]
37. Zweifel, O. The spacing of Turbo-Machine Blading, Especially with Large Angular Deflection. *Brown Boveri* **1945**, *32*, 436–444.
38. Schwer, D.A.; Kailasanath, K. Characterizing NOx emissions for air-breathing rotating detonation engines. In Proceedings of 52nd AIAA/SAE/ASEE Joint Propulsion Conference, Salt Lake City, UT, USA, 25–27 July 2016. [CrossRef]
39. Délery, J.; Dussauge, J.P. Some physical aspects of shock wave/boundary layer interactions. *Shock Waves* **2009**, *19*, 453. [CrossRef]

International Journal of
Turbomachinery
Propulsion and Power

MDPI

Article

Numerical Steady and Transient Evaluation of a Confined Swirl Stabilized Burner

Federica Farisco *,†, Luisa Castellanos, Jakob Woisetschläger and Wolfgang Sanz

Institute of Thermal Turbomachinery and Machine Dynamics— ITTM, Graz University of Technology, 8010 Graz, Austria; lmcastellanos07@gmail.com (L.C.); jakob.woisetschlaeger@tugraz.at (J.W.); wolfgang.sanz@tugraz.at (W.S.)

* Correspondence: federica.farisco@dlr.de or federica.farisco@tugraz.at; Tel.: +43-660-2622508

† Current address: German Aerospace Center (DLR), Institute of Combustion Technology, 70569 Stuttgart, Germany.

Abstract: Lean premixed combustion technology became state of the art in recent heavy-duty gas turbines and aeroengines. In combustion chambers operating under fuel-lean conditions, unsteady heat release can augment pressure amplitudes, resulting in component engine damages. In order to achieve deeper knowledge concerning combustion instabilities, it is necessary to analyze in detail combustion processes. The current study supports this by conducting a numerical investigation of combustion in a premixed swirl-stabilized methane burner with operating conditions taken from experimental data that were recently published. It is a follow-up of a previous paper from Farisco et al., 2019 where a different combustion configuration was studied. The commercial code ANSYS Fluent has been used with the aim to perform steady and transient calculations via Large Eddy Simulation (LES) of the current confined methane combustor. A validation of the numerical data has been performed against the available experiments. In this study, the numerical temperature profiles have been compared with the measurements. The heat release parameter has been experimentally and numerically estimated in order to point out the position of the main reaction zone. Several turbulence and combustion models have been investigated with the aim to come into accord with the experiments. The outcome showed that the combustion model Flamelet Generated Manifold (FGM) with the k-ω turbulence model was able to correctly simulate flame lift-off.

Keywords: confined swirl stabilized burner; CFD; combustion

check for updates

Citation: Farisco, F.; Castellanos, L.; Woisetschläger, J.; Sanz, W. Numerical Steady and Transient Evaluation of a Confined Swirl Stabilized Burner. *Int. J. Turbomach. Propuls. Power* **2021**, *6*, 46. https://doi.org/10.3390/ijtpp6040046

Academic Editor: Michael Pfitzner

Received: 6 August 2021
Accepted: 24 November 2021
Published: 30 November 2021

Publisher's Note: MDPI stays neutral with regard to jurisdictional claims in published maps and institutional affiliations.

Copyright: © 2021 by the authors. Licensee MDPI, Basel, Switzerland. This article is an open access article distributed under the terms and conditions of the Creative Commons Attribution (CC BY-NC-ND) license (https://creativecommons.org/licenses/by-nc-nd/4.0/).

1. Introduction

The correct modelling of the flow field in lean premixed combustors requires a deep understanding of the phenomena directly resulting in instability. It is, therefore, necessary to know the thermo-chemical processes that are influencing the main reaction zone in order to obtain more insight into the prediction of lean combustion.

The flow field in swirl-stabilized combustors was investigated and explained in different papers (see [1,2]). The first cited work reviewed the knowledge gained on vortex breakdown over the past 45 years. The paper was divided in three subsections (experimental, numerical and theoretical) where a clear structure of the flow pattern was underlined.

The next cited study [2] described in detail the main parameters influencing industrial dry-low emission (DLE) swirl-stabilized combustors. The authors outlined also the progress concerning numerical investigations of swirl-stabilized combustion.

One of the most common method used for the measurement of heat release concerns the analysis of OH* radical chemiluminescence in the flame [3,4]. A large amount of research [5–8] has been carried out to provide an overview of different techniques applied to analyze the flame dynamics. Chemiluminescence has proved to be an efficient method for investigating global heat release fluctuations (see [9,10]). Balachandran et al. [9] performed measurements of heat release with OH* and CH* chemiluminescence pointing out that

the global heat release estimated for both chemiluminescence parameters was in good agreement with respect to magnitude and phase. The work of Greiffenhagen et al. [10] investigated Laser Interferometric Vibrometry (LIV) as an addition to chemiluminescence in order to analyze heat release perturbations in the flame. Laser Interferometric Vibrometry (LIV) records directly the time derivative of density fluctuations along the laser beam path in unconfined and confined flames. Local measurements are obtained from integrals data by tomography or Abel inversion (Greiffenhagen et al. [11]). Numerical RANS (Reynolds Averaged Navier–Stokes) simulations have been presented in [12] for the same geometry analyzed in [10].

Detailed models and up to date experimental techniques are required to estimate combustor capabilities [13]. In the previous paper [13], the authors underlined the importance of an optimal three-step global reaction mechanism for methane-air mixtures that were used in their numerical analysis. Review papers by [13–15] present recent numerical progress related to the evaluation of swirl-stabilized flames. In [14] few swirl stabilized burner configurations have been investigated by comparing several turbulence models such as the standard k-ϵ model, the RNG k-ϵ model and the Realizable k-ϵ model. The authors observed that the calculations predicted correctly the experimental profile shapes; in particular, the application of RNG k-ϵ carried out a slight advantage compared to Realizable k-ϵ.

The work of [15] described the derivation of a Flamelet Generated Manifold model and its use for turbulent flames with Large Eddy Simulation (LES) and RANS. The flame front was modeled in these cases through the Probability Density Function (PDF) approach that takes into consideration non-equilibrium aspects [16]. The results pointed out that this chemical method is an accurate technique for modeling premixed combustion. In the work of [16], the authors proved also that the transient Scale Adaptive Simulation (SAS) model was capable for depicting the trademark of the unsteady flame in a more accurate manner compared to RANS.

However, accurate RANS flow simulations represent a standard tool applied within industrial design process suitable to reproduce the main flow characteristics using less computational time compared to LES or Detached Eddy Simulation (DES) methods.

This paper combines an analysis of several turbulence and combustion models of diverse complexity. The model's capability to reproduce the characteristics of the investigated combustor is studied. The CFD code Ansys Fluent v2020 R1 is used in the current study and is applied as combustion models with respect to the Eddy Dissipation Model (EDM) developed by Magnussen and Hjeertager [17], Steady Laminar Flamelet model (SLF) [18] and Flamelet Generated Manifold (FGM).

The scope of this work is to identify the most accurate combustion and turbulence model able to predict the correct behavior of the investigated combustor by using the estimation of temperature contours and species concentration.

This study is a follow-up of the paper of Farisco et al. [12] where a steady numerical analysis was performed with a different combustor compared to the current confined one in order to see if the results can be improved.

The current RANS (Reynolds Averaged Navier Stokes) numerical procedure is the same compared to [12]. Whereas in [12], the unconfined burner could not be correctly reproduced by any turbulence or combustion models, in the current confined case, the simulations will show a better agreement with the experimental data available. Furthermore, in this study, the results obtained by an unsteady investigation via Large Eddy Simulation (LES) of the confined combustor are also included. The outcomes of this research could be used as baseline for further industrial applications. Nevertheless, more research needs to be performed with a focus on understanding the complex flow effects and limitations of combustion models.

2. Combustor Domain Investigated

The numerical domain represents the geometry used for the experiments. The data were obtained on a lean, swirl-stabilized methane combustor with a cylindrical confinement under atmospherically conditions. A quartzglass cylinder was used with a height of 210 mm, an outer diameter of 120 mm and a wall thickness of 3 mm. The thermal power of the combustor was 3.44 kW and the mean equivalence ratio had the value of 0.88. Figure 1 presents the configuration of the confined configuration investigated. The burner (outer diameter of D = 18 mm) consists of a premixed axial and tangential line and a cooling air supply (see Greiffenhagen et al., 2020 [19]).The tangential air is premixed with the fuel and is then transferred into the inner area of the methane burner by a swirler consisting of 32 feed lines with a tangential alignment. The fuel-oxidizer mixture streams swirl into the combustion chamber, and it is ignited. The axial and radial pressure gradients that are produced by this swirling flow into the combustion chamber, create a recirculation zone which reduces the turbulent flow speed of the injected mixture compared to the flame speed. This effect operates as a stabilizing mechanism where the flame can burn at a fixed location, and additionally it guarantees that sufficient heat is available to ignite the upcoming fuel-oxidizer mixture. A swirl number value of 0.53 is obtained, taking into account the formulation of Candel et al. (2014) [20].

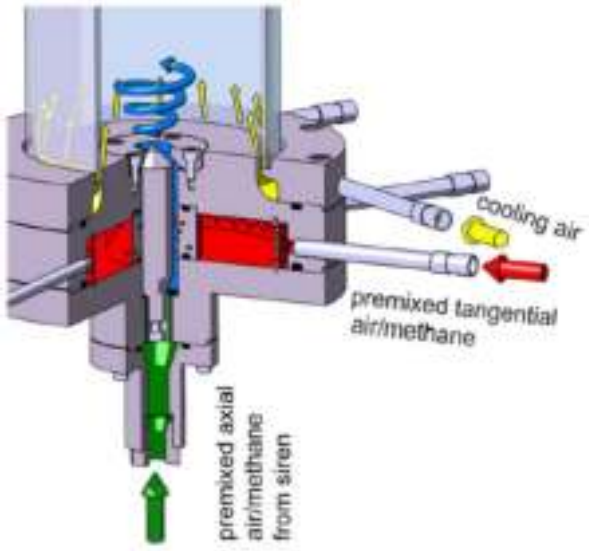

Figure 1. Schematic burner section.

Swirl Flow Structure

To clearly understand the outcomes of this work, a short description of the flow structures present in a swirl stabilized flame is provided. The flow field produces (see Figure 2) an outer recirculation zone (ORZ) that is a toroidal recirculating area due to the fast evolution of the nozzle into the combustor; an inner recirculation zone (IRZ or vortex breakdown) related to the vortex breakdown characterized by stagnation points and reversing flows that increases flame stabilization; and the high velocity annular fluid jet delimited by the inner and outer shear layers.Velocity perturbations modify the speed of this annular jet, resulting in oscillations of the flame. Another common type of a coherent vortex in swirl flames is the precessing vortex core (PVC) (see Figure 3). It develops when a central vortex core starts to precess around the axis of symmetry at a certain frequency [21].

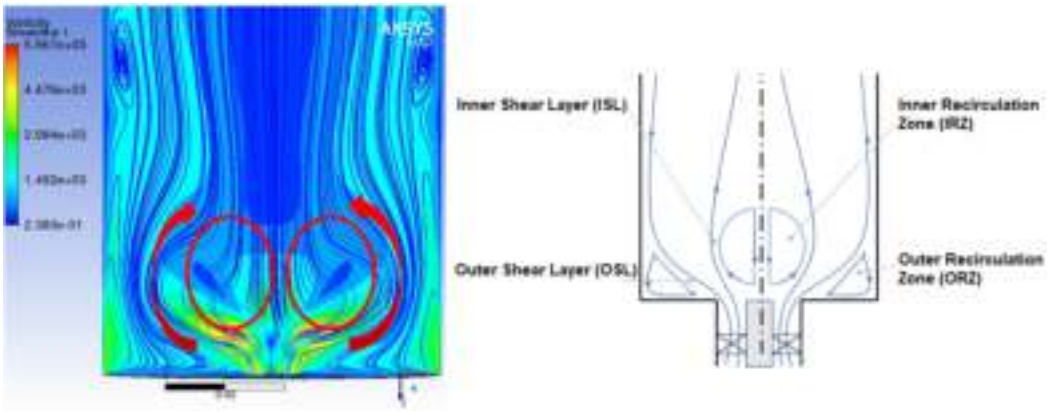

Figure 2. Vortex core overview. (**left**) current combustor; (**right**) sketch of flow patterns in a confined, premixed swirl stabilized combustor [22].

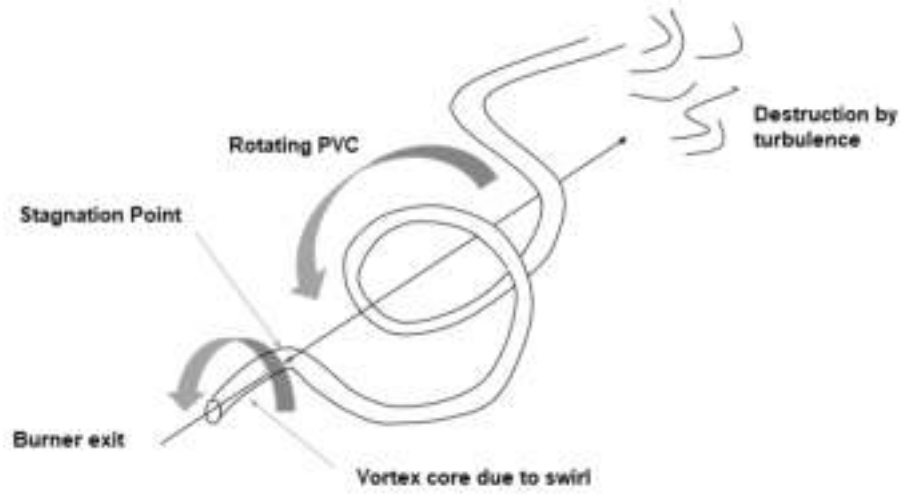

Figure 3. Vortex structure of PVC [21].

3. Experimental Setup

Experimental data are taken from a published study (see [19]). For more details concerning the LIV measurement technique and equipment, refer to papers [11,19].

4. Mesh Generation

Several meshes are performed within this work, and a mesh independency study is carried out. The commercial tools ANSYS mesher and ICEM are used in order to generate meshes. Figure 4 underlines the numerical domain of the confined combustor analyzed in the simulations.

The coarsest mesh is obtained with a first cell-center positioned at a non-dimensional wall distance of $y^+ = 3$. It consists of 4,165,157 cells, and it is refined in order to investigate the sensitivity of the numerical results. In addition to the coarsest mesh, two other refined meshes are generated. The one with $y^+ = 2$ has 1.5 times the number of nodes in each segment, and the $y^+ = 1$ mesh has two times the number of nodes. However, mesh independency is obtained with the coarsest mesh used. Simulations with cold flow and the RNG k-ϵ and k-ω turbulence models are performed with all meshes analyzed. The swirl number and the axial velocity profiles are used to investigate the behavior of different refined meshes.

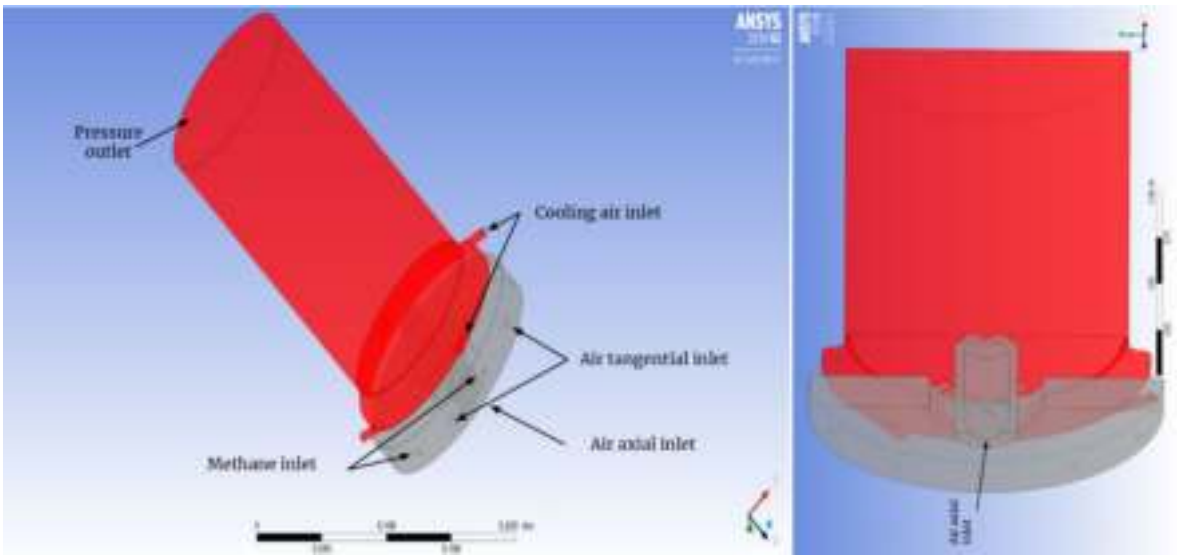

Figure 4. Sketch of the combustor and computational domain.

The simplified form of the swirl number equation is taken according to the experiments [8,20]. The same method for the calculation of the swirl number applied in the experiments is used also in the numerics to obtain a more accurate comparison between the two approaches. For the swirl number analysis, the simplified swirl number is calculated at two different distances, respectively: a quarter and half of the inlet diameter D. In order to obtain it, velocity profiles are extracted from line sampling in the x and y directions. The integration of absolute velocity values is performed by using a Riemann sum. The results of this integration are used for calculating the swirl number. A value of swirl number is obtained for an x-parallel line of samples and for the y-parallel line, then an averaging of both values is performed (as shown in Equations (1)–(3)). The suggestions shown in the literature [7] have been used to select the burner exit diameter as an integral boundary.

$$S_x = \frac{2\int_0^{\frac{D}{2}} vwx^2 dx}{D\int_0^{\frac{D}{2}} w^2 x dx} \tag{1}$$

$$S_y = \frac{2\int_0^{\frac{D}{2}} uwy^2 dy}{D\int_0^{\frac{D}{2}} w^2 y dy} \tag{2}$$

$$S = \frac{S_x + S_y}{2} \tag{3}$$

For the cold flow simulations, the averaged swirl numbers obtained with the coarsest mesh $y^+ = 3$ and with the finer mesh $y^+ = 1$ with both RNG k-ϵ and k-ω turbulence models are presented in Tables 1 and 2 at both $D/4$ and $D/2$ calculated distances. It can be observed that the higher swirl numbers are reached by the coarsest mesh with $y^+ = 3$. Figure 5 shows the axial velocity profile on the middle plane for the k-ϵ model with $y^+ = 3$ mesh (on the left side) and k-ϵ with $y^+ = 1$ mesh (on the right side). This parameter underlines, for the k-ϵ model with the $y^+ = 3$ mesh, a flow type II according with respect to the nomenclature of the International Flame Research Foundation. This case presents a V-shaped or M-shaped expansion of the flame with an angle of about 40°, pointing out a similar trend as observed in the measurements (for more details see the section "Results"). Instead, the axial velocity profile for the k-ϵ with the $y^+ = 1$ mesh shows a type of flow quite different and more similar to a flow type I. For this reason, the coarsest mesh with $y^+ = 3$ is chosen because the swirl is slightly better conserved along the burner exit region with values slightly higher

and closer to the experiments, and it guarantees less numerical time compared to the finer meshes generated.

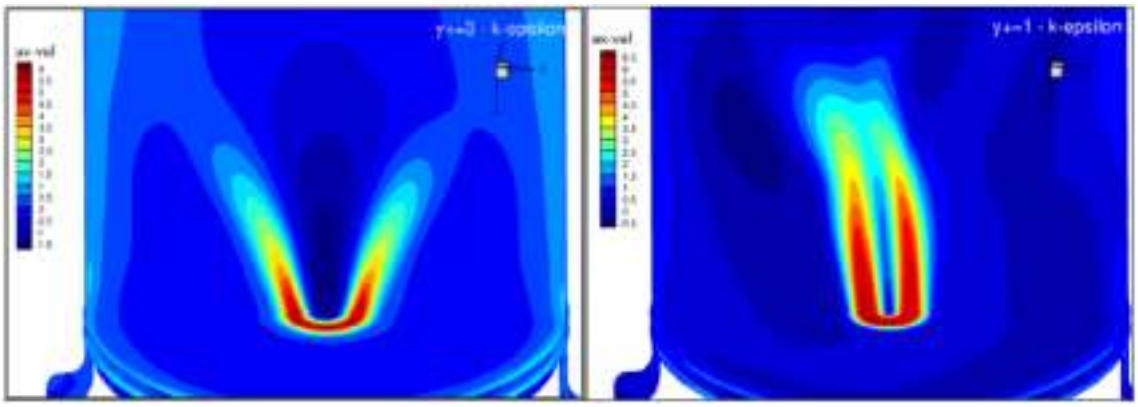

Figure 5. Axial velocity field comparison between k-ϵ $y^+ = 3$ (**left**) and k-ϵ $y^+ = 1$ (**right**).

Table 1. Cold flow case with $y^+ = 3$.

$y^+ = 3$	k-ϵ	k-ω
$S - D/4$	0.5684	0.4548
$S - D/2$	0.53625	0.54065

Table 2. Cold flow case with $y^+ = 1$.

$y^+ = 1$	k-ϵ	k-ω
$S - D/4$	0.48035	0.4278
$S - D/2$	0.43935	0.40995

A detail of the mesh used for the simulations is shown in Figure 6. A hybrid mesh is proposed for a better resolution of the domain. In order to decrease computational time, a reduced domain consisting of the entire hexahedral cylindrical exit burner is adopted for the combustion simulations.

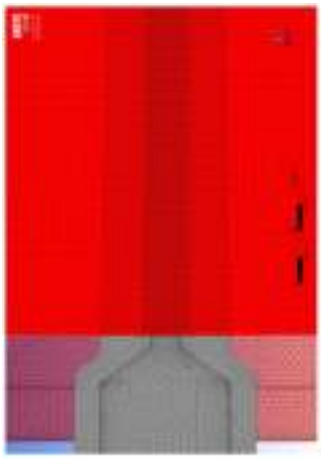

Figure 6. View of the chosen mesh.

The cell structure applied in the generated meshes is presented in Figure 6. In the area where the flame occurs, which is influenced by high velocity and temperature gradients, hexahedral cells are used to ensure high numerical reliability. The hex-cells produce reduced numerical dissipation compared to the tetrahedral cell shape, seeing that they are

aligned with the flow direction and they decrease the number of cells (the reader is referred to [13]). Due to the fact that the region inside the burner is represented by a configuration with the swirler consisting of small tubes, it is modelled using tetrahedral cells. This mesh is also used in the transient simulation. An approximate estimation for the integral length scale l_0 could be evaluated using k, ϵ and ω values from the RANS simulations. In order to resolve an eddy with a length scale l, it is necessary to have a couple of cells in each direction. Then, a resolution of the eddies with sizes larger than half size of the integral length scale ($l_0/2$) is required to obtain 80% of the turbulent kinetic energy (as stated in [23,24]). Approximately five cells are needed across the integral length scale l_0 [23], and the current mesh is also used in the unsteady simulation presented this feature.

5. Numerical Approach

In this work, the RANS numerical method is applied through the CFD code ANSYS Fluent to identify the main flow features within the cold flow and combustion processes. The simulations are performed in such a manner that the effects of the turbulence model are isolated. The SIMPLE method is used pressure–velocity coupling. The segregated solver is applied since partially premixed models do not allow the use of the coupled one. Concerning spatial discretization, the second order upwind scheme is preferred over the quadratic upwind scheme QUICK for the turbulent kinetic energy, momentum and specific dissipation rate in order to ensure a smoother simulation trend. The Peclet number is calculated as the ratio of the hyperbolic part of the Navier–Stokes equations relative to the parabolic part and using the first cell height for each mesh elaborated. The minimum value computed is 70, which indicates a considerable amount of advection. Pressure discretization type PRESTO is used. The Reynolds number 2554 is calculated based on inlet conditions. The convergence obtained with several parameters, such as velocity, temperature, CH_4 and CO_2 species, is detected through monitor points that are positioned at few locations close to the burner's exit.

FGM with premixed flamelets approach is also applied for transient simulation since it shows accurate results in RANS simulations and ensures reduced computational time. The SIMPLE approach for pressure-velocity coupling is considered. For LES, the Subgrid-Scale model (SGS) Kinetic Energy Transport is applied since it ensures lower computational cost, and it should be suitable for flows with strong recirculation zones. For the LES numerical simulation, a time step of Δt = 0.000025 s is taken with a time duration up to 0.75 s.

5.1. Boundary Conditions Applied

The numerical boundary conditions are derived by the measurements in order to ensure a validation of the numerics against the experimental data available. The mean equivalence ratio of $\Phi = \frac{1}{\lambda} = 0.88$ (λ set as fixed air excess parameter) and a constant thermal power of P_{th} = 3.44 kW are considered for the current numerical study. For cold flow calculations, the density is maintained constant, while it has an effect in the combustion process. The following values are taken for the mass flows: $\dot{m}_{CH4}$ = 0.068 g/s, $\dot{m}_{ax}$ = 0.705 g/s, $\dot{m}_{tan}$ = 0.628 g/s and $\dot{m}_{cooling}$ = 1.2 g/s, matching the experimental values. The domain is specified by setting mass flow and total temperature at the inlets and atmospheric pressure at the burner's outlet. Concerning the smaller region used for combustion simulations, one inlet mass flow is assigned in the axial direction consisting of premixed fuel, axial and tangential air. For the LES case, a forced response approach has been also used in the simulations, imposing a pressure wave excitation at the inlet of the combustor. The signal applied is a sine signal. Due to the fact that at a perturbation frequency of 225 Hz, a sharp peak of thermo-acoustic oscillations was recorded during the measurements, the same excitation frequency has been used also in the simulations. The formula applied for the mass flow fluctuations at the geometry inlet is shown in Equation (4) .

$$\dot{m}' = 0.001366 + 0.000035025 sin(2\pi \times 225 \times t) \quad (4)$$

The fluctuating mass flow value of 0.000035025 represents almost 3% of the constant mass flow term 0.001366. Pressure signals have been recorded at various points along the flow path during numerical calculations. The walls of the combustor have been set as diabatic taking the same glass temperature measured in the experiments. The Discrete Ordinates (DO) model is also applied to include the thermal radiation. Enhanced wall treatment is adopted as model for the flow near the wall (see [24,25]) assigning the value $y^+ = 3$ along the burner walls.

5.2. Turbulence-Chemistry Models

Many elementary reactions and species are included within the methane-air combustion. In order to lower computational effort in CFD combustion calculations, the species number has to be reduced. In order to describe the chemistry of methane-air mixtures, several reaction mechanisms are available in literature. The two-step mechanism introduced by Westbrook [26] is applied for the ED model in this work. The GRI-3.0 detailed mechanism of methane-air combustion is also adopted for the cases with flamelets formulation. This last chemical method is described by Smith et al. [27] for hydrocarbon combustion and is further verified in the literature.

Within the current study, the Eddy Dissipation Model was analyzed, and the outcomes are compared against FGM and SLF flamelet approaches.

Laminar flames are used to model the turbulent flame front in the flamelet formulations. Density, temperature and species concentration are obtained as results of the equations in every location of the laminar flamelet main reaction zone. The mixture fraction and scalar dissipation are used as main parameters to define the concentrations of fuel and oxidant. A Probability Density Function (PDF) combines instantaneous temperature and species values obtained from flamelet calculation with the turbulent flow [24]. For this study, both premixed and diffusion flamelets are selected to calculate the flamelet manifold. Finite Rate is used for the progress variable source. The turbulence-chemistry interaction approach in FGM is described by the variances of the progress variable and mixture fraction.

6. Results

6.1. Cold Flow

For the cold flow case, a converged solution with RNG k-ϵ turbulence model is obtained. RNG k-ϵ turbulence model with enhanced wall treatment is chosen because it is suited low Reynolds flows. Figure 7 shows the velocity magnitude profile for the cold flow along the middle plane. The radial section of the velocity field is introduced for all cold flow and combustion simulations due to its axial symmetry (x = 0 burner axis). With a similar but unconfined burner geometry, different turbulence and combustion models were already investigated in Fluent by Farisco et al. [12].

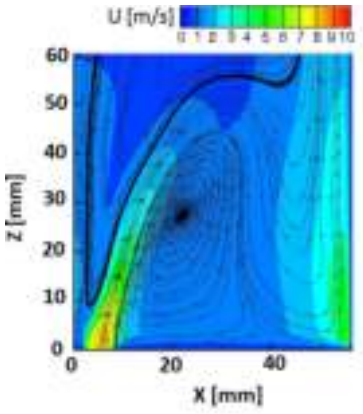

Figure 7. Velocity magnitude profile for the cold flow case with RNG k-ϵ turbulence model.

The swirl-induced jet opening at the exit burner area produces a narrow shape of the velocity magnitude profile. The highest velocity values of around U = 7.5 m/s are observed up to d = 10 mm above the burner. The velocity in the cold flow is reduced to U = 3 m/s beyond d = 15 mm above the burner, due to the lack of combustion processes that would cause a gas expansion in this region with enhanced absolute and tangential velocities. The numerical cold flow velocity profile is placed in line with the central axis in contrast with the cases with combustion. This is related to the fact that in the hot cases, the coming flow is accelerated and diverted at the flame front. The density differences between reactants and products and the entering swirl angle flow influence this flow deflection in the combustion process. For the cold flow simulation with RNG k-ϵ turbulence model, the averaged swirl number obtained is presented in Table 1. Figure 8a presents the cold flow axial velocity profile along the middle plane and at the burner exit (inlet plane for the combustion simulations). In Figure 8b, the 2D axial velocity profile is shown along a line taken at the burner exit plane. Figure 9a underlines the velocity magnitude contour obtained along a z-plane 5 mm above the nozzle opening. The 2D plot observed in Figure 9b points out the velocity trend along the black line shown in Figure 9a on the z-plane = 5 mm. The velocity magnitude reaches the highest values of about 7.5 m/s in the simulations, and it represents a good approximation compared to the measurements. The velocity magnitude U = (7.67 $\pm$ 0.03) m/s has been recorded also in the experiments (with DANTEC Dynamics CTA module 91C10, three components at 150 kS/s, StreameWare Pro Software and DANTEC PRO Calibrator) for the cold flow case at the same plane 5 mm above the nozzle opening. For this reason this current result is used as input for the following combustion simulations.

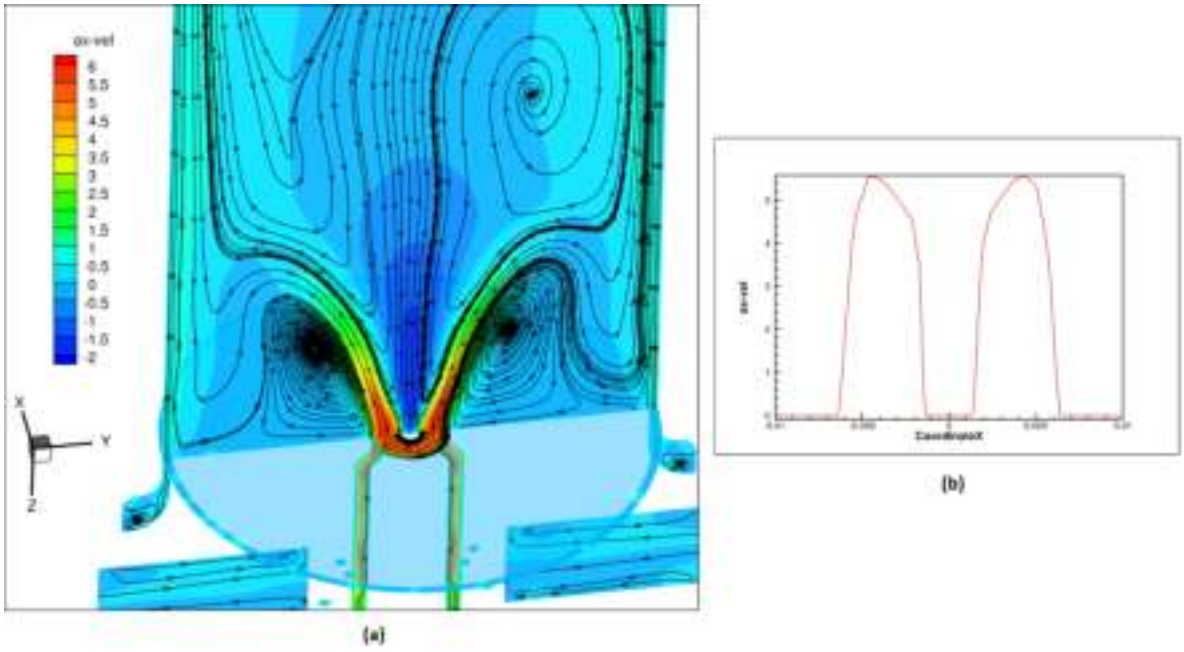

Figure 8. Axial velocity profile for the cold flow case with RNG k-ϵ turbulence model (**a**) and axial profile 2D plot set at the inlet of the combustion simulations (**b**).

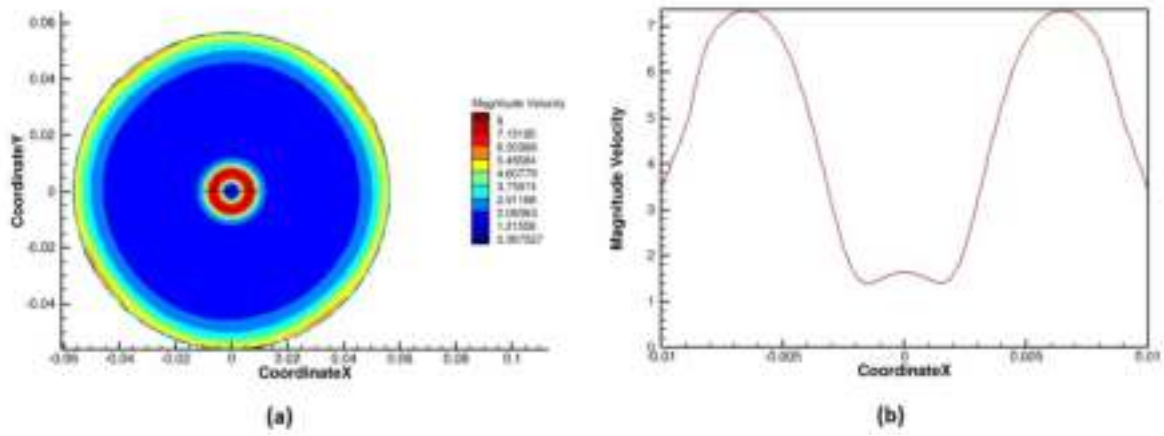

Figure 9. Velocity magnitude profile for the cold flow case with RNG k-ϵ turbulence model at the z-plane = 5 mm (**a**) and velocity magnitude profile 2D plot along the black line on z-plane = 5 mm (**b**).

6.2. Hot Flow Using Combustion Models

Concerning the combustion models, the Eddy Dissipation Model (EDM), the Steady Flamelet (SF) partially premixed model and Flamelet Generated Manifold (FGM) model with both premixed and diffusion flamelets approaches are applied. Each one of the combustion models is used in combination with the following turbulence models: RNG k-ϵ with enhanced wall treatment, k-ω and k-ω SST with low Reynolds corrections.

Table 3 points out the swirl number values calculated for all combustion and turbulence models used. The Steady Flamelet approach shows overall the lowest swirl number values compared with all turbulence models. Both EDM and FGM present similar swirl numbers for the k-ϵ and SST models with lower values than in the experimental case. EDM and FGM with both premixed and diffusion flamelets with k-ω turbulence model conserve swirls along the entire axial direction, showing an accurate approximation with experimental values. For this reason, velocity contour plots for EDM and FGM are shown in this study. FGM with premixed flamelets is chosen instead of FGM with diffusion flamelets because both models did not show substantial differences.

Table 3. Swirl number for the combustion and turbulence models analyzed.

Eddy Dissipation	**k-ϵ**	**k-ω**	**SST**
S	0.38505	0.605785	0.3929925
Steady Flamelet	**k-ϵ**	**k-ω**	**SST**
S	0.36569	0.27741	0.36799
FGM Premixed Flamelet	**k-ϵ**	**k-ω**	**SST**
S	0.378645	0.5313975	0.3744125
FGM Diffusion Flamelet	**k-ϵ**	**k-ω**	**SST**
S	0.3799175	0.523415	0.374775

Combustion data were available and comparisons with experiments were carried out for temperature and heat release contours. As first, the temperature and heat release contours for the FGM are presented, because the swirl numbers calculated for this combustion model and k-ω represent the closest approximation to the experimental values. Figure 10 shows the numerical temperature profiles for LES and for FGM with both k-ϵ and k-ω compared with the experimental data in Figure 10a. The temperature contours for FGM

and k-ω SST turbulence models are omitted because they present a similar behavior and swirl number value compared to the k-ϵ model.

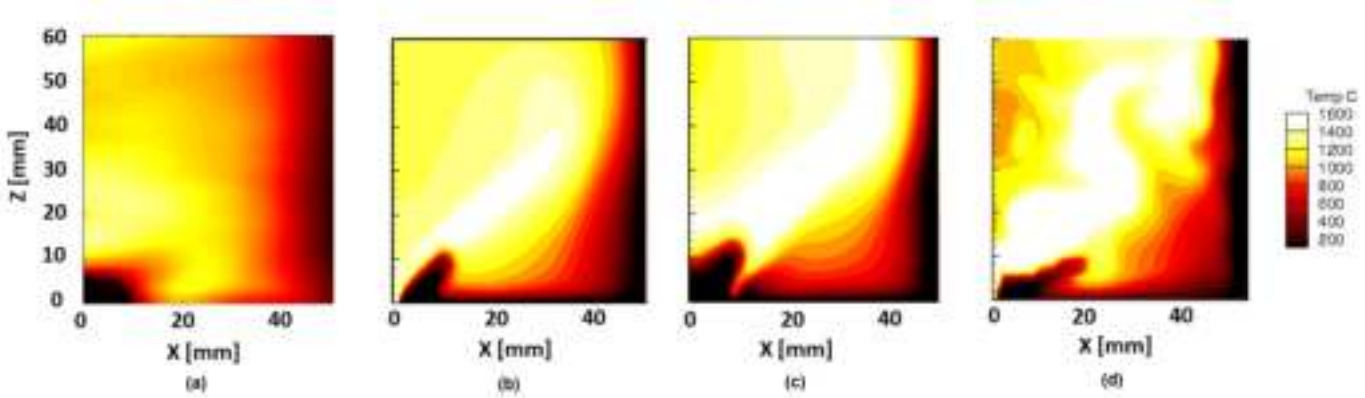

Figure 10. Flow comparison-temperature profile shown for (**a**) experiments, (**b**) FGM premixed with RNG k-ϵ, (**c**) FGM premixed with k-ω and (**d**) LES.

In order to obtain a temperature profile more accurate and similar to the experiments in the numerics, a radiation model was added to the already converged FGM simulation with premixed flamelet. In order to define which radiation model to use, the optical thickness parameter was taken into account:

$$OpTh = \alpha L \tag{5}$$

where $\alpha = (-ln(1-\epsilon))/S$ stands for a representative absorption, and L is the characteristic length of the combustor. Domain emissivity is represented by ϵ, and S is a geometric parameter of the domain ($S = V/A$) with V being the total volume of the domain, and A being the total surface of the domain. After evaluating the optical thickness as $OpTh$ = 0.049046 (the emissivity taken from the quartz glass that was used for the confinement in the experiments), model Discrete Ordinates (DOs) were chosen since it requires $OpTh < 1$.

The numerical temperature fields present maximum values that are higher compared to the experimental investigation. The reason could be related to the simulated combustion process where simplified and limited chemical reactions need to be taken into account due to computational efforts. During the simulations, it was observed that the radiation model DO decreased the temperature to about 100 °C compared to the case with adiabatic walls. Moreover, in the measurements, the energy loss due to radiation was only 3% (see as reference page 323 of [10]). For this reason, it would be more effective in correctly simulating heat loss through the walls. In this study, a fixed temperature wall with value taken from the experiments was set, but it would be necessary to perform a Conjugate Heat Transfrer (CHT) analysis as the next step.

The main difference that is observed between Figure 10b,c is related to the flame shape. The k-ϵ model produces a V-flame attached, and the k-ω model generates a detached flame with M-shape. All simulations present a flow type II generating a V-shaped or M-shaped flame with angle of about 45° pointing out a similar trend as in the experiments shown in Figure 10a.

The averaged temperature profile for LES in Figure 10d shows also a flame with an overall accurate shape and trend compared to the experiments. The region located at an axial distance from the burner above d = 10–20 mm shows the highest temperature values compared to the experiments. This area represents the main reaction zone.

As already shown in the section "Swirl flow structure," due to velocity and pressure, differences significant vortex structures form, and a vortex spiral evolves from the shear layer. This is related to the Kelvin–Helmoltz instability. This vortex turns around the centerline before breaking into small fragments. Figure 11 (left) presents a slice cut along the symmetry axis with temperature as contour for the LES simulation and isosurfaces at a

temperature of T = 1600 °C. Figure 11 (right) presents a slice cut along the symmetry axis with vorticity magnitude as contour for LES and isosurfaces at a vorticity magnitude of $\omega = 2000\ s^{-1}$. LES provides better accuracy in terms of larger vortex structure resolution, as already observed in Figure 10d. The toroidal Kelvin–Helmholtz vortices are observed clearly around the central axis. The LES simulation presents the development of large eddies and toroidal isosurfaces that rapidly transition into small vortex fragments.

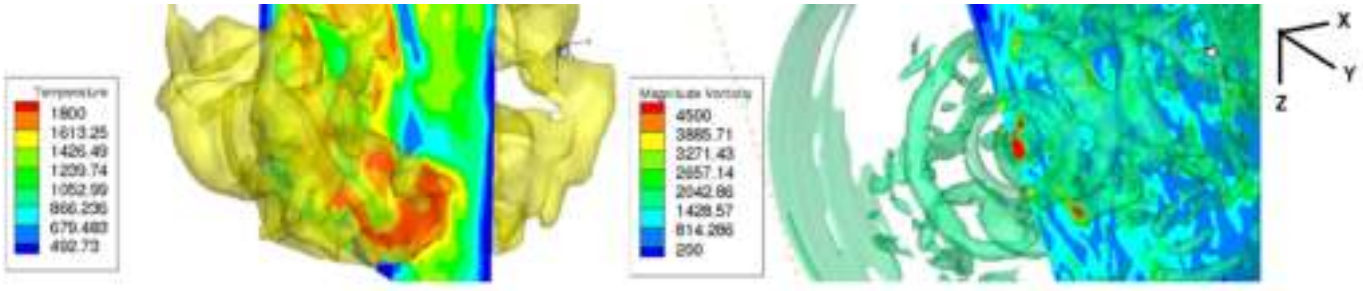

Figure 11. Snapshot of isosurfaces at temperature T = 1600 °C (**left**) and isovorticity surface $\omega = 2000\ s^{-1}$ (**right**) for LES.

Next, the flame's chemiluminescence is taken in order to characterize the overall structure of the flame. The heat release in the numerics has different units compared to OH* emission in the experiments. For this reason, a relative value in the simulations is calculated, and a qualitative comparison between the numerical results and the experiments can be carried out. For the simulations, the total heat release relative profile is shown in order to allow a clearer comparison of the main reaction zone position between numerics and experiments.

In Figure 12a, the local amplitude of OH* chemiluminescence emission is presented as recorded for [19]. Local data were derived from experimental line-of-sight-data by Abel transform. OH* chemiluminescence resembles heat release [28]. As already discussed in Section 5.2, the RANS simulation results represent steady flow, and they are obtained as the baseline for the LES simulation, where pressure fluctuations were also considered, as in the experiments. Thus, LES represents the final numerical step that also includes a perturbation frequency of 225 Hz. Figure 12a shows a maximum of heat release located at about x = 8 mm. In the numerics, the total heat release that corresponds to the temperature contour is shown for the FGM test case with both k-ϵ and k-ω in Figure 12b,c and for LES in Figure 12d. In LES in Figure 12d, the highest heat release values are located in a similar position compared to the measurements. Thus, the LES simulation shows the most accurate flow behaviour and stabilization mode compared to the experiments. Concerning the RANS simulations, one reason that could explain the performance of the k-ω model is related to the new formulation of the Wilcox model implemented in ANSYS Fluent that has reduced the dependency of the model to freestream. Production terms have been added to both the k and ω equations, which have improved the accuracy of the model for predicting free shear flows. A low Reynolds number modification term was also enabled in this setup for the k-ω model because the low Reynolds number term can result in a delayed onset of the boundary layer transition and, therefore, constitute a quite accurate model for laminar to turbulent transitions.

A RNG model was also chosen for the k-ϵ approach because it has shown substantial improvements over the standard model where the flow features include strong streamline curvature, vortices and rotation. This model would provide probably the best estimation for a strong swirl flow, whereas the present burner points out a moderate swirl.

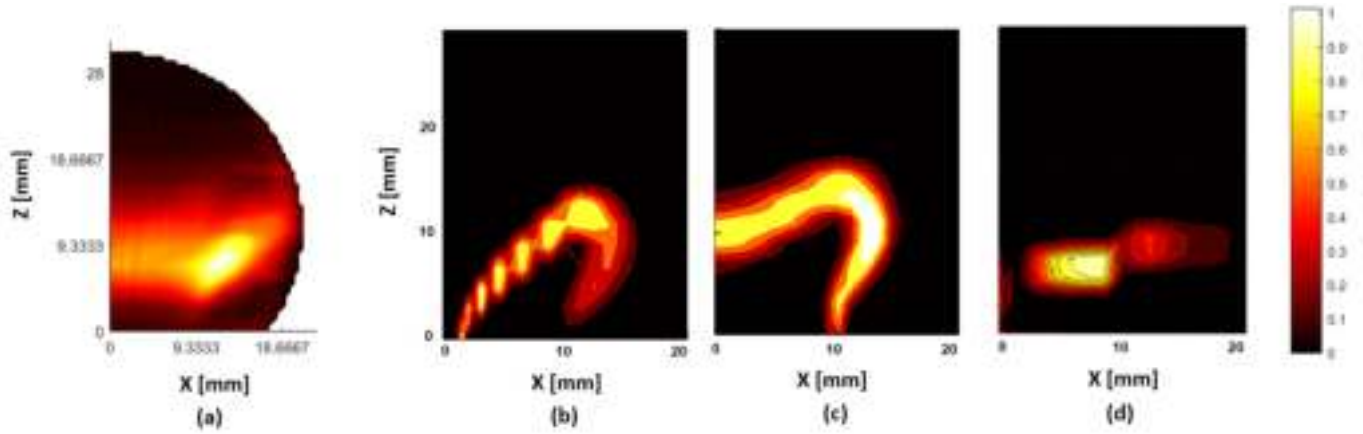

Figure 12. Flow comparison heat release profile shown for (**a**) OH* chemiluminescence experiments, (**b**) FGM premixed with RNG k-ϵ, (**c**) FGM premixed with k-ω and (**d**) LES.

A progress variable and its variances are added to the mixture fraction in the numerical formulation of FGM model. These included parameters can affect the location of the flame in the numerics. It is notable that the same RANS procedure applied to an unconfined burner resulted in much higher temperature values (see paper of Farisco et al. [12]). This outcome could be related to fact that the solver was not able to simulate correctly a sufficient entrainment of fresh ambient air that cools down the mixture in an unconfined configuration.

Figures 13 and 14 present the axial and tangential velocity profiles and streamlines for the simulations with the EDM and the three turbulence models analyzed in this study, RNG k-ϵ, k-ω and k-ω SST, with low Reynolds corrections. Both axial and tangential velocity components are also shown because the swirl number depends on the ratio of these parameters.

Figure 13 points out a similar axial velocity shape for the turbulence models k-ϵ and SST with higher overall values for the k-ϵ model. The k-ω model presents the core of the vortical structure (C) highlighted in Figure 13b located at higher axial distance from the burner exit compared with the other two turbulence models. This behavior underlines the flame lift-off in the k-ω model.

In Figure 14 the tangential velocity plots do not show significant differences between the different turbulence models, highlighting the negative velocity values within the inner recirculation zone.

A similar trend for the axial velocity contours is presented in Figure 15 for the FGM premixed flamelet model with several turbulence models investigated. The highest velocities in FGM k-ω are reached further downstream above d = 20 mm compared to Figure 13b. On the contrary, the other two models show the highest velocity close to the burner axis up to d = 15 mm. This results in lower swirl numbers evaluated for the k-ϵ and SST models compared to k-ω. The tangential velocity component for the FGM model is omitted because it shows the same trend that is already observed in Figure 14 for the ED model.

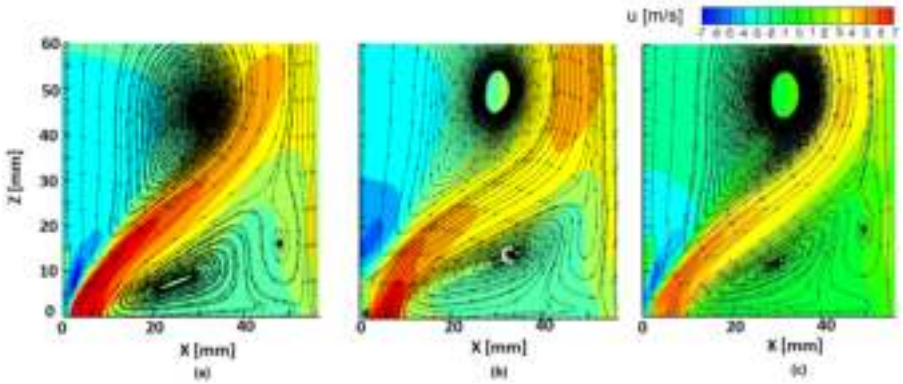

Figure 13. Flow comparisons-axial velocity profile shown for the combustion model ED and different turbulence models: (**a**) RNG k-ϵ, (**b**) k-ω and (**c**) SST.

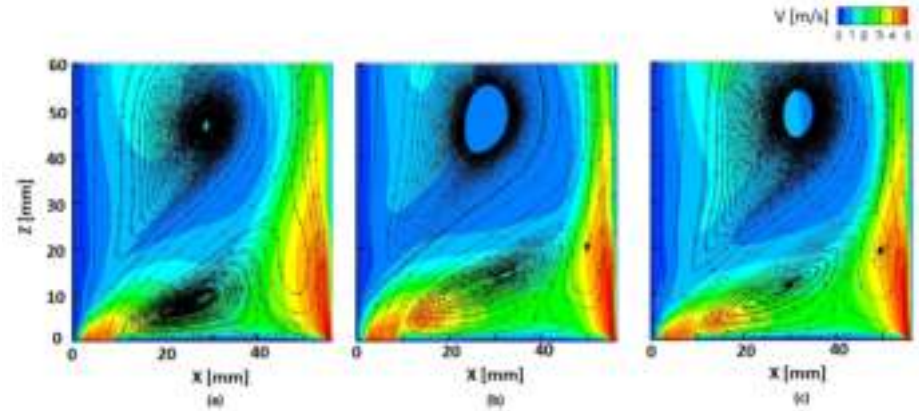

Figure 14. Flow comparisons-tangential velocity profile shown for the combustion model ED and different turbulence models: (**a**) RNG k-ϵ, (**b**) k-ω and (**c**) SST.

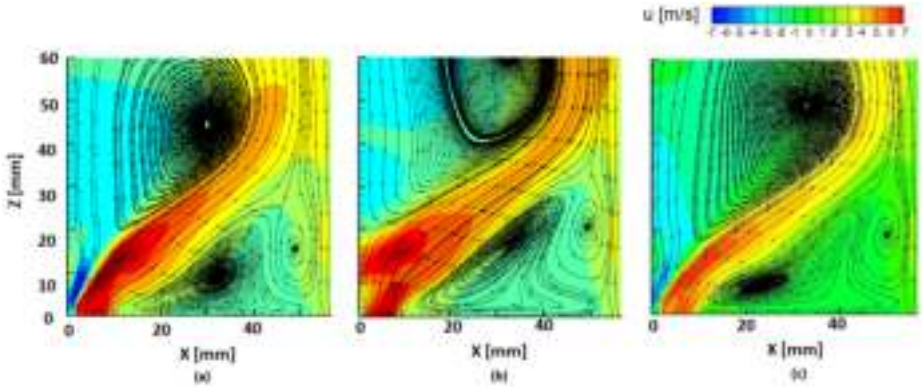

Figure 15. Flow comparisons-axial velocity profile shown for FGM premixed and different turbulence models: (**a**) RNG k-ϵ, (**b**) k-ω and (**c**) SST.

Figure 16 shows the velocity magnitude profile for the simulations with EDM and FGM. Figure 16a,b present the velocity magnitude contour for EDM with RNG k-ϵ and k-ω. The SST turbulence model is now neglected since it is a combination of the two previous cited models, and its results did not present substantial differences compared with the other models.

In EDM with both k-ϵ and k-ω models, the main reaction zone is located near the central axis along the burner exit. This can be explained by the fact that the ED model is based on the fast chemistry approach where the reaction starts as the reactants come into contact. The area with the lowest velocity values around the central burner axis represents

the inner recirculation zone or vortex breakdown region. K-ϵ in Figure 16a presents higher velocity magnitude in the range d = 5–15 mm compared to k-ω in Figure 16b.

Figure 16c,d present the absolute velocity contour for FGM model also with k-ϵ and k-ω. K-ϵ model points out a similar behaviour for both combustion models ED and FGM. K-ω model underlines in FGM a wider main reaction zone located at higher axial distance (in the range between d = 10–25 mm) that is extended until the burner axis in Figure 16d. FGM with k-ω shows also the core of the vortical structure (C) located at higher axial distance from the burner exit compared to the other cases. It can be clearly observed that the simulations show a flow of type II according to the nomenclature of the International Flame Research Foundation with stabilization at the inner recirculation producing a V-shaped or M-shaped expansion of the flame with an angle of 45°. Figure 11 taken from the study of [19] also presents the different flow types observed in the combustor confined analysed in the current paper compared to an unconfined case. These results were obtained via Density Tagging Velocimetry (DVT) and show the difference in inner recirculation between the confined flame analysed in the current paper and the unconfined flame. We observe that the confined case has a stronger inner recirculation zone compared to the unconfined case. This type of flow has been already observed in Figure 12a, where the position of heat release underlines also an expansion of the flame with an angle of about 40°.

Both experiments and simulations show in the current confined case a type II of flow with stabilization at the inner recirculation.

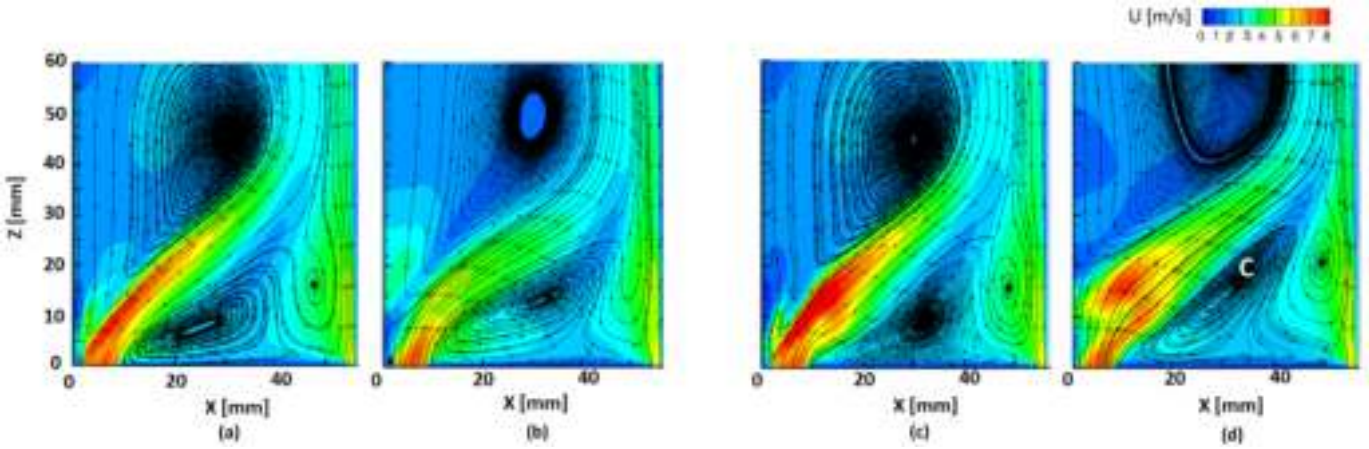

Figure 16. Velocity magnitude profile for combustion model ED with (**a**) RNG k-ϵ, (**b**) k-ω and FGM with (**c**) RNG k-ϵ and (**d**) k-ω.

7. Conclusions

The commercial CFD code ANSYS Fluent is used in this investigation to analyze a confined swirl stabilized combustor configuration. Several different turbulence and combustion models were compared, and the numerical outcomes were validated against available experimental data. The current study represents a follow-up work of the paper of Farisco et al. [12], where the same RANS numerical procedure was applied to a different unconfined combustor. In that case, no turbulence and combustion models were able to correctly predict the type of flow and stabilization mode of the flame, and the predicted temperature values were too high compared to the experiments.

In the present work, a better agreement was found. Steady and unsteady calculations were carried out with the aim to validate the combustion model's performances by examining temperature and heat release profiles. The ED model predicts the main reaction region to be closer to the burner's exit, and this is explained with the infinitely fast chemistry approach used as a basis of this combustion model. The same outcome is also confirmed by the results shown in [12] for the unconfined burner geometry.

The remarkable improvement compared to the previous analysis in [12] was found for the coupling of the combustion model FGM with the k-ω turbulence model that could conserve the swirl along the entire axial direction, resulting in an accurate approximation of the experimental values.

This RANS approach and especially the LES results demonstrated the most accurate agreement in terms of temperature and heat release profile shape with the experiments. The same RANS procedure applied to the previous similar but unconfined burner resulted in much higher temperature values, resulting in the conclusion that the solver is not able to correctly simulate a sufficient entrainment of fresh ambient air that cools down the combustion gases. Instead, in this study, both RANS and especially the transient simulations could predict the main combustion features for the the current confined combustor analyzed. In a follow-up study, an investigation will be performed in order to further decrease the effect of backward flow at the outlet of the combustion chamber in the simulations. For this reason, different boundary conditions at the combustor outlet will be tested next. Moreover, an acoustic analysis of the oscillations influencing the flame and the flow field should be performed with a more accurate method.

Author Contributions: Conceptualization, F.F., J.W., W.S. and L.C.; methodology, L.C., F.F., W.S. and J.W.; software, L.C. and F.F.; validation, F.F., L.C., W.S. and J.W.; formal analysis, L.C. and F.F.; investigation, L.C. and F.F.; resources, W.S.; data curation, F.F. and L.C.; writing—original draft preparation, F.F.; writing—review and editing, F.F., W.S., J.W. and L.C.; visualization, F.F., W.S., J.W. and L.C.; supervision, W.S. and J.W.; project administration, W.S., J.W. and F.F.; funding acquisition, J.W. All authors have read and agreed to the published version of the manuscript.

Funding: The project is a Lead-Agency D-A-CH project in cooperation between Graz University of Technology, Austria and Technische Universität Dresden, Germany, and was funded by the Austrian Science Fund FWF within Grant No. FWF-I2544-N30. Open Access Funding by the Austrian Science Fund (FWF).

Conflicts of Interest: The authors declare no conflict of interest. The funders had no role in the design of the study; in the collection, analyses or interpretation of data; in the writing of the manuscript; or in the decision to publish the results.

Abbreviations

The following abbreviations are used in this manuscript:

d	Flame length above burner exit (mm)
D	Burner exit diameter (mm)
f_D	Frequency shift of laser light (Hz)
U	Velocity magnitude (m/s)
u	Axial velocity component (m/s)
V	Tangential velocity component (m/s)
λ	Air/fuel ratio (-)
Φ	Equivalence ratio (-)
CFD	Computational Fluid Dynamics
DES	Detached Eddy Simulation
DLE	Dry-Low Emission
DO	Discrete Ordinates
ED	Eddy Dissipation
FGM	Flamelet Generated Manifold
FM-DGV	Frequency Modulated Doppler Global Velocimetry
IRZ	Inner Recirculation Zone
LES	Large Eddy Simulation
LIV	Laser Interferometric Vibrometry
ORZ	Outer Recirculation Zone
PDF	Probability Density Function
PIV	Particle Image Velocimetry

QUICK	Quadratic Upstream Interpolation for Convective Kinematics;
RANS	Reynolds-averaged Navier–Stoke
SAS	Scale Adaptive Simulation
SLF	Steady Laminar Flamelet

References

1. Lucca-Negro, O.; O'Doherty, T. Vortex breakdown: A review. *Prog. Energy Combust. Sci.* **2001**, *27*, 431–481. [CrossRef]
2. Huang, Y.; Yang, V. Dynamics and stability of lean-premixed swirl-stabilized combustion. *Prog. Energy Combust. Sci.* **2009**, *35*, 293–364. [CrossRef]
3. Schuermans, B.B.; Guethel, H.F.; Pennell, D.; Guyot, D.; Paschereit, D.O. Thermoacoustic modeling of a gas turbine using transfer functions measured under full engine pressure. *J. Eng. Gas Turbines Power* **2010**, *132*, 111503. [CrossRef]
4. Peterleithner, J.; Marn, A.; Woisetschläger, J. Interferometric investigation of the thermoacoustics in a swirl stabilized methane flame. In *Turbo Expo: Power for Land, Sea, and Air*; GT2015-42743; ASME Turbo Expo: Montreal, QC, Canada, 15–19 June 2015.
5. Sattelmayer, T.; Polifke, W. Assessment of methods for the computation of the linear stability of combustors. *Combust. Sci. Technol.* **2003**, *175*, 453–476. [CrossRef]
6. Lauer, M.R.W. Determination of the Heat Release Distribution in Turbulent Flames by Chemiluminescence Imaging. Ph.D. Thesis, University of Technology Munich, Munich, Germany, 2011.
7. Peterleithner, J.; Stadlmair, N.V.; Woisetschläger, J.; Sattelmayer, T. Analysis of measured flame transfer functions with locally resolved density fluctuation and OH-Chemiluminescence Data. *J. Eng. Gas Turbines Power* **2016**, *138*, 031504. [CrossRef]
8. Peterleithner, J.; Basso, R.; Heitmeir, F.; Woisetschläger, J.; Schlüssler, R.; Czarske, J.; Fischer, A. Comparison of flame transfer functions acquired by chemiluminescence and density fluctuation. In *Turbo Expo: Power for Land, Sea, and Air*; GT2016-57485; ASME Turbo Expo: Seoul, Korea, 13–17 June 2016.
9. Balachandran, R.; Ayoola, B.O.; Kaminski, C.; Dowling, A.P.; Mastorakos, E. Experimental investigation of the nonlinear response of turbulent premixed flames to imposed inlet velocity fluctuations. *Combust. Flame* **2005**, *143*, 37–55. [CrossRef]
10. Greiffenhagen, F.; Peterleithner, J.; Woisetschläger, J.; Fischer, A.; Gürtler, J.; Czarske, J. Discussion of laser interferometric vibrometry for the determination of heat release fluctuations in an unconfined swirl-stabilized flame. *Combust. Flame* **2018**, *201*, 315–327. [CrossRef]
11. Greiffenhagen, F.; Woisetschläger, J.; Gürtler, J.; Kuschmierz, R.; Czarske, J. Camera based full-field laser interferometric vibrometry for combustion diagnostics. In Proceedings of the 19th International Symposium on the Application of Laser and Imaging Techniques to Fluid Mechanics, Lisbon, Portugal, 16–19 July 2018.
12. Farisco, F.; Notsch, P.; Prieler, R.; Greiffenhagen, F.; Woisetschlaeger, J.; Heitmeir, F.; Hochenauer, C. Numerical investigation of a swirl stabilized methane fired burner and validation with experimental data. In *Turbo Expo: Power for Land, Sea, and Air*; GT2019-90452; ASME Turbo Expo: Phoenix, AZ, USA, 17–21 June 2019.
13. Abou-Taouk, A.; Whiddon, R.; Sigfrid, I.R.; Eriksson, L.E. CFD Investigation of Swirl-Stabilized Flexi-Fuel Burner using Methane-Air Mixture for Gas Turbines. In Proceedings of the Conference ISABE, Gothenburg, Sweden, 12–16 September 2011; pp. 2011–2122.
14. Hatziapostolou, A.; Orfanoudakis, N.G.; Koukou, M.K.; Raptis, G. CFD modeling of the swirl-stabilised flame produced by a laboratory-scale combustor. selection of the turbulence model. In Proceedings of the 4th WSEAS International Conference on Heat Transfer, Thermal Engineering and Environment, Elounda, Greece, 21–23 August 2006; pp. 83–88.
15. Van Oijen, J.A.; Donini, A.; Bastiaans, R.J.M.; ten Thije Boonkkamp, J.H.M.; de Goey, L.P.H. State-of-the-art in premixed combustion modeling using flamelet generated manifolds. *Prog. Energy Combust. Sci.* **2016**, *57*, 30–74. [CrossRef]
16. Puggelli, S.; Bertini, D.; Mazzei, L.; Andreini, A. Scale Adaptive Simulations of a swirl stabilized spray flame using Flamelet Generated Manifold. *Energy Procedia* **2016**, *101*, 1143–1150. [CrossRef]
17. Magnussen, B.F.; Hjertager, B.H. On Mathematical Modelling of Turbulent Combustion with Special Enphasis on Soot Formation and Combustion. In *Symposium (International) on Combustion*; Elsevier: Amsterdam, The Netherlands, 1977; Volume 16, pp. 719–729.
18. Peters, N. Laminar diffusion flamelet models in non-premixed turbulent combustion. *Prog. Energy Combust. Sci.* **1984**, *10*, 319–339. [CrossRef]
19. Greiffenhagen, J.; Woisetschläger, A.; Gürtler, J.; Czarske, J. Quantitative measurement of density fluctuations with a full-field laser interferometric vibrometer. *Exp. Fluids* **2020**, *61*, 1–15.
20. Candel, S.; Durox, D.; Schuller, T.; Bourgouin, J.; Moeck, J.P. Dynamics of swirling flames. *Annu. Rev. Fluid Mech.* **2014**, *46*, 147–173. [CrossRef]
21. Yiheng, T. Experimental and Numerical Investigations of Flames Stabilized by Swirl Flow and Bluff-Body: Flame Structures and Flame Instabilities. Ph.D. Thesis, Lund University, Lund, Sweden, October 2017.
22. Bompelly, R.K. Lean Blowout and Its Robust Sensing. Ph.D. Thesis, Georgia Institute of Technology, Atlanta, GA, USA, May 2013.
23. ANSYS. *Quick Guide to Setting Up LES-Type Simulations*; ANSYS FLUENT Version 1.4; Prepared and Compiled by Aleksey Gerasimov; ANSYS Sweden AB: Stockholm, Sweden, 2016.
24. ANSYS. *ANSYS FLUENT Theory Guide*; ANSYS FLUENT Release 14.5; ANSYS: Canonsburg, PA, USA, 2012.

25. Tanneberger, T.; Reichel, T.G.; Krüger, O.; Terhaar, S.; Paschereit, C.O. Numerical investigation of the flow field and mixing in a swirl-stabilized burner with a non-swirling axial jet. In *ASME Turbo Expo: Power for Land, Sea, and Air*; GT2015-43382; ASME Turbo Expo: Montreal, QC, Canada, 15–19 June 2015.
26. WestBrook, C.K.; Dryer, F.L. Simplified reaction mechanism for the oxidation of hydrocarbon fuels in flames. *Combust. Sci. Technol.* **1981**, *27*, 31–43. [CrossRef]
27. Smith, G.P.; Golden, D.M.; Frenklach, M.; Moriarty, N.W.; Eiteneer, B.; Goldenberg, M.C.; Bowman, T.; Hanson, R.K.; Song, S.; Gardiner, W.C.; et al. GRI-Mech. Available online: http://www.me.berkeley.edu/grimech/ (accessed on 20 January 2021).
28. Hardalupas, Y.; Orain, M. Local measurements of the time-dependent heat release rate and equivalence ratio using chemiluminescent emission from a flame. *Combust. Flame* **2004**, *139*, 188–207. [CrossRef]

International Journal of
Turbomachinery
Propulsion and Power

MDPI

Article

Transport of Swirling Entropy Waves through an Axial Turbine Stator †

Andrea Notaristefano and Paolo Gaetani *

Department of Energy, Politecnico di Milano, 20156 Milano, Italy; andrea.notaristefano@polimi.it
* Correspondence: paolo.gaetani@polimi.it
† This paper is an extended version of our contribution to the 14th European Turbomachinery Conference, Gdansk, Poland, 12–16 April 2021.

Abstract: The transport of entropy waves and their impact on the stage aerodynamics are still open questions. This paper shows the results of an experimental campaign that focuses on the swirling entropy waves advection through an axial turbine stator. The research aims at quantifying the aerodynamic impact of the swirling entropy waves on the first nozzle and characterizing their transport. The disturbance is generated by a novel entropy wave generator that ensures a wide set of different injection parameters. The device injects the disturbance axially, four different clocking positions are investigated. Measurements show a severe temperature attenuation of the swirling entropy wave at stator outlet. The high temperature location changes with the injection position as a result of the different interaction with the stator secondary flows. Depending on the injection position, the aerodynamic flow field is strongly perturbed by the injected swirl profile, instead the entropy wave effect is negligible.

Keywords: entropy wave; swirling entropy wave; combustor-turbine interaction; stator; high pressure turbine

check for updates

Citation: Notaristefano, A.; Gaetani, P. Transport of Swirling Entropy Waves through an Axial Turbine Stator. *Int. J. Turbomach. Propuls. Power* **2021**, *6*, 45. https://doi.org/10.3390/ijtpp6040045

Academic Editor: Marcello Manna

Received: 24 May 2021
Accepted: 19 November 2021
Published: 26 November 2021

Publisher's Note: MDPI stays neutral with regard to jurisdictional claims in published maps and institutional affiliations.

Copyright: © 2021 by the authors. Licensee MDPI, Basel, Switzerland. This article is an open access article distributed under the terms and conditions of the Creative Commons Attribution (CC BY-NC-ND) license (https://creativecommons.org/licenses/by-nc-nd/4.0/).

1. Introduction

Combustor-turbine interaction is a research topic that needs to be further addressed in order to understand all the phenomena there involved. In aero-engines, the strict requirements to minimize the fuel consumption ask for a complete knowledge of the flow physics to enhance the design, therefore the effects related to combustor-turbine interaction cannot be neglected. Modern lean-burn combustors are characterized by an unsteady heat release rate that, combined with a strong swirl motion, produces significant velocity and temperature non-uniformities [1,2]. The latter consists in temperature perturbations labeled as hot streak or entropy wave (EW), depending on whether they are steady or unsteady, respectively. The non-uniformities generated inside the combustion chamber are advected towards the turbine maintaining their intensity and strength, as [3,4] have shown in their investigations. The injection of the aforementioned disturbances in the 1st turbine stage produces significant problems that have to be accounted by turbine designers. First, the aerodynamic flow field is strongly affected by the swirl profile [5,6] and temperature disturbance [7]. A direct implication of the modified aerothermal field regards the blade heat transfer [6,8] that is significantly altered, thus, to design the blade cooling the combustor non-uniformities have to be considered. Finally, the acceleration of vorticity and temperature perturbation contributes to the production of indirect combustion noise [9], considered a significant source of engine noise [1,2].

Although there are several works that presented and discussed the effect of injecting swirl profile [10], hot-streak [11,12] and entropy waves [13,14], to authors knowledge there are no published experimental studies that combine the effects of a swirl profile and unsteady temperature perturbation (EW) in an annular turbine cascade. The only experimental campaign getting close to the present one has been carried out at Oxford university

and it is based on the combustor simulator developed in Adams et al. [15]: this campaign combines the generation of a swirl profile with a steady temperature perturbation [16]. According to Khanal et al. [17] computational study, a superimposition of the isolate cases considering either a swirl profile or a temperature perturbation leads to misleading results, hence they should be considered together, their effects being strongly non-linear.

In this work an experimental study of combustor-turbine interaction is carried out on the turbine test rig of Politecnico di Milano. The rig is equipped with a novel designed combustor simulator able to reproduce engine-representative turbine inlet conditions combining the generation of a swirl profile and EWs. The outlet conditions at the first stator is deeply analyzed and results shown. Steady aerodynamic measurements are carried out by a 5-hole pressure probe, whereas a fast response S-type micro-thermocouple is used to characterize the unsteady temperature field. The combustor simulator is moved azimuthally to inject the disturbance at four different stator relative positions, i.e., at leading edge, mid pitch, suction side and pressure side. Furthermore, the entropy wave is injected at two different frequencies, i.e., 10 and 110 Hz, chosen as the most representative. At these frequencies, the peak-to-mean flow temperature ratio is approximately 1.3 at 10 Hz and 1.08 at 110 Hz. These values are comparable with other works [3,18,19] where models have been developed to predict the EW dispersion. These authors agree that the higher the frequency, the higher is the EW dissipation caused by diffusion and dispersion inside the duct from the combustor to the turbine inlet. Therefore, an EW is expected to preserve a significant magnitude at turbine inlet only at low frequencies: 10 and 110 Hz seem to match the previous statement, as also showed in Notaristefano and Gaetani [20].

The geometry of the combustor simulator allows to carry out experiments injecting a swirl profile alone, while the isolation of the entropy wave is not possible. Therefore, the former case is also investigated. For a sake of comparison, the last case considered regards the uniform situation, where no swirl profile or entropy wave are injected.

After a brief description of the test rig and the EWG, the measuring techniques are introduced. The main features of the inlet disturbance are shown and finally the measurements at the stator outlet are discussed.

2. Materials and Methods

2.1. Test Rig and Entropy Wave Generator

The experimental campaign has been carried out on the high-speed closed-loop test rig at the Laboratory of Fluid Machines (Politecnico di Milano, Milano, Italy). A centrifugal compressor feeds the circuit allowing to set the mass flow rate and the turbine inlet conditions. Between the compressor and the turbine there is a cooler to control the turbine inlet flow conditions. The turbine is single stage, and it is representative of a high pressure turbine stage. Figure 1A shows a meridional view of the turbine test rig. The vane blades have a leaned geometry with a lean angle of 12°. Further details of the test rig operating principle can be found in Gaetani et al. [21].

The operating condition analyzed in this paper exploits an expansion ratio of 1.4 that means subsonic conditions throughout all the stage. The stator outlet Mach number at midspan is close to 0.6 with a Reynold number of 9×10^5 based on the stator chord; the average relative Mach number at rotor outlet is 0.45 with a Reynolds number of 5×10^5, based on rotor chord. The turbine aerodynamic in this condition is well known as a result of extensive previous studies [21]. The main operating conditions parameters and blade geometry are shown in Table 1.

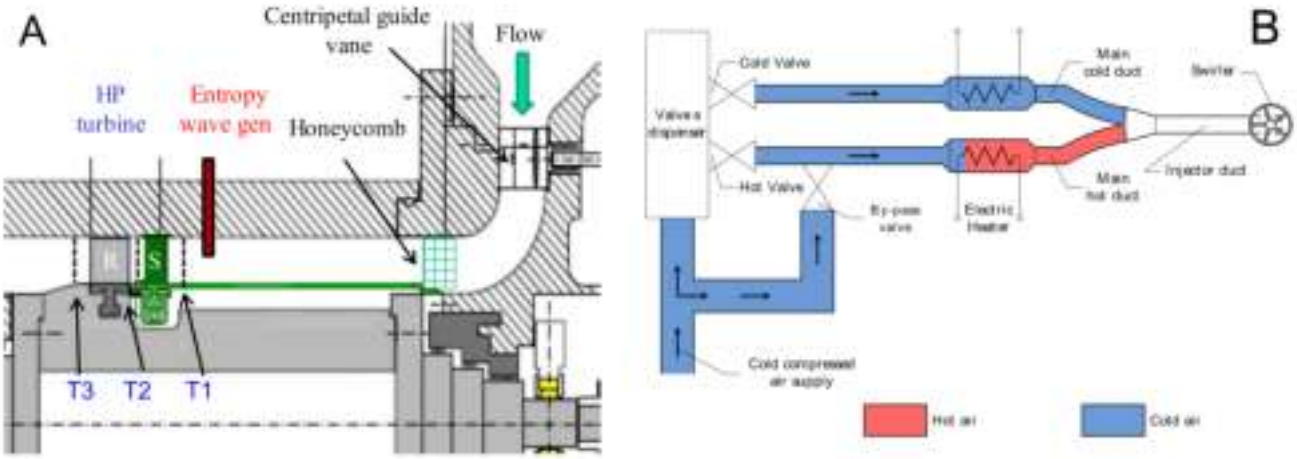

Figure 1. Turbine meridional view (**A**) and EWG layout (**B**).

Table 1. Turbine geometry and operating conditions.

Operating Condition	**β**	**n (rpm)**	**$\dot{m}$ (kg/s)**	**$T_{T,in}$(K)**
	1.4	7000	3.78	313
Geometry	**h (mm)**	**t_c/h**	**D_m (mm)**	**Gap/$C_{x,v}$**
	50	0.02	350	1.00
Blade rows	N_b	**σ**	**AR**	**Δθ**
Vane	22	1.20	0.83	75.2
Rotor	25	1.25	0.91	115.3

A combustor simulator, called entropy wave generator (EWG) and shown in Figure 1B, is placed upstream of the stator in order to carry out experiments aimed at characterizing the combustor-turbine interaction. The EWG injects an entropy wave (EW) in streamwise direction through a specifically designed injector. A swirler generator placed at the injector outlet produces a swirl profile that puts in rotation both the mainstream air and partially the EW. The working principle of the EWG is simple: two automotive valves feed alternatively two ducts, one of which has an electric heater to heat up the air passing through. The two ducts are then coupled in the injector head which injects the EW in the turbine. This novel EWG, extensively described in [20], allows to tune different parameters: the valves frequency that is the corresponding EW fluctuation frequency, the valves duty cycle, the feeding pressure and the heater power. For each frequency, the aforementioned parameters are set to guarantee the best EW penetration in the mainstream and the highest peak-to-trough temperature value.

Aerodynamic measurements are carried out using only three EWG for a sake of simplicity. Notwithstanding that the test rig can host eleven injectors, one out of two stator blades, the usage of three EWG requires to carry out measurements on the central one to satisfy the azimuthal periodicity. The EW is injected at blade midspan at four different circumferential positions with respect to the stator blade (Figure 2): mid-pitch, leading edge, pressure side and suction side. The outlet of the injector is 50 mm upstream the stator leading edge, as shown in Figure 2.

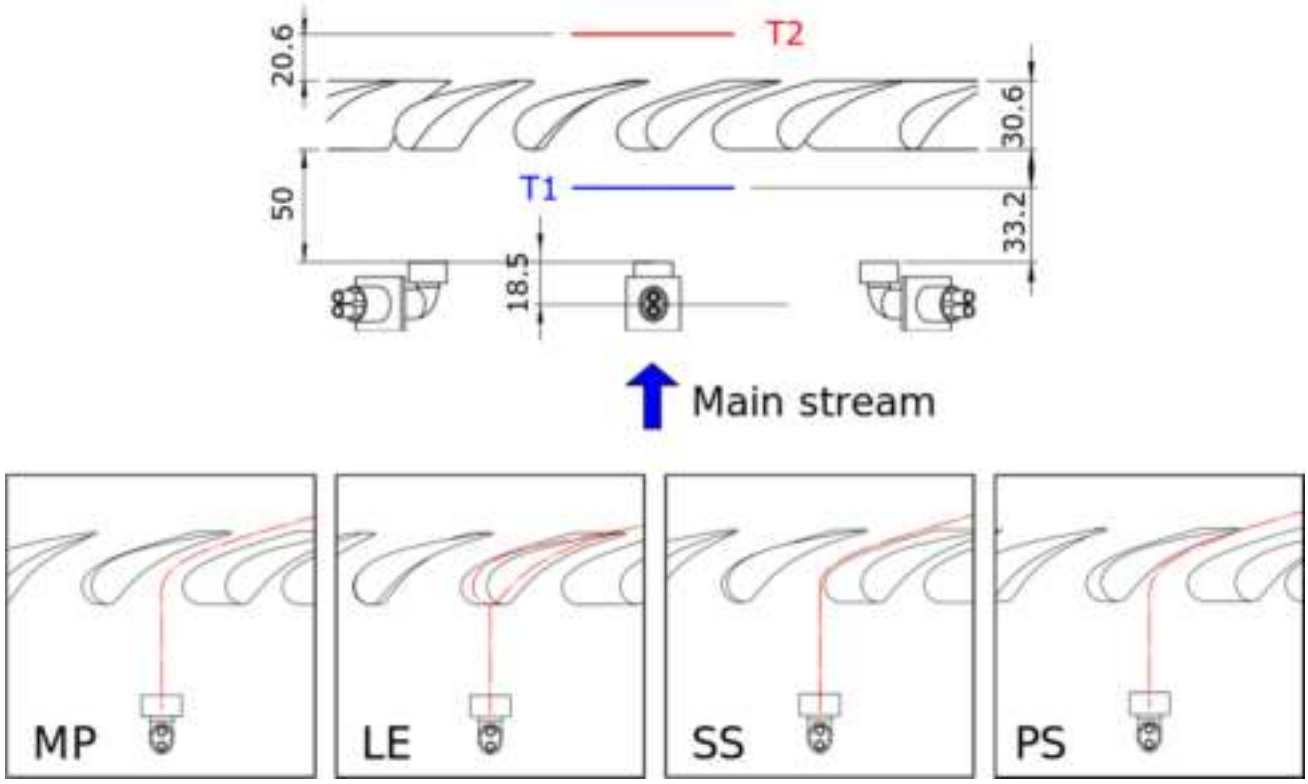

Figure 2. EWG set-up. Top: main geometrical distances. Bottom: injection positions.

2.2. Measuring Devices

This section is organized in two subsections: the first describes the measuring set-up of the turbine and EWG, the second introduces the probes that are used to characterize the flow field.

2.2.1. Turbine and EWG Set-Up

The turbine inlet total pressure is measured by a total pressure probe with head dimension of 0.5 mm and uncertainty 60 Pa. An inlet free stream turbulence intensity of 2.5% is measured by a hot wire probe. Inlet total temperature is measured by means of a K-type thermocouple. At the rotor outlet, T-type thermocouple gives the total temperature, a Kulite XT190 (Kulite, Leonia, NJ, USA) series pressure transducer measures the static pressure. A venturi tube gives information on the mass flow with an uncertainty of 1%.

The EWG is fully instrumented to measure its flow properties, necessary for control purposes. A T-type thermocouple measures the EWG supply air temperature and a Kulite XT190 pressure transducer (full scale 50 psi) the total pressure. A calibrated nozzle gives information on the mass flow rate given the pressure drop measured by a Kulite XT190 transducer (full scale 10 psi). The heater outlet temperature is measured by a K-type thermocouple: this value is used to control the power supply of the heater. In order to ensure that the heaters are switched off when no air is passing through, a Kulite XT190 (full scale 50 psi) measures the pressure difference between the heater inlet pressure and the turbine static pressure. A Kulite XT190 transducer (full scale 10 psi) measures the pressure in the cold duct to be used as trigger signal to phase-average the unsteady measurements. Pressure transducers have an uncertainty of 0.1% on the full scale, while thermocouples uncertainty is 0.2 K.

2.2.2. Flow Field Measurements

Several probes are used to characterize the flow quantities. These are mounted on a stepping motor that allows to measure at different spans, instead the stator and

EWG annulus are moved synchronously in circumferential direction to complete the traversing. The measuring grid covers two blade passages, that is about 32.5°, to have the full periodicity, being the combustor simulator pitch twice the stator one. Four different positions of the EWG with respect to the stator are analyzed (see Figure 2):

1. LE: aligned to the stator leading edge;
2. PS: at 1/3 of the pitch close to the pressure side;
3. MP: at mid pitch;
4. SS: at 1/3 of the pitch close to the suction side.

The traversing probes are positioned approximately at 67.3% stator axial chord downstream of the stator trailing edge. Unsteady temperature measurements are carried out by means of a fast response miniaturized S-type thermocouple with a junction size of 25.4 µm. The probe is calibrated in an oven and in a shock tube and exhibits a 1st order instrument response with a time constant of 2.4 ms. Temperature measurements are compensated applying the transfer function. The extended uncertainty of this probe is ±0.3 K.

The steady aero-dynamic flow field is measured by a 5-hole pressure probe that is able to reconstruct a 3D flow field. The probe has 1.4 mm head dimension and is calibrated in a reference nozzle in the range of 0.2 to 0.8 Mach numbers. On average the probe exhibits an uncertainty of 0.15° for the flow angles, 80 Pa for the total pressure and 40 Pa for the static pressure. A detailed analysis on the determination of these uncertainties can be found in [22].

3. Results and Discussion

3.1. Generated Disturbance

In this section the injected disturbance into the stator is characterized for the two frequencies of interest, 10 and 110 Hz. These are the lowest and highest, respectively, among the five frequencies tested and are chosen as representative. The complete assessment of the flow field downstream the EWG can be found in [20]. For each frequency, the best combination of feeding pressure, valves duty cycle and heater power can be set to maximize the EW penetration and the peak-to-trough temperature difference while keeping the same averaged momentum. The parameters outcoming the aforementioned maximization can be found in Table 2 for the two frequencies of interest. The first of the two numbers of the "Duty cycle" row refers to the hot period while the second refers to the cold injection time so that valves are modulated to have longer cold injection time than hot.

Table 2. EWG injection parameters.

Frequency (Hz)	10 Hz	110 Hz
Duty cycle	40–60	35–65
Feeding pressure (bar_G)	1.2	0.7
Heater power (W)	600	600

In addition to "10 Hz" and "110 Hz" cases, to better compare and analyze the results, other two cases are considered: the first ("EWG off") with the injector hosted, but the EWG switched off, i.e., only the swirl profile is injected; the second ("Clean") investigates the uniform condition when the injector is removed, thus no disturbance is generated.

Figure 3 shows the measured temperature disturbance produced by the EWG. The mean temperature contours (frames A and B) indicate that the mean temperature is similar for the two frequencies, but higher for the "110 Hz" case. Despite the EW is injected at mid-span, the swirled motion transports radially upward the temperature disturbance whose peak is found at 65% blade span, 8 mm over the mid span. If the frequency does not influence significantly the mean temperature, it dramatically changes the peak-to-trough temperature difference (frames C and D) due to the severe mixing process taking place at high frequency, as discussed in [20]. Overall, the local peak-to-trough temperatures are 70 K at 10 Hz and 25 K at 110 Hz. Peak-to-mean temperature ratio is approximately 1.30

at 10 Hz and 1.08 at 110 Hz and they are comparable with other combustor simulators documented in literature [3,18,19].

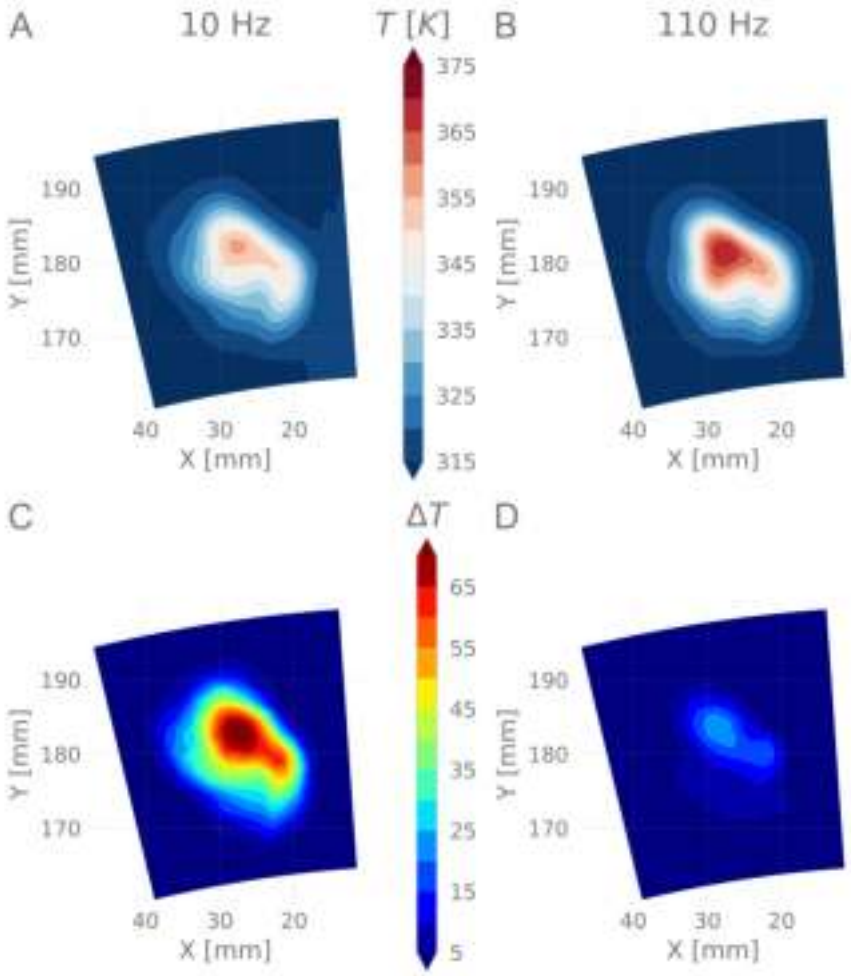

Figure 3. EWG generated disturbance assessment (Plane T1). Contour plots of: total temperature in frames (**A**,**B**); peak-to-trough temperature value in (**C**,**D**). (**A**,**C**) "10 Hz" case; (**B**,**D**) "110 Hz" case.

The aerodynamic flow field is shown in Figure 4, where the total pressure contours and the velocity vectors are shown for the cases "10 Hz", "EWG off" and "110 Hz". The velocity vectors highlight the generation of a well-defined vortex which has a central recirculation zone, typical of intense swirled flows [23]. The swirl number computed through the correlation showed in [24] is 0.6 that agrees with the calculations through experimental data. Furthermore, the generated vortex exhibits swirl angles of approximately $\pm 50°$. The two peaks of the total pressure have to be attributed to the hot and cold jets exiting the injector that do not completely mixed with the main flow. This conclusion comes from the comparison among "10 Hz" and "110 Hz" cases with "EWG off": when the EWG works, total pressure has higher values than when only the mainstream is swirled. Figure 4 results are consistent with Table 2: EW pressure is larger for the "10 Hz" case than "110 Hz". Furthermore, a comparison between EW injection cases and "EWG off" one highlights a stabilization and a reinforcement of the vortex. The stabilization is due to the axial injection that avoids, or at least reduces, the recirculation at vortex core. In addition to this, the injection of EWs increases the mass flow that is turned in the swirler generator, thus increasing its strength.

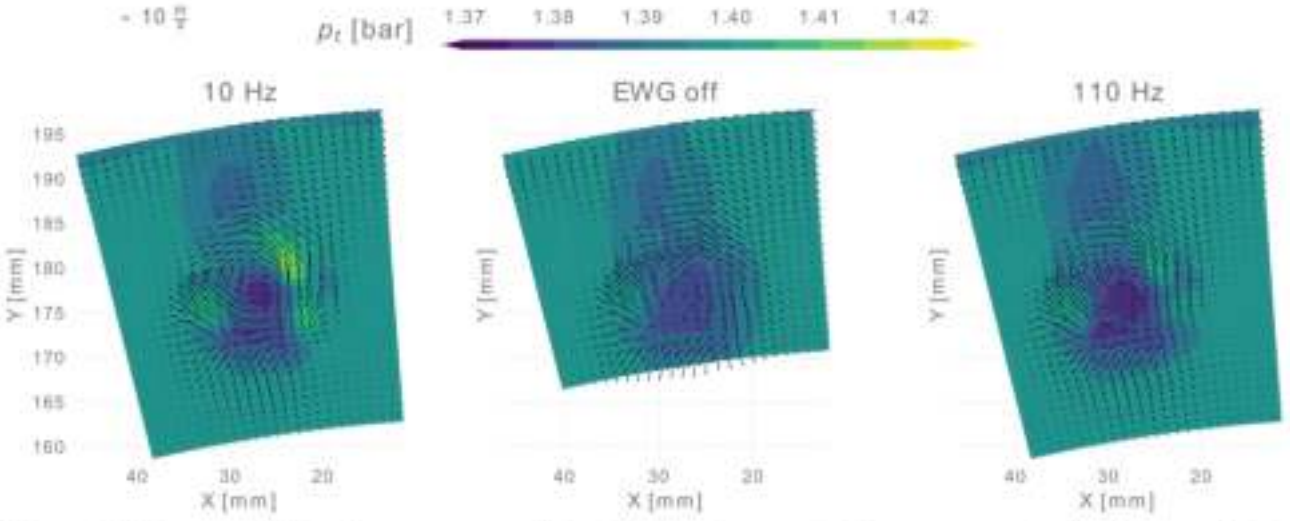

Figure 4. EWG generated disturbance assessment (Plane T1). Total pressure field as a contour and velocities magnitudes as vectors (viewed upstream the injector). From left to right: "10 Hz", "EWG off" and "110 Hz" cases.

Finally, an unavoidable drawback of the employed injector is the significant wake released by the stem. However, previous experimental campaigns in a wind tunnel have shown that the wake is completely reabsorbed at stator leading edge [20]. As such, the aforementioned flow features of the generated swirl make the generated vortex comparable to what documented in literature [16,17,25,26].

3.2. Downstream Stator Measurements

This section shows and discusses the flow field measurements downstream of the stator. The section is divided into subsections, each one showing the results obtained with a different probe. The goal is to study the EW advection and dissipation through the stator. Quantities are averaged on two stator pitches to preserve the full periodicity.

3.2.1. 5-Hole Pressure Probe

The 5-hole pressure measures the steady flow field exiting the stator. The measurements allow to calculate a total pressure loss coefficient defined as:

$$Y_{loss} = \frac{p_{t,U} - p_t}{p_t - p_s} \tag{1}$$

where p_t and p_s are the local total and static pressure measured by the 5-hole probe, respectively. $p_{t,U}$ is the average upstream turbine total pressure and it is the same for all the 4 cases, being measured upstream the EWG. Please consider that the total pressure loss across the EWG is negligible with respect to the total pressure level.

Figure 5 shows the circumferential mass average loss coefficient for the four stator clocking positions and the different injection cases. Particularly, the condition labeled as "Clean" refers to a uniform inlet flow field, whereas in the "EWG off" case the EWG is in place but the EW is not injected. Table 3 summarizes the results highlighting the mass average total pressure loss coefficient.

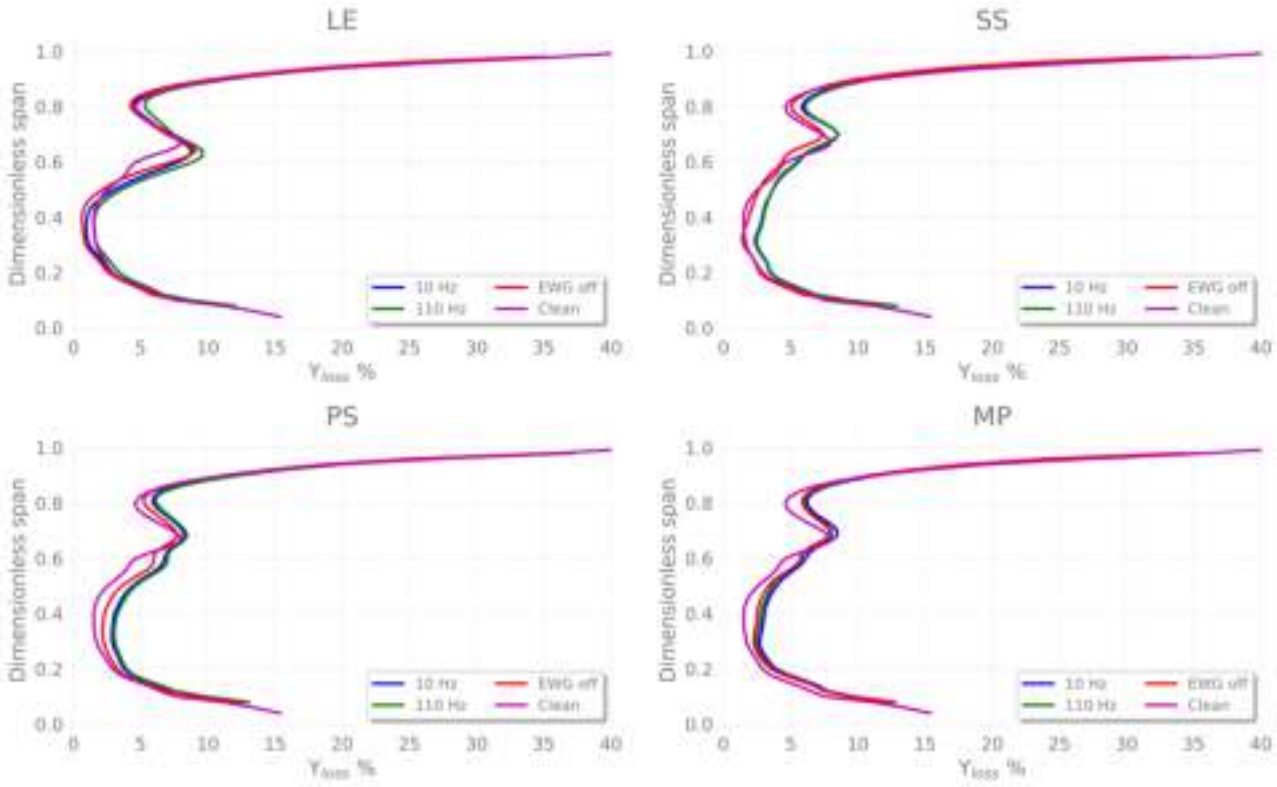

Figure 5. Circumferential mass average loss coefficient downstream of the stator (plane T2) at different injection positions. Measurements are carried out with EWG switched off ("EWG off"), injecting EW at 10 and 110 Hz ("10 Hz" and "110 Hz" respectively) and without the EWG in exploiting uniform inlet condition ("Clean").

In all the configurations, the regions close to the hub and tip do not change the loss intensity meaning that they are dominated by the casing boundary layers at tip and by the hub leakage at hub due to a slot in the trailing edge region: hence, the effect of the introduced perturbation is negligible. Instead, the impact on the central region is significant and changes for the different cases: the lowest losses are achieved with the "Clean" condition (see Table 3). The presence of the isolated swirler, i.e., case "EWG off", and the EW injection as well increase the losses and shift the peak in the central region. Generally speaking, in the midspan region the injected swirl has a positive incidence while it is negative close to the tip; moreover, the introduced swirl co-rotates with the tip passage vortex interacting with it and leading to an overall loss increase. The highest local losses magnitude is found at the LE injection position, whereas the clocking position PS has the widest region of high losses. Although the LE position has the highest peak, the loss profile in the other radial positions overlap with the "Clean" case, showing that EW and swirl profile have a small influence on the downstream stator aerodynamics. Considering that the case "EWG off" imposes only a swirl profile and that the cases "10 Hz" and "110 Hz" combine the swirl profile and the EW, the swirl profile is the biggest contribution to the losses. A proof of this trend can be obtained comparing the relative change between the cases "Clean" and "EWG off" with "EWG off" and the remaining others: the former is the largest, as also shown in Table 3, where the mass average values are shown. The last consideration on Figure 5 regards the effect of the frequency on the aerodynamic flow field: no clear trend can be evidenced comparing outcomes at 10 and 110 Hz. The differences among the perturbed injections cases are still an open question. In authors' opinion, they could be attributed to the pressure correction implemented on data to take into account of the plant drifts and not to some important flow feature: anyhow, the loss increase due to the inlet perturbation injection is unquestionable. Therefore, regardless the frequency, the EW impact on the downstream flow field is the same, as it will be also pointed out in the yaw angle analysis.

Table 3. Mass average total pressure loss coefficients.

Position	10 Hz	110 Hz	EWG off	Clean
MP	6.0	5.7	5.6	4.5
LE	5.0	5.7	4.7	
PS	6.1	6.3	5.4	
SS	5.6	5.7	4.7	

Figure 6 shows the spanwise profile of the azimuthal mass average yaw angle at stator outlet for passage aligned injections, i.e., MP, PS and SS and its difference with the clean case: this difference is supposed to be helpful in supporting the discussion.

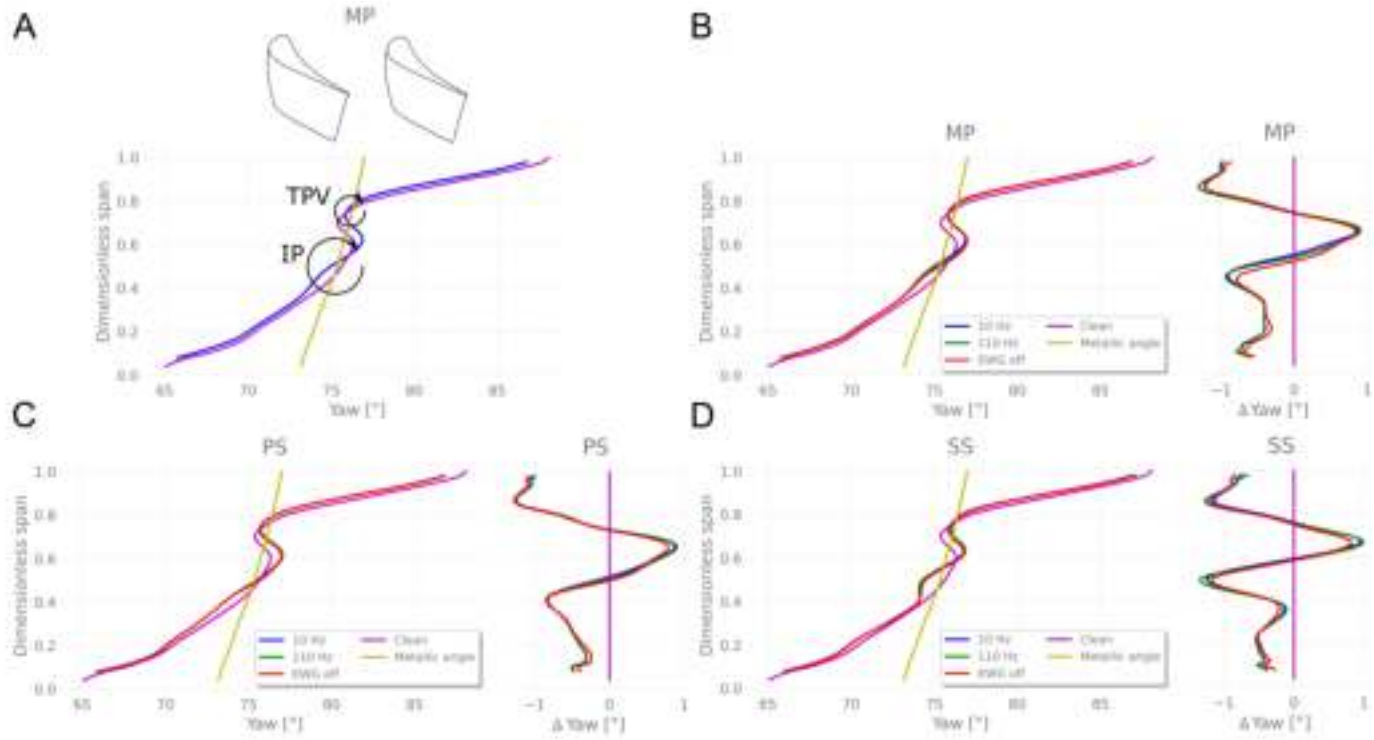

Figure 6. Circumferential mass average flow angle downstream of the stator (plane T2) at different passage aligned injecting positions (MP, PS and SS). Measurements are carried out with EWG switched off ("EWG off"), injecting EW at 10 and 110 Hz ("10 Hz" and "110 Hz" respectively) and without the EWG exploiting uniform inlet condition ("Clean"). Metallic angle line represents the geometric stator exiting angle. Frame (**A**): "Clean" and "10 Hz" cases comparison for MP. Frames (**B**–**D**): flow angle and its difference with respect to the "Clean" case for MP, PS and SS cases, respectively. Blade mirrored in frame A to ease the reading compared to flow angle.

In order to understand the yaw angle trend, a brief description of the "Clean" case, i.e., purple line, is helpful. The stator blade has a leaned geometry that produces an overturning at the tip and underturning at the hub. The overturning at the tip can be explained by the strong pressure gradient that is established between the blade pressure side and the suction side, as found in [27–29]. The lean geometry produces an accumulation of mass flow at the hub that makes the flow more axial, thus this effect produces the aforementioned underturning at the hub. Furthermore, this blade geometry shifts the tip passage vortex towards midspan.

The effect of the swirl profile injected upstream is appreciable at midspan where, for the passage aligned injections it interacts significantly with the secondary flows. The injected disturbance for these cases can be found around mid-span, as it will be shown in the vorticity discussion. To aid the comprehension of the flow physics, Figure 6A shows the MP case, comparing only "Clean" and "10 Hz" cases. The undisturbed injection, i.e.,

the purple line, shows an overturning at the tip and underturning at the hub as previously discussed. The tip passage vortex (TPV) is found at approximately 75% of the span and it is highlighted in Figure 6A. Its main effect is at 70% of the span where produces a significant underturning. When the swirl profile is injected (IP vortex in Figure 6A), it is against the bottom TPV branch reducing the underturning found in the "Clean" case; however, the IP produces an overturning and underturning at approximately 60% and 40% span, respectively, according to its turning direction. The core of the swirl profile results at midspan, confirming the previous statement.

Comparing Figure 6B,C profiles, the SS case shows a more confined effect around midspan while for the PS and MP cases the influence arrives till 20% of the span. In fact, in the SS case the lean geometry keeps the IP at its original injection radial position, thus confining its effect and reducing the interaction with the tip secondary flow. The three cases discussed up to now do not show significant differences in the steady aerodynamic flow field injecting or not EW at different frequencies.

The LE case shows a different trend (Figure 7): independently of the EW frequency, its injection produces differences with respect to the "EWG off" and "Clean" cases. The injected swirl impacting on the blade is weakened but kept confined and moves radially towards the tip, as found in Figure 8, due to a sort of climbing on the suction side blade surface. The swirl profile produces a more pronounced underturning at 60% span than the "Clean" condition, that is in agreement with swirl profile bottom branch (Figure 7A). The interaction between the swirl profile (climbed upward) and the tip passage vortex (pushed downward from the lean geometry) reduces the underturning at 70% span (Figure 7A). Although the two vortexes are corotating, their interaction reduces their impact: the swirl upper branch weakens the bottom tip passage vortex branch. Furthermore, the partial stagnation of the injected perturbation on the LE, thus its weakening, causes a more localized and weaker flow perturbation than passage aligned cases (MP, PS and SS). When the EW is injected (Figure 7B), the swirl profile mass flow increases, thus its intensity. Therefore, the impact discussed regarding Figure 7A is reduced in the case "EWG off", as highlighted in the ΔYaw plot (Figure 7B).

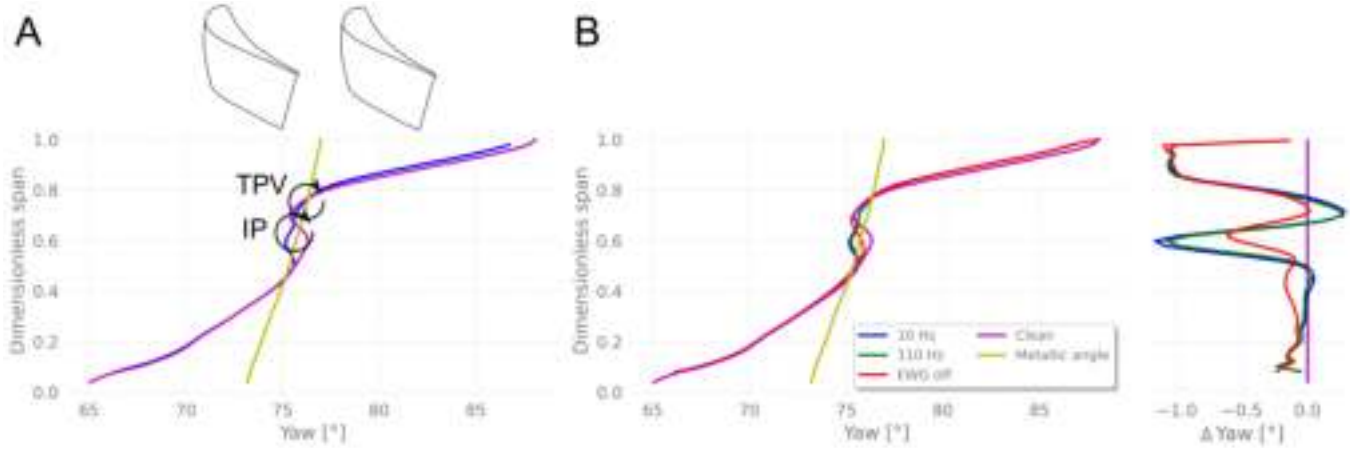

Figure 7. Circumferential mass average yaw angle downstream of the stator (Plane T2) at vane aligned position (LE). Measurements are carried out with EWG switched off ("EWG off"), injecting EW at 10 and 110 Hz ("10 Hz" and "110 Hz" respectively) and without the EWG exploiting uniform inlet condition("Clean"). Metallic angle line represents the geometric stator exiting angle. Frame (**A**): "Clean" and "10 Hz" cases. Frame (**B**): flow angle and its difference with respect to the "Clean" case. Blade mirrored in frame A to ease the reading compared to flow angle.

The vorticity field aids the comprehension of the previous results and discussions (Figure 8). The velocity vectors in Figure 8 are calculated as the projection of the flow velocity (measured by 5-hole probe) on a plane perpendicular to the local metallic angle. According to Persico et al. [30] they are not the secondary velocity vectors but provide a useful picture of the vorticity structures. The central frame shows the "Clean" case. The

description of the main vortical structures of the "Clean" condition allows to have a clear overview and aid the discussion of the cases with the injected perturbation (labeled as "IP" in Figure 8). By convention, the vorticity is positive when the vortical structures rotate clockwise. The main vorticity field is positive as a result of the leaned geometry [27]: it strengthens the hub passage vortex "HPV", while it weakens the tip passage vortex "TPV", being counter-rotating. The vorticity is positive on all the blade height meaning that the vortical structure produced by the lean geometry is stronger than the TPV, which has negative vorticity. In the hub region the lean vorticity strengthens the HPV generating a high vorticity region. The negative vorticity region that extends radially represents the wake vorticity: the viscous shear between the wake and the positive vorticity (generated by the lean) produces a negative vorticity. Leakage at the hub produces an important vortical structure (hub leakage vortex: HLV) that is negative and highlighted in Figure 8.

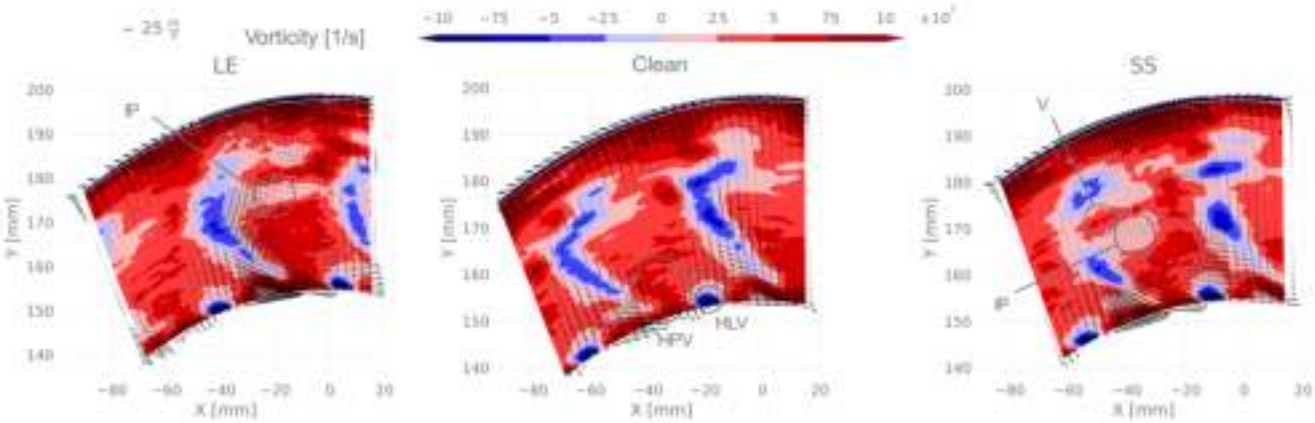

Figure 8. Vorticity contours at plane T2 for the cases "Clean", "LE 10 Hz" and "SS 10 Hz". Vectors represent the velocity magnitudes projected on a plane perpendicular to the stator geometrical discharge direction.

The left and right frames of Figure 8 show the LE and SS cases for an injection frequency of 10 Hz. Only this frequency is considered since previous outcomes showed that the EW frequency does not affect significantly the aerodynamic flow field, thus the vorticity pattern. Furthermore, the "EWG Off" case is very similar to the "10 Hz" case, confirming that the EW has negligible influence on the steady aerodynamic flow field. Considering that the aerodynamic flow field of SS, MP and PS cases is very similar, SS is shown as representative of the aforementioned three cases. A comparison between the two injection cases with the "Clean" one clearly evidences how significantly the swirling entropy wave affects the stator downstream vorticity. Given that the injected perturbation has a negative vorticity, as shown in Figure 9, in the LE case the EW interacts dramatically with the blade, hence with its wake, lowering the vorticity magnitudes. The experiments show that the injected perturbation remains on the blade suction side, thus interacting with its boundary layer. Furthermore, the injected perturbation is released at the trailing edge close to the wake: this causes a non-negligible reduction of the vorticity in the wake region. In fact, the wake at LE has the widest extension with respect to the other two cases shown.

In the SS case, the IP remains in the central region very close to the blade SS, as shown by the grey circle. The counter-rotating viscous structures, that result from the interaction of the swirling entropy wave and the mainstream, produce an increase in the vorticity field, i.e., the "V" region in Figure 9, around the EW core that affects also the wake.

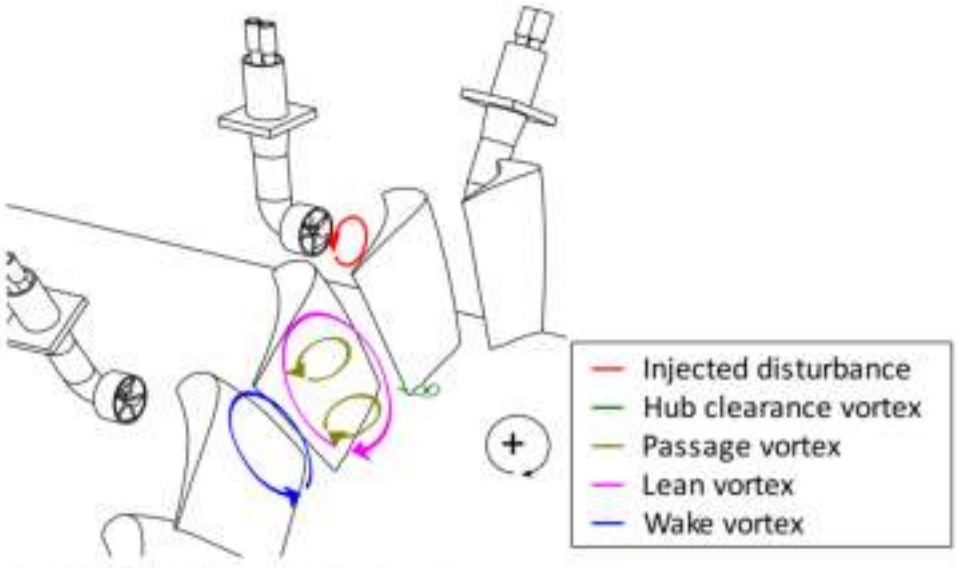

Figure 9. Vortical structures stator downstream.

3.2.2. Fast-Thermocouple

In this section the results of the fast-thermocouple are discussed. This experimental campaign aims at detecting the remaining magnitude of the injected EW downstream of the stator. Furthermore, the temperature field helps in investigating where the EW is released and which secondary structures it interacts with. Figure 10 shows the peak-to-trough temperature value for the different injection positions; each figure also shows the total pressure level as contour-lines.

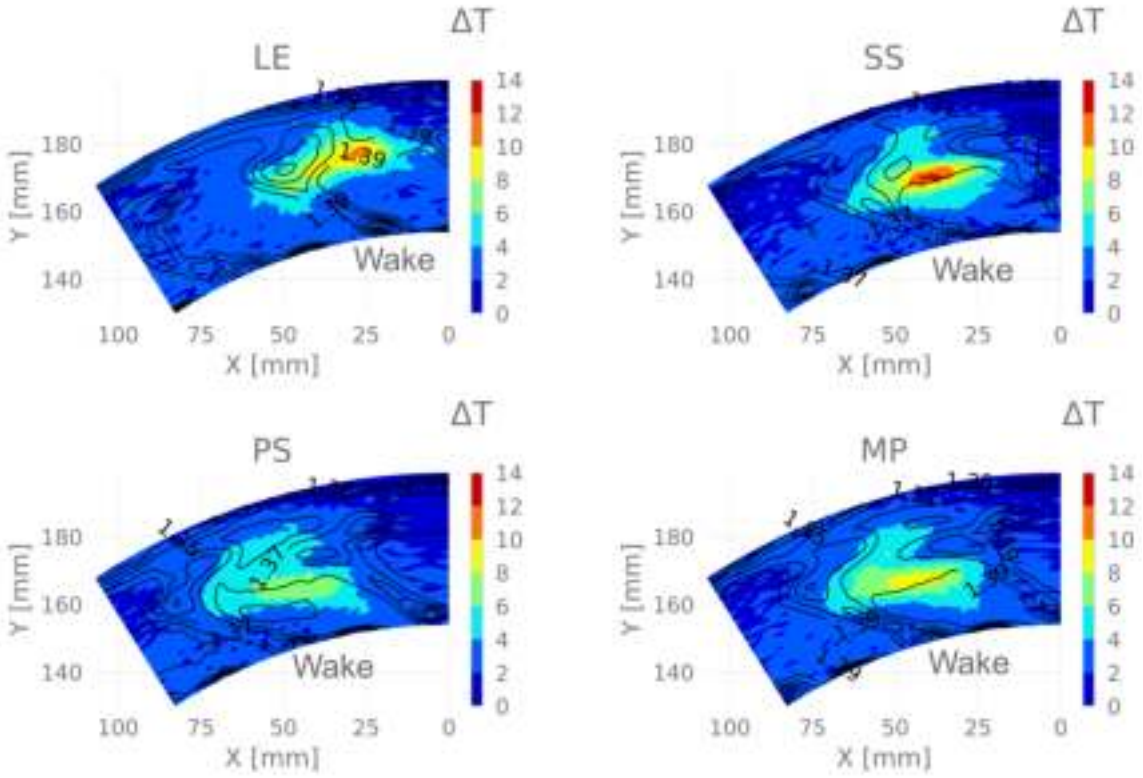

Figure 10. Peak-to-trough temperature contours at different injection positions at plane T2. The black line contour is the total pressure (bar_A).

In each position, the temperature perturbation is found mainly at the center of the blade passage that corresponds in the "Clean" case to the isentropic region. The differences regard the shape of the temperature disturbance that is differently stretched in radial and azimuthal direction depending on the injection position. The highest peak-to-trough temperature is found at the SS: the interaction between the injected EW and stator secondary flows is the lowest. In fact, the shape is also preserved, it is just stretched in radial direction due to its interaction with pressure field generated by the lean geometry. In the PS and MP cases, the temperature level is lower due to the mixing and spreading of the EW over the whole channel. Excluding the LE case, in all the others the EW is not entrained in the blade boundary layer, thus it does not affect significantly the wake temperature. In the LE case, the EW is injected on the blade LE and it interacts significantly with boundary layer so that at stator outlet the EW is partially inside the wake. Although the LE has a different shape, it shares with all the other cases a transport in azimuthal direction towards the pressure side. It can be justified by the interaction of the EW with the bottom branch of the tip passage vortex.

Khanal et al. [17] have found that in case of passage aligned injection the temperature disturbance is transported in the tip region, however in these experiments the injected EW in the passage region, i.e., cases MP, SS and PS, is found at mid span due to the lean blade geometry that pushes the mean flow towards the hub, compensating the aforementioned behavior. Furthermore, Khanal et al. [17] found that given a positive inlet swirl and a hot-streak injected vane aligned (corresponding to the LE case in the present work), it splits in two branches that move on the suction and pressure side respectively. The positive swirl transports the hot-streak on the pressure side towards the tip region, towards the hub on the suction surface. No evidence of this behavior is found in the present work. However, the injected EW is transported partially towards the tip, i.e., the core region, and partially towards the hub in the wake region.

A second comparison can be done with previous works on the same turbine performed at Politecnico di Milano where the injection of an isolated no-swirling EW disturbance discussed [13]. The two works have in common the EW transport towards the pressure side, independently on the injection position. However, in the SS case this transport was lower than what found in this work. The main difference regards the LE case: in their work, Gaetani and Persico [13] found that the EW injected on the LE spreads on the blade surface and mixed with the wake all along its span. These differences can be attributed to the imposed swirl profile that modifies significantly the EW interaction with the blade and secondary flows, as deeply discussed in previous section. As for the intensity, the SS case shows also in [13] the highest temperature level. A large difference is for the PS case where, in case of swirl, the magnitude is strongly weakened with respect to the purely axial no swirled EW injection.

4. Conclusions

This work has shown the strong impact on the flow field at the nozzle vane outlet injecting a combined swirl profile and entropy wave disturbance. Results strengthen the idea that, when designing the first stator blade, the perturbations generated in the combustion chamber cannot be neglected.

The effect on the downstream stator flow field is strongly affected by the injection position. When the disturbance is injected vane aligned (LE), it impinges on the blade vane causing a reduction of its vortical structure strength. Furthermore, the flow has a complex interaction with the secondary flows generating a lower under/overturning with respect to the "Clean" case; the temperature disturbance is strongly stretched in azimuthal direction. In the passage aligned cases (SS, MP, PS cases), the total pressure losses increase on 70% of the blade height, especially in the region between midspan and hub where the swirl profile produces a positive incidence that locally increases the loading, thus the strength of the secondary flows.

Generally, the temperature perturbation is found close to the pressure side of the passage where it is injected, regardless of the cases. This behavior can be attributed to the bottom branch of the tip passage vortex that pushes the injected temperature disturbance towards the pressure side. However, this interaction will require further investigation supported by CFD computations, especially for the LE case.

The comparison between the cases without the injector, with the injector placed but not fed, and the combined swirl profile and entropy wave injection have demonstrated that the aerodynamic steady flow field is mainly affected by the swirl profile, the temperature perturbation having negligible effects. This will be deeply investigated carrying out unsteady pressure measurements to analyze the effects of the temperature perturbation on the unsteady flow field downstream the stator. Furthermore, the EW frequency seems not to have an important effect, besides the attenuation of the injected peak-to-trough temperature difference.

Author Contributions: A.N. and P.G. contributed to the experimental campaign and the data reduction. A.N. gave the major contribution to the paper writing. All authors have read and agreed to the published version of the manuscript.

Funding: This research received no external funding.

Data Availability Statement: The datasets generated during the current study are available from the authors.

Acknowledgments: Authors want to thank Giorgio Scherini and Sofia Sagliocco for their help in the experimental campaigns.

Conflicts of Interest: The authors declare no conflict of interest.

References

1. Morgans, A.S.; Duran, I. Entropy noise: A review of theory, progress and challenges. *Int. J. Spray Combust.* **2016**, *8*, 285–298. [CrossRef]
2. Dowling, A.N.; Mahmoudi, Y. Combustion noise. *Proc. Combust. Inst.* **2015**, *35*, 65–100. [CrossRef]
3. Morgans, A.S.; Goh, C.S.; Dahan, J.A. The dissipation and shear dispersion of entropy waves in combustor thermoacoustic. *J. Fluid Mech.* **2013**, *733*, R2. [CrossRef]
4. Sattelmayer, T. Influence of the combustor aerodynamics on combustion instabilities from equivalence ratio fluctuations. *J. Eng. Gas Turb. Power* **2003**, *125*, 11–19. [CrossRef]
5. Beard, P.F.; Smith, A.; Povey, T. Impact of severe temperature distortion on turbine efficiency. *J. Turbomach.* **2013**, *135*, 011018. [CrossRef]
6. Jacobi, S.; Mazzoni, C.; Chana, K.; Rosic, B. Investigation of unsteady flow phenomena in first vane caused by combustor flow with swirl. *J. Turbomach.* **2017**, *139*, 041006. [CrossRef]
7. Beard, P.F.; Smith, A.; Povey, T. Effect of combustor swirl on transonic high pressure turbine efficiency. *J. Turbomach.* **2014**, *136*, 011002. [CrossRef]
8. Gundy-Burlet, K.L.; Dorney, D.J. Influence of 3D Hot Streak on Turbine Heat Transfer. *Int. J. Turbo Jet Eng.* **1997**, *14*, 123–131.
9. Cumpsty, N.A.; Marble, F.E. The interaction of entropy fluctuations with turbine blade rows; A mechanism of turbojet engine noise. *Proc. R. Soc. Lond.* **1997**, *357*, 323–344.
10. Qureshi, I.; Smith, A.D.; Povey, T. HP Vane Aerodynamics and Heat Transfer in the Presence of Aggressive Inlet Swirl. *J. Turbomach.* **2013**, *135*, 021040. [CrossRef]
11. Butler, T.L.; Sharma, O.P.; Joslyn, H.D.; Dring, R.P. Redistribution of an Inlet Temperature Distortion in an Axial Flow Turbine Stage. *J. Propuls. Power* **1989**, *5*, 64–71. [CrossRef]
12. Basol, A.M.; Jenny, P.; Ibrahim, M.; Kalfas, A.I.; Abhari, R.S. Hot Streak Migration in a Turbine Stage: Integrated Design to Improve Aerothermal Performance. *J. Eng. Gas Turb. Power* **2011**, *133*, 061901. [CrossRef]
13. Gaetani, P.; Persico, G. Transport of Entropy Waves Within a High Pressure Turbine Stage. *J. Turbomach.* **2019**, *141*, 031006. [CrossRef]
14. Pinelli, L.; Marconcini, M.; Pacciani, R.; Gaetani, P.; Persico, G. Computational and Experimental Study of the Unsteady Convection of Entropy Waves Within a High Pressure Turbine Stage. *J. Turbomach.* **2021**, *143*, 091011. [CrossRef]
15. Adams, M.G.; Povey, T.; Hall, B.F.; Cardwell, D.N.; Chana, K.S.; Beard, P.F. Commissioning of a combined hot-streak and swirl profile generator in a transonic turbine test facility. *J. Eng. Gas Turb. Power* **2020**, *142*, 031008. [CrossRef]
16. Adams, M.G.; Beard, P.F.; Stokes, M.R.; Wallin, F.; Chana, K.S.; Povey, T. Effect of a Combined Hot-Streak and Swirl Profile on Cooled 1.5-Stage Turbine Aerodynamics: An Experimental and Computational Study. *J. Turbomach.* **2021**, *143*, 021011. [CrossRef]

17. Khanal, B.; He, L.; Northall, J.; Adami, P. Analysis of Radial Migration of Hot-Streak in Swirling Flow Through High-Pressure Turbine Stage. *J. Turbomach.* **2013**, *135*, 041005. [CrossRef]
18. Giusti, A.; Worth, N.A.; Mastorakos, E.; Dowling, A.P. Experimental and Numerical Investigation into the Propagation of Entropy Waves. *AIAA J.* **2017**, *55*, 446–458. [CrossRef]
19. Christodoulou, L.; Karimi, N.; Cammarano, A.; Paul, M.; Navarro-Martinez, S. State prediction of an entropy wave advecting through a turbulent channel flow. *J. Fluid Mech.* **2020**, *882*, A8. [CrossRef]
20. Notaristefano, A.; Gaetani, P. Design and commissioning of a Combustor Simulator combining Swirl and Entropy Wave generation. *Int. J. Turbomach. Propuls Power* **2020**, *5*, 27. [CrossRef]
21. Gaetani, P.; Persico, G.; Spinelli, A. Coupled effect of expansion ratio and blade loading on the aerodynamics of a high-pressure gas turbine. *Appl. Sci.* **2017**, *7*, 259. [CrossRef]
22. Notaristefano, A.; Gaetani, P.; Dossena, V.; Fusetti, A. Uncertainty evaluation on multi-hole aerodynamic pressure probes. *J. Turbomach.* **2021**, *143*, 091001. [CrossRef]
23. Ruith, M.R.; Chen, P.; Meiburg, E.; Maxworthy, T. Three-dimensional vortex breakdown in swirling jets and wakes: Direct numerical simulation. *J. Fluid Mech.* **2003**, *486*, 331–378. [CrossRef]
24. Gupta, A.K.; Lilley, D.G.; Syred, N. *Swirl Flows*; Energy and Engineering Science Series; Abacus Press: Kent, UK, 1985.
25. Andreini, A.; Bacci, T.; Insinna, M.; Mazzei, L.; Salvadori, S. Hybrid RANS-LES modeling of the aerothermal field in an annular hot streak generator for the study of combustor—Turbine interaction. *J. Eng. Gas Turb. Power* **2016**, *139*, 021508. [CrossRef]
26. Werschnik, H.; Schneider, M.; Herrmann, J.; Ivanov, D.; Schiffer, H.P.; Lyko, C. The influence of combustor swirl on pressure losses and the propagation of coolant flows at the Large Scale Turbine Rig (LSTR): Experimental and numerical investigation. *Int. J. Turbomach. Propuls. Power* **2017**, *2*, 12. [CrossRef]
27. D'Ippolito, G.; Dossena, V.; Mora, A. The Influence of Blade Lean on Straight and Annular Turbine Cascade Flow Field. *J. Turbomach.* **2011**, *133*, 011013. [CrossRef]
28. Harrison, S. The Influence of Blade Lean on Turbine Losses. *J. Turbomach.* **1992**, *114*, 184–190. [CrossRef]
29. Denton, J.D.; Xu, L. The exploitation of three-dimensional flow in turbomachinery design. *Proc. Inst. Mech. Eng. Part C J. Mec.* **1999**, *213*, 125–137. [CrossRef]
30. Persico, G.; Gaetani, P.; Dossena, V.; D'Ippolito, G.; Osnaghi, C. On the definition of the secondary flow in three-dimensional cascades. *Proc. Inst. Mech. Eng. Part A J. Power Energy* **2003**, *223*, 667–676. [CrossRef]

International Journal of
Turbomachinery Propulsion and Power

MDPI

Article

Data Driven Modal Decomposition of the Wake behind an NREL-5MW Wind Turbine †

Stefania Cherubini [1,*], Giovanni De Cillis [1,*,‡], Onofrio Semeraro [2], Stefano Leonardi [3] and Pietro De Palma [1]

[1] Dipartimento di Meccanica, Matematica e Management, Politecnico di Bari, 70126 Bari, Italy; pietro.depalma@poliba.it
[2] Laboratoire iNterdisciplinaire des Sciences du Numerique, CNRS, Université de Paris-Saclay, 91405 Orsay, France; semeraro@limsi.fr
[3] Department of Mechanical Engineering, University of Texas at Dallas, Dallas, TX 75080, USA; Stefano.Leonardi@utdallas.edu
* Correspondence: stefania.cherubini@poliba.it (S.C.); giovanni.decillis@poliba.it (G.D.C.)
† This paper is an extended version of our contribution to the 14th European Turbomachinery Conference, Gdansk, Poland, 12–16 April 2021.
‡ Current address: Euro-Mediterranean Center on Climate Change Foundation, Ocean Predictions and Applications Division, 73100 Lecce, Italy.

Abstract: The wake produced by a utility-scale wind turbine invested by a laminar, uniform inflow is analyzed by means of two different modal decompositions, the proper orthogonal decomposition (POD) and the dynamic mode decomposition (DMD), in its sparsity-promoting variant. The turbine considered is the NREL-5MW at tip-speed ratio $\lambda = 7$ and a diameter-based Reynolds number of the order 10^8. The flow is simulated through large eddy simulation, where the forces exerted by the blades are modeled using the actuator line method, whereas tower and nacelle are modeled employing the immersed boundary method. The main flow structures identified by both modal decompositions are compared and some differences emerge that can be of great importance for the formulation of a reduced-order model. In particular, a high-frequency mode directly related to the tip vortices is found using both methods, but it is ranked differently. The other dominant modes are composed by large-scale low-frequency structures, but with different frequency content and spatial structure. The most energetic 200 POD modes account for ≈20% only of the flow kinetic energy. While using the same number of DMD modes, it is possible to reconstruct the flow field to within 80% accuracy. Despite the similarities between the set of modes, the comparison between these modal-decomposition techniques points out that an energy-based criterion such as that used in the POD may not be suitable for formulating a reduced-order model of wind turbine wakes, while the sparsity-promoting DMD appears able to perform well in reconstructing the flow field with only a few modes.

Keywords: modal decomposition; NREL-5MW wind turbine; wind turbine wake; coherent structures

check for updates

Citation: Cherubini, S.; De Cillis, G.; Semeraro, O.; Leonardi, S.; De Palma, P. Data Driven Modal Decomposition of the Wake behind an NREL-5MW Wind Turbine. *Int. J. Turbomach. Propuls. Power* **2021**, *6*, 44. https://doi.org/10.3390/ijtpp6040044

Academic Editor: Marcello Manna

Received: 2 August 2021
Accepted: 19 November 2021
Published: 25 November 2021

Publisher's Note: MDPI stays neutral with regard to jurisdictional claims in published maps and institutional affiliations.

Copyright: © 2021 by the authors. Licensee MDPI, Basel, Switzerland. This article is an open access article distributed under the terms and conditions of the Creative Commons Attribution (CC BY-NC-ND) license (https://creativecommons.org/licenses/by-nc-nd/4.0/).

1. Introduction

Low-dimensional models based on modal decomposition of complex flows are often sought in many different fields and among those in wind energy. The orthogonality of the resulting modes makes the proper orthogonal decomposition (POD) the commonly chosen basis for the formulation of a reduced-order model (ROM). In the wind-energy field, POD was at first applied to two-dimensional data. Andersen et al. [1] applied this modal decomposition to planes perpendicular to the streamwise direction of large eddy simulations (LES) of the flow impinging on an infinite series of rows of wind turbines, each one consisting of three turbines modeled by the actuator line technique. Bastine et al. [2] applied two-dimensional POD to the case of a single wind turbine, impinged by a turbulent neutrally stratified atmospheric boundary layer. POD analysis was then applied to three-dimensional flow fields behind a wind turbine array by VerHulst and Meneveau [3], both

in the presence and in the absence of atmospheric turbulence. Hamilton et al. [4,5] used POD applied to velocity measurements for investigating wake interaction and recovery dynamics in different wind turbine array configurations. More recently, Hamilton et al. [6] applied POD to LES data in order to construct a ROM of turbine wakes using polynomial reconstruction based on POD modes. Among others, Fortes-Plaza et al. [7] developed a ROM based on POD of LES data of yaw-controlled wake-interacting wind turbines. Very recently, De Cillis et al. [8] used POD analysis of LES of the flow behind a model wind turbine to determine the effect of the tower and nacelle on the development of coherent structures linked to given instability mechanisms within the flow.

POD is extensively used in the analysis of complex flow fields as it provides a finite set of orthogonal modes whose linear combination optimally reconstructs the energy of a set of stochastic flow data. However, in some particular cases, the most energetic POD modes may not be dynamically relevant; therefore, the selection of a low-dimensional basis for the realization of a reduced-order model may be not trivial [9]. In fact, POD ranks the modes depending on their energy, where the most energetic modes are often characterized by large-scale coherent structures which, in some cases, may not be the most dynamically relevant. Moreover, POD modes represent statistically steady structures, thus being unable to describe transient states which might arise from the interaction of the flow field with environmental disturbances, such as atmospheric turbulence. Finally, POD modes have a non-trivial temporal evolution, being composed by several temporal wavenumbers, while in some cases it can be interesting to capture structures characterized by a given frequency that can be more easily associated with well-defined physical processes (for instance, the wake meandering) or instabilities.

Another data-driven modal-decomposition technique that has all these capabilities and gained popularity in the last ten years is the dynamic mode decomposition (DMD), introduced by Schmid [10]. This technique finds eigenvalues and eigenvectors of a linear operator approximating the nonlinear dynamics embedded in the data sequence and it has been recently exploited for the formulation of ROMs of wind turbine relevant flows. Iungo et al. [11] realized a reduced-order model of wind turbine wakes based on the dynamic mode decomposition of LES flow data of wind turbines operating under different operational regimes. Le Clainche et al. [12] used the dynamic mode decomposition of LIDAR measurements to build a reduced-order model of the wind velocity upstream of a horizontal axis wind turbine. DMD modes are usually ranked according to their amplitude at the first snapshot of the data sequence. Such a criterion for the selection of a limited subset of dynamic modes can lead to poor quality of approximation of numerically generated snapshots and, therefore, to poor predictive capability of low-dimensional models. For this reason, different variants of the standard algorithm, aiming at extracting a limited subset of flow features that optimally approximate the original data sequence, have been developed, i.e., the optimized [13] or the sparsity-promoting DMD [14]. In the present work we use, for the first time in wind turbine wakes characterization, the sparsity-promoting (SP) algorithm for ranking the most relevant DMD modes.

The novelty of the current work is, therefore, to provide a direct comparison of the dominant POD and SP-DMD modes in the wake of a wind turbine, discussing possible reasons for their similarities and discrepancies and their potential relevance for the development of ROMs. As discussed before, POD is well fitted for flows whose coherent structures are to be ranked in terms of their energy content. However, in some cases the energy content of the coherent structures is not a well-fitted criterion to accurately describe the dynamical behaviour of the flow, which can be better modeled using a decomposition ranking the temporal dominant frequencies in terms of amplitude, such as DMD. In the literature, a few examples of comparative analyses of the performance of these two modal decompositions for different flows can be found. Reference [15] presents a comparative analysis of the POD and DMD modes extracted from experimental measurements of a turbulent jet flow. In this particular flow case, the modes arising from the different decompositions bear many similarities and the main physical instabilities are easily identified

using both methods. In Reference [16], both modal decompositions are used to study the complex turbulent flow around a wall-mounted finite cylinder at high Reynolds number. Both methods were able to capture dominant phenomena, mostly characterized by large energy content. However, POD was found to not clearly separate frequencies and scales, while DMD yielded the most relevant physical phenomena, with distinct frequencies and growth rates. In Reference [17], the most dominant flow structures of a simulated flow in the wake of a high-speed train model were extracted using both POD and DMD. Comparison between the modes from the two different decomposition methods shows that the second and third POD modes correspond to the same flow structure as the second DMD mode. More recently, the performance of these two methods have been compared for several flows [18], finding relevant differences depending on the selected flow case. In general, it was found that POD is able to correctly reproduce time-localized events, but produces a severe spectral mixing between different modes. Contrariwise, DMD allows for proper frequency identification but may yield poor convergence and redundancy in the spatial structures [18]. However, this comparison has never been assessed directly for the case of the flow behind a utility-scale wind turbine at realistic Reynolds number. This type of flow is characterized by coherent structures at different scales, where the largest, most energetic scales are not deemed to be the most dynamically relevant. Moreover, the interaction of the rotating tip vortices generated by the blades with the non-rotating ones, originated by the tower and the nacelle, might potentially lead to transient events within the flow that might not be accurately described by the statistically steady POD modes. Finally, DMD analysis might be better suited to describe typical phenomena at given frequencies, such as the wake meandering [19].

The present study is motivated by the need to clarify the connection and differences between DMD and POD modes, as well as their physical meaning and performance in reconstructing the flow field, for the flow behind a utility-scale wind turbine. In the present paper, we identify the most relevant coherent structures embedded in the turbulent wake flow developing downstream of the NREL-5MW wind turbine, using the two mentioned modal decompositions, addressing convergence, selection and physical interpretation of both POD and DMD modes. The flow is computed through large eddy simulation using the actuator line method to simulate the rotor and the immersed boundary method to simulate tower and nacelle. Coherent structures are isolated by means of the POD and the sparsity-promoting DMD. The results obtained with the two modal-decomposition techniques are compared and differences are highlighted, particularly in regard to a low-order representation of the wake. In conclusion, the DMD modes selected by the sparsity-promoting algorithm are found to be similar to the most energetic POD modes, but strong differences are found in their capability of reconstructing the flow field.

2. Methodology

The present study is based on the numerical simulation of the flow over a wind turbine using the LES approach. The large-scale structures of the flow are directly computed integrating the filtered Navier–Stokes equations, whereas the effect of smaller-scale structures on the resolved ones is modeled [20]. The governing equations for the filtered non-dimensional velocity, $\boldsymbol{u}= (u, v, w)^T$, and pressure, p, derived from the Navier–Stokes equations for incompressible flows read as follows:

$$\frac{\partial u_i}{\partial t} + \frac{\partial u_i u_j}{\partial x_j} = -\frac{\partial p}{\partial x_i} + \frac{1}{Re}\frac{\partial^2 u_i}{\partial x_j \partial x_j} - \frac{\partial \tau_{ij}}{\partial x_j} + f_i, \tag{1}$$

$$\frac{\partial u_i}{\partial x_i} = 0, \tag{2}$$

where the subscripts $i, j \in \{1, 2, 3\}$ indicate the streamwise, x, vertical, y, and transverse, z, directions, respectively, and $Re = U_\infty D/\nu$ is the Reynolds number, defined using the inlet velocity U_∞, the rotor diameter D and the kinematic viscosity of the fluid ν. Throughout the paper, upper-case (respectively, lower-case) notation denotes dimensional (respectively,

non-dimensional) variables. The subgrid-scale stress tensor, τ_{ij}, is modeled using the Smagorinsky model with constant C_S set to 0.17, about equal to the theoretical value typically used for LES.

Equations (1) and (2) are discretized using a finite difference scheme based on second-order centered discretization on a staggered Cartesian grid. Time integration is performed using a hybrid low-storage third-order accurate Runge–Kutta scheme [21]. The term f_i in Equation (1) accounts for the aerodynamic forces per unit volume exerted by the turbine blades on the fluid via the actuator line method [22]. These forces are modeled making use of the lift and drag coefficients of the rotor blades, which are treated as rotating rigid lines divided into discrete segments. In each segment, given the angle of attack and the relative inflow velocity, the lift and drag forces per unit length are estimated and then spread on areas perpendicular to each segment using a Gaussian distribution kernel. The tower and nacelle are taken into account by using the immersed boundary method, which avoids the use of a body-fitted grid, reducing the computational cost of the simulations. In particular, the approach proposed in Reference [23] has been used.

2.1. Proper Orthogonal Decomposition

The proper orthogonal decomposition (POD) is a statistical numerical technique able to identify the most energetic coherent structures characterizing the flow. The method is based on the eigendecomposition of the two-point spatial correlation tensor C, where the eigenvectors represent the POD modes and the associated eigenvalues represent their energy. A discrete approximation of the tensor C can be obtained from data consisting of a large number M of snapshots of the flow field. The entire dataset is usually organized into a single matrix $\mathbf{Q} \in \mathbb{R}^{N \times M}$, in which each column is a single instantaneous velocity field, represented by N scalars. The two-point correlation tensor can be approximated by the matrix $\mathbf{C} \in \mathbb{R}^{N \times N}$, computed as follow:

$$\mathbf{C} = \frac{1}{M}\mathbf{Q}\mathbf{Q}^T. \tag{3}$$

The eigendecomposition of $\mathbf{C}$ can be easily performed by computing the singular value decomposition of the snapshot matrix $\mathbf{Q}$, divided by the square root of the number of snapshots M,

$$\frac{\mathbf{Q}}{\sqrt{M}} = \mathbf{U}\mathbf{S}\mathbf{V}^T, \tag{4}$$

where the columns $\boldsymbol{u}_k$ of the matrix $\mathbf{U}$ of size $N \times M$ correspond to the POD modes, and the singular values squared correspond to the eigenvalues $\mathbf{L}$ of $\mathbf{C}$, namely $\mathbf{L} = \mathbf{S}^2$. The i-th snapshot can then be represented as a linear combination of POD modes:

$$\mathbf{q}^i(t) = \sum_{k=1}^{M} \mathrm{a}_k(t_i)\boldsymbol{u}_k \tag{5}$$

where the time coefficients of each POD mode, a_k, are given by the rows of the matrix $\sqrt{M}\mathbf{S}\mathbf{V}^T$. In addition, due to the orthogonality of the modes, it can be shown that the time coefficients a_k are uncorrelated at zero time lag:

$$\overline{\mathrm{a}_j \mathrm{a}_k} = \lambda_j \delta_{jk} \tag{6}$$

where $\bar{\cdot}$ indicates the long-time average.

2.2. Sparsity-Promoting Dynamic Mode Decomposition

The dynamic mode decomposition (DMD), proposed by [10], is a data-driven technique which allows one to extract relevant flow features, namely the DMD modes, whose dynamics are governed by correspondent eigenvalues. The key steps of the basic algorithm

are outlined hereafter.

As for the POD, a series of snapshots $\mathbf{q}^i$ is collected at a constant sampling frequency. We assume that a linear time-invariant mapping $\boldsymbol{A}$ connects every pair of successive snapshots,

$$\mathbf{q}^{i+1} = \boldsymbol{A}\mathbf{q}^i, \qquad i = \{0, \dots, M-1\}. \tag{7}$$

Using Equation (7) we can write:

$$\mathbf{Q}^1 = \boldsymbol{A}\mathbf{Q}^0, \tag{8}$$

where $\mathbf{Q}^0$ and $\mathbf{Q}^1$ are:

$$\mathbf{Q}^0 = \left[\mathbf{q}^0\, \mathbf{q}^1\, \dots\, \mathbf{q}^{M-1}\right], \qquad \mathbf{Q}^1 = \left[\mathbf{q}^1\, \mathbf{q}^2\, \dots\, \mathbf{q}^{M}\right]. \tag{9}$$

The linear operator $\boldsymbol{A}$, as suggested by [10], can be projected onto the $r-$dimensional basis $\mathbf{U}$ consisting of the first r POD modes of the snapshots matrix $\mathbf{Q}^0$,

$$\mathbf{Q}^0 \approx \mathbf{U}\mathbf{S}\mathbf{V}^T \tag{10}$$

$$\boldsymbol{A} \approx \mathbf{U}\boldsymbol{F}\mathbf{U}^T. \tag{11}$$

The dynamics in the low-dimensional subspace defined by the POD modes $\mathbf{U}$ is governed by

$$\boldsymbol{x}^{i+1} = \boldsymbol{F}\boldsymbol{x}^i. \tag{12}$$

where $\boldsymbol{x}^i$ is the projection of the snapshot matrix $\mathbf{Q}^i$ in the low-dimensional subspace defined by the chosen POD modes, with $i = 0, M-1$. Dynamic modes are then extracted by computing the eigendecomposition of the matrix $\boldsymbol{F}$:

$$\boldsymbol{F} = \underbrace{\begin{bmatrix}\boldsymbol{y}_1 & \dots & \boldsymbol{y}_r\end{bmatrix}}_{\boldsymbol{Y}} \underbrace{\begin{bmatrix}\mu_1 & & \\ & \ddots & \\ & & \mu_r\end{bmatrix}}_{\boldsymbol{D}_\mu} \underbrace{\begin{bmatrix}\boldsymbol{z}_1^* \\ \vdots \\ \boldsymbol{z}_r^*\end{bmatrix}}_{\boldsymbol{Z}^*} \tag{13}$$

where $\boldsymbol{y}_i$ and $\boldsymbol{z}_i^*$ are the right and left eigenvectors of $\boldsymbol{F}$, which are scaled such that $\boldsymbol{y}_i^*\boldsymbol{y}_i = 1$ and $\boldsymbol{z}_i^*\boldsymbol{y}_j = \delta_{ij}$. Notice that the frequency of the DMD modes is then given by the eigenvalues μ_i via the following relation: $\omega_i = -\dfrac{log(\mu_i)}{i\Delta t}$. Therefore, using Equation (12), we can approximate the solution $\boldsymbol{x}^n$ as follows:

$$\boldsymbol{x}^n = \boldsymbol{Y}\boldsymbol{D}_\mu^n\boldsymbol{Z}^*\boldsymbol{x}^0 = \sum_i^r \boldsymbol{y}_i\mu_i^n\boldsymbol{z}_i^*\boldsymbol{x}^0 = \sum_i^r \boldsymbol{y}_i\mu_i^n\alpha_i, \tag{14}$$

where $\alpha_i = \boldsymbol{z}_i^*\boldsymbol{x}^0$ represents the component of the initial condition $\boldsymbol{x}^0$ in the $\boldsymbol{z}_i^*$ direction. The snapshots can be approximated by mapping $\boldsymbol{x}^n$ on the higher dimensional space $\mathbb{C}^N$,

$$\mathbf{q}^n \approx \mathbf{U}\boldsymbol{x}^n = \sum_i^r \mathbf{U}\boldsymbol{y}_i\mu_i^n\alpha_i = \sum_i^r \boldsymbol{\phi}_i\mu_i^n\alpha_i, \tag{15}$$

and can be seen, therefore, as a linear combination of the DMD modes $\boldsymbol{\phi}_i = \mathbf{U}\boldsymbol{y}_i$ where α_i is the amplitude of the corresponding DMD mode. Equation (15) can be written also in matrix form:

$$\underbrace{\begin{bmatrix}\mathbf{q}^0 & \mathbf{q}^1 & \dots & \mathbf{q}^{M-1}\end{bmatrix}}_{\mathbf{Q}^0} \approx \underbrace{\begin{bmatrix}\boldsymbol{\phi}_1 & \boldsymbol{\phi}_2 & \dots & \boldsymbol{\phi}_r\end{bmatrix}}_{\mathbf{P}} \underbrace{\begin{bmatrix}\alpha_1 & & & \\ & \alpha_2 & & \\ & & \ddots & \\ & & & \alpha_r\end{bmatrix}}_{\boldsymbol{D}_\alpha} \underbrace{\begin{bmatrix}1 & \mu_1 & \dots & \mu_1^{M-1} \\ 1 & \mu_2 & \dots & \mu_2^{M-1} \\ \vdots & \vdots & \ddots & \vdots \\ 1 & \mu_r & \dots & \mu_r^{M-1}\end{bmatrix}}_{\boldsymbol{V}_{and}} \tag{16}$$

which highlights that the temporal evolution of the dynamic modes is governed by the Vandermonde matrix $\boldsymbol{V}_{and}$. Once the eigendecomposition of (13) is performed, the amplitudes' vector $\alpha = [\alpha_1 \dots \alpha_r]^T$ is computed solving the following optimization problem:

$$\underset{\alpha}{\text{minimize}} \;\; J(\alpha) = \left\| \mathbf{Q}^0 - \mathbf{P}\boldsymbol{D}_\alpha \boldsymbol{V}_{and} \right\|_F^2 \tag{17}$$

The superposition of all the DMD modes, weighted by their amplitudes and evolving according to their frequency and growth rate, optimally approximates the data sequence. Moreover, the sparsity-promoting DMD aims at finding a low dimensional representation of the snapshots' sequence in order to capture the most relevant dynamic structures. This objective is achieved in two steps. Firstly, a sparsity structure is sought, which achieves a user-defined trade-off between the number of modes and the approximation error, which depends on the sparsity parameter γ. This step is carried out by augmenting the objective function to be minimized with an additional term, $\mathbf{card}(\alpha)$, that penalizes the number of non-zero elements in the amplitudes' vector α,

$$\min_{\alpha} \quad J(\alpha) + \gamma\, \mathbf{card}(\alpha). \tag{18}$$

where γ is the parameter that influences the sparsity level, with higher values of the parameter promoting sparser solutions. Then the sparsity structure of the amplitudes' vector is fixed and the optimal values of the non-zero amplitudes are calculated. The metrics defining the performance of the algorithm are the cardinality of the optimal amplitude vector $\mathbf{card}(\alpha)$ and the performance loss, defined as:

$$\%\Pi_{loss} = 100 \frac{\left\| \mathbf{Q}^0 - \mathbf{P}\boldsymbol{D}_\alpha \boldsymbol{V}_{and} \right\|_F^2}{\left\| \mathbf{Q}^0 \right\|_F^2}. \tag{19}$$

For further details, the reader is referred to Reference [14].

3. Simulation Setup

The turbine considered in this study is the NREL-5MW with a diameter $D = 126$ m and hub height $h = 87.5$ m. The turbine is simulated at rated conditions with tip-speed ratio $\lambda = 7$, which implies a constant dimensionless angular frequency of the rotor $\omega = 2\lambda = 14$. The reference incoming wind speed at rated conditions is $U_\infty = 11.4$ m/s; therefore, the resulting diameter-based Reynolds number is $Re \approx 10^8$.

The size of the computational domain is $12.5 \times 5 \times 3$ diameter units in the streamwise (x), vertical (y) and transverse (z) directions, respectively. The turbine is located at 4 diameter units from the inlet, where a uniform velocity U_∞ is imposed, and it is centered in the transverse direction. We should remark that in real-life applications the turbine is impinged by an atmospheric turbulent boundary layer, which can potentially affect the dynamics of the wake.

Therefore, the scenario we discuss can be considered representative of real-life applications for low values of the inlet turbulence intensity. At the outlet, a radiative boundary condition is employed, with uniform convection velocity $c = 0.9$ [24]. No-slip and free-slip conditions are imposed at the bottom- and the top-wall, respectively, whereas the lateral boundaries are periodic. The computational grid used consists of $2048 \times 512 \times 512$ grid-points in x, y and z directions, respectively. The grid is uniform along the streamwise and

transverse directions, whereas it is stretched in the vertical direction, with finer (uniform) spacing in the part of the domain where the turbine's wake develops. The convergence of the numerical results with respect to the mesh has been assessed in Reference [8] for the mean flow. Concerning the POD and DMD modes, we have performed a sampling convergence study finding a moderate sensitivity of intermediate-frequency DMD modes, whereas low- and high- frequency DMD modes have shown robustness with respect to the sampling points.

4. Modal Decomposition of the Wake

Both modal-decomposition techniques used for identifying coherent structures in the wake are based on the same dataset. Snapshots of the velocity field are taken each 10° rotation of rotor, in a reduced three-dimensional subdomain enclosing the wake, whose extent is $[4\ \ 12.4] \times [-0.7\ \ 0.63] \times [0.8\ \ 2.2]$ in x, y and z direction, respectively. The entire dataset comprises 3052 snapshots; one of them is shown in Figure 1. The ensemble average of the snapshots, shown in Figure 2, is then subtracted from each snapshot.

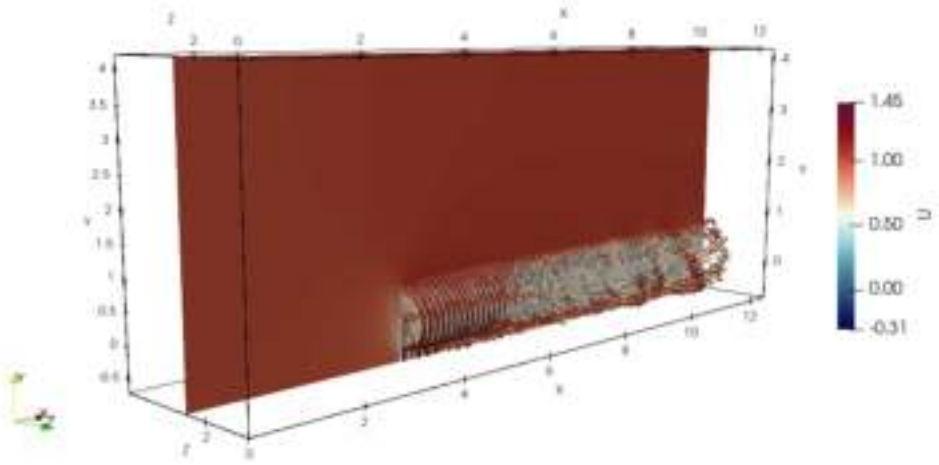

Figure 1. Streamwise velocity contours of a flow snapshot extracted from LES.

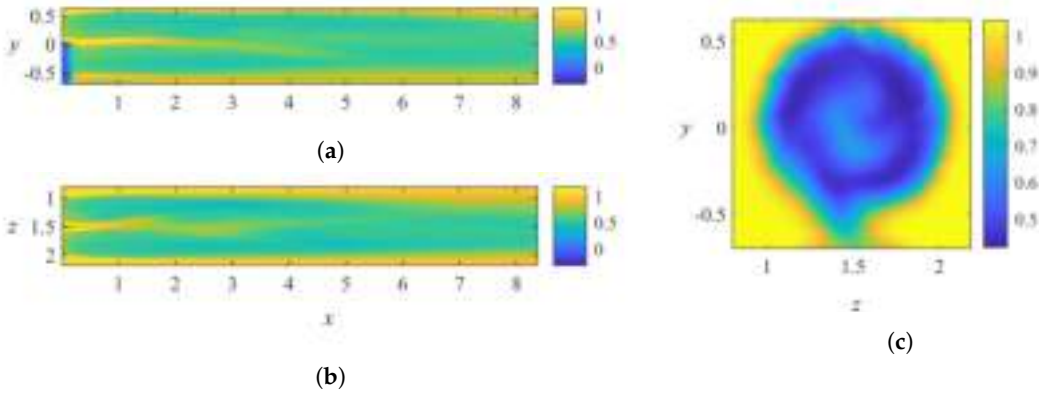

Figure 2. Streamwise velocity contours of the snapshots' ensemble mean. (**a**) $x-y$ plane at $z = 1.5$. (**b**) $x-z$ plane at $y = 0$. (**c**) $z-y$ plane at $x = 4$.

4.1. POD Results

In Figure 3a, the distribution of the singular values is shown. A fast energy decay for the first 2–3 hundreds of modes can be observed; then, the slope of the curve decreases and a nearly null energy is reached for $k \approx 2500$. A closer look to the singular values for the first 20 POD modes highlights a step-wise distribution, suggesting that successive modes characterized by a similar energy are paired. Figure 3b shows the cumulative percentage

distribution of turbulent kinetic energy versus the fraction of POD modes considered, computed as:

$$\bar{k}[\%] = \frac{\sum_{k=1}^{m} s_k}{\sum_{k=1}^{M} s_k} \times 100 \quad m \in \{1, \ldots, M\} \tag{20}$$

$$\text{modes}[\%] = \frac{m}{M} \times 100. \tag{21}$$

A total of 50% of the turbulent kinetic energy is due to only 15% of POD modes (∼457 modes), and 50% of modes (∼1525 modes) accounts for about 90% of the turbulent kinetic energy.

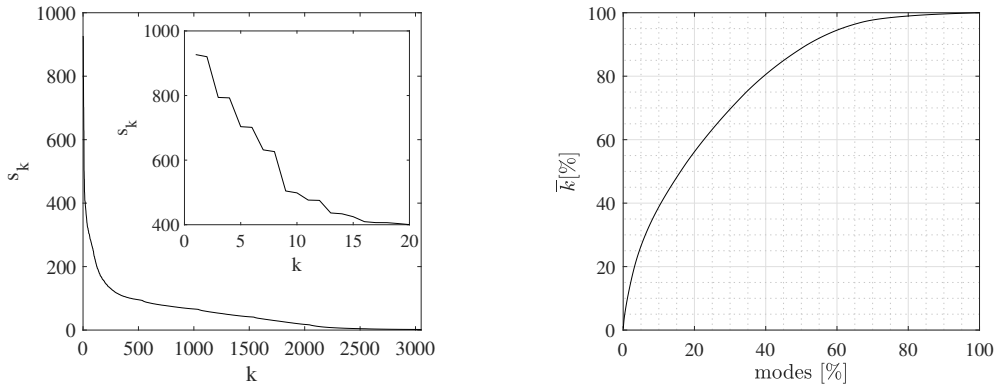

(**a**) (**b**)

Figure 3. (**a**) Singular values distribution with a close up for the first 20 modes. (**b**) Cumulative turbulent kinetic energy distribution versus the fraction of POD modes.

The most energetic POD modes are shown in Figure 4 (streamwise component) and Figure 5 (vertical and transverse components). The second pair, provided in Figures 4b and 5c,d, clearly corresponds to the tip vortices, which are localized very close to the turbine. The remaining modes are mostly localized in the far wake and are all characterized by low-frequency large-scale coherent motions. In fact, in the region close to the turbine, the tip vortices quickly break down and their energy is redistributed towards the smaller scales, until reaching the dissipative range, where the very small eddies are dissipated. Thus, far from the turbine, where tip vortices have broken down, other low-frequency coherent structures emerge that can be linked to the instability of the mean flow or to the nonlinear interactions between the vortices released by the turbine. In the case under consideration, the observed large-scale structures can be linked to the vortices shed by the tower and nacelle, as observed by De Cillis et al. [8]. Fourier transform of the time coefficients $a_k(t)$ associated with the most energetic POD modes is provided in Figure 6. While the third mode, which is associated with the tip vortices, has dominant wavenumber $\omega \approx 42$ ($f \approx 6.45$), roughly corresponding to three times the angular frequency of the rotor, the other energetic modes are characterized by low-frequency oscillations in the range $\omega \in [2.44 - 4.58]$ ($f \in [0.44 - 0.73]$). However, Figure 6 shows that most of the POD modes are characterized by more than one frequency peak, showing a higher/lower frequency content which appears not to be merely due to the development of harmonics of the main frequency. This confirms the fact that POD does not allow to clearly separate frequencies and scales of the main coherent structures developing in the flow. The main temporal wavenumbers of the eight most energetic pairs are reported in Table 1, for further comparison with the DMD most relevant modes.

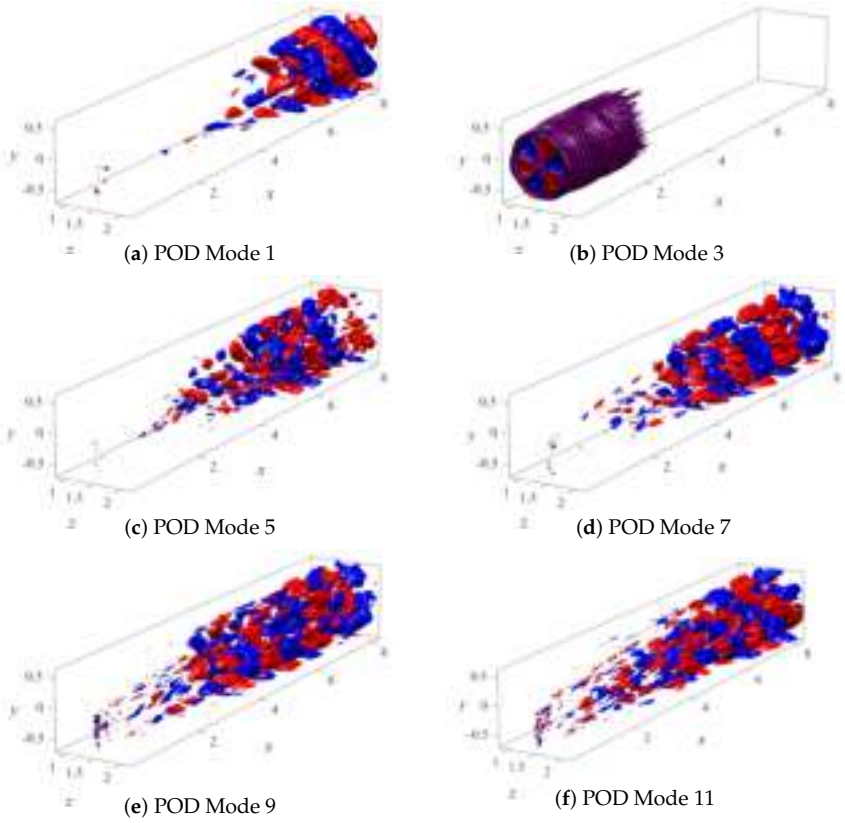

(**a**) POD Mode 1 (**b**) POD Mode 3

(**c**) POD Mode 5 (**d**) POD Mode 7

(**e**) POD Mode 9 (**f**) POD Mode 11

Figure 4. Streamwise velocity iso-surfaces of the most energetic POD modes (red for $u = 0.001$, blue for $u = -0.001$).

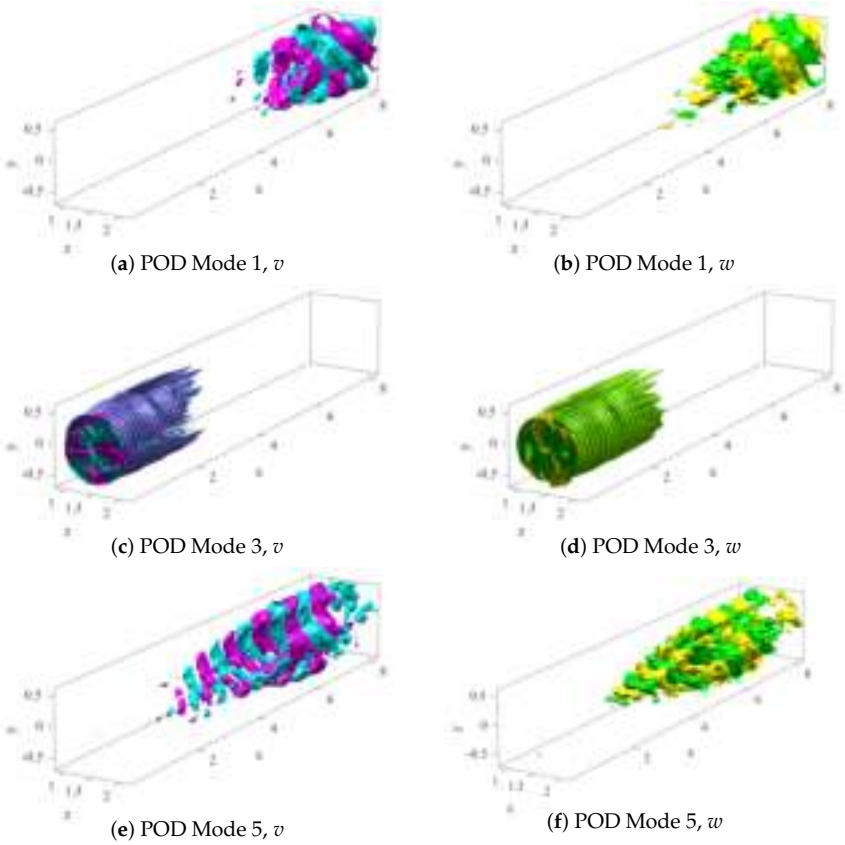

(**a**) POD Mode 1, v (**b**) POD Mode 1, w

(**c**) POD Mode 3, v (**d**) POD Mode 3, w

(**e**) POD Mode 5, v (**f**) POD Mode 5, w

Figure 5. Vertical (**left**) and transverse (**right**) velocity iso-surfaces of the most energetic POD modes (magenta/green for $v, w = 0.0008$, cyan/yellow for $v, w = -0.0008$).

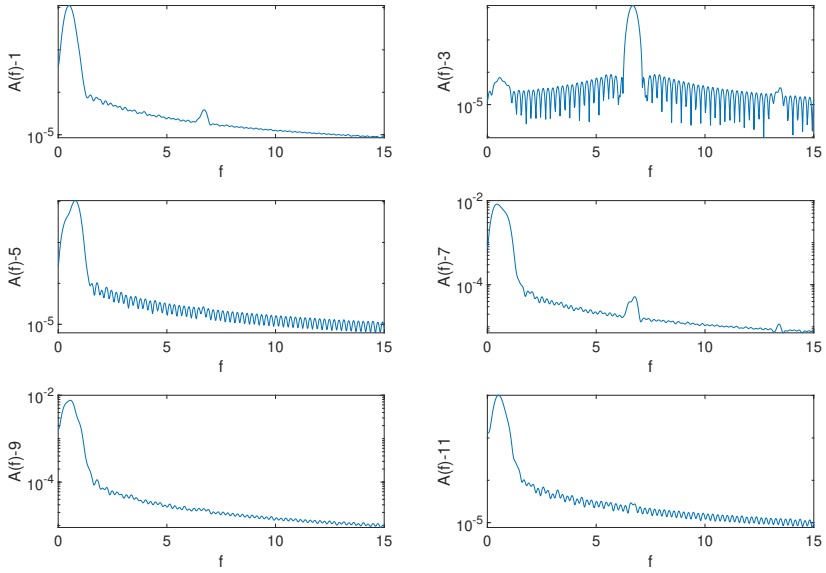

Figure 6. Fourier transform of the time coefficients $a_k(t)$ associated with the most energetic POD modes shown in Figure 4.

Table 1. Frequencies and amplitudes of the selected complex conjugate dynamic modes' pairs, computed with the standard and sparsity-promoting DMD.

	$\Re(\omega)$-POD	$\Re(\omega)$-DMD	$\lvert\alpha\rvert$ (std. DMD)	$\lvert\alpha\rvert$ (SP-DMD)
Pair 1	3.26	42.0	14.34	14.86
Pair 2	42.0	5.20	11.39	9.55
Pair 3	4.58	2.13	8.54	8.53
Pair 4	2.23	3.92	9.26	7.89
Pair 5	2.44	2.30	7.50	7.80
Pair 6	3.76	2.96	8.26	7.48
Pair 7	2.64	4.25	6.39	6.02
Pair 8	1.13	3.58	4.22	4.06

4.2. SP-DMD Results

The sparsity-promoting DMD has been performed on a subspace made of 251 POD modes, for increasing values of the sparsity parameter γ, in order to investigate the performance of the algorithm, as shown in Figure 7. It can be noted that the performance loss is not null, even for low values of γ, because the DMD is computed on the low-dimensional space defined by the first 251 POD modes. Notice that the first 251 POD modes allow a reconstruction of only ≈30% of the flow kinetic energy (see Figure 3). However, the same number of DMD modes leads to a loss in reproducing the whole velocity field of 20% only (see Figure 7, showing the percentage of loss as defined in Equation (19)). Thus, when comparing the performance of POD and DMD, we will refer to the relative performance loss, computed with respect to the baseline value obtained when retaining all 251 modes used for the projection on the POD base (namely, $20\% Pi_{loss}$). In Figure 7, we can see that, for $\gamma < 4 \times 10^3$, approximately all 250 modes are retained, leading to a relative performance loss close to zero. For $4 \times 10^3 < \gamma < 10^4$, the retained modes drop to ≈150, leading to a performance loss only slightly larger than the baseline value. Further increasing the sparsity parameter leads to a further drop of the number of selected modes, but at the price of a relative performance loss of more than 45% when less than 100 modes are retained. This analysis shows that ≈200 modes are sufficient for reconstructing the flow field with an almost negligible relative performance loss. As a comparison, we can observe in Figure 3 that 200 POD modes lead to the reconstruction of only 20% of the flow energy, while the same number of DMD modes leads to a performance loss of only 20%. This

clearly indicates that the kinetic energy may not be a relevant measure of the dynamical relevance of the flow structures for the considered flow. Thus, DMD modes appear to be better fitted for building reduced order models aiming at reconstructing the flow field with a small number of degrees of freedom.

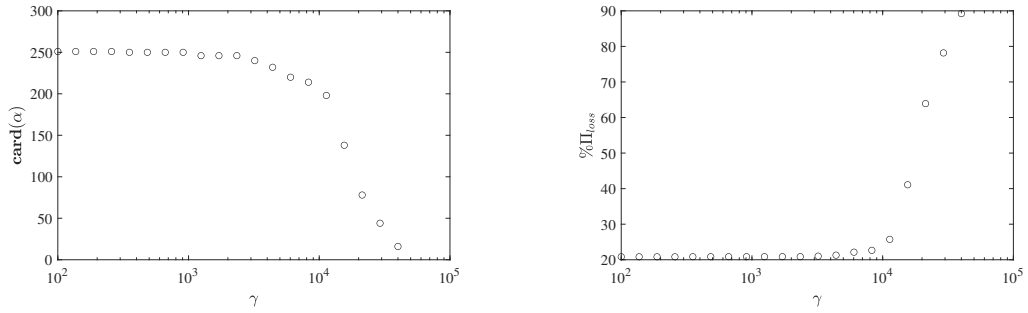

(**a**) (**b**)

Figure 7. The sparsity level **card**(α) (**a**) and the optimal performance loss $\%\Pi_{loss}$ (**b**) for different values of the sparsity parameter γ.

For reducing the dynamics on a very low dimensional space, and comparing the relevant modes with the most energetic ones recovered using POD, in the remainder of the paper we select the value of sparsity-promoting parameter γ = 40,000. This particular choice, despite being characterized by a high performance loss, leads to the nontrivial selection of just 16 relevant dynamic modes. In the left panel of Figure 8, the eigenvalues μ of the linear operator $\boldsymbol{F}$ (see Equations (12) and (13)) are shown, along with the unit circle. The modes selected by the sparsity-promoting algorithm are marked with a black circle. As expected for a turbulent statistically stationary flow, all eigenvalues are very close to the unit circle, describing the periodic dynamics of the associated modes. It is noticeable, furthermore, the unbalance between high- and low-frequency modes, the high frequency ones being, essentially, harmonics of the tip vortices. The right panel of Figure 8 shows the logarithmic mapping of the eigenvalues, computed according to $\omega = -\frac{log(\mu)}{i\Delta t}$ where Δt is the temporal separation between two consecutive snapshots and i the imaginary unit. Since the analyzed dataset is real, the eigenvalues with non-zero frequency form complex conjugate pairs, and so do the associated dynamic modes. Therefore, the 16 dynamic modes selected by the sparsity-promoting DMD consist of eight complex conjugate pairs. Frequencies and amplitudes of the selected dynamic modes' pairs are summarized in Table 1, compared to the main frequencies of the most energetic POD modes.

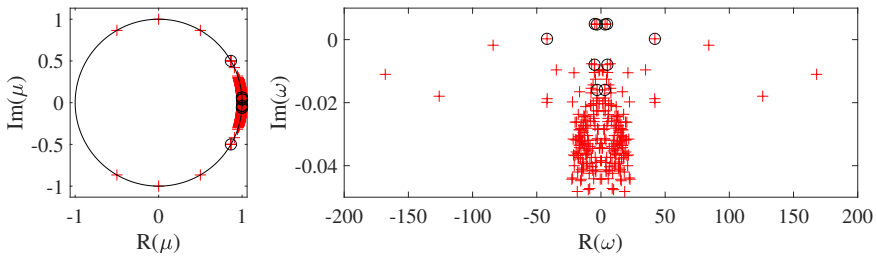

Figure 8. Eigenvalues resulting from the standard DMD algorithm (red crosses) and the sparsity-promoting algorithm (black circles). The right panel shows the logarithmic mapping of the eigenvalues, $\omega = -\frac{log(\mu)}{i\Delta t}$, where Δt is the temporal separation between two consecutive snapshots and i the imaginary unit.

Figures 9 and 10 provide the velocity components of the most relevant DMD modes, ordered by their amplitude $|\alpha|$. It is apparent that their main structure is similar to that of the most energetic POD modes, despite the ranking is different and the associated frequencies are not exactly the same (except for the high-frequency mode). Among the modes selected by the SP-DMD, the ones that have the largest amplitude correspond to the tip vortices, as one can see in Figure 9a for the streamwise velocity and Figure 10a,b for the vertical and transverse components. Notice that this mode oscillates at a characteristic angular frequency $\omega = 42$, equal to three times the rotational angular frequency of the turbine. It is interesting to note that the POD ranked the mode associated with the tip-vortices as the second one in terms of energy, probably because it is characterized by smaller-scale structures than the other ones (large-scale structures bearing, in general, more energy than small-scale ones). The remaining selected modes are characterized by low frequencies and large-scale spatial structures, as can be observed in Figures 9b–h and 10c–f. These low-frequency modes are probably linked to the interaction of tip vortices and tower vortices, as recently found by modal analysis of the wake of a wind turbine with and without tower and nacelle [8]. Compared to the POD modes, one can notice that these modes occupy a larger part of the domain, being characterized by smaller-scale structure in the near wake and large-scale structures in the far wake, while the POD low-frequency modes were found to be mostly localized in the far wake, probably due to the larger energetic content of large-scale structures which develop downstream once smaller-scale ones have dissipated. Moreover, in all the low-frequency DMD modes, one can clearly identify the footprint of the tower close to the inlet (see Figure 9b–h), which was seen only in POD modes 9 and 11. This direct connection with the near-wake small-scale structures is highlighted in Figure 11, providing the streamwise velocity contours of the most relevant DMD modes in two different wall-parallel planes. One can observe that the coherent structures of the DMD modes are almost equally distributed in the streamwise direction, except for the high-frequency mode which is mostly localized in the near wake, at least in the planes closest to the hub. Contrariwise, as shown in Figure 12, the most energetic POD modes are much more concentrated in the far wake (once again, except the high-frequency mode). Moreover, concerning the low-frequency POD modes, one can see a relevant scale separation between the structures closer to the hub (left frames) and those located closer to the wall (right frame). In particular, the coherent structures located farther from the hub have a much larger scale than those closer to it, probably being directly linked to the shedding of the tower (see De Cillis et al. [8] for a discussion of this type of POD mode). Instead, the coherent structures characterizing the DMD mode appear to maintain roughly the same wavelength, no matter the wall-normal position. It is worth to note that all the most energetic POD modes suffer from the same scale separation in the y and x direction, probably due to the fact that they are associated with more than one temporal frequency.

Finally, concerning the frequencies reported in Table 1, the DMD modes are characterized by slightly larger frequencies and are ordered with a different ranking with respect to the POD modes. In conclusion, the DMD modes selected by the sparsity-promoting algorithm are found to be structurally similar to the most energetic POD modes. Nevertheless, some non-trivial differences exist in ranking, frequencies and spatial structures, probably linked to the fact that DMD isolates structures associated with one frequency only, leading to relevant differences in the performance of the two sets of modes in reconstructing the flow field.

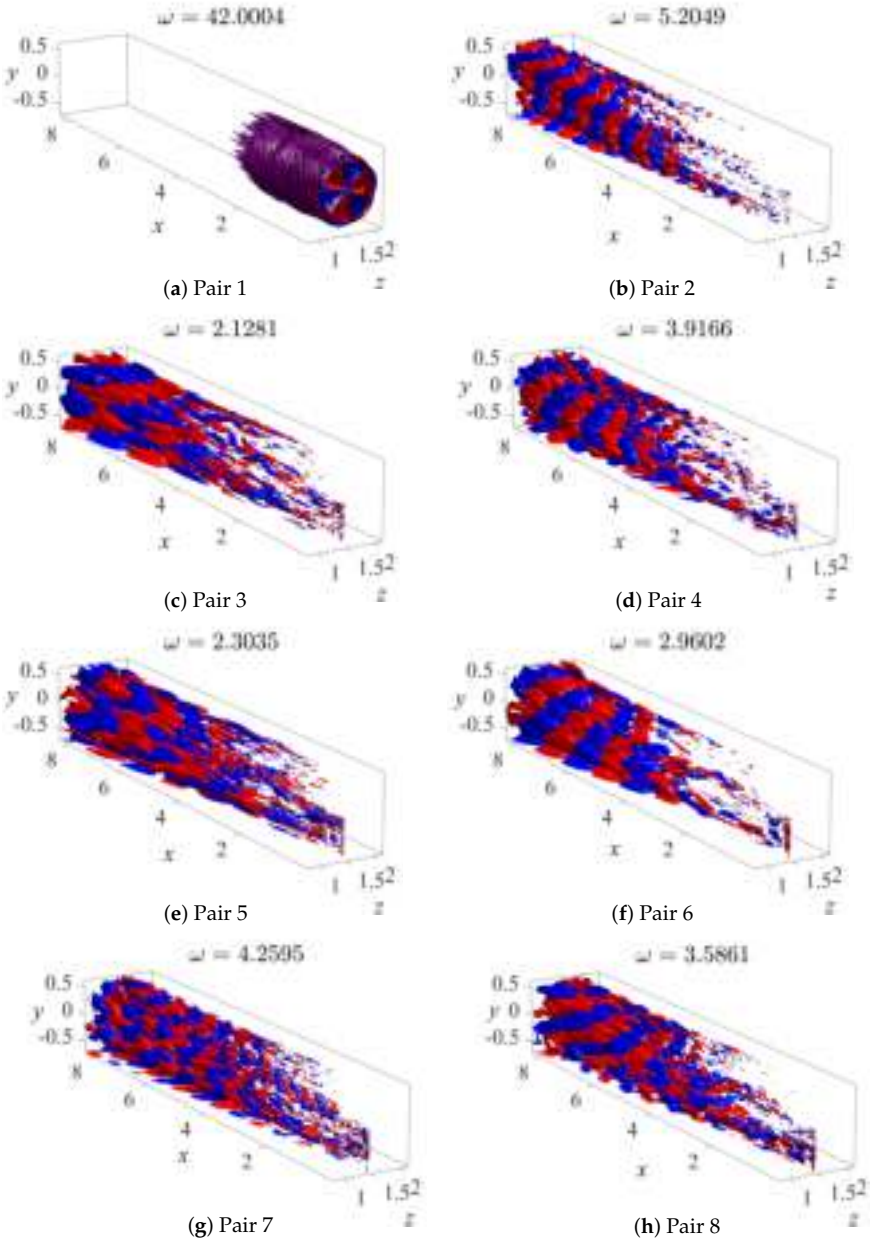

(**a**) Pair 1 (**b**) Pair 2

(**c**) Pair 3 (**d**) Pair 4

(**e**) Pair 5 (**f**) Pair 6

(**g**) Pair 7 (**h**) Pair 8

Figure 9. Streamwise velocity iso-surfaces (red for $u = 0.001$, blue for $u = -0.001$ values) of the real part of the eight dynamic modes' pairs selected by the sparsity-promoting algorithm, ordered according to their amplitude $|\alpha|$.

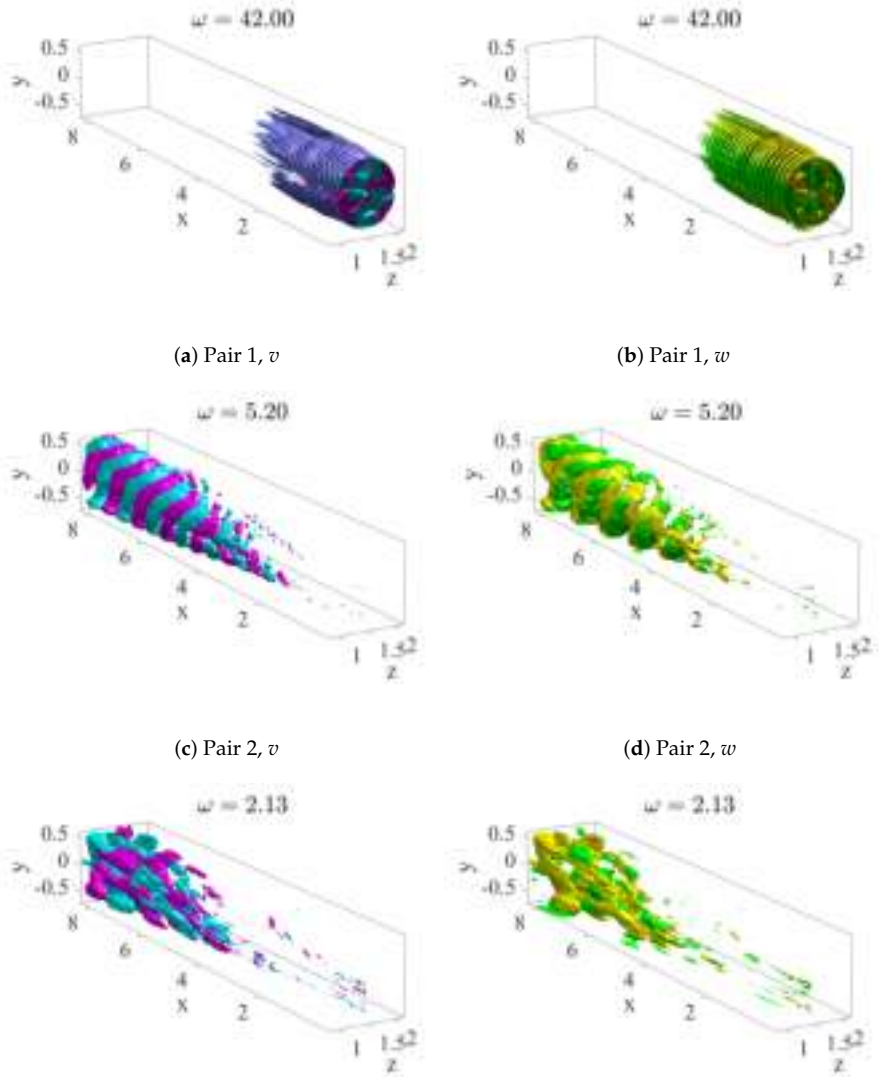

(**a**) Pair 1, v (**b**) Pair 1, w

(**c**) Pair 2, v (**d**) Pair 2, w

(**e**) Pair 3, v (**f**) Pair 3, w

Figure 10. Vertical (**left**) and transverse (**right**) velocity iso-surfaces (magenta/green for $v, w = 0.0008$, cyan/yellow for $v, w = -0.0008$ values) of the real part of the most relevant three dynamic modes' pairs selected by the sparsity-promoting algorithm, ordered according to their amplitude $|\alpha|$.

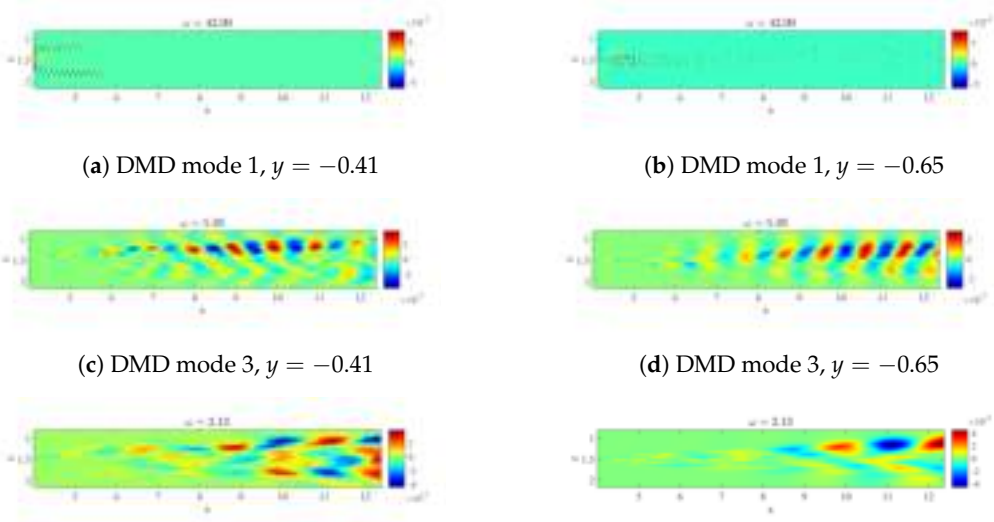

(**a**) DMD mode 1, $y = -0.41$ (**b**) DMD mode 1, $y = -0.65$

(**c**) DMD mode 3, $y = -0.41$ (**d**) DMD mode 3, $y = -0.65$

(**e**) DMD mode 5, $y = -0.41$ (**f**) DMD mode 5, $y = -0.65$.

Figure 11. Streamwise velocity contours of the most relevant DMD modes on two y-constant planes.

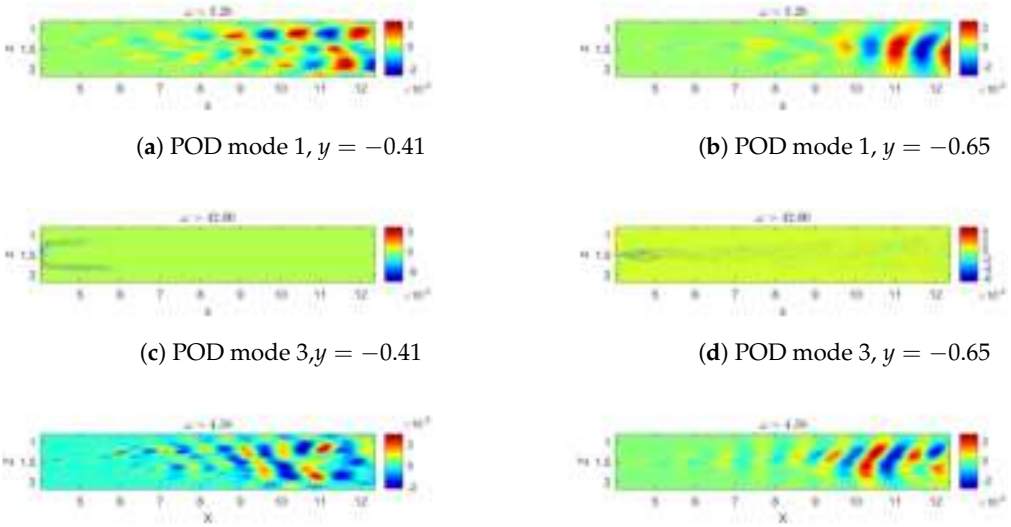

(**a**) POD mode 1, $y = -0.41$ (**b**) POD mode 1, $y = -0.65$

(**c**) POD mode 3,$y = -0.41$ (**d**) POD mode 3, $y = -0.65$

(**e**) POD mode 5,$y = -0.41$ (**f**) POD mode 5, $y = -0.65$

Figure 12. Streamwise velocity contours of the most energetic POD modes on two y-constant planes.

5. Discussion

The present work provides a numerical analysis of the dynamics of the wake developing behind the NREL 5-MW reference wind turbine, for laminar inflow conditions, using the proper orthogonal decomposition (POD) and the sparsity-promoting dynamic mode decomposition (SP-DMD) of the unsteady flow field. While POD provides a set of highly energetic, mutually orthogonal modes, these modes may not be the most dynamically relevant; therefore, the selection of a low-dimensional basis for the realization of a reduced-order model may be not trivial. On the other hand, DMD, in the sparsity-promoting variant, has the capability of selecting the most dynamically relevant motion, using a decomposition that ranks the temporal dominant frequencies in terms of amplitude. In the literature, some examples of comparative analyses of the performance of these two modal decompositions have been performed for different flows, showing the appropriateness of either of the two modal decompositions depending on the flow cases. However, such a comparison has never been assessed directly for the case of the flow behind a utility-scale wind turbine at realistic Reynolds number. In the present paper, the flow behind the NREL-5MW wind turbine was simulated employing an LES approach, in which the rotor blades are mod-

eled using the actuator line method, whereas tower and nacelle are simulated using an immersed boundary method. The most energetic modes identified by the POD are mostly characterized by large-scale structures localized in the far wake, except for the second most energetic mode which develops in the near wake and closely resembles the tip vortices. Notably, 50% of the whole flow field's turbulent kinetic energy is due to only 15% of POD modes, namely ≈457 modes. However, ≈1525 modes are needed to account for about 90% of the turbulent kinetic energy. Thus, using an energy-based criterion, it appears that a large number of modes is needed to appropriately reconstruct the flow field.

Attempting to reduce the degrees of freedom of the system, the sparsity-promoting DMD was performed on a subspace made of 251 POD modes. Depending on the value of the sparsity parameter, the SP-DMD selected different non-trivial subsets of dynamic modes that optimally reconstruct the entire data sequence. Comparing the reconstructed flow with the original one, it appears that for low values of the sparsity parameter the SP-DMD algorithm selects ≈200 modes, leading to a performance loss of ≈20% with respect to the reference snapshots. For high values of the sparsity parameter, the number of selected modes decreases considerably at the price of a larger loss. In all cases, the most relevant mode appears to be directly linked to the tip vortices, while the other most relevant modes are characterized by low-frequency oscillations filling a large part of the domain. While the coherent structures characterizing the DMD modes maintain roughly the same wavelength, no matter the wall-normal/streamwise position, the POD modes show a clear scale separation in the different spatial directions, probably due to the fact that they are associated with more than one temporal frequency. Moreover, the DMD modes are characterized by slightly larger frequencies and are ordered with a different ranking with respect to the POD modes.

6. Conclusions

Comparing the outcome of the DMD analysis with that of POD, we have to remark that a reconstruction using the most energetic 200 POD modes induces a loss of ≈80% of the flow kinetic energy, while reconstructing the flow field using the most relevant 200 DMD modes leads to a performance loss of only ≈20%. Despite the overall similarities between the two set of modes, the differences in ranking, temporal frequencies and spatial structures between the two modal-decomposition techniques points out that an energy-based criterion, such as that used in the POD, may not be suitable for formulating a reduced-order model of wind turbine wakes. Thus, sparsity-promoting DMD should be preferred for finding an optimal low-dimensional representation of flow data. Future work will aim at developing reduced-order models based on SP-DMD and evaluating their performance in different flow conditions.

Author Contributions: Data curation, formal analysis, draft preparation: G.D.C.; data curation, conceptualization, supervision, writing, original draft preparation, review and editing: S.C.; data curation, supervision, review and editing: O.S.; conceptualization, supervision, writing—review and editing: P.D.P.; conceptualization, supervision, review and editing: S.L. All authors have read and agreed to the published version of the manuscript.

Funding: This research received no external funding.

Institutional Review Board Statement: Not applicable

Informed Consent Statement: Not applicable.

Data Availability Statement: Not applicable.

Conflicts of Interest: The authors declare no conflict of interest.

References

1. Andersen, S.J.; Sørensen, J.N.; Mikkelsen, R. Simulation of the inherent turbulence and wake interaction inside an infinitely long row of wind turbines. *J. Turbul.* **2013**, *14*, 1–24. [CrossRef]
2. Bastine, D.; Witha, B.; Wächter, M.; Peinke, J. Towards a simplified dynamicwake model using pod analysis. *Energies* **2015**, *8*, 895–920. [CrossRef]
3. VerHulst, C.; Meneveau, C. Large eddy simulation study of the kinetic energy entrainment by energetic turbulent flow structures in large wind farms. *Phys. Fluids* **2014**, *26*, 025113. [CrossRef]
4. Hamilton, N.; Tutkun, M.; Cal, R.B. Wind turbine boundary layer arrays for Cartesian and staggered configurations: Part II, low-dimensional representations via the proper orthogonal decomposition. *Wind Energy* **2015**, *18*, 297–315. [CrossRef]
5. Hamilton, N.; Tutkun, M.; Cal, R.B. Anisotropic character of low-order turbulent flow descriptions through the proper orthogonal decomposition. *Phys. Rev. Fluids* **2017**, *2*, 014601. [CrossRef]
6. Hamilton, N.; Viggiano, B.; Calaf, M.; Tutkun, M.; Cal, R.B. A generalized framework for reduced-order modeling of a wind turbine wake. *Wind Energy* **2018**, *21*, 373–390. [CrossRef]
7. Fortes-Plaza, A.; Campagnolo, F.; Wang, J.; Wang, C.; Bottasso, C. A POD reduced-order model for wake steering control. *J. Phys. Conf. Ser.* **2018**, *1037*, 032014. [CrossRef]
8. De Cillis, G.; Cherubini, S.; Semeraro, O.; Leonardi, S.; De Palma, P. POD-based analysis of a wind turbine wake under the influence of tower and nacelle. *Wind Energy* **2021**, *24*, 609–633. [CrossRef]
9. Ilak, M.; Rowley, C.W. Modeling of transitional channel flow using balanced proper orthogonal decomposition. *Phys. Fluids* **2008**, *20*, 034103. [CrossRef]
10. Schmid, P.J. Dynamic mode decomposition of numerical and experimental data. *J. Fluid Mech.* **2010**, *656*, 5–28. [CrossRef]
11. Iungo, G.V.; Santoni-Ortiz, C.; Abkar, M.; Porté-Agel, F.; Rotea, M.A.; Leonardi, S. Data-driven reduced order model for prediction of wind turbine wakes. *J. Phys. Conf. Ser.* **2015**, *625*, 012009. [CrossRef]
12. Le Clainche, S.; Lorente, L.S.; Vega, J.M. Wind predictions upstream wind turbines from a LiDAR database. *Energies* **2018**, *11*, 543. [CrossRef]
13. Chen, K.K.; Tu, J.H.; Rowley, C.W. Variants of dynamic mode decomposition: Boundary condition, Koopman, and Fourier analyses. *J. Nonlinear Sci.* **2012**, *22*, 887–915. [CrossRef]
14. Jovanović, M.R.; Schmid, P.J.; Nichols, J.W. Sparsity-promoting dynamic mode decomposition. *Phys. Fluids* **2014**, *26*, 024103. [CrossRef]
15. Semeraro, O.; Bellani, G.; Lundell, F. Analysis of time-resolved PIV measurements of a confined turbulent jet using POD and Koopman modes. *Exp. Fluids* **2012**, *53*, 1203–1220. [CrossRef]
16. Frederich, O.; Luchtenburg, D.M. Modal analysis of complex turbulent flow. In *Seventh International Symposium on Turbulence and Shear Flow Phenomena*; Begell House Digital Library: Danbury, CT, USA, 2011.
17. Muld, T.W.; Efraimsson, G.; Henningson, D.S. Flow structures around a high-speed train extracted using Proper Orthogonal Decomposition and Dynamic Mode Decomposition. *Comput. Fluids* **2012**, *57*, 87–97. [CrossRef]
18. Mendez, M.; Balabane, M.; Buchlin, J.M. Multi-scale proper orthogonal decomposition of complex fluid flows. *J. Fluid Mech.* **2019**, *870*, 988–1036. [CrossRef]
19. Medici, D. Experimental Studies of Wind Turbine Wakes: Power Optimisation and Meandering. Ph.D. Thesis, Kungliga Tekniska Hogskolan (KTH): Stockholm, Sweden, 2005.
20. Pope, S.; Pope, S.; Eccles, P.; Press, C.U. *Turbulent Flows*; Cambridge University Press: Cambridge, UK, 2000.
21. Orlandi, P. *Fluid Flow Phenomena: A Numerical Toolkit*; Volume 55, Fluid Mechanics and Its Applications; Springer: Dordrecht, The Netherlands, 2000. [CrossRef]
22. Sørensen, J.N.; Shen, W.Z. Computation of wind turbine wakes using combined Navier-Stokes/actuator-line Methodology. In Proceedings of the 1999 European Wind Energy Conference and Exhibition, Nice, France, 1–5 March 1999; pp. 156–159.
23. Orlandi, P.; Leonardi, S. DNS of turbulent channel flows with two-and three-dimensional roughness. *J. Turbul.* **2006**, *7*, N73. [CrossRef]
24. Orlanski, I. A simple boundary condition for unbounded hyperbolic flows. *J. Comput. Phys.* **1976**, *21*, 251–269. [CrossRef]

International Journal of
Turbomachinery Propulsion and Power

MDPI

Article

Experimental and Numerical Analysis of a Compressor Stage under Flow Distortion

Alberto Baretter [1], Benjamin Godard [2], Pierric Joseph [1], Olivier Roussette [1], Francesco Romanò [1], Raphael Barrier [2] and Antoine Dazin [1,*]

[1] Univ. Lille, CNRS, ONERA, Arts et Métiers Institute of Technology, Centrale Lille, UMR 9014-LMFL-Laboratoire de Mécanique des Fluides de Lille -Kampé de Fériet, F-59000 Lille, France; alberto.baretter@ensam.eu (A.B.); pierric.joseph@ensam.eu (P.J.); olivier.roussette@ensam.eu (O.R.); francesco.romano@ensam.eu (F.R.)
[2] Onera—The French Aerospace Lab. F-92190 Meudon, France; benjamin.godard@onera.fr (B.G.); raphael.barrier@onera.fr (R.B.)
* Correspondence: antoine.dazin@ensam.eu

Abstract: On many occasions, fan or compressor stages have to face azimuthal flow distortion at inlet, which affects their performance and stability. These flow distortions can be caused by external events or by some particular geometrical features. The aim of this work is to propose a joined numerical and experimental analysis of the flow behavior in a single axial compressor stage under flow distortion. The distortions are generated by different grids that are placed upstream to the rotor. Experimentally, the flow analysis is based on the measurements obtained by a series of unsteady pressure sensors flush-mounted at the casing of the machine rotor. URANS computations are conducted using the elsA software. The flow distortion is simulated by a drop of stagnation pressure ratio at the inlet boundary condition. The study is focusing first on the ability of a pressure drop, imposed as an inlet boundary condition in CFD, to reproduce accurately the effect of a flow distortion. The analysis is conducted using singular value decomposition (SVD) and dynamic mode decomposition (DMD). A special attention is then paid, on the experimental level, to the arising of rotating stall, from the onset of the instability up to completely developed stall cells.

Keywords: axial compressor; inlet distortion; rotating stall

check for updates

Citation: Baretter, A.; Godard, B.; Joseph, P.; Roussette, O.; Romanò, F.; Barrier, R.; Dazin, A. Experimental and Numerical Analysis of a Compressor Stage under Flow Distortion. *Int. J. Turbomach. Propuls. Power* **2021**, *6*, 43. https://doi.org/10.3390/ijtpp6040043

Received: 30 September 2021
Accepted: 17 November 2021
Published: 23 November 2021

Publisher's Note: MDPI stays neutral with regard to jurisdictional claims in published maps and institutional affiliations.

Copyright: © 2021 by the authors. Licensee MDPI, Basel, Switzerland. This article is an open access article distributed under the terms and conditions of the Creative Commons Attribution (CC BY-NC-ND) license (https://creativecommons.org/licenses/by-nc-nd/4.0/).

1. Introduction

Inlet distortion is the situation in which the flow entering turbomachinery is nonuniform. This can occur in jet engines because the curvature of the intake induces secondary flows, or because the intake is close to the fuselage, so that the boundary layer is ingested. In principle, the boundary layer ingestion (BLI) has a potential benefit on fuel consumption for civil aircrafts [1]. It consists of reducing the drag using the aircraft engines, which are partially embedded at the back of the fuselage of the aircraft and ingest the boundary layer developed on the fuselage. Other situations in which distortion can occur relate to the operation of the engine in highly turbulent or in crosswind flows. A typical feature of a distorted flow is the co-existence of regions of lower and higher total pressure. Indeed, turbomachines are normally designed to work under a circumferentially uniform inflow, so that the rotating blades see the same angle of incidence and experience equal blade pressure profiles. However, in a circumferential distorted flow, the blades rotate in and out of the low pressure region and thus they will experience a cyclically varying incidence.

A simple model to describe the circumferential distortion was given by [2]. The response of the blades to a sinusoidal oscillation of the incidence angle consists of an oscillation of lift coefficient and, since the variations in pressure ratio are proportional to the variations in lift coefficient, the cyclic behavior of the lift coefficient induces a cyclic behavior of the pressure ratio in the compressor map. This cyclic behavior causes a

degradation of the performances of the machine, which cannot sustain the same pressure ratio as in nondistorted operational regimes. Moreover, as far as the compressor stability is concerned, the distorted flow region causes a higher incidence, and thus operation closer to the stall limit. Stall margin is reduced and instabilities will be triggered for a higher flow coefficient.

From the early studies in the 1970s [3,4] up to more recent studies [5], the effect of inlet distortion on turbomachines has been tested mostly by means of screens [6] placed in front of the machine; the attention has been concentrated on the characterization of the steady state performance under inlet distortion, and on rotating stall mostly in terms of stall margin reduction. Two aspects appear to deserve further investigation.

The first relates to the characterization of the effect of screens to represent a distortion. A better understanding of the effect of the geometry of the screen on the flow is needed to improve the understanding of the effects of screen-generated inlet flow distortion. A second aspect is the lack of investigation of the detailed dynamics of stall inception under distortion [7].

To address the first topic, experimental and numerical signals in steady state and transient operation of an axial flow compressor were compared, both in the case of clean undistorted flow operation and distorted flow operation created by a screen placed in front of the machine. Experimental and numerical casing pressure signals were compared for a stable operating point close to nominal conditions. As far as the stable operation is concerned, instantaneous casing pressure measurements were analyzed using dynamic mode decomposition to extract the modal content of the signal and to highlight the effect of the screen.

As far as the detailed dynamics of the transient operation towards rotating stall are concerned, casing static pressure has been acquired with sensors distributed circumferentially and used to track the evolution of the perturbation during transient.

2. Experimental Setup

The experiments were performed on the low speed CME2 axial compressor operating at Arts et Métiers, Lille, France. Its main operating and geometrical parameters are listed in Table 1.

Table 1. Compressor parameters.

Rotational speed	3200	rpm
Design mass flow rate at 3200 rpm	5.3	kg/s
Design total to static pressure ratio at	1.03	
Rotor blade number	30	
Stator blade number	40	
Casing diameter	550	mm
Rotor tip chord	84	mm
Rotor tip stagger angle	54	°
Rotor tip gap	0.5	mm
Number of structural struts	4	

The test bench (Figure 1b,c) is equipped with 14 casing flash-mounted pressure sensors (Figure 2). Seven piezoresistive pressure transducers ENDEVCO 8510B are placed circumferentially at mid chord, while seven other piezoresistive pressure transducers ENDEVCO 8507C are mounted onto an instrumented window (Figure 1c) and form a line in the axial direction starting from 2 mm ahead of the leading edge of the blades and continuing up to the trailing edge. The 0° position is chosen at noon in Figure 1b, and positive angles are in the blades' rotation direction. The sampling rate is 100 kS/s. The rated pressure of

the transducers is 6.89 kPa, and the sensitivity after calibration varies between 23.1 and 29.8 mV/kPa. The error in % of the full scale is between 0.3 and 1.2.

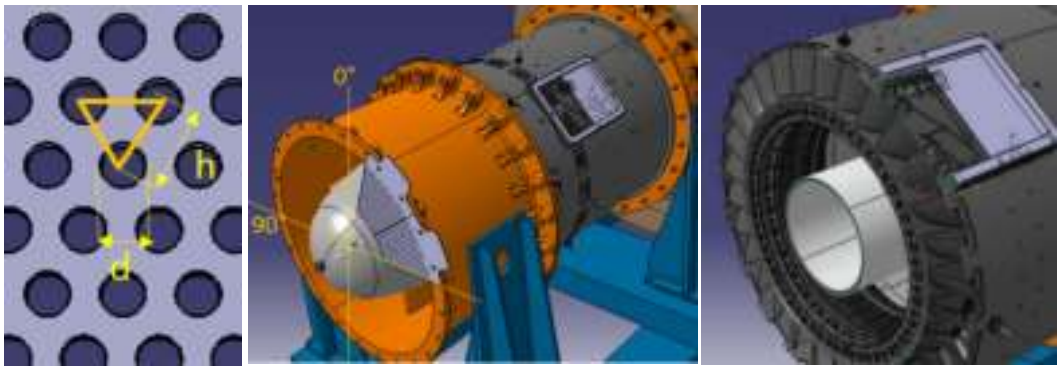

(**a**) (**b**) (**c**)

Figure 1. (**a**) CAD representation of the equilateral triangular pattern of the grid holes; (**b**,**c**) CAD representation of the CME2 compressor showing grid position with respect to instrumented window.

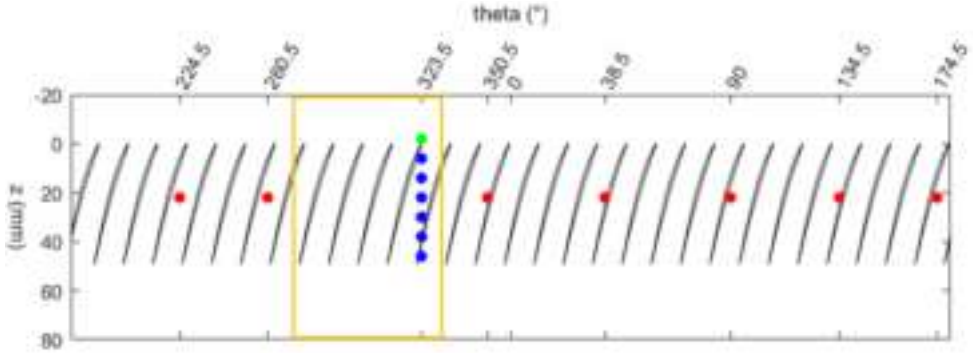

Figure 2. Scheme representing rotor blades and pressure probe locations highlighted in red (mid chord circumferential positions) and blue (axial position from $z = -2$ mm to $z = 50$ mm); probe used for DMD (green), wake of the grid (yellow).

The distortion is generated through distortion screens created from steel perforated plates installed one hydraulic diameter in front of the compressor. The plates are 2 mm thick with 3 mm diameter holes (d in Figure 1a) and 5 mm inter-hole distance (h in Figure 1a) and an equilateral triangle pattern (Figure 1a). The porosity, defined as perforated area divided by total area is $f = \frac{\pi}{2\sqrt{3}}\left(\frac{d}{h}\right)^2 = 33\%$. The plates were cut into angular sectors to mimic a circumferential distortion (Figure 1b). For the experiments, a sector of 60° has been installed between 270° and 330°; the estimated nondimensional pressure drop based on the velocity where the screen is placed (22 m/s) is 1.05.

3. Numerical Setup

Unsteady RANS computations are performed on this configuration with the ONERA compressible solver elsA [8] using a second-order in space Roe scheme, a first-order in time Backward Euler scheme and a scalar LUSSOR implicit method. The turbulent quantities are determined using the k-l two-equation model of [9]. The full annulus geometry is computed with the struts, rotor and stator rows, leading to a mesh of 122 million nodes as illustrated in Figure 3. The nodes in the strut, rotor and stator meshes are respectively 10, 70, 42 million. There are 88 and 121 nodes in the spanwise direction for the strut and stator components, respectively. In the rotor tip clearance, the number of spanwise nodes is 33. The geometry of the screen is not simulated; rather, the screen-induced distortion has been modelled by a total pressure drop directly applied at the inlet boundary condition. The inlet condition consists of of applying total pressure, total temperature, velocity direction and

turbulence variables (turbulent rate of 2%); the outlet boundary condition is applied with a static pressure at the hub and a radial equilibrium condition, and it has been used for both simulations with and without the grid. There were 3600 iterations per rotor revolutions used for the computations, and 6 complete revolutions were simulated for both clean and distorted cases. As far as the time periodicity of the numerical simulations is concerned, the criterion used consists of a periodic repeatability of the instantaneous mass flow for two consecutive revolutions with discrepancies of less than 0.1%. Time averaging was performed on a full rotation of the rotor.

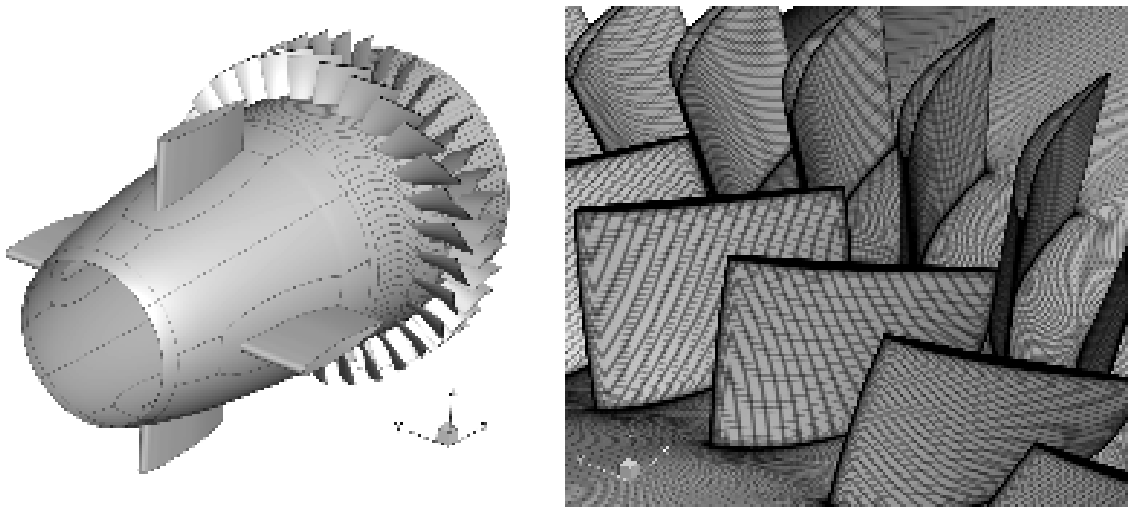

(**a**) (**b**)

Figure 3. (**a**) CFD domain; (**b**) grid views.

Two simulations were performed: a first one with a clean inlet flow, a second one with a pressure drop corresponding to the first screen used in the test. The two simulations without the grid and with the 60° grid converged toward a stable operating point, without rotating stall, at an average mass flow respectively of 4.853 kg/s and 4.848 kg/s respectively. Unsteady pressure was extracted from the calculations at the same fixed positions as the piezoresistive pressure transducers of the test bench.

4. Results

4.1. Stable Operation

A comparison was performed between the signals measured ahead of the rotor for the nondistorted and 60°-screen-distortion cases. The comparison was made using the Dynamic Mode Decomposition (DMD). The DMD was first proposed by [10], and it is a data-driven method that provides a way to decompose spatio–temporal measurements into a set of dynamic spatio–temporal modes derived from a local linearization of the system dynamics. The modes were limited to the postprocessing of the time-dependent pressure measurements as we did not combine multiple probes to include the spatial information in our DMD analysis.

The measurements of pressure in time were rearranged in a matrix H (Hankel matrix) by shifting them in time according to the number of modes we employed for reproducing each signal. Hence, the number of columns of H was equal to the number of modes that were used to approximate the signal (500 in the study); the number of rows corresponded to the number of time measurements considered in the postprocessed time window (5 s × 100 kS/s).

From the H matrix, two matrices X_1 and X_2 were created, X_2 being the time shifted matrix, and X_1 the matrix of the individual snapshots. The DMD computed the leading eigenmodes of the linear operator A that best advanced the data X_1 to X_2, i.e., ${X_2}^{\mathrm{N}} \approx \mathrm{A}\ {X_1}^{\mathrm{N}-1}$,

where N denotes the time of the current snapshot. For N→∞, hence marching continuously in time, the corresponding linear system reads

$$\frac{dX}{dt} = \mathcal{A}X. \tag{1}$$

When subjected to initial condition $X(0)$, the equation has the solution:

$$x(t) = \sum_{k=1}^{N} \psi_k \ \exp(\omega_k t) b_k \tag{2}$$

where ψ_k and ω_k are the eigenvectors and eigenvalues of the matrix $\mathcal{A}$, while b_k are the coordinates of $x(0)$ in the eigenvector basis. Getting back to the analogous time-discrete system with time step Δt, it yields

$$X_2 = A \ X_1 \tag{3}$$

with $A = \exp(\mathcal{A}\,\Delta t)$. Since the A matrix has generally a very large dimension, instead of computing directly the eigenvalues of A, we employed a rank-reduced representation of A. This rank-reduced representation of A was obtained using Singular Value Decomposition (SVD). The full algorithm employed in our study is explained in more details in [11].

First, DMD was applied to the experimental signals. In the present experiments, two different mass flow rates were chosen and casing static pressure from the sensors placed at $z = -2$ mm (green in Figure 2) was recorded for 5 s, which was approximatively 265 rotor revolutions. The first mass flow rate was 5 kg/s and it corresponded to a flow coefficient ϕ of 0.506 close to design point.

The second mass flow rate we investigated was 4.2 kg/s and it corresponded to a ϕ of 0.425, i.e., the last stable configuration before the onset of rotating stall in CME2. Figure 4a,b depicts the comparison between the DMD reconstruction and the raw signals experimentally obtained. On the same Figure, the error of the DMD reconstruction is plotted in orange. The DMD reconstruction is good, but it loses some accuracy when some nonperiodic peaks occur in the experimental signal at 5 kg/s, and it does not provide an accurate approximation of the grid distorted signal at a mass flow rate of 4.2 kg/s (not represented in Figure 4) because the signal was strongly nonperiodic.

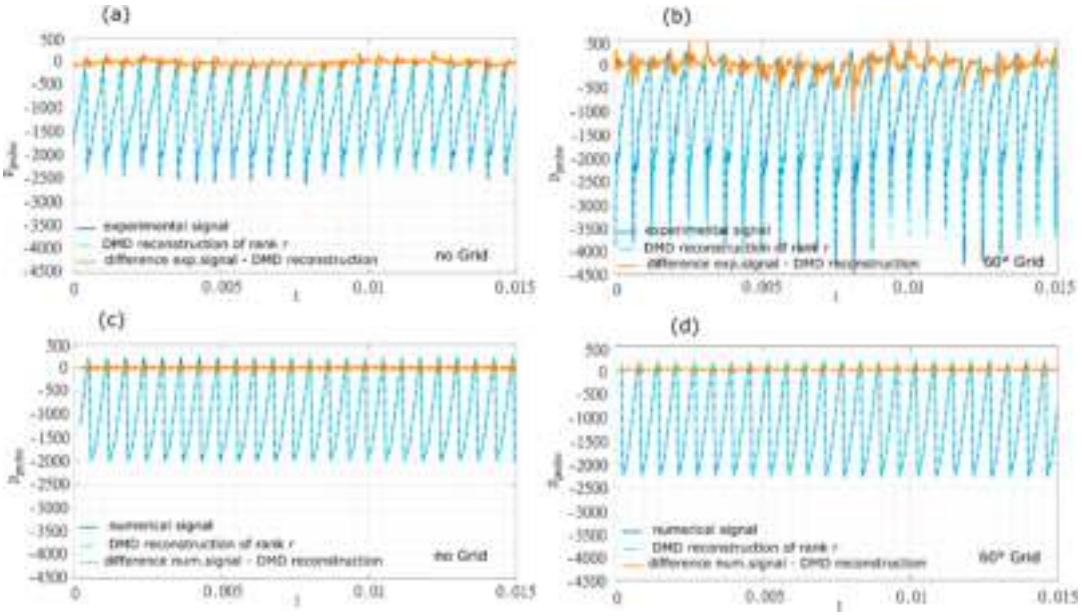

Figure 4. (**a**,**b**) Comparison between raw signal (blue) and DMD reconstruction (light blue) for the case of 5 kg/s; (**c**,**d**) comparison between raw numerical signal (blue) and DMD reconstruction (light blue) for the case of 4.85 kg/s. Difference between raw signal and DMD reconstruction plotted in orange.

A partial DMD reconstruction is shown in Figure 5a,b, where p_{DMD} indicates the reconstruction with 21 modes, p_1 the first mode reconstruction (the linear least-squares fit of the signal), p_2 the reconstruction up to the second order (linear least-squares fit plus the second mode with its complex conjugate), and so on. In Figure 5a,b, p_5 and p_9 respectively represent the DMD reconstruction with the minimum number of modes that have an error less or equal to 5% with respect to the DMD with 21 modes.

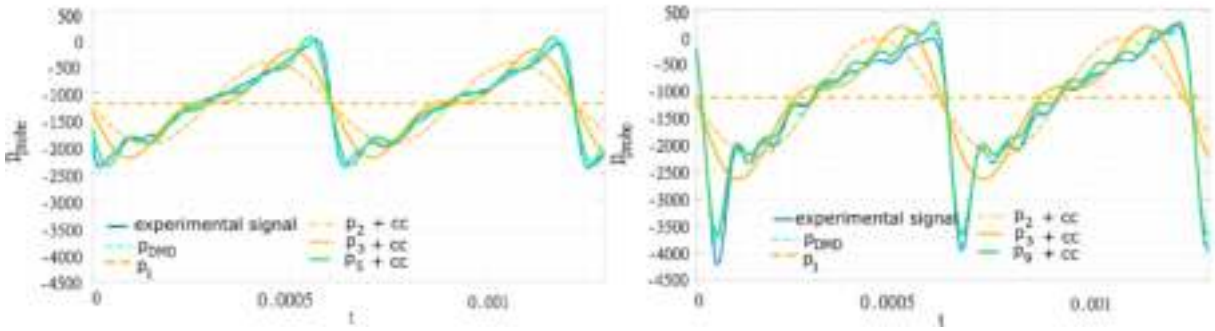

(**a**) (**b**)

Figure 5. Partial DMD reconstruction; p_1: least-squares fit, p_i + cc: DMD modes plus complex conjugate (cc) up to i th order. (**a**) 11 modes 5 kg/s without grid; (**b**) 19 modes 5 kg/s with 60° grid.

According to this criterion, the minimum number of DMD modes required to well reproduce the experimental signal was 11 for the nondistorted case at a mass flow rate of 5 kg/s. The required minimum number of modes grew to 19 when the grid was introduced. These additional modes can be partly explained by the presence of a low pressure peak in the signal, a trace of increased blade loading due to the locally reduced mass flow rate behind the grid. But we anticipate that this is not the only effect of the presence of the grid.

The DMD was then applied to numerical signals. The reconstruction (Figure 4c,d) was very good. For the numerical signals, the required number of DMD modes to well reproduce the signal was 13 no matter the presence of the grid (Figure 6a,b). Numerical simulations are thus losing some information compared to experiments.

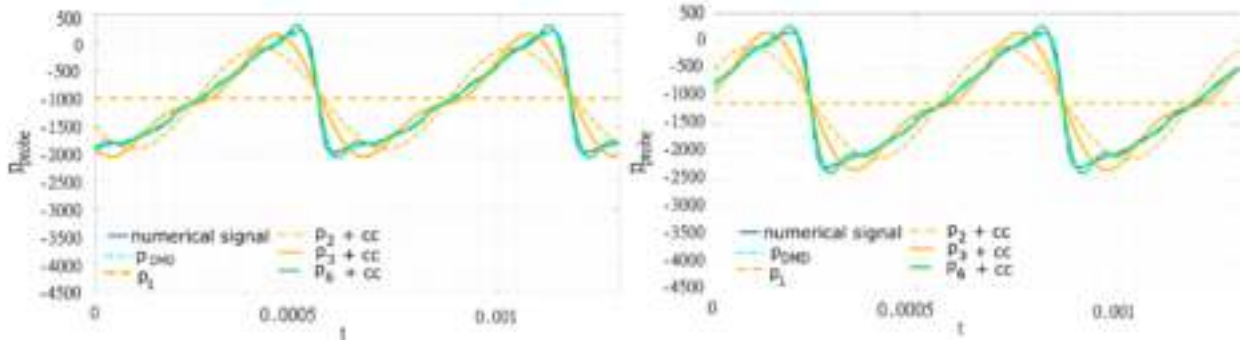

(**a**) (**b**)

Figure 6. Partial DMD reconstruction; p_1: least-squares fit, p_i + cc: DMD modes plus complex conjugate (cc) up to i th order; (**a**) 13 modes 4.85 kg/s without grid, (**b**) 13 modes 4.85 kg/s with 60° grid.

The first qualitative difference between the experimental and numerical signals was the presence of a sharp pressure drop in the experimental signal. Such a feature was not captured by the numerical simulation. A second difference was the presence of high-frequency oscillations in the experimental signal (Figure 5b). Modes with 5 and 10 oscillations per blade channel emerged. Their amplitudes were respectively the 25% and 7.5% of the amplitude of the main harmonic. Such modes can be related to the jets created by the holes of the grid. The blade channel measures 57 mm and the distance between the holes is 5 mm

so that there are 11 holes per blade channel. This feature already highlights the limitation of using a grid to reproduce a generic distortion since the grid geometry introduces in the flow some characteristic scales that are not existing in other types of distortion. Consistently, the comparison between Figures 5 and 6 shows that an inlet total pressure drop is too simplistic for modeling a screen-generated distortion.

In Figure 7, the eigenvalues obtained from applying SVD to the experimental signals are represented for the two mass flow rates investigated experimentally, with and without the presence of the 60° grid. The SVD eigenvalues are also represented for the numerical signals with and without the grid. The eigenvalues are normalized on the value of their total sum such that they represent the relative energy content of the various SVD modes. In the numerical signals (Figure 7b), the presence of the grid did not change the relative energy content of the modes. Moreover, in the experimental signals (Figure 7a,c) there were significant differences. We stress that the distribution of energy was different depending on the mass flow rate, even for nondistorted experimental flow. The first mode of the SVD (violet in Figure 7) had a relative energy of 32% at 5 kg/s, that decreased to 15% at 4.2 kg/s.

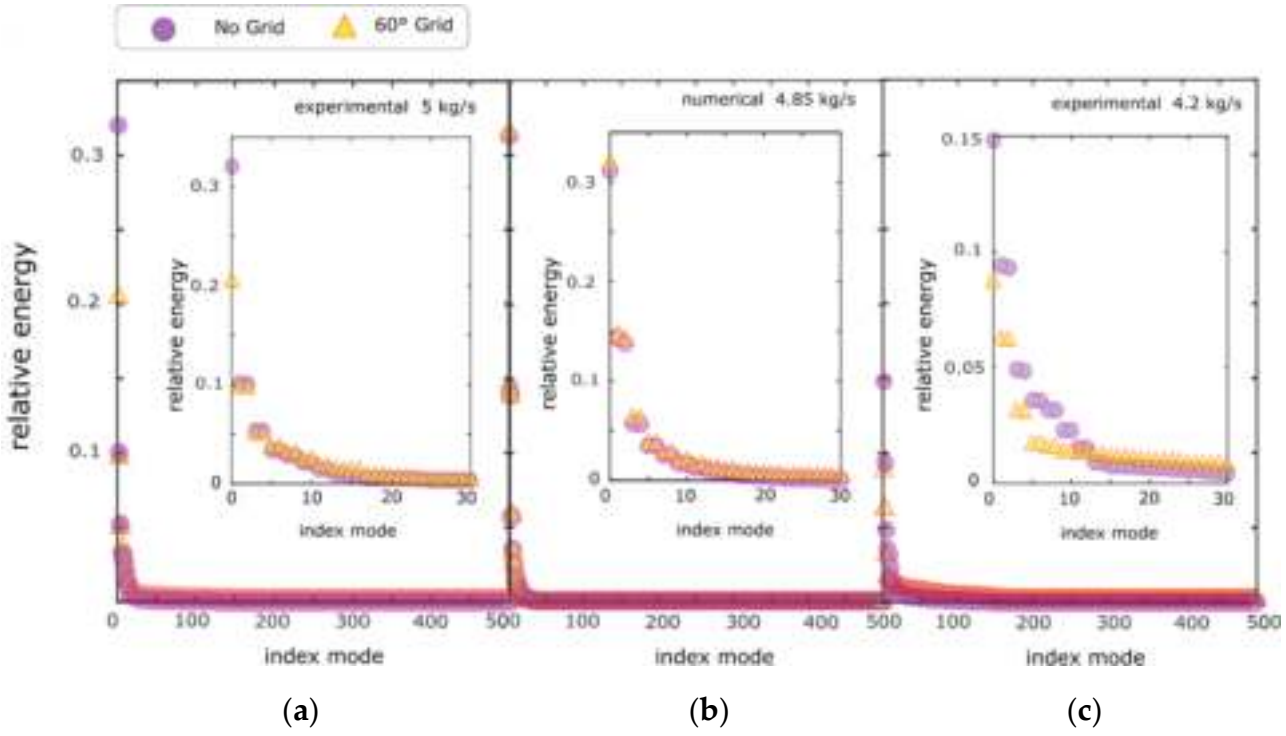

Figure 7. Relative energy in the modes calculated from SVD. Experimental signals. (**a**) 5 kg/s; (**c**) 4.2 kg/s; numerical signal (**b**) 4.85 kg/s.

Thus, as the stall limit is approached, signals were less periodic and the energy was redistributed from low frequencies to higher frequencies corresponding to higher index eigenvalues. The presence of the 60° screen had a similar effect on the redistribution of the energy of the SVD modes, i.e., part of the low-modes energy of the configuration without the grid was transferred to higher modes for the system with the grid. In fact, with the grid (orange in Figure 7), the relative energy of low index modes was lower than without the grid (violet in Figure 7), while the relative energy of high index modes with the grid was higher than without the grid.

The tendency was reproduced for both 5 kg/s and 4.2 kg/s. We speculate that a part of the energy redistribution was caused by the additional presence of the modes introduced by the local geometry of the grid.

4.2. Stall Inception

As shown in the previous section, the numerical simulations well captured the leading-order effect measured in the experimental signals for distorted configurations. We anticipate, however, that the grid-geometry-induced features observed in the experimental pressure measurements play a major role in the onset and decay of rotating instabilities. Since the numerical perturbation was modeled as a pressure drop, such a physical phenomenon cannot be studied with our computational simulations. Hence, in the following, only experimental measurements are presented.

As far as the stall inception process is concerned, the case without distortion screen and the case with the 60° distortion screen upstream of the instrumented window were compared. The throttling valve was closed progressively, starting from the last stable point to induce rotating stall. It has been observed, in previous works [12,13] that the perturbation arising in CME2 is always of spike type. A typical transition to stall is represented in Figure 8. The signals were filtered (cut frequency 800 Hz) to eliminate the blade passing frequency (1600 Hz). The tracking of the perturbation development was done by using cross correlation between each signal and a reference piece-wise signal composed of a typical spike, a stall cell and a transition between the two. The peaks of the correlation represent the time position of the perturbation for each sensors (red dots in Figure 8).

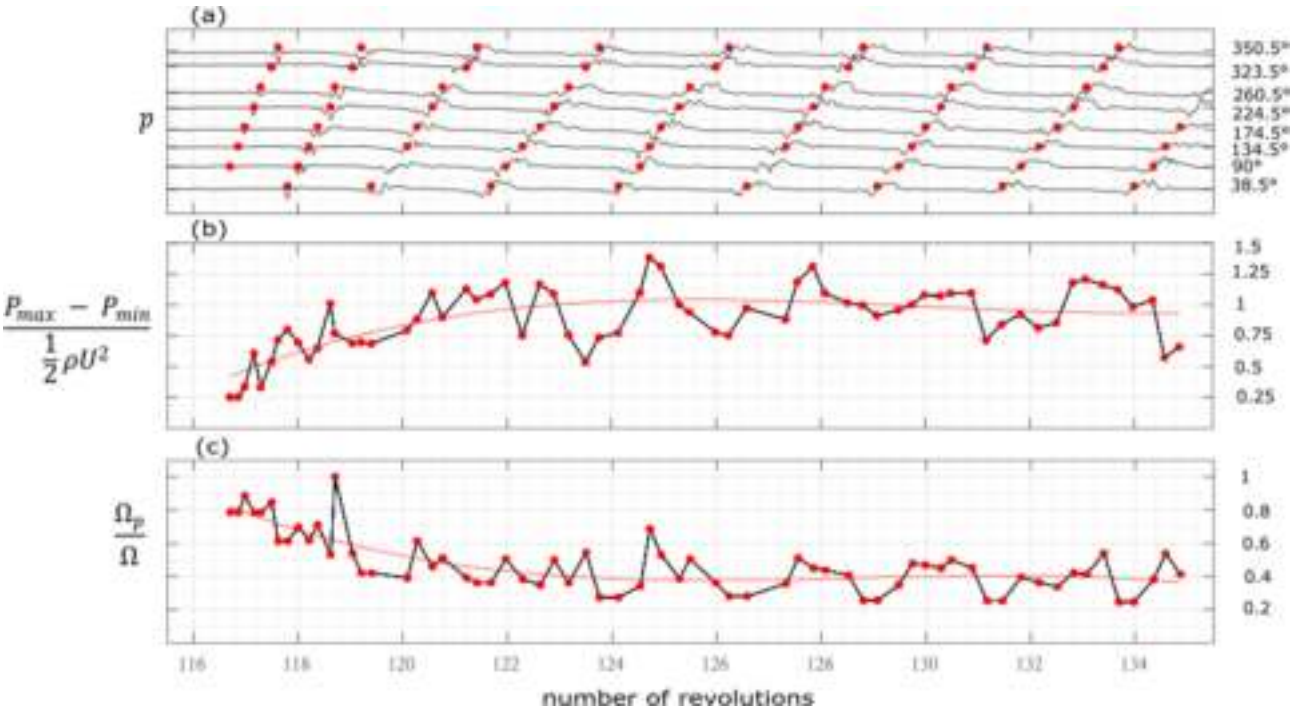

Figure 8. Stall transient with no grid; on the x axis the number of revolutions, on the y axis: (**a**) angular position of the signal, (**b**) non-dimensional pressure amplitude, (**c**) non-dimensional perturbation speed.

They were then used to derive the perturbation speed (Figure 8c). The peak-to-peak amplitude of the perturbation is also reported (Figure 8b). The main differences concern the starting point of the perturbation and the development of the perturbation during the first revolutions. The first difference is the stalling mass flow rate observed experimentally: 4.15 kg/s without grid and 4.23 kg/s with the 60° grid.

In the undistorted case, the spike usually starts in the region between 90° and 135°.

Such a feature has a very high reproducibility, most likely because the tip clearance in that region decreases and reaches the minimum value due to the imperfect circularity of the casing as already observed [13]. The perturbation then develops rapidly (in about

5 rotor revolutions) in amplitude, while its speed decreases from about 90% to 40% of the rotor speed.

In the distorted case, however (Figure 9), the perturbation arises just after the grid (around 30°). The explanation can be attributed to the fact that the region of highest incidence was located at the exit of the distorted region (in the direction of rotation) [14]. This is due to the pressure gradients created by the interaction of the low-pressure distorted stream and the undistorted one: these gradients created an upstream flow redistribution, so that the incidence at the entrance of the distorted region was reduced and the incidence at the exit was increased. In Figure 10, four repetitions of stall transient with the 60° grid are reported. The four transients were obtained throttling the compressor at a constant throttle speed, starting from the same mass flow rate corresponding to the last stable point of its characteristic curve. In the two cases in Figure 10a,c, after a period of growth, the perturbation vanished just before entering in the distorted region (represented with a black rectangle), which is exactly in the region of reduced incidence argument just discussed. The disappearance of the spike, however, was not always reproducible. It can occur multiple times before rotating stall, or it can also never occur (two cases in Figure 10b,d). The results reported in Figure 10 suggest that a threshold value in the perturbation amplitude at the beginning of the distorted region exists, above which the perturbation continues to grow. This threshold value is about 0.425 of the dynamic pressure based on the blade tip speed. There is thus a clear competition between the stabilizing effects of the low-incidence region existing at the distortion inlet and the proper dynamic of the instability.

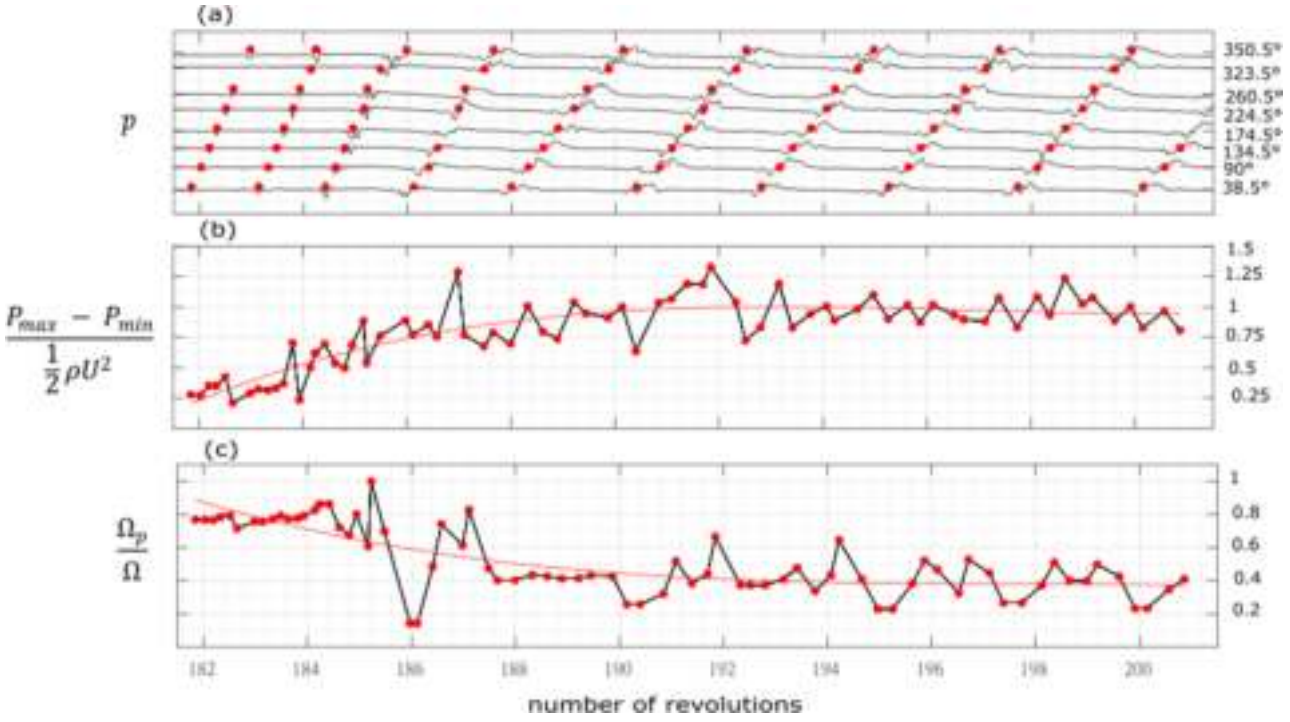

Figure 9. Stall transient with 60° grid; on the x axis the number of revolutions, on the y axis: (**a**) angular position of the signal, (**b**) non-dimensional pressure amplitude, (**c**) non-dimensional perturbation speed.

Moreover, this threshold value also marks two different stages of the development of instability (Figure 10): a first stage characterized by amplitudes lower than the threshold and constant rotational speed of the perturbation, and a second stage characterized by amplitudes higher than the threshold and decreasing speed of the perturbation.

This reflects the fact that when the perturbation started, nonlinear effects were weak, and were responsible for the saturation that limited the intensification of the perturbation, but the process of intensification of the perturbation did not affect the speed of the perturbation. Instead, as soon as the perturbation reached a high enough amplitude, nonlinear

effects became significant and led to a saturation of the intensification process, as well as to a remarkable slowdown of the convective velocity due to the enhanced inertia of the established perturbation.

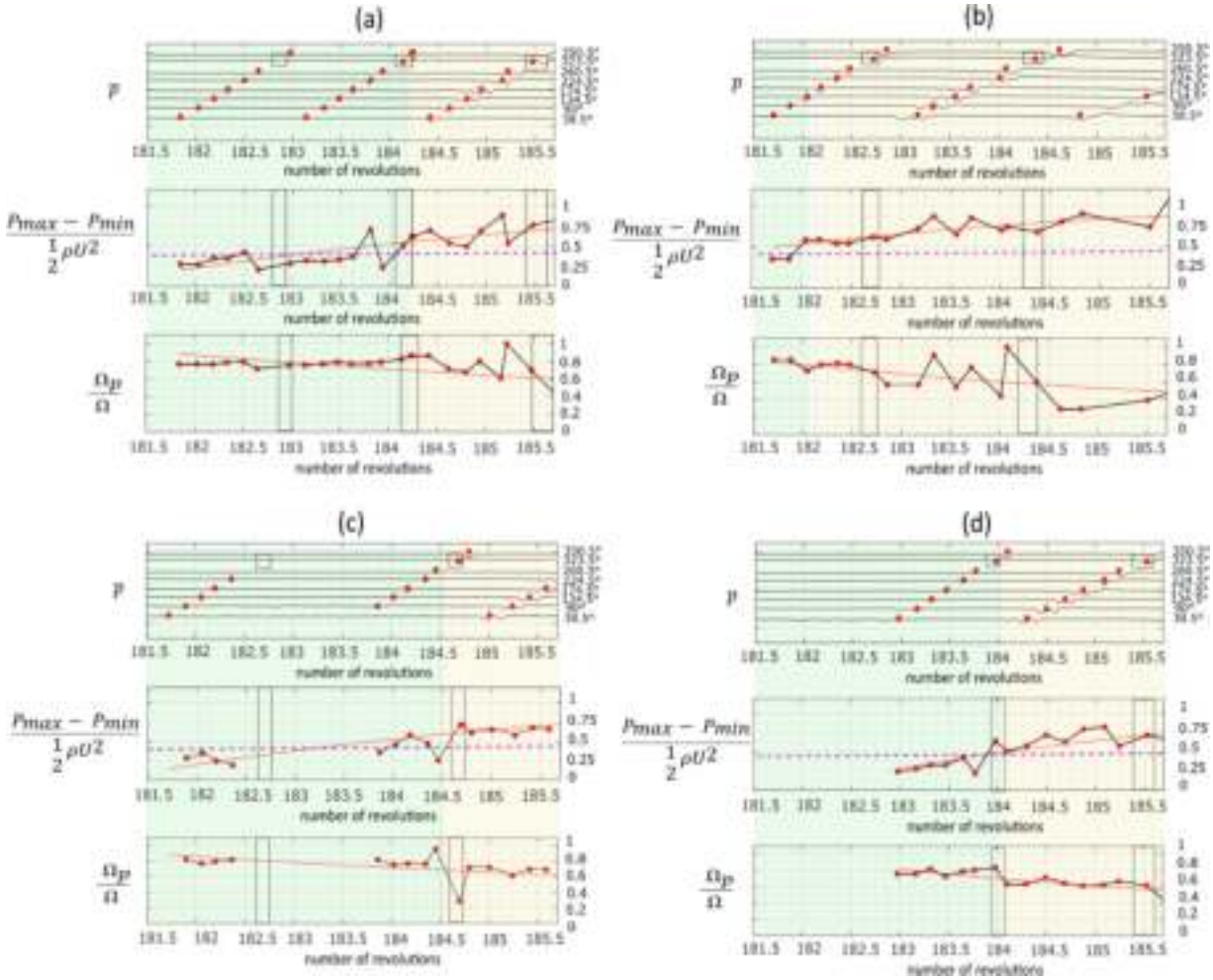

Figure 10. Four (**a**–**d**) repetitions of rotating stall transient with 60° grid. Black rectangles: position of the 60° grid. Dashed line in the bottom panel: threshold for spike development; red continuous line: polynomial fit, which appears also in Figures 8 and 9. Green background: part of the signal below threshold; yellow background: part of the signal above the threshold.

Apart from the initial stages of the perturbation, the experiments showed that the development into rotating stall is very similar, independently of the presence of the grid. The developed rotating stall cell has a speed corresponding to 40% of the rotational speed of the rotor, while its pressure amplitude is equal to the dynamic pressure based on the blade speed.

5. Conclusions

Unsteady casing pressure measurements were performed on an axial flow compressor, under clean flow and circumferential distorted flow, at two mass flow rates in the stable part of the compressor characteristics and at a varying mass flow rate, obtained throttling the valve from the last stable point to induce rotating stall. The analysis through DMD showed that the effect of the grid was to introduce new modes in the signal (both in the case of a real perforated plate and in the case of a simulated uniform low total pressure region). The modes introduced in the experimental signal have multiple oscillations per blade channel, reasonably due to the geometry of the holes of the grid, which are not

simulated in the numerical case. Moreover, the grid induces a redistribution of energy from low frequency modes to higher frequency modes.

Some variability in time of the onset of the spike perturbation was found, even if a correlation was confirmed between the spike occurrence and the location of the grid. Moreover, the spike dynamics seems to be determined by a critical pressure amplitude criterion.

Author Contributions: A.B.: experimental work, formal analysis, writing manuscript; B.G.: numerical work; P.J.: validation; O.R.: validation; F.R.: formal analysis, validation; R.B.: numerical work, validation, project administration, funding; A.D.: validation, supervision, project administration, funding. All authors have read and agreed to the published version of the manuscript.

Funding: The APC was founded by Euroturbo.

Institutional Review Board Statement: Not applicable.

Informed Consent Statement: Not applicable.

Data Availability Statement: The data will be available provided the consent of all the authors.

Acknowledgments: The work is supported by DGAC (the French Agency for Civil Aviation) through the SUBLIME research program.

Conflicts of Interest: The authors declare no conflict of interest.

Nomenclature

Roman		t	Time [s]
b	Initial amplitude of DMD modes	$U = \Omega r$	Blade velocity [m/s]
d	hole diameter of the grid [m]	v	Axial velocity [m/s]
DMD	Dynamic Mode Decomposition		
f	Porosity of the grid [-]	Greek	
h	grid inter-hole distance [m]	σ	Real part of ω
p	Static pressure [Pa]	$\phi = v/U$	Flow coefficient [-]
p_{DMD}	DMD reconstruction	ψ	Eigenvectors of DMD
r	Compressor mean radius [m]	ω	Growth rate of DMD modes
s	Diagonal matrix of the SVD	Ω	Compressor Angular velocity [rad/s]
SVD	Singular Value Decomposition	Ω_p	Perturbation angular velocity [rad/s]

References

1. Plas, A.P.; Sargeant, M.A.; Madani, V.; Crichton, D.; Greitzer, E.M.; Hynes, T.P.; Hall, C.A. Performance of a Boundary Layer Ingesting (BLI) Propulsion System. In Proceedings of the 45th AIAA Aerospace Sciences Meetings and Exhibit, Reno, NV, USA, 8–11 January 2007; p. 450.
2. Melick, H.C. *Analysis of Inlet Flow Distortion and Turbulence Effects on Compressor Stability*; NASA Technical Report No. 2-57110/3R-3071; NASA: Washington, DC, USA, 1973.
3. Reid, A.P. *The Response of Axial Flow Compressors to Intake Flow Distortion*; American Society of Mechanical Engineers: Newyork, NY, USA, 1969; Volume 79832. [CrossRef]
4. Calogeras, J.E.; Mehalic, C.M.; Burstadt, P.L. *Experimental Investigation of the Effect of Screen-Induced Total Pressure Distortion on Turbojet Stall Margin*; NASA TM X-2239; NASA: Washington, DC, USA, 1971.
5. Gunn, E.J.; Tooze, S.E.; Colin, Y. An experimental study of loss sources in a fan operating with continuous inlet stagnation pressure distortion. *J. Turbomach.* **2013**, *135*, 051002. [CrossRef]
6. Davis, M.; Hale, A.; Beale, D. An argument for enhancement of the current inlet distortion ground test practice for aircraft gas turbine engines. *J. Turbomach.* **2002**, *124*, 235–241. [CrossRef]
7. Perovic, D.; Hall, C.A.; Gunn, E.J. Stall Inception in a Boundary Layer Ingesting Fan. In Proceedings of the ASME Turbo Expo 2015, Montréal, QC, Canada, 15–19 June 2015. [CrossRef]
8. Cambier, L.; Heib, S.; Plot, S. The Onera elsA CFD software: Input from research and feedback from industry. *Mech. Ind.* **2013**, *14*, 159–174. [CrossRef]
9. Smith, B.R. A near wall model for the k-l two equation turbulence model. In Proceedings of the 25th Fluid Dynamics Conference, Colorado Springs, CO, USA, 20–23 June 1994; p. 2386. [CrossRef]
10. Schmid, P.J. Dynamic mode decomposition of numerical and experimental data. *J. Fluid Mech.* **2010**, *656*, 5–28. [CrossRef]
11. Kutz, J.N.; Brunton, S.L.; Brunton, B.W.; Proctor, J.L. *Dynamic Mode Decomposition*; Society for Industrial and Applied Mathematics: Philadelphia, PA, USA, 2016.

12. Veglió, M.; Dazin, A.; Bois, G.; Roussette, O. Unsteady Pressure Measurements of Spike Type Inception in Axial Compressor: Time Frequency Analysis and Averaging Procedure. In Proceedings of the 11th European Conference of Turbomachinery, Madrid, Spain, 23–27 March 2015.
13. Margalida, G.; Joseph, P.; Roussette, O.; Dazin, A. Comparison and sensibility analysis of warning parameters for rotating stall detection in an axial compressor. *Int. J. Turbomach. Propuls. Power.* **2020**, *5*, 16. [CrossRef]
14. Lesser, A.; Niehius, R. Transonic Axial Compressor with Total Pressure Inlet Flow Field Distortions. In *ASME Turbo Expo 2014: Turbine Technical Conference and Exposition*; American Society of Mechanical Engineers Digital Collection: New York, NY, USA, 2014. [CrossRef]

International Journal of
Turbomachinery Propulsion and Power

MDPI

Article

Turbine Broadband Noise Predictions Using Linearised Frequency Domain Navier-Stokes Solvers †

Ricardo Blázquez-Navarro * and Roque Corral

Department of Fluid Mechanics and Aerospace Propulsion, School of Aeronautics and Space, Universidad Politécnica de Madrid, 28040 Madrid, Spain; roque.corral@upm.es
* Correspondence: ricardo.blazquez@upm.es
† This paper is an extended version of our contribution to the 14th European Turbomachinery Conference, Gdansk, Poland, 12–16 April 2021.

Abstract: A linear frequency domain Navier-Stokes solver is used to retain the influence of turning, thickness, and main geometric parameters on turbine broadband noise. The methodology has been applied to predict the broadband interaction noise produced by a representative low-speed low-pressure turbine section. The differences in the spectra with respect to those yielded by state-of-the-art flat plate based methodologies are up to 6 dB. The differences are caused by multiple effects that semi-analytical methodologies do not account for. The most important are blade thickness and turning, which have been studied separately to quantify their impact on the broadband noise footprint. The influence of changing the turbine operating conditions has been discussed as well. The outlet sound pressure level scales with the third and second power of the inlet and outlet Mach number, respectively, for constant turbulence intensity, within most of the frequency range considered.

Keywords: aeroacoustics; broadband noise; low-pressure turbine; linearised Navier-Stokes

check for updates

Citation: Blazquez-Navarro, R.; Corral, R. Turbine Broadband Noise Predictions Using Linearised Frequency Domain Navier-Stokes Solvers. *Int. J. Turbomach. Propuls. Power* **2021**, *6*, 42. https://doi.org/10.3390/ijtpp6040042

Academic Editor: Antoine Dazin

Received: 3 August 2021
Accepted: 10 November 2021
Published: 12 November 2021

Publisher's Note: MDPI stays neutral with regard to jurisdictional claims in published maps and institutional affiliations.

Copyright: © 2021 by the authors. Licensee MDPI, Basel, Switzerland. This article is an open access article distributed under the terms and conditions of the Creative Commons Attribution (CC BY-NC-ND) license (https://creativecommons.org/licenses/by-nc-nd/4.0/).

1. Introduction

Since the last decade, there has been an increasing concern regarding the impact of turbine-generated broadband noise in the context of civil aviation. Nesbitt [1] described what he considered a 'turbine noise storm' caused by the confluence of several design choices. Namely, their reduced blade-count and solidity, the removal of acoustic liner treatments to reduce engine weight, and the reduction of noise emissions by other engine components. Nesbitt claimed that it is necessary to develop tools that can predict turbine noise with sufficient accuracy to understand its sources and reduce them in the future. Regarding turbine noise sources break-down, Serrano et al. [2] quantified experimentally the relative importance of turbine broadband noise, which can result in being dominant in many operating points and designs and hence, there is a need of industrial methods to predict it accurately. Turbulent wakes generated by a turbine row (see Figure 1) impinge on the downstream one, giving rise to acoustic waves with a broadband energy content.

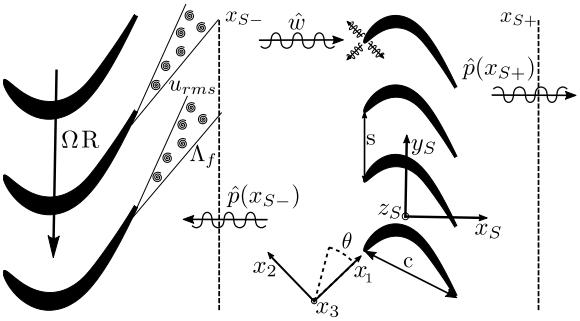

Figure 1. General Scheme of rotor-stator interaction broadband noise.

While industrial predictions of fan broadband noise have been based traditionally on the flat plate response to incoming vortical disturbances, this is much less justified for turbines. This approach can be valid for plate-like shapes such as fans, but it is unclear how to define an equivalent flat plate for a turbine, and more importantly, what the accuracy of such predictions would be. Several physical effects are not modelled by flat-plate methodologies. Among them, the influence of blade thickness and blade turning stands out, which entails a relevant flow acceleration.

The effect of blade thickness on broadband noise has been studied analytically by Gershfeld [3] and Evers and Peake [4], numerically by Gill et al. [5] and Gea-Aguilera et al. [6], and experimentally by Devenport et al. [7] within the past years, to cite some examples. The most extended conclusions are that thick airfoils lead to weaker broadband noise footprints, especially at high frequencies and in the downstream arc, as numerically shown by Gea-Aguilera et al. [6].

On the other hand, the impact of blade turning has been analysed analytically by Myers and Kerschen [8] and Evers and Peake [4], numerically by Gea-Aguilera et al. [6] and Paruchuri et al. [9], and experimentally by Devenport et al. [7], among other authors. There is a general agreement that camber has a very limited impact on the broadband noise footprint, impacting only the azimuthal modal decompositions, i.e., directivity, as shown by Myers and Kerschen [8] and Paruchuri et al. [9].

All these works, and some others not mentioned here, are either asymptotic studies or are applied to geometries with moderate thickness and low camber as those found in Fan/OGV interaction. However, for turbine geometries, thickness and camber can be very important, and the conclusions extracted from the past may not be applicable.

To shed light on the influence of the turning, thickness, and main geometric parameters on turbine broadband noise, the use of a computationally efficient linear frequency domain Navier-Stokes solver [10] is proposed. The solver runs on commodity GPUs [11], enabling the computation of the broadband noise spectra within an industrial design loop. The method has been validated previously for Fan/OGV interaction against experimental data and in a numerical benchmark in the context of the TurboNoiseBB EU project [12,13].

The objective of the present work is to assess quantitatively and qualitatively the effect of the airfoil geometry on turbine broadband noise, compare the results to the flat plate simplifications, and finally, investigate the impact of the operating point. The comparison of the present methodology to experimental data is postponed for the future since it requires other building blocks such as accurate turbulence modelling, and transmission effects through the turbine stages.

2. Methodology

The methodology has been thoroughly described for multi-stage applications [13] however, for completeness, it will be briefly described herein. Synthetic turbulence methods aim at reproducing a given turbulent spectrum by explicitly introducing vortical content into the simulation domain. They consist of three well-differentiated steps, namely incoming turbulence modelling, computation of the blade's acoustic response to the synthetic turbulence, and post-processing of the radiated acoustic power. The original methodology can retain certain 3D effects by using several strips at different radial positions. However, the analyses will be restricted here to a single strip for simplicity. For more information about three-dimensional effects, please refer to Blázquez-Navarro and Corral [13].

2.1. Turbulence Modelling

When turbulent wakes impact a turbine row, they give rise to broadband sound generation. These wakes can be characterised by their velocity power spectral density (PSD). Synthetic turbulence methods aim at reproducing the turbulence spectral characteristics through the summation of individual vortical gusts [14]. Their interaction with the turbine cascade is modelled under the Rapid Distortion Theory (RDT) hypothesis [15], which allows

linearising their propagation through the airfoil if the fluctuations are small compared to the mean flow and the eddies remain coherent through the blade passage.

Since usually experimental data or results from scale-resolved simulations are not available, certain assumptions shall be made to build the turbulent spectrum. In the present work, the synthetic turbulent spectrum is built using the Liepmann isotropic model Liepmann [16]. Its upwash component (x_2 direction in Figure 1), which is the most relevant one for noise generated by thin bodies [17], results:

$$\tilde{\Phi}_{22}(\tilde{\mathbf{k}}) = \frac{2}{\pi^2}\frac{(\tilde{k}_1^2 + \tilde{k}_3^2)}{(1+\tilde{k}^2)^3} \tag{1}$$

where $\tilde{\Phi}_{22} = \Phi_{22}/(u_{\text{rms}}^2 \Lambda_f^3) = \tilde{\Phi}_{22}(\tilde{\mathbf{k}})$ is the dimensionless velocity wave-number spectrum, which is a function of the wave-vector, $\mathbf{k}$, non-dimensionalised by the turbulence longitudinal integral length-scale, Λ_f: $\tilde{\mathbf{k}} = \mathbf{k}\Lambda_f = (\tilde{k}_1, \tilde{k}_2, \tilde{k}_3)$ and $\tilde{k}^2 = \tilde{k}_1^2 + \tilde{k}_2^2 + \tilde{k}_3^2$. The turbulence integral length-scale, Λ_f, and the velocity root mean square value, u_{rms}, are usually characterised by the RANS simulation of the previous row [18]. Since the purpose of this paper is not to compare numerical predictions against empirical data, reference data from the literature will be used.

The non-dimensional wave-vector $\tilde{\mathbf{k}} = (\tilde{k}_1, \tilde{k}_2, \tilde{k}_3)$ of the perturbation is not a degree of freedom that can be chosen when performing a numerical simulation. Instead, the excitation frequency, ω, and the azimuthal, β, and spanwise, γ, wave-numbers have to be explicitly imposed. The former is related to the streamwise wave-number using the hypothesis of Frozen Turbulence, i.e., the turbulent waves are assumed to be convected at the mean flow speed. The rest are computed using trigonometric relationships:

$$\tilde{k}_1 = \frac{\omega \Lambda_f}{V_0};\ \ \tilde{k}_2 = -\frac{\omega \Lambda_f}{V_0}\tan\theta + \frac{\tilde{\beta}}{\cos\theta};\ \ \tilde{k}_3 = \tilde{\gamma} \tag{2}$$

where V_0 is the mean flow velocity and θ is the velocity mean flow angle, depicted in Figure 1. The spectrum is discretised into upwash vortical gusts of prescribed frequency and wavelength, $w = \hat{w}_{\mathbf{k}} e^{i(\mathbf{k}.\mathbf{x}+\omega t)}$. Its amplitude, $\hat{w}_{\mathbf{k}}$, is a function of the wavenumber and the bandwidth used in the discretisation, $(\Delta k)^3 = \Delta k_1.\Delta k_2.\Delta k_3$. We can define a dimensionless perturbation, $\hat{\tilde{w}}$, which is directly related to the turbulent spectrum:

$$\hat{\tilde{w}}_{\mathbf{k}}^2 = \left(\frac{\hat{w}_k}{(\Delta\tilde{k})^{3/2} u_{rms}}\right)^2 = \frac{1}{(\Delta\tilde{k})^3} \int_{k_1}^{k_1+\Delta k_1} \int_{k_2}^{k_2+\Delta k_2} \int_{k_3}^{k_3+\Delta k_3} \tilde{\Phi}_{22}(\tilde{\mathbf{k}}) d\tilde{k}_1.d\tilde{k}_2.d\tilde{k}_3 \simeq \tilde{\Phi}_{22}(\tilde{\mathbf{k}}) \tag{3}$$

To keep a simpler formulation than in a previous publication [13], and as previously done by Ju et al. [19], the vortical gusts, which are sub-critical, i.e., do not produce any cut-on response, are a priori filtered out. This is performed to avoid an over-prediction of the number of cut-on modes that would occur in a purely 2D case leading to large over-predictions of the resulting spectra. Thus:

$$\hat{\tilde{w}}_{\mathbf{k}}^2|_{2D} = 2\int_0^{k_3^*} \tilde{\Phi}_{22}(\mathbf{k}) d\tilde{k}_3 \tag{4}$$

with

$$\tilde{k}_3^* = M\tilde{k}_1(1 - M_x^2)^{-1/2} \tag{5}$$

After this pre-filtering process, the problem becomes fully bi-dimensional.

2.2. Response Computation

The modelling of the interaction of the turbulent spectrum with the turbine gives rise to the resolution of a large number of gusts with different ω, β which build-up the unsteady response of the OGV cascade, $\mathbf{u}(\mathbf{x}, t)$:

$$\mathbf{u}(\mathbf{x}, t) = \sum_{n=-\omega_{max}/\Delta\omega}^{\omega_{max}/\Delta\omega} [\sum_{\mu=\mu_n^-}^{\mu_n^+} \hat{\mathbf{u}}_{\omega(n)}(\beta(\mu), \mathbf{x}) e^{i\omega(n)t}] \tag{6}$$

where $\omega(n) = n\Delta\omega$, $\beta(\mu) = \mu\Delta\beta$ are a discrete set of frequencies and inlet wavenumbers. The summation limit $\mu_n^{\pm}$ is chosen at each frequency to sample a certain fraction of the TKE, which in this work is 90% of the total. The explicit dependence of the wave-numbers on the summation indices will be omitted whenever possible to avoid unnecessary overloading of the nomenclature. The interaction of the airfoil cascade with each individual gust is solved in the frequency domain. Thus, thousands of linearised Navier-Stokes (LNS) simulations are required to compute the noise spectrum. A time instant solution can be reconstructed through the summation of all the simulations as shown in Equation (6) and displayed in Figure 2 for illustrative purposes.

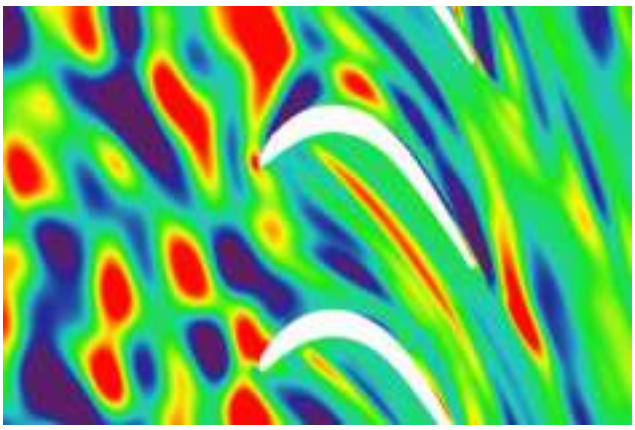

Figure 2. Time-instant reconstruction of vertical velocity, v', associated with the synthetic turbulent spectrum.

As mentioned above, the acoustic response is computed using a frequency-domain linearised Navier-Stokes Solver [10]. The methodology is explained with the Linearised Euler Equations (LEE) for simplicity even though the problem actually solved retains viscous effects. The extension of the ideas presented here to the solution of high Reynolds number viscous flows is straight forward. The flow is decomposed into a mean base flow, $\mathbf{U}_0(\mathbf{x})$ and a small perturbation $\mathbf{u}(\mathbf{x}, t) \ll \mathbf{U}_0$, i.e., $\mathbf{U}(\mathbf{x}, t) = \mathbf{U}_0(\mathbf{x}) + \mathbf{u}(\mathbf{x}, t)$. The base flow is obtained solving the nonlinear problem $\mathbf{A}(\partial\mathbf{U_0}/\partial x) + \mathbf{B}(\partial\mathbf{U_0}/\partial y) = \mathbf{F}$, which in practice is done using a RANS code known as Mu^2s^2T [20]. The perturbations are solved with the linear counter-part of the same code [10]. If the problem is assumed harmonic in time, i.e., $\mathbf{f} = \hat{\mathbf{f}}_\omega e^{i\omega t}$ and $\mathbf{u} = \hat{\mathbf{u}}_\omega e^{i\omega t}$, the linearised Euler equations can be Fourier-transformed, leading to:

$$\left(i\omega\mathbf{I} + \mathbf{A}_0\frac{\partial}{\partial x} + \mathbf{B}_0\frac{\partial}{\partial y}\right)\hat{\mathbf{u}}_\omega = \mathcal{L}(\mathbf{U}_0, \omega)\hat{\mathbf{u}}_\omega = \hat{\mathbf{f}}_\omega \tag{7}$$

where $\mathbf{A}_0(\mathbf{U}_0)$ and $\mathbf{B}_0(\mathbf{U}_0)$ are the Jacobian matrices particularised at $\mathbf{U} = \mathbf{U}_0 = (\rho_0\, u_0\, v_0\, p_0)^T$, $\hat{\mathbf{u}}_\omega = (\hat{\rho}_\omega\, \hat{u}_\omega\, \hat{v}_\omega\, \hat{p}_\omega)^T$ is the vector of perturbed variables, and $\hat{\mathbf{f}}_\omega$ contains just the small unsteady perturbations injected through the inlet. $\mathbf{I}$ is the identity matrix and $\mathcal{L}$ a linear operator which depends on the base flow and the frequency. The latter is actually discretised using a second-order accurate scheme to obtain the discrete operator $\mathcal{L}^D$, but the super-index is omitted for clarity. The harmonic solution can be formally solved as $\hat{\mathbf{u}}_\omega$=$\mathcal{L}^{-1}\hat{\mathbf{f}}_\omega$,

though in practice the inverse of $\mathcal{L}$ is never computed. The forcing term associated with the synthetic turbulent spectrum, $\hat{\mathbf{f}}_\omega$, in practice also depends on β and is expressed as:

$$\hat{\mathbf{f}}_\omega(\mathbf{x}_S^-, \beta) = \hat{v}_{\omega,\beta}\mathbf{e}_w^R e^{i(\omega t+\beta y_S)} = \hat{v}_{\omega,\beta}(0 \quad -\beta/k_x \quad 1 \quad 0)^T e^{i(\omega t+\beta y_S)} \tag{8}$$

where $\mathbf{e}_w^R$ is the right eigenvector associated with a vortical wave and $\hat{v}_{\omega,\beta}$ is the Fourier component of the perturbed velocity along the inlet, which is proportional to the upwash velocity component, $\hat{w}_{\omega,\beta}$. The readers are referred to Corral et al. [10], Burgos et al. [20] and Blázquez-Navarro and Corral [13], respectively, for detailed information about the solver numerics and the mesh criteria established to perform broadband noise predictions.

2.3. Post-Processing

The incoming vortical perturbation with azimuthal wavenumber β is scattered by the airfoils, giving rise to acoustic modes that conform the solution $\hat{\mathbf{u}}_\omega(\beta)$. In order to post-process $\hat{\mathbf{u}}_\omega(\beta)$, the solution at the inlet and the outlet ($x = x_S^-$ and $x = x_S^+$ in Figure 1, respectively) is Fourier transformed in the azimuthal direction:

$$\hat{\mathbf{u}}_\omega(\beta, x_S^\pm) = \sum_{\epsilon=-\infty}^{\infty} \hat{\mathbf{u}}^\pm_{\omega,\varphi(\epsilon)} e^{i\varphi(\epsilon)y} = \sum_{r=-\infty}^{\infty} \hat{\mathbf{u}}^\pm_{\omega,\check{\beta}(r)} e^{i\check{\beta}(r)y}. \tag{9}$$

where $\varphi(\epsilon) = \epsilon\Delta\varphi$ is an azimuthal wave-number used to compute the Fourier Transform. Nonetheless, the only non-null azimuthal modes that result from the Fourier Transform are the Tyler and Sofrin Modes, $\check{\beta}(r) = \beta + rV/R$. $\hat{\mathbf{u}}^\pm_{\omega,\check{\beta}(r)}$ is the r^{th} Tyler-Sofrin mode of the solution $\hat{\mathbf{u}}_\omega(\beta)$ at $x_S^\pm$, obtained applying the spatial Fourier operator in the circumferential direction, i.e., $\hat{\mathbf{u}}^\pm_{\omega,\check{\beta}} = \mathcal{F}_\theta \hat{\mathbf{u}}_\omega(\beta, x_S^\pm)$. Next, the pressure associated with the outgoing waves, $\hat{p}^{(a)}_{\omega,\check{\beta}}(x_S^\pm)$, is obtained assuming a uniform flow-field in these regions.

$$\hat{p}^{(a)}_{\omega,\check{\beta}}(x_S^\pm) = \mathbf{e}^L_{p^\pm} \hat{\mathbf{u}}_{\omega,\check{\beta}} \tag{10}$$

where $\mathbf{e}^L_{p^\pm}$ is the left eigenvector of the 2D LEEs of either the downstream (+) or upstream (−) running pressure waves. Within the same wave-splitting process, the cut-off acoustic waves are filtered out and do not contribute to the pressure spectrum. Thus, the acoustic perturbations upstream and downstream of the turbine row, $\hat{p}_{\omega,\check{\beta}}(x_{S\pm})$, are the result of applying a concatenation of different linear operators over each harmonic of the turbulent spectrum. These can be more conveniently expressed in non-dimensional form, thus obtaining:

$$\hat{\tilde{p}}^{(a)}_{\omega,\check{\beta}} = \frac{\hat{p}^{(a)}_{\omega,\check{\beta}}}{(\Delta\tilde{k}_1\Delta\tilde{k}_2)^{1/2}\rho_0(x_S^-)V_0(x_S^-)u_{\text{rms}}} = \tilde{\mathbf{e}}^L_{p^\pm}\mathcal{F}_\theta\widetilde{\mathcal{L}}_S^{-1}\mathbf{e}^{\mathbf{R}}_{\mathbf{w}}\hat{\tilde{v}}_{\omega,\beta} \tag{11}$$

where $\widetilde{\mathcal{L}}^{-1}$is the dimensionless linearised Navier-Stokes operator. It is readily seen that the acoustic response is proportional to the incoming gust strength, $\hat{\tilde{v}}_{\omega,\beta}$. The pressure PSD can be then computed as:

$$S^{pp}_{\omega,\beta}(x_{S\pm}) = \frac{1}{\Delta\omega\Delta\beta}\sum_{r=-\infty}^{\infty}\sum_{\mu=-\infty}^{\infty}|\hat{p}_{\omega,\check{\beta}(\mu,r)}|^2\delta(\beta - \check{\beta}(\mu,r)) \tag{12}$$

where $S^{pp}_{\omega,\beta}$ contains the squared summation of all the vortical waves with impinging azimuthal wave-number $\beta(\mu) = \mu\Delta\beta$ that produce an acoustic response with wave-number $\check{\beta}(\mu,r) = \beta(\mu) + rV/R$. This actually means that sources with different β are assumed to

be uncorrelated. This result can be expressed more generally by using the non-dimensional variable $\hat{\tilde{p}}$, as defined in Equation (11), leading to a non-dimensional pressure PSD:

$$S^{pp}_{\omega,\beta} = \frac{1}{\Delta\omega\Delta\beta}\sum_{r=-\infty}^{\infty}\sum_{\mu=-\infty}^{\infty}\left(|\hat{\tilde{p}}_{\omega,\breve{\beta}}|(\Delta\tilde{k}_1\Delta\tilde{k}_2)^{1/2}\rho_0(x_S^-)V_0u_{\text{rms}}\right)^2\delta(\beta-\breve{\beta}) \tag{13}$$

where the subindices have been omitted for clarity. Hence:

$$\tilde{S}^{pp}_{\omega,\beta} = S^{pp}_{\omega,\beta}\left(\frac{\Lambda_f^2\rho_0^2V_0u_{\text{rms}}^2}{\cos\theta}\right)^{-1} = \sum_{r=-\infty}^{\infty}\sum_{\mu=-\infty}^{\infty}||\hat{\tilde{p}}_{\omega,\breve{\beta}}|^2\delta(\beta-\breve{\beta}) \tag{14}$$

where the identities $\Delta k_2\cos\theta = \Delta\beta$ and $\Delta\tilde{k} = \Delta k\Lambda_f$ have been used. Finally, upon integration along the azimuthal wave number and expressing S^{pp}_{ω} in non-dimensional form it is readily obtained:

$$\tilde{S}^{pp}_{\omega}(x_{S\pm}) = S^{pp}_{\omega}\left(\Lambda_f\rho_0^2V_0u_{\text{rms}}^2\right)^{-1} = \sum_{\epsilon=-\infty}^{\epsilon=\infty}\tilde{S}^{pp}_{\omega,\beta(\epsilon)}(x_{S\pm})\Delta\tilde{k_2} \tag{15}$$

where $\beta(\epsilon) = \epsilon\Delta\beta$ and $\Delta\beta = \Delta k_2\cos\theta$ is the bandwidth employed to discretise the azimuthal wave-numbers.

The cross contribution to the acoustic power of pairs of waves with either different, ω, or β is as well null since they are considered uncorrelated sources with random phases between them. As usually in aeroacoustics applications, the sound loudness is represented in logarithmic scale, by means of a Normalised Sound Pressure Level, $\text{NSPL} = 10\log(\tilde{S}^{pp}_{\omega}/10^{-11})$, where no reference pressure is needed as $\tilde{S}^{pp}_{\omega}$ is already non-dimensional, but an arbitrary factor is introduced to obtain a positive spectrum.

3. Results

The presented methodology has been applied to a representative section of a modern aeronautical low-pressure turbine. The geometry selected corresponds to a section that has been analysed numerically [21] and tested [22] for aeroelastic purposes. The total turning is slightly higher than 100°, and its maximum relative thickness is about 12%. Several Operating Points (OP) have been considered however, as they all share the following parameters:

$$\text{Re}\sim 5\cdot 10^5 \quad \tilde{\Lambda}_f = 0.075 \quad s/c = 0.855 \quad \text{V} = 70 \quad \theta_1 = 44^\circ \quad \theta_2 = -59^\circ$$

where V represents the number of blades of the cascade, s/c is the pitch to chord ratio and Re is the Reynolds number. Note that the sub-indices 1 and 2 indicate respectively properties at the inlet and outlet axial stations, i.e., $\theta(x_S^-) = \theta_1$. A baseline operating point, OP1, which can be considered as the On-Design conditions, has been run. Several modifications have been performed to the boundary conditions, leading to the rest of the OPs described in Table 1.

Table 1. Definition of the operating points.

OP	$p_2/p_{t,1}$	i	M_1	M_2
OP1	0.68	0°	0.43	0.75
OP2	0.68	10°	0.56	0.75
OP3	0.83	10°	0.43	0.51
OP4	0.86	0°	0.30	0.44
OP5	0.86	10°	0.38	0.44
OP6	0.919	10°	0.30	0.34

3.1. Comparison with Flat Plate Based Methods

The first part of the analysis assesses the suitability of industry state-of-the-art flat plate methodologies to predict broadband noise of low-pressure turbine airfoils. The impact of the airfoil geometry on broadband noise predictions has been studied thoroughly in the literature with a focus on the fan outlet-guide-vanes. For these configurations, there is an extended agreement that the airfoil geometry impact on broadband noise is small, up to the highest frequencies of interest [4,6,23], since the airfoils are thin and feature a low camber. Recently, the present methodology has been applied to a modern Fan, concluding that the effect of the OGV detailed geometry on sound generation is, in general, small [12,13]. This section compares the results obtained accounting for the airfoil geometry with those obtained by replacing it with a flat plate cascade. Since which one is the best-suited equivalent flat plate is not apparent, several approaches are compared herein.

A broadband noise prediction has been performed at OP1, for reduced frequencies between $f_{\text{red}} = 2\pi fc/V_0 = 0.75$ and 25. The maximum reduced frequency corresponds approximately to 10^4 Hz. Figure 3 compares the NSPL obtained accounting for the actual airfoil geometry and substituting it by two different flat plates. The flat plate A has been constructed using the turbine inlet mean flow properties, whereas the flat plate B is defined by the outlet conditions (see Table 2 for their definition and flow conditions).

Table 2. Geometrical and flow parameter definitions of the airfoil and its equivalent flat plates.

OP	M_1	M_2	s/c	θ_1	θ_2	$\tilde{\Lambda}_f$
Airfoil	0.43	0.75	0.855	44°	−59°	0.075
Flat Plate A	0.43	0.43	0.855	44°	44°	0.075
Flat Plate B	0.75	0.75	0.855	−59°	−59°	0.075

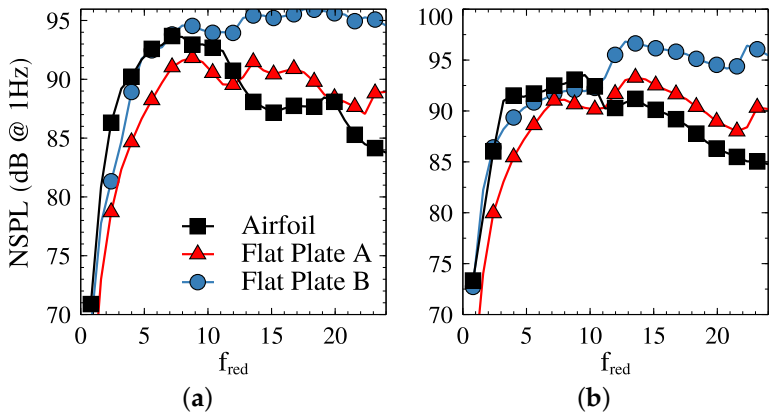

Figure 3. Non dimensional sound pressure level (NSPL) comparison between actual airfoil and equivalent flat plates, A and B. (**a**): inlet; (**b**): outlet. Note that the dimensionless pressure and reduced frequency of the flat plate B have been computed using the inlet properties for consistency.

The comparison of the flat plate A with the LPT airfoil yields the following conclusions. The pressure spectra obtained with the actual geometry in the inlet and outlet are up to 6 dB higher, at reduced frequencies lower than 12. At higher frequencies, the predictions using a flat plate cascade result in higher noise levels (about 4 dB), especially in the outlet. If the spectra are integrated along the frequency range, both effects are somehow compensated, as shown in Figure 4. The inlet prediction accounting for the airfoil geometry is overall 0.75 dB higher than the corresponding flat plate approximation while the outlet is 0.25 dB lower. Despite this similarity, the spectral distributions are very different, which can also lead to different perceived noisiness because the low-mid frequency octave bands are penalised by noise regulations.

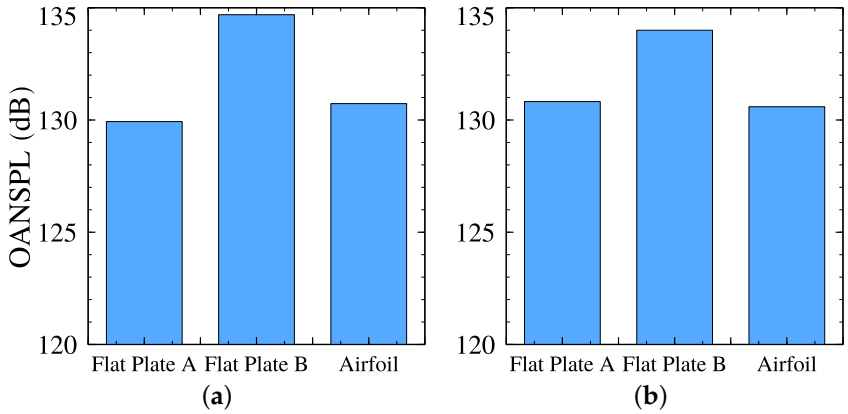

Figure 4. Overall NSPL at the inlet, (**a**) and outlet, (**b**), for the three modelling approaches considered.

Alternatively, the spectra retrieved by the flat plate B overestimate the Airfoil results by up to 10 dB. At low frequencies, i.e., $f_{\text{red}} < 10$, there is a reasonable agreement between the airfoil's results and flat plate B. Nonetheless, at higher frequencies, the differences between both approaches become large. Consequently, flat plate A yields a better agreement with the airfoil's result than flat plate B, as shown in Figure 4. This highlights the role of the leading edge as the major contributor to sound generation, especially at $f_{\text{red}} > 10$. The following analyses will therefore focus on further comparing the flat plate A results with the airfoil.

To provide a more detailed broadband noise footprint, the NSPL modal decomposition is depicted in Figure 5. The y axis corresponds to the reduced frequency, while the x-axis represents the azimuthal mode index: $m = \beta \text{V}s/(2\pi)$. Figure 5a,c show the results obtained at the inlet with the actual and flat plate geometry. The latter exhibits a straight line of extremely low pressure, caused by the dipole behaviour of the flat plate, corresponding to a directivity $-\theta$, because the plate's dipole cannot radiate in directions parallel to itself. The highest noise levels arise close to the cut-off condition for positive m because the regions of maximum radiation are normal to the plate. On the other hand, the simulations accounting for the actual geometry do not show such preferred directions. At low frequency, $f_{\text{red}} < 10$, noise is radiated fairly homogeneously along the whole cut-on region. This is likely to be produced by the presence of additional noise sources that do not arise in flat plates and also by the reflection of acoustic waves between neighbouring blades.

Regarding the downstream noise (Figure 5b,d), the differences are even greater. The results obtained with the equivalent flat plate, (d), have the same cut-on region as in the inlet since the flow properties are uniform. The observed behaviour is analogue to that in the inlet, but with opposite directivities. Contrarily, the cut-on region exhibited by the actual geometry is broader and tilted towards positive directivities due to the effect of the swirl. At low frequencies, $f_{\text{red}} < 10$, the directivity pattern is quite uniform while at higher frequencies there are very low-pressure levels close to the cut-on line, for positive m. It turns out that the cut-off transition of upstream-travelling waves has an effect on the downstream radiated noise because the pattern of the inlet cut-on line at positive m is seen also in Figure 5b. At $f_{red} \simeq 5$, the pressure level clearly increases through the cut-on-cut-off transition of the inlet ($m \simeq 20$). This is, upstream travelling modes are reflected towards the outlet, analogously as trapped modes [24], leading to an increase of downstream noise.

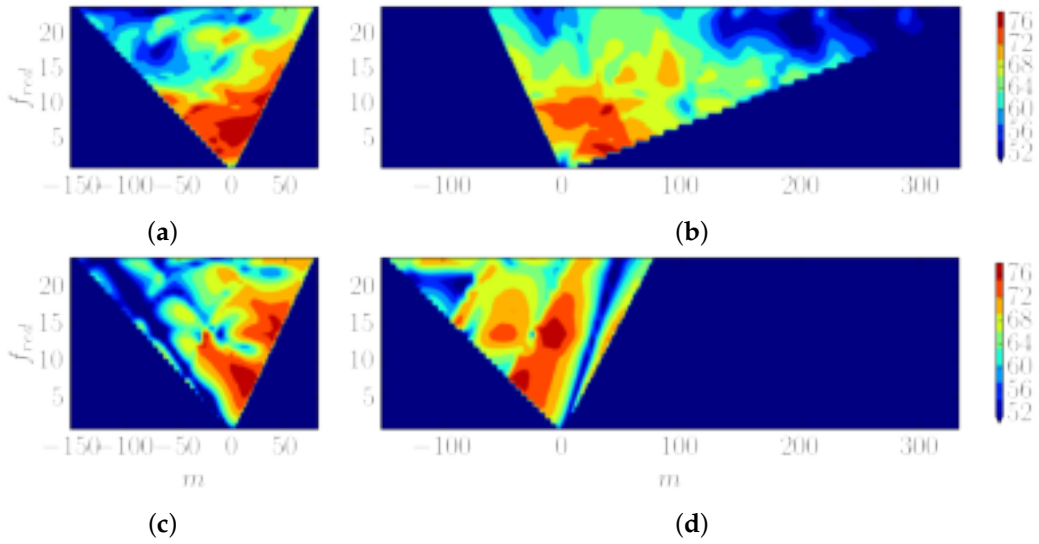

Figure 5. NSPL modal decomposition accounting for the actual geometry and for the equivalent flat plate cascade as a function of the azimuthal mode index. (**a**): Airfoil Geometry-Inlet; (**b**): Airfoil Geometry-Outlet; (**c**): Flat Plate Geometry-Inlet; (**d**): Flat Plate Geometry-Outlet.The scale is saturated below the lower limit for enhanced visualisation.

The information depicted in Figure 5 certainly shows that the resemblance of the integrated noise spectra is caused by statistical averaging and not by the accurate modelling of the physics. The reasons underlying the aforementioned qualitative differences will be explored next.

Figure 6 shows the pressure root mean square value (RMS) at three different frequencies for both the airfoil and flat plate geometries, where a different colour scale is used in each column for enhanced visualisation. This figure highlights the different acoustic sources present in both geometries. However, a note of caution is sounded as a high pressure RMS region is not directly equivalent to a sound source because the hydrodynamic pressure does not lead to sound generation. Anyhow, the pressure RMS can provide valuable information to understand the effect of the airfoil on noise generation, compared to flat plate geometries. At low reduced frequency, $f_{\text{red}} = 3$, the flat plate clearly presents a dipole pattern in the leading-edge, justifying the observations performed in Figure 5c,d. The regions with high-pressure RMS are located in the leading-edge, as predicted by quasi-steady aerodynamic theories. On the other hand, the turbine airfoil presents several regions of high levels of unsteady pressure, namely the leading-edge, the suction side peak Mach number region, and the pressure side where the flow starts to accelerate. These may correspond to volumetric noise sources, associated with the stretching of vorticity, which are known to produce sound [4]. Moreover, as the acoustic wave-length normalised with the chord $\tilde{\lambda}_{ac} = a_0/(f \cdot c)$ is about 0.2, the case can be considered acoustically compact and we may relate the pressure directly with the radiated noise, as deduced from Curle's analogy [25]. This explains the larger noise levels exhibited by the airfoil at low frequencies, compared with the flat plate case (see Figure 3). This noise mechanism is analogue to that described by Marble and Candel [26] for entropy waves, which lead to sound generation when they propagate through a non-uniform mean flow.

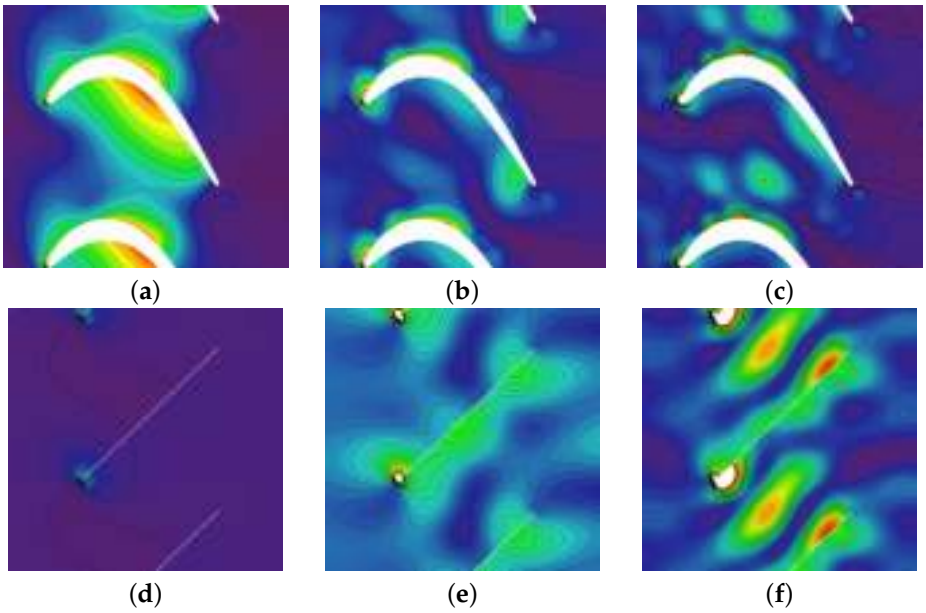

Figure 6. Pressure RMS at different reduced frequencies, with $M_1 = 0.42$. (**a**–**c**): Actual airfoil. (**d**–**f**): Flat Plate. (**a**,**d**): $f_{red} = 3$; (**b**,**e**): $f_{red} = 15$; (**c**,**f**): $f_{red} = 21$. A different colour scale is used in each column.

At higher frequencies, $f_{\text{red}} = 15$ and $f_{\text{red}} = 21$, the behaviour observed on the airfoil is rather similar to the previous one, although the large pressure regions on the suction side shift slightly forward. On the other hand, the flat plate cascade exhibits new pressure lobes which are not present in the low frequency case. The plates do not behave any more as compact acoustic sources and the interference of multiple leading and trailing edge scatterings lead to the more complex pressure pattern observed in Figure 6e,f. It is also seen that the high pressure regions at the plate's leading-edge are more prominent than those of the airfoil. The reason for that is the finite blade thickness and leading edge radius of the airfoil, which according to Gill et al. [5] at high frequencies $(f_{\text{red}}.t/c) > 1.5$ reduces the radiated noise compared to the flat plate case. This limit corresponds in this case to approximately $f_{\text{red}} = 15$. The effect of blade thickness and leading-edge radius on broadband noise have been studied by several authors previously and there is a general agreement that it diminishes the radiated noise, especially the downstream component, which is in agreement with Figure 3 where the NSPL roll-off increases at $f_{\text{red}} > 10$. This point will be further explored in the next section.

3.2. Separation of Geometrical Features

The objective of this section is to highlight the origin of the discrepancies between the results produced by the flat plate approximation and the actual geometry. For that aim, the effect of blade turning and thickness will be separated as follows. The blade camber line and thickness profile are computed, so that a new uncambered airfoil with the same thickness profile as the original turbine is built. This process is sketched in Figure 7. The base flow around the cambered plate is computed using the same boundary conditions as those used with the original geometry. Alternatively, the base flow around the uncambered airfoil is computed so that the inlet Mach number is the same as in the airfoil.

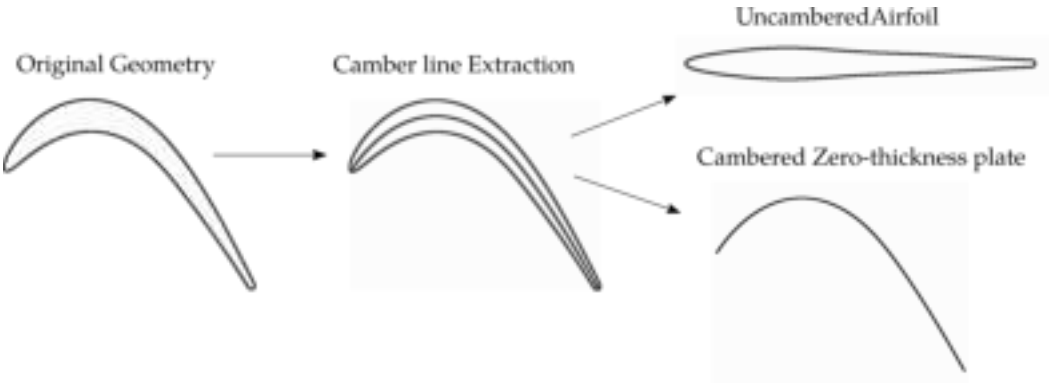

Figure 7. Extraction of the camber line from turbine airfoil and construction of cambered plate and uncambered airfoil with original thickness profile.

The selected approach to separate the thickness and turning effects relies on the assumption that the impact of the geometry on the flow is linear. Therefore the results obtained with the uncambered airfoil with a flat plate cascade will be compared first to derive a thickness correction. Next, we will compare the results obtained with the cambered plate with those of the original airfoil. We will apply the thickness correction to the cambered plate results to assess if the combined effect explains the results seen in the previous section.

Figure 8 compares the spectra retrieved by the uncambered airfoil cascade to the equivalent flat plate. In agreement with other authors, it is observed that the thickness decreases the radiated noise at high frequencies. As proposed by Gershfeld [3], the thickness-based reduced frequency ($f t_{\max}/V_\infty$) is displayed, so the results may be compared with others in the literature. Figure 8a,b compare the absolute spectra obtained with the airfoil and flat plate geometries at the inlet and outlet, respectively. Clearly, the airfoil thickness has a stronger effect on the downstream radiated noise. This point can be better observed in Figure 8c, which displays the difference between the flat plate and the airfoil. In spite of some large oscillations, most likely attributed to the effect of resonances and the 2D simplification, a clear trend can be observed.

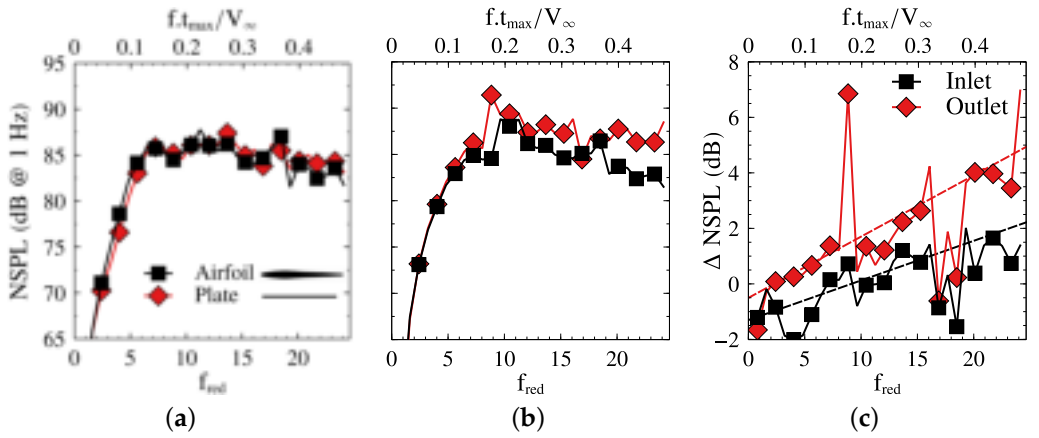

Figure 8. Assessment of the impact of zero-camber airfoil thickness on the broadband noise footprint at OP1. Subfigures (**a**,**b**) compare, respectively, the results with the airfoil and flat plate approximation at the inlet and outlet. Subfigure (**c**) shows the difference between both approaches at the inlet and outlet. The least-squares linear fittings are shown, given by equation: $\Delta\text{PWL} = -1.30 + 5.79 f.t_{\max}/V_\infty$ (inlet) and $\Delta\text{PWL} = -0.50 + 10.15 f.t_{\max}/V_\infty$ (outlet).

A least-squares fit has been computed, which highlights that at very low frequencies, thickness appears to increase the noise, especially in the upstream direction. On the other hand, the slope of the outlet least-squares fitting is larger than that of the inlet,

denoting a stronger effect of thickness on the downstream arc. These conclusions are well in agreement with the literature; Gea-Aguilera et al. [6] show remarkably similar trend lines for NACA0012 profiles for Mach Numbers between 0.3 and 0.5. The present analysis has also been performed with a cascade with a stagger angle of 44°, similarly as the inlet flow angle at OP1, yielding remarkably similar results.

The impact of flow turning is assessed by comparing the results obtained with the original airfoil with those obtained by the cambered plate. The spectra retrieved are displayed in Figure 9. Figure 9a compares the spectra at the inlet. Three curves are displayed, namely, the spectrum produced by the original airfoil, that of the cambered plate, and the latter modified by the previously derived thickness correction law. The cambered plate features a significantly similar shape compared to the spectra obtained with the original airfoil, but the levels are up to 3 dB higher at some frequencies. The thickness correction improves the agreement with the airfoil results but is insufficient to obtain a good matching. Moreover, the cambered plate results exhibit a resonant behaviour at $f_{red} \sim 9$, which is not seen when the actual airfoil geometry is included.

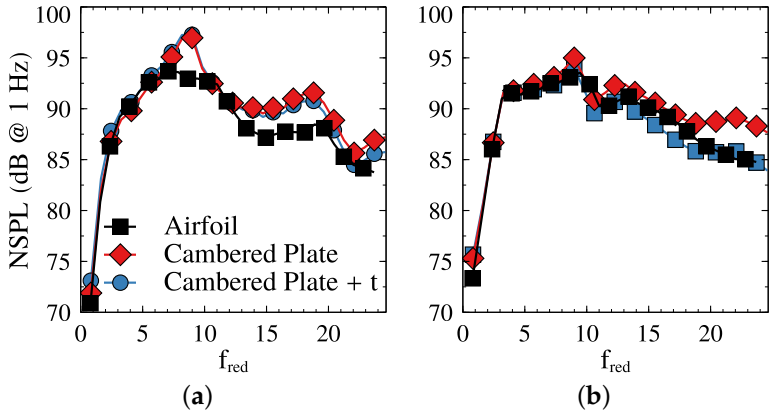

Figure 9. Assessment of the impact of blade turning on the broadband noise footprint at OP1. Subfigures (**a**,**b**) compare, respectively, the results with the airfoil and the cambered plate approximation at the inlet and outlet.

On the other hand, the outlet results, displayed in Figure 9b, show a better agreement between the two approaches. At the highest frequencies, the cambered plate results overpredict those of the airfoil by ∼3 dB. When the thickness correction law previously derived is applied, the matching between the curves improves. Overall, the outlet spectra are remarkably well reproduced by the cambered plate with a thickness correction.

To further explore the similarities and differences between the different spectra, their modal decomposition is analysed next. Figure 10 displays the NSPL modal decomposition for the original airfoil and the cambered plate. At first glance, their modal content exhibits a remarkable qualitative agreement. The inlet and outlet cut-on regions are very similar, as the OP1 boundary conditions were attempted to be matched. There are slight differences because a perfect agreement in the inlet cannot be achieved because the geometries are different. The same high-pressure structures appear in both geometries. At low reduced frequencies ($f_{red} < 10$) the modal content is fairly uniform, while at higher frequencies, the pressure decreases substantially and shifts closer to the cut-on lines, especially at the inlet.

At the inlet, higher pressure levels are observed close to the positive cut-on line, denoting an important contribution of positive modes to the overall footprint. This suggests strong leading-edge radiation at those frequencies, similarly as it occurred in the flat plate case (see Figure 5c). On the other hand, the inlet NSPL obtained with the cambered plate exhibits some high-pressure structures at $5 < f_{red} < 10$ and at $15 < f_{red} < 20$, which are responsible for the mismatching of the spectra observed in Figure 9a. The origin of such a high-pressure structure is yet unknown.

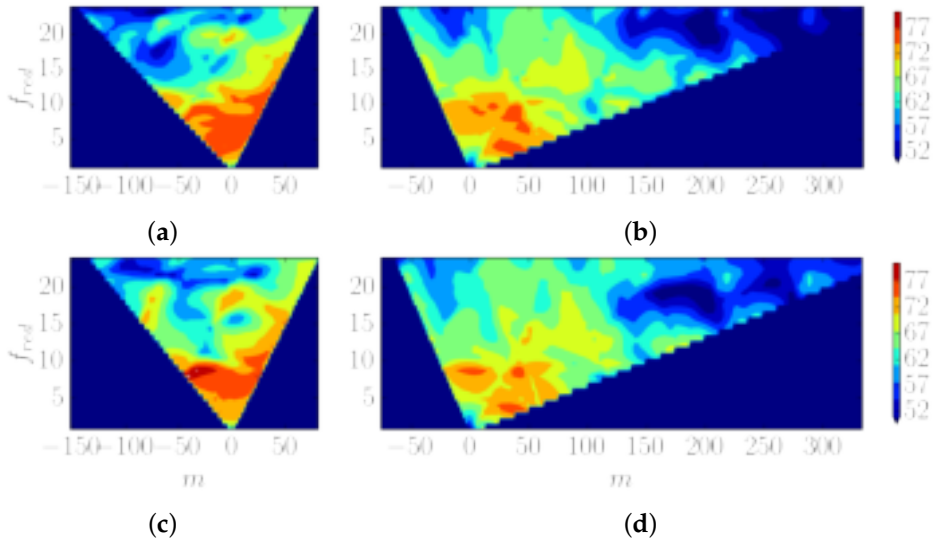

Figure 10. NSPL modal decomposition accounting for the actual geometry and for the cambered plate cascade as a function of the azimuthal mode index. (**a**): Airfoil Geometry-Inlet; (**b**): Airfoil Geometry-Outlet; (**c**): Cambered Plate Geometry-Inlet; (**d**): Cambered Plate Geometry-Outlet. The scale is saturated below the lower limit for enhanced visualisation.

At the outlet, the high-pressure structures occurring at $f_{\text{red}} < 10$ seem peakier in the case of the cambered plate but are qualitatively similar. Moreover, for both geometries, there are very low-pressure levels at $f_{\text{red}} > 15$ and $m > 150$ and at $m \sim -20$. Unlike at the inlet, there is not a clear preferred direction of radiation at high frequency. The reason for that resides most likely in the multiple reflections suffered by the acoustic waves when they propagate from the leading edge through the inter-blade channel.

As shown by this analysis, the similarity among the spectra shown in Figure 9 is due to a similar noise generation mechanism and not to an averaging process. Turbine broadband noise generation, in comparison with flat plates, can be better understood through the separation of the two main geometrical features: thickness and camber. At the highest frequencies considered, tthe hickness reduces the radiated noise in low-speed low-pressure turbines by up to 1 and 4 dB, in the upstream and downstream direction, respectively. On the other hand, highly cambered lines, similar to those featured by turbine airfoils, increase the noise levels at low and middle frequencies ($f_{\text{red}} \lesssim 12$) strongly.

3.3. Effect of the Operating Conditions

Six different Operating Points (OPs) have been run to unravel the effect of varying the Mach number on the spectra (see Table 1). Their isentropic Mach number distributions over the airfoil are shown in Figure 11. The fundamental changes between the different OPs have been the incidence and Mach number. Some changes can be adressed using the flat plate theory, but others require a detailed simulation of the flow. There are two different groups, the high Mach number cases, i.e., OPs 1-3 (see Figure 11a), and the low Mach number ones, i.e., OPs 4-6 (see Figure 11b). Among them, OP2 and OP5 increase the incidence, i, by 10°, which leads to an increase of the inlet Mach number and the airfoil loading. On the other hand, OP3 and OP6 keep the higher incidence but reduces the pressure ratio to retrieve the same inlet Mach number as OP1 and OP4, respectively with a significant decrease in the exit Mach number.

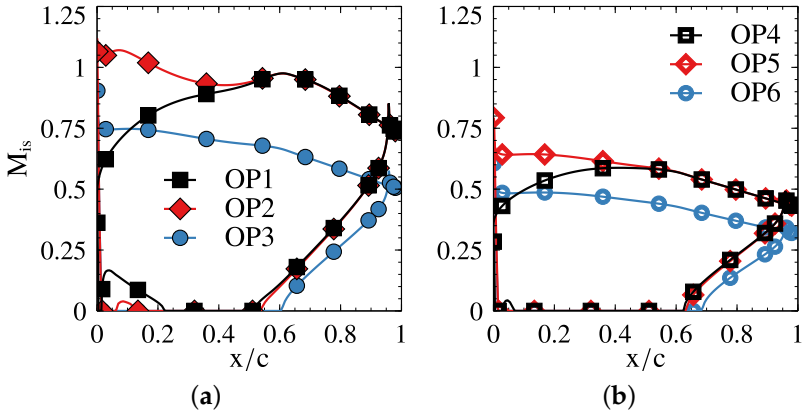

Figure 11. Isentropic Mach number distribution on the airfoil at the different OP considered. (**a**): OP1-3, (**b**): OP4-6.

Figures 12 and 13 show, respectively, the inlet and outlet NSPL at all the OPs considered obtained. Figure 12a,b show respectively the results of OPs 1–3 and 4–6, which have been segregated into two sub-figures for clarity. Figure 12c shows the spectra of OP1-3 and OP6 scaled as explained in the lines below; the spectra of OP4-5 are not included for readability purposes. The information depicted in these Figures is complemented by Figure 14, where the spectra modal decompositions are shown, and the cut-on regions at all the OP are seen.

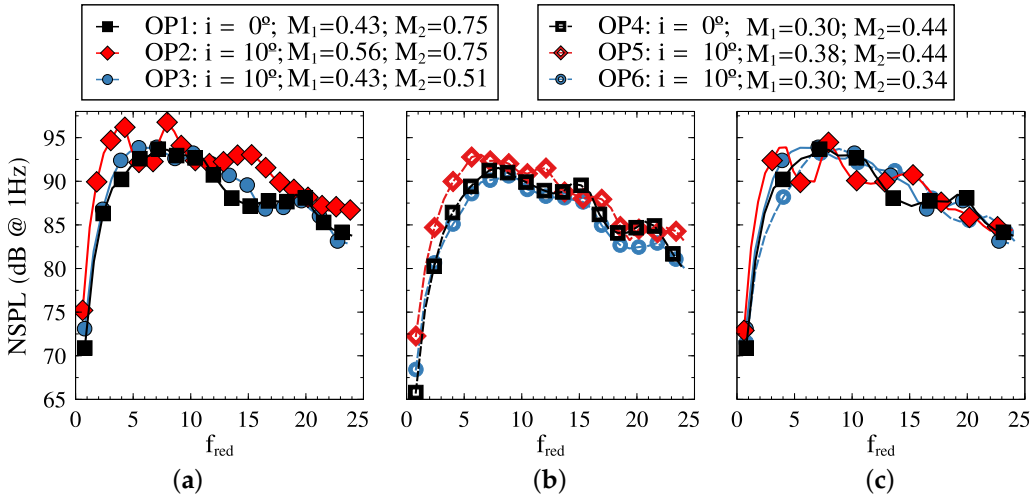

Figure 12. Inlet NSPL for different between operating points. (**a**,**b**) compare respectively the results of OP1-3 and OP4-6. (**c**) shows the NSPL of OP1-3 and 6 scaled with the inlet Mach number squared, M_1^2.

The inlet NSPL is weakly affected by changes in the outlet Mach number, as long as the inlet Mach number remains constant. Figure 12a shows differences between OP1 and OP3 smaller than 2.5 dB, while Figure 12b depicts an even better agreement between OP4 and OP6. Their modal decomposition exhibits significant similarities as well (See Figure 14a,e,g,k), denoting very similar physics and not just an artifact of statistical averaging.

Interestingly, the inlet NSPL scales as NSPL $\sim M_1^2$ due to the increase of the cut-on region, which has the same scaling. The cut-on regions displayed in Figure 14 scale as M, but there is an additional M factor whose origin is the spanwise wavenumber integration limit of Equation (4). In other words, the total number of modes is a combination of circumferential and span-wise modes whose cut-on regions scale with M. The consistency of this scaling is demonstrated by the rather good collapse of the curves shown in Figure 12c.

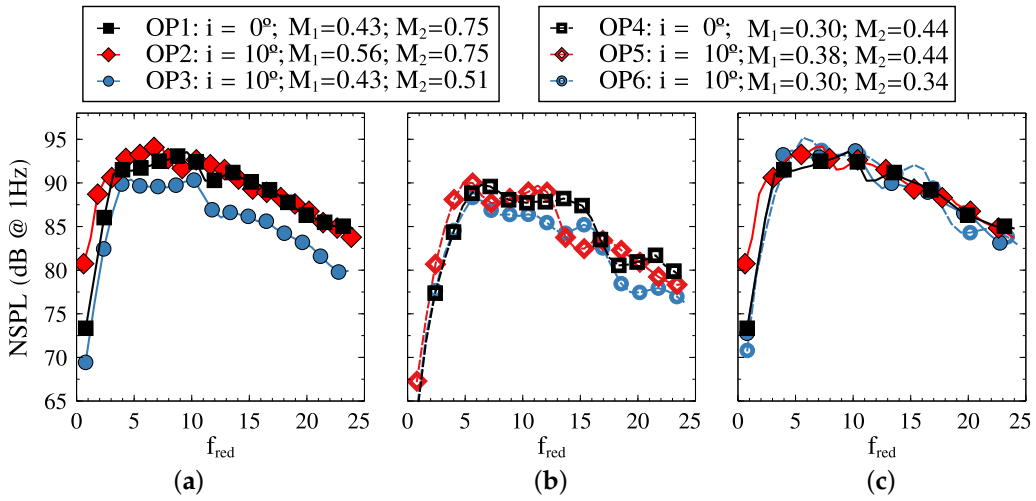

Figure 13. Outlet NSPL for operating points 1–6. (**a**,**b**) compare, respectively, the results of OP1-3 and OP4-6. (**c**) shows the NSPL of OP1-3 and 6 scaled with the outlet Mach number squared, M_2^2.

On the other hand, the outlet noise levels do not vary significantly with the inlet Mach number, except at low frequency ($f_{\text{red}} < 5$). OP1 and OP2 (see Figure 13a) and OP4 and OP5 (see Figure 13b) exhibit a close agreement. Figure 14b,d,h,j respectively show as well similar NSPL modal decompositions. The outlet Mach number widens or shortens the downstream cut-on region, as seen in Figure 14, and therefore controls the noise radiated in that direction through the number of modes that are cut-on or cut-off. Changes in the inlet Mach number seem to have a small impact on the outlet NSPL. However, it must be kept in mind that the physical noise is changed as it is scaled with the inlet speed, as clearly reflected by Equation (15). At low reduced frequency, it appears that loading increases by about 3 dB the outlet spectra, which may be related to a stronger stretching of the vortical waves by the flow field.

Following the same argument as for the inlet NSPL, the Outlet noise scales as NSPL $\sim M_2^2$ due to the increase of cut-on modes. The OP1 and OP3 curves in Figure 13a and the OP4 and OP6 curves in Figure 13b can be fairly well collapsed when these are scaled with M_2^2, which supposes, respectively a +3.3 and +6.9 dB shift on OP3 and OP6 outlet spectra. The collapsed curves are shown in Figure 13c. The agreement between the OP3 and OP1 is remarkable. The scaled OP6 slightly over-estimates the NSPL up to $f_{\text{red}} < 17$. However, the matching is still quite good considering the high difference in mean flow properties.

The inlet Mach number is the key parameter for noise generation as it modifies the spectral shapes. The outlet Mach number merely acts as a scaling factor on the noise due to the cut-on region variation. This is justified by the fact that noise is generated mainly at the leading-edge, within most of the frequency range. Therefore, the outlet physical noise, i.e., not normalised with the inlet conditions, scales as SPL $\propto M_1^3 M_2^2$. The first factor arises from assuming constant turbulence intensity and the response scaling with the inlet velocity (see Equation (15)). The second arises from the effect of the Mach number on the cut-on condition, as previously discussed. Only at low reduced frequencies does the loading seem to produce relevant changes in the radiated noise. The conclusions obtained herein are not a by-product of statistical averaging as they are also sustained by the NSPL modal decompositions. The trends found in the non-dimensional noise spectra and modal decompositions are consistent in the OP noise analysed, which explore changes in loading at low and medium Mach number levels.

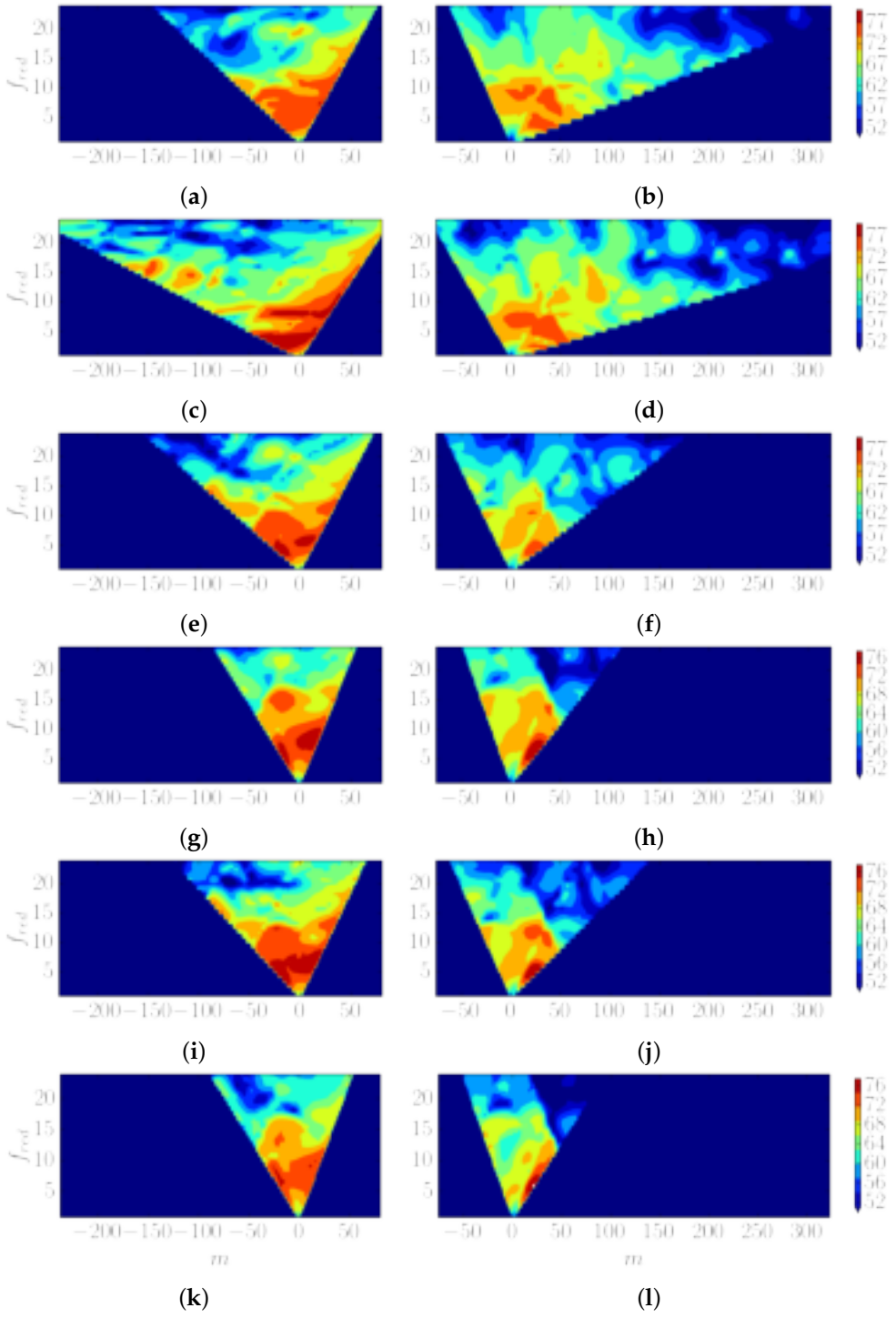

Figure 14. NSPL modal decomposition at all the OP considered. Left column: inlet. Right column: outlet. (**a**,**b**): OP1; (**c**,**d**): OP2; (**e**,**f**): OP3; (**g**,**h**): OP4; (**i**,**j**): OP5; (**k**,**l**): OP6.The scale is saturated below the lower limit for enhanced visualisation.

4. Conclusions

A methodology to include the effect of real geometry on the prediction of turbine broadband noise has been presented. The methodology has been applied to a representative low-speed low-pressure turbine airfoil and compared to state-of-the-art industrial techniques, based on the flat plate cascade theory response. Unlike in Fan/OGV noise, the airfoil geometry becomes relevant. The differences in the spectra between the actual airfoil and the equivalent flat plate analysis are up to 6 dB. At low reduced frequency ($f_{red} < 12$),

the turbine airfoil produces substantially higher noise levels than the flat plate, while at higher frequencies, the flat plate becomes louder. Furthermore, the spectrum modal decomposition using both approaches has been shown as well, exhibiting big discrepancies resulting from different physics. On the other hand, when the spectra are integrated in frequency, the differences become much smaller, of the order of 1dB, due to the compensation of the aforementioned effects. The reason for such a small discrepancy is the statistical averaging of the response, which could become much larger under anisotropic turbulence, as pointed out by Devenport et al. [7].

The geometrical effects, namely blade camber, and thickness have been studied separately to understand their impact on the broadband noise footprint. For a typical low-pressure turbine airfoil, the thickness decreases the downstream radiated noise by up to 4 dB at the highest frequencies considered. The blade camber produces a large change of the mean flow properties through the turbine. As described by Evers and Peake [4], amongst other authors, the stretching of vortical waves by a non-uniform flow gives rise to sound generation. This noise generation mechanism seems to appear in highly cambered airfoils up to $f_{\text{red}} < 12$, giving rise to the aforementioned 6 dB extra noise compared to flat plate methodologies.

The effect of the operating conditions of the turbine airfoil has been assessed by running six different operating points with different Mach numbers and incidences. The inlet Mach number does not significantly affect the outlet NSPL within the OP considered. Conversely, the outlet Mach number acts as a scaling factor of M_2^2 on the outlet noise through the cut-on condition. The loading increase due to the incidence increases the downstream dimensionless noise at low reduced frequencies ($f_{red} < 5$) but seems to have little effect at higher frequencies. Since the results are non-dimensionalised with the inlet properties, the outlet physical noise scales with $M_1^3 M_2^2$, assuming constant turbulence intensity, within most of the frequency range considered. On the other hand, the inlet noise remains relatively unaffected by changes in the incidence that lead only to a change in the outlet Mach number if the pressure ratio is kept. These conclusions are also supported by the NSPL modal decomposition, which shows that the rather good collapse of the spectra is not just a product of the statistical averaging. This is the first time that the impact of the turbine airfoil geometry has been included in a broadband noise prediction and compared against state-of-the-art methodologies.

Author Contributions: Conceptualization, R.B.-N. and R.C.; methodology, R.B.-N.; investigation, R.B.-N.; writing—original draft, R.B.-N.; software, R.B.-N.; visualization, R.B.-N.; writing—review & editing R.C.; supervision, R.C.; resources, R.C.; funding acquisition, R.C.; project administration, R.C. All authors have read and agreed to the published version of the manuscript.

Funding: This research was funded by the European Commission through the 2020 Horizon Project TurboNoiseBB under grant number 690714.

Institutional Review Board Statement: Not applicable.

Informed Consent Statement: Not applicable.

Data Availability Statement: Not applicable.

Acknowledgments: The financial support of the European Commission through the European 2020 Horizon project TurboNoiseBB under grant agreement number 690714 is greatly acknowledged. We would like to thank A. Serrano and P. Carrasco (ITP Aero) for all the fruitful discussions during these past years, which have helped to the development of this work. Moreover, we would like to thank ITP Aero for its support during the project.

Conflicts of Interest: The authors declare no conflicts of interest.

Abbreviations

The following abbreviations are used in this manuscript:

a	Speed of sound
c	Blade chord
f_{red}	Reduced Frequency
$\mathbf{k}$	Wave vector
i	Incidence Angle | imaginary unit
m	Azimuthal Mode Index
M	Mach number
r	Stator Tyler and Sofrin scatter index
R	Radius
p, p_t	Pressure, total pressure
s	Blade spacing
S^{pp}	Pressure Power Spectral Density
t	Airfoil thickness
V	Number of stator vanes
V_0	Streamwise Base flow velocity
$\mathbf{U}_0$	Base flow primitive variables
u_{rms}	Velocity root mean square value
w	Upwash velocity
$\mathbf{u}$	Primitive perturbed variables
β	Acoustic azimuthal wavenumber
γ	Acoustic spanwise wavenumber
Φ	Velocity power spectral density
$\mathcal{F}_\theta$	Fourier Transform Operator
Λ_f	Turbulence length scale
$\mathcal{L}$	Linearised Navier-Stokes Operator
ρ	Density
θ	Mean flow angle
ω	Angular frequency
Ω	Rotor angular speed
NSPL	Normalised Sound Pressure Level
OANSPL	Overall Normalised Sound Pressure Level
PSD	Power Spectral Density
0	Flow average variable
$\tilde{}$	Dimensionless Variable
$\hat{}$	Fourier Transform
1, 2	Inlet and Outlet Axial Stations

References

1. Nesbitt, E. Towards a quieter low pressure turbine: Design characteristics and prediction needs. *Int. J. Aeroacoustics* **2010**, *10*, 1–15. [CrossRef]
2. Serrano, A.; Aparicio, J.; Vázquez, R. On the estimation and relevance of internally generated turbine broadband noise. *Int. J. Aeroacoustics* **2010**, *10*, 51–74. [CrossRef]
3. Gershfeld, J. Leading edge noise from thick foils in turbulent flows. *J. Acoust. Soc. Am.* **2004**, *116*, 1416–1426. [CrossRef]
4. Evers, I.; Peake, N. On sound generation by the interaction between turbulence and a cascade of airfoils with non-uniform mean flow. *J. Fluid Mech.* **2002**, *463*, 25–52. [CrossRef]
5. Gill, J.; Zhang, X.; Joseph, P. Symmetric airfoil geometry effects on leading edge noise. *J. Acoust. Soc. Am.* **2013**, *134*, 2669–2680. [CrossRef]
6. Gea-Aguilera, F.; Gill, J.; Zhang, X. On the effects of fan wake modelling and vane design on cascade noise. *J. Sound Vib.* **2019**, *459*, 114859. [CrossRef]
7. Devenport, W.J.; Staubs, J.K.; Glegg, S.A. Sound radiation from real airfoils in turbulence. *J. Sound Vib.* **2010**, *329*, 3470–3483. [CrossRef]
8. Myers, M.R.; Kerschen, E.J. Influence of camber on sound generation by airfoils interacting with high-frequency gusts. *J. Fluid Mech.* **1997**, *353*, 221–259. [CrossRef]
9. Paruchuri, C.C.; Coupland, J.; Joseph, P. Airfoil geometry effects on turbulence interaction noise in cascades. In Proceedings of the 22nd AIAA/CEAS Aeroacoustics Conference, Lyon, France, 30 May–1 June 2016; p. 2738. [CrossRef]

10. Corral, R.; Escribano, A.; Gisbert, F.; Serrano, A.; Vasco, C. Validation of a linear multigrid accelerated unstructured Navier-Stokes solver for the computation of turbine blades on hybrid grids. In Proceedings of the 9 th AIAA/CEAS Aeroacoustics Conference, Hilton Head, SC, USA, 12–14 May 2003; p. 3326. [CrossRef]
11. Corral, R.; Gisbert, F.; Pueblas, J. Execution of a parallel edge-based Navier–Stokes solver on commodity graphics processor units. *Int. J. Comput. Fluid. Dyn.* **2017**, *31*, 93–108. [CrossRef]
12. Guérin, S.; Kissner, C.; Seeler, P.; Blázquez, R.; Carrasco, P.; de Laborderie, H.; Lewis, D.; Chaitanya, P.; Polacsek, C.; Thisse, J. ACAT1 Benchmark of RANS-informed Analytical Methods for Fan Broadband Noise Prediction: Part II—Influence of the Acoustic Models. *Acoustics* **2020**, *2*, 617–649. [CrossRef]
13. Blázquez-Navarro, R.; Corral, R. Prediction of fan acoustic blockage on fan/outlet guide vane broadband interaction noise using frequency domain linearised Navier–Stokes solvers. *J. Sound Vib.* **2021**, *500*, 116033. [CrossRef]
14. Bechara, W.; Bailly, C.; Lafon, P.; Candel, S.M. Stochastic approach to noise modeling for free turbulent flows. *AIAA J.* **1994**, *32*, 455–463. [CrossRef]
15. Batchelor, G.; Proudman, I. The effect of rapid distortion of a fluid in turbulent motion. *Q. J. Mech. Appl. Math.* **1954**, *7*, 83–103. [CrossRef]
16. Liepmann, H. Extension of the statistical approach to buffeting and gust response of wings of finite span. *J. Aeronaut. Sci.* **1955**, *22*, 197–200. [CrossRef]
17. Goldstein, M.E. *Aeroacoustics*; McGraw-Hill International Book Co.: New York, NY, USA, 1976; p. 130
18. Jaron, R.; Herthum, H.; Franke, M.; Moreau, A.; Guérin, S. Impact of Turbulence Models on RANS-Informed Prediction of Fan Broadband Interaction Noise. In Proceedings of the 12th European Turbomachinery Conference (ETC), Stockholm, Sweden, 3–7 April 2017; pp. 3–7. [CrossRef]
19. Ju, H.; Mani, R.; Vysohlid, M.; Sharma, A. Investigation of fan-wake/outlet-guide-vane interaction broadband noise. *AIAA J.* **2015**, *53*, 3534–3550. [CrossRef]
20. Burgos, M.A.; Contreras, J.; Corral, R. Efficient edge-based rotor/stator interaction method. *AIAA J.* **2011**, *49*, 19–31. [CrossRef]
21. Corral, R.; Vega, A. Physics of vibrating turbine airfoils at low reduced frequency. *J. Propuls. Power* **2016**, *32*, 325–336. [CrossRef]
22. Corral, R.; Beloki, J.; Calza, P.; Elliott, R. Flutter generation and control using mistuning in a turbine rotating rig. *AIAA J.* **2019**, *57*, 782–795. [CrossRef]
23. Paruchuri, C.; Gill, J.R.; Subramanian, N.; Joseph, P.; Vanderwel, C.; Zhang, X.; Ganapathisubramani, B. Aerofoil geometry effects on turbulence interaction noise. In Proceedings of the 21st AIAA/CEAS Aeroacoustics Conference, Dallas, TX, USA, 22–26 June 2015, p. 2830.
24. Cooper, A.; Peake, N. Trapped acoustic modes in aeroengine intakes with swirling flow. *J. Fluid Mech.* **2000**, *419*, 151–175. [CrossRef]
25. Curle, N. The influence of solid boundaries upon aerodynamic sound. *Proc. R. Soc. Lond. Ser. A Math. Phys. Sci.* **1955**, *231*, 505–514.
26. Marble, F.; Candel, S. Acoustic disturbance from gas non-uniformities convected through a nozzle. *J. Sound Vib.* **1977**, *55*, 225–243. [CrossRef]

International Journal of
Turbomachinery Propulsion and Power

MDPI

Article

Machine Learning Based Sensitivity Analysis of Aeroelastic Stability Parameters in a Compressor Cascade †

Marco Rauseo *, Mehdi Vahdati and Fanzhou Zhao

Department of Mechanical Engineering, Imperial College London, London SW7 2AZ, UK; m.vahdati@imperial.ac.uk (M.V.); fanzhou.zhao11@imperial.ac.uk (F.Z.)

* Correspondence: m.rauseo18@imperial.ac.uk

† This paper is a revised version of our paper published in Proceedings of the European Turbomachinery Conference ETC14, Gdansk, Poland, 12–16 April 2021.

Abstract: Aeroelastic instabilities such as flutter have a crucial role in limiting the operating range and reliability of turbomachinery. This paper offers an alternative approach to aeroelastic analysis, where the sensitivity of aerodynamic damping with respect to main flow and structural parameters is quantified through a surrogate-model-based investigation. The parameters are chosen based on previous studies and are represented by a uniform distribution within applicable intervals. The surrogate model is an artificial neural network, trained and tested to achieve an error within 1% of the test data. The quantity of interest is aerodynamic damping and the datasets are obtained from a linearised aeroelastic solver. The sensitivity of aerodynamic damping with respect to the input variables is obtained by calculating normalised gradients from the surrogate model at specific operating conditions. The results show a quantitative comparison of sensitivity across the different input parameters. The outcome of the sensitivity analysis is then used to decide the most appropriate action to take in order to induce stability in unstable operating conditions. The work is a preliminary study, carried out on a simplified two dimensional compressor cascade and it is aimed at proving the validity of a data-driven approach in studying the aeroelastic behaviour of turbomachinery. To the best of the authors' knowledge, this is the first time a data-driven flutter model has been investigated. The initial results are encouraging, indicating that this approach is worth pursuing in the future. The presented framework can be used as a redesign tool to enhance the flutter stability of an existing blade.

Keywords: flutter; machine learning; sensitivity analysis

check for updates

Citation: Rauseo, M.; Vahdati, M.; Zhao, F. Machine Learning Based Sensitivity Analysis of Aeroelastic Stability Parameters in a Compressor Cascade. *Int. J. Turbomach. Propuls. Power* **2021**, *6*, 39. https://doi.org/10.3390/ijtpp6030039

Academic Editor: Damian Vogt

Received: 19 May 2021
Accepted: 7 September 2021
Published: 15 September 2021

Publisher's Note: MDPI stays neutral with regard to jurisdictional claims in published maps and institutional affiliations.

Copyright: © 2021 by the authors. Licensee MDPI, Basel, Switzerland. This article is an open access article distributed under the terms and conditions of the Creative Commons Attribution (CC BY-NC-ND) license (https://creativecommons.org/licenses/by-nc-nd/4.0/).

1. Introduction

The development of highly loaded, three-dimensional, long compressor and fan blades yields a great challenge in terms of aeroelastic stability of turbomachinery. The task of assessing blade stability is only made more compelling by the recent trend towards blisks, in which mechanical damping is hardly present. Self-excited vibration, or flutter, is among the several aeroelastic phenomena which can limit the operating range of turbomachinery and eventually lead to blade failure. Flutter has been extensively studied by several authors, through analytical, experimental and computational methods, leading to a wealth of literature in which several driving parameters have been identified [1–3]. In [4], Srinivasan associates flutter with high steady loading and low reduced frequency, for blades vibrating in first bending or twist modes. The reduced frequency is addressed here as $k = \omega c / U_{rel}$, where ω is the angular vibration frequency, c is the blade chord and U_{rel} is the inlet relative flow velocity. In an early analytical work [5], Whitehead presents unsteady lift calculations for a two-dimensional cascade of flat plates, emphasising that stability is affected, in different fashions depending on the flow variables (e.g., inlet Mach number), by the nature (cut-on waves propagate without attenuation, whereas cut-off waves decay as they travel) of acoustic waves produced by the vibration. The strong correlation between mean flow incidence and stability is shown in [6], using results from a complete analytical model

for loaded cascades in incompressible flow developed in [7]. All of the above claims are corroborated by more recent computational studies. In [8], Vahdati and Cumpsty performed a three-dimensional CFD analysis of a state-of-the-art fan blade, and observed that (1) 3D separation (high loading), followed by radial migration of flow along the span towards the casing, reduces aerodynamic damping; (2) flutter occurs in the frequency and nodal diameter range where the generated acoustic waves are cut-on upstream and cut-off downstream (for an exhaustive explanation of acoustic modes in turbomachinery ducts see [9]); (3) aerodynamic damping decreases as the twist component in the first flap mode increases, in agreement with the study on turbines in [10]. Flutter is, therefore, influenced by steady and unsteady flow features, aeroacoustics and structural properties.

At early design stages, most of the attention is focused on performance, while aeroelastic stability is investigated only in terms of simple parameters such as reduced frequency. The influence of flow variables and other structural parameters is assessed only later in the process, or when in-service failure occurs. Although recent CFD-based methods have been successful in predicting flutter [11], the condition at which flutter occurs is unknown at the design stage; if unsteady CFD is to be used for such analysis, it can be very computationally expensive and cannot be used routinely. Moreover, given a specified range of design parameters variability, it is unclear in what measure these variables influence stability and how they quantitatively compare to one another. For example, is blade stiffening as effective as changing bending-twist ratio or the design point aerodynamics? How do flow features influence stability in different acoustic waves regimes?

The present paper will focus on the instability commonly known as stall flutter, which occurs at part-speed regime, when airfoils operate at an incidence higher than nominal [12]. It is misleadingly named so, since stall is not a necessary condition for its occurrence (Isomura and Giles [13] reported shock oscillations as instability exciting mechanism for their case, yet they referred to it as stall flutter). Inspired by the recent success of machine-learning-based uncertainty quantification of turbulence model coefficients [14–16], this paper attempts to answer the previous questions by means of a forward-propagation sensitivity analysis of selected design parameters, based on a machine-learnt surrogate model. The proposed method represents an alternative approach to current numerical stall flutter predictions which rely on ever growing computational methods [11,17]. The successful development of the proposed strategy would provide significant improvement over current CFD-based methods, as it requires significantly less computational resources. In addition, the machine-learnt model can provide quantitative measures of sensitivity, in the form of gradients of aerodynamic damping with respect to design parameters, offering optimum remedies for flutter issues of an existing design.

In this work, a simplified geometry is used to demonstrate the validity of a machine-learning-based framework to study the impact of flow and structural parameters on aerodynamic damping. The objective of the present work is to develop a redesign tool to enhance the flutter stability of an existing blade. The long term goal is to develop a simple model to assess stability of compressor and fan blades in order to provide early design guidelines focused on improving aeroelastic stability.

In the following sections, the choice of input coefficients, with their relative ranges, will be explained. Flow solver, machine learning model and forward-propagation strategy will be discussed and, finally, the results will be presented.

2. Methodology

2.1. Test Case

The test case selected for this study is the Standard Configuration 10 [18], a 2D compressor cascade. The chord length and pitch to chord ratio are fixed at 0.1 m and 1.0, respectively; the stagger angle is 45°; inlet total pressure and temperature are 101.3 kPa and 300 K throughout the study and finally, at design point, the cascade operates with inlet Mach number $M_1 = 0.7$ and inflow angle $\alpha_1 = 55°$. The incidence angle of flow onto the blade is referred to as β_1, with $\beta_1 = 0°$ corresponding to $\alpha_1 = 55°$, and therefore to

nominal incidence. Figure 1 shows an example of a steady state solution with $M_1 = 0.85$ and nominal incidence. The choice of a 2D geometry preserves the driving physics of flutter apart from two effects: three-dimensional flow profiles and presence of radial acoustic modes in the duct. Although relevant, these are not considered essential in the early design stage this work is targeting; moreover, this approach decouples the influence of tip leakage flow, which represents a cumbersome turbulence modelling problem in its own merit. Three-dimensional flow features will be included in future work.

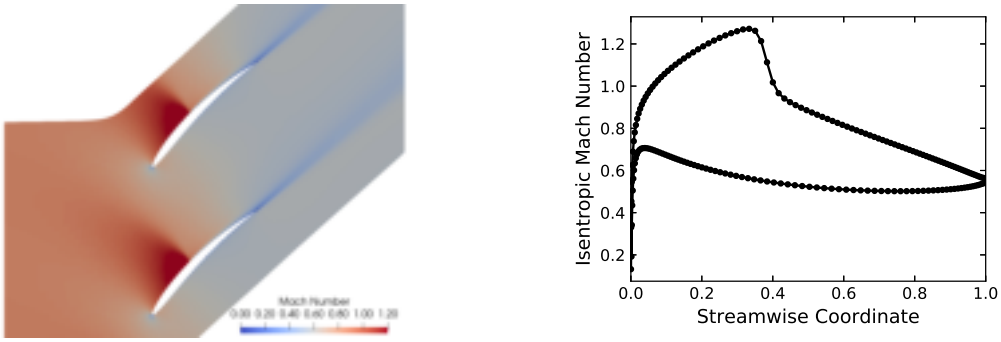

(**a**) Mach Number contour plot (**b**) Isentropic Mach Number

Figure 1. Example of steady state solution.

2.2. Flow Solver

The CFD solver used in this work, LUFT, is developed by Dr. Paul Petrie-Repar from RPMTurbo. LUFT steady-state solver solves the 3D RANS equations on a hexahedral mesh, using a cell-centered finite volume scheme. The fluxes are calculated with an upwind Roe scheme (other schemes are available), the flow is reconstructed using a MUSCL interpolation with van Albada limiter and a local time stepping with residual smoothing is applied. The unsteady flow solver is linearised, casting the URANS equations in the frequency domain and the calculated unsteady pressures are used to evaluate aerodynamic work on the blade and subsequently aerodynamic damping, ζ. A linearised Spalart-Allmaras turbulence model is adopted, with no wall functions. Two-dimensional non-reflecting boundary conditions are applied throughout the study. The solver has been validated against other established codes [19,20].

2.3. Selection of Design Parameters

The relevant parameters chosen for this work are based on the literature presented in the previous section: inlet Mach number, M_1, incidence angle, β_1, reduced frequency k, bending-twist ratio of modeshape and Interblade Phase Angle, σ.

β_1 is imposed as boundary condition, M_1 is varied by changing the pressure ratio (inlet total pressure over outlet static pressure) across the cascade, k is imposed in the unsteady solver which, in turn, calculates the correct structural frequency using the steady state inlet flow velocity as reference. σ is specified in degrees and imposed as phase lag at the passage interfaces in the unsteady solver. The bending-twist ratio requires a little discussion.

The modeshape chosen for this work is a rigid body rotation about a given axis, referred to as twist axis. The bending-twist ratio is varied by keeping a fixed leading edge displacement, while changing the parameter X_t, defined as:

$$X_t = \frac{\mathbf{X}_{LE} + \mathbf{X}_{TE}}{\mathbf{X}_{LE} - \mathbf{X}_{TE}} \tag{1}$$

where $\mathbf{X}_{LE}$, $\mathbf{X}_{TE}$ are signed leading and trailing edge displacements, respectively. The limiting cases are pure twist with $X_t = 0$ and pure bending with $X_t \to \infty$ ($\mathbf{X}_{LE} \to \mathbf{X}_{TE}$); all other cases, i.e., $X_t \in (0, \infty)$, are referred to as flap mode. The effect of increasing X_t is, essentially, to move the twist axis further downstream from the blade (e.g., $X_t = 2$

locates the twist axis half a chord away from the trailing edge); therefore, decreasing the twist component of the modeshape. Figure 2 shows a schematic illustration of the effect of increasing X_t.

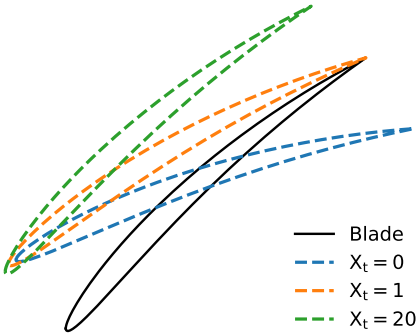

Figure 2. Schematic illustration of modeshape at different X_t.

The next step is to decide the intervals in which the input parameters will vary. The interval for inlet Mach number is chosen to be symmetric about the nominal value of 0.7, to study both subsonic flow, where no shock appears, and transonic flow conditions, where a shock is present on the suction side. M_1, thus, changes between 0.5, anything lower is discarded as excessively low speed, and 0.9, so that the shock stays on the suction side and does not move too far upstream (Figure 1a). The incidence of incoming flow onto the blade is varied between 0° and 6°, which is the largest value before inception of stall for all the Mach numbers studied in this work. σ ranges from $-180°$ to 180°; the extremes are the same point, although no special treatment has been specified for them in the training phase of the surrogate model. In practice, the combination of reduced frequency and modeshape is not arbitrary: the same blade will be characterised by very different reduced frequencies whether it is vibrating in a pure twist or in a flap mode. Moreover, this combination also depends on the machine being considered: the flap mode of a fan blade will have a lower reduced frequency [17,21] compared to an embedded compressor blade [22]. Nevertheless, to cover the whole spectrum of combinations, modeshape and frequency in this study are assumed to be independent from each other during training of the surrogate model and, therefore, take large intervals. Table 1 summarises the space of input variables.

Table 1. Intervals of design parameters.

Parameter		Min	Max
M_1	Inlet Mach Number	0.5	0.9
β_1	Incidence (difference with nominal)	0°	+6°
k	Reduced Frequency	0.4	1.5
X_t	Non dimensional Twist Axis distance	0.0	4.0
σ	Interblade Phase Angle	−180°	180°

2.4. Sensitivity Analysis Method

The sensitivity analysis in this work is carried out by means of a surrogate model-based approach, in order to alleviate the computational load required by a conventional CFD-based method.

The Latin Hypercube sampling method [23] is applied to generate five independent databases of input parameters within the range in Table 1: this approach ensures a uniform distribution of the samples in the space of interest and that arbitrary samples from different databases are mutually independent. The databases have size 128, 256, 512, 1024, 2048, and are referred to as db1 to db5. The databases are applied to train and test a surrogate

model of the CFD solver which will approximate aerodynamic damping without solving the aeroelastic equations:

$$\mathbf{q} \approx \hat{\mathbf{q}} = \mathbf{S}(\mathbf{x}) \tag{2}$$

where $\mathbf{x}$ is the input parameters vector, $\mathbf{S}$ is the surrogate model, $\hat{\mathbf{q}}$ and $\mathbf{q}$ are the quantity of interest, predicted by the surrogate model and CFD, respectively.

Finally, the PDF (probability density function) of aerodynamic damping can be obtained. The sensitivity of input coefficients on the prediction is quantified by the normalised gradient computed by the surrogate model, which will be briefly discussed.

The surrogate model $\mathbf{S}$ is a nonlinear function which given an input $x \in \mathbb{R}^d$ outputs $\hat{\mathbf{q}} \in \mathbb{R}^m$; the Jacobian of the outputs with respect to input is:

$$J_{ij}(x) = \frac{\partial S_i(x)}{\partial x_j} = \nabla S_i(x) \tag{3}$$

The value of $\nabla S_i(x)$ will give a measure of how sensitive the output i is to the input j in the vicinity of x. In order to have a comparison between the inputs and across different locations of the sample space, the gradient is normalised by its magnitude $|\nabla S_i(x)|$, yielding the normalised gradient.

2.5. Artificial Neural Network Based Surrogate Model

The artificial neural network (ANN) is used as a surrogate model of the CFD solver. The ANN is composed of multiple layers of nonlinear activation units called neurons. The input, hidden and output layers store input variables, intermediate outputs and quantity of interest, respectively. The vector of input variables $\mathbf{x}$ and quantity of interest $\mathbf{q}$ are below:

$$\begin{aligned} \mathbf{x} &= [M_1, \beta_1, k, X_t, \sigma] \\ \mathbf{q} &= \zeta \end{aligned} \tag{4}$$

The principles, training strategy and results are the following.

2.5.1. Forward Propagation

The input variables are normalised by their maximum and minimum and then rescaled in the range $\{-1, 1\}$:

$$\mathbf{a}_i^{(0)} = 2\frac{\mathbf{x}_i - min(\mathbf{x}_i)}{max(\mathbf{x}_i) - min(\mathbf{x}_i)} - 1 \tag{5}$$

where $\mathbf{x}_i$ is the vector of input variable i, with dimension m, where m is the number of samples. The outputs at intermediate layers are propagated as below:

$$\mathbf{a}^{(l+1)} = f(\mathbf{z}^{(l+1)}) = f(\mathbf{w}^{(l+1)}\mathbf{a}^{(l)} + \mathbf{b}^{(l+1)}) \tag{6}$$

where $\mathbf{w}$ is the weights matrix, $\mathbf{b} = diag(\mathbf{I})$ is the bias vector and $f(\cdot)$ is the activation function. The function $f(x) = Atanh(Hx)$ with $A = 1.7159$ and $H = \frac{2}{3}$ is a rescaled hyperbolic tangent as proposed by [24]. The results at the output layer $(L+1)$ are then denormalised to yield the quantity of interest:

$$\hat{\mathbf{q}} = (max(\mathbf{q}) - min(\mathbf{q})) \cdot \frac{\mathbf{a}^{(L+1)} + A}{2A} + min(\mathbf{q}) \tag{7}$$

The max-min normalisation of the aerodynamic damping is symmetric with respect to zero so that $\frac{|\hat{\mathbf{q}}|}{\hat{\mathbf{q}}} = \frac{|\zeta|}{\zeta}$, i.e., negative $\hat{\mathbf{q}}$ (output of ANN) corresponds to negative aerodynamic

damping. Lastly, the accuracy of ANN predictions is measured by the relative error on the test database:

$$\varepsilon = \frac{1}{m}\sum_{j=1}^{m}\frac{|\mathbf{q}_j - \hat{\mathbf{q}}_j|}{max(\mathbf{q}) - min(\mathbf{q})} \tag{8}$$

2.5.2. Backpropagation

The ANN solves an optimisation problem by iteratively updating the weights w that connect the neurons. These are initialised randomly and are updated by minimising the cost function J:

$$J(\mathbf{w},\mathbf{b}) = \frac{1}{2m}\sum_{j=1}^{m}(\mathbf{q}_j - \hat{\mathbf{q}}_j)^2 + \frac{\lambda}{2m}\sum_{l=1}^{L+1}(\mathbf{w}^{(l)})^2 \tag{9}$$

where λ regularises the weights norm so to avoid overfitting. The optimiser used in this work is the Broyden–Fletcher–Goldfarb–Shanno (BFGS, [25]). The gradient of the cost function is calculated as:

$$\begin{aligned}\frac{\partial J}{\partial \mathbf{w}^{(l)}} &= \frac{1}{m}\sum_{j=1}^{m}\Delta^{(l)}\cdot(\mathbf{a}^{(l-1)})^T + \frac{\lambda}{2m}\mathbf{w}^{(l)}\\ \frac{\partial J}{\partial \mathbf{b}^{(l)}} &= \frac{1}{m}\sum_{j=1}^{m}\Delta^{(l)}\end{aligned} \tag{10}$$

where:

$$\Delta^{(l)} = \begin{cases}(\hat{\mathbf{a}}^{(l)} - \mathbf{a}^{(l)})\cdot f'(\mathbf{z}^{(l)}), & l = L+1\\ (\mathbf{w}^{(l+1)})^T\Delta^{(l+1)}\cdot f'(\mathbf{z}^{(l)}), & 1 \le l \le L\end{cases} \tag{11}$$

2.5.3. Choice of Hyperparameters

The weights determined in the optimisation process are influenced by multiple parameters, the hyperparameters, namely number of layers L and number of neurons per layer N_L, training database size and regularisation factor λ. A baseline ANN with $L = 2$, $N_L = 12$ and $\lambda = 10^{-4}$ will be used for the hyperparameters study. First, a training database independence study is carried out, using 5 different combinations of databases summarised in Table 2. The training/test split is kept constant at 80/20 for all the combinations. The gradient-based optimisation can lead to local minima of the cost function; therefore, 16 networks with different initial conditions and randomly reshuffled datasets are trained in parallel.

Table 2. Data for training database independence study.

Data	Total Size	Training Data	Test Data	Trained ANNs
db1 ∪ db2	384	80%	20%	16
db2 ∪ db3	768	80%	20%	16
db3 ∪ db4	1536	80%	20%	16
db4 ∪ db5	3072	80%	20%	16
All dbs	3967	80%	20%	16

The difference between test and training error (ε_{TE}, ε_{TR}) is plotted in Figure 3. As the training database size increases, the difference between the test and training errors reduces to nearly zero, and thus, the accuracy of the ANN becomes independent of the training database size. Moreover the max-min envelope in Figure 3 converges to the mean value when all the datasets are used, indicating independence from initial conditions. The rest of the hyperparametric study is carried out using all data, with the training/test split discussed above.

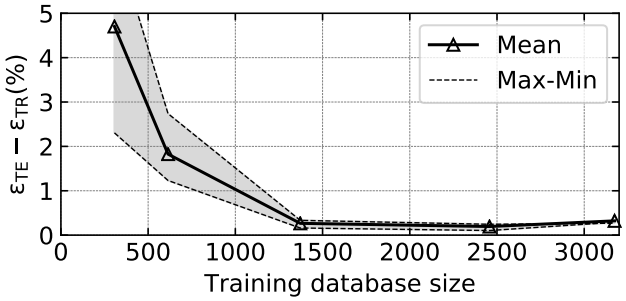

Figure 3. Training database independence study.

The hyperparameters are changed one at a time while keeping the others constant with the baseline setting; the number of neurons per layer, N_L, is kept constant at a value of 12 throughout the study. The most appropriate value of λ depends on the number of layers in the ANN; in Figure 4 it is shown that the minimum error is achieved with $\lambda = 10^{-1}$ when $L = 2$. As L increases, so does the cost associated with the ANN weights (see Equation (9)); therefore, it is inferred that with $L > 2$, the regularisation factor has to be $\lambda \leq 10^{-1}$. In order to find the best combination of the two hyperparameters, the study of number of layers L is repeated 4 times, with $\lambda = 10^{-1}, 10^{-2}, 10^{-3}, 10^{-4}$, respectively. This approach is known as "grid search" and it is described in the flowchart in Figure 5.

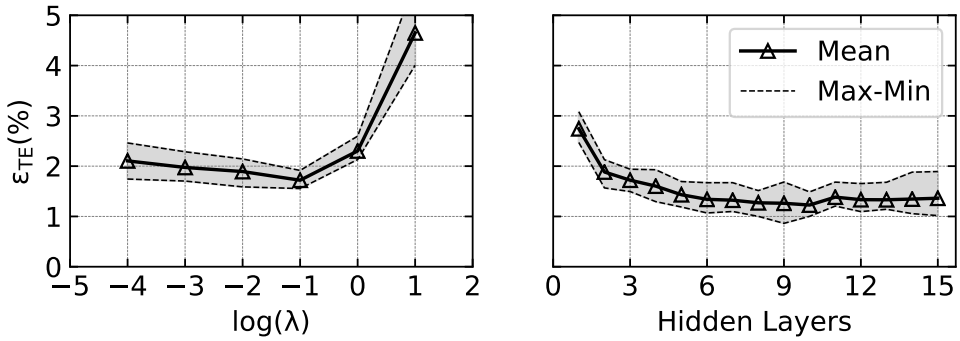

Figure 4. Hyperparameters study.

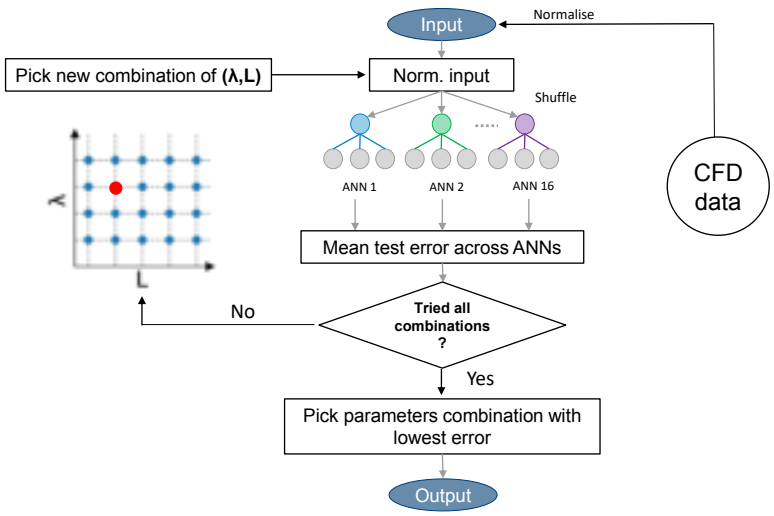

Figure 5. Flowchart for hyperparameters selection.

It is observed that the minimum mean error value ($\varepsilon_{TE} \approx 1\%$) is achieved with $\lambda = 10^{-4}$ and $L = 10$. The ANN employed in the rest of this work is, therefore, characterised by the following hyperparameters: $N_L = 12$, $L = 10$, $\lambda = 10^{-4}$.

Figure 6 shows a good agreement between the PDFs of CFD and ANN predictions; almost none of the test data lie outside the 5% confidence band (in grey).

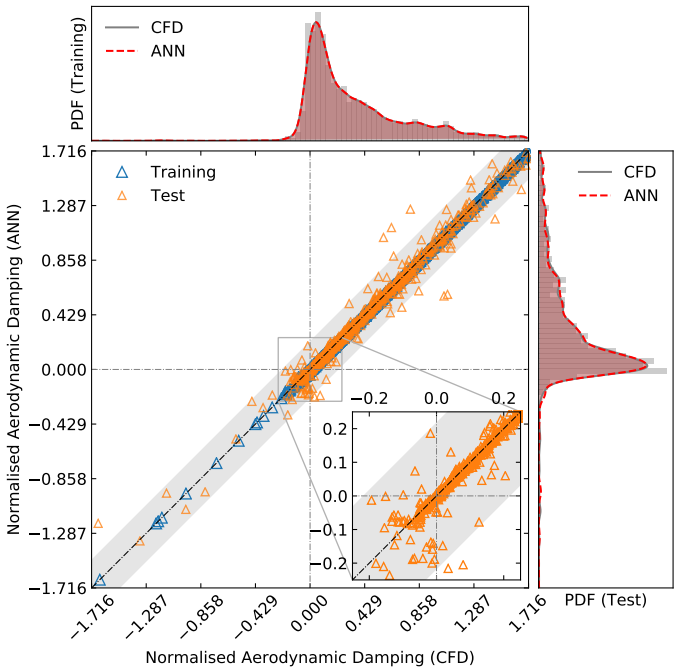

Figure 6. PDF and scatter plot of CFD data points and ANN "reproductions".

3. Results

3.1. Validation

The following results show a comparison between ANN and CFD predictions. Four cases are setup to demonstrate the capability of the ANN: 4 out of 5 input variables are fixed while the remaining one is swept. The CFD computations employed in this comparison do not explicitly coincide with any training sample, they will therefore represent a further, and final, test to evaluate the machine-learnt surrogate model. The combination of parameters for the four comparisons are reported in Table 3. The results in Figure 7 show good agreement between ANN and CFD.

Table 3. Input parameters for ANN sweep test.

	M_1	β_1	k	X_t	σ
Case 1	0.8	Sweep	0.5	3.0	20°
Case 2	0.55	+5°	Sweep	1.5	20°
Case 3	0.7	+6°	0.7	Sweep	0°
Case 4	0.55	+5°	0.5	1.0	Sweep

Figure 7a shows that for a blade vibrating in flap mode, in transonic flow, aerodynamic damping decreases with increasing flow incidence. The flow conditions for this case are very similar to what a fan blade section would experience as it moves up a constant speed characteristic. This behaviour has been already reported in the literature [8]. The ANN is able to follow the trend of the CFD closely, and to predict the flutter boundary within 0.2°, confirming that its predictions can be trusted for engineering-relevant cases. Figure 7b shows a reduced frequency sweep; at these flow conditions and with the given σ, the upstream and downstream cut-off frequencies are 0.230 and 0.408, respectively. As the

frequency of vibration is increased, the unsteady pressure fields upstream and downstream of the blade change from cut-on to cut-off. The frequencies at which this change takes place are the cut-off frequencies and their crossing is associated with a strong change in aerodynamic damping. The crossing in Figure 7b takes place at $k = 0.408$ and is visible by the drop in aerodynamic damping. The surrogate model captures the overall trend as well as the crossing of the zero damping line with good accuracy. Figure 7c shows a sweep of X_t; as the modeshape approaches a pure bending (increasing X_t), the aerodynamic damping increases, in agreement with the literature. The ANN is, again, able to follow the CFD closely. The peak in aerodynamic damping in Figure 7d is well predicted, both in location ($\sigma \approx 40^\circ$) and magnitude, and so is the overall shape of the curve.

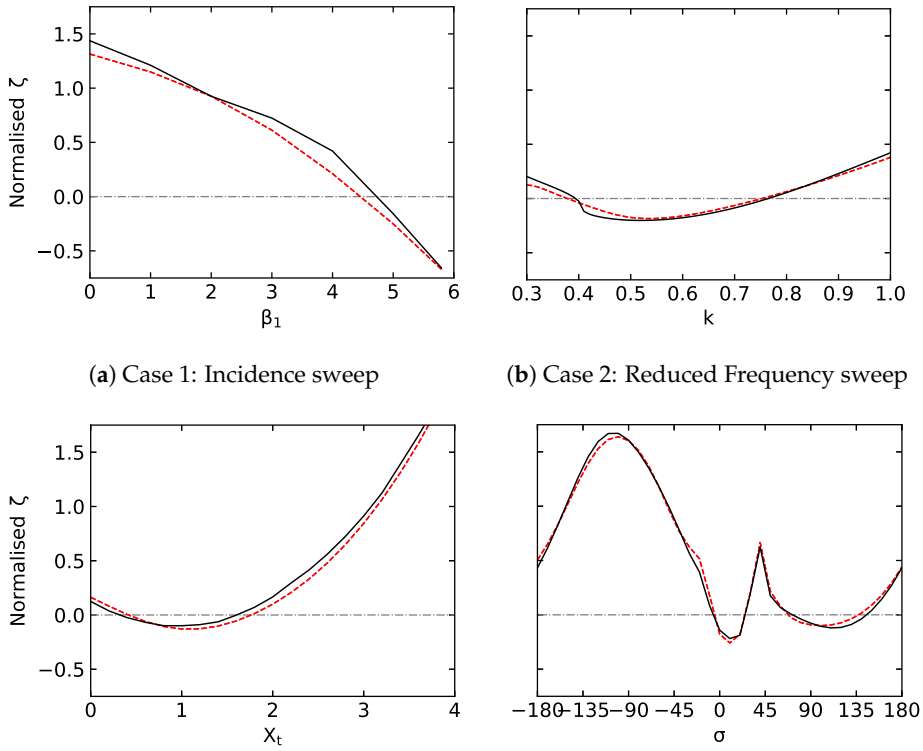

(**a**) Case 1: Incidence sweep (**b**) Case 2: Reduced Frequency sweep

(**c**) Case 3: Axis distance sweep (**d**) Case 4: Interblade Phase Angle sweep

Figure 7. Comparison of ANN (dashed red line) and CFD (solid black line) predictions.

The results discussed above show that the ANN is able to correctly predict aerodynamic damping across a range of flow conditions and structural parameters. Moreover, the surrogate model captures the zero damping crossing point (flutter boundary) with good accuracy. In the next subsection, an example of how the method can be used in a design environment is given.

3.2. Application

In this section, the application of this method to a hypothetical engineering problem is addressed. During the early design stage of a turbomachinery blade, the surrogate model predicts flutter for an aerodynamically optimised blade at some operating conditions. Even at the cost of reducing aerodynamic performance, the design parameters need to be adjusted to increase damping and regain stability. Under the assumption that a mechanical solution (e.g., introduction of under-platform dampers) is either not convenient or not possible at all (e.g., the blade is part of a blisk), the most viable solution is to increase aerodynamic damping. Traditional wisdom suggests that, for example, increasing reduced frequency is beneficial for aeroelastic stability. However, this generalisation has been shown to achieve mixed results in real applications (see Figure 7b). Therefore, there is a

need for tools which can provide guidelines for blade re-design or optimisation to improve aerodynamic damping. This is the problem that the present method tries to tackle.

Take a blade behaving like Figure 7d as test case. Two intervals of σ are affected by flutter: 0° to 30° and 60° to 140°. The objective is to adjust the design parameters so that instability can be avoided. In order to achieve this goal, one can compute the normalised gradients (Equation (3)), and use them as a guide for deciding the best action to take in order to increase damping in an unstable configuration.

The normalised gradients at $\sigma = 20^\circ$ and $\sigma = 120^\circ$ are shown in Figure 8. The bar height, value of normalised gradient, is a measure of aerodynamic damping sensitivity, while the sign on top gives the type of correlation between input and output, i.e., a (+) sign indicates that an increase in input variable results in greater aerodynamic damping. The most important parameter in both cases of Figure 8 is β_1 which is negatively correlated with damping. M_1 is important for $\sigma = 20^\circ$ but exerts negligible influence at $\sigma = 120^\circ$. The influence of k diminishes from $\sigma = 120^\circ$ to $\sigma = 20^\circ$, and, most importantly, the nature of its correlation with aerodynamic damping is opposite between the two cases; i.e., an increment in k is beneficial at $\sigma = 120^\circ$ but detrimental at $\sigma = 20^\circ$. Finally, X_t shows the same behaviour as k. The previous considerations lead to the conclusion that, varying only one parameter, the most effective action one can take (for both Interblade Phase Angles) is to reduce the incidence of incoming flow onto the blade (e.g., restaggering the blade).

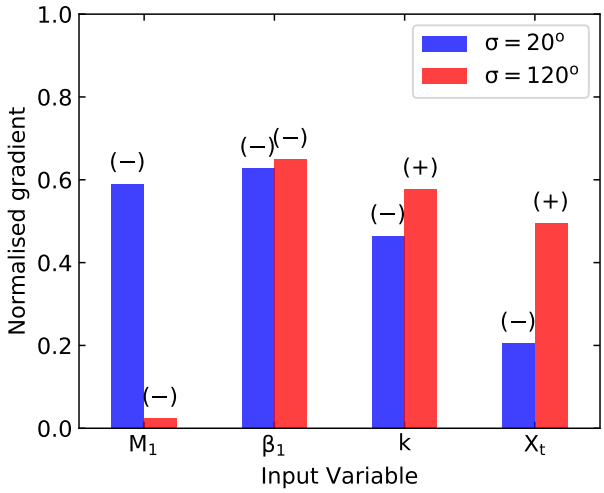

Figure 8. Normalised gradients for Case 4 at $\sigma = 20^\circ$ and $\sigma = 120^\circ$.

The change in aerodynamic damping due to variation in incidence angle and reduced frequency is shown in Figure 9. The predictions are results from the surrogate model. As expected, a reduction in incidence angle is beneficial for both Interblade Phase Angles (Figure 9a). In particular, a decrease of 0.3° is sufficient to stabilise $\sigma = 120^\circ$, whereas a reduction of 1.8° is necessary to stabilise $\sigma = 20^\circ$. Figure 9b confirms the contradicting behaviour of aerodynamic damping with respect to reduced frequency, for the two cases: an increase in k leads to a more stable blade at $\sigma = 120^\circ$, but aggravates the instability at $\sigma = 20^\circ$ in the vicinity of the design point. The method also provides an "exchange rate" between different parameters so that the designer can make the best choice for improving flutter margin. For example, in Figure 9 for $\sigma = 120^\circ$, a decrease of 0.3° in incidence is equivalent to an increase of, roughly, 0.06 in reduced frequency for eradicating flutter.

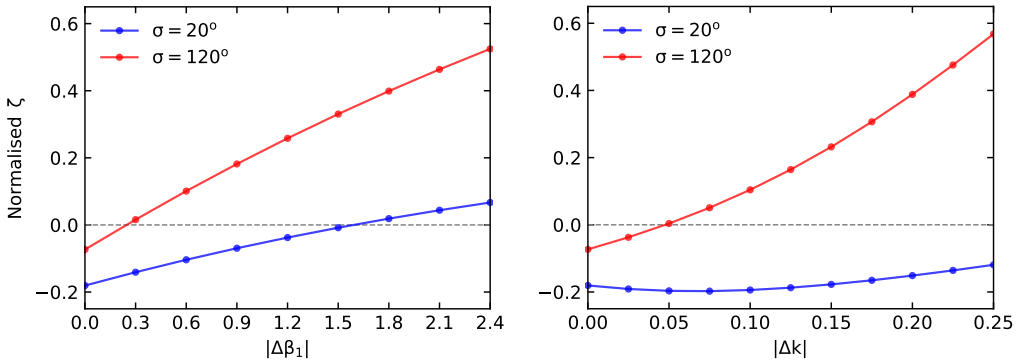

(**a**) Damping with decreasing incidence (**b**) Damping with increasing reduced frequency

Figure 9. Change in normalised damping at $\sigma = 20°$ and $\sigma = 120°$.

In summary, the surrogate model predicts that a decrease of 1.8° in flow incidence should stabilise the blade at both $\sigma = 20°$ and $\sigma = 120°$. To verify this claim, a "restaggered" case is setup, where the inflow angle is kept constant and the incidence is reduced by restaggering the blade by 1.8°. The other parameters are kept constant. The aerodynamic damping predicted by the CFD is shown in Figure 10. As anticipated by the surrogate model, $\sigma = 120°$ becomes highly stable while the point at $\sigma = 20°$ sits just above the zero damping line. Two unstable points at $\sigma = 0°$ and $\sigma = 10°$ are still present: the process described above can be repeated for them and appropriate changes to the input variables can be made to induce stability at these Interblade Phase Angles.

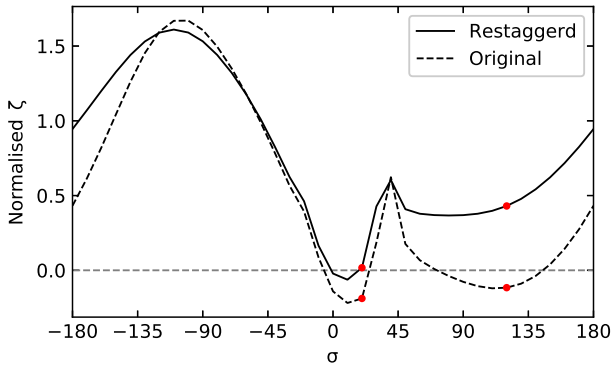

Figure 10. CFD prediction of normalised damping for "restaggered" blade.

4. Conclusions and Future Work

A machine-learning-based sensitivity analysis has been presented. The surrogate model has been trained on results from a linearised aeroelastic solver and its validity has been tested through evaluation of relative errors. The results concern a flap modeshape, with different Interblade Phase Angles, across a range of reduced frequencies, flow conditions and consequent acoustic waves regimes. It has been shown that the sensitivity analysis can be used as a guide to take appropriate measures to stabilise two unstable operating points; therefore, constituting a redesign tool for the given airfoil geometry. This preliminary study shows how summary measures of influence of design parameters can be easily extracted and presented with data-driven approaches, such as machine learning, rather than classical methods of investigation. The results in this work are obtained with a simple artificial neural network which makes no assumption regarding the flow physics of turbomachinery. Furthermore, the results are only valid for the airfoil geometry used in the training phase. Future work will focus on addressing these limitations by embedding known physics into the cost function (e.g., continuity), and by training the model on physically relevant steady state features (e.g., shock strength), independent of geometry.

Author Contributions: Conceptualization, M.R., M.V. and F.Z.; methodology, M.R., M.V., F.Z.; software, M.R.; formal analysis, M.R.; investigation, M.R., M.V., F.Z.; data curation, M.R.; writing—original draft preparation, M.R.; writing—review and editing, M.R., M.V. and F.Z.; visualization, M.R.; supervision, M.V. and F.Z.; funding acquisition, M.V. All authors have read and agreed to the published version of the manuscript.

Funding: This research received no external funding.

Institutional Review Board Statement: Not applicable.

Informed Consent Statement: Not applicable.

Data Availability Statement: Not applicable.

Acknowledgments: The authors would like to thank Paul Petrie-Repar from RPMTurbo for providing the aeroelastic solver used in this work.

Conflicts of Interest: The authors declare no conflict of interest.

Abbreviations

The following abbreviations are used in this manuscript:

ANN	Artificial Neural Network
CFD	Computational Fluid Dynamics
MUSCL	Monotonic Upstream-Centered Scheme for Conservation Laws
URANS	Unsteady Reynolds-averaged Navier–Stokes
PDF	Probability Density Function
GMRES	Generalized Minimal Residual Method

Appendix A. Computational Cost

The steady state solver uses a pseudo-time stepping technique to bring the solution to convergence. In this study, a steady CFD solution is considered converged if every point in the domain has a density residual of order 10^{-6}. On average, the equivalent CPU time elapsed to obtain a converged solution for this case is 8400 s.

The unsteady solver uses a preconditioned GMRES scheme to find the solution to the system arising from the linearisation of the URANS equations. In this study, an unsteady CFD solution is considered converged if the residual is of order 10^{-6}. On average, the equivalent CPU time elapsed to obtain a converged solution for this case is 20 s.

In total, the creation of the 5 databases employed in this study took an estimated 9280 CPU hours.

The ANN employed in this study runs on CPU and the optimisation process performs a fixed number of steps, 750. The number of iterations was chosen so that the different ANNs would not suffer from excessive underfitting or overfitting, so called "early stopping" regularization. The cost function convergence history for the ANN employed in this work is shown in Figure A1.

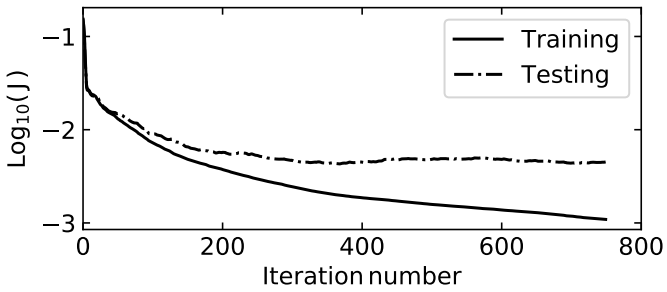

Figure A1. Plot of cost function convergence.

A total of 1072 different ANNs have been trained to find the best combination of parameters, yielding an estimated 194 equivalent CPU hours. The results in Figure 7 consist of 8 steady and 135 unsteady simulations. The predictions from the CFD have been obtained in an estimated 19 equivalent CPU hours, whereas the ANN produced its results in 4.6 CPU milliseconds.

References

1. AGARD. *Manual on Aeroelasticity in Axial-Flow Turbomachines*; AGARD-AG-298; North Atlantic Treaty Organization: Neuilly sur Seine, France, 1987.
2. Chi, R.M.; Srinivasan, A.V. Some Recent Advances in the Understanding and Prediction of Turbomachine Subsonic Stall Flutter. *J. Eng. Gas Turbines Power* **1985**, *107*, 408–417. [CrossRef]
3. Crawley, E.F.; Ducharme, E.H. Parametric Trends in the Flutter of Advanced Turboprops. *J. Turbomach.* **1990**, *112*, 741–750. [CrossRef]
4. Srinivasan, A.V. Flutter and Resonant Vibration Characteristics of Engine Blades. *J. Eng. Gas Turbines Power* **1997**, *119*, 742–775. [CrossRef]
5. Whitehead, D.S. Vibration and Sound Generation in a Cascade of Flat Plates in Subsonic Flow. 1972. Available online: https://reports.aerade.cranfield.ac.uk/bitstream/handle/1826.2/2959/arc-rm-3685.pdf?sequence=1&isAllowed=y (accessed on 31 January 2020).
6. Akai, T.J.; Atassi, H. Aerodynamic and Aeroelastic Characteristics of Oscillating Loaded Cascades at Low Mach Number-Part II: Stability and Flutter Boundaries. *J. Eng. Power* **1980**, *102*, 352–356. [CrossRef]
7. Atassi, H.; Akai, T.J. Aerodynamic and Aeroelastic Characteristics of Oscillating Loaded Cascades at Low Mach Number-Part 1: Pressure Distribution, Forces, and Moments. *J. Eng. Power* **1980**, *102*, 344–351. [CrossRef]
8. Vahdati, M.; Cumpsty, N. Aeroelastic Instability in Transonic Fans. *ASME J. Eng. Gas Turbines Power* **2016**, *138*, 022604. [CrossRef]
9. Tyler, J.M.; Sofrin, T.G. *Axial Flow Compressor Noise Studies*; SAE Technical Pape; SAE International: Warrendale, PA, USA, 1962. [CrossRef]
10. Panovsky, J.; Kielb, R.E. A Design Method to Prevent Low Pressure Turbine Blade Flutter. *J. Eng. Gas Turbines Power* **1999**, *122*, 89–98. [CrossRef]
11. Lee, K.B.; Wilson, M.; Vahdati, M. Numerical Study on Aeroelastic Instability for a Low Speed Fan. *J. Turbomach.* **2016**, *139*, 071004. [CrossRef]
12. Dowell, E.H. (Ed.) *A Modern Course in Aeroelasticity*; Springer: Berlin/Heidelberg, Germany, 2015; pp. 428–429.
13. Isomura, K.; Giles, M.B. A Numerical Study of Flutter in a Transonic Fan. *J. Turbomach.* **1998**, *120*, 500–507. [CrossRef]
14. He, X.; Zhao, F.; Vahdati, M. Uncertainty Quantification of Spalart-Allmaras Turbulence Model Coefficients for Simplified Compressor Flow Features. *J. Fluids Eng.* **2020**, *142*, 091501. [CrossRef]
15. Duraisamy, K.; Iaccarino, G.; Xiao, H. Turbulence Modeling in the Age of Data. *Annu. Rev. Fluid Mech.* **2019**, *51*, 357–377. [CrossRef]
16. Xiao, H.; Cinnella, P. Quantification of model uncertainty in RANS simulations: A review. *Prog. Aerosp. Sci.* **2019**, *108*, 1–31. [CrossRef]
17. Stapelfeldt, S.; Vahdati, M. On the Importance of Engine-Representative Models for Fan Flutter Predictions. *J. Turbomach.* **2018**, *140*, 081005. [CrossRef]
18. Frannson, T.; Verdon, J. Update Report on Standard Configurations for Unsteady Flow through Vibrating Axial-flow Turbomachine Cascades. *Rep. R. Inst. Technol. Stock. Swed.* **1991**. Available online: https://www.rpmturbo.com/testcases/STCF/STCF1to10/Documents/SC2110.92update.pdf (accessed on 31 March 2020).
19. Petrie-Repar, P.J.; McGhee, A.; Jacobs, P.A.; Gollan, R. Analytical Maps of Aerodynamic Damping as a Function of Operating Condition for a Compressor Profile. In Proceedings of the Turbo Expo: Power for Land, Sea, and Air, Barcelona, Spain, 8–11 May 2006; Volume 5, pp. 1133–1144.
20. Frey, C.; Ashcroft, G.; Kersken, H.P.; Schlüß, D. Flutter Analysis of a Transonic Steam Turbine Blade with Frequency and Time-Domain Solvers. *Int. J. Turbomach. Propuls. Power* **2019**, *4*, 15. [CrossRef]
21. Rendu, Q.; Vahdati, M.; Salles, L. Radial Decomposition of Blade Vibration to Identify a Stall Flutter Source in a Transonic Fan. *J. Turbomach.* **2019**, *141*, 101011. [CrossRef]
22. Zhao, F.; Nipkau, J.; Vahdati, M. Influence of acoustic reflections on flutter stability of an embedded blade row. *Proc. Inst. Mech. Eng. Part A J. Power Energy* **2016**, *230*, 29–43. [CrossRef]
23. McKay, M.D.; Beckman, R.J.; Conover, W.J. A Comparison of Three Methods for Selecting Values of Input Variables in the Analysis of Output from a Computer Code. *Technometrics* **1979**, *21*, 239–245.
24. Lecun, Y. Generalization and network design strategies. In *Connectionism in Perspective*; Pfeifer, R., Schreter, Z., Fogelman, F., Steels, L., Eds.; Elsevier: Amsterdam, The Netherlands, 1989.
25. Fletcher, R. *Practical Methods of Optimization*; Number v. 2 in A Wiley-Interscience Publication; Wiley: Hoboken, NJ, USA, 1987.

International Journal of
Turbomachinery
Propulsion and Power

MDPI

Article

Experimental Study of the Leakage Flow in an Axial-Flow Fan at Variable Loading †

Edward Canepa, Andrea Cattanei *, Mehrdad Moradi and Alessandro Nilberto

Dipartimento di Ingegneria Meccanica, Energetica, Gestionale e dei Trasporti (DIME), DIME-Università di Genova, via Montallegro, 1, I-16145 Genova, Italy; edward.canepa@unige.it (E.C.); mehrdad.moradi@edu.unige.it (M.M.); alessandro.nilberto@unige.it (A.N.)

* Correspondence: Andrea.Cattanei@unige.it; Tel.: +39-010-335-2445

† This is an extended version of our paper ETC2021-783 presented at the 14th European Turbomachinery Conference on Fluid Dynamics & Thermodynamics ETC14, Gdansk, Poland, 12–16 April 2021.

Abstract: The present paper reports a 2D-PIV (particle image velocimetry) study of the effect of the operating point on the leakage flow in a low-speed ring fan. First, the flow pattern has been studied at 12 operating points covering the whole characteristic curve. At very low loading, the leakage flow streams along the rotor ring and is directly reingested; then, a separation bubble attached to the ring forms that, approaching the design point, modifies in a flow streaming radially outward. As the loading further increases, a separated flow region appears in the blade tip region that finally merges with the leakage flow. A further, more detailed study has been performed at eight operating points in the neighborhood of the design one. Very small loading variations may yield the leakage flow pattern modification, but no intermittence is present during the transition, as instantaneous flow patterns of any intermediate type continuously alternate. These results provide a consistent explanation for the ones of previous acoustic measurements.

Keywords: axial-flow fan; rotating shroud; leakage flow; fan noise; PIV

check for updates

Citation: Canepa, E.; Cattanei, A.; Moradi, M.; Nilberto, A. Experimental Study of the Leakage Flow in an Axial-Flow Fan at Variable Loading. *Int. J. Turbomach. Propuls. Power* **2021**, *6*, 40. https://doi.org/10.3390/ijtpp6040040

Academic Editor: Antoine Dazin

Received: 28 July 2021
Accepted: 13 October 2021
Published: 20 October 2021

Publisher's Note: MDPI stays neutral with regard to jurisdictional claims in published maps and institutional affiliations.

Copyright: © 2021 by the authors. Licensee MDPI, Basel, Switzerland. This article is an open access article distributed under the terms and conditions of the Creative Commons Attribution (CC BY-NC-ND) license (https://creativecommons.org/licenses/by-nc-nd/4.0/).

1. Introduction

Axial fans employed in automotive cooling systems are commonly provided with a rotating shroud, i.e., a ring connecting the blade tips. This ring improves the volumetric efficiency and also strengthens the whole assembly, but it has a number of undesired effects. For instance, in a recent study, Carassale et al. [1] showed that the leakage flow may cause low-frequency flutter, but the typically reported effect is a strong increase in the radiated noise due to the presence of large-scale turbulent structures, Longhouse [2]. They are contained in the leakage flow released from the gap between the ring and the stationary enclosure and are eventually reingested by the rotor. Their interaction with the rotor blades results in noise in the low- to medium-frequency range, with the appearance of narrowband humps at subharmonic frequencies and a general increase in the broadband noise. In fact, a low-speed axial-flow fan may radiate noise as a consequence of a number of noise-generating mechanisms (mainly, large- and small-scale inlet turbulence, rotor-stator interaction, leakage flow, and interaction of boundary layer turbulence with the blade trailing edge). However, sealing the gap, Canepa et al. [3] could inhibit the leakage flow; this showed that not only the leakage flow noise may constitute the major contribution to the low-frequency noise but to the overall radiation also, e.g., see Canepa et al. [4]. Although the main features of the leakage flow are known, very few works related to it are available in the literature, e.g., see Fukano et al. [5], Fukano and Jang [6], Piellard et al. [7], Magne et al. [8], Moreau and Sanjose [9], Zenger et al. [10], Na et al. [11], Canepa et al. [3,4,12,13], and Zhu et al. [14]. In order to find effective solutions for noise reduction, a deeper insight in the leakage flow features and in the effect of relevant parameters is necessary.

The present paper continues the aerodynamic and acoustic investigation reported in Canepa et al. [4]. In such a study, a correspondence between SPL spectra and leakage flow pattern was sought. Namely, a detailed analysis of the effect of both rotational speed and operating point on the noise features was reported that suggested that local modifications in the SPL trend as a function of the loading are related to modifications of the leakage flow pattern but also to the appearance of separated flow regions at the blade tip. However, aerodynamic measurements were performed at only four operating points, proving to be insufficient for a complete description. Thus, a number of questions remained open that regard the dependence of the flow pattern on the operating point and some new ones arose. The present work reports PIV measurements of the leakage flow at a large number of operating points, thus providing a detailed description of the effect of the operating point on the leakage flow pattern.

As a general remark, it should be considered that the noise generation in low-speed fans depends on the instantaneous features of the flow. Hence, the possibility of simultaneously surveying the whole measurement domain makes PIV a suitable technique indeed. Unfortunately, the complexity of the rotor geometry and the highly distorted flow constitute serious limitations to the full exploitation of the present PIV system, preventing from taking measurements inside the rotor or in planes other than the meridional one. Noise yields from the loading fluctuations resulting from the interaction between flow and blade; thus, measurements of the instantaneous blade pressure would also provide very useful information. Unfortunately, the small blade thickness and the difficulties related to taking measurements in the rotating frame constitute serious hindrances. All this results in a situation that is typical when dealing with aerodynamic noise, i.e., having to gather information on physical phenomena on the basis of limited data sets. Fortunately, this problem is mitigated by the fact that, when dealing with aeroacoustic problems, the quality of phenomena is often more important than quantitative information.

2. Experimental Procedure

2.1. Experimental Facility

The measurement campaign has been carried out in the DIME Aeroacoustics laboratory with the fan mounted on a test rig specifically conceived and designed based on ISO 5801 norms, see Figure 1a. The tested rotor is a 9-blade aluminum prototype obtained by means of a numerically controlled milling machine; hence, it is geometrically very precise and, differently from rotors commonly employed in real cooling modules, it may be considered stiff. This prevents the geometry from being altered by the aerodynamic load or by the centrifugal force, an effect that could strongly affect leakage flow and radiated noise, e.g., see Canepa et al. [12]. The rotor has a tip radius r_{tip} of 222 mm, a hub-to-tip diameter ratio r_{hub}/r_{tip} of 0.374, and a chord c which varies between 43 mm and 50 mm from hub to tip. At the design point, the flow coefficient is $\varphi_{des} = \frac{Q_{des}}{u_{tip}\pi {r_{tip}}^2} = 0.0869$, and the pressure rise coefficient is $\psi_{des} = \frac{\Delta p_{des}}{0.5\rho_0 {u_{tip}}^2} = 0.0993$, with Q the volume flow rate and Δp the fan pressure rise (outlet static pressure minus inlet total one). The measurements have been carried out at constant rotational speed Ω of 2400 rev/min; depending on the operating point, the chord-based Reynolds number approximately ranges between 31,000 and 41,000 at the hub and between 186,000 and 188,000 at the tip. During the tests, Δp and Ω have been continuously monitored; Ω has been measured by means of a one-per-revolution TTL signal generated by an optical tachometer. The gap between the rotating ring and the stationary casing is constituted by 5-mm-width axial and radial parts, see Figure 1d. No acoustic measurements have been taken in the present work.

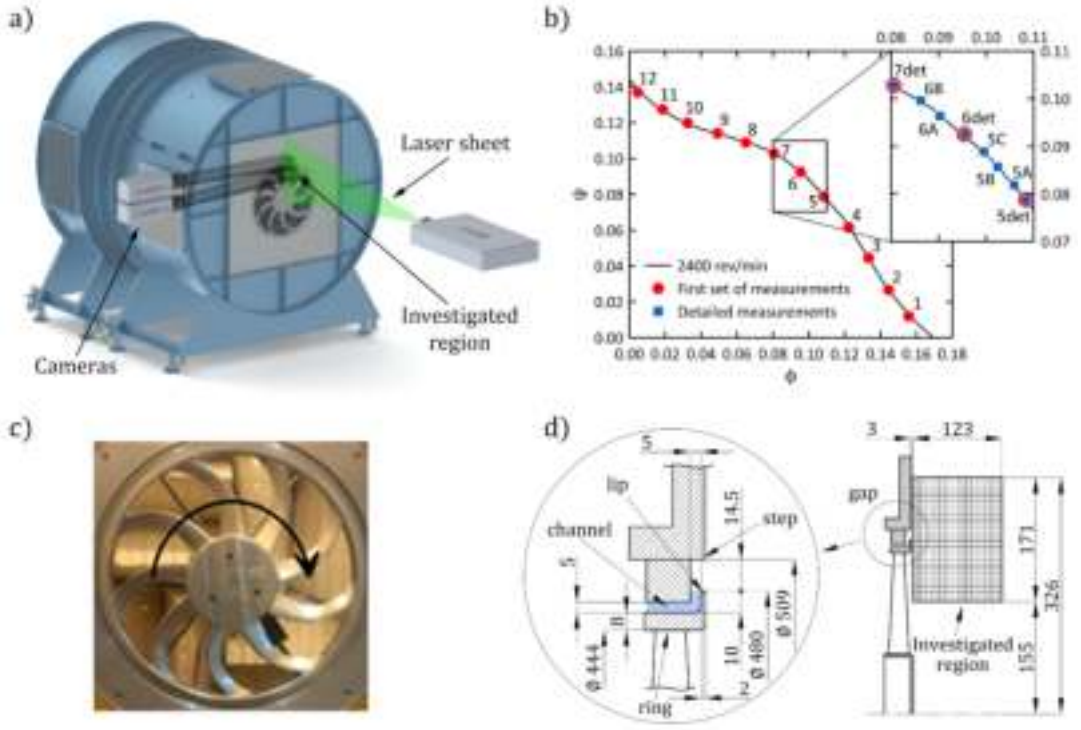

Figure 1. Experimental facility: (**a**) test rig; (**b**) rotor characteristic curve and investigated conditions; (**c**) rotor prototype; (**d**) rotor geometry.

2.2. Measurement Procedure and Data Processing Technique

In order to study the effect of the pressure rise on the leakage flow pattern, 12 ψ values covering the whole characteristic curve have been first considered, see Figure 1b; these operating points included the ones already investigated by Canepa et al. [4]. Subsequently, in order to obtain deeper insight into the flow pattern modification already observed about the design point (from a recirculation bubble attached to the ring to a broad recirculation bubble), a second, more detailed measurement campaign has been carried out at eight ψ values, see Table 1.

Table 1. Investigated operating conditions.

First Set of Measurements	ψ	Set of Detailed Measurements	ψ
1	0.0120	-	-
2	0.0267	-	-
3	0.0445	-	-
4	0.0617	-	-
5	0.0788	5det	0.0788
-	-	5A	0.0819
-	-	5B	0.0857
-	-	5C	0.0889
6	0.0925	6det	0.0925
-	-	6A	0.0964
-	-	6B	0.0996
7	0.103	7det	0.103
8	0.109	-	-
9	0.114	-	-
10	0.120	-	-
11	0.127	-	-
12	0.137	-	-

The flow field has been investigated in the meridional plane close to the tip gap by means of a 2D-PIV system. Namely, in a rectangular area located at x = 3 mm from the ring with an extension of L_x = 123 mm × L_r = 171 mm, i.e., r/r_{tip} = 0.698–1.468 and x/r_{tip} = 0.014–0.581, see Figure 1d. The PIV system is constituted by a double-cavity Nd:Yag pulsed laser and by two Dantec High Sense Mk II digital cameras with a maximum frame rate (i.e., sampling frequency) of 6 Hz. In order to increase the radial extension of the investigated area without losing spatial resolution, the two cameras have been mounted radially shifted with a 25-mm overlapping region used to join the two instantaneous vector fields correctly. The flow has been seeded by means of a fog generator. The velocity fields (i.e., the axial and radial velocity components v_a and v_r) have been obtained using a spatial cross-correlation function yielding instantaneous vector fields constituted by 83 × 116 points on a square grid of steps $\Delta x = \Delta r$ = 1.5 mm.

The first measurement campaign constitutes a basic survey of the flow field based on 800 instantaneous vector fields per working point; for such measurements, the available data are too few for performing sufficiently accurate ensemble averages; therefore, only time averages have been taken. In the second measurement campaign, 2000 instantaneous vector fields have been collected, and the TTL signal generated by the optical tachometer has been employed as a reference signal for the ensemble average technique. Then, the instantaneous vector fields have been sorted into 90 phase bins per revolution, each representing a particular instant within the rotational period, i.e., a 4-degree window in the relative frame. Other details may be found in Canepa et al. [4,13].

In order to increase the statistical reliability, the data related to a specific position within a blade passage have been further averaged, yielding 10 ensemble averaged meridional distributions per blade pitch based on about 198 samples, i.e., about 22 samples per each bin multiplied by nine blade passages. The 10 velocity fields may be related to 4-degree-spacing meridional planes. This further average is expected not to add fake turbulence, since the rotor geometry is very precise and the differences between blade passages should be negligible. For this set of measurements, the time averaged flow fields have been computed by means of the arithmetic average of flow fields on the 10 planes.

The following quantities will be employed for the analysis of the flow: the time-averaged velocity obtained averaging the instantaneous velocity components v_a and v_r, the time averaged turbulence intensity $\overline{Tu}$, and the unresolved unsteadiness $\overline{\widetilde{Tu}}$. Both $\overline{Tu}$ and $\overline{\widetilde{Tu}}$ are based on u_{tip}, but the former contains all of the velocity fluctuations, while the latter contains the non-periodic part of the velocity fluctuations only, i.e., v'_a and v'_r. In fact, v'_a and v'_r may also contain periodic components not related to the blade passage frequency (BPF) and harmonics. In the present case, as in most of low-speed turbomachines, no such periodic components are present; hence, $\overline{\widetilde{Tu}}$ cumulates the effects of both small-scale turbulence and large-scale flow structures only. As the 2D-PIV system does not allow to measure v_ϑ, $\overline{Tu}$ and $\overline{\widetilde{Tu}}$ only provide qualitative information about the flow unsteadiness. For the sake of space, only the definition of $\overline{\widetilde{Tu}}$ is reported, see Equation (1), since the definition of $\overline{Tu}$ is very similar; the reader is addressed to Hussain and Reynolds [15] or to Canepa et al. [13] for the details of the velocity decomposition technique.

$$\overline{\widetilde{Tu}} = \frac{\sqrt{\frac{\left(\overline{\widetilde{v'_a}^2}+\overline{\widetilde{v'_r}^2}\right)}{2}}}{u_{tip}} \tag{1}$$

According to the PIV error analyses of Grant [16] and Prasad et al. [17], the experimental uncertainty for the instantaneous velocity has been estimated to be 3% for the present case. Such an estimate represents an indicative value for the whole investigated domain and the chosen operating points.

In the present case, the cross-plane velocity component v_ϑ constitutes the main source of systematic bias (other causes are related to timing and synchronization, installation

and alignment, peak-locking and evaluation technique, particles tracing capability, and illumination) and hence a proper estimation is difficult since v_ϑ may not be measured. Such an effect increases close to the boundaries of the investigated domain, possibly yielding a spatially variable uncertainty.

Statistical errors have been computed based on a 20% $\overline{Tu}$ value. With a 95% confidence level, this results in statistical uncertainties of 1.5% for the time averaged velocity components $\overline{v_a}$ and $\overline{v_r}$, of 5% for $\overline{Tu}$ (800 instantaneous flow fields employed) and of 3% for $\overline{\widetilde{Tu}}$ (2000 instantaneous flow fields employed).

As already discussed, periodic oscillations provide a spurious contribution to time averaged quantities such as $\overline{Tu}$, since they may not be distinguished from fluctuations not correlated with the rotor revolution. The rotating pressure field anchored to the rotor yields an upstream potential-flow effect that, in the absolute frame, results in periodic velocity oscillations that typically take place in front of the rotor blades. As reported by Canepa et al. [13], this upstream effect may also extend to the gap region, thus yielding an erroneous contribution to $\overline{Tu}$ that is expected to increase with ψ, since such a pressure field strengthens as ψ increases.

Although this point is deepened in the following paragraphs, it is worthy to disclose that, depending on the operating conditions, two different patterns mainly characterize the leakage flow field (e.g., see Canepa et al. [4,12,13] and Magne et al. [8]): a recirculation bubble attached to the rotor ring, which for the present rotor approximately forms below the design pressure rise, and a large separated-flow zone that forms above it. Based on the observation of the time averaged velocity fields, the cases ψ = 0.0788 and 0.103 have been assumed as references for the two flow patterns and have been chosen as the lower and the upper limits for the ψ range of the second measurement campaign. Then, the resemblance of the instantaneous flow fields with the two reference flow patterns has been sought; to this aim, the resemblance index RI has been employed as a quantitative metric for comparing the instantaneous vector fields with the reference ones, see Liu and Haworth [18] and Willman et al. [19]. RI is obtained by projecting one velocity field onto the other one:

$$\mathrm{RI}\left(\vec{x}\right) = \frac{v_1\left(\vec{x}\right)\cdot v_2\left(\vec{x}\right)}{\left|v_1\left(\vec{x}\right)\right|\left|v_2\left(\vec{x}\right)\right|} \tag{2}$$

where $\vec{x}$ is a point in the measurement domain, and the indexes 1 and 2 may refer to two operating conditions ψ_1 and ψ_2 or to two time instants t^1 and t^2 at the same ψ. As a consequence of its definition, RI equals to the cosine of the angle between the velocities $v_1\left(\vec{x}\right)$ and $v_2\left(\vec{x}\right)$ and may vary in the range $[-1, 1]$, where 1 corresponds to aligned vectors with same direction and -1 corresponds to aligned vectors but in the opposite direction. In this way, RI compares the alignment of the two vectors independently of their magnitudes. Hence, for each comparison, a matrix of 83×116 RI values is generated which may be spatially averaged to produce a single value that quantifies the resemblance between the two fields, i.e., the overall match in the alignment.

In the present work, RI is employed to evaluate whether a velocity field acquired at the time instant t^n and related to a ψ value is similar to the time averaged velocity field related to a reference case for which $\psi = \psi_{ref}$ (either $\psi_{ref} = 0.0788$ or $\psi_{ref} = 0.103$):

$$\mathrm{RI}^n_{\psi_{ref}}(\psi) = \frac{1}{(i_{max}-i_{min}+1)(j_{max}-j_{min}+1)} \sum_{i=i_{min}}^{i=i_{max}} \sum_{j=j_{min}}^{j=j_{max}} \frac{\vec{v}^n_{ij}(\psi)\cdot\vec{v}^{av}_{ij}\left(\psi_{ref}\right)}{\left|\vec{v}^n_{ij}(\psi)\right|\left|\vec{v}^{av}_{ij}\left(\psi_{ref}\right)\right|} \tag{3}$$

where the i and j indexes represent the points in the x and r directions, i.e., $x_i = 3 + (i-1)\Delta x$ and $r_j = 155 + (j-1)\Delta r$ (quantities expressed in millimeters). n identifies the instanta-

neous velocity field and ranges between 1 and 2000, and the superscript av indicates that the velocity field related to the reference case is the mean one. Eliminating from the summations in Equation (3) those parts of the measurement domain where the two reference velocity fields show a similar behavior allows to highlight the differences and to better evaluate the resemblance. Hence, based on visual inspection of the vector plots, the computation of $RI^{n}_{\psi_{ref}}(\psi)$ has been arbitrarily restricted to the rectangular area in front of the gap sub-domain, choosing suitable values for i_{min}, i_{max}, j_{min} and, j_{max}. More details are given in the following.

3. Experimental Results

3.1. Previous Measurements

Canepa et al. [3] showed that for low-speed fans of the present kind, the leakage flow mainly affects the low-frequency part of the spectrum and may constitute the major noise source, e.g., see also Longhouse [2]. However, the studied rotor was made of plastic and the deformations due to the centrifugal force and to the blade loading resulted in a sudden flow pattern transition from the attached separation bubble to the large separated-flow zone, see Canepa et al. [12]. A simultaneous decrease in the low-frequency part of the SPL spectrum was also observed. Furthermore, acoustic measurements were repeated with the rotor mounted in different axial positions with respect to the standard one in which the ring lip is flush with the mounting panel. It was found that even a few-millimeters difference in the rotor position may vary the ψ value at which the transition takes place: a rotor protruding from the panel could decrease it, while a backward mounted rotor could have the opposite effect. This suggested that the relative position of ring lip and edge of the panel (the step in Figure 1) may vary the orientation of the flow leaving the gap and, hence, its ability to penetrate the incoming flow, thus moving away from the rotor rather than being immediately reingested. A possible effect of rotor deformation was also reported by Moreau et al. [9].

All this has suggested to study a different rotor made of aluminum, Canepa et al. [4], and to focus attention on the sound pressure level (SPL) in the low-frequency range (i.e., St = 6–90, with $St = 60f/\Omega$ the Strouhal number). It was found that, as expected, the flow pattern transition takes place in stiff rotors also, and that it depends on the ψ value. The plots reported in Figure 2, adapted from Canepa et al. [4], show the importance of the leakage flow noise. The effect of ψ on the following acoustic quantities is considered: OASPL (the overall SPL), SPL_{low} and SPL_{high} (the SPL in the low- and high-frequency range), and the SPL spectrum. The integral quantities provide overall information on the generated noise, while the spectrum helps identify and discriminate different noise-generating mechanisms.

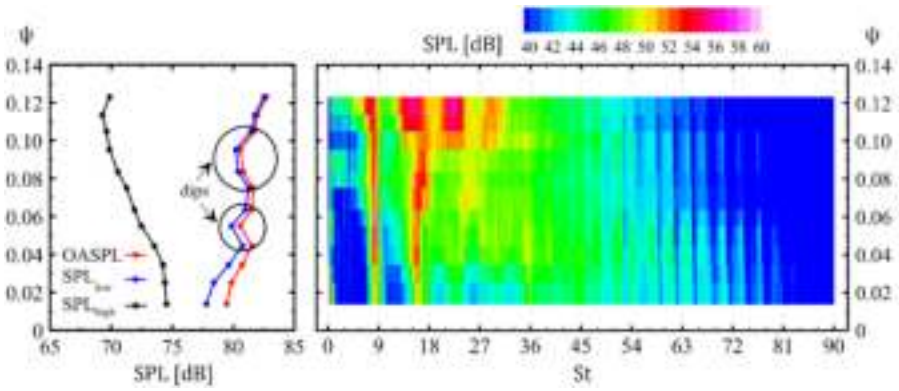

Figure 2. Dependence of the SPL on the operating conditions.

The comparison between OASPL, SPL_{low}, and SPL_{high} shows that the difference between OASPL and SPL_{low} decreases from 2 dB to 0 dB as ψ increases from the minimum to the maximum value. This means that the contribution from the high-frequency part is

negligible. Hence, at all ψ, SPL_{low} provides the major contribution to OASPL. Furthermore, the SPL spectrum contour plot indicates that crests and humps below the first three BPF harmonics ($St = 9,\ 18,\ 27$) provide the major contribution to SPL_{low}. The ingestion of non-rotating large-scale flow structures results in spectral peaks or narrowband humps at BPF harmonics, see Hanson [20] or Majumdar and Peake [21]. Peaks and humps at subharmonic frequencies are necessarily generated by the interaction of the rotor blades with co-rotating flow disturbances, e.g., see Magne et al. [8] and Moreau et al. [9]. In the present configuration, the upstream flow has no prerotation; hence, such disturbances may only be contained in flow coming from the rotor, either through the gap or from the blades due to the reverse flow. Evidences of the existence of such a reverse flow were provided by Canepa et al. [4], and blade stall in the tip region, possibly related to flow separation on the ring connection from radial to axial, is likely its cause. Flow separation in the hub region could also result in such a flow reversal, but it should affect the lower part of the blade span only, where the low velocity should result in minor contributions to the radiated noise.

Should SPL_{low} be related to the leakage flow rate only, it would increase with ψ, as the leakage flow also strengthens with it. On the contrary, SPL_{low} has a non-monotonic trend, since its growth is interrupted by two local minima at $\psi \cong 0.05$ and 0.09; an OASPL trend with a minimum about the design point has been reported by Moreau et al. [9]. This suggests that the noise-generating mechanism changes, i.e., that some flow features change at those operating points. A possible explanation is either a leakage flow pattern change or a flow reversal in the blade tip region. The comparison between the SPL_{low} plot and the SPL spectrum contour shows that the SPL_{low} trend is closely related to the modifications in the height of the crests at St smaller than 9 and 18, as such modifications take place at similar ψ values. Attention was focused on the behavior at approximately $\psi \cong 0.09$, since that point is close to the design one, and also since at $\psi \cong 0.05$ the SPL is smaller and the situation is of lesser interest. The discussion of the results suggested that: (1) the decrease that takes place from $\psi \cong 0.08$ to $\psi \cong 0.09$ is likely due to a leakage flow pattern transition from an attached recirculation bubble shortly reingested by the rotor to an outward radial flow following a long path before reingestion, and (2) the observation of the SPL spectrum shows that at $\psi \geq 0.103$, the crest at $St < 18$ shifts to lower St and becomes a broad hump; the crest at $St < 9$ has a similar behavior and a further hump appears at $St < 27$. This indicates that a change in the generating mechanism takes place. The possible explanation is that the further increase beyond $\psi \cong 0.09$ may likely be due to a flow separation taking place in the ring rounding/blade suction side region, i.e., that, at large ψ, the low-frequency noise is not due to the leakage flow. This effect may seem of lesser practical interest as it takes place at ψ values higher than the design one, where the fan is usually not operated, but it should be considered that a different design of the ring or of the shroud could move such a separation to a lower ψ. As a general consideration, this highlights that prerotating large-scale structures may be related to flow phenomena other than the leakage flow and, hence, subharmonic humps in the SPL spectrum may be caused by different kinds of generating mechanisms.

However, the aerodynamic measurements were taken at too few ψ values to properly investigate the flow pattern modifications. The present work stems from the need for a more systematic study.

3.2. General Trend of the Time-Averaged Flow Field

In order to provide an overall picture of the leakage flow in the gap region, 12 operating points have been first considered, see Table 1. The time averaged velocity fields are reported in Figure 3 together with the $\overline{Tu}$ contour plots. At all ψ values, the leakage flow may be identified by means of the high $\overline{Tu}$ zone about the gap region, i.e., in the range $r/r_{tip} = 1.081$–1.146. A higher $\overline{Tu}$ stripe is present in front of the blade at all ψ. Physically, high turbulence may depend either on convection or on local production. As the upstream flow entering the rotor has low $\overline{Tu}$, a physical explanation for such higher values could be the presence of blade stall, which could result in an instantaneous reverse flow possibly not

detected in the time averaged vector plot. In fact, as already remarked, such a $\overline{Tu}$ increase is likely due to the periodic flow fluctuations associated with the blade passage, and, in such a case, it should be disregarded as it has no physical meaning. On the contrary, $\widetilde{\overline{Tu}}$ is not affected by periodic oscillations and, hence, it provides information that is more physically reliable. The comparison between the $\widetilde{\overline{Tu}}$ contour plots of Figure 4 and the $\overline{Tu}$ ones of Figure 3 shows that, at the same operating point (5det vs. 5, 6det vs. 6, and 7det vs. 7), no high $\widetilde{\overline{Tu}}$ stripe is present in front of the blade. Hence, it may be concluded that, at least at those conditions, no abnormal flow situation takes place in front of the blade. As such a flow behavior is typical of high blade loading, this conclusion should also apply to operation at lower ψ, i.e., to points 1, 2, 3, and 4. On the contrary, in front of the gap region and at larger r, both $\overline{Tu}$ and $\widetilde{\overline{Tu}}$ attain similar values, thus indicating that periodicity in the leakage flow is likely weak. This observation contrasts with the case of the fan studied by Canepa et al. [13], in which a strong periodicity in the leakage flow was observed at high ψ. The geometrical differences between the two rotors prevent from providing a definite explanation for this flow difference.

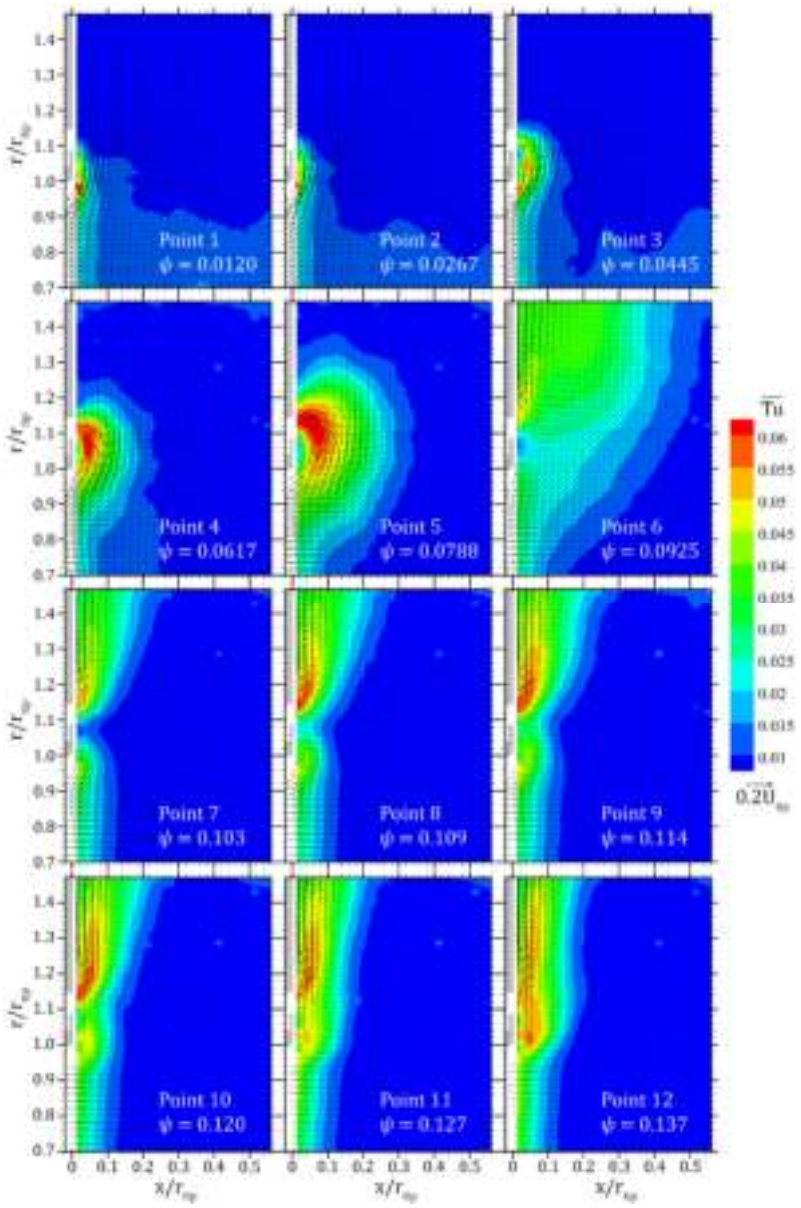

Figure 3. Time averaged flow field in the gap region: basic survey.

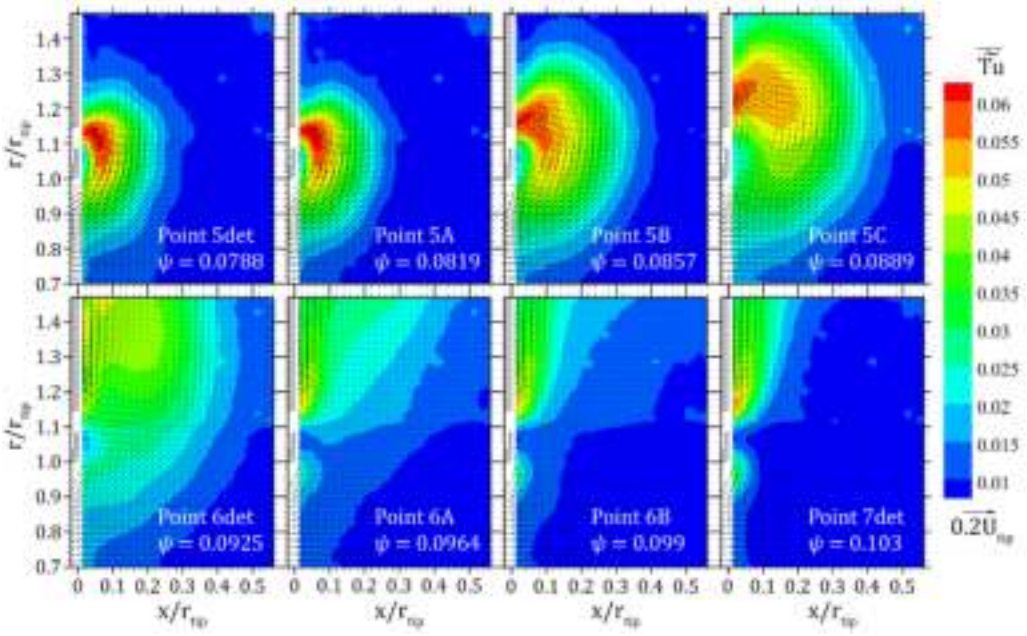

Figure 4. Time averaged flow field in the gap region: detailed survey.

In the present section, an intuitive description of the flow features related to low-frequency noise is reported in order to help interpret the relevant flow behavior. As ψ increases, the leakage flow rate increases due to the increase in the pressure difference in the gap, while the flow rate through the rotor decreases consistently with the negative slope of the characteristic curve. Depending on shape and proportions of the gap channel, the leakage flow leaves the gap in a direction that may be more radial or axial, e.g., see the study of the effect of the rotor axial position reported by Canepa et al. [12]. In the present rotor, see Figure 2, the radial part of the channel beyond the axial to radial bend presents a superposition of the rotor ring with the stationary walls 1.4 times longer than the meatus width. This suggests that the flow leaving the channel is likely radial. At a distance of almost three times the channel width, it encounters the step constituted by the panel edge that tends to turn the flow in the axial direction. Prerotation helps the leakage flow stream radially outwards, while the pressure gradient generated by the rotor has an opposite effect.

As a matter of fact, at high ψ, the leakage flow streams radially outwards and a large separated-flow region forms; at low ψ, the leakage flow has an important axial component and deflects towards the rotor resulting in a recirculation bubble attached to the ring. All this is related to the possibility for the leakage flow to penetrate the main one or being deflected. In the former case, the path followed by the leakage flow before being reingested by the rotor is longer than in the latter one. As a result, the mixing of the large-scale flow structures contained in the leakage flow with the main one is expected to be stronger than in the former case, resulting in stronger decay. Depending on the residual strength of the ingested flow structures, a stronger or weaker interaction with the rotor blades takes place, and stronger or weaker blade loading fluctuations yield. Eventually, stronger or weaker noise results. The ψ value at which the flow transition takes place depends on the above listed parameters. Such a behavior is consistent with the modifications of both the leakage flow and the SPL_{low} that take place at $\psi \cong 0.09$. These aspects have been also discussed in Canepa et al. [12,13].

The vector plots show that several flow patterns may be identified:

(1) Below the design Δp (points 1–5), a recirculation bubble attached to the ring lip may be clearly detected at $\psi = 0.0788$, and it is also present at $\psi = 0.0617$; at the interface between the leakage flow and the main one, high $\overline{Tu}$ values are present. At $\psi = 0.0617$, the high $\overline{Tu}$ stripe in front of the rotor lip suggests that the bubble should be present.

At very low ψ, that is at points 1 and 2, no bubble may be identified; should it be present, it would be very thin since the measurement domain extends up to 3 mm from the ring lip, but, likely, the leakage flow is attached to it. In all of the cases, due the limited extension of the bubble, the flow leaving the gap is reingested by the rotor within a short distance;

(2) At $\psi = 0.0925$ (point 6), the design operating point is approached and the flow pattern has an important change: the gap flow becomes centrifugal and a large separated-flow zone appears instead of the separation bubble attached to the ring. The center of such a zone is located away from the panel wall and at radial locations far from the ring; small $\overline{Tu}$ values are attained in the gap flow;

(3) Beyond the design conditions (i.e., at ψ =0.103–0.109, points 7 and 8), the leakage flow remains radial with large $\overline{Tu}$ values; the velocity direction, together with the absence of a center of the recirculation zone, indicates that the leakage flow leaves the measurement domain before turning towards the rotor and being eventually reingested. The large-$\overline{Tu}$ zone is still present in front of the blade;

(4) As ψ further increases (i.e., at $\psi = 0.114$–0.137, points 9 and 10), the features of the leakage flow are qualitatively unchanged, but the flow at the blade tip clearly modifies as it streams along the ring lip. It points radially outwards and then mixes with the leakage flow; at some locations $v_a < 0$. At large Δp and low Q ($\psi = 0.127$–0.137, points 11 and 12), the flow deteriorates: it probably separates in the lower part of the blade span as $v_r > 0$ at small r, and part of it leaves the rotor from the blade tip area consistently with the negative v_a; the remainder recirculates through the gap. Such a behavior may also be related to the radial breakdown of the flow downstream of the rotor, e.g., see Milanese et al. [22]. However, such operating points are of limited interest since the rotor efficiency is very small.

Furthermore, at all ψ, a large-$\overline{Tu}$ stripe is present in front of the blade but upstream of this area $\overline{Tu}$ is smaller. This indicates that turbulence is not convected there by the main flow. As already mentioned, such high values are only partially due to the blade passage unsteadiness, since that high unsteadiness area is present in front of the blade tip in some of the $\widetilde{\overline{Tu}}$ plots of Figure 4 also, i.e., at $\psi = 0.0964$, 0.0996, and 0.103. Such a local maximum is present at all of the higher loading points also, and its presence indicates that either turbulence is produced there or some related flow features are hidden in the time averaged vector plots; the observation of some instantaneous velocity fields, see Canepa et al. [4], showed that, at high ψ, a reverse flow may be present at the blade tip. In order to provide further evidence to this assumption, regions of reverse flow need to be identified. To this aim, a reverse flow index RI has been computed along the radial traverse closest to the blade ($x/r_{tip} = 0.0135$) for each ψ. Assuming that reverse flow in front of the blade is related to negative v_a values, such an index is simply defined as the percentage of instantaneous samples with $v_a < 0$ out of the 800 acquired ones. Its profiles related to operating points 4, 5, 6, 7, and 9 are reported in the plots of Figure 5 together with the $\overline{v_a}$ ones. The trend of RI is rather regular: it is very small or even null along most of the span and then it increases in front of the blade tip. At point 4, it does not reach 0.05, indicating that instantaneous negative v_a is statistically not significant. At points 5 and 6, the trends are rather similar, and the maximum value is approximately 0.15. At point 7, the maximum value increases to more than 0.3 and at point 9 it reaches 0.65. The region where the reverse flow index is not null gradually increases in size with ψ, but it extends from $r/r_{tip} = 0.97$ to 1 at point 4 and from 0.92 to 1 at point 7. The $\overline{v_a}$ profiles have qualitatively similar trends, but at points 7 and 9 a change in convexity takes place at $r/r_{tip} \cong 0.96$; furthermore, at point 9, slightly negative $\overline{v_a}$ values are attained beyond $r/r_{tip} \cong 0.99$. Instantaneous negative v_a values may be related to the presence of reverse flow coming from the blade but also to turbulent vortexes convected by the mean flow. However, compared to the low ψ cases, at high ψ, the strength of the turbulent vortexes associated with the leakage flow is smaller due to the higher decay that has already been discussed. Furthermore, they should not significantly contribute to the mean velocity sign, as the flow sampling

is not synchronized with their passage, which is random. Hence, their contribution to the instantaneous negative v_a, i.e., to RI, is expected to be less important at high ψ. This supports the assumption that, at least at point 9 but likely at point 7 also, a reverse flow coming from the rotor is present.

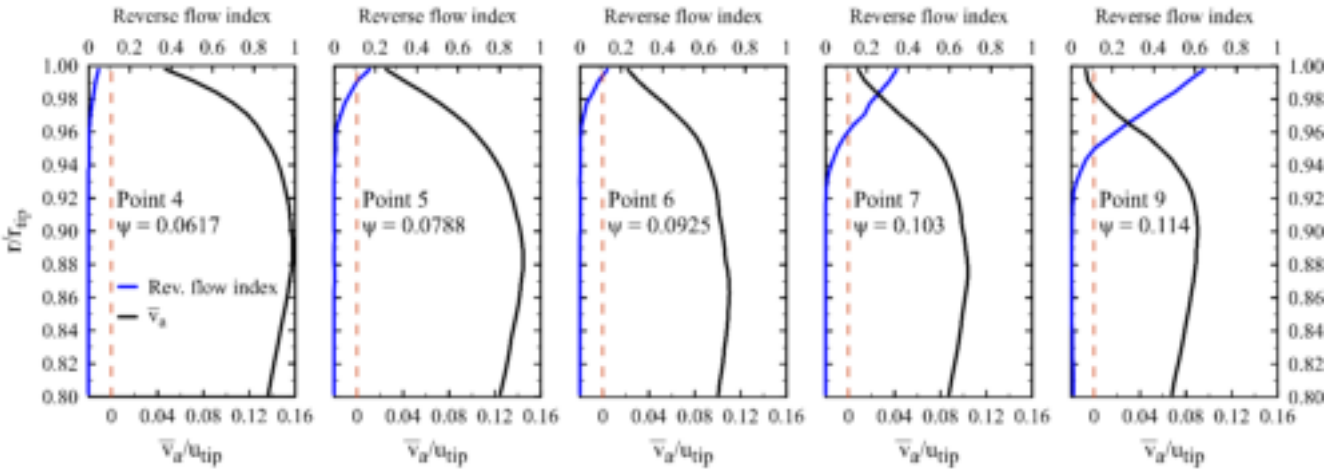

Figure 5. Radial profiles of the reverse flow index, time averaged axial velocity, and turbulence intensity ($x/r_{tip} = 0.0135$).

Overall, the above described trend is consistent with the SPL_{low} growth beyond $\psi \cong 0.05$ and also with the explanation hypothesized in Canepa et al. [4] for such a growth. More precisely, it was assumed that the leakage flow rate increase results in a noise increase followed by a sudden decrease as the transition from the attached recirculation bubble to a large separated-flow zone takes place; then, a further strong increase takes place as separation takes place in the blade tip region. A transition from a leakage flow attached to the ring lip to a separated flow region is a possible explanation for the SPL_{low} dip at $\psi \cong 0.05$ but, though reasonable, this remains a conjecture only, since at such low ψ the leakage flow is weak and is restrained between the main flow and the ring lip. On the other hand, the laser light reflections from the ring further complicate taking PIV measurements close to the wall. Hence, the study focuses on the flow transition at approximately $\psi \cong 0.09$.

3.3. Flow Pattern Modification about $\psi \cong 0.09$

The SPL_{low} decrease that takes place between ψ = 0.08 and 0.09 suggests that a way to decrease the leakage noise is realizing a leakage flow that points radially outwards instead of a more axial one, as the latter is directly reingested by the rotor with a lesser decay of large-scale structures. Hence, it is interesting to deepen how the transition from the attached recirculation bubble to such a flow takes place. In Canepa et al. [12], the flow pattern modification was sudden, but it was observed during a constant ψ rotational speed ramp with a continuous rotor deformation. Despite the differences between the two cases, this showed that even small modifications in geometrical parameters or operating conditions may have relevant effects on both flow pattern and noise level. In the present stiff rotor, the SPL decrease is less abrupt, suggesting that in the absence of deformation either the flow changes more gradually or an intermittent behavior between two different flow patterns takes place. In order to deepen insight into such an aspect, cases $\psi = 0.0788$ and $\psi = 0.103$ have been assumed as references for the attached recirculation bubble and the large recirculating flow zone, respectively. Then, measurements have been repeated at eight intermediate operating conditions with a Δp spacing of about 6 Pa, see Table 1. The related time averaged vector plots are reported in Figure 4. They show that the modification in the flow pattern seems rather gradual, as the separation bubble increases in size, its center displaces away from the wall and at larger radii, and eventually it exits the measurements domain upper boundary. However, a more careful observation shows that in cases $\psi = 0.0788$, 0.0819, 0.0857, and 0.0889, the time averaged leakage flow is directly

reingested by the rotor, while in cases $\psi = 0.0925$, 0.0964, 0.0996, and 0.103, it streams radially outwards along the panel. This would suggest that the transition between the two flow patterns takes place between $\psi = 0.0889$ and $\psi = 0.0925$.

However, the flow features are related to the instantaneous flow field, which may largely differ from the time averaged one especially across a flow modification or in presence of intermittency. In order to evaluate how much the flow pattern related to each operating point resembles either of the two reference flow fields, the 2000 instantaneous flow fields related to each of the eight operating points have been compared to the time averaged reference flow fields. To this aim, the flow in the rectangular region close to the wall (r/r_{tip} = 1.120–1.468 and x/r_{tip} = 0.014–0.176) has been considered since it is either centripetal (case $\psi = 0.0788$) or centrifugal (case $\psi = 0.103$) and, hence, it easily allows distinguishing the flow patterns; for the sake of simplicity, the two cases will be referred to as B (recirculation Bubble) and R (Radial flow), respectively. Then, for each ψ, $RI_B^n(\psi)$ and $RI_R^n(\psi)$ have been computed according to Equation (3) for any $n = 1$, 2000 (i.e., for each instantaneous flow field); this has yielded eight sets of 2000 RI_B and eight sets of 2000 RI_R values. Then, the mean value and rms of the sets $RI_B^n(0.0788)$ and $RI_R^n(0.103)$ have been computed, yielding the pairs $RI_B^{av}(0.0788)$ and $\sigma_B(0.0788)$ and $RI_R^{av}(0.103)$ and $\sigma_R(\ 0.103)$, see Figure 6a. As expected, for these cases the mean value is large, but it does not equal 1, and the rms is smaller than in the other cases, since fluctuations in the instantaneous flow fields are present anyway.

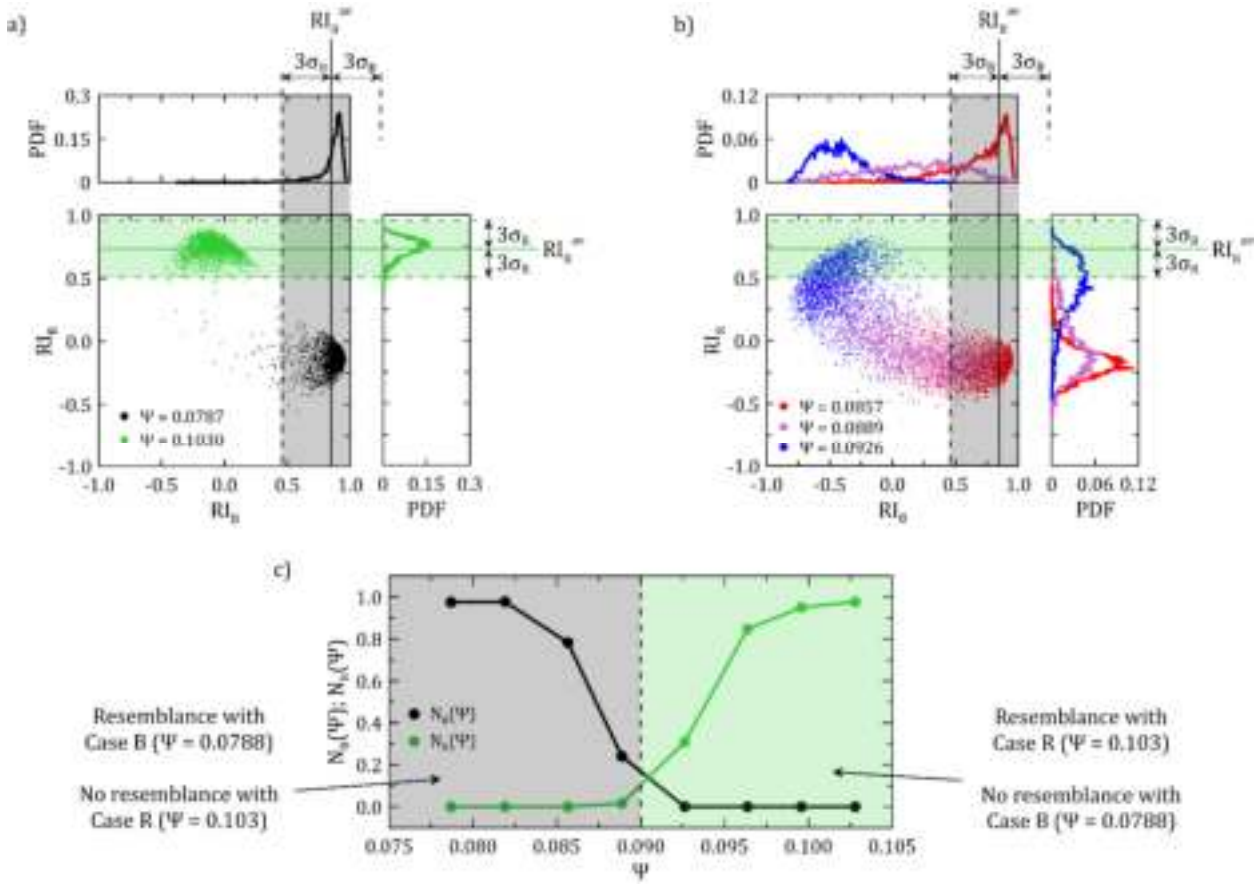

Figure 6. Resemblance index properties: (**a**) scatter plots of RI_B and RI_R for the reference cases; (**b**) scatter plots of RI_B and RI_R at ψ = 0.0857, 0.0889, and 0.0925; (**c**) N_B and N_R dependence on ψ.

For any ψ, the resemblance of the instantaneous flow fields with the two reference cases has been evaluated building the probability density functions (PDFs) of both $RI_B^n(\psi)$ and $RI_R^n(\psi)$. Then, the percentages of $RI_B^n(\psi)$ and $RI_R^n(\psi)$ belonging to the ranges $RI_B^{av}(0.0788) \pm 3\sigma_B(0.0788)$ and $RI_R^{av}(\ 0.103) \pm 3\sigma_R(0.103)$ have been computed, see

Figure 6b. Such percentages are referred to as $N_B(\psi)$ and $N_R(\psi)$, respectively, and are plotted in Figure 6c versus ψ. Based on that criterion, for $\psi \leq 0.09$, there should not be any resemblance with the radial flow of case $\psi = 0.103$ since $N_R(\psi) \cong 0$, while for $\psi \geq 0.09$, there should not be any resemblance with the recirculating flow of case $\psi = 0.0788$ since $N_B(\psi) \cong 0$. For both $N_B(\psi)$ and $N_R(\psi)$, only two points lay in the range 0.2–0.85: $\psi = 0.0857$, 0.0889 and $\psi = 0.0925$, 0.0964, respectively; this suggests that the transition takes place at approximately $\psi = 0.09$. However, low RI absolute values not only are due to completely different flow fields but also to the sensitivity of the scalar product to vector misalignment; for instance, such a misalignment may result from a different location of the center of a recirculation bubble. Hence, small values do not necessarily indicate an absence of resemblance. Furthermore, the employed criterion has a certain degree of arbitrariness and, thus, a deeper analysis has been performed which also considers the vector fields. To this aim, the pairs $RI_R^n(\psi)$ and $RI_B^n(\psi)$ have been plotted for the reference cases ($\psi = 0.0788,\ 0.103$), yielding the scattered plots of Figure 6a. Cases $\psi = 0.0857$, 0.0889, and 0.0925 have been selected out of the eight ones since they are close to $\psi = 0.09$; the related scattered plots are reported in Figure 6b. The comparison of such plots with the ones related to the reference cases (see Figure 6a) shows that a certain similarity exists between cases $\psi = 0.0857$ and $\psi = 0.0788$ on the one hand and between cases $\psi = 0.0925$ and $\psi = 0.103$ on the other hand. On the contrary, case $\psi = 0.0889$ (see Figure 7a) shows a continuous spread about a regression line with a negative slope. The cluster is denser in the IV quadrant where $RI_B^n > 0$ and $RI_R^n < 0$, (56% of points) than in the II quadrant where $RI_B^n < 0$ and $RI_R^n > 0$ (23% of points). It is straightforward to assume that high density in the IV quadrant implies high resemblance with case $\psi = 0.0788$ and, conversely, with case $\psi = 0.103$ when density in the II quadrant is high. Hence, the instantaneous vector fields related to the two quadrants have been averaged, showing that, basically, resemblance to either the former case or the latter one exists, see Figure 7b. The rather uniform cluster does not suggest the presence of any bimodality. However, an intermittent behavior between the two reference flow patterns could be present, but it could not have been detected due to the arbitrariness of the resemblance criterion. Hence, the whole set of instantaneous flow fields has been divided in five square subsets with side $\Delta RI = 0.35$, and the related averaged vector fields have been compared to the reference ones. They are plotted in Figure 7c and show that a gradual modification from one reference flow pattern to the other one is present. It appears as a displacement of the recirculation zone center away from the ring and in a leakage flow which becomes more radial as RI_B^n decreases and RI_R^n increases. This excludes the presence of an intermittent behavior. In terms of Δp, the operating points are uniformly spaced at approximately 6 Pa, thus showing that, overall, the flow pattern is very sensitive to the pressure rise as the transition from one flow pattern to the other one takes place in less than a 12-Pa-Δp variation, i.e., $\Delta\psi = 0.0064$. Furthermore, this analysis shows that, despite the arbitrariness in the way RI_B^n, RI_R^n, N_B, and N_R have been computed, the choice done allows to properly identifying the actual features of the flow pattern.

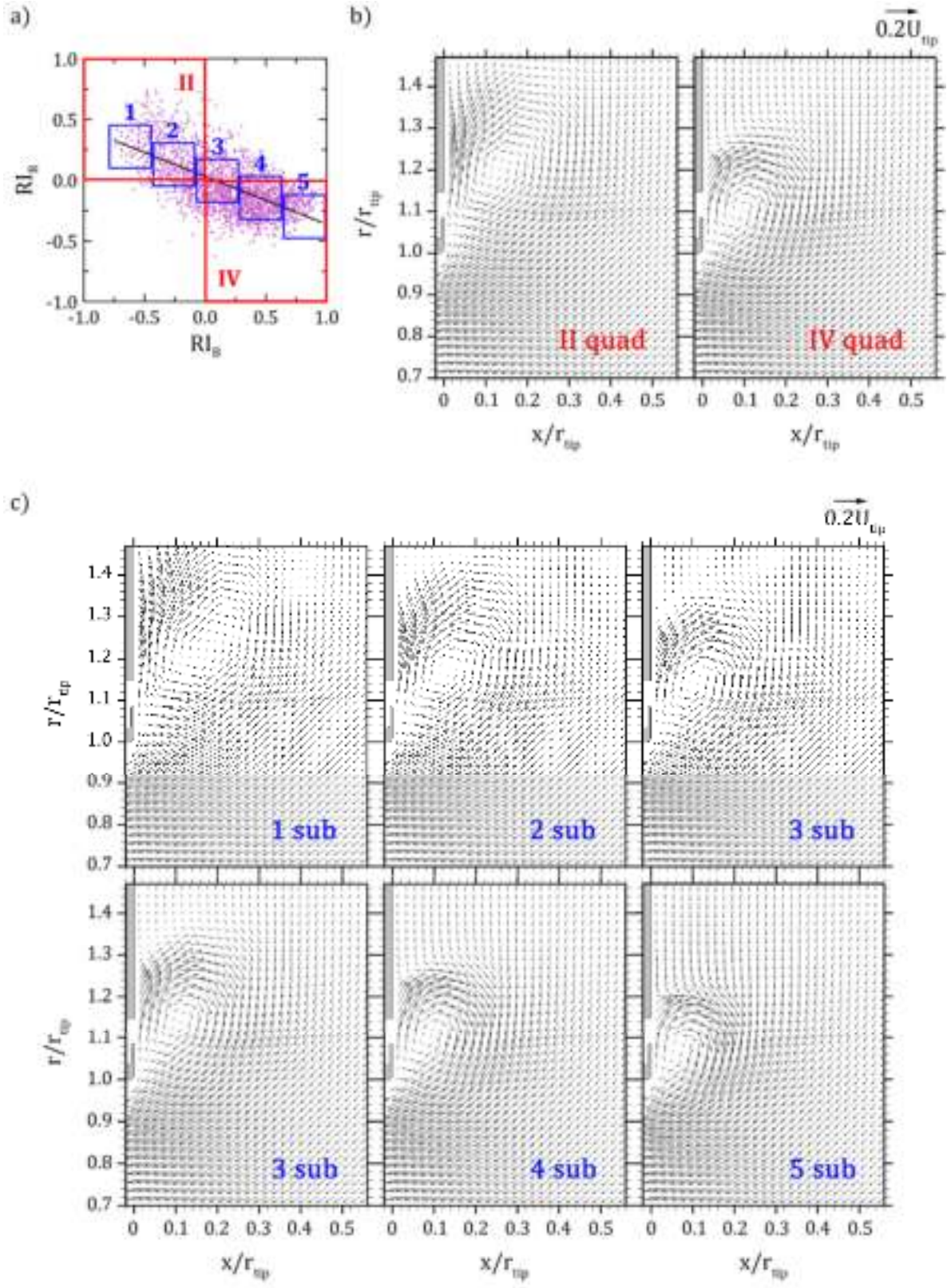

Figure 7. Averaged velocity fields at ψ = 0.0889: (**a**) subsets employed for the averaged velocity fields; (**b**) averaged fields related to the II and IV quadrants; (**c**) averaged fields related to smaller subsets (the case 3 sub was reported in both rows in order to ease comparisons).

4. Conclusions

The present work regards the leakage flow in axial fans provided with a rotating shroud and stems from a previous study, based on the comparison between aerodynamic and acoustic measurements. Such a study provided useful information about the noise generating mechanisms influencing the low-frequency range. Unfortunately, the limited number of operating points at which PIV measurements were taken resulted in a number of unsolved questions. To this aim, in the present investigation, the characteristic curve has been surveyed at a large number of points yielding a thorough study of the leakage flow development as the pressure rise varies. The results of the work are:

(1) A detailed description of the evolution of the leakage flow as a function of the loading.

It has been found that, starting from very low pressure rise, the leakage flow streams along the rotor ring and is immediately ingested by the rotor. Then, a recirculation bubble attached to the ring forms with a large turbulent fluctuation interface. As the pressure rise further increases, the separation bubble also increases in size together with the highly turbulent region. Finally, as the design point is approached, a flow pattern transition takes place with the leakage flow streaming radially outward and forming a large separated flow zone. Such a configuration is stable and nearly unchanged in the remainder of the characteristic curve with a general decrease of the turbulence intensity. Such a transition depends on a combination of factors that include the loading, but it may be expected that changing shape and/or size of the gap clearance may change the operating point at which it takes place;

(2) A detailed analysis of the flow pattern transition that, for the present geometry, takes place about the design operating point.

In light of these results, the investigation has focused on the flow pattern transition; two operating points, above and below the design one, have been assumed as the reference for flow patterns and the measurements have been repeated with very small pressure rise steps. At each operating condition, a statistical quantitative metric, based on the resemblance index, has allowed to identify the percentage of instantaneous vector fields resembling to the reference cases. This has shown that the shift from the attached recirculation bubble to the large separated-flow zone takes place within a pressure rise range of less than 5% of the maximum pressure rise. Namely, at all surveyed operating conditions but one, either one flow pattern or the other one is present. At that single point, the behavior is not intermittent, since the velocity field may resemble both reference ones or any intermediate pattern where the separation bubble is progressively displaced apart from the fan ring. This indicates that, within a very small pressure rise range, the interaction between the leakage flow and the main one is far from being univocal. Despite the arbitrariness in its computation, the resemblance index has proven effective in detecting and analyzing the transition process and the different flow patterns. Considering the strong sensitivity of the leakage flow to the details of the gap geometry, this indicates that a careful design of the gap may have a positive effect on the radiated noise;

(3) The establishment of a correspondence between leakage flow and SPL growth.

The comparison of the flow patterns with a previously reported trend of the SPL shows that interruptions in the SPL growth with increasing head may be due to modifications in the leakage flow pattern; this may also help interpret the results of acoustic measurements that sometimes may appear inconsistent;

(4) Further evidence of the existence of a flow reversal at the blade tip has been provided.

Such a flow separation at the blade tip is likely responsible for the low-frequency noise generation at high-loading; unfortunately, a detailed study of that phenomenon has not been performed for reasons of space, but it will be the next extension of the present work.

Author Contributions: E.C.: Conceptualization, Supervision, Investigation, Writing—original draft. A.C.: Conceptualization, Supervision, Writing—review. M.M.: Investigation, Data curation, Visualization, Writing—original draft. A.N.: Investigation, Visualization, Writing—original draft. All authors have read and agreed to the published version of the manuscript.

Funding: This research received no external funding.

Institutional Review Board Statement: Not applicable.

Informed Consent Statement: Not applicable.

Data Availability Statement: Not applicable.

Acknowledgments: The authors kindly acknowledge Johnson Electric Asti srl for having provided the tested rotor.

Conflicts of Interest: The authors declare no conflict of interest.

Nomenclature

OASPL	overall sound pressure level, ref. 20 μPa
N	percentage of instantaneous flow fields similar to the reference one
Q	volume flow rate
r	radial coordinate
SPL	sound pressure level spectrum, ref. 20 μPa
SPL_{low}	sound pressure level in the range 6 < St < 90, ref. 20 μPa
SPL_{high}	sound pressure level in the range 90 < St < 300, ref. 20 μPa
RI	resemblance index
St	Strouhal number (frequency normalized with $\Omega/60$)
Tu	turbulence intensity based on u_{tip}
u_{tip}	peripheral speed of the blade
v_a, v_r, v_ϑ	components of the absolute velocity
x	axial coordinate
Δp	pressure rise through the rotor (static outlet minus total inlet)
ϑ	tangential (azimuthal) coordinate
ρ_0	air density
φ	flow coefficient, $\frac{Q}{u_{tip}\pi {r_{tip}}^2}$
ψ	pressure rise coefficient, $\frac{\Delta p}{0.5\rho_0 {u_{tip}}^2}$
Ω	rotational speed (expressed in rev/min)

Superscripts

$\sim$	related to the ensemble average
$\overline{}$	related to the time average
$'$	related to non-periodic instantaneous fluctuations

Subscripts

B	related to the reference case with recirculation bubble
R	related to the reference case with radial leakage flow
tip	related to the blade tip

References

1. Carassale, L.; Cattanei, A.; Mazzocut Zecchin, F.; Moradi, M. Leakage flow flutter in a low-speed axial-flow fan with shrouded blades. *J. Sound Vib.* **2020**, *475*, 115275. [CrossRef]
2. Longhouse, R. Control of tip-vortex noise of axial flow fans by rotating shrouds. *J. Sound Vib.* **1978**, *58*, 201–214. [CrossRef]
3. Canepa, E.; Cattanei, A.; Mazzocut Zecchin, F.; Milanese, G.; Parodi, D. An experimental investigation on the tip leakage noise in axial-flow fans with rotating shroud. *J. Sound Vib.* **2016**, *375*, 115–131. [CrossRef]
4. Canepa, E.; Cattanei, A.; Mazzocut Zecchin, F. Leakage Noise and Related Flow Pattern in a Low-Speed Axial Fan with Rotating Shroud. *Int. J. Turbomach. Propuls. Power* **2019**, *4*, 17. [CrossRef]
5. Fukano, T.; Takamatsu, Y.; Kodama, Y. The effects of tip clearance on the noise of low pressure axial and mixed flow fans. *J. Sound Vib.* **1986**, *105*, 291–308. [CrossRef]

6. Fukano, T.; Jang, C.-M. Tip clearance noise of axial flow fans operating at design and off-design condition. *J. Sound Vib.* **2004**, *275*, 1027–1050. [CrossRef]
7. Piellard, M.; Coutty, B.; Le Goff, V.; Vidal, V.; Pérot, F. Direct Aeroacoustics Simulation of Automotive Engine Cooling Fan System: Effect of Upstream Geometry on Broadband Noise. In Proceedings of the 20th AIAA/CEAS Aeroacoustics Conference, Atlanta, GA, USA, 16–20 June 2014. AIAA Paper 2014–2455.
8. Magne, S.; Moreau, S.; Berry, A. Subharmonic tonal noise from backflow vortices radiated by a low-speed ring fan in uniform inlet flow. *J. Acoust. Soc. Am.* **2015**, *137*, 228–237. [CrossRef] [PubMed]
9. Moreau, S.; Sanjose, M. Sub-harmonic broadband humps and tip noise in low-speed ring fans. *J. Acoust. Soc. Am.* **2016**, *139*, 118–127. [CrossRef] [PubMed]
10. Zenger, F.J.; Renz, A.; Becher, M.; Becker, S. Experimental investigation of the noise emission of axial fans under distorted inflow conditions. *J. Sound Vib.* **2016**, *383*, 124–145. [CrossRef]
11. Na, G.-D.; Kameier, F.; Springer, N.; Mauß, M.; Paschereit, C.O. URANS Simulations and Experimental Investigations on Unsteady Aerodynamic Effects in the Blade Tip Region of a Shrouded Fan Configuration. In Proceedings of the ASME Turbo Expo 2017: Turbomachinery Technical Conference and Exposition, Charlotte, NC, USA, 26–30 June 2017. ASME Paper GT2017-6.
12. Canepa, E.; Cattanei, A.; Jafelice, F.; Mazzocut Zecchin, F.; Parodi, D. Effect of rotor deformation and blade loading on the leakage noise in low-speed axial fans. *J. Sound Vib.* **2018**, *433*, 99–123. [CrossRef]
13. Canepa, E.; Cattanei, A.; Mazzocut Zecchin, F.; Parodi, D. Large-scale unsteady flow structures in the leakage flow of a low-speed axial fan with rotating shroud. *Exp. Therm. Fluid Sci.* **2019**, *102*, 1–19. [CrossRef]
14. Zhu, T.; Lallier-Daniels, D.; Sanjose, M.; Moreau, S.; Carolus, T. Rotating coherent flow structures as a source for narrowband tip clearance noise from axial fans. *J. Sound Vib.* **2018**, *417*, 198–215. [CrossRef]
15. Hussain AK, M.F.; Reynolds, W.C. The mechanics of an organized wave in turbulent shear flow. *J. Fluid Mech.* **1970**, *41*, 241–258. [CrossRef]
16. Grant, I. Particle image velocimetry: A review. *Proc. Inst. Mech. Eng. Part C J. Mech. Eng. Sci.* **1997**, *211*, 55–76. [CrossRef]
17. Prasad, A.K.; Adrian, R.J.; Landreth, C.C.; Offutt, P.W. Effect of resolution on the speed and accuracy of particle image velocimetry interrogation. *Exp. Fluids* **1992**, *13*, 105–116. [CrossRef]
18. Liu, K.; Haworth, D.C. Development and Assessment of POD for Analysis of Turbulent Flow in Piston Engines. In Proceedings of the SAE 2011 World Congress and Exhibition, Detroit, MI, USA, 12–14 April 2011. SAE Technical Paper: 2011-01-0830.
19. Willman, C.; Scott, B.; Stone, R.; Richardson, D. Quantitative metrics for comparison of in-cylinder velocity fields using particle image velocimetry. *Exp. Fluids* **2020**, *61*, 62. [CrossRef]
20. Hanson, D.B. Spectrum of rotor noise caused by atmospheric turbulence. *J. Acoust. Soc. Am.* **1974**, *56*, 110–126. [CrossRef]
21. Majumdar, S.J.; Peake, N. Noise generation by the interaction between ingested turbulence and a rotating fan. *J. Fluid Mech.* **1998**, *359*, 181–216. [CrossRef]
22. Milanese, G.; Cravero, C. Analysis of the Design Bounds in Performance Limits for Industrial Axial Flow Fans. In Proceedings of the ASME Turbo Expo 2020: Turbomachinery Technical Conference and Exposition, Virtual, Online, 21–25 September 2020. ASME Paper no. GT2020-16058.

International Journal of
Turbomachinery Propulsion and Power

MDPI

Article

The High-Speed Cascade Wind Tunnel at the Bundeswehr University Munich after a Major Revision and Upgrade †

Reinhard Niehuis * and Martin Bitter

Institute of Jet Propulsion, Bundeswehr University Munich, Werner-Heisenberg-Weg 39, 85577 Neubiberg, Germany; martin.bitter@unibw.de

* Correspondence: reinhard.niehuis@unibw.de

† This paper is an extended version of our contribution to the 14th European Turbomachinery Conference, Gdansk, Poland, 12–16 April 2021.

Abstract: Since its first operation in 1956 at DFL Braunschweig and after its movement to Munich, the High-Speed Cascade Wind Tunnel (HGK) at Bundeswehr University Munich is intensively used for fundamental and application-oriented research on aero-thermodynamics of turbomachinery bladings. Numerous systematic airfoil design studies were performed over the last decades. Thanks to the HGK facility, which enables thorough and detailed cascade testing at turbomachinery-relevant conditions, many of those airfoils for different purposes finally made it into turbomachinery applications. Nowadays, the HGK still provides very useful contributions to the understanding of the complicated flow in compressor and turbine bladings, and thereby extends the knowledge on relevant physical phenomena. As a consequence of the intense usage, this unique test facility was subject to a major revision and upgrade. The performed changes are presented within this paper including an overview on new capabilities in terms of the extended operating range, the data acquisition system, and the recently available measurement equipment.

Keywords: high-speed cascade wind tunnel; engine-relevant conditions; linear cascade; operation range

check for updates

Citation: Niehuis, R.; Bitter, M. The High-Speed Cascade Wind Tunnel at the Bundeswehr University Munich after a Major Revision and Upgrade. *Int. J. Turbomach. Propuls. Power* **2021**, *6*, 41. https://doi.org/10.3390/ijtpp6040041

Academic Editor: Ralf Obertacke

Received: 24 June 2021
Accepted: 26 October 2021
Published: 29 October 2021

Publisher's Note: MDPI stays neutral with regard to jurisdictional claims in published maps and institutional affiliations.

Copyright: © 2021 by the authors. Licensee MDPI, Basel, Switzerland. This article is an open access article distributed under the terms and conditions of the Creative Commons Attribution (CC BY-NC-ND) license (https://creativecommons.org/licenses/by-nc-nd/4.0/).

1. Introduction

The High-Speed Cascade Wind Tunnel (HGK) of the Bundeswehr University Munich is a well-established test facility in the turbomachinery community. Due to its ability to change two similarity parameters, namely, Mach and Reynolds number, independently from each other at jet engine relevant flow conditions, it is a unique test facility worldwide, whose performance map is very well suited for research on airfoil aero-thermodynamics. The facility's large test section dimensions of up to $500 \times 300\,mm^2$ (height × width) enabled very detailed experimental performance characterizations on numerous compressor and turbine airfoil generations which finally made it into service.

Initially, based on a design proposal by Scholz, the facility was erected in 1956 at DFL Braunschweig by one of Germany's pioneers on experimental fluid mechanics, see Schlichting [1]. A first comprehensive documentation of its performance was published by Scholz and Hopkes [2]. In 1984, the entire test facility was moved to the Bundeswehr University Munich, where it got operational in 1985 after an overhaul of the main components as documented in Sturm and Fottner [3]. As a major change, the original pressure tank (2.4 m in diameter and 9.0 m in length) was replaced by one of significantly bigger volume (4.0 m in diameter and 11.8 m in length) allowing the realization of a longer settling chamber providing much better flow homogeneity and, moreover, a much better access to the wind tunnel components.

Nowadays, there is still a high demand on cascade testing under engine relevant test conditions from industry, which, more than ever, seeks for highly efficient airfoils, especially to fulfill the goals of "Flight Path 2050" published by the European Commission [4].

Beside this, there is also a particular and long-lasting request for fundamental research on aero-thermodynamic flow phenomena in turbomachinery bladings in order to gain better physical understanding and to provide sound data to validate and further mature numerical methods. In order to stay fully operational and to upgrade the facility for future research requirements, it was decided to carry out a major revision of the test facility, more than 60 years after its first run and tens of thousands hours of intensive testing. In particular, the main components, i.e., drive train, compressor, and oil system, date back to when the test facility first got into service in 1956. Some of these components exhibited already some pre-damages, cracks, and wear. Due to their age spare parts were not available off the shelf in most cases. Therefore, a spontaneous fatal damage to one of these components would result in enormous downtime of the test facility, high costs, and severe delays of running and planned research projects performed at this tightly booked and heavily used research environment. In order to avoid this, a major revision was performed in 2017/2018 and critical hardware components were replaced by new ones of the latest technology. Thanks to a careful and detailed project planning the entire revision could successfully be realized within a very short time frame of four months only. The new components now feature a higher power level providing a significantly extended operating range of the test facility. Parallel to the hardware, a high level of automation was introduced into the facility. Together with a state-of-the-art real-time data acquisition system, the wind tunnel finally satisfies raised demands on automated long-term operating stability. Relevant features and the raised potential of the revised test facility are described in this paper. The picture of the new HGK is rounded by presenting the available portfolio of measurement techniques, both classical probe-based and non-intrusive techniques.

2. The New High-Speed Cascade Wind Tunnel

2.1. Working Principle and Main Components

The HGK is a continuous operation, open-loop test facility with an open test section located inside a big pressure tank, as shown in Figure 1. The static pressure of the air inside the tank can be lowered down to slightly less than 40 hPa and pressurized up to 1200 hPa. By controlling the fluid's stagnation pressure, static chamber pressure, and the total temperature, an independent variation of two major flow similarity parameters—Reynolds and Mach number—can be achieved, which allows experiments to be conducted under turbomachinery-relevant flow conditions. For a detailed description of the performance and the components of the HGK before the major revision in 2017, the reader is referred to the publications mentioned above.

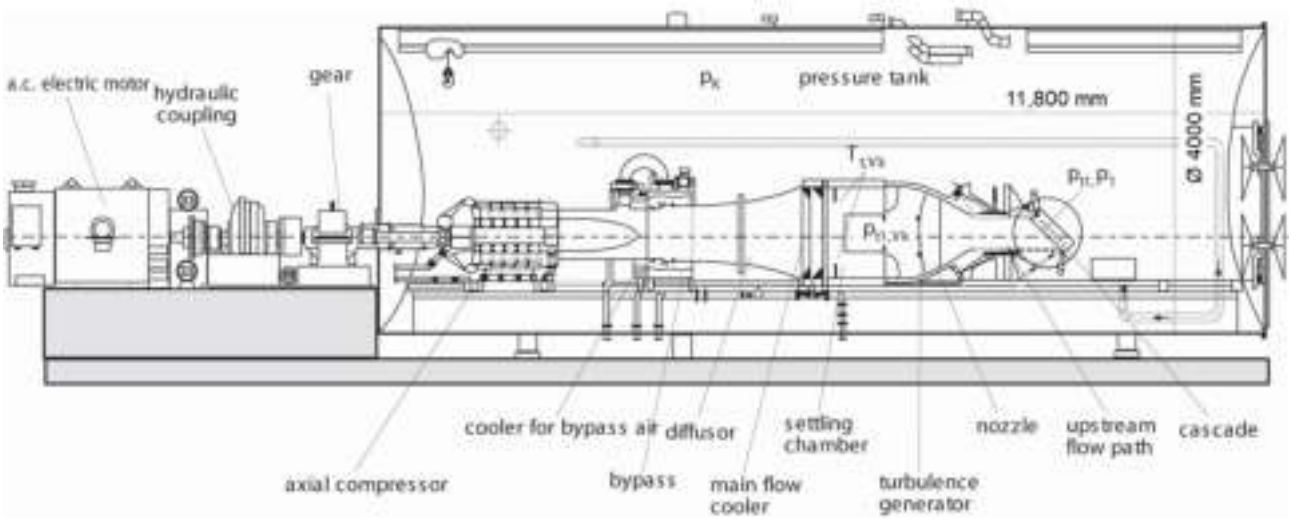

Figure 1. Main components of the High-Speed Cascade Wind Tunnel before revision.

The air flow was formerly generated by an axial compressor driven by a 1300 kW AC electric motor placed outside the tank. The electric motor and the axial compressor were connected via shaft, hydraulic coupling, and gear box. After leaving the axial compressor, the air passes through a twin-bypass device. By the larger butterfly bypass the compressor can instantly be un-throttled in situations it gets prone to exceed the surge limit. A second annular slide bypass is used for fine adjustment of the dynamic pressure in the range of few Pascal providing higher precision than an adjustment via the shaft speed. Further downstream, the bypass is followed by a diffuser and a main cooler before entering the settling chamber. The water-cooled heat exchanger of the main cooler extracts the fluid energy introduced by the compressor to maintain the air's total temperature constant within a range of $20 \leq T_t \leq 60$ °C. After leaving the settling chamber, the flow is accelerated in the convergent nozzle to the requested Mach number (max. up to $Ma = 1.06$) before entering the test section and its outlet (i.e., a plane 40 mm downstream of the measurement positions for p_{t1} and p_1), where the test specimen (typically linear cascades) can be installed. Different turbulence grid types allow the adjustment of the turbulence level to realistic turbomachinery-relevant levels. Upon request, periodic unsteady inflow conditions, typically caused in turbomachines by the relative motion between rotor and stator, can be simulated by installing a wake generator in the test section, see Acton and Fottner [5].

The majority of the wind tunnel components, except for the pressure tank, the heat exchanger, and the settling chamber, originate from the test facility's early years in 1956 as it was erected in Braunschweig. Therefore, both the Bundeswehr University as well as the Institute of Jet Propulsion felt the urgency to replace all major components of the test facility, namely, the drive train, the compressor, the oil system, and the main cooler, in order to assure full availability and fail-safe testing for prospective research purposes and to extend the operating range significantly for future needs.

2.2. Performed Revisions and Modifications

The existing six-stage axial compressor of the "old HGK" was a drive unit specifically designed by the Voith company to operate this facility. During project planning for the "new HGK", an extensive exploration of the market was performed by an external recognized engineering office. It turned out that the replacement of this component will be the most challenging issue, as no commercial compressor off the shelf was available matching all major requirements in terms of size, volume flow, pressure ratio, power, and the operability at very low pressures in the HGK environment. Finally, and once again, the new compressor as a centerpiece of the "new HGK" had to be tailored for the specific demands of this wind tunnel, as it had been already done for the old one.

At the end, an excellent customized solution was realized in close collaboration with MAN Energy Solutions (formerly MAN Diesel and Turbo SE). The propulsor for the new HGK is based on MAN's latest design of the industrial compressor MAX-1, compare Ziegler et al. and Anding et al. [6,7]. During its development phase a configuration consisting of the first seven stages of the novel axial compressor design was tested in a test bed at MTU Aero Engines, scaled down by a factor of 3. It turned out that the first three stages of that scaled version perfectly match all requirements for the requested operation range of the new HGK, in case that all three stages would be equipped with variable guide vanes. For this purpose, however, a new casing including inlet and outlet, a new rotor, as well as a new bearing system were needed. The outcome was a rather compact and powerful compressor unit which was installed and commissioned successfully in December 2017, as depicted in Figure 2. The compressor is designed at a nominal speed of 11,550 rpm. At maximum speed of 12,705 rpm, it can deliver a maximum pressure ratio of 2.4 and a maximum volume flow of 32.8 m^3/s. Regarding the remaining components of the drive train, the replacement was rather straight forward with state-of-the-art components off the shelf, i.e., an 1800 kW Siemens asynchronous electric motor (type 1RQ65004JT60-Z) in combination with a Sinamics Perfect Harmony GH180 medium volt-

age driver for frequency conversion. The 38% power increase compared to the old motor (1300 kW) is the prerequisite for a significant extension of new HGK's operating range, as it is explained below. As the new electric motor can be controlled to individual rotational speeds by means of the frequency converter, the hydraulic turbo coupling, which took over this job in the old HGK by energy dissipation, was not longer needed. One of the main advantages of getting rid of the turbo coupling is a stable and continuous operation of the wind tunnel across the entire chamber pressure range in particular at static chamber pressures around atmospheric conditions or higher (i.e., at high Reynolds numbers). In order to match the rotational speed between the new compressor ($N_{max} = 12{,}700\,\mathrm{min}^{-1}$) and the new electric motor ($N_{max} = 1650\,\mathrm{min}^{-1}$), a Renk gear box TS-450 with a gear ratio of 7.7 was installed outside the pressure tank connecting the high- and the low-speed shafts. The new configuration required a completely new oil circuit for supplying the compressor and the gear box, too. This system had to overcome the challenge to deal with different relative oil feeding pressures for the individual components inside and outside the pressure tank whose required oil pressure ratio is far below or even 1.8 times above atmosphere, respectively. An active pressure control and level balancing system was finally installed to get the system operating safely.

As a consequence of the increased electrical power, a new main cooler had to be installed in order to allow testing at constant total temperature even at the new performance limits. Accordingly, the new heat exchanger was designed to extract energy from the flow which is roughly in the same order as the maximum power of the electric motor (1800 kW). The cooler was delivered by the Güntner company, Germany. It is a special construction of their GCO type heat exchanger, which is particularly designed in order to match the operation requirements of the HGK and to provide excellent flow homogeneity in terms of velocity and temperature distribution as well as low pressure losses. In contrast to the old main cooler, which consisted out of six single elements, the new cooler is a single heat exchanger block consisting of aluminum fins and stainless steel tubes which leads to a compact design and ensures utmost uniform flow quality. The cooling water header outlet is carried out in four sections, in which the volume flow can individually be controlled by valves in order to achieve best temperature uniformity in the flow field. The flow quality behind the main cooler is further raised by a single stage flow straightener integrated directly upstream the settling chamber.

At the end, the testing downtime for dismantling the old test facility and assembly of all components of the "new HGK" was 4 months only, thanks to a very careful project planning. The new test facility, as depicted in Figure 3, got operational on 26 January 2018. However, the full electric power is not yet available as electricity is still provided by the old existing transformer, which cannot convert the maximum power for the new motor. The replacement of the old with a more powerful transformer has already been started and the finalization is envisaged in the year 2022. After its accomplishment, the full operating range of the new HGK test facility will finally become available.

Figure 2. New 3-stage axial compressor (**left**: during installation, **right**: final assembly).

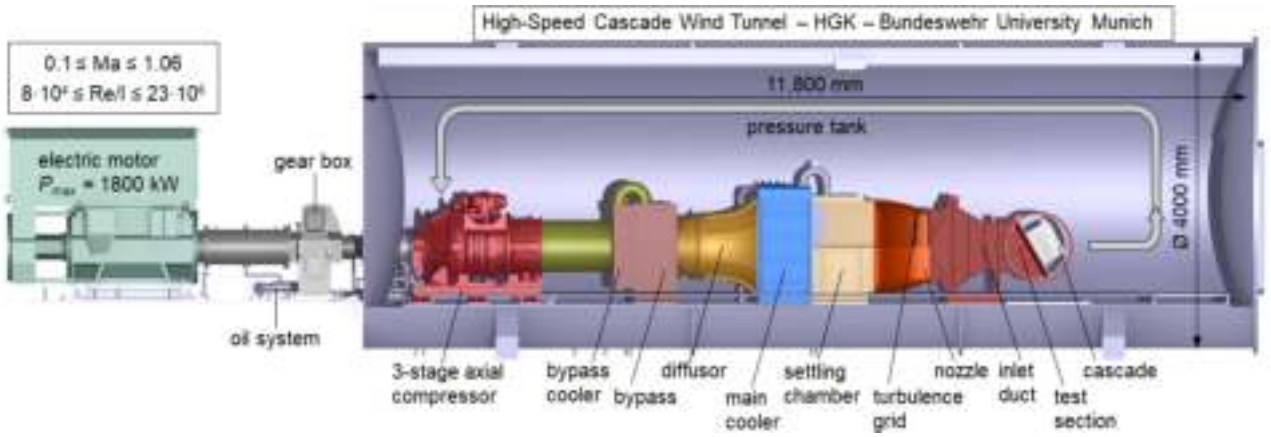

Figure 3. Main components of the High-Speed Cascade Wind Tunnel after revision.

Performance Map after Revision and Upgrade

It was mainly the main air cooler which limited the old HGK's maximum performance (i.e., the maxima of Reynolds and Mach number) as steady-state total flow temperatures up to 303 K were only possible up to 940 kW electrical power. In Figure 4, the operation limits of the old and new HGK are plotted for min. and max. duct heights (i.e., 250 mm or 500 mm, respectively) in terms of maximum mass flow at atmospheric conditions, pressure ratio, unit Reynolds number, and Mach number depending on the power input. The higher compressor mass flow as well as the re-designed main cooler of the new HGK after the revision revealed already an enormous increase in the operating range, even at the maximum power of 1300 kW which is presently available. Once the new transformer gets operational, expected to happen in the year 2022, the final (extrapolated) operating range can be achieved and the new test facility, labeled "new HGK*" in Figure 4, significantly and even further extends the achievable Reynolds and Mach number range.

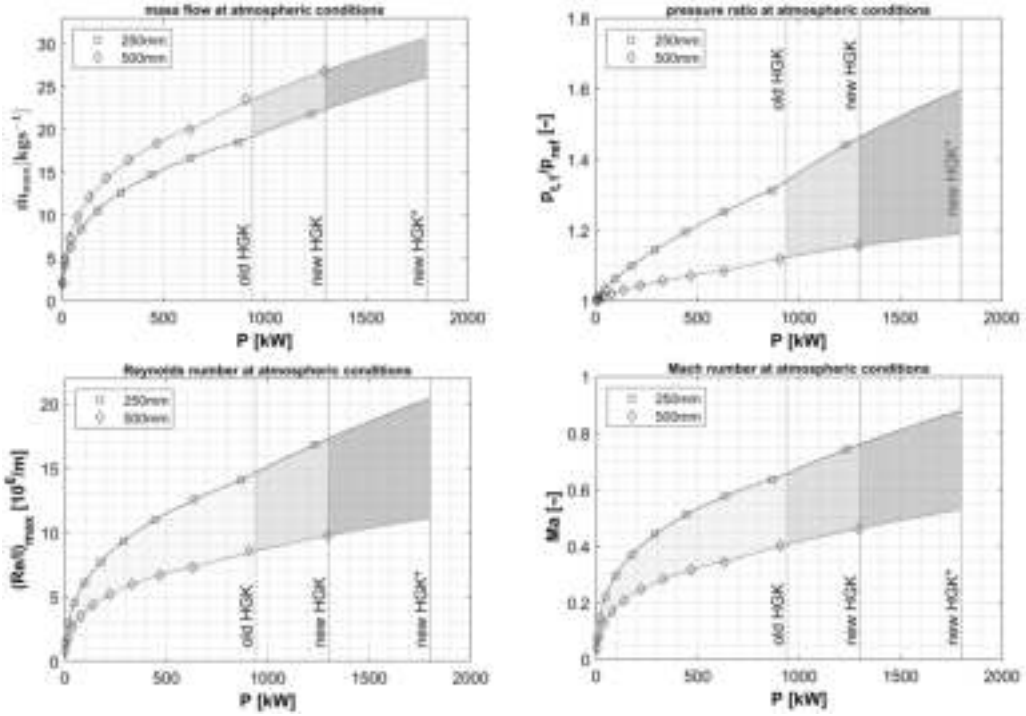

Figure 4. Maximum achievable mass flow, total pressure ratio, unit Reynolds number, and Mach number versus old and new facility's power setting under atmospheric condition ($p_{ref} = 958$ hPa).

In order to emphasize the main dimensionless flow quantities for aerodynamic testing, the performance map of the HGK is typically plotted in terms of a Mach number and unit Reynolds number diagram as shown in Figure 5. The unit Reynolds number is related to a characteristic length of $l = 1\,\mathrm{m}$. Test specimen typically feature smaller characteristic lengths, which scales the values for the final testing Reynolds number. The diagram contains operating lines of constant static chamber pressure (p_{ref}-solid blue) and dynamic pressure (q_{ref}-dashed blue), which can be realized for various absolute duct heights ranging from 250 to 500 mm. Highest Mach numbers at the test section outlet (inlet to the test specimen) can be achieved for the smallest duct height of 250 mm. For larger duct dimensions, the maximum available mass flow inevitably leads to lower achievable maximum Mach numbers, compare previous plot. The minimum unit Reynolds number is limited by the absolute chamber pressure slightly less than $p_{ref} = 40\,\mathrm{hPa}$ (I) which, in turn, is limited by the 2 NASH liquid ring vacuum pumps whose nominal absolute pressure minimum is 33 hPa. The chamber can be evacuated to minimum pressure level within 60 min. The compressor speed limits restrict the minimum and maximum Mach number (II and V). The maximum Reynolds number is result of the available electrical power limiting the maximum dynamic pressure q_{ref} (III) and the vessel structural strength at 1200 hPa (IV). The shaded areas visualize the extended operating range from the new HGK as of now and after the availability of the full power (new HGK*) compared to the old HGK for the smallest and largest duct dimensions. Especially, the potential for testing at higher Reynolds number is significantly extended. The new HGK* in its final stage after the revision will allow testing at much higher Mach and Reynolds number levels as before (e.g., up to 50% higher Reynolds number under atmospheric conditions) which has often been requested many times in the past but could not be serviced with the old HGK. Furthermore, testing can now be performed at stable operating conditions over several hours even at very low Mach number, which was also not possible in the past due to limitations of the hydraulic coupling.

The performance map in Figure 5 mainly supports the design of the cascade test specimen prior to testing for targeted aerodynamic test conditions under several design constraints, i.e., among others, to scale the characteristic blade size l. At the end, it is always a trade-off between best possible local resolution for the respective measurement tasks/test objectives and best possible flow periodicity under the consideration of requested maximum Mach and Reynolds number levels.

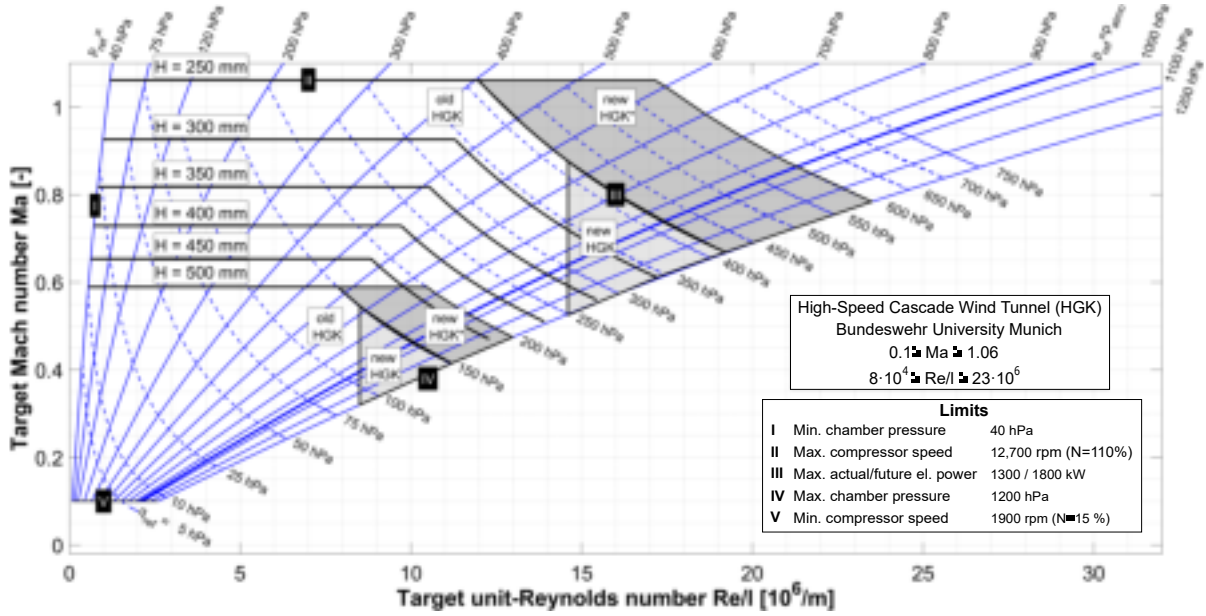

Figure 5. Performance map of the HGK for different test section heights H over the facility's static and dynamic pressure range p_{ref} (solid blue) and q_{ref} (dashed blue), respectively (at $T_t = 30\,^{\circ}\mathrm{C}$).

3. Operating Point and Compressor Health Monitoring

The HGK is typically operated at constant Mach and Reynolds number conditions over several hours depending on the test matrix. Since the new electric motor is frequency controlled, the setting and stability of the stagnation pressure is way more precise compared to the old drive train with the hydraulic coupling. The revolutions of the high-speed shaft driving the compressor is stable by better than 0.1%.

The planning of an experimental campaign necessitates the definition of target Mach and Reynolds numbers. These test conditions are usually specified far prior before testing. Targeted Ma and Re conditions are controlled by measuring and monitoring just three flow properties: the stagnation pressure p_t, the reference pressure p_{ref} and the total temperature T_t, which define the operating conditions for a given blade chord length l according to Equations (1) and (2):

$$Ma = \sqrt{\frac{2}{\gamma - 1} \cdot \left[\left(1 + \frac{p_t - p_{ref}}{p_{ref}} \right)^{\frac{\gamma - 1}{\gamma}} - 1 \right]} \tag{1}$$

$$Re/l = \sqrt{\frac{\gamma}{R}} \cdot \frac{Ma \cdot p_{ref}}{C_1} \left[\frac{T_t}{1 + \left(\frac{\gamma - 1}{2} \right) Ma^2} + C_2 \right] \cdot \left[\frac{T_t}{1 + \left(\frac{\gamma - 1}{2} \right) Ma^2} \right]^{-2}. \tag{2}$$

R, C_1, and C_2 represent the specific gas constant as well as the Sutherland's constant values for air and p_{ref} is measured at the cascade's inlet plane for compressor tests and at the outlet plane in case of a turbine test specimen. A Mensor CPG 2500 precision pressure scanner was installed, allowing to measure the static reference pressure p_{ref} and the dynamic pressure q_{ref} ($= p_t - p_{ref}$) referenced to the atmospheric pressure within 0.008% full scale accuracy (i.e., 7.5 Pa and 10 Pa, respectively).

In the course of the revision, the wind tunnel control system was migrated to a state-of-the-art PLC (Programmable Logic Controller) control system which continuously monitors and controls all relevant status values for operating point or system health monitoring and exports a 10-Hertz data log. All measures as well as the dedicated limits for experimental safety are provided and controlled by the SPS. The surveillance data comprises the wind tunnel environment (e.g., all operating pressures and temperatures) as well as the drive train and compressor status (e.g., actual power ratings, motor and compressor speed, vibrations sensors, temperatures in inlet, outlet, and bearings and compressor pressure ratio) and all secondary systems (e.g., cooling power, oil pressures, or actuator positions). In particular, the compressor stability limit (i.e., surge limit) was determined experimentally during commissioning runs in the HGK test facility by MAN prior to any measurement campaigns. Since that time, all relevant values to prevent compressor surge are continuously monitored. In case the surge limit is critically approached during operation, a two-stage warning system forces the operator (and in future the fully integrated bypass actuator, see above) to intervene and unload the critical operating point setting. In case the limits are still exceeded, the system trips and shuts down in a controlled manner. Anyhow, as the change of an operational set point usually happens slowly within several seconds there is no need for unsteady surveillance or instantaneous actuators.

Due to the full online data availability, a software controller was implemented recently, which will enable fully automated operation on a longer term. At the moment, this control algorithm is intensively tested and trained under various operating point combinations also including safety limit approach and recovery. First fully automated tests without user input were successfully carried out in summer 2021 but need further tuning.

The evaluation of the main three flow properties which define the target Mach and Reynolds number conditions from the continuous data log allows an assessment of the operating point stability as outlined in Figure 6.

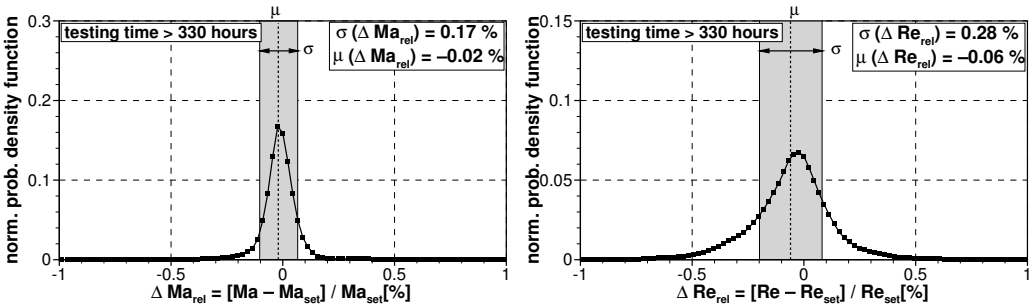

Figure 6. Statistics of the operating point stability for Mach number (**left**) and Reynolds number (**right**) extracted from the continuous logs for more than 330 h of HGK testing.

The data were extracted from the last testing hours (>330 h) throughout the wind tunnel's entire operating field. The statistical quantities μ and σ result from fitting all data by a normal distribution, whereas μ is the mean deviation and σ gives the standard deviation and hence a quantitative measure (e.g., 1-, 2-, or 3-sigma) for the deviation of the actual Ma and Re values from their target points. Therefore, the long-term operating point stability for the target Mach and Reynolds number are determined to be $\sigma_{Ma} = 0.17\%$ and $\sigma_{Re} = 0.28\%$, respectively. As an example, for a low-pressure turbine cascade being tested at $Ma = 0.65$ and Re = 100,000 this results in $\Delta Ma = 0.0011$ and $\Delta Re = 280$. It is expected that the fully automated testing can reduce the standard deviation even further, in particular to control the static chamber pressure and hence the Reynolds number.

The repeatability and temporal stability of both, Ma and Re, are mainly dominated by the precision and leakage rate of the butterfly valve which controls the HGK's reference pressure in the tank. It is situated in the peripherical infrastructure of the wind tunnel in between the pressure tank and the vacuum pumps. Considering the fairly large volume of the vessel of 150 m^3, the operating pressure can be stabilized over the long term within absolute reference pressure better than $p_{ref} = \pm 50$ Pa and dynamic pressure better than $q_{ref} = \pm 10$ Pa. As a consequence of the big vacuum chamber, a huge amount of thermal energy leads to a tardy temperature settlement and a continuous heat radiation from the vessel to the lab building, which is unfortunately not temperature controlled. Therefore, the flow temperature can typically be stabilized and measured better than 0.3 K during several hours of testing.

4. Data Acquisition

Beside the continuous log for operation, the main architecture for test data acquisition (DAQ) was migrated to the National Instruments real-time platform PXI-8880 combined with a state-of-the-art LabView user interface developed in-house. The new platform enables the direct application of a large number of onboard measurement equipment, or the linked control of third-party test equipment. A brief overview of the available portfolio at the HGK is presented in the last chapter of this paper.

The DAQ allows for the recording of real-time streaming data and control of hardware in the loop (HIL) processes at high-frequency (HF) up to 250 kHz and at ultra-HF up to 1.25 MSamples/s at various digital channels (recently 96 HF and 12 ultra-HF channels). A local data streaming network allows the integration of the RJ-45 based communication with more than 384 pressure channels (Pressure Systems NetScanner type 98-RK1 and type 9116) and a five axes traversing unit. The measurement data including all meta data from the facility status is stored in a TMDS binary format which allows high streaming rates, important especially for long-term unsteady data recordings. Typical DAQ sampling rates of 10 to 20 Hz over several seconds during steady state measurements allow the calculation of uncertainty and standard deviations for all data channels, whereas the long-term stability over a test day is recorded within the continuous data log as outlined above.

5. Qualification of the Flow Field in the Cascade Inlet Plane

The flow quality of the old HGK facility was excellent. Anyhow, the old facility was operated and monitored in a widely analogue manner. There was no major need to improve the flow quality but to replace the old components and to extend the limits in the operating range. One overall constraint was that the new components shall provide comparably good or even better inflow quality to the test specimen in order to allow a comparison between data form the old and new test facility. Therefore, the flow quality in the test section was carefully checked with detailed flow measurements after re-commissioning. The goal of these experiments was the qualification of the flow homogeneity in the wind tunnel outlet plane where the test specimen is typically installed. For the sake of ease, the wind tunnel outlet was set vertically for these experiments providing the outflow vector co-aligned with the wind tunnel coordinate system. The horizontal duct width was kept constant at $W = 300\,\text{mm}$, whereas three different duct heights $H = [250; 310; 500]\,\text{mm}$ were characterized starting 15 mm downstream of the test section outlet plane. To create a holistic view on the flow field across the entire operating range, traverses with a spherical-head five-hole pressure probe (5HP) and total temperature probe in tandem configuration were performed covering the full duct channel cross section normal to the main flow component by up to 315 data points each. Both probes enabled the assessment of the homogeneity of the flow properties p_t, p and T_t, which usually define cascade inlet conditions.

The thermodynamic data were complemented by 3-component flow velocity fields measured with far higher spatial resolution by means of stereoscopic Particle Image Velocimetry (2D-3C PIV) at the same operating points and duct heights as above. These PIV measurements were performed in a vertical plane downstream of the test section outlet originating from the plane of the probe traverses and being aligned in parallel to the main flow direction at half duct width. Similar to the work presented in Chemnitz and Niehuis [8], up to 10,000 PIV images were recorded for statistical relevance of a converged turbulence intensity. The PIV images were analyzed for each operating point using a state-of-the-art commercial PIV image processing toolbox based on interrogation-window cross-correlation. For the sake of brevity and to focus on the general evidence, a detailed discussion of the experimental setup is skipped here, and the reader is referred to the corresponding literature discussed in the last chapter of this paper.

This campaign comprises the outlet plane characterization at a clean test section duct (i.e., no turbulence grid installed) featuring wind tunnel ground turbulence level as well as at elevated turbulence levels generated by two separately installed grids, named VIIIk and IXgK. These grids are typically used during cascade testing to simulate turbomachinery relevant turbulence intensities, see Figure 7 or Kiock et al. [9].

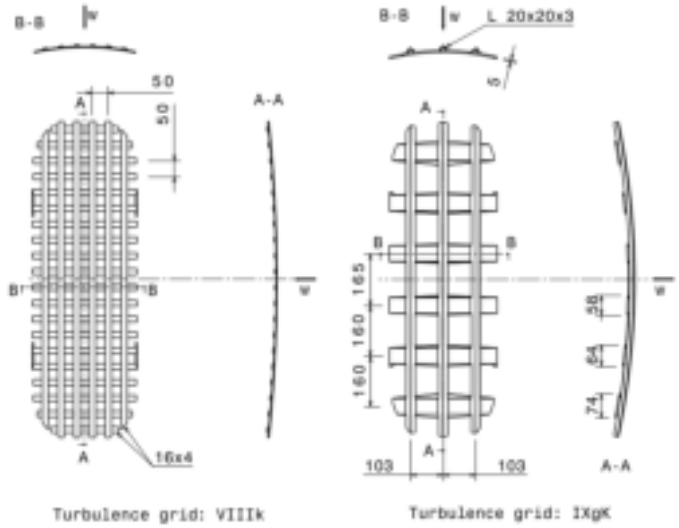

Figure 7. Geometry details of two commonly used turbulence grids VIIIk (**left**) and IXgK (**right**).

At first, outflow profiles for various outlet Mach numbers ranging from 0.1 to 0.9 are shown on the left in Figure 8. These profiles were extracted from the PIV fields at 310 mm duct height along the intersection line between the PIV and the 5HP plane. The central and right hand side plots of Figure 8 show profiles of the local PIV measurement uncertainty as well as the turbulence intensity TI derived from the PIV data at the same positions for the clean test section (black) and individually equipped with the two turbulence grids (blue and orange) for two typical turbine and compressor cascade inlet Mach number levels $Ma = [0.3; 0.59]$. All profiles are widely homogeneous over ~75% of the normalized tunnel height, except for the boundary layer regions in the proximity of the lower and upper duct walls. As loss characterization in case of cascade testing is typically performed for the central blade(s) placed around mid-duct height, the flow homogeneity is very good and the deficit in the boundary layer regimes is of less relevance.

Apparently, the TI distribution exhibits a specific profile, which is a consequence of the installed turbulence grids. Anyway, the results prove that the profiles of the velocity fluctuations in the clean test section are widely homogeneous over a large duct area and that the homogeneity is widely perfect for reliable loss characterization of airfoils in the core flow region. Note that cascade testing typically is not performed without any use of a turbulence grid. As the flow in turbomachinery is featuring higher turbulence levels, usually either grid VIIIk or IXgK is selected.

For the representation in Figure 9, each individual TI profile was averaged over $y/H = \pm 10\%$ duct height around the centerline for all available PIV results across the HGK's entire performance map. The symbols in the figure represent all measured operating points. The colored regions indicate the TI range for a specific turbulence setting in between the smallest and largest duct heights and over the tested operating range. The line style distinguishes between high (dashed) and low (solid) Reynolds numbers, i.e., $Re/l \geq 4.8 \times 10^6$ and $Re/l \leq 1 \times 10^6$, respectively. In case of the largest duct height, a small influence of Reynolds number is observed. In combination with the performance map discussed above, this chart allows the assessment of expected turbulence intensity at the cascade inlet plane during test campaign planning.

A holistic assessment of the flow quality in the measurement planes is provided in Figure 10 by some exemplary results. The individual fields display all acquired data from the pneumatic, thermal, and velocity field measurements for three Mach and Reynolds number combinations(left: $Re/l = 1 \times 10^6$ at $Ma = 0.3$, mid: $Re/l = 4.8 \times 10^6$ at $Ma = 0.3$, right: $Re/l = 4.8 \times 10^6$ at $Ma = 0.59$), all shown for the clean test section duct without turbulence grid. For this purpose, the five-hole probe data were converted into absolute flow velocities (U_{5HP}). Both the PIV and 5HP velocity fields were normalized by the target velocity of the respective operating point ($U_{set} = 103\,\mathrm{m/s}$ and $U_{set} = 196\,\mathrm{m/s}$, respectively). The velocity fields in both the axial and lateral plane are in very good accordance with each other and reveal widely homogeneous core flow regions. The dashed iso-thermal lines represent the difference between the local total temperature T_t and the target temperature setting of the respective operation point. Locally scattered deviations of only several tenth Kelvin are present in the outflow temperature fields. The measurement uncertainty of conventional resistant thermal probes, which are installed in the settling chamber to control the operating total temperature, is usually in the same order of magnitude. This demonstrates a very good homogeneity of the temperature field as long as the main cooler is not operating at its limits. When operating the main cooler at its power limit in combination with maximum mass flow rates, local temperature deviations of up to 2 K were observed.

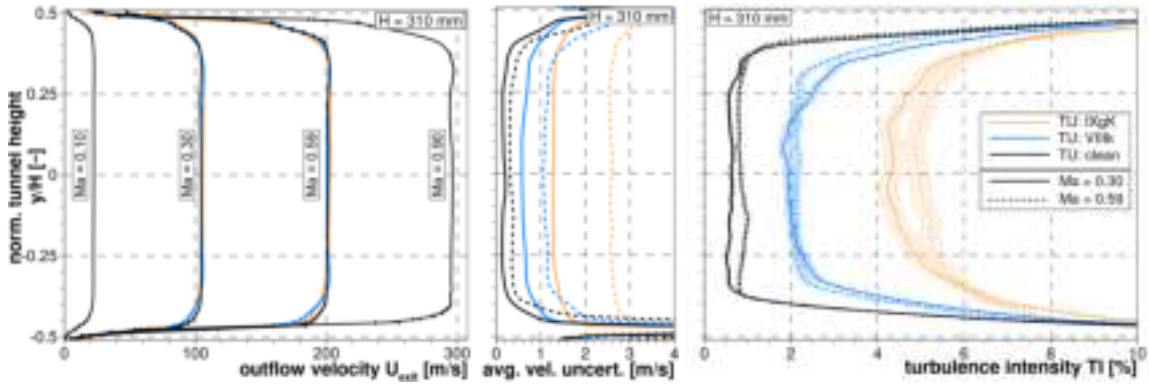

Figure 8. Left: Outflow velocity profiles across the entire channel height of $H = 310\,\text{mm}$ at different operating Mach numbers measured with 2D-3C PIV; **center**: absolute velocity uncertainty of avg. vector field; **right**: corresponding turbulence intensity profiles including the local error bars for the clean test section duct (black-clean) and equipped with the turbulence grids (blue-VIIIk; orange-IXgK) at two outflow Mach numbers $Ma = 0.3$ (solid) and $Ma = 0.59$ (dashed).

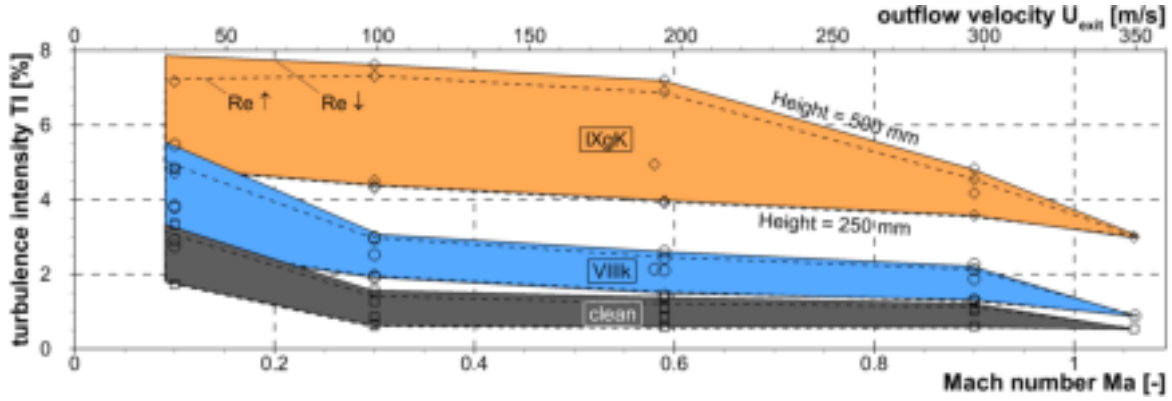

Figure 9. Distribution of the integral turbulence intensity TI across the HGK's entire performance map. TI was measured with 2D-3C PIV and averaged between $y/H = \pm 0.1$ without turbulence generator (black-clean) and for both turbulence grids (blue-VIIIk) and (orange-IXgK).

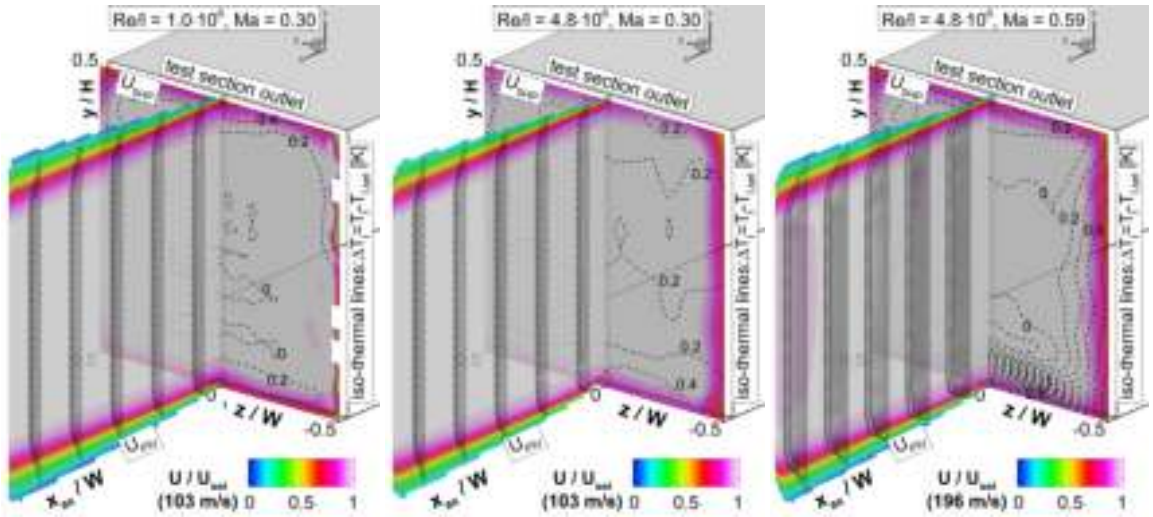

Figure 10. Outflow topology at the HGK's test section outlet measured with 5-hole probe, stereo-PIV and a total temperature probe for $Re/l = 1 \times 10^6\,\text{m}^{-1}$ at $Ma = 0.30$ (**left**), $Re/l = 4.8 \times 10^6\,\text{m}^{-1}$ at $Ma = 0.30$ (**middle**) and $Re/l = 4.8 \times 10^6\,\text{m}^{-1}$ at $Ma = 0.59$ (**right**). The dashed iso-thermal lines show the local difference in the flow temperature according to the total temperature setting $T_t = 30\,^\circ\text{C}$.

6. Repeatability of Test Results in the Old and New Facility

Especially in terms of airfoil performance characterization (e.g., determination of profile loss or outflow angle), it had to be demonstrated that the results of the old and revised wind tunnel facility are quantitatively comparable among each other after re-commissioning. The repeatability was tested on a transonic low pressure turbine cascade, which was investigated latest before the revision and directly after the re-commissioning using the entirely new HGK facility. As an operating point at a transonic Mach number is known to react very sensitive to any changes, e.g., caused by newly installed hardware components in the wind tunnel, the cascade's exit Mach number of 0.95 was chosen for this specific assessment. Exemplary results of these investigations are presented in Figure 11 in terms of the local total pressure loss coefficient ζ and outflow angle β, whereas the loss coefficient was normalized with the integral value from the test campaign prior to the revision. The data were measured in a wake traverse at 40% axial chord length downstream of the transonic turbine cascade across the central blades passage with a miniaturized wedge probe developed in-house. Both, the loss coefficient as well as the outflow angle distributions show an overwhelming agreement before and after the revision of the HGK. The difference in the integral total loss is only 0.11% and only 0.06° for the exit flow angle, which can be determined by the measurement uncertainty indicated by the error bars in Figure 11. These experiments proof both, an unchanged high quality test environment after the revision and an excellent repeatability of testing in this test facility in general.

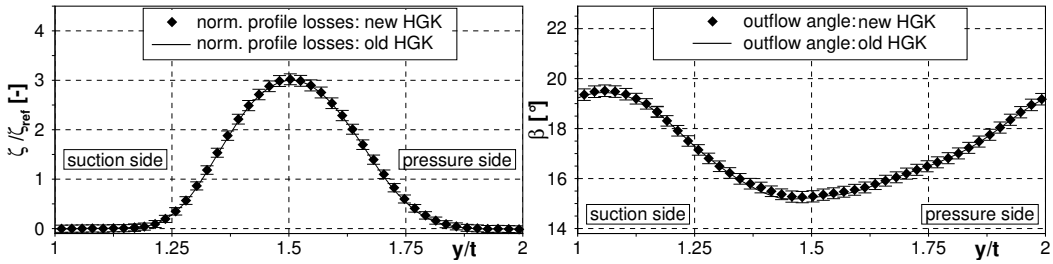

Figure 11. Profile loss characterization (**left**) and outflow angle measurements (**right**) on a transonic turbine cascade, before and after revision.

7. Available Measurement Techniques

A large spectrum of measurement techniques for all requirements on steady-state or unsteady flow characterization are routinely applied in the HGK, including both probe-based as well as non-intrusive optical techniques as depicted in Figure 12. A particular challenge for all these techniques is the testing environment at very low ambient pressure down to several hecto-Pascal and the limited access to the test specimen inside the pressure tank. This requires that the majority of the listed techniques have to be adapted for the specific use in the HGK. Due to space limitations in this paper, only a brief summary of the testing equipment portfolio can be given here and the reader is referred to the latest publications of the institute.

Details of the design and additive-manufacturing of the miniaturized five-hole wedge type probe which was already mentioned in the section above can be found in Börner and Niehuis [10]. This probe was particularly calibrated for reliable wake traverses at high exit Mach number up to $Ma = 1.55$. At these conditions, conventional blunt five-hole probes with a spherical head fail. Aberle-Kern et al. [11] successfully proposed a methodology for loss determination downstream of cascades under consideration of thermal gradients in non-adiabatic flow fields by utilizing a newly developed combined thermal- and multi-hole probe.

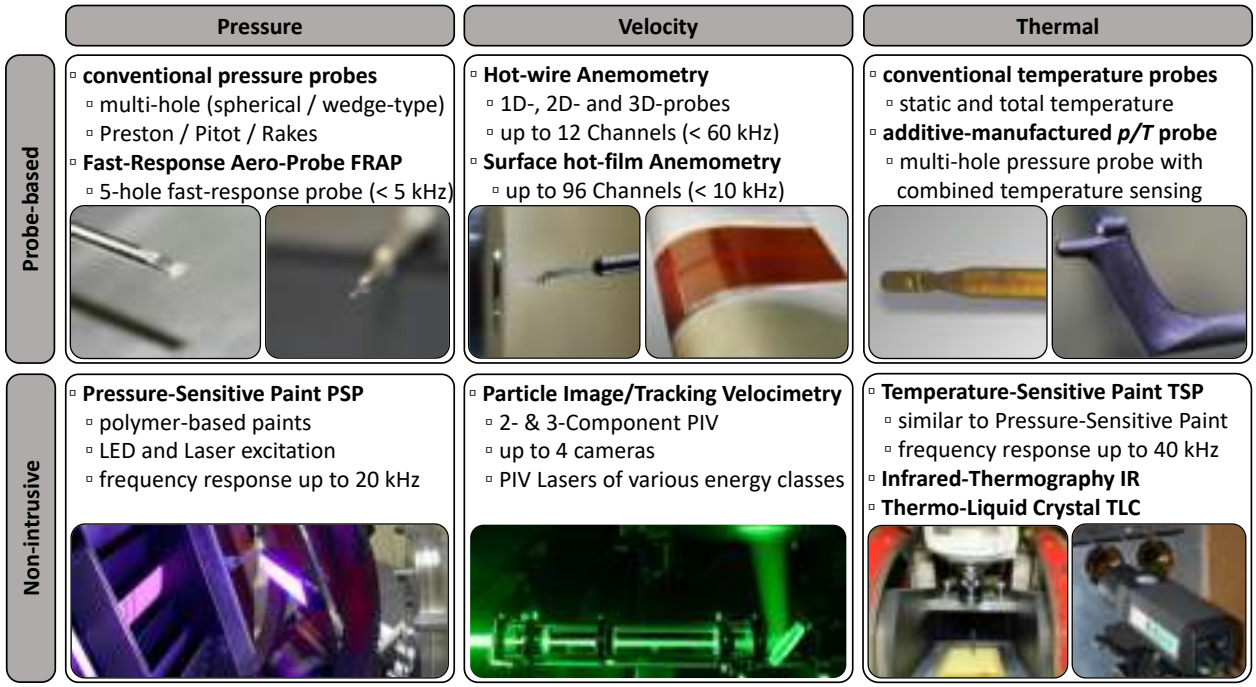

Figure 12. Portfolio of measurement techniques commonly applied in the HGK.

Apart from the newest probe-based pressure measurements, the application of non-intrusive optical flow sensing techniques, i.e., Particle Image Velocimetry (PIV), Pressure- and Temperature-Sensitive Paints (P-/TSP) or Infrared Thermography (IR-T), was heavily raised within the last years. As all these diagnostic methods have in common the need of at least one camera, the optical access to the test specimen is inevitably required. In case, the test design requests the application of one of these techniques, the test specimen must be designed in an appropriate manner. Actively cooled LED light sources as well as CCD or CMOS cameras perfectly illuminate and capture the flow images even in the low-pressure environment. In order to prevent calibrated cameras (e.g., IR cameras) from the vacuum conditions, usually a special housing is required which can complicate an experimental setup. A PIV laser setup is also more complex compared to an atmospheric wind tunnel facility, since the laser head has to be placed outside the pressure chamber at atmospheric conditions and the routing path inside the test chamber can be very long. Therefore, it is inevitably required to couple the beam into the low-density environment with a severely different refraction index and deflect it with several mirrors to the location of interest. This is realized through a precision window and a very careful alignment of the optical path. Starting in 2016, Bitter et al. [12] presented the application of combined PIV and PSP measurements in the HGK in order to gain a holistic view on the flow field around an LPT blade at a glance. Chemnitz and Niehuis [8] reported on successful turbulence measurements in the 3D flow field downstream of an LP turbine cascade at high subsonic Mach numbers referencing 2D-3C PIV measurements to 3D hot-wire anemometry under low-density conditions. Bitter and Niehuis [13] applied the same PIV technique to characterize the impact of periodically changing inlet turbulence on statistical flow quantities in the wake of an LPT cascade. Based on this, in the meanwhile, long-lasting experience in the application of non-intrusive techniques in the HGK environment has been gained. The latest achievements were the precise measurement of unsteady surface pressure fluctuations on an LPT cascade down to several Pascal by means of unsteady Pressure-Sensitive Paint (iPSP) at 6 kHz sampling rate, as reported in Bitter et al. [14]. Recent activities seek to adapt unsteady optical temperature measurements by means of unsteady Temperature-Sensitive Paint (iTSP). First promising results of a cylinder in transonic cross flow sampled at acquisition rates of more than 20 kHz are presently under investigation. A non-intrusive but

steady-state surface temperature sensing methodology for precise heat transfer estimations based on the Infrared Thermography is already available in the HGK, see Aberle et al. [15].

8. Summary

After more than 60 years of intensive and successful operation of the High-Speed Cascade Wind Tunnel at Bundeswehr University Munich, this unique test facility was subject to a major revision and upgrade recently. In this context the entire drive train, the axial compressor, oil system, and the main air cooler were exchanged by more powerful components featuring state-of-the-art technologies. For the most challenging component, which turned out to be the axial compressor, finally a very attractive and tailored solution was found for replacement. Within a remarkably short downtime of only four months, the entire revision as well as the successful re-commissioning of the test facility was realized. The new HGK finally features an extended operation range (e.g., up to 50% higher Reynolds number) which extends the research portfolio to stationary gas turbine applications or HPT (high-pressure turbine) investigations which have often been requested in the past but could never be serviced before. The test facility with its new features and equipment now fulfills all demands on a modern test facility. The new actuators together with the control systems very soon enable long lasting test campaigns under very stable and automatically controlled operating conditions down to $\Delta Ma = 0.17\%$ and $\Delta Re = 0.28\%$ never having been reached in the past. A huge variety of machine operating data not just simplifies trouble shooting during testing but also enables health monitoring and lifetime surveillance. With a powerful real-time data acquisition system in combination with many classical and modern measurement techniques, the new HGK is now well prepared and even more attractive for research needs and challenges in the future.

Author Contributions: Investigation, methodology, software, visualization, and validation, M.B.; conceptualization, writing, reviewing and editing, formal analysis, and data curation, R.N. and M.B.; resources, project administration, supervision, and funding, R.N. All authors have read and agreed to the published version of the manuscript.

Funding: The authors express their special thanks to the chancellor of the Bundeswehr University Munich, Siegfried Rapp, for his kind support of the project making the necessary budget available.

Institutional Review Board Statement: Not applicable.

Informed Consent Statement: Not applicable.

Data Availability Statement: The authors provide no supplemantary data.

Acknowledgments: The authors thank Ingenieurbüro Isler AG for the planning, project management, and successful completion of the entire revision. Thanks are also due to MAN for their support and willingness to develop and manufacture a tailored compressor for the HGK. In particular, it was Kai Ziegler at MAN, who had an open ear for all wishes and demands of the institute and made the successful cooperation possible right from the start. Special thanks go to the two technicians of the institute, Wilfried Ehrlich and Franz Grabendorfer, who actively supported the revision, and to the former chief engineer of the institute, Reinaldo Gomes, being a very valuable support with his profound experience during the planning phase.

Conflicts of Interest: The authors declare no conflict of interest.

Abbreviations

5HP	five-hole probe
HGK	High-Speed Cascade Wind Tunnel at the Bundeswehr University in Munich
IR-T	Infrared-Thermography
LPT	Low-Pressure Turbine
PIV	Particle Image Velocimetry
P-/TSP	Pressure-/Temperature-Sensitive Paint
ref	reference condition

Symbols

$H; W$	test section dimensions (height, width)
l	characteristic length
Ma	Mach number
$\dot{m}$	mass flow
N	shaft rotational speed
p; p_t	static; total pressure
P	electrical power
q	dynamic pressure
Re; Re/l	Reynolds number; Re based on unit length $l = 1\,\mathrm{m}$
T; T_t	static; total temperature
TI	turbulence intensity
U	velocity vector $U = [u; v; w]$
β	cascade outflow angle
γ	specific heat ratio
$\mu; \sigma$	statistical quantities for operating stability
ζ	total pressure loss coefficient $(p_{t,1} - p_{t,2})/(p_{t,1} - p_{ref})$

References

1. Schlichting, H. *The Variable Density High Speed Cascade Wind Tunnel of the Deutsche Forschungsanstalt für Luftfahrt Braunschweig*; AGARD Report; NATO: Paris, France, 1956; Volume 91.
2. Scholz, N.; Hopkes, U. Der Hochgeschwindigkeits-Gitterwindkanal der Deutschen Forschungsanstalt für Luftfahrt Braunschweig. *Forsch. Auf Dem Geb. Des Ingenieurwesens* **1959**, *25*, 5. (In German) [CrossRef]
3. Sturm, W.; Fottner, L. The High-Speed Cascade Wind Tunnel of the German Armed Forces University Munich. In Proceedings of the 8th Symposium on Measuring Techniques for Transonic and Supersonic Flows in Cascades and Turbomachines, Genoa, Italy, 24–25 October 1985.
4. European Commission. *Flightpath 2050 Europe's Vision for Aviation, Report of the High-Level Group on Aviation Research*; European Commission: Brussels, Belgium, 2011. [CrossRef]
5. Acton, P.; Fottner, L. The Generation of Instationary Flow Conditions in the High-Speed Cascade Wind Tunnel of the German Armed Forces University Munich. In Proceedings of the 13th Symposium on Measurement Techniques, Zurich, Switzerland, 5–6 September 1996.
6. Ziegler, K.; Eisenberg, B.; Hörmeyer, K.; Emmrich, R.; Ressing, H. Development of a Novel Axial Compressor Generation for Industrial Applications–Part 1: Compressor Design and Performance. In Proceedings of the ASME Turbo Expo 2014, Düsseldorf, Germany, 16–20 June 2014.
7. Anding, D.; Ressing, H.; Hörmeyer, K.; Pisch, R.; Ziegler, K. Development of a Novel Axial Compressor Generation for Industrial Applications–Part 2: Blade Mechanics. In Proceedings of the ASME Turbo Expo 2014, Düsseldorf, Germany, 16–20 June 2014.
8. Chemnitz, S.; Niehuis, R. A Comparison of Turbulence Levels from Particle Image Velocimetry and Constant Temperature Anemometry Downstream of a Low-Pressure Turbine Cascade at High-Speed Flow Conditions. *J. Turbomach* **2020**, *142*, 071008. [CrossRef]
9. Kiock, R.; Laskowski, G.; Hoheisel, H. *Die Erzeugung Höherer Turbulenzgrade in der Meßstrecke des Hochgeschwindigkeits-Gitterwindkanales, Braunschweig, zur Simulation Turbo-Maschinenähnlicher Bedingungen*; Technical Report, DFVLR-FB 82-25; DFVLR: Braunschweig, Germany, 1982.
10. Börner, M.; Niehuis, R. Development of an Additive Manufactured Miniaturized Wedge Probe Optimized for 2D Transonic Wake Flow Measurements. In Proceedings of the XXIV Biannual Symposium on Measuring Techniques in Turbomachinery, Prague, Czech Republic, 29–31 August 2018.
11. Aberle-Kern, S.; Niehuis, R.; Ripplinger, T. Loss determination at a linear cascade under consideration of thermal effects. *Aeronaut. J.* **2020**, *124*, 1592–1614. [CrossRef]
12. Bitter, M.; Kurz, J.; Kähler, C.J.; Niehuis, R. Investigations of a low pressure turbine blade by means of simultaneous optical velocity and pressure measurements. In Proceedings of the 18th International Symposium on Applications of Laser Techniques to Fluid Mechanics, Lisbon, Portugal, 4–7 July 2016.
13. Bitter, M.; Niehuis, R. Effects of Periodic Inflow Turbulence on the Statistics in the Wake of a Linear LPT Cascade at Jet-Engine Relevant Test Conditions. In Proceedings of the 13th International Symposium Particle Image Velocimetry-ISPIV 2019, Munich, Germany, 22–24 July 2019.
14. Bitter, M.; Stotz, S.; Niehuis, R. On High-Resolution Pressure Amplitude and Phase Measurements Comparing Fast-Response Pressure Transducers and Unsteady Pressure-Sensitive Paint. *J. Turbomach* **2021**, *143*, 031012. [CrossRef]
15. Aberle, S.; Bitter, M.; Hoefler, F.; Carretero Benignos, J.; Niehuis, R. Implementation of an In-situ Infrared Calibration Method for Precise Heat Transfer Measurements on a Linear Cascade. *J. Turbomach* **2019**, *141*, 021004. [CrossRef]

International Journal of
Turbomachinery Propulsion and Power

MDPI

Article

Design Parameter Influence on Losses and Downstream Flow Field Uniformity in Supersonic ORC Radial-Inflow Turbine Stators

Alessandro Cappiello * and Raffaele Tuccillo

Department of Industrial Engineering, "Federico II" University of Naples, 80125 Naples, Italy; raffaele.tuccillo@unina.it
* Correspondence: alessandro.cappiello@unina.it

Abstract: The design of organic Rankine cycle (ORC) turbines often requires dealing with transonic flows due to the cycle efficiency requirements and the matching of the temperature profiles with heat sources and sinks, as well as the nature of organic fluids, often featuring high molecular weight. Consequently, the use of convergent–divergent turbine stators has been widely established as a solution in the published literature for use in both axial- and radial-inflow machines. With respect to the latter layout in particular, the available design guidelines are still limited. The present work shows the results of an investigation into a series of ORC radial-inflow convergent–divergent nozzles that differ with respect to the vane count and the designed metal angle of the outlet. These stators were designed by fitting the divergent portion of a sharp-edged minimum-length nozzle, designed by means of the method of characteristics (MoC) adapted to dense gases, into a radial-inflow turbine stator. The geometries were analysed by means of steady-state RANS CFD calculations, and the results were used to assess the influence of the design parameters on the nozzle losses and downstream flow field uniformity, showing that conflicting trends exist between optimum stator efficiency and optimum downstream flow field uniformity.

Keywords: organic Rankine cycle; method of characteristics; supersonic stator; radial inflow turbine

check for updates

Citation: Cappiello, A.; Tuccillo, R. Design Parameter Influence on Losses and Downstream Flow Field Uniformity in Supersonic ORC Radial-Inflow Turbine Stators. *Int. J. Turbomach. Propuls. Power* **2021**, *6*, 38. https://doi.org/10.3390/ijtpp6030038

Academic Editor: Francesco Martelli

Received: 26 May 2021
Accepted: 12 August 2021
Published: 6 September 2021

Publisher's Note: MDPI stays neutral with regard to jurisdictional claims in published maps and institutional affiliations.

Copyright: © 2021 by the authors. Licensee MDPI, Basel, Switzerland. This article is an open access article distributed under the terms and conditions of the Creative Commons Attribution (CC BY-NC-ND) license (https://creativecommons.org/licenses/by-nc-nd/4.0/).

1. Introduction

Organic Rankine cycles (ORC) require an organic medium to operate through thermodynamic states determined by the matching of temperature profiles to heat sources and sinks, often resulting in large expansion ratios. Additionally, the high molecular weight often exhibited by organic fluids leads to low values of the speed of sound [1], resulting in turn in the onset of highly supersonic flows at stator discharge [2]. The authors [3] carried out an investigation of the radial-inflow turbine (RIT) design space using a mean-line model and parametric analyses, showing that, in order to achieve satisfactory efficiency with typical cycle configurations on the scale of tens of kilowatts, the stator discharge Mach numbers attain levels that commonly require convergent–divergent stators.

With respect to the design of convergent–divergent nozzles, the axial flow turbine configuration benefits from the broader pre-existing knowledge related to ideal gases, e.g., [4–6], mainly derived from previous experience with highly loaded stages [7] and auxiliary power turbines such as rocket turbo-pumps [8]. On the other hand, the published literature concerning the use of RIT supersonic stators for the expansion air or other ideal gases is scarce. A noticeable exception is the work by Reichert and Simon [9], who presented the design and analysis of convergent–divergent RIT nozzles for different discharge Mach numbers.

The established design practice for transonic stators, regardless of whether the turbine layout is in an axial or radial arrangement, makes use of the well-known method of characteristics [10] for the design of the diverging section, which is then arranged into a

row of nozzles. However, the conventional MoC, which assumes the fluid to be an ideal gas, cannot be used for an organic medium, and its first extension to dense gas vapours was reported by Aldo and Argrow [11]. Since then, several authors have dealt with the design and the analysis of single test cases of ORC radial-inflow convergent–divergent stators, e.g., the adaptation of the existing RANS solver to real gas flows [12], and subsequently the comparison of different flow solvers, turbulence models and fluid models [13], as well as shape optimization studies, e.g., [14,15]. Furthermore, several design methods for the design of ORC radial-inflow supersonic vanes have been presented over the years, e.g., the one by Wheeler and Ong [16] under the assumption of a polytropic relationship in fluid modelling, and the one by Anand et al. [17]; furthermore, the replacement of the working fluid for radial-inflow supersonic stators was investigated by White et al. [18]. However, comprehensive design guidelines are still unavailable with respect to several of the design variables.

From axial turbine cascades, it is known that under supersonic discharge conditions, the shape of the rear suction side plays a crucial role, as it reflects the expansion waves from the Prandtl–Meyer expansion around the trailing edge (TE), as well as the shock waves originating at the TE of the adjacent blade. Eventually, a curved uncovered suction side would also be responsible for the formation of additional waves. Therefore, the shape of the rear suction side can affect the uniformity of the downstream flow field.

With respect to convergent–divergent RIT nozzles, a straight uncovered suction side was found to increase downstream non-uniformity, affecting the Mach number and flow angle pitch-wise distributions [17]. This might eventually result in an increase in loss due to the resulting mixing process, as well as enhanced unsteadiness, as observed in the subsequent blade row, which might also be of concern from a structural point of view. In this regard, Rinaldi et al. [19] performed unsteady calculations using a highly supersonic ORC RIT, finding that torque fluctuated widely (even changing sign under certain operative conditions), as well as the presence of tangential and radial forces on the rotor blade resulting from the shock waves impinging on and detaching from the rotor blade; furthermore, one of the major contributors to loss was observed to be the boundary layer separation due to shock wave interaction in the rotor passages.

The stator design aims to meet some typical specifications, such as the outlet Mach number and the flow angle. The independent variables selected to achieve these goals include the vane count and the metal angle at the trailing edge. This choice allows the activation of a design procedure for the stator passage, whose effectiveness is then checked using a CFD base flow simulation. With respect to the first variable, conflicting trends can be envisaged: increasing the vane count increases the flow guidance, but on the other hand it also increases the wetted area and eventually the losses. Under supersonic discharge conditions, the picture is further complicated by the existence of waves reflecting on the uncovered suction side and playing a role in the uniformity of the downstream flow field. With respect to the outlet flow angle, from an efficiency point of view, it is desirable to increase its value (particularly at low specific speeds) [20]. For axial turbine convergent–divergent stators, it has been demonstrated that increasing the outlet flow angle leads to higher downstream mixing losses and flow field non-uniformity, since the wake is closer to the suction side of the adjacent vane [21]. On the other hand, related literature in this topic concerning RIT convergent–divergent nozzle is scarce. Finally, the discharge Mach number determines the level of compressibility and the magnitude of losses due to shock waves if supersonic discharge takes place.

This work aims at assessing the influence of combined effects of ORC convergent–divergent vane count and outlet metal angle on losses and downstream flow field uniformity and to investigate the existence of optimal combinations of these parameters. To do so, a series of RIT convergent–divergent nozzles with different values of vane count and outlet metal angle has been designed by means of an in-house code based on the *method of characteristics* (MoC) adapted to dense gases. The geometries have been then analysed and compared by means of CFD calculations.

2. Methodology

This section describes the methodology used to set up and analyse the test cases and it is organized as follows: the *Method of Characteristics* section describes the algorithm implementation to perform the sizing of the divergent side of the RIT nozzle; the *Radial Vane Design* section presents the methods used to fit the divergent part of the nozzle into a radial vane as well as the vane parametrization method and its input data; and *CFD Setup* describes the setting of numerical calculations for analysis and comparison of several geometries.

2.1. Method of Characteristics

As is well established, assuming a shape for the sonic line allows the supersonic region of a transonic nozzle to be designed independently of the subsonic one [22]. The latter can then be designed to produce the desired sonic line shape [23]. The design of the divergent portion is commonly made by means of the MoC [10], although an adaptation is required for the application to dense gases.

In the present study, the design of the divergent part of supersonic nozzles is performed by means of an adapted Method of Characteristics for a two-dimensional sharp-edged Minimum Length Nozzle with a straight sonic line, under the assumption of steady, isentropic, inviscid flow. The code is implemented in MATLAB environment and fluid properties are computed via link to CoolProp thermodynamic library [24].

The design of the divergent region implies the assignment of inlet total temperature and total pressure, which are equal to those at nozzle inlet, as well as the target Mach number at nozzle outlet together with the working fluid specification. Corresponding static pressure at the throat (M = 1) and at target Mach number (both reached through an isentropic expansion) are computed iteratively by means of bracketing method. Subsequently, the Prandtl–Meyer function ν corresponding to target Mach number is computed via numerical integration of the system of Equation (1)–(4), adapted from Cramer and Crickenberger [25], with initial flow property values evaluated at the nozzle throat.

Once known the overall Prandtl–Meyer function required to bring the fluid to the desired outlet Mach number, the divergent nozzle shape and flow property calculation on the characteristics network is carried out based on the algorithm by Vanco and Goldman [26].

$$\frac{d\nu}{dV} = \frac{\left(M^2-1\right)^{1/2}}{VM^2} \tag{1}$$

$$\frac{dM}{dV} = -\frac{M}{V}\,J \tag{2}$$

$$J = 1 - \Gamma - M^{-2} \tag{3}$$

$$\Gamma = EoS(V, \mathrm{s}^*) \tag{4}$$

The Prandtl–Meyer expansion originated at the throat corner is discretized into a user-specified number of right-running (RR) waves, blue lines in Figure 1a, which are reflected as left-running (LR) waves, red lines in Figure 1a, at the centreline. The latter family of waves meets the upper nozzle contour that is shaped to cancel them.

Flow angle φ, Prandtl–Meyer function ν and Mach angle μ in each of the cells bounded by the characteristics net can be computed as in the ideal gas case; however, since the relationship between ν, local velocity-to-sonic speed in the throat and local Mach number used in [26] is not applicable to dense gases, the algorithm is modified making use of the ν-Mach number relation from Ref. [25]. The slopes of Mach lines for RR and LR waves are given by $\tan(\mu + \varphi)$ and $-\tan(\mu - \varphi)$, respectively. Like in Ref. [26], average values of adjacent cells are used.

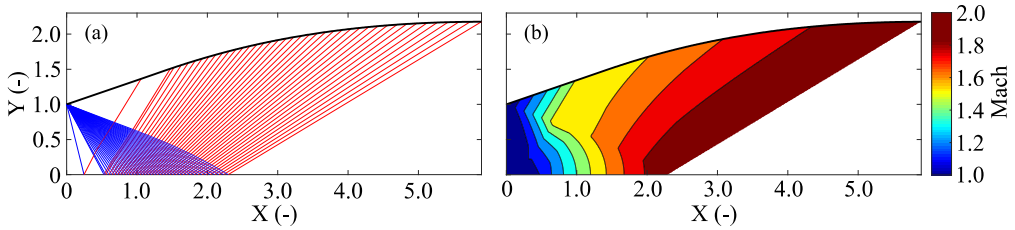

Figure 1. Convergent-divergent nozzle design: (**a**) Characteristic net-blue line: right-running waves, red lines: left-running waves; (**b**) Mach number contour of nozzle divergent region from method of characteristics.

The knowledge of characteristic line slopes allows identification of the location (in terms of X and Y coordinates) of each intersection between characteristic lines, so building the characteristic net (Figure 1a), although different equations are required for interior points, nozzle centreline and nozzle contour points. Further details about the calculation procedure can be found in Ref. [26].

The application of the method of characteristics adapted to dense gases leads to the calculation of the non-dimensional nozzle contour shape with respect to half throat width, together with flow properties distribution starting from M = 1 (straight sonic line at divergent duct inlet) up to a uniform target Mach number value at the nozzle outlet. Figure 1 show the resulting characteristic net (with a reduced number of waves for legibility purpose) obtained by the MoC for a sample half-nozzle expanding R245fa to a target Mach number of 1.89; blue and red lines refers to RR and LR waves, respectively. Figure 1b presents the related Mach number distribution computed by MoC for the same nozzle.

Figure 2 presents the resulting upper half shape (made non-dimensional by the inlet width) of nozzle divergent section obtained by means of the adapted MoC for several working fluids expanding from the same reduced total pressure (p_0/p_c) and total temperature (T_0/T_c) as those in Figure 1, for two discharge Mach number values. This figure allows an impressive insight into the effect of both working fluid and target Mach number on nozzle dimensions. In this regard, it can be seen in Figure 2 that, for a given target Mach number value, the working fluid affects both length and discharge area of the nozzle. The latter can be better visualized by means of the close-up view of the outlet region, provided in Figure 2a, which also reports the average polytropic exponent k. This parameter is computed by a linear regression of $\log(\rho/\rho_0)$ and $\log(p/p_0)$ along 1000 points within the isentropic expansion from inlet to outlet pressure. This approach allows a qualitative understanding of the working fluid effects on nozzle shape, although larger discrepancies between the average value of k and the local slope of $\log(p/p_0)$ vs. $\log(\rho/\rho_0)$ arise as far as the critical point is approached. However, it is worth mentioning that in all cases presented in Figure 2a, the R^2 of the linear regression was fairly higher than 0.998.

As one can notice from Figure 2a, the lower the average polytropic exponent k the larger the nozzle length and outlet width. This occurrence is a consequence of the effect of k on the Prandtl-Meyer function value ν. In fact, it is known that for a target Mach number, decreasing the value of k leads to a higher required Prandtl–Meyer function value ν and, ultimately, to a larger nozzle size [16]. As expected, an increase in the target Mach number increases nozzle length and outlet width, Figure 2.

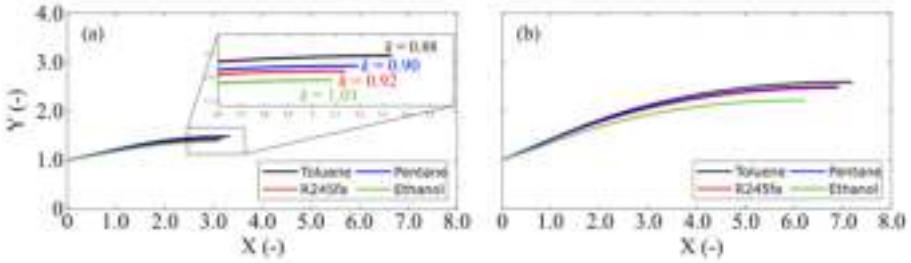

Figure 2. Upper half of nozzle divergent section from adapted MoC for several organic fluids at p_{0r} = 0.767, T_{0r} = 1.028: (**a**) target Mach number = 1.6; (**b**) target Mach number 2.0.

2.2. Radial Vane Design

Once the non-dimensional shape of the nozzle divergent part has been computed, it is possible to resize it and to arrange it into a RIT vane according to the following procedure.

First, the nozzle contour must be scaled to the right size in order to comply with the design mass flow rate. In this regard, it should be reminded that the vane height is generally not a free choice, because it usually results from the rotor preliminary design. Consequently, in the present design method, it is treated as a user-specified value and used to compute the actual throat width as follows:

$$A^* = \frac{\dot{m}}{Z\,\rho^*\,a^*\,b} \tag{5}$$

Subsequently, the nozzle contour is scaled by $A^*/2$ and its specular half with respect to the horizontal axis is created. In this regard, it is worth mentioning that no boundary layer correction is applied to compute nozzle throat width (A*), which might lead to a slightly lower mass flow rate than the design one.

Furthermore, the suitability of the approximations has been checked against CFD results and it appeared to be satisfying, since the mass-average Mach number from CFD at A* is 1.04, and the difference between CFD mass-weighted average and target Mach number at A_E is within 1% as well.

The first trailing edge (TE) is drawn by setting half circle of radius R_{TE} at coordinates $(0, R_{out} + R_{TE})$ and aligning it to the design outlet metal angle, Figure 3. Then, the right-scaled divergent region of the nozzle is shifted such that the last point of right-hand side contour lies at point f and it is rotated in order to be aligned with the outlet metal angle with respect to radial direction.

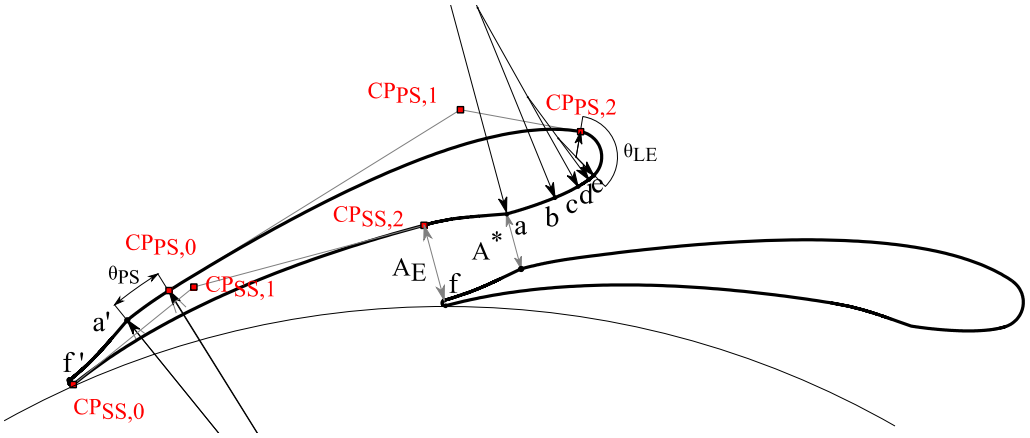

Figure 3. Radial inflow turbine vane parametrization method.

The TE and the right-hand side nozzle contour are rotated around an angular pitch $(2\pi/Z)$ building the supersonic part of the vane pressure side (a'–f').

The uncovered suction side is built by means of a 2nd order Bezier polynomial whose two legs are tangent to the end of nozzle contour suction side and to the TE circle; control points $CP_{SS,\,0}$, $CP_{SS,\,2}$ and $CP_{SS,\,1}$ are given by the first point of the rotated TE circle, last point of nozzle contour suction side and the intersection between the two tangent to $CP_{SS,\,0}$ and $CP_{SS,\,2}$, respectively.

The subsonic part of the suction side, together with the leading edge (LE), is built according to the vane parametrization by Reichert and Simon [9] by means of a series of circular arcs of decreasing radius from the inner throat (A^* in Figure 3) to the leading edge, so that the radius of curvature is larger where gradients are higher.

The subsonic part of the pressure side consists of a circle (a'-$CP_{PS,0}$) with the same radius and angular extension (θ_{PS}) as the first circle of the subsonic suction side construction (a–b), and a 2nd order Bezier polynomial defined as in the uncovered suction side case.

Finally, it should be highlighted that, while the vane count is an independent variable, the present design method does not allow the vane row solidity to be assigned, since the vane chord results from the design procedure.

2.3. CFD Setup

The stator design specifications, say inlet and outlet flow angles and vane height, are derived from one of the test cases investigated in the authors' previous work [3] that describes a RIT preliminary design performed by mean of an in-house mean-line code linked to CoolProp thermodynamic library [24]. More specifically, the chosen test case assumes R245fa as working fluid, which is undergoing a volumetric expansion ratio of 14 with upstream total temperature and pressure of 439 K and 28 bar, respectively. The turbine candidate was selected among the converged cases of the parametric analysis discarding those with unfeasible geometries, excessive rotor flow turning and too short stator vane height (below 2 mm).

The RIT vanes built with the procedure outlined above have been later investigated by means of viscous, steady-state RANS 3D CFD calculations performed by ANSYS Fluent® solver v 17.1. All calculations have been carried out by means of a density-based solver with implicit formulation, and Courant number = 5. Roe-FDS method for flux scheme was selected. Concerning the spatial discretization, a least square cell based scheme has been used for gradient reconstruction, whereas second order upwind discretization has been selected for flow and turbulence. Finally, the $k-\omega\ SST$ model has been employed for the turbulent problem closure. Real gas thermodynamic properties have been evaluated by means of REFPROP [27], via the built-in fluent routines. Regarding the convergence check, a first order solution was achieved before switching to second order spatial discretization.

The fluid domain, shown in Figure 4 together with the mesh for the 15 vanes–75° outlet metal angle case, was extended upstream and downstream with respect to the vane in order to avoid non-physical solutions, with rotationally periodic boundary condition on the sides of the domain. Hub, shroud, and blade walls were considered to be adiabatic with no-slip conditions. Flow boundary conditions were set in terms of total pressure and temperature and flow direction angles at the inlet and static pressure at the outlet. An outlet static pressure of 3.25 bar was assigned to reach a static pressure at rotor inlet plane (R_4 in Figure 4) close to the one computed by the turbine preliminary design mentioned above. Finally, a strong-averaging option was activated to avoid wave reflection on the outlet boundary.

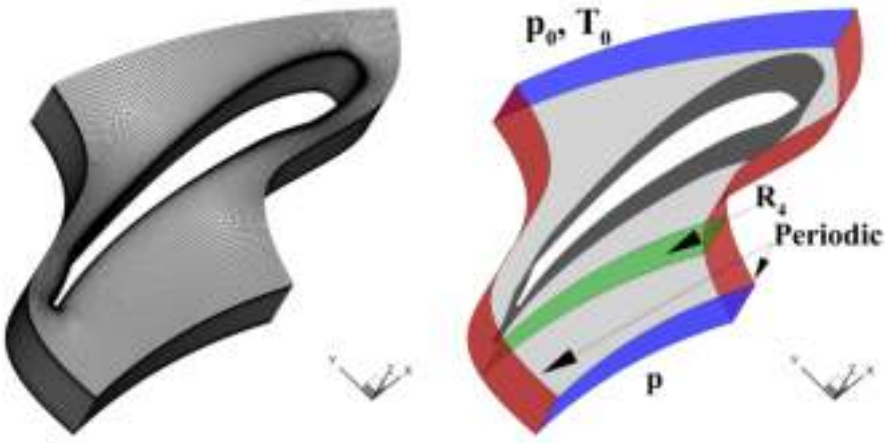

Figure 4. Mesh and computational domain for 15 vane–75° outlet metal angle case.

All meshes have been set-up in ANSYS TurboGrid; to reduce the computational effort, y^+ was set to 25 on the walls, making use of wall functions.

2.4. Mesh Sensitivity

A mesh sensitivity analysis was carried out on a single geometry with intermediate characteristics with respect to the investigated set of profiles, as reported in Table 1. Four grid sizes have been used for the grid convergence study, established by refining the average spacing $h = \sqrt[3]{\text{Volume/Cells Number}}$, and by keeping the refinement factor r = $h_{coarser}/h_{finer}$ always above 1.3 from each mesh to the finer one, Table 2.

Table 1. Mesh sensitivity analysis vane features.

Re_c	Ma_4	c (mm)	Z	β_m (°)	A* (mm)	R_3 (mm)
5.86×10^6	1.66	12.8	15	75	1.36	≈22

Table 2. Mesh data for grid convergence analysis.

Mesh #	Volume (m^3)	Cells Number (10^6)	h (m)	r
1	1.54×10^{-7}	0.122	1.08×10^{-4}	-
2	1.54×10^{-7}	0.287	8.12×10^{-5}	1.33
3	1.54×10^{-7}	0.679	6.10×10^{-5}	1.33
4	1.54×10^{-7}	1.604	4.58×10^{-5}	1.33

Number.

Table 3 reports the variation with mesh size of the mass-averaged results of performance coefficients and of several quantities of interest, expressed as percentage difference with respect to the finest mesh. As one can notice, such differences are already very low starting from the second mesh. However, despite such very small variations of the mass-averaged quantities with mesh size, the analysis of mid-span pitch-wise distributions (at rotor inlet radius R_4) displayed in Figure 5 highlights very sharp variations. The latter may be explained by both expansion fans and shock waves originating from vane trailing edge, which appears dramatically smoothed out by the coarser grids.

Table 3. Percentual variation of relevant quantities with mesh size: finest mesh taken as reference.

	Mesh #			
	1	**2**	**3**	**4**
Δp4 (%)	2.2710	1.0476	0.4601	0
Δα4 (%)	0.2484	0.0786	0.0418	0
ΔEk4 (%)	−0.7188	−0.3013	−0.0959	0
ΔM4 (%)	−0.3212	−0.2014	−0.1476	0
Δζ (%)	−8.4196	−2.3310	0.6954	0
Δs (%)	−12.031	−3.8900	0.0304	0
Δηs (%)	0.6587	0.1997	−0.0247	0
Δp4 (%)	2.2710	1.0476	0.4601	0

Number.

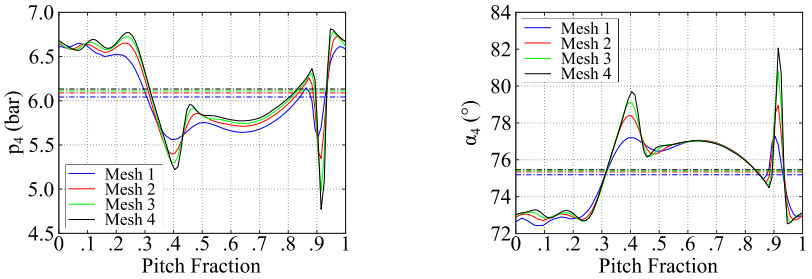

Figure 5. Influence of mesh size on mid-span pitch-wise distributions at rotor inlet radius (solid line) and average value (dash-dot line): static pressure; absolute flow angle.

In particular, pitch-wise pressure and flow angle distributions at mid-span computed in the coarsest mesh case, Figure 5, present differences with peaks of about 20% with respect to the finest mesh. Based on these considerations, since the focus of the work is mainly on the downstream flow field uniformity, it was decided to proceed with an average mesh spacing h corresponding to the one of the third mesh. This choice allowed a resolution enhancement of the expansion fans and shock waves, which appear to give the largest contributors to the pitch-wise non-uniformities.

3. Results

Different RIT vanes have been designed by means of the method presented in the methodology section. The nine geometries for the parametric analysis differ by vane count Z (10, 15 and 20) and outlet metal angle β_m (70°, 75° and 80°). The distance between stator trailing edge and rotor inlet has been kept constant for all the cases and equal to the value found in the mean-line design. TE thickness was set as a percentage of the inner throat area (A^*), so to induce the same blockage effect in each case. In this way, the actual blockage is only dependent on the of the boundary layer growth. The resulting TE thickness-to-pitch ratio is of nearly 1.49×10^{-2}.

Regarding the target Mach number (M_E) input for the method of characteristics, it was decided to keep it at a fixed value of 1.55. The latter is lower than the design Mach number at the stator outlet plane from mean-line design (1.66), thus ensuring that the flow undergoes a further expansion up to the stator exit pale. This expansion from nozzle core outlet (plane E in Figure 3) to the TE plane might have a stabilizing effect on the boundary layer and might hence be beneficial. The resulting design expansion ratios in the nozzle core (throat-plane E) and semi-bladed region are 2.14 and 1.27, respectively.

In the following, the results of the numerical calculations on the geometries are presented. First, static pressure, Mach number and total pressure distributions at mid-span are shown for the 15 vane–75° outlet metal angle case in Figure 6, with the superposition of streamlines. This allows visualization of expansion fans and compression waves, which can be clearly distinguished by means of the streamline deflection, Figure 6a,b; and by the total pressure defect in the wake behind the trailing edge, Figure 6c.

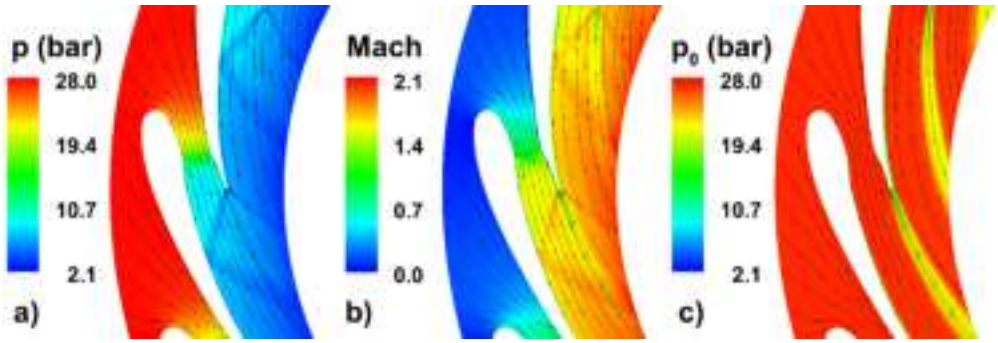

Figure 6. 15 vanes–75° outlet metal angle mid-span distributions: (**a**) static pressure; (**b**) Mach number; (**c**) total pressure.

A more accurate insight into both flow field features and downstream non-uniformities is provided in next section by mid-span blade-to-blade contours together with mid-span pitch-wise distributions, so allowing assessment of metal angle and vane number influence.

3.1. Flow Structures

With the aim of investigating the characteristic features of the flow structures along with the influence of the design parameters, mid-span blade-to-blade pressure gradient distributions are presented for the 9 geometries in Figure 7. Some common features can be identified in terms of right-running (RR) and left-running (LR) expansion fans, at the inner throat A* in Figure 3, together with the well-known trailing edge supersonic flow pattern, which is also typical of axial turbine stators. In particular, the latter consists of:

- LR expansion fan (tag A, Figure 6);
- LR shock (tag B), located after the expansion fan A;
- RR expansion fan, which is then reflected on the suction side of the adjacent vane as LR expansion wave (tag C);
- RR shock reflected as a LR shock (tag D) on the suction side of the adjacent vane.

Besides the above-mentioned sets of waves, another peculiar structure (tags E′ and E″, Figure 7) can be observed, i.e., two sets of *in-passage LR compression waves*, originated by the non-straight rear suction side shape. The first one is located approximately at the beginning of the uncovered suction side (tag E′, Figure 7), and the second one can be detected towards the trailing edge (tag. E″, Figure 7). It is worth-noting that the locations of *in-passage LR compression waves* appear to be strongly affected by vane count and outlet metal angle combination, as a result of the vane parametrization method.

In fact, in the highest metal angle cases only the *in-passage LR compression waves* located right after the nozzle core exit plane can be found (tag E′). Conversely, in the intermediate metal angle cases, the first set (tag E′) is shifted downstream and the second set of compression waves (although of very weak intensity) can be seen toward the trailing edge (tag E″).

Eventually, in the low metal angle cases, only the second set (tag E″) is present, because of the different curvature distribution of the rear suction side. Finally, it is worth- noting that in the 20 vane count–70° outlet metal angle case, Figure 7, the placement of *in-passage LR compression waves* is so close to the trailing edge that it is rather difficult to distinguish it from the trailing edge LR shock (tag B). Actually, such waves almost merge while travelling downstream, making the expansion fan (tag A) difficult to identify.

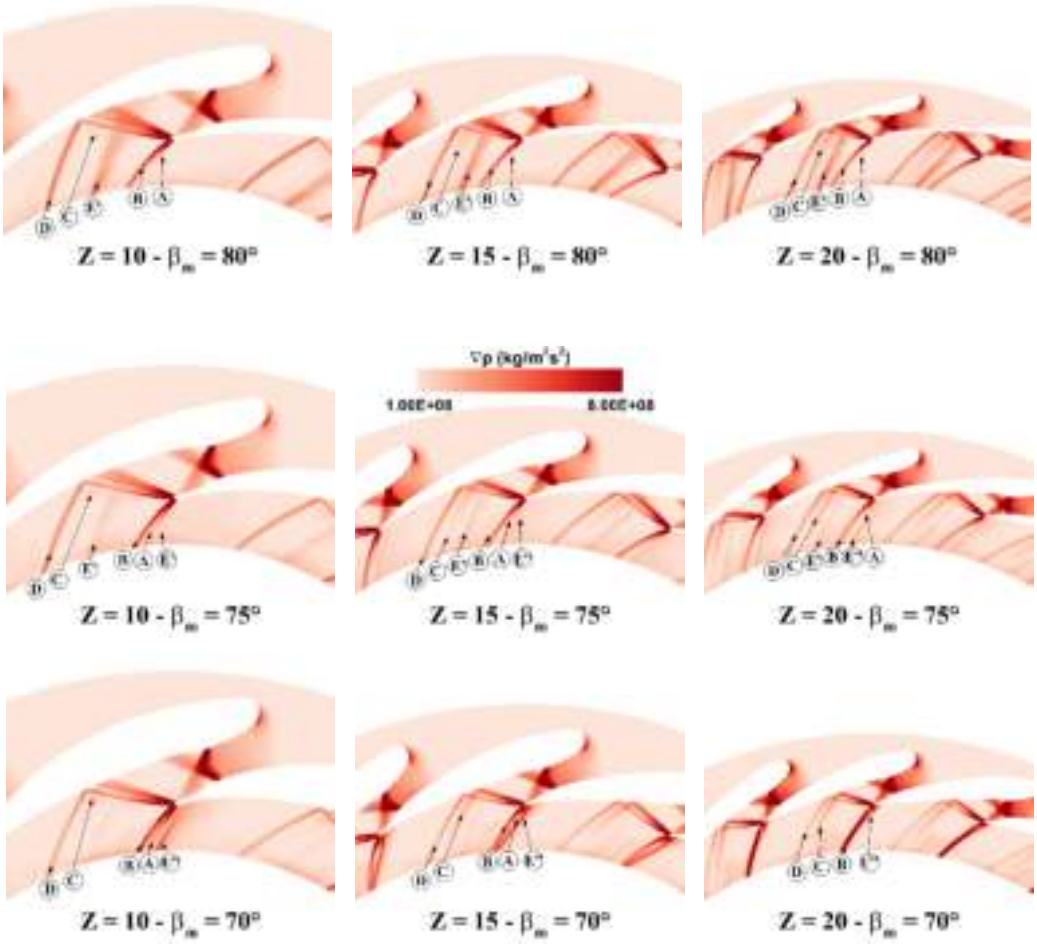

Figure 7. Pressure gradient contours.

3.2. Pitch-Wise Distributions

Figures 8 and 9 display the pitch-wise pressure distribution at mid-span (expressed as percent deviation from the average value) at rotor inlet radius (R_4) as a function of the relative angular coordinate with respect to the angular pitch. It is worth mentioning that a pitch fraction of zero corresponds to the RHS corner of the computational domain (Figure 4), whereas the unity corresponds to the LHS one.

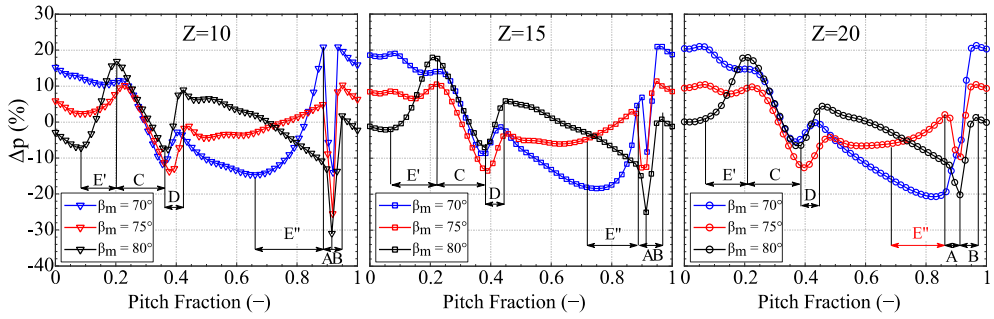

Figure 8. Mid-span pitch-wise static pressure distribution at rotor inlet radius expressed as a percent deviation with respect to mean value, grouped by vane count.

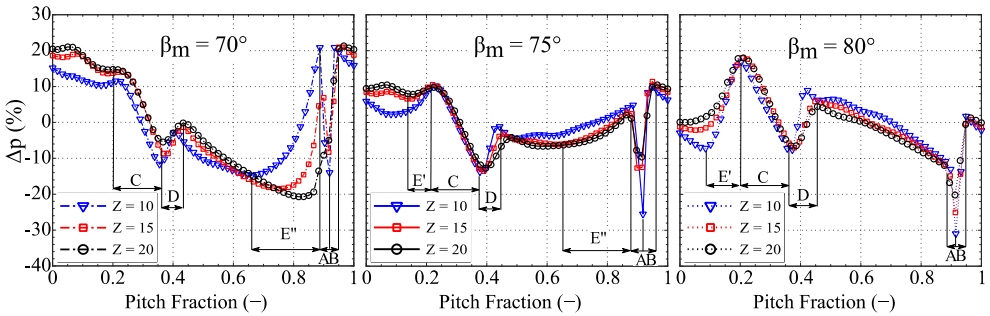

Figure 9. Mid-span pitch-wise static pressure distribution at rotor inlet radius expressed as a percent deviation with respect to mean value, grouped by outlet metal angle.

Referring to the 10 vane configurations (Figure 8, Z = 10), a slightly decreasing trend can be observed in the distribution behind the trailing edge location (lowest fractions of the pitch), which can be ascribed to the wake effect.

Then, cases with outlet metal angles of 75° and 80° show a sudden pressure rise (due to *in-passage compression waves* E′), which is instead not detected for 70° case. This occurrence can be explained by the pressure gradients in Figure 7, if observing that in 70° cases only the second set of *in-passage LR compression waves* E″ is present and located near the trailing edge. Moreover, for the 80° case, the pressure rise due to the *in-passage LR compression waves* (E′) is much larger than the one in the 75° case, consistently with the higher curvature induced by the 80° case right after the nozzle core outlet section.

Moving towards higher pitch fraction values, all three distributions undergo rapid expansion of comparable intensity because of the presence of the reflected *left-running expansion fan*, tag C in Figure 7. After the valley, pressure rises again because of the fluid passing through the *reflected left-running shock wave*, tag D in Figure 7.

If moving further towards the unit pitch fraction, different trends can be identified, depending on metal angle:

In the 70° case, the pressure distribution, after an initial decrease, starts rising very sharply due to the *in-passage compression waves*, tag E″ (which in this case are located almost at the vane trailing edge, as a consequence of the uncovered suction side curvature distribution).

Conversely, the 80° case shows a decreasing trend, thanks to a lower curvature of the terminal part of vane suction side.

An intermediate trend takes place in the 75° arrangement (which is also characterized by a weak second set of *in-passage compression waves*, tag E″). In this case, an initially decreasing trend is followed by an increasing one due to the compression waves.

Subsequently, a sudden expansion can be noticed in all three cases (although much larger in the 70° case) due to the *left-running expansion fan*, tag A in Figure 7. The pressure rises again in all three cases due to the *left-running shock wave* tag B, Figure 7. Finally, a slight expansion behind the trailing edge occurs in all these cases.

The same pressure pattern can be found in Figure 8 (Z = 15 and 20), although with different values. The only relevant exception occurs in the 20 vane–70°, Figure 8, for which the second set of *in-passage compression waves*, tag E″, is practically merged with the trailing edge shock wave.

3.2.1. Vane Number Effect

As one can notice from Figure 9, the overall effect of the vane count is modest particularly in the 75° and 80° outlet metal angle cases, with the major differences segregated firstly in the LR expansion fan (tag A, Figure 7) and LR shock wave (tag B, Figure 7), with sharper trends pertaining to the lowest vane count case, and secondly to pressure rise magnitude due to the *in-passage compressions waves* (tag E′).

Differences induced by the vane count are more evident only in the 70° outlet metal cases, in the region between the reflected LR shock wave (tag D) and LR expansion fan (tag A), Figure 9. Actually, in this region such cases are affected by the presence of the *in-passage compressions waves* (tag E", Figure 7), which occur much earlier as the vane count is decreased.

3.2.2. Discharge Metal Angle Effect

Substantially different trends can be detected in the 80° and 75° metal angle cases, Figure 9, inside the region between reflected LR shock wave (tag D, Figure 7) and LR expansion fan (tag A, Figure 7). In particular, in the former case a monotonically decreasing trend is noticed, whereas in the latter case an increasing pattern is present after a certain pitch fraction, as a result of a weaker *in-passage compression wave* (tag E"). Concerning the 70° case, a monotonically decreasing trend can be observed up to the pressure rise induced by *in-passage compression waves* (tag E").

Furthermore, 80° metal angle cases always show the deeper valley associated to the LR expansion fan (tag A).

Finally, since most of the above-mentioned features of pitch-wise pressure distributions are induced by streamlines crossing Mach waves, similar trends can be detected for flow angle pitch-wise distributions in Figure 10. In this case, however, maximum deviations from mean value do not exceed 15%, with unaltered vane count and outlet metal angle effects.

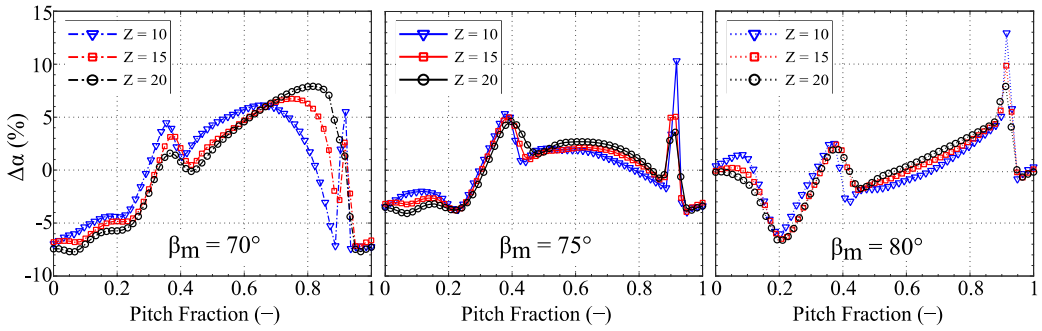

Figure 10. Mid-span pitch-wise flow angle (abs. frame of reference) distribution at rotor inlet radius expressed as a percent deviation with respect to mean value, grouped by outlet metal angle.

3.3. Global Trends

Several figures of merit have been considered to provide a global sketch of each stator performance in terms of losses and downstream flow field uniformity. For what concerns the former, total pressure loss Y, kinetic loss coefficient ζ, and stator efficiency η have been considered. In Equation (6), outlet properties are evaluated at rotor inlet radius surface.

$$Y = \frac{p_{0\ in} - p_{0\ out}}{p_{0\ out} - p_{out}} \cdot 100 \qquad \zeta = \frac{v^2_{out\ is} - v^2_{out}}{v^2_{out\ is}} \cdot 100 \qquad \eta = \frac{h_{0\ in} - h_{out}}{h_{0\ in} - h_{out\ is}} \cdot 100, \tag{6}$$

The pitch-wise non-uniformity level of each geometry has been evaluated for several quantities with reference to the mid-span pitch-wise distribution at the rotor inlet radius, by means of the figure of merit defined by Equation (7), χ being a general quantity of interest. This figure quantifies the average deviation of each distribution from its average value (designated by the overbar) normalized by the angular pitch.

$$\frac{\int_0^{\theta_{pitch}} |\chi - \overline{\chi}|\, d\theta}{\Delta\theta_{pitch}} \cdot \frac{100}{\overline{\chi}}, \tag{7}$$

Figure 11 presents the contour plots for total pressure loss, kinetic loss coefficient and stator efficiency as a function of vane count Z and outlet metal angle β_m. A clear and consistent trend can be identified for all three parameters. As a matter of fact, higher losses occur at both low vane count Z and high outlet metal angle β_m, and a progressive decrease occurs as the vane count is increased and the outlet metal angle is lowered. A minimum level is reached at the opposite corner of the map, with the lowest outlet metal angle and the highest vane count.

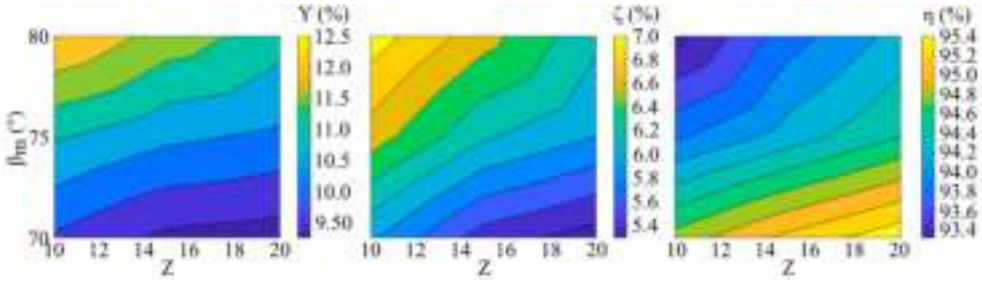

Figure 11. Distribution of stator performance index as a function of vane count and outlet metal angle: total pressure loss Y, kinetic loss coefficient ζ and stator efficiency η.

Figure 12 shows the contour plots of non-uniformity index for mid-span outlet Mach number and outlet flow angle (both in the absolute reference frame) at rotor inlet radius, as a function of vane count Z and outlet metal angle β_m. It is worth-noting that an opposite trend with respect to losses can be observed, since the lowest non-uniformity coefficients are attained by low vane count–high outlet metal angle configurations. Furthermore, the outlet flow angle non-uniformity level appears to be only weakly affected by the vane count. Generally speaking, despite the sharper trends in Figure 9, lower vane counts show globally lower non-uniformity levels, Figure 12.

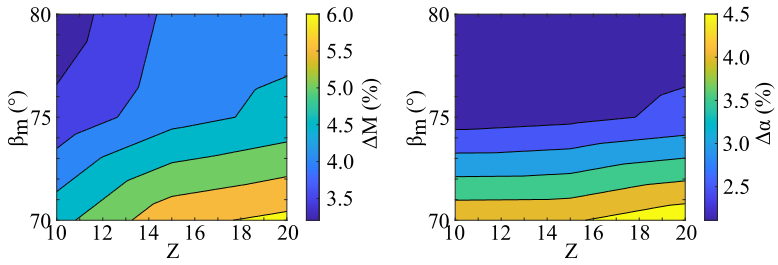

Figure 12. Distribution of non-uniformity index as a function of vane count and outlet metal angle: Mach number and absolute flow angle.

As a concluding remark, overall conflicting trends can be found in Figures 11 and 12 between the optima from a loss perspective and downstream flow field uniformity, so suggesting the need for multi-objective optimization strategies.

4. Conclusions

The present work was founded on an adaptation to dense gases of the method of characteristics for the inverse design of the diverging section of sharp-edged minimum length nozzles.

The adapted method of characteristics was used to design supersonic vanes of radial flow turbines for organic Rankine cycles, by means of a simple vane parametrization method, fitting the inverse design of the nozzle divergent section into the turbine vane. The method fits well in a conventional design procedure, allowing the designer to set vane height (usually determined in the preliminary design stage), vane count and outlet metal angle independently.

The method was used to investigate the combined effect of vane count and outlet metal angle on stator losses and downstream flow field uniformity for nine stators designed

to expand R245fa, while keeping the same MoC target Mach (at A_E) lower than the stator design discharge Mach number.

The boundary conditions, together with the preliminary design specifications, were derived from a previous publication by the authors, in which an in-house mean-line code was used to perform the turbine preliminary design and to carry out a parametric analysis of the design space. The CFD analyses of the nine geometries unveiled conflicting trends between optimal stator efficiency and downstream flow field uniformity, so envisaging the need for multi-objective optimization strategies. To gain further insight in the mechanisms driving this occurrence, mid-span pressure gradients were used to visualize the Mach wave patterns. Their influence is correlated with mid-span pitch-wise distributions at the rotor inlet, and the effect of vane count and outlet metal angle on their structure is highlighted. The overall effect of vane count appeared to be slight, even if locally sharper trends take place as the vane count is reduced. The outlet metal angle was seen to induce a larger effect on the overall mid-span pitch-wise distribution at stator outlet, and particularly on the trend in the rear suction side region. Furthermore, the higher the outlet metal angle the sharper the local trends.

Despite the simple vane parametrization method used in this work, results provide novel contribution particularly for the effect of outlet metal angle and vane count and the conflicting trends of optimum stator efficiency and downstream flow field uniformity.

Developments of the present work include the unsteady simulation for the stator-rotor interaction [28]. Possible future works might include the investigation of the effect of the target Mach number for the MoC, in terms of expansion ratio sharing between bladed and semi-bladed portion of the vane passage. Improvements to the vane parametrization method might include the use of higher order Bezier polynomials specially for the rear suction side, so allowing more degrees of freedom for the curvature distribution, although reducing simplicity of use for generating a first guess geometry.

Author Contributions: Conceptualization, A.C. and R.T.; methodology, A.C. and R.T.; software, A.C.; validation, A.C., R.T.; investigation, A.C. and R.T.; data curation, A.C.; writing—original draft preparation, review, and editing, A.C. and R.T.; visualization, A.C.; supervision, R.T. All authors have read and agreed to the published version of the manuscript.

Funding: This research received no external funding.

Institutional Review Board Statement: Not applicable.

Informed Consent Statement: Not applicable.

Data Availability Statement: The data presented in this study are available on request from the corresponding author.

Acknowledgments: The method of characteristics and supersonic radial vane design method are implemented in MATLAB R2019a. CFD calculations have been performed in ANSYS Fluent® 17.1.

Conflicts of Interest: The authors declare no conflict of interest.

Nomenclature

Abbreviations

EoS	Equation of State
ORC	Organic Rankine Cycle
LE	Leading Edge
LR	Left Running
MoC	Method of Characteristics
PS	Pressure Side
RIT	Radial-Inflow Turbine
RR	Right-Running

RR	Right-Running
SS	Suction Side
TE	Trailing Edge

Symbols

A	Area
M	Mach number
R	Radius
V	Specific volume
Y	Total pressure loss
Z	Vane count
a	Speed of sound
b	Vane height
c	Chord
h	Mesh spacing
p	Pressure
r	Mesh refinement
s	Entropy
v	Flow velocity

Greeks

Γ	Fundamental derivative of gas dynamics
α	Absolute flow angle (°)
β_m	Metal angle (°)
θ	Angle
μ	Mach angle
ν	Prandtl-Meyer function
ρ	Density
φ	Flow angle in MoC
η	Efficiency
ζ	Kinetic loss coefficient

Subscripts

0	Total quantity
3	Stator exit surface
4	Rotor inlet surface
E	Nozzle core exit
c	Critical point
r	Reduced
in	Inlet
is	Isentropic
out	Outlet

Superscripts

*	Property at the throat

References

1. Astolfi, M.; Martelli, E.; Pierobon, L. Thermodynamic and technoeconomic optimization of Organic Rankine Cycle systems. In *Organic Rankine Cycle (ORC) Power Systems*; Woodhead Publishing: Sawston, UK, 2017; pp. 173–249. [CrossRef]
2. Colonna, P.; Casati, E.; Trapp, C.; Mathijssen, T.; Larjola, J.; Turunen-Saaresti, T.; Uusitalo, A. Organic Rankine Cycle Power Systems: From the Concept to Current Technology, Applications, and an Outlook to the Future. *J. Eng. Gas Turbines Power* **2015**, *137*, 100801. [CrossRef]
3. Cappiello, A.; Tuccillo, R. Design and CFD Analysis of a Radial-Inflow Turbine for Small Scale ORC Applications. In Proceedings of the E3S 75th National ATI Web Congress—#7 Clean Energy for All (ATI. 2020), Rome, Italy, 15–16 September 2020; Volume 197, p. 11005. [CrossRef]

4. Moffitt, T.P. Maximum Theoretical Tangential Velocity Component Possible from Straight-Back Converging and Converging-Diverging Stators at Supercritical Pressure Ratios, Cleveland. 1958. Available online: https://ntrs.nasa.gov/search.jsp?R=19930085040 (accessed on 10 November 2019).
5. Ohlsson, G.O. Supersonic Turbines. *J. Eng. Power* **1964**, *86*, 7–12. [CrossRef]
6. Goldman, L.J. Supersonic Turbines. In *NASA-SP-290*; NASA: Washington, DC, USA, 1994; pp. 249–278. Available online: https://ntrs.nasa.gov/search.jsp?R=19950015924 (accessed on 20 May 2019).
7. Johnston, I.H.; Dransfield, D.C. The Test Performance of Highly Loaded Turbine Stages Designed for High Pressure Ratio, London, 1959. Available online: http://citeseerx.ist.psu.edu/viewdoc/download?doi=10.1.1.227.2268&rep=rep1&type=pdf (accessed on 23 September 2019).
8. Fu, C.; Zou, Z.; Kong, Q.; Cheng, H.; Zhang, W. Aerodynamic Design and Numerical Analysis of Supersonic Turbine for Turbo Pump. *Int. J. Turbo Jet-Engines* **2016**, *33*. [CrossRef]
9. Reichert, A.W.; Simon, H. Design and Flow Field Calculations for Transonic and Supersonic Radial Inflow Turbine Guide Vanes. *J. Turbomach.* **1997**, *119*, 103–113. [CrossRef]
10. Shapiro, A.; Edelman, G. *Method of Characteristics for Two-Dimensional Supersonic Flow: Graphical and Numerical Procedures*; Massachusetts Institute of Technology: Cambridge, MA, USA, 1947.
11. Aldo, A.C.; Argrow, B.M. Supersonic minimum length nozzle design for dense gases. In *The Fifth Annual Thermal and Fluids Analysis Workshop*; NASA, Lewis Research Center: Cleveland, OH, USA, 1993. Available online: https://ntrs.nasa.gov/search.jsp?R=19940019183 (accessed on 11 March 2020).
12. Hoffren, J.; Talonpoika, T.; Larjola, J.; Siikonen, T. Numerical Simulation of Real-Gas Flow in a Supersonic Turbine Nozzle Ring. *J. Eng. Gas Turbines Power* **2002**, *124*, 395–403. [CrossRef]
13. Harinck, J.; Turunen-Saaresti, T.; Colonna, P.; Rebay, S.; Van Buijtenen, J. Computational Study of a High-Expansion Ratio Radial Organic Rankine Cycle Turbine Stator. *J. Eng. Gas Turbines Power* **2010**, *132*, 054501. [CrossRef]
14. Harinck, J.; Pasquale, D.; Pecnik, R.; van Buijtenen, J.; Colonna, P. Performance improvement of a radial organic Rankine cycle turbine by means of automated computational fluid dynamic design. *Proc. Inst. Mech. Eng. Part A J. Power Energy* **2013**, *227*, 637–645. [CrossRef]
15. Pasquale, D.; Ghidoni, A.; Rebay, S. Shape Optimization of an Organic Rankine Cycle Radial Turbine Nozzle. *J. Eng. Gas Turbines Power* **2013**, *135*, 042308. [CrossRef]
16. Wheeler, A.P.S.; Ong, J. The Role of Dense Gas Dynamics on Organic Rankine Cycle Turbine Performance. *J. Eng. Gas Turbines Power* **2013**, *135*, 102603. [CrossRef]
17. Anand, N.; Vitale, S.; Pini, M.; Otero, G.J.; Pecnik, R.; Otero-Rodríguez, G.J. Design Methodology for Supersonic Radial Vanes Operating in Nonideal Flow Conditions. *J. Eng. Gas Turbines Power* **2018**, *141*. [CrossRef]
18. White, M.T.; Markides, C.N.; Sayma, A.I. Working-Fluid Replacement in Supersonic Organic Rankine Cycle Turbines. *J. Eng. Gas Turbines Power* **2018**, *140*, 091703. [CrossRef]
19. Rinaldi, E.; Pecnik, R.; Colonna, P. Unsteady Operation of a Highly Supersonic Organic Rankine Cycle Turbine. *J. Turbomach.* **2016**, *138*, 121010. [CrossRef]
20. Rohlik, H.E. *Analytical Determination of Radial Inflow Turbine Design Geometry for Maximum Efficiency*; National Aeronautics and Space Administration: Washington, DC, USA, 1968.
21. Anand, N.; Colonna, P.; Pini, M. Design guidelines for supersonic stators operating with fluids made of complex molecules. *Energy* **2020**, *203*, 117698. [CrossRef]
22. Argrow, B.M.; Emanuel, G. Comparison of Minimum Length Nozzles. *J. Fluids Eng.* **1988**, *110*, 283–288. [CrossRef]
23. Argrow, B.M.; Emanuel, G. Computational Analysis of the Transonic Flow Field of Two-Dimensional Minimum Length Nozzles. *J. Fluids Eng.* **1991**, *113*, 479–488. [CrossRef]
24. Bell, I.H.; Wronski, J.; Quoilin, S.; Lemort, V. Pure and Pseudo-pure Fluid Thermophysical Property Evaluation and the Open-Source Thermophysical Property Library CoolProp. *Ind. Eng. Chem. Res.* **2014**, *53*, 2498–2508. [CrossRef] [PubMed]
25. Cramer, M.S.; Crickenberger, A.B. Prandtl-Meyer function for dense gases. *AIAA J.* **1992**, *30*, 561–564. [CrossRef]
26. Vanco, M.R.; Goldman, L.J. *Computer Program for Design of Two Dimensional Supersonic Nozzle With Sharp Edged Throat*; NASA: Cleveland, OH, USA, 1968. Available online: https://ntrs.nasa.gov/search.jsp?R=19680005278 (accessed on 14 March 2020).
27. Lemmon, E.W.; Huber, M.L.; McLinden, M.O. *NIST Standard Reference Database 23, Reference Fluid Thermodynamic and Transport Properties (REFPROP), Version 9.1*; National Institute of Standards and Technology: Gaithersburg, MD, USA, 2013.
28. Cappiello, A.; Tuccillo, R. Influence of Supersonic Nozzle Design Parameters on the Unsteady Stator-Rotor Interaction in Radial-Inflow Turbines for Organic Rankine Cycles, ASME Paper GT2021-59123. In Proceedings of the Turbo Expo Technical Conference, Virtual Conference, 7–11 June 2021.

International Journal of
Turbomachinery Propulsion and Power

MDPI

Article

Influence of Spanwise and Streamwise Film Hole Spacing on Adiabatic Film Effectiveness for Effusion-Cooled Gas Turbine Blades

Matthew Courtis [1,*], Alexander Murray [1], Ben Coulton [1], Peter Ireland [1] and Ignacio Mayo [2]

[1] Oxford Thermofluids Institute, University of Oxford, Oxford OX2 0ES, UK; alexander.murray@eng.ox.ac.uk (A.M.); ben.coulton@eng.ox.ac.uk (B.C.); peter.ireland@eng.ox.ac.uk (P.I.)
[2] Rolls-Royce PLC, Derby DE24 8BJ, UK; mayo@rolls-royce.com
* Correspondence: matthew.courtis@eng.ox.ac.uk or matthew.courtis.10@gmail.com

Abstract: To meet the challenges of increased thermal loads and performance demands on aero-engine turbine blades, more advanced cooling techniques are required. This study used a modification of the well-known Goldstein equation to predict film effectiveness for an individual film cooling hole and applied the Sellers' superposition method to apply these films across effusion-cooled configurations. In doing so, it tackles a relatively unchallenged problem of film holes in close spanwise proximity. An experimental set-up utilised infrared cameras to assess the film effectiveness of nine geometries of varying spanwise and streamwise spacings. Higher porosity led to increased thermal protection, and the spanwise spacing had the most profound impact, with film effectiveness approaching 0.9. Additionally, greater uniformity in the spanwise direction was observed. The modified Goldstein-Sellers method showed good agreement with experimental results although lateral mixing was underestimated. This method represents a tool that could be easily implemented in the industry for rapid assessment of novel cooling geometries.

Keywords: gas turbine; effusion cooling; heat transfer; turbine cooling; superposition

check for updates

Citation: Courtis, M.; Murray, A.; Coulton, B.; Ireland, P.; Mayo, I. Influence of Spanwise and Streamwise Film Hole Spacing on Adiabatic Film Effectiveness for Effusion-Cooled Gas Turbine Blades. *Int. J. Turbomach. Propuls. Power* **2021**, *6*, 37. https://doi.org/10.3390/ijtpp6030037

Academic Editor: Tony Arts

Received: 15 June 2021
Accepted: 30 August 2021
Published: 31 August 2021

Publisher's Note: MDPI stays neutral with regard to jurisdictional claims in published maps and institutional affiliations.

Copyright: © 2021 by the authors. Licensee MDPI, Basel, Switzerland. This article is an open access article distributed under the terms and conditions of the Creative Commons Attribution (CC BY-NC-ND) license (https://creativecommons.org/licenses/by-nc-nd/4.0/).

1. Introduction

Over the last several decades, the operating temperature of gas turbines has continued to increase by about 10 K per year. As a result of the second law of thermodynamics, an increase in temperature leads to an increase in overall engine efficiency. The consequence is high inlet temperatures seen by the turbine, imposing high thermal stresses, especially on the guide vanes and first several blade rows. To resolve such issues and maintain suitable dependability of engines, there is a need for turbine blade cooling systems. Major milestones, such as internal cooling and film cooling, have enabled inlet temperatures of up to 2000 K. The coolant flow rate should be minimised to limit aerodynamic losses, and consequently, as temperatures continue to move beyond 2000 K more advanced cooling methods are required. Increased engine efficiency will reduce fuel costs and, in turn, has the capability to reduce CO_2 emissions by over 180,000 kg per engine per year [1].

Transpiration cooling takes advantage of porous walls and injects coolant into the flow, creating a protective film between the surface wall and hot gas. Two main processes are involved to produce cooling:

1. Convective cooling—between the cooling fluid and porous wall;
2. Film cooling—a layer of coolant air over the blade reduces the convective heat flux from the hot gas cross flow,

Consequently, the study of turbine cooling performance generally takes two distinct forms: film effectiveness and metal effectiveness. The former represents the performance of only the films and is measured by how closely the adiabatic wall temperature can be kept to to the coolant temperature, as shown in Equation (1). Metal effectiveness combines

both the film cooling and internal convective cooling, providing a representation of the overall cooling performance.

$$\eta_f = \frac{T_\infty - T_{aw}}{T_\infty - T_c} \tag{1}$$

While transpiration cooling has been intensively researched for many years, such as early work produced in 1951 by NASA [2] or more recently by Polezhaev [3], successful application in engines has remained unattainable due to limitations of the porous materials available. Additionally, accurately modelling the aerothermal and mechanical stress fields remains a challenge as coupling is required between the flow, thermal and stress fields. These are made even more complex, given the shear number of film holes present in highly porous cooling schemes.

Despite this, there is a move from traditional film cooling methods to effusion cooling. Krewinkel [4] highlighted that the difference between transpiration and effusion cooling is not always clear, although the former tends to be associated with porous media and the latter with discrete film holes. Nevertheless, effusion cooling represents a path on the way to transpiration cooling that theoretically occurs when the solid and coolant reach thermal equilibrium. A significant number of studies on effusion cooling have been performed in recent years [5–9], which is unsurprising given the major benefits of film superposition. This occurs with reduced film hole spacing as a result of film jet interaction with the consequence of augmented film protection offered by each subsequent downstream film hole.

Superposition was first proposed by Sellers [10], who found that the summation of films from a single hole could be used to replicate multiple rows of films. This takes the form of Equation (2).

$$\eta_f(x,y) = 1 - \prod_{i=1}^{n}\Big(1 - \eta_{f,i}(x,y)\Big) \tag{2}$$

Experiments by Muska et al. [11] and more recently Murray et al. [12] reaffirm the superposition method and its usefulness in predicting multi-row film cooling. The latter used a modified Goldstein Equation [13] (described later, but in the form of Equation (3)) to predict the film distribution of an individual hole and, when combined with Sellers' superposition, found the additive effect of multiple film hole rows. Jiang et al. [14] found that even one additional staggered row (offset by half the primary spacing in both streamwise and spanwise directions, x and y) produced much higher film effectiveness. Even at high injection velocities, where the coolant flow detached from the metal surface, the vortex pairs of the first cooling row pushed the second row films toward the surface resulting in quick reattachment and enhanced film protection.

Murray et al. [15] used the Sellers method as part of a decoupled solver (separately solving the internal and external thermal fields) and showed good agreement between experimental and numerical results, as well as an exhibit for efficient numerical studies for complex double-walled effusion systems. Despite these successes, no account was made for the proximity of adjacent holes (spanwise consideration) and, as such, were deemed to be independent. This causes an issue for more porous geometries, and most studies have focused on film cooling with relatively large spanwise distances. This study builds upon this work to incorporate the method to more porous geometries, which are required to move from effusion towards transpiration-like cooling.

The present study investigates the influence of streamwise and spanwise spacing on film effectiveness using a modified Goldstein–Sellers approach, which is explained in the next section. An infrared methodology measures the cooling performance for nine geometries at six coolant flow rates. Numerical results for varying film spacing are presented, and a more advanced cooling layout is explored. Experimental results are presented before a comparison between the two result sets are evaluated. The work

represents a preliminary step in understanding the importance of film hole proximity and extensions to the Goldstein–Sellers method.

2. Materials and Methods

2.1. Research Object

Film cooling performance was assessed using flat plate geometries, all of which had a staggered configuration of film holes inclined at 30° to the plate surface, as illustrated in Figure 1. The hole diameter in all cases was 4.0 mm, with additional dimensions also stated. Spacing between film holes was varied in both the streamwise and spanwise direction for S_x/D = 3.0, 4.5 and 6.0, and similarly for S_y/D, to produce a test matrix of nine geometries. The area of coverage of film holes was based on a 6×6 array for $S_y/D = S_x/D = 6.0$, and the other spacings had more rows and columns in order to meet the same coverage area.

Geometric Properties	
D	4.0 mm
H	10 mm
S_x/D	3.0 , 4.5 , 6.0
S_y/D	3.0 , 4.5 , 6.0
Rows	11 , 8 , 6
Columns	11 , 8 , 6
L/D	5.0
l_1	248 mm
l_2	178 mm
l_3	20 mm
l_4	29 mm
$l_{i,x}$	140 mm
$l_{i,y}$	100 mm
γ	30°

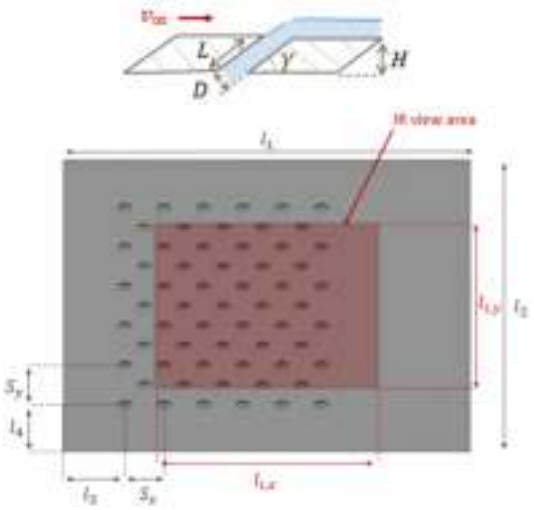

Figure 1. A schematic showing the dimensions of the flat plate geometry, where the red section highlights the visible portion for the IR camera. The illustration here shows the $S_x/D = S_y/D = 6.0$ geometry.

A more advanced film cooling system was also numerically investigated. A baseline design (TD2) was used and represents a transpiration-like cooling system with a porosity of 19%. This design was originally modelled on a double-wall effusion system developed by Murray et al. [16] at the Oxford Thermofluids Institute (OTI) (URL retrieved 1 September 2021) but with an increase in the number of film holes. The film hole diameter was also reduced to be 1/5 the size of conventional holes. The hole spacing was $S_x/D = S_y/D = 3.5$ with a hole diameter of 2 mm and a 'hole blockage' of 25%. The latter is defined as the ratio of film holes removed due to proximity to internal design features (pedestals and impingement jets). For direct comparison, the spanwise spacing was varied and the streamwise spacing altered to maintain porosity, as tabulated in Table 1. The film's effectiveness was found using the modified Goldstein–Sellers approach for each configuration at four blowing ratios ($M = 0.20, 0.25, 0.30, 0.35$) across the extent of the domain.

Table 1. Properties for the TD2 film spacing variation study.

TD2 Study Geometric Properties					
D			2.0 mm		
S_x/D	4.9	4.1	3.5	3.1	2.7
S_y/D	2.5	3.0	3.5	4.0	4.5

2.2. Numerical Method

An in-house MATLAB code was used to predict the film effectiveness of any given film using a modified Goldstein correlation. This method attempts to model the decay of films in both the streamwise and spanwise directions and is defined in Equation (3). M is the blowing ratio of the film, specified as the product of the ratios of density and velocity between the coolant and free-stream fluid, $M = (\rho_c v_c)/(\rho_\infty v_\infty)$. This parameter influences the following constants: turbulent thermal diffusivity α_t and x_{decay}, which captures changes in the streamwise direction. The spanwise distance constant (c_1) and the spanwise shaping constant (c_2), which influence the spanwise film decay, are variables dependent on both the blowing ratio M and distance downstream of the film hole x. The values for these are based on experimental and correlation data, which can be found in [12,17].

$$\eta_f(x,y) = M\frac{V_\infty D}{8\alpha_t\left(x/D + x_{decay}\right)}\exp\left\{-\left(\frac{y}{c_1}\right)^{c_2}\right\} \tag{3}$$

Films were placed individually on a global grid and subject to the Sellers' superposition, as illustrated in Figure 2. This method could take into account variable blowing ratios and any form of spatial configuration. It is worth noting that the empirical data used had a hole aspect ratio (L/D) of 2.0, compared to $L/D = 5.0$ for geometries investigated in this study. Lutum and Johnson [18] demonstrated that a lower aspect ratio reduced film effectiveness, and consequently, the film effectiveness calculated here may represent a conservative estimate of the actual value.

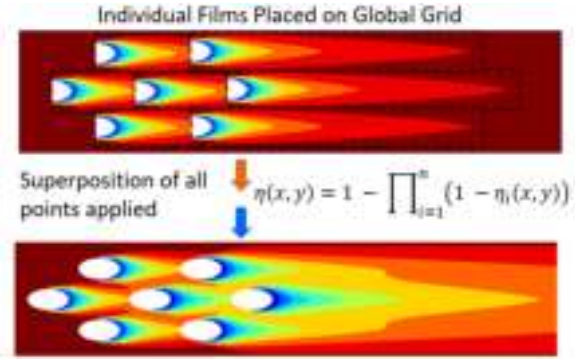

Figure 2. Visualisation of Sellers' superposition method.

2.3. Experimental Method

2.3.1. Experimental Facility

The **D**ouble-Walled **E**ffusion **C**ooling **A**erothermal **F**acility (DECAF) at the Oxford Thermofluids Institute was used for the experimental study—see Figure 3. The facility provides conditions for scaled tests of flat plate cooling geometries. Murray et al. [19] provides a detailed description of the facility and measurement procedure, although a brief summary is also provided here.

The facility provides Reynolds number similarity to engine conditions and has been specified for high-temperature capabilities. ROHACELL was used for test geometries to investigate film effectiveness, assuming an adiabatic surface. This material was chosen due to its low thermal conductivity ($\lambda \sim 0.030$ W/m-K), and a high grade with a closed cell structure was selected (71 HERO) to reduce the impact that roughness would have on film holes with small diameters. The film effectiveness is calculated by measuring the surface temperature through an infrared camera, and the back-side surface temperature is also monitored. A range of mass flows between 0.01 kg/s and 0.035 kg/s were investigated for each geometry. This was achieved by varying the coolant mass flow into the plenum while keeping the mainstream velocity constant. The typical experimental mainstream Reynolds number based on the film hole diameter, mainstream temperature, coolant-mainstream temperature ratio and density ratio are tabulated in Table 2.

Table 2. Approximate experimental conditions.

Re_∞	T_∞	T_c/T_∞	ρ_c/ρ_∞
1.12×10^4	373 K	0.8	1.2

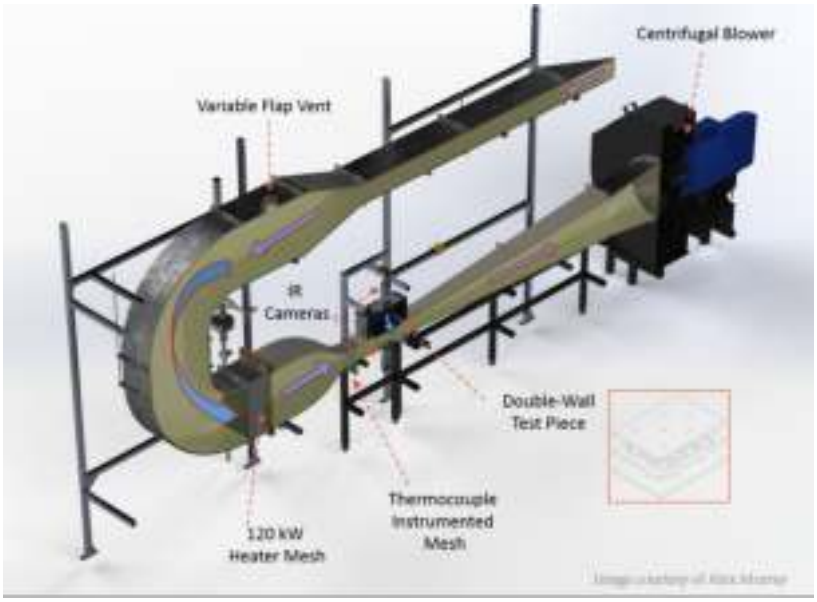

Figure 3. Annotated schematic of the OTI experimental facility.

2.3.2. Infrared Methodology

Temperatures of the external surface were made through the use of two *FLIR A655sc* infrared cameras, with optical access provided by Zinc Selenide windows. Thin wire thermocouples were attached to both the hot-gas and coolant plenum external surfaces of the test geometry. These are within the IR camera field of view, permitting an in situ calibration. External surfaces were painted matt black to minimise IR reflections from the surroundings. The calibration method is described in detail by Murray et al. [19], in which both the blackbody and greybody calibration were used to calculate temperatures from the raw data output of the cameras. The former finds the ideal blackbody parameters, and the latter finds parameters due to non-ideal surface IR emission. The frame rate of the camera was set at 25 Hz to allow an assessment of flow unsteadiness, and data are averaged over 10 s (250 frames) to provide a mean steady-state temperature. Using these temperatures, the film effectiveness was calculated using Equation (1).

3. Results and Discussion

3.1. Numerical Results

To determine the affect of changing streamwise (S_x) and spanwise (S_y) spacing on the film effectiveness, the modified Goldstein method with Sellers' superposition was implemented across a standardised geometry. The first study focused on maintaining a constant blowing ratio with three rows and three columns for a staggered array, which were varied as $3.0 \leq S_y/D \leq 5.0$ and $3.0 \leq S_x/D \leq 8.0$. A visualisation of this, along with the comparison area, can be seen in Figure 4. Another set of calculations were based on the assumption of constant mass flow between geometries. To achieve this, each geometry was made to cover the same surface area, and the coolant mass flow kept constant, as illustrated in Figure 5.

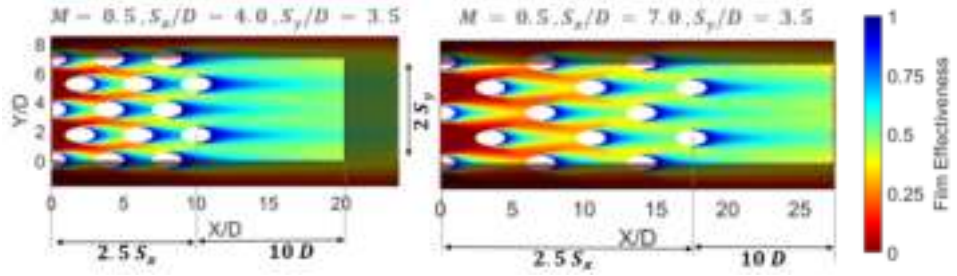

Figure 4. Comparison area for the mean film effectiveness with varying S_x/D and S_y/D, using a constant blowing ratio. Enhanced superposition occurs with reduced streamwise spacing.

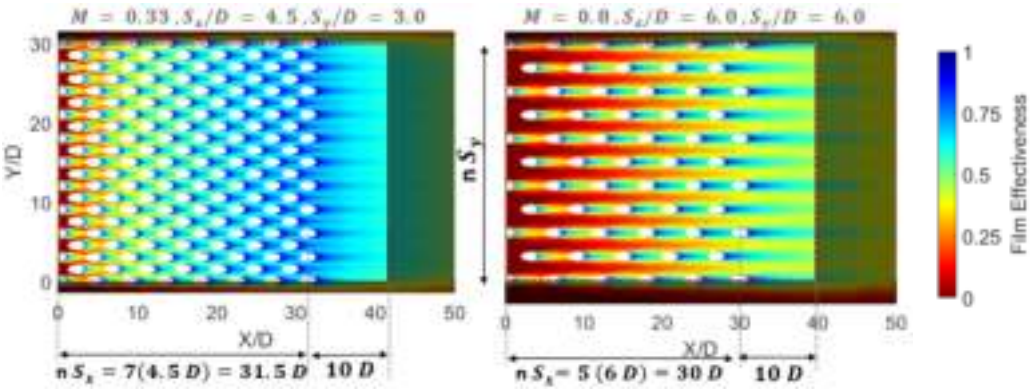

Figure 5. Comparison area for the mean film effectiveness with varying S_x/D and S_y/D, with a constant coolant mass of $\dot{m}_c = 2.56$ kg/s/m^2. Hot streaks are minimised as the spanwise spacing reduces.

For a fixed mass flow rate, increasing the porosity reduces the blowing ratio. While this reduces the performance of any individual film, the proximity of neighbouring holes may compensate for this detriment. Figure 5 illustrates that as spanwise distance increases, the films become more isolated, and distinct hot-streaks can be observed between film columns. As S_y decreases, the extent of the hot streaks is reduced given the adjacency of a staggered film, and less of the exterior wall is subject to the mainstream temperature, a benefit even without accounting for film interaction. Additionally, the lower spanwise distance resulted in the merging of the adjacent films. Film effectiveness is enhanced by reducing S_x, as would be predicted by Sellers superposition, but since films propagate with the mainstream flow, the proximity in the streamwise direction is less influential than that for the spanwise direction.

The averaged film effectiveness for the first study is compared to porosity in Figure 6, where the symbols correspond to a constant S_y. Here, porosity is defined as the geometric porosity, the surface area of the film holes (A_h) compared to the area these holes cover (A_s), and is defined in Equation (4).

$$\phi = \frac{A_h}{A_s} = \frac{\pi}{2(S_x/D)(S_y/D)\sin(\gamma)} \tag{4}$$

As spanwise spacing was reduced, the area-averaged film effectiveness increased at a greater rate than the influence of streamwise spacing. This is made clear on the figure by two arrows indicating the general trend of film effectiveness for a reduction in S_y and S_x, respectively. Consequently, for an increase in porosity and to reduce the added mass flow required, having films with a lower S_y was advantageous.

To investigate constant mass flow across all geometries, the area-averaged film effectiveness is shown in Figure 7, alongside isobars of constant porosity. As one moves along a constant porosity curve, the film effectiveness benefits from decreasing S_y and increasing

S_x. This was true for all three mass flow rates, confirming that increasing the porosity will enhance the overall film effectiveness.

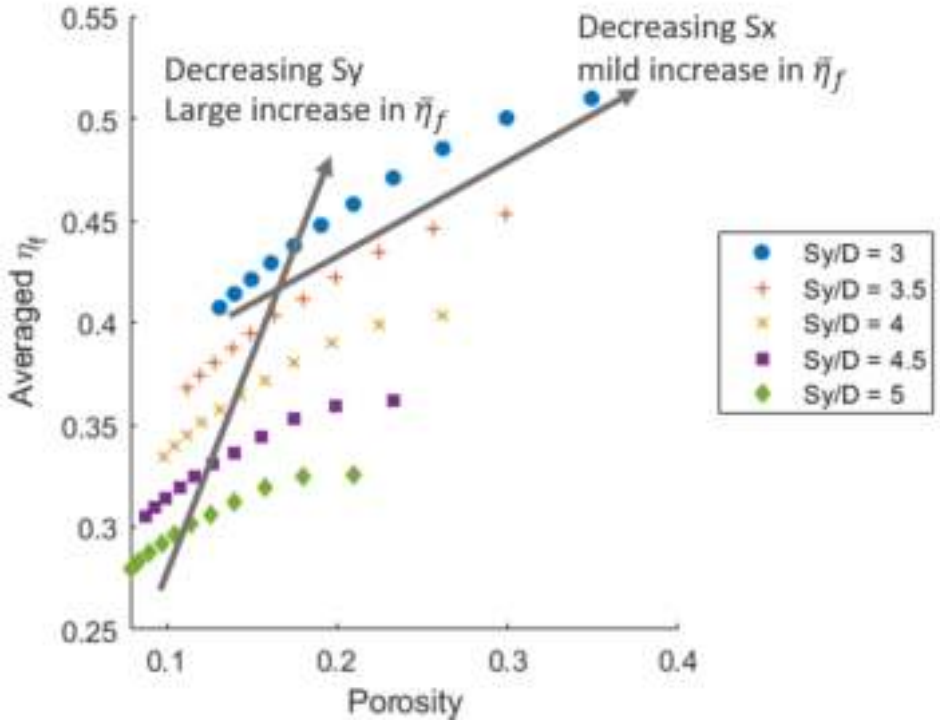

Figure 6. The effect of film spacing (S_x,S_y) on area-averaged film effectiveness, for $M = 0.5$

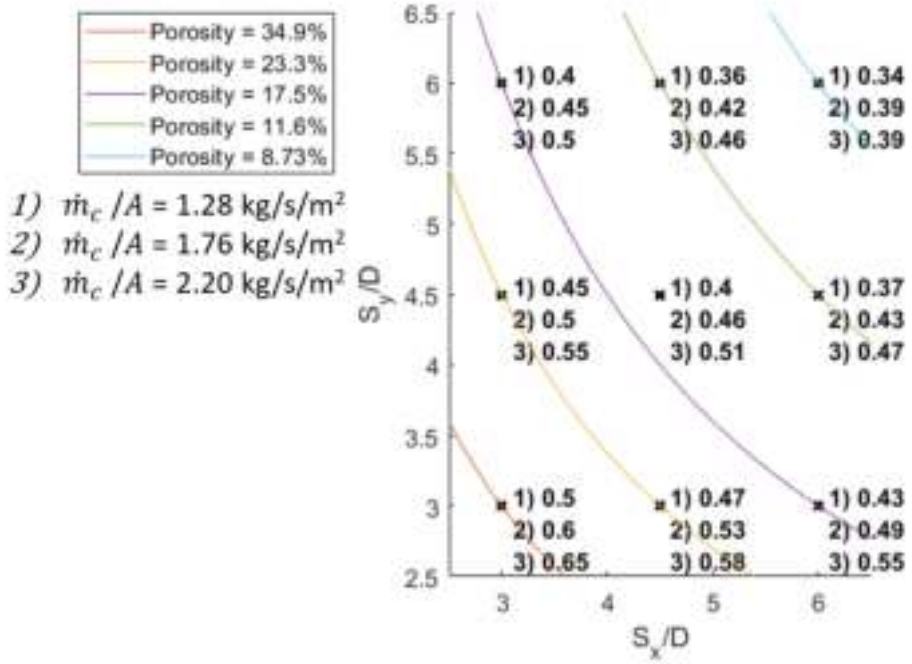

Figure 7. The effect of film spacing (S_x,S_y) on area-averaged film effectiveness, for three coolant mass flows. Isobars of constant porosity are displayed.

3.2. Td2 Results

High film effectiveness was demonstrated by TD2, as well as the design variants. Figure 8 plots the area-averaged film effectiveness of each variant characterised by the

ratio of streamwise to spanwise spacing (S_x/S_y) for four blowing ratios. The same trend of increased film effectiveness with a reduction in S_y is observed. Increasing the blowing ratio increased the film effectiveness throughout, although with diminishing returns for each blowing ratio increment. Film effectiveness contours for two TD2 variants and the base geometry are shown in Figure 9 at $M = 0.3$. It can be seen that the leftmost plot (smallest S_y) has increased spanwise uniformity and the reduction of hot spots observed at the location where film holes were removed. The increased lateral spread compensates for a missing film hole and maintains the uniformity of film coverage. This is consistent with results by Yang et al. [20], which demonstrated that while the blockage ratio was an important parameter affecting film effectiveness for a porous metal plate, ratios of up to 30% had only a small influence.

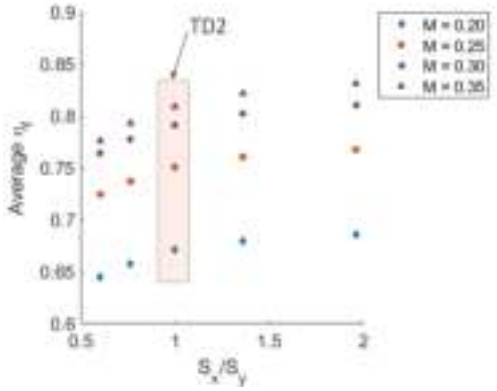

Figure 8. The area-averaged film effectiveness is compared to the ratio of spanwise and streamwise spacing for TD2-base geometry for four blowing ratios. The original design with $S_x = S_y = 3.5D$ is highlighted for reference.

For streamwise columns without hole removal (the second column from the bottom and for figures as we move left to right at Y/D = 2.5, Y/D = 3.5 and Y/D = 4.5), the increased streamwise spacing reduced the superposition effect, but given these are well protected areas and reach saturation after several rows, one would expect this not to be a concern for the overall blade design. These results suggest that further double-walled effusion designs should consider implementing low spanwise spacing if feasible.

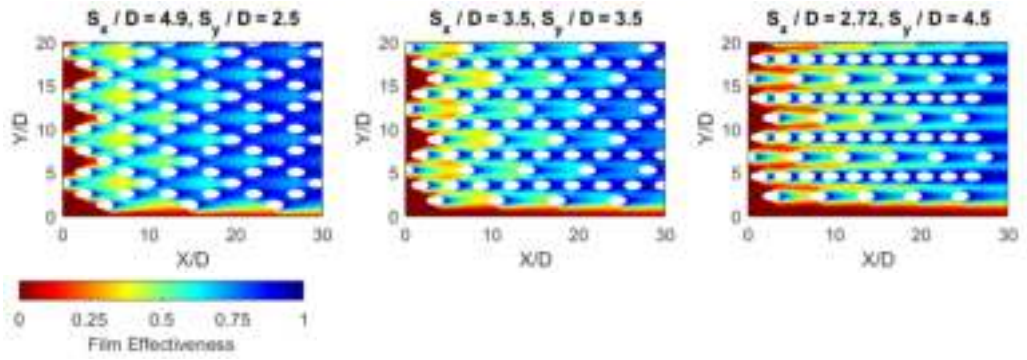

Figure 9. Film effectiveness contours for TD2 and two film spacing variations, for $M = 0.30$. TD2 ($S_x = S_y = 3.5$) is the central plot.

3.3. Experimental Results

To account for differences in tunnel velocity and fluid properties between experimental runs, a non-dimensional mass flow was used for comparison, defined in Equation (5), where $\bar{h}$ is the mean heat transfer coefficient (W/m^2/K) and A is the surface area of the flat plate.

$$m^* = \frac{\dot{m}_c c_p}{\bar{h} A} \tag{5}$$

The averaged film-effectiveness for the visible camera area was calculated for each condition and is displayed in Figure 10. At m^* near 1, there are three distinct groupings of film effectiveness, each with constant S_y. Between the three groups, as S_y decreases, the film effectiveness increases. For larger values of m^*, these lines diverge, and the porosity (i.e., S_x) determines the film effectiveness range. For clarity, the lowest spanwise spacing results ($S_y/D = 3.0$) are highlighted and exhibited the best performance, across the entire range of m^*. This indicates that S_y is more crucial to film protection than S_x. Furthermore, the line plotted with triangles ($S_x/D = 4.5$, $S_y/D = 6.0$) and stars ($S_x/D = 6.0$, $S_y/D = 4.5$) can be seen when comparing two geometries with the same porosity. Across the entire range of m^*, the latter geometry, with a lower S_y, has a higher average film-effectiveness.

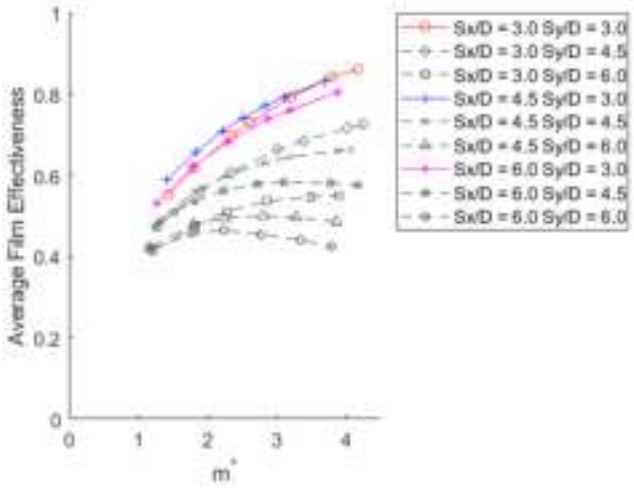

Figure 10. Experimental overall film effectiveness against non-dimensional mass flow (m^*). Geometries with $S_y/D = 3.0$ are highlighted and have the highest averaged film protection, illustrating the benefits associated with low spanwise film spacing.

The general characteristic of these curves is an increase in film protection with coolant flow, which plateaus as the coolant saturates, and for $S_y = 3.0$ geometries, they approach a film effectiveness of 0.9. For lower porosity cases, not only is a plateau reached, but the film effectiveness reduces. This is a consequence of high blowing ratios, and the occurrence of jet lift-off. An unexpected observation was a higher average film effectiveness for $S_x/D = 4.5, S_y/D = 3.0$ compared to the most porous geometry ($S_x/D = S_y/D = 3.0$) for all but the highest mass flow, discussed in more detail below.

Contours of film effectiveness for two mass flows, approximately $m^* = 1.8$ and $m^* = 3.2$, are illustrated in Figures 11 and 12, respectively. Enhanced film protection is evident for the most porous geometries, as well as the benefit of low spanwise spacing. The most striking feature is that film hole proximity to adjacent ('staggered') rows enhances the superposition of films. This is still present at $S_y/D = 4.5$, albeit to a lower extent. However, for $S_y/D = 6.0$, it is almost absent.

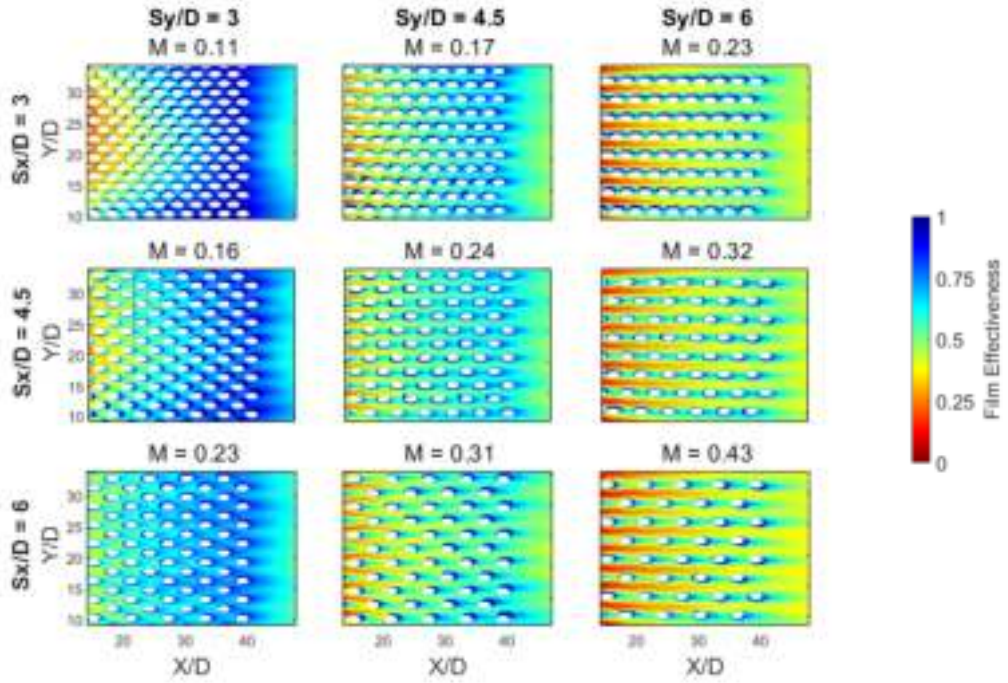

Figure 11. Experimental film effectiveness contours for $m^* \approx 1.8$. The blowing ratio (M) of each geometry is displayed above each contour plot. In general, increased porosity results in a more uniform film coverage.

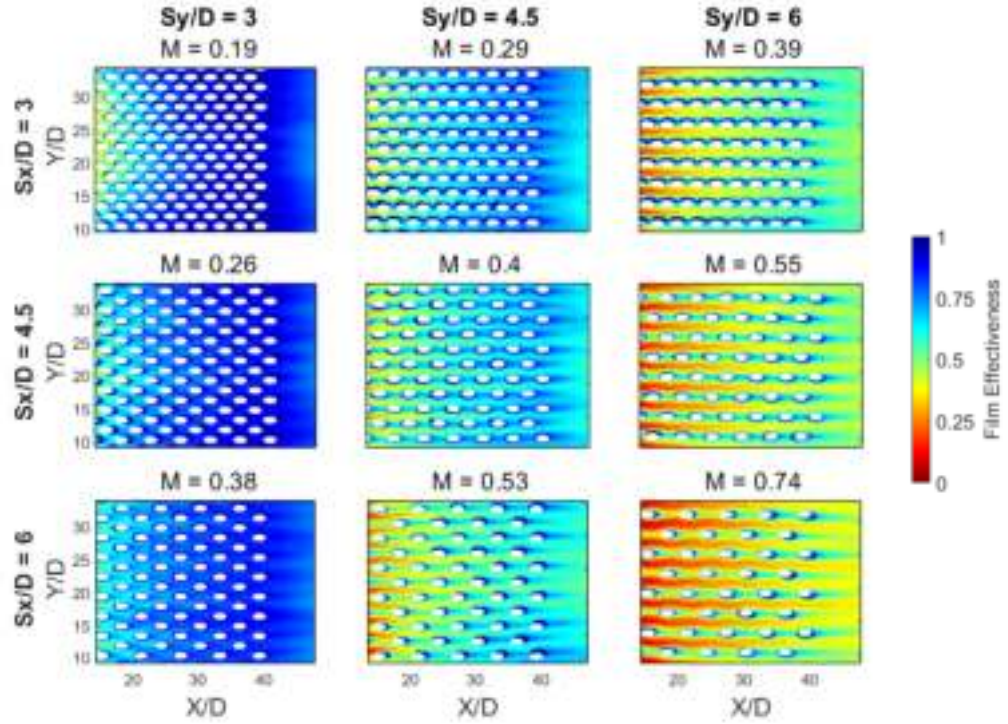

Figure 12. Experimental film effectiveness contours for $m^* \approx 3.2$. The blowing ratio (M) of each geometry is displayed above each contour plot. High porosity geometries form saturated films, leading to uniform and almost complete protection. For lower hole counts, higher blowing ratio leads to jet liftoff, reducing film effectiveness.

At the two highest porosities with $S_y/D = 3.0$ (S_x/D of 3.0 and 4.5), there is a variation in film effectiveness across the spanwise direction. A similar feature was observed

by Murray et al. [12], where a flat plate with hole spacings of $S_x/D = S_y/D = 3.0$ was investigated using pressure-sensitive paint for a range of blowing ratios. It was suggested to be a result of variations in the blowing ratio between film holes across the span, and a product of the side-wall boundary layer reducing the mainstream flow velocity in the vicinity of the side film holes. In this study, given the distance between the side walls and the test piece, another explanation for the variation in blowing ratio is provided here. At large spanwise spacings, the mainstream flow can migrate around individual film holes, evidenced by hot streaks. However, as S_y decreases, the mainstream flow must also divert around the nearby staggered holes. Consequently, the increased upwards curvature of the mainstream flow imposes an increased static pressure on the film hole outlet. Given the finite lateral boundary of the cooling array, film holes at the edge do not pose as large of a obstacle for the mainstream flow, as it can curve both upwards and laterally; thus, the static pressure is lower at the edge of the cooling array compared to the middle. This explains the higher averaged film effectiveness for $S_x/D = 4.5, S_y/D = 3.0$ compared to $S_x/D = S_y/D = 3.0$, as the coolant deviates to the periphery holes rather than those that are central. Additionally, the upstream central holes for the latter geometry may struggle due to the lower blowing ratio, which may lead to hot-gas ingestion at the leading central film holes. Despite this feature, geometries with $Sy = 3.0$ still exhibit a high film effectiveness throughout the visible domain, even along the centreline..

The streamwise-averaged film effectiveness is introduced here and shown in Figures 13 and 14, with a constant S_y for each plot. This metric is an indication of how uniform the protection is perpendicular to the mainstream flow. For film holes spaced with $S_y/D = 6.0$, the difference between the peak and trough streamwise-average film effectiveness is approximately 0.4, compared to 0.2 for $S_y/D = 4.5$ and 0.15 for $S_y/D = 3.0$. This highlights that a reduction in S_y increases the mean film effectiveness, as well as reducing the variance. Hence one can conclude that if a uniform protection is desired, the spanwise film spacing is crucial to this aim. On the contrary streamwise spacing has only a small influence on this but acts to increase the mean film effectiveness.

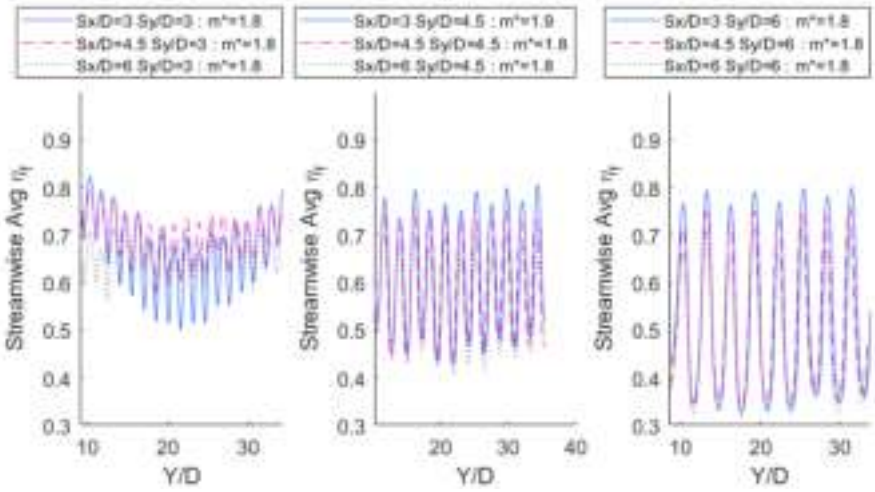

Figure 13. Streamwise-average film effectiveness for $m^* \approx 1.8$. In each individual plot, geometries with constant S_y are shown.

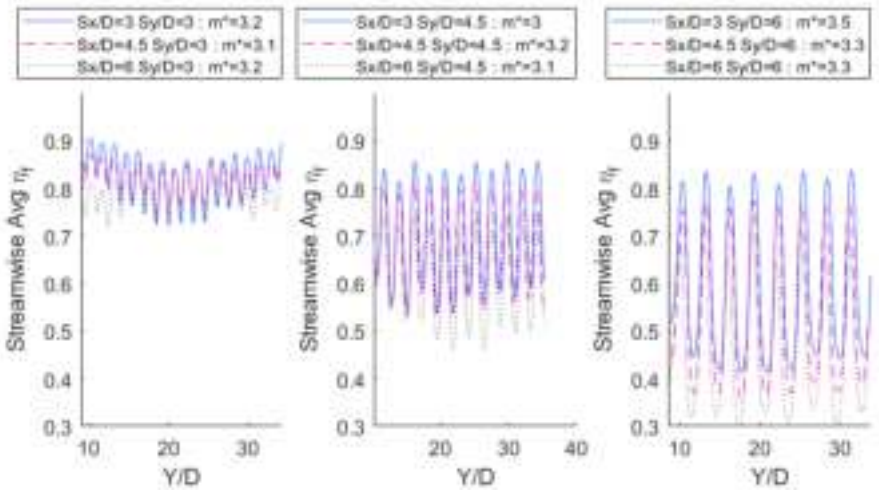

Figure 14. Streamwise-average film effectiveness for $m^* \approx 3.2$. In each individual plot, geometries with constant S_y are shown.

3.4. Numerical and Experimental Comparison

Spanwise and streamwise averaged film effectiveness were calculated using the modified Goldstein–Sellers across the same area as the infrared camera: $14D < x < 48D$ and $9D < y < 34D$. Results for $m^* = 1.8$ are shown in Figures 15 and 16 and results for $m^* = 3.8$ by Figures 17 and 18, with the solid and dashed line representing experimental and numerical results, respectively.

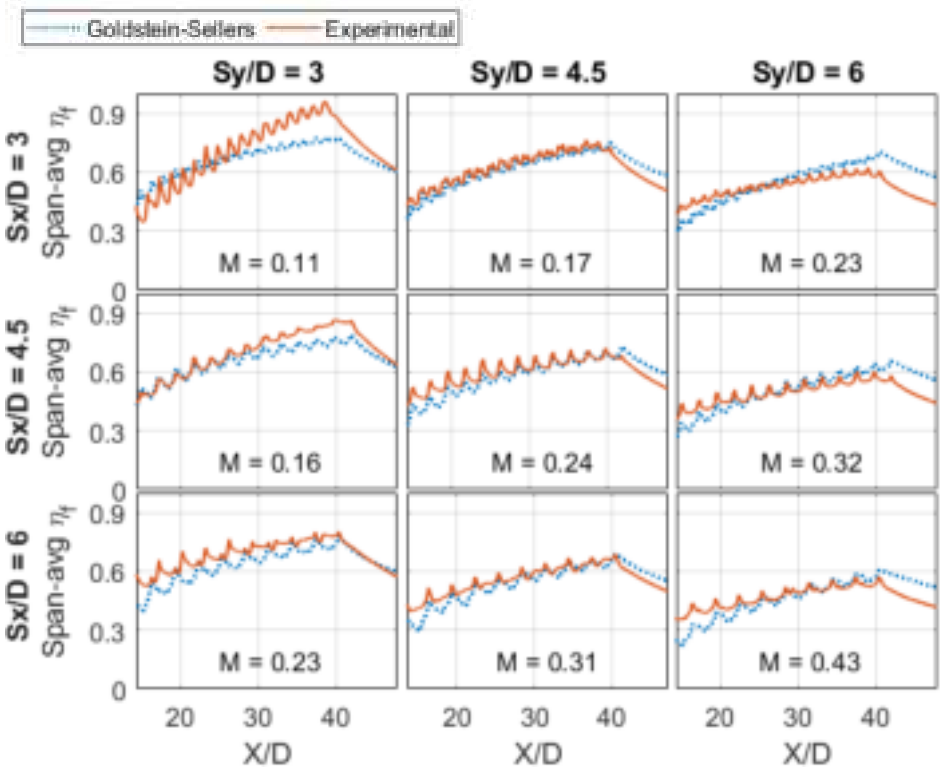

Figure 15. A comparison of numerical and experimental spanwise-averaged film effectiveness for $m^* = 1.8$.

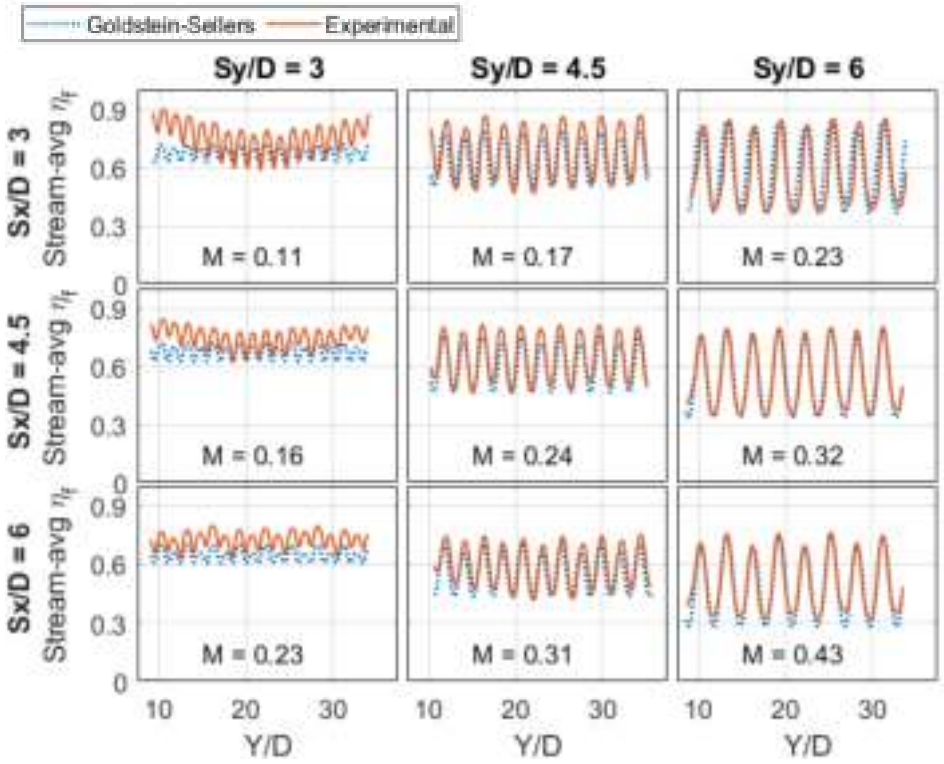

Figure 16. A comparison of numerical and experimental streamwise-averaged film effectiveness for $m^* = 1.8$.

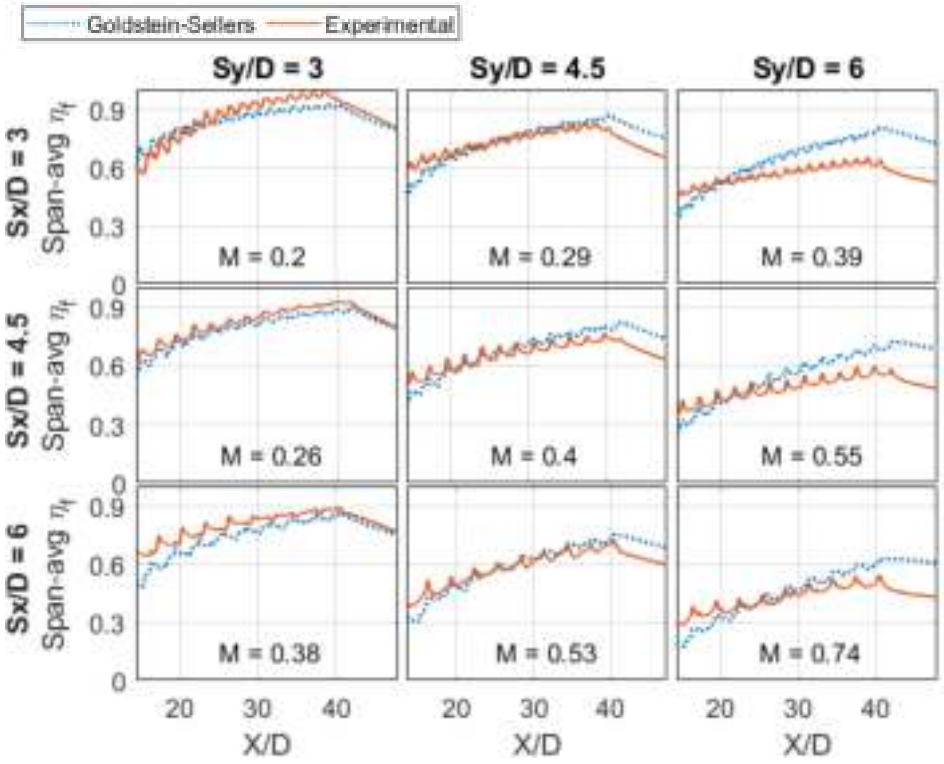

Figure 17. A comparison of numerical and experimental spanwise-averaged film effectiveness for $m^* = 3.8$.

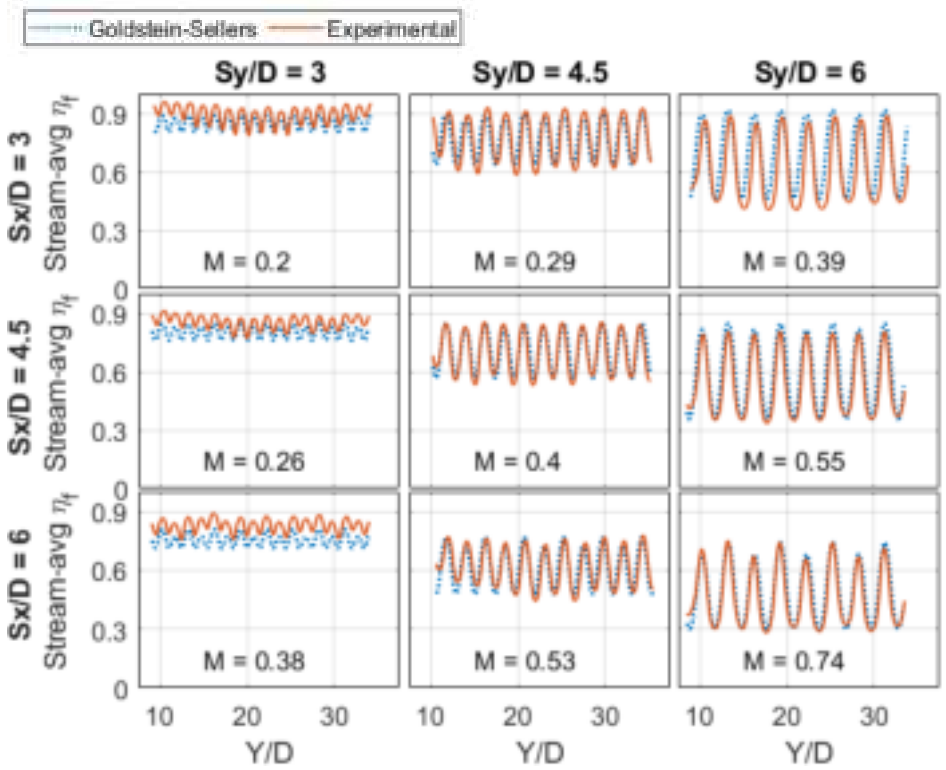

Figure 18. A comparison of numerical and experimental streamwise-averaged film effectiveness for $m^* = 3.8$.

The modified Goldstein–Sellers captures the general trend of the spanwise-average film effectiveness across all geometries. For the largest spanwise spacing ($S_y = 6D$), the spanwise-average η_f is under-predicted for the leading film holes up to $X/D = 20$ but over-predicted beyond $x/D = 40$, indicating that while the initial film protection was underestimated, the effect of superposition was overly optimistic. The same trend can be observed for $S_y = 4.5D$ but to a lesser extent. For the lowest spanwise spacing ($S_y = 3D$), spanwise-averaged η_f was well captured despite a small under-prediction throughout the domain, with a deviation for $S_x = 3D$, $S_y = 3D$ due to the suspected variable mass flow distribution, as previously discussed.

The streamwise-average film effectiveness indicates that films are well-matched for $S_y = 6D$ and $S_y = 4.5D$, with numerical results having a higher film effectiveness directly downstream of the film holes and a lower film effectiveness in the gaps between film hole columns. This would suggest a lack of lateral spread film coverage was predicted numerically. For $S_y = 3D$, the numerical model under-predicts throughout the plate; however, the level of variation between film rows was similar.

Spanwise and streamwise averaged film effectiveness indicate that the modified Goldstein–Sellers method can predict the superposition of staggered film arrays for both densely packed and moderately spaced film holes. This is further examined by the film effectiveness contours for both experiments and the numerical method in Figure 19a,b. Three geometries with evenly spaced film holes ($S_x = S_y$) are shown at two mass flows, with blowing ratios indicated above each plot. For the lowest film spacing ($S_x = S_y = 3D$), the two mass flows paint a contrasting picture. At $m^* = 1.8$, the experiments had lower film effectiveness at upstream film rows, and this was more pronounced at the centre-line of the array. Conversely, film effectiveness builds up more as you move downstream compared to Goldstein–Sellers. This was largely due to the variable mass flow distribution observed for highly porous geometries. As mass flow increases to $m^* = 3.8$, this phenomenon was less pronounced and may be due to earlier saturation of film effectiveness, and thus, differences are constrained to upstream rows outside the IR camera view. The authors suggest that

investigation of the upstream rows for densely packed film arrays should be made in future work.

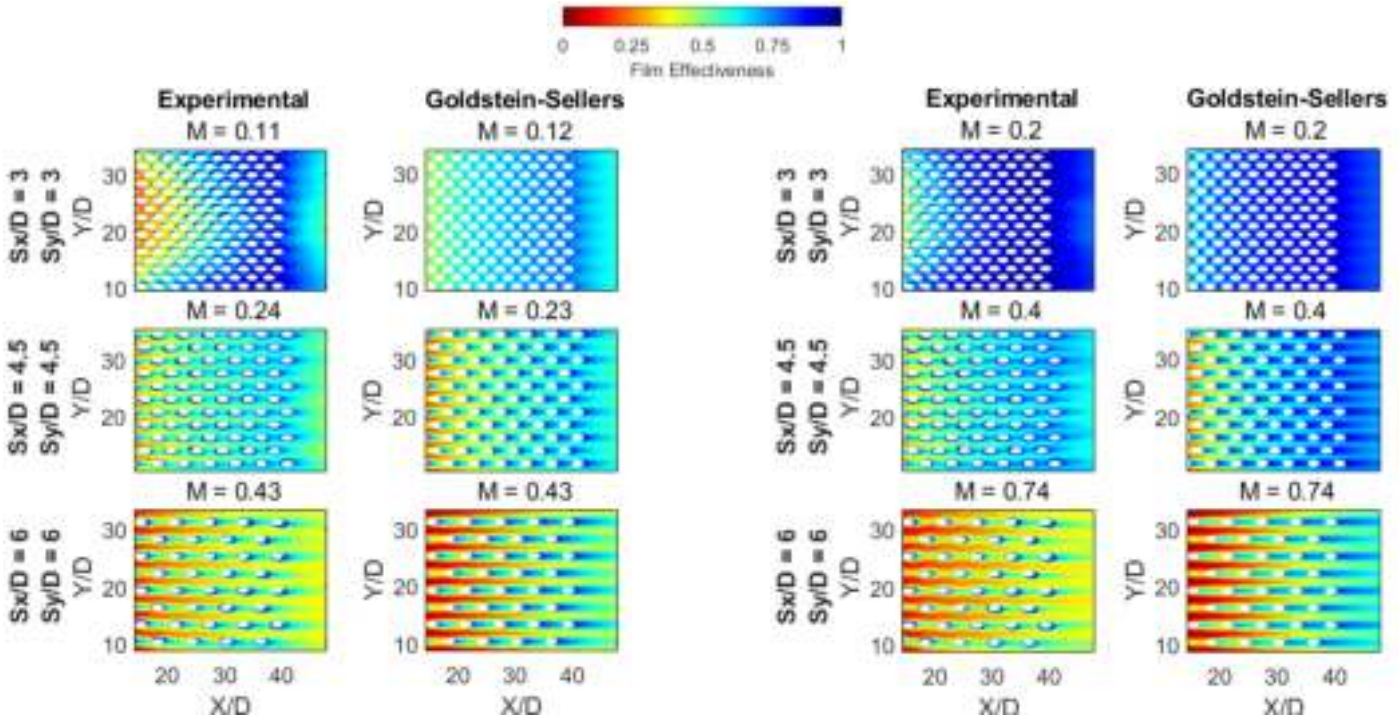

(**a**) $m^* \approx 1.8$ (**b**) $m^* \approx 3.8$

Figure 19. A comparison of film effectiveness contours between experiments and Goldstein–Sellers. Film hole spacing is stated for each row, and the corresponding blowing ratios are displayed above each plot.

For the two other geometries shown in Figure 19 ($S_x = S_y = 4.5D$ and $S_x = S_y = 6D$), film effectiveness was over-predicted for film hole centre-lines; however, this appears to be at the expense of hot streaks between film holes. This is an indication of increased mixing in the experimental study that is not accounted for by the Sellers approach. Some of the discrepancy may be due to manufacturing differences between the experimental pieces in this study compared to that used by [12,17] in the formulation of the modified Goldstein equation. In this study, the flat plates were made from ROHACELL, and consequently, the hole boundaries had significant deviations that may enhance the lateral spread of films and increase the turbulence of the film jets.

4. Conclusions

The effect of variable spanwise and streamwise film hole spacing was investigated for staggered hole arrays. While a decrease in both spacings enhances the film effectiveness, the spanwise spacing is more effective, and jet lift off at higher mass flows can be avoided. Additionally, the range of streamwise-averaged film effectiveness is reduced by half when moving from S_y = 6.0 to S_y = 4.5, indicating a more uniform coverage. It is thus worth considering moving away from equal spanwise and streamwise spacing for effusion designs, despite this being common practice in the industry. This could be important in designs looking to increase film hole porosity, as manufacturing realities may introduce the need for missed rows for structural purposes. Further work needs to address variable mass flow distribution between film holes for geometries with porosity in excess of 20%.

Highly porous film-hole coverage represents an efficient cooling method with film effectiveness approaching 0.9. However, metal effectiveness and mechanical stresses should be considered for a better understanding of the overall consequences on more engine-like designs. This is an area of research investigated by Elmukashfi et al. [21], and something that the authors of this study look to expand upon.

A modified Goldstein–Sellers film superposition method was compared to experimental results for a range of staggered film hole spacings. This method was shown to predict the behaviour of film superposition relatively well but did not completely account for lateral mixing. Consequently, this method could be a useful tool for preliminary evaluations and use in de-coupled conjugate studies.

Author Contributions: M.C.: Research and conceptualisation, methodology, experimental and numerical work and writing manuscript; A.M.: methodolody, review and editing; B.C.: methodology; P.I.: Supervisor; I.M.: Supervisor. All authors have read and agreed to the published version of the manuscript.

Funding: This research was funded by the EPSRC Transpiration Cooling grant (EP/P000878/1).

Acknowledgments: The authors wish to express their thanks for the on-going support provided by Rolls-Royce plc, and the EPSRC Transpiration Cooling grant (EP/P000878/1). The authors would also like to thank the technicians and staff at the Oxford Thermofluids Institute.

Conflicts of Interest: The funders had no role in the design of the study; in the collection, analyses, or interpretation of data; or in the writing of the manuscript.

Nomenclature

The following abbreviations are used in this manuscript:

Acronyms		
IR	Infrared	
OTI	Oxford Thermofluids Institute	
Non-Dimensional Numbers		
η_f	Film Effectiveness	
ϕ	Porosity	
c_1	Spanwise distance constant	
c_2	Spanwise shaping constant	
M	Blowing ratio	
m^*	Non-dimensional mass flow	
x_{decay}	Streamwise distance film-decay	
Properties		
α_t	Turbulent thermal diffusivity	m^2/s
$\dot{m}$	Mass flow rate	kg/s
γ	Hole inclination angle	deg
λ	Thermal conductivity	W/m·K
ρ	Density	kg/m^3
A_f	Hole surface area	m^2
A_s	Surface coverage of film holes	m^2
c_p	Specific heat capacity	J/kg·K
D	Diameter	m
H	Plate thickness	m
h	Heat transfer coefficient	$W/m^2·K$
k	Thermal conductivity	W/m·K
S_x	Streamwise spacing	m
S_y	Spanwise Spacing	m
T	Temperature	K
V	Velocity	m/s
Subscripts		
∞	Free stream	
aw	Adiabtic wall	
c	coolant	
f	film	

References

1. Research Councils UK. *Transpiration Cooling Systems for Jet Engine Turbines and Hypersonic Flight*; Research Councils UK: Swindon, UK, 2018.
2. Eckert, R.G.; Esgar, J.B. *Survey of Advantages and Problems Associated with Transpiration Cooling and Film Cooling of Gas-Turbine Blades*; NACA-RM-E50K15; Nationa Advisory Committee for Aeronautics Research Memorandum: Washington, DC, USA, 1951.
3. Polezhaev, J. Transpiration cooling for blades of high temperatures gas turbine. *Energy Convers. Manag.* **1997**, *38*, 1123–1133. [CrossRef]
4. Krewinkel, R. A review of gas turbine effusion cooling studies. *Int. J. Heat Mass Transf.* **2013**, *66*, 706–722. [CrossRef]
5. Battisti, L.; Fedrizzi, R.; Cerri, G. Novel Technology for Gas Turbine Blade Effusion Cooling. In Proceedings of the ASME Turbo Expo 2006: Power for Land, Sea, and Air, Barcelona, Spain, 8–11 May 2006; Volume 3, pp. 491–501.
6. Rogers, N.; Ren, Z.; Buzzard, W.; Sweeney, B.; Tinker, N.; Ligrani, P.; Hollingsworth, K.; Liberatore, F.; Patel, R.; Ho, S.; et al. Effects of Double Wall Cooling Configuration and Conditions on Performance of Full-Coverage Effusion Cooling. *J. Turbomach.* **2017**, *139*, 051009. [CrossRef]
7. Jiang, Y.; Murray, A.; Ireland, P.; Di Mare, L. *Coolant Jets Interaction in Effusion Cooling System: Experimental and Numerical Study*; American Society of Mechanical Engineers: New York, NY, USA, 2019.
8. Ngetich, G.C.; Ireland, P.T.; Murray, A.V.; Romero, E. A 3D Conjugate Approach For Anaysing A Double-Walled Effusion-Cooled Turbine Blade. In Proceedings of the ASME Turbo Expo 2018: Turbomachinery Technical Conference and Exposition, Oslo, Norway, 11–15 June 2018.
9. Bernhard Gustafsson, K.M.; Gunnar Johansson, T. An experimental study of surface temperature distribution on effusion-cooled plates. *J. Eng. Gas Turbines Power* **2001**, *123*, 308–316. [CrossRef]
10. Sellers, J.P. Gaseous Film Cooling With Multiple Injection Stations. *AIAA J.* **1963**, *1*, 2154–2156. [CrossRef]
11. Muska, J.F.; Fish, R.W.; Suo, M. The Additive nature of film cooling from rows of holes. *J. Eng. Gas Turbines Power* **1976**, *98*, 457–463. [CrossRef]
12. Murray, A.; Ireland, P.; Wong, T.; Tang, S.; Rawlinson, A. High Resolution Experimental and Computational Methods for Modelling Multiple Row Effusion Cooling Performance. *Int. J. Turbomach. Propuls. Power* **2018**, *3*, 4. [CrossRef]
13. Goldstein, R.J. Film Cooling. *Adv. Heat Transf.* **1971**, *7*, 321–379. [CrossRef]
14. Jiang, Y.; Capone, L.; Ireland, P.; Romero, E. A detailed study of the interaction between two rows of cooling holes. *ASME. J. Turbomach.* **2018**, *140*, 041008. [CrossRef]
15. Murray, A.V.; Ireland, P.T.; Rawlinson, A.J. An Integrated Conjugate Computational Approach for Evaluating the Aerothermal and Thermomechanical Performance of Double-Wall Effusion Cooled Systems. In Proceedings of the ASME Turbo Expo 2017: Turbomachinery Technical Conference and Exposition, Charlotte, NC, USA, 26–30 June 2017. [CrossRef]
16. Murray, A.V.; Ireland, P.T.; Romero, E. Development of a steady-state experimental facility for the analysis of double-wall effusion cooling geometries. *J. Turbomach.* **2019**, *141*, 041008. [CrossRef]
17. Baldauf, S.; Schulz, A.; Wittig, S. High resolution measurements of local effectiveness by discrete hole film cooling. In Proceedings of the ASME 1999 International Gas Turbine and Aeroengine Congress and Exhibition, Indianapolis, IN, USA, 7–10 June 1999. [CrossRef]
18. Lutum, E.; Johnson, B.V. Influence of the Hole Length-to-Diameter Ratio on Film Cooling With Cylindrical Holes. *J. Turbomach.* **1999**, *121*, 209. [CrossRef]
19. Murray, A.V.; Ireland, P.T.; Romero, E. Experimental and Computational Methods for the Evaluation of Double-Wall, Effusion Cooling Systems. *J. Turbomach.* **2020**, *142*, 111003. [CrossRef]
20. Yang, L.; Min, Z.; Parbat, S.N.; Chyu, M.K. Effect of Pore Blockage on Transpiration Cooling With Additive Manufacturable Perforate Holes; In Proceedings of the ASME Turbo Expo 2018: Turbomachinery Technical Conference and Exposition, Oslo, Norway , 11–15 June 2018; ASME: New York, NY, USA, 2018; p. V02DT47A004. [CrossRef]
21. Elmukashfi, E.; Murray, A.V.; Ireland, P.T.; Cocks, A.C. Analysis of the thermomechanical stresses in double-wall effusion cooled systems. *J. Turbomach.* **2020**, *142*, 051002. [CrossRef]

International Journal of
Turbomachinery Propulsion and Power

MDPI

Article

Effect of Different Subgrid-Scale Models and Inflow Turbulence Conditions on the Boundary Layer Transition in a Transonic Linear Turbine Cascade

Ettore Bertolini [1,*], Paul Pieringer [2] and Wolfgang Sanz [1]

[1] Institute of Thermal Turbomachinery and Machine Dynamics, Graz University of Technology, 8010 Graz, Austria; wolfgang.sanz@tugraz.at
[2] ABES Pircher and Partner GmbH, 8010 Graz, Austria; paul.pieringer@abes-austria.com
* Correspondence: ettore.bertolini@tugraz.at

Abstract: The aim of this work is to study the influence of different subgrid-scale (SGS) closure models and inflow turbulence conditions on the boundary layer transition on the suction side of a highly loaded transonic turbine cascade in the presence of high free-stream turbulence using large eddy simulations (LES) of the MUR237 test case. For the numerical simulations, the MUR237 flow case was considered and the incoming free-stream turbulence was reproduced using the synthetic eddy method (SEM). The boundary layer transition on the blade suction side was found to be significantly influenced by the choice of the SGS closure model and the SEM parameters. These two aspects were carefully evaluated in this work. Initially, the influence of three different closure models (Smagorinsky, WALE, and subgrid-scale kinetic energy model) was evaluated. Among them, the WALE SGS closure model performed best compared to the Smagorinsky and KEM models and, for this reason, was used in the following analysis. Finally, different values of the turbulence length scale, eddies density, and inlet turbulence for the SEM were evaluated. As shown by the results, among the different parameters, the choice of the turbulence length scale plays a major role in the transition onset on the blade suction side.

Keywords: LES; laminar-to-turbulent transition; subgrid-scale model; synthetic eddy method

check for updates

Citation: Bertolini, E.; Pieringer, P.; Sanz, W. Effect of Different Subgrid-Scale Models and Inflow Turbulence Conditions on the Boundary Layer Transition in a Transonic Linear Turbine Cascade. *Int. J. Turbomach. Propuls. Power* **2021**, *6*, 35. https://doi.org/10.3390/ijtpp6030035

Academic Editor: Antoine Dazin

Received: 19 May 2021
Accepted: 18 August 2021
Published: 27 August 2021

Publisher's Note: MDPI stays neutral with regard to jurisdictional claims in published maps and institutional affiliations.

Copyright: © 2021 by the authors. Licensee MDPI, Basel, Switzerland. This article is an open access article distributed under the terms and conditions of the Creative Commons Attribution (CC BY-NC-ND) license (https://creativecommons.org/licenses/by-nc-nd/4.0/).

1. Introduction

In modern aero engines, the turbine stages have to deal with extreme conditions due to the presence of high pressures, high temperatures, and high levels of turbulence. In order to ensure the performance and the lifetime of the components, precise knowledge and control of the flow field inside the machine is required. Particularly critical is the region of the flow closest to the solid surfaces. This region is called the boundary layer (BL), and it is here that viscous effects drive the exchanges of energy and momentum. The boundary layer can be both laminar and turbulent, and this has a great influence on the transport processes such as wall friction and heat transfer. Furthermore, the ability of the boundary layer to remain attached to the blades in the condition of adverse pressure gradients changes dramatically from laminar to turbulent. Therefore, the control of the boundary layer becomes essential in modern aero engines where high loads and high efficiency are required from every stage.

Much research has been undertaken in the last few decades in order to understand all the complex mechanisms occurring in the boundary layer region. Besides the experimental approach, the numerical solution of the Navier–Stokes (NS) equations has also been used since it can provide a priori useful information for the designers. Consequently, a substantial amount of numerical models has been developed and refined in order to accurately predict the evolution of the boundary layer. While RANS models played a big role concerning simulations of near-wall flows, more recently, thanks to the fast growth of

computational resources, more accurate numerical models such as large eddy simulation (LES) and direct numerical simulation (DNS), which were considered almost impossible to use a decade ago for engine-relevant flow conditions, are becoming more and more popular. Among the three, LES seems to be especially attractive due to a lower computational cost compared to DNS and better accuracy and adaptability in comparison with RANS, making it a valuable choice not only in research fields, but also in industrial ones.

One of the biggest challenges for LES when dealing with turbomachinery flows is the prediction of the laminar-to-turbulent transition on the blade surface in the presence of free-stream turbulence. The incoming turbulence has a great impact on the BL evolution and needs to be carefully modeled in order to reach accurate results. However, the specification of the inlet flow data is a bit more complex and challenging in LES compared to RANS since an unsteady turbulence velocity signal has to be superimposed at the inlet boundary in order to reproduce the turbulence statistics of the real flow. Dhamankar et al. [1] provided an overview of the different approaches used for reproducing turbulence. Among the different methods, the synthetic eddy method (SEM) of Jarrin et al. [2] was chosen in this work since it can be used to describe a large number of inlet turbulence conditions in terms of turbulence length scale, anisotropy, and intensity with a relatively low computational cost and a good replicability of the turbulence statistics. Furthermore, it is easy to change the inflow boundary conditions since the method does not require precursor simulations.

The ability of LES to predict the BL transition on a highly loaded turbine blade in the presence of inlet turbulence was investigated in the works of [3–7]. In these works, the flow case investigated was the MUR cascade tested at the von Karman Institute for Fluid Dynamics [8]. The cascade was composed of a linear arrangement of five blades, where the central one was instrumented for both pressure and heat transfer measurements. In the cascade, the influence of free-stream turbulence, the free-stream Reynolds number, and the Mach number on the boundary layer transition and on the heat transfer on the blade was evaluated. Different methods for reproducing the inflow turbulence statistics and different LES setups were used by every author. However, all the numerical configurations exhibited weaknesses in some flow configurations, showing that a reliable prediction of the BL laminar-to-turbulent transition is still a challenge. In the work of Jee et al. [7] in particular, it was found that the boundary layer transition on the blade suction side is significantly influenced by the choice of the subgrid-scale (SGS) closure model and the SEM parameters.

The aim of this paper is to investigate the influence of different LES setups on the boundary layer transition on the blade suction side of a MUR cascade in the presence of synthetic inlet turbulence. For the simulations, the in-house code LINARS was used. The inflow turbulence is described using the SEM routine proposed by [2], and the numerical simulations refer to the MUR237 flow case.

The paper is arranged as follows. Firstly, the influence of three different closure models is evaluated. Starting from the results of [7], the standard Smagorinsky model is compared to the WALE model and the one-equation subgrid-scale kinetic energy model (KEM). Afterwards, the influence of the SEM parameters such as the turbulence intensity, turbulence length scale, and number of turbulent eddies is investigated.

2. Numerical Method

2.1. Flow Case

The flow case investigated in the simulations was the MUR237 test case. This flow case is part of a campaign of measurements (MUR132, MUR218, and MUR237), where the influence of the inflow turbulence intensity on the heat transfer and boundary layer transition on the blade surface was evaluated. The cascade counts in total 5 blades with a chord length, blade height, and blade pitch of 67.647 mm, 100 mm, and 57.5 mm, respectively. The main flow parameters can be found in Table 1. MUR237 involves a higher level (6%) of inflow turbulence and an earlier laminar-to-turbulent transition of the boundary layer on the suction side of the blade compared to the MUR218 (4%) and MUR132 (0.8%) flow cases.

Table 1. Flow parameters and boundary conditions for the numerical investigation.

MUR237			
Parameter	**Symbol**	**Value**	
Total temperature inlet	T_{1tot}	417.3	K
Static temperature inlet	T_{1s}	415.43	K
Total pressure inlet	p_{1tot}	1.753	bar
Static pressure inlet	p_{1s}	1.726	bar
Velocity inlet	v_1	61.29	m/s
Static pressure outlet	p_{2s}	1.179	bar
Wall temperature	T_{wall}	299.85	K
Reynolds number outlet	Re_{out}	1.0×10^6	-
Freestream turbulence	Tu	6.0%	-
Incidence angle	β_1	0	deg
Exit Mach number	M_{2is}	0.775	-

2.2. Computational Mesh

For the MUR237 flow case, the flow at midspan has been proven to be independent of the hub and shroud secondary vortices and reasonably periodic in the circumferential direction for the central vane [8]. Hence, the numerical grid considers only one vane channel, and only part of the entire blade span is considered. The numerical span was equal to 10% of the entire blade height since it was shown in the work of [5] that by a further increase of the numerical span, no significant improvement in the results can be achieved. Figure 1 displays the computational grid used. A configuration with O-blocks around the blade was used in order to guarantee higher accuracy close to the blade wall while maintaining a low number of grid points in the free-stream region where such a grid resolution is not needed. As can be seen in the black frame in Figure 1, the number of grid points along the streamwise direction was doubled moving towards the blade surface from one O-block to the consecutive one. A total of 3 layers of O-blocks was used. At the outlet, two coarser blocks were added in order to increase the dissipation of the flow structures of the wake and reduce the reflections at the outlet boundary. The grid counts a total of 38M grid points, and it was designed in order to achieve a maximum value of y^+, x^+, and z^+ of 1.2, 40, and 30, respectively. Furthermore, in the free-stream region, the maximum grid spacing was equal to 0.3 mm.

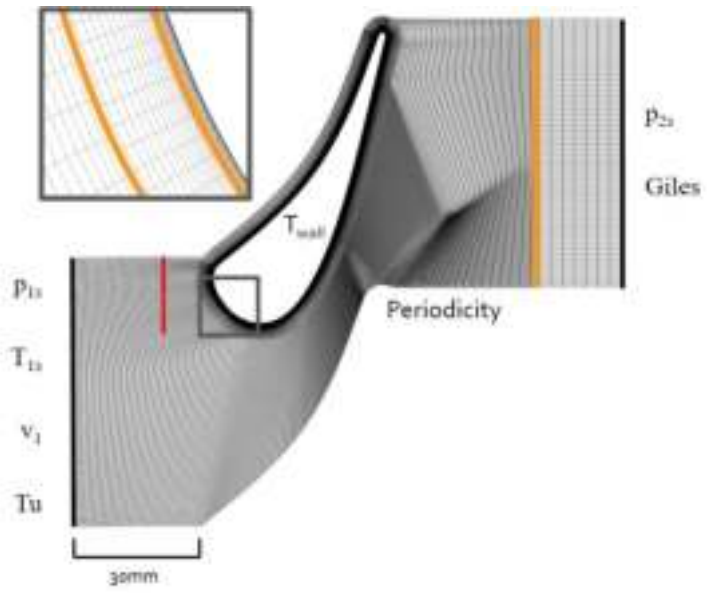

Figure 1. Computational grid and O-blocks.

2.3. Boundary Conditions

At the inlet and outlet, the boundary conditions were assigned according to Figure 1 the parameters in Table 1. At the outlet, the static pressure was assigned, as well as a Giles nonreflective boundary condition [9] in order to improve the stability of the simulations. At the inlet, the static temperature, static pressure, and mean velocity were imposed, whereas the inlet turbulence intensity was prescribed using the SEM. At the blade wall, a constant temperature equal to 299.85 K was set. Between the O-blocks around the blade and the coarser blocks in the outer layers, an interpolation of second-order was used to connect the faces. Further information about the interpolation used can be found in [7]. Finally, periodicity was used in the circumferential and spanwise direction.

2.4. Numerical Schemes

For the time iteration, the fourth-order explicit Runge–Kutta method (RK4) was used with a time step of 4×10^{-9} s and a maximum value of $CFL < 1$. For the computation of the cell fluxes, a weighted essentially nonoscillatory (WENO) scheme was used since it was proven by [10] to give better performance compared to the central schemes and the TVD schemes in terms of numerical stability and dissipation.

2.5. Computational Time

The simulations were performing using the in-house code LINARS. The numerical domain was split into several blocks for parallel computing and a total of 160 cores was used for each simulation. Approximately 2.5×10^5 core hours were needed to carry out every simulation.

2.6. Subgrid-Scale Models

In this work, three different SGS models were used: Smagorinsky–Lilly, wall-adapting local eddy-viscosity (WALE), and the one-equation subgrid-scale kinetic energy model (KEM).

2.6.1. Smagorinsky–Lilly Model

The standard Smagorinsky–Lilly model was used in this paper. Lilly originally found a value of the Smagorinsky coefficient C_s equal to 0.17 [11]. This value gives good results for isotropic turbulence in the free-stream region, but it introduces a too high dissipation when dealing with near-wall flows. For this type of flow, a value equal to 0.1 is usually recommended. However, in [7] it was found that with a Smagorinsky coefficient equal to 0.1, the boundary layer evolution on the MUR blade could not be accurately predicted because the closure model was still too dissipative. Different values of the Smagorinsky coefficient were tested for the MUR132 flow case, and a value equal to 0.05 was found to give the best performance. For this reason, this value was also used in this work.

A damping function acting on the Smagorinsky length scale was also applied in order to reduce the viscosity in the near-wall region:

$$\ell_s = min(\kappa d, C_s V^{1/3}) \tag{1}$$

where d is the distance from the solid wall, κ represents the von Karman constant $\kappa = 0.41$, and V is the volume of the computational cell.

2.6.2. WALE Model

The WALE model [12] is a subgrid-scale model based on the square of the velocity gradient tensor. Compared to the standard Smagorinsky–Lilly model, in the WALE model the eddy viscosity with this formulation goes naturally to zero close to the wall, and it is also zero in the case of pure shear stress. The eddy viscosity is rewritten as:

$$\mu_t = \rho L_s^2 \frac{(S_{ij}^d S_{ij}^d)^{3/2}}{(\overline{S}_{ij}\overline{S}_{ij})^{5/2} + (\overline{S}_{ij}\overline{S}_{ij})^{5/4}} \tag{2}$$

$\overline{S}_{ij}$ is the rate-of-strain tensor for the resolved scale, which can be expressed as:

$$\overline{S}_{ij} = \frac{1}{2}\left(\frac{\partial \overline{u_i}}{\partial x_j} + \frac{\partial \overline{u_j}}{\partial x_i}\right) \tag{3}$$

whereas the mixing length L_s and the parameter S_{ij}^d are defined respectively as:

$$L_s = min(\kappa d, C_\omega V^{1/3}) \tag{4}$$

$$S_{ij}^d = \frac{\partial \overline{u_i}}{\partial x_j} \tag{5}$$

The coefficient C_ω was set equal to 0.325 since this value has been proven to produce satisfactory results for a wide range of flows.

2.6.3. KEM Model

In the KEM closure model, the eddy viscosity is expressed as:

$$\mu_t = C_k \sqrt{k_{sgs}} V^{1/3} \tag{6}$$

where k_{sgs} is the kinetic energy related to the subgrid scales of turbulence, and it is obtained from the additional transport equation:

$$\frac{\partial k_{sgs}}{\partial t} + \overline{u}_j \frac{\partial k_{sgs}}{\partial x_j} = -\tau_{ij}\frac{\partial \overline{u}_i}{\partial x_j} - C_c \frac{k_{sgs}^{3/2}}{\Delta} + \frac{\partial}{\partial x_j}\left[\left(\frac{\nu_k}{\sigma_k} + \nu\right)\frac{\partial k_{sgs}}{\partial x_j}\right] \tag{7}$$

In the equation, the terms on the right-hand side are, respectively, production, dissipation, and diffusion. The constants were set according to the work of [13] as $C_k = 0.05$, $C_c = 1.0$, and $\sigma_k = 1.0$, whereas Δ was obtained from the cell volume as $\Delta = V^{1/3}$. Finally, the inlet condition for the subgrid-scale kinetic energy was set equal to 6% of the inlet turbulence kinetic energy.

2.7. SEM

The main principles of the SEM are as follows. The eddies that constitute a set of velocity fluctuations are contained in a box outside of the computational domain. The eddies are defined in the box by the coordinates of their center, their velocity fluctuation distribution, and their size. The location of the eddies is randomly defined, as well as the direction of the fluctuation, which is assigned using a random variable taken from the distribution $\{-1; 1\}$ with equal probability to take one or the other value. The eddies are then convected from the SEM box to the computational domain by using Taylor's frozen hypothesis [2].

The setup of the SEM used in this work was the same as in [7], and the main points are recalled here. An isotropic turbulent inflow was considered, so the intensity of the turbulence fluctuations was the same for the three velocity components and equal to the product between the average inlet velocity and the turbulence intensity ($a_{ii} = TuU$). The dimension of the box was the same in the circumferential and spanwise direction as the inlet boundary of the main computational domain, whereas the length in the streamwise direction was found by multiplying the average inlet velocity by a time constant τ as $L_x = \tau U$. Finally, the number of eddies was found as recommended in the work of [14] by dividing the volume of the SEM box (V_{SEM}) by the cube of the turbulence length scale (σ) as:

$$N = V_{SEM}/\sigma^3 \tag{8}$$

It is important to mention that when all the eddies inside the SEM box are transported inside the computational domain, a new SEM box is generated. The new SEM box is defined by a new set of random eddies. The random eddies were picked from an external pool previously generated with MATLAB. The total number of eddies contained in the

pool was chosen in order to avoid the time periodicity of the inlet turbulence in the time frame of the simulation. As a consequence, τ did not have any influence on the generated turbulence, but it was only used to build an initial SEM box used for flow visualization and for checking the correctness of the turbulence statistics.

Different SEM boxes were defined for this investigation. The main parameters of each of them are displayed in Table 2. In all boxes, 6.5% inlet turbulence was prescribed apart from SEM5T8, where 8% was used. The turbulence length scale was equal to 5 mm for SEM5 and SEM5T8, 3 mm for SEM3 and SEM3N4, and 2 mm for SEM2. The time constant τ was chosen in order to have enough eddies in the streamwise direction inside the SEM box and good turbulence statistics. The number of eddies was then obtained from Equation (8), apart from SEM3N4, where the number of eddies that was prescribed was 4-times larger. Finally, in the last column of Table 2, the density of the eddies in the SEM box is reported. As can be seen, the density of the eddies increased by reducing the turbulence length scale.

Table 2. SEM box parameters.

Name	σ	Tu	τ	N	N/V_{SEM}
SEM2	2 (mm)	6.5 (%)	0.0006 (s)	2643 (-)	0.125 $(1/mm^3)$
SEM3	3 (mm)	6.5 (%)	0.006 (s)	7831 (-)	0.037 $(1/mm^3)$
SEM5	5 (mm)	6.5 (%)	0.01 (s)	2819 (-)	0.008 $(1/mm^3)$
SEM3N4	3 (mm)	6.5 (%)	0.0005 (s)	2610 (-)	0.148 $(1/mm^3)$
SEM5T8	5 (mm)	8.0 (%)	0.01 (s)	2819 (-)	0.008 $(1/mm^3)$

For the SGS closure model comparison, only the SEM5 box was used for the definition of the inlet turbulence. For the investigation of the influence of the inlet turbulence length scale, SEM2, SEM3, and SEM5 were used. Regarding the influence of the number of eddies, the simulation using SEM3 was compared to the one with SEM3N4. Finally, SEM5 and SEM5T8 were compared in order to investigate the effect of the turbulence intensity.

3. Results

In this section, the results of the current investigation are presented and discussed. The experimental convective heat transfer coefficient (h) on the blade surface was compared with the predicted one of the LES simulations. In order to obtain h, the main flow parameters were recorded every 5000 iterations. Then, an average in time was performed, as well as along the spanwise direction. In order to prove that the solution had converged, the integral of the convective heat transfer coefficient over a region on the suction side of the blade close to the trailing edge was evaluated over time. After convergence was reached, 250,000 time steps were performed, and a total number of 50 samples were taken. h was then obtained by the definition:

$$h = \frac{\dot{q}_{wall}}{T_{1tot} - T_{wall}} \tag{9}$$

where $\dot{q}_{wall}$, T_{1tot}, and T_{wall} are the wall heat flux, total inlet temperature, and wall temperature, respectively. Finally, in order to compare with the experiments, the convective heat transfer coefficient was plotted along the curvilinear abscissa (S) for both the pressure side (PS) and suction side (SS). In the heat transfer measurements of the MUR test case, an uncertainty of 5% was estimated, so it was taken into account in the graphs using error bars.

3.1. SGS Closure Model Influence

The convective heat transfer coefficient predicted by the three different SGS models for the MUR237 test case is displayed in Figure 2. Looking at the suction side (SS), the three models reached similar levels at the blade leading edge (0 mm $<$ S $<$ 20 mm). Starting

from $S = 20$ mm and up to $S = 58$ mm, WALE and SMAG predicted slightly lower levels of h compared to KEM. However, starting from $S = 58$, this trend changed, and both WALE and SMAG predicted a sudden increase of h due to the laminar-to-turbulent transition of the boundary layer (a visualization of the boundary layer for the WALE simulation is provided in Figure 6). On the other hand, KEM did not show a complete transition, and consequently, lower levels of h were reached. Focusing now on the pressure side, even though the heat transfer was similar at the blade leading edge, starting from the position $S = -5$, the three models exhibited some differences. KEM in particular predicted the highest levels of h all over the PS, whereas SMAG and WALE showed similar behavior, with the latter giving slightly lower levels of heat transfer.

To further analyze the differences between the tested SGS models, the wall shear stress on the blade wall was also computed. Looking at Figure 3, contrary to what was found for the convective heat transfer, the three models showed very similar levels of wall shear stress at the blade pressure side, with the WALE giving slightly lower values compared to KEM and SMAG. Concerning the SS, the predicted wall shear stress was similar in the first part of the suction side up to $S = 20$ mm. From this point on, some small differences could be found within the region 20 mm $<$ S $<$ 60 mm, but it was again closer to the trailing edge where the greatest deviations between the models could be found due to a different prediction of the laminar-to-turbulent transition.

In Figure 4, the velocity profiles are reported. The velocity profiles were extrapolated in two locations on the SS at $S = 60$ mm (beginning of the laminar-to-turbulence transition) and $S = 80$ mm (more turbulent BL) and one on the PS at $S = -20$ mm. In the graphs, theoretical solutions of the flat plate flow for both the viscous sublayer (dashed line) and the logarithmic law of the wall (dashed-dotted line) are also included. Generally, the velocity profiles of the different SGS models were very similar when the boundary layer was laminar (positions $S = -20$ mm and $S = 60$ mm), and they matched the viscous sublayer theoretical shape well. On the contrary, at position $S = 80$ mm, the models behaved very differently. The KEM velocity profile was still laminar compared to the ones of WALE and SMAG, which showed a more turbulent profile. Among the three models, WALE seemed to perform best in both the viscous sublayer and in the log-law region.

Looking again at position $S = 80$, none of the SGS models matched the turbulence velocity profile given by the logarithmic law of the wall. In order to find the reason for the discrepancy, the velocity profiles were also drawn in this location for a RANS solution with the k-ω SST model combined with the γ-Re_θ transition model. As can be seen in Figure 4, the RANS model predicted the theoretical line in the log-law region better compared to the LES models. Looking now at the heat transfer coefficient in Figure 2, it can be clearly seen that the RANS model exhibited a much more rapid transition compared to LES and also predicted a much higher level of convective heat transfer once that transition had occurred. This indicates that the LES models did not predict a full transition of the boundary layer which could explain the discrepancy in the log-law region of the velocity profiles and in the heat transfer.

Overall, by comparing the experimental and the numerical results, h was underpredicted in all three LES simulations, and this difference was larger in the aft part of the blade SS, where the transition occurred much more downstream than in the experiments. Furthermore, as was previously found in [6,7], the predicted heat transfer better agree with the experimental results of the MUR218 flow case where a lower level of turbulence (4%) at the inlet was generated (see Figure 2).

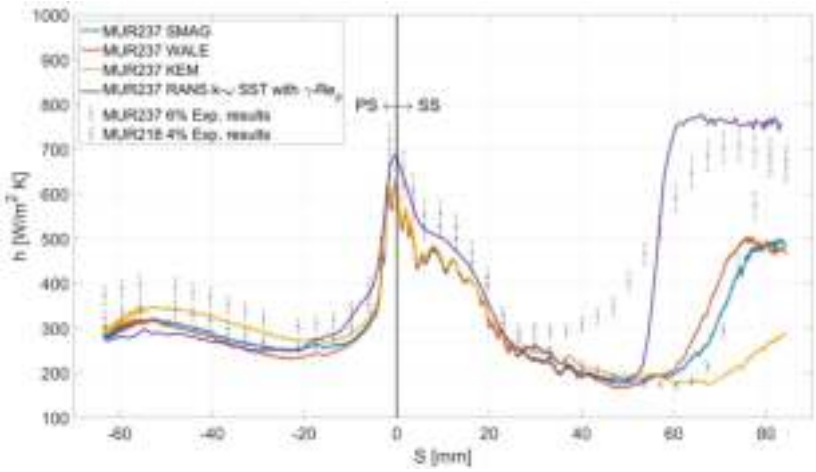

Figure 2. Influence of the SGS closure models: convective heat transfer coefficient.

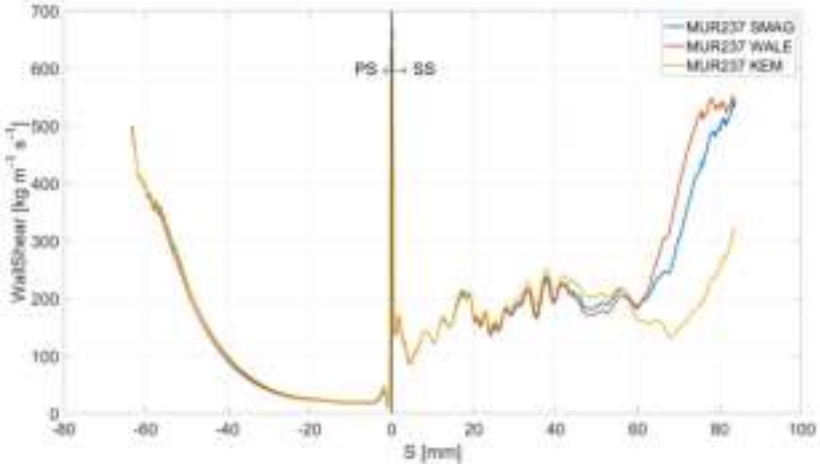

Figure 3. Influence of the SGS closure models: wall shear stress.

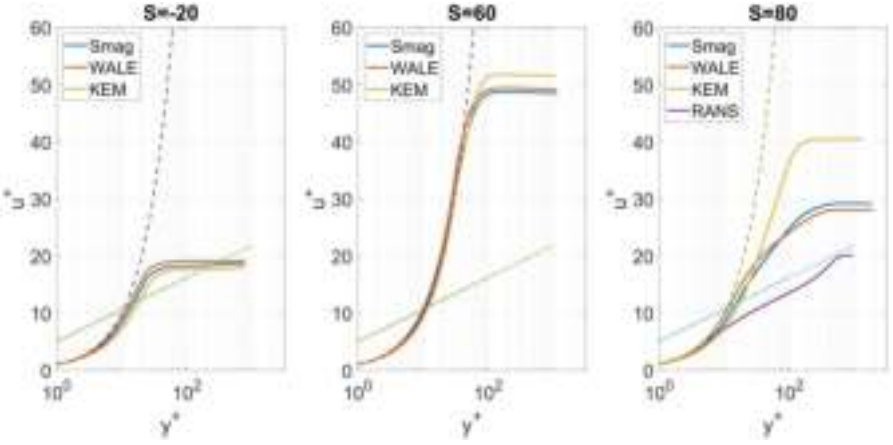

Figure 4. Influence of the SGS closure models: velocity profile.

In [7], some open questions remained regarding the origin of the deviation between the experimental and numerical results and whether it was connected to the chosen SGS closure model or the SEM parameters. From these results, it can be concluded that the choice of the SGS model influences the prediction of the heat transfer on the blade surface at both the pressure and suction side, whereas on the SS the influence seems to be restricted to the BL laminar-to-turbulent transition region when looking at the wall shear stress. KEM had more subgrid-scale viscosity than WALE and SMAG, and this caused a suppression of the laminar-to-turbulent transition on the blade SS. WALE and SMAG gave similar results,

but the first one seems to be slightly less dissipative than SMAG and also performed better in the subviscous layer of the boundary layer. Therefore, for this reason, it was used in the further investigations of this work.

3.2. Influence of SEM Box Parameters

As the next step, the impact of the SEM parameters on the convective heat transfer and the laminar-to-turbulent BL transition is discussed. In particular, the influence of the turbulence length scale, the number of eddies prescribed in the SEM box, and the turbulence intensity are treated separately.

3.2.1. Turbulence Length Scale

In the experiments, no information regarding the turbulence length scales was given. However, the mixing length is well known to have a great influence on the boundary layer transition. In the works of [5,6,15], a deep discussion on the choice of the mixing length for the simulation of the MUR flow case can be found, and the typical values chosen in their investigations varied between 1.5 and 8 mm. According to the range of values found in the literature, three different turbulence length scales were chosen, 2 mm, 3 mm, and 5 mm, for the current investigation.

For this set of simulations, the WALE model was used, whereas turbulence was prescribed by the 2 mm, 3 mm, and 5 mm turbulence length scale cases, respectively, using SEM2, SEM3, and SEM5 (see Table 2). Looking at the convective heat transfer in Figure 5, some differences can be already noticed at the blade leading edge where larger values of heat transfer can be found for the 3 mm and 2 mm flow cases. On the blade pressure side, the predicted heat transfer was very similar between SEM5 and SEM3, whereas SEM2 predicted slightly higher levels of h from $S = -20$ mm to the trailing edge. On the suction side, the differences were more remarkable. Starting from the leading edge and up to $S = 20$ mm, the heat transfer was closer to the experimental results for the 3 mm flow case, whereas only slight differences could be found between 2 mm and 5 mm. Between $S = 20$ mm and $S = 40$ mm, it seemed that h converged to similar levels for all three turbulence length scales, but starting from $S = 40$ mm, the heat transfer for SEM3 rose considerably, showing a much earlier laminar-to-turbulent transition compared to SEM5 and SEM2, where the transition onset was at $S = 60$ mm. By comparing the numerical and experimental results, it is interesting that an inlet turbulence length scale equal to 3 mm remarkably improved the results, whereas a larger (5 mm) and smaller (2 mm) length scale showed similar, but worse results.

In order to better understand the reason for such a difference in the results between the 3 mm and the 5 mm flow cases, the interaction between the incoming turbulence and the boundary layer was investigated by looking at the instantaneous flow field around the blade. As can be seen by the isosurfaces of the Q criterion colored by the velocity magnitude in Figure 6, the density of eddies in the near-wall region was much larger when a 3 mm length scale was prescribed. It has to be remembered that the number of eddies was chosen according to Equation (8), so that a lower density of eddies was expected when a larger turbulence length scale was used (see Table 2). As Figure 6 suggests, this had a great impact on the boundary layer even though the same turbulence intensity was prescribed at the inlet boundary. By observing the contour of spanwise vorticity, it can also be clearly seen that the 3 mm inlet turbulence influenced the pressure side BL as well as the suction side, where the onset of transition occurred much earlier. On the other hand, even though the density of the eddies was the highest for the 2 mm flow case, a later transition was found compared to the 3 mm flow case and similar to the 5 mm case. This was probably caused by a higher dissipation of the smaller turbulence length scale that occurred in the free-stream region. Due to the faster dissipation, the eddies that hit the boundary layer were weaker and could not properly trigger the BL transition.

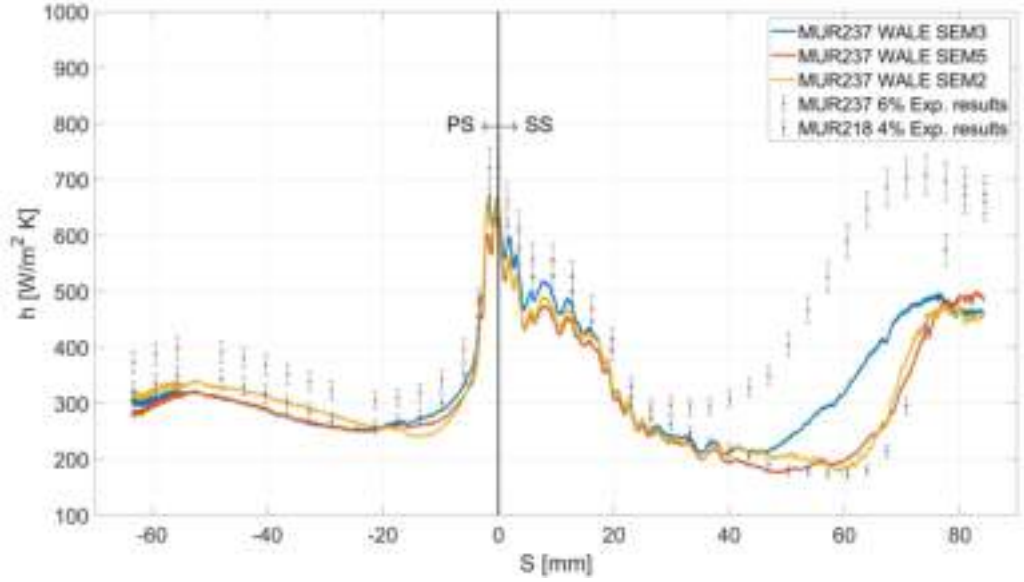

Figure 5. Influence of the turbulence length scales: convective heat transfer coefficient.

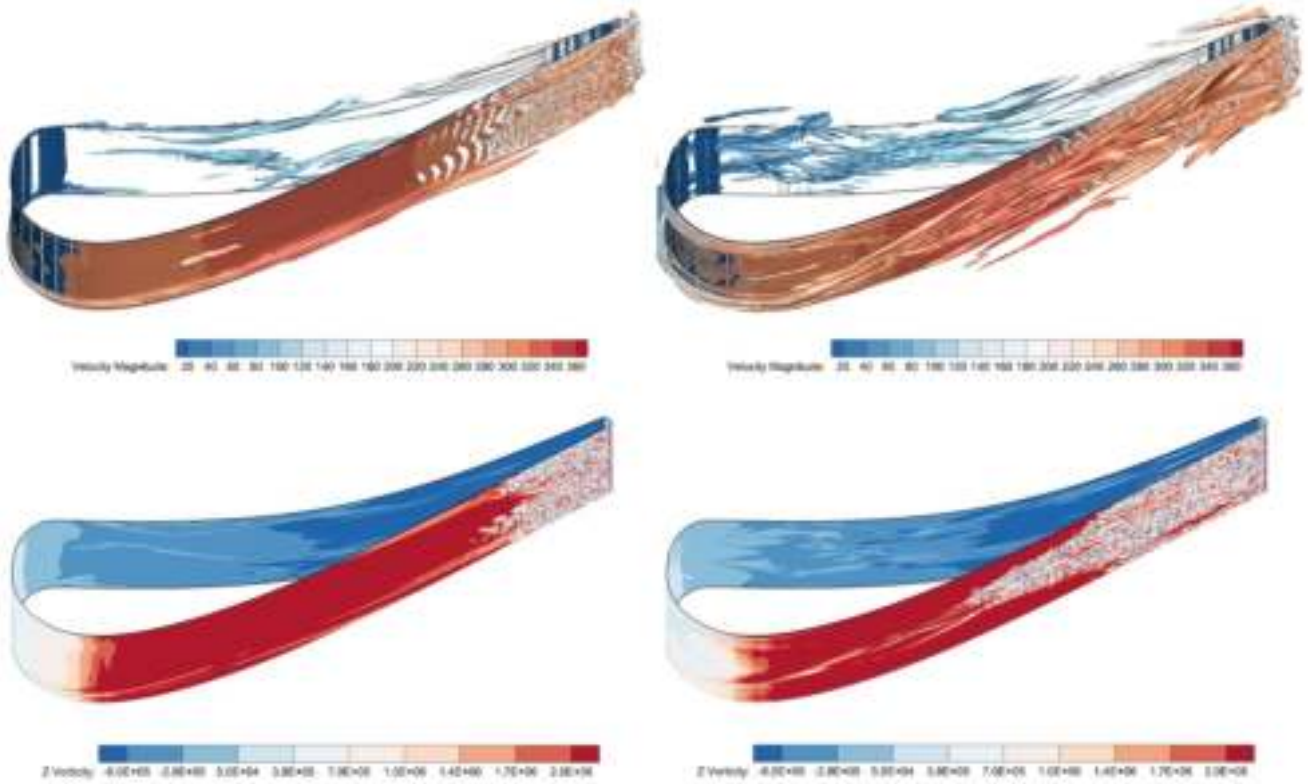

Figure 6. Interaction of the incoming turbulent eddies with the boundary layer for the 3 mm and 5 mm cases: isosurfaces of $Q = 1 \times 10^8$ colored by velocity magnitude (**top**) and the contour of spanwise vorticity at 1×10^{-5} mm from the blade surface (**bottom**).

3.2.2. Number of Eddies

In Figure 7, the results of the investigation regarding the influence of the number of eddies in the SEM box are displayed. Increasing the number of eddies by a factor of four from SEM3 to SEM3N4 led to a degradation of the result quality, and in particular, a later onset of transition could be found. A comparison of the turbulence kinetic energy (TKE) level between the two flow cases was performed at 10 mm upstream the leading

edge of the blade (see the red plane in Figure 1). SEM3N4 showed at this point almost 6% less TKE compared to SEM3 despite having the same value at the inlet boundary. When a larger number of eddies was used compared to the recommended one of Equation (8), more regions exist inside the SEM box where the eddies overlap. This could lead to a deterioration of the turbulence fluctuations and, consequently, to a faster dissipation of the TKE along the streamwise direction.

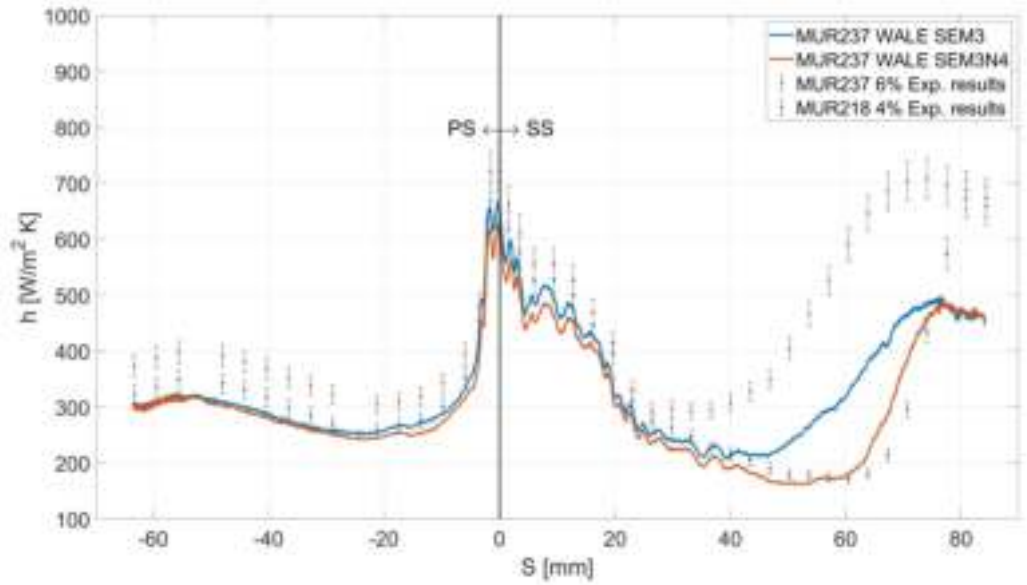

Figure 7. Influence of the number of eddies: convective heat transfer coefficient.

3.2.3. Turbulent Intensity

Looking at Figure 8, it can be seen that by increasing the turbulence intensity from 6% to 8% for the 5 mm flow case, very few changes in the convective heat transfer coefficient could be found. The onset of transition on the SS remains unchanged between the two flow cases, although a slightly higher level of h was predicted for the higher turbulence case between $S = 0$ and $S = 20$ mm. However, a faster transition could be observed for SEM5T8.

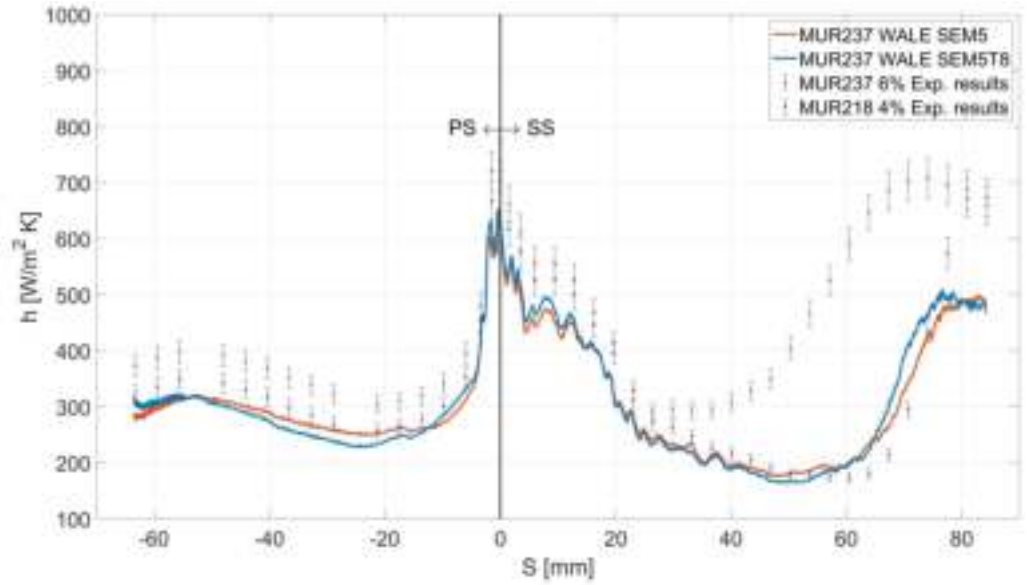

Figure 8. Influence of the turbulence intensity: convective heat transfer coefficient.

4. Conclusions

In this work, the influence of different LES setups on the boundary layer transition on the blade suction side of a highly loaded turbine cascade in the presence of synthetic inlet turbulence was discussed. From the investigation with the different SGS closure models (SMAG, WALE, and KEM), it was found that the choice of the SGS model influenced the prediction of the heat transfer at both pressure and suction side of the blade. In particular, the main differences existed in the region of the suction side where the laminar-to-turbulent transition of the boundary layer occurred. Here, KEM proved to be much more dissipative than WALE and SMAG, and this caused a suppression of the laminar-to-turbulent transition. WALE and SMAG gave similar results, but the first one seemed to be slightly less dissipative than SMAG and also performed better in the subviscous layer of the boundary layer. Regarding the influence of the SEM parameters for prescribing the inlet turbulence such as the turbulence intensity, turbulence length scale, and number of turbulent eddies, it was found that the turbulence length scale had a greater impact on the boundary layer transition and consequently on the heat transfer compared to the other two. In particular, with a turbulence length scale equal to 3 mm, a remarkable improvement of the numerical results compared to the experimental one for the convective heat transfer coefficient was found, especially for the transition onset location. Finally, the increased turbulence intensity seems not to have great impact on the heat transfer, whereas a larger number of eddies in the SEM box resulted in a decrease of turbulence and a deterioration of the turbulence statistics.

Author Contributions: Conceptualization, E.B., P.P. and W.S.; methodology, E.B., P.P. and W.S.; software, E.B., P.P. and W.S.; validation, E.B.; formal analysis, E.B. and W.S.; investigation, E.B. and W.S.; resources, E.B., P.P. and W.S.; data curation, E.B. and W.S.; writing—original draft preparation, E.B.; writing—review and editing, E.B., P.P. and W.S.; visualization, E.B.; supervision, W.S.; project administration, W.S.; funding acquisition, W.S. All authors read and agreed to the published version of the manuscript.

Funding: This research was conducted in the framework of the project ALESIA (Advanced Large Eddy Simulation in Aeroengines) supported by the Austrian Federal Ministry for Transport, Innovation and Technology within the Austrian Aeronautics Program TAKE OFF.

Institutional Review Board Statement: Not applicable.

Informed Consent Statement: Not applicable.

Data Availability Statement: Not applicable.

Acknowledgments: The authors would like to acknowledge the use of the HPC resources provided by the ZID of Graz University of Technology.

Conflicts of Interest: The authors declare no conflict of interest.

Abbreviations

The following abbreviations are used in this manuscript:

BL	Boundary Layer
CFL	Courant–Friedrichs–Lewy
DNS	Direct numerical simulation
KEM	Subgrid-scale Kinetic energy model
LES	Large eddy simulation
NS	Navier–Stokes
PS	Pressure side
RANS	Reynolds-averaged Navier–Stokes
SGS	Subgrid scale
SEM	Synthetic eddy method
SMAG	Smagorinsky
SS	Suction side
WALE	Wall-adapting local eddy-viscosity

Roman Symbols

C_c	Constant of the KEM model
C_k	Constant of the KEM model
C_s	Smagorinsky coefficient
C_ω	Constant of the WALE model
d	Distance to the wall
ℓ_s	Smagorinsky length scale
h	Convective heat transfer coefficient
L_S	Mixing length
k_{sgs}	Kinetic energy of the the subgrid scale
M_{2is}	Isentropic Mach number outlet
p_{1tot}	Inlet total pressure
p_{1s}	Inlet static pressure
p_{2s}	Outlet static pressure
$\dot{q}_{wall}$	Wall heat flux
Re_{out}	Reynolds number at the outlet
S	Curvilinear coordinate
$\overline{S}_{ij}$	Rate-of-strain tensor
S^d_{ij}	Rate-of-strain tensor for the resolved scale
T_{1s}	Inlet static temperature
T_{1tot}	Inlet total temperature
T_{wall}	Wall temperature
Tu	Turbulence level
$u+$	Dimensionless velocity
v_1	Inlet velocity
V	Volume of the computational cell
V_{SEM}	Volume of the SEM box
$y+$	Dimensionless wall distance

Greek Symbols

κ	von Karman constant
μ_t	Eddy viscosity
ρ	Density
σ	Turbulent length scale of the SEM box
σ_k	Constant of the KEM model
τ	Time constant of the SEM box

References

1. Dhamankar, N.; Blaisdell, G.; Lyrintzis, A. An Overview of Turbulent Inflow Boundary Conditions for Large Eddy Simulations (Invited). In Proceedings of the 22nd AIAA Computational Fluid Dynamics Conference, Dallas, TX, USA, 22–26 June 2015. [CrossRef]
2. Jarrin, N.; Benhamadouche, S.; Laurence, D.; Prosser, R. A synthetic-eddy-method for generating inflow conditions for large-eddy simulation. *Int. J. Heat Fluid Flow* **2006**, *27*, 585–593. [CrossRef]
3. Bhaskaran, R.; Lele, S.K.; Eaton, J.K.; Moin, P. *Large Eddy Simulation of High Pressure Turbine Cascade*; Stanford University: Stanford, CA, USA, 2010.
4. Gourdain, N.; Gicquel, L.Y.M.; Morata, E. Comparison of RANS simulation and les for the prediction of heat transfer in a highly loaded turbine guide vane. In Proceedings of the 9th European Conference on Turbomachinery: Fluid Dynamics and Thermodynamics, Istanbul, Turkey, 21–25 March 2011; Volume 2, pp. 847–862. [CrossRef]
5. Morata, E.C.; Gourdain, N.; Duchaine, F.; Gicquel, L. Effects of free-stream turbulence on high pressure turbine blade heat transfer predicted by structured and unstructured LES. *Int. J. Heat Mass Transf.* **2012**, *55*, 5754–5768. [CrossRef]
6. Jee, S.; Joo, J.; Medic, G. Large-Eddy Simulation of a High-Pressure Turbine Vane with Inlet Turbulence. In Proceedings of the ASME Turbo Expo 2016, Seoul, Korea, 13–17 June 2016; Volume 2D; Turbomachinery, GT2016–56980. [CrossRef]
7. Bertolini, E.; Pieringer, P.; Sanz, W. Large Eddy Simulation of a Transonic Linear Cascade with Synthetic Inlet Turbulence. In Proceedings of the ASME Turbo Expo 2020, London, UK, 22–26 June 2020; Volume 2C; Turbomachinery, GT2020–14461.
8. Arts, T.; Lambert de Rouvroit, M.; Rutherford, A.W.; Von Karman Institute for Fluid Dynamics. *Aero-Thermal Investigation of a Highly Loaded Transonic Linear Turbine Guide Vane Cascade: A Test Case for Inviscid and Viscous Flow Computations*; Technical Note Von Karman Institute for Fluid Dynamics; von Karman Institute for Fluid Dynamics: Sint-Genesius-Rode, Belgium, 1990.

9. Giles, M.B. Nonreflecting boundary conditions for Euler equation calculations. *AIAA J.* **1990**, *28*, 2050–2058. [CrossRef]
10. Bertolini, E.; Pieringer, P.; Sanz, W. Prediction of Separated Flow Transition Using LES and Transitional RANS Model. In Proceedings of the ASME Turbo Expo 2019, Phoenix, AZ, USA, 17–21 June 2019; Volume 2C; Turbomachinery, GT2019–90214.
11. Pope, S.B. *Turbulent Flows*; Cambridge University Press: Cambridge, UK, 2000.
12. Franck, N.; Ducros, F. Subgrid-Scale Stress Modelling Based on the Square of the Velocity Gradient Tensor. *Flow Turbul. Combust.* **1999**, *62*, 183–200. [CrossRef]
13. Yoshizawa, A.; Horiuti, K. A Statistically-Derived Subgrid-Scale Kinetic Energy Model for the Large-Eddy Simulation of Turbulent Flows. *J. Phys. Soc. Jpn.* **1985**, *54*, 2834–2839. [CrossRef]
14. Poletto, R.; Craft, T.; Revell, A. A New Divergence Free Synthetic Eddy Method for the Reproduction of Inlet Flow Conditions for LES. *Flow Turbul. Combust.* **2013**, *91*, 1–21. [CrossRef]
15. Liu, Y. Aerodynamics and heat transfer predictions in a highly loaded turbine blade. *Int. J. Heat Fluid Flow* **2007**, *28*, 932–937. [CrossRef]

International Journal of
Turbomachinery
Propulsion and Power

MDPI

Article

Unsteady Simulation of a Transonic Turbine Stage with Focus on Turbulence Prediction

Wolfgang Sanz * and David Scheier

Institute for Thermal Turbomachinery and Machine Dynamics, Graz University of Technology, 8010 Graz, Austria; david.scheier@hotmail.com
* Correspondence: wolfgang.sanz@tugraz.at; Tel.: +43-316-873-7229

Abstract: The flow in a transonic turbine stage still poses a high challenge for the correct prediction of turbulence using an eddy viscosity model. Therefore, an unsteady RANS simulation with the k-ω SST model, based on a preceding study of turbulence inlet conditions, was performed to see if this can improve the quality of the flow and turbulence prediction of an experimentally investigated turbine flow. Unsteady Q3D results showed that none of the different turbulence boundary conditions could predict the free-stream turbulence level and the maximum values correctly. Luckily, the influence of the boundary conditions on the velocity field proved to be small. The qualitative prediction of the complex secondary flows is good, but there is lacking agreement in the prediction of turbulence generation and destruction.

Keywords: transonic turbine stage; unsteady flow simulation; secondary flow; turbulence prediction; turbulence boundary conditions

check for updates

Citation: Sanz, W.; Scheier, D. Unsteady Simulation of a Transonic Turbine Stage with Focus on Turbulence Prediction. *Int. J. Turbomach. Propuls. Power* **2021**, *6*, 36. https://doi.org/10.3390/ijtpp6030036

Academic Editor: Antoine Dazin

Received: 21 July 2021
Accepted: 24 August 2021
Published: 27 August 2021

Publisher's Note: MDPI stays neutral with regard to jurisdictional claims in published maps and institutional affiliations.

Copyright: © 2021 by the authors. Licensee MDPI, Basel, Switzerland. This article is an open access article distributed under the terms and conditions of the Creative Commons Attribution (CC BY-NC-ND) license (https://creativecommons.org/licenses/by-nc-nd/4.0/).

1. Introduction

Although CFD codes are already highly developed and able to predict the flow even through very complex geometries, still assumptions and simplifications are necessary concerning turbulence. The correct prediction of turbulence in a highly loaded turbine stage using a RANS approach still poses a challenge. Therefore, experiments in test rigs at realistic flow conditions where turbulence data are also acquired support the development and evaluation of CFD codes.

Therefore, at Graz University of Technology, Göttlich et al. [1] performed Laser Doppler Velocimetry (LDV) in a transonic turbine stage, where they measured the unsteady velocity and turbulence in planes after the stator and rotor. Based on the experimental data, Pieringer et al. [2] studied the secondary flow effects and the interaction of the rotor tip leakage vortex with the main flow with a steady CFD simulation. Since the agreement with the measurements was not completely satisfying, the fillets of the nozzle blades were additionally modelled, but the agreement with the measurements did not improve [3].

In a new attempt, Pecnik et al. [4] applied different turbulence models in the steady simulation of the transonic stage, where the k-ω SST model by Menter [5] could best predict the flow separation at the trailing edge of the stator blade, but deviations to the measurement data still remained. Therefore, in this work, based on [6], a further attempt with an unsteady simulation of the transonic stage flow using the k-ω SST model is presented where particular attention was paid to the comparison of the measured turbulence after the rotor with the predicted one. This shall help to clarify the limitations of RANS simulations in predicting turbulence in highly loaded transonic turbine stages.

2. Test Facility and Experimental Data

The Institute for Thermal Turbomachinery and Machine Dynamics at Graz University of Technology has been operating a transonic test turbine as a cold-flow, open-circuit facility since 2001. The first test object was a transonic turbine stage where laser Doppler

velocimetry (LDV) was used to measure the unsteady flow [1]. Figure 1 (left) shows the meridional flow contour with stator and rotor blade and the main dimensions. The convergent–divergent flow path accelerates the flow to supersonic velocities. Stagnation values of pressure and temperature were measured with probes 66 mm in front of the stator leading edge and the outlet static pressure was measured in a plane 158 mm downstream of the stator leading edge. Geometrical data of the blades and important operating conditions are summarized in Table 1. The profile geometry of the 24 stator blades and the 36 rotor blades is indicated in Figure 1 (right). These blade numbers implicate a circumferential periodicity of 30 deg.

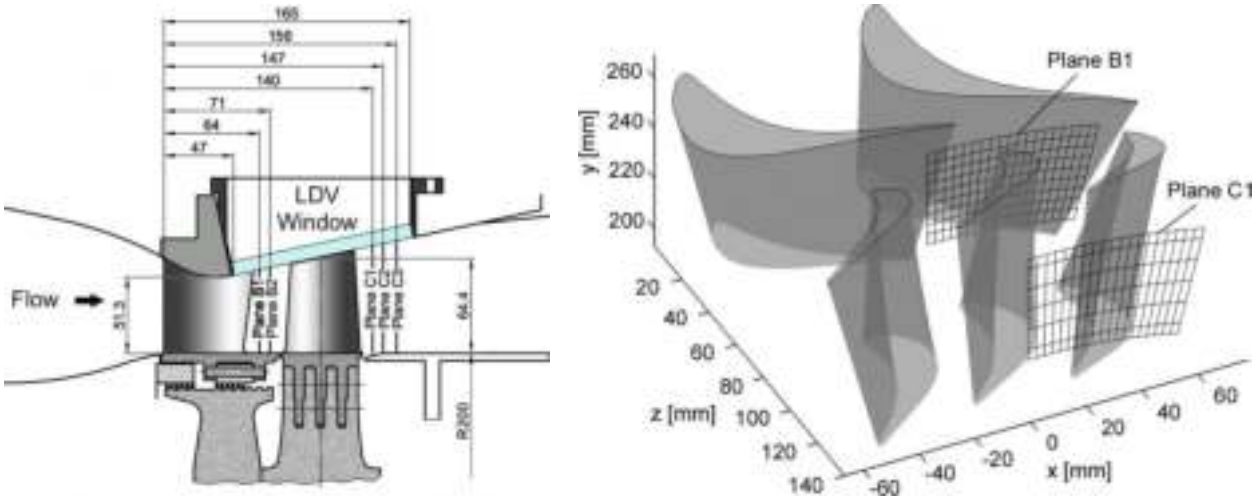

Figure 1. Meridional view of flow channel (**left**) and blade contours with measurement planes (**right**).

Table 1. Stage geometrical data and operating conditions.

Number of nozzle guide vanes	24
Number of rotor blades	36
Nozzle chord (mid-span) [mm]	78.9
Nozzle turning angle [deg.]	70
Rotor blade chord (mid-span) [mm]	55.9
Rotor blade turning angle [deg.]	107
Nozzle height at exit [mm]	55.1
Rotor blade height at exit [mm]	69.2
Tip clearance/blade height [%]	1.4
Pressure ratio $p_{tot,in}/p_{out}$	3.50
Reynolds number nozzle exit	2.57×10^6
Reynolds number rotor blade exit	1.69×10^6

In the outer casing a glass window was mounted to allow LDV access to the flow channel. LDV data were collected in plane B1 after the stator and plane C1 after the rotor (see Figure 1). The measurement domain covered 15 deg. circumferential spacing (=1 stator pitch), so that by correct phase shifting the full periodic domain of 30 deg. corresponding to 2 stator and 3 rotor channels could be obtained. Due to reflections at the hub and the glass window, the measurements covered approximately 25% to 88% relative span in B1 and 25% to 80% relative span in C1 (see Figure 1, right). Nine radial lines in plane B1 and seven radial lines in plane C1 were traversed with 20 measurement positions per line, where approximately 80,000 velocity bursts were collected. They were assigned to the proper rotor position, i.e., 40 different stator-rotor positions per rotor blade pitch (=10 deg.), with the help of a trigger signal provided by the shaft monitoring system.

In order to get the turbulence locally and over time by the variance, the instantaneous velocity vector $\mathbf{v}_i$ of each burst was decomposed as follows

$$\mathbf{v}_i = \bar{\mathbf{v}} + \mathbf{v}' = \bar{\bar{\mathbf{v}}} + \tilde{\mathbf{v}} + \mathbf{v}' \quad (1)$$

where $\bar{\mathbf{v}}$ is the ensemble-averaged velocity, $\bar{\bar{\mathbf{v}}}$ is the time-averaged velocity, $\tilde{\mathbf{v}}$ is the periodic velocity component, and $\mathbf{v}'$ is the unresolved velocity component, i.e., the turbulent fluctuation. With 40 evaluation windows, the number of velocity samples per window was still high enough to allow the determination of mean value and level of turbulence at reasonable uncertainty. For a confidence level of 95%, an uncertainty of 3.5 m/s in and 0.9 m/s outside the rotor wake for the ensemble-averaged velocity as well as 11 m/s in and 2.5 m/s outside the rotor wake for the unresolved velocity were found.

Since a two-dimensional LDV system was applied, only the velocities in the axial and circumferential direction were measured. Therefore, for the calculation of the turbulence kinetic energy k reliable estimations on the fluctuations in radial direction were needed. For this, turbulence measurements with a CTA system, performed by Bauinger et al. [7] inside a two-stage configuration in our test rig, were analyzed and the ratio of the radial fluctuations to the mean of the axial and circumferential fluctuations was evaluated. In a plane after the turning strut of the turbine center frame, the average ratio was 1.08 with a standard deviation of 0.4. In a plane shortly after the LP blade, the average ratio was 0.77 with a standard deviation of 0.17. Based on this ratio, the turbulence kinetic energy k can be estimated as

$$k = (0.69 \div 0.77)(\overline{u'^2} + \overline{v'^2}) \quad (2)$$

For the following comparisons with the measurement data, a ratio of 0.75 was used, which corresponds to the variance of the radial fluctuations as the mean of the variances in the two other directions. Compared to the lower value of 0.69, this means an overestimation of k by 8%.

Another uncertainty comes from the definition of the turbulence kinetic energy in the simulations based on a Favre- (mass-) averaging of velocity (see Equation (3)). A simple estimation of the error due to the different definitions showed only for the case of very high turbulence deviations of 2%, whereas it is mostly below 1% [6].

$$k_{Favre} = \frac{1}{2\bar{\rho}}(\overline{\rho u''^2} + \overline{\rho v''^2} + \overline{\rho w''^2}) \quad (3)$$

3. Numerical Setup

3.1. Flow Solver

The computations were performed with the Navier–Stokes code LINARS, developed at the Institute for Thermal Turbomachinery and Machine Dynamics (ITTM) by Pecnik et al. [4], which has been successfully utilized for the solution of numerous applications. The code solves the compressible Reynolds averaged Navier–Stokes equations in conservative form by means of a fully implicit, time-marching, finite-volume method. Structured grids are utilized in multi-block assignment. The code is parallelized based on the grid blocks.

The inviscid fluxes are discretized with the upwind flux difference splitting method by Roe. A higher order of spatial accuracy for the convective fluxes is achieved through a monotone upstream-centered scheme (MUSCL). A limiter is applied to avoid numerical instabilities. The viscid flux vector at the cell interfaces is constructed in a central-differencing manner using Green's theorem. A linear set of algebraic equations is obtained by discretization in time with the Newton–Raphson procedure. For this investigation, turbulence was modelled with the k-ω SST turbulence model [5].

3.2. Computational Mesh

The block-structured computational mesh was generated with the in-house meshing tool AIGrid3D. In order to have full flow periodicity in the unsteady simulation, a 30-deg.

segment comprising two stator blades and three rotor blades had to be modelled. Figure 2 (left) shows the resulting mesh, consisting of 57 blocks. Special care was laid on the mesh quality in the rotor tip leakage, as shown by the block structure in Figure 2 (right). The total number of cells was nearly 10 million. The y+ value of all wall cells was evaluated and showed a mean value of 0.8; 97% of all cells exhibited a value below 1.2. From preceding mesh studies on similar configurations, this mesh quality proved sufficient to obtain grid independent results (see, e.g., [8]).

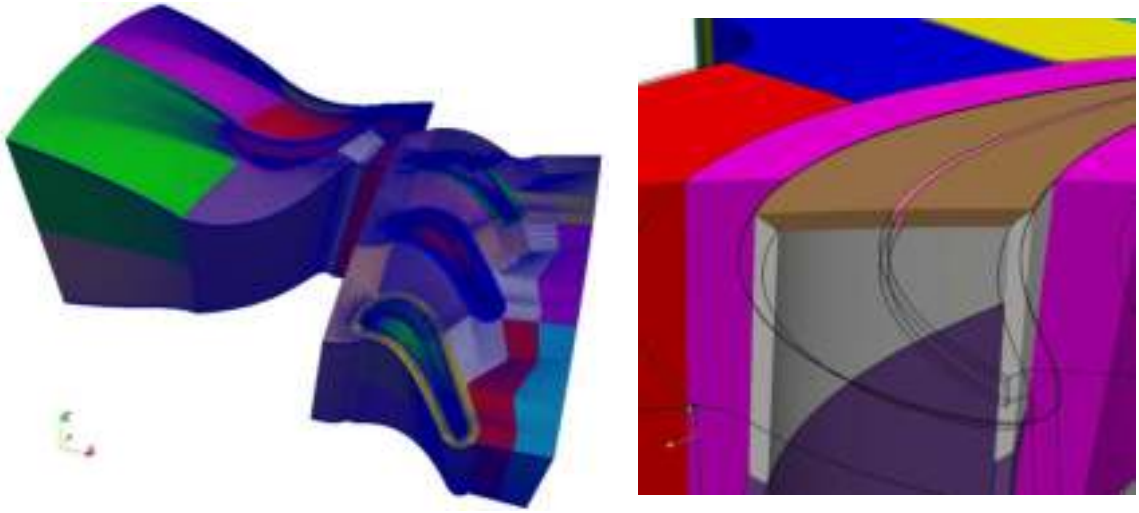

Figure 2. Computational mesh consisting of 57 blocks and nearly 10 million cells (**left**), block arrangement in the tip leakage region (**right**).

3.3. Boundary Conditions and Solver Parameters

The boundary conditions are given in Table 2. Constant total pressure and total temperature as well as axial inflow were prescribed at the inlet boundary. At the beginning, a turbulence intensity of 12% and a mixing length of 1 mm was applied and later adapted based on the comparison with the measurements (see below). At the outlet, the static pressure was prescribed at the inner contour; radial equilibrium was applied. The rotational speed was 10,617 rpm.

Table 2. Boundary Conditions.

Rotational speed [rpm]	10,617
Inlet total pressure [Pa]	3.332×10^5
Inlet total temperature [K]	402.7
Inlet turbulence intensity [%]	12/18
Inlet turbulent length scale [mm]	1/5
Outlet static pressure at inner casing [Pa]	0.90×10^5

For the unsteady simulation, a constant time-step corresponding to 1/40 deg. of rotor rotation was used, so that 1200 time iterations were necessary to cover one periodic segment of 30 deg. Periodic fluctuations were monitored and periodic convergence was achieved after 180 deg. of rotation. Data evaluation was done after one full rotation. Two Newton subiterations were used to improve the temporal accuracy. The computational time for one rotation was approx. 190 h, using 24 Intel(R) Xeon(R) X7560 8-core 2.26 GHz CPUs.

4. Results

4.1. Study of Inlet Turbulence

Figure 3 shows the absolute and relative velocity at mid-span from a 3D steady simulation illustrating the main flow features. In the stator as well as in the rotor, the flow

was strongly accelerated, resulting in two shock systems emanating from the trailing edge. The pressure-side shock was reflected at the neighboring blade suction side. The stator flow remained supersonic to the rotor inlet. In the rotor, the reflected shock was still very strong and formed a parallel shock to the suction-side trailing-edge shock leaving the rotor.

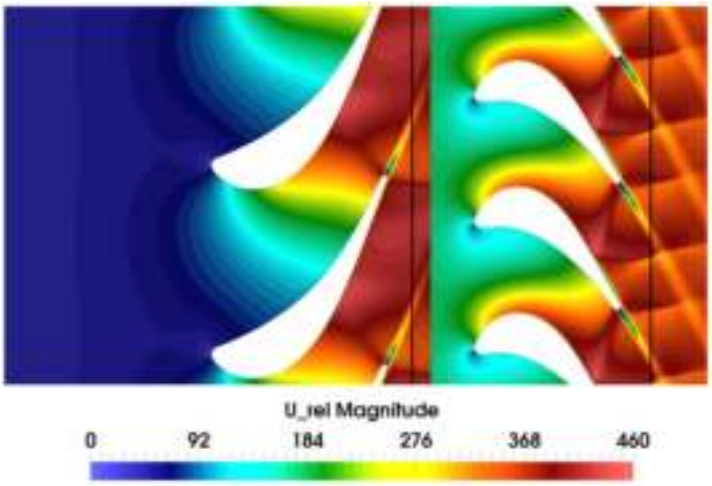

Figure 3. Absolute (stator) and relative velocity (rotor) at mid-span (steady solution).

In a steady simulation, at the mixing plane between stationary and rotating domain the turbulence kinetic energy was averaged, leading to an increase in the free-stream turbulence and an extinction of the wake turbulence. Therefore, an unsteady simulation needed to be performed in order to study turbulence generation and transport.

For the used test case, turbulence measurements in the inflow were not performed, but for other test configurations a very high turbulence intensity of 12–15% was found for the test rig. However, no data on the turbulent length scale were known. In order to find reasonable turbulence inlet boundary conditions, an unsteady Q3D flow study for varying turbulence inlet conditions was performed. The turbulence intensity was varied between 12% and 21% and the length scale between 1 mm and 50 mm. The results were compared with the measurements of the turbulence kinetic energy in planes B1 and C1, and are shown for a turbulence intensity of 12% and 18% in Figures 4 and 5, respectively. The values were averaged over time and between the flow channels.

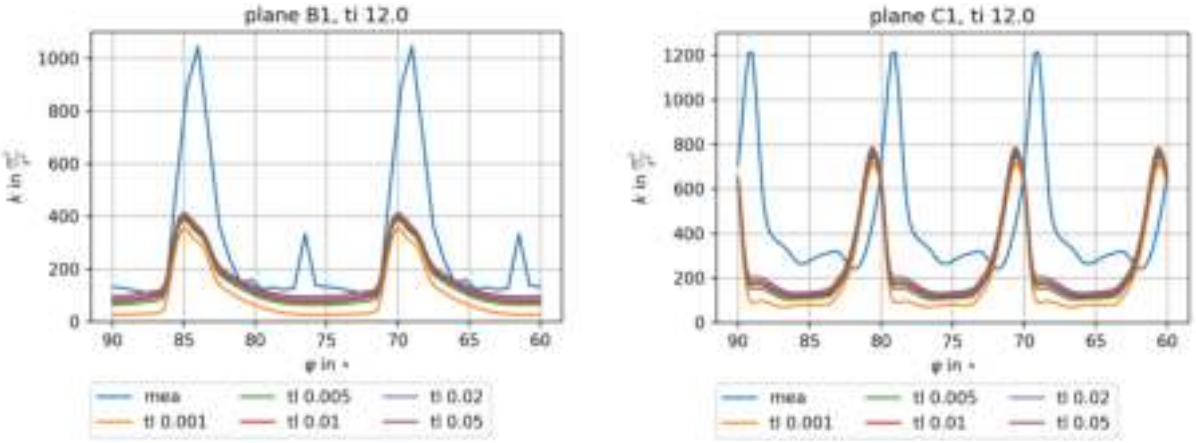

Figure 4. Comparison of turbulence kinetic energy in planes B1 (**left**) and C1 (**right**) for an inlet turbulence intensity of 12% and varying turbulence length scale (1–50 mm) (mea . . . measured) (Q3D simulation at mid-section).

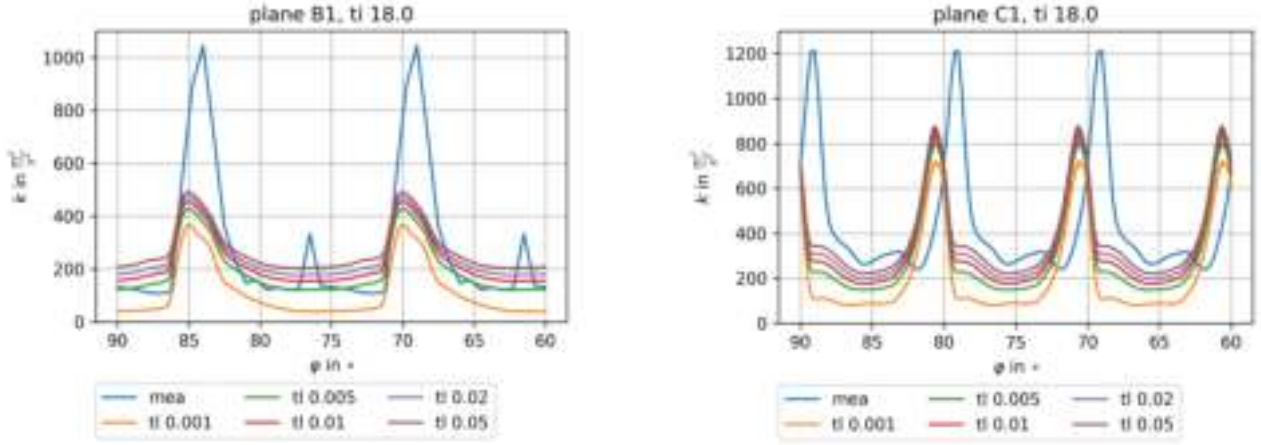

Figure 5. Comparison of turbulence kinetic energy in planes B1 (**left**) and C1 (**right**) for an inlet turbulence intensity of 18% and varying turbulence length scale (1–50 mm) (mea . . . measured) (Q3D simulation at mid-section).

The measured maximum values in the wake of approx. 1000 m^2/s^2 after the stator and 1200 m^2/s^2 after the rotor could not be achieved by far by any inlet condition. Additionally, the small second peak in B1 and C1 in mid-channel was not found. There was also a clear shift in the circumferential position of the rotor wake, which was attributed to difficulties in determining the exact rotor position with the used trigger signal.

For a turbulence intensity of 12%, there was little influence of the chosen value of the turbulent length scale. In the free-stream, a slight underprediction occurred after the stator and a strong deviation after the rotor. For an inlet turbulence of 18%, the influence of the turbulent length scale was more pronounced. For a value of 5 mm, the free-stream level after the stator was well captured, whereas the rotor free-stream turbulence was again underpredicted for all values of the turbulent length scale. The turbulence level there depends strongly on the turbulent mixing process of the incoming stator flow, which was difficult to accurately predict with a linear eddy-viscosity model. On the other hand, the high values in the stator wakes were also not found in the simulation, so that these two effects can partly explain the discrepancy in the rotor free-stream turbulence. As a compromise between stator and rotor flow agreement, a turbulence intensity of 18% and a turbulent length scale of 5 mm were chosen for the succeeding unsteady, full 3D flow simulations.

4.2. Rotor Secondary Flow

In order to better understand the turbulence generation and structures in the stage, at first the secondary flow in the rotor was presented. In Figure 6, contours of normalized streamwise vorticity (SWV) and streamlines colored by SWV explain the formation of the secondary flow in the hub region. Positive values of SWV indicate clockwise rotation. In the left figure, the streamlines originating from the horseshoe vortex at the leading edge are depicted. The pressure-side leg moved immediately towards the suction side of the neighboring blade and was pushed towards mid-span at the channel exit. It kept its strong counterclockwise sense of rotation. The suction-side leg kept its original sense of rotation only for a short term and then also switched to counterclockwise rotation. The right figure is a view from the bottom in span-wise direction. The large blue zone of counterclockwise rotation, where the pressure-side leg of the horse-shoe vortex ends, was caused by the lower channel vortex. The suction side-leg rotated slowly around the vortex core. A small zone of clockwise vorticity starting at mid-chord in the corner of hub and blade suction side was a corner vortex driven by the channel vortex. At the trailing edge region, the channel vortex moved radially upwards, resulting in a trailing edge vortex sheet together with flow coming from the pressure side. This description of the secondary flow structure followed the work by Wang et al. [9].

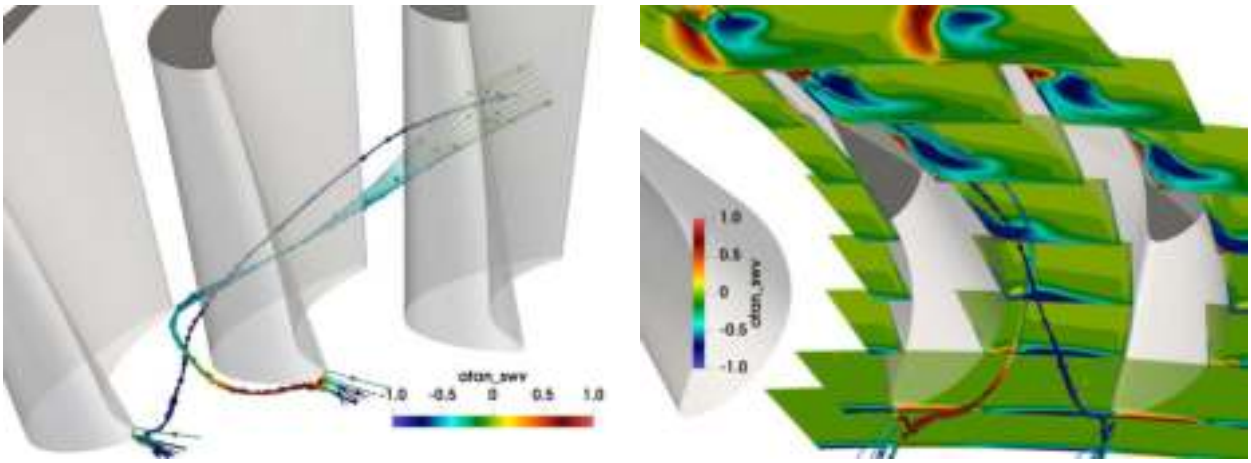

Figure 6. Streamlines and contours of normalized streamwise vorticity in the rotor hub region.

The flow in the tip region was dominated by the tip leakage vortex. In Figure 7 (left), the red streamlines coming from the pressure side and passing the tip gap and the blue slightly rotating streamlines coming from the leading edge formed together the tip leakage vortex. The diameter of the vortex increased in the aft section due to a strong backflow region in its center, as depicted in Figure 7 (right). In Figure 7 (middle), additional streamlines coming from the neighboring blade pressure side are turned towards mid-span by the tip leakage vortex, forming a strong counter-rotating vortex, the upper channel vortex. These secondary flows are also well seen in the SWV contours in Figure 8 (left). The tip leakage vortex (blue zone of counter-clockwise vorticity) formed after the leading edge and strongly grew in streamwise direction. The clockwise-rotating channel vortex wrapped around the tip leakage vortex and stretched towards mid-span. Figure 8 (right) shows the secondary flow at the channel outlet. The backflow zone dissolved, and a strong, but smaller, tip leakage vortex can be seen surrounded by the channel vortex.

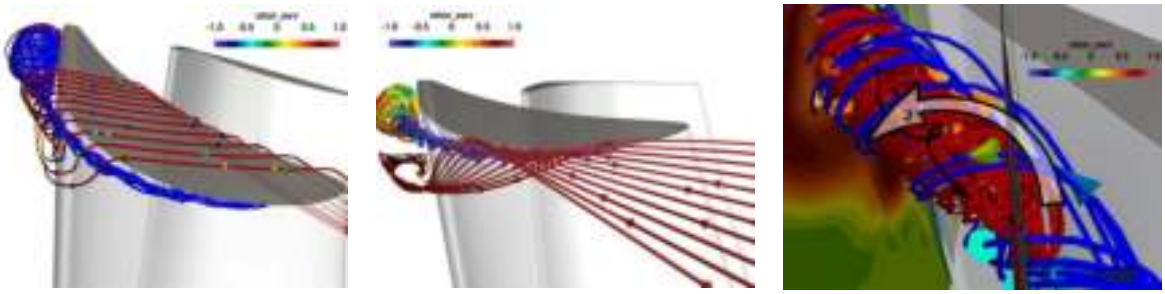

Figure 7. Streamlines in the tip region (not colored by SWV).

The effect of the described secondary flows can be clearly seen in the wall streamlines based on the wall shear stress on the rotor blade in Figure 9. On the pressure side, the flow moved towards the hub, driven by the lower channel vortex. In the tip region, there was a strong radial movement caused by the common effect of upper passage vortex and tip leakage flow. On the suction side, there was a distinct movement towards mid-span at hub and shroud. In the tip region, the limit streamline separated the counter-rotating tip leakage vortex and the upper channel vortex, as described above. A similar strong radial movement was found in the hub region. The small zone of low wall shear at mid-span indicated flow separation caused by the impinging shock there. Additional small backflow regions were found at the hub and tip.

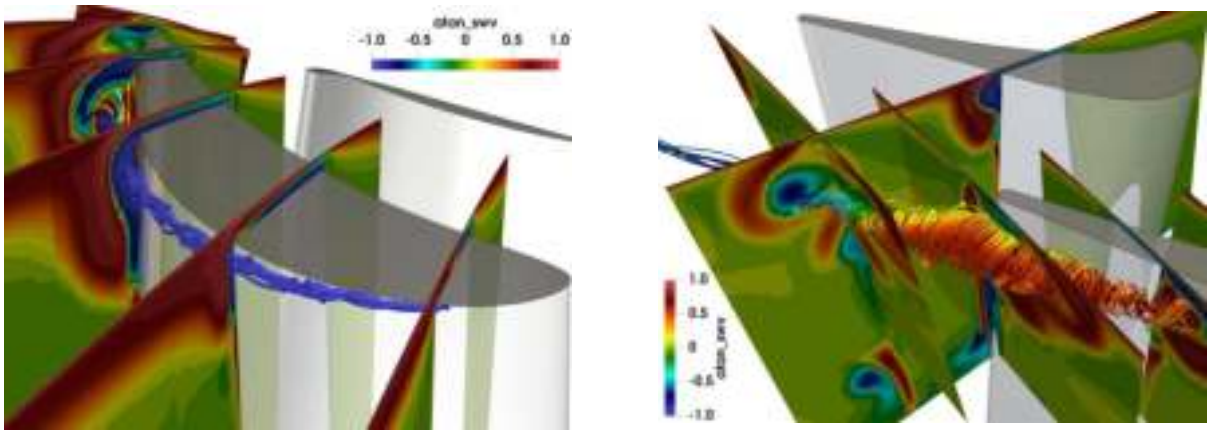

Figure 8. Contours of streamwise vorticity in the tip region.

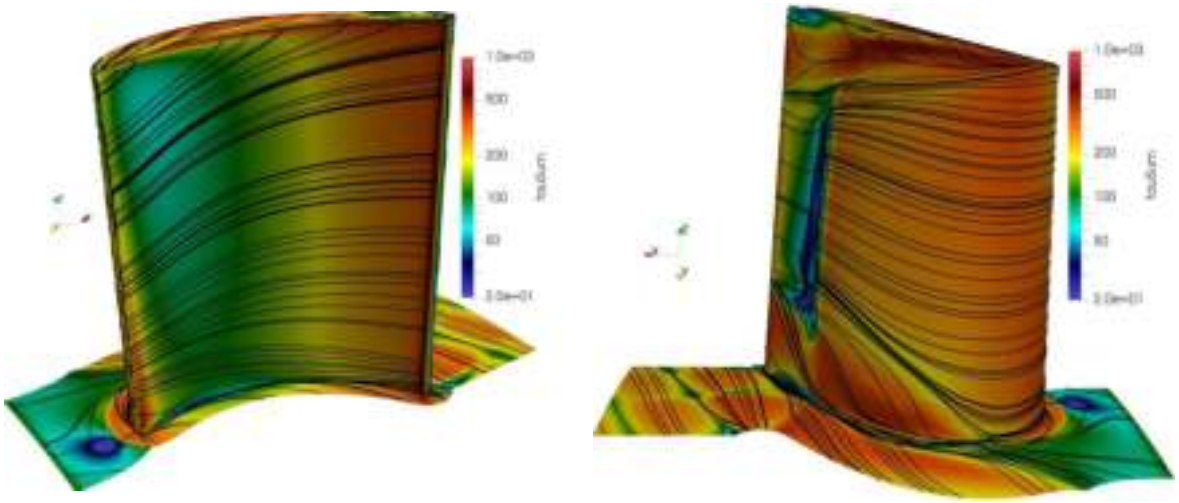

Figure 9. Wall shear stresses and streamlines on rotor blade pressure and suction side.

4.3. Unsteady Velocity Field

A comparison of the unsteady velocity field between measurements and simulation for plane C1 after the rotor is given in Figure 10. Results are shown for four time instants during 5 deg. of rotation, so that the flow repeats in the channel to the left. Simulation results are shown for turbulence inlet conditions of 18%/5 mm and 12%/1 mm to illustrate their influence. Looking at the simulation results, the three rotor wakes of lower velocity are slightly visible, moving from left to right. The flow differed remarkably between the three channels under the influence of the stator flow. The zone of higher velocity, clearly visible in the first two time instants, dissolves, whereas a new zone appears on the left in the next two time instants. In the shroud region, strong differences in velocity occurred, mainly due to the tip leakage flow. Zones of highest velocity appear close to the blue zones, indicating the backflow in the core of the leakage vortex, which varied strongly during the rotation. Comparing the numerical results of the two different turbulence inlet conditions, the main flow features were very similar, but slight differences regarding the backflow region, the shape of the wakes, and the zone of high velocity in the main flow can be clearly seen. Regarding the difference to the experimental results, it was larger than the one between the different turbulence conditions. The zone of high velocity was well predicted, but the phase lag already seen in Figures 4 and 5, led to an earlier emergence of the high-velocity zone on the left side.

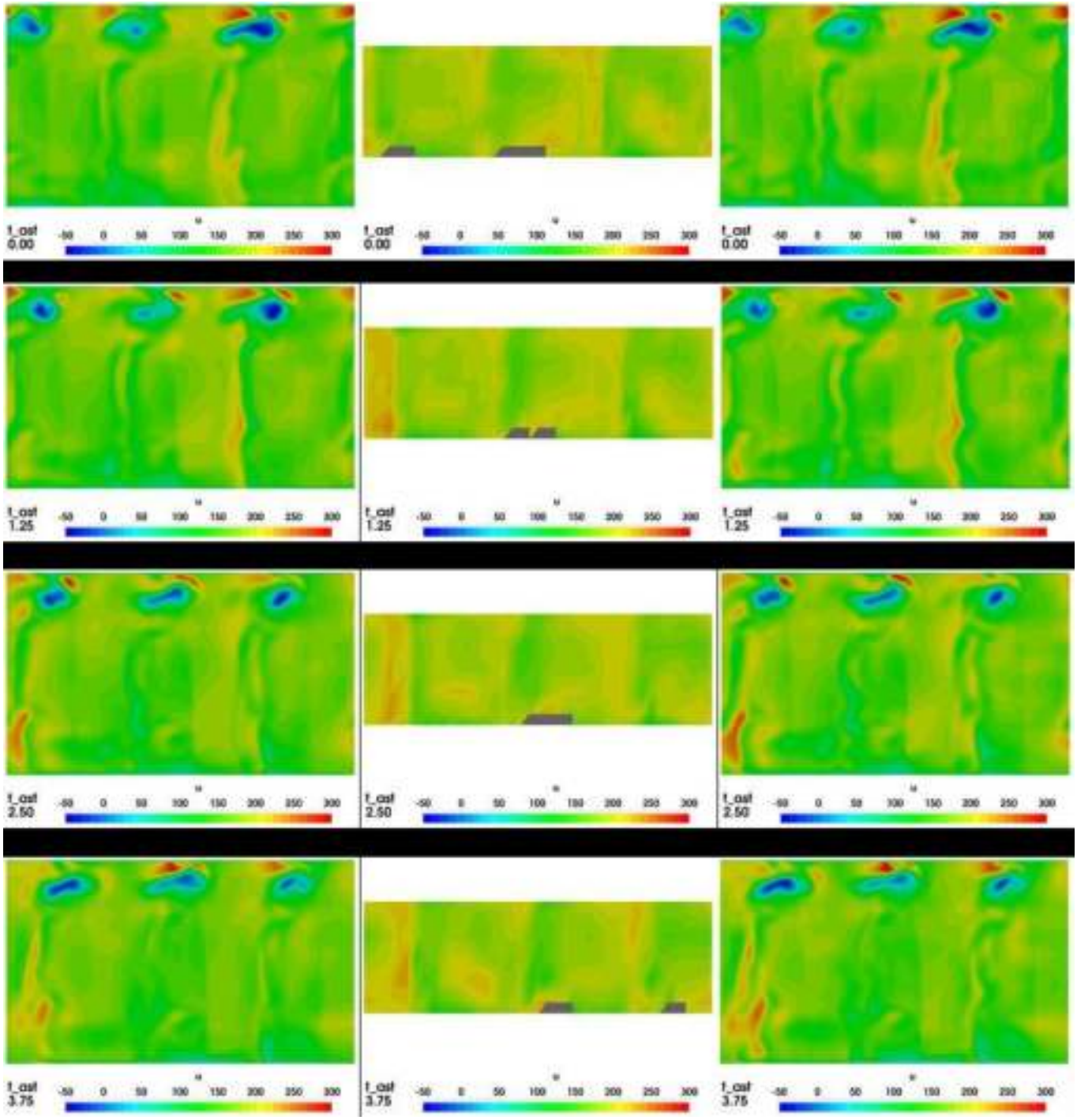

Figure 10. Instantaneous measured (**middle**) and computed (**left**: 18%/5 mm inlet turbulence, **right**: 12%, 1 mm inlet turbulence) velocity in plane C1 after the rotor (view in upstream direction).

4.4. Unsteady Turbulence Prediction

A comparison of the unsteady turbulence kinetic energy between measurements and simulation for the higher inlet turbulence case in plane C1 after the rotor is given in Figure 11. As shown in Figure 5, the predicted turbulence in the main flow was mostly lower than in the measurements, even considering the uncertainty of the measurements.

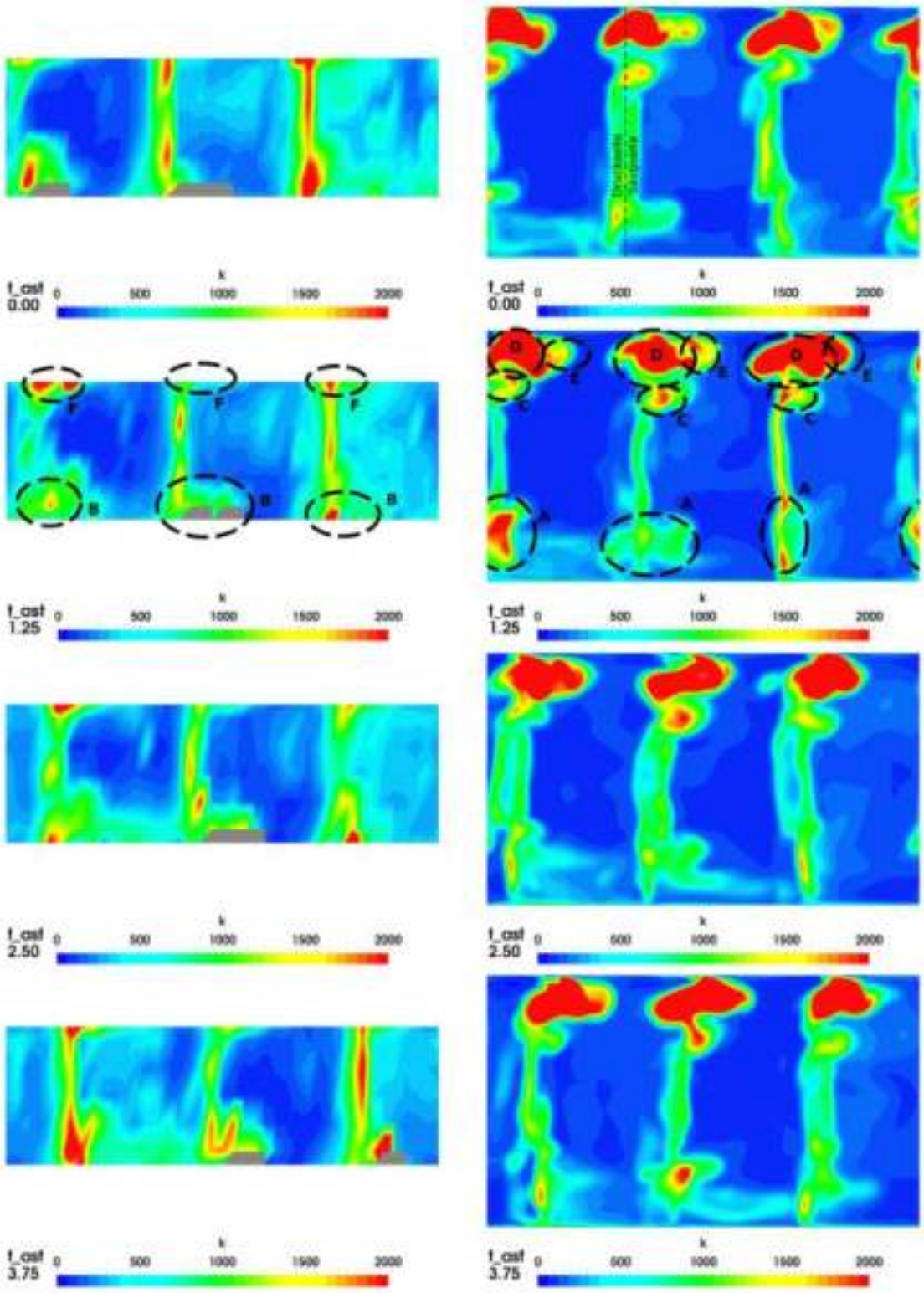

Figure 11. Comparison of instantaneous measured (**left**) and computed (**right**) turbulence kinetic energy in plane C1 after the rotor (view in upstream direction).

The maximum values in the wake flow were about half the ones in the measurements. The very high turbulence there can be explained with the secondary flows described above. Zone A at the hub came from the lower channel vortex and the trailing edge vortex sheet there. They remarkably varied in strength over time, due to the influence of the preceding

stator blades. The corresponding zone B in the measurements was located slightly more towards mid-span.

In the tip region, the zones of high turbulence correspond to the zones of high SWV in Figure 8. The zones C and D in the predictions and corresponding zone F in the measurements can be explained by the interaction of tip leakage vortex and upper channel vortex, which generated further rotating structures in the outflow region. Again, the strong variations during the rotation were remarkable. The measurements also showed temporally high values in the wake region, which can only be partly found in the computations. Measured local maxima of turbulence in the mid-channel could not be predicted.

A more quantitative comparison of the unsteady turbulence after the rotor (plane C1) is given in Figure 12, where radial distributions of the circumferentially averaged turbulence kinetic energy are given for the experimental and computational data. Additionally, the minimum and maximum values at each time instant are displayed. At most radial positions the measurements showed a distinct higher averaged turbulence kinetic energy. The minimum values were nearly identical, whereas the maximum values were remarkably higher in the measurements at all time instants. Only in the outer region similar maxima occurred, indicating that the secondary flows extended more towards mid-span in the simulations. The highest turbulence values in the simulations appeared in the tip region, where the tip leakage vortex and the upper channel vortex interacted. Strong variations over time can be detected in this region. Figure 12e displays the time average and the temporal variations of the mean distributions, which were surprisingly small despite high local and instantaneous fluctuations.

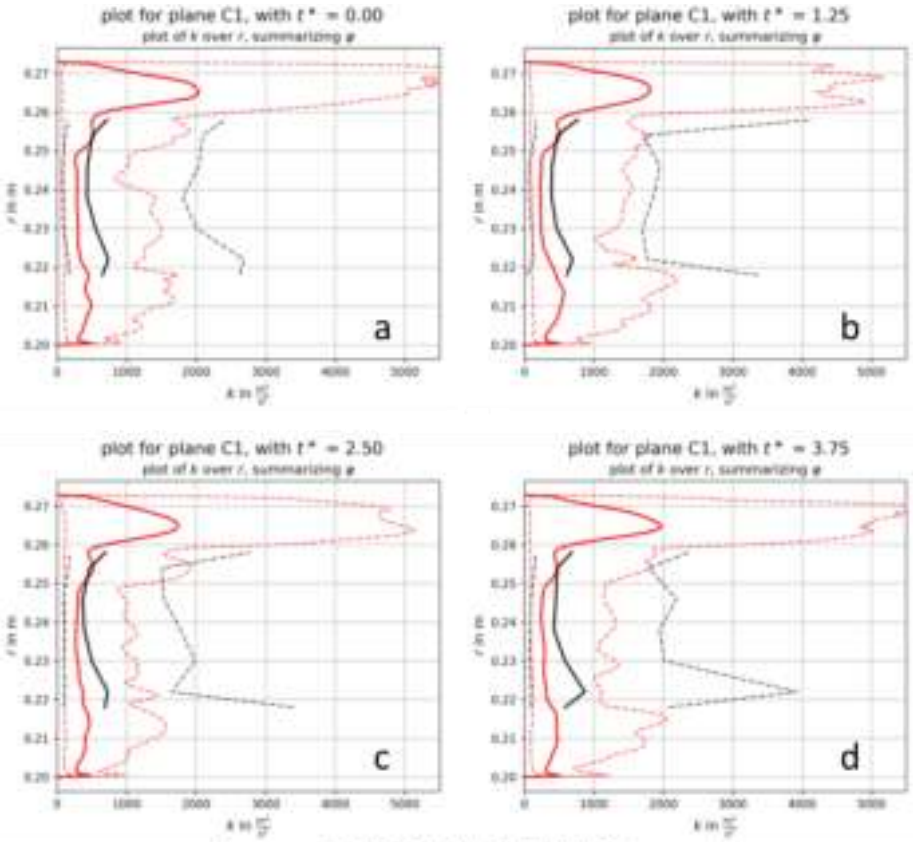

Figure 12. *Cont.*

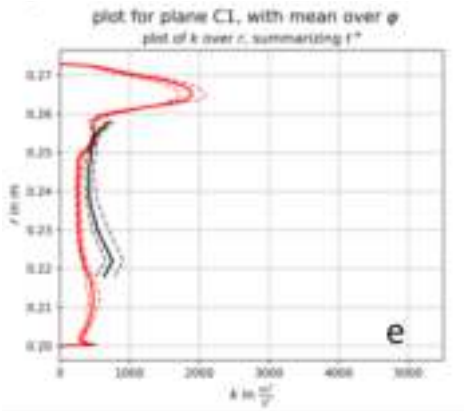

Figure 12. (**a**–**d**) Circumferentially averaged turbulence kinetic energy and minimum and maximum values in plane C1 at different time instants; (**e**) Time average of all mean distributions with variations (black: experiments; red: computations).

5. Conclusions

An unsteady flow simulation of a transonic turbine stage was performed in order to study if an unsteady simulation can give a better agreement with the measurement data than steady simulations done in the past. The turbulence inlet boundary conditions were first varied in an unsteady Q3D simulation to see their influence. None of the boundary conditions could predict the free-stream turbulence level after the rotor or the maximum values of turbulence kinetic energy in the wake, whereas the stator free-stream value could be captured.

Regarding the secondary flow, it could be well captured by the unsteady 3D simulation, although the quantitative agreement was not satisfying. Luckily, the velocity field itself after the rotor was only slightly influenced by the inlet conditions of turbulence, so that especially the time-averaged solution should be independent of them.

Regarding turbulence, it was predicted very high in the shroud region where backflow occurs inside the tip leakage vortex. However, in the mid-span region, where measurements are available, the predicted values were lower in the free-stream as well as in the wakes. This indicated that a linear eddy viscosity model is not sufficient to model the intricate generation, destruction, and mixing out of turbulence in a complex turbine flow.

Author Contributions: Conceptualization, W.S.; methodology, W.S. and D.S.; software, W.S. and D.S.; validation, D.S.; CFD investigation, D.S.; writing—original draft preparation, W.S.; writing—review and editing, W.S. and D.S.; visualization, D.S. All authors have read and agreed to the published version of the manuscript.

Funding: This research was partly funded by the Austrian Federal Ministry for Transport, Innovation and Technology within the Austrian Aeronautics Program TAKE OFF, project ALESIA.

Institutional Review Board Statement: Not applicable.

Informed Consent Statement: Not applicable.

Data Availability Statement: The measurement data this work is based on can be obtained from https://www.tugraz.at/institutes/ittm/research/downloads/measurement-data-tttf/ (accessed on 5 December 2015).

Acknowledgments: The authors gratefully acknowledge the use of HPC resources provided by the ZID of Graz University of Technology.

Conflicts of Interest: The authors declare no conflict of interest.

References

1. Göttlich, E.; Neumayer, F.; Woisetschläger, J.; Sanz, W.; Heitmeir, F. Investigation of Stator-Rotor Interaction in a Transonic Turbine Stage Using Laser-Doppler-Velocimetry and Pneumatic Probes. *J. Turbomach.* **2004**, *126*, 297–305. [CrossRef]
2. Pieringer, P.; Sanz, W.; Neumayer, F.; Gehrer, A.; Heitmeir, F. Numerical Investigation of the Three Dimensional Flow through a Transonic Turbine Stage. In Proceedings of the 5th European Conference on Turbomachinery, Prague, Czechia, 17–21 March 2003; pp. 1115–1131.
3. Pieringer, P.; Sanz, W. Influence of the Fillet between Blade and Casing on the Aerodynamic Performance of a Transonic Turbine Vane. In Proceedings of the ASME Turbo Expo, Vienna, Austria, 14–17 June 2004. Paper GT2004-53119.
4. Pecnik, R.; Pieringer, P.; Sanz, W. Numerical Investigation of the Secondary Flow of a Transonic Turbine Stage Using Various Turbulence Closures. In Proceedings of the ASME Turbo Expo, Reno, NV, USA, 6–9 June 2005. Paper GT2005-68754.
5. Menter, F.R. Two-equation eddy-viscosity turbulence models for engineering applications. *AIAA J.* **1994**, *32*, 1598–1605. [CrossRef]
6. Scheier, D. Numerische Turbulenzuntersuchung an Einer Turbinenstufe (Numerical Turbulence Investigation in a Turbine Stage). Master's Thesis, Graz University of Technology, Graz, Austria, 2016.
7. Bauinger, S.; Behre, S.; Lengani, D.; Guendogdu, Y.; Heitmeir, F.; Göttlich, E. On Turbulence Measurements and Analyses in a Two-Stage Two-Spool Turbine Rig. *J. Turbomach.* **2017**, *139*, 071008. [CrossRef]
8. Mangani, L.; Sanz, W.; Darwish, M. Comparing the performance and accuracy of a pressure based and a density-based coupled solver. In Proceedings of the ISROMACH, Honolulu, HI, USA, 10–15 April 2016. Paper No. 345.
9. Wang, H.P.; Olson, S.J.; Goldstein, R.J.; Eckert, E.R.G. Flow Visualization in a Linear Turbine Cascade of High Performance Turbine Blades. *J. Turbomach.* **1997**, *119*, 1–8. [CrossRef]

International Journal of
Turbomachinery Propulsion and Power

MDPI

Technical Note

Improvement of the Parallel Compressor Model and Application to Inlet Flow Distortion

Emmanuel Benichou *,†, Nicolas Binder *,†, Yannick Bousquet † and Xavier Carbonneau †

ISAE-SUPAERO, Université de Toulouse, 31013 Toulouse, France; yannick.bousquet@isae-supaero.fr (Y.B.); xavier.carbonneau@isae-supaero.fr (X.C.)

* Correspondence: emmanuel.benichou@isae-supaero.fr (E.B.); nicolas.binder@isae-supaero.fr (N.B.)

† These authors contributed equally to this work.

Abstract: This paper introduces a semi-analytical approach which enables one to deal with distorted inflow in axial fans or compressors. It is inspired by the classical parallel compressor (PC) theory but relies on a local flow-loading coefficient formalism. It is applied to non-uniform flow conditions to study the aerodynamic behavior of a low-speed fan in response to upstream flow distortion. Experimental measurements and 3D RANS simulations are used to evaluate the prediction of fan performance obtained with the local PC method. The comparison proves that, despite its simplicity, the present approach enables to correctly capture first order phenomena, offering interesting perspectives for an early design phase if different fan geometries are to be tested and if the upstream distortion maps are available.

Keywords: boundary layer ingestion; inlet distortion; axial fan; parallel compressors

check for updates

Citation: Benichou, E.; Binder, N.; Bousquet, Y.; Carbonneau, X. Improvement of the Parallel Compressor Model and Application to Inlet Flow Distortion. *Int. J. Turbomach. Propuls. Power* **2021**, *6*, 34. https://doi.org/10.3390/ijtpp6030034

Academic Editor: Francesco Martelli

Received: 22 June 2021
Accepted: 19 August 2021
Published: 25 August 2021

Publisher's Note: MDPI stays neutral with regard to jurisdictional claims in published maps and institutional affiliations.

Copyright: © 2021 by the authors. Licensee MDPI, Basel, Switzerland. This article is an open access article distributed under the terms and conditions of the Creative Commons Attribution (CC BY-NC-ND) license (https://creativecommons.org/licenses/by-nc-nd/4.0/).

1. Introduction

Increasingly stringent environmental constraints push the aeronautical industry to drastically decrease airplane emissions. Many theoretically promising innovative airplane technologies can be collected under the umbrella term "integrated propulsion airplanes". These are characterized by the propulsive system being conceived to operate in synergy with other airplane parts for an overall system-level energy benefit [1].

Consequently, the interactions between the propulsive system and its environment are enhanced and often lead to additional flow complexity, especially when involving Boundary Layer Ingestion (BLI). In that case, quantifying the fuel savings at the system level for a whole mission remains a very challenging issue. The StarC-ABL from NASA provides a good example: in 2016, this hybrid-electric single-aisle concept was expected to save 12% of block fuel compared to the reference baseline [2]. Later work brought the block fuel reduction to 3.4% [3] and more recent work even concluded that this configuration leads in fact to increasing block fuel up to 5.4% [4,5], largely due to a huge increase in the mass of the propulsive system. This illustrates how difficult it is to predict the performance of an innovative configuration during preliminary design with an adequate accuracy.

For this reason, new methods are needed to provide reliable performance prediction during an early design phase and, as stated by Hall [4], this means improving individual component models. Concerning propulsion with BLI, special attention must be paid to the fan aerodynamic behavior under distorted inflow conditions, in terms of stability margin and efficiency penalty, among others. Some 3D parametric studies have recently been conducted, for example, by Fernandez et al. [6], Schmollgruber et al. [7] or Habermann et al. [8]. However, the cost and complexity of these simulations remain prohibitive and the design space they explore is limited in terms of geometries, propulsor characteristics or operating conditions. Thus, usual Computational Fluid Dynamics (CFD) tools may not be adapted to a preliminary design.

This work presents an adaptation of the parallel compressor (PC) theory. This approach classically considers independent circumferential flow zones evolving through a compressor, without interacting between each other. In the present work, this theory has been modified in order to locally use a flowloading coefficient (ϕ–ψ) formalism. Instead of relying on a global performance curve, the user inputs are some basic geometric elements of the blades and flow deviation correlations. It enables dealing with any upstream flow distortion map, and the downstream flow field provided can then be averaged in order to update the corresponding fan performance.

In the first section of this paper, the local PC formulation is described in detail. Next, it is applied to a low-speed fan for two operating points with distortion. The results are compared to experimental measurements and higher-fidelity CFD simulations in order to validate the approach and discuss its limitations.

2. Local Parallel Compressor Model

The approach referred to as the parallel compressor theory was first introduced by Pearson [9] and has been extensively used to predict the impact of an inlet flow distortion on the stability limit of a fan or a compressor. The idea consists of subdividing the compressor in different segments along the circumferential direction (for an azimuthal distortion), considering each of them as independent and fed by a uniform inflow. The initial formulation assumes a steady behavior and a uniform outlet static pressure distribution, each compressor segment operating at the same rotational speed and different pressure ratios. A lot of research work has been carried out to enrich the physical modeling:

- Defining a critical extent for the distorted angular sector [10];
- Combining an analytical description with empirical results in order to determine an appropriate characteristic time [11–15];
- Coupling this approach with dynamic system modeling tools to better capture the inertia of multi-stage configurations [16–22].

Most of the time, the use of PC involves global performance, e.g., fan pressure ratio maps and efficiency penalties or pressure loss correlations when available. An example of implementation and application of classical PC can be found in [23], for example. Additional research has been carried out in order to achieve a local flow prediction. Doulgeris combined the classical parallel compressor approach with a streamline curvature (SLC) method to account for the variations in the radial direction [24]. Valencia also started from meanline modeling but added local loss correlations based on Miller's work [25], which is described as the discretized Miller approach [26]. More recently, Menegozzo presented a similar approach intended for enhancing performance prediction [27].

Less work is available with regard to the modeling of distortion itself. A two-zone model has been proposed by Budziszewski [28]: it involves boundary layer integral quantities, namely displacement and momentum thicknesses, and creates an equivalent 1D upstream distortion profile. This two-zone profile is then combined with classical parallel compressors based on clean flow performance curves, which gives access to the fan performance under distortion. This semi-analytical modeling is promising but there is room for improvement in the fan stage treatment.

In line with this philosophy, the present work aims at establishing a local method, discretizing the fan blade geometry and relying on Euler's theorem in order to produce a customized outlet flow field. This improvement makes it possible to access the 2D distortion map downstream of the rotor, from which the fan performance under distortion can then be deduced. Thus, it is a relevant tool to study a BLI propulsive configuration without resorting to costly unsteady CFD simulations.

The parallel compressor model is implemented here using a flowloading coefficient (ϕ–ψ) formalism. Given the low-speed test case, an incompressible formulation is adopted for ϕ (Equations (1) and (2)). In this framework, the fan iso-speed performance curves are all superimposed in a unique line, as pictured in Figure 1, which provides a relevant and practical linearized relationship between massflow rate and work exchange. ϕ_P represents

the transition point between compressor and turbine modes, for which there is zero global work exchange, referred to as free windmill in the following.

$$\phi = \frac{V_z}{U} \tag{1}$$

$$\psi = \frac{\Delta h_i}{U^2} \tag{2}$$

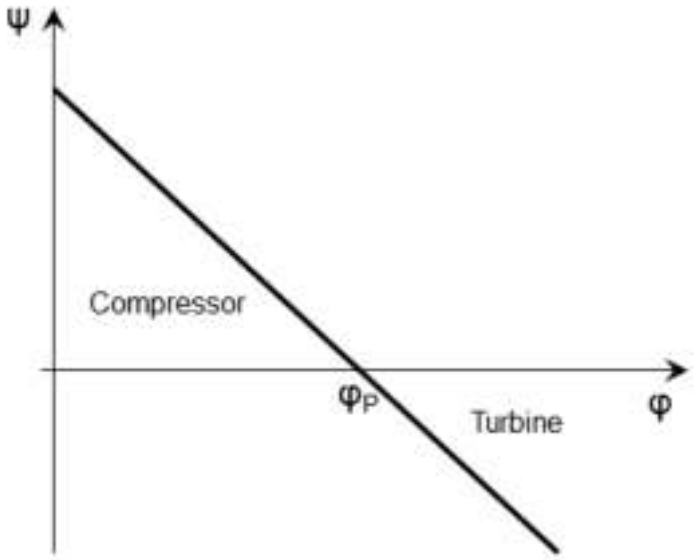

Figure 1. Performance curve plotted in the ϕ–ψ framework.

The necessary inputs are the rotor LE and TE stagger angles, the rotational speed, the target massflow rate and the 2D upstream distortion maps for total temperature, total pressure, axial velocity and absolute flow angle. Whether global or local, this type of simplified modeling requires additional information at some point. In the following, two experimental inputs are also used (see Figure 2):

- A loss correlation for the fan stage, expressed as a function of massflow rate with a second-order polynom;
- A modification of McKenzie's original law (Equation (3)) for flow deviation angle at the rotor outlet [29], based on measured radial profiles (Equation (4)). θ_c and σ refer to the blade camber and solidity, respectively. This correlation is used in the following for both presented operating points, although it should ideally be adapted to the operating conditions.

All radial velocity components are neglected. No radial equilibrium is prescribed at the outlet, which means that no radial flow redistribution is taking place. This point can be limiting, especially for off-design operating points, but as discussed by Cousins [30], it is particularly difficult to implement and has been put on hold for now.

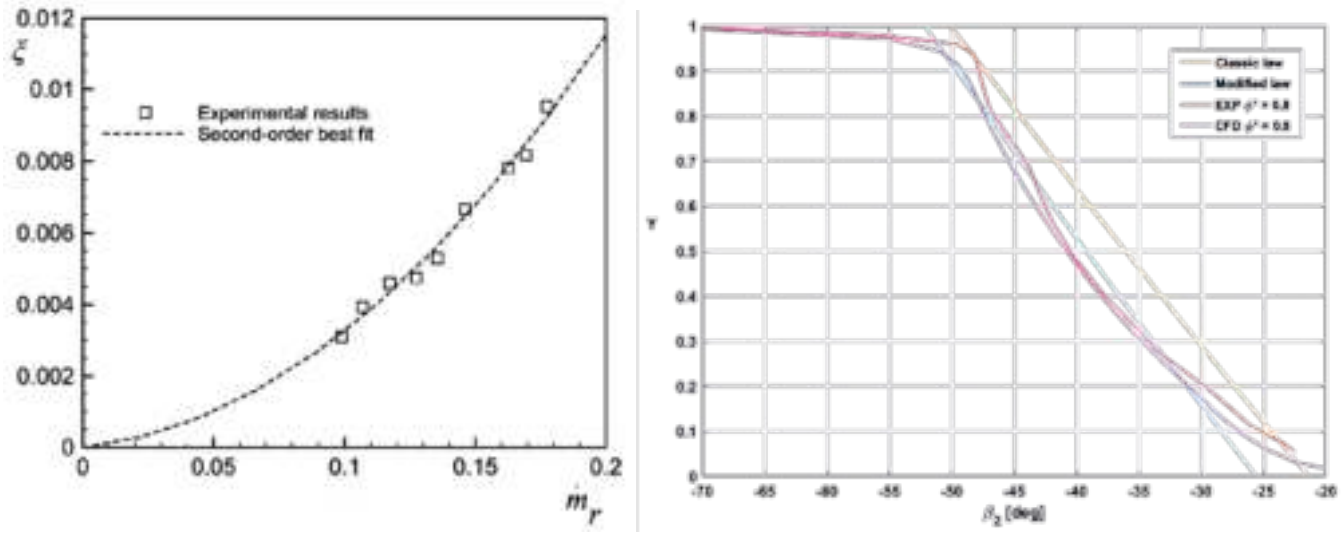

Figure 2. Loss correlation (**left**) and modified MacKenzie's law at rotor TE (**right**).

Figure 3 introduces the notations used in the following to describe the velocity triangles at the rotor LE and TE. In order to apply this model to the fan stage, two 2D meshes are created to represent the rotor LE and TE sections, as illustrated in Figure 4. In line with the principle of parallel compressors, there is no interaction between a mesh cell and its neighbors. In the following, all the quantities are mass-averaged, but in case some have to be area-averaged, the spatial discretization ensures that the surface of all the cells is the same, in order to not create an unwanted geometric weighting. In the present work, the 2D mesh is composed of 64 and 360 cells in the radial and circumferential directions, respectively. For each cell, the method follows the steps below:

1. Section 1 is initialized by sampling URANS results for four quantities: V_z, P_i, T_i, α (Figures 8 and 9) and the velocity triangles in Section 1 are calculated. Indeed, URANS maps are coherent with experimental ones (see, for example, Figure 10 for the upstream swirl angle α) and enable the use of an adequate 2D mesh while importing the exact same boundary conditions at the rotor LE for a proper comparison to 3D CFD. Section 2 is initialized by calculating the rotor relative outlet angle β_2 thanks to the modified McKenzie's law for flow deviation (Equation (5)). The axial velocity V_{z2} is initialized using massflow conservation for an incompressible flow (Equation (4)).
2. The loading coefficient ψ of the fan is calculated using a simplified analytical model (Equations (6)–(9)), valid under certain assumptions (see [31]);
3. Section 2 is updated accordingly: keeping V_{z2} and β_2 constant, accounting for pressure loss and modifying the velocity triangles. The massflow rate in Section 2 is computed and V_{z2} is corrected until massflow conservation is reached (Equation (10));
4. ψ is re-evaluated based on Euler's theorem (Equations (11) and (12)) and ϕ is updated using the same value of n as in step 2;
5. Section 1 is updated using the new value of ϕ (Equation (14)). The massflow rate in Section 1 is computed and V_{z1} is corrected until massflow conservation is reached (Equation (15));
6. ϕ is mass-averaged in Section 1 (Equation (19)) and steps 2 to 6 are repeated until convergence is reached;
7. For each radius, a mean fluid particle passage time and circumferential displacement are calculated (Equations (16)–(18)), which reshapes the resulting field in Section 2.

$$\delta_{McK}^{original} = (1.1 + 0.31\theta_c)\,\sigma^{\frac{1}{3}} \tag{3}$$

$$\delta_{McK}^{modified} = (1.1 + 0.43\,\theta_c)\,\sigma^{\frac{1}{4}} \tag{4}$$

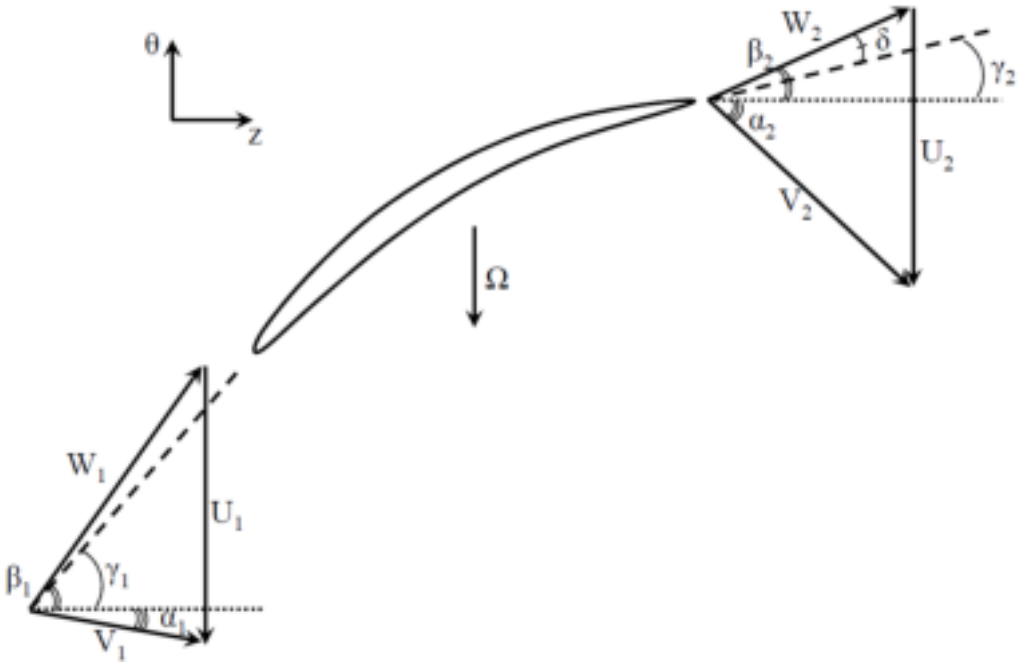

Figure 3. Velocity triangles upstream and downstream of the rotor row.

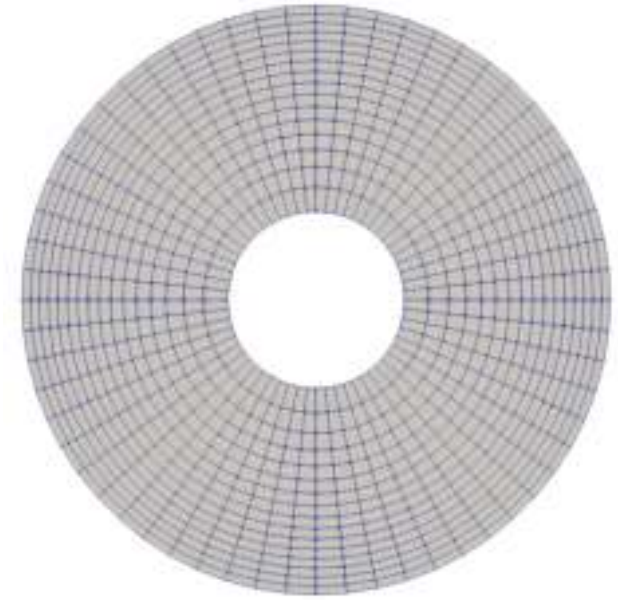

Figure 4. Example of coarsened mesh used for PC calculation.

Figure 5 depicts the associated workflow. $\dot{m}_{obj}$ refers to the target massflow rate, imposed from measurements or CFD results. $\tilde{X}$ represents the mass-averaged value of quantity X along a given annulus and depends on the radius. $\bar{X}$ represents the mass-averaged value of X in the whole 2D section. As mentioned by Valencia [32], although this method is very basic, it has some advantages, such as dealing with any distortion pattern, involving no pre-calculated fan performance map and requiring very low CPU resources.

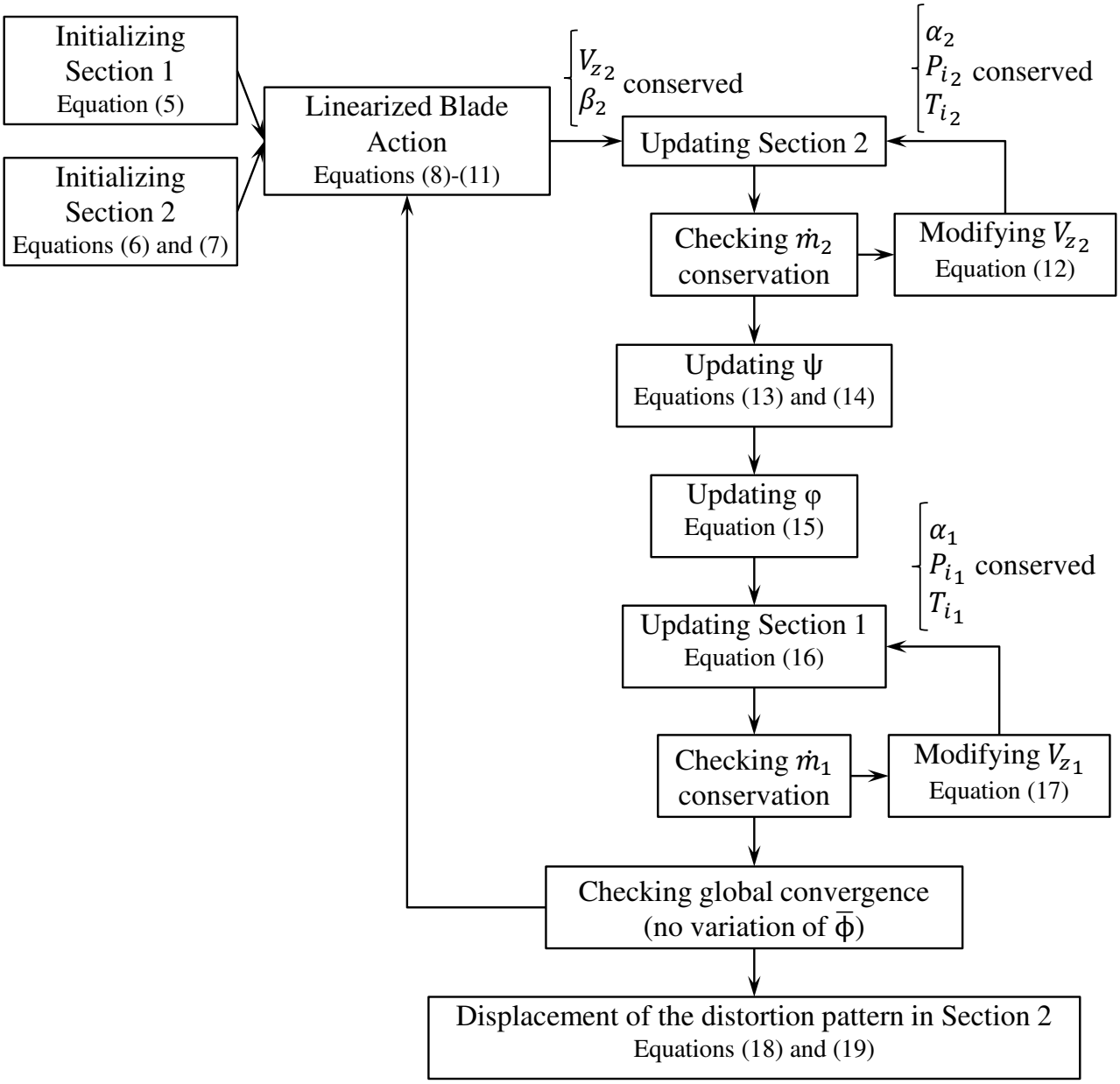

Figure 5. Local parallel compressor workflow.

$$\phi = \frac{V_{z1}}{U_2} \tag{5}$$

$$V_{z2} = V_z 1 \frac{S_1}{S_2} \tag{6}$$

$$\beta_2 = \gamma_2 + \delta_{McK} \tag{7}$$

$$k = \frac{V_{z2}}{V_{z1}} \tag{8}$$

$$u = \frac{R_1}{R_2} \tag{9}$$

$$n = k \tan \beta_2 - u \tan \alpha_1 \tag{10}$$

$$\psi = 1 + n\phi \tag{11}$$

$$V_{z2} = V_{z2} - \frac{\dot{m}_2 - \dot{m}_{obj}}{\bar{\rho}_2 S_2} \tag{12}$$

$$\Delta h_i = \frac{1}{2}\left[\left(W_1^2 - W_2^2\right) + \left(V_2^2 - V_1^2\right) + \left(U_2^2 - U_1^2\right)\right] \tag{13}$$

$$\psi = \frac{\Delta h_i}{U_2^2} \tag{14}$$

$$\phi = \frac{\psi - 1}{n} \tag{15}$$

$$V_{z1} = \phi U_2 \tag{16}$$

$$V_z 1 = V_{z1} - \frac{\dot{m}_1 - \dot{m}_{obj}}{\bar{\rho}_1 S_1} \tag{17}$$

$$\Delta t = \frac{c_z}{\frac{1}{2}\left(\tilde{V_{z1}} + \tilde{V_{z2}}\right)} \tag{18}$$

$$\Delta\theta = \frac{\frac{1}{2}\left(\tilde{V_{\theta_1}} + \tilde{V_{\theta_2}}\right)}{r}\Delta t \tag{19}$$

$$\tilde{X}(r) = \frac{\int_0^{2\pi} X\rho V_z r d\theta}{\int_0^{2\pi} \rho V_z r d\theta} \tag{20}$$

$$\bar{X} = \frac{\int_{r_{hub}}^{r_{tip}} \int_0^{2\pi} X\rho V_z r dr d\theta}{\dot{m}} \tag{21}$$

3. Higher-Fidelity CFD Simulations

In order to evaluate the local PC approach, two types of numerical simulations are presented:

- The first one is body force modeling (BFM), which consists of using source terms to reproduce the passage-averaged effect of the blades on the flow. Previous work already evaluated this approach in presence of an upstream flow distortion for a low-speed fan operating as a compressor [33]. This work is extended in this paper to a free windmilling operating point, keeping a simple distortion pattern at the inlet;
- The finest level of fidelity relies on unsteady Reynolds-averaged Navier–Stokes simulations (URANS) performed on the whole annulus of the fan stage. It represents a reference method to capture the aerodynamics of the fan with inflow distortion, but its cost still remains prohibitive for early design phases. It is shown here to complete the experimental results and to evaluate the other approaches.

3.1. Body Force Modeling (BFM)

The general idea of BFM is to avoid directly simulating the 3D geometry of a turbomachinery blade row and to fill in the bladed areas with source terms which represent the forces exerted by the blades on the fluid. The formulation retained in the present work is based on Hall's model [34] and extensively explained in Thollet's work [35]. Previous work showed that it provides satisfactory results in presence of a distorted inflow compared to URANS blade simulations for a compressor-like operating point (see [33] for the details of the implementation and the analysis). This method has also been validated using Gong's model in the case of a small turbofan under windmill conditions [36]. All the BFM simulations presented here rely on the Hall–Thollet model.

3.2. Unsteady RANS Simulations

The highest level of fidelity consists here of full-annulus URANS simulations, carried out with the *elsA* software. They feature two sliding mesh interfaces, between the inlet of the domain and the rotor and between the rotor and the stator. All the numerical

settings are presented in [33]. Except for the turbulence modeling, this approach requires no particular hypothesis. It enables oe to capture rotor-stator interactions and interblade passage phenomena and is therefore considered here as a numerical reference.

4. Validation Test Case

The test case is a low-speed cooling fan stage, designed and produced by Safran Ventilation Systems. A 3D view of the fan stage is shown in Figure 6 and its main characteristics are given in Table 1. More information about the test rig and the instrumentation used for experimental measurements can be found in Ortolan's PhD work [37].

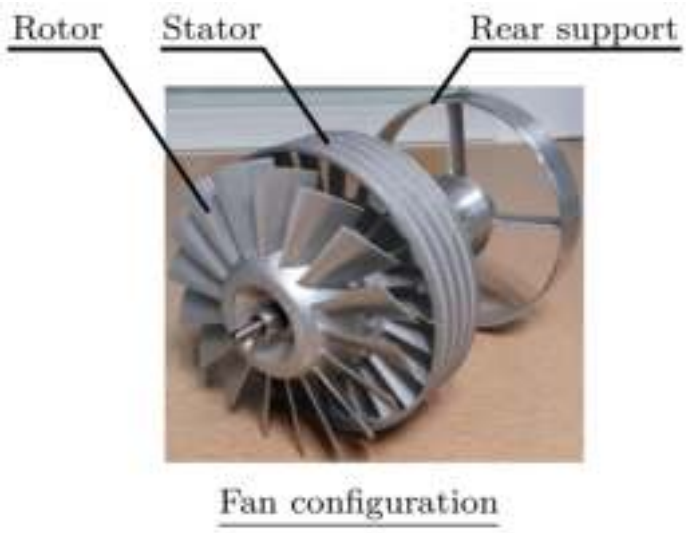

Figure 6. 3D view of the fan stage.

Table 1. Fan stage characteristics, from [37].

Diameter	$D < 200$ mm
Rotor blade count	$N_R = 17$
Stator blade count	$N_S = 23$
Design rotational speed	$\Omega \approx 12.000$ rpm
Axial Mach number	0.1–0.2

5. Distortion Patterns and Operating Points

In order to create simple patterns, two distortion grids with a uniform porosity were used (Figure 7), which results in a two-zone total pressure field for upstream conditions. The 1 mm grid was associated with a high mass-flow rate compressor-like operating point and led to a 1.7% total pressure deficit, i.e., $\frac{Pi_{min}}{Pi_{max}} = 0.983$. The 2.5 mm grid was associated with free windmill and led to a 0.3% total pressure deficit, i.e., $\frac{Pi_{min}}{Pi_{max}} = 0.997$. The combination of these operating conditions and these distortion grids was chosen in order not to operate too close to the fan stability limit and to not create too much aerodynamic blockage. The last situation actually corresponds to severe off-design flow conditions, possibly representative of a hybrid-electric aircraft configuration if a battery was to be reloaded during a descent flight phase—for example, the rotor operating as a turbine in that case. Such a combination of both windmilling regime and non-uniform upstream flow is currently not documented in the literature.

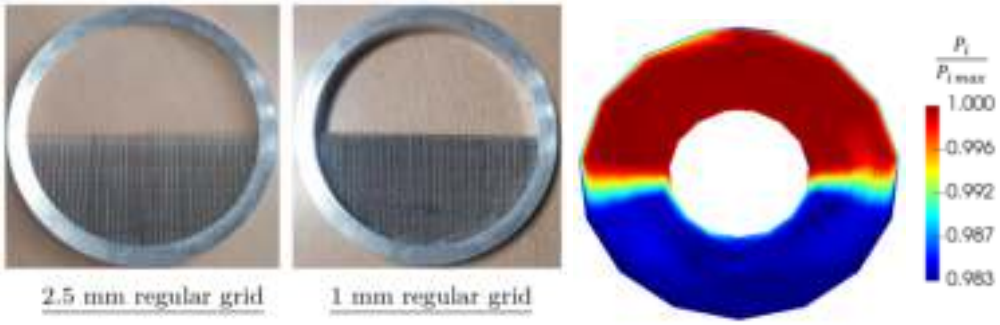

Figure 7. Distortion grids and example of measured total pressure pattern.

Figures 8 and 9 show the distortion maps extracted from the URANS results at the rotor LE. They are used as inputs to apply the local parallel compressor model as previously described. Although the targeted distortion aims at creating a total pressure deficit, a non-negligible swirl also exists near the hub in this section (Figure 10), attributed to the combination of the high radial curvature (see the front bulb in Figure 6) and the azimuthal pressure gradients at the 180° grid extremities. This point is discussed in the last paragraph.

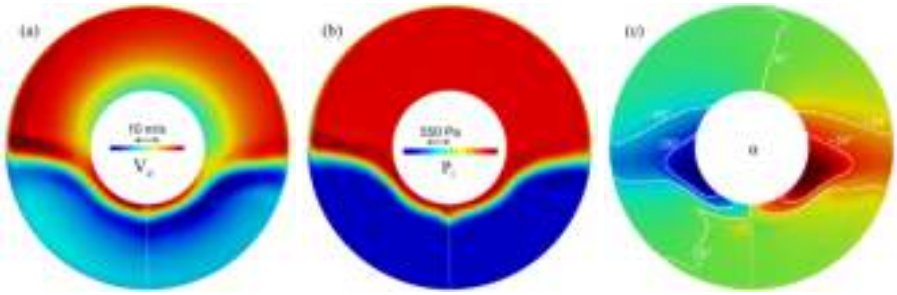

Figure 8. (**a**–**c**) Boundary conditions used in PC model for the compressor operating point (T_i is uniform).

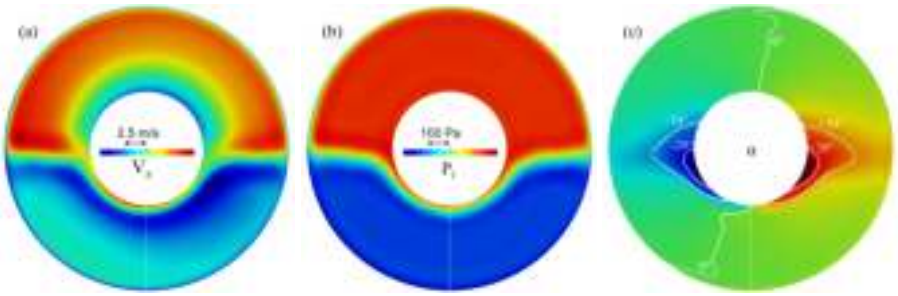

Figure 9. (**a**–**c**) Boundary conditions used in PC model at free windmill (T_i is uniform).

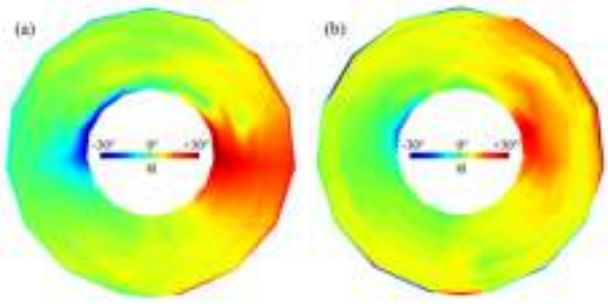

Figure 10. Swirl angle measured at rotor LE: compressor (**a**) and free windmill (**b**).

6. Results

BFM simulations are parallelized with 64 cores and URANS simulations with 512 cores, both using up-to-date CPU performance. Table 2 gives typical user times corresponding to the three approaches. The next paragraphs compare the results for the two sets of operating conditions.

Table 2. Typical user time for 1 operating point with distortion.

PC	BFM	URANS
<10 s	12 h	1 week

6.1. Compressor-Like Operating Point

Table 3 compares the prediction of global performance for the fan stage operating as a compressor: total-to-total pressure ratio π, isentropic efficiency η, total and static pressure rises across the stage ΔP_i, ΔP. These figures are not available from experimental results, as well as local values are not available downstream of the stator row. For a preliminary design phase, the accuracy of the results and the physics captured are quite satisfactory, both with parallel compressors and body force simulations. The main weakness of PC is the absence of downstream velocity redistribution; hence, the error in the static pressure rise.

Table 3. Relative discrepancy between URANS and lower-fidelity approaches.

	$\dot{m}$	π	η	ΔP_i	ΔP
BFM—URANS	+0.6%	<0.1%	+3.2%	+3.1%	+1.5%
PC—URANS	0%	+0.1%	+2.4%	+6.3%	−25.9%

Figures 11 and 12 show the stagnation pressure and temperature maps downstream of the rotor and the stator, respectively. What is shown as total temperature from the experiments is actually not directly measured but evaluated thanks to Euler's theorem from the flow turning, the main uncertainty coming in that case from the flow angle values.

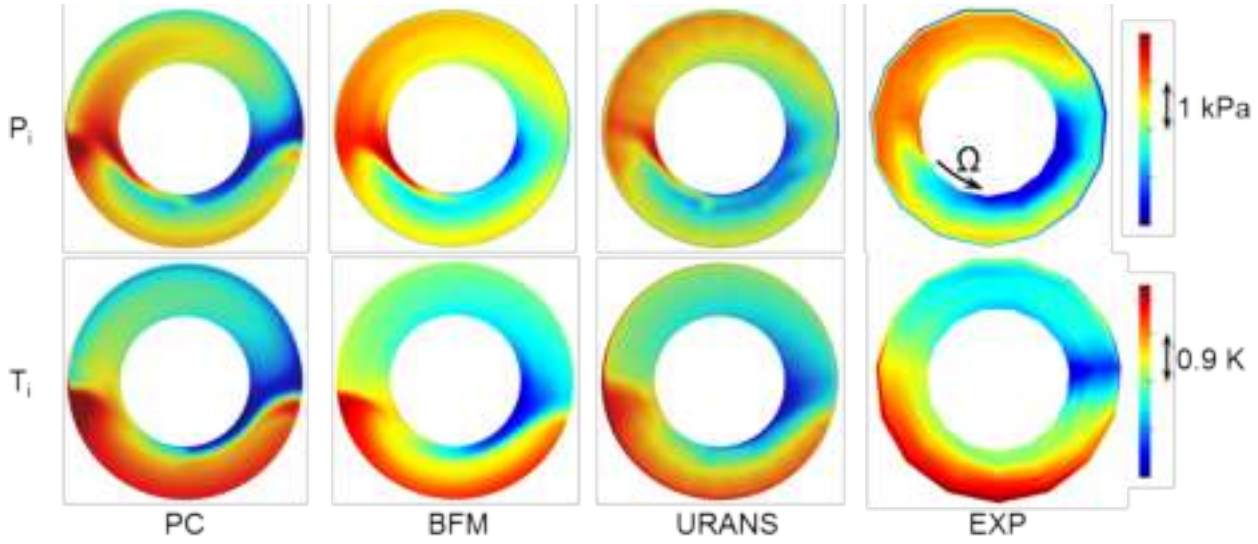

Figure 11. Total pressure (**top**) and total temperature (**bottom**) downstream of the rotor.

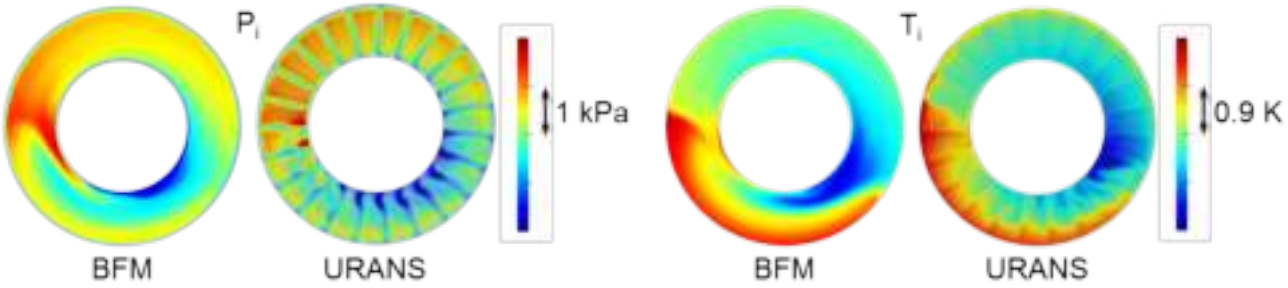

Figure 12. Total pressure (**left**) and total temperature (**right**) downstream of the stator.

6.2. Free Windmilling Operating Point

Table 4 compares the prediction of global performance for the fan stage operating under free windmill conditions: since the global work input is close to zero, the pressure ratio is close to 1 and calculating efficiency would not make sense, either as a compressor or as a turbine.

Table 4. Relative discrepancy between URANS and lower-fidelity approaches.

	$\dot{m}$	ΔP_i	ΔP
BFM—URANS	−0.1%	+51.7%	+47.2%
PC—URANS	0%	+63.2%	+50.1%

Qualitatively, the numerical results downstream of the rotor match fairly well with the experiments for total pressure (Figure 13). The local variations of total temperature are around 1K or below, which falls in the measurement uncertainty range. Experimental results are also affected by the higher level of flow unsteadiness which naturally appears for these operating conditions, which makes the flow angle values more difficult to accurately measure.

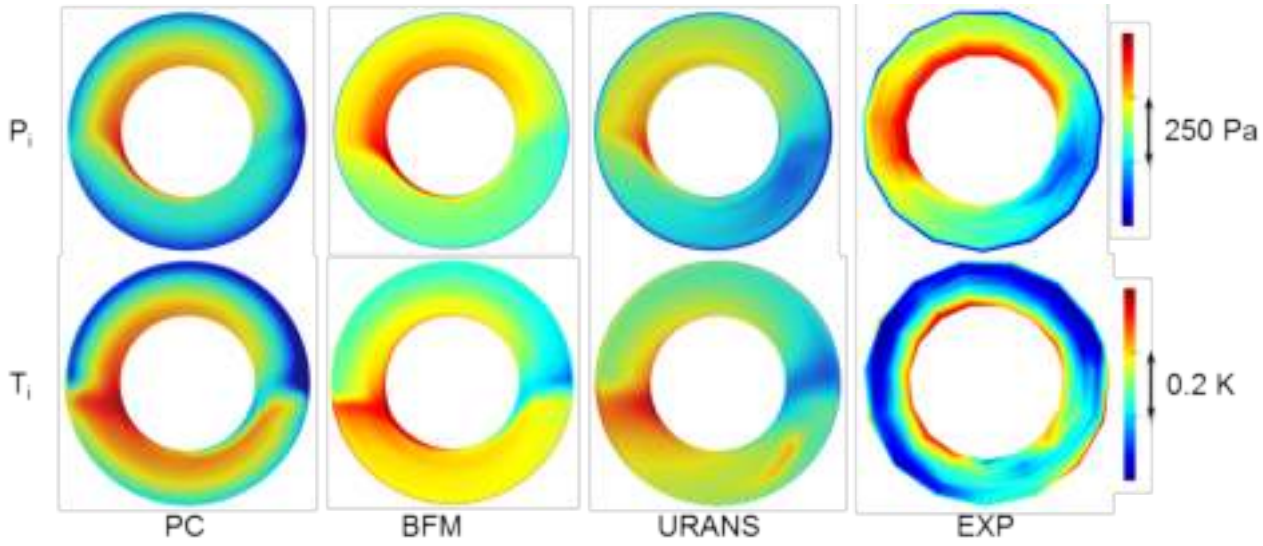

Figure 13. Total pressure (**top**) and total temperature (**bottom**) downstream of the rotor.

Concerning the stator (Figure 14), a notable discrepancy can be seen between the URANS and BFM results, despite the loss calibration. Indeed, the off-design term added in the parallel force globally increases the loss level, but not enough to account for 3D effects here. In the URANS results, each stator vane is massively separated at the LE, due to

severe flow under-incidence, and the wakes are much thicker than for the compressor-like operating point. A detailed description of the flow topology at free windmill is given by Courty-Audren et al. [38]. An interesting update of loss correlations at high negative incidence has recently been published [39,40] and could be useful in future work to improve this point. However, it should be underlined that the hypotheses behind the body force approach are particularly challenged, since the flow structures observed from URANS exhibit high gradients in the blade-to-blade direction, involving smaller length scales than for the compressor-like operating point. Figure 15 shows the axial velocity component downstream of the stator (the white line is an iso-line for the medium value of each case), revealing very different spatial distributions.

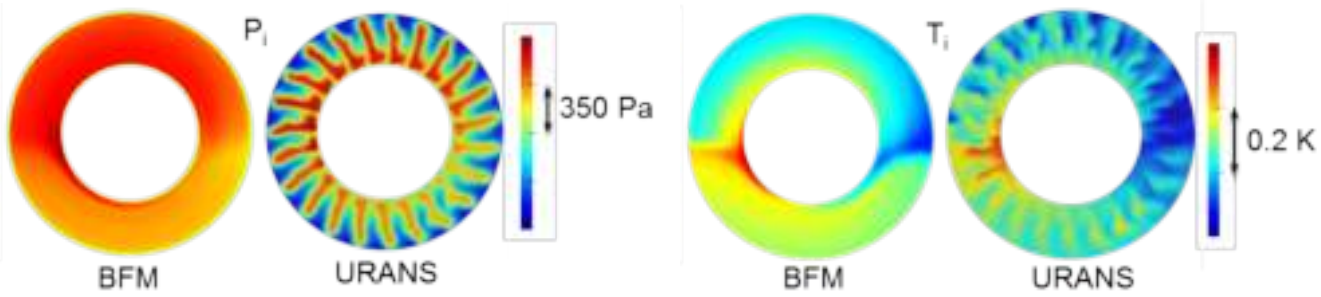

Figure 14. Total pressure (**left**) and total temperature (**right**) downstream of the stator.

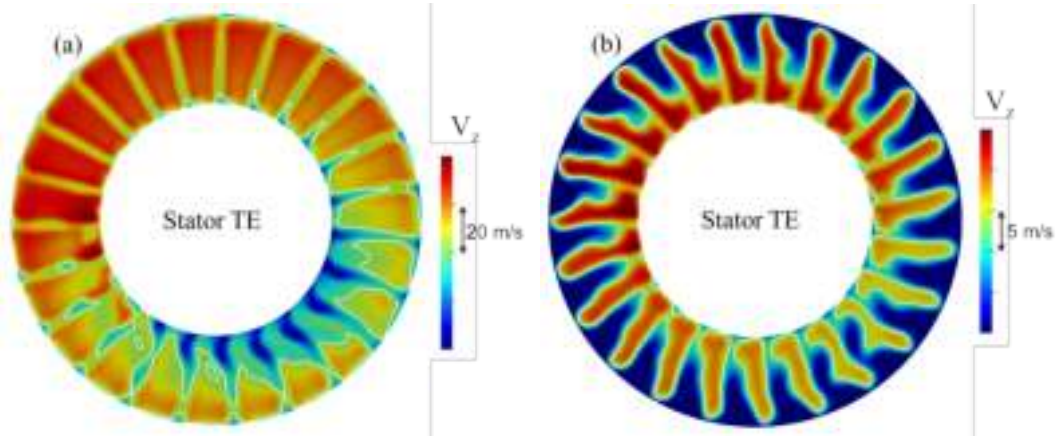

Figure 15. Axial velocity downstream of the stator: compressor (**a**) and free windmill (**b**).

6.3. Point of Attention

The previous two paragraphs show that the local parallel compressor model satisfactorily captures first order effects, provided that it is fed with correct upstream conditions. Particular attention should be paid to the upstream swirl angle, which is often neglected. In the present case, the model has been tested with uniform zero swirl and led to very different outputs (Figure 16, to be compared to Figures 11 and 13). It is in fact the main difficulty in a design context: this method is efficient for what concerns the propagation of the distortion across the fan stage but requires relevant inputs to accurately characterize the upstream distortion maps.

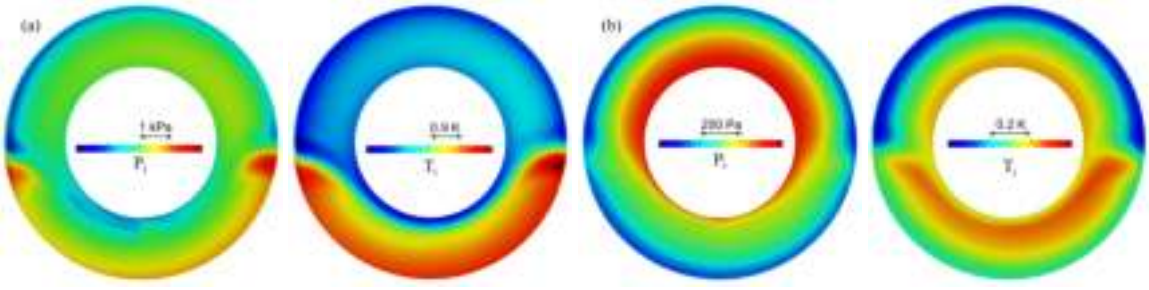

Figure 16. Total pressure and total temperature downstream of the rotor, assuming the same V_z, P_i, T_i conditions from URANS and uniform zero swirl angle: compressor (**a**) and free windmill (**b**).

7. Conclusions

This work introduces a low-fidelity method to tackle the prediction of fan performance under distorted inflow. It is compared with higher-fidelity simulations and experimental measurements. The main take-aways are the following:

- The idea of the present modeling is very simple since it relies only on the fan blade geometry and on Euler's theorem;
- Concerning the fan behavior, this tool can be used without additional inputs. However, a finer customization is possible, extracting loss or deviation calibrations from measurements or higher-fidelity CFD, for example. If this approach is to be used during an early design phase, the explored design space must be previously delimited, so that these inputs are reliable enough.
- Although the parallel compressor model can be considered as rather basic, it proves to be sufficient to provide relevant physical insight and to correctly quantify the impact of distortion on the performance near the design operating conditions;
- As could be expected, the most challenging point comes with off-design conditions and this part of the modeling can be improved;
- The use of the new formulation itself comes with a negligible CPU cost, provided that the upstream distortion maps are available.

This method provides an interesting alternative to avoid long and expensive simulations, which makes it compatible with a preliminary design phase. It can be combined with extra data and enriched in many ways. However, in addition to improving the modeling of individual components, a major perspective to increase the level of accuracy in global performance prediction remains the coupling of such an aerodynamic method with a performance tool at the system level, as recently illustrated by Pokhrel et al. [41], Lopez de Vega et al. [42] or Kolias et al. [43], so that aircraft design can beneficiate from an improved modeling of the propulsive subsystem, even for complex innovative configurations.

Author Contributions: Analytical investigation, N.B. and E.B.; numerical investigation, Y.B.; experimental validation, N.B.; supervision, X.C. All authors have read and agreed to the published version of the manuscript.

Funding: This research was funded by Safran Group.

Institutional Review Board Statement: Not applicable.

Informed Consent Statement: Not applicable.

Data Availability Statement: Not applicable.

Acknowledgments: This work was granted access to the HPC resources of CINES under the allocation 2019-A0072A06879 made by GENCI and to the HPC resources of CALMIP Supercomputing Center under the allocation 2019-P18021. The authors are grateful to Safran Ventilation Systems for the successful collaboration in the low-speed fan domain and to Safran Group for funding this study, which is part of the joint research initiative AEGIS engaged with ISAE-SUPAERO. Francesco Salvatori's contribution during his research project about parallel compressors at ISAE-SUPAERO is also acknowledged.

Conflicts of Interest: The authors declare no conflict of interest.

Abbreviations

The following abbreviations are used in this manuscript:

BLI	Boundary Layer Ingestion
CFD	Computational Fluid Dynamics
LE	Leading Edge
TE	Trailing Edge
PC	Parallel Compressors
BFM	Body Force Modeling
RANS	Reynolds-Averaged Navier–Stokes
URANS	Unsteady Reynolds-Averaged Navier–Stokes
P	pressure
T	temperature
W	relative velocity
V	absolute velocity
U	rotational speed
ρ	density
ϕ	flow coefficient
ψ	loading coefficient
δ	local deviation angle
π	pressure ratio
η	isentropic efficiency
$\dot{m}$	massflow rate
S	section surface
α	absolute flow angle
β	relative flow angle
c_z	axial chord length
θ_c	blade camber
σ	blade solidity
γ	blade metal angle
V	absolute velocity
h/H	relative span height
x, y, z	cartesian coordinates
z, r, θ	cylindrical coordinates
i	stagnation quantity
1, 2	relative to the rotor LE, TE sections

References

1. Bijewitz, J.; Seitz, A.; Hornung, M. A review of recent aircraft concepts employing synergistic propulsion-airframe integration. In Proceedings of the 30th Congress of the International Council of the Aeronautical Sciences, Daejeon, Korea, 25–30 September 2016.
2. Welstead, J.; Felder, J.L. Conceptual design of a single-aisle turboelectric commercial transport with fuselage boundary layer ingestion. In Proceedings of the 54th AIAA Aerospace Sciences Meeting, San Diego, CA, USA, 4–8 January 2016; p. 1027.
3. Bowman, C.L.; Felder, J.L.; Marien, T.V. Turbo-and Hybrid-electrified aircraft propulsion concepts for commercial transport. In Proceedings of the 2018 AIAA/IEEE Electric Aircraft Technologies Symposium (EATS), Virtual, 10–12 August 2018; pp. 1–8.
4. Hall, D.K.; Dowdle, A.; Gonzalez, J.; Trollinger, L.; Thalheimer, W. Assessment of a boundary layer ingesting turboelectric aircraft configuration using signomial programming. In Proceedings of the 2018 Aviation Technology, Integration, and Operations Conference, Atlanta, GA, USA, 25–29 June 2018; p. 3973.

5. Giannakakis, P.; Maldonado, Y.B.; Tantot, N.; Frantz, C.; Belleville, M. Fuel burn evaluation of a turbo-electric propulsive fuselage aircraft. In Proceedings of the AIAA Propulsion and Energy 2019 Forum, Virtual, 19–22 August 2019; p. 4181.
6. Fernández, A.M.; Smith, H. Effect of a fuselage boundary layer ingesting propulsor on airframe forces and moments. *Aerosp. Sci. Technol.* **2020**, *100*, 105808. [CrossRef]
7. Schmollgruber, P.; Donjat, D.; Ridel, M.; Cafarelli, I.; Atinault, O.; François, C.; Paluch, B. Multidisciplinary design and performance of the ONERA Hybrid Electric Distributed Propulsion concept (DRAGON). In Proceedings of the AIAA Scitech 2020 Forum, Virtual, 11–21 January 2020; p. 0501.
8. Habermann, A.L.; Gokhale, A.; Hornung, M. Numerical investigation of the effects of fuselage upsweep in a propulsive fuselage concept. *CEAS Aeronaut. J.* **2021**, *12*, 173–189. [CrossRef]
9. Pearson, H.; McKenzie, A. Wakes in axial compressors. *Aeronaut. J.* **1959**, *63*, 415–416. [CrossRef]
10. Reid, C. *The Response of Axial Flow Compressors to Intake Flow Distortion*; American Society of Mechanical Engineers: New York, NY, USA, 1969; Volume 79832.
11. Goethert, B.; Reddy, K. *Unsteady Aerodynamics of Rotor Blades of a Compressor under Distorted Flow Conditions (Interference Effect between Oscillating and Distorted Inlet Flow on Compressor Stall)*; Cranfield University: Bedford, UK, 1971.
12. Melick, H., Jr. *Analysis of Inlet Flow Distortion and Turbulence Effects on Compressor Stability*; Ames Research Center: Moffett Field, CA, USA, 1973 .
13. Kimzey, W. *An Analysis of the Influence of Some External Disturbances on the Aerodynamic Stability of Turbine Engine Axial Flow Fans and Compressors*; Technical Report; Arnold Engineering Development Center: Murfreesboro, TN, USA, 1977.
14. Mazzawy, R.S. Multiple Segment Parallel Compressor Model for Circumferential Flow Distortion. *J. Eng. Power* **1977**, *99*, 288–296. [CrossRef]
15. Hynes, M. Improvement of the parallel compressor model by consideration of unsteady blade aerodynamics. In Proceedings of the Propulsion and Energetics 68th (A) Specialists' Meeting, AGARD, Munich, Germany, 10–12 September 1987; Volume 400.
16. Hynes, T.; Chue, R.; Greitzer, E.; Tan, C. Calculations of inlet distortion induced compressor flowfield instability. In Proceedings of the Propulsion and Energetics 68th (A) Specialists' Meeting, AGARD, Munich, Germany, 10–12 September 1987; Volume 400.
17. Hale, A.; Davis, M. DYNamic turbine engine compressor code (DYNTECC)-theory and capabilities. In Proceedings of the 28th Joint Propulsion Conference and Exhibit, Nashville, TN, USA, 6–8 July 1992; p. 3190.
18. Shahrokhi, K.; Davis, J.M. Application of a modified dynamic compression system model to a low aspect ratio fan-effects of inlet distortion. In Proceedings of the 33rd Aerospace Sciences Meeting and Exhibit, Reno, NV, USA, 9–12 January 1995; p. 301.
19. Davis, R.L.; Yao, J. Computational approach for predicting stall inception in multistage axial compressors. *J. Propuls. Power* **2007**, *23*, 257–265. [CrossRef]
20. Fredrick, N.; Davis, M., Jr. Investigation of the Effects of Inlet Swirl on Compressor Performance and Operability Using a Modified Parallel Compressor Model. In Proceedings of the ASME 2011 Turbo Expo: Turbine Technical Conference and Exposition, Vancouver, BC, Canada, 6–10 June 2011; Volume 54617.
21. Davis, M.W., Jr.; Cousins, W.T. Evaluating complex inlet distortion with a parallel compressor model: Part 2—Applications to complex patterns. In *Turbo Expo: Power for Land, Sea, and Air*; American Society of Mechanical Engineers: New York, NY, USA, 2011; Volume 54617, pp. 13–23.
22. Floyd, R.S., Jr.; Davis, M.W., Jr.; Validation of a modified parallel compressor model for prediction of the effects of inlet swirl on compressor performance and operability. In *Turbo Expo: Power for Land, Sea, and Air*; American Society of Mechanical Engineers: New York, NY, USA, 2015; Volume 56628, p. V001T01A024.
23. Escudero Saiz, A. Investigation of Analytical Models for Evaluating the Impact of Distortion on Compressor Performance and Stability [BR]-Internship. Master's Thesis, Université de Liège, Liège, Belgium, 2020.
24. Doulgeris, G.; Khaleghi, H.; Kalfas, A.; Pilidis, P. Development of a method for enhanced fan representation in gas turbine modeling. *Int. J. Rotating Mach.* **2011**, *2011*. [CrossRef]
25. Miller, D.; Wasdell, D. *Off-Design Prediction of Compressor Blade Losses*; C279/87; Japan Science and Technology Agency: Tokyo, Japan, 1987; pp. 249–258.
26. Valencia, E.; Hidalgo, V.; Nalianda, D.; Laskaridis, P.; Singh, R. Discretized Miller approach to assess effects on boundary layer ingestion induced distortion. *Chin. J. Aeronaut.* **2017**, *30*, 235–248. [CrossRef]
27. Menegozzo, L.; Benini, E. Meanline calculation of surge margin loss due to inlet flow distortion. In *Turbo Expo: Power for Land, Sea, and Air*; American Society of Mechanical Engineers: New York, NY, USA, 2020.
28. Budziszewski, N.; Friedrichs, J. Modelling of a boundary layer ingesting propulsor. *Energies* **2018**, *11*, 708. [CrossRef]
29. McKenzie, A.B. Axial flow fans and compressors. In *Aerodynamic Design and Performance*; Gower Technical: Tokyo, Japan, 1997.
30. Cousins, W.T.; Davis, M.W., Jr. Evaluating complex inlet distortion with a parallel compressor model: Part 1–Concepts, theory, extensions, and limitations. In *Turbo Expo: Power for Land, Sea, and Air*; American Society of Mechanical Engineers: New York, NY, USA, 2011; Volume 54617, pp. 1–12.
31. Binder, N. *Aéro-Thermodynamique des Turbomachines en Fonctionnement Hors-Adaptation*; Université de Toulouse: Toulouse, France, 2016.
32. Valencia, E.; Nalianda, D.; Laskaridis, P.; Singh, R. Propulsion system analysis using a parametric and the parallel compressor approach to model distortion in Boundary Layer Ingestion systems. *Part G J. Aerosp. Eng.* **2014**. [CrossRef]

33. Benichou, E.; Dufour, G.; Bousquet, Y.; Binder, N.; Ortolan, A.; Carbonneau, X. Body Force Modeling of the Aerodynamics of a Low-Speed Fan under Distorted Inflow. *Int. J. Turbomach. Propuls. Power* **2019**, *4*. [CrossRef]
34. Hall, D.; Greitzer, E.; Tan, C. Analysis of fan stage conceptual design attributes for boundary layer ingestion. *J. Turbomach.* **2017**, *139*, 071012. [CrossRef]
35. Thollet, W. Body Force Modeling of Fan—Airframe Interactions. Ph.D. Thesis, ISAE-SUPAERO, Toulouse, France, 2017.
36. Dufour, G.; Thollet, W. Body Force Modeling of the Aerodynamics of the Fan of a Turbofan at Windmill. In *Turbo Expo: Power for Land, Sea, and Air*; American Society of Mechanical Engineers: New York, NY, USA, 2016; Volume 49712, p. V02CT39A045.
37. Ortolan, A. Aerodynamic Study of Reversible Axial Fans with High Compressor/Turbine Dual Performance. Ph.D. Thesis, ISAE-SUPAERO, Toulouse, France, 2017.
38. Courty-Audren, S.K.; Ortolan, A.; Carbonneau, X.; Binder, N.; Challas, F. Numerical analysis of secondary flow topologies of low-speed axial fans from compressor to load-controlled windmill. In Proceedings of the 12th European Conference on Turbomachinery Fluid dynamics & Thermodynamics ETC12, Stockholm, Sweden, 3–7 April 2017.
39. Ferrer-Vidal, L.E.; Schneider, M.; Allegretti, A.; Pachidis, V. A Loss and Deflection Model for Compressor Blading at High Negative Incidence. *J. Turbomach.* **2019**, *141*, 121001. [CrossRef]
40. Righi, M.; Ferrer-Vidal, L.; Pachidis, V. Body-force and mean-line models for the generation of axial compressor sub-idle characteristics. *Aeronaut. J.* **2020**, *124*, 1–19. [CrossRef]
41. Pokhrel, M.; Shi, M.; Ahuja, J.; Gladin, J.; Mavris, D.N. Conceptual Design of a BLI Propulsor Capturing Aero-Propulsive Coupling and Distortion Impacts. In Proceedings of the AIAA SciTech 2019 Forum, San Diego, CA, USA, 7–11 January 2019; p. 1588.
42. López de Vega, L.; Dufour, G.; García Rosa, N. Fully Coupled Body Force–Engine Performance Methodology for Boundary Layer Ingestion. *J. Propuls. Power* **2021**, *37*, 192–201. [CrossRef]
43. Kolias, I.; Alexiou, A.; Aretakis, N.; Mathioudakis, K. Axial Compressor Mean-Line Analysis: Choking Modelling and Fully-Coupled Integration in Engine Performance Simulations. *Int. J. Turbomach. Propuls. Power* **2021**, *6*, 4. [CrossRef]

International Journal of
Turbomachinery Propulsion and Power

MDPI

Article

Dimensionless Numbers Relationships for Outer Air Seal of Low Pressure Turbine †

Kacper Pałkus [1,2,*] and Piotr Strzelczyk [1]

[1] The Faculty of Mechanical Engineering and Aeronautics, Rzeszow University of Technology, al. Powstańców Warszawy 8, 35-959 Rzeszów, Poland; piotstrz@prz.edu.pl
[2] Doctoral School of Engineering and Technical Sciences, Rzeszow University of Technology, 35-959 Rzeszów, Poland
* Correspondence: kacp.palkus@gmail.com
† This paper is an extended version of our paper published In Proceedings of the European Turbomachinery Conference ETC14, Gdansk, Poland, 12–16 April 2021.

Abstract: The dimensional analysis and the numerical parametric study of the typical outer air seal from a low-pressure turbine were performed in the framework of the presented paper. The most crucial variables for the flow through the outer air seal were identified and further dimensionless numbers were derived. The dependent quantities resulting from the analysis were: the axial Reynolds number (formulated with the bulk velocity, corresponding to the mass flow through the seal), the outlet swirl ratio (incorporating the exit flow angle, important for mixing) and the windage heating (related to the internal losses). Additionally, the discharge coefficient was cross-checked enabling further comparison with the available literature. The comprehensive numerical parametric study included all important contributors for the flow through the seal with a parameter operating range appropriate for engine outer air seals.

Keywords: outer air seal; dimensional analysis; low pressure turbine; CFD

check for updates

Citation: Pałkus, K.; Strzelczyk, P. Dimensionless Numbers Relationships for Outer Air Seal of Low Pressure Turbine. *Int. J. Turbomach. Propuls. Power* **2021**, *6*, 33. https://doi.org/10.3390/ijtpp6030033

Academic Editor: Francesco Martelli

Received: 28 May 2021
Accepted: 19 August 2021
Published: 24 August 2021

Publisher's Note: MDPI stays neutral with regard to jurisdictional claims in published maps and institutional affiliations.

Copyright: © 2021 by the authors. Licensee MDPI, Basel, Switzerland. This article is an open access article distributed under the terms and conditions of the Creative Commons Attribution (CC BY-NC-ND) license (https://creativecommons.org/licenses/by-nc-nd/4.0/).

1. Introduction

Recent advances in the Low-Pressure Turbines (LPT), dealing with super-critical profiles, ultra-thin trailing edges, and ultra-high lift blade shapes, to name a few, lead to the borders of maximal efficiency of these machines. However, there are still several areas that need further development because of their efficiency potential margin. One such field is the Outer Air Seals (OAS). In LPT, the most frequently applied concept is the labyrinth seal combined with abradables such as honeycombs. Labyrinth seals are already a very well-known solution—effective and reliable. Thus, they are the perfect choice for aircraft engines.

The majority of the labyrinth seals research was carried out for Inner Air Seals (IAS). Both kinds of seals operate under very different conditions. Since OAS are located at the outer diameter, they work at a much bigger radius than IAS. Due to that, there are locally very high circumferential Mach numbers. Moreover, at the outer diameter, configurations with two or three fins are typically applied. This is due to the fact that every additional mass at such a radius is unfavorable for the stresses of the rotating blade. Furthermore, the relative movements of the sealing parts are incomparably bigger at OAS, so that it is extremely demanding to maintain relatively small clearances between rotating and nonrotating parts. Last, but not least, OAS experience much less cooling and thus they operate at much higher temperatures, a limiting factor for many practical solutions.

1.1. Previous Work

For the previously mentioned reasons, the IAS regions were the first to attract the interest of many research groups attempting to optimize the device performance. There exist

well-performing solutions of IAS, such as the brush seals investigated for instance by Dinc et al. [1], or the turning devices by Mahle [2].

Historically, one of the first studies of labyrinth seals is due to Wittig et al. [3], who performed systematic series of measurements on the straight-through seals. They mainly concentrated on the discharge characteristics and the friction factors for various configurations. The authors indicated that the scale has a significant impact on the seal performance. This is in agreement with the current knowledge stating that when flow phenomena "scale", the similarity numbers must be preserved.

Waschka et al. [4], based on experimental evidence, suggested that the discharge behavior is dependent on the pressure ratio, the Reynolds, and the Taylor numbers. The other way to derive proper similarity numbers is through the application of Dimensional Analysis (DA). Denecke et al. [5] performed such an analysis for IAS and scaled engine conditions to the laboratory ones for 2D and 3D cases. The authors have further carried out a numerical parametric study to ascertain the influence of the derived parameters. To this aim, they have kept constant the discharge behavior and looked for the appropriate scaling of the windage heating and of the exit swirl. The main outcome of their Dimensional Analysis was that the ratios U/V_{ax}, σ, K_{out} are dependent on the following dimensionless parameters: c/R, Π, Mu, Re_U, K_{in} k, Pr, Tu.

In another work by Denecke et al. [6], the dimensionless quantities were applied to prepare the experimental research in terms of total temperature increase due to losses and swirl development in convergent and divergent stepped labyrinth IAS. The authors also indicated that accurate measurements within such small devices are extremely difficult to complete, so that that the windage heating uncertainty was estimated to lie in the 2–30% range. Their work allowed Yan et al. [7] to carry further numerical studies of stepped IAS with and without the honeycomb. Those authors have shown a good agreement of their simulations with the experiments from Denecke et al. [6]; they further provided additional characterization of the seal windage heating and leakage flow.

A lot of correlations based on measurements were presented by Zimmermann and Wolff [8]. The researchers provided a complete study of the seal discharge characteristics as a function of the pressure ratio, the clearance size, the grooves, the fins number, the honeycomb cells size, and a few other parameters typical of straight and stepped configurations.

Recently, OAS have also been extensively investigated. Szymanski et al. [9] performed CFD simulations of these devices. They studied the effects of roughness and rotational speed on flow characteristics. The authors observed the influence of the very high rotational speeds (above 15,000 RPM) on the flow characteristics for small pressure ratios. Conversely, for low roughness at higher pressure ratios (above 1.5), they indicated a very limited impact of the rotational speed. Later on, Szymanski et al. [10] also compared two different experiments with the CFD outcomes, showing good agreements. Another very detailed numerical study about OAS with honeycomb is due to Fraczek et al. [11]. They have provided radial profiles both at the seal inlet and outlet including the honeycomb rubbing. Kluge et al. [12] have shown good agreement of the numerical predictions with the experimental data obtained on a new seal rig. The authors also indicated that the local flow parameters and vortices are not captured correctly. Wein et al. [13] compared experimental data with numerical computations checking multiple variants of different turbulence models with miscellaneous corrections to find the best setup for OAS. They have shown that general vortex structures and flow characteristics in comparison to PIV and 3D-PVT measurements are well captured. Nevertheless, the local flow behavior was still not adequately predicted.

Unsteady phenomena occurring in IAS were investigated for labyrinth seals by Gao et al. [14]. They showed that LES and URANS yield reasonably good agreement with steady-state measurements. Kluge et al. [15], for isolated OAS investigated in a novel rig, have also reported some unsteady pressure fluctuations at the outlet of the device, in a certain range of operation. Their comparison of numerical and experimental results shows that CFD models are able to capture the right frequency fluctuations modes.

In the above-mentioned publications, the CFD results for IAS and OAS are found to reflect well the general flow characteristics of labyrinth seals. The literature data show that steady simulations are able to capture the trends but misrepresent the local parameters estimate. Further, extensive studies for the local flow behavior, including LES, are already under investigation to compensate for the RANS modeling deficiencies in terms of the local flow features prediction.

1.2. Objectives of the Current Work

As mentioned in the previous section, the available literature does not frequently cover OAS. It is conjectured that due to the fairly different operating conditions characterizing IAS and OAS, the existing results and achievements may deviate in the case of OAS.

The present research facilitates comparison with other researchers' outcomes, considering the significance of the already developed relations on Outer Air Seals.

To better understand the dependencies between the relevant quantities, localization of the key parameters which are crucial for OAS is needed, which is a simultaneous result of the application of DA.

A comprehensive parametric study of OAS, including all important contributors of the flow, with an appropriate parameters range for OAS and dependencies between similarity numbers, has not yet been carried out.

The present work contributes to deepening the understanding of several OAS issues and dependencies between the flow quantities; it further allows to find room for improvements in the performance of these devices.

2. Methodology

The present research deals with the aerodynamic investigation of OAS (see Figure 1). The investigation is divided into two parts. The first one consists of a Dimensional Analysis resulting in a set of dimensionless numbers characterizing the flow through the seal. The second part relies on a set of CFD investigations of typical stepped labyrinth OAS used in engine applications.

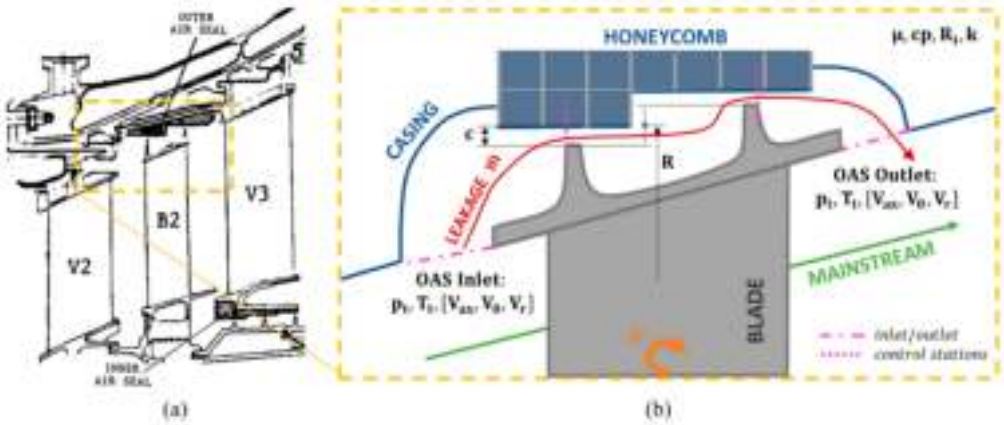

Figure 1. (**a**) A typical OAS of LPT [16]. (**b**) Meaningful quantities considered for flow through the OAS.

The aim of the research was the identification of the key factors influencing the flow through OAS and their mutual dependency. Recent studies have proven that CFD results show good agreement with experiments in terms of general flow characteristics, see e.g., [7,10]. Therefore, RANS are the proper choice for this kind of investigation. RANS directly provide averaged values of the flow quantities and, for general nondimensional relations, they are considered sufficient. Nevertheless, for several cases, URANS were also performed.

The most important quantitates used for the study (DA) are shown in Figure 1. These quantities were assumed to mainly contribute to the characteristics of the flow through the

seal. The control stations where the flow quantities were mass averaged are also marked in Figure 1.

2.1. Dimensional Analysis

The DA allowed the identification of the key parameters controlling the flow in OAS and their reduction to dimensionless numbers. The DA is based on a mathematically proven theorem by Buckingham. It leads to the proper formulation of the similarity numbers and further to the similarity laws. As described by Qing-Ming [17], the DA method at first requires the appropriate selection of the fundamental quantities which drive the physical phenomenon. It is the most crucial step in a properly carried DA. While reviewing a physical problem, one shall consider the quantities which essentially influence the phenomenon. Following this concept, in the presented study, the variables most influencing the OAS characteristics were first found. The list of quantities relevant for the flow through OAS is given in Table 1.

Table 1. Selection of quantities applied for Dimensional Analysis of OAS.

Quantities Considered Meaningful for OAS DA	c, R, N, a, R_i, μ, $p_{t,in}$, $p_{t,out}$, $T_{t,in}$, $T_{t,out}$, $\dot{m}$, $V_{\theta,in}$, $V_{\theta,out}$, $V_{r,in}$, $V_{r,out}$, $V_{ax,in}$, $V_{ax,out}$
Base units	[s], [m], [kg], [K]
Chosen independent variables	R, N, μ, $T_{t,in}$ ~[m], [s^{-1}], [kg·m^{-1}·s^{-1}], [K]
Chosen dependent variables	c, a, R_i, $p_{t,in}$, $p_{t,out}$, $T_{t,out}$, $\dot{m}$, $V_{\theta,in}$, $V_{\theta,out}$, $V_{r,in}$, $V_{r,out}$, $V_{ax,in}$, $V_{ax,out}$

A choice was made about the dependent and independent variables. This was determined by analyzing the crucial OAS aspects for LPT. Subsequently, on the basis of the DA theorem, the relations between these variables were determined. When too many quantities are prescribed they are reduced by the chosen measurement system and the redundancy is removed. The natural outcome of the procedure is a set of dimensionless numbers. It is also worth mentioning that the final form of the similarity numbers is conditioned by the choice of the fundamental unit system. In the present study, the most appropriate nondimensional numbers from the authors' perspective are given in Equation (1). For OAS, they are: the axial Reynolds number Re_{ax} (representing the mass flow behavior), the outlet swirl ratio K_{out} (corresponding to the exit flow angle, important for mixing problems), and the windage heating σ (related to the internal losses). The dimensionless relations in general form are:

$$Re_{ax}, K_{out}, \sigma = f\left(\frac{c}{R}, \Pi, K_{in}, M_u, k, \frac{p_{t,in}}{N\mu}\right) \quad (1)$$

More details on the performed dimensional analysis are given in Appendix A.

In the present study, the quantities on the right-hand side were varied and their influence on Re_{ax}, K_{out}, σ was checked. The relative clearance c/R was varied by the gap change at both fins. The geometrical features other than c/R were not varied, as this would generate too many configurations. Such geometrical dependencies were already thoroughly studied by Zimmermann and Wolf [8]. The other geometrical details of the investigated seal configuration having an impact on the seal performance are given in Appendix B. The Pressure Ratio Π was adjusted by varying the static pressure at the outlet. The inlet swirl ratio was prescribed through the velocity angle at the inlet. The circumferential Mach number M_u has been calculated at the OAS inlet for the prescribed rotational speed. The ratio of the specific heats resulted from the assumed temperature corresponding to the engine conditions. The ratio $p_{t,in}/N\mu$ was varied by changing independently the rotational speed and the total pressure at the inlet.

Another commonly used quantity for air seals is the so-called discharge coefficient defined as:

$$C_d = \frac{\dot{m}}{\dot{m}_{id}}, \quad \dot{m}_{id} = \frac{p_{t,in} \cdot A \cdot f(\Pi)}{\sqrt{T_{t,in}}}, \quad f(\Pi) = \left(\frac{1}{\Pi}\right)^{\frac{1}{k}} \cdot \sqrt{\frac{2k}{R_i(k-1)}\left[1 - \left(\frac{1}{\Pi}\right)^{\frac{k-1}{k}}\right]} \tag{2}$$

This coefficient is not an outcome of the DA. It rather refers to the velocity in an ideal nozzle according to the Saint-Venant–Wenzel formula. Denecke et al. [5] state that it incorporates much more information than just the mass flow, as it also embodies losses and flow characteristics for a specific geometry. This parameter is widely used in the engineering practice in many secondary airflow systems. Knowing the proper C_d value and the basic flow variables, with the help of Equation (2) it is possible to calculate the mass flow through gaps, orifices, wyes, connectors, or any other system. Unfortunately, C_d depends upon many parameters. Thus, it is not easy to predict its correct value. In the present research, C_d will serve only as a comparison with the available literature, rather than as an outcome of the study. Here, the OAS flow characteristics are considered to be sufficiently well described by the numbers resulting from the DA. With this approach, the factors influencing particular flow phenomena can be separated.

2.2. Numerical Setup

2.2.1. Geometry

To study the influence of the nondimensional numbers on the behavior of the general OAS flow characteristics, a series of CFD analyses were performed employing the ANSYS Workbench package.

The study was performed on a model OAS typically used in the first stage of the LPT of the Energy Efficient Engine [16]. An overview of the studied configuration is given in Figure 1. The geometry is typical of LPTs. It is an OAS cavity volume of shrouded turbine blades with two fins positioned at a considerable average radius (R = 0.538 [m]), forming, together with the honeycomb, a stepped labyrinth. For simplicity reasons, a honeycomb itself was not modeled. The influence of the honeycomb can be superimposed a-posteriori to the general behavior of the seal, as confirmed by [7,8]. The minor, irrelevant features in the OAS geometry were simplified, according to standard good practices commonly followed in CFD, to avoid potential problems and numerical errors with improper grids.

2.2.2. Mesh

The model spans a 6° sector of the outer cavity in the tangential direction (according to the engine data, [16]), and it was meshed in ICEM CFD with hexahedral structured elements. A few variants of the mesh were checked. First, following [10], the analyses with $y^+ \sim 1$ (approx. 3M cells) were prepared. Subsequently, the mesh was coarsened for the application of standard Wall Functions, resulting in $y^+ \sim 30 \div 50$ (about 300 K cells, see Figure 2). The coarse mesh quality statistics were still satisfying. Table 2 shows the influence of the spatial discretization on the parameters of interest in the presented study. For this crosscheck, three grids were built. Two with $y^+ \sim 1$ and one with coarser resolution (adopting WF) which was applied in this study.

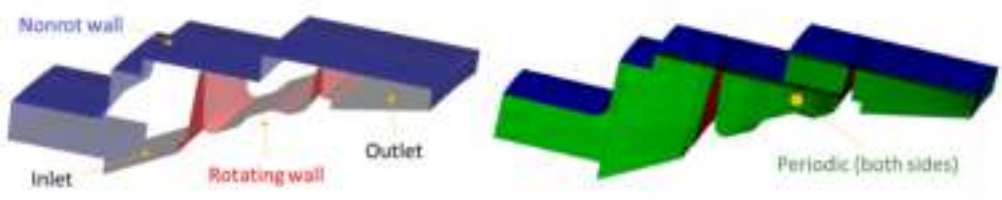

Figure 2. OAS model, boundary conditions, and mesh.

Table 2. Grid Convergence Index for the most important dimensionless OAS parameters.

	r_{21}	r_{32}	ϵ_{21}	ϵ_{32}	p	GCI_{21}	GCI_{32}
Re_{ax}	1.3	1.4	0.005	0.034	6.0	1.8×10^{-3}	2.2×10^{-3}
K_{out}	1.3	1.4	0.001	0.019	10.2	1.0×10^{-4}	1.3×10^{-4}
σ	1.3	1.4	0.011	0.047	4.2	6.6×10^{-3}	7.7×10^{-3}
Cd	1.3	1.4	0.002	0.017	6.7	5.7×10^{-4}	7.1×10^{-4}

Although there appear to be some differences in the outcomes of the different meshes in terms of the general dependencies of the characteristic parameters, in the forthcoming part of the study only the coarse grid results were considered to reduce the computational costs.

2.2.3. Boundary Conditions

The rotational periodicity was imposed on both sides of the model. The other Boundary Conditions are shown in Figure 2. At the walls, viscous flow conditions were prescribed. The rotating wall had a particular speed for each case. All walls were set to adiabatic. This assumption was considered reasonable for the general flow dependencies. The outlet was not lengthened, and use was made of the CFX functionality that automatically places a wall at each outlet section where backflow occurs. Such a solution was intended to model the flow near the outer diameter where the passing mainstream acts as a blockage for the leakage (see Figure 1). The leakage usually injects flow into the mainstream in the rear part of the cavity, and a vortex is typically created behind the second fin.

At the inlet boundary, total pressure and total temperature were set, based on the engine data. Depending on the case, the circumferential velocity angle was prescribed at the inlet, to include the pre-swirl into the simulation. The radial velocity angle at the inlet was assumed constant throughout the analyses, and equal to 45°. In engine applications, this parameter is strongly driven by the geometry. Due to the considerable extension of the OAS keep-out zones at the inlet and outlet of the device, it is impractical to influence this parameter, which is also considered to have a minor influence on the OAS operation. At the outlet boundary, a constant static pressure was imposed to keep the pressure ratio to the target value for the particular scenario. The modeled fluid was assumed compressible with a perfect gas equation of state. The specific heats and viscosity (Sutherland's formula) were considered to be dependent on the temperature (thermally perfect gas). Throughout the analyses, a medium value of the turbulence intensity $Tu = 5\%$ was assumed at the inlet boundary. Such a value was considered to well represent the flow conditions typically occurring in OAS. The Prandtl number throughout the parametric study was set to be close to 0.7.

2.2.4. Solver

The analyses were performed using ANSYS CFX. Most of them were steady state. The SST was applied as a turbulence model as advised in [10,11,15]. The limiting convergence value was set to 1×10^{-4} (rms value), but frequently it dropped below 1×10^{-5}. The simulations were carried out until all monitored parameters of interest had shown a pseudo-time constant behavior. Transient simulations were initialized from a steady solution. The numerical setup for the unsteady simulations was kept unchanged. The transient simulations were performed for several rotational speeds. The physical timestep corresponding to 1/1600 of the rotor revolution time, resulted in a maximum CFL number of about 20.

3. Results and Discussion

3.1. Axial Reynolds Number

The first dependent quantity according to Equation (1) is the axial Reynolds number Re_{ax}, expressing the ratio of the inertia to the viscous forces. Thus, applied to OAS, Re_{ax}

incorporates information about the mass flow behavior, since it can be conveniently defined as follows:

$$Re_{ax} = \frac{\rho V_{ax} c}{\mu} = \frac{\rho V_{ax} c R 2\pi}{\mu R 2\pi} = \frac{\dot{m}}{2\pi R \mu} \tag{3}$$

The outcomes from the numerical study on the axial Reynolds number are presented in Figure 3. From Equation (3), it is clear that, the bigger leakage mass flow through the OAS, the bigger the Re_{ax}. The data show that the Reynolds number strongly depends on the pressure ratio Π and the relative clearance c/R. At the higher pressure ratios (approx. 1.7), the changes in the Reynolds number and, correspondingly, in the mass flow are smaller. This is due to the chocking occurring at the fins. It is also seen that for higher pressure ratios the growth rate in the Re_{ax} weakens. Current aircraft LPT operate at considerably higher OAS pressure ratios $(1.5 \div 1.7)$ then twenty years ago (~ 1.3). For this reason, OAS regions are even more important for nowadays engines because about 20–30% more leakage mass flow goes through the seals. Another parameter that drastically influences the axial Reynolds number is the clearance size, or in terms of nondimensional quantities, the relative clearance. It is obvious that with the increasing cross-sectional area, the mass flow and the corresponding Re_{ax} will be higher. The present results and the dependencies of Re_{ax} upon Π and c/R are in agreement with [7,10].

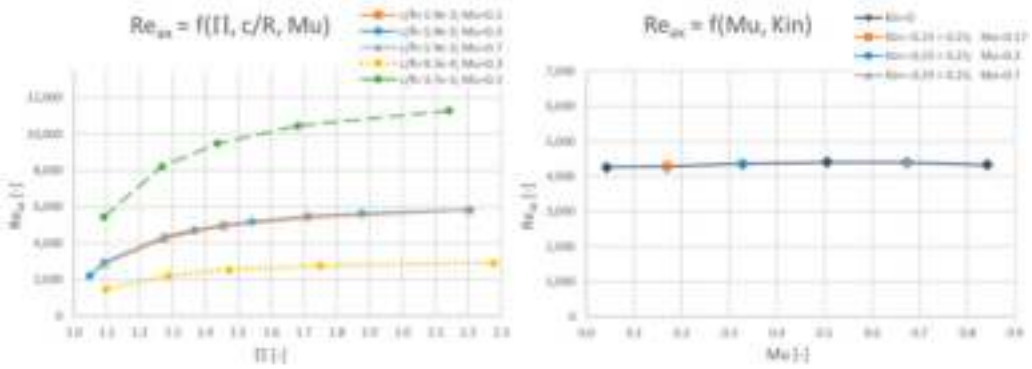

Figure 3. Dependency of axial Reynolds number on Π, c/R, M_u, and K_{in}.

Figure 3 also shows that the Reynolds number is independent of the circumferential Mach number, thereby also from the rotational speed. Furthermore, a different inlet swirl has no influence on the Re_{ax} (and consequently on the leakage mass flow). In conclusion, for the wide range of variables considered herein, the OAS leakage mass flow is generally independent of the rotation and the inlet velocity angle. Denecke et al. [5] stated that the mass flow is independent of rotational effects as long as the ratio U/V_{ax} stays below 1. This is usually the case for IAS. From the outcomes of the presented study, for the practical cases of OAS, it is clear that the rotation and inlet velocity angle do not influence the mass flow even when the U/V_{ax} ratio spans the $0.02 \div 2.4$ range, corresponding to the M_u range shown in Figure 3.

In addition, few other researchers point to independence from rotation. Zimmermann et al. [8] and Szymanski et al. [4] state that the influence of the rotation on the characteristics of the discharge coefficient C_d can be neglected when $Re_{ax} > 10,000$. These rotation effects become significant with decreasing Reynolds number, because the pressure losses increase, due to the growing friction losses. Figure 4 presents C_d plotted against Re_{ax} with varying relative clearance, pressure ratio, and circumferential Mach number to facilitate the comparison with the available literature. The above-mentioned small dependency of C_d on the rotation rate is clearly visible in Figure 4, already near $Re_{ax} \sim 6000$.

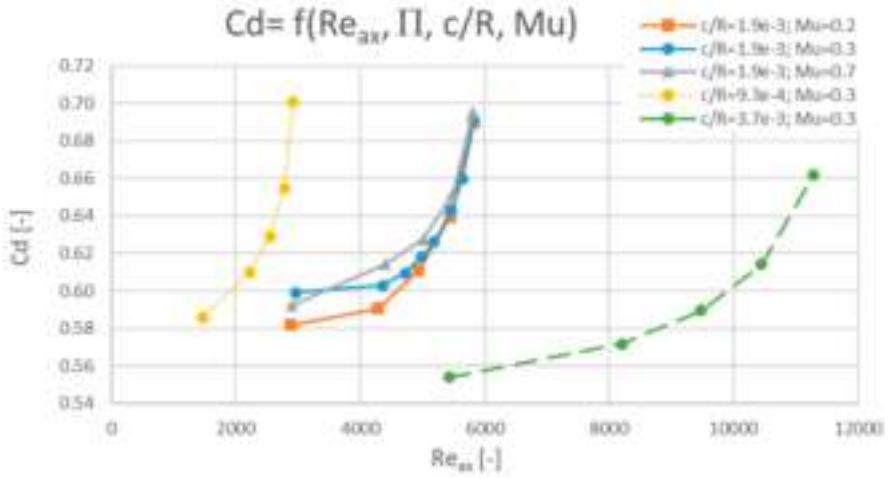

Figure 4. Discharge coefficient for the researched OAS for different e_{ax}, Π, c/R, and M_u.

Despite the generally good agreement with the literature results of the rotational effects with respect to the relative clearance, two different trends are found in the available research reports. Wittig et al. [3] and Waschka et al. [4] demonstrated that for the straight labyrinth seal with various fins configurations, C_d decreases with a clearance reduction. Conversely, in the current study and similarly to Willenborg et al. [18], Schramm et al. [19], and Zimmermann and Wolff [8] in stepped labyrinths cases, C_d has been found to decrease with increasing clearance. Moreover, Szymanski et al. [10], comparing two experiments with CFD, also observed two different unexplained trends of C_d with respect to the clearance in both analyzed experiments.

The first and most basic difference between the mentioned cases is the seal configuration—straight or stepped. In the case of straight-through seals (still commonly applied at cylindrical parts of the engines), the bigger the gap, the bigger the C_d. Whereas for stepped ones, the bigger the gap, the smaller the C_d. Thus, for different types of geometries, there is a completely reverse discharge behavior. Similar conclusions were also drawn by Denecke et al. [20] who studied straight, forward, and backward stepped configurations with and without rub-grooves. They indicated that the outcomes valid for the stepped seals should not be put together with those of the straight seal type. Furthermore, the differences in the geometry result in a modified flow guidance and a visibly altered discharge behavior. In the case of the straight-through geometry, the leakage directly enters the downstream seal chamber, and it reduces the sealing. The step in the configuration serves as an additional stagnation point and redirects the jet towards the bottom of the seal improving the sealing.

All these findings show that accurate correlations and dependencies for the discharge coefficient are difficult to determine. Both Re_{ax} and C_d provide some information about the leakage mass flow. While the Reynolds quantifies the ratio of the inertia to viscous forces, the discharge coefficient C_d compares the true mass flow to the ideal value as a result of the miscellaneous losses. It is also possible that the C_d studied by other researchers was influenced by different geometric features such as the distance between the fins, the radii of the fins, and their shapes. That could have an impact on the results. Already, Zimmermann and Wolff [8] stated that the generalized correlation of C_d cannot be very accurate. This is also addressed in the presented paper, because C_d depends on very many variables. Nevertheless, the C_d parameter is eagerly used, due to its convenient use in engineering applications as discussed in the previous section.

3.2. Leakage Exit Swirl Ratio

The dimensionless expression for the inclination of the flow velocity vector, resulting from the performed DA, is the swirl ratio K. This parameter indicates how big is the circumferential velocity of the flow with respect to the circumferential velocity of the rotor. In the case of OAS, the velocity of the blade tip reaches significant numbers, due to the high

rotational speeds and the considerable radii. The outlet swirl is thus a very big contributor to the mixing of the OAS leakage and of the mainstream flow in LPT.

When it comes to the exit swirl ratio, parametrized with the rotational speed and the clearance decrease, the dependency on the pressure ratio is marginally higher. However, it can be assumed that even for high speeds and very small clearances, beginning with a certain value of the pressure ratio (approximately 1.4), the swirl ratio is independent from Π (see Figure 5). Such a behavior is present for different relative clearances and circumferential Mach numbers.

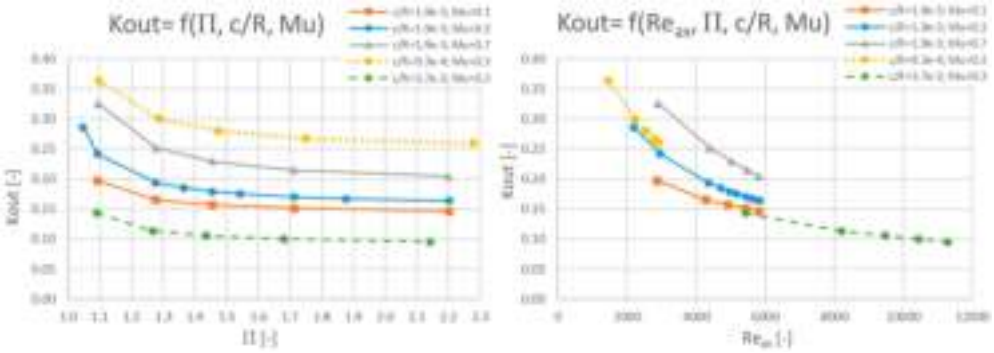

Figure 5. Exit swirl ratio dependency on π, Re_{ax}, c/R, and M_u.

From Figure 5 it can be concluded that with a relative clearance increase and a M_u decrease, the swirl ratio at the outlet of the cavity tends towards 0, that is the flow tends to be unturned. This is because the bigger the gap at the fins and the smaller the revolutions, the more flow crosses the OAS without undergoing any particular effect. Such a behavior, compared to the small relative clearances, indicates that the flow is especially strongly turned at the fins themselves. For smaller clearances, the shear layer dominates in the smallest cross-sectional area (at fins). In other words, very little flow is free from the boundary layer influence. The leakage is subjected then to viscous effects. Since the rotor is turning, the flow due to viscosity effects is also turned. The same conclusion is achieved in terms of the meaning of the Reynolds number, expressing the ratio of the inertia to the viscous forces. For small Reynolds, viscous forces are dominating, which is visible for small gaps in Figure 5. This is reflected in the higher swirl ratio at the outlet.

Figure 6 shows that the outlet swirl ratio is strongly dependent especially on two parameters: the circumferential Mach number of the rotor M_u and the level of the swirl ratio at the inlet K_{in}. The inlet swirl corresponds to the initial inclination of the leakage velocity vector entering the cavity. It is obvious that when the swirl at the entrance of the cavity is higher, in the same manner, the outlet swirl will be higher. This is well visible from the curves presented in Figure 6, highlighting that the outlet swirl ratio linearly depends on the inlet pre-swirl. The slope of the lines for different M_u is almost the same; only the level changes. This slope remains also unchanged when the velocity vector is directed against the rotational speed. It additionally confirms that both numbers M_u and K_{in} resulting from the DA describe separate phenomena. Figure 6 also shows that a M_u increase results in a linear increase of the outlet swirl ratio. The induced, additional turning at OAS is in the direction of the rotation. It is partly an effect of the flow turning at the rotating walls due to the viscosity of the fluid and partly to the interaction with the mid-chamber vortices. The results agree well with those reported in [5].

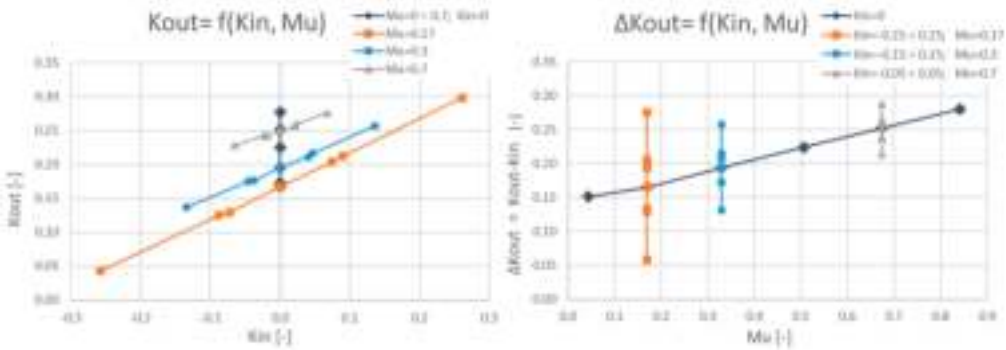

Figure 6. Exit swirl ratio dependency on M_u and K_{in}.

3.3. Windage Heating

Windage heating corresponds to the outlet temperature rise and is a measure of the power losses due to vortices, friction, etc. The outlet temperature increase comes from the work input by the rotating blade through viscous forces. In the present study, due to the assumption of adiabatic walls, the heat transfer associated with the effects of the cooling at the walls (normally present in the experiments) cannot be accounted for. Figure 7, providing windage heating dependency on the pressure ratio Π, indicates that σ shows very similar trends to K_{out}. With increasing Π and c/R, windage losses tend to drop.

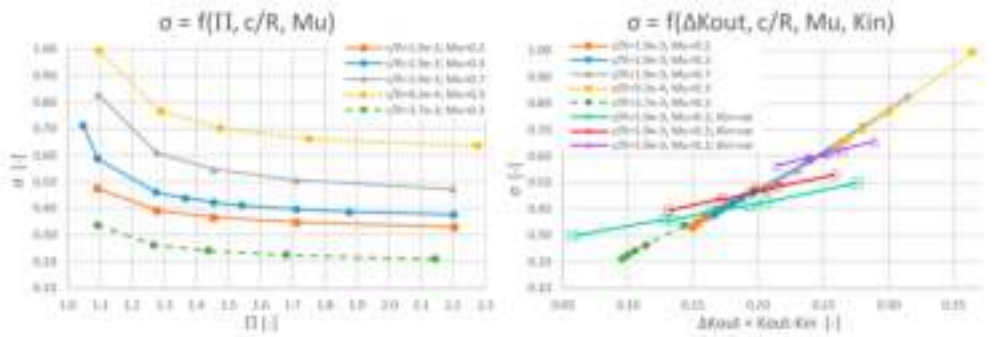

Figure 7. Windage heating dependency on π, Re_{ax}, c/R and M_u and K_{in}.

The smaller the leakage (smaller Reynolds number), the bigger the relative contribution of the viscous forces. Thus, the lesser flow in the axial direction (either due to the tight gaps or due to small pressure difference), the bigger the contribution of the circumferential stresses. Then, the more enhanced mixing due to the relatively bigger contribution of the viscous forces on the circumferential direction and the more increased windage heating. Much in the same way as for the exit swirl ratio, at higher pressure rations (approx. 1.4), σ is almost independent from Π. This leads to the conclusion that both quantities σ and K_{out} should have similar trends. This is confirmed by the results presented in Figure 7, however, only when the inlet swirl does not vary. To compare cases with different pre-swirl levels, a difference operator (delta) between outlet and inlet swirl values is applied (see Figure 7, right panel). The right panel shows that the drivers for both σ and K_{out} are identical with respect to the relative clearance, the pressure ratio, and the circumferential Mach number, that is to say, the trends of σ and K_{out} are linear with respect to the changes in the mentioned parameters. However, the influence of the pre-swirl ratio is different, as shown by the decreasing slopes contrary to the increasing ones in the case of K_{out}.

Figure 8 presents the influence of the circumferential Mach number and of the inlet swirl ratio on σ. Clearly, the increase in M_u leads to a linear increase in the windage losses. With the higher speed of the rotor, the vortices generated by the enhanced circumferential component become stronger, yielding more windage losses. This was also shown in [5,7].

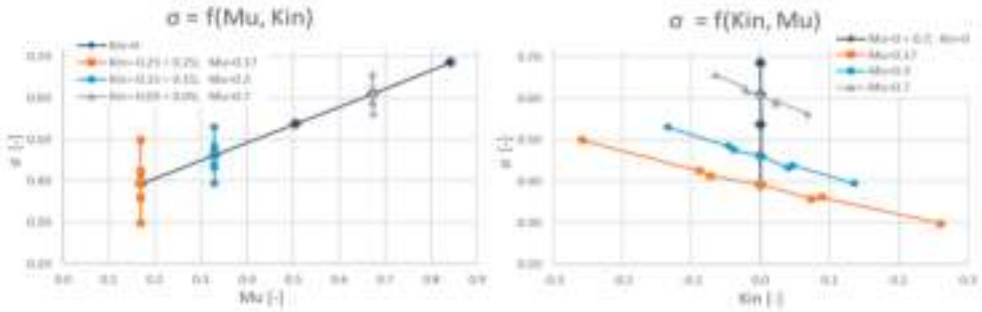

Figure 8. Windage heating against the circumferential Mach number and inlet pre-swirl ratio.

A reverse trend is visible in the second chart of Figure 8. A negative value of K_{in} indicates that the velocity vector points against the direction of rotation. The data clearly show that if velocity is inclined towards the rotation direction, the windage losses becomes smaller. On the other hand, if the velocity acts against the rotation, a larger interaction of the leakage with the vortices (induced by the rotation) will occur, leading to more losses. This contributes to the different trends between windage heating and exit swirl ratio.

3.4. Other Parameters Resulting from Dimensional Analysis

There are two other dimensionless numbers stemming from the performed DA: $p_{t,in}/N\mu$ and k. The ratio of specific heats k is considered to have a minor influence on Re_{ax}, K_{out} and σ. Additionally, it is impossible to influence this parameter during the design, because it is one of the characteristics of the fluid itself for a given case. Conversely, the ratio $p_{t,in}/N\mu$ can vary with respect to the inlet total pressure and the rotational speed. The effects of variations in this quantity on the dependent variables resulting from the DA is presented in Figure 9. For all below cases, the pressure ratio was kept at the same level.

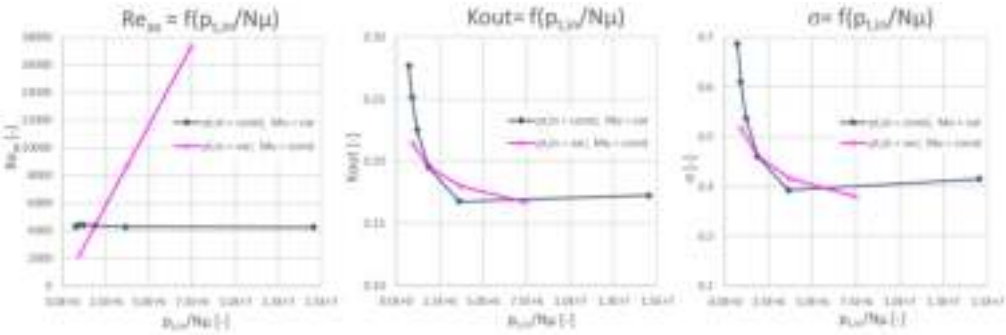

Figure 9. Influence of $pt_{in}/N\mu$ on axial Reynolds number, outlet swirl ratio, and windage heating.

Firstly, the impact of the ratio $p_{t,in}/N\mu$ on the Re_{ax} is affected by other groups. It was already shown that the axial Reynolds does not vary with M_u. On the other hand, it is obvious that an increase of the inlet pressure, that is of the density, will also lead to a proportional increase of the mass flow. This effect needs to be accounted for when evaluating the Reynolds number.

However, with respect to the other parameters, K_{out} and σ, the ratio $p_{t,in}/N\mu$ exhibits almost the same trends, regardless of the $p_{t,in}$ or M_u variations. Both charts also show that the above-mentioned trends tend to show asymptotic behavior for large values of the $pt_{in}/N\mu$ ratio, and have steep gradients for smaller ones. The high gradients refer to the situation when the inlet total pressure is small and the rotation big. It leads to the conclusion that the bigger the total pressure (the bigger the leakage), the smaller the additional outlet swirl ratio and the windage losses. Since in LPT the total pressure decreases strongly along the machine, the downstream stations will experience higher turning of the leakages, higher windage losses, and correspondingly smaller leakages.

3.5. Unsteady Effects at OAS in Dimensionless Numbers

It has already been mentioned that RANS calculations provide time-averaged values of the flow quantities, and for general nondimensional relations they are sufficiently accurate. Nevertheless, for several cases with different rotational speeds, a set of URANS calculations was also performed to investigate the influence of the vortices' unsteadiness on the dimensionless numbers. The differences between the steady and transient cases are shown in Table 3.

Table 3. Differences on dimensionless numbers between steady and unsteady solutions for OAS cases with $c/R = 1.9 \times 10^{-3}$; $\Pi = 1.3$; $K_{in} = 0$; for different rotational speeds.

	***Mu*=0.17**	***Mu*=0.3**	***Mu*=0.6**
Re_{ax}	0%	−0.5%	−0.3%
K_{out}	0.2%	−0.1%	−1.1%
σ	−0.4%	0.8%	0.9%
Cd	−0.7%	−0.2%	0.1%

The unsteady simulations have shown minor variations in the nondimensional parameters resulting from the DA. The largest percentage difference yields a −1.1% value for the outlet swirl ratio. The vortices in the OAS configuration presently investigated do not show noticeable unsteady effects. RANS are still considered to representatively capture the trends of the nondimensional numbers. Nevertheless, some other additional effects could appear if the influence from the mainstream flow was considered.

4. Conclusions

The Dimensional Analysis and a numerical parametric study of an OAS were performed in the framework of the present paper. The most crucial variables were identified and further nondimensional numbers were derived. To investigate the influence of the parameters, a few CFD models of the typical LPT OAS were built. The general dependencies between the nondimensional quantities were found to be well modelled by RANS, offering a comprehensive overview of the OAS characteristics.

The Reynolds number has been found to be independent of the rotational speed and pre-swirl effects, and strongly depended on the relative clearance, pressure ratio, and $p_{t,in}/N\mu$ ratio.

Both the outlet swirl ratio and the windage heating, have shown the same trends, suggesting that they are driven by similar phenomena. The only different behavior was found with respect to the inlet swirl ratio. Both parameters appeared to be almost independent of the pressure ratio.

Additionally, the discharge coefficient relations were cross-checked to offer a ground for comparison with the available literature data. It was found that C_d is essentially driven by multiple parameters. In the first place, it is chiefly influenced by the geometry: c/R ratio, seal configuration (number of stagnation points, steps), and pressure ratio Π. Of some importance are also M_u, K_{in}, $p_{t,in}/N\mu$, and k. The obtained results are in good agreement with the literature data. All findings show that accurate correlations and dependencies for the discharge coefficient are difficult to determine in a quantitative manner.

For the presently investigated OAS, and with reference to the parameters operating range corresponding to nowadays LPT conditions, the following dependencies were found:

$$Re_{ax} = f\left(c/R, \Pi, \frac{p_{t,in}}{N\mu}\right) \tag{4}$$

$$K_{out} = f\left(c/R, M_u, \frac{p_{t,in}}{N\mu}, K_{in}\right) = f\left(Re_{ax}, M_u, K_{in}\right) \tag{5}$$

$$\sigma = f\left(c/R, M_u, \frac{p_{t,in}}{N\mu}, K_{in}\right) = f(\Delta K_{out}, K_{in}) \tag{6}$$

To facilitate the comparison of specific phenomena and prediction of OAS behavior, proper dimensionless numbers should be retained. With respect to the mass flow behavior, the axial Reynolds Re_{ax} turns out to be the most important. The outlet swirl ratio K_{out} is crucial for mixing, while the windage heating σ controls the internal losses.

Author Contributions: Conceptualization, K.P. and P.S.; methodology, K.P. and P.S.; software, K.P.; validation, K.P. and P.S.; formal analysis, K.P.; investigation, K.P.; resources, K.P.; data curation, K.P.; writing—original draft preparation, K.P.; writing—review and editing, K.P. and P.S.; visualization, K.P.; supervision, P.S.; project administration, K.P. All authors have read and agreed to the published version of the manuscript.

Funding: This research received no external funding.

Data Availability Statement: The data presented in this study are available on request from the corresponding author.

Conflicts of Interest: The authors declare no conflict of interest.

Abbreviations

The following symbols and abbreviations are used in this manuscript:

a	Local speed of sound
b, b_i	any dimensional quantity c Clearance size
c_p	Specific heat capacity
$\frac{c}{R}$	Relative clearance
k	Ratio of specific heats
$\dot{m}$	Leakage mass flow
p	Pressure
A	Cross-sectional area at fin
C_d	Discharge coefficient
$K = \frac{V_\theta}{NR}$	Swirl ratio
$M_u = \frac{U}{\sqrt{kR_iT_{in}}}$	Circumferential Mach number
N	Rotational speed
Pr	Prandtl number
R	Average radius of fins
R_i	Individual gas constant
$Re_{ax} = \frac{\rho V_{ax} c}{\mu} = \frac{\dot{m}}{2\pi R \mu}$	Axial Reynolds number
T	Temperature
Tu	Turbulence intensity
$U = \frac{\pi N}{30} R$	Rotor fins circumferential velocity
V_{ax}	Axial velocity component
V_r	Radial velocity component
V_θ	Circumferential velocity component
α, β, δ	any exponents
μ	Viscosity
ρ	Density
$\Pi = p_{t,in}/p_{out}$	Pressure Ratio
Ψ, Ψ_i	any dimensionless quantity $\sigma = \frac{2cp(T_{t,out} - T_{t,in})}{U^2}$ Windage heating
Subscripts:	
t	Total quantities
in, out	Inlet, Outlet
Acronyms:	
CFD	Computational Fluid Dynamics
DA	Dimensional Analysis
IAS/OAS	Inner/Outer Air Seal
LES	Large Eddy Simulations
LPT	Low Pressure Turbine(s)
PIV	Particle Image Velocimetry
PVT	Particle Velocimetry Tracking
(U)RANS	(Unsteady) Reynolds-Averaged Navier-Stokes

Appendix A. Main Steps of the Dimensional Analysis

The basis for the dimensional analysis is the mathematically proven Buckingham's theorem. Qing-Ming [17] indicated that the power law formula can express the dimension of any quantity. In the method, an emphasis is placed on the careful selection of fundamental quantities in solving problems. As noted by Qing-Ming [17], it is possible, based on the theorem, to find from the regular dimensional relationship:

$$b = f(b_1,\ b_2\ \ldots,\ b_n), \tag{A1}$$

of a physical problem, where the variables in a function are independent, the dimensionless relationship between the variables. After adopting the power formula, the relation can be presented as:

$$\Psi = const{\cdot}\Psi_1^{\alpha},\ \Psi_2^{\beta},\ldots\Psi_{N-k}^{\delta}, \tag{A2}$$

In addition, as indicated by Qing-Ming [17], one should only consider the numbers essential for the problem being investigated. The irrelevant independent variables should be omitted.

When attempting to the analysis of a physical phenomenon, frequently it is better to start from the relationship in dimensionless form. Then, units do not need to be converted, and also the amount of work is considerably reduced because the number of independent variables is reduced, in addition, the results are more universal.

In the presented work, the essential for the researched phenomena were variables listed in the Table 1. Additionally, the set of variables is given in the form of function in Equation (A3).

$$f\left(c,\ R,\ N,\ a,\ R_i,\ \mu,\ p_{t,in},\ p_{t,out},\ T_{t,in},\ T_{t,out},\ \dot{m},\ V_{\theta,in},\ V_{\theta,out},V_{r,in},\ V_{r,out},V_{ax,in},\ V_{ax,out}\right) = 0 \tag{A3}$$

Base units were chosen: [Time], [Length], [Mass], and [Heat], which corresponds to [s], [m], [kg], and [K], respectively.

The chosen independent variables were: $R,\ N,\ \mu,\ T_{t,in}$ and their units: $[m],\ \left[s^{-1}\right],\ \left[kg{\cdot}m^{-1}{\cdot}s^{-1}\right],\ [K]$.

The dependent variables though: $c,\ a,\ R_i,\ p_{t,in},\ p_{t,out},\ T_{t,out},\ \dot{m},\ V_{\theta,in},\ V_{\theta,out},V_{r,in},\ V_{r,out},\ V_{ax,in},\ V_{ax,out}$.

Afterwards, each parameter was evaluated in terms of independent variables. Then, based on Buckingham's theorem and the power low, the units were compared. As an example, in the presented work, mass flow through the seal considered with respect to the chosen independent variables:

$$\dot{m} = f(R,\ N,\ \mu,\ T_{t,in}) = \text{const}{\cdot}R^{\alpha}{\cdot}N^{\beta}{\cdot}\mu^{\gamma}{\cdot}T_{t,in}^{\delta} \tag{A4}$$

consideringly on the units:

$$\left[\text{kg}{\cdot}s^{-1}\right] = [m]^{\alpha}{\cdot}\left[s^{-1}\right]^{\beta}{\cdot}\left[kg{\cdot}m^{-1}{\cdot}s^{-1}\right]^{\gamma}{\cdot}[K]^{\delta} \tag{A5}$$

Then, one obtains:

$$\begin{cases} [Time]: -1 = -\beta - \gamma \\ [Length]:\ \ 0 = \alpha - \gamma \\ [Mass]:\ \ \ 1 = \gamma \\ [Mass]:\ \ \ 0 = \delta \end{cases} \rightarrow \begin{cases} \alpha = 1 \\ \beta = 0 \\ \gamma = 1 \\ \delta = 0 \end{cases} \rightarrow \dot{m} = f(R,\ \mu) \rightarrow \text{const}{\cdot}R^1{\cdot}\mu^1 \rightarrow 1 = \frac{\dot{m}}{R\mu} \sim\ Re_{ax} \tag{A6}$$

The outcome is the quantity in the dimensionless form.

Next, one should look for the other known numbers and relate them to the investigated phenomenon. In the case of mass flow through the outer air seal, the corresponding number is axial Reynolds number, Equation (A6). The resultant dimensionless numbers for the outer air seal are given in Equation (1).

Appendix B. Details of the Investigated Seal Geometry

It is known from the works of other researchers, for example Zimmermann and Wolf [8], that the seal performance is influenced by the geometry itself. To provide better

insight into the investigated seal, in Figure A1 and in Table A1 are given geometrical details of the configuration.

Table A1. Geometrical details of the outer air seal investigated in the study.

Clearance Size, *c*	**0.001 [m]**
Average radius of the fins, *R*	*0.538* [m]
1st fin height	$20\frac{c}{R}$
2nd fin height	$10\frac{c}{R}$
Width of the fins	$2\frac{c}{R}$
Distance between the fins	$40\frac{c}{R}$
Step height	$10\frac{c}{R}$
Distance from the step to the 2nd fin	$20\frac{c}{R}$
Corner radii of the fins	0 (sharp fins)

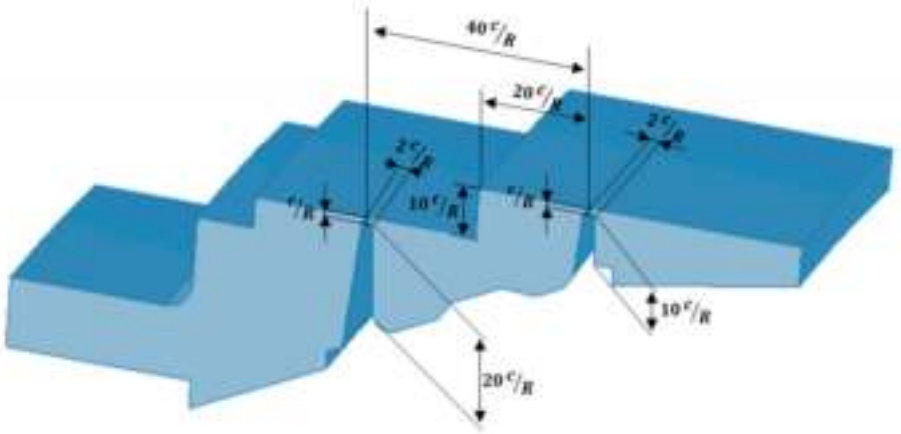

Figure A1. Geometrical details of the outer air seal investigated in the study.

References

1. Dinc, S.; Demiroglu, M.; Turnquist, N.; Mortzheim, J.; Goetze, G.; Maupin, J.; Hopkins, J.; Wolfe, C.; Florin, M. Fundamental Design Issues of Brush Seals for Industrial Applications. *J. Turbomach.* **2002**, *124*, 293–300. [CrossRef]
2. Mahle, I. Improving the Interaction Between Leakage Flows and Main Flow in a Low Pressure Turbine. *ASME J. Turbomach.* **2010**, *7*, 1177–1186. [CrossRef]
3. Wittig, S.L.K.; Dorr, L.; Kim, S. Scaling Effects on Leakage Losses in Labyrinth Seals. *J. Eng. Power* **1983**, *105*, 305–309. [CrossRef]
4. Waschka, W.; Wittig, S.; Kim, S. Influence of High Rotational Speeds on the Heat Transfer and Discharge Coefficients in Labyrinth Seals. *J. Turbomach.* **1992**, *114*, 462–468. [CrossRef]
5. Denecke, J.; Farber, J.; Dullenkopf, F.; Bauer, H.J. Dimensional Analysis and scaling of rotating seals. *ASME J. Turbomach.* **2005**, *47268*, 1149–1160. [CrossRef]
6. Denecke, J.; Dullenkopf, K.; Wittig, S.; Bauer, H.-J. Experimental Investigation of the Total Temperature Increase and Swirl Development in Rotating Labyrinth Seals. *ASME J. Turbomach.* **2005**, *3*, 1161–1171. [CrossRef]
7. Yan, X.; Li, J.; Song, L.; Feng, Z. Investigations on the Discharge and Total Temperature Increase Characteristics of the Labyrinth Seals with Honeycomb and Smooth Lands. *J. Turbomach.* **2009**, *131*, 041009. [CrossRef]
8. Zimmermann, H.; Wolff, K.H. *Air System Correlations: Part 1—Labyrinth Seals*; ASME Paper 98-GT-206; ASME: New York, NY, USA, 1998.
9. Szymanski, A.; Wroblewski, W.; Dykas, S. Flow Analysis of the Turbine Rotor Tip Seal on a Highly Rotary Test Rig. In Proceedings of the 11th European Conference on Turbomachinery Fluid dynamics & Thermodynamics, ETC11, Madrid, Spain, 23–27 March 2015; pp. 23–27.
10. Szymanski, A.; Dykas, S.; Wroblewski, W.; Fraczek, D. Experimental and Numerical Validation Study of the Labyrinth Seal Configurations. In Proceedings of the 12th European Conference on Turbomachinery Fluid Dynamics & Thermodynamics ETC12, Stockholm, Sweden, 3–7 April 2017. [CrossRef]

11. Fraczek, D.; Wroblewski, W.; Chmielniak, T. Influence of Honeycomb Rubbing on Tip Seal Performance of Turbine Rotor. In Proceedings of the 11th European Conference on Turbomachinery Fluid Dynamics & Thermodynamics, Madrid, Spain, 23–27 March 2015. [CrossRef]
12. Kluge, T.; Wein, L.; Schmierer, R.; Seume, J.R. Sensitivity analysis, instrumentation and design, and experimental validation of a novel labyrinth seal rig. In Proceedings of the 13th European Conference on Turbomachinery Fluid dynamics & Thermodynamics ETC13, Lausanne, Switzerland, 8–12 April 2019. [CrossRef]
13. Wein, L.; Kluge, T.; Seume, J.R.; Hain, R.; Fuchs, T.; Kähler, C.; Schmierer, R.; Herbst, F. Validation of RANS Turbulence Models for Labyrinth Seal Flows by Means of Particle Image Velocimetry. In Proceedings of the ASME Turbo Expo 2020: Turbomachinery Technical Conference and Exposition, London, UK, 21–25 September 2020. [CrossRef]
14. Gao, F.; Chew, J.W.; Beard, P.; Amirante, D. Numerical Studies of Turbine Rim Sealing Flows on a Chute Seal Configuration. In Proceedings of the 12th European Conference on Turbomachinery Fluid dynamics & Thermodynamics ETC12, Stockholm, Sweden, 3–7 April 2017. [CrossRef]
15. Kluge, T.; Lettmann, I.S.; Oettinger, M.; Wein, L.; Seume, J.R. Unsteady Flow Phenomena in Turbine Shroud Cavities. In Proceedings of the Global Power and Propulsion Society, Chania, Greece, 7–9 September 2020. [CrossRef]
16. Leach, K.; Thulin, R.; Howe, D. Energy Efficient Engine. In *Tubrine Indermediate Case ad Low Pressure Turbine Component Test Hardware Detailed Design Report*; NASA CR-167973; PWA-5594-191; NASA Lewis Research Center: Cleveland, OH, USA, 1982; p. 44135.
17. Qing-Ming, T. *Dimensional Analysis with Case Studies in Mechanics*; Springer: Berlin/Heidelberg, Germany, 2011; pp. 1–41.
18. Willenborg, K.; Kim, S.; Wittig, S. Effects of Reynolds Number and Pressure Ratio on Leakage Loss and Heat Transfer in a Stepped Labyrinth Seal. *J. Turbomach.* **2001**, *123*, 815–822. [CrossRef]
19. Schramm, V.; Willenborg, K.; Kim, S.; Wittig, S. Influence of a Honeycomb Facing on the Flow Through a Stepped Labyrinth Seal. *J. Eng. Gas Turbines Power* **2000**, *124*, 140–146. [CrossRef]
20. Denecke, J.; Schramm, V.; Kim, S.; Wittig, S. Influence of Rub-Grooves on Labyrinth Seal Leakage. *J. Turbomach.* **2003**, *125*, 387–393. [CrossRef]

International Journal of
Turbomachinery Propulsion and Power

MDPI

Article

Experimental Study on Flow Behavior of Unshrouded Impeller Centrifugal Pumps under Inlet Air Entrainment Condition

Minquan Liao [1], Qiaorui Si [1,*], Meng Fan [2], Peng Wang [1], Zhonghai Liu [3], Shouqi Yuan [1], Qianglei Cui [1] and Gérard Bois [2]

[1] National Research Center of Pumps, Jiangsu University, Zhenjiang 212013, China; liaominquanujs@163.com (M.L.); pwang@ujs.edu.cn (P.W.); shouqiy@ujs.edu.cn (S.Y.); cuiqiangleiujs@163.com (Q.C.)
[2] LMFL, FRE CNRS 3723, Arts et Métiers Paris Tech, 59046 Lille, France; Devin99988@outlook.com (M.F.); Gerard.BOIS@ENSAM.EU (G.B.)
[3] Changsha Dewater Machanical Technology Co., Ltd., Changsha 410100, China; liuzhonghai@csdewater.com
* Correspondence: siqiaorui@ujs.edu.cn; Tel.: +86-136-5529-3881

Abstract: Results on overall pump head and efficiency performance, pressure pulsation and high speed camera visualization of flow patterns behavior are presented for different inlet air-water void fractions at a given rotational speed. With the increase of inlet void fractions and decrease of the flow rates, the size of bubbles increase and tend to agglomerate in specific impeller passage locations along the blade chord. The starting point of pump breakdown is related to a strong inward reverse flow occurring in a specific location near the shroud gap of the impeller and volute tongue region. Using a constant air void fraction value of 2%, pressure pulsation frequency results are analyzed in relation with local flow mixture patterns and flow rate modification.

Keywords: centrifugal pump; two-phase flow pattern; pressure pulsation; visualization

check for updates

Citation: Liao, M.; Si, Q.; Fan, M.; Wang, P.; Liu, Z.; Yuan, S.; Cui, Q.; Bois, G. Experimental Study on Flow Behavior of Unshrouded Impeller Centrifugal Pumps under Inlet Air Entrainment Condition. *Int. J. Turbomach. Propuls. Power* **2021**, *6*, 31. https://doi.org/10.3390/ijtpp6030031

Academic Editor: Giorgio Pavesi

Received: 9 May 2021
Accepted: 26 July 2021
Published: 28 July 2021

Publisher's Note: MDPI stays neutral with regard to jurisdictional claims in published maps and institutional affiliations.

Copyright: © 2021 by the authors. Licensee MDPI, Basel, Switzerland. This article is an open access article distributed under the terms and conditions of the Creative Commons Attribution (CC BY-NC-ND) license (https://creativecommons.org/licenses/by-nc-nd/4.0/).

1. Introduction

Centrifugal pumps, as one of the core components of fluid transfer, are widely used in various sectors such as nuclear power, petrochemistry and oil extraction. In engineering practice of above field, it is sometimes often impossible to avoid air entrainment into the fluid delivery system. Air entrainment as well as internal vapor generation by cavitation is known as being detrimental and critical to the operation of centrifugal pumps, since decrease the pump performance and take negative influences on the plant system [1,2]. Several studies have been made, investigating the theoretical pump performance and the flow behavior of centrifugal pumps under gas-liquid two-phase flow conditions [3–6]. Due to the rapid development of new measurement and Computational Fluid Dynamics (CFD) technologies, pump performance deterioration caused by air entrainment problem has been better understood [7–11]. However, investigation on unsteady flow-induced characteristics of the centrifugal pump under air entrainment conditions hasn't been treated with enough attention. Experimental flow visualization studies have been conducted in Jiangsu University together with pump performance analysis for centrifugal pumps under inlet air- water two-phase flow [12]. It was found that a particular two-phase flow pattern observed near the shroud gap between the impeller and volute tongue area is closely related to the starting point of the pump break down point. Consequently, the present paper intends to reveal the unsteady flow-induced characteristics of centrifugal pumps under inlet air entrainment condition by combining pump performance tests, inner flow visualization and pressure pulsation measurements.

2. Experimental Set-Up

The pump model used for the present investigation has a transparent plexiglass impeller with a semi-open unshroud three-dimensional blade and a rectangular section

volute, as shown in Figure 1. Pump main geometrical parameters are given in Table 1. Rotational speed has been reduced to 1000 rpm (compared with the normal shroud impeller one of 2900 rpm) to avoid impeller failure due to plexiglass. An open-type test loop, shown in Figure 2, is built to assess the experiment. Ambient atmospheric pressure is close to 101,325 Pa (water level reaches 2 m inside the inlet tank) and temperature is about 298.15 K. Pump performance, such as head and global efficiency values, were obtained in accordance with ISO 9906:2012 [13]. Stable air mass flow rate is measured and controlled by a micro-electro-mechanical flow sensor system (Bürkert 8107) at ambient atmospheric conditions, while the flow rate of pure water is measured using an electromagnetic flow meter placed upstream the injection device (mixer). More details can be found in Si et al. [12]. For low inlet water flow rates, slug flow mixture configuration can be observed inside the horizontal inlet pipe, but after entering the impeller, bubbles are gradually broken up under the rotating action of the impeller leading edge, achieving a quasi-homogeneous air-water mixing.

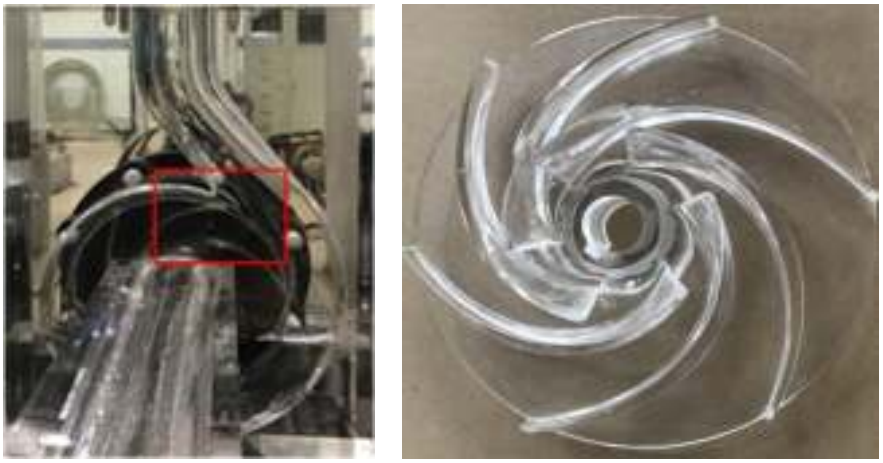

(**a**) scan of the pump (**b**) unshroud impeller

Figure 1. Plexiglass pump model.

Table 1. Pump geometry.

Parameter	Value	Parameter	Value
Rotating speed, n(rpm)	1000	Inlet diameter, D_1/mm	74
Design Head, H/m	4	Outlet diameter, D_2/mm	174
Design flow rate, Q_d/m^3 h^{-1}	17.25	Outlet tube diameter, D_O/mm	65
Design flow coefficient	0.1	Impeller blade inlet angle, $\beta_1/^\circ$	28
number of blades, Z	6	Impeller blade outlet angle, $\beta_2/^\circ$	30
Specific speed, Ω	0.484	Outlet blade width, b_2/mm	12
Specific radius	3.141	——	——

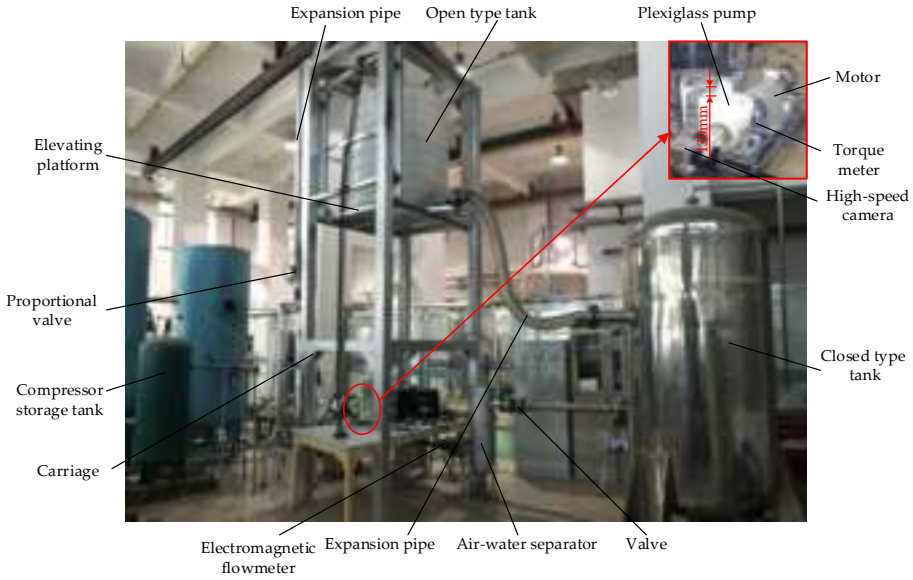

Figure 2. Test rig.

3. Experimental Uncertainties

Overall performance uncertainty is within ±2% for the water flow rate (device measuring range: 0–50 m^3/h) and ±3.5% for head increase, including device accuracies.

For unsteady pressure measurements, the following parameters are used.

$$U = \sqrt{X_S^2 + \Delta_{ins}^2} \tag{1}$$

$$Ur = \frac{U}{\overline{X}} \times 100\% \tag{2}$$

where Xs is the standard deviation, Δ_{ins} is the sensor error, set at 300 Pa, U is the total uncertainty and $\overline{X}$ is the average value.

According to the basic working conditions of this test measurement, the relative uncertainty of each measurement result is shown in Table 2. The relative uncertainty of the test results of the present centrifugal pump are all within 5%.

Table 2. Average relative uncertainties Ur for different inlet void fractions.

n/(rpm)	Q/Q_d	α = 0%	α = 1%	α = 2%	α = 3%	α = 4%
1000	0.3	3.16	—	—	—	—
	0.48	3.35	3.82	3.42	3.65	—
	0.75	3.76	4.38	4.20	3.94	4.19
	0.87	3.87	—	—	—	—

4. Results and Discussion

4.1. Pump Performance

Figure 3 shows all performance curves of the pump model with different inlet air void fraction at 1000 rpm, respectively, head coefficient (Figure 3a), global efficiency (Figure 3b) and shaft power coefficient (Figure 3c). The maximum flow coefficient that can be reached is below the nominal value of 0.1, due to large loop loss that limits the maximum flow coefficient to 0.08.

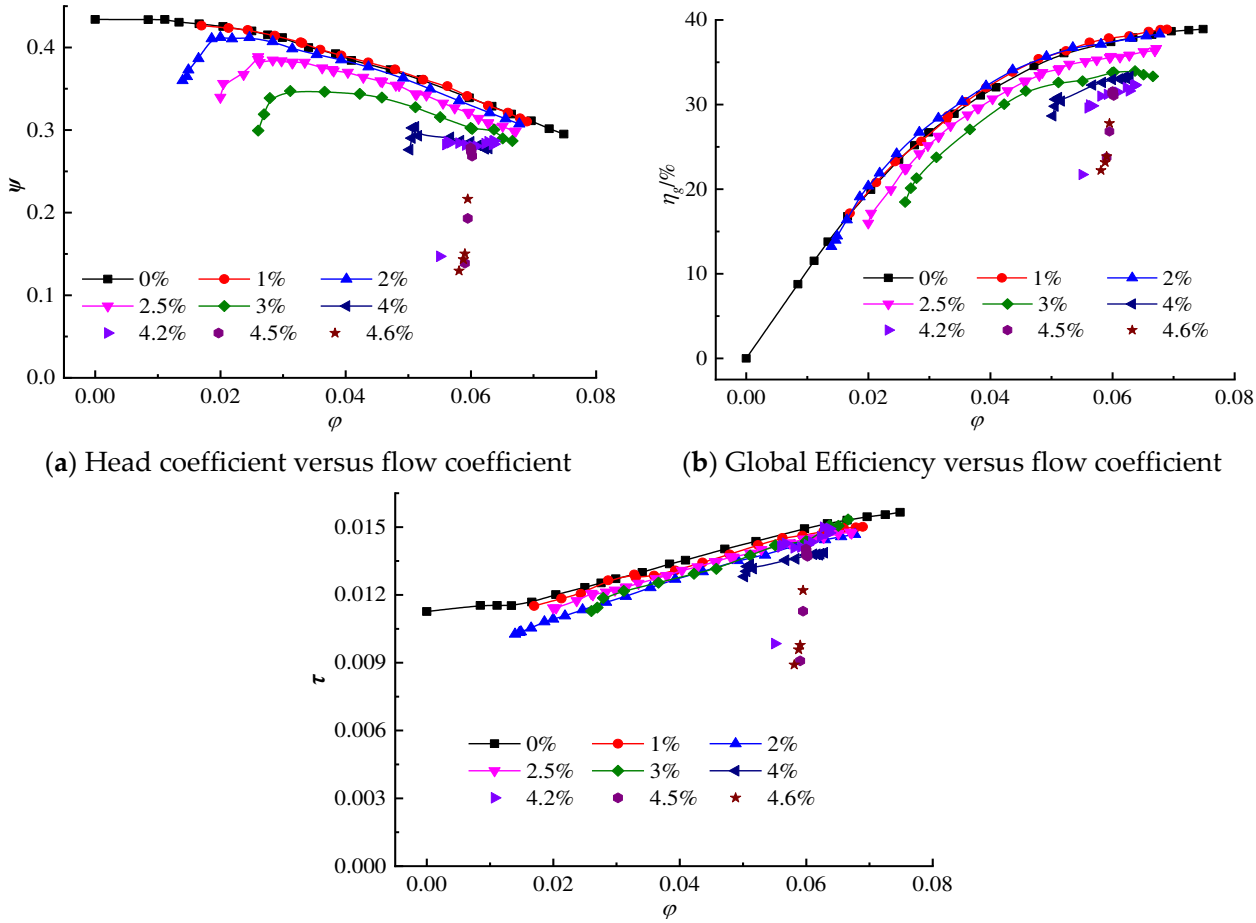

(**a**) Head coefficient versus flow coefficient

(**b**) Global Efficiency versus flow coefficient

(**c**) Shaft power coefficient versus flow coefficient

Figure 3. Pump performance curves. (values in % correspond to different inlet void fraction α) ((**a**,**b**) are adapted from ref. [11]).

Maximum efficiency value is small compared with existing pumps having the same specific speed and specific radius. This pump model is derived from a shrouded pump made of stainless steel which reaches a global efficiency of 0.70. To perform visualizations, it has been manufactured using plexiglass with an unshrouded version. Tip clearance gap has been found bigger than expected; this gap is about 0.8 to 1 mm so that the gap ratio related to the outlet blade width is about 8%. In addition, the gap cannot be easily controlled during operation. It is believed that its value may increase due to plexiglass deformation due to rotation and pressure effects and consequently affects the efficiency.

As for any pump design, the water flow range of the pump decreases as the inlet volume of air increases. The maximum air void fraction value the pump can work before shut-down is 4.6% for the present rotational speed, the corresponding water volume flow rate being equal to 13.0 m^3/h. The pump performance is almost unaffected compared with pure water when the inlet air void fraction is 1%, which means the pump is not sensitive to such gas content for a wide range of water flow rate. When the inlet air void fraction reaches 2%, the pump performance drops sharply at small flow coefficient ($\varphi < 0.02$), while the performance curve remains parallel to the pure water condition for higher flow coefficients. For inlet void fraction values higher than 2%, the pump model becomes more sensitive to the incoming air-water mixture; the higher the void fraction, the more pronounced pump degradation becomes. Under high flow coefficient values, the pump performance drops sharply and the flow coefficient drops down up to $\varphi = 0.06$. Compared with the pure water condition, when operating in the range of 4.2–4.6% inlet air void fraction, the head will decrease by 30–53%, global efficiency will decrease by 26–50%. It is found that the pump

cannot work normally for long time when operating at this critical unstable air content range and that flow passage can be rapidly blocked. The head coefficient delivered by the pump suddenly drops and exhibits a vertical line.

4.2. Pressure Fluctuation

The rotation frequency (shaft frequency) is f_0 = 16.67 Hz, and the blade passing frequency is $f = 6\,f_0$ = 100.02 Hz. The outlet monitoring point is located twice downstream the outlet pipe diameter of the volute outlet flange corresponding to a distance of 130 mm as shown in Figure 2. Transient pressure sensors (Shuang-Qiao company, Suzhou, China CYG1102F type, with a manufacturer measuring range of 0–200 KPa and an accuracy class of 0.15%) mounted perpendicular to the outlet pipe are used to obtain the pressure pulsations with 20,000 Hz sampling. Figure 4 shows the pressure pulsation of the outlet monitoring point under pure water conditions. As expected, the main frequency of pressure pulsation under different flow rates corresponds to the blade passing frequency. The value of the pulsation increases when the flow rate decreases, which is also expected as off design conditions always increase flow instabilities inside the impeller due to increasing positive incidence and stronger interactions from volute tongue.

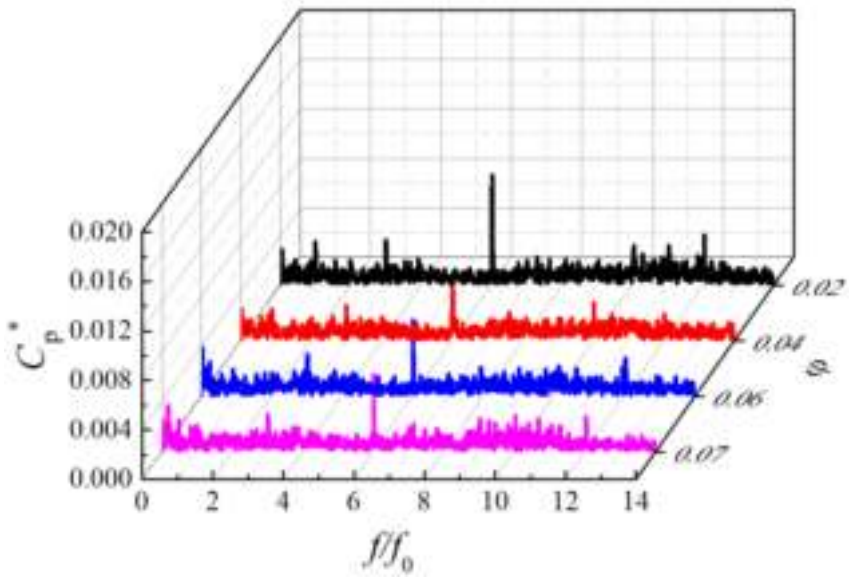

Figure 4. Frequency domain of pressure fluctuation for different flow rates and $\alpha = 0$.

In Figure 5, pressure pulsation frequency charts are compared for two selected flow rates under different inlet void fractions. These two flow rates have been chosen because they correspond to the usual head curve variation with a negative slope. The main frequency of pressure pulsation corresponds to the blade passing frequency for both flow coefficients. The amplitude of pressure pulsation at the blade passing frequency shows a tendency to first increase and then decrease for increasing values of inlet void fraction. Moreover, the pressure pulsation amplitude at the blade passing frequency decreases significantly when the inlet air void fraction reaches the critical unstable air content rate.

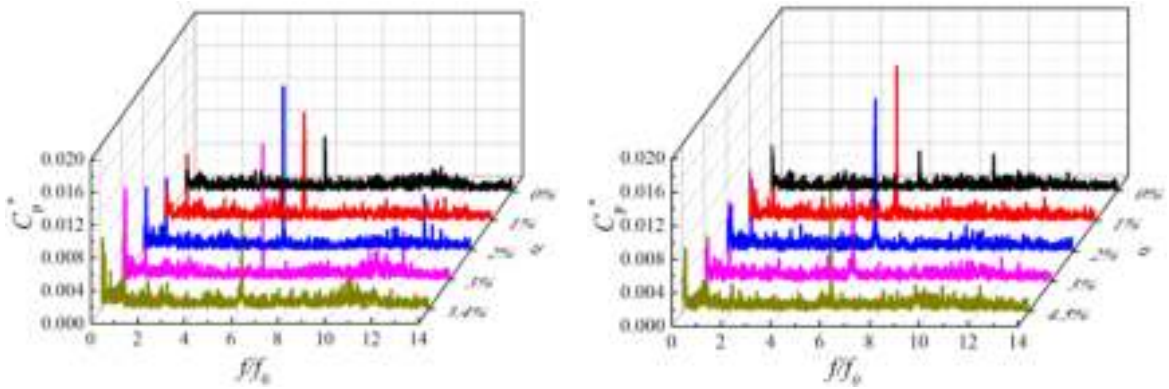

(**a**) $\varphi = 0.04$ (**b**) $\varphi = 0.06$

Figure 5. Frequency domain diagram of outlet pressure fluctuations for several inlet air void fractions and two different flow coefficients.

As far as the pressure pulsations are concerned, the inlet void fraction of 2% corresponds to the maximum value of the outlet pressure fluctuations.

Figure 6 presents the comparative performance curve for two different inlet air void fractions, respectively, 0% and 2%. To facilitate the study, the area corresponding to a negative slope zone is defined as Area I, and the area corresponding to a positive slope zone, is defined as Area II. Comparisons are processed among six flow rates with two different inlet void fractions of 0% and 2%, as shown in Figure 7A. It shows that the change of pressure pulsation amplitude is intrinsically related to the head curve modification.

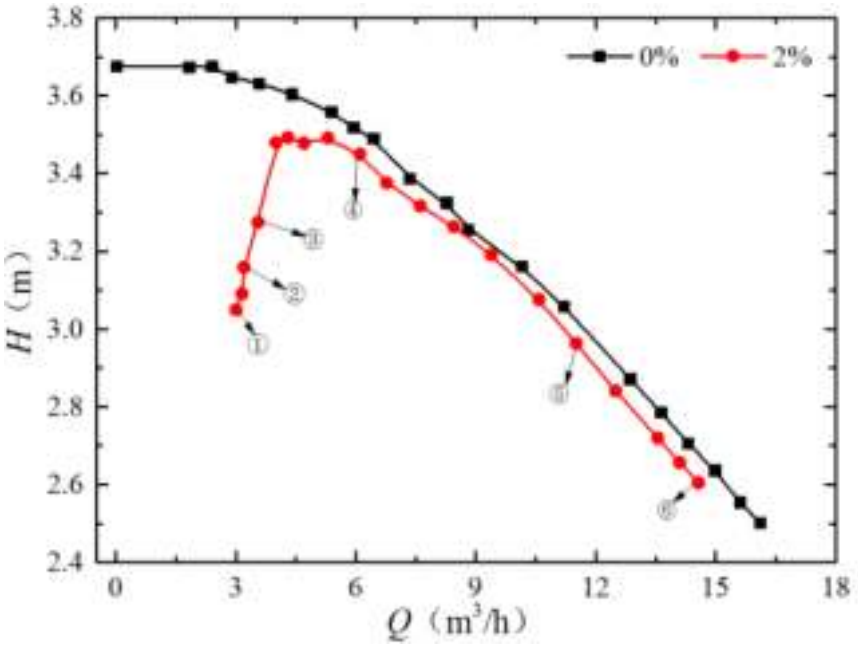

Positions: ① $\varphi = 0.014$ ② $\varphi = 0.015$ ③ $\varphi = 0.016$
④ $\varphi = 0.028$ ⑤ $\varphi = 0.056$ ⑥ $\varphi = 0.07$

Figure 6. Pump performance head coefficient versus flow coefficient for α = 0% and 2%.

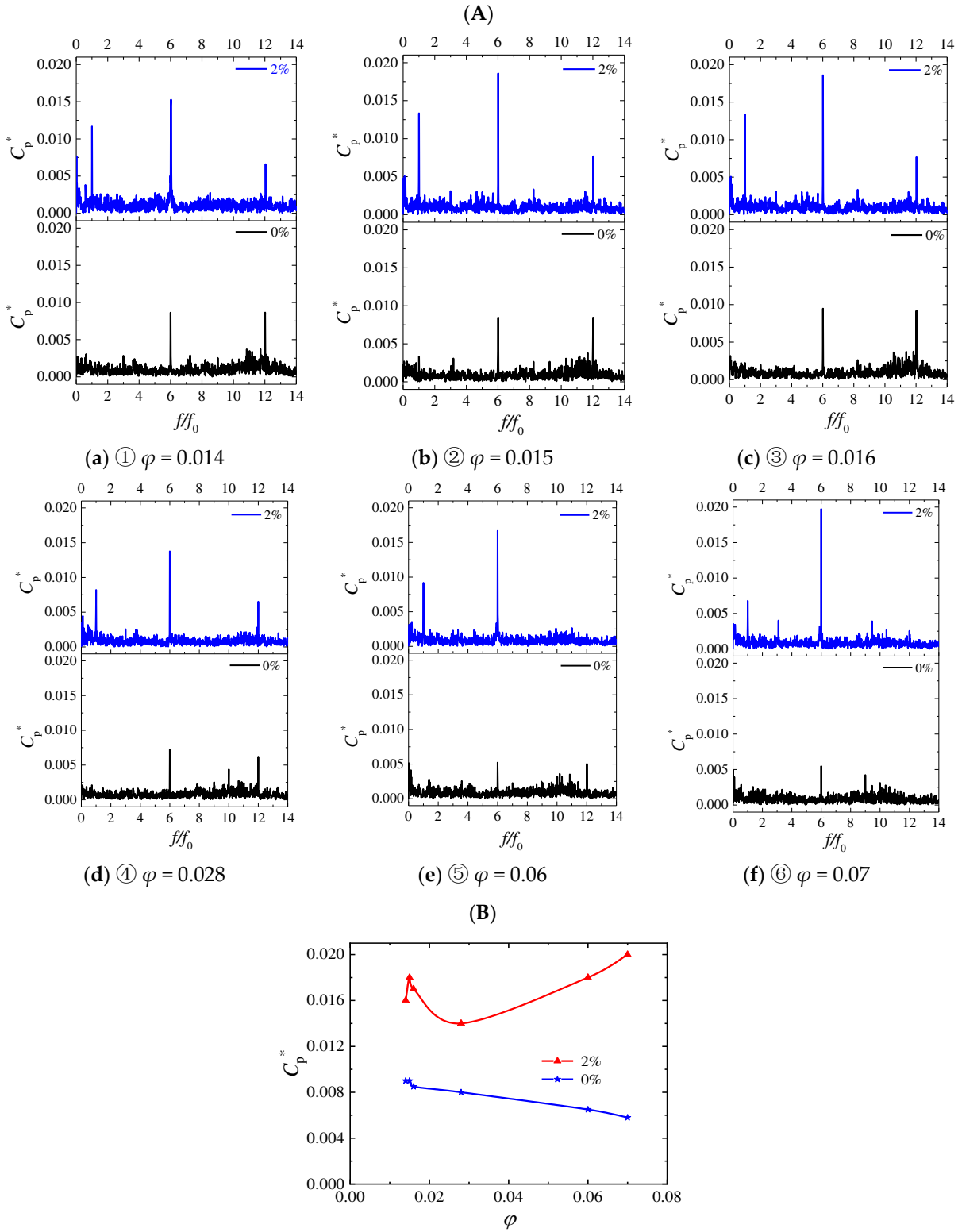

Figure 7. (**A**). Frequency domain charts of pressure fluctuation at α = 0% and 2%. (**B**). Maximum C_p values at BPF for several flow coefficients.

It can be seen that the main frequency of pressure pulsation for all working condition is the blade passing frequency with its first harmonic. The amplitude of the pressure pulsation at blade passing frequency increases gradually in area I and area II as the flow rate decreases for a given value of the inlet void fraction of 2%, but it decreases from area I (flow coefficient ③) to area II (flow coefficient ④) when the head slope trend is opposite.

This can be seen on Figure 7B, where maximum pressure pulsation is plotted versus flow coefficients at BPF. Compared with pure water condition, it will produce larger pulsation amplitude at shaft passing frequency and shaft frequency increasing amplitude for 2% void fraction. At flow coefficient values corresponding to flow coefficient ①, ② and ③, amplitudes are larger than that the ones that correspond to flow coefficient ④, ⑤ and ⑥, mainly because the mean fluid velocity slows down and the local gas content will gradually block parts of the impeller flow channel in a non-periodic pattern. Location of each position in Figure 7A are corresponding to those in Figure 6.

4.3. Flow Visualization Inside the Impeller and Volute Channel

A high-speed camera typed Phantom 710S (Vision Research, Wayne, NJ, USA) is used for the two-phase flow visualization. The shooting frame rate is 8000 fps, the corresponding image resolution is 1024 × 800 and the exposure duration is 30 µs. The selected shooting area is shown in the red rectangular box of Figure 1a. The camera points at the middle of the picture, perpendicular to the camera lens axis to minimize the arc and angle errors. In addition, due to the high frame rate during shooting, supplemental light processing is managed on the scene. The speed of the centrifugal pump is adjusted to 1000 rpm and the high-speed camera is triggered accordingly.

Figure 8 show the visualization test results of the air-liquid two-phase distribution inside the pump, respectively, for six decreasing flow rates with 2% inlet air void fraction and for a given impeller passage location close to the volute tongue. Each corresponding flow coefficient value is reported on Figure 6. From the instantaneous pictures extracted from video, the air-liquid two-phase flow patterns inside the pump impeller at low flow rate mainly corresponds to the so-called gas-pocket flow regime and segregated flow regime. It gradually changes to agglomerated bubble flow regime and bubbly flow regime for increasing flow rates.

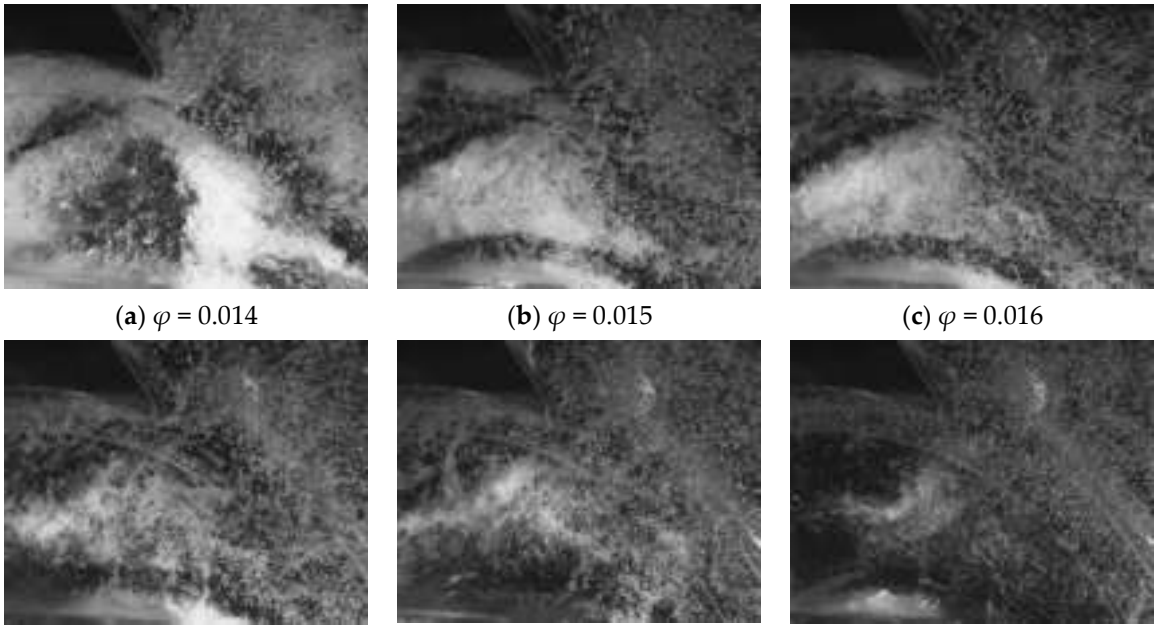

(**a**) φ = 0.014 (**b**) φ = 0.015 (**c**) φ = 0.016

(**d**) φ = 0.028 (**e**) φ = 0.06 (**f**) φ = 0.07

Figure 8. Flow behavior at different flowrate for α = 2% for a fixed rotor-stator position.

Instantaneous flow pattern suddenly changed between Figure 8c,d, which corresponds to the pump performance slope modification that occurs for φ = 0.022 between positions ③ and ④ in Figure 6, and possibly corresponding to unstable flow condition inside the pump. It was previously experimentally observed that, when approaching a value of the flow coefficient φ = 0.014 (corresponding to a water flow rate of 3 m^3/h), for increasing

values of α, the pump could no longer provide sufficient head and shut down after a few seconds of operation.

For bubble-flow type conditions, bubbles generally collect near the blade suction surface and then extend inside the blade passage when being transported toward the impeller outlet. In the selected area close to the volute tongue, part of the air bubble area locks in a stagnant position and another one is pushed back into the impeller blade passage. These could cause the unsteady pump operation, corresponding to lower frequency pulsations in the frequency domain, especially as the amplitude of the shaft frequency becomes larger.

Figure 9 presents the instantaneous flow path of air-liquid two-phase flow at $\varphi = 0.014$ for $\alpha = 2\%$. The global time value T corresponds to 0.06 s. Figure 8a corresponds to Figure 9d for which leakage flow pattern due to the shroud gap cannot be detected. With the addition of Figure 9a–c, strong reverse flow can be observed within the impeller shroud gap when a blade passes close to the volute tongue. Due to the rotation of the impeller, the gas-pocket flow, segregated flow and the water structures were simultaneously transported in the tangential direction as well as in the inward radial direction due to the strong reverse flow occurring in the shroud gap area. Therefore, three-dimensional separated flow vortices were watched at the pump inlet position. This locally special two-phase flow pattern migration is believed to be related to the starting point of pump surge shut-off and never being pointed out before. However, it is difficult to relate this strong reverse flow only to the two-phase pattern evolution. Additional flow visualization should be performed in pure water for the same flow rate obtained close to the shut-off conditions to confirm that such behavior mainly corresponds to the consequence of two-phase flow conditions.

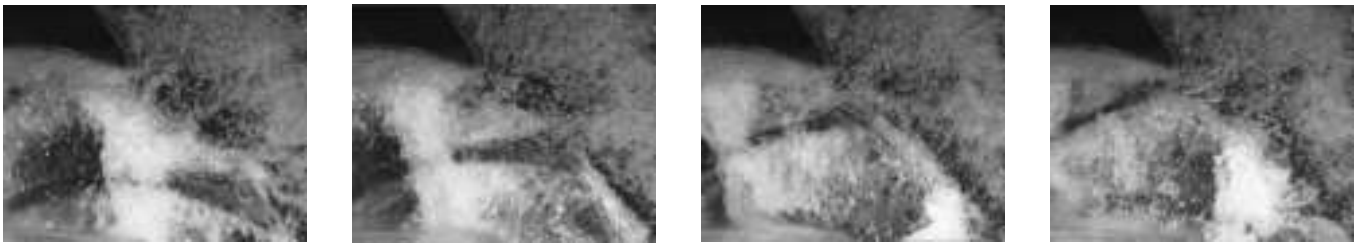

(**a**) $t_0+T/4$ (**b**) $t_0+T/2$ (**c**) $t_0+3T/4$ (**d**) t_0+T

Figure 9. Flow tracing at $\varphi = 0.014$ for $\alpha = 2\%$ at different timestep.

Finally, an important point is that homogeneous bubbly flow regime can be found inside the volute regardless to the flow rate. It is so considered that, inside the volute, pressure loss coefficient may not increase compared with pure water condition.

5. Conclusions

A flow visualization technique was used in relation with pump performance and pressure pulsation in a semi-open unshrouded transparent centrifugal impeller pump model under different air-entrainment. The main conclusions are as follows:

(1) Two-phase flow pump performance degradations have been experimentally obtained for a given rotational speed of 1000 rpm and several inlet void fractions up to 4.6%.

(2) For an inlet void fraction of 2%, the pump outlet pressure pulsation reaches its maximum value, which is found to be the first critical point for pump performance modification in relation with pressure pulsation amplitude evolutions.

(3) Results from visualization have shown that local void fraction increases as the bubble sizes increase when decreasing flow rates. Air bubbles tend to agglomerate near the impeller suction side shroud at mid-chord and close to the pressure side close to the impeller outlet plane. The starting point of pump break down is related to a strong inward reverse flow occurring in a specific location near the shroud gap of the impeller and volute tongue region. However, it is still one question that if this phenomenon related to the low flow rate value only for pure water.

(4) Additional visualization should however be performed in the whole pump area, including inlet tube flow patterns, close to the performance head curve slope modification just before pump break down starting point.

Author Contributions: Investigation-writing-review and editing, M.L. and Q.S.; data curation, M.F. and Q.C.; methodology-funding acquisition, S.Y.; validation, P.W. and Z.L.; formal analysis, G.B. All authors have read and agreed to the published version of the manuscript.

Funding: This research was funded by National Key R&D Program of China (2020YFC1512403), National Natural Foundation of China (51976079, 51779107) and Postdoctoral Science Foundation of China (2019M661745).

Institutional Review Board Statement: Not applicable.

Informed Consent Statement: Not applicable.

Data Availability Statement: Not applicable.

Acknowledgments: The authors gratefully acknowledge the financial support of the National Key R&D Program of China, National Natural Foundation of China and Postdoctoral Science Foundation of China. We are also grateful to Giorgio Pavesi from the University of Padua for his comments on the revision of this paper.

Conflicts of Interest: The authors declare no conflict of interest.

Nomenclature

A	Cross-sectional area
C_p	Pressure pulsation coefficient: $C_p = p - \overline{p}/0.5\rho u_2^2$
C_p*	Amplitude of C_p after Fast Fourier analysis
H	Pump head
P	Shaft power
p	Static pressure
Q	Volume flow rate
R	Radius
u	Impeller rotational speed: $u = \omega \cdot R$
Ω	Specific speed: $\Omega = \omega \cdot Q^{0.5}/(g \cdot H)^{0.75}$
Λ	Specific radius: $\Lambda = R \cdot (g \cdot H)^{0.25}/Q^{0.5}$
α	Inlet air void fraction: $\alpha = Q_{\text{air}}/(Q_{\text{air}} + Q_{\text{water}})$
β	Blade angle (from tangential direction)
η_g	Global efficiency: $\eta = \rho g Q_{\text{water}} H/P$
η_{int}	Internal efficiency
φ	Flow coefficient: $\varphi = Q_{\text{water}}/(2\pi \cdot R_2 \cdot b_2 \cdot u_2)$
ψ	Head coefficient: $\psi = gH/(u_2)^2$
ρ	Density of mixed fluid: $\rho = \rho_{\text{water}} \times (1 - \alpha) + \rho_{\text{air}} \times \alpha$
$\psi_{\text{t,int}}$	Internal head coefficient: $\psi_{\text{t}} = \psi/\eta_{int}$
ω	Angular velocity
τ	Shaft power coefficient: $\tau = P/\rho A_2 (u_2)^3$
1	Impeller inlet
2	Impeller outlet
t	Impeller inlet tip

References

1. Schäfer, T.; Neumann, M.; Bieberle, A.; Hampel, U. Uwe Hampel. Experimental investigations on a common centrifugal pump operating under gas entrainment conditions. *Nucl. Eng. Des.* **2017**, *316*, 1–8. [CrossRef]
2. Li, X.; Jiang, Z.; Zhu, Z.; Si, Q.; Li, Y. Entropy generation analysis for the cavitating head-drop characteristic of a centrifugal pump. *Proc. Inst. Mech. Eng. Part C J. Mech. Eng. Sci.* **2018**, *232*, 4637–4646. [CrossRef]
3. Minemura, K.; Murakami, M.; Katagiri, H. Characteristics of centrifugal pumps handling air-water mixtures and size of air bubbles in pump impellers. *Bull. JSME* **1985**, *28*, 2310–2318. [CrossRef]
4. Clark, A.P. Numerical prediction of bubble flow in a centrifugal pump. *Adv. Multiph. Flow* **1995**, *64*, 175–181.

5. Schäfer, T.; Bieberle, A.; Neumann, M.; Hampel, U. Application of gamma-ray computed tomography for the analysis of gas holdup distributions in centrifugal pumps. *Flow Meas. Instrum.* **2015**, *46*, 262–267. [CrossRef]
6. Jiang, Q.; Heng, Y.; Liu, X.; Zhang, W.; Bois, G.; Si, Q. A review on design considerations of centrifugal pump capability for handling inlet gas-liquid two-phase flows. *Energies* **2019**, *12*, 1078. [CrossRef]
7. Si, Q.; Cui, Q.; Zhang, K.; Yuan, J.; Bois, G. Investigation on centrifugal pump performance degradation under air-water inlet two-phase flow conditions. *La Houille Blanche* **2018**, *3*, 41–48. [CrossRef]
8. Müller, T. Numerical 3D RANS simulation of gas-liquid flow in a centrifugal pump with an euler-euler two-phase model and a dispersed phase distribution. In Proceedings of the 11th European Conference on Turbomachinery Fluid dynamics & Thermodynamics, ETC11, ETC2015-076, Madrid, Spain, 23–27 March 2015.
9. Si, Q.R.; Bois, G.; Zhang, K.Y.; Yuan, J.P. Air-water two-phase flow experimental and numerical analysis in a centrifugal pump. In Proceedings of the 12th European Conference on Turbomachinery Fluid dynamics and Thermodynamics, ETC12, Paper ID: ETC2017-54, Stockholm, Sweden, 3–7 April 2017.
10. Stel, H.; Ofuchi, E.; Sabino, R.; Ancajima, F.; Bertoldi, D.; Marcelino, N.; Morales, R. Investigation of the motion of bubbles in a centrifugal pump impeller. *J. Fluids Eng.* **2019**, *141*, 031203. [CrossRef]
11. Si, Q.; Bois, G.; Liao, M.; Zhang, H.; Cui, Q.; Yuan, S. A comparative study on centrifugal pump designs and two-phase flow characteristic under inlet gas entrainment conditions. *Energies* **2020**, *13*, 65. [CrossRef]
12. Si, Q.; Zhang, H.; Bois, G.; Zhang, J.; Cui, Q.; Yuan, S. Experimental investigations on the inner flow behavior of the centrifugal pumps under inlet air- water two-phase conditions. *Energies* **2019**, *12*, 4377. [CrossRef]
13. ISO 9906: 2012. Rotodynamic Pumps-Hydraulic Performance Acceptance Tests—Grades 1, 2 and 3. Available online: https://max.book118.com/html/2017/0914/133901920.shtm (accessed on 31 May 2012).

International Journal of
Turbomachinery Propulsion and Power

MDPI

Article

Loss Characterization of a Conventional Variable Inlet Guide Vane †

Roman G. Frank [1,*], Christian Wacker [2] and Reinhard Niehuis [1]

[1] Institute of Jet Propulsion, Bundeswehr University Munich, 85577 Neubiberg, Germany; reinhard.niehuis@unibw.de
[2] MAN Energy Solutions SE, 13507 Berlin, Germany; christian.wacker@man-es.com
* Correspondence: roman.frank@unibw.de
† This paper is an extended version of our contribution to the 14th European Turbomachinery Conference, Gdansk, Poland, 12–16 April 2021.

Abstract: Variable inlet guide vanes (VIGVs) are most commonly used as the major control unit of integrally geared centrifugal compressors (IGCCs). In order to enhance the efficient operating range of the compressor, the loss mechanisms and utilization limits of state-of-the-art VIGVs need to be better understood. Field measurements in the wake of a typical, commercially used configuration were therefore conducted at the VIGV test facility of the Bundeswehr University Munich. The investigations were carried out at application oriented subsonic flow conditions and stagger angles from 50° to 90° covering the full low-loss operating range, including the limits of efficient operation. For a precise local loss characterization, an inflow correlation was developed and applied to consider total pressure inhomogeneities caused by the radial inflow velocity profile and minor circumferential velocity deviations. Contrary to previous research efforts, not only the profile losses, but also the secondary flow losses induced by the open blade tips and wall-blade interactions were resolved in full detail. For this reason, a more precise and comprehensive loss assessment of realistic VIGV cascades is acquired.

Keywords: variable inlet guide vane; inflow correlation; secondary flow; annular cascade flow

check for updates

Citation: Frank, R.G.; Wacker, C.; Niehuis, R. Loss Characterization of a Conventional Variable Inlet Guide Vane. *Int. J. Turbomach. Propuls. Power* **2021**, *6*, 30. https://doi.org/10.3390/ijtpp6030030

Received: 25 May 2021
Accepted: 14 July 2021
Published: 26 July 2021

Publisher's Note: MDPI stays neutral with regard to jurisdictional claims in published maps and institutional affiliations.

Copyright: © 2021 by the authors. Licensee MDPI, Basel, Switzerland. This article is an open access article distributed under the terms and conditions of the Creative Commons Attribution (CC BY-NC-ND) license (https://creativecommons.org/licenses/by-nc-nd/4.0/).

1. Introduction

Based on the international efforts to reduce greenhouse gas emissions, the electricity supply is progressively governed by intermittent renewable resources like solar and wind energy. One concept to cope with the rise of supply fluctuations is the demand side management (DSM). The power consumption is thereby established alongside the power supply to balance the electricity market as outlined by Gellings [1]. Particularly for energy intensive industries, this concept becomes interesting, as it is able to access the wholesale electricity markets. In such a way, price peaks can be avoided by market oriented production rates. A flexible electricity consumer could furthermore capitalize by providing a balancing reserve to the transition system operator as described by Häfner [2]. For this reason, most diverse industrial sectors intensify their efforts towards more flexible production rates. Examples are outlined by Sauer et al. [3]. One particularly promising electricity consumer, however, are IGCCs, which are widely used in facilities of the process industry, the petrochemistry or air separation units, see Beaty et al. [4].

Generally, IGCCs feature up to ten stages. Each stage is driven via one bull gear, which in turn is most commonly propelled by a synchronous motor at 50 or 60 Hz grid frequency. Hence, the load shift crucial for the DSM is usually carried out by variable inlet guide vanes (VIGVs) generating varied relative impeller inlet velocities. Details regarding the pre-swirl operation are well described by Stark and Böhle [5] and Mohseni et al. [6]. Once the generated swirl or flow deflection at the VIGV exceeds a critical value, however, open flow separation and increasing secondary flow effects cause a rapid drop of the vane performance. Rising costs based on such decreased compressor efficiency will then certainly

negate the incentives of the DSM. For this reason, a widened operational range of the VIGV becomes particularly worthwhile. Previous research efforts on an enhanced efficient operating range already focused on promising blade concepts like split blades or S-cambered profiles. The experimental investigations, however, were performed solely on either linear cascade measurements carried out by Stark and Böhle [5], Bross and Stark [7] and Händel et al. [8], or full compressor stage tests conducted by Kassens and Rautenberg [9] and Mohseni et al. [6], for instance. Highly resolved data in the wake of an isolated, annular VIGV was still pending. In the context of this work, an in-depth experimental investigation of a customary, annular VIGV was therefore performed across the total efficient operating range and its operating limits.

2. Experimental Setup

2.1. VIGV Test Facility

The present characterization of the VIGV performance was conducted at the VIGV test facility of the Institute of Jet Propulsion at the Bundeswehr University Munich. Unlike the previous investigations on linear cascades, the annular measurement section depicted in Figure 1b provides the formation of a complete flow pattern, including secondary flow effects caused by open blade tips or wall-blade interactions. The relevant flow characteristics from the casing to the center are therefore reproduced and quantifiable by five-hole probe measurements. These can either be performed in the two upstream cross sections a_i or the four cross sections b_i in the wake of the VIGV. The investigations were performed at one application oriented, stationary operating point of $Ma = 0.125$ and $Re_D = 1.16 \times 10^6$. Both Mach and Reynolds numbers refer to integral, inlet flow conditions and the inlet diameter D of the VIGV. Variations of the operating point were maintained below $\pm 0.2\%$.

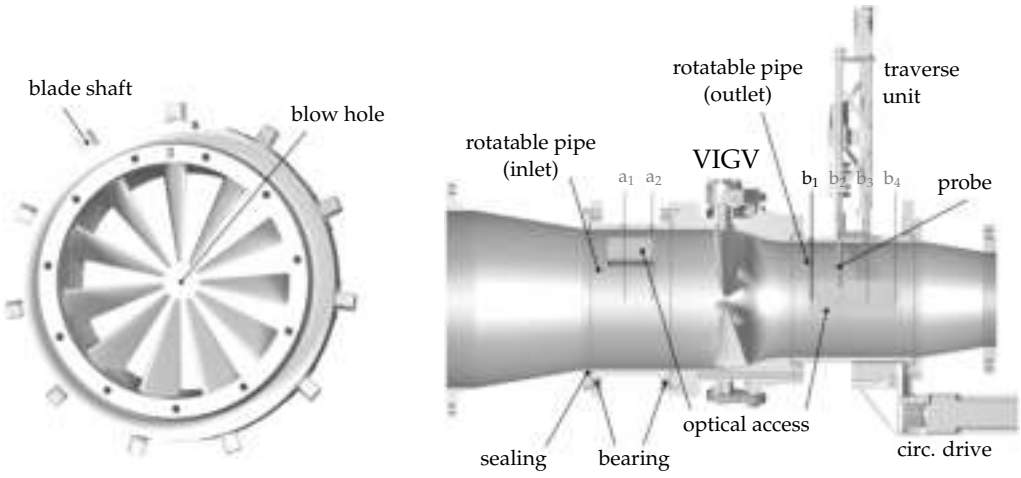

(**a**) Annular VIGV geometry (**b**) Measurement section

Figure 1. Design of the VIGV and the measurement section.

2.2. VIGV Cascade

A state-of-the-art VIGV cascade provided by MAN Energy Solutions SE served as the test specimen for the following experimental study. An illustration of the vane is found in Figure 1a. It features three major characteristics: Eleven sharply tapered, symmetric blades enabling stagger angles down to $\beta_S = 0°$, see Figure 2, linked blade shafts for joint stagger angle variations, and open blade-tips with the associated blow hole in the center region of the annular cascade. The blade geometry corresponds to the V410 profile investigated by Händel et al. [10,11] in various linear cascade measurements. The turning of the blades is maintained at minimal clearance losses between the blade hub and the casing by a spherically shaped cascade duct as illustrated by Figure 3a and Coppinger and Swain [12].

Generally, the linearly increasing chord length along the radius has a significant effect on the local Reynolds number Re_c. Although the incoming velocity profile counteracts the effect of increasing chord lengths with the radius, the general trend towards larger local Reynolds numbers closer to the casing is not reversed for wide parts of the blade height as shown in Figure 3b.

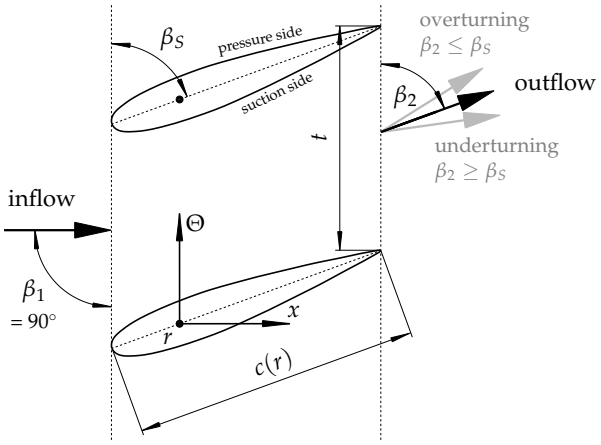

Figure 2. Scheme of the cascade in a plane of constant radius.

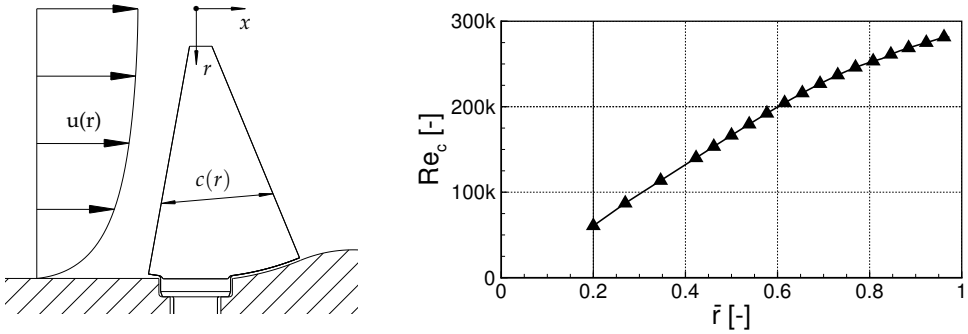

(**a**) Annular VIGV geometry (**b**) Distribution of the local Re_c along $\bar{r}$

Figure 3. Influence of the tapered blade design and inflow velocity distribution on Re_c.

2.3. Measurement Techniques and Operation

The wake field measurements presented in the following were conducted by a cranked five-hole probe in measurement plane b_1 0.61 times the cascade inlet diameter D downstream of the blade axis, which is also illustrated in Figure 1b. Due to the inevitable, radial penetration of the probe into the measurement plane, a short headed elbow probe with a spherical probe head of 3 mm was utilized. The automated positioning of the probe within the measurement section is performed by a traversing unit controlled by stepper motors. It features a rotatable pipe segment and a radial drive unit. The positioning uncertainty is considered below ± 0.1 mm and $\pm 0.1°$. Furthermore, circumferential incidence angles off the calibration range can be avoided by pivoting the probe into the flow. More detailed in-depth specifications of the utilized probe, the traversing unit, and the general test facility are provided by Frank et al. [13].

The differential pressures of the conducted measurements were recorded by a Netscanner 98 RK. Depending on the VIGV stagger angle and the expected pressure levels, the utilized pressure transducers varied from 10″ WC to 5 PSI modules. Considering each measurement as fully independent, the uncertainty provided in the following plots is based on the Gauss' law of error propagation and includes both the calibration and sensor uncertainties.

The field measurements were performed at the stagger angles $50° \leq \beta_S \leq 90°$ in increments of 10°. This covers the full low-loss operating range of the VIGV down to

$\beta_S = 60°$ as assessed by Händel et al. [8] plus one additional stagger angle at 50° off these bounds. The largely symmetric flow character and rampant measurement expenses in mind, the measurements were limited to a circular sector of two pitches only. The spatial resolution of each stagger angle setup was furthermore customized to ensure a sufficient resolution at reasonable costs. Each individual grid features between 1050 and 1250 measurement points at up to 39 radial positions.

2.4. Loss Characterization and Flow Deflection

To assess the performance of the VIGV, the generated total pressure loss $p_{t1} - p_{t2}$ and the achieved flow deflection $\Delta\beta$ is decisive. Due to negligible lateral velocity components in the inflow, the latter is provided solely by five-hole probe measurements in the wake field whereas $p_{t1} - p_{t2}$ requires a reasonable reference p_{t1} unaffected by the VIGV. This obstacle will be addressed in the following subsection. In order to parameterize the issue, the local total pressure loss is nevertheless provided by the local pressure loss coefficient

$$\zeta = \frac{p_{t1} - p_{t2}}{q_1}. \tag{1}$$

In contrast to the local $p_{t1} - p_{t2}$ probe measurements, the dynamic pressure q_1 at the VIGV inlet represents an integral variable based on the integral total mass flow.

By means of the highly resolved flow field, the local information of $\Delta\beta$ and ζ provides the foundation for the evaluation of the local primary and secondary flow phenomena. For an overall quantification of the vane performance, data reduction becomes indispensable. Mass averaged mean values (marked by the subscript Θ and r) are therefore used in the following.

2.5. Inflow Correlation of the Total Pressure Loss

In order to measure the total pressure p_{t1} to determine ζ, the application of a sole, representative Pitot probe upstream the test specimen is common practice in wind tunnel testing. This represents an adequate method in homogeneous total pressure fields without local gradients. In the present case, however, extensive boundary layer effects and local inflow inhomogeneities are present. The undisturbed total pressure field is therefore hardly detectable by one fixed Pitot probe only. For this reason, the correlation

$$\zeta = \frac{\zeta^o q_1^o - \zeta^i q_1^i}{q_1^o} = \frac{p_{t2}^i - p_{t2}^o + \left[p_{t1}^o - p_{t1}^i\right]}{q_1^o} \tag{2}$$

between the two independent measurements i and o was performed. Both ζ^i and ζ^o still refer to one local Pitot reference p_{t1}. Assuming only minor variations of the operating point, the influence of the term $\left[p_{t1}^o - p_{t1}^i\right]$ in Equation (2) and the Pitot probe measurement vanishes. Although i and o were both recorded downstream the VIGV, the guide vane was not equipped with blades in the case of i. Thus, the measurement of ζ^i does include the inflow inhomogeneities and the influence of the narrowing contour of the VIGV, but not the loss induced by the blades. To still perform a meaningful correlation, the locations of the measurement points i and o need to match one streamline. A previous approach by Frank et al. [13] already considered the dominating radial gradients along the radius assuming a negligible flow deflection over the local radius relative to the pipe radius ($\bar{r}$). Subordinate circumferential total pressure gradients of the incoming flow field were neglected, though. The necessity, however, to correlate circumferential deviations is highlighted by two exemplary 360°-traverses at $\beta_S = 90°$ in Figure 4a,b. Not only the general offset from zero caused by significant boundary layer effects, but also considerable circumferential variations of the incoming flow, which partly exceed a delta of $\Delta\zeta/\zeta_{ref} = 2.5\%$, are thus excellently eliminated. Striving for a complete approach, which includes the circumferential discontinuities, the generated, local angular flow deflection $\Delta\Theta$ between the VIGV blades and the measurement plane as depicted in Figure 5 must

therefore be considered. Due to a negligible flow deflection at $\beta_S = 90°$, this has not been an issue at the previously illustrated cases in Figure 4, yet. With decreasing stagger angles, the flow field is, however, largely distorted from the VIGV inlet to the measurement plane. At comparable circumferential velocities generated by the straight VIGV blades, the distortion is mainly caused by the inverse proportionality of the angular velocity and the radius $\omega \propto r^{-1}$. Therefore, the angular velocity and the covered angular flow deflection $\Delta\Theta$ increase rapidly towards the center as highlighted in Figure 5b. The flow in the blow hole region in turn is not disturbed by the vane, which causes an additional sheer layer downstream the blade tips.

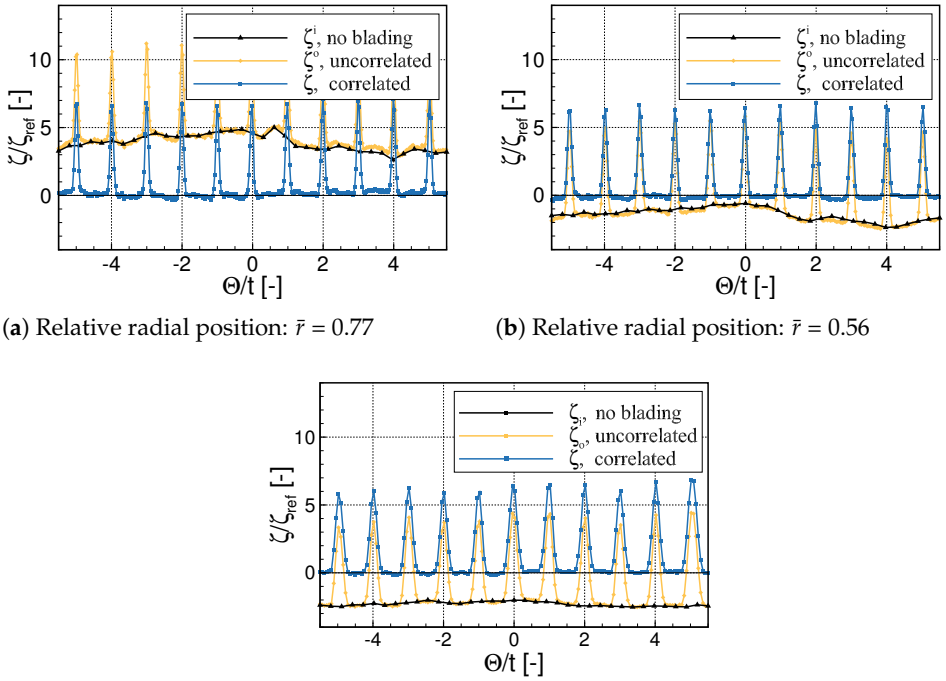

(**a**) Relative radial position: $\bar{r} = 0.77$ (**b**) Relative radial position: $\bar{r} = 0.56$

(**c**) Relative radial position: $\bar{r} = 0.35$

Figure 4. Inflow correlation at $\beta_S = 90°$ over 360° at selected radii.

To emulate the angular flow deflection $\Delta\Theta$ of the streamlines of i and o, a trigonometric approach based on the measured, circumferential flow angle β_2^o and the axial distance x between the VIGV and the measurement plane was chosen as a first approximation

$$\Delta\Theta(r) = \frac{x}{r\tan(\beta_2^o)} + \Theta_{off}. \tag{3}$$

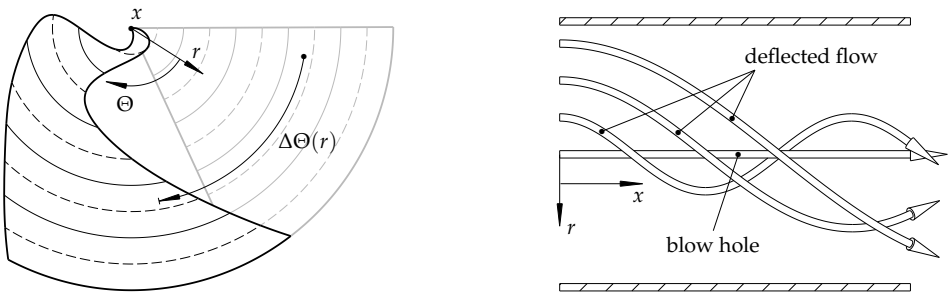

(**a**) Matching segments with (o, black) and without blading (i, gray)

(**b**) Exemplary streamlines of constant circumferential velocities

Figure 5. Stretching of the flow field at $\beta_S \neq 90°$.

Mindful of the gross assumption of a constant circumferential flow angle along x, a correction factor Θ_{off} is introduced to obtain a more reliable correlation. An illustration of the approach is provided in Figure 6. Downstream the blade at central height, where the flow is highly dominated by profile losses, the determination of Θ_{off} is performed by a matching of the actual and the trigonometrically predicted blade position identified by the blade wake. Close to the casing at large radii, however, secondary losses increasingly dominate the profile losses previously used as a marker. Thus, Θ_{off} has to be assumed constant in this region. The thereby caused error remains minor as the angular velocity gradients are relatively small, and Θ_{off} is still much smaller than the pitch t. Towards decreasing radii and small stagger angles of the guide vane, Θ_{off} potentially exceeds the magnitude of t due to the significantly increased covered angle $\Delta\Theta$. This obstacle to reliably determine Θ_{off} at small radii is caught by a radial cross-comparison. Significant radial gradients of Θ_{off} from one radial position to the next would be nonphysical and are thus disallowed. The success of the streamline correlation is demonstrated by the physically meaningful contour plots in Figure 7. Since the underlying data interpolation of the following plots is based on the same algorithm as the introduced correlation, the reliability of the approach is graphically ensured. In the pipe center governed by the blade tip vortex, a precise local correlation becomes increasingly difficult, though. As flow inhomogeneities are weak in the core region, see Figure 4c, an extensive angular correlation is dispensable in this particular region, anyway. Naturally, the described procedure must be performed individually for each setting of the guide vane and each operating point.

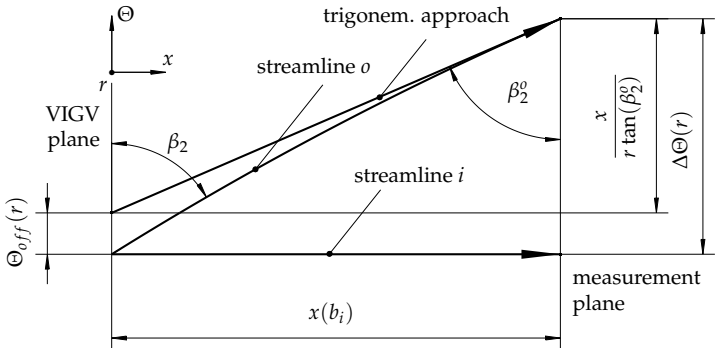

Figure 6. Approach of the circumferential correlation at the radius r.

3. Results and Discussion

The spatially resolved distributions of ζ at the five investigated stagger angles are provided in Figure 7. Each measurement position is marked by a velocity vector. Despite gross differences in the loss distribution and rates, the contour plots reveal common characteristics and underlying trends towards decreased stagger angles. At $\beta_S = 90°$, the loss is mainly dominated by profile losses (I) reaching as an elongated loss field from near the casing to $\bar{r} \approx 0.22$ downstream the bounds of the blow hole at the blade tips (IV). At decreasing stagger angles, this region is progressively stretched in the circumferential direction, resulting in an exit of one blade wake at the one side of the investigated circular sector and an entering of another wake from the other side. At $\beta_S \leq 70°$, an accelerated growth of the profile losses, as well as a broadening of the wakes, is observed. This characteristic is traced back to higher losses and wider wakes generated at larger flow deflections, as it was already observed in linear cascade measurements of the same profile by Händel et al. [10]. To a certain extent, the broadening of the wakes is also considered to be driven by an increased mixing of the flow based on the elongated streamlines between the VIGV and the measurement plane with higher swirl, see Amecke [14].

Besides the analysis of the primary profile losses, it has been the main objective to trace and to quantify the secondary flow losses inevitably generated by the open blade-tips (III) and the finite casing dimensions (II). Wall-blade flow interactions at radii $\bar{r} \to 1$ are well-known in turbomachinery flow. Sieverding [15] and Denton [16], for instance, provide

an in-depth review about the findings of the previous decades. Most commonly the effects are classified into passage, horse shoe, and corner vortices. Even if the loss region caused by the blade-wall interaction is clearly identified by the undertaken measurements, the subdivision of the different vortex structures is not feasible due to the high mixing length between the cascade and the measurement plane of at least 1.5 times $c(r)$. A steady increase of the blade-wall induced losses is nevertheless apparent with smaller stagger angles.

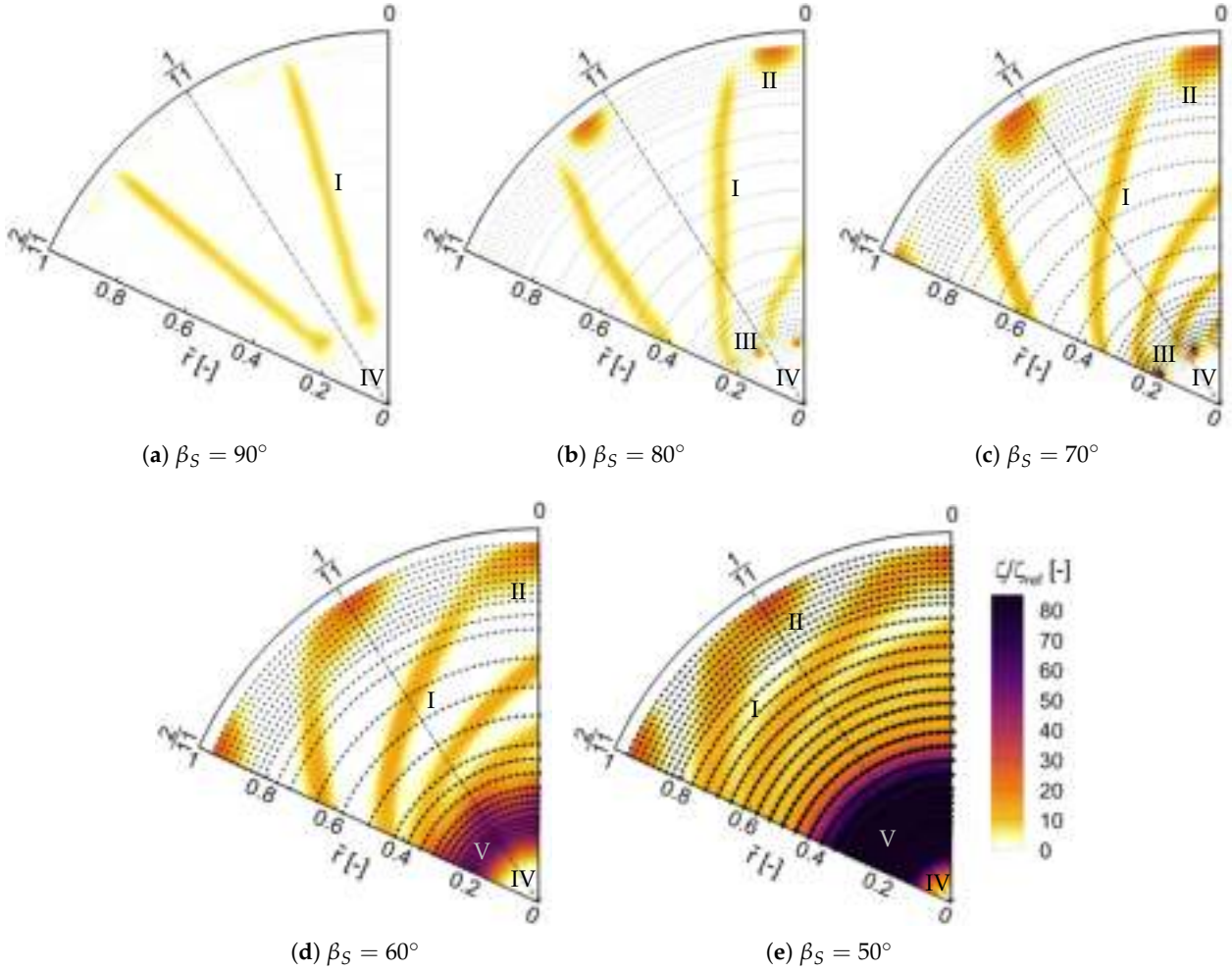

(**a**) $\beta_S = 90°$ (**b**) $\beta_S = 80°$ (**c**) $\beta_S = 70°$

(**d**) $\beta_S = 60°$ (**e**) $\beta_S = 50°$

Figure 7. Wake field measurements from $\beta_S = 90°$ to 50° [I: profile losses, II: wall-blade interaction losses, III: blade tip losses, IV: blow hole flow, V: suspected open flow separation].

Unlike secondary flow losses at the endwall, the blade tip loss is a rather exceptional phenomenon in turbomachinery applications as the development of blade tip vortices is usually hindered by the hub. The observed effects, however, compare well to the widely known wing tip vortex at airfoil structures as described by Green [17], for instance. The development of the loss at the blade tip is prefigured as a diminutive loss region at $\beta_S = 90°$ and $\bar{r} \approx 0.2$ in Figure 7a. With decreased stagger angles by 10 and 20°, the loss region grows progressively in size and intensity. From $\beta_S = 60°$ on, the locally bounded loss is merged in a large ring-shaped loss region (V), which considerably intensifies at $\beta_S = 50°$. In the previous linear cascade measurements of Händel et al. [10], the development of an open separation bubble was detected at $Re_c \leq 100$ k and $\beta_S \leq 60°$. These conditions match the flow conditions at the noticed ring-shaped area of high loss very well. Thus, rather the development of an open separation than a disproportionate rise of the blade tip losses is suspected as the source for the rapidly growing losses in this particular region.

Further measurements have been recorded in the cross section b_3, $1.01D$ downstream the VIGV. As expected by the increased axial distance x, the wake fields are further distorted, loss peaks flattened, and the region affected by loss is widened. For this reason, the hereby presented measurements in b_1 were considered to be more revealing in this context.

3.1. Performance along the Radius

Subsequent to the previous qualitative discussion, the mass averaged mean values ζ_Θ and $\Delta\beta_\Theta$ are illustrated in Figure 8 to enable a quantitative assessment of the losses along the radius. The blade tip position at $\bar{r} = 0.2$ is marked by a solid, vertical line.

Each of the previously defined regions of loss dominated by either profile, wall-blade interaction or blade tip losses is still well distinguished in Figure 8a,b. Successively rising and widening losses induced by the wall-blade interactions are found between $\bar{r} = 0.8$ and 1, whereas the losses enforced by the blade tip vortex are located in the region around the blade tips at $\bar{r} = 0.2$. From $\beta_S \leq 60°$, the losses, especially in the latter region downstream of the blade tips at the comparable low local Reynolds numbers Re_c, drastically increase. As already discussed, this severe rise is traced back to open flow separation effects. In the area of moderate profile losses at mid blade height around $\bar{r} = 0.6$ between the latterly discussed loss region of the blade tip vortex or open flow separation effects and the deploying wall-blade interactions, a stable decrease of the losses with higher radii or larger local Re_c is observed throughout all stagger angles, interrupted only by the highly mixed flow field at $\beta_S = 50°$. This effect is in good accordance with the observations of a decreasing profile loss with higher Re_c made by Händel et al. [10].

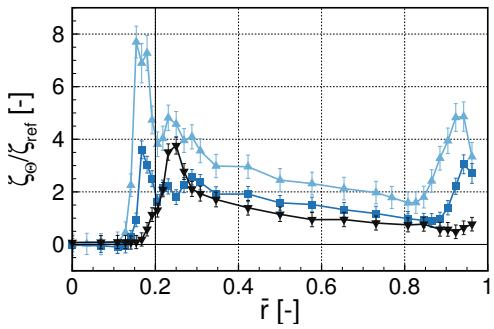

(**a**) ζ at $\beta_S \geq 70°$

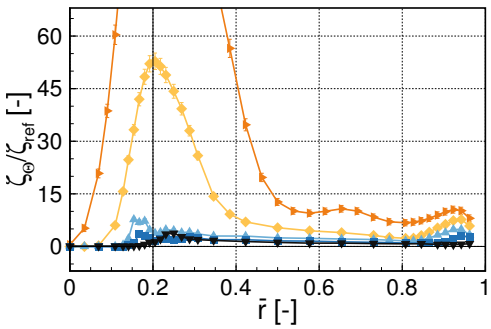

(**b**) ζ across the entire stagger angle range

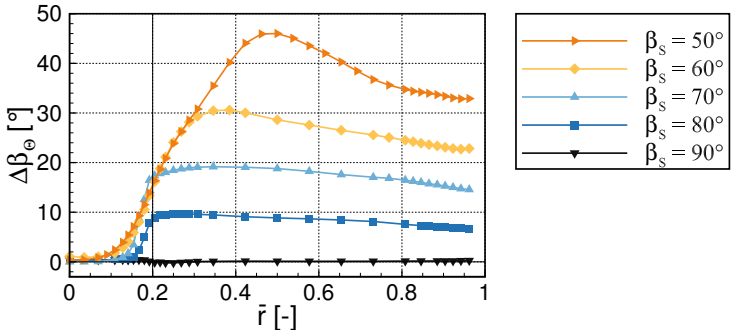

(**c**) $\Delta\beta$ across the entire stagger angle range

Figure 8. Radial loss and deflection assessment.

The obtained circumferential flow deflection $\Delta\beta_\Theta$ depicted in Figure 8c naturally starts at zero in the pipe center, increases downstream the blade tip region until a flow deflection of approximately $90° - \beta_S$ is reached, and slowly decreases in the following again. Radial velocity components, in contrast, remain nearly negligible as already indicated in Figure 7. At $\beta_S = 50°$ and $0.39 \leq \bar{r} \leq 0.66$ an exceptional overturning of $\Delta\beta_\Theta$ of up to 6° compared

to the set blade angle is noticed. A comparable local overturning of the circumferential velocity was already observed by Kassens and Rautenberg [9] at a similar VIGV cascade geometry in a centrifugal compressor stage and stagger angles of 60 and 30°. The authors ascribe this effect to the converging pipe geometry leading to a fluid transport towards smaller radii and thus an acceleration of the angular velocity. Chen et al. [18], in contrast, trace the overturning observed by Kassens and Rautenberg [9] from the vortex structure enforced by the VIGV to the development of a Rankine vortex. The outer region of the Rankine vortex is governed by a potential vortex, which represents the analytical solution of a vortex field in total pressure equilibrium without radial velocity components. The outer flow field is therefore postulated to evolve into a potential vortex whereby a local rise of the tangential velocity is explained. Neither of the two publications considers the possible influence of a solid open flow separation, however. Händel's [19] linear cascade tests at identical profile geometries revealed a strong tendency towards flow overturning due to an open flow separation at $\beta_S = 50°$. In this respect, a deploying open flow separation represents a highly plausible explanation for the observed flow overturning.

3.2. Overall Losses

For a global assessment of the VIGV performance at varied stagger angles, Figure 9a features the mass averaged total pressure loss coefficient $\zeta_{r,\Theta}$ versus the flow deflection $\Delta\beta_{r,\Theta}$. It was expected from Figure 8a that the loss remains similar at $\beta_S = 90$ and 80° and rises only moderately at $\beta_S = 70°$. A further decrease of the stagger angles increases the loss more dramatically. This trend was especially indicated by the significant losses in the blade tip region of Figure 8b. A progressive shortfall of $\Delta\beta_{r,\Theta}$ compared to the blade angle $90° - \beta_S$ is moreover observed in Figure 9a. The discrepancy is partly due to the observed underturning at the blades and to the natural lack of deflection in the blow hole. At $\beta_S = 50°$, this deficit is partly counteracted by the previously described overturning at parts of the blade height.

To finally evaluate the efficiency of the achieved flow deflection, the total pressure loss coefficient per generated flow deflection is illustrated in Figure 9b. Due to the singularity at $\Delta\beta_{r,\Theta} = 0°$, the field measurement at $\beta_S = 90°$ is thereby not considered. At $\beta_S = 80$ and 70°, the index reveals moderate, relative losses in each case. At further decreased stagger angles, a progressive rise is observed. In alignment with the previous recommendation of Händel et al. [10], the utilization of the VIGV cascade is not recommended at stagger angles below 60° to maintain an adequate vane and compressor efficiency.

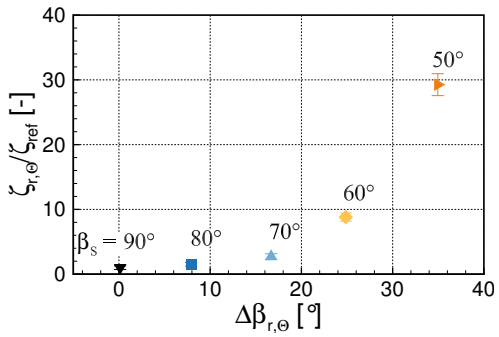

(**a**) Total pressure loss coefficient against the generated flow deflection

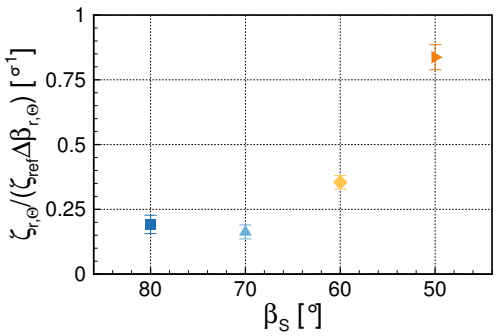

(**b**) Total pressure loss coefficient per flow deflection against the stagger angle

Figure 9. Overall loss assignment.

4. Conclusions and Outlook

The objective of the present work is the evaluation of the losses generated by a state-of-the-art VIGV at varied stagger angles. Due to the annular geometry of the test section,

both profile and secondary flow effects induced by wall-blade interactions and open blade tips were reproduced and metrologically recorded.

In order to deliver reliable data, an advanced correlation of the pressure loss ζ^o measured in the wake to ζ^i in the unaffected flow field has been introduced. Compared to a previous approach, not only radial gradients of ζ caused by the wall boundary layer, but also circumferential deviations reaching up to at least $\Delta\zeta/\zeta_{ref} = 2.5\%$, are thereby eliminated.

Based on the findings of the wake fields exceeding the total working range of the investigated VIGV, two suggestions are made in the following to minimize dominant loss regions and to ultimately increase the efficient operating range of the vane and the associated compressor:

- From $\beta_S = 60^\circ$ on, an increasing region of notable losses was observed downstream the region of the blade tips. Previous linear cascade measurements at an identical profile geometry by Händel et al. [10] already proved the tendency of the profile towards an open flow separation at the referred stagger angle and comparable local Reynolds numbers. Therefore, the reconsideration of the current blade design is recommended to ensure attached flow at further decreased stagger angles. Especially split blade geometries as investigated in linear cascade measurements by Bross and Stark [7] and Händel et al. [8] show promise to extend the efficient operational range of the annular VIGV.
- Moreover, the blocking of the center by a hub is suggested. Low local Reynolds numbers Re_c are hence prevented by accelerated flow conditions and the elimination of short chord lengths in the core region. Thus, lower profile losses as they were observed along higher Re_c, a certain shift of the devastating open flow separation towards lower stagger angles β_S, and the suppression of the blade-tip vortex are expected. Instead of the blade tip losses, blade-hub flow interactions and tip gap effects will induce new losses. It is to be investigated if the expected benefits prevail with the induced hub-blade and tip clearance losses.

Author Contributions: Conceptualization, R.G.F., C.W. and R.N.; methodology, software and validation, R.G.F.; formal analysis, R.G.F. and R.N.; investigation, R.G.F.; resources, R.N. and C.W.; data curation, R.G.F. and R.N.; writing—original draft preparation, R.G.F.; review and editing, R.G.F. and R.N.; visualization, R.G.F.; supervision, C.W. and R.N.; project administration, R.N.; funding acquisition, C.W. and R.N. All authors have read and agreed to the published version of the manuscript.

Funding: This research was funded by the German Federal Ministry of Education and Research (Kopernikus project—SynErgie). The test specimen was kindly provided by the MAN Energy Solutions SE.

Institutional Review Board Statement: Not applicable.

Informed Consent Statement: Not applicable.

Data Availability Statement: The non-dimensionalized data presented in this study is available on request from the corresponding author.

Acknowledgments: The authors gratefully acknowledge the financial support of the Kopernikus project SynErgie by the German Federal Ministry of Education and Research (BMBF) and the project supervision by the project management organization Projektträger Jülich (PtJ).

Conflicts of Interest: The authors declare no conflict of interest. The funders had no role in the design of the study; in the collection, analyses, or interpretation of data; in the writing of the manuscript; or in the decision to publish the results.

Abbreviations

Symbols

b_i	Measurement plane i [-]
c	Chord length [m]
Ma	Mach number [-]
p	Pressure [Pa]
q	Dynamic pressure [Pa]
r	Radial axis [m]
$\bar{r}$	r relative to local pipe radius [-]
Re_D	Integral Reynolds number [-]
Re_c	Local Reynolds number [-]
t	Pitch [°]
x	Pipe center line axis [m]
β_S	Stagger angle [°]
$\Delta\beta$	Circumferential flow deflection [°]
Θ	Pipe circumferential axis [°]
$\Delta\Theta$	Angular flow deflection [°]
ζ	Total pressure loss coefficient [-]

Sub-/Superscripts

1, 2	Without or with effect of VIGV
D	Inlet diameter of VIGV
i	Measurement without blading
o	Wake measurement incl. blading
off	Offset
ref	Integral reference at $\beta_S = 90°$
t	Total value
Θ, r	Mass averaged over Θ, r

Acronyms

DMS	Demand side management
VIGV	Variable inlet guide vane
IGCC	Integrally geared centrifugal compressor

References

1. Gellings, C.W. The Concept of Demand-Side Management for Electric Utilities. *Proc. IEEE* **1985**, *73*, 1468–1470. [CrossRef]
2. Häfner, L. Demand Side Management: Entscheidungsunterstützungssysteme für die flexible Beschaffung von Energie unter integrierten Chancen- und Risikoaspekten. *HMD. Theor. Und Prax. Der Wirtsch.* **2018**, *55*, 627–645. [CrossRef]
3. Sauer, A.; Abele, E.; Buhl, H.U. *Energieflexibilität in der deutschen Industrie*; Frauenhofer Verlag: Stuttgart, Germany, 2019; ISBN 978-3-8396-1479-2
4. Beaty, P.J.; Eisele, K.; Maceyka, T.D.; Schwarz, C. *Integrally Geared API 617 Process Gas Compressors*; Texas A&M University, Turbomachinery Laboratories: College Station, TX, USA, 2000; pp. 239–246. [CrossRef]
5. Stark, U.; Böhle, M. Theoretische und experimentelle Untersuchungen an ungestaffelten Gittern aus Profilen mit mechanischen Klappen. *Forsch. Im Ingenieurwesen* **1990**, *56*, 169–182. [CrossRef]
6. Mohseni, A.; Goldhahn, E.; Van den Braembussche, R.A.; Seume, J.R. Novel IGV Designs for Centrifugal Compressors and Their Interaction with the Impeller. *ASME J. Turbomach.* **2012**, *134*, 021006. [CrossRef]
7. Bross, S.; Stark, U. Entwicklung neuer Schaufelgitter aus Profilen variabler Geometrie zum Einsatz in Leiträdern drallgerelgeter Turbomaschinen-Teil I. *Forsch. Im Ingenieurwesen* **1994**, *60*, 120–132. [CrossRef]
8. Händel, D.; Niehuis, R.; Klausmann, J. *Aerodynamic Investigation of an Advanced VIGV Design of Adjustable Geometry for Very High Flow Turning*; ASME Turbo Expo: Montreal, QC, Canada, 2015. [CrossRef]
9. Kassens, I.; Rautenberg, M. *Flow Measurements Behind the Inlet Guide Vane of a Centrifugal Compressor*; ASME Turbo Expo: Stockholm, Sweden, 1998; doi:10.1115/98-GT-086 [CrossRef]
10. Händel, D.; Niehuis, R.; Rockstroh, U. *Aerodynamic Investigation of a Variable Inlet Guide Vane with Symmetric Profile*; ASME Turbo Expo: Düsseldorf, Germany, 2014. [CrossRef]
11. Händel, D.; Rockstroh, U.; Niehuis, R. Experimental Investigation of Transition and Seperation Phenomena on an Inlet Guide Vane with Symmetric Profile at Different Stagger Angles and Reynolds Numbers. In Proceedings of the International Symposium on Transport Phenomena and Dynamics of Rotating Machinery, Honolulu, HI, USA, 24–28 February 2014; FR305
12. Coppinger, M.; Swain, E. Performance Prediction of an Industrial Centrifugal Compressor Inlet Guide Vane System. *Proc. Inst. Mech. Eng.* **2000**, *214*. [CrossRef]

13. Frank, R.; Wacker, C.; Niehuis, R. *A New Test Facility for Advanced Testing of Variable Inlet Guide Vanes*; MTT Measuring Techniques in Turbomachinery; 2020, MTT2520A18. Available online: https://www.measTechturbo.com/paper-archives/mtt2520-santorini-2020 (accessed on 16 July 2021).
14. Amecke, J. *Auswertung von Nachlaufmessungen an ebenen Schaufelgittern*; Messbericht 67 A 49; AVA Göttingen: Gottingen, Germany, 1967
15. Sieverding, C.H. Recent Progress in Understanding of Basic Aspects of Secondary Flows in Turbine Blade Passages. *ASME J. Eng. Gas Turbines Power* **1985**, *107*. [CrossRef]
16. Denton, J.D. Loss Mechanisms in Turbomachinery. *ASME J. Turbomach.* **1993**, *115*, 621–656. [CrossRef]
17. Green, S.I. Wing Tip Vortices. In *Fluid Mechanics and Its Applications*; Springer: Dordrecht, The Netherlands, 1995; Volume 30.
18. Chen, Y.N.; Hagelstein, D.; Kassens, I.; Hasermann, H.; Haupt, U.; Rautenberg, M. *Overshoot of the Rankine Vortex Formed in the Flow Field Behind the Inlet Guide Vane of Centrifugal Compressors*; ASME Turbo Expo: Indianapolis, IN, USA, 1999. [CrossRef]
19. Händel, D. *Experimentelle Untersuchung und Weiterentwicklung eines variablen Eintrittsleitapparates für die Vordrallregelung in Turbomaschinen*; Verlag Dr. Hut: Munich, Germany, 2018; ISBN 978-38439-3874-7.

International Journal of
Turbomachinery
Propulsion and Power

MDPI

Article

Flow Coefficient and Reduced Frequency Effects on Wake-Boundary Layer Interaction in Highly Accelerated LPT Cascade

Edward Canepa, Davide Lengani, Alessandro Nilberto, Daniele Petronio *, Daniele Simoni, Marina Ubaldi and Pietro Zunino

DIME, Department of Mechanical, Energy, Management and Transport Engineering, University of Genova, I-16143 Genova, Italy; Edward.Canepa@unige.it (E.C.); davide.lengani@edu.unige.it (D.L.); alessandro.nilberto@unige.it (A.N.); daniele.simoni@unige.it (D.S.); marina.ubaldi@unige.it (M.U.); pietro.zunino@unige.it (P.Z.)
* Correspondence: daniele.petronio@edu.unige.it

Abstract: The paper presents a detailed analysis of particle image velocimetry (PIV) measurements performed in a turbine cascade representative of highly accelerated low-pressure turbine (LPT) blades. Two cameras have been simultaneously used to observe a great portion of the suction side boundary layer with the highest possible spatial resolution, thus allowing us to solve the interaction process between impinging upstream wakes and the blade boundary layer. Four unsteady inflow conditions, characterized by different incoming wake reduced frequencies and flow coefficients, have been examined at fixed Reynolds number. The highly resolved flow fields have been processed to explore reduced frequency and flow coefficient effects on the boundary layer unsteady transition process and, consequently, on loss production. For a deep physical insight on the mechanisms responsible for loss generation, proper orthogonal decomposition (POD) has been applied at different phases of the wake passing period. This has provided the dominant structures affecting the cascade aerodynamics during the wake period. Moreover, the examination of POD modes has allowed us to show the effects induced by the parameter variation on the turbulent kinetic energy production and thus to the unsteady loss production mechanisms.

Keywords: POD; LPT; wake-boundary layer interaction; production of turbulent kinetic energy (TKE)

check for updates

Citation: Canepa, E.; Lengani, D.; Nilberto, A.; Petronio, D.; Simoni, D.; Ubaldi, M.; Zunino, P. Flow Coefficient and Reduced Frequency Effects on Wake-Boundary Layer Interaction in Highly Accelerated LPT Cascade. *Int. J. Turbomach. Propuls. Power* **2021**, *6*, 32. https://doi.org/10.3390/ijtpp6030032

Academic Editor: Claus Sieverding

Received: 24 May 2021
Accepted: 2 August 2021
Published: 4 August 2021

Publisher's Note: MDPI stays neutral with regard to jurisdictional claims in published maps and institutional affiliations.

Copyright: © 2021 by the authors. Licensee MDPI, Basel, Switzerland. This article is an open access article distributed under the terms and conditions of the Creative Commons Attribution (CC BY-NC-ND) license (https://creativecommons.org/licenses/by-nc-nd/4.0/).

1. Introduction

The investigation of the physical sources involved in the generation of profile losses represents a central topic in the optimization process of low-pressure turbines. The study is very complex because of the presence of periodic wakes shed from upstream rows, that makes the flow strongly unsteady. For this reason, several research works were carried out in the past. In the numerical simulation by Wu and Durbin [1], the dynamics of the upstream wake evolving in the blade passage is accurately described. It is shown that the wake is conveyed by the cascade potential field towards the blade suction side where it interacts with the boundary layer. Consequently, the transition and separation processes along the blade suction side are strongly influenced by upstream wakes. Especially, relevant effects have been observed in high-lift cascades at low Reynolds numbers, where large separation bubble can be present in the steady condition (see for instance Michelassi et al. [2]). Further investigations [3] captured the formation of two counter-rotating vortices developing at the boundaries of the wake, that are responsible for inducing periodic accelerations and decelerations inside the boundary layer. The consequent intermittent evolution of the near wall flow is also shown in the tests performed by Gompertz and Bons [4]. The process is even more complicated by smaller scale structures carried within the bulk of the wake, as documented by the measurements carried out by Stieger and Hodson [5], that revealed high turbulent activity just in the region of impinging wakes. In this scenario, a step forward in the understanding of wake related effects is provided in [6], where

the capability of proper orthogonal decomposition (POD) in identifying different flow structures is discussed, allowing the identification of different mechanisms responsible for loss generation.

The dynamics of the wake-boundary layer interaction process is strongly affected by the upstream wake reduced frequency and the flow coefficient, since they characterize both timing and direction of incoming wakes. Michelassi et al. [7] investigated different inflow conditions, showing that the reduced frequency directly represents the forcing frequency acting on the boundary layer, while the flow coefficient induces different wake trajectories during advection in the downstream cascade passage. Similar flow dynamics are also shown in the simulations reported in [8], carried out for different combinations of both the parameters. Funazaki et al. [9] presented an investigation that quantified losses to the variation of some flow and geometric parameters, including the Strouhal number, closely related to the reduced frequency. However, in this work, reduced frequency and flow coefficient have not been varied independently.

In the present work, particle image velocimetry (PIV) measurements have been carried out in the rear part of the blade suction side to solve the wake-boundary layer interaction process in a highly accelerated turbine cascade. Four different combinations of reduced frequency and flow coefficient have been tested, at constant Reynolds number. Incoming wakes have been characterized at the inlet of the cascade by phase-locked velocity data acquired with an hot-wire anemometer (HWA). The time-mean and fluctuating parts of PIV velocity fields have been analyzed in order to discuss the effects of both reduced frequency and flow coefficient on the blade boundary layer development. Fluid dynamic losses have been quantified in the measuring domain for the different flow cases. Hence, for a deeper investigation of the mechanisms responsible for loss production, POD has been applied at six different phases of the wake passing period. POD modes have allowed us to separate deterministic and stochastic flow structures and to follow their temporal evolution through the inspection at different phases. The turbulent kinetic energy production per POD mode has also revealed loss contributions due to different flow structures, while its spatial distribution has exhibited the regions where losses are mainly produced for the different combinations of the flow parameters here tested.

2. Test Facility and Data Analysis

Measurements were performed in the low-speed wind tunnel installed in the Aerodynamic and Turbomachinery Laboratory of the University of Genova. The test section was constituted of a seven-blade planar cascade, representative of a highly accelerated low-pressure turbine row. The blade chord was 190 mm, the deflection 40° and the solidity 1.2. The cascade, designed to operate with a fully laminar suction side boundary layer in the steady condition, is further characterized by a diffusion factor of $DF = 0.09$, a diffusion rate of $Ds = 0.15$ and a velocity ratio of $VR = 2.8$. Measurements were carried out at fixed Reynolds number Re = 160k for four different combinations of reduced frequency and flow coefficient (see Table 1). The Reynolds number, slightly lower than the design one, was selected to maximize the spatial resolution of the PIV measurements. Instead, the combinations of reduced frequency and flow coefficient were chosen to investigate a large range of parameter variation around their nominal values. All the tests were performed with an inlet homogeneous free-stream turbulence of about $Tu = 6\%$, generated by means of a turbulence generating grid and measured at the cascade inlet section in the steady condition. Upstream wakes were simulated by the moving bar system schematically presented in Figure 1, that allows the variation of reduced frequency and flow coefficient by controlling the bar velocity and spacing. The bars used for the present investigation were characterized by a diameter of 3 mm, appositely chosen to generate momentum defect and losses typical of an upstream LPT row. A detailed characterization of the wake entering the downstream cascade is reported in the following.

Table 1. Test flow conditions.

	Reduced Frequency f^+	Flow Coefficient φ
C1	1.2	0.6
C2	0.6	0.6
C3	1.2	0.3
C4	2.4	0.3

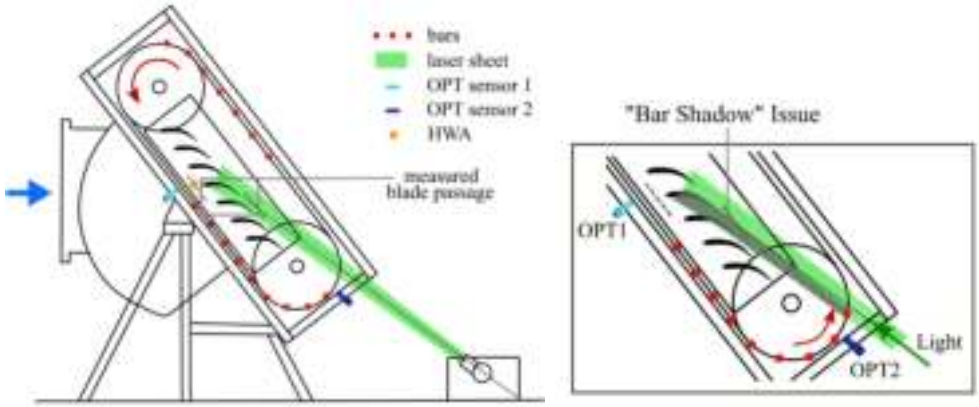

Figure 1. Test section (on the **left**) and detail of the "bar shadow" issue (on the **right**).

2.1. Experimental Setup

Figure 1 shows the test section. The light source, a dual cavity Nd:Yag pulsed laser with 100 mJ energy per pulse at 6 Hz and pulse duration 8 ns, was located to light the test section from behind. The flow was seeded at the wind tunnel entrance section with Vaseline oil droplets with a mean diameter of 1.5 µm. The seeding flow rate was chosen in order to obtain a particle concentration of 4/5 particles per interrogation area. Measurements were performed in order to solve the wake-boundary layer interaction process on the blade suction side with the highest possible spatial resolution. To this end, two Dantec HighSense Mk II digital cameras (Dantec Dynamics, Skovlunde, Denmark), with a resolution of 1344 × 1024 pixels, were used simultaneously. The positions of the cameras are schematically reported in Figure 2. The left camera (cam1) observed the flow field just behind the velocity peak region for $0.35 < s/s_{MAX} < 0.6$, where the incoming wakes start to interact with the boundary layer, while the right camera (cam2) was located downstream close to the blade trailing edge, looking at the flow region in between $0.75 < s/s_{MAX} < 1$. In order to allow the measurement of the velocity gradients in the boundary layer, couples of PIV images were acquired with a time delay of 40 µs. The magnification factor was 0.263. The cross-correlation has been calculated over a 32 × 32 pixels interrogation area with 50% overlap, obtaining a vector spacing of 0.30 mm. For each flow condition, a total amount of about 2000 couples of images were collected.

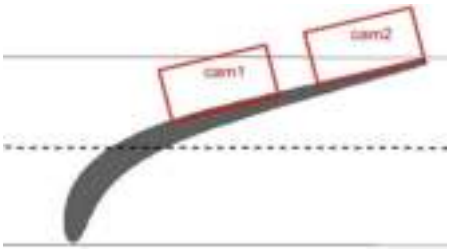

Figure 2. Detail of the positions of the two cameras.

A particular setting of the test section was adopted to avoid shadows generated by the bars passing in front of the light source may corrupt the acquired images. The detail reported on the right of Figure 1 highlights the "bar shadow" issue. To overcome this problem, the bars (marked by red points in the figure) were assembled in two trains,

constituted of 14 bars for conditions C1 and C4 (higher reduced frequency) and 7 bars for conditions C2 and C3 (lower reduced frequency). At the same time, two optical sensors were located in front of the cascade (OPT1) and in front of the laser (OPT2) to capture the passage of the bars. The transistor-transistor logic (TTL) signals generated by the sensors are reported in Figure 3 together with the laser pulses. The first spike from OPT1 switches on an acquisition window, that will be closed by the first spike from OPT2. The laser pulses in between the acquisition window correspond to images with wakes and without shadows, so they were kept for further post-processing, whereas the other images were discarded. The selected snapshots can be also phased in the wake period by computing the difference between the time instant t_{piv} of PIV pulse with the time instant t_1 of the closer previous TTL pulse emitted by the optical sensor in front of the cascade (OPT1) and reffering it to the bar passing period $T = t_2 - t_1$, as in Equation (1):

$$t/T = \frac{t_{piv} - t_1}{t_2 - t_1} \tag{1}$$

In order to evaluate the velocity defect and the turbulence intensity peak characterizing the incoming wake for the different conditions, a single-element HWA (type 55P15) was also installed at the cascade entrance (Figure 1). The TTL signal from OPT1 has been used to phase-lock also these data. The signals of the optical sensors, the HWA and the PIV pulses were sampled with a DAQ NI acquisition board, with a sampling frequency of 6.3 kHz.

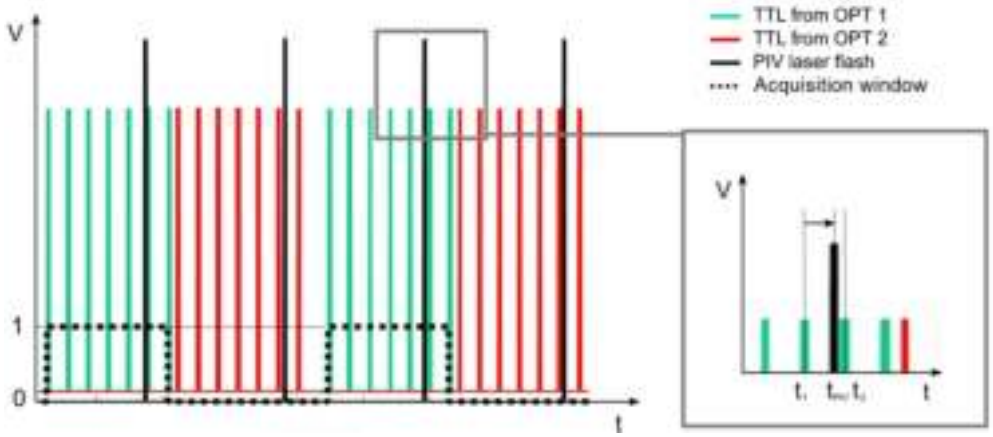

Figure 3. TTL signals and phasing procedure.

2.2. Data Processing

A fluid dynamic loss analysis was performed to quantify the effects due to reduced frequency and flow coefficient variation on the cascade efficiency. In the mean flow energy equation losses are related to the viscous dissipation D_{visc} and the turbulent kinetic energy production P_{TKE} terms, reported in Equation (2) and Equation (3), respectively. For clarity, U_i indicates the i^{th} component of the time-mean velocity, while u_i indicates the i^{th} component of the fluctuating velocity. The viscous term represents the contribution to entropy generation due to the shear work (see for instance [10]) and depends only on the time-mean flow velocity gradient, while the turbulent kinetic energy production is also related to the fluctuating velocity field. In particular, turbulence production occurs where the principal direction of the Reynolds stresses and the mean flow strain tensor are aligned [3]. Since the integral of these two terms on a control volume gives the total pressure losses from the inlet to the outlet of the measuring domain [6], a loss coefficient ω can be defined in order to quantify the overall fluid dynamic losses produced in the volume Ω as in Equation (4), where p_{ref} is the reference dynamic pressure at the outlet

of the cascade. In the present work, the overall region framed by the cameras has been considered as the control volume.

$$D_{visc} = \sum_{i,j} \nu \left(\frac{dU_i}{dx_j} \right)^2 \tag{2}$$

$$P_{TKE} = \sum_{i,j} -\overline{u_i u_j} \frac{dU_i}{dx_j} \tag{3}$$

$$\omega = \frac{\int_\Omega \rho D_{visc} d\Omega}{p_{ref}} + \frac{\int_\Omega \rho P_{TKE} d\Omega}{p_{ref}} \tag{4}$$

Once estimated the effects on the losses due to the parameter variation, POD has been applied for a deep analysis of the mechanisms responsible for loss generation in the different flow cases. As discussed in previous works (see for example [8]), POD provides a triplet of information: the eigenvalues $\lambda^{(k)}$, the eigenvectors $\chi^{(k)}$ and the POD modes $\phi^{(k)}$. Each POD mode is able to capture a particular spatial flow structure, the relative eigenvector provides its temporal evolution and the relative eigenvalue expresses the associated energy content. In the present work, POD has been applied at different phases of the wake period to follow the flow structure evolution during the wake-boundary layer interaction process. To this end, PIV snapshots have been split in 6 intervals equally spaced in time. The number of the time intervals has been defined in order to conserve at least about 300 snapshots for each phase bin, thus ensuring the convergence of the first low order (most energetic) POD modes, as documented in Lacarelle et al. [11]. Then, the turbulent kinetic energy production was evaluated per POD mode per phase. This allows us to identify the flow structures responsible for loss production and to investigate where losses are mainly produced. To this end, Reynolds stresses are expressed in the POD space according to Equation (5), where k indicates the mode index.

$$P_{TKE}{}^{(k)} = -\sum_{i,j} \lambda^{(k)} \phi_i{}^{(k)} \phi_j{}^{(k)} \frac{dU_i}{dx_j} \tag{5}$$

3. Results

3.1. HWA Measurements

The phase-locked velocity data measured at the inlet of the cascade with HWA are presented in Figure 4 for the four examined conditions. The plot on the top reports the phase-locked velocity, while the bottom one shows the phase-locked turbulence intensity. Referring to the C1 case (blue lines), the plots show four wake passing periods. Incoming wakes are hardly visible in the velocity plot, while they can be identified more clearly in terms of turbulence intensity peaks. The reason why the wakes do not appear as velocity defects can be explained looking at the sketches presented in Figure 5. The dynamics of the wakes at the entrance of the cascade is here schematically reported by velocity triangles, where c_1 is the absolute flow velocity, u is the bar velocity and w_1 is the relative flow velocity. The flow inside the wake is slower than the surrounding flow, thus, it develops with a lower velocity w_{1w}. Once combined with the bar velocity, the absolute velocity of the flow inside the wake c_{1w} can be obtained. In the sketch on the left, the triangles are calculated for $\varphi = 0.6$ (C1 and C2 cases). It results that the modules of the unperturbed absolute velocity (c_1) and of the velocity inside the wake (c_{1w}) are very similar. For this reason, the wakes in the C1 case are hardly visible in the velocity plot of Figure 4. This also occurs for the C2 case (black line), since it is characterized by the same flow coefficient of the C1 case. At the same time, in the C2 case the reduced frequency is halved with respect to the C1 case. Consequently, the distance between two consecutive peaks in the turbulence intensity plot is doubled and only two wakes can be observed. In between adjacent wakes the flow is unperturbed, as in the steady state, thus, the turbulence intensity resets almost to the inlet homogeneous free-stream turbulence intensity imposed by the

turbulence generating grid (about 6%). On the other hand, the C3 case (green line) reveals the effect of the flow coefficient variation. Indeed, the reduced frequency is the same and the flow coefficient is a half with respect to the C1 case. The dynamics of the entering wakes is now reported by the sketch on the right of Figure 5, obtained for $\varphi = 0.3$. The bar velocity is doubled and, consequently, the module of the velocity inside the wake (c_{1w}) becomes larger than the module of the unperturbed velocity (c_1). Thus, the wakes are visible in the velocity plot derived from single-element HWA measurements as peaks, which is a completely different situation with respect to classic LPT blades, where upstream wakes are well known to be seen as velocity defect (see for example the work of Praisner et al. [12]). This is due to the small absolute flow angle jointly with the low value of the flow coefficient characterizing the operation of such a kind of highly accelerated turbine profiles. Looking at the turbulence intensity plot, the wakes appear with a higher and wider peak than in the previous cases. Nevertheless, the distance between two successive peaks is the same as the C1 case, since the reduced frequency is the same. Lastly, the C4 case (red line), characterized by high reduced frequency and low flow coefficient, exhibits the combined effect of both parameter variation. According with the previous observations, a larger number of wakes can be observed into the plot. The overall turbulence intensity is higher because the flow is continuously perturbed by wakes and, interestingly, any unperturbed flow region can be observed in between adjacent wakes, since they collapse and merge together. This will have a great impact on the loss generation mechanisms discussed below.

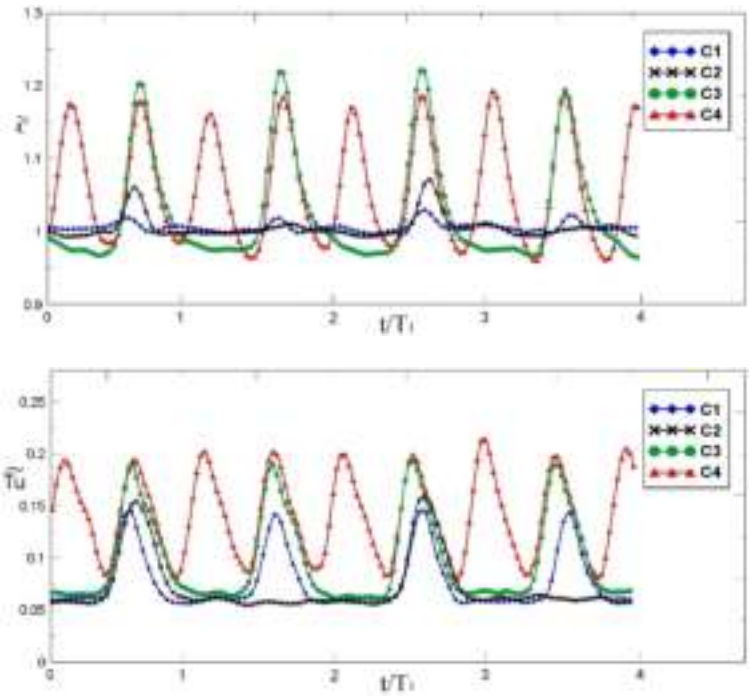

Figure 4. Phase-locked velocity $\widetilde{c}$ and phase-locked turbulence intensity $\widetilde{Tu}$ distributions.

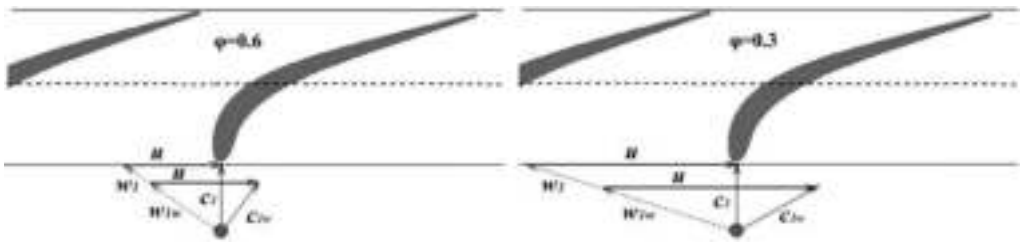

Figure 5. Sketches of the wake dynamics at different flow coefficients.

3.2. Time Mean and Phase-Locked Distributions

The time-mean flow field is exemplary presented in Figure 6 for the C1 case. The contour plot represents the streamwise velocity component U, while the grey line highlights the boundary layer thickness. The velocity vectors (U,V) are also superimposed to the plot (one every eight vectors are shown to improve plot readability). The plot shows that the boundary layer continuously develops, without any separated flow region, from the velocity peak position to the blade trailing edge. In the fore part of the measuring domain (camera on the left), the boundary layer remains very thin, while it significantly grew in the rear part of the diffusive region captured by the right camera.

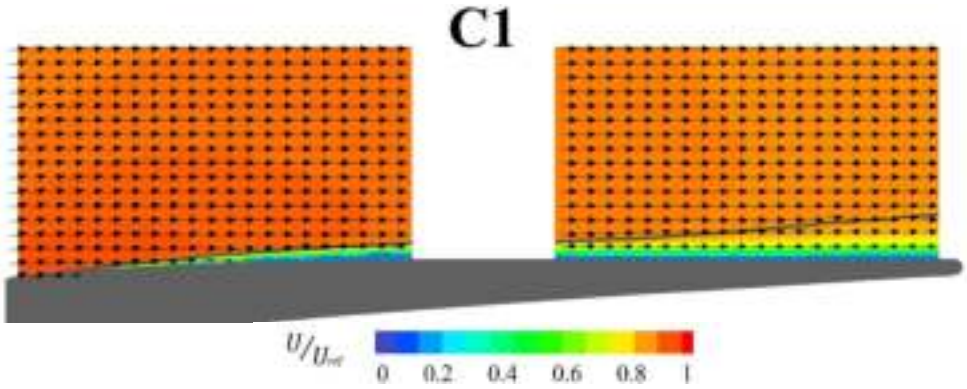

Figure 6. Time-mean velocity vectors in the C1 case. Contour of streamwise velocity component U. Grey line represents the boundary layer thickness.

Reduced frequency and flow coefficient variation modifies the boundary layer evolution. Figure 7 shows the boundary layer thickness distribution referred to the blade chord in the plot on the left. It was directly calculated from PIV snapshots with an estimated accuracy of $\delta/C = \pm 0.75 \times 10^{-3}$, that corresponds to $\pm 2.5\%$ of its value at the trailing edge in the C1 case, where the boundary layer velocity profile is solved by 16 measuring points. The maximum growth of the boundary layer was observed in the C1 and C4 cases, with a maximum thickness $\delta/C = 0.027$ at the blade trailing edge, while the minimum thickness was observed for the C2 case ($\delta/C = 0.022$ at the trailing edge). On the other side, Figure 7 presents the momentum thickness distribution normalized by its maximum value. It was obtained applying trapezoidal rule to integrate the velocity defect, with an estimated resultant accuracy at the trailing edge of $\pm 8\%$. The momentum thickness shows similar trends with respect to the boundary layer thickness, with values in the C4 case higher than in the C1 case. Since this latter parameter is commonly related to the boundary layer losses, higher losses are expected in the C4 case, characterized by high reduced frequency and low flow coefficient.

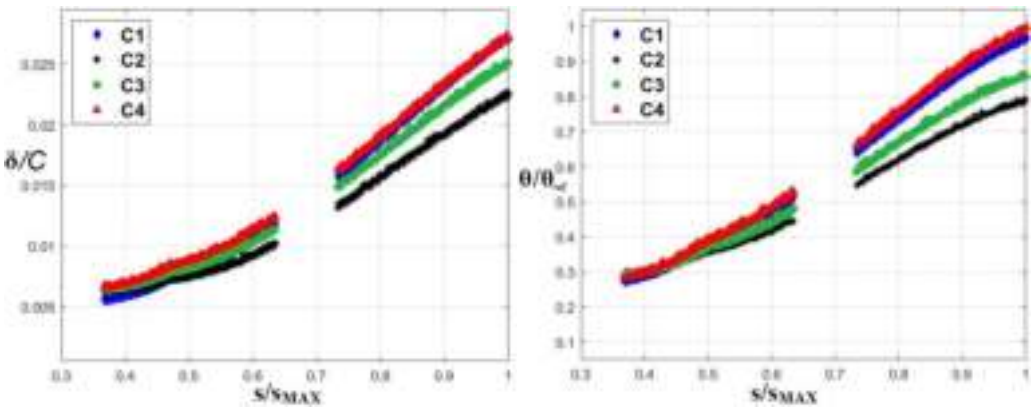

Figure 7. Boundary layer thickness δ and momentum thickness θ along the suction side.

To better appreciate the transition mechanisms induced by upstream wakes, Figure 8 shows the time-space phase-locked evolution of the momentum thickness and of the shape factor for the different flow cases. Plots are extended over three wake passing periods of the C1 case. The intermittent nature of the boundary layer is clearly captured. Particularly, referring to the top-left plot (momentum thickness, C1 case) the yellow-red stripes are related to the momentum thickness increase consequent to the wake passage. Indeed, as explained in [5], the flow at the trailing boundary of the wake is subjected to a strong deceleration that leads to higher momentum thickness. Coherently, the shape factor (C1 case) reduces from value in the surround of 2.5, typical of the laminar state prior than the wake arrival, to around 1.8 as a consequence of the induced transition, as highlighted by the blue stripes observable downstream of $s/s_{MAX} = 0.6$. It is worth noting that transition is locally induced by the wake passage, that promotes a turbulent state. However, a fully turbulent condition, typically identified by values of $H_{12} = 1.4$, is never achieved in these operating conditions.

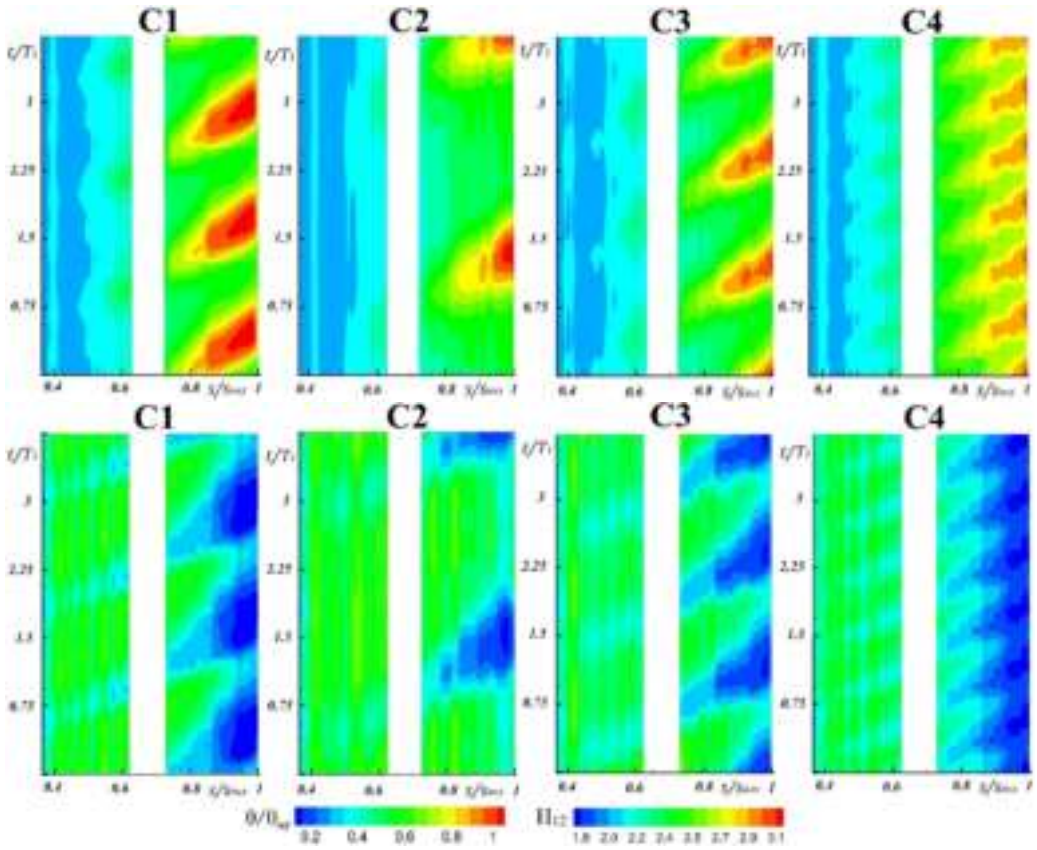

Figure 8. Time-space diagrams of momentum thickness θ and shape factor H_{12}.

The comparison with the other flow cases allows a direct visualization of the effects induced by both reduced frequency and flow coefficient variation. The reduced frequency effect is clearly visible in terms of number of wake patches present into the plot. In the C2 case only one wake path can be recognized, with the following one just appearing at the end of the ordinate axis. In the C1 and C3 cases three nuclei at high momentum thickness and low shape factor can be observed, while in the C4 case six wake induced transition zones can be observed. The flow coefficient variation is responsible for shifting in time the transitional patch induced by upstream wakes, as observable comparing the C1 and C3 cases.

In order to quantify the effects on the losses due to the observed different transition processes induced by the wakes, Figure 9 presents the fluid dynamic losses calculated in the PIV measuring domain for the different flow cases. The blue part of the bars is related to the contribution of the viscous term, while the green part represents the contribution

of the turbulent kinetic energy production term. Data are scaled with the maximum loss value. Highest losses are produced in the C4 case, at high reduced frequency and low flow coefficient. This is due to the large number of wakes inducing a prompter transition, that leads to a higher momentum thickness and, at the same time, a greater turbulent kinetic energy production. The C1 and C3 cases are characterized by similar losses, although the momentum thickness at the trailing edge was slightly higher in the C1 case than in the C3 case. At the same time, Figure 8 has shown similar dynamics of the transition process induced by wakes, that appeared only shifted in time. On the other hand, the C2 case clearly exhibits the lowest losses, due to the reduced frequency reduction, in accordance with the smaller number of turbulent patches observed in Figure 8. It is worth noting that the main differences appear predominantly due to the different amount of turbulent kinetic energy production process (green bars). Indeed, the turbulent kinetic energy produced in the C2 case is 40% lower than in the C4 case, while the differences between the viscous terms are less pronounced and close to their measurement uncertainty. For this reason, in the following chapter a deep discussion of the turbulent kinetic energy production in the different cases is analyzed by means of POD.

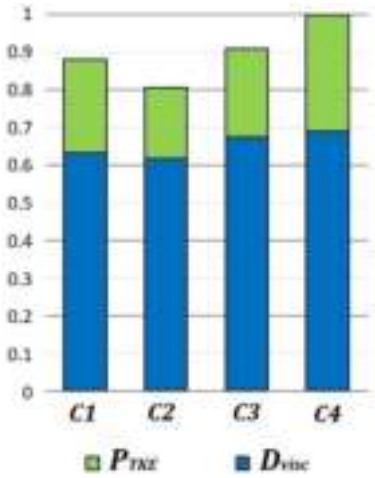

Figure 9. Quantification of different loss contributions in the four flow cases.

3.3. POD Analysis

POD modes at different phases are presented in the following figures in order to identify the main flow structures carried by upstream wakes and how they interact with the boundary layer for the different cases. The turbulent kinetic energy production per POD mode is also reported to highlight the mechanisms leading to the loss variation depicted in Figure 9. Figure 10 presents the vectorial representation of the first POD mode computed at $t/T = 0.00$, $t/T = 0.33$ and $t/T = 0.67$ (on the left) and two exemplary higher order modes representative of finer scale fluctuations carried by wakes (on the right) for the C1 case. The color levels provide the turbulent kinetic energy produced by the related POD mode, while the green lines superimposed to the plot indicate the boundary layer thickness. Previous applications have already shown the capability of the first POD mode to capture the deterministic part of the fluctuating field (see, for instance, [13–15]), identifying the wake as a negative jet and showing two large scale vortices, referred as Q1 and Q2 in the literature (see, for example, [4]), attached to the leading and trailing boundaries of the wake. Here, the application of POD at different phases of the wake passage period also provides the possibility to follow the temporal evolution of these deterministic structures, simply by looking at the first POD mode for different phases. With reference to Figure 10, the wake is leaving the measuring domain at $t/T = 0.00$ and the clockwise rotating Q2 vortex attached to the trailing boundary of the wake is visible in the region captured by the right camera. Its passage causes a strong deceleration into the boundary layer region, responsible for turbulent kinetic energy production (yellow-red contour in the plot). Subsequently, at

t/T = 0.33 the wake has completely left the blade passage (only the last part of the induced deceleration is visible on the right), while the new wake is entering on the left side of the domain. The left camera clearly shows the negative jet and the counter-clockwise rotating Q1 vortex. At t/T = 0.67 the wake is passing in the gap between the two cameras and both the Q1 and Q2 vortices can be observed on the right and on the left cameras, respectively. The boundary layer is now subjected to an acceleration induced by the Q1 vortex. The 3rd POD mode at t/T = 0.00 exhibits structures forming inside the boundary layer in the rear part of the suction side by the passage of the Q2 vortex. Regions of intense turbulent kinetic energy production can be identified by yellow-red areas where the magnitude of the vectors is higher. On the other side, the 2nd POD mode at t/T = 0.67, related to boundary layer structures just before the arrive of the wake, exhibits limited turbulent kinetic energy production, suggesting that loss production intensifies only after the passage of the wake centerline.

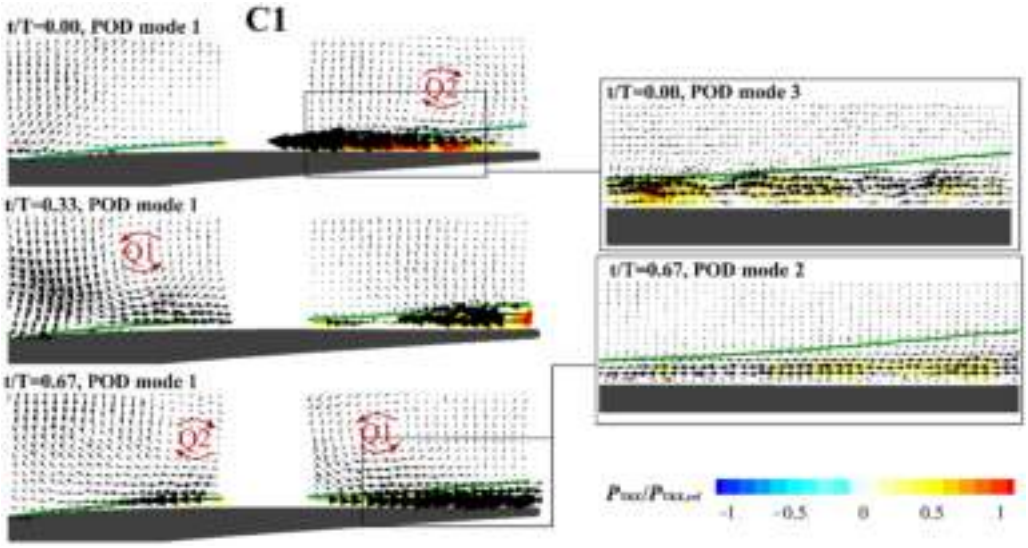

Figure 10. Exemplary POD modes at different phases for the C1 flow case (f^+ = *1.2*, φ = *0.6*). Contour plots report the turbulent kinetic energy production per mode.

Figure 11 shows analogous POD modes for the C2 case. With respect to the previous condition, the wake can be observed to enter at t/T = 0.00, it leaves the blade at t/T = 0.33, while at t/T = 0.67 the flow is completely unperturbed as a consequence of the lower reduced frequency characterizing this case. The negative jet and related vortices appear bigger, but the induced fluctuations are of minor magnitude. In addition, in this case, the turbulent kinetic energy is mainly produced in the decelerating region induced immediately after the wake passage, as visible at t/T = 0.33 looking at both the 1st mode (right camera) and the 3rd mode (detail on the rear part of the suction side). The mode 3 at t/T = 0.00 shows limited turbulent kinetic energy production when the boundary layer is unperturbed, confirming again that loss production is intensified immediately after the passage of the negative jet. Just because of the presence of large unperturbed areas (see t/T = 0.67 for example), the overall turbulent kinetic energy production is lower than in the previous case.

The flow coefficient effect on the structures captured by POD can be discussed comparing Figure 12 (C3 case) with Figure 10 (C1 case). Comparison of the first mode at t/T = 0.00 for the C3 case and the first mode at t/T = 0.33 for the C1 case makes evident that the wake enters in the measuring domain with a more tangential inclination at low flow coefficient. Looking at t/T = 0.33 for the C3 case and at t/T = 0.67 for the C1 case, when the wake is passing in the gap between the two cameras, it can be also noted that Q1 and Q2 vortices are stretched in the outflow direction at low flow coefficient. Subsequently, at t/T = 0.67, the wake is interacting with the rear part of the suction side, while the successive wake is

appearing on the left. Therefore, with respect to the C1 case, the wake motion is shifted in phase as a consequence of the different wake trajectory related to the flow coefficient, while the incoming wake frequency is the same. The 3rd mode at $t/T = 0.67$ captures again the deceleration induced in the boundary layer responsible for high turbulent kinetic energy production, as in the previous cases. Interestingly, the 2nd mode at $t/T = 0.67$ also shows a not negligible amount of turbulent kinetic energy produced in the acceleration region. It occurs at the leading boundary of the wake where the negative jet carries finer-scale fluctuations into the boundary layer, as observed by Berrino et al. [16] that measured high turbulence intensity just in this region.

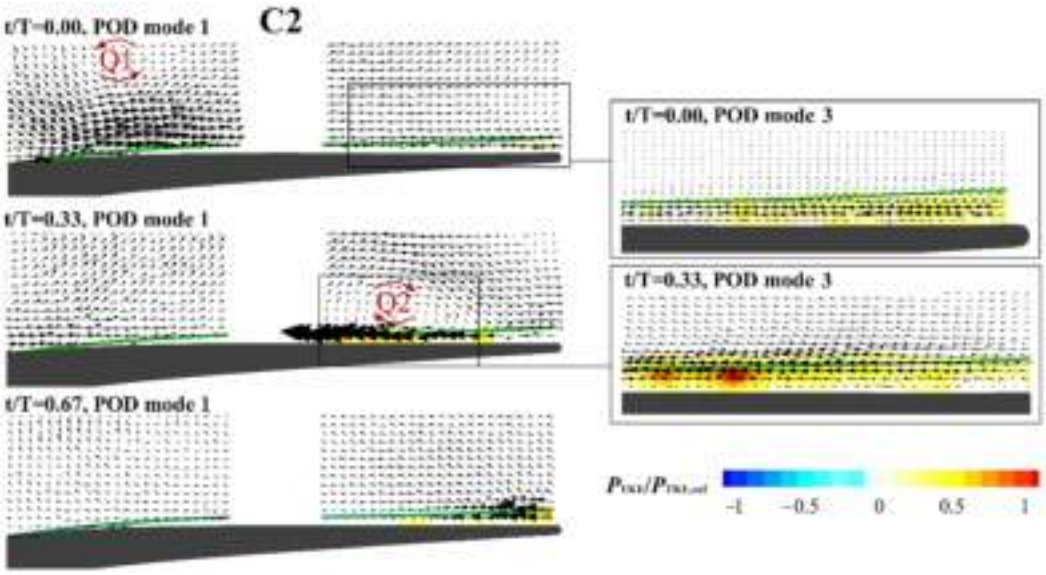

Figure 11. Exemplary POD modes at different phases for the C2 flow case ($f^+ = 0.6$, $\varphi = 0.6$). Contour plots report the turbulent kinetic energy production per mode.

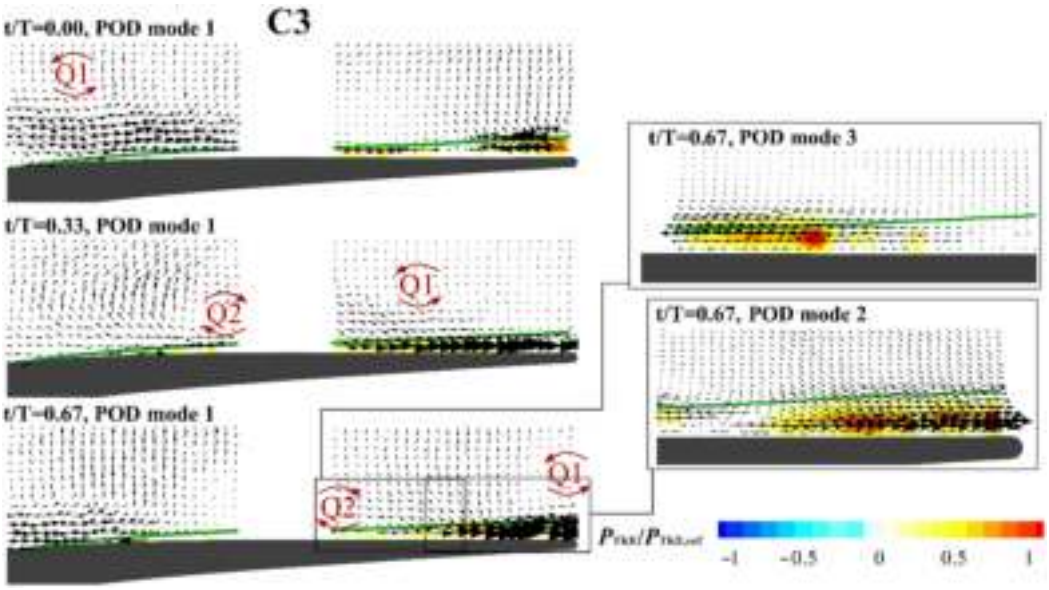

Figure 12. Exemplary POD modes at different phases for the C3 flow case ($f^+ = 1.2$, $\varphi = 0.3$). Contour plots report the turbulent kinetic energy production per mode.

The C4 flow case, characterized by high reduced frequency and low flow coefficient, is reported in Figure 13. The first POD mode simultaneously represents two distinct negative jet like motions, related to two consecutive wakes. At $t/T = 0.00$, the jets are well

centered in the two cameras. The Q1 and Q2 vortices appear evidently smaller and more distorted than in the previous cases, probably because of the strong interaction with the previous/successive wake. Turbulent kinetic energy is produced at every phase into the boundary layer. The 3rd mode at $t/T = 0.33$ exhibits very high turbulent kinetic energy production at the blade trailing edge, as consequence of the Q2 vortex effects. The 3rd mode at $t/T = 0.67$ shows an accelerating region above the decelerating one leading again to high turbulent kinetic energy production.

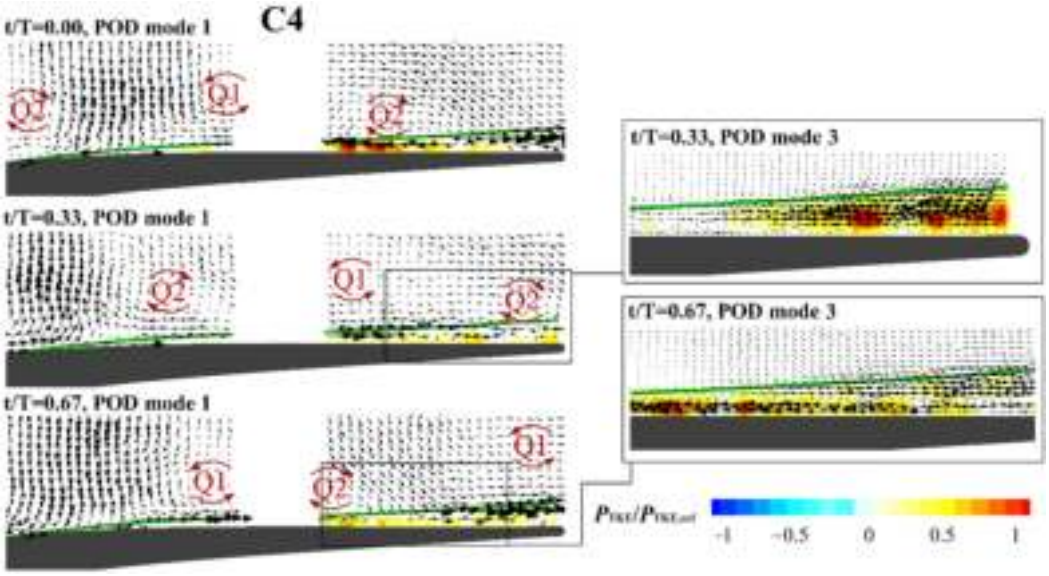

Figure 13. Exemplary POD modes at different phases for the C4 flow case ($f^+ = 2.4$, $\varphi = 0.3$). Contour plots report the turbulent kinetic energy production per mode.

The inspection of POD modes has shown that turbulent kinetic energy is mainly produced during the passage of the large-scale vortices in the diffusive part of the boundary layer. In particular, the decelerations induced by the Q2 vortex are related to high loss production. On the other hand, loss production decreases in the unperturbed regions, before the arrive of the successive wake. Therefore, loss differentiation between the flow cases is mainly driven by the reduced frequency. At low reduced frequency, the large areas of unperturbed flow cause a lower loss production, while at high reduced frequency the continuous action of successive vortices drives to higher loss production. On the other hand, the effect of the flow coefficient on the overall losses is difficult to isolate. Indeed, despite of the different wake trajectory and the different shape of the vortices, the turbulent kinetic energy production in the C1 and C3 cases is very similar.

4. Conclusions

A detailed analysis of the wake-boundary layer interaction process has been carried out by means of PIV measurements in the rear part of the suction side of a highly accelerated LPT cascade. Four flow conditions with different reduced frequency and flow coefficient have been investigated. Incoming wake characterization at the inlet of the cascade has revealed different dynamics induced by the flow coefficient variation. Interestingly, in the examined flow conditions, the wakes cannot be identified as velocity defects as in classic LPT cascades, but mainly as turbulent intensity peaks. Indeed, the small absolute flow angle and the low flow coefficient characterizing the operation of highly accelerated profiles induce a particular dynamic where the flow inside the wake results equal or slightly faster than the surrounding flow.

The analysis of the flow fields has shown different loss production, with higher losses at low flow coefficient and high reduced frequency as a consequence of the prompter transition process induced by incoming wakes. Loss variation between the flow cases

appeared mainly due to the turbulent kinetic energy production; thus, POD has been applied to investigate the main flow structures involved in the wake-boundary layer interaction process and to discuss their contribution to loss generation. The first POD mode at different phases has described the deterministic part of the fluctuations, including negative jet and large-scale vortices at the boundaries of the wake. Reduced frequency affects the dimensions of the vortices. They are bigger at low reduced frequency, while the flow coefficient acts on their shape, causing stretching in the outflow direction at low flow coefficient. Higher order modes have instead shown oscillations induced inside the boundary layer. The turbulent kinetic energy is mainly produced by the decelerations induced immediately after the wake passing, while it decreases in the unperturbed flow regions in between adjacent wakes. Thus, loss variation between the different cases is mostly due to the effect of the reduced frequency, that determines the population of structures during the wake passage period.

Author Contributions: Conceptualization, D.L. and D.S.; data curation, E.C., A.N., D.P., M.U. and P.Z.; methodology, D.S. and D.L.; writing—original draft preparation, E.C., A.N., D.P., M.U. and P.Z.; writing—review and editing, E.C., A.N., D.P., M.U. and P.Z.; supervision, D.L. and D.S. All authors have read and agreed to the published version of the manuscript.

Funding: AvioAero originally founded the rig set up.

Institutional Review Board Statement: Not applicable.

Informed Consent Statement: Not applicable.

Data Availability Statement: Not applicable.

Acknowledgments: The authors would like to acknowledge AvioAero for the financing of the cascade tests.

Conflicts of Interest: The authors declare no conflict of interest. The funders had no role in the design of the study; in the collection, analyses, or interpretation of data; in the writing of the manuscript. The funders approved publication of the manuscript.

Abbreviations

The following abbreviations are used in the manuscript:

Re	Reynolds number $[c_2 C/\nu]$
f^+	reduced frequency $[(u/S)/(c_2/C)]$
φ	flow coefficient $[c_{1,ax}/u]$
c	absolute flow velocity
C	blade chord
DF	diffusion factor $[(c_{peak} - c_{te})/c_{te}]$
Ds	diffusion rate $[DF/(s_{dec} - s_{tot})]$
s	coordinate along the blade suction side
S	bar pitch
t	time
T	wake passing period
Tu	turbulence intensity
u	bar velocity
VR	velocity ratio $[cos\ (\alpha_1)/cos\ (\alpha_2)]$
w	relative flow velocity
α	cascade angles
ρ	density
ν	kinematic viscosity
Subscripts	
ax	cascade axial direction
ref	reference value
te	trailing edge
$1,2$	inlet/outlet section of the cascade

References

1. Wu, X.; Durbin, P.A. Evidence of longitudinal vortices evolved from distorted wakes in a turbine passage. *J. Fluid Mech.* **2001**, *446*, 199–228. [CrossRef]
2. Michelassi, V.; Chen, L.-W.; Pichler, R.; Sandberg, R.D. Compressible Direct Numerical Simulation of Low-Pressure Turbines—Part II: Effect of Inflow Disturbances. *J. Turbomach.* **2015**, *137*, 071005. [CrossRef]
3. Stieger, R.D.; Hodson, H.P. The Unsteady Development of a Turbulent Wake through a Downstream Low-Pressure Turbine Blade Passage. *J. Turbomach.* **2005**, *127*, 388–394. [CrossRef]
4. Gompertz, K.A.; Bons, J.P. Combined Unsteady Wakes and Active Flow Control on a Low-Pressure Turbine Airfoil. *J. Propuls. Power* **2011**, *27*, 990–1000. [CrossRef]
5. Stieger, R.D.; Hodson, H.P. The Transition Mechanism of Highly Loaded Low-Pressure Turbine Blades. *J. Turbomach.* **2004**, *126*, 536–543. [CrossRef]
6. Lengani, D.; Simoni, D.; Pichler, R.; Sandberg, R.D.; Michelassi, V.; Bertini, F. On the Identification and Decomposition of the Unsteady Losses in a Turbine Cascade. *J. Turbomach.* **2019**, *141*, 031005. [CrossRef]
7. Michelassi, V.; Chen, L.; Pichler, R.; Sandberg, R.; Bhaskaran, R. High-Fidelity Simulations of Low-Pressure Turbines: Effect of Flow Coefficient and Reduced Frequency on Losses. *J. Turbomach.* **2016**, *138*, 111006. [CrossRef]
8. Lengani, D.; Simoni, D.; Pichler, R.; Sandberg, R.; Michelassi, V.; Bertini, F. Identification and quantification of losses in a LPT cascade by POD applied to LES data. *Int. J. Heat Fluid Flow* **2018**, *70*, 28–40. [CrossRef]
9. Funazaki, K.-I.; Murakami, D.; Okamura, Y. Parametric Studies on Aerodynamic Performance of Various Types of LP Turbine Airfoils for Aero-Engines Under the Influence Periodic Wakes and Freestream Turbulence. In Proceedings of the ASME Turbo Expo 2019: Turbomachinery Technical Conference and Exposition, Phoenix, AZ, USA, 17–21 June 2019.
10. Denton, J.D. Loss Mechanisms in Turbomachines. *J. Turbomach.* **1993**, *115*, 621–656. [CrossRef]
11. Lacarelle, A.; Faustmann, T.; Greenblatt, D.; Paschereit, C.O.; Lehmann, O.; Luchtenburg, D.M.; Noack, B.R. Spatiotemporal Characterization of a Conical Swirler Flow Field Under Strong Forcing. *J. Eng. Gas Turbines Power* **2009**, *131*, 031504. [CrossRef]
12. Praisner, T.J.; Clark, J.P.; Nash, T.C.; Rice, M.J.; Grover, E.A. Performance Impacts Due to Wake Mixing in Axial-Flow Turbomachinery. In Proceedings of the ASME Turbo Expo 2006, Barcelona, Spain, 11 May 2006; pp. 1821–1830.
13. Lengani, D.; Simoni, D.; Nilberto, A.; Ubaldi, M.; Zunino, P.; Bertini, F. Synchronization of multi-plane measurement data by means of POD: Application to unsteady boundary layer transition. *Exp. Fluids* **2018**, *59*, 184. [CrossRef]
14. Legrand, M.; Nogueira, J.I.; Lecuona, A. Flow temporal reconstruction from non-time-resolved data part I: Mathematic fundamentals. *Exp. Fluids* **2011**, *51*, 1047–1055. [CrossRef]
15. Legrand, M.; Nogueira, J.I.; Tachibana, S.; Lecuona, A.; Nauri, S. Flow temporal reconstruction from non time-resolved data part II: Practical implementation, methodology validation, and applications. *Exp. Fluids* **2011**, *51*, 861–870. [CrossRef]
16. Berrino, M.; Lengani, D.; Simoni, D.; Ubaldi, M.; Zunino, P. POD Analysis of the Wake-Boundary Layer Unsteady Interaction in a LPT Blade Cascade. In Proceedings of the 11th European Conference on Turbomachinery, Fluid Dynamics & Thermodynamics, Madrid, Spain, 23–27 March 2015.

International Journal of
Turbomachinery Propulsion and Power

MDPI

Article

Flow and Ingestion in a Turbine Disc Cavity under Rotationally-Dominated Conditions

Anna Bru Revert [1,*], Paul F. Beard [2] and John W. Chew [3]

[1] Rolls-Royce plc, P.O. Box 3, Bristol BS34 7QE, UK
[2] Oxford Thermofluids Institute, University of Oxford, Oxford OX2 0ES, UK; paul.beard@eng.ox.ac.uk
[3] Thermo-Fluid Systems UTC, University of Surrey, Guildford GU2 7XH, UK; j.chew@surrey.ac.uk
* Correspondence: anna.brurevert@rolls-royce.com

Abstract: An investigation of hot gas ingestion driven by the disc pumping effect in a chute seal was conducted at the Oxford Rotor Facility. Measurements of mean pressure, unsteady pressure and gas concentration have been logged and analysed under different operating conditions. The sensitivity of mean cavity pressure coefficient, frequency spectra of the unsteady pressures and sealing effectiveness to changing conditions of purge flow, annulus flow, rotor disc speed and seal clearance have been studied. The steady pressures revealed the development of two vortices in the cavity, induced by the sharp change in geometry of the stator wall. The increased shear at the interface between these two vortices strengthened the unsteady activity at this location. The addition of mainstream flow improved the sealing capability of the chute seal under certain operating conditions. The excitation of further frequencies when an axisymmetric annulus flow was introduced suggests a complex interaction between annulus and purge flows.

Keywords: rim seal; ingestion; disc pumping effect; turbine; seal performance; unsteady

check for updates

Citation: Bru Revert, A.; Beard, P.F.; Chew, J.W. Flow and Ingestion in a Turbine Disc Cavity under Rotationally-Dominated Conditions. *Int. J. Turbomach. Propuls. Power* **2021**, *6*, 29. https://doi.org/10.3390/ijtpp6030029

Academic Editor: Emil Göttlich

Received: 18 May 2021
Accepted: 13 July 2021
Published: 20 July 2021

Publisher's Note: MDPI stays neutral with regard to jurisdictional claims in published maps and institutional affiliations.

Copyright: © 2021 by the authors. Licensee MDPI, Basel, Switzerland. This article is an open access article distributed under the terms and conditions of the Creative Commons Attribution (CC BY-NC-ND) license (https://creativecommons.org/licenses/by-nc-nd/4.0/).

1. Introduction

Decades of research in the topic of hot gas ingestion point towards disc pumping, circumferential annulus pressure asymmetries and, more recently, rim seal flow instabilities as the main drivers for hot gas ingestion. These three mechanisms are depicted in Figure 1. Ingress of high temperature flow from the main gas path is undesired. Rotor discs are not thermally insulated and the ingestion of hot gas from the mainstream can significantly damage the mechanical integrity of these highly stressed components and reduce their operating life. To prevent this from occurring, cool air is injected between the stator and rotor discs to purge and pressurise the cavity. However, this comes at the detriment of engine efficiency. The intrinsically convoluted flow field in the turbine rim region creates a complex environment in which fundamental understanding of the basic flow physics becomes paramount to comprehend the synergetic effect of each of the mechanisms mentioned above. This investigation focuses on the performance of a chute rim seal with no blades and vanes in the annulus, such that ingestion is expected to be driven by the effects of rotation. Bru Revert et al. [1] showed that this scenario is relevant for high pressure turbines at low flow coefficients.

The spacing between the stator ring and the rotor disc is sufficient to allow for separate boundary layers and turbulent flow to develop in the cavity as established by Daily and Nece [2]. Shear forces transfer angular momentum from the rotating disc to the adjacent fluid and the centrifugal force then projects the flow radially out towards the rim gap. The purge flow introduced in the inner region of the cavity feeds the boundary layer on the rotor disc. A core of rotating inviscid flow develops in the cavity volume inducing a pressure gradient that leads to lower pressures in the cavity than in the annulus. The flow structure inside the cavity volume is influenced by the ingress and egress of flow through the rim seal. To balance any excess of egress over the supplied purge flow rate,

mainstream flow from the outside environment may be drawn into the cavity through the rim seal. After mixing with purge flow in the outer part of the cavity, ingressed flow entrains the boundary layer on the stator disc and progresses radially inward. The mixed flow in the stator boundary layer travels axially across the inviscid core to enter the rotor boundary layer.

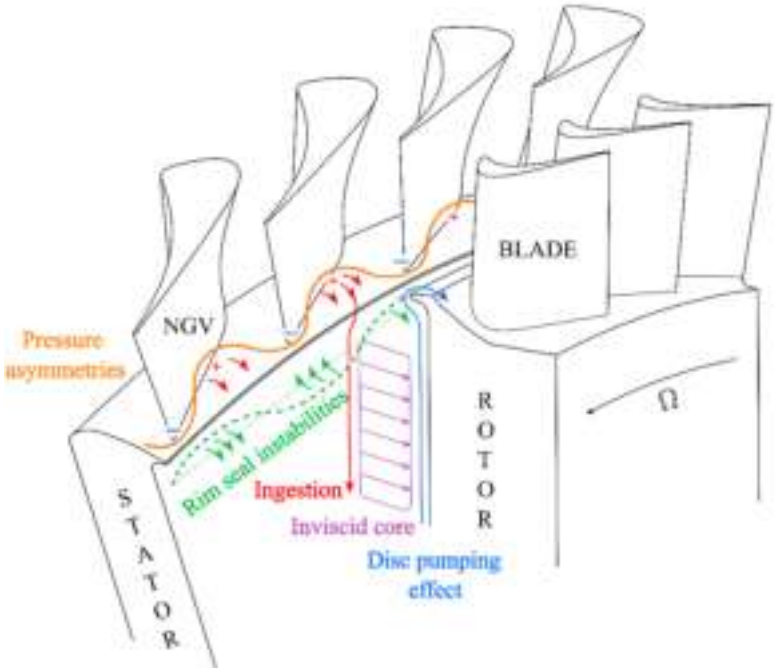

Figure 1. Driving mechanisms for hot gas ingestion.

Initial studies of the disc pumping effect, such as that of Bayley and Owen [3], derived empirical correlations to quantify the minimum amount of purge flow necessary to fully seal the cavity. With the introduction of the tracer gas technique to study hot gas ingestion, experimental data quantifying sealing effectiveness became available. Several rim seal geometrical arrangements were studied revealing that the radial seal over-performed the axial seal. Chew [4] developed an orifice model to estimate the sealing effectiveness under dominance of the disc pumping effect. Chew's correlation could be fitted to different seal geometries by adjusting the empirical constant k which indicates the ability to prevent ingestion of each rim seal design. The model is detailed in Equation (1), where U_m is the mean flow velocity through the rim seal, Ω is the angular speed and b is the rotor disc radius.

$$\frac{U_{m,min}}{\Omega b} = 0.1214\,k;\ \varepsilon = \frac{1}{0.8 + 0.02428\,k\left(\frac{\Omega b}{U_m}\right)} \quad \text{for } 0 < U_m < U_{m,min} \tag{1}$$

Further studies simulated more engine-realistic scenarios with pressure asymmetries in the main gas path and showed that the ingestion of annulus flow at the rim seal region could be dominated by rotation or pressure asymmetries, e.g., Phadke and Owen [5]. Later, advances in computational methods and measurement techniques allowed Cao et al. [6] to numerically and experimentally identify large scale unsteady flow features in the rim seal cavity that could also dominate ingress of hot gas. Further details of previous work are given in the extensive reviews by Scobie et al. [7] and Chew et al. [8].

The results of an investigation of the disc pumping effect in a turbine disc cavity with a chute rim seal arrangement are presented in this paper extending the preliminary study by Bru Revert et al. [9]. The effect of annulus pressure asymmetries created by the presence of NGVs in the gas path is compared by Bru Revert et al. [1] to the results of this study. The

sealing performance is assessed based on pressure measurements and values of sealing effectiveness derived from readings of gas concentration in the absence of external flow and with an axial axisymmetric annulus flow. The sensitivity of these variables to changes in purge flow, annulus flow, rotor disc speed and seal clearance are discussed.

The experimental configuration of the Oxford Rotor Facility is briefly described first, followed by the discussion of the cavity flow based on steady pressure measurements. Next, the sensitivities of the sealing effectiveness and cavity pressure coefficient to rotor disc speed, purge flow, mainstream flow and seal clearance are thoroughly analysed under different test conditions. A summary of the main findings of the study is given in the concluding section.

2. Experimental Setup

The Oxford Rotor Facility (ORF) was modified to study rim sealing flows and an extensive description of the modifications to the facility was published by Bru Revert et al. [1]. To investigate purely rotationally induced ingestion, the NGVs and rotor blades were not included in the working section and therefore the pressure asymmetries in the annulus were removed. Instead, dummy rotor and stator discs were installed in the facility (see Figure 2).

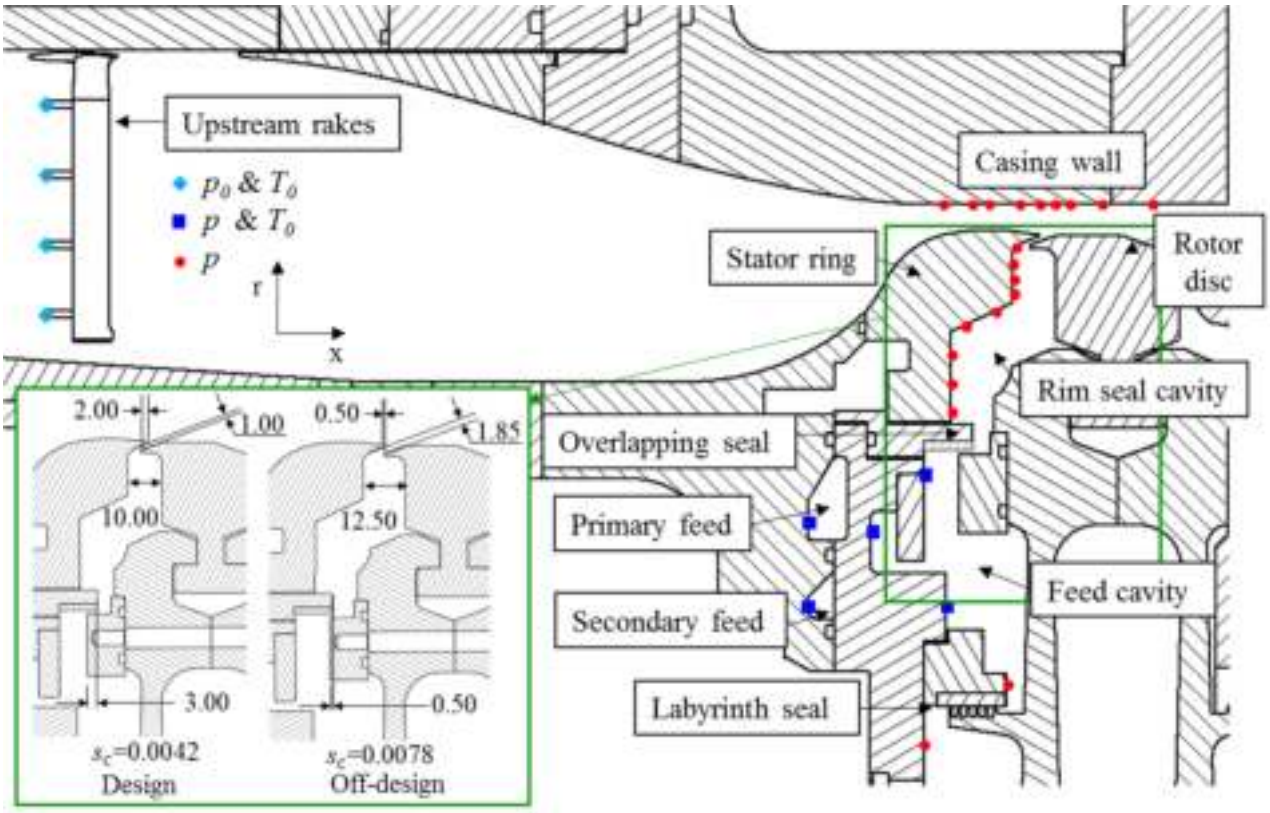

Figure 2. Longitudinal cross section of the facility with instrumentation.

A nominal rim gap of 1 mm was studied. This was measured between the stator and rotor surfaces in the angled region of the chute rim seal which corresponded to a 2 mm overlap in the axial direction. An increased seal clearance of 1.85 mm was also studied representing an off-design engine condition in which rear axial displacement of the turbine may occur. The gap increase was achieved by introducing a spacer ring between the shaft and the rotor disc. However, due to the movement of the rotor disc, the overlap was lost and replaced by a 0.5 mm axial displacement. The purge flow was supplied through 60 holes of 2.5 mm diameter in the primary feed with a discourager surface to prevent jetting. A secondary feed was available but was not used.

Pressure and temperature measurements were acquired at strategic points in the working section to monitor the flow conditions as specified in Figure 2. Temperature measurements were obtained with k-type bare bead thermocouples with exposed tips (uncertainty ±0.45%). Absolute pressures were acquired through First Sensor CTE8000 transducers (uncertainty of ±0.1% of full-scale output), whilst the differential measurements inside the cavity were logged with First Sensor BTEM5000 (±0.2% of full-scale output uncertainty) pressure sensors. Total pressure and total temperature rakes were located upstream of the working section at four circumferential positions to ensure the mainstream flow, when present, was axisymmetric (0.2% maximum deviation from the mean pressure of the four rakes). Likewise, static pressure and total temperature were registered in the purge flow feed system. Pressure taps were distributed radially along the stator wall and were used to log static pressures as well as to sample tracer gas concentration in the cavity. The measurements presented here were recorded at 97° from top dead center in the clockwise direction when looking from downstream. Unsteady pressures were acquired with Kulite™ XCQ-062 series pressure sensors mounted in the stator wall at equivalent radial positions to those of the steady taps in Figure 2, with a circumferential offset of 160°. Unsteady pressures were logged for 1 s at a sampling frequency of 1 MHz. The data were filtered after acquisition with a low pass band Butterworth filter.

The tracer gas technique was used to assess the sealing performance of the chute seal. Sample gas from the cavity was extracted and directed, through pneumatic tubes, to the measurement cell of a gas analyser as thoroughly described by Bru Revert et al. [1]. The Signal Group multi-channel gas analyser provided readings of foreign gas content (CO_2) in the air mixture that were used to derive the sealing effectiveness with Equation (2).

$$\varepsilon = \frac{c_{\text{stator}} - c_{\text{ann}}}{c_{\text{purge}} - c_{\text{ann}}} \tag{2}$$

The influence of purge mass flow, rotor disc speed, rim seal gap size and annulus mass flow over the output variables of cavity pressure coefficient, C_p, and sealing effectiveness, ε, has been investigated. The test matrix is summarised in Table 1. Note that $\text{Re}_{ax} = 0$ corresponds to the absence of annulus flow, although in the sealing effectiveness test campaign a weak axial flow vented the gas path to avoid build-up of CO_2 above the rim giving false readings. The axial Reynolds number has been calculated based on the axial chord of the NGVs that would be placed in the gas path, C_{ax} = 0.034 m, and the equivalent flow coefficient at $\text{Re}_{\varnothing} = 3 \times 10^6$ is $U_{ax}/(\Omega b) = 0.45$.

Table 1. Experimental test matrix.

Re_{ax}	C_w	$\text{Re}_{\varnothing}$	s_c
0	800 to 9000	1.5×10^6 2.1×10^6	4.2×10^{-3}
2.6×10^5		2.7×10^6 3×10^6	7.8×10^{-3}

3. Cavity Flow Structure

This section provides insight into the flow structure within the rim seal cavity when subject to the disc pumping effect and the supplied purge flow without annulus flow.

The radial distributions of mean pressure coefficient inside the cavity, C_p, are shown in Figure 3 at different operating conditions in the absence of external flow. C_p is included as a measure of the vortex strength in the rim seal cavity, calculated as the pressure difference to the innermost measurement point available in each test case and non-dimensionalised using the dynamic head at the disc rim speed. The radial distribution of C_p in Figure 3 indicates coexistence of two different swirl velocities in the cavity rotating core. Lines corresponding to forced vortices at several fractions of disc speed (assuming radial equilibrium) represent vortex rotation and are included to aid visualisation. A change in slope at r/b~0.93 reflects

an increase in the vortex strength in the outer part of the cavity, consequence of the abrupt change in geometry in the stator wall. For a fixed rotor disc speed, an increase in purge reduces the pressure gradient in the cavity. At the lower purge flow rate, results for two different rotor speeds are almost identical. As shown in Figure 3, the throughflow parameter $\lambda_T = C_w/Re_\varnothing^{0.8}$ varies from 0.01 to 0.006 at these conditions. A value of $\lambda_T = 0.219$ marks the point at which the purge flow rate equals disc pumping flow given by von Kármán's rotating free disc solution. For the lower values of λ_T, it seems that the influence of purge flow on the cavity flow has severely diminished. Ingestion rates are also expected to vary with λ_T, and the results indicate that effects of ingestion on the mean cavity flow are also small.

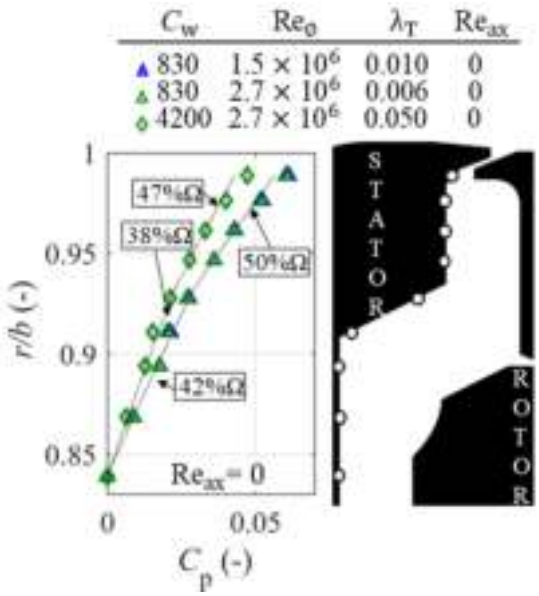

Figure 3. Cavity radial pressure distribution.

The measurements by Beard et al. [10] evidenced the presence of unsteady flow structures in the axisymmetric rim cavity geometry of the ORF without external mainstream flow. The frequency spectra revealed distinct peaks at f/Ω~21 that correspond to large scale flow features rotating in the cavity at approximately 80% of the rotor disc speed. The frequency spectra of the fluctuating component of the unsteady pressure acquired during this test campaign can be seen in Figure 4a. Please note these correspond to the full time history of the signal, including 50 rotor revolutions in the case of $Re_\varnothing = 3 \times 10^6$. The rebuild of the facility did not affect the frequency nor the rotating speed of these structures although a reduction in the overall unsteadiness was registered. This was associated with a more axisymmetric geometry of the front face of the rotor disc in the feed cavity.

In addition, the new results are consistent with the increase in distinct peak amplitude with decreasing radius reported by Beard et al. [10]. They speculated that the measured unsteadiness may originate further inboard, potentially at the overlapping seal. Extended instrumentation was installed in the ORF registering negligible unsteadiness at either side of the overlapping seal as shown in Figure 4b. This indicated that the unsteady flow features inside the cavity did not originate there. This conclusion agrees with the findings of Gao et al. [11] who showed that a change in radius is required to generate unsteady inertial waves in seals. Interestingly, the most intense peak in the frequency spectra appears at $r/b = 0.95$, consistent with the change of slope of C_p in Figure 3 (note no unsteady pressure measurements were available at $r/b = 0.93$). Relating the findings of Figures 3 and 4, it is thought that increased shear between the two different swirl velocities observed in the mean cavity pressure coefficient causes the highest unsteadiness detected at the geometrical discontinuity.

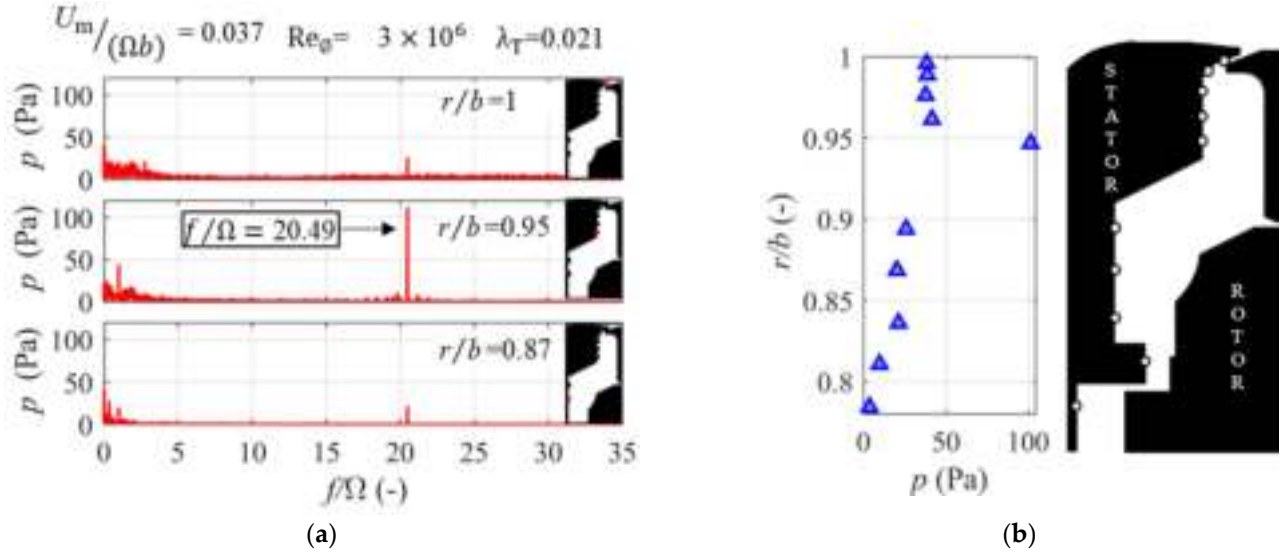

(**a**) (**b**)

Figure 4. (**a**) Frequency spectra of the pressure signal FFT at three radial positions and (**b**) peak amplitude of the pressure FFT across the stator cavity wall.

4. Sensitivity Studies

This section presents the impact of the non-dimensional handle variables C_w, $Re_\varnothing$, Re_{ax} and s_c on the steady state output variables ε, C_p and the flow unsteadiness through the frequency spectra.

4.1. Effect of Rotor Disc Speed

At low rates of purge flow (C_w = 830), Figure 5a left shows that disc pumping draws relatively large amounts of external flow through the rim seal, leading to low values of sealing effectiveness. This is due to the pressurisation of the cavity not being sufficient to overcome the disc pumping effect at any of the rotor disc speeds studied. Figure 5a right shows how a higher non-dimensional purge flow rate (C_w = 7400) reduces the gradient of the radial pressure distribution. A drastic increase in sealing effectiveness occurs as a direct consequence of the drop in pressure coefficient. A fully sealed cavity is achieved at $Re_\varnothing = 1.5 \times 10^6$. Larger sensitivity of both C_p and sealing performance to the rotational Reynolds number is observed for the highest purge flow supply. A significant contrast in ε between results at $Re_\varnothing = 1.5 \times 10^6$ and all the other rotor disc speeds is visible in Figure 5a both at C_w = 830 and C_w = 7400, with the difference also being noticeable in the C_p of the right plot.

The frequency spectra presented in Figure 5b show an increase in the peak amplitude proportional to the rotor disc angular velocity, typical for all the purge supplies and seal clearances tested. The stronger pressure gradient in the cavity, as a consequence of the intensification of the disc pumping effect, translates into an isolated outstanding peak of higher amplitude and frequency. This confirms that the phenomena is rotationally driven and potentially caused by the increased shear of the cavity vortices at r/b = 0.93. However, when non-dimensionalised by rotor disc speed, a slight shift towards lower non-dimensional peak frequencies is observed. Please note that the spike at $f/\Omega = 1$ corresponds to the frequency of the rotating disc and it could be caused by a slight eccentricity of the rotor disc.

4.2. Effect of Purge Flow

Larger supplies of purge flow to the seal increase the cavity pressure and counteract the disc pumping, ultimately preventing ingestion. A rise in sealing effectiveness with purge flow rate at all the radial positions considered is observed in Figure 6. A decrease

in sealing effectiveness for the wider gap is evident when comparing data for constant $U_m/(\Omega b) = 0.02$ ($C_w = 850$) looking at the blue markers across the two plots.

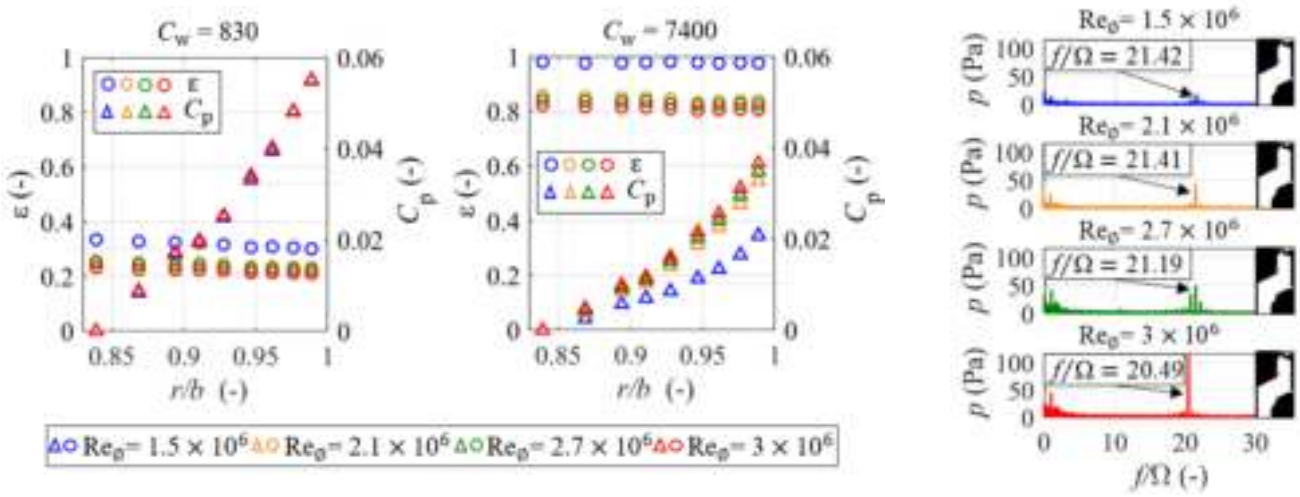

(**a**) (**b**)

Figure 5. (**a**) Sealing effectiveness and pressure coefficient radial distributions at different $Re_\varnothing$ for $s_c = 0.0078$ and (**b**) frequency spectra at $r/b = 0.95$ for $C_w = 3500$ and $s_c = 0.0042$.

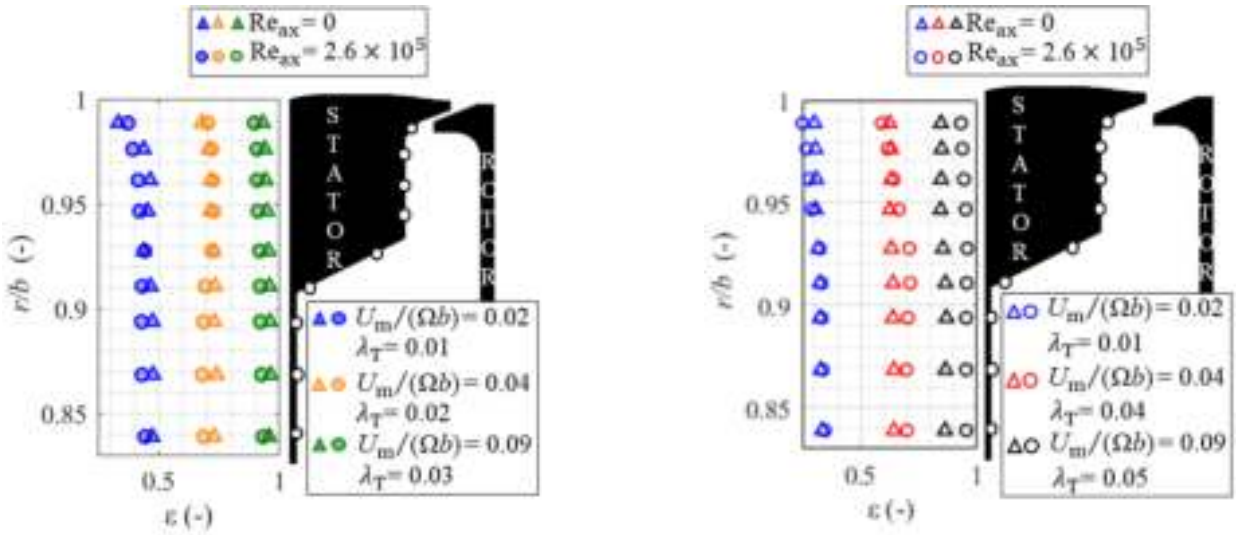

(**a**) $s_c = 0.0042$ (**b**) $s_c = 0.0078$

Figure 6. Radial distribution of sealing effectiveness under different conditions of purge supply and annulus flow at $Re_\varnothing = 1.5 \times 10^6$ for (**a**) $s_c = 0.0042$ and (**b**) $s_c = 0.0078$.

The radial profile of sealing effectiveness can be explained by the cavity flow structure. When ingestion occurs, the external flow that reaches the cavity mixes with the outward purge flow in the outer part of the volume. The combined flow then merges with the stator boundary layer and migrates radially downwards. A constant radial distribution of sealing effectiveness is observed in Figure 6 at the inner part of the cavity ($r/b < 0.93$) indicating that the flow is fully mixed all along the stator boundary layer. On the contrary, at higher radii ($r/b > 0.93$) radial variations in the sealing effectiveness distribution indicate partial mixing of ingested annulus and cavity flows. It is also worth noting that the geometrical discontinuity of the stator wall joining the flat vertical and angled faces at $r/b = 0.93$ aids this effect and the change consistently takes place at this radial coordinate.

Higher values of turbulent flow parameter, λ_T, reduce the swirl velocity thus generating lower pressure gradients across the cavity. Interestingly, Figure 7b reveals that for $\lambda_T > 0.1$, the pressure coefficient tends to an asymptotic value. When the purge flow satisfies disc pumping for $\lambda_T = 0.219$ as shown by Childs [12], the recirculation and formation of a rotating core in the cavity is suppressed. Estimates of free disc pumping with allowance for the effect of a non-zero inner radius of the disc are consistent with a change of flow behaviour at $\lambda_T \sim 0.1$ as reflected in Figure 7b.

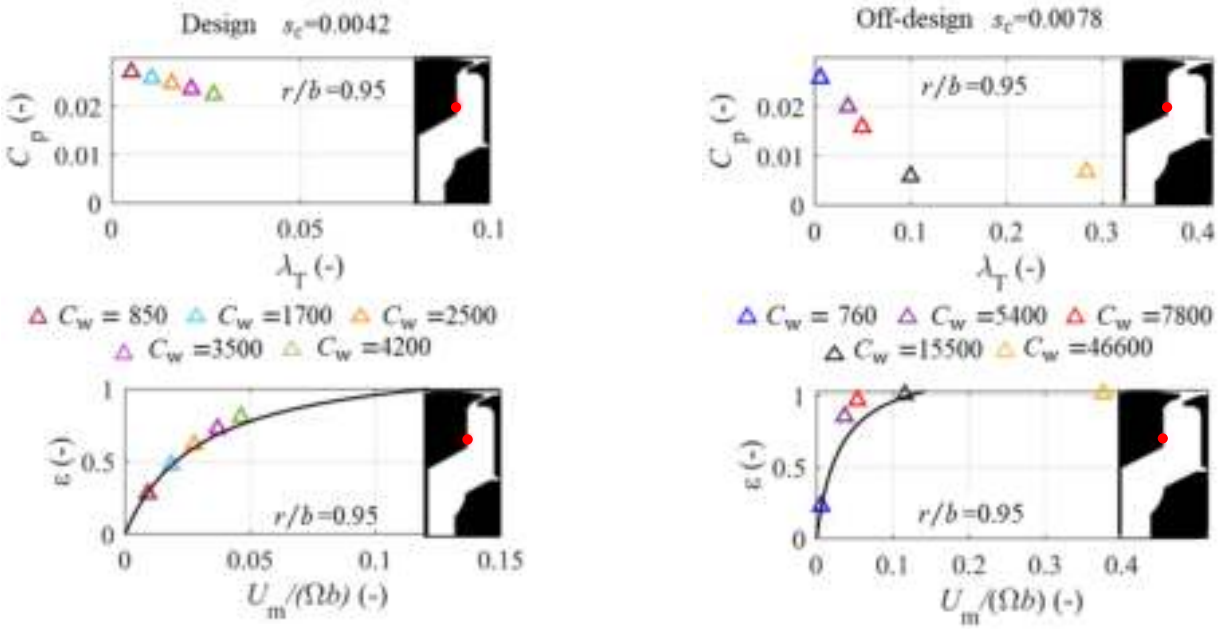

(**a**) (**b**)

Figure 7. Cavity pressure coefficient and sealing effectiveness as function of λ_T and $U_m/(\Omega b)$ evaluated at $r/b = 0.95$ for (**a**) $s_c = 0.0042$ and (**b**) $s_c = 0.0078$.

4.3. Effect of Seal Clearance

Figure 7a,b show pressure coefficient and sealing effectiveness results for the two seal clearances at $r/b = 0.95$. Sealing effectiveness data show reasonable agreement with the disc pumping correlation derived by Chew [4] and shown in Equation (1), although the data for the larger seal clearance generally sit above the analytical prediction. This suggests a superior sealing capability of the open rim geometry as shown in Figure 7b (please note the wider range of purge flows tested at off-design). Here, the empirical constant in the model, k, is set to 1, as it was shown to best fit the experimental data for a chute seal by Bru Revert et al. [9]. Therefore, the underprediction for the larger clearance suggests that a slightly lower value of k is needed to represent this seal. The increase in gap size was achieved by axially displacing the rotor disc rearwards, and consequently the overlap in the chute seal was lost. This change in configuration intrinsically modified the rim seal geometry into an axial seal of 0.5 mm clearance. This is consistent with the comparison against available experimental data of an axial rim seal reported by Bru Revert et al. [1] that fitted Chew's orifice model with $k = 0.8$.

4.4. Effect of Mainstream Flow

The effect of the annulus flow on the sealing performance of the chute seal has been investigated for a wide range of conditions and is summarised in Figure 8. Data correspond to $Re_\varnothing = 1.5 \times 10^6$ (left) and $Re_\varnothing = 2.7 \times 10^6$ (right) for the test cases without and with axial annulus flow. The results presented were measured at the rim, $r/b = 0.99$, for the larger seal

clearance, s_c = 0.0078. The imposed annulus flow was purely axial with a Mach number of 0.34 (axial Reynolds number of 2.6 × 10^5 referenced to the nominal NGV axial chord).

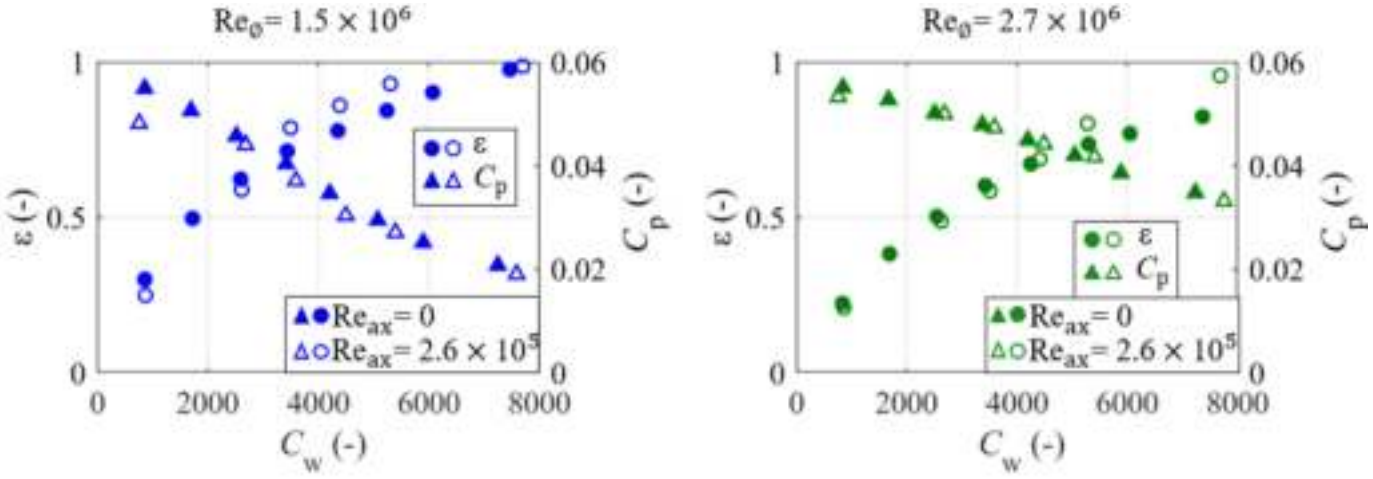

Figure 8. Effect of the axial annulus flow on the sealing effectiveness and cavity pressure difference as a function of the purge supply measured at r/b = 0.99 and s_c = 0.0078.

Figure 8 reveals that the addition of axial annulus flow aids the sealing performance of the chute seal under certain circumstances. There is a value of C_w at which the sealing effectiveness under axial annulus flow equals that of the configuration without it. As purge flow rate increases from this point, the presence of mainstream flow seems to exert a beneficial effect on the sealing capability of the chute seal. The pressure coefficient shows little sensitivity to the presence of annulus flow.

The study conducted by Phadke and Owen [5] reported an improvement of the sealing capability when the external environment presented a weak quasi-axisymmetric flow. Past a certain threshold ($Re_{ax} \geq 2 \times 10^5$ for s_c = 0.01), their data revealed a detrimental effect of the external flow. Note that different definitions of Reynolds number across studies may apply. These results are in broad agreement with the measurements obtained in the ORF. Bear in mind that Phadke and Owen's experimental set up struggled to achieve an axisymmetric mainstream flow and the pressure non-uniformities in the gas path amplified with higher flow rates.

The sealing effectiveness is sensitive to the annulus flow conditions at high purge flow rates when $\varepsilon > 0.75$. In this particular case, it appears that a purge supply able to satisfy C_p = 0.04 is sufficient to overcome the disc pumping effect and could benefit the sealing performance. The value of C_w at which this occurs depends on the rotor disc speed. A stronger pressure gradient in the cavity is generated at higher rotational Reynolds number, thus demanding larger flow rates to pressurise the cavity and outbalance the disc pumping effect. In the specific cases depicted in Figure 8, values of C_w~3000 and C_w~5000 are required to satisfy the condition for the low and high rotational Reynolds number respectively. This improvement in sealing capability in the presence of external flow could be a consequence of the flow recirculation in the rim seal region due to the interaction between purge and annulus flows that intensifies at higher rates of sealing air supply. The flow visualisation technique employed by Phadke and Owen revealed a separation bubble at the rim that reduced the effective separation between the stator and rotor discs therefore restricting ingestion. The CFD analysis of Savov and Atkins [13] showed that the gap recirculation zone reduced in size and was blown out of the rim seal passage into the main gas path at high flow rates. The turbulent mixing of the purge and annulus flow would then occur in the annulus and ingestion would be inhibited. Experimental evidence supporting this hypothesis is provided here.

The effect of the seal clearance can be assessed by examining Figure 9a. The gap size appears to more largely impact the amplitude of the frequency spike than the non-

dimensional frequency of the peak. This suggests that the intensity of the unsteady pressure fluctuations decreases in the off-design axial-like seal geometry. The methodology detailed by Beard et al. [10] to obtain the lobe count and rotational speed of the unsteady flow structures was applied to this experimental campaign, obtaining 27 lobes rotating at 76% of rotor disc speed at the highest rotational speed. The results from this study are in good agreement with those previously reported by Beard et al. [10] and show that at higher rotor disc speeds both the lobe count and the angular speed of the structures slightly reduced.

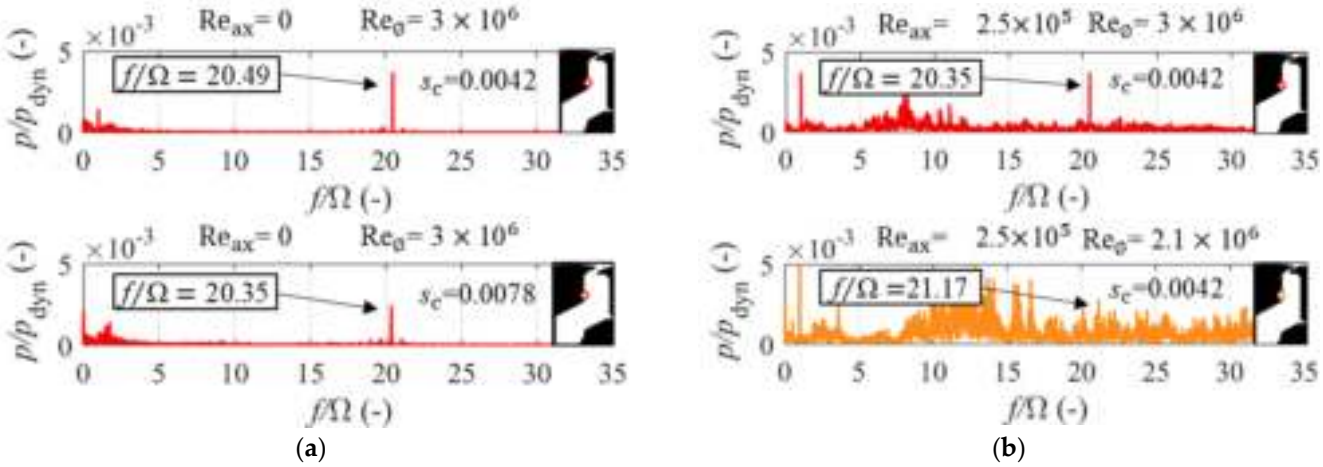

Figure 9. Frequency spectra of the unsteady pressures at C_w = 3500, r/b = 0.95 in (**a**) absence of annulus flow at constant rotational Reynolds number for two seal clearances and (**b**) with axial axisymmetric annulus flow at constant gap size for two rotational Reynolds numbers.

The frequency spectra of the unsteady pressure signals across the test matrix reveal that the introduction of external axial flow does not have a strong impact on the non-dimensional frequency of the distinct peak (top plots in Figure 9a,b). However, an increase in the unsteady activity under an axial axisymmetric mainstream flow is registered around f/Ω~8 and is attributed to the complex interaction and shear between the annulus and purge flows in the rim seal region. Indeed, a lower rotational Reynolds number reduces the intensity of the disc pumping effect as discussed in Figure 5b which in turn translates into a distinct peak of decreased amplitude. Under the influence of the mainstream annulus flow, the bottom plot in Figure 9b reveals an intensification of the broadband unsteadiness and the characteristic spike of the disc pumping effect no longer stands out. Interestingly, the increased unsteadiness originated by the interaction of the annulus and purge flows appears at a constant frequency. Nonetheless, the frequency non-dimensionalisation with rotor disc speed gives a false illusion of a shift towards higher frequencies. A more detailed analysis of this dataset will be the subject of a future publication.

5. Conclusions

The Oxford Rotor Facility has been modified to investigate rim sealing flows with more extensive instrumentation installed in the stator-rotor cavity to measure pressure and gas concentration.

Steady pressure measurements have revealed the presence of different vortex strengths in the outer and inner sections of the cavity, implying that the change in geometry in the stator wall is inducing two different, coexisting vortices. The frequency spectra of the unsteady pressure signals present a maximum amplitude peak at r/b = 0.95, which is close to the change in stator wall geometry. Extended radial unsteady pressure transducers investigated the possible origin of the excitation further inboard in the cavity down to the overlapping seal and concluded this was not the source of the unsteadiness. The cavity flow unsteadiness is therefore associated with flow effects of the interface of the

two vortices and is linked to rotating flow structures in the rim seal region identified in previous experimental and computational studies.

The effect of the rotor disc speed has been found to be dependent on the purge flow rate: at low supplies of sealing flow a large pressure gradient across the cavity appears to be insensitive to disc speed, whilst rotational effects have been identified at large rates of purge flow. The frequency spectra reveal an increase in the amplitude of the distinct frequency peak with angular speed of the rotor disc, indicating this is a rotationally dominated phenomenon.

The sealing performance is better for the larger seal clearance tested than for that of the smaller gap at the same value of $U_m/(\Omega b)$. That is, increasing the seal clearance requires a lower increment in purge flow than simple, proportional scaling would suggest. The frequency spectra from the unsteady pressure traces reveal that an increase in the gap size has a larger impact on the amplitude of the pressure fluctuations of the unsteady flow structures than on the speed at which they travel.

The introduction of mainstream annulus flow exerts a beneficial effect in the sealing capability of the chute seal at conditions where sealing effectiveness is greater than ε~0.75. At the two conditions investigated this has been found to occur at C_p~0.04. The interaction between the purge and annulus flows has been registered as an excitation of a band of frequencies at f/Ω~8. The broadband unsteadiness is further increased when the effect of the disc pumping effect reduces at lower rotor disc speeds until the distinct peak no longer stands out in the frequency spectra.

The study by Bru Revert et al. [1] showed that rotationally induced ingestion may be the dominant mechanism in cases of low flow coefficient in which pressure asymmetries derived from NGVs exist in the gas path, such as high pressure turbines. This publication contributes towards an improvement of the understanding of the disc pumping effect and the flow behavior in the rim seal region through a more comprehensive analysis allowed by three different sets of measurement techniques complementing each other.

Author Contributions: Conceptualisation, methodology, formal analysis, investigation, data curation, writing—original draft preparation, A.B.R.; supervision and project administration, P.F.B.; writing—review and editing, P.F.B. and J.W.C. All authors have read and agreed to the published version of the manuscript.

Funding: This research was funded Rolls-Royce plc and Innovate UK through the TSB 113076 grant.

Data Availability Statement: Not applicable.

Acknowledgments: The authors wish to acknowledge the guidance provided by Sebastiaan Bottenheim and Peter Smout as well as the technical support of Gregory King, Sunny Chana and James Carter.

Conflicts of Interest: The authors declare no conflict of interest.

Nomenclature

b	disc radius, m
c	tracer gas concentration, %
C_{ax}	NGV axial chord, m
C_w	non-dimensional purge flow rate $= \dot{m}/\mu b$
C_p	cavity pressure coefficient, $= (p - p_{1011})/0.5\rho(\Omega b)^2$
g	rim seal gap size, m
k	empirical constant
$\dot{m}$	mass flow, kg s^{-1}
p	pressure, Pa
Re_{ax}	axial flow Reynolds number $= \rho U_{ax} C_{ax}/\mu$
$Re_{\varnothing}$	rotational Reynolds number $= \rho\Omega b^2/\mu$
s_c	seal clearance $= g/b$
T	temperature, K
U_{ax}	axial velocity, m s^{-1}
U_m	mean flow velocity through seal, $= \dot{m}/\rho 2\pi b s_c$, m s^{-1}

Greeks

ε	sealing effectiveness
λ_T	turbulent flow parameter $= C_w/Re_{\varnothing}{}^{0.8}$
μ	dynamic viscosity, Pa s
ρ	fluid density, kg m^{-3}
Ω	angular rotational speed, rad s^{-1}

Subscripts

0	total conditions
ax	axial component value
min	minimum value
purge	purge flow value

Acronyms

CFD	computational fluid dynamics
NGV	nozzle guide vane
ORF	Oxford Rotor Facility

References

1. Bru Revert, A.; Beard, P.F.; Chew, J.W.; Bottenheim, S. Performance of a Turbine Rim Seal Subject to Rotationally-Driven and Pressure-Driven Ingestion. *J. Eng. Gas Turbines Power* **2021**, *143*, 081025. [CrossRef]
2. Daily, J.W.; Nece, R.E. Dimension Effects on Induced Flow and Frictional Resistance of Enclosed Rotating Discs. *J. Basic Eng.* **1960**, *82*, 217–230. [CrossRef]
3. Bayley, F.J.; Owen, J.M. The Fluid Dynamics of a Shrouded Disk System with a Radial Outflow. *J. Eng. Power* **1970**, *92*, 335–341. [CrossRef]
4. Chew, J.W. A Theoretical Study of Ingress for Shrouded Rotating Disk Systems with Radial Outflow. *J. Turbomach.* **1991**, *113*, 91–97. [CrossRef]
5. Phadke, U.P.; Owen, J.M. An Investigation of Ingress for an "Air-Cooled" Shrouded Rotating Disk System with Radial-Clearance Seals. *J. Eng. Power* **1983**, *105*, 178–182. [CrossRef]
6. Cao, C.; Chew, J.W.; Millington, P.R.; Hogg, S.I. Interaction of Rim Seal and Annulus Flows in an Axial Flow Turbine. *J. Eng. Gas Turbines Power* **2004**, *126*, 786–793. [CrossRef]
7. Scobie, J.A.; Sangan, C.M.; Owen, M.; Lock, G.D. Review of Ingress in Gas Turbines. *J. Eng. Gas Turbines Power* **2016**, *138*, 120801. [CrossRef]
8. Chew, J.W.; Gao, F.; Palermo, D.M. Flow mechanisms in axial turbine rim sealing. *Proc. Inst. Mech. Eng. Part C J. Mechan. Eng. Sci.* **2018**, *233*, 7637–7657. [CrossRef]
9. Bru Revert, A.; Beard, P.F.; Chew, J.W.; Bottenheim, S. Sealing Performance of a Turbine Rim Chute Seal Under Rotationally-Induced Ingestion. *J. Phys. Conf. Ser.* **2020**, *1909*, 012035. [CrossRef]
10. Beard, P.F.; Gao, F.; Chana, K.S.; Chew, J. Unsteady Flow Phenomena in Turbine Rim Seals. *J. Eng. Gas Turbines Power* **2017**, *139*, 032501. [CrossRef]
11. Gao, F.; Chew, J.W.; Marxen, O. Inertial waves in turbine rim seal flows. *Phys. Rev. Fluids* **2020**, *5*, 024802. [CrossRef]
12. Childs, P.R.N. *Rotating Flow*; Elsevier: Amsterdam, The Netherlands, 2010.
13. Savov, S.S.; Atkins, N.A.; Uchida, S. A comparison of Single and Double Lip Rim Seal Geometries. *J. Eng. Gas Turbines Power* **2017**, *139*, 112601. [CrossRef]

International Journal of
Turbomachinery Propulsion and Power

MDPI

Article

Influence of the Rotor-Driven Perturbation on the Stator-Exit Flow within a High-Pressure Gas Turbine Stage †

Paolo Gaetani and Giacomo Persico *

Laboratory of Fluid-Machines, Energy Department, Politecnico di Milano Via Lambruschini 4, 20156 Milano, Italy; paolo.gaetani@polimi.it

* Correspondence: giacomo.persico@polimi.it; Tel.: +39-02-2399-8605

† This manuscript is an extended version of our meeting paper published in the Proceedings of the 14th European Turbomachinery Conference, Gdansk, Poland, 12–16 April, 2021.

Abstract: In stator–rotor interaction studies on axial turbines, the attention is commonly focused on the unsteady rotor aerodynamics resulting from the periodic perturbations induced by the stator flow structures. Conversely, less interest has been historically attracted regarding the influence of the rotor on the flow released by the stator, correlated to propagation of the blade potential field upstream of the rotor leading edge. In this paper, experiments in the research high-pressure turbine of the Laboratory of Fluid-Machines of the Politecnico di Milano, performed by applying a fast-response aerodynamic pressure probe, alongside fully-3D time-accurate CFD simulations of the flow, are combined with the aim of discussing the rotor-to-stator interaction. While rotating, the rotor induces periodic perturbations on the pressure and velocity field in the stator–rotor gap, altering the evolution of the total quantities and the flow rate discharged by each stator channel and eventually triggering energy-separation effects which result in total pressure and total temperature oscillations in the stator-exit flow. Such oscillations were found to rise up to almost ±10% of the stage total temperature drop.

Keywords: high-pressure turbines; blade-row interaction; cascade potential field; energy separation; unsteady measurements; time-accurate CFD

check for updates

Citation: Gaetani, P.; Persico, G. Influence of the Rotor-Driven Perturbation on the Stator-Exit Flow within a High-Pressure Gas Turbine Stage. *Int. J. Turbomach. Propuls. Power* **2021**, *6*, 28. https://doi.org/10.3390/ijtpp6030028

Academic Editor: Claus Sieverding

Received: 26 June 2021
Accepted: 6 July 2021
Published: 13 July 2021

Publisher's Note: MDPI stays neutral with regard to jurisdictional claims in published maps and institutional affiliations.

Copyright: © 2021 by the authors. Licensee MDPI, Basel, Switzerland. This article is an open access article distributed under the terms and conditions of the Creative Commons Attribution (CC BY-NC-ND) license (https://creativecommons.org/licenses/by-nc-nd/4.0/).

1. Introduction

The need for continuous improvements in gas turbine performance, in terms of efficiency and rangeability, alongside the need of a deeper understanding of the flow physics, still asks for important theoretical and experimental efforts and research. A key field of interest—among the many involved in gas turbine studies—is thermo-fluid-dynamics, pillar for getting a holistic comprehension of turbomachinery and for their optimal design. In this context, one of the major interests in present-day research is the interaction between system components, as well as stationary and rotating rows of turbomachinery. Multiple classes of problems can be acknowledged, such as the combustor–1st turbine stage interaction, the stator–rotor interaction in both high-pressure and low-pressure turbines, the last turbine stage–diffuser interaction, the impeller–diffuser interaction and the surge in compressors.

With specific reference to turbines stages, the stator–rotor interaction consists of potential field interference, wake/shock/vortex-blade interaction, wake-wake interaction and wake/vortex-secondary flow interaction [1–13]. In general, most of the papers focus on the effect of the stator flow structures on the rotor aerodynamics and performance, as the spatial non uniformities at the stator exit result in time-varying inlet boundary conditions for the rotor. Only a few studies report about the effects of the rotor potential field on the stator, for example, [14] for subsonic turbines and [15] for transonic high-pressure turbines; these studies typically include measured data on the stator blade surface. Thanks to the recent improvements in measuring techniques—such as fast response aerodynamic

pressure probes—and CFD codes, it is now possible to more proficiently track these features, also considering the detailed flow configuration in-between the blade rows, i.e., in the stator–rotor axial gap.

When discussing the flow unsteadiness in turbomachines, one basic observation is the inherent link between unsteady flow and work exchange [16], related to the coupling, valid for inviscid flows, between the material derivative of the total enthalpy and the local time-derivative of the static pressure:

$$\rho \frac{Dh_t}{Dt} = \frac{\partial p}{\partial t} \tag{1}$$

The same concept, when applied to a wake incoming on a turbine cascade and impinging on the blades, was observed to produce a local increase in the total enthalpy and pressure, due to onset of energy separation effects [17].

Similar features may apply also to the potential field, with the important difference that the pressure field also propagates upstream of a cascade (at least up to the sonic throat of the upstream cascade, if this latter is choked) which might lead, in case of a rotor, to the onset of unexpected flow features within the stator–rotor axial gap. Such features, not visible if applying time-mean measurement techniques or steady computational models, can instead be highlighted by resorting to unsteady measurements and time-accurate CFD simulations. This is indeed the focus of the present paper, which aims at discussing the effect of the rotor potential field on the flow released by the stator, thanks to a combined experimental and numerical approach.

The paper is structured as follows: at first the experimental and numerical approaches are described, then the experimental results are discussed with the support of CFD results for physical interpretations and, finally, some conclusions are derived.

2. Test Facility and Measuring Techniques

The test rig and instrumentation applied in the present research work are already described in other papers: see, for example, [18]. In this section, they are briefly recalled.

2.1. Test Rig and Axial Turbine Stage

The test rig run for the present investigation is the high-speed test rig for turbine and compressor located at the Laboratory of Fluid Machine (LFM) of the Energy dept. of the Politecnico di Milano. It consists of a radial section where a centrifugal compressor is run and, in the present investigation, it feeds the turbine with the proper pressure ratio and flow rate; its maximum rotational speed is 45,000 rpm with a power available upstream of the gearbox of 800 kW. The radial section is then followed by a cooler to set the temperature level of the rig, a venturi pipe to measure the flow rate and a throttling section to control the expansion ratio made available to the turbine. The turbine is located in an axial section, whose maximum rotational speed is 20,000 rpm.

The axial turbine stage is a single stage, not cooled, representative of a high pressure one. The main features are reported in Table 1; in addition, the stator blade is leaned by 12° on the pressure side and at midspan it has a geometrical discharge angle of 75.4°. The rotor is bowed with a constant outlet angle of −67.7°, it has a clearance at tip of 0.6 mm and a blade height of 50 mm (clearance included). The axial distance between the stator and the rotor is equal to one stator axial chord (30.6 mm), easing the probe insertion.

Table 1. Stage geometry and operating conditions.

Operating Condition	β	n [rpm]	G [kg/s]	Tt_{in} [K]
	1.35	**7000**	**3.5**	**323**
Geometry	h [mm]	t_C/h	D_M (mm)	$gap/c_{x,V}$
	50	0.015	350	1.00
Blade Rows	Nb	σ	AR	ε
Vane	22	1.20	0.83	75.2
Rotor	25	1.25	0.91	115.3

Measurements were taken at 71% of the stator axial chord downstream of the stator trailing edge, all over the channel height: the measurement grid counts 320 points (16 points on the stator pitch, 20 points along the blade span) on each stator channel. Figure 1 reports a picture of the stage and a sketch of the meridional section.

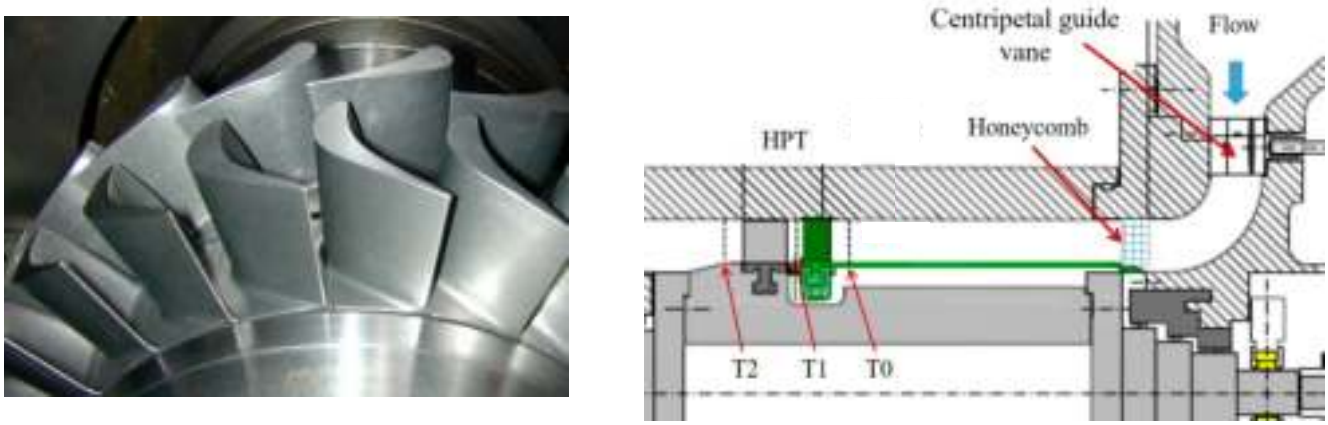

(**a**) (**b**)

Figure 1. Picture of the turbine stage (**a**) and sketch of the meridional section (**b**).

2.2. Measurement Techniques

In the present study, besides the instrumentation for the rig management, only a Fast Response Aerodynamic Pressure Probe (FRAPP) was applied. The reader is referred to [19] for a picture of the present-day FRAPP, design, operation and technology available at Politecnico di Milano and to [11,13,18] for the FRAPP application in the rig.

The FRAPP here applied has a cylindrical head (diameter of 2 mm) where a single sensor is inserted (Kulite, model XCQ062) and connected to the external environment by a hole whose diameter is 0.35 mm. The probe promptness, evaluated on a shock tube, is 100 kHz after digital compensation thanks to the very small size of the line-cavity system facing the sensor. The probe is applied in the absolute frame of reference as a virtual 3 holes probe by rotating it around its own stem and then re-phasing the measurements making use of the key-phasor. Each pressure data set is acquired at 500 kHz and has 500,000 samples.

In addition to the standard use described in the aforementioned papers, by applying the methodology proposed in [20], it is possible to have a qualitative evaluation of the turbulence level. Thanks to this quantity, it is possible to track and evaluate the viscous structure released by the stator.

For the specific investigation, each rotor pitch has been discretized by means of 40 points.

As for the rig instrumentation, the inlet and outlet temperatures are monitored by T thermocouple, whose uncertainty after calibration is 0.3 °C.

The stage inlet and outlet pressure level are measured by means of Kulite transducers (model XT190) whose uncertainty, after calibration, is 60 Pascal.

FRAPP data reduction is based on the phase-averaging techniques. First, the pressure measurements are phase averaged by referring to the key-phasor signal: the averaged value in each interval (40 per rotor pitch) is thus the result of about 12,000 samples. Second, by applying the calibration matrices, they are used to derive the flow quantities in terms of total and static pressure, flow angle. Finally, assuming a total temperature constant across the stator, the velocity field is determined and—by the peripheral speed—the flow conditions in the rotating frame of reference are calculated. As it will be discussed in the last section, the total temperature fluctuates by about ± 1 K; the corresponding velocity fluctuation is expected to be of the order of 0.1% and, hence, negligible, also considering that the Mach number is correct coming from a phase-resolved data reduction.

Overall, pressure values have an averaged uncertainty of 0.5% of the kinetic head measured by the FRAPP.

The phase averaged signals for the different stator positions (in all the blade span positions) are re-organized in order to map the stator—rotor interaction for the different stator to rotor positions. The time mean quantities in the absolute frame of reference are calculated by averaging in time the phase averaged flow quantities. The time mean quantities in the rotating frame of reference are calculated by averaging the stator to rotor interaction positions, acknowledging the rotor pitch periodicity.

3. CFD Model and Experimental Validation

In this study, CFD simulations mainly act as support to the interpretation of the experimental result. The calculations were performed using ANSYS-CFX, applying the flow model developed at Politecnico di Milano for turbomachinery flow simulations, discussed in detail in [21] and briefly summarized in the following. Fully 3D and time-resolved calculations were performed, modeling the fluid as perfect gas and introducing turbulence effects by resorting to the fully-turbulent k-ω SST model. The near-wall resolution was specified so to guarantee $y^+ < 1$ on endwalls and on blade surfaces, thus avoiding the use of wall functions. Unsteady terms are discretized with an implicit second order scheme, the advection terms with a high-resolution total-variation-diminishing scheme, the diffusive terms with a second order central scheme. Simulations were performed by assigning, at the inlet, the measured radial profile of total pressure, uniform total temperature, axial flow direction and a uniform turbulence intensity of 2.5%, resulting from dedicated hot-wire measurements (the eddy viscosity ratio was set equal to 25, following the recommended expression proposed by the solver). A radial-equilibrium distribution of static pressure was assigned at the outlet.

Coupled stator–rotor simulations were performed, first resolving the flow in steady-state fashion using a mixing-plane stator–rotor interface for initialization and then moving to time-resolved analysis. Given the different blade numbers between the stator and the rotor, to simulate the full stator–rotor coupling (i.e., also the rotor-to-stator interaction and not only the stator-to-rotor interaction as was conducted in [21] where only the unsteady flow in the rotor was solved) while saving computational cost, the time-inclined solution strategy proposed in [22] was adopted. By virtue of this method, spatial-temporal solutions are obtained so to guarantee automatically the phase-lag between periodic boundaries and neither multiple channels nor alteration of the cascade solidity (or blade scaling) are required.

The solver integrates the equations over structured meshes composed by hexahedral elements. A grid-dependence study was performed to select the proper spatial resolution. The study was conducted by keeping constant the near-wall resolution so that the boundary layer is properly resolved on both blade walls and hub and shroud walls for each of the tested meshes. The mesh dimension ranged from 2.2 million to 18.4 million cells for the entire stage; overall cascade/stage performance data as well as detailed spanwise profiles were considered to judge the influence of spatial resolution. Grid-independent results were achieved for stator and rotor meshes composed by 4.6 million cells, for a total of 9.2 million cells (the difference in stage efficiency with respect to the result obtained with the finest

mesh resulted below 0.1%). The final meshes of each blade row, reported in Figure 2, are composed by 140 cells in spanwise direction and 33,000 cells in each blade-to-blade layer.

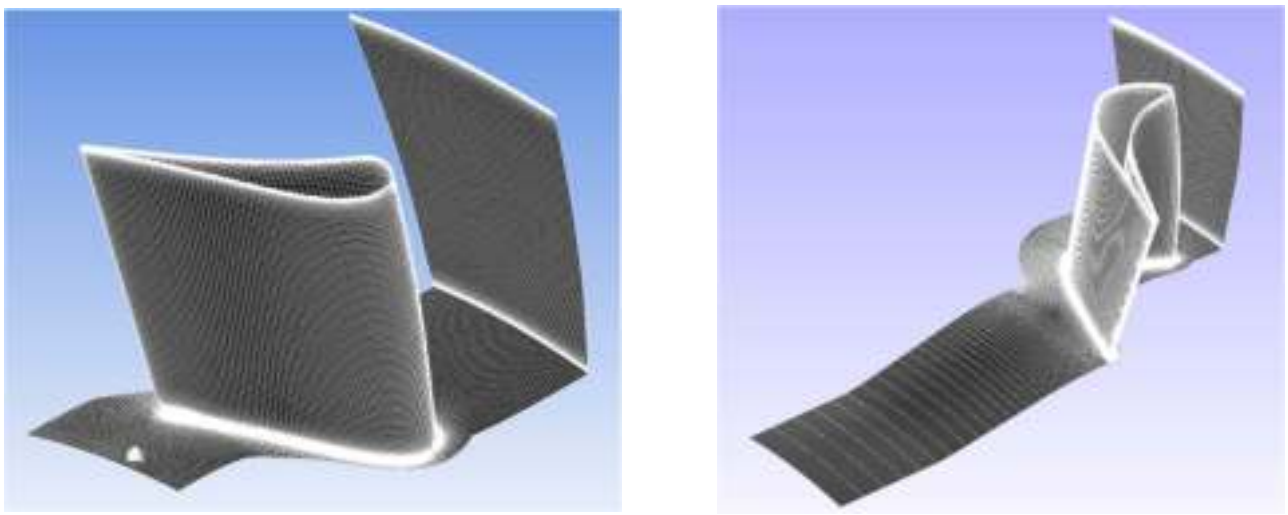

(**a**) (**b**)

Figure 2. Computational meshes of the stator (**a**) and rotor (**b**) blade rows after grid-dependence study.

The time step was set to 1/56 of the rotor blade passing period (corresponding to about 0.25°); the unsteady solution resulted smooth (due to the subsonic flow regime) and further reductions of the time step were not found to alter the performance prediction and the flow morphology. The specific time step value was selected to optimize the sampling of the 3D solution for post-processing (since the stage periodicity 22 × 25 is close to 7 × 8 and 56 is the least common value of these two numbers). The periodic solution was achieved after 20 periods (the first 12 ones run with a larger time step, 1/25 of the rotor blade passing period). The computational cost of the time-resolved simulation was about one week on a 40-processor cluster.

Before simulations are used to aid the interpretation of the experiments, experiments are used to assess the simulation results. Figure 3 shows a set of spanwise profiles, comparing the computations and measurements both at the stator and rotor exit. The top-left frame of Figure 3 reports the distribution of total pressure loss coefficient (Yloss) at the stator exit and shows a remarkable agreement between experiment and calculations. It is to be noted that the experimental trend interrupts at 10% span, due to limitations in the probe traversing, so the severe increase of loss in the hub region predicted by the numerical trend cannot be entirely visible in the measurements (but it is outlined in the bottom part of the experimental profile). This generation of loss in the hub region is driven by a hub clearance in the region of the blade tail, whose effect combines with the inherent cascade corner vortex to generate a wide vortex counter-rotating with the hub passage vortex. More details on the stator aerodynamic will be discussed later, when analyzing the flow configuration.

The remaining three frames of Figure 3 report the spanwise profiles of Mach number, deviation angle (defined as the difference between the relative flow angle and the blade metallic angle) and absolute flow angle downstream of the rotor. Again, a good agreement was found between simulations and experiments, especially below 80% span. The spanwise flow configuration appears highly non uniform, marking the presence of large over-turning (i.e., low/negative deviation angle) region at 20% and 80% span caused by the secondary flows and an underturning region at midspan, where the two large rotor passage vortices come to interact. The simulations capture well the radial extension and the spanwise migration of the vortices, as well as their impact on the flow angle. Larger discrepancies appear only in the top 20% span, where a wide tip leakage vortex develops and proves to be challenging for the turbulence modeling used in this study.

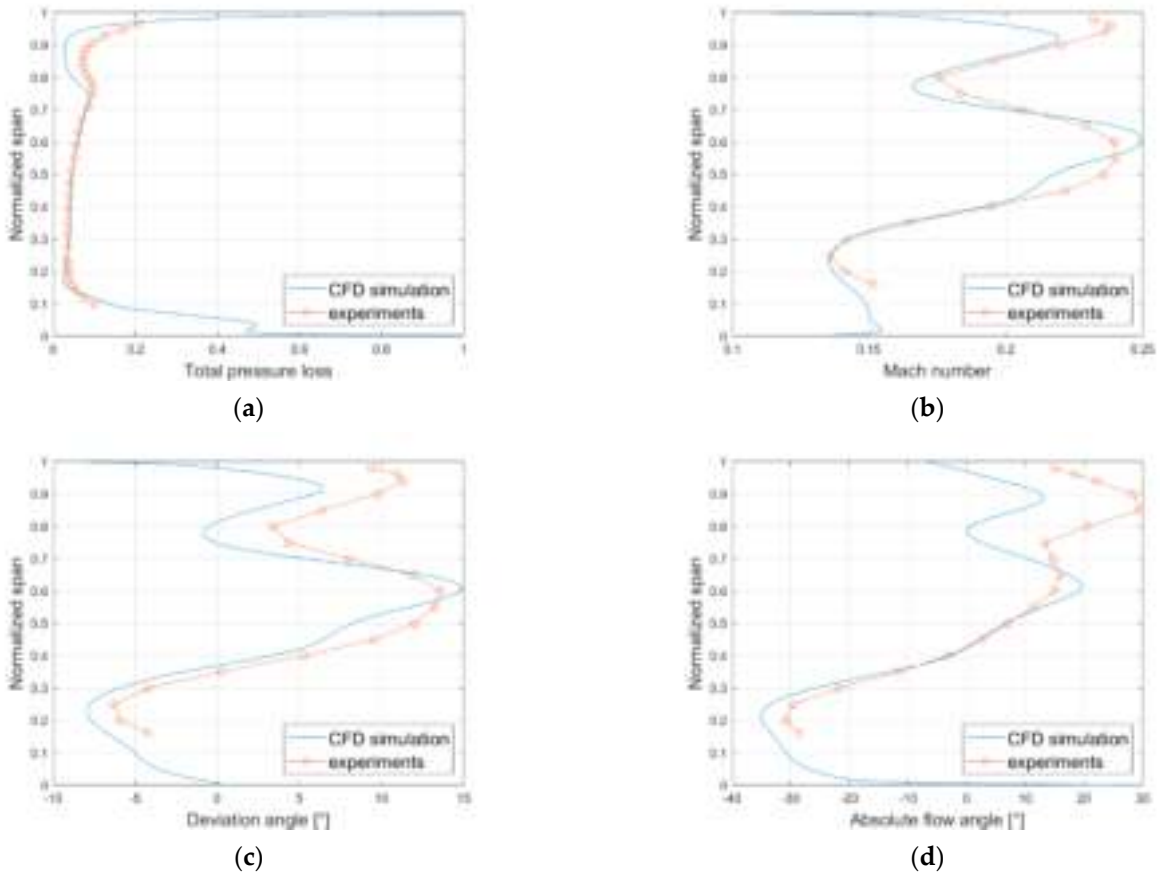

Figure 3. Measured and computed spanwise profiles. (**a**) Yloss at stator- exit; (**b**) Mach number at rotor exit. (**c**) rotor-exit deviation angle; (**d**) and absolute flow angle.

Accordingly, a very good quantitative agreement is also obtained in terms of cascade and stage efficiency. The overall stator loss coefficient, estimated from the experiments equal to 5.9%, resulted 5.4% from the simulation (averaging over the span covered by the measurement traverse). The total-total stage efficiency, calculated as the ratio between the Euler work (computed as the difference between the UV_t terms weighted on the flow rate upstream and downstream of the rotor) and the total to static isentropic enthalpy drop, is estimated as 86.4% from experiments, with an uncertainty quantified in $\pm 0.5\%$ and resulted equal to 85.5% in the CFD simulation.

The quantitative and qualitative reliability resulting from this assessment study indicate that the present simulation can be used as an effective tool for the physical interpretation of experimental data.

4. Results

This section presents the results of the flow downstream of the stator, first neglecting the stator–rotor interaction and then highlighting its effect. The flow field is discussed first from the perspective of a stationary observer, to show what discharged by the stator and then in the rotating frame of reference, to present what enters into the rotor according to its own perspective.

Results will be presented first in a time-mean form to evidence the gross features of the flow and secondly by the description of the different interaction phases between the stator and the rotor.

4.1. Time Averaged Quantities

4.1.1. Absolute Frame of Reference

One of the most important physical quantity to describe is the total pressure and its related total pressure loss coefficient. In stators, losses are generated by the blade boundary layers, the wake shed downstream of the blade trailing edge and the secondary vortices and their mutual interaction (shock losses being absent due to subsonic character of the flow). Given such occurrence, a typical distribution of total pressure loss coefficient downstream of the stator located in the present test rig is reported in the frame (a) of Figure 4, as measured by FRAPP (top) and predicted by CFD (bottom) within the stator–rotor gap.

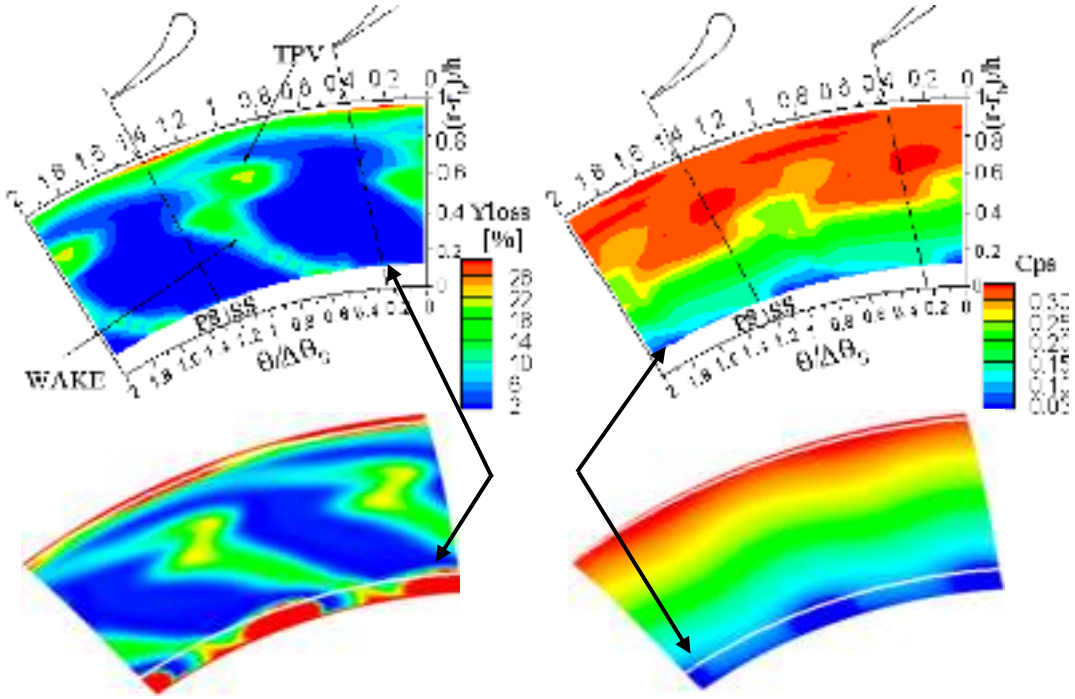

(**a**) (**b**)

Figure 4. Time-averaged contours at the stator exit. Left-to-right: (**a**) Total pressure loss (Yloss); (**b**) Static pressure coefficient (Cps). Top: experiment. Bottom: CFD predictions.

As extensively discussed in [11,18] the narrow loss trace along the span is the wake, whereas the two cores, one at the hub and the second one at 75% span, are related to the secondary flows and to their interaction with the wake. The wake, evidenced both in the total pressure and loss field, is distorted by the action of the secondary flows, by the blade twist and lean resulting in a spanwise variation of flow angle from 85° at the tip to 64° at the hub. These features are properly captured by the code, demonstrating the fidelity of the simulation tool also on a distributed level. In the hub region, a wide loss core appears, induced by the hub clearance. Even though measurements are not available in this region (the bottom and top limits of the measurement surface are marked in the computed field by white lines), the very bottom part of the measurement plane indicates an increase of loss coefficient in the central part of the channel (far away from the wake) consistent with what predicted by the code. While this feature is weakly visible here (though present and marked by black arrows), it clearly appeared in the five-hole probe measurement data presented in [18] for that the probe design allowed to extend the measurement grid closer to the hub end wall. The static pressure field, shown in Figure 4b evidences the usual radial pressure gradient due to the radial equilibrium, combined to a circumferential perturbation resulting from the suction/pressure gradient across the blade passage still not completely

decayed at this axial position. The pressure field marks the perturbation produced by the hub vortex, also evident in the experiment.

All frames appearing at the top of Figure 4 were obtained by time-averaging the FRAPP data and for this reason the periodic unsteadiness given by the rotor is filtered. Exploiting the FRAPP promptness and applying the so-called triple decomposition to the pressure signal, it is possible to extract the resolved (periodic) and unresolved unsteadiness of the flow. Filtering only the periodic component, the resulting signal can be interpreted as the random total pressure oscillation due to turbulence and its standard deviation RMSP can be used as marker of regions of high turbulence [22]. All the low total pressure regions identified above find perfect correspondence with high RMSP regions, as visible from the RMSP map reported in Figure 5, assessing the interpretation of such regions as viscous flow structures released by the stator. This observation, which appears trivial on a time-averaged basis, will become less trivial when we will focus on the stator–rotor interaction in Section 4.2 of the paper.

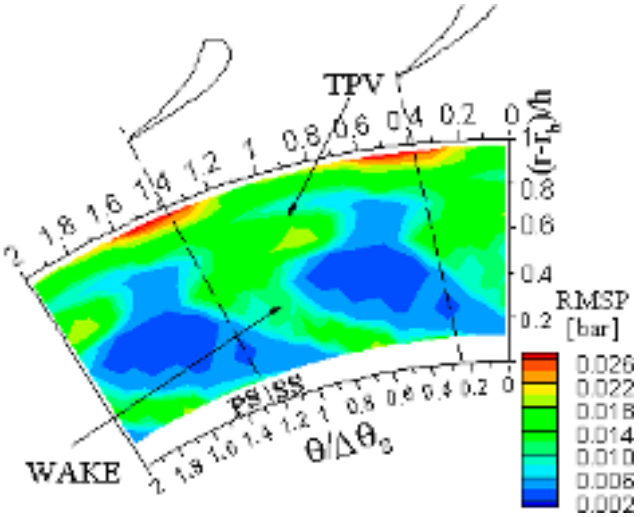

Figure 5. Standard deviation of the absolute total pressure (RMSP) at the stator exit.

4.1.2. Rotating Frame of Reference

When the perspective is changed from the stationary to the rotating frame of reference, different flow features can be highlighted. In the rotating frame, usual meaningful quantities are the relative total pressure (and its related coefficient Cptr) and the relative Mach number (Mr) entering the rotor, whose measured distributions are reported in the two top frames of Figure 6.

As for the Cptr distribution in circumferential direction, it shows a peak and a sink per pitch, thus evidencing a periodic trend; the same feature is found for the Mach number, which presents a trend opposite to that of the static pressure. The shape of the low Cptr region (highlighted by black dashed lines in Figure 6), which has a nearly constant extension in circumferential direction along the whole channel span, suggests that it is not related to the stator wake (which, instead, is strongly bended); thus, another effect is acting here, clearly related to the rotor.

If, somehow artificially, the time-mean distribution of absolute total pressure perceived by a rotating observer is analyzed, one may expect to see a uniform trend in circumferential direction; the same conclusion applies to the RMSP, whose distribution was found to correspond to the one of the absolute total pressure for stationary observers. This expectation is disregarded by measurements, also being visible in the two bottom frames of Figure 6. As a matter of fact, only the RMSP evidences an azimuthally uniform distribution, whereas the Pt distribution shows an evident perturbation whose spatial periodicity coincides with that of the rotor. The low total pressure region cannot be acknowledged as the stator wake

or as the secondary loss region since no characteristic features of those phenomena can be found.

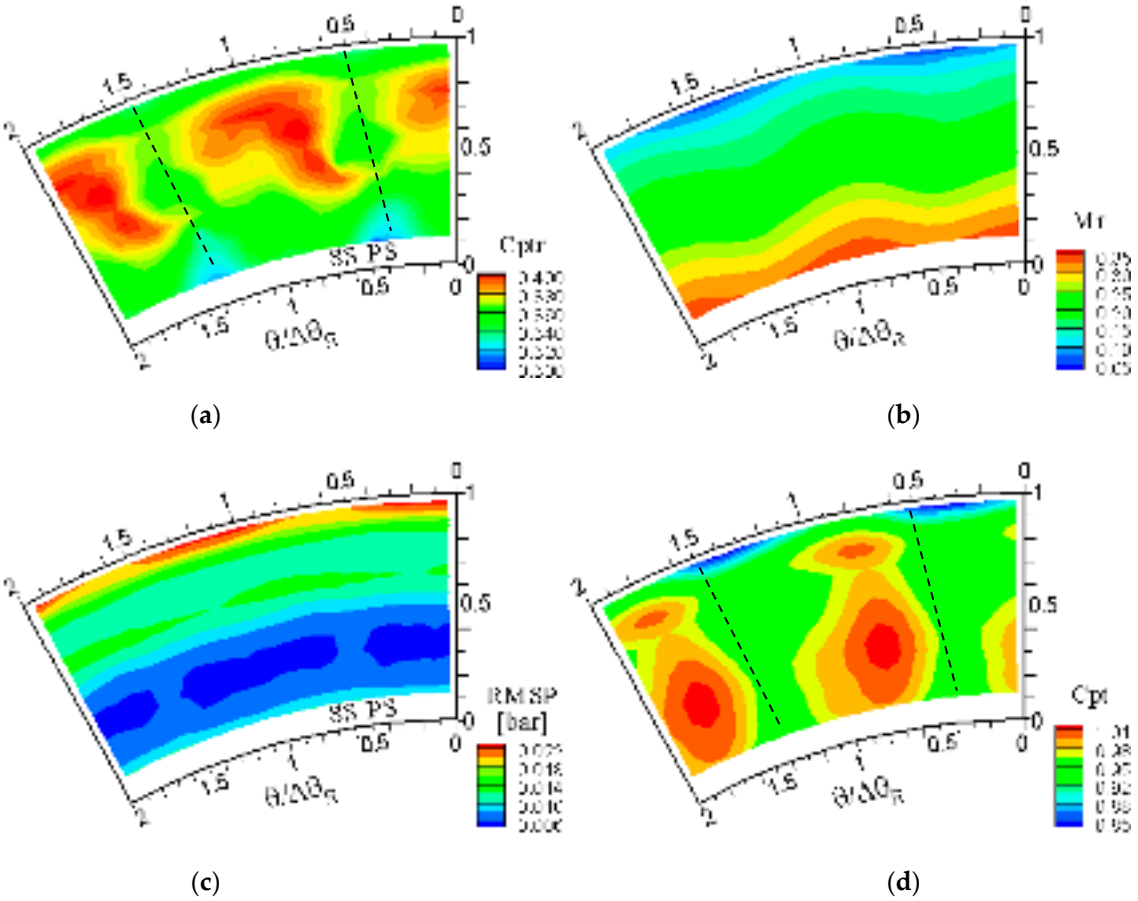

(**a**) (**b**)

(**c**) (**d**)

Figure 6. Experimental time-averaged flow in the rotating frame of reference; (**a**) relative total pressure coefficient Cptr; (**b**) relative Mach number Mr; (**c**) unresolved total pressure unsteadiness RMSP; (**d**) total pressure coefficient Cpt.

CFD simulation results, reported in Figure 7, confirm the regular and typical trend of relative Mach number and, especially, the unexpected distribution of absolute total pressure. The reason for these results must be searched for in the stator–rotor interaction phenomena, deeply presented and discussed in the following section.

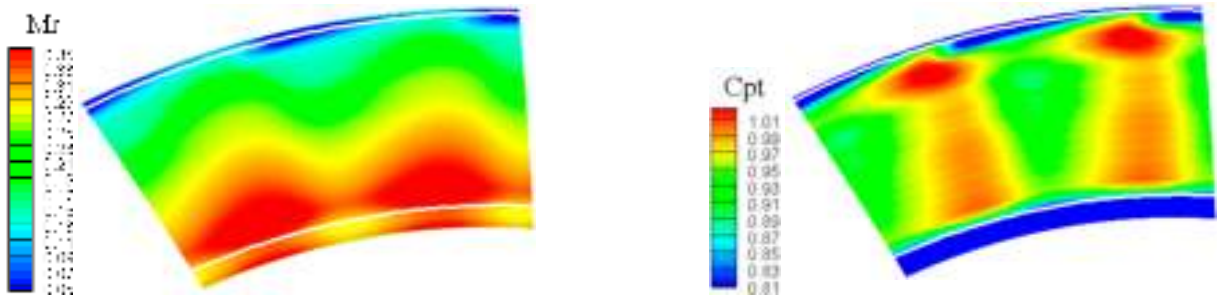

(**a**) (**b**)

Figure 7. Computed time-averaged relative Mach number (**a**) and absolute total pressure (**b**) in the rotating frame of reference at the stator exit.

4.2. Rotor–Stator Interaction Effects

By exploiting the FRAPP promptness and the phase averaging techniques, it is possible to map the different instants of the stator–rotor interaction and, specifically for this analysis, the effect of the rotor on the flow field released by the stator.

The first quantity described is the RMSP, plotted over half of the stator blade row in Figure 8. As a preliminary note, in this kind of plots adjacent channels reproduce different stator–rotor interaction phases, due to the phase-lag resulting from the different number of stator and rotor blade rows. As clearly visible, the distribution is nearly periodic with the stator pitch, being mainly related to the stator viscous structures (labelled as W) that are only marginally affected by the rotor–stator interaction. It is also clearly visible a periodicity over the whole crown of about 120° degrees as a consequence of the rotor and stator blade number ($25/22 \approx 8/7$, that means 3 nearly periodic configurations over the whole annulus). The outlines of eight rotor adjacent channels are also marked by black lines and the resulting total arc is also reported.

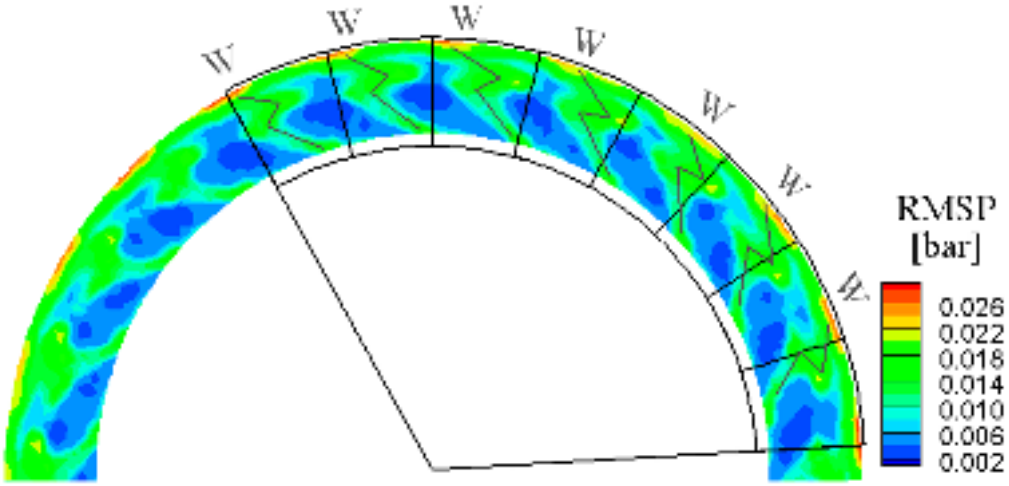

Figure 8. Snapshot of RMSP distribution over multiple channels in different stator–rotor positions.

When studying the instantaneous distribution of Pt, reported in Figure 9, the stator wakes, acknowledged as regions of low Pt/high RMSP in the stationary time-averaged maps, become no longer clearly visible, as shown in Figure 8. In the Figure 9 and in the following two figures, the black lines labelled with "W" mark the wake traces identified from RMSP in Figure 8, and are also renamed from A to G to consider the different channel.

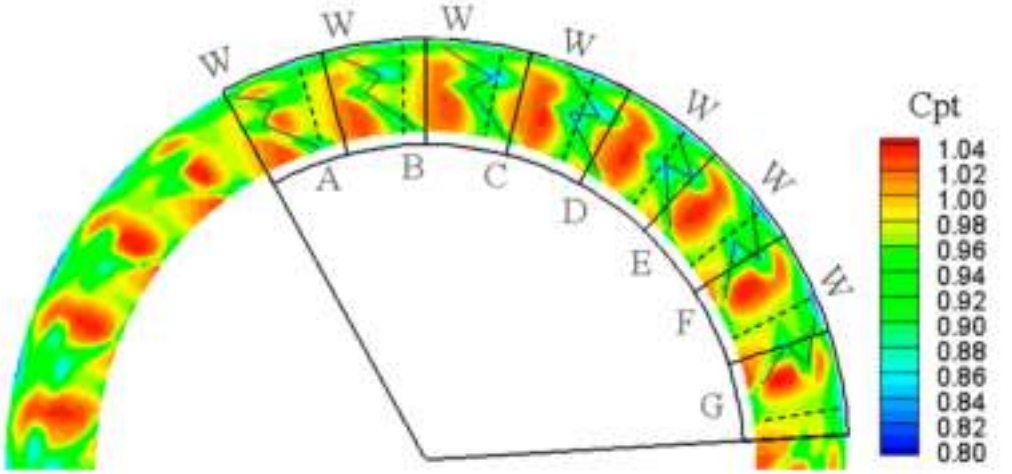

Figure 9. Snapshot of Cpt distribution over multiple channels in different stator–rotor positions.

With reference to Figure 9 and starting from left, a low Pt region coincides with black continuous line A, i.e., the stator wake, but another low Pt zone appears on the right (highlighted with a dashed line), not merged with the former; this second low Pt region is nearly uniform in spanwise direction. As the adjacent channel is considered (wake B), the low Pt zone corresponding to the black line still remains (with marginal difference with respect to the wake A), while the low Pt region 'moves' towards the wake and partially overlaps with the latter. For wake C, the two low Pt zones perfectly overlap, leading to the deepest total pressure deficit. Furthermore, shifting from one channel to the adjacent one (wake C to wake D, to E, etc.) the second low Pt region progressively 'moves' leftward with respect to the stator wake. The same consideration can be done on the high total pressure region, typically referred to as the isentropic region, where the level is modulated passing from one channel to the adjacent one. The time average of this process in the absolute frame, which is the average among the different stator channels appearing in this plot, has been already reported in Figure 4. Moreover, if the pressure level is considered, the time-averaged value Pt in the free stream is 1.345 bar (which corresponds to the upstream one), while the phase resolved one is up to 1.36 bar. Since across the stator the total pressure cannot increase, the azimuthal perturbation of Pt discussed above is clearly an effect of the rotor on the flow released by the stator.

As a further proof of that, this Pt perturbation rotates consistently with the sweeping of the rotor blades. In fact, as the rotor sweeps downstream of the stator outlet section, the rotor potential field propagates upstream with a wave of high and low static pressure, which also induces corresponding changes in the local flow direction. This also induces a local redistribution of mechanical energy, conceptually corresponding to an 'internal' work exchange between different portions of the flow, which ultimately alters the total pressure. In Section 5 a quantification of the periodic change in total temperature on the fluid upstream of the rotor, resulting from the process discussed above, will be proposed.

Considering the absolute flow angle, reported in Figure 10, the rotor-induced perturbation is observed to alter the flow direction. In particular, the interaction positions labelled as wake C and D show the maximum over-turning (high angles) in the midspan region and the maximum under-turning (low angles) condition at hub. The maximum cross flow at the tip is for the interaction position E, F, where also the lowest total pressure is found. The Mach number field, reported in Figure 11, shows a modulation among the adjacent channels. This feature evidences that changes in the flow rate released by the stator channel depend on the rotor position, as the blade leading edge creates a blockage at the outlet of the stator channel. The lowest Mach number, as an average on the passage, is found in the channel between wakes D and E.

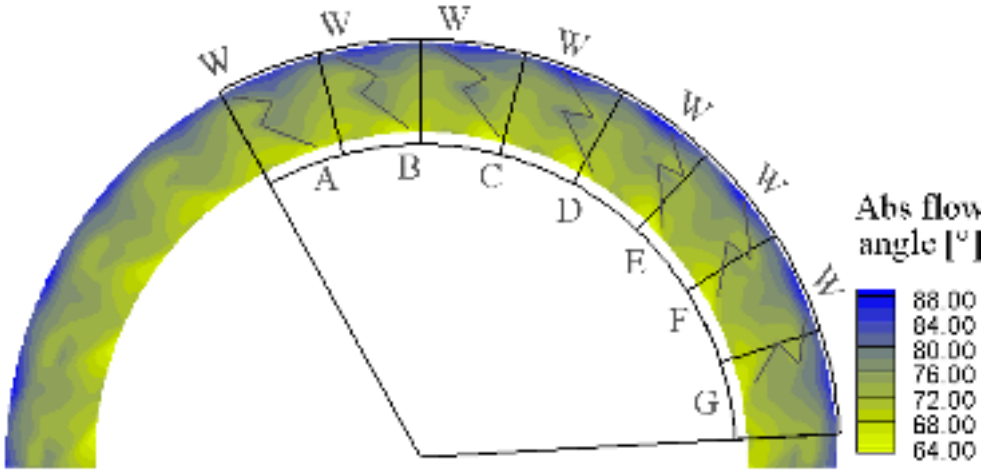

Figure 10. Snapshot of absolute flow angle distribution over multiple channels in different stator–rotor positions.

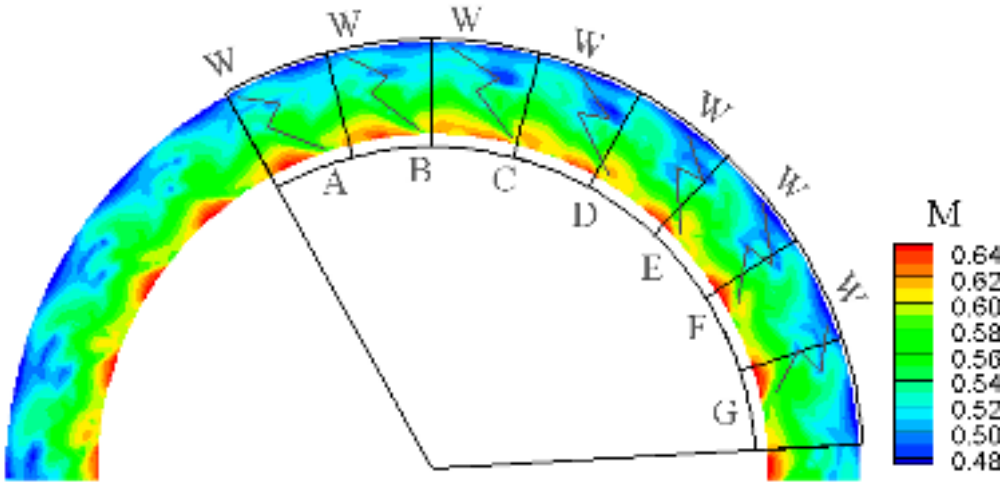

Figure 11. Snapshot of M distribution over multiple channels in different stator–rotor positions.

The scenario resulting from the analysis of the time-resolved experiments in-between the stator–rotor gap demonstrates a significant interference between the stator and rotor aerodynamics. While several effects are well known and properly discussed in Literature, for other quantities (like the absolute total pressure) an explanation is required. To this end, the CFD simulations were considered and Figure 12 summarizes relevant features—unavailable in the experiments—such as the flow configuration and the distribution of absolute total quantities, entropy and pressure on a blade-to-blade surface at midspan. The left frame of Figure 12 shows the streamlines constructed with the absolute velocity vector upstream and within the rotor channel. Streamlines clearly mark the local flow turning occurring around the rotor leading edge and in particular the absolute flow undergoes a local acceleration and deflection close to the front suction side of the rotor blade. This is the motivation for the azimuthal variability of flow angle observed in the experiments, recognized when commenting Figure 10.

The change in flow angle is associated to a change in the angular momentum of the fluid, which increases locally, because the rotor blade has locally imparted torque to the flow: this process has ultimately increased the mechanical energy of the flow upstream of the blade. This variation of mechanical energy has opposite sign with respect to the one expected in a turbine, thus leading to the local absolute total pressure increase and explaining the unexpected rise of Pt upstream of the rotor. This phenomenon is clearly visible in the corresponding Pt distribution reported in Figure 12, which shows how the high Pt region propagates upstream, producing a significant effect also on the stator wake, as appearing in this interaction phase. It is interesting to note that this process does not alter the entropy level in the flow upstream of the rotor: the entropy field shows how the stator wake is bowed by the interaction with the rotor blade, but it also highlights that no further entropy production occurs, thus confirming the quasi-isentropic character of the effect here discussed.

The field of Tt at midspan exhibits an azimuthal perturbation propagating upstream, along the black dashed lines reported in Figure 12, thus testifying that the flow deflection upstream of the rotor is the main player of the process. Thanks to the near-uniformity of the total temperature background field, one can properly appreciate the sinusoidal character of the perturbation, as well as its crucial dependence on the design of the front part of the blade, especially on the suction side. From this perspective, the comparison with the static pressure field indicates that the Pt-Tt perturbations are not linked to the recompression induced by the rotor leading edge (which propagates upstream along the red dashed line), but it conversely occurs in a region of the flow featuring a relatively low static pressure; in particular, the total temperature/total pressure rise begins exactly where maximum (in absolute value) negative azimuthal pressure gradients is found.

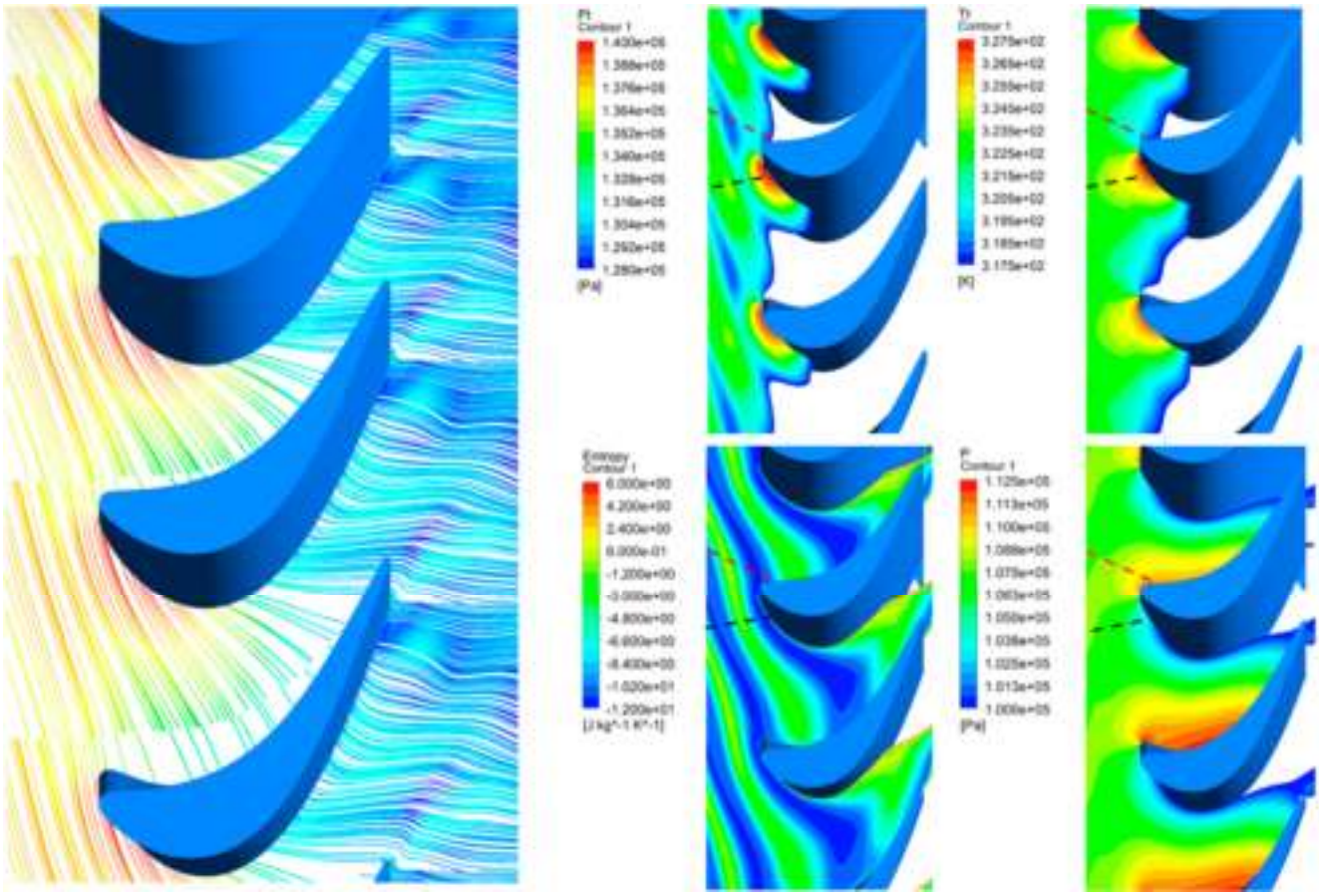

Figure 12. Computed instantaneous absolute flow field across the rotor at midspan. Left: streamlines of absolute velocity vector (coloured by the velocity magnitude). Center: Pt (**top**) and entropy (**bottom**) fields. Right: Tt (**top**), P (**bottom**) fields.

5. Discussion: Energy Separation Effect

One of the consequences of the rotor-induced periodic flow fluctuation is that the rotor pressurises and depressurizes the flow field in the stator–rotor gap: if, as in this case, the flow is subsonic, no shock waves establish and the time-average of this perturbation is null, namely the time-mean flow corresponds to the steady-state flow condition. As shown by CFD results, the rotation of the rotor potential field induces quasi-isentropic unsteady perturbations of total temperature (or total enthalpy) propagating upstream. The observed effect can be analytically justified by resorting to equation 1, which establishes a link, rigorously valid only for inviscid flows, between the material derivative of the total enthalpy and the local (partial) derivative of the static pressure. The capability of static pressure unsteadiness to 'redistribute' total quantities is often called, in Literature, energy separation effect. Energy separation was widely documented to occur in the Von Karman vortex streets featuring the wake of cylinders in cross-flow [23,24] and was also observed to occur in the blade-wake interaction phenomena [18]. In the present case, the source of the static pressure unsteadiness has to be found in the rotor pressure field travelling with the blade itself. As a result of the blade motion, the azimuthal gradients of pressure on the relative frame covert into static pressure unsteadiness according to the formula [25]:

$$\frac{\partial p}{\partial t} = -\mathrm{U}\frac{\partial p}{\partial y}|_{rel} \tag{2}$$

By plugging expression (2) into Equation (1), one gets a differential relation between the rotor pressure field and the total enthalpy rise:

$$\rho \frac{Dh_t}{Dt} = -\mathrm{U} \frac{\partial p}{\partial y}|_{rel} \tag{3}$$

Equation (3) demonstrates analytically the experimental and computational finding of this study, i.e., that the rotor pressure field is able to trigger energy separation effects in the stator–rotor axial gap of a high pressure gas turbine. If the rotor aerodynamic loading is high (as usual in present-day gas turbine stages) and the stator–rotor axial gap is small (as usual in turbines) this effect might influence in a non-negligible way the stator blade aerodynamics and heat transfer.

The statements above and, in a broader sense, the technical relevance of the energy separation effect here discussed demand for a proper quantification. In fact, a direct quantitative evaluation of the total enthalpy/total temperature oscillation upstream of the rotor is not feasible, since no unsteady measurements of total temperature are available (neither a fast-response temperature probe nor a rotating probe are available for such high speed rotors). Nevertheless, the isentropic character of the energy separation effect allows estimating the total temperature increase from experiments, by applying the isentropic thermodynamic relations to the measured total pressure perturbations. Considering as reference values the pitchwise-averages of the measured total pressure and total temperature distributions, the local phase-resolved total temperature is calculated by the phase-resolved total pressure as follows:

$$Tt = \overline{Tt} \left(\frac{Pt}{\overline{Pt}} \right)^{\frac{\gamma-1}{\gamma}} \tag{4}$$

It is interesting to note that the pitchwise averages $\overline{Pt}$ and $\overline{Tt}$ are effective reference conditions, as the average filters the effect of the rotor potential field. The total temperature fluctuation due to energy separation can be finally evaluated as $\Delta Tt = Tt - \overline{Tt}$.

The results of this quantification are reported in Figure 13a over two rotor pitches and show—for the present operating condition—a temperature fluctuation ΔTt of ± 0.9 K; this value corresponds to about 8% of the total temperature drop across the stage ($\approx$21.5 K). The slight tangential shift between the high temperature level at the hub and at the tip depends on the rotor blade twisting, on the spanwise trend of the azimuthal leading edge position of the rotor blade and on the leading edge loading. Interestingly, Figure 13b reports the distribution of ΔTt over two rotor pitches as directly extracted from CFD simulation (i.e., using the actual unsteady total temperature values predicted by the solver). The excellent comparison between the experimental estimate and the simulation demonstrates not only the 'qualitative' validity of the interpretation, but also the quantitative relevance of the energy separation approach.

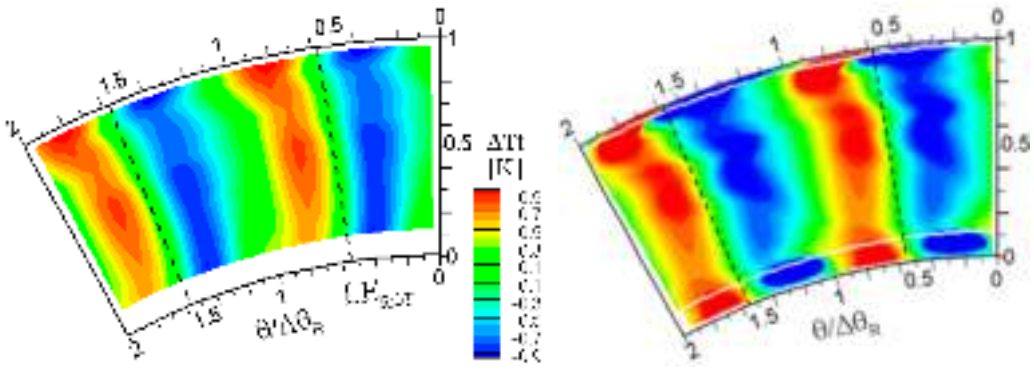

(**a**) (**b**)

Figure 13. Amplitude of the periodic fluctuations of total temperature upstream of the rotor due to rotor-driven perturbation; (**a**) estimated from total pressure measurements; (**b**) predicted by CFD.

Ultimately, the operating condition here presented is one out of the four ones actually available, taken at higher and lower expansion ratio (though still all subsonic) and here not shown for sake of brevity: it is important to highlight that, for all such different operating conditions, the total temperature fluctuation always results of about 10% of the stage total temperature drop.

6. Conclusions

The paper has presented, by combining experiments and CFD simulations, the flow within the stator–rotor gap of a subsonic high-pressure turbine and on how this is influenced by the rotor potential field propagating upstream.

First, a validation of the CFD model against the experimental data has been provided, showing a very good agreement in terms of overall cascade and stage performance, spanwise profiles of pitch-wise averaged data and distributed flow field.

Then, the flow released by the stator has been investigated considering two alternative perspectives, i.e., for stationary and rotating observers, both in terms of time mean and phase-resolved quantities. The analysis in the stationary frame shows the well-known wake and secondary flows pattern, the radial equilibrium issues and loss mechanisms typical of a subsonic modern stator. In the rotating frame of reference, the relative quantities show a periodic pattern with a shape and periodicity related to the rotor pitch. On the contrary, the absolute total pressure perceived by a rotating observer evidences a periodic pattern featuring the rotor angular periodicity, thus revealing an influence of the rotor potential field on the total pressure field in the stator–rotor gap.

When the phase-resolved flow field is analyzed, the impact of the rotor aerodynamics on the flow in the stator–rotor gap is found on most quantities, such as the total pressure, the Mach number, the flow angle, while the viscous dissipative structures released by the stator appear only weakly affected by the rotor. These effects can only be connected to the rotor potential field, which is the unique rotor feature which can propagate upstream. The Mach number distribution exhibits a periodic blockage of the stator channel flow rate. The flow angle also shows a periodic increase in the tangential component of the absolute velocity. The total pressure experiences a periodic increase with respect to the stator upstream, thus apparently violating the energy and momentum balances. CFD simulations reveal the inherent link between these observations, suggesting that the total pressure rise is caused by the deflection imposed to the absolute flow when turning around the front part of the rotor blade. Predictions also show local and periodic total temperature rise in correspondence to the total pressure one, also marking a nearly-isentropic process.

An analytical approach allows explaining the observed feature and to classify it as a new energy separation effect, not described up to now in the scientific literature according to authors' knowledge, in which the static pressure unsteadiness is triggered by the rotation of the rotor potential field. On the quantitative ground, this energy separation effect impacts the total temperature field, which is periodically altered by about $\pm 8\%$ with respect to the mean temperature drop across the stage.

Such an effect might play a role on the aerodynamics and, especially, on the heat transfer in the rear section of the stator blade, especially for new-generation gas turbines stages featuring high rotor loading and small axial gap in-between the blade rows. Moreover, in case of transonic turbines (except for the very rare, saturated condition) the onset of supersonic flows and shock wave patterns within the stator–rotor gap would likely alter the isentropic character of the process, with potential impact on the performance. Future works will extend the present study considering transonic stages and more realistic axial gaps, with special focus on the aero-thermal stator behavior.

Beside the physical aspects, the present findings also show the importance of the design of the front part of the rotor blade, that is, one of the main geometrical features that determines the propagation upstream of the rotor potential field. Further studies on this feature and its implication may lead to novel design remarks for both the rotor and the stator optimization.

Author Contributions: Conceptualization, P.G. and G.P.; methodology, P.G. and G.P.; software, P.G. and G.P.; experiments, P.G.; CFD and its validation, G.P.; formal analysis, P.G. and G.P.; writing—original draft preparation, P.G. and G.P.; writing—review and editing, G.P. All authors have read and agreed to the published version of the manuscript.

Funding: This research received no external funding.

Data Availability Statement: Not applicable.

Conflicts of Interest: The authors declare no conflict of interest.

Nomenclature

Latin	
$c_{x:V}$	stator axial chord
D_M	stage mean diameter
G	mass flow rate
h	blade height
h_t	Total Enthalpy
Mr	relative Mach number
n	rotational speed
N_b	blade number
Ps	static pressure
Pt	absolute total pressure
Ptr	relative total pressure
$\overline{Pt}$	pitchwise-averaged total pressure
t	time
t_c	tip clearance
Tt	absolute total temperature
$\overline{Tt}$	pitchwise-averaged total temperature
Tt_{in}	inlet total temperature
U	peripheral speed
Vt	tangential velocity
Yloss	total pressure loss coefficient
Greek	
β	total to static expansion ratio
Δ	difference
ε	flow deflection at midspan
γ	ratio of specific heat capacities
ρ	density
σ	blade solidity at midspan (chord/pitch)
Θ	circumferential coordinate
$\Delta\theta_R$	angular rotor pitch
Subscripts	
ref	reference condition
Abbreviations	
AR	blade aspect ratio (height/chord)
CFD	Computational Fluid Dynamics
$Cps = (P-P_{ref})/(Pt_{ref}-P_{ref})$	pressure coefficient
$Cpt = (Pt-P_{ref})/(Pt_{ref}-P_{ref})$	total pressure coefficient
$Cptr = (Ptr-P_{ref})/(Pt_{ref}-P_{ref})$	relative total pressure coefficient
FRAPP	fast response aerodynamic pressure probe
TPV	Tip Passage Vortex

References

1. Sharma, O.P.; Pickett, G.F.; Ni, R.H. Assessment of unsteady flows in turbines. *J. Turbomach.* **1992**, *114*, 79–90. [CrossRef]
2. Zaccaria, M.A.; Lakshminarayana, B. Unsteady flow field due to nozzle wake interaction with the rotor in an axial flow turbine: Part I-Rotor passage flow field. *J. Turbomach.* **1997**, *119*, 210–222. [CrossRef]
3. Chaluvadi, V.S.P.; Kalfas, A.I.; Benieghbal, M.R.; Hodson, H.P.; Denton, J.D. Blade-row interaction in a high-pressure turbine. *J. Propul. Power* **2001**, *17*, 892–901. [CrossRef]
4. Schlienger, J.; Kalfas, A.I.; Abhari, R.S. Vortex-wake-blade interaction in a shrouded axial turbine. *J. Turbomach.* **2005**, *127*, 699–707. [CrossRef]
5. Dénos, R.; Arts, T.; Paniagua, G.; Michelassi, V.; Martelli, F. Investigation of the unsteady rotor aerodynamics in a transonic turbine stage. *J. Turbomach.* **2001**, *123*, 81–89. [CrossRef]
6. Chaluvadi, V.S.P.; Kalfas, A.I.; Hodson, H.P.; Ohyama, H.; Watanabe, E. Blade row interaction in a high-pressure steam turbine. *J. Turbomach.* **2003**, *125*, 14–24. [CrossRef]
7. Miller, R.J.; Moss, R.W.; Ainsworth, R.W.; Horwood, C.K. Time-resolved vane-rotor interaction in a high-pressure turbine stage. *J. Turbomach.* **2003**, *125*, 1–13. [CrossRef]
8. Hodson, H.P.; Howell, R.J. Bladerow interactions, transition, and high-lift aerofoils in low-pressure turbines. *Annu. Rev. Fluid Mech.* **2005**, *37*, 71–98. [CrossRef]
9. Dénos, R.; Paniagua, G. Effect of vane-rotor interaction on the unsteady flowfield downstream of a transonic high pressure turbine. *Proc. Inst. Mech. Eng. Part A J. Power Energy* **2005**, *219*, 431–442. [CrossRef]
10. Göttlich, E.; Woisetschläger, J.; Pieringer, P.; Hampel, B.; Heitmeir, F. Investigation of vortex shedding and wake-wake interaction in a transonic turbine stage using laser-doppler-velocimetry and particle-image-velocimetry. *J. Turbomach.* **2006**, *128*, 178–187. [CrossRef]
11. Gaetani, P.; Persico, G.; Dossena, V.; Osnaghi, C. Investigation of the flow field in a HP turbine stage for two stator-rotor axial gaps: Part II–Unsteady flow field. *J. Turbomach.* **2007**, *129*, 580–590. [CrossRef]
12. Paniagua, G.; Yasa, T.; De La Loma, A.; Castillon, L.; Coton, T. Unsteady strong shock interactions in a transonic turbine: Experimental and numerical analysis. *J. Propul. Power* **2008**, *24*, 722–731. [CrossRef]
13. Gaetani, P.; Persico, G.V.; Osnaghi, C. Effects of axial gap on the vane-rotor interaction in a low aspect ratio turbine stage. *J. Propul. Power* **2010**, *26*, 325–334. [CrossRef]
14. Dring, R.P.; Joslyn, H.D.; Hardin, L.W.; Wagner, J.H. Turbine rotor-stator interaction. *J. Eng. Power* **1982**, *104*, 729–742. [CrossRef]
15. Miller, R.J.; Moss, R.W.; Ainsworth, R.W.; Harvey, N.W. Wake, shock and potential field interaction in a 1.5 stage turbine–Part I: Vane-rotor and rotor-vane interaction. *J. Turbomach.* **2003**, *125*, 33–39. [CrossRef]
16. Dean, R.C. On the necessity of unsteady flow in fluid machines. *J. Basic Eng.* **1959**, *81*, 24–28. [CrossRef]
17. Hodson, H.P.; Dawes, W.N. On the Interpretation of measured profile losses in unsteady wake turbine blade interaction studies. *J. Turbomach.* **1998**, *120*, 276–284. [CrossRef]
18. Gaetani, P.; Persico, G.; Spinelli, A. Coupled effect of expansion ratio and blade loading on the aerodynamics of a high-pressure gas turbine. *Appl. Sci.* **2017**, *7*, 259. [CrossRef]
19. Gaetani, P.; Persico, G. Technology development of Fast-Response Aerodynamic Pressure Probes. *Int. J. Turbomach. Propuls. Power* **2020**, *5*, 6. [CrossRef]
20. Persico, G.; Mora, A.; Gaetani, P.; Savini, M. Unsteady aerodynamics of a low aspect ratio turbine stage: Modeling issues and flow physics. *J. Turbomach.* **2012**, *134*. [CrossRef]
21. Giles, M.B. Stator/rotor interaction in a transonic turbine. *J. Propul. Power* **1990**, *6*, 621–627. [CrossRef]
22. Persico, G.; Gaetani, P.; Paradiso, B. Estimation of turbulence by single-sensor pressure probes. In Proceedings of the XIX Symposium on Measuring Techniques in Transonic and Supersonic Flow in Cascades and Turbomachines, Rhode-St-Genese, Belgium, 7–8 April 2008.
23. Eckert, E.R.G. Cross transport of energy in fluid streams. *Wärme-und Stoffübertragung* **1987**, *21*, 73–81. [CrossRef]
24. Aleksyuk, A.I. The Eckert–Weise effect and energy separation under the flow interference behind side-by-side cylinders. *J. Fluid Mech.* **2021**, *915*. [CrossRef]
25. Hodson, H.P.; Hynes, T.P.; Greitzer, E.M.; Tan, C.S. A physical Interpretation of Stagnation Pressure and Enthalpy Changes in Unsteady Flow. *J. Turbomach.* **2012**, *134*, 060902.